

Formation of Semiconductor Interfaces

Proceedings of the
Fifth International Conference on the
Formation of Semiconductor Interfaces

Princeton, NJ, USA, June 26-30, 1995



Edited by
A. Kahn
R. Plafie

North-Holland

FORMATION OF SEMICONDUCTOR INTERFACES

ICFSI-5

Proceedings of the Fifth International Conference on the Formation of Semiconductor Interfaces

Princeton University, Princeton, NJ, USA, June 26–30, 1995



DISTRIBUTION STATEMENT 1

Approved for public release
Distribution Unlimited

No 0014-95-1-0377

DTIC QUALITY INSPECTED 4

Edited by:

A. Kahn

Princeton University, Princeton, NJ, USA

and

R. Ludeke

IBM T.J. Watson Research Center, Yorktown Heights, NY, USA



1996

ELSEVIER

Amsterdam – Lausanne – New York – Oxford – Shannon – Tokyo

19970530 160

Copyright © 1996 Elsevier Science B.V. All rights reserved.

This journal and the individual contributions contained in it are protected by the copyright of Elsevier Science B.V., and the following terms and conditions apply to their use:

Photocopying. Single photocopies of single articles may be made for personal use as allowed by national copyright laws. Permission of the Publisher and payment of a fee is required for all other photocopying, including multiple or systematic copying, copying for advertising or promotional purposes, resale, and all forms of document delivery. Special rates are available for educational institutions that wish to make photocopies for non-profit educational classroom use.

In the USA, users may clear permissions and make payment through the Copyright Clearance Center Inc., 222 Rosewood Drive, Danvers, MA 01923, USA. In the UK, users may clear permissions and make payment through the Copyright Licensing Agency Rapid Clearance Service (CLARCS), 90 Tottenham Court Road, London W1P 0LP, UK. In other countries where a local copyright clearance centre exists, please contact it for information on required permissions and payments.

Derivative works. Subscribers may reproduce tables of contents or prepare lists of articles including abstracts for internal circulation within their institutions. Permission of the Publisher is required for resale or distribution outside the institution.

Permission of the Publisher is required for all other derivative works, including compilations and translations.

Electronic storage. Permission of the Publisher is required to store electronically any material contained in this journal, including any article or part of an article. Contact the Publisher at the address indicated.

Except as outlined above, no part of this publication may be reproduced, stored in a retrieval system or transmitted in any form or by any means, electronic, mechanical, photocopying, recording or otherwise, without prior written permission of the Publisher.

No responsibility is assumed by the Publisher for any injury and/or damage to persons or property as a matter of products liability, negligence or otherwise, or from any use or operation of any methods, products, instructions or ideas contained in the material herein.

Although all advertising material is expected to conform to ethical (medical) standards, inclusion in this publication does not constitute a guarantee or endorsement of the quality or value of such product or of the claims made of it by its manufacturer.

∞ The paper used in this publication meets the requirements of ANSI/NISO Z39.48-1992 (Permanence of Paper).

Printed in The Netherlands

Reprinted from:
APPLIED SURFACE SCIENCE 104/105 (1996)

The manuscripts for the Proceedings were
received by the Publisher: December 28, 1995

PRINTED IN THE NETHERLANDS

Preface

This special volume contains the proceedings of the Fifth International Conference on the Formation of Semiconductor Interfaces (ICFSI-5). ICFSI had been previously held in Marseille, France (1985), Takarazuka, Japan (1988), Rome, Italy (1991) and Jülich, Germany (1993). This fifth edition of the conference, aimed at providing a review of state-of-the-art experimental and theoretical research on structural and electronic properties of semiconductor interfaces, was held for the first time in the United States, on the campus of Princeton University, Princeton, New Jersey on June 26–30, 1995.

The scientific program, organized in a traditional format of single oral session and poster presentations, focused on various aspects of *semiconductor nanostructures, thin insulators on semiconductors, highly lattice-mismatched heterostructures, passivation and surfactants, atom manipulation on semiconductor surfaces, wide band gap semiconductors, interfaces of organic semiconductors, semiconductor heterojunctions, metal–semiconductor interfaces, as well as clean surfaces and adsorbates*. A technical summary of the conference and its scientific highlights have been expertly outlined in the invited Conference Summary by Professor Hans Lüth, the last paper of these proceedings.

The conference was attended by 175 scientists from 21 countries. A total of 159 presentations were made, including 18 invited talks, 37 contributed talks and 104 poster presentations. The schedule of the oral and poster sessions was designed to maximize the time for discussions. These were extensive and often lively, and comments from the participants indicated that this goal was at least partially achieved at ICFSI-5, and should remain an overriding priority in future conferences.

The composition of the program shows that traditional semiconductor surface and interface issues, such as clean surfaces and adsorbates or metal–semiconductor interfaces, still constitute an important fraction of the concerns and interest of our community. However, recent development in nanostructures, atom manipulation, organic semiconductors and wide band gap semiconductors are generating a large interest that will continue to expand the program of future conferences along these and yet-to-be identified new directions. To strike a proper balance between these various fields of interest will be a challenge for prospective organizers of this excellent series.

The next meeting of this series will be held in June 1997 in Cardiff, United Kingdom, and will be chaired by Professor R.H. Williams and Dr. J.E. Macdonald.

We wish to thank particularly Mrs. Emmalee Morrison who played an essential role in all aspects of the preparation and of the smooth running of the conference. Our deep appreciations also go to the members of the local organization committee for their dedication and hard work: V. Bulovic, J. Kahn, C. Kendrick, H. Manoharan, M. Mitchell, M. Petrov, S. Shukla, A.St. Amour, L. Xu. We also wish to thank Dean James Wei and Associate Dean Richard Golden of the School of Engineering and Applied Science for their early and strong support of the conference. Last, but not least, we would like to acknowledge our financial sponsors, without whom this conference would not have been possible. They are listed on page x.

The Editors

A. Kahn and R. Ludeke

Conference Organization

Conference Co-Chairs

A. Kahn, Princeton University
R. Ludeke, IBM, Yorktown Heights

Conference Secretary

E. Morrison, Princeton University

International Advisory Committee

M. Aono, Japan
C. Calandra, Italy
R. Car, Switzerland
J.D. Chadi, USA
L. Feldman, USA
V. Grazhulis, Russia
A. Hiraki, Japan
H.-L. Hwang, Taiwan
B.A. Joyce, UK
G. Le Lay, France
I. Lindau, Sweden
H. Lüth, Germany
W. Mönch, Germany
C. Sébenne, France
J.F. van der Veen, The Netherlands

International Program Committee

G. Allan, France
E. Garfunkel, USA
R.L. Gunshor, USA
J. Kanski, Sweden
N. Karl, Germany
A. Koma, Japan
M.G. Lagally, USA
J.-P. Landesman, France
F.K. Le Goues, USA
I.T. McGovern, Ireland
R. Miranda, Spain
B.O. Nesterenko, Ukraine
J.E. Northrup, USA
I. Ohdomari, Japan
C. Palmstrom, USA
P. Perfetti, Italy
P. Petroff, USA
J. Pollmann, Germany
M. Sauvage-Simkin, France
L.J. Schowalter, USA
J.C. Sturm, USA
K. Tsutsui, Japan

Sponsors

Advanced Technology Center for Photonics and Optoelectronic Materials, Princeton University
David Sarnoff Research Center
Epitaxx
Evans East
IBM
International Rectifier Corporation
Office of Naval Research
Oxford Instruments, Inc.
Princeton Materials Institute, Princeton University
School of Engineering and Applied Science, Princeton University
Sensors Unlimited
West Windsor-Plainsboro H.S. German Club

Contents

Preface	vii
Conference Organization	ix
Sponsors	x

Semiconductor surfaces

Ab initio calculations of structural and electronic properties of prototype surfaces of group IV, III-V and II-VI semiconductors	
J. Pollmann, P. Krüger, M. Rohlfing, M. Sabisch and D. Vogel	1
Plasmon excitations and the effects of surface preparation in n-type InAs(001) studied by electron energy loss spectroscopy	
G.R. Bell, C.F. McConville and T.S. Jones	17
Investigation of the space charge regime of epitaxially grown GaAs (100) by high-resolution electron energy-loss spectroscopy	
V.M. Polyakov, A. Elbe, J. Wu, G.J. Lapeyre and J.A. Schaefer	24
Kinematical RHEED simulation of different structure models for the GaAs (311)A surface	
W. Braun, O. Brandt, M. Wassermeier, L. Däweritz and K. Ploog	35
Ab initio calculations of the reconstructed (100) surfaces of cubic silicon carbide	
P. Käckell, J. Furthmüller and F. Bechstedt	45
Chemical preparation of CdTe(100) and (110) surfaces using atomic hydrogen	
Y. Luo, D.A. Slater, M. Levy and R.M. Osgood Jr.	49
Photoexcited carrier diffusion near a Si(111) surface and in the Si bulk	
C.M. Li, T. Sjödin, Z.C. Ying and H.L. Dai	57
In-situ monitoring of surface chemistry and charge transfer at semiconductor surfaces	
E. Fefer, L. Kronik, M. Leibovitch, Y. Shapira and W. Riedl	61
Electronic structure of the valence band of GdS_x and Gd_3S_4	
V.A. Grazhulis, S.I. Bozhko, I.L. Bolotin, O.R. Bulanov and A.M. Ionov	68

Surfaces and adsorbates

Sb or Cs covered InAs(110) surfaces: moving E_F into conduction band and quantized 2D electron channel	
V.Yu. Aristov, M. Grehk, V.M. Zhilin, A. Taleb-Ibrahimi, G. Indlekofer, Z. Hurych, G. LeLay and P. Soukiassian	73
Synchrotron radiation study of Cs/carbon-rich β -SiC(100) and Cs/silicon-rich β -SiC(100) surfaces: metallization and interface formation	
F. Semon, P. Soukiassian, P.S. Mangat, Z. Hurych, L. di Cioccio and C. Jaussaud	79
Surface core-level shift photoelectron diffraction from As/Si(111)	
L.S.O. Johansson, R. Gunnella, E.L. Bullock, C.R. Natoli and R.I.G. Uhrberg	88
Fluorine adsorption on GaAs(110) surfaces and the onset of etching after XeF_2 exposures	
H. Nienhaus and W. Mönch	95
An ARUPS/NEXAFS study of the H_2S /InP(110) adsorbate system	
E. Dudzik, A. Leslie, E. O'Toole, I.T. McGovern, A. Patchett and D.R.T. Zahn	101
Preparation of H-terminated Si surfaces and their characterisation by measuring the surface state density	
H. Angermann, K. Kliefoth and H. Flietner	107
Ge(111)3 \times 1:K/Sn; on the influence of tin substitution in a metal induced 3 \times 1 reconstruction	
M. Göthelid, S. Odasso, G. LeLay, M. Björkqvist, E. Janin, U.O. Karlsson and T.M. Grehk	113

Si(110) 16×2 and Si(110) 2×3 -Sb surfaces studied by photoemission and optical spectroscopy A. Cricenti, P. Perfetti, B. Nesterenko, G. LeLay and C. Sébenne	118
The atomic structure of the Si(111) $(2\sqrt{3} \times 2\sqrt{3})R30^\circ$ -Sn reconstruction A.H. Levermann, P.B. Howes, K.A. Edwards, H.T. Anyele, C.C. Matthai, J.E. Macdonald, R. Feidenhans'l, L. Lottermoser, L. Seehofer, G. Falkenberg and R.L. Johnson	124
Atomic phenomena on Si surfaces at adsorption of transition metals B.Z. Olshanetsky	130
Hydrogenated and oxidized vicinal Si(001) surfaces investigated by reflectance-difference spectroscopy U. Rossow, L. Mantese, T. Yasuda and D.E. Aspnes	137
Se-induced 3d core-level shifts of GaAs(110) P. Käckell, W.G. Schmidt and F. Bechstedt	141
Optical study of potassium growth on the Si(100) surface M. Roy and Y. Borensztein	147
A surface extended X-ray absorption fine structure study of tellurium adsorbed onto Si(100) S.R. Burgess, B.C.C. Cowie, S.P. Wilks, P.R. Dunstan, C.J. Dunscombe and R.H. Williams	152
Optical spectroscopy study of hydrogenation of the Si(111)- 7×7 surface M. Roy, C. Beitia, Y. Borensztein, A. Shkrebtii, C. Noguez and R. Del Sole	158
Dissolution and segregation of monolayer Cu, Ni and Co atoms on the Si(111)- $\sqrt{3} \times \sqrt{3}$ -Ag surface induced by thermal annealing J. Yuhara, R. Ishigami, D. Ishikawa and K. Morita	163
Segregation of In atoms at clean and hydrogen passivated InP(100) surfaces F. Stietz, Th. Allinger, V. Polyakov, J. Woll, A. Goldmann, W. Erfurth, G.J. Lapeyre and J.A. Schaefer	169
Electronic properties of antimony monolayers on III-V (110) surfaces: a comparative study by reflectance anisotropy spectroscopy and microscopic tight-binding calculations A.I. Shkrebtii, N. Esser, M. Köpp, P. Haier, W. Richter and R. Del Sole	176

Metals on semiconductors

Schottky-barrier formation at passivated surfaces: covalent and ionic semiconductors R. Saiz-Pardo, R. Rincón, P.L. de Andrés and F. Flores	183
Midgap states observed by nonlinear optical spectroscopy of metal:GaAs junctions J. Qi, W. Angerer, M.S. Yeganeh, A.G. Yodh and W.M. Theis	188
Spatially resolved internal and external photoemission of Pt/n-GaP Schottky barrier C. Coluzza, J. Almeida, T. dell'Orto, F. Barbo, M. Bertolo, A. Bianco, S. Cerasari, S. Fontana, O. Bergossi, M. Spajer and D. Courjon	196
Structural properties of epitaxial silicide layers on Si H. von Känel, E. Müller, S. Goncalves-Conto, C. Schwarz and N. Onda	204
Atomistic study of the formation process of Ni silicide on the Si(111)- 7×7 surface with scanning tunneling microscopy T. Yao, S. Shinabe and M. Yoshimura	213
Analytical studies of nickel silicide formation through a thin Ti layer F. Fenske, A. Schöpke, S. Schulze and B. Selle	218
Scanning tunneling spectroscopy examination of surface electronic structures of Si(111) $(2\sqrt{3} \times 2\sqrt{3})30^\circ$ -Sn surface X.F. Lin, I. Chizhov, H.A. Mai and R.F. Willis	223
Unpinned behavior of the Fermi level and photovoltage on p-(100)GaAs surface facilitated by deposition of cesium V.L. Alperovich, A.G. Paulish, H.E. Scheibler, V.I. Tynnyi and A.S. Terekhov	228
Development of the Na/GaAs(111)A-(2×2) interface at room and low temperature J.M.C. Thornton, P. Weightman, P. Bailey, D.A. Woolf, A.D. Laine and D.A. Evans	234

Metal overlayers on the MBE-grown ZnSe(001) surface D.A. Evans, D. Wolfframm, D. Gnoth, J. Cairns, A.C. Wright, M. Evans, J. Riley, D. Westwood and D.A. Woolf	240
Metal-insulator transition for K on GaAs(100)-As rich surfaces A. Levy Yeyati, A. Martín-Rodero, F. Flores, J. Ortega and R. Rincón	248
Quantitative analysis of degradation in Schottky diode characteristics induced by single ion implantation M. Koyama, Y. Akita, C. Cheong, M. Koh, T. Matsukawa, K. Horita, B. Shigeta and I. Ohdomari	253
A normal incidence X-ray standing wave study of sulphur adsorption on InP(110) T.K. Johal, P. Finetti, V.R. Dhanak, A.W. Robinson, A. Patchett, D.R.T. Zahn and R. McGrath	257
The Schottky barrier of Co on strained and unstrained $\text{Si}_x\text{Ge}_{1-x}$ alloys J.-H. Ku and R.J. Nemanich	262
Characterization of cobalt-diamond (100) interfaces: electron affinity and Schottky barrier P.K. Baumann and R.J. Nemanich	267
Hot-electron scattering at Au/Si(100) Schottky interfaces measured by temperature dependent ballistic electron emission microscopy C.A. Ventrice Jr., V.P. LaBella, G. Ramaswamy, H.-P. Yu and L.J. Schowalter	274
Valence band of $\text{Cd}_{1-x}\text{Fe}_x\text{Se}/\text{Fe}$ in resonant photoemission spectra B.A. Orlowski, B.J. Kowalski, N. Barrett, D. Martinotti, C. Guillot, J.-P. Lacharme and C.A. Sébenne	282

Atom manipulation on surfaces

Intrinsic surface atom manipulations in STM and AFM K. Cho and J.D. Joannopoulos	286
Surface diffusion limitation in laser focused atomic deposition R.E. Behringer, V. Natarajan and G. Timp	291

Surface dynamics and simulation

Graphitization of diamond (111) studied by first principles molecular dynamics A. De Vita, G. Galli, A. Canning and R. Car	297
A comparative study of the adsorption and thermal decomposition of triethylgallium and trimethylgallium at GaAs(100) surfaces studied by electron energy loss spectroscopy A.A. Aquino and T.S. Jones	304
Smoothing of crystal surfaces during growth interruption A.Yu. Kaminski and R.A. Suris	312

Thin insulators on semiconductors

Comparison of structurally relaxed models of the Si(001)- SiO_2 interface based on different crystalline oxide forms A. Pasquarello, M.S. Hybertsen and R. Car	317
Initial stage of oxidation of hydrogen-terminated silicon surfaces T. Hattori, T. Aiba, E. Iijima, Y. Okube, H. Nohira, N. Tate and M. Katayama	323
The initial oxidation of silicon: new ion scattering results in the ultra-thin regime E.P. Gusev, H.C. Lu, T. Gustafsson and E. Garfunkel	329
Local atomic structure and electrical properties of nitrided Si-SiO ₂ interfaces produced by low-temperature plasma processing and rapid thermal annealing, and explained by ab-initio quantum chemistry calculations G. Lucovsky, D.R. Lee, S.V. Hattangady, H. Niimi, S. Gandhi, C. Parker, Z. Jing, J.L. Whitten and J.R. Hauser	335

Density of states and relaxation spectra of etched, H-terminated and naturally oxidized Si-surfaces and the accompanied defects	
H. Flietner, W. Füssel, N.D. Sinh and H. Angermann	342
Synchrotron radiation photoelectron spectroscopy of the O(2s) core level as a tool for monitoring the reducing effects of ion bombardment on SnO ₂ thin films	
P. De Padova, R. Larciprete, C. Ottaviani, C. Quaresima, P. Perfetti, E. Borsella, C. Astaldi, C. Comicioli, C. Crotti, M. Matteucci, M. Zacchigna and K. Prince	349
Influences of hydrogen on initial oxidation processes of H-terminated Si(100) surfaces	
H. Ikeda, K. Hotta, S. Furuta, S. Zaima and Y. Yasuda	354
Effect of chemical preoxidation treatment on the structure of SiO ₂ /Si interfaces	
H. Nohira, H. Sekikawa, M. Matsuda and T. Hattori	359
Radiation immunity of pMOSFETs and nMOSFETs examined by means of MeV He single ion microprobe	
M. Koh, K. Horita, B. Shigeta, T. Matsukawa, A. Kishida, T. Tanii, S. Mori and I. Ohdomari	364
Weak fluence dependence of charge generation in ultra-thin oxides on silicon	
K.R. Farmer, C.P. Debauche, A.R. Giordano, P. Lundgren, M.O. Andersson and D.A. Buchanan	369
Studies on low temperature silicon grain growth on SiO ₂ by electron cyclotron resonance chemical vapor deposition	
K.C. Wang, H.L. Hwang, J.J. Loferski and T.R. Yew	373
Characterization of nitrided SiO ₂ thin films using secondary ion mass spectrometry	
M.R. Frost and C.W. Magee	379
Plasma assisted oxidation of SiGe layers at 500°C: interface characterization	
C. Tételin, X. Wallart, L. Vescan and J.P. Nys	385
Diffraction spot profile analysis for heteroepitaxial surfaces applied to the initial growth stages of CaF ₂ adlayers on Si(111)	
J. Wollschläger and A. Meier	392
Structural transformations at CaF ₂ /Si(111) interfaces	
N.S. Sokolov, J.C. Alvarez, Yu.V. Shusterman, N.L. Yakovlev, R.M. Overney, Y. Itoh, I. Takahashi and J. Harada	402
Molecular beam epitaxial growth of thin CaF ₂ films on vicinal Si(111) surfaces	
B.M. Kim, C.A. Ventrice, Jr., T. Mercer, R. Overney and L.J. Schowalter	409
Growth of CdF ₂ /CaF ₂ Si(111) heterostructure with abrupt interfaces by using thin CaF ₂ buffer layer	
A. Izumi, K. Kawabata, K. Tsutsui, N.S. Sokolov, S.V. Novikov and A.Yu. Khilko	417
Hydrogen ion treatments of oxidized GaAs(100) and AlGaAs(100) surfaces: surface stoichiometry and electronic properties	
Y.-L. Chang, S.I. Yi, S. Shi, E. Hu, W.H. Weinberg and J. Merz	422
Interface properties of PN _x /InP structures by in-situ remote plasma processes	
T. Sugino, Y. Sakamoto, T. Miyazaki and J. Shirafuji	428

Surfactants and passivation

Sulfur passivated InP(100): surface gaps and electron counting	
C.E.J. Mitchell, I.G. Hill, A.B. McLean and Z.H. Lu	434
GaAs surface passivation using in-situ oxide deposition	
M. Passlack, M. Hong, R.L. Opila, J.P. Mannaerts and J.R. Kwo	441
Influence of physisorbed arsenic on RHEED intensity oscillations during low-temperature GaAs molecular beam epitaxy	
R. Venkatasubramanian, V.K. Pamula and D.L. Dorsey	448

Wide band gap semiconductors

UV photoemission study of heteroepitaxial AlGaIn films grown on 6H-SiC	
M.C. Benjamin, M.D. Bremser, T.W. Weeks, Jr., S.W. King, R.F. Davis and R.J. Nemanich	455

Initial stage of growth of GaN/GaAs(001) in plasma-assisted molecular beam epitaxy H. Yang, O. Brandt, A. Trampert and K.H. Ploog	461
Nitridation of GaAs surfaces stimulated by nitrogen glow discharge Q.J. Xu, X.M. Ding, X.Y. Hou and X. Wang	468
Growth and characterization of ZnSe/GaAs single quantum well structures J.L. House, D.J. Dougherty, G.S. Petrich, L.A. Kolodziejski, E.P. Ippen and G.-C. Hua	472
Photomodulation Raman scattering spectroscopy of ZnSe/GaAs heterostructure interface H. Talaat, L. Elissa, S. Negm and E. Burstein	479
Raman monitoring of selenium decapping and subsequent antimony deposition on MBE-grown ZnSe(100) D. Drews, A. Schneider, D.R.T. Zahn, D. Wolfframm and D.A. Evans	485
Heterocrystalline SiC: ab initio calculations for the interface structure of combinations of cubic and hexagonal SiC P. Käckell and F. Bechstedt	490

Growth and characterization of nanostructures

Highly mismatched heteroepitaxy: 2D platelets assisted nucleation of self-assembled 3D quantum dots C. Priester and M. Lannoo	495
Photoluminescence and transmission electron microscopy investigation of SiGe quantum wires grown on patterned Si substrates A. Hartmann, C. Dieker, U. Bangert, R. Loo, L. Vescan and H. Lüth	502
AFM and RHEED study of Ge islanding on Si(111) and Si(100) P.W. Deelman, T. Thundat and L.J. Schowalter	510
Surface and subsurface imaging of indium in InGaAs by scanning tunneling microscopy M. Pfister, M.B. Johnson, S.F. Alvarado, H.W.M. Salemink, U. Marti, D. Martin, F. Morier-Genoud and F.K. Reinhart	516
Characterization of arsenide/phosphide heterostructure interfaces by scanning tunneling microscopy A.Y. Lew, C.H. Yan, C.W. Tu and E.T. Yu	522
Atomic force microscopy of III-V nanostructures in air F. Reinhardt, B. Dwir, G. Biasiol and E. Kapon	529
Site occupation of Si atoms deposited on vicinal GaAs(001)-(2 × 4) surfaces A.R. Avery, J.L. Sudijono, T.S. Jones and B.A. Joyce	539
Characterization of nanostructures by virtue of the phenomena due to the electron-phonon interaction E.P. Pokatilov, V.M. Fomin, S.N. Klimin and S.N. Balaban	546
Porous silicon layers as a model system for nanostructures U. Rossow, U. Frotscher, C. Pietryga, D.E. Aspnes and W. Richter	552

Lattice mismatched systems

Influence of surface reconstruction on MBE growth of layered GaSe on Si(111) substrates H. Reqqass, J.-P. Lacharme, M. Eddrief, C.A. Sébenne, V. Le Thanh, Y.L. Zheng and J.-F. Pétroff	557
Heteroepitaxial growth of InSb on Si(001) surface via Ge buffer layers M. Mori, D.M. Li, M. Yamazaki, T. Tambo, H. Ueba and C. Tatsuyama	563
Ga-Se films grown on a GaAs(001) surface at high temperature using a thermal evaporation of GaSe T. Izumi, H. Nishiwaki, T. Tambo and C. Tatsuyama	570
MOCVD growth of Ga ₂ Se ₃ on GaAs(100) and GaP(100): a Raman study M. von der Emde, D.R.T. Zahn, T. Ng, N. Maung, G.H. Fan, I.B. Poole, J.O. Williams and A.C. Wright	575
Temperature dependence of interdiffusion-induced III-V compound formation at the interface between Al, Ga, In layers and Sb substrates V. Wagner, W. Richter and J. Geurts	580

STM study of the organic semiconductor PTCDA on highly-oriented pyrolytic graphite C. Kendrick, A. Kahn and S.R. Forrest	586
---	-----

Semiconductor heterostructures

Low-energy yield spectroscopy determination of band offsets: application to the epitaxial Ge/Si(100) heterostructure L. Di Gaspare, G. Capellini, C. Chudoba, M. Sebastiani and F. Evangelisti	595
Ultra-thin AlAs films on GaAs (001) investigated by high-resolution electron-energy-loss spectroscopy J.-L. Guyaux, Ph. Lambin, M.D. Lange, R. Sporken, P.A. Thiry and R. Caudano	601
Band structure evolution in InAs overlayers on GaAs(110) Z.Q. He, L. Ilver, J. Kanski, P.O. Nilsson, P. Songsiriritthigul, G. Holmén and U.O. Karlsson	608
Measurements of the energy band offsets of $\text{Si}_{1-x}\text{Ge}_x/\text{Si}$ and $\text{Ge}_{1-y}\text{C}_y/\text{Ge}$ heterojunctions F. Chen, M.M. Waite, S. Ismat Shah, B.A. Orner, S.S. Iyer and J. Kolodzey	615
The conduction barrier at the interface between low temperature grown GaAs and undoped GaAs K.D. Maranowski, J.P. Ibbetson, K.L. Campman and A.C. Gossard	621
$(\text{II-VI})_m/(\text{IV}_2)_n$ (110) superlattice: interfacial chemistry, electronic structure, and optical property E.G. Wang	626
Charge transfer and electronic activation at an Sb δ -layer in Si(001) J.M.C. Thornton, R.J. Cole, D.J. Gravesteijn and P. Weightman	631

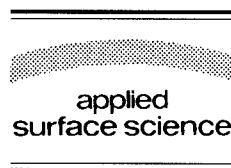
Strained layers

A scanning tunnelling microscopy study of local surface modifications induced by misfit dislocation formation in strained-layer heteroepitaxy G. Springholz and G. Bauer	637
Reconstruction and chemical ordering at the surface of strained (In, Ga)As epilayers M. Sauvage-Simkin, Y. Garreau, R. Pinchaux, A. Cavanna, M.B. Véron, N. Jedrecy, J.P. Landesman and J. Nagle	646
Interface abruptness in strained III-V heterostructures M.R. Bruni, S. Kačiulis, G. Mattogno and G. Righini	652
Ab-initio electronic structure calculation of the InAs multiple quantum wells in bulk GaAs N. Tit and M. Peressi	656
Medium energy ion scattering (MEIS) studies on Si/GaSb/Si- and Si/CaF ₂ /Si(111) layer systems T. Tappe, A. Chatziparaskewas, J. Schäffer, J. Schlosser, J. Schmalhorst and B. Schmiedeskamp	661
Clustering on surfaces at finite areal coverages R. Barel, Y. Mai, G.R. Carlow and M. Zinke-Allmang	669
Preparation and properties of thin polycrystalline $\text{MnSi}_{1.73}$ films St. Teichert, R. Kilper, J. Erben, D. Franke, B. Gebhard, Th. Franke, P. Häussler, W. Henrion and H. Lange	679
A summary and perspective on the Fifth International Conference on the Formation of Semiconductor Interfaces, Princeton, NJ H. Lüth	685
Author index	690
Subject index	699



ELSEVIER

Applied Surface Science 104/105 (1996) 1–16



Ab initio calculations of structural and electronic properties of prototype surfaces of group IV, III–V and II–VI semiconductors

J. Pollmann^{*}, P. Krüger, M. Rohlffing, M. Sabisch, D. Vogel

Institut für Theoretische Physik II, Universität Münster, Wilhelm-Klemm-Str. 10, D-48149 Münster, Germany

Received 28 June 1995; accepted 30 August 1995

Abstract

In this brief review, structural and electronic properties of technologically important semiconductor surfaces are presented and discussed with particular emphasis on most recent ab initio results for semi-infinite and supercell geometries. Most of the results are based on the local density approximation of density functional theory but GW quasiparticle band structures and results of calculations incorporating self-interaction-corrections are included as well. A general picture of the surface reconstruction or relaxation behaviour is developed and the resulting electronic properties of prototype surfaces of diamond-, zincblende- and wurtzite-structure crystals are discussed. The systems addressed comprise reconstructed (001) surfaces of diamond, Si, Ge and SiC, the relaxed (110) surface of SiC and GaAs and nonpolar (10 $\bar{1}0$) surfaces of wurtzite-structure SiC, ZnO and CdS. A comparing discussion of the relaxed surfaces of SiC, GaAs and of II–VI compound semiconductors allows to address the physical origins of the relaxation behaviour of these compounds and to identify characteristic differences and similarities in their relaxation behaviour related to the specific heteropolarity or ionicity of these systems. Our results show excellent agreement with a whole body of experimental data.

1. Introduction

Semiconductor surfaces continue to attract large interest both in fundamental and applied research. The wide range of their technological applications is a strong stimulus to fully understand their structural and electronic properties on a microscopic level. We have witnessed the developments and applications of quite a number of fascinating and pretentious surface sensitive experimental and theoretical methods and techniques. The field of electronic structure theory of

clean semiconductor surfaces has matured within the last decade and total energy minimization calculations have become a very powerful tool for theoretically determining equilibrium configurations of surfaces. A most complete account on structural and electronic properties of semiconductor surfaces has been compiled in two recent volumes of Landolt-Börnstein [1,2]. Although semiconductor surfaces have been studied for decades, a number of systems remain under debate because of their complex structural properties. While surfaces like GaAs(110) or Si(111) are well-understood, by now, other systems like the (001) surfaces of elemental semiconductors continue to attract large attention. In addition, new

^{*} Corresponding author.

systems like surfaces of SiC move into the focus of interest because of their paramount potential for microelectronic devices. Likewise, surfaces of cubic and hexagonal II–VI semiconductors attract increasing interest because of their importance for optoelectronic devices and heterogeneous catalysis.

In this relatively short paper, we certainly can not review the whole field. For a fair account of by now ‘classical’ results, we refer the reader to the review articles by Hansson and Uhrberg [3] and LaFemina [4], concerning extensive discussions of related experimental and theoretical work, respectively. Here we rather focus on a brief discussion of most recent theoretical developments for prototypical systems that are under intensive study currently. We first address the ‘backbone of semiconductor technology’, i.e. the Si(001) surface, in connection with diamond (001) and Ge(001) and discuss the physical origin and quantitative nature of the dimer reconstruction of these surfaces. Next we address the surface structural and electronic properties that occur if one of the two Si atoms in each bulk unit cell is replaced by a C atom and the lattice constant concomitantly shrinks by some 20%, i.e. we discuss surface properties of SiC. The properties of the polar SiC(001) surfaces will be presented and discussed in comparison with those of Si(001) and C(001), respectively. We then move to the nonpolar (110) surface of cubic SiC. It is most revealing to discuss the respective results in comparison with those of the probably best well-known semiconductor surface, namely GaAs(110). While in the above comparisons the changing ionicity is the main theme, in the systems to be discussed next, a change in crystal structure is important, as well. To highlight the related effects, we present the surface structure and band structure of the nonpolar (10 $\bar{1}$ 0) surface of wurtzite-structure SiC and discuss the properties of α -SiC(10 $\bar{1}$ 0) in comparison with those of β -SiC(110). Finally, we address wurtzite-crystal surfaces of prototypical II–VI semiconductors. Here we discuss ZnO(10 $\bar{1}$ 0) and CdS(10 $\bar{1}$ 0) in comparison with SiC(10 $\bar{1}$ 0). A systematic discussion of all of these systems allows to identify characteristic differences and similarities in the relaxation behaviour, which are related to the specific types of heteropolarity or ionicity of these systems.

The paper is organized as follows. In Section 2 we briefly address the theoretical approach. In Sec-

tion 3 we discuss characteristic results for prototype surfaces as outlined above. A short summary concludes the paper in Section 4.

2. Theoretical approach

The results reviewed in this paper have been calculated employing theoretical methods that have been described in detail elsewhere. Therefore, we refrain from repeating any equations here. Most of our *ab initio* calculations [5–8] have been carried out in the local density approximation (LDA) of density functional theory (DFT). We employ nonlocal, norm-conserving pseudopotentials in separable form, as suggested by Kleinman and Bylander [9]. We use the norm-conserving pseudopotentials of Sabisch [7] for C and for Si in SiC and those of Gonze, Stumpf and Scheffler [10] for Si, Ge, Ga, As, S and O. The Zn^{12+} and Cd^{12+} pseudopotentials have been used in separable form in Ref. [8] employing the Bachelet, Hamann and Schlüter potentials [11]. The exchange–correlation potential (XC) is taken into account in the Ceperley–Alder [12] form as parameterized by Perdew and Zunger [13]. One distinctive technical aspect of our calculations, as compared to many others is, that we use linear combinations of *Gaussian orbitals* of s, p, d and s* type to represent the wave functions. In most LDA calculations of other groups plane wave basis sets are used. They are easier to handle but lead to much larger Hamiltonian matrices when supercell geometries are used to describe surface systems. For semi-infinite systems that can be described by potential scattering theory and Green functions [5,14], plane waves are inadequate. In that case the calculations can be carried out very efficiently with Gaussian orbital basis sets [5,14]. Total energies for the surface structure optimizations are calculated selfconsistently using the momentum–space formalism of Ihm, Zunger and Cohen [15]. Optimal surface relaxations or reconstructions are determined within the supercell approach [16]. We optimize the structure by calculating the forces. When a Gaussian basis is employed, Pulay forces have to be taken into account in addition to the Hellmann–Feynman forces [14,17]. Eliminating the forces iteratively is achieved by employing the Broyden scheme [18]. We move all atoms in

the unit cell until all forces vanish to within 10^{-3} Ry/au. For further details related to particular systems the reader is referred to the respective literature [5–8,14].

Now it is well-known, that band gaps in semiconductors are underestimated by some 50% or more within LDA and that this shortcoming transfers to the surface electronic structure. To overcome these problems, quasiparticle bandstructure calculations have proven to be a very powerful tool [19,20]. Based on the formalism of Hedin [21] and Hedin and Lundqvist [22], presented some 30 years ago, they have been successfully carried out within the GW approximation for bulk solids (see, e.g., Refs. [19,20]), as well as, for a small number of surface systems (see, e.g., Refs. [23–26]). Our approach to calculate GW quasiparticle bandstructures has been described in detail elsewhere [20,26]. Here we will only use the respective results [26,27] for Si(001)-(2 \times 1) to highlight the self-energy shifts in the quasiparticle bandstructure with respect to the LDA results and to assess and identify the character and the importance of these effects.

In the case of II–VI semiconductor surfaces, LDA results suffer from a further deficiency in addition to the above mentioned shortcomings in that the occupied cationic d-bands result roughly 3 eV too high in energy as compared to experiment (see, e.g., Ref. [28]). This leads to an unphysically increased interaction between the cation d- and the anion-p valence bands closing the gap even further than is typical for the LDA. Due to the overestimated p–d interactions one could expect that prominent gap surface states [8] are strongly influenced by the inadequate d-band positions. To overcome this problem to a very large extent, we have developed an approximate approach to take dominant self-interaction-corrections into account [29]. The lack of these corrections in standard LDA calculations is thought to be largely responsible for the above mentioned deficiencies [8,28]. We construct atomic self-interaction-corrected pseudopotentials (SIC-PP's) which are then transferred to the bulk solid and to the surface calculations. The reader is referred to Ref. [29] for more details of this approach. Using these SIC-PP's, the calculations can again be carried out along the lines indicated in the first paragraph of this section.

We have applied the above mentioned theoretical

techniques very recently for studying prototype surface systems which will be discussed in the next section.

3. Electronic and structural properties of prototype surfaces

3.1. Diamond, Si and Ge(001) surfaces

The origin and nature of dimer reconstructions at (001) surfaces of elemental semiconductors has been one of the most intensively discussed issues in semiconductor surface physics. Large efforts have concentrated on the Si(001) surface, since this is the technologically most important surface system and its surface reconstruction is the most subtle of the three systems (see, e.g., Ref. [6]). Very recently a consistent picture of the reconstruction of these three surfaces has emerged from a number of ab initio total energy minimization calculations, the results of which are in very good agreement with a whole body of experimental surface structure and surface spectroscopy data. The investigations of the Ge(001)-(2 \times 1) surface (see, e.g., Refs. [6,30–34]) have rather quickly converged to the asymmetric dimer model (ADM) and those of C(001)-(2 \times 1) surface (see, e.g., Refs. [6,35–37]) agreeingly find the symmetric dimer model (SDM) to be the equilibrium configuration of this surface. In the case of Si(001)-(2 \times 1), there has been a long-standing discussion whether this surface reconstructs in the SDM or ADM. The original motivation for the introduction of asymmetric dimers by Chadi [38] was the finding that empirical tight-binding band structure calculations which assumed a symmetric dimer reconstruction of Si(001)-(2 \times 1) invariably resulted in a metallic surface in disagreement with the results of angle-resolved photoelectron spectroscopy (ARPES) data [39]. The picture of asymmetric dimers was supported, e.g., by core-level spectroscopy [40], surface-photovoltage [41], low-energy electron diffraction [42] (LEED) and ion-scattering experiments [43]. In scanning-tunnelling-microscopy (STM) studies [44], carried out later on, the dimers appeared to be symmetric. The most recent experimental data [45–53], however, show convincingly that the dimers are buckled. This is in agreement

with the results of well-converged ab initio total energy LDA calculations [6,30,54–58]. They provide agreeing evidence that, in the case of the SDM, the electronic surface bands deriving from the dangling bonds at the two atoms of each dimer overlap in energy at the Fermi level leading to a metallic surface. Buckling of the dimers leads to an energy gain of some 0.14 eV per unit cell by opening up a Jahn–Teller like gap between the surface-induced dangling bond states. Therefore a semiconducting Si(001)-(2 × 1) surface results for the ADM in agreement with experiment [39,47,52].

From a systematic comparative study [6] of the reconstructions of the three surfaces using our Green function technique for semi-infinite systems [5,14] we have obtained the electronic band structures shown in Fig. 1. The three panels on the left hand side show our results for the optimal SDM of each surface. In each case, we obtain a bonding π band and an antibonding π^* band originating from symmetric and antisymmetric linear combinations of the dangling bond orbitals at the dimer atoms. Obviously, the SDM of C(001)-(2 × 1) yields a semiconducting surface while it yields metallic surfaces for

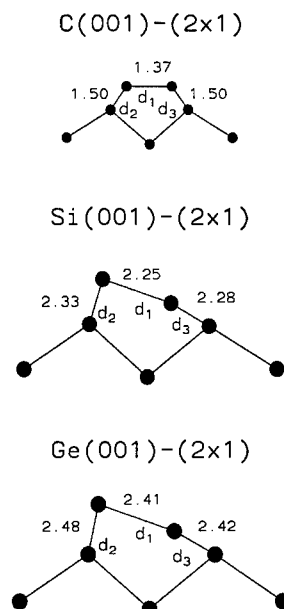


Fig. 2. Side views of energy-optimized configurations of the C-, Si-, and Ge(001)-(2 × 1) surfaces. The bond lengths are given in Å.

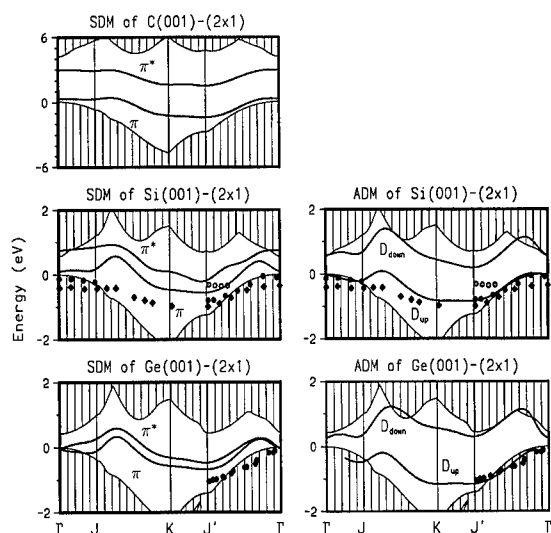


Fig. 1. Section of the surface band structure of C, Si, and Ge(001)-(2 × 1) as resulting from LDA Green function calculations for the symmetric dimer model (SDM) and the asymmetric dimer model (ADM) in comparison with experimental ARPES data of Ref. [59] (diamonds) and Ref. [60] (dots) for Si(001) and of Ref. [61] for Ge(001).

Si and Ge(001)-(2 × 1). Tilting the dimers with respect to the surface plane raises the total energy for C(001)-(2 × 1) and leads to an energy gain of 0.14 eV per unit cell for Si(001)-2 × 1) and of 0.30 eV per unit cell for Ge(001)-(2 × 1). The optimal surface configurations of these three systems, as resulting from our Green function calculations [6], are shown in Fig. 2. Our calculated dimer bond lengths and back bond lengths included in the figure are in excellent agreement with the results of other most recent ab initio calculations for the three systems (see Table 1 for that matter). Table 1 shows agreeing evidence from most recent ab initio calculations for these structural models. For C(001)-(2 × 1) there is beautiful agreement between the results of the four independent calculations [6,35–37]. So far, there are no experimental data in the literature on the structure of this surface, to our knowledge. For Si(001)-(2 × 1) we observe very good agreement between the results of most recent, well-converged calculations [6,24,30,58]. The experimental data show a relatively large scatter which might be related to surface imperfections (dimer defects, etc.). For Ge(001)-(2 × 1)

Table 1
Bond lengths and tilt angles at the (2×1) -reconstructed diamond, Si and Ge(001) surfaces from theoretical (T) and experimental (E) surface structure determinations (see Fig. 2 for the definition of $d_1 - d_3$)

	d_1 (Å)	d_2 (Å)	d_3 (Å)	φ (deg)	Ref.
C(001)- (2×1)	1.37	1.50	1.50	0	[6] T
	1.37			0	[35] T
	1.37	1.50	1.50	0	[36] T
	1.38			0	[37] T
Si(001)- (2×1)	2.21			7	[55] T
	2.25			8	[54] T
	2.25	2.33	2.28	19	[6,30] T
	2.26	2.34	2.29	18	[58] T
	2.27			14	[56] T
				15	[57] T
	2.20			5	[49] E
	2.25			19	[53] E
	2.34			7	[45] E
	2.36			14	[43] E
Ge(001)- (2×1)	2.41	2.48	2.42	19	[6,30] T
	2.46			13	[31] T
	2.46			19	[32] T
	2.44			20	[33] E
				21	[34] E

close agreement between the calculations and the experimental data is found.

The calculated reconstruction-induced energy gain per surface dimer is very closely related to the cohesive energy per bulk bond in diamond, Si and Ge, as has been shown in Ref. [6]. These energies agree within some 0.3 eV in each case. This energy difference is surface-specific and is due to the back bond rotations accompanying the dimer formation.

The surface electronic structure for the ADM of Si and Ge(001)- (2×1) is shown in the two panels on the right-hand side of Fig. 1. Both surfaces turn out to be semiconducting for the ADM in agreement with experiment. The calculated occupied dangling bond bands D_{up} are in good agreement with the ARPES data [59–61] for the ADM while the occupied π -bands for the SDM are hard to reconcile with the data.

The origin of the different reconstruction behaviour of the diamond surface as opposed to the Si and Ge surfaces can be traced back to the drastically different strengths in σ - and π -bonding between the orbitals at the atoms of the symmetric dimers and to

the fact that C 2p orbitals are more localized than C 2s orbitals, while Si 3p (Ge 4p) orbitals are more extended than Si 3s (Ge 4s) orbitals. This occurs, since there are no p states in the C core, as opposed to Si and Ge. At C(001)- (2×1) , neighbouring surface atoms form double-bonded dimers with a bond length of 1.37 Å, which is very close to the double-bond length of 1.34 Å in, e.g., the C_2H_4 molecule. At the Ge(001)- (2×1) surface they form single-bonded dimers whose bond length of 2.41 Å is close to the single-bond length of 2.40 Å in Ge_2H_6 molecules. The case of Si(001)- (2×1) resides in the middle of these two limiting cases [6]. In consequence of the short dimer bond, the π -interaction between the dangling bonds at the C(001)- (2×1) surface is strong enough to clearly separate the π - and π^* -bands energetically. Thus the SDM of C(001)- (2×1) is already semiconducting and tilting the dimers does not lead to any additional energy gain. In contrast, in the SDM of Si and Ge(001)- (2×1) , the π -interactions are not strong enough to open up a surface gap (see the left panels of Fig. 1).

While the surface band structures in the right panels of Fig. 1 nicely agree with the ARPES data [59–61], they fail to correctly describe the measured surface gaps [41,62,63]. This is, of course, related to the well-known shortcoming of the LDA which underestimates band gaps of bulk semiconductors and surfaces considerably. These problems can be overcome by carrying out quasiparticle bandstructure calculations as mentioned in Section 2. In Fig. 3 we show the quasiparticle bandstructures for the SDM and the ADM of Si(001)- (2×1) as obtained by our GW calculations employing Gaussian orbital basis sets [27]. The respective LDA results are given by dashed lines for comparison. It should be noted at this point, that the band structures in Fig. 3 have been calculated for a supercell geometry with 8 atomic and 6 vacuum layers per supercell while those in Fig. 1 were calculated for semi-infinite geometries. The figure reveals two important results. First of all we note, that the SDM remains metallic, even if the quasiparticle band structure is considered. This result, together with the evidence from total energy minimization, convincingly rules out the SDM. Second we note, that the D_{up} band for the ADM hardly changes while the D_{down} band strongly moves up in energy opening up the LDA gap of only

0.2 eV to the GWA gap of 0.65 eV. Our results in Fig. 3 have been obtained using a model dielectric matrix in the GW calculations [27]. They are very close to those of our full RPA calculation [26] yielding a surface gap of 0.7 eV. The calculated gap energies are well within the range of the experimental values of 0.44 eV from optical absorption spectroscopy [62], 0.64 eV from surface photovoltage measurements [41] and 0.9 eV from tunnelling spectroscopy [63].

Concerning the comparison of the D_{up} band in the top right panel of Fig. 1 and the quasiparticle D_{up} band in the top panel of Fig. 3 with the data, it is obvious, that the calculated bandwidth is somewhat larger than the experimental bandwidth. In addition, there are further experimental features (open symbols) which can not be reconciled with the theoretical bands resulting for the (2×1) surface. Northrup [24] has carried out GW calculations for the low temperature $c(4 \times 2)$ phase of Si(001). On the basis of a comparison of his results with ARPES data of

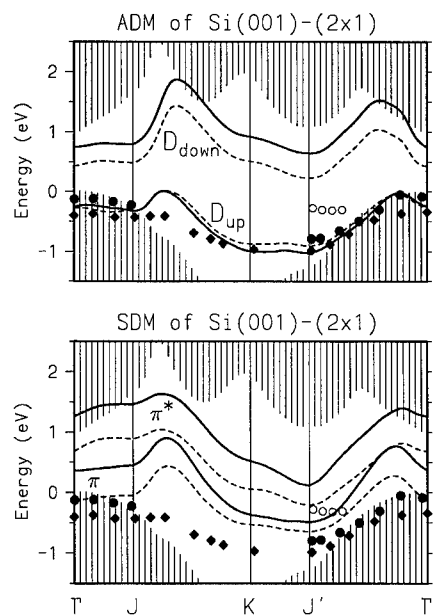


Fig. 3. Calculated dangling bond bands of Si(001)-(2 \times 1) for the asymmetric (ADM) and the symmetric dimer model (SDM). Solid lines display GWA results and dashed lines display LDA results in each figure. The symbols refer to photoemission data of Ref. [59] (diamonds) and Ref. [60] (dots). The shaded regions show the projected quasiparticle bulk band structure as resulting from our GWA calculations.

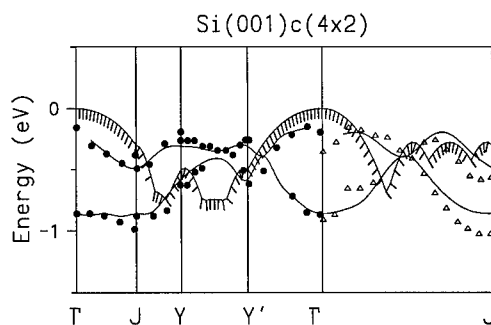


Fig. 4. Section of the calculated LDA surface band-structure of Si(001)- $c(4 \times 2)$ in comparison with photoemission data of Ref. [64] (triangles) and Ref. [65] (dots). The shaded region indicates the top of the projected bulk bands of Si.

Landmark [64] it seems very likely that the above-mentioned features originate from $c(4 \times 2)$ islands at the nominal (2×1) room temperature surface. We note in passing that Northrup observes an opening of the surface gap by 0.48 eV for the $c(4 \times 2)$ surface due to quasiparticle corrections, while we observed 0.50 eV, respectively, for the (2×1) surface. These results are convincingly close. Using the surface geometry as given by Northrup, we have carried out Green function LDA calculations to evaluate the surface band structure for the semi-infinite $c(4 \times 2)$ surface. A small section of the band structure near the top of the valence bands is compared in Fig. 4 with ARPES data of Landmark [64] and Enta et al. [65]. There is a very good agreement to be noted between the occupied bands of our LDA surface band structure of the $c(4 \times 2)$ surface and the data.

3.2. Polar (001) surfaces of β -SiC

While the (001) surfaces of diamond, Si and Ge have been studied by very many groups within the last decades, SiC(001) surfaces are moving into the focus of interest only recently. A number of different LEED patterns, depending sensitively on surface preparation techniques, have been observed [66]. The atomic structure of various reconstructions was investigated by dynamical tensor LEED analyses [67,68]. Using their slab-MINDO approach, Craig and Smith [69] have investigated structural properties of (2×1) - and $c(2 \times 2)$ -reconstructed surfaces. The results to be presented in this subsection and those of

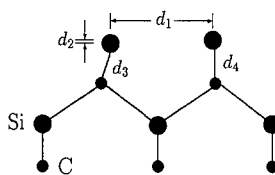
Käckell et al. [70] in these proceedings are the first ab initio results on structural and electronic properties of SiC(001) surfaces, to our knowledge.

SiC crystallizes in the zincblende- (β -phase) and in the wurtzite-structure (α -phase). Cubic β -SiC has one Si and one C atom per bulk unit cell. Si acts as cation and C as anion in this compound semiconductor. Its ionicity ($g = 0.475$) has been discussed in detail in Ref. [7]. In consequence of the heteropolarity of SiC, the (001) surfaces are polar since they are either Si- or C-terminated. This heteropolarity stems from the very different covalent radii of the two atoms rather than from different valencies of the anion and cation as is the case in III–V or II–VI compound semiconductors. Nevertheless, the stronger C potential as compared to that of Si leads to a considerable charge transfer from the Si cations to the C anions. The charge density along the Si–C bonds is strongly asymmetric (see Ref. [7]). This has important consequences for the reconstruction of SiC surfaces. The β -SiC lattice constant of 4.36 Å is larger than that of diamond and smaller than that of Si. Thus in β -SiC we will encounter physical properties of Si orbitals on a lattice with a 20% smaller lattice constant than in bulk Si and physical properties of C orbitals on a lattice with a 22% larger lattice constant than in bulk diamond.

Considering the (001) surfaces of β -SiC, one might expect that the Si- and C-terminated surfaces show a similar reconstruction behaviour as the respective Si or C(001)-(2×1) surfaces discussed in Section 3.1. It is very important to note, however, that the Si orbitals in the Si surface layer at the Si-terminated SiC(001)-(2×1) surface reside at a much smaller distance than at Si(001)-(2×1), while the C orbitals in the C surface layer at C-terminated SiC(001)-(2×1) reside at much larger relative distance than at C(001)-(2×1). The atoms at the latter surface, therefore, are free to move and to form strong C dimer bonds, while those at the former are strongly hindered in their movement by the reduced lattice constant and the concomitantly increased Coulomb repulsions with the backbonds. In addition, the valence charge of Si and C is four in both elemental semiconductors, while it is larger than four at the C ion and smaller than four at the Si ion in SiC.

We have carried out LDA structure optimizations

Si-term. SiC(001)-(2×1)



C-term. SiC(001)-(2×1)

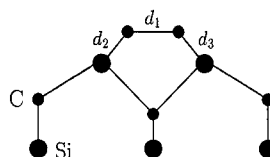


Fig. 5. Side view of the energy-optimized configurations of Si- (top panel) and C-terminated (bottom panel) β -SiC(001) surfaces. The actual values of the structure parameters are given in Table 2.

and electronic structure calculations for these two surfaces using supercells with eight atomic layers and seven vacuum layers. The bonds on one side of the slabs have been saturated with adsorbed hydrogen atoms. In the calculations discussed here we have only considered (2×1) reconstructions.

The optimal structure of the Si- and the C-terminated SiC(001)-(2×1) surface is shown in Fig. 5 and our structural data are compared with the Slab-MINDO results of Craig and Smith [69] in Table 2. The optimal reconstructions of the two (2×1) surfaces are vastly different. Contrary to the Si(001)-(2×1) surface, Si surface dimers are not stable at the Si-terminated SiC(001)-(2×1) surface. Only a very slight buckling of the Si atoms occurs (see the top panel of Fig. 5 for that matter). This is certainly related to both the reduced lattice constant and the decreased charge density at the Si cations in SiC, as compared to the case of Si (see Ref. [7]). The energy gain is only 2 meV per unit cell (but see also the note added in proof). The optimal (2×1) structure of the C-terminated SiC(001)-(2×1) surface, on the contrary, forms very strong symmetric C surface dimers with an energy gain of 4.9 eV per unit cell (see bottom panel of Fig. 5). The large valence charge density at the C anions and the increased lattice constant as compared to C(001)-(2×1) easily

Table 2

Structural data for energy-optimized Si- and C-terminated SiC(001)-(2×1) surfaces as resulting from our ab initio calculations and the slab-MINDO calculations of Craig and Smith [69]

	d_1 (Å)	d_2 (Å)	d_3 (Å)	d_4 (Å)	Ref.
Si-terminated SiC(001)	2.73	0.08	1.88	1.90	this work
	2.33	0.20	1.78	1.85	[69]
C-terminated SiC(001)	1.36	1.86	1.86		this work
	1.36	1.86	1.86		[69]

For the definition of the parameters, see Fig. 5.

allow dimer formation. Our structural parameters for the C-terminated surface in Table 2 are identical to those of Craig and Smith [69] while they are very different from the results of those authors for the Si-terminated surface. We believe that the large differences in the latter case could be due to the very subtle nature of the (2×1)-reconstruction of the Si-terminated surface. In particular it might be difficult to describe ionicity-induced charge transfer relaxations by the slab-MINDO approach. In the case of the C-terminated surface, on the contrary, the reconstruction is extremely strong and local and can thus probably be described by that approach very well. It is interesting to note that at C-terminated SiC(001)-(2×1) double-bonded C dimers with a bond length of 1.36 Å are formed as in the case of C(001)-(2×1) (see Tables 2 and 1, for comparison).

Small sections of the surface band structures for both optimized configurations are shown in comparison with the related bandstructures for the ideal surfaces in Fig. 6. The latter have been backfolded onto the (2×1) surface Brillouin zone for a more meaningful comparison. The bands D_1 and D_2 at the reconstructed Si-terminated surface originate from the backfolded dangling bond bands D and the bands D_3 and D_4 originate from the backfolded bridge bond bands Br at the ideal, unreconstructed surface (see the left panels of Fig. 6). The bridge and dangling bond bands of the ideal surface are split and shifted by the symmetry breaking due to the (2×1) reconstruction. Contrary to the case of the ideal Si(001) surface, the D and Br bands are energetically separated already at the ideal SiC surface (see upper left panel of Fig. 6) because of the stronger C potentials on the second layer, as compared to that of Si. The electronic structure for the

reconstructed Si-terminated SiC surface is semiconducting, as well. As mentioned already, the energy gain per unit cell due to the reconstruction is only 2 meV, in spite of the strong influence of the reconstruction on the D and Br bands yielding the bands D_1 – D_4 . This is related to the fact, that the center of gravity of the four bands hardly changes from the ideal to the reconstructed surface although each individual band shows large reconstruction-induced effects. In view of the structural results of Craig and Smith [69] for this surface, we have imposed as a test the same buckling which is observed for the Si(001)-(2×1) surface (see Table 1) to this surface. A very strongly metallic surface results. Thus such a strong buckling has to be discarded for this reason and because of a concomitant increase of the total energy by 0.67 eV. The surface electronic structure of the C-terminated surface in the right panels of Fig. 6 shows distinctly different features. First we note that the D and Br bands at the ideal surface strongly overlap in energy such that the ideal surface is metallic. Second, we observe that the π and π^* bands originating from the symmetric C dimers at

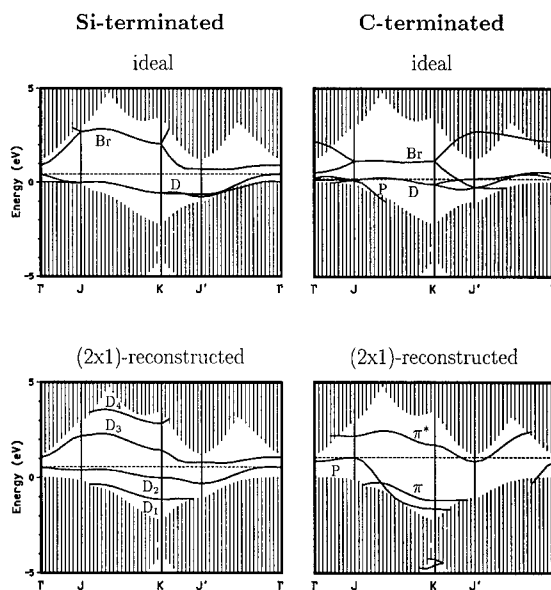


Fig. 6. Section of the surface band-structures of β -SiC(001)-(2×1) for the ideal lattice structures (top panels) and the energy-optimized configurations (bottom panels) together with the projected bulk band structure. Salient bands of localized states are shown for the Si-terminated (left panels) and C-terminated (right panels) surfaces. A dashed line indicates the Fermi-level in each case.

the reconstructed surface are clearly separated in energy as was the case for C(001)-(2 × 1) (see upper left panel of Fig. 1). But now an additional p-like band (P) occurs in the gap. It is related to occupied C 2p states that are perpendicular to the symmetric surface dimers. This P band is also to be observed at the ideal surface (see upper right panel of Fig. 6) where it resides lower in energy. It shifts into the gap at the reconstructed, C-terminated SiC(001)-(2 × 1) surface because of the reduced interaction with the Si sublayer, as compared to C(001)-(2 × 1). In consequence also the surface band structure for this (2 × 1)-reconstructed surface remains slightly metallic. Actually, more complicated c(2 × 2) reconstructions have been suggested for this surface [68]. We are currently studying such configurations by total energy minimization calculations (see the note added in proof).

Most of the results of this section are theoretical predictions. No ARPES data on these surfaces have been published to date. Concerning the (2 × 1)-reconstructed Si-terminated surface we are only aware of a tensor LEED investigation [67] which favours Si dimers with a bond length of 2.3 Å. This value is close to the dimer-bond length at Si(001)-(2 × 1) (see Table 1). For such a configuration we find, as mentioned above, an upward shift of the total energy by 0.67 eV and a strongly metallic surface band structure. Both findings do not favour such geometries. The tensor LEED results [67] might be

explained by an additional Si adlayer at this polar SiC(001) surface. We are currently investigating this issue (see the note added in proof).

3.3. Nonpolar surfaces of β -SiC, α -SiC and GaAs

Both the zincblende and the wurtzite modifications of SiC exhibit nonpolar surfaces, i.e. β -SiC(110) and, e.g., α -SiC(10 $\bar{1}$ 0). Both surfaces have been studied by empirical tight-binding calculations [71–73], as well as by ab initio LDA calculations [7,74]. Our supercell calculations [7] have been carried out with nine atomic layers and five vacuum layers in the unit cell using Gaussian orbital basis sets. The resulting optimal structures of the relaxed surfaces are shown in Fig. 7 and our structural data are compared with those of other calculations in Table 3. There is excellent agreement between the results of the two ab initio calculations [7,74] for the β -SiC(110)-(1 × 1) surface (see Table 3). Our calculated energy gain due to relaxation is 0.64 eV per unit cell for β -SiC(110) and 0.71 eV per unit cell for α -SiC(10 $\bar{1}$ 0). Wenzien et al. [74] found for the β -SiC(110) surface almost the same energy gain (0.63 eV) in their calculation. The top panel of Fig. 7 shows a rotation relaxation that is well-known, in general, from the (110) surfaces of III–V semiconductors, in particular for GaAs(110). The relaxation angle ω of about 17° for β -SiC(110) is considerably smaller than that of about 30° for GaAs(110). We will

Table 3
Structural data for energy-optimized, nonpolar β -SiC(110)-(1 × 1) and α -SiC(10 $\bar{1}$ 0) surfaces

SiC(110)	Ref. [7]	Ref. [74]	Ref. [73]	SiC(10 $\bar{1}$ 0)	This work	Ref. [71]	Ref. [73]
a_b (Å)	4.34	4.29	4.36	a (Å)	3.07	3.08	3.08
				c (Å)	5.03	5.05	5.05
d_b (Å)	1.88	1.86	1.89	d_b (Å)	1.88	1.88	1.88
$\Delta_{1,\perp}(d_b)$	0.14	0.13	0.05	$\Delta_{1,\perp}(d_b)$	0.06	0.04	0.03
$\Delta_{1,x}(d_b)$	1.86	1.82	1.86	$d_{1\parallel}(d_b)$	2.65	2.61	2.66
$d_{12,\perp}(d_b)$	0.65	0.67	0.71	$d_{12,\perp}(d_b)$	0.32	0.35	0.33
$d_{12,x}(d_b)$	1.27	1.27	1.21	$d_{12\parallel}(d_b)$	2.31	2.25	2.27
$\Delta_{2,\perp}(d_b)$	−0.02	−0.02	−0.01	$\Delta_{2,\perp}(d_b)$	−0.01	0.00	−0.03
				$d_0(d_b)$	0.37	0.39	0.38
ω (deg)	16.9	15.4	6.0	φ (deg)	3.8	2.6	1.7

Our results [7] are compared to literature data by Wenzien et al. [74], Lee and Joannopoulos [71], and Mehendru and Anderson [73]. For the definition of the parameters, see Fig. 7. The atomic shifts with respect to their ideal positions, as given in Refs. [71] and [73], have been converted to the structural parameters used in this work.

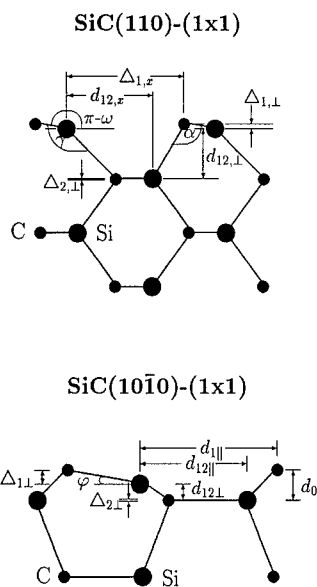


Fig. 7. Side view of the relaxed β -SiC(110)-(1×1) surface (top panel) and the relaxed α -SiC(10 $\bar{1}$ 0)-(1×1) surface (bottom panel). The actual values of the structure parameters are given in Table 3.

comment on this point in the next subsection where we also address the relatively small relaxation angle ω of 3.8° at the α -SiC(10 $\bar{1}$ 0) surface.

In Fig. 8 we compare the surface electronic structure for the optimally relaxed configurations of these two nonpolar surfaces with that of GaAs(110) from Ref. [7]. The band structure for the optimally relaxed β -SiC(110) surface in the middle panel is very similar to that of GaAs(110), in general. The A_5 band originates from the occupied dangling bonds at the surface anions, i.e. the C atoms, and the C_3 band

originates from the empty dangling bonds at the surface cations, i.e. the Si atoms. The surface band structure is semiconducting. The same result obtains for the α -SiC(10 $\bar{1}$ 0) surface. Its band structure in the right panel of Fig. 8 is very similar to that of the relaxed β -SiC(110) surface. Only the gap between the A_5 and C_3 band is more pronounced in this case since the bulk band gap of wurtzite α -SiC is already larger than that of cubic β -SiC. These similarities and the very similar energy gain due to relaxation for the two systems is related to the fact that the nearest-neighbour configuration of Si and C atoms is the same in both modifications and only the second-nearest neighbour configurations discern the structures. For the same reason, the different lattices give rise to similar charge densities for the pronounced A_5 and C_3 surface states. These are shown in Fig. 9 for both optimally relaxed surfaces and the similarities are most obvious even for the C_3 states if one takes the different spatial configurations of the ions into account.

3.4. Origin of the different surface relaxations

In order to highlight the differences in the observed surface relaxations, we have summarized our results for the optimal structure of GaAs(110), β -SiC(110) and α -SiC(10 $\bar{1}$ 0) in Fig. 10 together with the structure of the ideal (110) surface of a zincblende semiconductor. There are at least three driving forces for the structural relaxation at these surfaces as has been discussed in great detail in Ref. [7]. First, the more electronegative ions tend to reside as far above

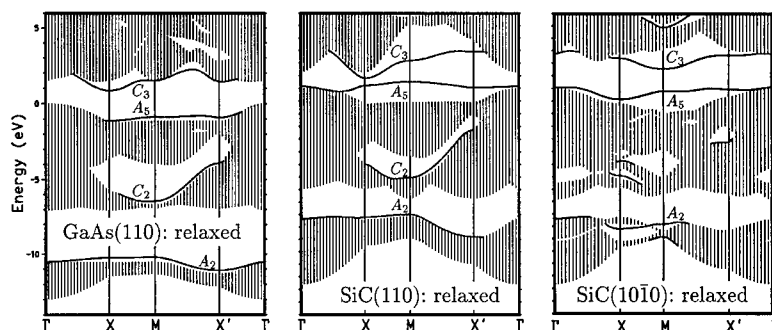


Fig. 8. Salient bands of localized surface states of the relaxed GaAs(110) (left), cubic SiC(110) (middle) and wurtzite SiC(10 $\bar{1}$ 0) (right) surfaces together with the respective projected bulk band structure.

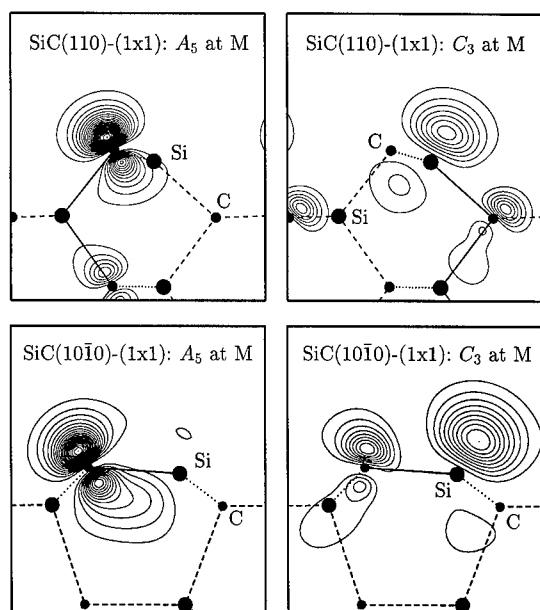


Fig. 9. Charge densities of the C- and Si-derived dangling-bond states A_5 and C_3 at the M-point of cubic SiC(110)-(1 \times 1) (top panels) and of wurtzite SiC(10 $\bar{1}$ 0)-(1 \times 1) (bottom panels) surfaces. Bonds within (parallel to) the drawing plane are shown by full (dashed) lines. Bonds forming an angle with the drawing plane are indicated by dotted lines.

the surface as possible. This reduces the Coulomb repulsion between the electrons. Second, the changes in hybridization at the surfaces as compared to the bulk lead to p^3 pyramidal configurations around the anions, while the cations tend to become sp^2 -like planar bonded at the surface. Therefore, anions tend to move above and cations below the ideal surface plane. This is a purely quantum mechanical driving force due to hybridization. Third, if the systems become more and more ionic, classical electrostatic interactions start to dominate and they have a tendency to form planar anion–cation arrays, maximizing the electrostatic attraction and minimizing the total energy, thereby. The result of the combined effects of these three mechanisms is to be observed in Fig. 10. In particular, the electrostatic forces lead to a bond contraction at the surface with increasing asymmetry of the charge density along the cation–anion bonds and a concomitant lowering of the relaxation angle (see Table 4). It is obvious from the table that the quantum mechanical hybridization mechanism is still very strong in the case of CdS

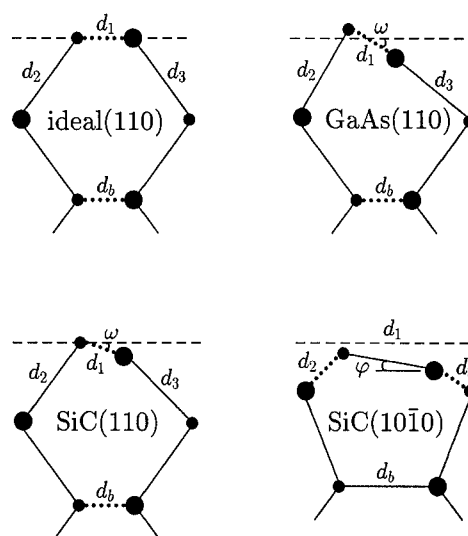


Fig. 10. Side views (drawn to scale) of the ideal GaAs(110) surface and of the energy-optimized relaxed GaAs(110), SiC(110), and SiC(10 $\bar{1}$ 0) surfaces. The ideal surface plane is indicated by a dashed line in each case. Bonds that form an angle with the drawing plane are shown by dotted lines. Bonds which lie in the drawing plane or which are parallel to the drawing plane are shown by full lines. Small dots show anions while large dots show cations. The actual values of the structure parameters are given in Table 4.

which behaves similar to III–V semiconductors in this respect. The asymmetry of its charge density is less pronounced than in SiC. In Table 4, we have summarized characteristic structural data resulting from our calculations for GaAs, SiC and CdS surfaces. The data show the trends in the surface-layer bond lengths and in the relaxation angles as discussed above. It should be noted at this point, that the relaxation angle ω at the (110) surfaces of zincblende crystals results from a projection of the anion–cation bonds onto the drawing plane in Fig.

Table 4

Bulk (d_b) and surface (d_1) bond-lengths as well as relaxation angles (ω) and tilt angles (φ) as defined in Fig. 10 for GaAs, SiC and CdS surfaces (for details, see text)

	Ideal	GaAs(110)	SiC(110)	SiC(10 $\bar{1}$ 0)	CdS(10 $\bar{1}$ 0)
d_b (Å)	$a_b\sqrt{3}/4$	2.40	1.88	1.88	2.51
d_1 (d_b)	1.00	0.99	0.94	0.91	0.96
ω (deg)	0	30.6	16.9	3.8	16.6
φ (deg)	0	16.7	8.2	3.8	16.6

10 while the anion–cation bonds at the wurtzite (10 $\bar{1}$ 0) surface lie in the drawing plane. In consequence, the tilt angle φ and the relaxation angle ω are the same only in the latter case. In general, we observe that cations (Ga, Si, Cd) reside closer to the substrate than anions (As, C, S) and the surface bonds are contracted in ionic systems while they are almost conserved in covalent systems, e.g., in GaAs(110). The different relaxation behaviour can very clearly be traced back to differences in the asymmetry of the charge density of the underlying bulk bonds as has been worked out in great detail in Ref. [7]. From these considerations it follows that the buckling angle ω decreases with increasing ionicity due to increasing electrostatic forces, as is confirmed by the results in Table 4. Since the quantum mechanical hybridization mechanism dominates in the III–V semiconductors, the anions move above and the cations move below the ideal surface plane of these crystals (see Fig. 10 and, e.g., Refs. [7] and [75]). In the more ionic systems in Fig. 10, the electrostatic mechanism dominates so that not only the cations but also the anions move below the ideal surface plane. Yet the anions reside above the cations because of the first mechanism mentioned above.

3.5. Nonpolar (10 $\bar{1}$ 0) surfaces of II–VI semiconductors

Electronic and structural properties of II–VI compound semiconductors and their surfaces are currently moving into the focus of interest because of their technological potential in optoelectronics (e.g. blue lasers based on ZnSe) and heterogeneous catalysis (e.g. ZnO surfaces). A number of experimental and theoretical investigations has been carried out over the years. LEED studies of, e.g., ZnO(10 $\bar{1}$ 0) have been carried out by Duke et al. [76,77]. Two different empirical tight-binding calculations for the surface electronic structure of ZnO(10 $\bar{1}$ 0) lead to strikingly different results for the surface bands in the gap energy region. Ivanov and Pollmann [78], who used an empirical tight-binding Hamiltonian incorporating only Zn 4s and O 2p orbitals did not find dangling bond bands in the gap but only ionic resonances within the projected bulk bands. Wang and Duke [79], on the other hand, included Zn 4p

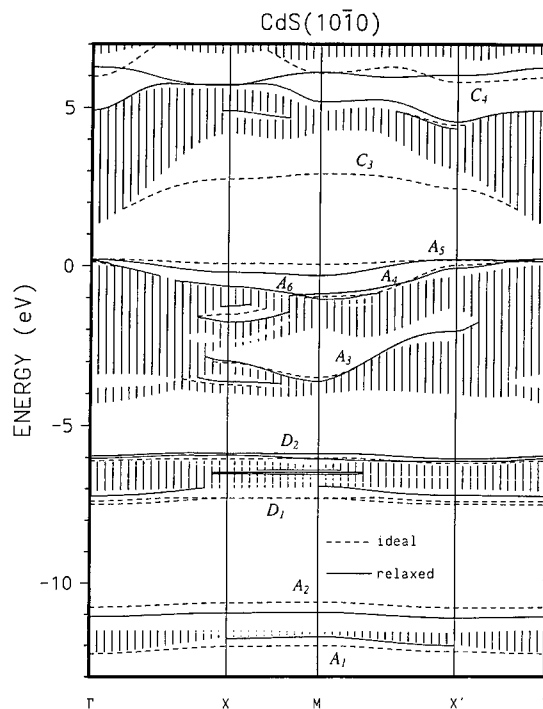


Fig. 11. Surface bandstructure of ideal and relaxed CdS(10 $\bar{1}$ 0). The localized surface states at the ideal surface are shown by dashed and at the relaxed surface by full lines.

orbitals in their Hamiltonian and found a dangling bond band of occupied O 2p states near the top of the projected bulk valence bands. To resolve this discrepancy, Schröer et al. [8] have carried out the first ab initio calculations for CdS(10 $\bar{1}$ 0) and ZnO(10 $\bar{1}$ 0) within LDA. They confirmed the results of Wang and Duke [79,80] and found anion-derived dangling bond bands near the top of the valence bands for both surfaces, as well.

As an example, the LDA surface bandstructure for CdS(10 $\bar{1}$ 0) is shown in Fig. 11. An anion-derived dangling bond band A_5 and two bands A_4 and A_6 are observed near the top of the valence bands for the relaxed surface. Wang and Duke [79,80] labeled their surface states S_1 to S_n (for surface bands), while Schröer et al. [8] labeled them P_1 to P_n in order to indicate the p-character of these anion-derived bands. For a more meaningful comparison with the results of SiC(110) and SiC(10 $\bar{1}$ 0), discussed in Section 3.3, we change the nomenclature here and label the anion-derived surface state bands accordingly as

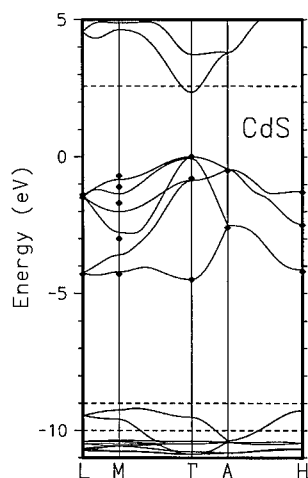


Fig. 12. Bulk bandstructure of wurtzite CdS as calculated using our SIC-PP approach in comparison with ARPES data of Ref. [81]. The horizontal lines indicate the measured energy gap and the measured d-band width.

A_1 to A_5 (see Fig. 11). Except for the A_4 and A_5 bands, the fundamental gap is free from surface states due to the large ionicity of this compound. Comparing the bandstructure in Fig. 11 with that of the relaxed α -SiC(10 $\bar{1}$ 0) surface in the right panel of Fig. 8, we observe a number of distinct differences. First, the heteropolar gap between the anion-derived s- and p-bands in II–VI semiconductors is much larger than in SiC due to the increased ionicity. Second, there is no C_3 band in the gap of ZnO(10 $\bar{1}$ 0) (see Ref. [8] for that matter) or CdS(10 $\bar{1}$ 0) and the A_5 bands are somewhat closer to the projected valence bands than at α -SiC(10 $\bar{1}$ 0). This is related to the larger ionicity and the concomitant smaller covalent character of CdS and ZnO, as compared to SiC. Third, there is a very specific additional feature in the II–VI semiconductors, that calls for particular attention. In these materials, there are occupied cationic d-states whose energies reside between those

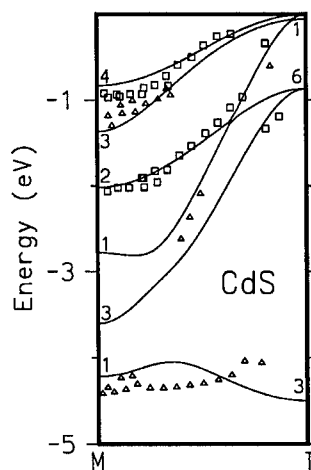


Fig. 13. Upper valence bands of wurtzite bulk CdS resulting from our SIC-PP calculations in comparison with polarization- and angle-resolved photoemission data of Ref. [82]. The experimental data refer to bands resulting from states that are even (triangles) or odd (squares) with respect to the mirror plane. The calculated bands 1 and 3 are even and the bands 2 and 4 are odd with respect to the mirror plane.

of the anion s- and p-states. They give rise to d-bands between the anion p- and s-valence bands. The semi-core d-states, that are highly localized in space, have to be retained in the valence electron shell in order to arrive at accurate theoretical lattice constants (see, e.g., Ref. [8] for that matter). Inclusion of the d-orbitals, however, leads to further problems, in that the d bands result roughly 3 eV too high in energy, as compared to experiment. In consequence the cation-d–anion-p interaction is much too strong. The p bands are shifted up in energy and the gap is almost closed in ZnO (0.23 eV instead of 3.4 eV, see Ref. [8]) and much too small in CdS (1.22 eV instead of 2.6 eV). In particular, the question arises, whether the A_5 dangling bond bands near the top of the projected valence bands of ZnO(10 $\bar{1}$ 0) and

Table 5
Structural parameters of the nonpolar CdS(10 $\bar{1}$ 0) surface as resulting from two theoretical surface structure determinations

	$A_{1\perp}$ (Å)	$d_{1\parallel}$ (Å)	$d_{12\parallel}$ (Å)	$A_{2\perp}$ (Å)	$d_{12\perp}$ (Å)	d_0 (Å)	φ (deg)	Ref.
CdS (10 $\bar{1}$ 0)	0.00	4.19	3.35	0.00	1.19	1.19	0	id. surface
	0.74	4.41	3.86	-0.08	0.62	1.19	17.9	[79]
	0.69	4.40	3.72	-0.15	0.61	1.15	16.6	this work

Our results are compared to literature data. For the definition of the parameters, see the lower panel of Fig. 7.

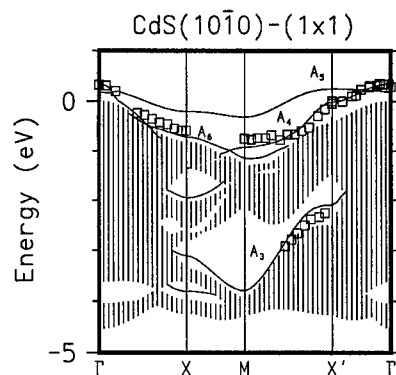


Fig. 14. Section of the surface band-structure of relaxed CdS(10 $\bar{1}$ 0)-(1 \times 1) in comparison with ARPES data of Ref. [83]. Salient bands of localized surface states resulting from our SIC-PP calculations are shown together with the respective projected bulk bandstructures (shaded regions).

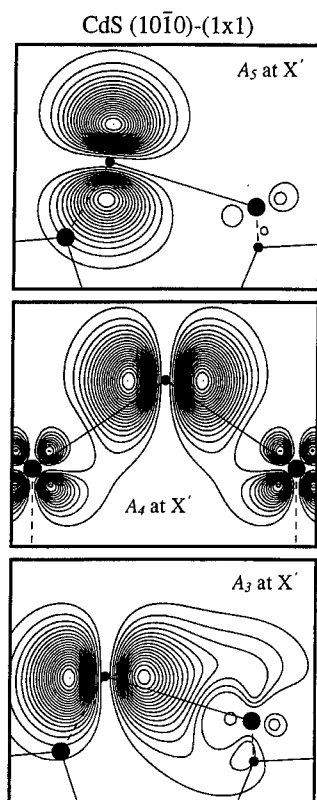


Fig. 15. Charge densities for representative surface states of CdS(10 $\bar{1}$ 0)-(1 \times 1) at the X' point. Bonds that form an angle with the drawing plane are shown by dashed lines. The Cd (S) atoms are indicated as large (small) dots.

CdS(10 $\bar{1}$ 0) are artifacts of the calculations in consequence of the unphysically strong p–d interactions.

To resolve this issue, we have developed an efficient approach to incorporate dominant self-interaction-corrections in our LDA calculation which is described in Ref. [29]. We construct appropriate self-interaction-corrected pseudopotentials (SIC-PP's). Using the SIC-PP's, we obtain bulk band structures in very good agreement with experiment (see Fig. 12). Compared to the standard LDA results, as given in Ref. [28], the d-bands are strongly down in energy, the gap is opened up almost to the experimental value and the bandwidth and dispersions of the S 3p valence bands are now in excellent agreement with ARPES data of Stoffel [81] and of Magnusson and Flodström [82], as can be seen in Fig. 12 and Fig. 13. Using our SIC-PP approach, we have also calculated the structure and the electronic properties of CdS(10 $\bar{1}$ 0). The structural relaxation is similar, in principle, to that of SiC(10 $\bar{1}$ 0) (see lower panel of Fig. 7). In our total energy minimization atomic relaxations of the first three layers are taken into account. With two atoms per layer unit cell, which are allowed to move only parallel to the *c*-axis and perpendicular to the (10 $\bar{1}$ 0) surface, due to the symmetry of the system, there are twelve structural degrees of freedom. We have minimized all related forces until they are less than 10 $^{-3}$ Ry/a.u. Structural data for CdS(10 $\bar{1}$ 0) are given in Table 5. There is very good agreement between the two different sets of theoretical data. In Fig. 14 we compare a small section of the CdS(10 $\bar{1}$ 0) surface band structure as resulting from our modified LDA (using our SIC-PP's) with experimental data of Magnusson and Flodström [83]. The existence of an anion-p-derived dangling bond band A₅ at the (10 $\bar{1}$ 0) surface of II–VI semiconductors is thus firmly established (see also Ref. [8]). Furthermore we note that our results are in very good agreement with the data. This holds in particular for the A₃, A₄ and the A₆ bands. The character of the most pronounced states A₃, A₄ and A₅ is shown by the respective charge densities at the X'-point in Fig. 15. It is obvious from the figure, that all three states have strong p_z-contributions and should therefore be accessible to ARPES measurements. In view of these theoretical results the question remains why the A₅ band does not seem to have been detected. A systematic comparing study of a

number of II–VI semiconductor surfaces is currently in progress in our group. The results will be given elsewhere.

4. Summary

In this paper we have briefly discussed structural and electronic properties of a number of prototype semiconductors. The results of well-converged *ab initio* total energy minimization and electronic structure calculations were found to be in good agreement with the available experimental data of surface structure determinations and high-resolution surface spectroscopy results. In the other cases they yield most useful and important predictions. The resulting structural and electronic properties have been analyzed and a general picture of the physical nature and origin of particular reconstruction or relaxation behaviours has been developed. A clear physical picture of a number of important surfaces has emerged. Shortcomings of LDA results have been identified and it has been exemplified in cases how they can be overcome by GW quasiparticle band structure calculations or by LDA calculations that include most important self-interaction-corrections. The good agreement of the theoretical results with most recent experimental data on these surfaces once more confirms the appropriateness and usefulness of most advanced ‘state of the art’ theoretical approaches for quantitative studies of well-ordered clean semiconductor surfaces.

Note added in proof

More recently, we have carried out very detailed additional structure optimization calculations for Si- and C-terminated SiC(001) surfaces. Our results for the C-terminated surface were fully confirmed while for the Si-terminated SiC(001)-(2 × 1) surface we have obtained a marginal refinement. As optimal surface geometry we find a symmetric configuration of the surface Si atoms with $d_1 = 2.73$ Å, $d_2 = 0.00$ Å, $d_3 = d_4 = 1.89$ Å and a concomitant energy gain of 10 meV. For details, see M. Sabisch, P. Krüger, A. Mazur, M. Rohlfing and J. Pollmann, *Phys. Rev. B* 53 (1996), issue of May 15.

Acknowledgements

Fruitful discussions with Dr. A. Mazur throughout the course of this work are gratefully acknowledged.

References

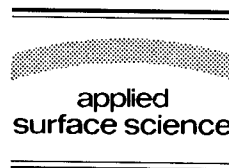
- [1] G. Chiarotti, Ed., *Numerical Data and Functional Relationships in Science and Technology*, Landolt–Börnstein, New Series Group III, Vol. 24a (Springer, Berlin, 1993).
- [2] G. Chiarotti, Ed., *Numerical Data and Functional Relationships in Science and Technology*, Landolt–Börnstein, New Series Group III, Vol. 24b (Springer, Berlin, 1994).
- [3] G.V. Hansson and R.I.G. Uhrberg, *Surf. Sci. Rep.* 9 (1988) 197.
- [4] J.P. LaFemina, *Surf. Sci. Rep.* 16 (1992) 133.
- [5] P. Krüger and J. Pollmann, *Phys. Rev. B* 38 (1988) 10578.
- [6] P. Krüger and J. Pollmann, *Phys. Rev. Lett.* 74 (1995) 1155.
- [7] M. Sabisch, P. Krüger and J. Pollmann, *Phys. Rev. B* 51 (1995) 13367.
- [8] P. Schröer, P. Krüger and J. Pollmann, *Phys. Rev. B* 49 (1994) 17092.
- [9] L. Kleinman and D.M. Bylander, *Phys. Rev. Lett.* 48 (1983) 1425.
- [10] X. Gonze, R. Stumpf and M. Scheffler, *Phys. Rev. B* 44 (1991) 8503.
- [11] G.B. Bachelet, D.R. Hamann and M. Schlüter, *Phys. Rev. B* 26 (1982) 4199.
- [12] D. Ceperley and B.J. Alder, *Phys. Rev. Lett.* 45 (1980) 566.
- [13] J.P. Perdew and A. Zunger, *Phys. Rev. B* 23 (1981) 5048.
- [14] P. Krüger and J. Pollmann, *Physica B* 172 (1991) 155.
- [15] J. Ihm, A. Zunger and M.L. Cohen, *J. Phys. C* 12 (1979) 4409.
- [16] M. Schlüter, J.R. Chelikowsky, S.G. Louie and M.L. Cohen, *Phys. Rev. B* 12 (1975) 4200.
- [17] M. Scheffler, J.P. Vigneron and G.B. Bachelet, *Phys. Rev. B* 31 (1985) 6541.
- [18] C.G. Broyden, *Math. Comput.* 19 (1965) 577; D.D. Johnson, *Phys. Rev. B* 38 (1988) 12807.
- [19] M.S. Hybertsen and S.G. Louie, *Phys. Rev. B* 34 (1986) 5390.
- [20] M. Rohlfing, P. Krüger and J. Pollmann, *Phys. Rev. B* 48 (1993) 17791.
- [21] L. Hedin, *Phys. Rev.* 139 (1965) A796.
- [22] L. Hedin and S. Lundqvist, in: *Solid State Physics, Advances in Research and Application*, Vol. 23, Eds. F. Seitz, D. Turnbull and A. Ehrenreich (Academic Press, New York, 1969) p. 1.
- [23] X. Zhu, S.B. Zhang, S.G. Louie and M.L. Cohen, *Phys. Rev. Lett.* 63 (1989) 2112; X. Zhu and S.G. Louie, *Phys. Rev. B* 43 (1991) 12146; J.E. Northrup, M.S. Hybertsen and S.G. Louie, *Phys. Rev. Lett.* 66 (1991) 500.
- [24] J.E. Northrup, *Phys. Rev. B* 47 (1993) 10032.

- [25] C. Kress, M. Fiedler and F. Bechstedt, in: *Proceedings of the 4th Int. Conf. on the Formation of Semiconductor Interfaces*, Jülich 1993, Eds. B. Lengeler, H. Lüth, W. Mönch and J. Pollmann (World Scientific, Singapore, 1994) p. 19.
- [26] M. Röhlfing, P. Krüger and J. Pollmann, *Phys. Rev. B* 52 (1995) 1905.
- [27] M. Röhlfing, P. Krüger and J. Pollmann, *Phys. Rev. B* 52 (1995) 13753.
- [28] P. Schröder, P. Krüger and J. Pollmann, *Phys. Rev. B* 47 (1993) 6971; P. Schröder, P. Krüger and J. Pollmann, *Phys. Rev. B* 48 (1993) 18264.
- [29] D. Vogel, P. Krüger and J. Pollmann, *Phys. Rev. B* 52 (1995) R14316.
- [30] P. Krüger and J. Pollmann, *Appl. Phys. A* 59 (1994) 487.
- [31] M. Needels, M.C. Payne and J.D. Joannopoulos, *Phys. Rev. Lett.* 58 (1987) 1765.
- [32] J. Cho and M.H. Kang, *Phys. Rev. B* 50 (1994) 17139.
- [33] R.J. Culbertson, Y. Kuk and L.C. Feldmann, *Surf. Sci.* 167 (1986) 127.
- [34] R. Rossmann, H.L. Meyerheim, V. Jahns, J. Wever, W. Moritz, D. Wolf, D. Dornisch and H. Schulz, *Surf. Sci.* 279 (1992) 199.
- [35] C. Kress, M. Fiedler, W.G. Schmidt and F. Bechstedt, *Phys. Rev. B* 50 (1994) 17697.
- [36] J. Furthmüller, J. Hafner and G. Kresse, *Europhys. Lett.* 28 (1994) 659.
- [37] Z. Zhang, M. Wensell and J. Bernholc, *Phys. Rev. B* 51 (1996) 5291.
- [38] D.J. Chadi, *Phys. Rev. Lett.* 43 (1979) 43.
- [39] F.J. Himpsel and D.E. Eastman, *J. Vac. Sci. Technol.* 16 (1979) 1297.
- [40] F.J. Himpsel, P. Heimann, T.C. Chiang and D.E. Eastman, *Phys. Rev. Lett.* 45 (1980) 1112.
- [41] W. Mönch, P. Koke and S. Krueger, *J. Vac. Sci. Technol.* 19 (1981) 313.
- [42] B.W. Holland, C.B. Duke and A. Paton, *Surf. Sci.* 140 (1984) L269.
- [43] R.M. Tromp, R.J. Hamers and J.E. Demuth, *Phys. Rev. Lett.* 55 (1985) 1303.
- [44] R.J. Hamers, R.M. Tromp and J.E. Demuth, *Phys. Rev. B* 34 (1986) 5343.
- [45] N. Jedrecy, M. Sauvage-Simkin, R. Pinchaux, J. Massies, N. Greiser and V.H. Etgens, *Surf. Sci.* 230 (1990) 197.
- [46] R.A. Wolkow, *Phys. Rev. Lett.* 68 (1992) 2636.
- [47] E. Landemark, C.J. Karlsson, Y.-C. Chao and R.I.G. Uhrberg, *Phys. Rev. Lett.* 69 (1992) 1588.
- [48] E. Fontes, J.R. Patel and F. Comin, *Phys. Rev. Lett.* 70 (1993) 2790.
- [49] G. Jayaram, P. Xu and L.D. Marks, *Phys. Rev. Lett.* 71 (1993) 3489.
- [50] H. Tochiwara, T. Amasuka and M. Iwatsuki, *Phys. Rev. B* 50 (1994) 12262.
- [51] D. Badt, H. Wengelink and H. Neddermeyer, *J. Vac. Sci. Technol. B* 12 (1994) 2015.
- [52] A.W. Munz, C. Ziegler and W. Göpel, *Phys. Rev. Lett.* 74 (1995) 2244.
- [53] E.L. Bullock, R. Gunnella, L. Patthey, T. Abukawa, S. Kono, C.R. Natoli and L.S.O. Johansson, *Phys. Rev. Lett.* 74 (1995) 2756.
- [54] M.T. Yin and M.L. Cohen, *Phys. Rev. B* 24 (1981) 2303.
- [55] N. Roberts and R.J. Needs, *Surf. Sci.* 236 (1990) 112.
- [56] K. Kobayashi, Y. Morikawa, K. Terakura and S. Blügel, *Phys. Rev. B* 45 (1992) 3469.
- [57] J. Dabrowski and M. Scheffler, *Appl. Surf. Sci.* 56 (1992) 15.
- [58] A. Ramstad, G. Brocks and P.J. Kelly, *Phys. Rev. B* 51 (1995) 14504.
- [59] R.I.G. Uhrberg, G.V. Hansson, J.M. Nichols and S.A. Flodström, *Phys. Rev. B* 24 (1981) 4684.
- [60] L.S.O. Johansson, R.I.G. Uhrberg, P. Martensson and G.V. Hansson, *Phys. Rev. B* 42 (1990) 1305.
- [61] E. Landemark, C.J. Karlsson, L.S.O. Johansson and R.I.G. Uhrberg, *Phys. Rev. B* 49 (1994) 16523.
- [62] Y.J. Chabal, S.B. Christmann, E.E. Chaban and M.T. Yin, *J. Vac. Sci. Technol. A* 1 (1983) 1241.
- [63] R.J. Hamers and U.K. Köhler, *J. Vac. Sci. Technol. A* 7 (1989) 2854.
- [64] E. Landemark, PhD Thesis, University of Linköping, 1993, unpublished.
- [65] Y. Enta, S. Suzuki and S. Kono, *Phys. Rev. Lett.* 65 (1990) 2704.
- [66] R. Kaplan, *J. Vac. Sci. Technol. A* 6 (1988) 829; R. Kaplan, *Surf. Sci.* 215 (1989) 111.
- [67] J.M. Powers, A. Wander, M.A. van Hove and G.A. Somorjai, *Surf. Sci.* 260 (1992) L7.
- [68] J.M. Powers, A. Wander, P.J. Rous, M.A. van Hove and G.A. Somorjai, *Phys. Rev. B* 44 (1991) 11159.
- [69] B.I. Craig and P.V. Smith, *Surf. Sci.* 233 (1990) 255; B.I. Craig and P.V. Smith, *Surf. Sci.* 256 (1991) L609.
- [70] P. Käckell, J. Furthmüller and F. Bechstedt, *Appl. Surf. Sci.* 104/105 (1996) 45.
- [71] D.H. Lee and J.D. Joannopoulos, *J. Vac. Sci. Technol.* 21 (1982) 351.
- [72] T. Takai, T. Halicioglu and W.A. Tiller, *Surf. Sci.* 164 (1985) 341.
- [73] S.P. Mehandru and A.B. Anderson, *Phys. Rev. B* 42 (1990) 9040.
- [74] B. Wenzien, P. Käckell and F. Bechstedt, *Surf. Sci.* 307 (1994) 989.
- [75] C.B. Duke, in: *Surface Properties of Electronic Materials*, Eds. D.A. King and D.P. Woodruff (Elsevier, Amsterdam, 1988) pp. 69–118.
- [76] C.B. Duke, A.R. Lubinsky, S.C. Chang, B.W. Lee and P. Mark, *Phys. Rev. B* 15 (1977) 4865.
- [77] C.B. Duke, A. Paton and P. Mark, *Phys. Rev. B* 18 (1978) 4225.
- [78] I. Ivanov and J. Pollmann, *Phys. Rev. B* 24 (1981) 7275.
- [79] Y.R. Wang and C.B. Duke, *Surf. Sci.* 192 (1987) 309.
- [80] Y.R. Wang and C.B. Duke, *Phys. Rev. B* 37 (1988) 6417.
- [81] N.G. Stoffel, *Phys. Rev. B* 28 (1983) 3306.
- [82] K.O. Magnusson and S.A. Flodström, *Phys. Rev. B* 38 (1988) 1285.
- [83] K.O. Magnusson and A. Flodström, *Phys. Rev. B* 38 (1988) 6137.



ELSEVIER

Applied Surface Science 104/105 (1996) 17–23



Plasmon excitations and the effects of surface preparation in n-type InAs(001) studied by electron energy loss spectroscopy

G.R. Bell^a, C.F. McConville^{a,*}, T.S. Jones^b

^a Department of Physics, University of Warwick, Coventry CV4 7AL, UK

^b Department of Chemistry, Imperial College, London SW7 2AY, UK

Received 28 June 1995; accepted 30 August 1995

Abstract

High resolution electron energy loss spectroscopy (HREELS) has been used to study the surface plasmon excitations on n-type InAs(001) surfaces prepared either by decapping a protective As layer or by argon ion bombardment and annealing (IBA) procedures. The plasmon frequency for heavily doped decapped samples indicates a free carrier concentration in good agreement with the nominal bulk doping level ($n \sim 5.0 \times 10^{18} \text{ cm}^{-3}$). Subjecting the decapped sample to IBA results in a much higher carrier concentration ($\sim 10^{19} \text{ cm}^{-3}$). Measurements from a lower doped InAs(001) sample ($n \sim 2.0 \times 10^{16} \text{ cm}^{-3}$) prepared by IBA also show an increased carrier concentration ($\sim 10^{18} \text{ cm}^{-3}$), suggesting the presence of additional free carriers as a consequence of the structural damage induced by the sputtering process. For both surface preparations, the plasmon frequency does not vary as a function of the incident electron beam energy and suggests a homogeneous free carrier profile. Measurements of the plasmon frequency as a function of the incident electron beam energy indicate that the depth of electronic damage extends at least 400 Å into the material. The frequency of the surface plasmon is also strongly affected by the ion bombardment and annealing conditions. In particular, the use of high ion beam energies ($> 2 \text{ keV}$) directed along the surface normal, gives rise to the highest residual carrier concentrations, consistent with the generation of higher degrees of structural damage in the material.

1. Introduction

Studies of III–V semiconductor materials have received considerable attention in recent years with the aim of using this knowledge in a variety of novel device applications [1,2]. To this end, several surface sensitive and bulk material analysis techniques have been applied to elucidate the physical and electronic structure of these compound semiconductor materials. Of the binary III–V semiconductor materials,

InAs is of particular interest for certain device applications because of the natural electron accumulation layer formed at the (001) surface: a recent example is the use of InAs for inter sub-band infrared detection [3]. The surface accumulation behaviour of InAs differs from that of other III–V materials such as GaAs, which forms a natural depletion layer at the surface.

An important area of study in III–V semiconductor materials is the preparation of clean, ordered substrates prior to epitaxial growth by techniques such as molecular beam epitaxy (MBE). To date there is limited information on MBE growth of

* Corresponding author. Tel.: +44-1203-524236; fax: +44-1203-692016; e-mail: spcm@spec.warwick.ac.uk.

homoepitaxial InAs(001) because of the small window for epitaxial growth [4], and hence most published growth studies use InP(001) and GaAs(001) substrates [5]. Work has been published on the substrate preparation of InAs [6,7], primarily for epitaxial growth of high In-content $\text{In}_x\text{Ga}_{1-x}\text{As}$ alloys for optical modulators [8] and for the growth of lattice-matched $\text{InP}_{1-x}\text{Sb}_x$, a material used for quantum-well lasers and detectors in the 2.0–3.5 μm band [9].

Surface preparations of all III–V semiconductor materials basically fall into three categories: oxide desorption under a group V over-pressure, group V decapping in-vacuum and ion bombardment and annealing (IBA). Oxide desorption tends to produce rough surfaces (although quite adequate for epitaxial growth) which are free of contaminants and electronic damage. Capped samples, which must first be grown by MBE and then decapped in vacuum, also produce crystalline surfaces free from contamination and damage. The third of these preparation techniques, IBA, again results in clean, ordered surfaces but always leaves residual damage in the near surface region that has a dramatic effect on the electronic structure of the material. For example, in a previous study of InSb(001), the damage induced by IBA produced carrier concentrations in the near surface region much higher than the bulk doping level [10–12]. In contrast, decapping Sb from InSb(001) samples grown by MBE resulted in a near surface carrier concentration unchanged from the bulk value, apart from the presence of the natural depletion layer [13]. In both cases, high resolution electron energy loss spectroscopy (HREELS) was used to obtain the plasmon frequency, which is a direct measure of the carrier concentration [10–13].

HREELS is a sensitive probe of plasmon excitations in the near surface region of doped semiconductor materials [14]. In the dipole scattering process, which dominates the small angle electron scattering by these long-wavelength excitations, the *effective* probing depth is not determined by the mean free path of the electrons in the solid, but is governed by the inverse of the wave-vector transfer parallel to the surface (q_{\parallel}). By changing the kinetic energy of the incident electrons, it is possible to probe free carrier concentrations at different depths in the solid. In this paper, plasmon excitations in InAs(001) have been investigated to monitor changes in the near

surface electronic structure (at depths up to ~ 500 Å) as a function of the surface preparation, in particular the use of ion bombardment and annealing (IBA). The parameters associated with IBA were systematically varied for two different n-type bulk doping samples and the effect on the carrier concentration in the near surface region of InAs(001) surfaces was monitored.

2. Experimental

The experiments were carried out in an ultra-high vacuum chamber (base pressure $\sim 1 \times 10^{-10}$ mbar) equipped with HREELS and low energy electron diffraction (LEED). Two n-type InAs(001) samples were used in this study. The first was bulk grown InAs (Si doped, $n \sim 2 \times 10^{16} \text{ cm}^{-3}$) and the second was grown by MBE with Si doping ($n \sim 5 \times 10^{18} \text{ cm}^{-3}$) and an As cap to protect the surface during transfer from the MBE chamber to the HREELS system. The MBE grown sample was then decapped in the HREELS chamber by annealing to 650 K for 15 min. The bulk grown samples were subjected to half-hour cycles of ion bombardment and annealing (IBA), varying the angle of ion incidence, the ion beam energy and the post-bombardment annealing temperature, the temperature being measured by a chromel–alumel thermocouple attached to the side of the samples. The maximum annealing temperature following bombardment was 600 K to minimise degradation of the sample surface by As-desorption and subsequent surface In-clustering. After completion of the HREELS measurements the decapped samples were also prepared using IBA. The decapping procedure resulted in the appearance of a rather disordered (4×1) LEED pattern. Ion bombardment and annealing gave a much sharper (4×1) LEED pattern.

The HREEL spectrometer consists of a fixed monochromator and rotatable analyser, both of a 180° hemispherical deflector type with a four element entrance and exit lens system. Incident electron energies (E_i) in the range 4–100 eV were used and all HREEL spectra were collected in specular scattering geometry ($\theta_i = \theta_s = 45^\circ$) and at room temperature. The instrumental resolution was typically 10 meV as measured by the full width at half maximum

(FWHM) of the elastic peak, although this was often degraded to ~ 15 meV for some measurements to increase the count rates and reduce the scan times. Peak positions are accurate to ± 1 meV.

3. Results and discussion

A series of HREEL spectra, recorded with $E_i = 25$ eV from n-type ($n \sim 5 \times 10^{18} \text{ cm}^{-3}$) InAs(001) samples following different surface preparation methods, are shown in Fig. 1. Decapping at 650 K to completely remove the As cap results in a strong surface plasmon feature at 96 meV (Fig. 1a). The resulting spectra after IBA cleaning procedures are strongly dependent on the sputtering conditions. For example, Fig. 1b and c show the effects on the HREELS spectra of changing the angle of incidence of the 500 eV Ar ion beam, with the angle defined relative to the surface normal. Both spectra are again dominated by a characteristic surface plasmon excitation, however, the frequency of this feature shifts with changing angle of ion incidence. Incident angles of 10° and 50° give plasmon frequencies of 133 and 120 meV respectively.

The free carrier concentration (n) is related to the surface plasmon frequency (ω_s) by

$$\omega_s^2 = \frac{ne^2}{\epsilon_0(\epsilon_\infty + 1)m^*} \quad (1)$$

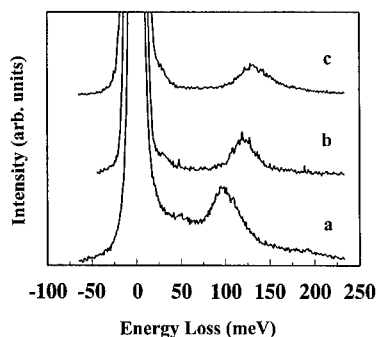


Fig. 1. Specular ($\theta_i = \theta_s = 45^\circ$) HREELS spectra recorded at 25 eV for n-type (Si doped, $n \sim 5 \times 10^{18} \text{ cm}^{-3}$) InAs(001) after (a) decapping a protective As capping layer by heating to 650 K, (b) ion bombardment with 500 eV Ar ions incident at 50° to the surface normal followed by annealing to 600 K and (c) ion bombardment with 500 eV Ar ions incident at 10° to the surface normal followed by annealing to 600 K.

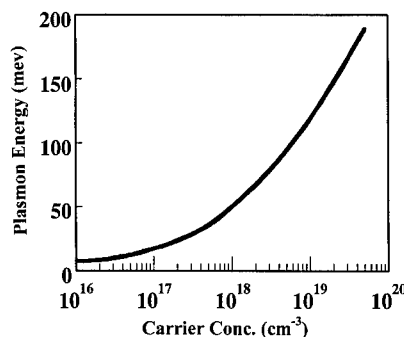


Fig. 2. The calculated surface plasmon frequency (meV) plotted as a function of free carrier concentration (cm^{-3}) for InAs at room temperature.

where m^* is the conduction band electron effective mass [15,16], ϵ_∞ is the high frequency dielectric constant (12.25 for InAs) and ϵ_0 is the permittivity of free space. The calculated relationship between ω_s and n , obtained using Eq. (1), is plotted in Fig. 2.

The plasmon frequency of 96 meV obtained for the decapped sample corresponds to a carrier concentration of $5.0 \times 10^{18} \text{ cm}^{-3}$, a value consistent with the nominal bulk doping level. This indicates that decapping InAs samples does not lead to a measurable change in the free carrier concentration in the near surface region of the material. This is consistent with previous HREELS studies of n-type InAs(001), also prepared by decapping methods [17], which showed that the choice of a higher bulk doping level ($n \sim 8.0 \times 10^{18} \text{ cm}^{-3}$) results in essentially flat band behaviour, since the bulk Fermi level coincides with the surface state energy.

In contrast, the plasmon frequencies observed in Fig. 1b and c for the ion bombarded samples correspond to carrier concentrations of 1.0×10^{19} (120 meV) and $1.5 \times 10^{19} \text{ cm}^{-3}$ (133 meV). Both of these values are significantly higher than the bulk doping level of these samples ($5.0 \times 10^{18} \text{ cm}^{-3}$) and indicate the presence of additional free carriers in the near surface region of the material. Similar effects have been seen on InSb(001) surfaces prepared by IBA [10–12]. The increase in the number of free carriers (electronic damage) is a direct consequence of the surface preparation procedure.

The dominant plasmon wave-vector parallel to the surface ($q_{||}$) depends strongly on the incident electron energy, E_i . The electric fields of the plasmon

normal to the surface decay exponentially from the plane of localisation of the plasmon with a decay length $\sim q_{\parallel}^{-1}$, where

$$q_{\parallel} = k_i \sin \theta_i \left(\frac{\hbar \omega_p}{2 E_i} \right) \quad (2)$$

and

$$k_i = \frac{(2mE_i)^{1/2}}{\hbar}$$

is the wave-vector of the incident electrons. This means that electrons can be scattered by a plasmon localised deep within the sample even though they do not significantly penetrate the sample. Consequently, by simply varying the kinetic energy of the incident electrons it is possible to tune the effective probing depth. Measurements of the plasmon frequency as a function of E_i can therefore be used to determine the free carrier profile to a depth of several hundred Angstroms into the material [11,18].

A plot of the surface plasmon frequency as a function of E_i for both the decapped and ion bombarded (500 eV, 45°) samples is shown in Fig. 3. For the decapped sample, the plasmon frequency remains at a constant value of 96 meV as E_i is varied from 5 to 100 eV. A similar trend is observed in the case of the ion bombarded sample, with the plasmon frequency remaining at the higher constant value of 124 meV. This indicates that the free carrier profile is essentially homogeneous in both cases. The effective

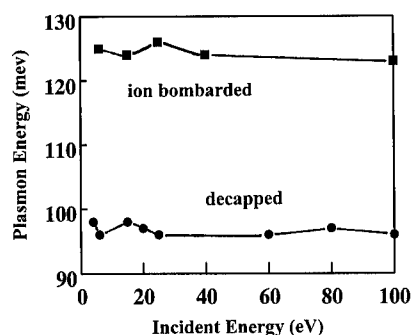


Fig. 3. The experimental surface plasmon frequency (meV) plotted as a function of incident electron energy (eV) for n-type (Si doped, $n \sim 5 \times 10^{18} \text{ cm}^{-3}$) InAs(001) after either decapping a protective As capping layer by heating to 650 K or ion bombardment with 500 eV Ar ions incident at 45° to the surface normal followed by annealing to 600 K.

probing depths for a 96 meV and a 124 meV excitation at $E_i = 100 \text{ eV}$ are 480 Å and 360 Å respectively. The depth of electronic damage induced by the IBA process therefore extends at least 400 Å into the bulk of the material.

Inhomogeneity in the carrier concentration profile near the surface is also caused by band bending due to Fermi level pinning at the surface. For InAs(001), intrinsic surface states in the conduction band cause an accumulation layer to be formed on samples doped to $n < 8.0 \times 10^{18} \text{ cm}^{-3}$ [17]. The ion bombarded samples show a carrier concentration of $n \sim 1.0 \times 10^{19} \text{ cm}^{-3}$ resulting in a bulk Fermi level close to the surface state energy and displaying approximately flat band behaviour. In contrast, the decapped samples should form an accumulation layer less than 50 Å thick, significantly less than the minimum probing depth in these experiments ($\sim 100 \text{ Å}$). Spatial dispersion of the plasmon also contributes to changes in the plasmon energy as a function of incident electron energy [17,18]. However, in the range of q_{\parallel} used in these experiments, the expected contribution to the plasmon energy due to spatial dispersion is less than 3 meV, based on a spatial dispersion parameter determined previously from HREELS measurements on decapped InAs samples [17]. Therefore the observed plasmon energy is effectively independent of the incident electron beam energy.

The electronic damage resulting from the ion bombardment process is strongly dependent on the specific sputtering and annealing conditions used. The effects on the free carrier concentration of changing the ion beam energy are shown in Fig. 4 for a sample having a bulk doping level of $2.0 \times 10^{16} \text{ cm}^{-3}$. The carrier concentration was obtained from the surface plasmon frequency (Eq. (1)) for HREEL spectra recorded at 25 eV on samples cleaned at a fixed angle of incidence (45°) and subsequently annealed to 600 K for 2 h. The carrier concentration in all cases is well in excess of the nominal bulk doping level and rises dramatically with increasing ion beam energy up to a maximum value of $5.0 \times 10^{18} \text{ cm}^{-3}$ at $\sim 2.0 \text{ keV}$ ion beam energy.

As already indicated in Fig. 1b and c, the angle of incidence of the Ar ions also has a dramatic effect on the surface plasmon frequency. Fig. 5 shows the free carrier concentration after ion bombardment of a

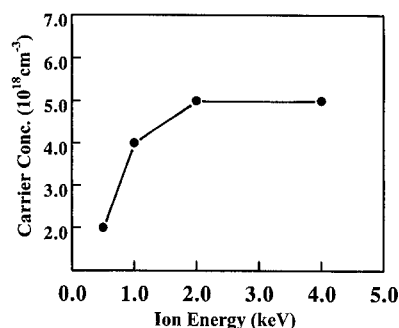


Fig. 4. The free carrier concentration plotted as a function of Ar ion beam energy for n-type (Si doped, $n \sim 2 \times 10^{16} \text{ cm}^{-3}$) InAs(001) after ion bombardment with Ar ions incident at 45° to the surface normal followed by annealing to 600 K. The carrier concentration was obtained from the experimentally determined surface plasmon frequency using Eq. (1).

InAs(001) sample, having a bulk doping level of $5.0 \times 10^{18} \text{ cm}^{-3}$, at different incident angles, with a fixed ion beam energy of 500 eV and after post-bombardment annealing at 600 K. As the angle of incidence is varied between 80° and 40° with respect to the surface normal, the free carrier concentration remains at a constant value of $1.0 \times 10^{19} \text{ cm}^{-3}$. For angles approaching the surface normal ($\theta = 0^\circ$), the carrier concentration rises to $2.0 \times 10^{19} \text{ cm}^{-3}$. Whilst the carrier concentration in all cases is significantly larger than the bulk doping level, these results indicate that the degree of electronic damage is higher for sputtering at close to normal incidence.

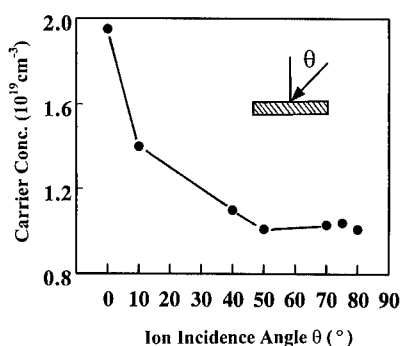


Fig. 5. The free carrier concentration plotted as a function of the incident angle of 500 eV Ar ions during the ion bombardment of n-type (Si doped, $n \sim 5 \times 10^{18} \text{ cm}^{-3}$) InAs(001) followed by annealing to 600 K. The carrier concentration was obtained from the experimentally determined surface plasmon frequency using Eq. (1).

It is well known from ion beam damage studies in bulk III–V semiconductor materials (using ions in the energy range 20–200 keV) that residual electronic damage is detectable in amounts well below the detectability limits for structural damage [19]. The presence of significant electronic damage near the surface of these InAs samples, together with good crystalline order, as indicated by LEED, extends this conclusion to the *near-surface* region where damage is caused by low energy ions (0.5–4 keV). Bulk damage studies also indicate a close connection between the degrees of structural damage and electronic damage. The degree of structural damage in the near-surface case can be related to the sputtering yield, as a function of ion energy and angle. Although sputtering yield measurements from III–V semiconductor materials have concentrated almost exclusively on GaAs and InP [19], similar trends should be apparent on InAs. In the range of ion energies from 500 eV to 5 keV, the sputtering yield from GaAs increases by a factor of three, saturating at a maximum around 10 keV. For InP, the sputtering yield approximately doubles between 500 eV and a broad maximum at 1.5–2.0 keV. The measurements shown in Fig. 4 indicate that the residual electronic damage in InAs follows a similar pattern, with an increase in the sputter yield by a factor of 2.5 between 500 eV and 4 keV. The measured carrier concentration is entirely due to electronic damage in this case, since the bulk doping level is two orders of magnitude less. The measurements do not extend to sufficiently high ion energies to define a clear maximum.

The sputtering yield for 300 eV Ar ions incident on GaAs approximately doubles between grazing ion incidence and normal ion incidence, with a maximum at about 40° in some studies [19]. The preferential sputtering of As from GaAs is not strongly angle-dependent. For 500 eV Ar ions incident on InP there is a smaller variation in sputtering yield, although the preferential sputtering of P is strongly angle-dependent [20], increasing markedly towards normal incidence. Fig. 5 indicates that the residual electronic damage in InAs is enhanced by a factor of 3 at normal incidence compared with grazing incidence (note that the bulk doping level is comparable to the ion-induced carrier concentration in this case). Again, the behaviour of the residual electronic dam-

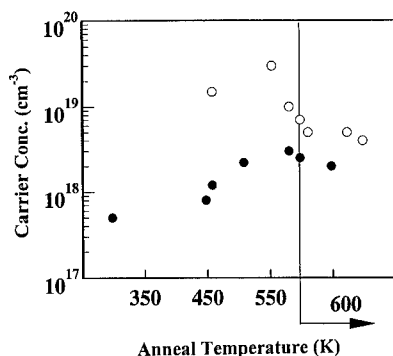


Fig. 6. The free carrier concentration plotted as a function of postbombardment annealing temperature after ion bombardment of n-type (Si doped, $n \sim 2 \times 10^{16} \text{ cm}^{-3}$) InAs(001). Ion bombardment was carried out with Ar ions of 1 keV (open circles) and 500 eV (dark circles) incident at 45° to the surface normal. The carrier concentration was obtained from the experimentally determined surface plasmon frequency. The vertical line indicates the maximum annealing temperature used (600 K). Points to the right of this line represent extended annealing times at 600 K (3 h for the point at the extreme right).

age follows a similar pattern to that of the sputtering yield, indicating a correlation between structural damage and electronic damage. It is also likely that group V preferential sputtering is less significant in the case of InAs than for InP, but more so than for GaAs, influencing the level of residual damage [19]. The angular effects were fully reversible: it was possible to lower the carrier concentration in a sample by re-bombarding at a more grazing angle followed by annealing.

The influence of post bombardment annealing temperature in determining the free carrier concentration is shown in Fig. 6 for n-type ($n \sim 2.0 \times 10^{16} \text{ cm}^{-3}$) InAs(100) cleaned by ion bombardment with both 500 eV and 1 keV argon ions incident at 45° . In both cases the free carrier concentration rises to a maximum after annealing to $\sim 550 \text{ K}$; $n \sim 3.0 \times 10^{18}$ and $3.5 \times 10^{19} \text{ cm}^{-3}$ for 500 eV and 1 keV ions respectively. Higher annealing temperatures and extended annealing at 600 K results in a decrease in these values, although in both cases the free carrier concentration is always significantly higher than the bulk doping level. This suggests that the electronic damage induced by the structural damage cannot be repaired simply by annealing. Ordered LEED pat-

terns appear at an annealing temperature of $\sim 500 \text{ K}$ indicating the removal of most of the structural damage. The behaviour of the free carrier concentration with temperature is very similar to that observed for InSb(100) in a previous HREELS study [10,11], where the surface plasmon energy indicated substantial residual electronic damage even after extended annealing close to the melting point.

4. Conclusions

The surface plasmon excitations on n-type InAs(001) surfaces, prepared either by decapping a protective As capped layer from an MBE grown sample, or by specific argon ion bombardment and annealing procedures, have been studied using HREELS. The plasmon frequency for the As-decapped samples indicates a free carrier concentration which is in agreement with the nominal bulk doping level, whereas the effects of ion bombardment and annealing result in much higher carrier concentrations ($\sim 10^{19} \text{ cm}^{-3}$) suggesting the presence of additional free carriers arising as a consequence of the structural damage induced by the sputtering process. For both surface preparations, the plasmon frequency is independent of the incident electron beam energy, indicative of a homogeneous free carrier profile. The energy dependent studies indicate that the depth of electronic damage extends at least 400 \AA into the material. The frequency of the surface plasmon is also strongly affected by the ion bombardment and annealing conditions. In particular, the use of ion beams always results in additional carriers in the near surface region. The level of this electronic damage is correlated with the degree of structural damage caused by varying the IBA parameters, as indicated by comparison with sputtering yield data from InP and GaAs.

Acknowledgements

We are grateful to Prof. R.A. Stradling and his group for the As-capped MBE samples and for the financial support and a studentship for GRB from the Engineering and Physical Sciences Research Council (EPSRC), UK.

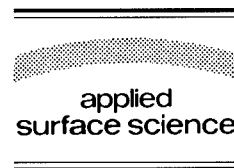
References

- [1] S.L. Eglash and C.K. Choi, *Appl. Phys. Lett.* 57 (1990) 1292.
- [2] H. Mani, A. Joullie, G. Boissier, E. Tournie, F. Pitard, A.-M. Jouille and C. Alibert, *Electron. Lett.* 24 (1988) 1543.
- [3] M.T. Emery, private communication.
- [4] Y. Yamaguchi and Y. Horikoshi, *J. Appl. Phys.* 64 (1990) 1610.
- [5] M.L. Dotor, J. Melendez, P. Huertas, M. Garriga, D. Gollmayo and F. Briones, *J. Cryst. Growth* 127 (1993) 46.
- [6] R. Ludeke, *IBM J. Res. Dev.* 22 (1978) 304.
- [7] H.F. Hsieh, C.C. Yeh and H.C. Shih, *J. Electrochem. Soc.* 140 (1993) 463.
- [8] D.J. Goodman, A.C. Walker, C.R. Stanley, M.C. Holland and M. McElhinny, *Appl. Phys. Lett.* 64 (1994) 1192.
- [9] M. Behet, B. Stoll and K. Heime, *J. Cryst. Growth* 124 (1992) 389.
- [10] T.S. Jones, M.Q. Ding, N.V. Richardson and C.F. McConville, *Appl. Surf. Sci.* 45 (1990) 85.
- [11] T.S. Jones, M.Q. Ding, N.V. Richardson and C.F. McConville, *Surf. Sci.* 247 (1991) 1.
- [12] W.T. Yuen, M.O. Schweitzer, T.S. Jones, C.F. McConville, E.A. Johnson, A. Mackinnon, N.V. Richardson and R.A. Stradling, *Semicond. Sci. Technol.* 8 (1993) S396.
- [13] S.D. Evans, L.L. Cao, R.G. Egdell, R. Droopad, S.D. Parker and R.A. Stradling, *Surf. Sci.* 226 (1990) 169.
- [14] H. Luth, *Vacuum* 38 (1988) 223.
- [15] Landolt-Bornstein, *Numerical Data and Functional Relations in Science and Technology, New Series Volume III/17a*.
- [16] W. Nakwaski, *Physica B* 210 (1995) 1.
- [17] R.G. Egdell, S.D. Evans, R.A. Stradling, Y.B. Li, S.D. Parker and R.H. Williams, *Surf. Sci.* 262 (1992) 444.
- [18] T.S. Jones, M.O. Schweitzer, N.V. Richardson, G.R. Bell and C.F. McConville, *Phys. Rev. B* 51 (1995) 17675.
- [19] J.B. Malherbe, *Solid State Mater. Sci.* 19(2) (1994) 55; 19(3) (1994) 129, and references therein.
- [20] X. Wang, *Appl. Surface Sci.* 33/34 (1988) 88.



ELSEVIER

Applied Surface Science 104/105 (1996) 24–34



Investigation of the space charge regime of epitaxially grown GaAs (100) by high-resolution electron energy-loss spectroscopy

V.M. Polyakov^a, A. Elbe^a, J. Wu^b, G.J. Lapeyre^b, J.A. Schaefer^{c,*}

^a *Fachbereich Physik, Universität Kassel, D-34132 Kassel, Germany*

^b *Department of Physics, Montana State University, Bozeman, MT 59717, USA*

^c *Institut für Physik, Technische Universität Ilmenau, D-98684 Ilmenau, Germany*

Received 28 June 1995; accepted 4 November 1995

Abstract

High-resolution electron energy-loss spectroscopy (HREELS) has been used in situ to investigate the space charge regime of homogeneously doped and delta-doped (Si) GaAs (100) samples, which were grown by molecular beam epitaxy (MBE). The simplest model we applied to fit the experimental energy-loss spectra of homogeneously doped samples is based on a step-like distribution of free electrons with the Drude dielectric response function. In this case, the spatial dispersion of plasmon excitations is neglected, whereas in the Thomas–Fermi (or Debye–Hückel) model it is considered. The results of the fitting carried out show that the Drude model gives the higher values for both the free-electron density and the plasmon damping when compared to the Thomas–Fermi model. It thus appeared to provide a more adequate description of the collective dynamic response of free electrons. Post-annealing of the homogeneously doped GaAs (100) samples reveals a significant reduction (compensation) of the free-electron density due to the localization of free electrons on defects diffused from the surface to the bulk.

For the delta-doped samples the free-electron density profiles are calculated self-consistently in the effective-mass approximation. The profiles obtained are then approximated by a finite number of rectangles simulating sublayers to calculate the effective dielectric function by virtue of a continued-fraction expansion. The spatial dopant spreading is estimated from the best fit to experimental energy-loss spectra. The change of fitted plasmon damping with the primary electron-beam energy showing a significant decrease for the lowest primary energy applied, is briefly discussed.

1. Introduction

Detailed knowledge of the characteristics of the space charge layers like dopant spreading and free-carrier density profiles, barrier height, band bending, electron/hole mobility etc. are of great importance in order to control semiconductor devices [1–5]. This information can be provided by theoretical calculations of scattering cross sections and their comparison with data from high-resolution electron energy-loss spectroscopy (HREELS).

* Corresponding author.

The application of HREELS is based on the observation of collective surface excitations (phonons and plasmons) in the scattering experiment of electrons impinging on the semiconductor surface. The transferred wave vector parallel to the surface is a measure for the spatial penetration of the polarization electric field of collective surface excitations into the solid. The value of the parallel wave vector q_{\parallel} is usually in the range from 10^{-3} to 10^{-2} \AA^{-1} , which corresponds to a penetration depth of about a few hundred ångström. As the free-electron density profile defines the surface plasmon excitations, space charge layer parameters can be extracted from HREELS. The basic concepts of HREELS and its application have been demonstrated in the past [5–10]. In this study we compare calculated energy-loss spectra with experimental spectra, taken at doped (Si) GaAs (100) surfaces.

All samples were grown in a Perkin-Elmer molecular-beam epitaxy (MBE) system at a substrate temperature of 550°C and a Si-flux of $1 \times 10^{11} \text{ cm}^{-2} \text{ s}^{-1}$. The crystal quality and surface reconstruction was checked by means of reflection high-energy electron diffraction (RHEED) during and after the growth. The MBE growth chamber is connected directly to an analysis chamber equipped with a HREELS spectrometer (Leybold-ELS-22), low-energy electron-diffraction (LEED) and photoelectron spectroscopy (XPS, UPS). HREELS spectra were measured in specular geometry with primary electron beam energies ranging from 0.5 to 20 eV at an incidence angle of 45° . The energy resolution was set at 8 meV. For the homogeneously doped samples post-annealing as an effective mechanism of free-electron compensation is investigated.

The delta-doped samples consist of an undoped GaAs buffer layer of $0.4 \text{ }\mu\text{m}$ thickness and one delta-layer in 100 Å or 200 Å depth beneath the surface. Samples were grown with two doping levels $N_{\text{Si}} = 1.3 \times 10^{13} \text{ cm}^{-2}$ and $6.0 \times 10^{13} \text{ cm}^{-2}$. For these samples we use a symmetric rectangular and asymmetric Gaussian dopant profile for our calculations for the low and high doping levels, respectively. Further, we discuss the significant change of the plasmon damping versus the primary electron-beam energy in terms of free-electron scattering on the optical phonons.

The spatial dispersion of the quasi-two-dimensional plasmon excitations is taken into account as the long-wavelength limit of the Lindhard dielectric response function.

The remainder of the paper is outlined as follows. In Section 2 we present different models used for fitting the experimental energy-loss spectra, taken at homogeneously doped GaAs (100). The main features of these models are discussed. Section 3 contains the fitting results of HREELS-spectra for delta-doped GaAs (100) samples with low and high doping levels. We discuss qualitatively the competition of different scattering mechanisms of the plasmon excitations.

2. Homogeneously doped GaAs (100)

For the energy-loss calculation a two-layer model was chosen, which consists of a semi-infinite substrate with a bulk free-electron density n and an overlayer depleted of free electrons [2,5,6]. This approach is justified by an abrupt decrease of the free-electron density from the unperturbed bulk value to zero towards the surface over a distance, estimated by the screening length in the Thomas–Fermi theory as

$$\lambda_{\text{TF}} = \left[\frac{\epsilon_0 E_F}{6\pi e^2 n} \right]^{1/2},$$

where E_F is the Fermi energy, n the free-electron density and ϵ_0 the low-frequency dielectric constant [11]. This parameter is 45–60 Å in the case of high-doped GaAs ($n = 10^{18}$ – 10^{19} cm^{-3} in the present study).

The general case of multi-layered structures was presented by Lambin et al. [8]. The effective surface dielectric function of such systems was approximated by virtue of the continued-fraction expansion

$$\epsilon_{\text{eff}}(q_{\parallel}, \omega) = a_1 - \frac{b_1^2}{a_1 + a_2 - \frac{b_2^2}{a_2 + a_3 - \dots}} \quad (1)$$

with $a_i = \varepsilon_i \coth(q_{\parallel} d_i)$ and $b_i = \varepsilon_i / \sinh(q_{\parallel} d_i)$, where ε_i and d_i are the dielectric function and the thickness of the i -th layer, respectively; $q_{\parallel} = |\mathbf{q}_{\parallel}|$ is the parallel wave-vector transfer from impinging electrons to surface excitations.

In the simplest case of a two-layer model the effective dielectric function (1) is rewritten as

$$\varepsilon_{\text{eff}}(q_{\parallel}, \omega) = \varepsilon_{\text{ph}}(\omega) \frac{1 + \Delta(q_{\parallel}, \omega) \exp(-2q_{\parallel} d)}{1 - \Delta(q_{\parallel}, \omega) \exp(-2q_{\parallel} d)} \quad (2)$$

with

$$\Delta(q_{\parallel}, \omega) = \frac{\varepsilon_{\text{sub}}(q_{\parallel}, \omega) - \varepsilon_{\text{ph}}(\omega)}{\varepsilon_{\text{sub}}(q_{\parallel}, \omega) + \varepsilon_{\text{ph}}(\omega)}$$

and

$$\varepsilon_{\text{ph}}(\omega) = \frac{\varepsilon_{\infty} + (\varepsilon_0 - \varepsilon_{\infty}) \omega_{\text{TO}}^2}{\omega_{\text{TO}}^2 - \omega^2 - i\gamma\omega},$$

where ε_0 and ε_{∞} are the low and the high frequency dielectric constants, respectively, ω_{TO} the transverse optical phonon frequency, and γ the phonon damping [6].

In the Drude model the spatial dispersion of plasmon excitations is neglected [15–17] and the substrate dielectric function $\varepsilon_{\text{sub}}(q_{\parallel}, \omega)$ is given by

$$\varepsilon_{\text{sub}}(q_{\parallel}, \omega) = \varepsilon_{\text{sub}}(\omega) = \varepsilon_{\text{ph}}(\omega) - \frac{\omega_{\text{p}}^2}{\omega^2 + i\Gamma\omega} \quad (3)$$

with $\omega_{\text{p}}^2 = 4\pi e^2 n / m^*$. Here Γ is the plasmon damping, m^* the effective electron mass and ω_{p} the bulk plasmon frequency [6].

Taking into account the spatial dispersion of plasmons, the bulk dielectric function including the phonon contribution in the long-wavelength limit of the Lindhard dielectric function [10] of the electron gas is given by

$$\varepsilon_{\text{bulk}}(\mathbf{q}_{3\text{D}}, \omega) = \varepsilon_{\text{ph}}(\omega) - \frac{\omega_{\text{p}}^2}{\omega^2 - D(\mathbf{q}_{3\text{D}}) + i\Gamma\omega} \quad (4)$$

with $D(\mathbf{q}_{3\text{D}}) = \frac{3}{5} v_{\text{F}}^2 \mathbf{q}_{3\text{D}}^2$ in the Thomas–Fermi model, and v_{F} the electron velocity at the Fermi level.

For the evaluation of the substrate dielectric function $\varepsilon_{\text{sub}}(q_{\parallel}, \omega)$, entering the formula (2), additional boundary conditions are applied [12,13], that results in

$$\frac{1}{\varepsilon_{\text{sub}}(q_{\parallel}, \omega)} = \frac{2}{\pi} \int_0^{\infty} dq_z \frac{q_{\parallel}}{q_{\parallel}^2 + q_z^2} \frac{1}{\varepsilon_{\text{bulk}}(\mathbf{q}_{3\text{D}}, \omega)} \quad (5)$$

with $\mathbf{q}_{3\text{D}} = \{\mathbf{q}_{\parallel}, q_z\}$ and $q_{\parallel} = |\mathbf{q}_{\parallel}|$.

Multiple-scattering energy losses and gains for arbitrary temperature are accounted for through a suitable thermodynamic average [8].

In order to elucidate the main differences between the Drude and Thomas–Fermi models, we calculated the dispersion relations of plasmon modes, which are defined by the poles of the energy-loss function

$$\text{Im}[1/(\varepsilon_{\text{eff}}(q_{\parallel}, \omega) + 1)],$$

where the effective surface dielectric function $\varepsilon_{\text{eff}}(q_{\parallel}, \omega)$ is determined by Eqs. (2)–(5). It is obvious from Fig. 1 that the Drude model predicts a downward dispersion (curve c) in the case of the presence of a depletion layer and no dispersion for the flat band conditions (not shown here). On the contrary, the Thomas–Fermi model (curve a in Fig. 1) shows a general trend to upward dispersion in both cases. The dispersion curve for the

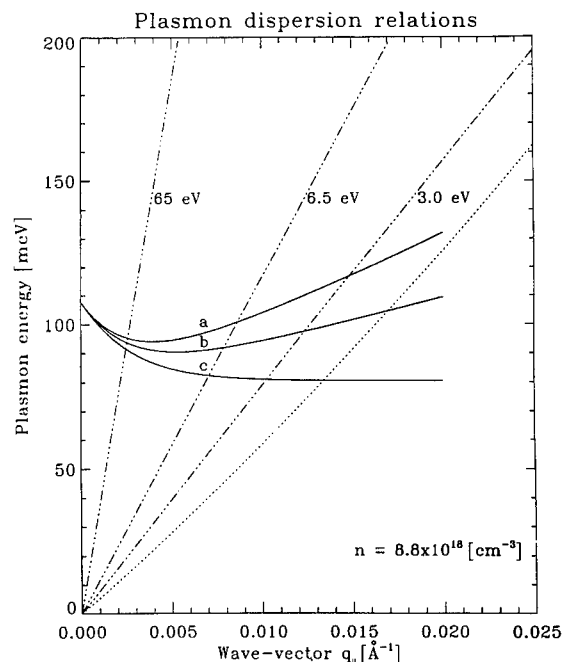


Fig. 1. Calculated dispersion relations of the surface plasmon for $n = 8.8 \times 10^{18} \text{ cm}^{-3}$ and depletion layer thickness $d = 200 \text{ Å}$: (a) Thomas-Fermi model; (b) Debye-Hückel model; (c) Drude model. The dotted line indicates the low energy boundary of the domain for electron-hole pair excitations. The dash-dotted lines indicate parallel wave-vector transfer for different primary electron-beam energies (eV).

Debye-Hückel model (Fig. 1, curve b) runs between those of the two former models. From this observation it follows, that the bulk free-electron density in the Drude model has to be significantly higher than that in the Thomas-Fermi (or Debye-Hückel) model in order to fit the same surface plasmon energy. Further analysis of the dispersion relations shows, that the Thomas-Fermi model predicts a decrease of the plasmon energy when a higher primary electron-beam energy is applied within a certain range, in contrast to the Drude model.

The plasmon damping factor obtained from the best fit by the Drude model is higher than that estimated in the frame of the Thomas-Fermi model. This discrepancy is attributed to the absence of plasmon peak broadening due to the plasmon dispersion in the Drude model. Thus, the Thomas-Fermi model, which takes into account the spatial plasmon dispersion, allows a distinction between broadening caused by dispersion and intrinsic broadening by scattering of free electrons on ionized dopants and phonons. It is worth mentioning, that broadening of the plasmon peak due to dispersion is caused by the limited sizes of the acceptance aperture of the HREELS-system.

We fitted the experimental energy-loss spectra for MBE-growth GaAs (100)-c(4 × 4) in the frame of the Thomas-Fermi (Fig. 2a), Debye-Hückel and Drude (not shown here) models by varying the bulk free-electron density and depletion layer width to fit the plasmon peak position. Despite a good agreement between theory and experiment, the main parameters fitted are rather different (Table 1), in accordance with the discussion above.

We analyzed in detail experimental data on high-doped GaAs (100) samples, which were post-annealed after the growth at elevated temperatures and/or exposed to atomic hydrogen. After annealing the sample at the temperature of 850 K, the free-electron density is reduced from 8.8×10^{18} to $2.9 \times 10^{18} \text{ cm}^{-3}$. This is indicated by a drastic downward shift of the plasmon energy from 106 meV (Fig. 2a) to 65 meV (Fig. 2b). Simultaneously, the As-rich c(4 × 4)-surface is converted to the Ga-rich c(8 × 2)-surface. We assume that this

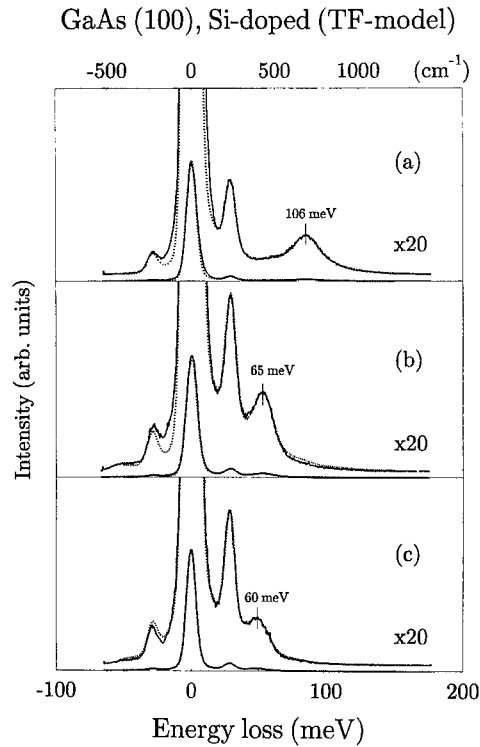


Fig. 2. (a) Calculated by Thomas–Fermi model (dashed line) and experimental (solid line) energy-loss spectra for GaAs (100)-c(4×4): $E_0 = 6.5$ eV, $\vartheta_i = 45^\circ$. (b) Same as in (a), but for GaAs (100)-c(8×2). For further details see text. (c) Same as in (b), but after subsequent hydrogen exposure of 10^5 L (1 Langmuir = 1 Torr s). At this stage the LEED-pattern shows a (1×1)-structure.

strong free-electron compensation is caused by indiffusion of the native acceptor-like defects, formed at the surface during heating of the sample. Further details are discussed in [36]. After the annealing the sample was exposed to hydrogen up to 10^5 L. The hydrogenation of GaAs (100) is accompanied by effective indiffusion of hydrogen atoms, chemically bonding to silicon dopants [14]. Due to this process the free-electron density decreases, which results in a further downward shift of the plasmon energy from 65 to 60 meV (Fig. 2c).

Table 1

Parameters after fitting the HREELS spectrum from the homogeneously doped GaAs(100)-c(4×4) sample using different models: Drude, Debye–Hückel, Thomas–Fermi. The values listed are: $\hbar\omega_{pl}$ — measured plasmon energy, n — electron density, d — depletion layer width, Γ — plasmon damping constant, μ_n — electron mobility, V_{bb} — band bending, Q_{ss} — density of occupied surface states, m^* — effective electron mass

Parameter	Drude model	Debye–Hückel model	Thomas–Fermi model
$\hbar\omega_{pl}$ (meV)	106	106	106
n (10^{18} cm $^{-3}$)	17.3	11.5	8.8
d (Å)	75	60	45
Γ (meV)	30	26	21
μ_n (cm 2 /V·s)	340	460	630
V_{bb} (meV)	745	315	155
Q_{ss} (10^{12} cm $^{-2}$)	13.5	7.0	4.0
m^* (m_0)	0.114	0.097	0.089

3. Delta-doped GaAs (100): dopant spreading estimation

The present study of delta-doped GaAs (100) has been motivated by investigations of delta-doped semiconductors by virtue of different techniques as secondary-ion mass spectrometry (SIMS) [18–24], magneto-transport measurements [25], capacitance–voltage ($C-V$) profiling [26–28] and Raman spectroscopy [29]. First investigations by HREELS [17,30] demonstrated that this very surface-sensitive technique may provide information upon spatial donor spreading and free-carrier density profiles of delta-doped layers in the vicinity of the surface, whereas other techniques mentioned above are limited when applying to the near-surface region.

To calculate theoretically HREELS-spectra for the delta-doped structures a knowledge of the electron-density profile is needed. In delta-doped n-type GaAs the silicon atoms are spread within the region from several tens to a few hundred ångström centered in the vicinity of the intended ideal doping plane. The electrons released from silicon atoms experience the Coulomb interaction with their parent ionized donors. This leads to a confinement of electrons in the potential well formed by dopants. If the confining potential is strong enough, the electron de Broglie wavelength is comparable to the width of the potential well. As a result, the electron motion in a direction perpendicular to the surface is quantized and an energy subband structure is formed. In order to obtain the electron-density profile we adopt the effective-mass approximation in the slab geometry [31]. The positive background of ionized dopants is presented by two Gaussians or rectangles, placed at equal depths beneath both sides of the slab.

The dopant distribution of the high-doped sample #17 is considered as Gaussian due to the expected wider spatial spreading. First, we assume an initial distribution at time $t = 0$ given by the delta-function

$$n_D(t, z)|_{t=0} = N_D \delta(z - z_0),$$

where N_D is the total areal density of electrically active dopant atoms and z_0 is a position of the doping plane.

The solution of the diffusion equation in the presence of the non-transparent boundary at the surface for the diffusing dopants is given by

$$\begin{aligned} n_D(t, z) &= \frac{4N_D}{w_1 + w_2} \sqrt{\frac{\ln 2}{\pi}} \exp \left[-\frac{(z - z_0)^2 4 \ln 2}{w_1^2} \right] && \text{for } z \geq z_0, \\ &= \frac{4N_D}{w_1 + w_2} \sqrt{\frac{\ln 2}{\pi}} \exp \left\{ \left[-\frac{(z - z_0)^2 4 \ln 2}{w_2^2} \right] + \exp \left[-\frac{(z + z_0)^2 4 \ln 2}{w_2^2} \right] \right\} && \text{for } 0 \leq z < z_0. \end{aligned} \quad (6)$$

where w_1^2 and w_2^2 are the widths of the right and the left halves of the total asymmetric Gaussian distribution, respectively, considered in the absence of the boundary. These values are related to the diffusion coefficients in both directions from the initial doping plane as

$$w_1 = 4\sqrt{\ln 2 D_1 t} \quad \text{and} \quad w_2 = 4\sqrt{\ln 2 D_2 t},$$

where D_2 and D_1 are the diffusion coefficients in the growth direction and back from the initial doping plane, respectively.

Since the surface boundary restricts the diffusion process in the growth direction, one obtains an accumulation of the dopants beneath the surface even in the case of the equality of the diffusion coefficients D_1 and D_2 , when the doping plane is placed close to the surface. The Eq. (6) defines an asymmetric dopant distribution, used in the self-consistent calculation of the electron-density profile.

At our growth temperature of 550°C (lower than the temperature explored by Lohe et al. [17] and subsequent thermal decapping of the As-passivation overlayer, which would cause an additional diffusion, was not necessary due to UHV transfer between growth chamber and HREELS spectrometer) we obtain the best ordered GaAs(100) layers as observed in our RHEED and LEED experiments when compared to lower growth temperatures. In addition Köhler et al. [37] reported a higher sheet carrier concentration for the same Si-doping

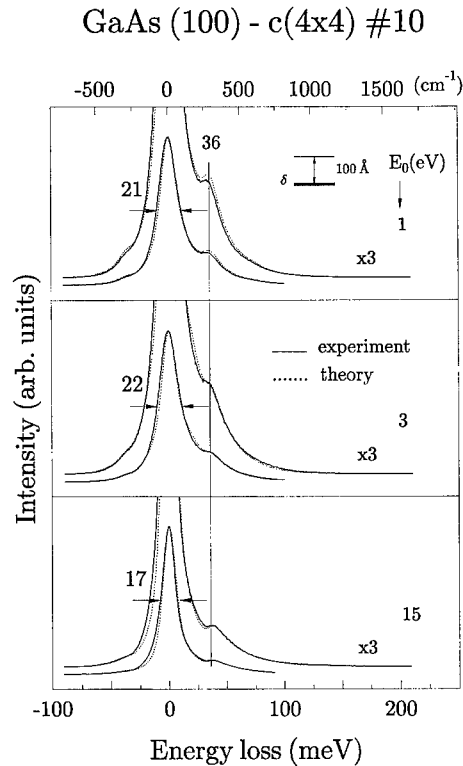


Fig. 3. The measured (solid lines) and the fitted (dotted lines) energy-loss spectra for primary beam energies $E_0 = 1, 3$ and 15 eV for the low-doped sample #10 with the doping plane at a depth of 100 \AA . The rectangular-shaped dopant distribution with $w = 40 \text{ \AA}$, the density of electrically active dopants $N_D = 8.0 \times 10^{12} \text{ cm}^{-2}$, and the free-electron density $N_E = 1.5 \times 10^{12} \text{ cm}^{-2}$ were estimated from the fitting.

level than for lower growth temperatures, whereas the Si-spreading is decreasing with lower growth temperatures. For these reasons, when fitting the measured energy-loss spectra of the low-doped sample #10, based on the smooth electron-density profile (approximated by a set of 20 sublayers), a symmetric spreading of the dopant atoms near the intended doping plane was assumed. Both rectangular and Gaussian distributions of dopant atoms were used in the calculations and no notable difference was found. During the fitting, first for the primary beam energy 9 eV , we adjusted the areal density of the electrically active dopants N_D , the width of the rectangular dopant spreading w , the surface trapped charge density N_s and the plasmon damping Γ . For the other primary beam energies only the plasmon damping was changed to obtain the best fits to the experimental data. The fitted energy-loss spectra for different primary energies are shown in Fig. 3.

The same fitting scheme was applied for the low-doped sample #11 with the intended doping plane at 200 \AA depth (Fig. 4) and for the high-doped 100 \AA depth sample #17 (Fig. 5). In the latter case, we assumed the ratio w_2/w_1 of 1.5 , i.e. the ratio D_2/D_1 of 2.25 between the diffusion coefficients of dopants towards the surface and backward from the doping plane, respectively. In this fashion, we simulated the preferential diffusion in the growth direction (segregation) [32], which is expected to be strong in the case of high doping. This results in a strong asymmetric distribution of the dopants with respect to the initial doping plane. The calculated self-consistent electron-density profile for the high-doped 100 \AA depth sample #17 is shown in Fig. 6. It should be noted, that even an approximation of the dopant spreading by a Gaussian with equal diffusion coefficients in both directions from the doping plane (Eq. 6) can result in an appreciable asymmetry of the dopant distribution if a doping plane is positioned close to the surface.

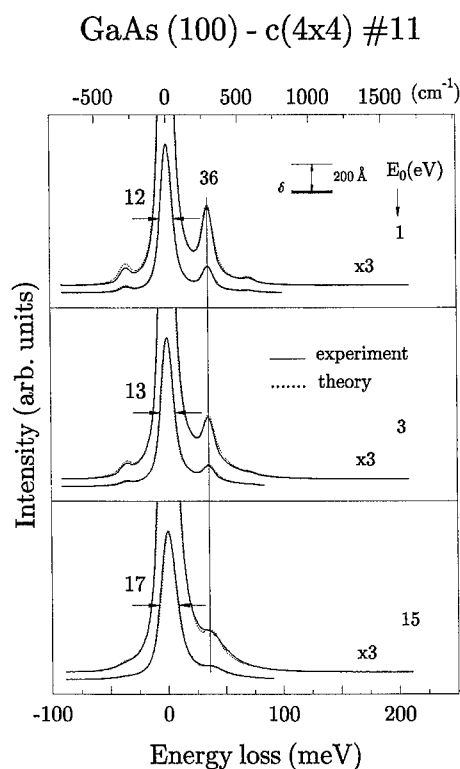


Fig. 4. The same as in Fig. 3, but for the low-doped sample #11 with the doping plane at a depth of 200 Å. The parameters $w = 80$ Å, $N_D = 8.0 \times 10^{12} \text{ cm}^{-2}$ and $N_E = 4.6 \times 10^{12} \text{ cm}^{-2}$ were estimated from the fitting.

The parameters of the dopant spreading and calculated electron-density profiles for all samples investigated are summarized in Table 2.

The fitted plasmon damping factors for all samples studied are presented in Table 3, where the probing depths of the phonon mode ω_0 are given too. The probing depth (effective spatial extent of the polarization electric field from the surface inward the bulk) can be roughly estimated [6] as $1/q_{\parallel}$ with $q_{\parallel} = (2m_0/\hbar^2)^{1/2} [E_0^{1/2} - (E_0 - \omega_0)^{1/2}] \sin \theta_i$.

The most striking feature of this data is the significant decrease of the plasmon damping at the low primary energies for the low-doped samples #10 and #11 (see Table 3). Such a decrease can be attributed to the spatial separation between the phonon mode, localized closely to the surface (for instance, the probing depth of the

Table 2
Summary of the dopant spreading parameters for the different delta-doped GaAs (100) samples (#10, #11 and #17). The values listed are: z_0 — depth of the initial doping plane, N_D — areal density of the electrically active dopant atoms, N_E — areal density of electrons in the conduction band, w — full width at a half maximum (FWHM) of the dopant distribution, $(E_C - E_F)_{\text{surf}}$ — Schottky barrier height

Sample	z_0 (Å)	N_D (cm^{-2})	N_E (cm^{-2})	w (Å)	$(E_C - E_F)_{\text{surf}}$ (eV)
#10	100	8.0×10^{12}	1.5×10^{12}	40 (rectangle)	0.72
#11	200	8.0×10^{12}	4.6×10^{12}	80 (rectangle)	0.73
#17	100	1.5×10^{13}	4.9×10^{12}	$w_1 = 100, w_2 = 150$	0.71

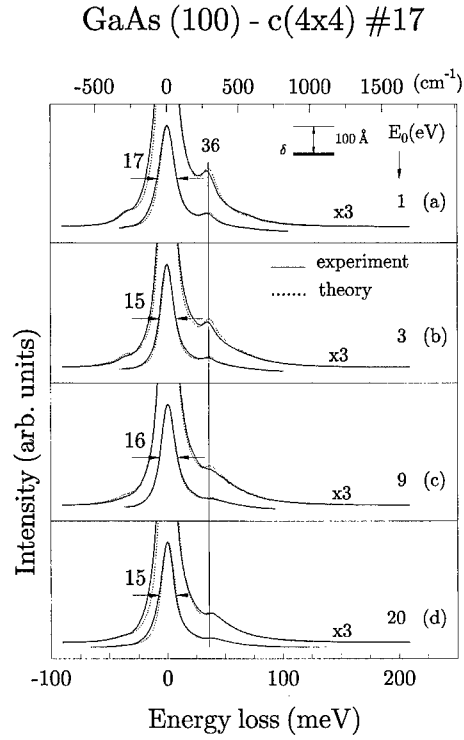


Fig. 5. The same as in Fig. 3, but for the high-doped sample #17 with the doping plane at a depth of 100 Å and for primary beam energies $E_0 = 1, 3, 9$ and 20 eV. The asymmetric Gaussian-shaped dopant distribution with $w_1 = 100$ Å and $w_2 = 150$ Å was estimated.

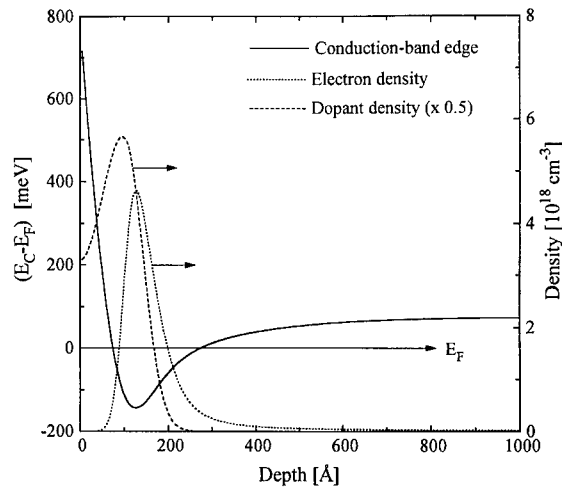


Fig. 6. The self-consistent electron-density profile (dotted line) and the conduction-band edge relative to the Fermi energy E_F (solid line) are displayed. The asymmetric Gaussian-shaped dopant distribution (dashed line), used when solving the Schrödinger and the Poisson equations, is shown too.

Table 3
The dependence of the plasmon damping factor Γ on the primary electron-beam energy E_0 for the different delta-doped GaAs (100) samples (#10, #11 and #17). The probing depths for the phonon mode $\hbar\omega_0 = 36$ meV are shown too

E_0 (eV)	Sample #10 Γ (meV)	Sample #11 Γ (meV)	Sample #17 Γ (meV)	Probing depth (\AA) for $\omega_0 = 36$ meV
0.5	8.7	9.9	18.6	89
1	6.0	5.0	16.1	126
3	5.6	8.7	12.4	220
6.5	31.0	14.9	—	325
9	26.7	21.1	21.1	382
12	19.8	22.3	21.1	441
15	19.8	27.3	17.4	493
20	13.6	—	21.1	570

phonon mode ω_0 is 126 \AA for $E_0 = 1$ eV) and the plasmon mode, confined within the potential well, formed by ionized dopants at depths of 100 \AA and 200 \AA for these two samples, respectively. One can also conclude from this finding, that a scattering of plasmon excitations on the optical phonons at room temperature is dominant, if compared to the scattering on the ionized dopants. In the case of the high-doped samples the spatial separation mentioned above is less, and thus such a decrease of the plasmon damping was not observed.

In summary of this section, we presented results of HREELS-investigations of the delta-doped GaAs (100) samples MBE-grown at 550°C with different doping levels and doping plane depths. From the comparison with the calculated spectra the dopant spreading has been estimated. It was shown that in low-doped samples the symmetric dopant distribution near the initial doping plane provides good fits to measured energy-loss spectra for the applied set of the primary electron-beam energies. In contrast, for high-doped samples the asymmetry in the dopant distribution was assumed to simulate a possible segregation process. This was done by virtue of the asymmetric Gaussian, which is a solution of the diffusion equation in the non-transparent surface boundary conditions for diffusing dopants.

The significant decrease of the plasmon damping at low primary beam energies for the low-doped samples is ascribed to a spatial separation between the surface optical phonon mode, strongly localized near the surface and plasmon excitations, confined within the potential well, positioned at 100 \AA and 200 \AA from the surface for samples #10 and #11, respectively. This provides additional evidence that scattering of free electrons on the optical phonons is dominant at room temperature [33–35].

Acknowledgements

One of the authors (V.M.P.) gratefully acknowledges the financial support of the Heraeus foundation and of the Deutsche Forschungsgemeinschaft.

References

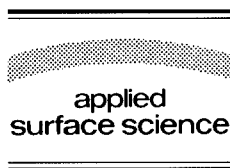
- [1] E.H. Rhoderick and R.H. Williams, *Metal–Semiconductor Contacts* (Clarendon, Oxford, 1988).
- [2] H. Lüth, *Surfaces and Interfaces of Solids* (Springer, Berlin, 1993).
- [3] W. Mönch, *Semiconductor Surfaces and Interfaces* (Springer, Berlin, 1993).
- [4] H. Lüth, *Festkörperprobleme/Advances in Solid State Physics*, Vol. 21, Ed. J. Treusch (Vieweg, Braunschweig, 1981).
- [5] H. Lüth, *Vacuum* 38 (1988) 233.
- [6] H. Ibach and D.L. Mills, *Electron Energy Loss Spectroscopy and Surface Vibrations* (Academic Press, New York, 1982).
- [7] D.H. Ehlers and D.L. Mills, *Phys. Rev. B* 34 (1986) 3939; S.R. Streight and D.L. Mills, *Phys. Rev. B* 37 (1988) 965.
- [8] Ph. Lambin, J.P. Vigneron and A.A. Lucas, *Phys. Rev. B* 32 (1985) 8203; *Comput. Phys. Commun.* 60 (1990) 351.

- [9] B. Rösen, H.Ch. Schäfer, Ch. Dieker, A. Rizzi and D. Gerthsen, *J. Vac. Sci. Technol. B* 11 (1993) 1407.
- [10] D.G. Kilday, G. Margaritondo and G.J. Lapeyre, *J. Vac. Sci. Technol. A* 8 (1990) 2755; Y. Chen, S. Nannarone, J.A. Schaefer, J.C. Hermanson and G.J. Lapeyre, *Phys. Rev. B* 29 (1989) 7653; Y. Chen, J.C. Hermanson and G.J. Lapeyre, *Phys. Rev. B* 39 (1989) 12682.
- [11] S.M. Sze, *Physics of Semiconductor Devices* (Wiley, New York, 1981).
- [12] W.L. Schaich, *Surf. Sci.* 122 (1982) 175.
- [13] Z. Penzar and M. Sunjic, *Phys. Scr.* 30 (1984) 631.
- [14] B. Pajot, R.C. Newman, R. Murray, A. Jalil, J. Chevallier and R. Azoulay, *Phys. Rev. B* 37 (1988) 4188; L. Pavesi, P. Giannozzi and F.K. Reinhart, *Phys. Rev. B* 42 (1990) 1864; L. Pavesi and P. Giannozzi, *Phys. Rev. B* 43 (1991) 2446; P.R. Briddon and R. Jones, *Phys. Rev. Lett.* 64 (1990) 2535.
- [15] Z.J. Gray-Grychowski, R.A. Stradling, R.G. Egdell, P.J. Dobson, B.A. Joyce and K. Woodbridge, *Solid State Commun.* 59 (1986) 703; Z.J. Gray-Grychowski, R.G. Egdell, B.A. Joyce, R.A. Stradling and K. Woodbridge, *Surf. Sci.* 186 (1987) 482.
- [16] R. Biagi, C. Mariani and U. del Pennino, *Phys. Rev. B* 46 (1992) 2467; U. del Pennino, R. Biagi and C. Mariani, *Appl. Surf. Sci.* 56–58 (1992) 44.
- [17] C. Lohé, A. Leuther, A. Förster and H. Lüth, *Phys. Rev. B* 47 (1993) 3819.
- [18] R.B. Beall, J.B. Clegg and J.J. Harris, *Semicond. Sci. Technol.* 3 (1988) 612.
- [19] A.M. Lanzillotto, M. Santos and M. Shayegan, *Appl. Phys. Lett.* 55 (1989) 1445.
- [20] E.F. Schubert, H.S. Luftman, R.F. Kopf, R.L. Headrick and J.M. Kuo, *Appl. Phys. Lett.* 57 (1990) 1799.
- [21] Ph. Jansen, M. Meuris, M. Van Rossum and G. Borghs, *J. Appl. Phys.* 68 (1990) 3766.
- [22] A.M. Lanzillotto, M. Santos and M. Shayegan, *J. Vac. Sci. Technol. A* 8 (1990) 2009.
- [23] M. Santos, T. Sajoto, A.M. Lanzillotto, A. Zrenner and M. Shayegan, *Surf. Sci.* 228 (1990) 255.
- [24] H.C. Nutt, R.S. Smith, M. Towers, P.K. Rees and D.J. James, *J. Appl. Phys.* 70 (1991) 821.
- [25] A. Zrenner, F. Koch and K. Ploog, *Surf. Sci.* 196 (1988) 671.
- [26] E.F. Schubert, J.B. Stark, B. Ullrich and J.E. Cunningham, *Appl. Phys. Lett.* 52 (1988) 1508.
- [27] A. Zrenner, *Appl. Phys. Lett.* 55 (1989) 156.
- [28] E.F. Schubert, R.F. Kopf, J.M. Kuo, H.S. Luftman and P.A. Garbinski, *Appl. Phys. Lett.* 57 (1990) 497.
- [29] J. Wagner, M. Ramsteiner, W. Stolz, M. Hauser and K. Ploog, *Appl. Phys. Lett.* 55 (1989) 978.
- [30] R. Biagi and U. del Pennino, *Phys. Rev. B* 50 (1994) 7573.
- [31] S.R. Streight and D.L. Mills, *Phys. Rev. B* 37 (1988) 965.
- [32] E.F. Schubert, J.M. Kuo, R.F. Kopf, A.S. Jordan, H.S. Luftman and A.S. Hopkins, *Phys. Rev. B* 42 (1990) 1364.
- [33] K. Hirakawa and H. Sakaki, *Phys. Rev. B* 33 (1986) 8291.
- [34] P.J. van Hall, T. Klaver and J.H. Wolter, *Semicond. Sci. Technol.* 3 (1988) 120.
- [35] W. Walukiewicz, H.E. Ruda, J. Lagowski and H.C. Gatos, *Phys. Rev. B* 30 (1984) 4571.
- [36] V. Polyakov, A. Elbe and J.A. Schaefer, *Appl. Phys. A* 60 (1995) 567.
- [37] K. Köhler, P. Ganser and M. Maier, *J. Cryst. Growth* 127 (1993) 720.



ELSEVIER

Applied Surface Science 104/105 (1996) 35–44



Kinematical RHEED simulation of different structure models for the GaAs (311)A surface

W. Braun^{*}, O. Brandt, M. Wassermeier, L. Däweritz, K. Ploog

Paul-Drude-Institut für Festkörperelektronik, Hausvogteiplatz 5–7, D10117 Berlin, Germany

Received 28 June 1995; accepted 25 October 1995

Abstract

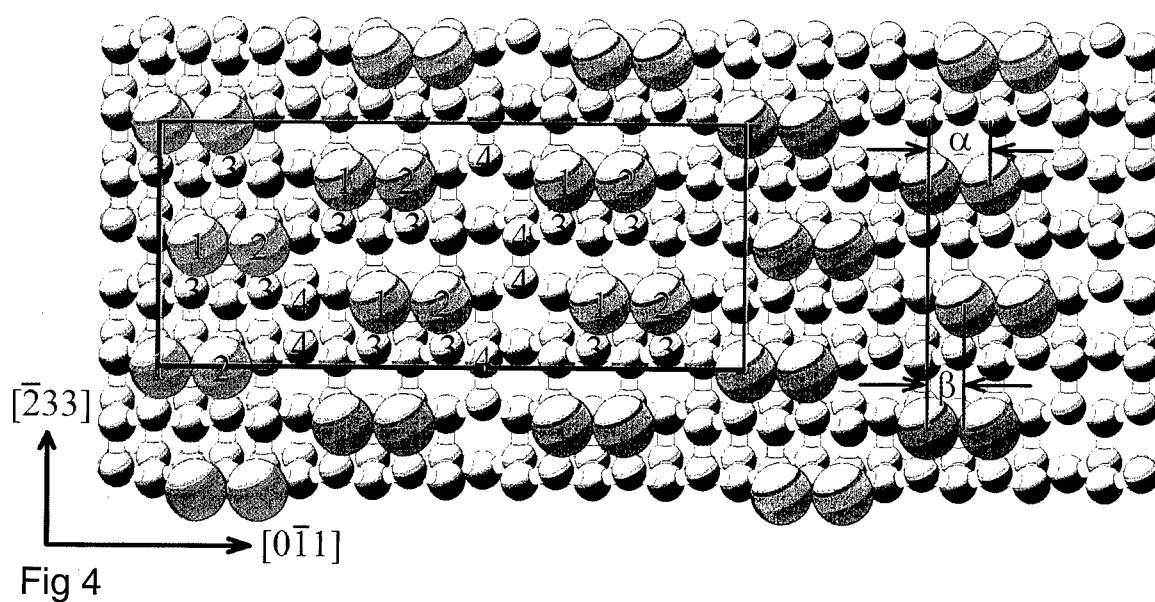
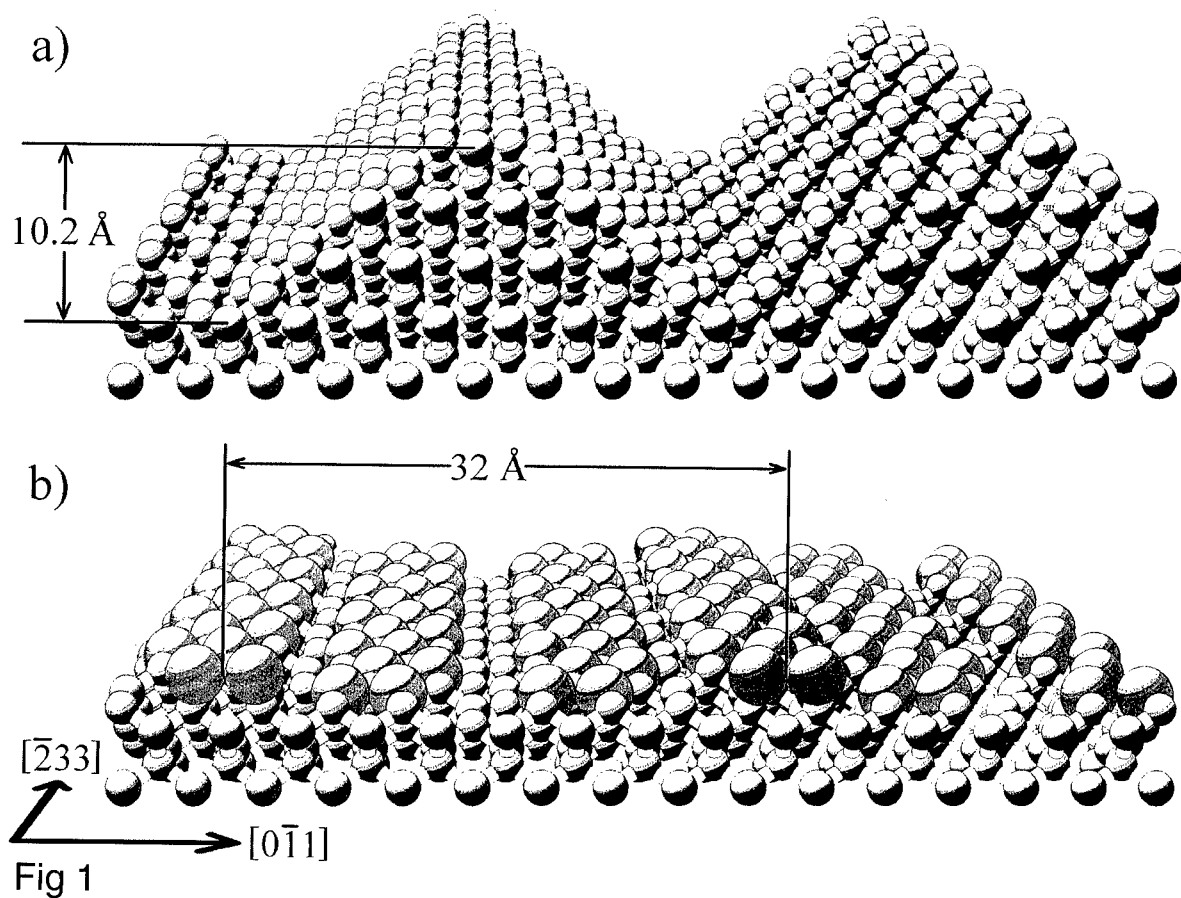
We compare two different structure models proposed recently for the GaAs (311)A surface using kinematical calculations of their reflection high-energy electron diffraction (RHEED) patterns. Whereas for one structure the calculated pattern does not fit very well, the agreement between calculation and experimental pattern is excellent for the other and allows even structural refinement of the relaxation parameters. Consideration of only the topmost atoms of the surface in the calculation yields the best agreement with the RHEED pattern, which indicates a very small sampling depth of RHEED. Therefore, at least in special cases, the kinematical theory is a valid approximation to calculate RHEED patterns.

Reflection high-energy electron diffraction (RHEED) is widely used as a sensitive technique for the in situ investigation of surface structures and growth processes in molecular beam epitaxy (MBE). The theoretical understanding and ability to model the observed phenomena, however, has not yet evolved to an accuracy comparable to other electron diffraction methods. In low electron diffraction (LEED) [1] or transmission electron microscopy (TEM), theoretical simulations can be used as reliable tools for structure determination or chemical lattice imaging [2]. The situation encountered in the case of RHEED is more complicated, mainly due to the effects of the glancing incidence at low angles. The interaction volume is strongly elongated along the beam and comprises many scatterers. Multiple

scattering events thus cannot generally be neglected and only dynamical calculations are expected to be appropriate [3]. These calculations are complex and computationally intensive. Moreover, the iterative algorithms employed do in general not converge due to the artificial truncation of the unit cell, and special corrective measures need to be taken [4].

Since the input to RHEED calculations, like possible surface unit cell configurations, already represents a multi-dimensional parameter field and the calculation itself contains still more fitting parameters, a comparison of different surface structure models with experiment is not straightforward. As a consequence of this inherent problem, there is an ongoing debate about the reliability of the obtained results [5,6]. For example, dynamical calculations showed good agreement with the three-dimer structure for the $\beta(2 \times 4)$ reconstruction of the GaAs (100) surface [7,8], but atomic resolution STM measurements revealed the two-dimer structure [9,10],

^{*} Corresponding author. Tel.: +49-30-20377356; fax: +49-30-20377201; e-mail: braun@pdi.wias-berlin.de.



supported by recent first-principles calculations [11].

In this paper, we discuss two surface structure models for the GaAs (311)A surface proposed recently by comparing their kinematically calculated diffraction patterns to the observed RHEED intensity distribution. We assume that if the two structure models are sufficiently different, even kinematical theory should be sensitive enough to show distinct differences between the respective RHEED patterns. The obtained results indeed demonstrate that the kinematical theory is sufficient to describe most features of the experimental RHEED pattern and that the fit is even sensitive enough to perform structure refinement.

The two different proposed structure models for the GaAs (311)A surface are shown in Fig. 1 with the viewing direction along the $[\bar{2}33]$ azimuth. Green and blue spheres indicate As and Ga atoms, respectively. Fig. 1a represents the model proposed by Nötzel et al. [12,13], which is based on the assumption that the (311) surface reconstructs into two sets of (331) and (313) facets because of the lower surface energy of these facet planes compared to (311). Together with the 32 Å periodicity along $[0\bar{1}1]$, this leads to a corrugation height of 10.2 Å. We refer to this model as model A. The second model, proposed by Wassermeier et al. [14], is shown in Fig. 1b. It is based on scanning tunnelling microscopy (STM) observations and the requirement that both excess charge density and dangling bond density are minimized. The As atoms are assumed to dimerize along $[0\bar{1}1]$ similar to the (100) surface, as indicated by the oversized blue spheres in Fig. 1b. Even and odd dimers along $[\bar{2}33]$ are shifted towards each other in the $[0\bar{1}1]$ direction, creating zigzagging rows of As dimers. This structure will be referred to as model B. Whereas the lateral periodicities of both structures are identical, the depth modulation of model B is only 3.4 Å, i.e., 1/3 of model A.

Two experimental RHEED patterns of the GaAs (311)A structure are shown in Fig. 2 taken along the $[\bar{2}33]$ azimuth with an acceleration voltage of 20 kV in both cases. For both samples, optimum growth conditions for GaAs (311)A were used, which we found to be at slightly less As pressure and about 25°C higher sample temperature than the optimum for the GaAs (100) $\beta(2 \times 4)$ reconstruction. The samples differ in the miscut angle, which is 0.9 degrees towards the RHEED screen in (a) and negligible for the purposes of our study in (b). For comparison with the simulations, a length marker corresponding to the reciprocal lattice constant of bulk GaAs is included in the photograph. The construction of model A was based on samples unintentionally miscut by an angle similar to (a). These samples show a triple splitting of the (00) rod close to the X-shaped Kikuchi line crossing from which the corrugation amplitude was deduced. While even for on-axis substrates a dual splitting can be observed due to the cut of the Ewald sphere at finite angle, additional structure arises from misorientation. A detailed discussion of misorientation and defect structure effects leading to this additional modulation will be presented in a separate publication.

The kinematic scattering theory is based on the assumption that multiple diffraction processes can be neglected. This is equivalent to the application of first-order perturbation theory. The diffracted intensity is proportional to $|F(\mathbf{G})|^2$, where $F(\mathbf{G})$ denotes the scattering amplitude for a pair of incident and scattered wave vectors differing by a reciprocal lattice vector \mathbf{G} . The calculation of $F(\mathbf{G})$ involves the summation of the phase factors of the waves scattered from the volume elements inside the interaction volume. Taking advantage of the crystal periodicity, the problem can be separated into the construction of the reciprocal lattice that determines the positions of the possible reflections and the calculation of the

Fig. 1. Two proposed models for the GaAs (311)A surface reconstruction. (a) shows model A by Nötzel et al. [12] with a corrugation of 10.2 Å, (b) model B by Wassermeier et al. [14] The dark blue spheres represent Ga atoms, the green spheres As atoms. As dimers are indicated by large light blue spheres.

Fig. 4. Surface of the B model in top view. The unit cell of the reconstruction is indicated by the rectangle. The red numbers denote the equivalent atoms included in the various calculations. Relaxation of the dimerized As atoms was modeled by the fitting parameters α and β .

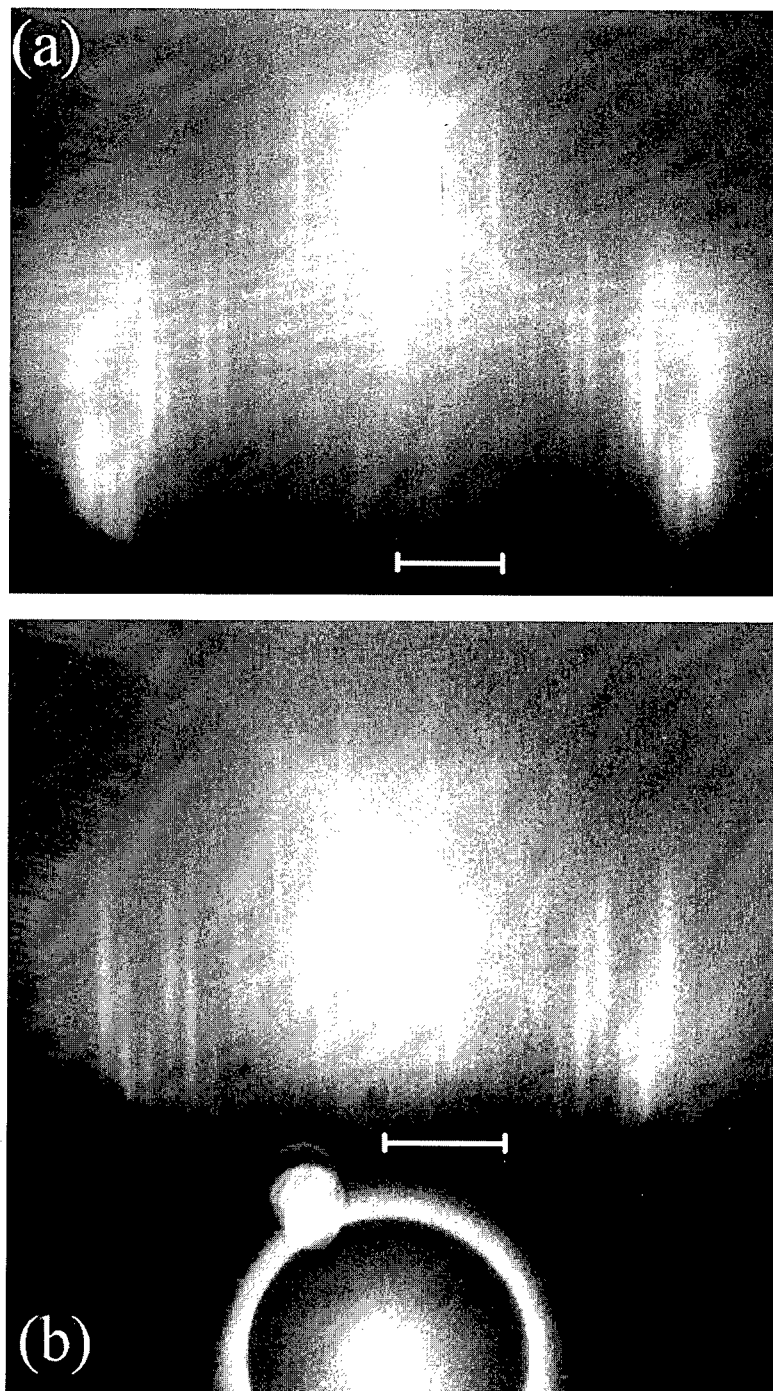
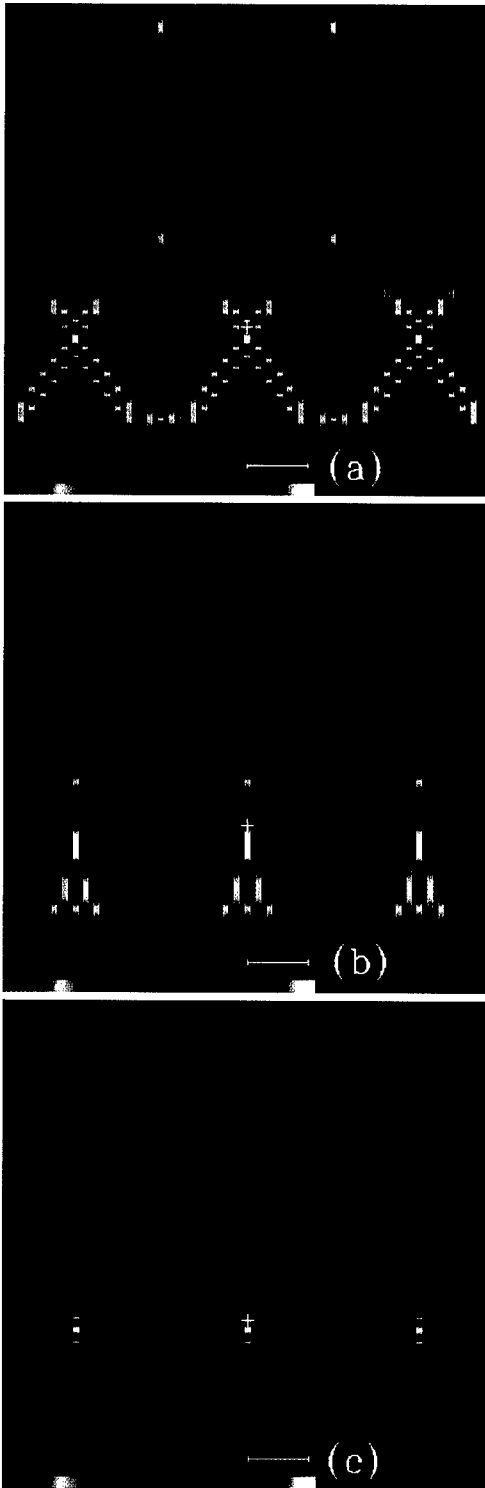


Fig. 2. Experimental RHEED patterns of the GaAs (311)A surface reconstruction. The observation direction is along the $[\bar{2}33]$ azimuth with an acceleration voltage of 20 kV and an incidence angle of 1.4° for (a) and $1.5(2)^\circ$ for (b) at a sample temperature of 605°C . The length of the marker corresponds to the reciprocal lattice constant of bulk GaAs. While (b) is exactly oriented, the sample used in (a) is miscut by 0.9° towards the RHEED screen. Samples unintentionally miscut by approximately the same angle were used in the study of Nötzel et al. [12].



structure factor for every reciprocal lattice point, which determines the intensity of the respective reflection. In the quasi-2D RHEED case, the reciprocal lattice consists of rods perpendicular to the surface. Therefore, the reciprocal lattice index perpendicular to the surface becomes a continuous variable. The scattering amplitude can then be written as

$$F(\mathbf{G}_{\parallel}, \gamma, s) = A \sum_i u_i(s) \exp(-B_i s^2) \times \exp[i(\mathbf{G}_{\parallel} \mathbf{r}_{i\parallel} + \gamma \mathbf{r}_{i\perp})]$$

where the subscripts \parallel and \perp denote the surface parallel and surface normal components of the respective vectors, \mathbf{r} and \mathbf{G} are discrete real-space and reciprocal-space vectors, γ is the continuous reciprocal space coordinate normal to the surface, and i is the summation index counting the scatterers inside the surface unit cell. The parameter s is defined as $s = (\sin \theta)/\lambda$; λ being the electron wavelength and θ denoting the angle between the incident and the scattered wave vector. For the scattering factors u_i , the Doyle–Turner formula was used [15]. The Debye–Waller factors [16] $\exp(-B_i s^2)$ describe the loss of intensity due to the thermal vibration of the lattice. For our purpose, they turn out not to be very important since the constant A is normalized to the maximum intensity and the Doyle–Turner scattering factors have the same dependence on s as the Debye–Waller attenuation.

The experimentally observed RHEED pattern is not the reciprocal lattice plane obtained by the calculations, but the intersection of this plane with the Ewald sphere. Within the approximations of our model, this intersection would yield a row of points on the Laue circle. In the experiment, however, both the reciprocal lattice rods and the Ewald sphere are broadened. Since at low angles the cut of the Ewald sphere through the reciprocal lattice plane is also almost parallel to this plane, the experimental image

Fig. 3. Simulated RHEED patterns in the $[\bar{2}33]$ azimuth (a) of model A, (b) model B and (c) 11 ML of bulk material. The markers represent the reciprocal lattice constant of GaAs, a hair cross marks the position of the specular spot for an incidence angle of 1.52° . The false colour conversion is given at the bottom of the squares with green and purple representing low and high intensities, respectively.

shows a wide region of the reciprocal lattice plane close to the origin instead of a row of points. The resulting two-dimensional intensity distribution includes many more data points and therefore allows a much better fit to the theoretical pattern. We therefore use the intensity distribution on the whole first-order plane for comparison with the experiment. One has to keep in mind, though, that intensities closer to the exact Laue circle position are higher when comparing the experiment with the intensity distribution of the reciprocal lattice. Since we assume perfect periodicity parallel to the surface plane, the rods are truly one-dimensional. Their width in the simulated pictures is arbitrarily adjusted for good visibility, but has no physical significance.

The calculation of a reciprocal lattice plane using the kinematical model takes a few min on a PC and therefore allows the fast inspection of a large number of possible unit cell configurations. Our starting point for comparing the two (311)A surface models are unrelaxed structures with both the surface As and Ga atoms at bulk positions. For simplicity, the Doyle–Turner factors were set to unity, since in first order they only introduce an intensity envelope decaying exponentially with the radial distance from the primary beam (000) spot. Only the surface Ga and As atoms are included in this first approximation which are those visible on the top of the structures of Fig. 1. The results are shown in Fig. 3a for model A and in Fig. 3b for model B. Fig. 3c shows a simulation of 22 layers (11 As and 11 Ga) of bulk material for comparison. Incidence angle and scale of the simulations are matched to the experimental picture given in Fig. 2b. The simulated images show a higher dynamic range compared to the experiment due to the neglect of disorder in the calculations. To show as many levels as possible, we have used a false colour representation shown in the horizontal bar at the bottom of each picture. The green end of the scale corresponds to low intensity, high intensity is shown purple-white. Both simulations (a) and (b) include the bulk spots since they are subsets of (c). Model A (a) exhibits a splitting of all streaks with a period corresponding to $2\pi/10.2 \text{ \AA}$ as expected for a two-level system [17]. Although the facet planes are narrow, emerging facet streaks perpendicular to the (331) and (313) begin to form as a modulation of the reconstruction streaks. None of these features are

present in the experimental intensity distribution of Fig. 2b. All streaks show a slowly varying intensity distribution normal to the surface. No clear evidence of the facet streaks can be seen. The X-shaped intensity enhancement centred about 0.5° above the specular spot is due to Kikuchi lines. Only streaks #8 to #13, counting from (00), resemble the simulated facet streaks, but they constitute a much lower angle towards the surface normal than expected for model A, rather resembling the angle present in model B. In addition, the simulation of Fig. 3a predicts dark areas opening on both sides next to the specular position as well as a strong reflection on the #8 streak close to the shadow edge. Both features are not seen in Fig. 2. The model B simulation of Fig. 3b is in closer agreement with the experimental pattern. The streak modulation is of about the same period, and there is some intensity adjacent to the specular beam position. Several streaks already show a staircase structure similar to streaks #8 through #13 in Fig. 2b.

Whenever more bulk atoms are included in simulating either the Nötzel or the Wassermeier structure, the pattern approaches Fig. 3c. The reconstruction features weaken and the relative intensity of the bulk reflection increases. The experimental picture, however, shows high intensity on the reconstruction reflections which is comparable to the intensity on the bulk streaks. Also, the modulation of the streaks along the surface normal is lower in Fig. 3b and Fig. 2b compared to the simulation of 22 bulk layers in Fig. 3c. This means that the intensity distribution present in Fig. 2b is dominated by the surface atoms of the reconstruction. Since the simulation of Fig. 3b is already closer to the bulk picture than the experimental pattern, we can conclude that less atoms participate in the formation of the experimental pattern and that the surface atoms relax from their bulk positions, thus redistributing intensity into the reconstruction streaks. In fitting the calculated pattern for model B to the observed one, we therefore employ two sets of fitting parameters, namely the number of scatterers and the relaxation of the surface atoms.

A top view of model B is given in Fig. 4. The unit cell of the surface reconstruction is indicated by the black rectangle. The larger blue spheres, similar to Fig. 1, denote the top As atoms that are assumed to form dimers similar to the (100) surface. Since

these atoms are able to relax along $[0\bar{1}1]$, the two fitting parameters α and β are introduced to describe these displacements, α denoting the dimer bond length and β describing the relative displace-

ment of the two sub-rows along $[\bar{2}33]$. For the unrelaxed structure with the top As atoms at bulk positions, $\alpha = 4 \text{ \AA}$ and $\beta = 2 \text{ \AA}$. The simplest approximation to the structure is to neglect the sub-structure

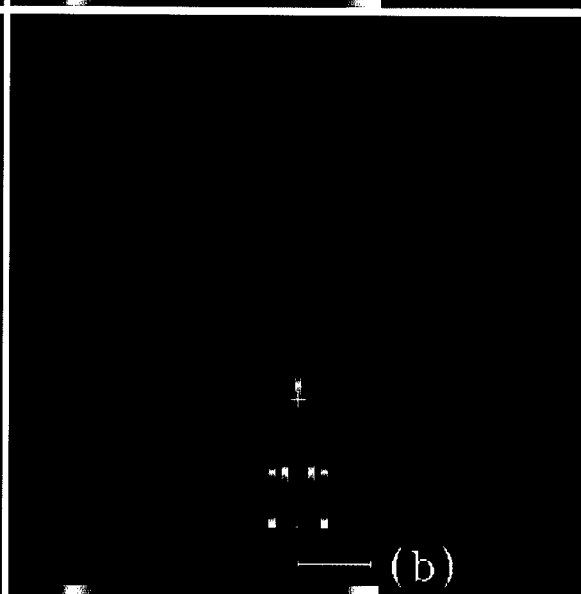
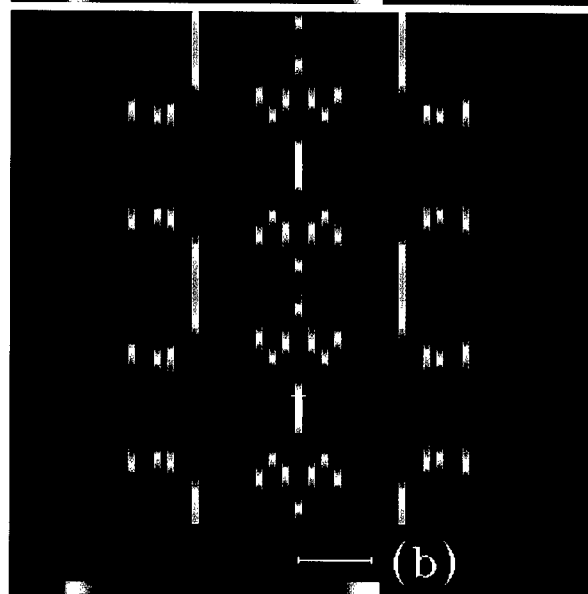
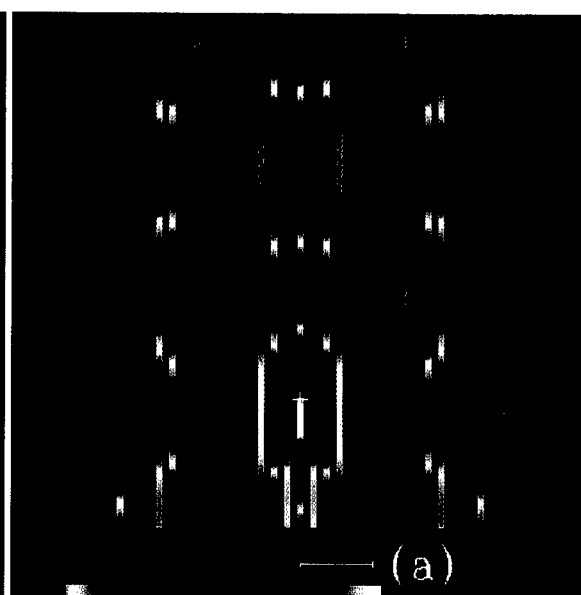
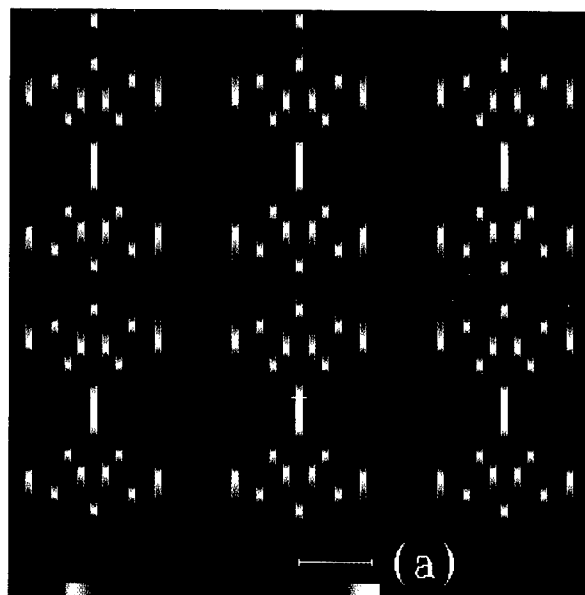


Fig. 5

Fig. 6

Fig. 5. Simulations obtained from (a) atoms 1 of Fig. 4 at unrelaxed positions and (b) atoms 1 and 2 of Fig. 4 with $\alpha = 2.7 \text{ \AA}$ and $\beta = 0.7 \text{ \AA}$. The central group of streaks is representative for model B and independent of relaxation and substructure for a wide range of parameters.

Fig. 6. Optimum fit of the kinematical model to the experimental picture. The picture in (a) was calculated for constant isotropic scattering, while (b) includes the effect of the Doyle–Turner scattering and Debye–Waller factors for a temperature of 880 K.

of the units comprising atoms 1, 2 and 3 in Fig. 4 and to use only the atoms 1. The resulting reciprocal lattice image is shown in Fig. 5a. Compared to Fig. 3b, the result is closer to the experimentally observed pattern in that the intensity is more evenly distributed in reciprocal space. Also, the intensity distribution on the individual rods is closer to the experiment. The calculation now correctly reproduces the first three streaks of the experimental pattern, counting from (00). This characteristic structure consists of alternating regions of high (h) intensity on streaks 0 and 3 or 1 and 2 and low (l) intensity on the others. The alternating h-l-h-l-h-l-h and l-h-h-l-h-h-l structure is characteristic for the GaAs (311)A reconstruction and can be found in any experimental RHEED pattern of this surface showing the 8-fold periodicity along $[0\bar{1}1]$.

The calculated pattern deviates from the experimental one in Fig. 2b on the streaks further away from (00). These streaks are more sensitive to the fine structure of the reconstruction than the ones closer to (00). Including atoms 1 and 2 of Fig. 4 and optimizing α (2.7 Å) and β (0.7 Å), one obtains the reciprocal space map of Fig. 5b. The value of α agrees well with estimates found by STM for (100) GaAs [10]. The sub-row relaxation parameter β is quite large, even if we consider a repulsive interaction of the empty-state dangling orbitals of the As dimers. Comparing Fig. 5a and b, the insensitivity of the streaks close to (00) to structure variation is evident. The dense reciprocal lattice of the (311)A reconstruction allows relatively easy fine-tuning of the relaxation parameters since any periodicity smaller than the unit cell size in real space shows up as an intensity variation larger than the streak separation in reciprocal space. The dimer bond length α is about 1/10 of the real space unit cell size along $[0\bar{1}1]$. It therefore shows up as an intensity variation with a period of about 10 reciprocal lattice rods in the simulation. The same behaviour holds for β , with a still larger period in reciprocal space. The accuracy of the simulation can therefore be improved by including rods far away from the (00) rod. Since the experimental pattern is the intersection of the reciprocal lattice plane with the Ewald sphere, the truncation of the higher-order streaks limits the accuracy of the simulation. This means that in our case β , due to its small value, is a less reliable parameter

in the fitting procedure than α . When comparing Fig. 5b with Fig. 2b, we find good semiquantitative agreement between the simulated and the experimental pattern out to the 13th streak. The intensity distributions both along and normal to the shadow edge are correctly reproduced. This remarkable agreement constitutes strong evidence that the kinematical approximation is valid approximation for this particular case.

The good fit can be explained by the smoothness of the surface along the $[233]$ direction. The low density of disorder steps revealed by STM [14] combined with the absence of depth modulation along $[233]$ in the surface unit cell itself produces dense and linear rows of scatterers along the beam direction. A modulated surface that exposes areas normal to the beam direction facilitates the entry as well as the exit of the high-energy electrons to and from the bulk. In our case, such modulation is not present and scattering is dominated by the surface atoms. This means that single scattering events dominate and therefore kinematical theory is adequate.

The streaks #4 and #12 of Fig. 5 do not show any modulation and do not change on variation of α or β . To obtain an intensity variation on these streaks, additional atoms need to be included in the simulation. It turns out, however, that even including only the Ga atoms, labelled 3 in Fig. 4, considerably worsens the agreement between theory and experiment. The Ga atoms located 1.27 Å below the As positions introduce a large-period intensity modulation normal to the surface that degrades the correct intensity distribution of Fig. 5b. Therefore, the form factor of the Ga atoms at positions 3 in Fig. 4 has to be reduced by at least a factor of 4 with respect to the As atoms 1 and 2 to achieve a good fit. The same is true for the atoms between the dimerized rows labelled 4 in Fig. 4. In a simple picture, their smaller contribution to the RHEED image can be explained by a shadowing of part of their scattering solid angle close to the shadow edge by the neighbouring dimerized rows, therefore reducing their contribution to the pattern. A calculation including atoms 1 through 4 of Fig. 4 is shown in Fig. 6a. The relative (still isotropic) form factors for the atoms at positions 1 through 4 are $u = 1$ for 1 and 2, $u = 1/4$ for 3, $u = 1/2$ for 4 As and $u = 1/8$ for 4 Ga. Rod 4 from the centre now shows some intensity variation that

matches the experimental distribution, although the Kikuchi line crossing in the experiment might overemphasize the intensity next to the specular spot on the 4th rod. The intensity on rod #12 is still too low, but the overall intensity distribution fits well with the experiment.

Fig. 6b shows a simulation of the same structure with the same relative form factors, but now including the Doyle–Turner scattering distribution and the Debye–Waller factors for a temperature of 880 K. Intensities away from the reciprocal lattice centre are strongly damped, but retain their relative magnitudes if one moves along a circle around the reciprocal lattice centre. Except for this exponential damping in the radial direction, the pattern remains unchanged. This justifies our neglect of both the scattering potentials and Debye–Waller factors in the simulations. The next step from Fig. 6b would be to convolute this picture with some radial function that models the intersection of a broadened Ewald sphere with a broadened reciprocal lattice plane. This would remove the excess intensity close to the origin and again cause it to approach the observed intensity distribution. We did not do this because it introduces two more fitting parameters in the calculation without significantly changing the pattern in comparison to Fig. 6a.

In conclusion we have confirmed the surface reconstruction model of Wassermeier et al. [14] for exactly oriented GaAs (311)A by simulating the RHEED intensity distributions using kinematical diffraction theory. Not only are we able to show distinct differences in the fit of the two models with experiment, but also to perform a refinement of the structural parameters of the surface reconstruction. The best agreement between simulation and experiment is achieved by including atoms at most 1.5 Å beneath the surface for an incidence angle of 1.5 degrees, where the contribution of the subsurface atoms is typically less by a factor of 4. The (311)A surface structure of GaAs in the $[\bar{2}33]$ azimuth is particularly well suited for the kinematical analysis. Since the intensity distribution close to the (00) streak is insensitive to the details of a structure, we expect our model to work in general for the distinction of different possible structure models. As the calculations are computationally economical, it seems feasible to use them also for the modelling of defect

structures using very large supercells or even for the simulation of RHEED intensity oscillations in combination with Monte Carlo methods.

The defect structure, especially for not exactly oriented surfaces, is expected to be of crucial importance for the properties of heterostructures grown on the (311) surface. Large-scan STM images revealed a highly anisotropic surface roughness which typically comprises five monolayers [14]. This mesoscopic surface modulation is very likely also present at the GaAs–AlAs heterointerfaces. Therefore the interface will be corrugated. The reconstruction is maintained on both sides of the heterointerface and since it contains two incomplete group III layers, a modulation of the interface due to the reconstruction can be expected. In real structures, however, this microscopic interface structure can be weakened or destroyed by segregation and mixing during heterointerface formation.

Acknowledgements

We would like to acknowledge the financial support of the Bundesministerium für Bildung und Wissenschaft of the Federal Republic of Germany.

References

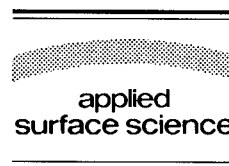
- [1] M. Henzler, *Appl. Surf. Sci.* 11/12 (1982) 450.
- [2] S. Thoma and H. Cerva, *Ultramicroscopy* 53 (1994) 37.
- [3] J.L. Beeby, *NATO ASI Ser.* 188 (1988) 29.
- [4] Y. Ma, S. Lordi, P.K. Larsen and J.A. Eades, *Surf. Sci.* 289 (1993) 47.
- [5] J.M. McCoy, U. Korte, P.A. Maksym and G. Meyer-Ehmsen, *Surf. Sci.* 306 (1994) 247.
- [6] Y. Ma, S. Lordi, P.K. Larsen and J.A. Eades, *Surf. Sci.* 306 (1994) 252.
- [7] Y. Ma, S. Lordi, P.K. Larsen and J.A. Eades, *Surf. Sci.* 289 (1993) 47.
- [8] J.M. McCoy, U. Korte, P.A. Maksym and G. Meyer-Ehmsen, *Phys. Rev. B* 48 (1993) 4721.
- [9] T. Hashizume, Q.-K. Xue, A. Ichimiya and T. Sakurai, *Phys. Rev. B* 51 (1995) 4200.
- [10] V. Bressler-Hill, M. Wassermeier, K. Pond, R. Maboudian, G.A.D. Briggs, P.M. Petroff and W.H. Weinberg, *J. Vac. Sci. Technol. B* 10 (1992) 1881.
- [11] J.E. Northrup and S. Froyen, *Phys. Rev. B* 50 (1994) 2015.
- [12] R. Nötzel, N.N. Ledentsov, L. Däweritz, M. Hohenstein and K. Ploog, *Phys. Rev. Lett.* 67 (1991) 3812.

- [13] R. Nötzel and K. Ploog, *J. Vac. Sci. Technol. A* 10 (1992) 617.
- [14] M. Wassermeier, J. Sudijono, M.D. Johnson, K.T. Leung, B.G. Orr, L. Däweritz and K. Ploog, *Phys. Rev. B* 51 (1995) 14721.
- [15] P.A. Doyle and P.S. Turner, *Acta Cryst. A* 24 (1968) 390.
- [16] J.S. Reid, *Acta Cryst. A* 39 (1983) 1.
- [17] M.G. Lagally, D.E. Savage and M.C. Tringides, *NATO ASI Ser.* 188 (1988) 139.



ELSEVIER

Applied Surface Science 104/105 (1996) 45–48



Ab initio calculations of the reconstructed (100) surfaces of cubic silicon carbide

Peter Käckell^{*}, Jürgen Furthmüller, Friedhelm Bechstedt

Institut für Festkörpertheorie, Friedrich-Schiller-Universität, Max-Wien-Platz 1, 07743 Jena, Germany

Received 28 June 1995; accepted 25 October 1995

Abstract

We have performed ab initio DFT–LDA supercell calculations for several reconstructions of the (100) surface of cubic silicon carbide. For the computations we have applied the Vienna ab initio molecular dynamic program (VAMP). We use ultrasoft Vanderbilt pseudopotentials which allow the use of an extremely small plane-wave cutoff energy. Interactions due to an artificial electric field between the two inequivalent slab surfaces are avoided by saturating one (carbon terminated) side with hydrogens. We discuss the geometries and energetics for several silicon and carbon terminated configurations (e.g. silicon-rich $c(2 \times 2)$, 2×1).

1. Introduction

During the last years, the group-IV compound silicon carbide has received considerable interest because of its attractive physical properties. Strong chemical bonding, physical stability and a rather large band-gap energy predestinate the material for applications in high-power devices at high temperatures. Furthermore, SiC crystallizes in more than two hundred different stable and long-range ordered modifications, called polytypes. The structural and electronic properties of the cubic and hexagonal bulk polytypes have been well investigated by first-principles calculations [1–6]. On the other hand, there exist only a small number of theoretical ab initio studies of the surface properties for the SiC polytypes. In Refs. [7] and [8], results for the geometric

and electronic structure of the SiC(110) surface of cubic silicon carbide are given, whereas in Ref. [6] a vacancy-induced (2×2) reconstruction of the SiC(111) surface is discussed. To our knowledge the SiC(100) surface has not yet been calculated with first-principles methods.

2. Method

In this paper, we present the results of ab initio calculations for the (100) surface of SiC. The calculations are performed within the framework of density functional theory (DFT) in the local density approximation (LDA). Explicitly we use the ‘Vienna ab initio molecular dynamic program’ (VAMP) [9]. The electronic ground state is evaluated using a conjugate-gradient technique. For the description of the electron-ion interaction we use ultrasoft pseudopotentials for carbon and hydrogen. This allows a

^{*} Corresponding author. Tel.: +49-3641-635910; fax: +49-3641-635182; e-mail: kaeckell@ifto.physik.uni-jena.de.

remarkable reduction of the necessary number of plane waves compared to the use of normconserving ones for first-row elements. Nevertheless, we use normconserving pseudopotentials for the bigger silicon atoms. An energy cutoff of 19 Ry is used for the plane-wave basis set. The k space integration is replaced by a summation over special k points according to the scheme of Chadi and Cohen [10]. In the case of a 2×1 supercell we use four special points in the irreducible part of the first Brillouin zone, whereas this number is reduced to one in the case of a 2×2 supercell. These are folded in the full Brillouin zone, which results in sixteen and four k points, respectively.

For the simulation of the surface, a repeated-slab method is applied. The supercell has a length of four conventional fcc cells, i.e. four times the cubic lattice constant. For the latter quantity we use a value of $a_0 = 4.33 \text{ \AA}$, the calculated equilibrium value for cubic SiC. Half of the slab is filled with silicon and carbon layers, in total eight layers. Such a slab configuration can cause several problems during the cycle of selfconsistency, since the two surfaces are inequivalent. At first, there might occur an artificial charge transfer, since the surface states of the cation (Si) dangling bonds lie above those of the anion (C) dangling bonds. Furthermore the surface states on both sides could interact which each other through the slab. Several possibilities exist to avoid these artificial effects. One way is to construct a slab containing a mirror plane. However, this slab would contain twice as many atoms, since the mirror plane had to lie in the 'bulk' part of the slab [6]. The approach we have taken is to saturate the dangling bonds at the carbon terminated surface with a hydrogen atom each. The four outermost layers on the other side are allowed to relax.

3. Results

3.1. Clean silicon terminated surface

We have performed calculations for silicon terminated clean and covered surfaces with $p(2 \times 1)$, $c(2 \times 2)$ and $p(2 \times 2)$ symmetry. As a first step, we calculate the reconstruction of the hydrogen terminated surfaces to make them force-free. In the equi-

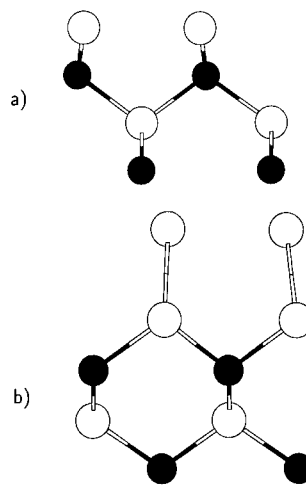


Fig. 1. Reconstructed silicon terminated SiC(100) 2×1 surfaces. Silicon atoms are indicated by empty circles, carbon atoms are indicated by filled circles. View direction is towards [011]. (a) clean surface, (b) additional Si layer on top (1×2 cell).

librium state, the carbon-hydrogen bonds have the same direction as they would have if two hydrogens were replaced by a silicon atom. In comparison to the C–Si bonds in cubic SiC ($d = 1.89 \text{ \AA}$) the C–H bonds are shortened, they have a length of $d = 1.08 \text{ \AA}$.

Considering the clean silicon terminated surfaces ($\Theta = 1$) with a full silicon layer on top, there exist detailed experimental data only for the $p(2 \times 1)$ surface, based on LEED measurements [11]. Powers et al. favour a buckled silicon dimer model as optimum structure. They find a Si–Si dimer bond length of 2.31 \AA and a buckling of 0.20 \AA . Our result, shown in Fig. 1a, is quite different. Even if we take their results as starting configuration for the calculation, we end up in a system showing almost no dimerization and no buckling at all. The surface silicon atoms move towards each other by about 0.15 \AA each. This results in a distance of 2.75 \AA , which is about 0.4 \AA larger than the one measured by Powers et al. [11]. As a consequence, the energy gain per surface atom is almost negligible ($\sim 10 \text{ meV}$). The same rather weakly pronounced tendency to dimerize is found for all other starting configurations, including symmetric and asymmetric buckled and nonbuckled $c(2 \times 2)$ and $p(2 \times 2)$ configurations. A reason for this small changes compared to the unreconstructed but relaxed structure might be the strong bonding of the

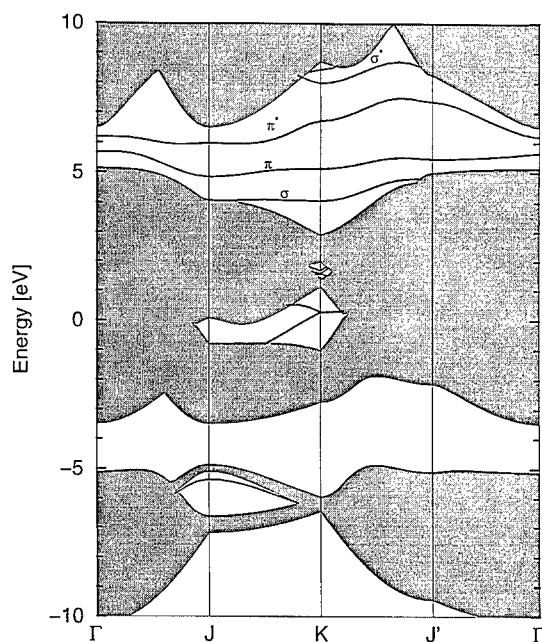


Fig. 2. Band structure for the clean silicon terminated SiC(100) 2×1 reconstruction of cubic silicon carbide.

surface silicon atoms to the second layer of C atoms. The energy loss due to subsurface strains would be larger than the energy gain due to charge transfer and stronger dimerization. Since these calculations are performed for nearly zero temperature, this conclusion might not hold at higher temperatures and a following annealing process where the energy barrier could be crossed more easily.

We have also calculated the band structure for the $p(2 \times 1)$ surface, which is shown in Fig. 2. π - and π^* -like as well as σ - and σ^* -like surface states appear in the fundamental gap region. The surface is nonmetallic. The indirect LDA surface band gap amounts to 0.26 eV. The occupied π -like band maximum and the unoccupied π^* -like band minimum are located on the ΓJ line. Due to the small interaction of the surface wave functions the gap remains small.

3.2. Non-stoichiometric silicon terminated surfaces

Another possible explanation for the discrepancy between the theoretical and experimental results might be the stoichiometry of the surface. The strong

dimerization found by tensor-LEED studies [11] could be interpreted to be performed for a SiC(100) surface with another layer of Si on top. Therefore, we have calculated the reconstruction of different $p(2 \times 1)$ and $p(1 \times 2)$ geometries with a coverage of $\Theta = 2$, i.e. an additional Si layer on top. The energetically most favorable reconstruction is displayed in Fig. 1b. Again, our preliminary results do not show a pronounced silicon dimer. The distance between the Si atoms on top amounts to 2.55 Å. Moreover, there is a tendency to weaken the bonds to the second layer of silicon atoms. The corresponding bond length amounts to 2.49 Å. The buckling is negligible.

Considering possible $c(2 \times 2)$ reconstructions with a coverage of only half a monolayer of Si ($\Theta = 1/2$), we have performed calculations for silicon atoms at hollow (Fig. 3a) and bridge (Fig. 3b) sites. In both cases the reconstructions are more important than for the clean case ($\Theta = 1$). However, the energy gain is smaller for the case of silicon at hollow sites. The Si atoms on top build single bonds to the second layer with a length of 2.34 Å and move inward by about 0.11 Å, whereas the second and third show a tendency to move outward. There are no lateral relaxations, except for the second silicon layer, where the atoms move away from the silicons at the hollow sites by about 0.07 Å each.

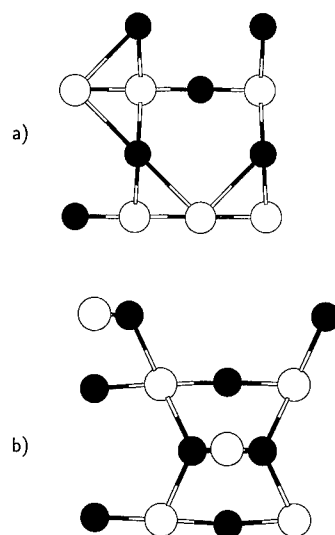


Fig. 3. Top view on the half covered silicon terminated $c(2 \times 2)$ surface with silicon at (a) hollow and (b) bridge sites.

Placing the Si atoms at bridge sites causes rather large reconstructions. The Si atoms form strong bonds with the carbon atoms of the second layer with a bond length of 1.86 Å, which is somewhat smaller than the bond length in cubic SiC (1.89 Å). The Si top layer moves 0.47 Å outward, whereas the second (carbon) layer moves 0.12 Å inward, compared to the ideal slab positions. In addition, the carbon atoms of the second layer show also a lateral movement of 0.79 Å, which results in an elongation of the bond lengths to the third layer atoms (1.92 Å). This might explain the inward movement of the carbon layer in spite of the strong Si–C bonds. However, as a consequence of the strong bonding the binding energy per surface atom is lower by about 58 meV for the bridge-site structure compared to the hollow-site structure.

3.3. Carbon terminated surface

The work for these surfaces is in progress. Until now we have calculated only the analogon for the silicon terminated $c(2 \times 2)$ surface ($\Theta = 1$) with staggered dimers (Fig. 4). In contrast to our findings for the silicon terminated surface, on the carbon terminated surface real double bonded C–C dimers are formed with a bond length of 1.38 Å. It is only slightly larger than the value 1.31 Å reported for aromatic carbon systems. No buckling occurs, but the first two layers move 0.21 Å (C) inward and 0.08 Å (Si) outward, respectively. The energy gain per surface carbon atom is 2.18 eV compared to the clean carbon terminated, relaxed surface.

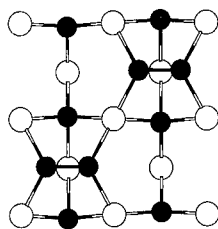


Fig. 4. Top view on the carbon terminated $c(2 \times 2)$ surface with staggered C–C dimers.

4. Conclusions

We have presented ab initio calculations for a variety of silicon terminated surfaces and for the carbon terminated $c(2 \times 2)$ surface with staggered dimers. In the case of the silicon terminated surfaces, no strong dimerization takes place, in contrast to the experimental data. Even taking into account a second Si layer on top, the experimental findings remain unexplained. Larger reconstructions occur for non-stoichiometric silicon terminated structures. On the other hand, there are C–C double bonded dimers formed at the carbon terminated surface.

Acknowledgements

We wish to thank W.G. Schmidt for fruitful discussions. The work was supported by the Sonderforschungsbereich 196 (Project No. A08) of the Deutsche Forschungsgemeinschaft.

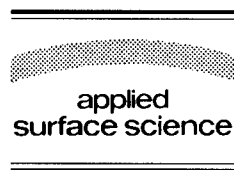
References

- [1] C. Cheng, R.J. Needs and V. Heine, *J. Phys. C* 21 (1988) 1049.
- [2] W.R.L. Lambrecht, B. Segall, M. Methfessel and M. van Schilfgaarde, *Phys. Rev. B* 44 (1991) 3685.
- [3] C. Park, B.-H. Cheong, K.-H. Lee and K.J. Chang, *Phys. Rev. B* 49 (1994) 4485.
- [4] P. Käckell, B. Wenzien and F. Bechstedt, *Phys. Rev. B* 50 (1994) 17037.
- [5] P. Käckell, B. Wenzien and F. Bechstedt, *Phys. Rev. B* 50 (1994) 10761.
- [6] B. Wenzien, P. Käckell and F. Bechstedt, *Surf. Sci.* 307–309 (1994) 989.
- [7] B. Wenzien, P. Käckell and F. Bechstedt, *Surf. Sci.* 331–333 (1995) 1105.
- [8] M. Sabisch, P. Krüger and J. Pollmann, *Phys. Rev. B* 51 (1995).
- [9] G. Kresse and J. Hafner, *Phys. Rev. B* 49 (1994) 14251.
- [10] D.J. Chadi and M.L. Cohen, *Phys. Rev. B* 8 (1973) 5747.
- [11] J. Powers, A. Wander, M.A. Van Hove and G.A. Somorjai, *Surf. Sci.* 260 (1992) L7.



ELSEVIER

Applied Surface Science 104/105 (1996) 49–56



Chemical preparation of CdTe(100) and (110) surfaces using atomic hydrogen

Y. Luo, D.A. Slater^{*}, M. Levy, R.M. Osgood Jr.

Department of Electrical Engineering and Columbia Radiation Laboratory, Columbia University, 500 West 120th Street, 1342 Mudd, New York, NY 10027, USA

Received 28 June 1995; accepted 11 September 1995

Abstract

We present the results of an AES, XPS, LEED and photoluminescence study of the reaction of oxide and contaminant overlayers on CdTe(100) and (110) surfaces with atomic hydrogen. For both surfaces exposure of an oxide overlayer to a flux of atomic hydrogen produced by ‘cracking’ ambient molecular hydrogen on a hot tungsten filament results, in contrast to the case of GaAs substrates, in a rapid, quantitative removal of the oxide overlayer at substrate temperatures as low as 300 K. This process results in surfaces free of contaminants which have sufficient surface order to produce clear LEED patterns characteristic of well known reconstructions of these surfaces. Additionally in situ photoluminescence spectroscopy allows direct correlation of surface cleaning with reduced nonradiative carrier recombination.

1. Introduction

Surface preparation is a crucial consideration in the fabrication of modern semiconductor devices. Issues to be addressed in this regard for the realization of optimal device performance include chemical composition (particularly with respect to the elimination of undesirable surface contaminants and impurities), the elimination or passivation of surface defects and the maintenance and production of abrupt interfaces in heterodevices. All of these considerations have become steadily more important as surface/area volume ratios have increased with progressive device miniaturization and have become especially important with the advent of nanostructure devices.

Whilst the preparation of II–VI surfaces is a

relatively unexplored topic, the most commonly employed technique for the preparation of III–V materials, particularly in ‘practical’ situations such as the preparation of substrates for epitaxial growth, is a simple thermal desorption or ‘blow-off’ of oxide and contaminant overlayers under an overpressure of the more volatile substrate component (i.e. arsenic in the case of GaAs). However it is now well known [1,2] that this can lead both to incomplete oxide removal and to the development of a very significant degree of surface roughness which in turn necessitates the homoepitaxial growth of a ‘smoothing’ layer before, for example, heteroepitaxy can proceed.

This, together with other potentially deleterious effects resulting from processes requiring high substrate temperatures, such as thermally activated dopant segregation and interdiffusion at pre-formed heterojunctions, have led to a growing interest in chemical preparation techniques which are able to

^{*} Corresponding author. Fax: +1-212-8606182; e-mail: daves@cuml.ctr.columbia.edu.

operate at low temperatures and generally involve the use of highly reactive, radical species generated in situ.

Early experiments [3–5] within this vein generally employed plasma discharges to generate such species. This approach however is less than ideal due to the inevitable generation of a flux of ionic species which can result in surface damage due to a variety of mechanisms.

More recently it has been recognized that it is possible to form neutral, radical species effective in the cleaning process without the ion formation associated with the use of plasma discharges. Consequently a number of studies of the surface modification of III–V materials using atomic hydrogen species have appeared recently, dealing with the application of such techniques to the manipulation of GaAs surface chemistry [6,7], although applications to the case of InP [8] and Si [9] have also appeared. The potential importance of the atomic hydrogen aided removal of oxide overlayers has been shown recently, on GaAs, by Kolodziejcki and coworkers [10] who have demonstrated, using photoluminescence, that oxide removal by hydrogen treatment followed by ZnSe epitaxial growth gives a superior interfacial quality to that produced by thermal ‘blow off’ of substrate oxides followed by re-growth.

In our recent investigations, work described below, we have attempted to extend this methodology to the processing of II–VI materials, specifically the CdTe(110) and (100) surfaces. We have previously given a brief report of the hydrogen atom processing of CdTe(110) surfaces [11], thus here we concentrate on the more complex but technologically important (100) surface.

2. Experimental

The nominally undoped CdTe (110) and (100) oriented crystals used in this study (II–VI incorporated) were supplied with surfaces which had been chemically polished. Before mounting in the ultra high vacuum (UHV) system the crystals were degreased by washing in trichloroethane. No sample heating to remove adsorbed species was performed before H-atom processing.

All experiments were performed in an UHV sys-

tem which will be described in detail elsewhere [11]. Briefly the system is equipped with a fast sample entry system and consists of two chambers between which the sample may be transported in vacuum.

The analysis chamber (base pressure $< 5 \times 10^{-11}$ mbar) is equipped with a hemispherical electrostatic energy analyzer for surface spectroscopy, an ion gun for sample sputter cleaning, a quadrupole mass spectrometer for residual gas analysis and a tungsten filament placed ~ 20 mm from the sample (only small temperature rises (ca. 10°C) were observed even when this device was in operation for extended periods). This filament may be resistively heated to temperatures ca. 1500 K in order to dissociate ambient molecular hydrogen and thus provide a source of atomic hydrogen. As no absolute measurement of the resulting flux of atomic hydrogen at the sample surface is available exposures are quoted in terms of the ambient hydrogen pressures. Analytical facilities include X-ray photoelectron spectroscopy (XPS) via a dual anode (Mg, Al) X-ray source, electron excited Auger electron spectroscopy (AES), ion scattering spectroscopy, low energy electron diffraction (LEED) and photoluminescence spectroscopy. An electron cyclotron resonance (ECR) plasma source is mounted in a second chamber (base pressure $< 1 \times 10^{-9}$ mbar).

All XPS spectra described below were obtained using unmonochromatized Mg $K\alpha$ radiation. The sample is mounted on a thin molybdenum foil which can be both cooled and resistively heated allowing temperatures between 80 and 1000 K to be attained. Sample temperatures were measured using a chromel/alumel (K-type) thermocouple spot welded to the molybdenum foil as close as possible to the edge of the sample. Photoluminescence spectra were recorded at 80 K.

In addition to experiments on native oxidized surfaces, as received from the supplier, experiments were conducted on oxide layers grown in situ. As oxidation of CdTe surfaces takes place only slowly under thermal conditions in an O_2 ambient, oxide overlayers were conveniently and more rapidly formed by exposure of clean surfaces to oxygen plasmas generated using the ECR apparatus. In contrast to the formation by ECR plasmas of oxide layers on GaAs surfaces [12] no species could be detected for overlayers produced in this manner

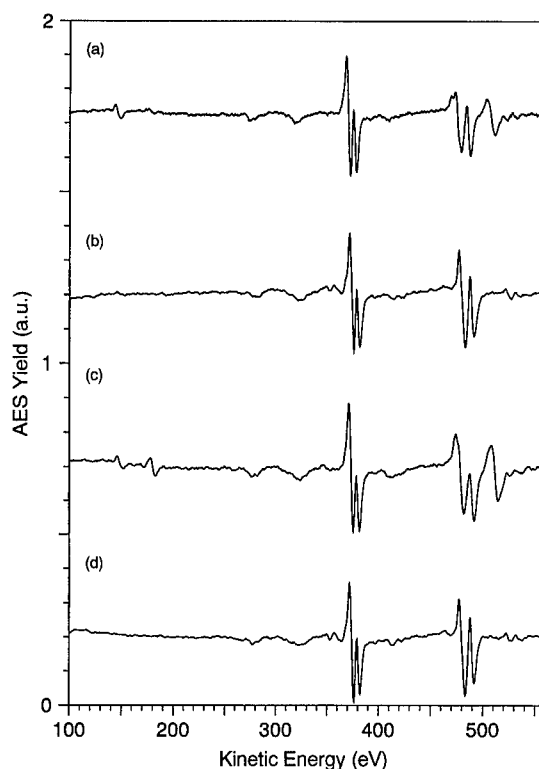


Fig. 1. Auger electron spectra of 'as received' CdTe (110) and (100) crystals (a, c) and the following hydrogen atom processing at room temperature (b, d).

which were not also observed for the case of the native oxide, i.e. the oxide chemistry appeared to be identical to that of the 'native' oxide.

3. Results and discussion

Representative Auger spectra of (110)- and (100)-oriented crystals 'as received' (a, c) and following H-atom processing at room temperature (b, d) are shown in Fig. 1. In addition to large features due to cadmium (280, 320, 375 and 380 eV) and tellurium (408, 480, 490 eV) the spectrum of crystals 'as received' also exhibits pronounced oxygen-derived features (512 eV) due to the presence of a surface oxide layer, large features (181 eV) due to chlorine contamination which were found to result from the degreasing procedure and occasional sulfur contamination (152 eV). No LEED pattern can be

observed for such samples indicating the presence of a disordered, amorphous layer (on the order of ~ 20 Å) at the surface, which was thick enough to suppress the transmission of electrons diffracted by the underlying, ordered, substrate. Attempts to thermally desorb such an overlayer from a (110) surface indicate that a temperature $\sim 600^\circ\text{C}$ is required to achieve total oxide desorption and that such a procedure can result in a very gross roughening of the surface easily visible to the naked eye.

Following H-atom processing with the substrate held at room temperature the removal from the spectra of the features at 510 and 181 eV indicates a reduction in surface oxygen and chlorine levels to below the AES detection limit ($\ll 5\%$ of a monolayer). This facile production of an atomically clean surface at room temperature contrasts with the behavior observed for GaAs surfaces where the formation of the gallium suboxide Ga_2O via reduction of Ga_2O_3 -like oxides limits further reaction unless the substrate temperature is raised to effect desorption of the resultant Ga_2O layer [3,6,7].

As we and others have previously shown [11,13–16] X-ray photoelectron spectroscopy can also provide information on the composition of oxide layers on CdTe surfaces, both through the intensity of the O 1s photoemission signal and a signal from strongly chemically shifted Te 3d peaks corresponding to Te^{4+} species. Representative spectra illustrating the H-atom stimulated removal of an oxide overlayer on CdTe(100) are shown in Fig. 2. These spectra clearly

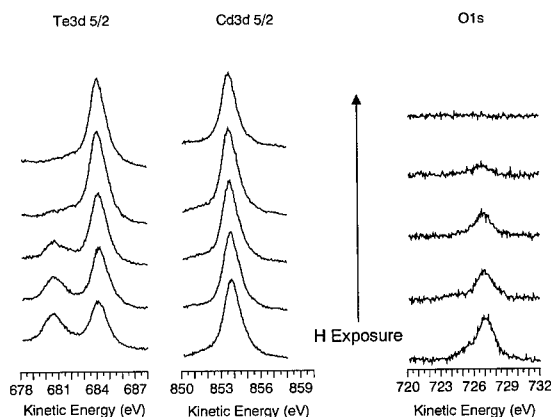


Fig. 2. X-ray photoelectron spectra illustrating the progressive removal of an oxide overlayer from a CdTe(100) surface.

show oxygen-1s and oxide-induced, chemically shifted Te 3d photoemission features and their removal by H-atom processing. Although the resolution of an unmonochromatic X-ray source does not allow the observation of distinct chemically shifted Cd species within the overlayer, our ability to grow rather thick oxide overlayers in situ has allowed us to show that such an overlayer does contain near stoichiometric quantities of Cd [11], a result which would be expected if the overlayer consists primarily of CdTeO_3 [17]. The detection of partially reduced intermediate species such as those implicated in the removal of oxides from GaAs substrates [3,6,7] would provide some insight into the microscopic mechanisms underlying the H-atom reduction process. We anticipate performing such experiments utilizing the higher resolution afforded by synchrotron radiation sources in the near future.

This efficiency of oxide removal at room temperature is further emphasized by the data of Fig. 3 which shows the change in the ratio of Te derived XPS signals obtained from an oxide overlayer and the underlying substrate for a CdTe(100) surface as a function of hydrogen atom exposure at various substrate temperatures. Clearly an increase in the effi-

ciency of oxide removal such as observed for GaAs substrates with increasing sample temperature is not found for CdTe. In fact the opposite effect, i.e. a decrease in the efficiency of oxide removal, is observed, suggesting that under these conditions thermally activated processes, arising, for example, from product desorption, are not rate limiting in the cleaning process. This behavior also contrasts to that found for the removal of sulfur layers from InP(100) using H-atom processing where the rate was found to increase strongly with increasing substrate temperature indicating the operation of a thermally activated reaction mechanism [8].

Also apparent following H-atom treatment at room temperature is a gross improvement in the order of the near surface atomic structure evidenced by the appearance, for both substrate orientations, of clear, albeit somewhat diffuse (1×1) LEED patterns with periodicity characteristic of the bulk material. An improvement of the 'sharpness' of the patterns which occurs on mild (ca. 350°C , 20 min for (110), 275°C , 20 min for (100)) annealing following such a treatment indicates a further improvement in the near surface order. Additionally, for the case of the (100) oriented crystal, a change in the periodicity of the

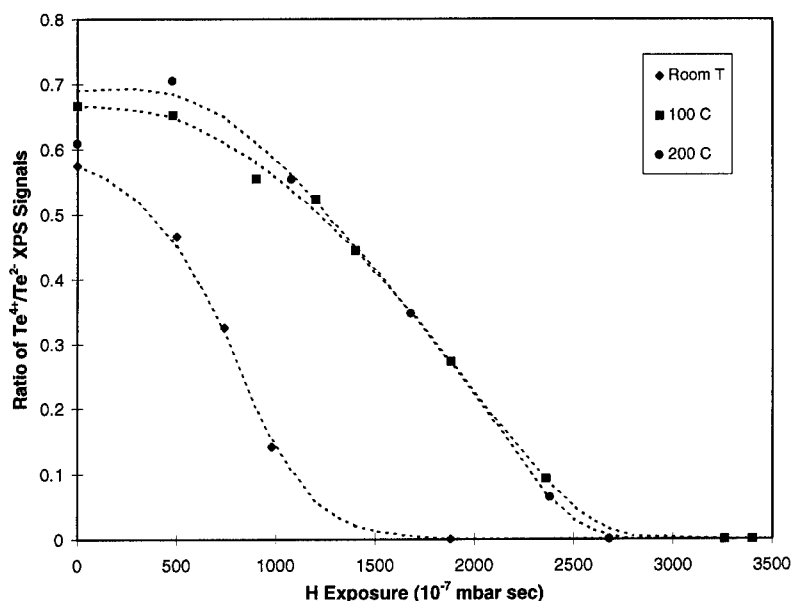


Fig. 3. Removal of oxide overlayers from CdTe(100) at various substrate temperatures. The ratio of chemically shifted Te 3d photoemission to that characteristic of the substrate is used as a measure of oxide thickness. This quantity is found to scale directly with oxygen 1s emission in all cases.

LEED pattern from (1×1) to $c(2 \times 2)$ (or equivalently $(\sqrt{2} \times \sqrt{2})R45$) following annealing indicates the formation of a specific well known, surface layer reconstruction for this orientation.

For the case of the (100) surface the $c(2 \times 2)$ pattern has been correlated with the occurrence of cadmium termination both during CdTe film growth by molecular beam epitaxy, and for CdTe substrates under 'static' conditions [18–20]. We have not observed the alternative tellurium termination, which is characterized by a (2×1) LEED pattern, following either H-cleaning and annealing or ion-sputter cleaning followed by annealing at 275°C. This observation is compatible with the faster sublimation rates which have been reported for surface tellurium in comparison to cadmium from the (100) surface in this temperature range [19]. Higher annealing temperatures do not in general result in an improvement in surface order. LEED in such cases frequently exhibits a marked reduction in microscopic surface planarity evinced by a diffuse $c(2 \times 2)$ pattern, superimposed upon which are a large number of extra features centered upon multiple new zeroth order diffraction features in directions non-normal to the (100) sur-

face, indicating the existence of surfaces other than CdTe(100). This indicates that surface facetting has occurred. This effect was not found to be a problem, if sample temperatures were not allowed to exceed approximately 300°C, even after multiple oxidation/reduction cycles were performed on the same surface.

A clear danger in the use of hydrogen atoms for surface chemical modification in a binary compound such as CdTe is that a preferential etching of one substrate component may occur producing a non-stoichiometric surface. Just such an effect has been observed in studies of hydrogen treatment of an InP(100) surface [8]. In that case hydrogen exposure at substrate temperatures in excess of 400 K were found to lead to a surface enriched in indium, presumably through formation of PH_3 . Analogous processes are obviously possible for the case of CdTe, particularly with respect to the formation of a cadmium rich surface due to etching of TeH_2 . This point is obviously of great importance to practical surface preparation procedures, especially given the propensity of excess metal to form three dimensional droplets on semiconductor surfaces [8].

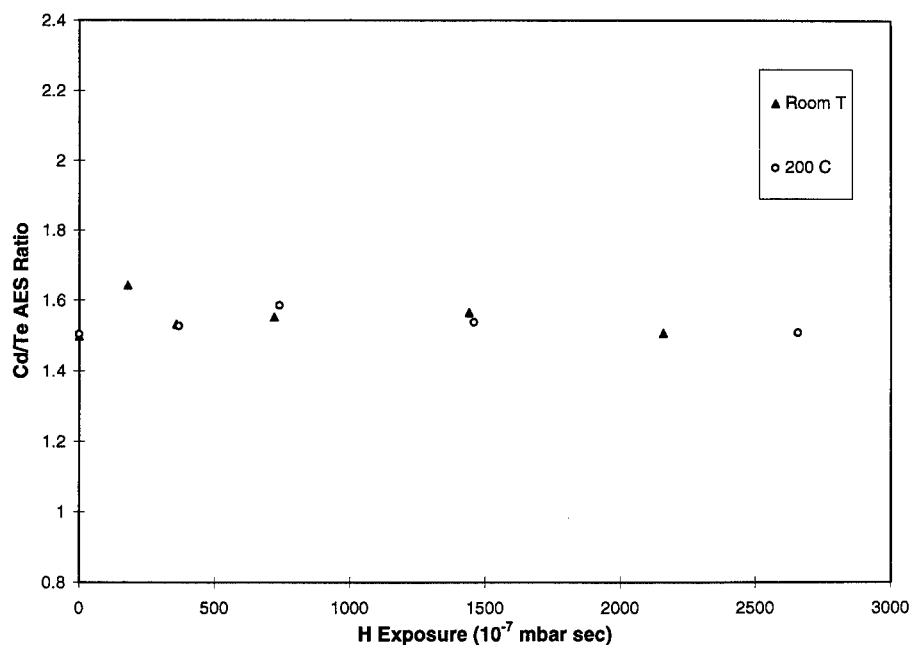


Fig. 4. Measured ratio of cadmium and tellurium signals following prolonged exposure of a clean, well ordered CdTe(100) surface to atomic hydrogen at room temperature and 200°C.

We have attempted to address this point in two ways. Firstly, comparisons of the relative intensities of Cd and Te Auger and XPS signals for a number of samples cleaned by sputter/annealing at 500 eV (an energy at which it has been shown that little preferential sputtering occurs [21]) and by atomic hydrogen suggests very similar stoichiometries are obtained using either technique. Secondly, we have studied the interaction of atomic hydrogen with clean surfaces in an attempt to observe preferential etching. Fig. 4 illustrates the measured variation in the ratio of Cd and Te AES ratio as a function of exposure to hydrogen atoms at room temperature and 200°C for a sputter/annealed surface (100) surface initially exhibiting a well defined $c(2 \times 2)$ reconstruction. Clearly little variation in stoichiometry is observed even for rather long exposures (compare with the exposures required for the removal of the rather thick oxide layers in Fig. 3). This is in contrast to results for H-plasma treatment of a somewhat less well defined CdTe(100) surface which indicates a very marked Te enrichment of the surface region [22].

Photoluminescence spectroscopy, though not an intrinsically surface sensitive technique, is expected to be, indirectly, extremely sensitive to the surface quality of the sample under investigation. This effect

can arise in at least two distinct ways. Most obviously the photoluminescence intensity obtained for radiative recombination at energies near the band gap might be expected to be strongly quenched both by the presence of surface 'defect' sites due either to crystallographic defects or impurity atoms which act to enhance the efficiency of non-radiative decay channels. Secondly modifications in surface band bending effects will effect the tendency of electrons and holes to become spatially separated in the near surface electric field responsible for the band bending. This will, in turn, modify the radiative recombination rate. As the band bending phenomenon has its origins in the presence of surface states within the band gap, removal or passivation of such states during surface treatment will enhance the photoluminescence yield.

Fig. 5(a) illustrates a typical photoluminescence spectrum obtained in situ from a cleaned CdTe(100) surface at 80 K. The spectrum is dominated by a broad near band gap envelope at 1.57 eV which clearly contains a number of distinct features assigned to excitonic transitions. Smaller features are observed at energies of 1.53 and 1.515 eV which have been [23–25] previously attributed to the presence of defects and impurities within the crystal. As might be expected from such an assignment, the

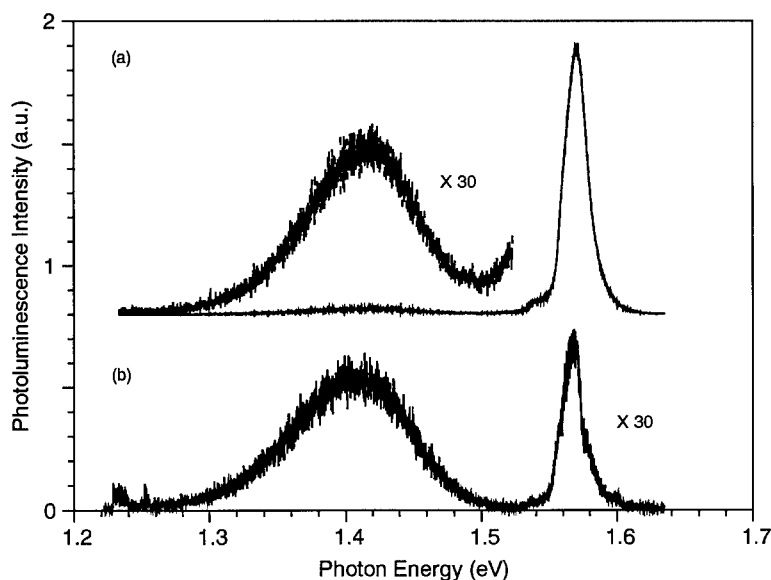


Fig. 5. Photoluminescence spectra of a CdTe(100) surface (a) exhibiting a well formed $c(2 \times 2)$ LEED pattern and (b) the same surface after deliberate overannealing.

intensities of these features are found to be somewhat dependent on the particular sample examined. This spectrum is in excellent agreement with previously published spectra recorded at similar temperatures [26,27] and shows little photoluminescence intensity from states within the bandgap, though for this particular sample a broad peak is observed at around 1.4 eV (shown expanded in the inset to Fig. 5). This is contrasted to spectrum (b) which was obtained from the same CdTe(100) surface following annealing to 400°C at which point it exhibited the 'faceted' LEED pattern described above, indicating a gross change in surface morphology. Obviously a much lower intensity is observed for the near bandgap states and though the feature at 1.4 eV is relatively unchanged and now dominates the spectrum. The dramatically lower luminescent intensity observed illustrates dramatically the potential for surface preparation procedures to drastically effect the carrier recombination properties of such a sample.

In situ photoluminescence spectroscopy allows monitoring of the effect of the cleaning procedure on the carrier recombination properties of the surface. This is illustrated in Fig. 6 which correlates the variation of photoluminescence intensity from the main near bandgap envelope with the intensities of

XPS signals from oxidized and unoxidized tellurium (and thus the thickness of an oxide overlayer) and with subsequent increasing annealing temperature. Clearly photoluminescence intensity is seen to increase as the oxide overlayer is reduced. The effect is most pronounced as the last trace of oxide contamination is removed to produce a clean surface and on annealing as crystallographic defects are removed.

Surface band bending effects are assessed through the measured position of the Cd 3d and photoemission features. Only small changes in peak position are observed (in contrast to peak shifts of up to 0.8 eV which have been measured during plasma processing of clean CdTe(100) surface [22]) and the overall trend is of a smooth shift in position as a function of processing. Certainly no large discontinuity is observed during the final stages of oxide removal and subsequent annealing which mirrors that in the photoluminescence intensity. In view of this latter observation we tentatively suggest that, for this surface at least, the primary mechanism for the modification of the near-band-gap photoluminescence yield is a reduction in non-radiative recombination, due to a removal of centers at which this process is enhanced, during the cleaning and annealing of the surface.

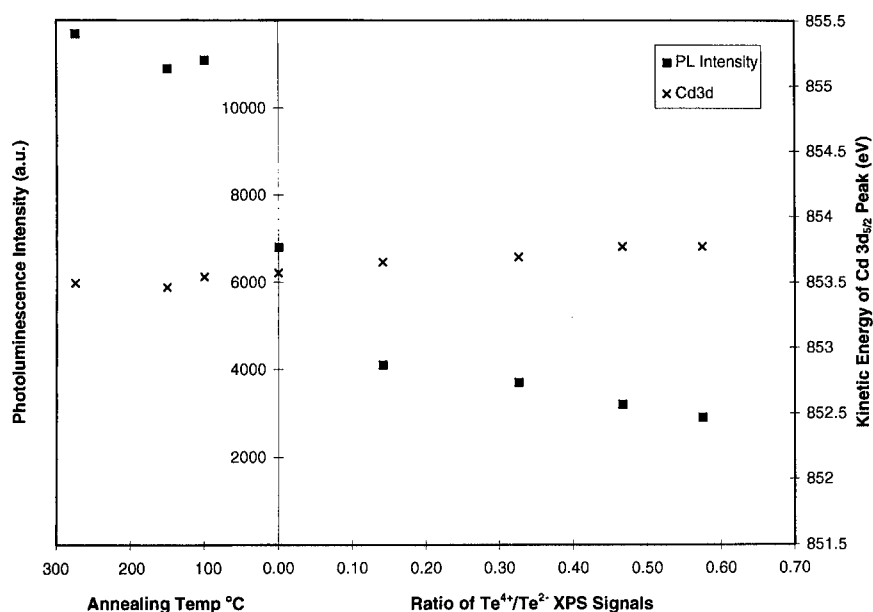


Fig. 6. Variation of near band gap photoluminescence signal and position of Cd 3d photoemission features with oxide removal via H-atom treatment.

4. Conclusions

We have shown that hydrogen atom processing of both CdTe(100) and (110) substrates can produce atomically clean surfaces which appear to be very close to stoichiometric in composition. This facile cleaning at room temperature contrasts with the situation encountered during the processing of oxide layers on III–V substrates using the same technique.

The surfaces produced in this manner exhibit a high degree of surface and near-surface order which can be somewhat improved by a mild annealing process. The upper limit for thermal processing of the (100) surface however appears to be set by the propensity of this surface to facet.

Monitoring of the cleaning process using in situ photoluminescence spectroscopy has allowed a direct correlation of the effect of this surface preparation procedure on the carrier recombination properties of the sample.

Acknowledgements

We gratefully acknowledge the support of this work by the NSF through award No. DMR-92-25134 and partial instrumentation support by the DOE through the provision of award No. DE-FG-02-09ER14104. Thanks are also due to Professor P. Sarachik of The City College of New York for the generous loan of equipment for photoluminescence experiments.

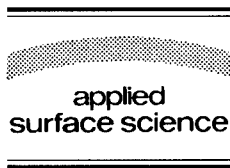
References

- [1] M.D. Pashley and D. Li, *Mater. Sci. Eng. B* 30 (1995) 73.
- [2] Y. Nomura, S. Goto and Y. Morishita, *Jpn. J. Appl. Phys.* 33 (1994) L1744.
- [3] Z. Lu, M.T. Schmidt, D. Chen, R.M. Osgood, Jr., W.M. Holber, D.V. Podlesnik and J. Forster, *Appl. Phys. Lett.* 58 (1991) 1143.
- [4] A. Takamori, S. Sugata, K. Asakawa, E. Miyauchi and H. Hashimoto, *Jpn. J. Appl. Phys.* 26 (1987) L142.
- [5] S. Sugata, A. Takamori, N. Takado, K. Asakawa, E. Miyauchi and H. Hashimoto, *J. Vac. Sci. Technol. B* 6 (1988) 1087.
- [6] M. Yamada and Y. Ide, *Jpn. J. Appl. Phys.* 33 (1994) L671.
- [7] Y. Ide and M. Yamada, *J. Vac. Sci. Technol. A* 12 (1994) 1858.
- [8] G.W. Anderson, M.C. Hanf, J.G. Schapter, P.R. Norton, Z.H. Lu and M.J. Graham, *Surf. Sci.* 318 (1994) 299.
- [9] A. Crossley, C.J. Sofield, S. Sugden, R. Clampitt and C. Bradley, *Vacuum* 46 (1995) 667.
- [10] L.A. Kolodziecki, private communication.
- [11] Y. Luo, D.A. Slater and R.M. Osgood, *Appl. Phys. Lett.* 66(26) (1995), to appear.
- [12] Z. Lu, M.T. Schmidt and R.M. Osgood, Jr., *J. Vac. Sci. Technol. A* 9 (1991) 1040.
- [13] J.G. Werthen, J.P. Haring and R.H. Bube, *J. Appl. Phys.* 54 (1983) 1159.
- [14] U. Solsbach and H.J. Richter, *Surf. Sci.* 97 (1980) 191.
- [15] M.K. Bahl, R.L. Watson and K.J. Irgolic, *J. Chem. Phys.* 66 (1977) 5526.
- [16] A.J. Ricco, H.S. White and M.S. Wrighton, *J. Vac. Sci. Technol. A* 2 (1984) 910.
- [17] C.R. Helms, *J. Vac. Sci. Technol. A* 8 (1990) 1178.
- [18] S. Tatarenko, F. Bassani, J.C. Klein, K. Saminadayer, J. Cibert and V.H. Etgens, *J. Vac. Sci. Technol. A* 12 (1994) 140.
- [19] J.D. Benson, B.K. Wagner, A. Torabi and C.J. Summers, *Appl. Phys. Lett.* 49 (1986) 1034.
- [20] Y.S. Wu, C.R. Becker, A. Waag, M.M. Kraus, R.N. Bicknell-Tassius and G. Landwehr, *Phys. Rev. B* 44 (1991) 8904.
- [21] J.B. Malherbe, *Appl. Surf. Sci.* 70/71 (1993) 322.
- [22] A.J. Nelson, S.P. Frigo and R.A. Rosenberg, *J. Appl. Phys.* 75 (1994) 1632.
- [23] J. Gonzalez-Hernandez, E. Loez-Cruz, D.D. Allred and W.P. Allred, *J. Vac. Sci. Technol. A* 8 (1990) 3255.
- [24] J.M. Figueroa, F. Sanchez-Sinencio, J.G. Mendoza-Alvarez, O. Zelaya, C. Vaquez-Lopez and J.S. Helman, *J. Appl. Phys.* 60 (1986) 452.
- [25] P.M. Amirtharaj and N.K. Dhar, *J. Appl. Phys.* 67 (1990) 3107.
- [26] A. Cricenti, L. Ferrari, B.A. Orłowski and B. Kowalski, *Vacuum* 46 (1995) 485.
- [27] C.B. Norris and K.R. Zanio, *J. Appl. Phys.* 53 (1982) 6347.



ELSEVIER

Applied Surface Science 104/105 (1996) 57–60



Photoexcited carrier diffusion near a Si(111) surface and in the Si bulk

C.M. Li, T. Sjodin, Z.C. Ying¹, H.L. Dai^{*}

Laboratory for Research on the Structure of Matter, University of Pennsylvania, Philadelphia, PA 19104, USA

Received 28 June 1995; accepted 25 October 1995

Abstract

Photocarrier diffusivities of Si have been measured near a surface covered with naturally grown oxide layer and in the bulk using the transient grating technique in reflection and transmission geometries, respectively. Within experimental uncertainty, the surface diffusivity near the surface is found to be essentially the same as that in the bulk, indicating that in the medium-high carrier density regime there is no significant surface effects such as surface recombination, surface state trapping or band bending, affecting band edge carrier diffusion.

PACS: 72.20.Jv; 73.50.Gr; 78.30.Fs

1. Introduction

It has been recently recognized that one of the most important mechanism for surface photo-chemistry is induced by photoexcited electrons in the substrate [1–3]. In this mechanism, excited electrons which are generated within the collisional mean free path of the surface may survive relaxation collisions and reach surface adsorbate, inducing chemical reactions. A quantitative characterization of this mechanism requires knowledge of the relaxation and transportation dynamics of the excited electrons in the surface region, which may be influenced by surface conditions such as band bending, surface recombina-

tion, and surface states. Furthermore, in recent studies of light induced chemical processes on surfaces, the intensity of the light used often induces a high carrier density in the substrate. Accurate measurements of carrier diffusivity at high carrier density region and comparison of carrier diffusivities in the surface and bulk regions are thus necessary for understanding and designing surface photo-chemistry.

In this paper, we will address issues related to carrier diffusion in silicon; specifically the ambipolar diffusivity of band edge carriers near the surface and in the bulk regions. The band edge carriers are generated by photon (energy 1.91 eV) excitation of electron–hole pairs above the indirect band gap (1.1 eV), which then rapidly relax to the band edge on subpicosecond timescale. Diffusivities in both the surface and bulk are measured around a carrier density of $2 \times 10^{18} \text{ cm}^{-3}$. The measurements are conducted on a Si(111) surface as well as a thin (2–4

^{*} Corresponding author. E-mail: dai@chem.upenn.edu.

¹ Present address: New Mexico State University, Las Cruces, NM 88003, USA.

μm) silicon film so that a comparison of the diffusivities in the surface versus bulk regions can be made for the observation of any possible surface effects.

For measuring the ambipolar diffusivity of band edge carriers in the surface and bulk regions, we have adopted the transient grating (TG) technique in reflection and transmission geometries, respectively. When performed in the reflection geometry where the first order diffraction beam is on the same side of the sample as the pump and probe beams, this technique measures diffusivity of band edge carriers within a few hundred Å of the Si surface region. This surface sensitivity of TG in reflection geometry has been shown by Fishman et al. [4]. In the reflection geometry, the TG signal from the sample bulk is greatly reduced because of phase mis-matching. As a result the magnitude of the TG signal is equivalent to that from surface layers of a thickness of $\lambda/4\pi\sqrt{n^2 + k^2}$. The surface contribution to the TG signal, if exists, is not affected by this phase mis-matching and is now much more likely to be observed. In the case of silicon the probing depth of reflective transient grating is only ~ 140 Å at the probe wavelength of 720 nm.

When operated in the transmission geometry where the first order diffraction beam is detected on the other side of the sample, the TG signal arises from the entire bulk where the pump and probe light penetrate and overlap. Unlike the TG in reflection geometry, TG in transmission geometry measures the ambipolar diffusivity of carriers in the bulk [4]. By measuring and comparing the diffusivity in the bulk and near a surface with the same carrier density generated by excitation with the same pump power, surface effect on carrier diffusion, if any, will be revealed.

2. Experimental

In both the transient reflection grating (TRG) and transient transmission grating (TTG) experiments, a mode-locked Nd:YAG laser (Spectra Physics) is used to synchronously pump two dye lasers to generate 5.3 ps, 652 nm pulses and 3.8 ps, 715 nm pulses both at 82 MHz repetition rate. The two pulse trains

are amplified by a three-stage (Quanta-Ray) or a two-stage homemade dye amplifiers, respectively. Both amplifiers are pumped by the 532 nm output of a 20 Hz Q-switched Nd:YAG laser (Continuum). The maximum pulse energy of the pump beam is 350 μJ /pulse while that of the probe beam is 80 μJ /pulse. The pulse energy of both beams can be adjusted with a half wave plate–polarizer combination. The probe beam energy is always kept one order of magnitude smaller than the pump beam energy in all the experiments to prevent probe interference.

The TRG experimental principles and setup have been described in detail in Ref. [5]. Briefly, the pump beam is split into two and re-crossed onto the (111) surface of a 300 μm thick Si sample in air with a crossing angle of $2\theta = 9.6^\circ$. In this geometry, a grating with a fringe period of $\Lambda = \lambda/2 \sin \theta = 3.9$ μm is formed ($\lambda = 652$ nm). The probe pulse with a variable time-delay after the pump pulse is directed onto the sample surface at an arbitrary incident angle ($\sim 6^\circ$) and spatially overlapped with the pump beams of 2 mm in diameter. The first order diffraction signal at $\sim 18^\circ$ reflection passes through a Corning 7-54 filter, which reduces the scattered light from the pump beams, and then a spatial filter with 200 μm pinhole, which reduces the probe beam scattered light and further enhances the signal to noise ratio. The diffracted light after the pinhole is detected by a photomultiplier tube and the signal is integrated by a gated CAMAC board interfaced with a micro-computer. A fraction of the probe beam is split off by a pellicle beam splitter and monitored by another photomultiplier tube after being attenuated by neutral density filters to provide a reference for laser intensity fluctuation correction. The zero time-delay position is determined by maximizing the sum frequency generation signal between the probe and either one of the pump beams on a 300 μm thick KDP crystal placed at the same position as the silicon sample.

In the TTG experiments, a 3 ± 1 μm thick Si(100) wafer was used. The crossing angle of two pump beams is $2\theta = 10.4^\circ$ and the grating fringe period is $\Lambda = 3.58$ μm . The probe beam was directed onto the sample surface at the Bragg angle (5.7°). The pump and probe beams entered from one side of the sample, while the first order scattering signal emerging at the Bragg angle from the other side was moni-

tored. The rest of the optical setup is exactly the same as the experiment in reflection geometry.

3. Results and analysis

As an example of the time-evolution of the TG signal, results from a TTG experiments are shown in Fig. 1. The TG signal is measured as a function of probe beam delay time. The pump and probe energies were set at 100 and 10 $\mu\text{J}/\text{pulse}$, respectively. This pump pulse energy generates a photoexcited electron–hole pair density of $1.8 \times 10^{19} \text{ cm}^{-3}$ at the grating peak. Following a sharp rise ($\sim 6 \text{ ps}$), the TTG signal in Fig. 1 has a monotonous decay on sub-nanosecond time scale.

The 1.9 eV photons excite electrons from the valence band into the conduction band through phonon mediation. The initially excited electron–hole pairs relax rapidly to the band edge through intraband thermalization to form a band edge carrier grating. Heat released during this process may also form a thermal expansion grating and an acoustic wave grating. The band edge carriers will eventually decay through photoluminescence, carrier–carrier annihilation and carrier–phonon thermalization. Again, this decay process may induce a thermal grating.

The generation and relaxation of the various grat-

ings happen on different time scales. Intraband thermalization of hot carriers in semiconductors occurs on a time scale of $\sim 1 \text{ ps}$ which is within the pump laser pulse. A possible thermal grating would occur in the same time scale as that of the observed diffraction signal decays and should not be ignored before further analysis. For example, Pennington et al. [6] have detected such thermal grating on a GaAs(100) surface using transient reflective grating technique. The signal rise has a time scale of $\sim 20 \text{ ps}$ and the signal decay has a time scale of $\sim 150 \text{ ps}$. The signal rise and decay were well explained by surface expansion and thermal diffusivity. In order to decide if the thermal expansion grating is also present in the case of Si, we calculated the diffraction signal rise from a possible thermal grating using the same algorithm as described in Ref. [6]. The calculated curve is shown in Fig. 1 as the dashed line. It appears that the curve is too slow to account for the observed sharp rise. This is a strong evidence for eliminating possible thermal grating contribution to the scattering signal. Thus, we conclude that the scattering signal must be attributed to the band edge carrier grating only. The reason that light scattering off a thermal grating is not observed here is because the light absorption coefficient is much less than GaAs. As described in detail in Ref. [6], the characteristic signal rising time from a thermal grating is roughly inversely proportional to the light absorption coefficient. A small absorption coefficient would result in a much weaker signal with a much longer rising time.

The decaying part of the TG signal is analyzed by an ambipolar diffusion differential equation that includes, single carrier decay channels, whose lifetime has been measured to be greater than 50 ns for Si [7], the radiative recombination channel with coefficient B reported to be $1.1 \times 10^{-14} \text{ cm}^3 \text{ s}^{-1}$ [8], and the Auger recombination channel with coefficient γ at a generally accepted value of $3.8 \times 10^{-31} \text{ cm}^6 \text{ s}^{-1}$ [9]. The ambipolar diffusivity D_a is defined along the x direction defined parallel to the silicon surface and perpendicular to the grating and the z direction along the surface normal into the bulk. This equation is solved numerically in x – z dimensions using the finite difference method [10]. The band edge carrier density distribution can be calculated as a function of time following the grating generation with an as-

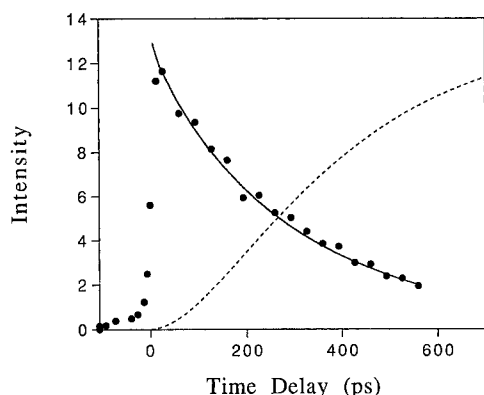


Fig. 1. The TTG diffraction signal as a function of probe pulse time delay. The solid line is a fit to a TTG signal decay due to band edge carrier diffusion. The dashed line is the calculated leading edge if there is a TG signal caused by photothermal surface expansion and diffusion.

sumed D_a value. The first order diffraction (TG) signal is calculated as the square of the first order component in the Fourier transform of the carrier density modulation along the x direction. The calculated first order diffraction signal was then fitted to the experimental data in Fig. 1 to obtain a diffusion coefficient D_a .

The ambipolar diffusivity data (D_a) at a couple of carrier densities N are shown in Table 1 for both the TRG measurements from the Si(111) surface and the TTG measurements on this film water.

4. Discussion and conclusion

From Table 1, it appears that the near surface diffusivity points are slightly lower than those of the bulk ones. However, the difference is within the experimental uncertainty, which is about 10% of the diffusivity value. Therefore, we conclude that for Si covered with a naturally grown oxide layer there appears no significant surface effects, such as surface recombination or surface state trapping, affecting the carrier dynamics. One other consideration is the possible effect by band bending. Due to surface charge, the band bends upwards or downwards depending on the intrinsic doping of the semiconductor. This band bending extends to $\sim 1 \mu\text{m}$ into the bulk. Thus, depending on how the band bends, the carrier velocity and mobility will be affected. However, this seems to be a negligible effect at least in the carrier density range where our experiments were performed. When the injected carrier density is high, the injected carriers can neutralize the net surface charges associated with band bending and flattens the bending band within 1 ps. With a flattened band, diffusivity near the surface or in the bulk should be identical.

Table 1
Diffusivity near a Si(111) surface versus diffusivity in the Si bulk

Carrier density (cm^{-3})	Surface diffusivity (cm^2/s)	Bulk diffusivity (cm^2/s)
Intrinsic		18.8 ^a
1.8×10^{19}	4.6	5.0
2.8×10^{19}	5.1	5.7

^a See Ref. [11].

The overall low diffusivity near carrier density $2 \times 10^{19} \text{ cm}^{-3}$ in comparison with the intrinsic diffusivity indicates that it is an optimal range for substrate electron mediated chemical processes. Because at such carrier densities carriers diffuse slower they would stay in the surface area longer, and therefore may have more chances to tunnel to surface adsorbate to induce chemical reactions. This carrier density region coincidentally is close to those generated by present high power pulsed lasers.

In conclusion, we have found from transient grating experiments performed on Si samples with both reflection and transmission geometries that carrier diffusivity near the Si(111) surface or in the Si bulk are identical with the experimental uncertainty ($\sim 10\%$). This indicates that band bending near surface or effects due to surface defects/impurities do not influence carrier diffusion in the high carrier density region (10^{19} cm^{-3}).

Acknowledgements

This work is supported by the National Science Foundation, MRL Program, under Grant No. DMR91-20668. Acknowledgment is made to the MRL Laser Facility at the University of Pennsylvania for the use of equipment.

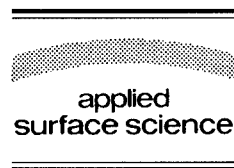
References

- [1] Z. Ying and W. Ho, *Phys. Rev. Lett.* 60 (1988) 57.
- [2] Z.C. Ying and W. Ho, *Phys. Rev. Lett.* 65 (1990) 741.
- [3] S.A. Buntin, L.J. Richter, R.R. Cavanagh and D.S. King, *Phys. Rev. Lett.* 61 (1988) 1321.
- [4] I.M. Fishman, C.D. Marshall, J.S. Meth and M.D. Fayer, *J. Opt. Soc. Am. B* 8 (1991) 1880.
- [5] C.M. Li, Z.C. Ying, T. Sjödin and H.L. Dai, *Proc. SPIE* 2125 (1994) 107.
- [6] D.M. Pennington and C.B. Harris, *IEEE J. Quantum Electron.* 28 (1992) 2523.
- [7] L. Jonikas, K. Jarasiunas and J. Vaitkus, *Phys. Status Solidi* 112 (1989) 375.
- [8] W. Gerlach, H. Schlagenotto and H. Maeder, *Phys. Status Solidi (a)* 13 (1972) 277.
- [9] M.W. Rowe, H. Liu, G.P. Williams, Jr. and R.T. Williams, *Phys. Rev. B* 47 (1993) 2048.
- [10] S.V. Patankar, in: *Numerical Heat Transfer and Fluid Flow* (Hemisphere, Washington, DC, 1980) pp. 59–61.
- [11] N. Neuberger, *Handbook of Electronic Materials*, Vol. 5 (Plenum, New York, 1971).



ELSEVIER

Applied Surface Science 104/105 (1996) 61–67



In-situ monitoring of surface chemistry and charge transfer at semiconductor surfaces

E. Fefer^a, L. Kronik^a, M. Leibovitch^a, Yoram Shapira^{a,*}, W. Riedl^b

^a Department of Electrical Engineering–Physical Electronics, Faculty of Engineering, Tel-Aviv University, Ramat-Aviv 69978, Israel

^b Siemens AG, Corporate Research and Development, ZFE T EP 2, Domagkstrasse 11, D-80807 München, Germany

Received 28 June 1995; accepted 26 September 1995

Abstract

A simple method for in-situ distinction between the effect of dipole formation/annihilation and charge transfer to/from surface gap states on the semiconductor work function is described. The technique is based on simultaneous monitoring of the work function and photovoltage at the semiconductor surface. The approach is illustrated by experiments performed on single crystalline InP(100) surfaces and polycrystalline Cu(In,Ga)Se₂.

1. Introduction

It is well known that chemical reactions at semiconductor surfaces may change the semiconductor surface work function (defined as the amount of energy required to remove a surface electron from the Fermi level into the vacuum). Indeed, monitoring the surface work function so as to determine such a change is a well established experimental technique [1]. A surface chemical reaction may change the surface work function due to two distinctly different processes: These are a change in the surface dipole and a change in the surface band bending [2–5]. The distinction between the two mechanisms is usually based on measuring the change in the surface photovoltage (which measures the band bending), in addition to the change in the work function in the dark

(which measures both changes in the band bending and in the surface dipole) [6–9]. However, such measurements are not conducted in-situ because that would require simultaneous measurements in the dark and under illumination. In particular, monitoring the dynamics of a photo-induced chemical reaction is difficult [10,11], because typically the optical excitation which drives the reaction also excites carriers to/from the surface and changes the band bending [12].

In this article, we provide a simple technique which makes it possible to monitor changes in the surface dipole and in the band bending independently, simultaneously and in-situ. The technique is suitable for both photo-induced and non-photo-induced surface chemical reactions. Thus, our approach may be a valuable tool in determining the dynamics of charge transfer electronic processes in surface chemical reactions. Such information is essential in studies of the initial stages of Schottky

* Corresponding author.

barrier formation, studies of chemisorption and heterogeneous catalysis at semiconductor surfaces, etc. [5].

2. Theoretical approach

In order to understand the different possible contributions to the work function, let us inspect the electronic band structure at a semiconductor surface, which is shown schematically in Fig. 1. Using the figure, the work function at the semiconductor surface in equilibrium may be expressed in the form:

$$W_s = (E_C - E_F)_b - qV_s + \chi + \Delta\phi_s \equiv (E_C - E_F)_b - qV_s + \chi^* \quad (1)$$

Here W_s is surface work function, $(E_C - E_F)_b$ is the difference between the bottom of the conduction band and the Fermi level in the semiconductor bulk, q is the (absolute value of) the electron charge, V_s is the surface band bending (defined as positive when the bands bend downwards). $\chi = E_1 - E_c$ is the electron affinity. E_1 is the local vacuum level, defined (following Marshak [13]) as the energy of an electron at a given point if it were at rest and free from the influence of the crystal potential (which determines the band structure). $\Delta\phi_s$ is the dipole at the semiconductor surface, which depends on surface ordering and adsorbed species [9,14]. We define $\Delta\phi_s$ as positive if its orientation increases the work function (i.e., negative side pointing outwards). Note that the term 'surface dipole' means the *additional* dipole contribution to the surface work function. The surface dipole manifests itself as a potential step in the local vacuum level at the surface. $\chi^* \equiv \chi + \Delta\phi_s$ is the 'effective electron affinity', which is defined as

the total barrier a surface electron must overcome to be emitted from E_c into the vacuum. Note that according to our definition the electron affinity is an inherent material property which remains unchanged upon any surface treatment. Changes in the affinity referred to in the literature (e.g. Ref. [14]) should be taken as changes in χ^* , i.e. in $\Delta\phi_s$ in our nomenclature.

As mentioned above, when a chemical reaction takes place at the semiconductor surface, the surface work function may change as a result of changes in the surface band-bending and/or the surface dipole.

The surface band-bending changes if the charge balance between the surface states and the semiconductor space charge region is modified due to the reaction. This may be a result of a change in surface state properties, e.g. density, energy position, etc. In the case of illumination-induced chemical reactions the change in band-bending may also be the result of excitation of carriers from a surface state into the conduction band (or from the valence band into a surface state) [15], or the result of trapping of excited carriers in surface states [16].

The surface dipole may change due to formation/annihilation of dipoles and/or a change in the ordering of the surface, which affects the net surface dipole [9]. Such a change does not entail charge transfer since the dipole is electrically neutral and hence does not affect the surface band-bending. When the surface work function is monitored one cannot, without additional measurements, determine the extent of the dipole and the surface band bending contributions.

Many experimental investigations (Refs. [6–8] are but a few examples) have utilized measurements of the surface band-bending (using the photosaturation technique) *and* the work function in the dark before and after the surface reaction. This makes it possible to distinguish between the changes in the band-bending and surface dipole ex-situ. The photosaturation technique involves applying illumination intensity which is strong enough to flatten the bands [7,8] while the surface dipole is unaffected: The small width of the dipole, which is about a lattice constant, and the strong bonding of its charge lead to its stability under external excitation. Also, the dipole may be considered as a neutral electrostatic system due to the weak dipole interaction [17].

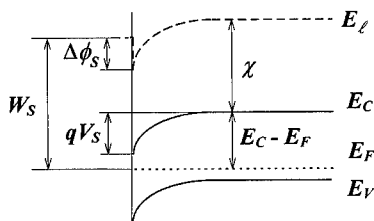


Fig. 1. Schematic diagram of the electronic band structure at a semiconductor surface.

Our approach is based on repeatedly exciting the semiconductor with an optical ‘probe beam’ for limited durations of time while continuously monitoring the surface work function throughout the chemical reaction. A plot of the surface work function versus time should feature ‘pulses’ caused by the illumination pulses. This is because during the ‘probe beam’ illumination (designed *not* to induce any chemical activity) the surface work function changes *only* due to changes in the band-bending (see Eq. (1)). If photosaturation is attained, the height of each ‘pulse’, or ‘spike’, would be exactly equal to the band-bending. Hence, the *dynamic* behavior of the surface band-bending (and by subtraction, the surface dipole) is obtained.

It is important to note that photosaturation is not

always experimentally obtainable: The bands may still be bent even at high illumination intensities due to the Demer effect, especially in low-doped semiconductors [18]. Also, the intensity required to flatten the bands might be higher than the optical damage threshold, inducing ‘parasitic’ chemical effects. Therefore, photosaturation must be verified for each specific sample separately. Nevertheless, even if photosaturation is unattainable, the relative change in the height of the ‘spikes’ may continue to reflect the trends of the change in the surface band-bending. Indeed, it has been shown that in order to determine whether formation/annihilation of dipoles takes place it is sufficient to draw both the work function and the surface photovoltage on a normalized scale [9]. Thus, although the experiments to be discussed below have been conducted using (relatively high) laser illumination, no attempt to reach rigorous photosaturation has been made.

Fig. 2 schematically shows three surface work function curves as a function of time: In curve (a) the chemical reaction changes the surface dipole, but not the band bending. Hence, the dark value of the work function changes, but the height of the ‘spikes’ due to illumination does not. Visually, the ‘spike envelope’ (dashed curve) follows the ‘dark’ curve. In curve (b), the chemical reaction changes the band bending, but not the surface dipole. Hence, the change in the ‘dark’ work function is equal and opposite to the change in ‘spike’ heights. Visually, the ‘spike envelope’ is constant. Curve (c) depicts a general case where both dipole and band bending change.

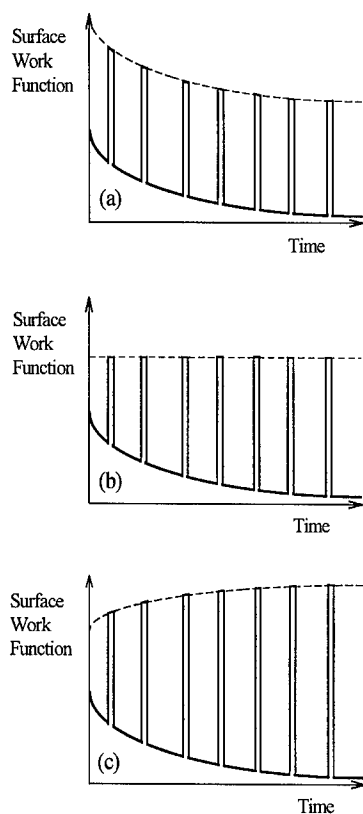


Fig. 2. Schematic work function versus time curves during a surface reaction: (a) change in surface dipole, no change in surface band bending; (b) no change in surface dipole, change in surface band bending; (c) change in both surface dipole and surface band bending.

3. Experimental setup and illustrations

Fig. 3 schematically shows the setup used in our experiments. Changes in the work function have been continuously monitored using a semi-transparent Kelvin probe [1] with a 1 mV sensitivity (Delta Phi Elektronik, Jülich). The contact potential difference (CPD) between the surface under study and the Kelvin probe is continuously monitored. Changes in the surface work function are equal to changes in the CPD [1]. Illumination from either a 5 mW HeNe laser or a 15 mW Ar⁺ laser was used as the ‘probe beam’. For photochemical excitation: $h\nu \gg E_g$ UV radiation from an Hg lamp was used.

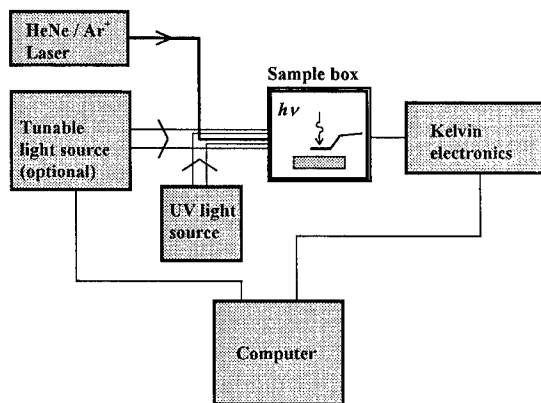


Fig. 3. Schematic diagram of the experimental setup.

The following cases are given as brief illustrations of the power of the technique under various conditions without going into further elaboration of their scientific implications.

We followed the in-air oxidation of the free surface of a $5 \times 10^{16} \text{ cm}^{-3}$ p-type InP(100) wafer, after its etching in 30% H_2O_2 solution for 30 s. Ar^+ laser radiation was used as the 'probe beam'. We independently verified that the 'probe beam' does not induce surface chemical activity. The results are shown in Fig. 4. Analysis of the data shows that the height of

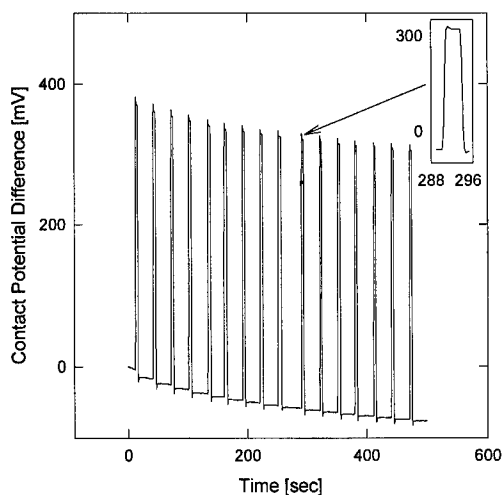


Fig. 4. CPD as a function of time at an InP(100) surface immediately after etching in H_2O_2 , with Ar^+ laser periodic 'probe beam' illumination. Inset features a zoom on a typical Ar^+ induced CPD 'spike'.

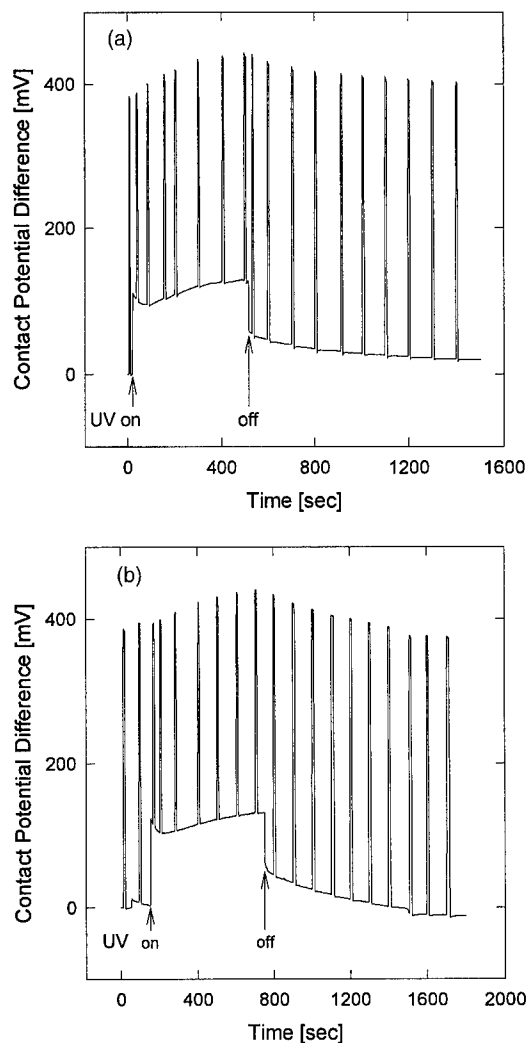


Fig. 5. CPD as a function of time at an InP(100) surface subject to UV irradiation and Ar^+ laser periodic 'probe beam' illumination: (a) in air; (b) in N_2 .

the 'spikes' and hence the surface band bending do not change with time (compare with Fig. 2a). This implies that all CPD changes are only due to dipole formation/annihilation. Since according to the previous analysis no surface states are formed, it follows that the change of about 75 mV in the CPD is due to a formation of a negative surface dipole (or the annihilation of a positive dipole). No significant change in band bending takes place.

Another example is the UV-induced photochemi-

cal response at the same InP surface. Fig. 5a and b show both the 'UV on' and 'UV off' parts of the work function curve, in air and in N_2 , respectively. Here, Ar^+ laser light was used as the probe beam. Using Fig. 5 we note that as soon as the UV radiation is turned on, the CPD signal which is due to the UV *only* (observed by following the position of the 'bottom' of the spikes) changes considerably (by more than 100 mV) and abruptly. However, the CPD signal due to the combined UV and Ar^+ laser illumination (observed by following the position of the 'spike envelope') changes by a few mV at most.

After this initial response, the UV-induced CPD decreases while the UV + laser-induced CPD increases (compare with Fig. 2c). After about 50 s, both CPD signals increase in parallel for the remainder of the 'UV on' part of the curve. During the 'UV off' part of the response, the opposite processes take place.

Analysis of the data shows that the initial response is consistent with a change of CPD *only* due to UV-induced band bending (compare with Fig. 2b). The following response shows that *both* the band-bending and the surface dipole change in this regime. Moreover, the height of the spikes increases. This means that the UV-induced charge transfer displays a decay from the initial overshoot, i.e., the amount of charge transferred between the surface and the bulk, immediately after the UV is switched on, is larger than its steady state value. Analysis of the response after about 50 s indicates a change in surface dipole *only*. This dipole change begins immediately after the UV irradiation is switched on, but occurs much more slowly than charge transfer processes (note the monotonously increasing 'spike envelope'). After the UV is turned off, the band bending increases immediately and the surface dipole slowly decreases.

Analysis of these representative data of our technique in comparison with a typical CPD experiment where only the UV-induced CPD behavior is followed, shows that much more information may be provided by the proposed technique. Moreover, Fig. 5 shows that all the three cases schematically depicted in Fig. 2 are obtained experimentally in one (apparently reversible) photochemical surface reaction. Also, the analysis permits a study of the effect of the ambient. It is quite clear that the surface dipole increases more rapidly upon UV switch-on

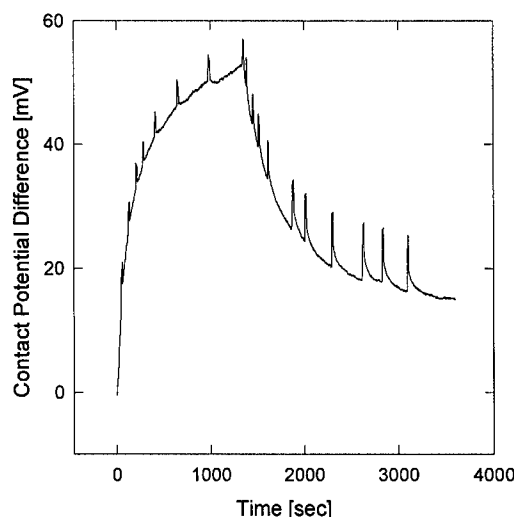


Fig. 6. CPD as a function of time at a $Cu(In,Ga)Se_2$ polycrystalline surface subject to UV irradiation and HeNe laser periodic 'probe beam' illumination in air.

and decreases more slowly upon UV switch-off in air than in N_2 .

Our technique has also been applied to the study of UV-induced photochemical effects at the surface of polycrystalline $Cu(In,Ga)Se_2$ (CIGS) samples (manufactured by Siemens AG, München). CIGS is a promising absorber material for high performance, low cost solar cells [19,20]. However, its chemistry is considerably more complicated and less well understood than that of Si or III–V semiconductors. Fig. 6 shows both the 'UV on' and 'UV off' parts of the work function curve. It is easily observed that the CPD, and hence the surface work function, increase upon exposure to the UV irradiation. However, the surface band-bending (as expressed by the heights of the 'spikes') does not change at all during the 'light on' part of the experiment. In the 'light off' part of the response, the surface work function decreases, whereas the surface band-bending *increases* (by 6 mV). The work function does not return to its initial value, but is 16 mV higher in its new steady state.

The analysis of the results is as follows: A positive surface dipole (according to the sign convention introduced above) is formed at the surface due to a photochemical reaction induced by the UV irradiation. Once the light is turned off, most of this dipole disappears. However, a 'residual' dipole remains.

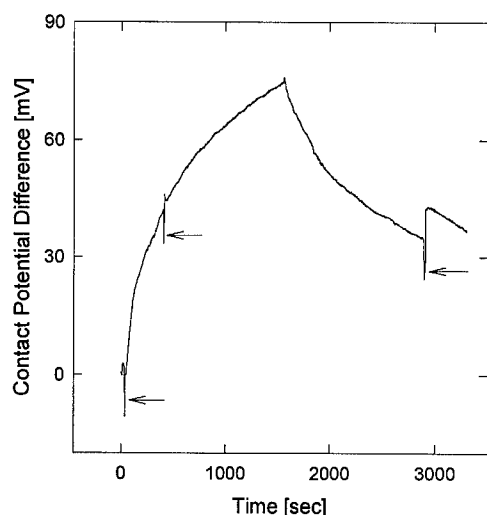


Fig. 7. CPD as a function of time at a Cu(In,Ga)Se_2 polycrystalline surface subject to UV irradiation and HeNe laser periodic 'probe beam' illumination in N_2 .

The work function increased by 16 mV, whereas the surface band-bending increased by 6 mV. Hence, the magnitude of the residual dipole is 22 mV (see Eq. (1)). We conclude that no charge transfer between the surface and the bulk takes place during the build-up of the dipole, as the surface band-bending does not change during the 'light on' part of the response. However, during the decay of the dipole, the surface becomes more positive, since the (p-type) band bending increases.

It is interesting to note that during the experiments on one of the CIGS samples, type conversion of the surface was observed. This is shown in Fig. 7, which is similar to Fig. 6, but with fewer 'probe pulses'. Despite the similar behavior under UV irradiation, the negative amplitude of the 'spikes' clearly shows a different direction of the band bending, in this case, which is typical of an n-type surface [15]. One possible explanation is that at this CIGS surface the UV irradiation created conditions under which the well known n-type ordered defect compound (ODC) [21] surface layer manifested itself. Another (less plausible) possibility could be a drastic chemical reaction induced by the UV irradiation. Indeed, type conversion of n-CuInSe₂ has been reported before [22].

4. Conclusions

The combination of work function measurements (using a Kelvin probe) together with probing pulses of laser illumination seems to be an effective, inexpensive and easy to use tool for in-situ independent monitoring of surface dipoles and surface charge transfer during chemical reactions. Moreover, the technique works equally well in any ambient, since the measurements are vacuum independent. This technique may be easily combined with surface photovoltage spectroscopy (SPS), which yields direct and quantitative information about surface states [15,23], in order to obtain a complete picture of the evolution of the electronic surface structure.

Acknowledgements

The research was partially supported by a grant from the Israeli National Council for R&D and the BMFT, Germany. E.F. wishes to thank the Eshkol Foundation (Ministry of Science and the Arts) for a doctoral scholarship.

References

- [1] D.P. Woodruff and T.A. Delchar, *Modern Techniques of Surface Science* (Cambridge University Press, Cambridge, 1986) ch. 7.
- [2] W. Chen, A. Kahn, P.S. Mangat, P. Soukiasian, L.T. Florez, J.P. Harbison and C.J. Palmstrom, *J. Vac. Sci. Technol. B* 11 (1993) 1571.
- [3] H. Nienhaus and W. Mönch, *Appl. Surf. Sci.* 65/66 (1993) 632.
- [4] K. Wandelt, in: *Physics and Chemistry of Alkali Metal Adsorption*, Eds. H.P. Bonzel, A.M. Bradshaw and G. Ertl (Elsevier, Amsterdam, 1989).
- [5] W. Göpel and G. Rocker, *J. Vac. Sci. Technol.* 21 (1982) 389.
- [6] R.D. Campbell and H.E. Farnsworth, *Surf. Sci.* 10 (1968) 197.
- [7] L.J. Brillson, *J. Vac. Sci. Technol.* 16 (1979) 1137.
- [8] M. Bruening, E. Moons, D. Yaron-Marcovich, D. Cahen, J. Libman and A. Shanzer, *J. Am. Chem. Soc.* 116 (1994) 2972; M. Bruening, E. Moons, D. Cahen and A. Shanzer, *J. Phys. Chem.* 99 (1995) 8368.
- [9] L. Kronik, M. Leibovitch, E. Fefer, V. Korobov and Y. Shapira, *J. Electron. Mater.* 24 (1995) 893.

- [10] L.J. Richter and R.R. Cavanagh, *Progr. Surf. Sci.* 39 (1992) 155.
- [11] Y. Shapira, R.B. McQuistan and D. Lichtman, *Phys. Rev. B* 15 (1977) 2163.
- [12] C.G.B. Garrett and W.H. Brattain, *Phys. Rev.* 99 (1955) 376.
- [13] A.H. Marshak, *IEEE Trans. Electron Devices* ED-36 (1989) 1764.
- [14] W. Mönch, in: *Chemistry and Physics of Solid Surface V*, Vol. 35, Springer Series in Chemical Physics, Eds. R. Vanselow and R. Howe (Springer, Berlin, 1984).
- [15] H.C. Gatos and J. Lagowski, *J. Vac. Sci. Technol.* 10 (1973) 130.
- [16] V.M. Buimistrov, A.P. Gorban and V.G. Litovchenko, *Surf. Sci.* 3 (1965) 445.
- [17] L.D. Landau and E.M. Lifshitz, *The Classical Theory of Fields*, 4th ed. (Pergamon, Oxford, 1975) ch. 5.
- [18] Q. Liu, C. Chen and H. Ruda, *J. Appl. Phys.* 74 (1993) 7492.
- [19] F. Karg, V. Probst, H. Harms, J. Rimmasch, W. Riedl, J. Kotschy, J. Holz, R. Treichler, O. Eibl, A. Mitwalsky and A. Kiendl, in: *Proc. 23rd IEEE Photovoltaic Specialists Conf.* (1993) p. 441.
- [20] H.-W. Schock, *Mater. Res. Soc. Bull.* 18 (1993) 42.
- [21] W. Riedl, J. Rimmasch, V. Probst, F. Karg and R. Guckenberger, *Sol. Energy Mater. Sol. Cells* 35 (1994) 129.
- [22] H.J. Lewerenz and E.R. Kötz, *J. Appl. Phys.* 60 (1986) 1430.
- [23] L. Kronik, M. Leibovitch, E. Fefer, L. Burstein and Y. Shapira, *J. Electron. Mater.* 24 (1995) 379.



ELSEVIER

Applied Surface Science 104/105 (1996) 68–72

applied
surface science

Electronic structure of the valence band of GdS_x and Gd_3S_4

V.A. Grazhulis^{*}, S.I. Bozhko, I.L. Bolotin, O.R. Bulanov, A.M. Ionov*Institute of Solid State Physics, Russian Academy of Sciences, Chernogolovka, Moscow District 142432, Russia*

Received 28 June 1995; accepted 2 October 1995

Abstract

Electronic structure of clean surfaces of single crystals of magnetic compounds of sulfides of gadolinium GdS_x ($x = 0.8\text{--}1.25$) with NaCl and Th_3P_4 structures has been investigated by ultra-violet and X-ray photoelectron, Auger and electron energy loss spectroscopy. Clean surfaces of GdS_x were obtained by cleavage in situ in ultra-high vacuum and by ion bombardment followed by annealing in vacuum. Photoelectron spectra of the valence band of GdS_x family have the similar structure with a maxima at 9 eV and 5 eV related to a photoemission from the 4f-states and valence band formed by 3p-states of S anions respectively and features in the region 0–2 eV associated with 6s–5d conduction band of GdS_x . An analysis of electron energy loss spectra has shown that the main features in loss spectra at high beam energy are associated with the 4d–4f giant resonance, 5p–5d resonance and plasmon excitation. At low incident energy a prominent multiplet structure is observed and interpreted in terms of the dipole-forbidden 4f → 4f electron transitions.

1. Introduction

GdS_x crystals (where $x = 0.8\text{--}1.5$) belong to a family of compounds with interesting physical properties [1]. Although GdS is an antiferromagnetic (T_N about 50 K) with the MnO (NaCl) structure, an increase of x leads to ferromagnetic ordering and transition to the Th_3P_4 structure for Gd_3S_4 and Gd_2S_3 . Earlier ultra-violet photoelectron spectroscopy studies [2] of GdS films have revealed the main features of electron spectra, associated with the conduction and valence bands, and position of the 4f-states which play an important role and determine interesting physical properties. However, no such investigations have yet been performed for GdS_x . In the present paper we report the first part of results of investigations of the electronic structure of GdS_x by

electron spectroscopy, namely, ultra-violet photoelectron spectroscopy (UPS), X-ray photoelectron spectroscopy (XPS), Auger electron spectroscopy (AES), low energy electron diffraction (LEED) and electron energy loss spectroscopy (EELS) on clean surfaces of single crystals of GdS_x .

2. Experiment

The single crystals of $\text{GdS}_{0.8}$ and $\text{GdS}_{1.25}$ (the composition close to Gd_3S_4) used in these experiments were grown by the Bridgman method in a sealed molybdenum crucible 10 mm in diameter and about 100 mm in length (polycrystalline GdS was prepared by annealing at 2100 K in vacuum 10^{-5} Torr). Light ‘golden’ crystals of GdS have the NaCl structure with $a = 5.560$ Å, display metallic conductivity and are antiferromagnetic with $T_N = 50$ K.

^{*} Corresponding author.

'Black' crystals with the $\text{GdS}_{1.25}$ composition (according to electron micro-probe analysis) have the cubic Th_3P_4 structure with $a = 8.35 \text{ \AA}$ (checked by X-ray diffraction), display also metallic conductivity and are ferromagnetic with T_c about 25 K. The samples were cut from a boule and mounted mechanically on a special sample holder or glued by a conductive epoxy. Clean surfaces were obtained either by cleaving in UHV (about 10^{-10} Torr) or by the ion bombardment and annealing.

All experiments were performed using the electron spectrometer ESCALAB-5 with a spherical sector analyzer (the resolution was 0.1 eV for UPS and low energy (10–100 eV) EELS, and 0.5 eV for higher energy loss spectroscopy). Photoemission experiments were carried out using He discharge lamp ($h\nu = 21.2$ and 40.8 eV) and Al K_α X-ray source ($h\nu = 1486.6$ eV). In the EELS measurements electron guns with the primary electron beam energy 10–100 eV (with a monochromator, FWHM 0.1 eV) and 400–2000 eV were used. Chemical composition of surfaces was checked by AES.

3. Results and discussion

Photoelectron spectra of rare earth (RE) compounds usually have a rather complicated structure due to the presence of 4f-states and their interaction with other electron shells [3,4]. The main electronic

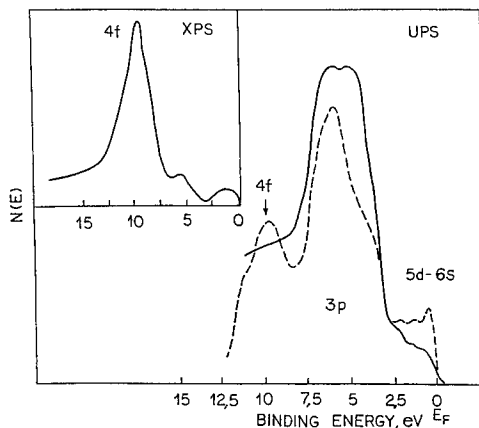


Fig. 1. UPS photoemission spectra of Gd_3S_4 : solid line He I, dashed line He II. Inset: XPS spectrum (Al K_α) of valence band Gd_3S_4 .

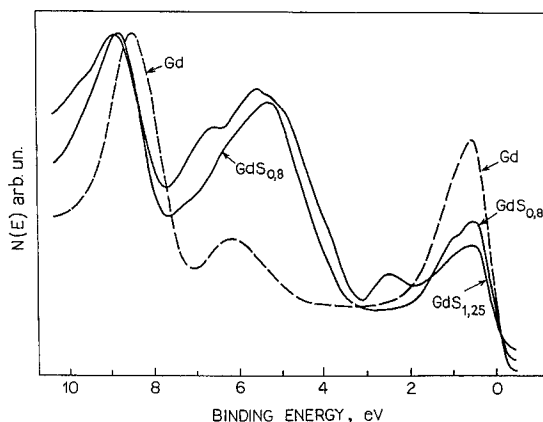


Fig. 2. Photoemission spectra (He II, $h\nu = 40.8$ eV) of Gd_3S_4 , $\text{GdS}_{0.8}$ and Gd (dashed line), normal emission. The spectra are normalized to the intensity of 4f peaks.

configuration of gadolinium ions Gd^{3+} in chemical compounds is $4f^7 5s^2 5p^6$ [2,3] and the wave functions of 4f-electrons are strongly localized and screened by the 5s, 5p electrons. Our UPS and XPS results revealed that the valence electron spectra of GdS_x have a comparatively simple structure (see Figs. 1 and 2) due to a stable half-filled $4f^7$ -shell of the Gd^{3+} ion with the $^8\text{S}_{7/2}$ configuration which transform to the ^7F -term after the photoemission process. The spectra exhibit maxima at 9 eV and about 5 eV related to photoemission from the 4f-states and from the valence band formed by 3p-states of S anions. Features in the 0–2 eV region seem to be associated with the conduction band formed by 6s and 5d electrons of Gd. The peak at about 9 eV dominates in the XPS spectra, reflecting the fact that the photoionization cross-section increases for higher azimuthal quantum numbers with the growth of the excitation energy. The UPS and XPS (Fig. 1) spectra are similar to those reported in Ref. [2] for GdS (NaCl-type). It should be noted that the positions of the 4f and 5d features in our UPS spectra correlate not only with the GdS data [2] but even with Gd [5], except for the fact that the intensity of photoemission near E_f is higher in GdS and Gd. A possible explanation of this fact is that the position of strongly localized 4f-states in gadolinium compounds is essentially determined by the stable $4f^7$ configuration of Gd and weakly dependent on the atomic environment, and the variation of photoemission intensity



Fig. 3. LEED pattern for $\text{GdS}_{0.8}(001)$: $E_p = 138$ eV, $T = 300$ K.

near E_f reflects the fact that the density of 5d electrons in the conduction bands of more closely packed Gd and GdS is higher than that of $\text{GdS}_{1.25}$ (Fig. 2).

Preliminary investigations of atomic structure show that clean (001) surfaces of $\text{GdS}_{0.8}$ cleaved in UHV are not reconstructed and exhibit a 1×1 LEED pattern (see Fig. 3). Our preliminary studies of (001) surfaces of $\text{GdS}_{0.8}$ in the temperature range 30–300 K did not reveal any important changes in the LEED picture and no superstructural spots below T_N (see for comparison [6,7]). We plan to investigate the temperature behavior of the LEED pattern of antiferromagnetic GdS near Neel temperature in more detail. It should be noted that all attempts to obtain a LEED patterns from cleaved or ion cleaned and

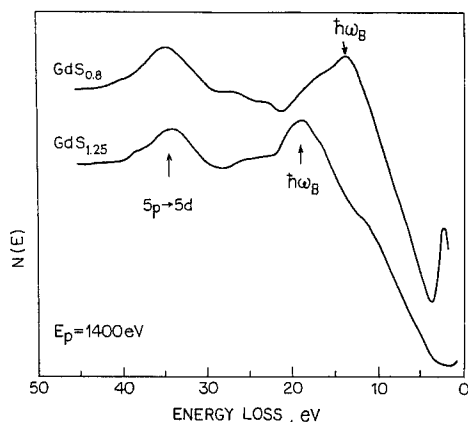


Fig. 4. Electron energy loss spectra of $\text{GdS}_{0.8}$ and Gd_3S_4 after cleavage in UHV $E_p = 1100$ eV.

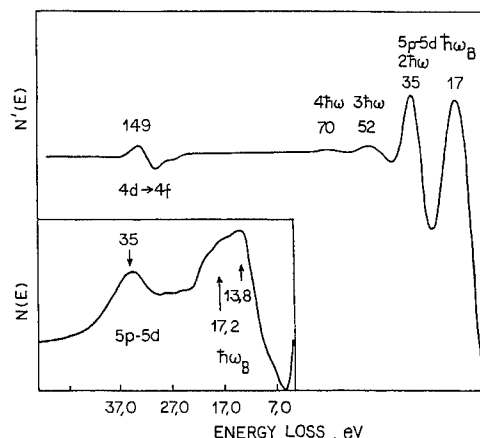


Fig. 5. The EELS spectra of Gd_3S_4 , after ion bombardment, $N'(E)$ mode $E_p = 3000$ eV. Inset: $N(E)$ mode, $E_p = 1000$ eV.

annealed (1100 K) in UHV surfaces of Gd_3S_4 were unsuccessful.

The electron excitation spectrum structure on the clean surface of GdS_x were investigated by EELS (reflection mode) in the 10–100 eV and 400–2000 eV incident energy ranges. The EELS spectra were obtained in the $N(E)$ mode, after numerical differentiation $N''(E)$ spectra (not shown on Figs. 4–6) were used for the precise identification of positions of the weak features in spectra.

The EELS spectra from GdS_x shows that the main features at higher incident beam energy are related to plasmon excitations, to a 4d–4f giant resonance and to the 5p–5d resonance (Figs. 4 and

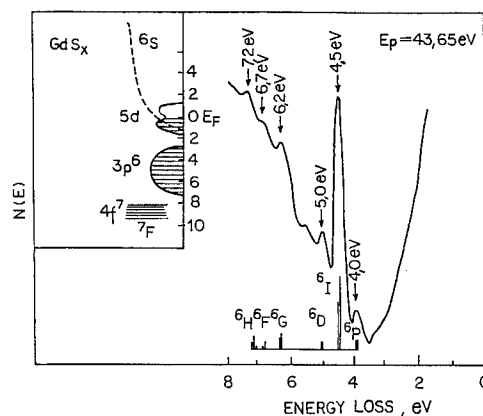


Fig. 6. EELS spectrum of Gd_3S_4 at low incident energy. Inset: possible model of the band structure of GdS_x family.

5). At low incident beam energies a prominent multiplet structure is observed (Fig. 6).

The loss features in the 140–160 eV range are attributed to the giant 4d–4f resonance process: $4d^{10}4f^7-4d^94f^8$. A clearly observed peak at about 35 eV may be associated with the 5p–5d resonance excitation. Both types of excitations are very characteristic of RE and are in good agreement with data reported in Ref. [8] for metallic Gd. The most prominent high incident energy peaks at about 18 and 13.8 eV in the loss spectra of $GdS_{1.25}$ and $GdS_{0.8}$ respectively becomes more clear as E_p is increased and may be associated with the bulk plasmon (see also a series of equally spaced features with decreasing intensity in Fig. 5, apparently due to creation of plasmons). It should be noted that the position of these peaks in EELS spectra depend on the surface composition. According to our Auger data, ion bombardment changes the surface composition of Gd_3S_4 decreasing the sulfur content on the surface, and shifts this plasmon peak close to that of $GdS_{0.8}$. A possible explanation of such a behavior of the plasmon peak is that ion bombardment produces sulfur vacancies on the surface, and reduces the electron density in the valence band as a result the plasmon peak moves towards low loss energy (Fig. 5).

The feature at about 2 eV (Fig. 4) observed in GdS and $GdS_{0.8}$ (and appearing in $GdS_{1.25}$ after ion bombardment) is not yet clearly identified, but is probably related to the collective excitation of conduction electrons.

Sharp electronic transitions in the 3–8 eV range are observed at low primary beam energy (10–100 eV), in Fig. 6. Our data are in good agreement with the data reported for metallic Gd in Refs. [9,10], where similar losses were interpreted in terms of dipole-forbidden transitions between $4f^n$ multiplets. In the case of Gd, the latter corresponds to $4f^7(^8S_{7/2}) \rightarrow 4f^7(^6X_j)$ electron transitions. A clear multiplet structure with energies 4.0, 4.5, 5.0, 6.2, 6.7 and 7.2 eV is observed in our case for GdS_x , in good agreement with results reported in Refs. [7,8] and may be associated with the excitation from the ground state $^8S_{7/2}$ to excited 6X_j multiplet with the 6P , 6I , 6D , 6G , 6F , and 6H components.

Good agreement in energy position and intensity of $4f \rightarrow 4f$ losses for GdS_x in our case, Gd and Gd silicide [9,10], their sharpness and insensitivity to

chemical environment confirm the quasiautomatic character of 4f electrons in Gd compounds. A more detailed analysis of electron energy loss spectra will be published elsewhere.

Thus, using the photoemission and loss spectroscopy, one may propose the band structure of $GdS_{1.25}$ (Th_3P_4 -type crystal structure) which is quite similar to GdS (NaCl structure). Gd chalcogenides have deep localized $4f^7$ states (see Fig. 6, inset), wide valence band formed by 3p-states of chalcogens, and a conduction band of the 6s–5d character near E_f .

4. Conclusion

Investigations of the electronic structure of the valence band of metallic conductor GdS_x with the Th_3P_4 structure by UPS, XPS, and EELS show that the band structure of Gd_3S_4 is similar to that of GdS and even Gd (with respect to the position of 4f-states and 6s–5d conduction band electrons) except for higher density of states near E_f for GdS and Gd. The latter may probably be explained by higher concentration of 5d electrons per cell for Gd and GdS .

Analysis of electron excitations in the case of EELS has shown that the main features in the loss spectra are associated with the plasmon excitation, and 4d–4f and 5p–5d resonances. At low incident energy, prominent loss structures are observed and interpreted in terms of the quasiautomatic dipole-forbidden $4f \rightarrow 4f$ electron transitions.

Acknowledgements

This work was supported by the Russian Foundation for Fundamental Research, Project No. 93-02-02053 and the International Science Foundation Grant RE8000, RE8300.

References

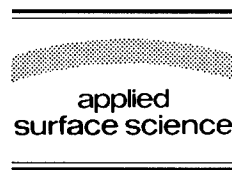
- [1] V.P. Zhuse, Ed., *Fizicheskie Svoistva Halkogenidov Redkozemelnih Elementov* (Nauka, Leningrad, 1973) (in Russian); Gmelin Handbook, Rare Earth-C7, p. 510.
- [2] D.E. Eastman and M. Kuznietz, *J. Appl. Phys.* 42 (1971) 1396.

- [3] M. Campagna, G.K. Wertheim and Y. Baer, in: *Photoemission in Solids II*, Eds. L. Ley and M. Cardona (Springer, Berlin, 1979) p. 216.
- [4] Y. Baer and W.-D. Schneider, in: *Handbook of the Physics and Chemistry of Rare Earths*, Vol. 10, Eds. K.A. Gschneider, L. Eyring and S. Hufner (North-Holland, Amsterdam, 1987) p. 1.
- [5] J.E. Ortega, F.J. Himpsel, D. Li and P.A. Dowben, *Solid State Commun.* 91 (1994) 807.
- [6] P.W. Palmberg, R.E. De Wames, L.E. Vredevoe and T. Wolfram, *J. Appl. Phys.* 40 (1969) 1158.
- [7] V.A. Grazhulis, A.M. Ionov and V.F. Kuleshov, *JETP Lett.* 46 (1987) 51.
- [8] G. Strasser, G. Rosina, J.A.D. Matthew and F.P. Netzer, *J. Phys. F: Met. Phys.* 15 (1985) 739, 753.
- [9] S. Modesti, G. Paolucci and E. Tosatti, *Phys. Rev. Lett.* 55 (1985) 2995.
- [10] J.A.D. Matthew, W.A. Henle, M.G. Ramsey and F.P. Netzer, *Phys. Rev. B* 43 (1991) 4897.



ELSEVIER

Applied Surface Science 104/105 (1996) 73–78



Sb or Cs covered InAs(110) surfaces: moving E_F into conduction band and quantized 2D electron channel

V.Yu. Aristov^{a,b,c}, M. Grehk^d, V.M. Zhilin^b, A. Taleb-Ibrahimi^e, G. Indlekofer^e,
Z. Hurych^a, G. Le Lay^{c,*}, P. Soukiassian^{a,f}

^a Department of Physics, Northern Illinois University, DeKalb, IL 60115-2854, USA

^b Institute of Solid State Physics, Russian Academy of Sciences, Chernogolovka, Moscow District 142432, Russia

^c CRMC2, CNRS, Campus de Luminy, Case 913, F-13288 Marseille Cedex 09, France

^d Materials Physics, KTH, Teknikringen 14, S-100 44 Stockholm, Sweden

^e LURE, Centre Universitaire Paris-Sud, Bat. 209D, F-91405 Orsay Cedex, France

^f Commissariat à l'Energie Atomique, DSM, DRECAM, SRSIM, Bat. 462, Centre d'Etudes de Saclay, 91191 Gif sur Yvette Cedex, France

Received 28 June 1995; accepted 10 October 1995

Abstract

With the study of the formation of Sb/InAs interface by synchrotron radiation photoemission, we add a new piece of evidence that a two-dimensional free electron gas can be created at room temperature, on the (110) cleaved surface of InAs upon adsorption of few metal atoms. In the case of Cs, we demonstrate that this very interesting feature results from 2D channels quantized in the direction normal to the surface.

1. Introduction

During the last few years it was proven in several experiments that upon deposition of minute amounts of noble metals at low temperature (≈ 20 K) [1,2] as well as alkali metals at room temperature (RT) [3–5] onto InAs(110) surfaces one induces a large movement of the Fermi level (E_F) high into the conduction band. This Fermi level movement is accompanied by a large downward band bending which creates an inversion and/or an accumulation layer at the surface. This property makes the study of the metal/InAs interfaces extremely attractive, especially in comparison to other metal/III–V semicon-

ductor systems which have been widely investigated in recent years.

Typically, alkali metals [6–8] and antimony [9–15] on large band gap III–V compounds have been considered as prototypical systems in these metal–semiconductor studies and models in the formation of Schottky barriers. However, for the large band gap semiconductors, the E_F position is found to remain within the gap, at variance with the narrow band gap III–V semiconductors, i.e. InAs and InSb, where E_F at the cleaved, almost bare, (110) surfaces can move, even at RT, to an extremely high pinning position above the conduction band minimum (CBM): up to 0.6 eV with ≈ 0.03 monolayer (ML) coverage of cesium on InAs (110) [3,4].

The narrow band gap semiconductors present very interesting and rather unique properties, such as high

* Corresponding author.

carrier densities, even at very low temperatures, and extremely high electron mobilities. This could lead to a new class of devices able to operate at very low temperatures, where the carriers for other semiconductors would already be frozen. Therefore the creation of a two-dimensional (2D) electron channel, deduced from the measured band bending changes at the free InAs(110) surface, is another striking feature of this semiconductor, which deserves further investigations.

The anomalously high E_F pinning positions, as compared to the theoretical predictions from the metal induced gap state (MIGS) mechanism [16–18], has suggested instead that a metal adatom induced donor type surface state driving mechanism would play a crucial role [1,3–5] as shown recently [19] and described theoretically [20–22], as a matter of fact for s-electron adatoms on GaAs(110). The calculated energies of these pinning states at the GaAs(110) surfaces are in excellent agreement with the experiments and correlate well with the first ionization energy of the free metal atoms.

We had also found a very nice correlation for InAs with adsorbed Cs, Na, Cu and Ag. As we will show later, the adsorption of Sb follows the same simple trend.

More strikingly we will present direct evidence of photoelectron emission in the normally empty conduction band, arising from the 2D electron channel created by the adsorption of minute amounts of metal atoms at RT (cesium in this case). Besides, photoemission from an accumulation layer at the InAs(111) and (100) surfaces has also been measured recently by angle resolved photoelectron spectroscopy (ARPES) [23], while few other examples of the creation of an inversion or an accumulation layer at a free InAs surface had been previously studied by high resolution electron energy loss spectroscopy [24,25]. Yet we present here, for the first time, *discrete* photoemission lines which result from quantization of the 2D electron gas in the direction normal to the surface.

The paper is organized as follows: after a brief description of our synchrotron radiation experiments, we will present results on the formation of the Sb/InAs interface and corresponding band bending at RT and after annealing before showing the *conduction* band electron distributions curves (EDC's)

resulting from the Cs-induced quantized 2D electron channel at the free, nearly pristine, InAs(110) surface.

2. Experimental details

The synchrotron radiation photoemission measurements were performed at RT, at two different places. The study of the Sb/InAs system was performed at the Synchrotron Radiation Center of the University of Wisconsin–Madison using the soft X-ray light emitted by the Aladdin 1 GeV storage ring and dispersed by the Mark II grasshopper monochromator. The photoelectron energies were analyzed by an angle integrated double-pass cylindrical mirror analyzer at a working pressure in the 10^{-11} Torr range. The overall instrumental resolution was better than 200 meV. The Sb evaporation flux (8 Å per min) was calibrated with a quartz microbalance. The Cs/InAs(110) system was studied at the Laboratoire pour l'Utilisation du Rayonnement Electromagnetique (LURE, Orsay, France) using the UV light emitted by the SuperACO storage ring and dispersed by a high resolution toroidal grating monochromator at the SU 3 beam line. The photoelectron energies were analyzed by an angle resolved hemispherical energy analyzer with a maximum acceptance angle of 5° , and overall instrumental energy resolution better than 100 meV. The pressure in the experimental chamber was below 7×10^{-11} Torr during data acquisition. Using very severe standards, pure Cs was deposited at RT from a SAES getters source, carefully outgassed, without any pressure rise during deposition [26]; at RT the maximum Cs coverage attainable is one monolayer.

Clean InAs (110) surfaces were obtained by cleaving in-situ InAs single crystal bars having doping concentrations $\approx 3 \times 10^{-17} \text{ cm}^{-3}$ for both p-type (Zn doped) and n-type (S doped) samples. Only mirror-like cleaved surfaces have been used for data collection. To achieve the best accuracy in the band bending measurements, that is to avoid any potential problem with the photon energy reproducibility, we have always kept the same photon energy within a specific series of measurements; to have high surface sensitivity for both In 4d and As 3d substrate core lines we used a photon energy of 82 eV. The valance

band photoemission experiments were performed at LURE using the optimum energy of 14 eV. The Fermi level positions were determined accurately from thick evaporated noble metal films. At this point it is important to note that at RT, for narrow gap, highly doped, semiconductors, a surface photovoltage effect is absolutely excluded. Further, we stress that we have shown earlier that for well-cleaved InAs samples, flat band conditions are realized for the (110) surfaces; therefore, with our doping concentrations, the Fermi level positions are the same as in the bulk, that is E_F practically coincides with the CBM for n-type samples, while it lies at 0.08 eV above the valence band maximum (VBM) for p-type ones [5].

3. Sb/InAs(110): band bending results

To our knowledge, no experimental work had been performed so far on the growth of Sb on InAs(110), although Sb is unreactive and forms ordered first monolayers on GaAs, InP and GaP. Just very recently, the adsorption of Sb on *n*-type InAs(110) was studied at RT deposition and subsequent annealing, by core-level photoemission and photoelectron diffraction [27]. On *n*-type samples E_F reaches its highest position at 0.3 eV above the CBM at about 2 ML coverage, thus leading to the formation of an accumulation layer (see Fig. 1). The photoelectron diffraction study [28] reveals that the ordered monolayer (after annealing) has essentially the same 1×1 structure as that proposed heuristi-

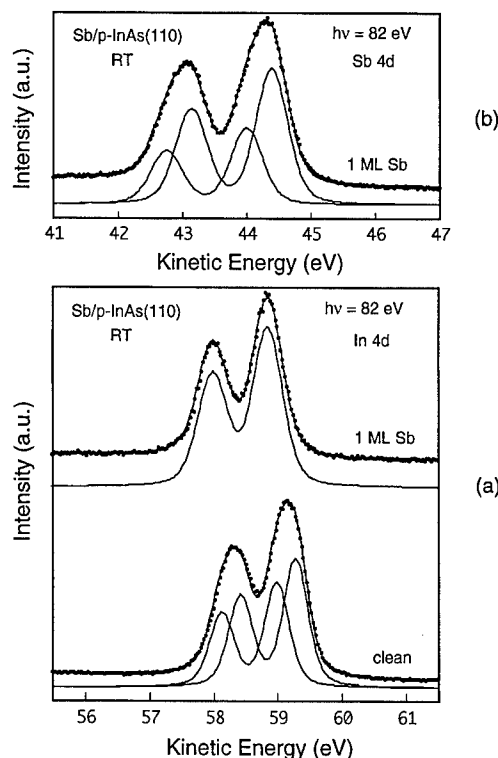


Fig. 2. Core-level spectra and their decompositions: (a) In 4d from the clean and 1 ML Sb covered p-type InAs(110) surface at RT; (b) Sb 4d from 1 ML of Sb on this surface.

cally by Goddard [29] and confirmed experimentally using low energy electron diffraction [30] and scanning tunneling microscopy [31].

At the same time, we have independently performed a detailed photoemission study (valence band and core levels) on *p*-type samples. Fig. 1 shows also the Fermi level positions at the Sb/p-InAs interface as a function of the Sb coverage and annealing temperature, derived from the In 4d and As 3d bend bending shifts. As a matter of fact, we have performed, as previously [1,13,27], a decomposition of these core levels to extract the positions of the bulk components (see Fig. 2); this allows to determine with great accuracy the true band bending and accordingly the changes of the Fermi level position upon Sb deposition.

The relevant point for our present study is that the Fermi level moves, once more, upon RT adsorption of Sb, into the conduction band: An inversion layer is thus created at the p-type InAs(110) surface, in the

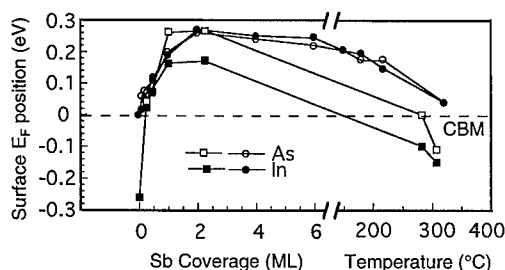


Fig. 1. Fermi level positions at the InAs(110) surfaces for p-type (squares) and n-type (circles) samples as a function of Sb coverage at RT; filled symbols: E_F positions derived from the In 4d shifts; open symbols: E_F positions derived from the As 3d shifts. The data for the n-type samples are taken from [27].

same way as an accumulation layer was formed at the n-type one. Following the noble and alkali metal adsorption studies, these new Sb absorption results confirm that the creation of a 2D electron channel at the InAs(110) surface upon metal adsorption is a general trend. We will see in the next section that eventually direct photoelectron emission from this channel inside the normally empty conduction band can be detected.

4. Cs/n-InAs(110): discrete line photoemission from a quantized 2D electron channel

By comparing in Fig. 3 the photoelectron spectra in the vicinity of the Fermi edge from the clean (a) and the 0.01 ML Cs covered (b) InAs(110) surfaces at RT we prove the presence of discrete filled electronic states inside the normally empty conduction band. These spectra were recorded at a polar emission angle of 45° along the (100) surface direction. The intensity of the emission after adsorption of a few Cs atoms is one order of magnitude less than the emission intensity arising from the valence band.

Two distinct features labeled E_0 and E_1 are clearly resolved; they point to discrete electronic levels arising from quantization, in the direction normal to the surface, of the 2D electron gas formed

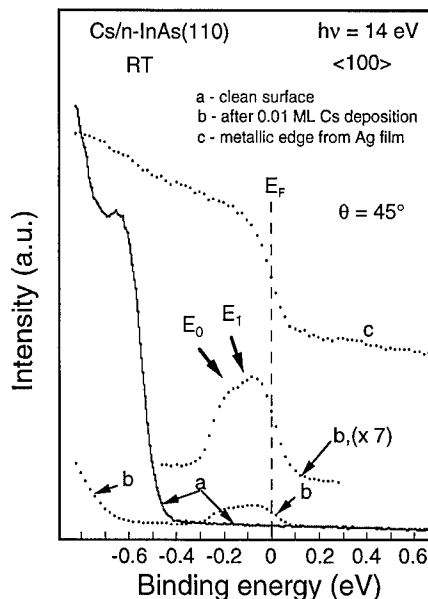


Fig. 3. Photoemission spectra near the Fermi level of Cs/n-InAs(110) at RT: (a) clean cleaved surface; (b) after deposition of ≈ 0.01 ML Cs at RT; (c) metallic edge from a silver film.

by the creation of the ≈ 0.4 eV deep, potential well at the InAs(110) surface as a consequence of the Fermi level movement above the CBM. Interestingly the positions of these two levels, respectively ≈ 0.2 and 0.3 eV above the CBM, qualitatively correspond

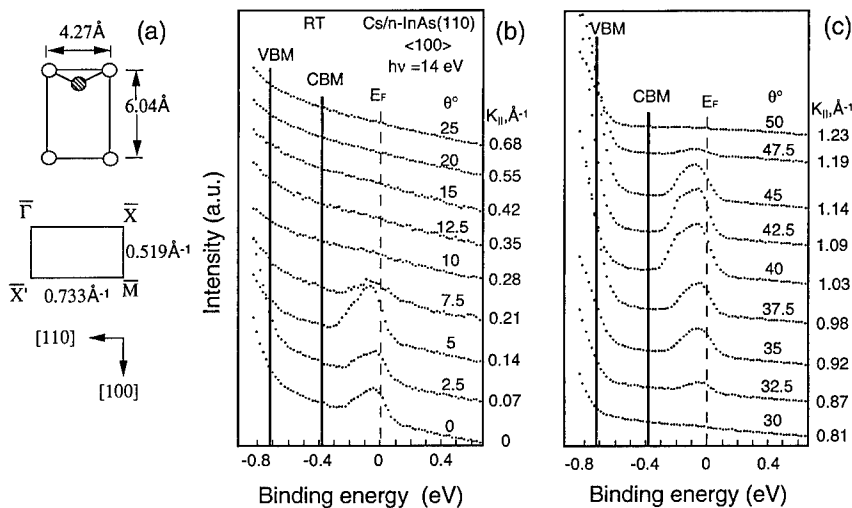


Fig. 4. (a) Direct and reciprocal surface cells of InAs(110); (b, c) photoemission spectra recorded at different emission angles along the Γ - X' direction from the InAs(110) surface after RT deposition of ≈ 0.01 Cs monolayer.

to theoretical predictions¹: to this end self-consistent Hartree-calculations of the potential well shape and charge densities were performed using an approach similar to that developed by Streight and Mills [33].

As may be seen in Fig. 4, which displays EDC's recorded as a function of the polar emission angle along the $\bar{\Gamma}$ – \bar{X}' direction of the surface Brillouin zone (SBZ), emission arises from the vicinities of the $\bar{\Gamma}$ the points of the first and second BZ. This localization is a proof of emission from the quantized energy levels of the 2D electron gas: as a matter of fact, emission from Cs valence electrons could be barely detectable at such a low coverage and would anyway be situated at a much deeper energy below E_F [26]. Furthermore, the adsorbed Cs atoms at such a low coverage produce donor type surface states located at ≈ 0.6 eV above the CBM [3,4]; this position is ≈ 0.2 eV above E_F leading in practice to totally ionized Cs atoms, in other words this state is empty. Finally, we underline that in the absence of quantization, we should observe a continuous distribution of electrons from the bottom of the conduction band (≈ 0.4 eV below E_F) up to the Fermi level instead of discrete lines. Thus our experimental results demonstrate for the first time the creation of a *quantized* electron channel, mediated by few Cs adsorbed atoms, at the free, almost bare InAs(110) surface.

5. Summary

We have shown that in addition to noble and alkali metals, adsorption of antimony on the InAs(110) surface can move the Fermi level *at room temperature* well above the conduction band minimum. In previous studies, chlorine and oxygen adsorbates [34] had also lead to a similar behaviour. The formation of an inversion or an accumulation layer, that is the creation of a two-dimensional electron channel at the free, almost pristine, surface is thus a general property of this narrow band gap

semiconductor. Although the presence of such a 2D electron channel could be inferred from previous experiments, no direct proof of its existence, except at the (111) and (100) InAs surfaces grown by molecular beam epitaxy [23], had been firmly established. Using angle-resolved high-resolution synchrotron radiation photoemission we have given the first direct evidence of this electron channel at the n-type InAs(110) surface, mediated by few Cs atoms. Furthermore, we could demonstrate that this two-dimensional electron gas is quantized in the direction normal to the surface.

Acknowledgements

This work was supported by the U.S. National Science Foundation (NSF) under contract No. DMR 92-23710 and by the Northern Illinois University Graduate School Fund. It is based upon research conducted in part at the Synchrotron Radiation Center (SRC), University of Wisconsin–Madison supported by NSF under contract No. DMR 92-12658. The authors want to acknowledge the SRC staff for expert and outstanding technical assistance. The authors are also grateful to F. Flores, J. Lapeyre and M.C. Asensio for valuable discussions.

References

- [1] V.Yu. Aristov, G. Le Lay, K. Hricovini, Le Thanh Vinh and J.E. Bonnet, Phys. Rev. B 47 (1993) 2138.
- [2] V.Yu. Aristov, Phys. Scr. 39 (1991) 333; V.Y. Aristov, I.L. Bolotin and S.G. Gelakhova, Surf. Sci. 251/252 (1991) 453.
- [3] V.Y. Aristov, G. Le Lay, P. Soukiassian, K. Hricovini, J.E. Bonnet, J. Osvald and O. Olsson, J. Vac. Sci. Technol. B 12 (1994) 2709.
- [4] V.Y. Aristov, G. Le Lay, P. Soukiassian, K. Hricovini, J.E. Bonnet, J. Osvald and O. Olsson, Europhys. Lett. 26 (1994) 359.
- [5] V.Y. Aristov, P.S. Mangat, P. Soukiassian and G. Le Lay, Surf. Sci. 331–333 (1995) 64.
- [6] T. Kendelewicz, P. Soukiassian, M.H. Bakshi, Z. Hurych, I. Lindau and W.E. Spicer, Phys. Rev. B 38 (1988) 7568.
- [7] P. Soukiassian and T. Kendelewicz, in: Metallization and Metal–Semiconductor Interfaces, Ed. I.P. Batra, NATO Advanced Study Institute, Serie B 195 (Plenum, New York, 1989) p. 465.
- [8] M. Prietsch, M. Domke, C. Laubschat, T. Mandel, C. Xue and G. Kaindi, Z. Phys. B 74 (1989) 21.

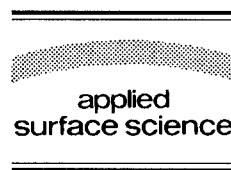
¹ A complete description of the calculation methodology and of the results for the energy levels obtained for different widths, depths and overall shape of some specific InAs channels is beyond the scope of the present paper; for more details see [32].

- [9] F. Schaffler, R. Ludeke, A. Taleb-Ibrahimi, G. Hughes and D. Rieger, *J. Vac. Sci. Technol. B* 5 (1987) 1048.
- [10] R. Cao, K. Miyano, I. Lindau and W.E. Spicer, *J. Vac. Sci. Technol. A* 7 (1989) 861.
- [11] T. Kendelewicz, K. Miyano, R. Cao, I. Lindau and W.E. Spicer, *J. Vac. Sci. Technol. B* 7 (1987) 991.
- [12] R.H. Williams, D.R.T. Zhan, N. Esser and W. Richter, *J. Vac. Sci. Technol. B* 7 (1989) 997.
- [13] N. Esser, D.R.T. Zhan, C. Muller, W. Richter, C. Stephans, R. Whittle, J.T. McGovern, S. Kulkarni and W. Braun, *Appl. Surf. Sci.* 56–58 (1992) 169.
- [14] C.B. Duke, C. Mailhot, A. Paton, K. Li, C. Bonaparte and A. Kahn, *Surf. Sci.* 163 (1985) 391.
- [15] J.P. Lafemina, C.B. Duke and C. Mailhot, *J. Vac. Sci. Technol. B* 8 (1990) 888.
- [16] J. Tersoff, *Phys. Rev. B* 32 (1985) 6968.
- [17] M. Cardona and N.E. Christensen, *Phys. Rev. B* 35 (1987) 6182.
- [18] J. Menendez, *Phys. Rev. B* 38 (1988) 6305.
- [19] W. Mönch, *Europhys. Lett.* 7 (1988) 275.
- [20] J.E. Klepeis and W.A. Harrison, *Phys. Rev. B* 40 (1989) 5810.
- [21] I. Lefebvre, M. Lannoo and G. Allan, *Europhys. Lett.* 10 (1989) 359.
- [22] J. Ortega and F. Flores, *Phys. Rev. Lett.* 63 (1989) 2500.
- [23] C.M.M. Andersson, U.O. Karlsson, L. Ilver, J. Kanski, P.O. Nilsson, L.Ö. Olsson and M.C. Håkansson, in: *Proc. 22nd Int. Conf. on the Physics of Semiconductors, ICPS-22, Vancouver, 1994*, Ed. D.J. Lockwood (World Scientific, Singapore, 1995) p. 489.
- [24] Y. Chen, J.C. Hermanson and G.J. Lapeyre, *Phys. Rev. B* 39 (1989) 12682.
- [25] M. Noguchi, K. Hirakawa and T. Ikoma, *Phys. Rev. Lett.* 66 (1991) 2243.
- [26] P. Soukiassian, J.A. Kubby, P. Mangat, Z. Hurych and K.M. Shirm, *Phys. Rev. B* 46 (1992) 13471.
- [27] C. Novak, J. Krujatz, A. Markl, A. Chasse, W. Braun, W. Richter and D.R.T. Zahn, *BESSY Jahresber.* (1994) 275.
- [28] W. Richter, private communication.
- [29] C.A. Swarts, W.A. Goddard and T.C. McGill, *J. Vac. Sci. Technol.* 17 (1982) 982.
- [30] W.K. Ford, T. Guo, D.L. Lessor and C.B. Duke, *Phys. Rev. B* 42 (1990) 8952.
- [31] P. Mårtensson and R.M. Feenstra, *Phys. Rev. B* 39 (1989) 7744.
- [32] V. Y. Aristov, G. Le Lay, M. Grehk, V.M. Zhilin, A. Taleb-Ibrahimi, G. Indlekofer and P. Soukiassian, *Surf. Rev. Lett.* 2 (1995) 723.
- [33] S.R. Streight and Mills, *Phys. Rev. B* 37 (1988) 965.
- [34] H.U. Baier, L. Koenders and W. Mönch, *Solid State Commun.* 58 (1986) 328; H.U. Baier, L. Koenders and W. Mönch, *J. Vac. Sci. Technol. B* 4 (1986) 1095.



ELSEVIER

Applied Surface Science 104/105 (1996) 79–87



Synchrotron radiation study of Cs/carbon-rich β -SiC(100) and Cs/silicon-rich β -SiC(100) surfaces: metallization and interface formation

F. Semond^a, P. Soukiasian^{a,b,*}, P.S. Mangat^{b,1}, Z. Hurych^b, L. di Cioccio^c,
C. Jaussaud^c

^a Commissariat à l'Energie Atomique, DSM-DRECAM-SRSIM, Bâtiment 462, Centre d'Etudes de Saclay, 91191 Gif sur Yvette Cedex, France, and Département de Physique, Université de Paris-Sud, 91405 Orsay Cedex, France

^b Department of Physics, Northern Illinois University, DeKalb, IL 60115-2854, USA

^c LETI (CEA – Technologies Avancées), DMEL, CEN / G, 85 X, 38041 Grenoble Cedex, France

Received 12 July 1995; accepted 5 October 1995

Abstract

The room temperature interface formation of the Cs/carbon-rich and silicon-rich β -SiC(100) single-domain surfaces is studied by core level and valence band photoemission spectroscopy using synchrotron radiation. For both surfaces, Cs deposition results in reactive interface formation. For the carbon-rich β -SiC(100), the presence of a Cs monolayer leads to surface metallization as evident from asymmetric shape tail at the Cs 4d core level indicating the presence of a plasmon and from metal-induced gap state near the top of the valence band. In contrast, the silicon-rich β -SiC(100) surface remains semiconducting in presence of a Cs overlayer at saturation coverage. This investigation stresses the central importance of initial surface composition.

1. Introduction

Silicon carbide belongs to the family of wide band gap semiconductors with gaps ranging from 2.3 eV to 2.9 eV depending of the crystallographic phase (cubic or hexagonal). In addition, it is a IV–IV compound semiconductor having very interesting properties from both fundamental and applied aspects. In fact, unlike silicon, silicon carbide is a

'refractory' semiconductor which, in its cubic β phase, could operate at rather elevated temperatures ($\approx 600^\circ\text{C}$). This potentially makes it a very promising material for electronic and opto-electronic devices working at high temperatures, high frequencies and high power [1]. Also, its chemical stability makes silicon carbide an attractive material able to operate in difficult environments, especially when compared to silicon and other compound semiconductors such as III–V [1]. However, silicon carbide has not, so far, been very much investigated, especially when compared to other elemental or compound semiconductors. Doping, surface passivation and metallization are among the important problems to be solved

* Corresponding author.

¹ Now at: Motorola, Inc., Austin, TX, USA.

in order to achieve practical device applications. There are few studies about surface passivation by native SiO_2 oxide growth using direct [2,3] or promoted oxidation [4,5]. In contrast, the formation of metal/silicon carbide interfaces has been more widely investigated primarily in the thin film regime using various metal (noble and transition metals) adsorbates having very different properties [6–11] in order to explore the thermal stability of metallic contacts. Theoretical calculations were also performed in the case of iron and aluminum/silicon carbide interfaces [12]. In most of the cases, the metal/SiC is reactive already at room temperature while the silicon carbide surface metallization was found to generally take place in the case of rather high metal coverages [6,7].

From a more basic aspect, ab-initio theoretical calculations have predicted that silicon carbide is a rather ionic semiconductor with a significant charge transfer from Si cation to C anion which makes it closer from III–V compound than from group IV semiconductors [12–16]. Depending on whether it is silicon-rich, stoichiometric or carbon-rich, the β -SiC(100) surface presents various reconstructions including 3×2 , 3×1 , 2×1 , $c(2 \times 2)$ and 1×1 when going from silicon-rich to carbon-rich surfaces respectively [2,10,11,17]. Among other metals, alkali metals, who could act as donors [18,19], are of special interest for such a metal/SiC surface/interface investigations. The first studies about alkali metal/SiC systems were performed only very recently [4,5,20]: we have shown that (i) Rb increases dramatically the oxidation rate of the stoichiometric β -SiC(100) surface [4,5] and (ii) Na in the monolayer range metallizes the carbon-rich- β -SiC(100) surface [20]. In this view, it is interesting to study the effect of β -SiC(100) surface composition upon alkali metal deposition in the monolayer range.

In this paper, we investigate the Cs/carbon-rich β -SiC(100) and Cs/silicon-rich β -SiC(100) interfaces by core level and valence band photoemission spectroscopies using synchrotron radiation, which has, so far, not been very much used to investigate silicon carbide. At saturation Cs coverage, both interfaces are found to be reactive. However, we also find striking differences between the two interfaces with clear evidence of Cs-induced surface metallization for the Cs/carbon-rich β -SiC(100) interface

while the corresponding silicon-rich interface remains semiconducting.

2. Experimental details

The experiments were performed at the Synchrotron Radiation Center, University of Wisconsin–Madison by valence band and core level photoemission spectroscopy techniques using the light emitted by the ‘Aladdin’ 1 GeV storage ring and dispersed by a grasshopper Mark II monochromator. A double-pass angle-integrating cylindrical mirror analyzer (CMA) was used to measure the photoelectron energy with an overall energy resolution better than 0.3 eV at the Si 2p and Cs 4d core levels while it was estimated to be around 1.2 eV at the C 1s core level. The data were taken at pressures better than 5×10^{-11} Torr in the experimental chamber with working pressure in the monochromator below 2×10^{-11} Torr during data acquisition. The single-domain n-type β -SiC(100) (zinc-blende structure) sample was grown at LETI (Grenoble) by chemical vapor deposition (CVD) onto a Si(100) wafer miscut by 4° , yielding a layer thickness of about $1 \mu\text{m}$ [21]. The formation of single crystal silicon carbide was evidenced by conventional X-ray diffraction. The sample was heated by through current. We were able to achieve contaminant free silicon or carbon-rich β -SiC(100) surfaces by thermal annealings treatments only at temperatures ranging from 1000°C to 1280°C . Additional thermal annealings induce Si surface depletion leaving carbon-rich β -SiC(100) surfaces meaning that a new sample has to be introduced into the chamber to obtain again silicon-rich β -SiC(100) surfaces. The Fermi edge was determined from a gold sample. Pure Cs deposition on the carbon and/or silicon-rich β -SiC(100) surfaces was performed at room temperature using a SAES Getters source outgassed to perfection with pressure increases remaining always below 2×10^{-11} Torr in order to avoid any problem related to the presence of low level impurities [22,23]. The present experiments have been performed at the Cs saturation coverage only. This amount of Cs corresponds to the amount necessary to achieve a coverage of one monolayer on the Si(100) 2×1 surface. Other infor-

mation about the experimental details are provided elsewhere [4,5,20–23].

3. Results

3.1. Clean surfaces

Depending on the surface composition, the β -SiC(100) surface could present several reconstructions including (3×2) , (5×2) , $c(4 \times 2)$, (2×1) , (1×1) and $c(2 \times 2)$. Surface models have been proposed for almost all the reconstructions [24–29]. Very recent photoemission spectroscopy experiments using synchrotron radiation for the β -SiC(100) surfaces have shown a clear correlation between surface reconstructions identified by low energy electron diffraction (LEED), and specific Si 2p core level shifts and valence band spectral features [17,30]. Therefore, a straightforward identification of the two clean surfaces used in this work, namely the Si terminated β -SiC(100) 3×2 and C terminated β -SiC(100) 1×1 surfaces, could be achieved using Si 2p core level and valence band data only (Fig. 1a and b).

Valence band for the clean surfaces (Fig. 1b) exhibit five structures at 14.0, 9.6, 7.2, 5.0 and 3.2 eV below the Fermi level (E_F). We use for these peaks the same labeling A, B, C_1 , X and C_2 as in former works [2,24]. The valence band is very sensitive to the surface composition. In particular, when the surface is silicon terminated, peak C_2 is the dominant feature while peak X becomes more and more intense when the surface becomes more and more carbon-rich [2,17,24]. Therefore, peak C_2 is related to surface silicon atoms while peak X is likely related to surface carbon atoms. From the energy position and line shape (including peak ratios) of the Si 2p core level (Fig. 1a) and from valence band spectral features (Fig. 1b), one can conclude that the top Si 2p spectrum (Fig. 1a) and the top valence band spectrum (Fig. 1b), correspond to a clean β -SiC(100) 3×2 surface reconstruction [17,30]. On the other hand, the bottom Si 2p spectrum (Fig. 1a) associated with the bottom valence band spectrum (Fig. 1b) indicate a β -SiC(100) 1×1 surface reconstruction [17]. Even if the exact structure of these surfaces is not perfectly known, there is

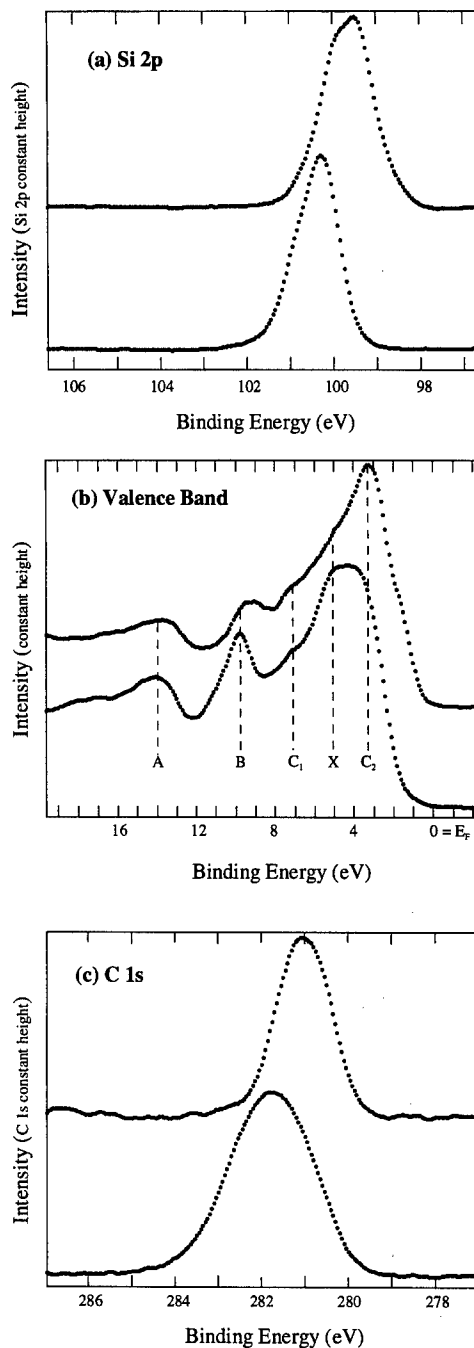


Fig. 1. Clean silicon-rich β -SiC(100) surface (top) and clean carbon-rich β -SiC(100) surface (bottom). (a) Si 2p core levels, the photon energy was 150 eV. (b) Valence band spectra, the photon energy was 150 eV. (c) C 1s core levels, the photon energy was 340 eV.

a general consensus that β -SiC(100) 3×2 and 1×1 surface reconstructions are respectively Si and C terminated [17,24,26,30].

Additional information about clean surface composition is provided by the C 1s core level (Fig. 1c) corresponding to the same surfaces than in Fig. 1a and b. The bottom spectrum indicates a C 1s energy position at 282 eV with a full width at half maximum (FWHM) of 2.5 eV while the top spectrum has a binding energy of 281 eV with a FWHM of 1.2 eV. The broadening of the C 1s core level is related to surface increasing stoichiometry in carbon atoms [17,24]. So, one can assign the bottom C 1s spectrum to a surface richer in carbon than for the top C 1s spectrum. This further supports the surface identification provided by the above Si 2p and valence band results. Therefore, using Si 2p and C 1s core levels, and valence band results, one can clearly identify clean Si-rich and C-rich surfaces (β -SiC(100) 3×2 and β -SiC(100) 1×1 respectively).

3.2. Cs on β -SiC(100)

We now look at the effect of one Cs monolayer (corresponding to the saturation coverage) deposition on carbon-rich and silicon-rich surfaces. Since this paper is primarily devoted to interface formation and not to band bending studies, all the spectra have been aligned to facilitate the identification of reactive components. This means that all rigid shifts (-0.16 eV for the C-rich β -SiC(100) surface and -0.65 eV for the Si-rich β -SiC(100) surface) resulting from the band bending upon Cs deposition have been removed and are not presented in this paper. The important issue of Schottky barrier formation will be presented elsewhere [17].

3.2.1. Si 2p and C 1s core levels

We first look at the formation of Cs/carbon-rich β -SiC(100) interface using the Si 2p and C 1s core levels which are displayed in Fig. 2a and b respectively. As can be seen in Fig. 2a, a new component R, shifted by 1.3 eV to lower binding energy arises upon Cs deposition. This indicates a reactive interface formation. Also of interest, is the slightly asymmetric shape of the Si 2p core level on the high binding energy side upon Cs deposition. This tail is very likely to indicate the presence of a surface

plasmon, suggesting surface metallization. The reactive component R is destroyed upon an oxygen exposure of 100 L while Si oxide formation results as evident from Si 2p core level shift and broadening on the high binding energy side (Fig. 2a). The behavior observed here for the Cs covered carbon-rich β -SiC(100) surface is very similar to the one we reported recently for the corresponding Na/carbon-

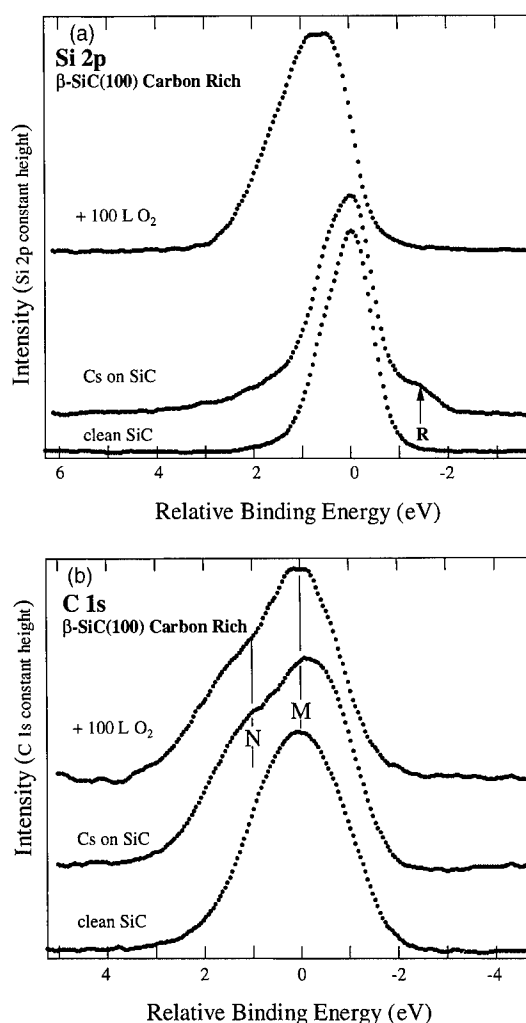


Fig. 2. (a) Si 2p core level photoemission spectra for the clean carbon-rich β -SiC(100) surface, the same surface covered by a Cs overlayer at saturation coverage and then exposed to 100 L O₂. The photon energy was 150 eV. (b) C 1s core level photoemission spectra for the clean carbon-rich β -SiC(100) surface, the same surface covered by a Cs overlayer at saturation coverage and then exposed to 100 L O₂. The photon energy was 340 eV.

rich β -SiC(100) interface [20]. However one should notice that the energy position of the plasmon loss feature observed in the present study is different from the one we observed for Na deposition, at 3 eV, which makes the plasmon clearly visible in the latter case [20]. This results from the large difference in the plasma frequency between Cs (1.5 eV) and Na (4 eV) in the case of adsorption on metal surfaces [31–34].

Fig. 2b displays the C 1s core level for the same sequence for the Cs/carbon-rich β -SiC(100) interface which provides the additional insights about interface formation. As can be seen in Fig. 2b, the C 1s core level clearly exhibits, upon the deposition of one Cs monolayer, a new component N, located at 1 eV higher binding energy. Again, this is very similar to the behavior that we observed for the corresponding Na/carbon-rich β -SiC(100) system [20]. Interestingly, the same shifted component is also observed upon thermal annealing of the clean β -SiC(100) surface. This feature has been interpreted as resulting of graphitic bonding due to Si desorption [24]. Therefore, the presence of peak N would correspond to graphite formation. This behavior suggests that Cs deposition results in the breaking of Si–C bonds leaving C atoms on the surface forming probably graphite clusters [9,24]. One can also imagine that, upon the deposition of Cs which has the lowest electronegativity, an important electronic charge redistribution takes place between carbon, silicon and cesium atoms without any bond breaking as in the case of some III–V compound semiconductors [35,36]. Upon an oxygen exposure at 100 L, the intensity ratio N/M is significantly decreased. This could results from Cs-induced carbon/graphite oxidation leading to the formation of CO or CO₂ species desorbing into the vacuum as previously suggested elsewhere [2,5].

We now turn to the Cs/Si-rich β -SiC(100) interface formation. Fig. 3a and b exhibit respectively the Si 2p and C 1s core levels for a similar sequence as in Fig. 2a and b. As can be seen in Fig. 3a, the Si 2p core level shows a very large component (peak R) located at about 0.8 eV lower binding energy. It suggests that the Cs/Si-rich β -SiC(100) interface is also reactive. However, in contrast to the carbon-rich surface, the Si 2p core level does not show any plasmon loss feature. The exposition to 100 L of

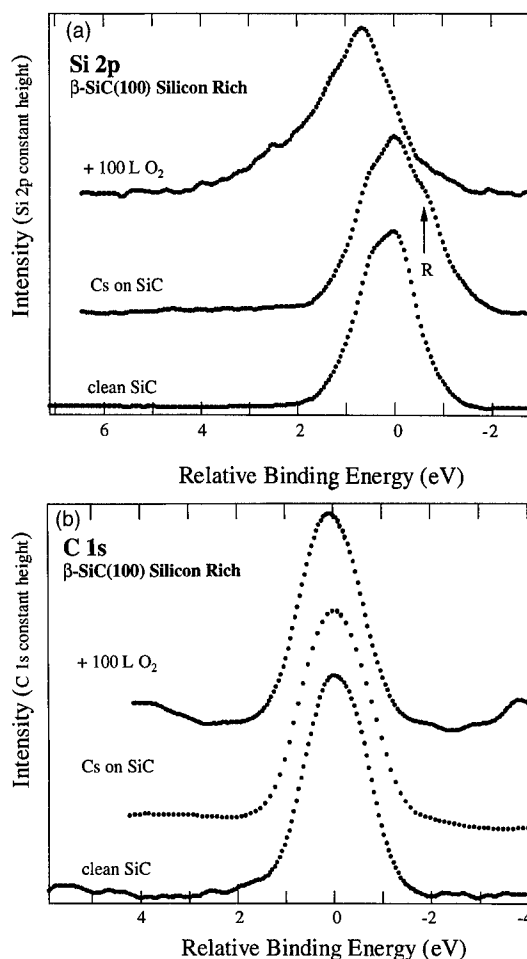


Fig. 3. (a) Si 2p core level photoemission spectra for the clean silicon-rich β -SiC(100) surface, the same surface covered by a Cs overlayer at saturation coverage and then exposed to 100 L O₂. The photon energy was 150 eV. (b) C 1s core level photoemission spectra for the clean silicon-rich β -SiC(100) surface, the same surface covered by a Cs overlayer at saturation coverage and then exposed to 100 L O₂. The photon energy was 340 eV.

oxygen apparently destroys the reactive component and results in silicon oxide growth as evident from the spectral features developing on the high energy side of the Si 2p core level [37]. The C 1s core level, shown in Fig. 3b, remains basically unaffected by Cs deposition and oxygen exposure.

3.2.2. Cs 4d core level

Additional insights about the process of surface metallization could be found by looking at the Cs 4d

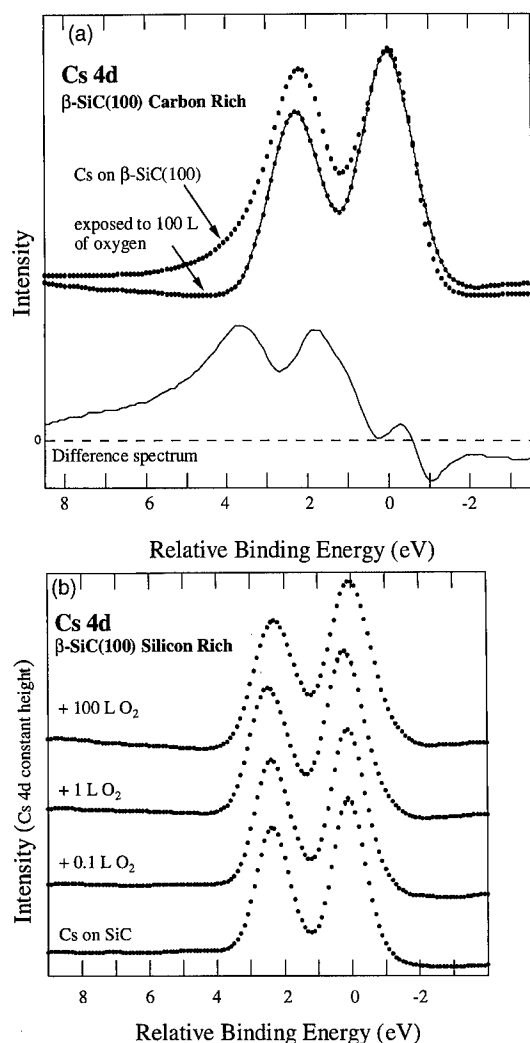


Fig. 4. (a) Cs 4d core level photoemission spectra for the Cs/carbon-rich β -SiC(100) surface and the same surface exposed to 100 L O_2 . The difference spectra (not on the same scale) is also presented below showing the Cs plasmon. The photon energy was 120 eV. (b) Cs 4d core level photoemission spectra for the Cs/silicon-rich β -SiC(100) surface and then exposed to various amount of O_2 . The photon energy was 120 eV.

core levels for both carbon-rich and silicon-rich surfaces. As can be seen in Fig. 4a for the carbon-rich Cs/ β -SiC(100) interface, the Cs 4d core level presents a clear asymmetric shape with a pronounced tail at the higher binding energy side which is likely to result from the presence of a Cs plasmon [38,39]. This tail is removed by an oxygen exposure which could easily be interpreted by the fact that oxygen,

an electron acceptor species is going to reduce the number of electrons involved in a collective process which would then destroy the plasmon. In order to better identify the presence of a Cs plasmon, we have performed a difference between these two spectra which basically give a similar spectrum shifted by 1.5 eV, corresponding exactly to the Cs plasmon, despite the fact that such an excellent agreement might be accidental. This feature further confirms the presence of a Cs plasmon at the Cs 4d core level as previously observed for other systems [38,39]. It is in excellent agreement with the picture of Cs-induced carbon-rich β -SiC(100) surface metallization already suggested above with the Si 2p core level result. Therefore, similarly to the case of Na/carbon-rich β -SiC(100) surface that we studied recently using the same technique [20], Cs induces surface metallization of the carbon-rich β -SiC(100).

We now turn to the effect of similar Cs deposition on the silicon-rich β -SiC(100) surface. Fig. 4b displays the Cs 4d core level for the clean and oxygen exposed Cs/silicon-rich β -SiC(100) surfaces. In strong contrast to the carbon-rich surface, one can clearly see by a simple visual inspection that the Cs 4d core level does not exhibit an asymmetric shape with a tail on the higher binding energy side resulting from a plasmon-like feature which would suggests surface metallization. Furthermore, unlike the C-rich β -SiC(100) surface, the shape of the Cs 4d remains basically not affected by oxygen exposures.

3.2.3. Valence band

We now examine the valence band spectra shown in Fig. 5a and b. The main feature resulting from Cs deposition onto the carbon-rich β -SiC(100) surface can be seen in Fig. 5a where Cs atoms induce the growth of a new peak (D) located at the top valence band. Peak D is mostly located into the band gap and therefore results from an adsorbate-induced gap state. This interesting feature should play a major role in the surface metallization observed above, as previously demonstrated for similar metal-induced gap states (MIGS) in the case of alkali metal/III–V compound semiconductor interfaces as GaAs and InP [35,36]. Also of interest is the change in the relative intensity of peaks X and C_2 . As mentioned above (Fig. 1b) and shown previously, the two spectral features X and C_2 are very specific of the

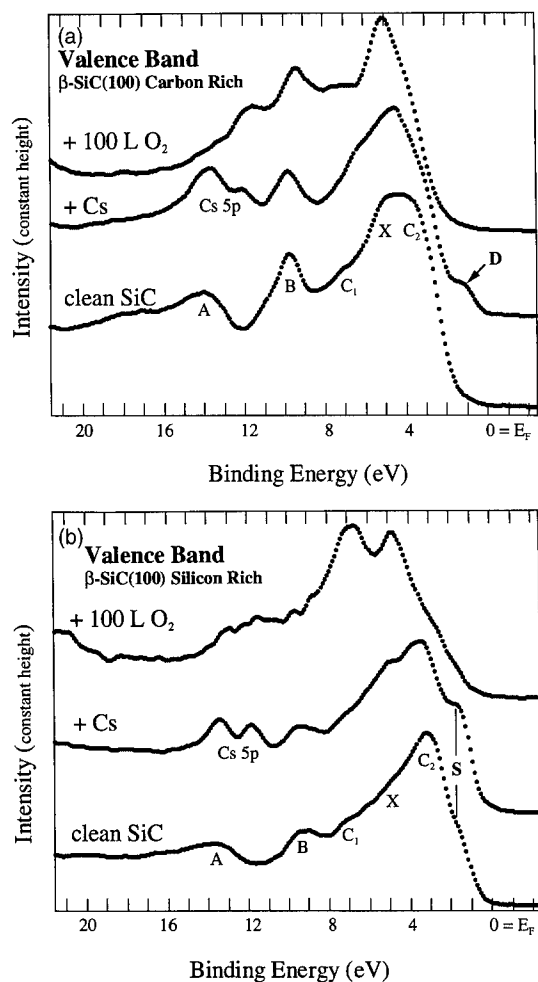


Fig. 5. (a) Valence band spectra for the clean carbon-rich β -SiC(100) surface, the same surface covered by a Cs overlayer at saturation coverage and then exposed to 100 L O₂. The photon energy was 150 eV. (b) Valence band spectra for the clean silicon-rich β -SiC(100) surface, the same surface covered by a Cs overlayer at saturation coverage and then exposed to 100 L O₂. The photon energy was 150 eV.

surface composition [17,24,30]. In agreement to what we observed at the C 1s core level upon Cs deposition, the change observed in the relative intensity of peaks X and C₂ indicates the growth of carbon species at the surface and/or a change in the electronic configuration of carbon surface atoms. Upon oxygen exposure, peak D is destroyed which could be correlated to the simultaneous removal of surface

metallization observed from the disappearance of the plasmon losses at Si 2p and Cs 4d (Fig. 2a and Fig. 4a).

We now follow the effect of the same sequence on the valence band of the silicon-rich β -SiC(100) surface. In contrast to the behavior of the C-rich surface, the deposition of Cs atoms does not induce any new feature above the valence band maximum (Fig. 5b) which seems to be consistent with the lack of surface metallization since we did not observe any plasmon at the Si 2p and Cs 4d (Fig. 3a and Fig. 4b). It could suggest that, unlike the carbon-rich surface, the silicon-rich β -SiC(100) surface remains semiconducting even when covered by Cs atoms. Interestingly, the intensity of peak S, which is likely related to Si dangling bonds, apparently increases upon Cs overlayer deposition. As observed for alkali metal covered silicon surfaces, this could result from the hybridization between surface dangling bonds and Cs valence electrons, giving rise to an electronic interface state [19,22,39]. However, one cannot totally rule out that the peak S intensity increase might result from the attenuation of peak C₂ upon Cs deposition. Upon oxygen exposure, spectral features related to the O 2p electronic levels [37] appear around 5 and 7 eV binding energies.

4. Discussion

Together with our recent results for the Na/carbon-rich β -SiC(100) interface [20], the above data for the Cs/carbon-rich β -SiC(100) and Cs/silicon-rich β -SiC(100) interfaces indicates that alkali metals form strongly reactive interfaces with β -SiC(100) as evident from the reactive components observed at substrate core levels which suggest adsorbate–substrate charge transfer. It shows that the alkali metal/ β -SiC(100) interface formation is different from that with silicon surfaces which are non-reactive (except with Li) [19]. In these views, the behavior of the β -SiC(100) surface is much closer from the one taking place with III–V compound semiconductors like e.g. GaAs(110), InP(110) and GaSb(110) [35,36,40]. Theoretical calculations [13,16] have concluded that a significant charge

transfer from the Si atom to the C atom is taking place which is exactly what could be expected by just considering the Pauling electronegativity difference between Si and C atoms [41]. The ionic character of silicon carbide (Si acts as cation and C acts as anion) is likely to explain its very different behavior upon Cs (or Na) deposition when compared to covalent semiconductors as silicon or germanium [19]. Therefore, when adsorbing low electron affinity species such as alkali metals like Na [20] or Cs on the β -SiC(100) surface, one can expect some important charge transfer from the alkali atoms to Si atoms resulting from the smaller charge density of Si atoms in silicon carbide. The large chemical shift observed at the Si 2p core level (peak R, in Fig. 2a and Fig. 3a) could in fact be taken as the signature of such a charge transfer, which would also influence significantly the C–Si bond. Concerning the possible interface state (peak S, Fig. 1b) induced below the Fermi level by Cs deposition onto the silicon-rich β -SiC(100) surface, it appears to be very similar to the one that we previously reported for the Cs/Si(100)2 \times 1 interface [39] and would probably result also for the β -SiC(100) surface, from hybridization between the Cs 6s orbital and surface dangling bonds. However, this point requires a more detailed investigation which is actually in progress [17].

Another very important and striking feature of Cs/ β -SiC(100) interface formation is the effect of surface composition on alkali metal-induced metallization. The β -SiC(100) carbon-rich system becomes metallic upon Cs adsorption as evidenced by plasmon losses features taking place at the Cs 4d and Si 2p core levels (Fig. 4a and Fig. 2a) and metal-induced gap state formation above the valence band maximum (Fig. 5a). Also, one cannot totally rule out that graphite (which is a semi-metal) formation, as mentioned above, would result in Cs intercalation, as previously demonstrated [42–44]. This could explain, at least in part, the observed surface metallization. On the other hand, the absence of plasmon loss features at the Cs 4d and Si 2p core levels (Fig. 4b and 3a) for the silicon-rich surface (which does not exhibits cluster/graphite formation), indicates that the latter remains semiconducting upon Cs deposition. In addition, unlike the C-rich β -SiC(100), we do not observe metal-induced gap state formation for the Si-rich surfaces upon Cs deposition.

5. Conclusions

Using valence band and core level photoemission spectroscopy, we have demonstrated that a Cs overlayer induces the metallization of the carbon-rich β -SiC(100) surface while the corresponding silicon-rich interface remains semiconducting. This effect could result from metal induced gap states upon Cs deposition while carbon/graphite cluster formation might also play an important role. Both Cs/carbon-rich β -SiC(100) and Cs/silicon-rich β -SiC(100) systems were found to form very reactive interfaces with significant charge transfer from the adsorbate to the surface. For the carbon-rich surface, such a surface reaction could also result in C–Si bond breaking possibly leading to carbon/graphite cluster formation as for the corresponding Na carbon-rich β -SiC(100) surface. The more ionic character of this binary IV–IV compound semiconductor seems to be of relevance in the observed differences between silicon carbide and elemental covalent semiconductors as silicon or germanium upon alkali metal deposition and interface formation. The very different behavior of Cs/Si-rich β -SiC(100) and Cs/C-rich β -SiC(100) interfaces switching from semiconducting to metallic, stresses the crucial importance of the initial surface composition.

Acknowledgements

This work was supported by the U.S. National Science Foundation under contract No. DMR 92-23710. It is based upon research conducted in part at the Synchrotron Radiation Center, University of Wisconsin–Madison which is supported by the U.S. National Science Foundation under award No. DMR 92-12658. Finally, we want to thank the staff of the Synchrotron Radiation Center for expert and outstanding technical assistance.

References

- [1] R.F. Davis, *J. Vac. Sci. Technol. A* 11 (1993) 829; H. Morkoç, S. Strite, G.B. Gao, M.E. Lin, B. Sverdlov and M. Burns, *J. Appl. Phys.* 76 (1994) 1363.

- [2] V.M. Bermudez, J. Appl. Phys. 66 (1989) 6084; J.M. Powers and G.A. Somorjai, Surf. Sci. 244 (1991) 39.
- [3] F. Semond, L. Douillard, P. Soukiassian, D. Dunham, F. Amy and S. Rivillon, App. Phys. Lett. 68 (1996) 2144.
- [4] M. Riehl-Chudoba, P. Soukiassian and C. Jaussaud, J. Appl. Phys. 76 (1994) 1932.
- [5] M. Riehl-Chudoba, P. Soukiassian, C. Jaussaud and S. Dupont, Phys. Rev. B 51 (1995) 14300.
- [6] L. Porte, J. Appl. Phys. 60 (1986) 635.
- [7] H. Höchst, D.W. Niles, G.W. Zajac, T.H. Fleisch, B.C. Johnson and J.M. Meese, J. Vac. Sci. Technol. B 6 (1988) 1320; D.W. Niles, H. Höchst, G.W. Zajac, T.H. Fleisch, B.C. Johnson and J.M. Meese, J. Appl. Phys. 65 (1989) 662.
- [8] K.M. Geib, C. Wilson, R.G. Long and C.M. Wilmsen, J. Appl. Phys. 68 (1990) 2796.
- [9] N. Lundberg, C.M. Zetterling and M. Östling, Appl. Surf. Sci. 73 (1993) 316.
- [10] T.M. Parrill and Y.W. Chung, Surf. Sci. 271 (1992) 395.
- [11] V.M. Bermudez and R. Kaplan, J. Mater. Res. 5 (1990) 2882.
- [12] W. Lu, K. Zhang and X. Xide, Phys. Rev. B 45 (1992) 11048; 48 (1993) 18159.
- [13] N. Churcher, K. Kunc and V. Heine, J. Phys. C 19 (1986) 4413.
- [14] B.I. Craig and P.V. Smith, Phys. Status Solidi (b) 154 (1989) K127.
- [15] P. Käckell, B. Wenzien and F. Bechstedt, Phys. Rev. B 50 (1994) 10761.
- [16] M. Sabisch, P. Krüger and J. Pollmann, Phys. Rev. B 51 (1995) 13367.
- [17] F. Semond, L. Douillard, D. Dunham, F. Amy, S. Rivillon and P. Soukiassian, recent results (1995).
- [18] H.P. Bonzel, A.M. Bradshaw and G. Ertl, Eds., Physics and Chemistry of Alkali Metal Adsorption, Materials Science Monographs, Vol. 57 (Elsevier, Amsterdam, 1989), and references therein.
- [19] P. Soukiassian, in: Fundamental Approach to New Materials Phases, Ordering at Surfaces and Interfaces, Eds. A. Yoshimori, T. Shinjo and H. Watanabe, Springer Series in Materials Science, Vol. 17 (Springer, Berlin, 1992) p. 197, and references therein.
- [20] F. Semond, P. Soukiassian, P.S. Mangat and L. di Cioccio, J. Vac. Sci. Technol. B 13 (1995) 1591.
- [21] N. Becourt, B. Cros, J.L. Ponthenier, R. Berjoan, A.M. Papon and C. Jaussaud, Appl. Surf. Sci. 68 (1993) 461.
- [22] P. Soukiassian, J.A. Kubby, P.S. Mangat, Z. Hurych and K.M. Schirm, Phys. Rev. B 46 (1992) 13471.
- [23] L. Spiess, P.S. Mangat, S.P. Tang, K.M. Schirm, A.J. Freeman and P. Soukiassian, Surf. Sci. 289 (1993) L631.
- [24] T.M. Parrill and Y.W. Chung, Surf. Sci. 243 (1991) 96.
- [25] R. Kaplan, Surf. Sci. 215 (1989) 111.
- [26] S. Hara, W.F.J. Slijkerman, J.F. van der Veen, I. Ohdomari, S. Misawa, E. Sakuma and S. Yoshida, Surf. Sci. 231 (1991) L196.
- [27] J.M. Powers, A. Wander, P.J. Rous, M.A. Van Hove and G.A. Somorjai, Phys. Rev. B 44 (1991) 11159.
- [28] J.M. Powers, A. Wander, M.A. Van Hove and G.A. Somorjai, Surf. Sci. 260 (1992) L7.
- [29] H. Yan, A.P. Smith and H. Jónsson, Surf. Sci. 330 (1995) 265.
- [30] V.M. Bermudez and J.P. Long, Appl. Phys. Lett. 66 (1995) 475.
- [31] S.A. Lindgren and L. Wallden, Phys. Rev. B 22 (1980) 5967.
- [32] P. Soukiassian, R. Riwan and Y. Borensztein, Solid State Commun. 44 (1982) 1375.
- [33] J. Cousty, R. Riwan and P. Soukiassian, J. Phys. (Paris) 46 (1985) 1693.
- [34] Y. Huttel, E. Bourdié, P. Soukiassian, P.S. Mangat and Z. Hurych, Appl. Phys. Lett. 62 (1993) 2437.
- [35] T. Kendelewicz, P. Soukiassian, M.H. Bakshi, Z. Hurych, I. Lindau and W.E. Spicer, Phys. Rev. B 38 (1988) 7568; J. Vac. Sci. Technol. B 6 (1988) 1331.
- [36] M. Prietsch, M. Domke, C. Laubschat, T. Mandel, C. Xue and G. Kaindl, Z. Phys. B 74 (1989) 21.
- [37] P. Soukiassian, M.H. Bakshi, Z.D. Hurych and T.M. Gentle, Phys. Rev. B 35 (1987) 4176.
- [38] H. Tochiwara, K. Kubota and Y. Murata, Solid State Commun. 57 (1986) 437.
- [39] P. Soukiassian, M.H. Bakshi, Z. Hurych and T.M. Gentle, Surf. Sci. 221 (1989) L759.
- [40] K.M. Schirm, P. Soukiassian, P.S. Mangat and L. Soonckindt, Phys. Rev. B 49 (1994) 5490.
- [41] L.N. Pauling, The Nature of the Chemical Bond (Cornell University, Ithaca, NY, 1939, 1960).
- [42] M.T. Johnson, H.I. Starnberg and H.P. Hughes, Solid State Commun. 57 (1986) 545.
- [43] H. Estrade-Szwarckopf and B. Rousseau, J. Phys. Chem. Solids 53 (1992) 419.
- [44] B. Rousseau and H. Estrade-Szwarckopf, Solid State Commun. 85 (1993) 793.



ELSEVIER

Applied Surface Science 104/105 (1996) 88–94

applied
surface science

Surface core-level shift photoelectron diffraction from As/Si(111)

L.S.O. Johansson^{a,*}, R. Gunnella^b, E.L. Bullock^c, C.R. Natoli^d, R.I.G. Uhrberg^e^a Department of Synchrotron Radiation Research, Institute of Physics, Lund University, Sölvegatan 14, S-223 62 Lund, Sweden^b Dipartimento di Fisica, Università di Camerino, Via Madonna delle Carceri, 62032 Camerino, Italy^c Institut de Physique Expérimentale, Université de Lausanne, 1015 Lausanne-Dorigny, Switzerland^d INFN, Laboratori Nazionali di Frascati, C.P. 13, 00044 Frascati, Italy^e Department of Physics and Measurement Technology, Linköping Institute of Technology, S-581 83 Linköping, Sweden

Received 28 June 1995; accepted 24 November 1995

Abstract

We have studied the arsenic-terminated Si(111)-(1 × 1) surface with low energy photoelectron diffraction. On this ideally terminated surface, the Si 2p core-level consists of a bulk component and a single well separated surface component shifted to 0.75 eV higher binding energy compared to the bulk component. We have measured the intensities of the surface and bulk components of the Si 2p core-level, and the single component As 3d core-level, as functions of azimuthal angle. The recorded azimuthal scans for the Si 2p surface component showed extremely large intensity variations. For a photon energy of 130 eV and emission angle of 45° for example, the intensity of this component was found to vary by 400 percent upon an azimuthal rotation of the sample by 45°. The experimental data were compared to model calculations of the photoelectron diffraction utilizing a fully convergent multiple scattering formalism. The best fit to the data was consistently found in all the azimuthal scans for an outward relaxation of the As atoms from the Si bulk positions by 0.2 Å. This is in good agreement with earlier structural determinations of this surface.

1. Introduction

Arsenic deposited onto a Si(111)-(7 × 7) surface results in a nearly ideal (1 × 1) bulk termination with high passivity [1–11]. Since this surface was first reported by Olmstead et al. [1], several studies have confirmed their conclusion that As replaces the first half of the topmost Si double layer with each As atom bonding to three Si atoms and possessing two valence electrons in a nonbonding lone-pair state (see Fig. 1). The remarkable consistency of the

results of these studies attests to the simplicity and high degree of order of this system. From the point of view of atomic structure, this simplicity reduces the number of geometric parameters of the ordered (1 × 1) phase essentially to one: the vertical interplanar distance between the As and uppermost Si layers. Measurement of this distance using both experimental [3,6,7] and theoretical [2,8,10] methods have also been quite consistent yielding a relaxation of the As layer toward the vacuum of $\Delta z = 0.16$ to 0.25 Å when compared to the bulk Si(111) lattice spacing.

Also reflecting the simplicity of this surface are the results of core-level photoemission measure-

* Corresponding author.

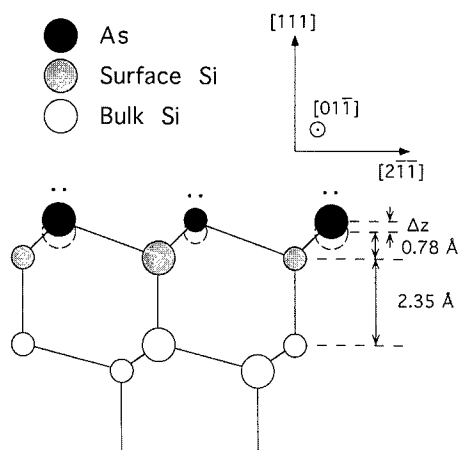


Fig. 1. Shown here is a side view in the $[01\bar{1}]$ plane of the 1 ML As/Si(111)-(1 × 1) surface. The As atoms replace the Si atoms in the upper layer of the topmost double layer. The structural parameter Δz is the movement of the As plane from the Si bulk position (shown with unfilled, broken circles).

ments [1,2,4]. The Si 2p core-level shows two very well defined components separated by 0.75 eV. The component to high binding energy is a surface core-level shifted (SCLS) peak due to the Si atoms bonded directly to the As atoms (shown in gray in Fig. 1 and designated 'Surface Si') while the component to low binding energy results from emission from bulk Si in lower layers. The As 3d core-level shows a single component. This structural and spectroscopic simplicity makes this system an ideal one for studying photoelectron diffraction (PD) effects from each of the core-level components separately, as intrinsic effects in angle resolved core-level photoemission experiments. PD is manifested as changes in core-level intensities as functions of angle or excitation energy and is due to the interference between the part of the outgoing photoelectron wave which is unaffected by the surrounding atomic potentials (the direct wave) and the part which undergoes elastic scattering by atoms in the vicinity of the emitting atom (the scattered waves). These intensity modulations thus contain information on the positions of the atoms surrounding the emitting atom [12–17]. Isolating the PD signal from SCLS peaks has recently been found to be a particularly sensitive method for obtaining the three dimensional geometry of clean surfaces when combined with multiple scattering calculations [16,17].

In this paper, we report azimuthal scanned PD measurements from the Si 2p SCLS peak for photon energies of $h\nu = 130$ and 150 eV and from the single component As 3d peak for $h\nu = 72$ eV. The Si 2p SCLS component shows very large intensity variations as functions of azimuthal angle. For $h\nu = 130$ eV and an electron emission angle of $\Theta = 45^\circ$ for example, the intensity of this component is found to vary by 400% upon an azimuthal rotation of 45° . This result indicates that PD effects can be very large in this important energy regime and that they must somehow be explicitly taken into consideration or averaged out to avoid potentially large errors in quantitative coverage determinations of surface or adsorbate atoms based on intensity variations between different atomic layers, which are modeled by a single parameter: the electron escape depth. A comparison of the measurements to model calculations using a fully convergent multiple scattering formalism is in good agreement with the accepted structure.

2. Experimental details

In order to perform these measurements, a preoxidized Si(111) substrate (n-type, Sb doped, $\sim 3 \Omega \text{ cm}$) with a misorientation of $< 0.3^\circ$ was mounted onto a high precision manipulator capable of a 180° rotation in the azimuthal sense (around the sample normal). The misalignment of the sample normal and the azimuthal rotation axis was $< 0.6^\circ$. After the preparation of the Si(111)-(7 × 7) surface using standard procedures, As was deposited onto the surface by evaporation from a well outgassed GaAs wafer. During the evaporation, which lasted 14 minutes, the sample was cooled from 700°C to 600°C and the background pressure was in the $1\text{--}3 \times 10^{-9}$ mbar range (compared with a base pressure of 2×10^{-10} mbar). After the source was turned off, the sample was cooled slowly to room temperature and then annealed to 450°C for 5 minutes to remove any superfluous As. The resulting surface exhibited a sharp (1 × 1) low energy electron diffraction (LEED) pattern with no streaking and photoemission mea-

measurements indicated sharp core-level profiles with no evidence of Ga or any other contaminant. The measurements were performed on beamline 41 of the MAX I storage ring in Lund, Sweden which is equipped with a toroidal grating monochromator (TGM) capable of delivering photons in the 15–200 eV range. The angle resolving electron analyzer had an angular acceptance of $\sim \pm 2.0^\circ$ in both the dispersive and nondispersive directions and the total instrumental energy resolution was ~ 0.15 eV under the conditions of the experiment.

3. Results and discussion

At the top of Fig. 2 are shown two Si 2p spectra using $h\nu = 130$ eV and $\Theta = 45^\circ$. The light incidence angle ($\Theta_{h\nu}$) was along the sample normal. The well separated surface component is shown as the shaded spin-orbit doublet on the low kinetic energy side of the signal in each spectrum. For all Si 2p spectra in this study, the total signal was fit to two spin-orbit split Voigt functions. All the peak parameters, including the spin-orbit branching ratios were free

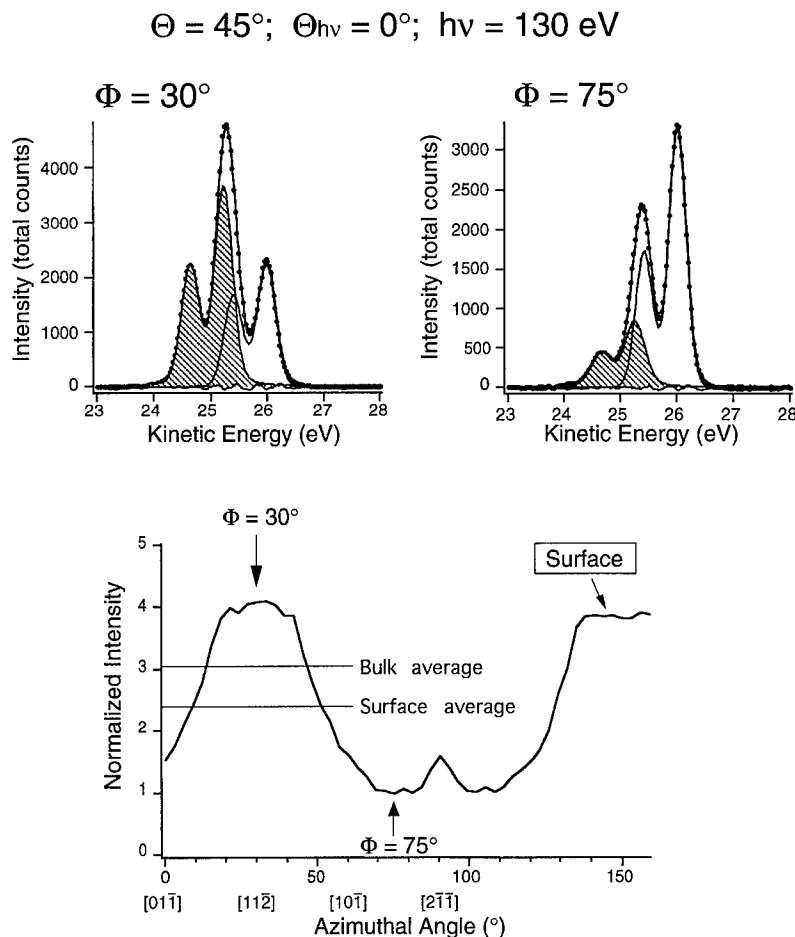


Fig. 2. At the top of this figure are two Si 2p core-level spectra which have been decomposed into two spin-orbit split Voigt functions. The shaded peak is due to the surface Si directly below and bonded to the As atoms. The only difference between the two spectra is a 45° rotation of the sample in the azimuthal direction. At the bottom is the normalized integrated intensity of this Si 2p SCLS peak as a function of azimuthal angle. The horizontal line represent the bulk and surface azimuthal averaged intensities.

parameters in the fit, with the exception of the spin–orbit splitting which was fixed at 0.600 eV. The least squares fits were excellent for all spectra yielding a surface–bulk separation of 0.75 ± 0.01 eV in agreement with previous work [1,2,4]. The fact that this separation is greater than the spin–orbit splitting allows one to rule out the possibility of additional components in the spectra and to determine the integrated intensities of the surface and bulk components with a high degree of accuracy. In the spectra, the black dots are the experimental data after background subtraction and the smooth curves are the results of the fits. The differences between the experimental data and the fits are also shown. These two spectra were taken at the same electron emission angle of $\Theta = 45^\circ$ with the only difference between them being a 45° azimuthal rotation of the sample with respect to the fixed light incidence and analyzer acceptance directions. It is clear upon inspection of these spectra that large changes in peak shape occur upon this azimuthal rotation with the most noticeable change being a strong increase in the relative intensity of the surface component at an azimuthal angle of $\Phi = 300^\circ$ compared to $\Phi = 75^\circ$. After normalization with respect to the background at a kinetic energy of 27.5 eV, this increase is found to be $\sim 400\%$. Changes in peak intensity as a function of azimuthal angle are not predicted using the single parameter electron escape depth model which is routinely used for determining surface atom or adsorbate atom coverages. As discussed below, this effect is due to diffraction of the outgoing Si 2p SCLS photoelectrons as they leave the crystalline surface.

The bottom of Fig. 2 reports the integrated, background normalized Si 2p SCLS peak intensity as a function of azimuthal angle over a 160° range using $h\nu = 130$ eV and $\Theta = 45^\circ$. Some crystallographic directions are indicated on the azimuthal angle scale. These data have not been symmetrized. Even so, the $[11\bar{2}]$ and $[2\bar{1}\bar{1}]$ mirror planes are very clear from the data with even some fine structure to $\sim 13^\circ$ on either side of the $[2\bar{1}\bar{1}]$ direction being reproduced. The high quality of these data is due principally to the large surface–bulk component separation and consequent accuracy of the SCLS peak intensity determination. Here, the large fluctuations in peak intensity are readily visible with the normalized peak

intensity varying from ~ 4 for $\Phi = 30^\circ$ to ~ 1 for $\Phi = 75^\circ$ with these two data points corresponding to the two spectra at the top of the figure. The bulk component exhibits weaker diffraction effects and its average value is indicated by a horizontal line. Also indicated by a horizontal line is the azimuthal averaged value of the surface component.

Based on the one parameter electron escape depth model for relative peak intensities, the coverage in monolayers (ML), x , of the atoms giving rise to the surface Si peak for this system is given by the following equation:

$$x = \frac{I_S [e^{a_1 / (\lambda_e \cos \Theta)} + 1]}{I_B [e^{a_2 / (\lambda_e \cos \Theta)} - 1]},$$

where I_S and I_B are the integrated surface and bulk peak intensities respectively extracted from the measurement, $a_1 = 0.78$ Å is the distance between the two layers of the double layer in bulk Si, $a_2 = 3.13$ Å is the distance between two double layers in bulk Si, λ_e is the electron mean free path, and Θ is the electron emission angle with respect to the surface normal. If one were to use this equation to determine the number of monolayers giving rise to the surface Si signal based on bulk and surface component intensities for the spectrum taken at $\Phi = 30^\circ$ and assuming an electron mean free path of 4 Å, the result would be 2.0 ML. On the other hand, if the same calculation were done using the spectrum taken at $\Phi = 75^\circ$, the result would be 0.4 ML (these results differ by a factor of 5 rather than 4 since the measured bulk intensities were used in the calculation rather than the azimuthal averaged value). It should be emphasized that this analysis is not intended to predict quantitatively the errors in coverage determinations based on core-level intensities since the majority of such determinations are done using ‘angle integrated’ instruments. These results instead serve as an indication of the magnitude of PD effects as an intrinsic part of angle resolved core-level photoemission measurements at energies near the minimum in the electron mean free path. However, angle integrated instruments generally accept electrons over a rather small fraction of the full 2π hemisphere above the surface. The large, long period PD oscillations observed in Fig. 2 suggest that such angle integrated measurements are still far from av-

eraging over diffraction effects in this energy regime for a general case. In addition, strong PD effects are known to occur as functions of energy, possibly further increasing the error introduced in coverage determinations based on core-levels measured at a single photon energy. Remarkably, PD effects are usually completely ignored in coverage determinations although Fadley in his review of PD and Auger electron diffraction (AED) [12] estimated that errors as high as $\pm 50\%$ may occur due to diffraction effects. The results of the present study, however, show that such effects may in fact be much greater than this value.

Fig. 3 shows measurements identical to those of Fig. 2 except that here $h\nu = 150$ eV was used. As in

Fig. 2, the diffraction curve shown at the bottom of the Figure is the raw data without any symmetrization and the mirror symmetries are very well reproduced. Again there are strong changes in relative peak intensities as functions of azimuthal angle although they are not as dramatic as the $h\nu = 130$ eV case. The Si 2p SCLS diffraction curve is noticeably different from the previous case both in its average value and its shape showing that the peak intensities are also functions of photon energy. In comparing Figs. 2 and 3, it is noted that the azimuthal averaged surface peak intensity is significantly closer to the azimuthal averaged bulk peak intensity in Fig. 3. This relative increase in the surface peak intensity indicates in a direct way that the electron mean free

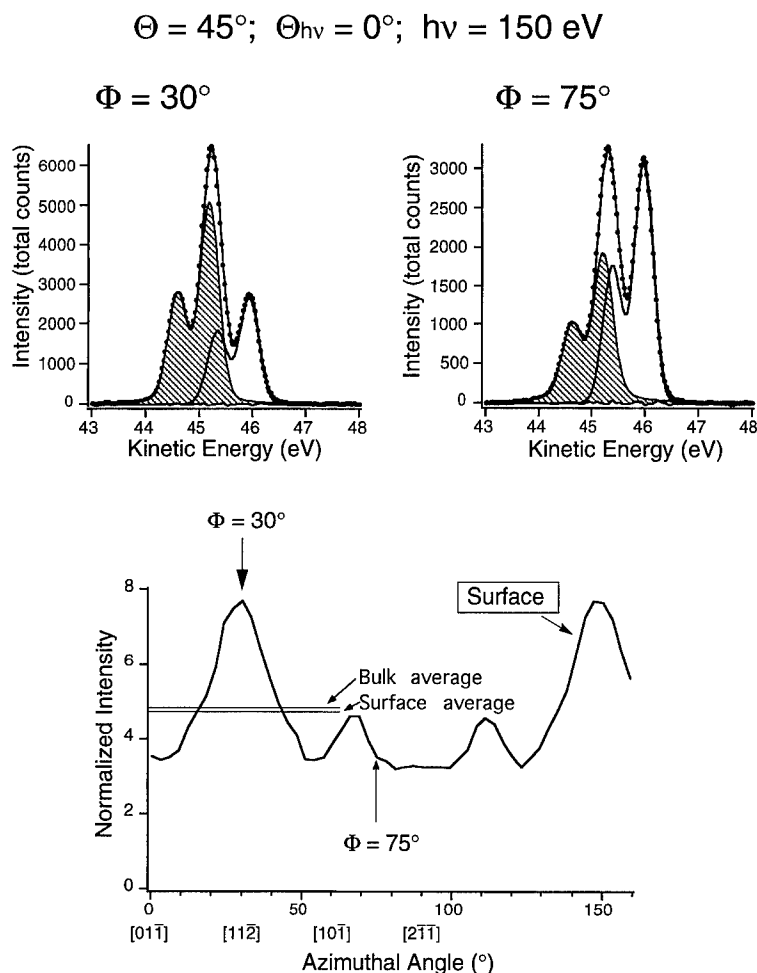


Fig. 3. This figure shows data identical to Fig. 2 except that the photon energy used was $h\nu = 150$ eV rather than $h\nu = 130$ eV.

path is smaller for $h\nu = 150$ eV than for $h\nu = 130$ eV. It is in fact possible to use the above equation and the azimuthal averaged values for the peak intensities to estimate the mean free path *if* one assumes that such azimuthal averaging effectively averages out PD effects. From the data in Figs. 2 and 3, such calculations yield electron mean free paths of 3.9 Å for the $h\nu = 130$ eV case and 3.4 Å for the $h\nu = 150$ eV case. Si 2p photoemission measurements are often performed at $h\nu = 130$ eV and the value of 3.9 Å found here for the electron mean free path in Si agrees very well with previous determinations of this quantity [18,19]. Thus, it appears for the

$h\nu = 130$ eV case that averaging the Si 2p intensity over the full azimuthal range does effectively average over PD effects although this cannot be expected to be true in general for the reasons given above.

The Si 2p SCLS PD data as well as the As 3d single component PD measured using $h\nu = 72$ eV have been modeled using a fully convergent multiple scattering formalism [20] with a complex Hedin–Lundqvist potential [21] for Δz values of 0.1, 0.2, and 0.3 Å. These numbers thus cover the range of values determined for this structural parameter by previous studies. The results of these calculations are shown in Fig. 4 as dashed lines with the upper curve in each set corresponding to $\Delta z = 0.3$ Å, the middle curve to 0.2 Å, and the bottom curve to 0.1 Å. The experimental data are shown as solid lines. In all three cases the calculations reproduce the experimental data rather well showing that the strong changes in peak intensities as functions of azimuthal angle can be successfully predicted using an appropriate scattering formalism. A detailed analysis of the very strong effects present in the Si 2p SCLS PD curve taken using $h\nu = 130$ eV indicates that these are due principally to single scattering by nearest neighbor As atoms with the strong constructive interference effects (at $\Phi = 30^\circ$) occurring for scattering angles considerably different from the forward scattering maxima which are prominent at much higher electron kinetic energies [22].

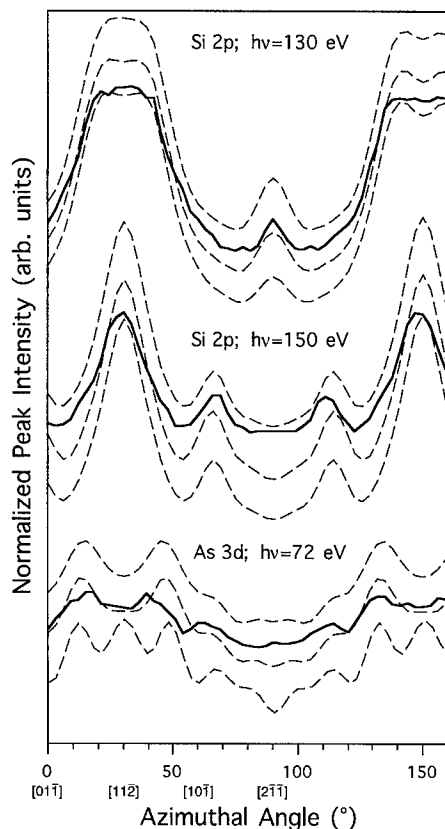


Fig. 4. Here, the photoelectron diffraction results from the Si 2p SCLS peak for $h\nu = 130$ eV (uppermost solid curve) $h\nu = 150$ eV (middle solid curve), and the As 3d single component for $h\nu = 72$ eV (bottom solid curve) are superimposed on the results of multiple scattering simulations (dashed curves). For each set, the upper dashed curve represents the results of the calculation for $\Delta z = 0.3$ Å, the middle dashed curve for $\Delta z = 0.2$ Å and the lower dashed curve for $\Delta z = 0.1$ Å.

4. Summary

In conclusion, photoelectron diffraction measurements of the very well resolved Si 2p surface core-level shifted peak and the single component As 3d peak from 1 ML As/Si(111)-(1 × 1) have been presented. Because the Si 2p surface component is so well resolved, there is very little error introduced in the deconvolution of the Si 2p signal and the intensity oscillations of the signal coming from the Si layer bonded to the As atoms can be isolated with a high degree of accuracy. This fact, along with the structural simplicity of the system, makes it an ideal one for studying photoelectron diffraction effects as an intrinsic part of angle resolved core-level photoemission experiments. It was found that such diffraction effects lead to differences of up to 500% in

coverage determinations of surface or adsorbate atoms based on relative peak intensities if a simple one parameter electron mean free path model is used. Azimuthal averaging of peak intensities appears to decrease this error so that angle integrated core-level measurements should be more appropriate for coverage determinations. However, since diffraction effects occur at all angles and angle integrated measurements sample only a relatively small part of the hemisphere above a surface, these measurements cannot be expected to average out diffraction effects completely. In addition relative peak intensities are also affected by energy dependent diffraction effects which may also introduce errors in quantitative coverage determinations. Simulations of the experiments using a fully convergent multiple scattering formalism successfully reproduce the experimental data for both the Si 2p and As 3d diffraction results when the accepted structure is used.

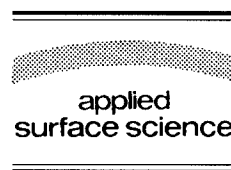
References

- [1] M.A. Olmstead, R.D. Bringans, R.I.G. Uhrberg and R.Z. Bachrach, *Phys. Rev. B* 34 (1986) 6041.
- [2] R.I.G. Uhrberg, R.D. Bringans, M.A. Olmstead, R.Z. Bachrach and J.E. Northrup, *Phys. Rev. B* 35 (1987) 3945.
- [3] J.R. Patel, J.A. Golovchenko, P.E. Freeland and H.-J. Gossman, *Phys. Rev. B* 36 (1987) 7715.
- [4] R.D. Bringans, M.A. Olmstead, R.I.G. Uhrberg and R.Z. Bachrach, *Phys. Rev. B* 36 (1987) 9569.
- [5] R.S. Becker, B.S. Swartzentruber, J.S. Vickers and M.S. Hybertsen, *Phys. Rev. Lett.* 60 (1988) 116.
- [6] R.L. Headrick and W.R. Graham, *Phys. Rev. B* 37 (1988) 1051.
- [7] M. Copel, R.M. Tromp and U.K. Köhler, *Phys. Rev. B* 37 (1988) 10756.
- [8] M.S. Hybertsen and S.G. Louie, *Phys. Rev. B* 38 (1988) 4033.
- [9] R.S. Becker, T. Klitsner and J.S. Vickers, *J. Microsc.* 152 (1988) 157.
- [10] C.H. Patterson and R.P. Messmer, *Phys. Rev. B* 39 (1989) 1372.
- [11] O. Sakata, H. Hashizume and H. Kurashina, *Phys. Rev. B* 48 (1993) 11408.
- [12] C.S. Fadley, in: *Synchrotron Radiation Research: Advances in Surface Science*, Ed. R.Z. Bachrach (Plenum, New York, 1990).
- [13] S.A. Chamber, *Adv. Phys.* 40 (1991) 357.
- [14] W.F. Egelhoff, Jr., in: *Ultrathin Magnetic Structures I, An Introduction to Electronic, Magnetic and Structural Properties*, Eds. J.A.C. Bland and B. Heinrich (Springer, Berlin, 1994).
- [15] L. Patthey, E.L. Bullock and K. Hricovini, *Surf. Sci.* 269/270 (1992) 28.
- [16] S. Gota, R. Gunnella, Z.-Y. Wu, G. Jézéquel, C.R. Natoli, D. Sébilleau, E. L. Bullock, F. Proix, C. Guillot and A. Quémerais, *Phys. Rev. Lett.* 71 (1993) 3387.
- [17] E.L. Bullock, R. Gunnella, L. Patthey, T. Abukawa, S. Kono, C.R. Natoli and L.S.O. Johansson, *Phys. Rev. Lett.* 74 (1995) 2756.
- [18] E. Landemark, C.J. Karlsson, Y.-C. Chao and R.I.G. Uhrberg, *Phys. Rev. Lett.* 69 (1992) 1588.
- [19] F.J. Himpsel, F.R. McFeely, A. Taleb-Ibrahimi, J.A. Yarmoff and G. Hollinger, *Phys. Rev. B* 38 (1988) 6084.
- [20] C.R. Natoli, M. Benfatto, C. Brouder, M.F. Ruiz Lopez and D.L. Foulis, *Phys. Rev. B* 42 (1992) 5997.
- [21] L. Hedin and S. Lundqvist, *Solid State Phys.* 23 (1969) 1; *J. Phys. (Paris) C* 3 (1972) 73; *J. Phys. (Paris) C* 4 (1971) 2064; *J. Phys. (Paris) C* 4 (1971) 2347.
- [22] E.L. Bullock, R. Gunnella, C.R. Natoli, R.I.G. Uhrberg and L.S.O. Johansson, unpublished results.



ELSEVIER

Applied Surface Science 104/105 (1996) 95–100



Fluorine adsorption on GaAs(110) surfaces and the onset of etching after XeF_2 exposures

H. Nienhaus^{*}, W. Mönch

Laboratorium für Festkörperphysik, Gerhard-Mercator-Universität Duisburg, Lotharstr. 1-21, D-47048 Duisburg, Germany

Received 28 June 1995; accepted 26 September 1995

Abstract

The interaction of XeF_2 molecules with GaAs(110) surfaces was investigated with high-resolution electron energy-loss (HREELS) and Auger electron spectroscopy (AES) in the exposure range between 1 and 1000 langmuir (L). The AES results show that up to XeF_2 doses of approximately 100 L, fluorine atoms are mainly chemisorbed on GaAs(110) surfaces. After XeF_2 exposures above 100 L, etching of the GaAs(110) surface occurs by removing arsenic atoms. Adsorbed xenon atoms were never detected. In the chemisorption range an energy-loss structure which is attributed to As–F valence vibrations is observed in the HREEL spectra. The excitation energy of the As–F vibration shifts from 670 cm^{-1} (84 meV) at very low fluorine coverages to 720 cm^{-1} (90 meV) at 0.3 monolayers. This finding may be explained by a mutual electrostatic interaction between As–F surface dipoles and their images. From that and by use of dielectric theory an effective dynamic charge of the vibrating As–F surface molecules is estimated. In the etching regime this As–F loss structure disappears and a broad feature at about 575 cm^{-1} (71.3 meV) is observed which may be due to vibrations of Ga–F_x groups.

1. Introduction

Fluorination of GaAs surfaces has attracted increasing attention as the chemical reaction produces a GaF_3 film on the surface which exhibits promising qualities as an insulator suitable for microelectronic devices. Hence, a variety of studies was focused on GaF_3 /GaAs interfaces and fluorinated surfaces after large exposures to F_2 [1,2], XeF_2 [3], F^+ ions [4] or excited fluorinated molecules ([3], and references therein). However, the low-exposure range is not well investigated. In case of XeF_2 on GaAs(110) X-ray photoemission spectroscopy (XPS) was ap-

plied [5]. From the chemically shifted components of Ga and As 3d core-levels XeF_2 was found to adsorb dissociatively, leaving atomic F at both substrate atoms behind. After higher exposures GaF_3 groups were detected.

In the present study, the interaction of XeF_2 molecules with GaAs(110) surfaces has been investigated with Auger electron (AES) and high-resolution electron energy-loss spectroscopy (HREELS). The experiments characterize the adsorbate–substrate bonds by respective valence vibrations and determine the onset of etching. They are motivated by recent HREELS results at chlorinated GaAs(110) surfaces [6]. In the energy-loss spectra, only Ga–Cl vibrations were detected as long as the surface was not disrupted. This finding is surprising because chlorine is supposed to chemisorb at both substrate

^{*} Corresponding author. Fax: +49-203-3793163.

atoms as it is also expected for fluorine on GaAs(110).

2. Experimental

The experiments were performed in a two-chamber ultrahigh vacuum system. In the preparation chamber, clean GaAs(110) surfaces were prepared *in situ* by cleaving single crystalline bars. During exposures, they were placed in front of a small tube through which XeF₂ molecules were let in. For this, a leak valve was opened between the preparation chamber and a vessel in which XeF₂ crystallites were sublimated. The dose was varied in the range of 1 and 1000 L (1 L = 10⁻⁶ Torr s) and monitored by measuring the background pressure in the preparation chamber with a cold-cathode ion gauge. Before any exposure, the whole dosing system was passivated with a large amount of XeF₂. No carbon or metal contaminations were observed on the surface. Residual oxygen was only detected after highest exposures.

In the analysis chamber, the Auger electron spectra were obtained by using a cylindrical mirror analyser. The primary electron beam with an energy of 3 keV was scanned across the surface to avoid electron-stimulated desorption (ESD) [7,8] of adsorbed fluorine. AES line intensities were measured as the peak-to-peak value of the first derivative signals.

The electron energy-loss spectra were recorded at a primary energy E_p of typically 5 eV and an instrumental resolution of 30 cm⁻¹ (3.7 meV). The incident electrons were specularly reflected from the surface with an angle of incidence of 55°. To provide a high resolution in the HREEL spectra, surfaces of semi-insulating material were investigated. Here, broadening of the loss peaks due to surface plasmon excitations of free charge carriers does not occur [9,10].

3. Results and discussion

3.1. AES results

After XeF₂ exposures, adsorbate-induced AES features corresponding to KLL lines of fluorine were

observed. Xe atoms were never detected on the surface. The same was found in the XPS study mentioned above [5]. To investigate the fluorine uptake the intensity ratio between the F(KLL) line at a kinetic energy of 650 eV and the Ga(LMM) peak at 1070 eV was measured as a function of the XeF₂ dose N . The results recorded with p- and n-type samples are shown in Fig. 1. The scatter of the data is due to uncertainties of determining the dose. Applying a simple layer model with calculated AES cross sections [11] an effective F-coverage Θ is deduced from the data. It is shown on the right-hand axis in Fig. 1. One monolayer (ML) is set equal to the number of possible adsorption sites per unit area on the GaAs(110) surface, i.e., $\sigma = 8.86 \times 10^{14}$ cm⁻².

Adsorption of fluorine atoms is first detected at a dose of approximately 10 L. After the highest XeF₂ exposures of 1000 L the coverage corresponds to $\Theta = 0.75$ ML. No saturation of the uptake is observed. For dissociative chemisorption of second order a relation

$$\Theta = \Theta_s \frac{S_0 N}{\sigma C + S_0 N} \quad (1)$$

is expected [12]. The curve in Fig. 1 is a fit to the experimental data following Eq. (1) with the parameters $\Theta_s = 1.1$ ML and $S_0 = 0.02$. The latter might not be identified with the initial sticking coefficient as the values of exposure are too uncertain. The con-

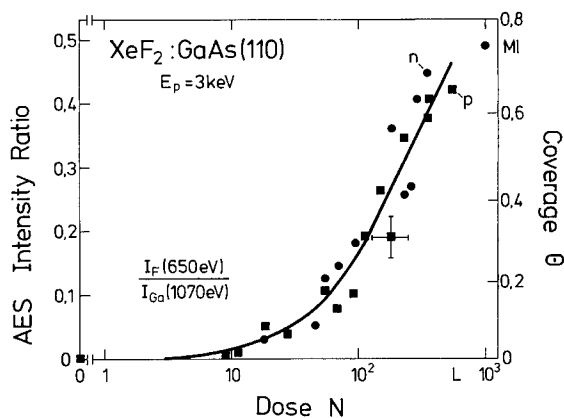


Fig. 1. Auger electron intensity-ratio I_F/I_{Ga} as a function of XeF₂ exposure. The coverage scale was calculated by use of a layer model.

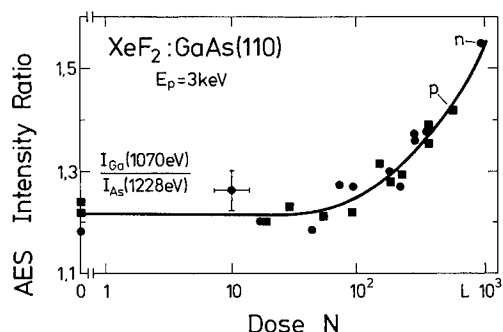


Fig. 2. Auger electron intensity-ratio of the high-energy substrate lines as a function of XeF_2 exposure. After doses above 100 L the GaAs(110) surface is etched.

stant $C = 6.58 \times 10^{-15} \text{ L cm}^2$ converts the unit cm^{-2} into L.

To study the etching of the GaAs(110) surface by XeF_2 , the intensity quotient of the high-energy Ga(1070 eV) and As(1228 eV) AES lines is plotted with varying exposure in Fig. 2. The solid line just follows the trend of the data. Up to doses of 100 L the ratio remains almost constant at 1.23 but increases after higher exposures. The analysis of the Auger spectra reveals that the absolute AES intensities of the As lines are significantly reduced while those of the Ga structures do not change. This finding implies a removal of arsenic atoms from the surface. It discriminates between the chemisorption range up to 100 L, which corresponds to a F-coverage of about 0.3 ML, and the etching regime for larger exposures.

3.2. HREELS results

Two typical HREEL spectra obtained from semi-insulating GaAs(110) surfaces after XeF_2 doses of 36 and 250 L are plotted in Fig. 3. The energy resolution is demonstrated by the width of the elastic peak at half maximum and varies between 32 and 38 cm^{-1} (4 and 4.7 meV). The energy-loss and -gain features due to the excitation of one or more Fuchs-Kliwer surface phonons at an energy of 289 cm^{-1} (35.8 meV) [13] are labeled as FK and $\overline{\text{FK}}$, respectively. In the lower panel of Fig. 3, i.e., when fluorine atoms are chemisorbed on GaAs(110), adsorbate-induced loss structures F, X_1 , X_2 and the combined excitation $\text{FK1} + \text{F}$ are observed. The

sharp peak F at a loss energy $\hbar\omega_F$ of about 700 cm^{-1} (86.8 meV) is also detected as an anti-Stokes line $\overline{\text{F}}$. Its intensity varies with the energy E_p of the primary electrons following an E_p^{-1} law which is expected for adsorbate vibrations. Since vibrational frequencies at surfaces are close to those known from infrared and Raman spectra of free molecules one may consider AsFH_2 and $\text{AsF}(\text{CH}_3)_2$ to get a reference value for the energy of the As-F valence vibration. That was measured between 650 and 720 cm^{-1} (80.6 and 89.3 meV) [14–16]. Infrared studies at gallium fluorine systems gave a Ga-F stretching frequency in the range from 590 to 620 cm^{-1} (64.5 to 76.9 meV) [17,18]. Taking these data into account, the HREELS structure F may be attributed to As-F valence vibrations. The weak double loss feature X was only resolved after long measuring times. Its

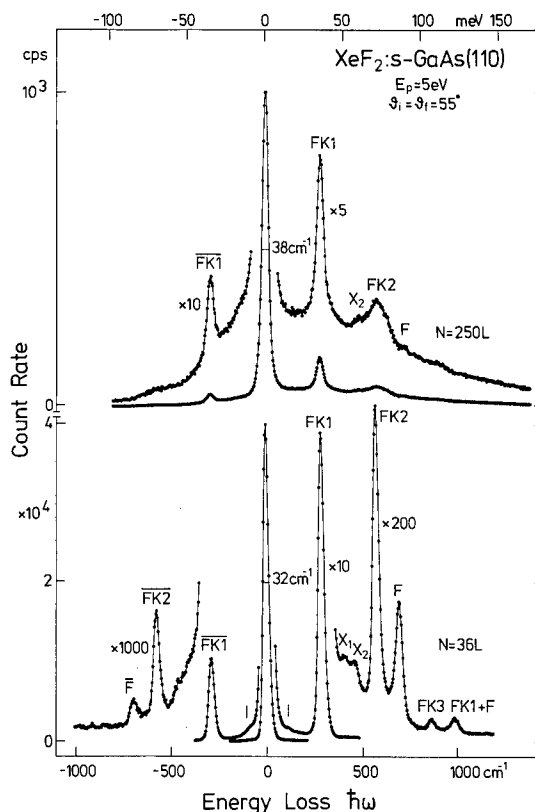


Fig. 3. HREEL spectra recorded with GaAs(110) surfaces after XeF_2 exposures of 36 and 250 L. FK: Fuchs-Kliwer phonon; $\overline{\text{F}}$: As-F valence vibration; X: weak adsorbate-induced feature with uncertain origin.

origin is uncertain. It might be due to vibrations of fluorine atoms located in the substrate backbonds since in cyclic molecules Ga–F–Ga vibrations were found at energies between 420 and 500 cm^{-1} (52.1 and 62 meV) [19].

XPS [5] and electron energy-loss spectroscopy at intermediate energies [20] have revealed that fluorine–gallium bonds already exist in the chemisorption range although they are not detected with HREELS. From that, one may conclude that Ga–F bonds are oriented almost parallel to the surface and the respective adsorbate vibration cannot be effectively excited in dipole scattering geometry.

After a XeF_2 dose of 250 L, etching of the surface starts. As shown in the upper panel of Fig. 3, the total HREELS intensity is reduced by a factor of 40, the background signal is increased and the structures F and X almost disappear. Instead, a broad HREEL feature at 575 cm^{-1} (71.3 meV) is observed and overlaps the double loss FK2. The same was found in infrared spectra from thin GaF_3 layers on GaAs(110) [1] where this loss is attributed to GaF_x vibrations.

The loss intensity and the excitation energy of the As–F valence vibration were extracted from HREEL spectra in the XeF_2 exposure range from 0 to 200 L, i.e., in the chemisorption regime. The results recorded with semi-insulating and n-doped samples are shown in Fig. 4. The solid lines are meant to guide the eye.

The intensity I_F/I_{el} of the F-induced line relative to the signal of elastically scattered electrons is plotted in the upper panel. It grows by a factor of about 100 when the exposure is increased from 3 to 100 L. With the disruption of the surface at higher doses, the relative intensity remains constant or becomes even smaller. In the lower panel the significant frequency shift of the As–F vibration is shown. The loss energy at small and large F-coverages is difficult to determine due to the low intensity and the high background signal, respectively. The excitation energy $\hbar\omega_F$ increases from 670 to 720 cm^{-1} (83.1 to 89.3 meV) in the chemisorption range.

Frequency shifts as a function of coverage were reported for vibrations of molecules as CO on metal surfaces ([21–28], and references therein). The enhanced vibrational polarizability was tried to be explained by the electrostatic dipole–dipole interaction of neighboring molecules [23–25] and the strong

response of the metal surface modeled by an image potential [26–28]. However, some experimental data were insufficiently described by these local field effects. Also in the present case where adsorbate–substrate vibrations are concerned, the large frequency shift and intensity increase may only be understood if a strong response of the substrate–electron system is considered. To demonstrate that, an effective dynamic charge e^* of the As–F surface molecule bond is deduced from the experimental data. A priori, one would expect that in a point-charge model e^* is close to the static charge transfer from arsenic to fluorine which is estimated as 0.4 e_0 from Pauling's electronegativity scale.

The data in Fig. 4 may be analysed by applying dielectric theory for inelastic electron scattering in dipolar geometry. The cross section for exciting a surface mode is proportional to the loss function $\text{Im}[-1/\epsilon_a(\omega)]$ where $\epsilon_a(\omega)$ is a frequency-dependent dielectric constant (DC) of a thin surface layer

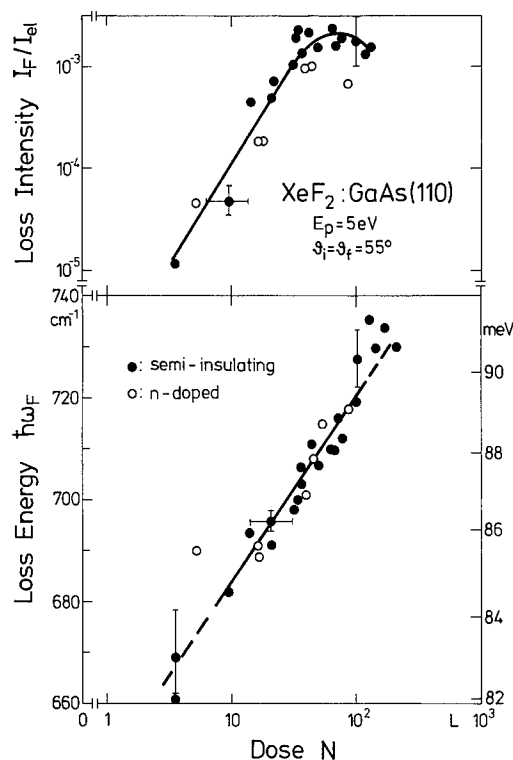


Fig. 4. Change of the relative HREEL intensity I_F/I_{el} and the loss energy $\hbar\omega_F$ due to As–F valence vibrations with increasing XeF_2 exposure. The solid lines are meant to guide the eye.

[22]. If the ensemble of the As–F surface molecules with reduced mass M_r is considered as a two-dimensional gas of harmonic oscillators interacting with each other via dipole fields, a DC

$$\epsilon_a(\omega) = 1 + \frac{n_{os}(ae^*)^2}{M_r \epsilon_0} \frac{1}{\omega_0^2 + \Delta^2 - \omega^2 - i\gamma\omega} \quad (2)$$

may be assumed in a first approximation. An electronic polarizability is neglected. In Eq. (2), $n_{os} = c\Theta\sigma/d$ denotes the spatial molecule density, d is the thickness of the adsorbate layer and $c\Theta$ the As–F coverage. The quantities ω_0 and γ are the frequency and the damping constant of a single non-interacting oscillator, respectively. The factor a describes a possible enhancement of e^* due to an image charge. The resonance frequency in Eq. (2) is shifted by

$$\Delta = \sqrt{\frac{\kappa\sigma^{3/2}(ae^*)^2}{4\pi\epsilon_0 M_r} c\Theta} \quad (3)$$

due to dipole–dipole interaction [20] if the molecules are randomly distributed on the surface [28]. The factor $\kappa \approx 9$ originates from the dipole sum.

If Eq. (2) is inserted into the loss function one finds that $[(\hbar\omega_F)^2 - (\hbar\omega_0)^2]$ and $\hbar\omega_F I_F/I_{el}$ are proportional to $c\Theta(ae^*)^2$ [20]. In Fig. 5 these relationships are illustrated. Within the limits of error the predicted linear dependences are confirmed. If equal probabilities for the existence of As–F and Ga–F bonds are assumed, i.e., $c = 0.5$, it follows from least-squares fits to the data plotted in Fig. 5

$$e^* = (1.0 \pm 0.3)e_0/a. \quad (4)$$

If e^* is close to the static charge transfer the factor a must be of the order of 2, i.e., the effective dipoles are doubled at the GaAs(110) surface by an additional image charge. Whether such a strong response of the semiconductor surface is reasonable can only be answered by a precise theoretical treatment of the coverage dependent dynamics of fluorine adsorbed on GaAs(110). However, such calculations for adsorbed atoms do not exist, yet. They would give a deeper insight into the mechanisms of vibrational interactions and frequency shifts.

4. Conclusion

In the present study, the interaction of XeF_2 with GaAs(110) surfaces at room temperature was investigated with AES and HREELS. The AES results demonstrate that fluorine atoms chemisorb on the surface up to a coverage of 0.3 monolayers. Further fluorine uptake is accompanied with a removal of arsenic atoms from the surface. AES structures due to Xe are not observed.

With HREELS an adsorbate-induced loss feature attributed to As–F valence vibrations is detected as long as the surface is not disrupted. This finding cannot rule out the existence of Ga–F bonds at low coverage which were reported before. The results indicate that those bonds are oriented almost parallel to the surface. At higher exposures the As–F loss structure disappears and a broad HREELS feature due to GaF_x groups is detected.

With increasing coverage the observed excitation energy of the As–F vibration shifts significantly. From this and the intensity variation one may deduce an effective dynamic charge of about $0.5e_0$ if an image potential is assumed. Further sophisticated theoretical work is necessary to reveal the physical

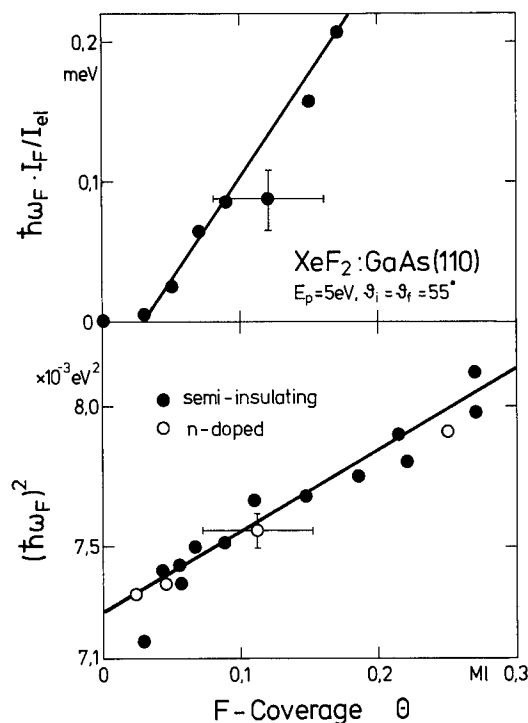


Fig. 5. Linear dependences predicted by dielectric theory between the quantities $\hbar\omega_F I_F/I_{el}$ and $(\hbar\omega_F)^2$ and the F-coverage Θ .

origin of such strong coverage dependent frequency shifts.

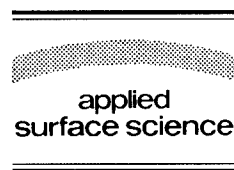
References

- [1] A.S. Barrière, B. Desbat, H. Guégan, L. Lozano, T. Séguélong, A. Tressaud and P. Alnot, *Thin Solid Films* 170 (1989) 259.
- [2] A.S. Barrière, B. Desbat, J. Granec, H. Guégan, T. Séguélong and J. Chazelas, *Thin Solid Films* 196 (1991) 65.
- [3] P.R. Varekamp, W.C. Simpson, D.K. Shuh, T.D. Durbin, V. Chakarian and J.A. Yarmoff, *Phys. Rev. B* 50 (1994) 14267; W.C. Simpson, P.R. Varekamp, D.K. Shuh and J.A. Yarmoff, *J. Vac. Sci. Technol. A* 13 (1995) 1709.
- [4] L.R. Williston, I. Bello and W.M. Lau, *J. Vac. Sci. Technol. A* 10 (1992) 1365.
- [5] A.B. McLean, L.J. Terminello and F.R. McFeely, *Phys. Rev. B* 40 (1989) 11778.
- [6] J. Pankratz, H. Nienhaus and W. Mönch, *Surf. Sci.* 307–309 (1994) 211.
- [7] D. Troost, H.J. Clemens, L. Koenders and W. Mönch, *Surf. Sci.* 286 (1993) 97.
- [8] G.B. Hoflund, *Scanning Electron Microsc. IV* (1985) 1391.
- [9] B.N.J. Persson and J.E. Demuth, *Phys. Rev. B* 30 (1984) 5968.
- [10] H. Ibach, *Surf. Sci.* 299/300 (1994) 116.
- [11] S. Mroczkowski and D. Lichtman, *J. Vac. Sci. Technol. A* 3 (1985) 1860.
- [12] W.H. Weinberg, *Kinetics of Interface Reactions*, in: Springer Series in Surface Science, Vol. 8, Eds. M. Grunze and H.J. Kreuzer (Springer, Berlin, 1987).
- [13] R. Matz and H. Lüth, *Phys. Rev. Lett.* 46 (1981) 500.
- [14] J. Breidung, W. Thiel and A. Komornicki, *Inorg. Chem.* 30 (1991) 1067, and references therein.
- [15] L. Andrews and T.C. McInnis, *Inorg. Chem.* 30 (1991) 2996.
- [16] E. Höfling, Thesis, Universität Stuttgart (1968).
- [17] J.W. Hastie, R.H. Hauge and J.L. Margrave, *J. Fluorine Chem.* 3 (1973–74) 285.
- [18] H. Uehara, K. Horiai, K. Nakagawa and H. Suguro, *Chem. Phys. Lett.* 178 (1991) 533.
- [19] H. Schmidbaur, J. Weidlein, H.F. Klein and K. Eiglmeier, *Chem. Ber.* 101 (1968) 2268.
- [20] H. Nienhaus, Thesis, Universität Duisburg (1994).
- [21] R.F. Willis, A.A. Lucas and G.D. Mahan, in: *The Chemical Physics of Solid Surfaces and Heterogeneous Catalysis*, Vol. 2, Eds. D.A. King and D.P. Woodruff (Elsevier, Amsterdam, 1983).
- [22] H. Ibach and D.L. Mills, *Electron Energy Loss Spectroscopy and Surface Vibrations* (Academic Press, New York, 1982).
- [23] S. Andersson and B.N.J. Persson, *Phys. Rev. Lett.* 45 (1980) 1421.
- [24] B.N.J. Persson and R. Ryberg, *Phys. Rev. B* 24 (1981) 6954.
- [25] M. Moskovits and J.E. Hulse, *Surf. Sci.* 78 (1978) 397.
- [26] S. Efrima and H. Metiu, *Surf. Sci.* 108 (1981) 329; 109 (1981) 109.
- [27] M. Scheffler, *Surf. Sci.* 81 (1979) 562.
- [28] G.D. Mahan and A.A. Lucas, *J. Chem. Phys.* 68 (1978) 1344.



ELSEVIER

Applied Surface Science 104/105 (1996) 101–106



An ARUPS/NEXAFS study of the H₂S/InP(110) adsorbate system

E. Dudzik^a, A. Leslie^a, E. O'Toole^a, I.T. McGovern^{a,*}, A. Patchett^b,
D.R.T. Zahn^b

^a Trinity College, Dublin 2, Ireland

^b TU Chemnitz, Chemnitz, Germany

Received 13 July 1995; accepted 2 October 1995

Abstract

The room temperature adsorption of H₂S on InP(110) may be understood as a cooperative dissociation in which H⁺ and SH[−] bond to the surface anion and cation, respectively. Synchrotron radiation angle resolved ultraviolet photoelectron spectroscopy (ARUPS) and near edge X-ray absorption fine structure (NEXAFS) are used to probe the filled and vacant orbital levels of the adsorbate complex. The NEXAFS results are consistent with the location of the sulphur in the continued layer anion site in agreement with recent X-ray standing wave measurements.

1. Introduction

The adsorption of H₂S on the (110) surface of indium phosphide appears paradoxical in many respects. For example, the adsorption occurs at room temperature [1,2] whereas it is necessary to cool the related GaAs(110) surface to 200 K for adsorption to occur [3,2]. Also, the adsorbate is easily removed by gentle annealing, yet the adsorption results in a relatively large surface anion core level shift more appropriate to strongly bound species [2]. These paradoxes may be understood in terms of a cooperative dissociation bonding of H⁺ and SH[−] to surface anion and cation atoms; this is in effect a proton exchange between the H₂S molecule and the surface anion dangling bond [4]. Recent normal incidence X-ray standing wave measurements [5] provide some

confirmation of this model, placing the sulphur atom at the location of a phosphorus atom in the continued layer structure.

This paper presents the results of a combined angle resolved ultraviolet photoelectron spectroscopy (ARUPS) and near edge X-ray absorption fine structure (NEXAFS) study using synchrotron radiation. These measurements probe the adsorbate filled and empty orbital levels, respectively, and the results are interpreted in terms of the dissociative adsorption model.

2. Experimental details

Pre-notched n-InP samples were cleaved in UHV at base pressures around 3×10^{-10} mbar. They were then dosed with 2–5 L of H₂S (purity 99.6%). The ARUPS experiments were carried out at the TGM2

* Corresponding author.

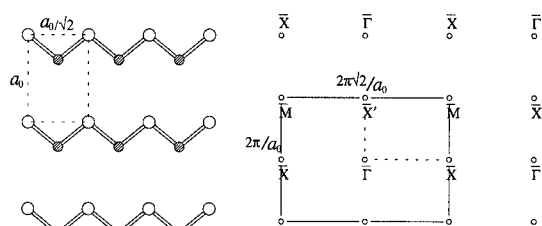


Fig. 1. Orientation of the surface unit cell and the surface Brillouin zone.

beamline of the Berlin electron synchrotron (BE-SSY). The electron spectrometer was an ADES 400 hemispherical analyser operated in the retarding field mode. The combined resolution was typically 0.2 eV at 24 eV. Valence band spectra were taken before and after dosing between $\bar{\Gamma}$ and \bar{X} and $\bar{\Gamma}$ and \bar{X}' at photon energies of 24 and 32 eV and between \bar{X}' and \bar{M} at 24 eV. The surface unit cell and the surface Brillouin zone (SBZ) are shown in Fig. 1.

The NEXAFS experiments were conducted at beamline 6.3 of the Daresbury Synchrotron Radiation Source. The UHV system contained an VSW HA100 hemispherical electron analyser; the combined resolution of beamline and analyser was about 0.6 eV at 2600 eV photon energy. Absorption spectra of the sulphur K-edge at 2466 eV were taken at different excitation geometries. The absorption was monitored using the sulphur KLL Auger line at 2106 eV kinetic energy. The separate contributions to the near edge structure were obtained by fitting a step function to the K-edge and then using a core level fit program to determine the peak areas.

3. Results and discussion

A sample set of polar angle dependent ARUPS spectra along $\bar{\Gamma}$ to \bar{X} at 24 eV photon energy from the H_2S dosed InP(110) surface is shown in Fig. 2. Adsorption leads to pronounced changes, including the quenching of the clean surface states and the generation of adsorbate orbital features. As discussed previously for the high symmetry points [4], there are at least three adsorbate levels in the valence band spectra; a non-dispersing feature γ at 6.8 eV binding

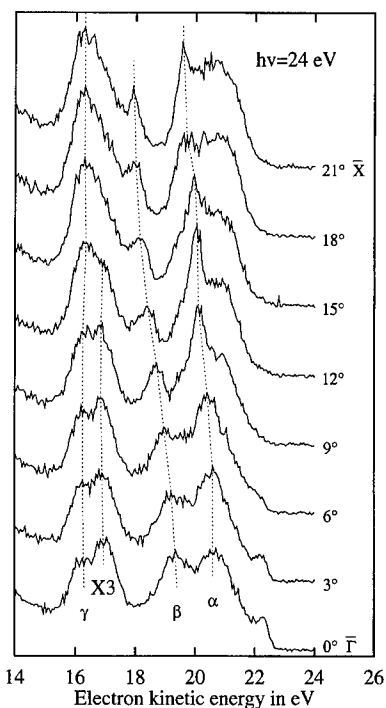


Fig. 2. Valence band spectra from H_2S dosed InP(110) at a photon energy of 24 eV taken along the $\bar{\Gamma}$ to \bar{X} direction of the SBZ. The angle of incidence was 45° . Adsorbate related features are labelled α , β and γ ; adsorption enhances the bulk density of states emission from X3 and quenches the anion dangling bond peak.

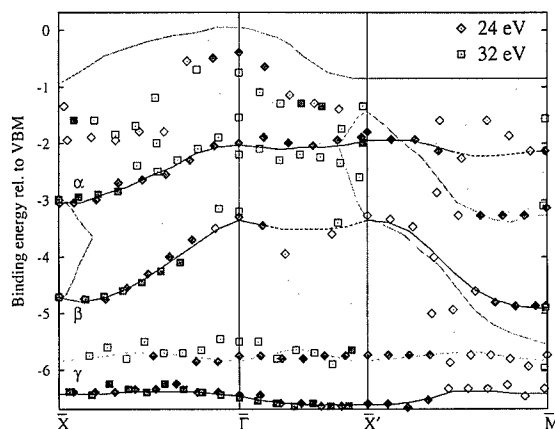


Fig. 3. Valence bandstructure of InP(110) dosed with 2 L of H_2S , showing the dispersion of α , β and γ . Well defined features are represented by filled symbols, weaker structures are marked with open symbols. The surface projection of the bulk bandstructure is shown as the shaded area.

energy (relative to the valence band maximum), and two lower binding energy features β and α dispersing downward from $\bar{\Gamma}$ to \bar{X} .

Assignment of these features is not unique. Comparison with experimental and theoretical studies of the dissociative adsorption of water on silicon sur-

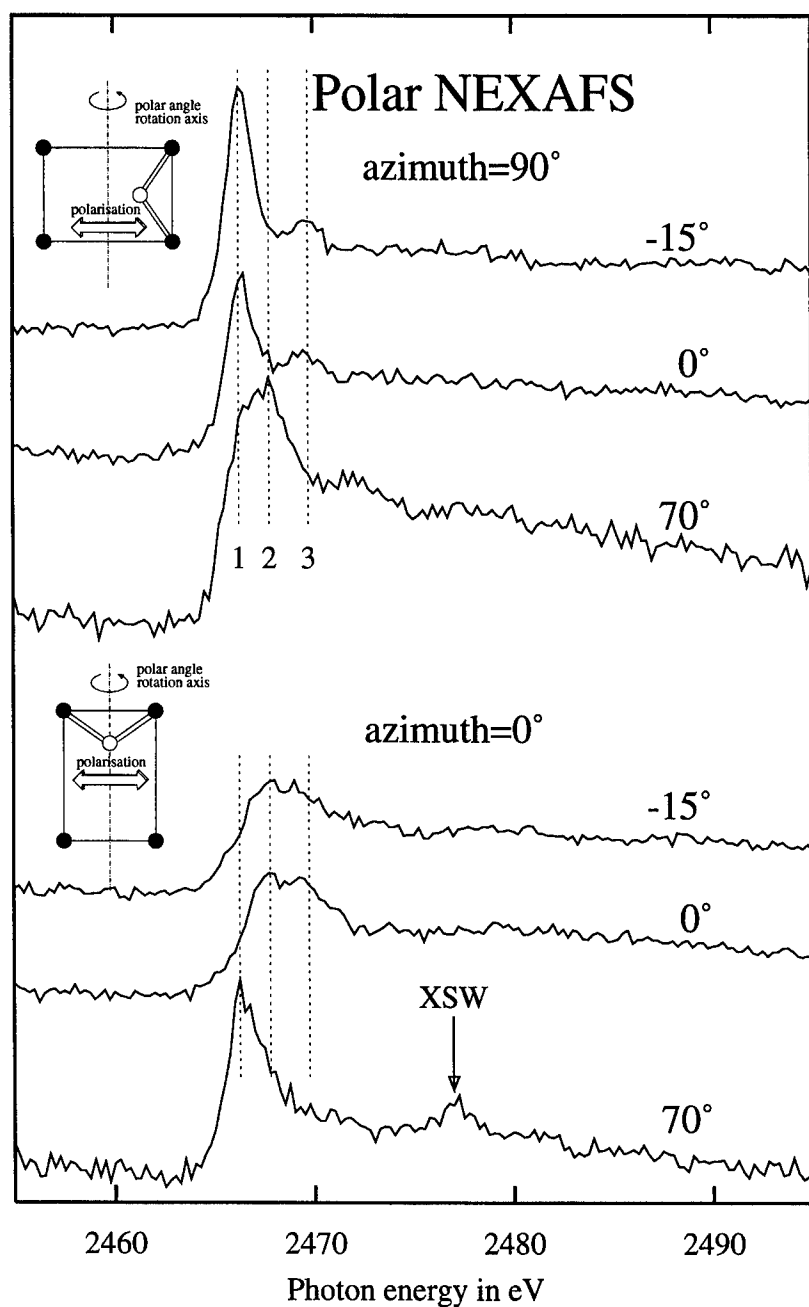


Fig. 4. NEXAFS scans of the sulphur K-edge at normal, -15° off normal and grazing incidence for azimuth = 90° (above) and 0° (below). The orientation of the surface unit cell and the polarisation are shown in the insets. Three features labeled 1, 2 and 3 can be identified in the near-edge region. There is an X-ray standing wave peak in the bottom spectrum.

faces [6,7] would suggest that α , β and γ are respectively the S–H π non-bonding orbital, the S–H σ bond and the In–S bond. A Hartree–Fock

molecular orbital calculation using the GAMESS program was carried out. Although this reproduces the ordering for SiH_3OH , a different ordering is

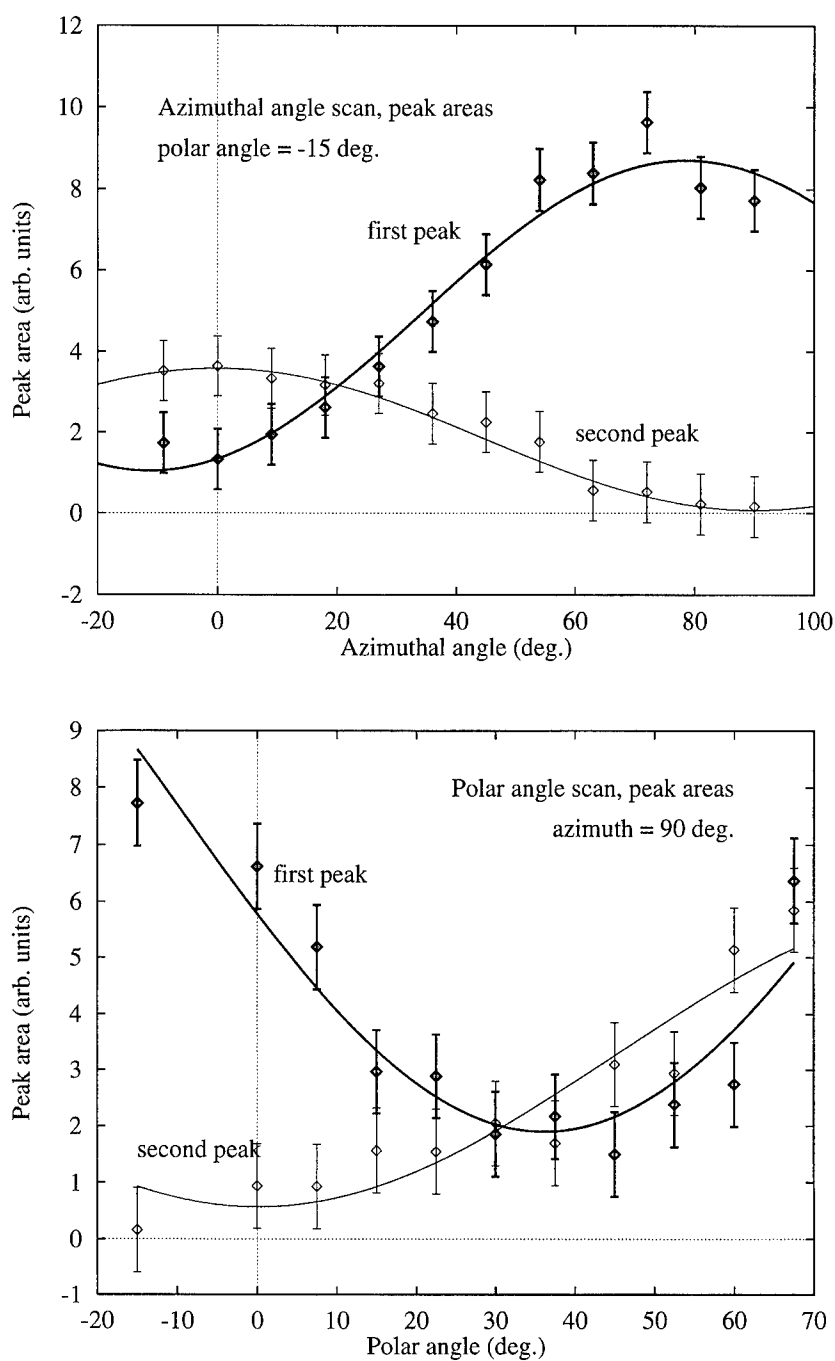


Fig. 5. Intensity of the first peak versus azimuth and polar angle. A \cos^2 function was fitted to both data sets.

obtained for InH_3SH^- . α is still a sulphur lone pair, but β and γ are now the In–S and the S–H bond. There is also the issue of the P–H bond, but this has probably a less favourable cross section.

The dispersion of these features along $\bar{\Gamma} \rightarrow \bar{X}$ and $\bar{\Gamma} \rightarrow \bar{X}'$ is shown in Fig. 3. The coincidence of valence band features for the two photon energies is an indication of their surface origin. Also shown are data along $\bar{X}' \rightarrow \bar{M}$ for 24 eV only, except at \bar{M} where there are data points for both photon energies.

Both α and β disperse between $\bar{\Gamma}$ and \bar{X} (along the direction of the (110) surface zigzag-chains and the short side of the surface unit cell). The greater dispersion might be expected from states which can overlap along the chain direction. In the simple continued layer structure both the In–S and the S–H bonds are perpendicular to the chain while the S–H π non-bonding orbital is parallel to the chain. This analysis would not be completely consistent with either of the binding energy orders considered above, where the greatest dispersion β is attributed to either the S–H or the In–S bonding levels. One possible conclusion is that the single continued layer model is not appropriate. The NEXAFS data afford further comment on this point.

A selection of sulphur K-edge near edge spectra is shown in Fig. 4. The geometry of the experiment limited the polar angle θ variation between -15° and $+70^\circ$ and the azimuthal angle variation between 0° and 90° . The azimuthal orientations of 90° and 0° are shown in the upper and lower insets respectively. θ is the angle of incidence of the light with respect to the surface normal and therefore the angle between the polarisation vector and the surface. Three features were found in the near-edge region spectra, which are labelled 1, 2 and 3 in Fig. 4. Feature 1 is most clearly seen at an azimuth of 90° and close to normal incidence and also at grazing incidence for an azimuth of 0° . Peak 2 can be seen most clearly at grazing incidence for an azimuth of 90° and peak 3 for example at normal incidence at an azimuth of 90° .

The intensity of the first two features has been monitored in detail by taking spectra both at a fixed azimuth of 90° , varying the polar angle, and by varying the azimuth at a polar angle of -15° . The intensity variation of peaks 1 and 2 with polar angle/azimuth are shown in Fig. 5. For peak 1 both

sets of data can be fitted with a \cos^2 function with the maximum in the azimuthal angle scans at about 90° and the minimum in the polar angle scans at 36° . The second peak has a rather different profile, reaching maximum intensity at 0° in the azimuthal angle scans and minimum intensity at 0° in the polar angle scans. The third peak data were not good enough for any detailed evaluation.

Assuming that SH^- bonds to the surface indium, this adsorbate has a similar configuration to methylmercaptan (CH_3SH). Gas phase NEXAFS data exist for this molecule [8,9]. The first two peaks in the NEXAFS spectrum were attributed to the S–C (here the S–In) and the S–H bond respectively; both have σ symmetry. The NEXAFS profile of feature 1 is fully consistent with the S–In bond in the continued layer structure; the maximum in the 90° azimuth is consistent with the S–In bond being perpendicular to the surface chain, the minimum at a polar angle of 36° corresponds to a geometry in which the polarisation vector is perpendicular to the continued tetrahedral bond (i.e. 54° from the surface). By contrast the NEXAFS profile of feature 2 would suggest that the S–H bond lies in the azimuth of the chain, i.e. perpendicular to the continued layer orientation. Possibly the HS molecule is rotated about the In–S bond axis. It is interesting to note that a possible effect of this is to overlap the S–H σ levels along the chain direction, i.e. increase dispersion which would favour the Si–OH type assignment of ARUPS features. However, the quality of the data for feature 2 in the present measurement is limited and a further investigation is planned.

4. Conclusions

The adsorption of H_2S on InP(110) was studied with ARUPS and NEXAFS. The results are interpreted within the model of dissociative adsorption of H^+ and SH^- at the surface anion and cation dangling bonds. Three features, two of which show dispersion, were identified in the ARUPS spectra at binding energies (at $\bar{\Gamma}$) of -6.8 eV, -3.5 eV and -2.2 eV relative to the VBM. A HF MO calculation would assign these to the S–H bond, the S–In bond and one sulphur lone pair. However, this assignment may not be correct. Further comment on the ob-

served dispersion requires a proper calculation. NEXAFS results were interpreted using CH_3SH as a model compound. The results are in good agreement with the sulphur being located in phosphorus sites of the continued layer structure but there are indications that the adsorbate complex departs from the simple tetrahedral structure. A more detailed investigation of the near edge profiles is planned.

Acknowledgements

The authors acknowledge the support of the Large Scale Installations Plan and the Science and Technology Cooperation Germany–Ireland for funding. These studies are facilitated by the HCM Network ‘Chalcogen Modification of Semiconductor Interfaces’ CHRX-CT93-0317-EU. We would like to thank Dr. W. Ranke of the Fritz-Haber-Institute in

Berlin for the loan of his H_2S dosing apparatus. The support of Dr. B. Cowie at the Daresbury Synchrotron is gratefully acknowledged.

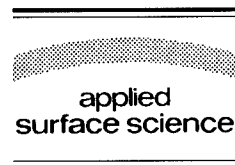
References

- [1] G. Hughes, T.P. Humphreys, V. Montgomery and R.H. Williams, *Vacuum* 31 (1981) 539.
- [2] E. Dudzik, R. Whittle, C. Müller, I.T. McGovern, C. Nowak, A. Märkl, A. Hempelmann, D.R.T. Zahn, A. Cafolla and W. Braun, *Surf. Sci.* 307–309 (1994) 223.
- [3] H.J. Kuhr, W. Ranke and J. Finster, *Surf. Sci.* 178 (1986) 171.
- [4] E. Dudzik, *Surf. Sci.* 344 (1995) 1.
- [5] E. Dudzik et al., to be published.
- [6] K. Fives, R. McGrath, C. Stephens, I.T. McGovern, R. Cimino, D.S.-L. Law, A.L. Johnson and G. Thornton, *J. Phys.: Condens. Matter* 1 (1989) SB105.
- [7] S. Ciraci and H. Wagner, *Phys. Rev. B* 27 (1983) 5180.
- [8] S. Bodeur and J.M. Esteve, *Chem. Phys.* 100 (1985) 415.
- [9] C. Dezarnaud, M. Tronc and A.P. Hitchcock, *Chem. Phys.* 142 (1990) 455.



ELSEVIER

Applied Surface Science 104/105 (1996) 107–112



Preparation of H-terminated Si surfaces and their characterisation by measuring the surface state density

H. Angermann^{*}, K. Kliefoth, H. Flietner

Abteilung Photovoltaik, Hahn-Meitner-Institut, Rudower Chaussee 5, 12489 Berlin, Germany

Received 28 June 1995; accepted 24 November 1995

Abstract

H-terminated n- and p-type Si(111) surfaces are characterised by the large-signal field-modulated photovoltage technique (SPV) measuring the surface potential and the energetic distribution of surface states $D_{it}(E)$. Using aqueous HF acid (HF) and buffered HF solution (BHF), different methods of chemical preparation were carried out characterising the treated surfaces repeatedly during the preparation process. The ideal H-terminated surface displays a very low density of surface states, comparable to well thermally oxidised surface and a significant decrease of HF-induced positive surface charge. The absence of these extrinsic defects indicates the successful preparation of H-terminated surfaces characterised by a nearly intrinsic surface state distribution. The surface state density was found to be mainly influenced by three aspects of the preparation: the doping type and the surface morphology of the substrate, the kind of chemical treatment, and the clean-room conditions as well. Very low surface state density ($5 \times 10^{10} \text{ cm}^{-2} \text{ eV}^{-1}$ and about $2 \times 10^{10} \text{ cm}^{-2} \text{ eV}^{-1}$ on n-type and p-type Si surfaces, respectively) were obtained using BHF as final etching solution, when the treatment was carried out in N_2 atmosphere.

1. Introduction

Wet chemical treatments are conventionally required in semiconductor processing to remove particles, organic and metallic contaminants. As a result of rapid advances in microelectronic device manufacturing, the thickness of typical gate oxides decreased to about 10 nm. The properties of thin oxide, epitaxial, and passivation layers are strongly influenced by the chemical integrity and morphological structure of the semiconductor surface prior to preparation. Wet chemical methods used to clean and

passivate silicon surfaces prior to the processing can be classified into two groups according to the different passivation mechanism. Hydrophilic methods, e.g. the RCA standard clean process [1], are mainly based on H_2O_2 containing solutions which increase the silicon surface micro-roughness as a side effect to the H_2O_2 decomposition [2]. Moreover, the resulting hydrophilic surfaces are contaminated by native oxide films and their impurities. To avoid both, micro-roughness and contamination by native oxides, various hydrophobic methods have been developed using HF and NH_4F solutions to dissolve the native oxide completely and to passivate the surface with hydrogen [3,4]. For control and optimization of these cleaning procedures a variety of surface sensitive

^{*} Corresponding author.

spectroscopical and structural methods has been applied to characterise the treated surfaces [5,6].

In this paper we report on investigations of surface Fermi level position and the surface state distribution of H-terminated surfaces carried out to achieve a better knowledge of the influence of the chemical treatment on electronic properties of the H-terminated surfaces. As recently reported we compared the surface electronic properties of electrolytically hydrogen terminated Si(111) surfaces after storage in nitrogen and in air and after hot water treatment [7]. The electrochemical H-termination is a laborious method, applicable on single wafers only. The present paper for the first time demonstrates the optimisation of simple preparation methods, compatible to the wet chemical technological process, resulting in H-terminated surfaces characterised by a very low surface state density about $2 \times 10^{10} \text{ cm}^{-2} \text{ eV}^{-1}$.

2. Dangling bond model of the Si surface

The electronic properties of Si-surfaces and interfaces are determined by surface and interface states. Surface states on clean Si surfaces after chemical etching originate from extrinsic and intrinsic dangling bonds (DB) with different back-bond configurations. The saturation of dangling bonds by adatoms removes these surface states and replaces them by adsorbate-induced states influencing the surface band-bending.

We utilised the large-signal field-modulated surface photovoltage technique (SPV) for contactless measurement of the surface band-bending and of the energetic distribution of surface states $D_{it}(E)$. The continuous energetic distribution of surface states as determined by $C(V)$ and SPV methods can be separated into several groups of states. Following the dangling bond model for the Si/SiO₂ interface [8] two groups of intrinsic states U_T (resulting from strained Si–Si bonds) and U_M (resulting from DB defects back-bonded only to silicon) give rise to U-shaped distributions while extrinsic states (correlated to Si atoms of lower state of oxidation, Si⁺¹ and Si⁺²) form additionally Gaussian distributions of extrinsic states P_L and P_H , respectively. The defect groups U_M and P_L are not only identified by the electronic model consideration but also by EPR

measurements [9]. Here we use the dangling bond model for the interpretation of surface state distributions obtained from SPV measurement on chemically treated and native oxidised Si surfaces.

3. Experimental

Polished thermally oxidised Si(111) n-type (5 and 70 $\Omega \cdot \text{cm}$) and p-type (1, 190 and 270 $\Omega \cdot \text{cm}$) samples were chemically cleaned by conventional SC1 and SC2 processes [1]. After removing the thermal oxide in a HF solution pH = 5 the samples were chemically reoxidised in a boiling solution of H₂SO₄:H₂O₂ (1:1) for 10 min, rinsed and afterwards placed into the final etching solution. Concentrated HF (48%, treatment time $t_{\text{HF}} = 30 \text{ s}$) were applied for conventional HF treatment. Pure NH₄F (40%) solution pH = 7.8 (treatment time $t_{\text{BHF}} = 6.5$ and 10 min) was used for the H-termination process. To investigate the influence of the RCA cleaning process itself already H-terminated samples were again treated by conventional SC1 and SC2 processes following the H-termination treatment.

H-terminated surfaces were prepared under three different conditions: chemical laboratory (using laminar flow boxes), clean-room conditions (particle class 100) and dry nitrogen (using a closed inert-sphere). After short pure water rinse ($t_{\text{H}_2\text{O}} = 1 \text{ s}$) the samples were blown dry by pure nitrogen and characterised by SPV immediately after the treatment and repeatedly during the preparation process. To improve the chemical stability of the treated surfaces the samples have been stored in clean-room air (temperature 25°C, humidity about 50%). The reoxidation was examined by SPV measurements after exposure times ranging from 10 min to 15 months. We used the pulsed field modulated SPV for contactless measurements of the surface potential using a mica foil dielectric spacer in the same experimental configuration as described in [10]. A pulsed laser diode (150 ns, wavelength $\lambda = 904 \text{ nm}$ and power $P = 150 \text{ W}$) is used for flashing the sample. A dc-bias voltage source provides the field voltage U_F to vary the surface band bending ϕ_s . The electron-hole pairs generated by the incoming laser light decreases the built-in electrical field of the space-charge region near the semiconductor surface. Con-

sequently the surface potential ϕ_{so} is reduced to ϕ_s and a surface photovoltage U_{ph} can be measured:

$$U_{ph} = \phi_s - \phi_{so} + U_D. \quad (1)$$

The Demmer voltage U_D results from the different electron and hole mobility. With reasonable assumptions for ϕ_{so} and U_D , ϕ_s can be obtained from U_{ph} [10]. The distribution of surface states $D_{it}(\phi_{so})$ is determined measuring U_{ph} as function of the external bias voltages U_F [11].

4. Results

Representative $U_{ph}(U_F)$ plots measured on HF treated and H-terminated p-type samples ($270 \Omega \cdot \text{cm}$) are presented in Fig. 1a. Their shift to lower field voltage values indicates a significant decrease of the positive charge component with more efficient procedures for the preparation of H-terminated surfaces. The reduced positive charge was found to be directly associated with a decrease of the surfaces state density (Fig. 1b).

Typical energetic distributions of the surface state density on p- and n-type Si are presented in Fig. 1b and Fig. 2, characterised by a superposition of intrinsic states forming the U-shaped background spectrum and extrinsic states (P_L) forming Gaussian distributions. While on p-type Si surfaces (Fig. 1b) the generation of extrinsic defects can be avoided by a short HF (48%) dip, on n-type surfaces (Fig. 2) the conventional HF (48%) treatment results in a high concentration of extrinsic states below midgap. The concentration of these HF induced extrinsic states

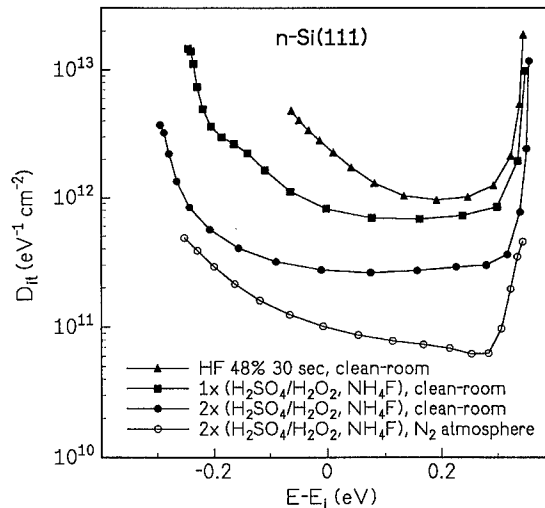


Fig. 2. $D_{it}(E)$ for p-Si(111) surfaces after different H-termination treatments.

was significantly reduced by using BHF as final etching solution. A $D_{it}(E)$ distribution dominated by only intrinsic states was observed when the chemical oxidation and the final etching step using NH_4F was repeated. Using NH_4F solution under clean-room conditions the concentration of intrinsic states was further reduced. Finally, performing the same treatment in N_2 atmosphere again a significant decrease of the surface state density is obvious.

Summarizing the results of these experiments we underline that the H-termination of Si(111) surfaces in N_2 atmosphere using NH_4F as final etching solution results in a minimum surface state density $D_{it,min}$.

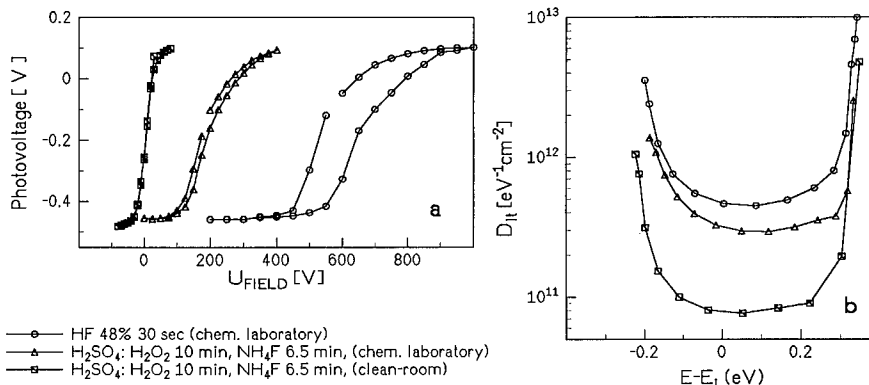


Fig. 1. SPV(U_F) curves (a) and $D_{it}(E)$ (b) for p-Si(111) surfaces after different H-termination treatments.

Table 1

Material	H-termination in N ₂ atmosphere $D_{it,min}$ (cm ⁻² eV ⁻¹)
p-Si 190 $\Omega \cdot \text{cm}$	4×10^{10}
p-Si 1 $\Omega \cdot \text{cm}$	2×10^{10}
n-Si 70 $\Omega \cdot \text{cm}$	5×10^{10}
n-Si 5 $\Omega \cdot \text{cm}$	6×10^{10}

The H-terminated surfaces are characterised by a smaller surface charge directly after the treatment and a significantly longer initial phase. The logarithmic decrease of surface charge during the following oxidation is equal for both types of treatments.

5. Discussion

Our investigation of Si(111) surfaces H-terminated by different methods shows that the ideal H-terminated surface is characterised by a very low density of surface states, comparable to the well thermally oxidised surface and by a significant decrease of HF-induced positive surface charge. The surface state distribution of chemically prepared samples was found to be mainly influenced by three aspects: the doping type and the surface roughness of the substrate, the kind of chemical preparation, and the clean-room conditions as well.

These influences should be explained by the mechanism of chemical reactions governing the process of H-termination. It is well known that the initial surface after removal of oxide layers by HF-containing solutions is characterised by F-termination of the Si dangling bonds yielding a strong polarisation of the Si–Si back-bonds. The H-termination process is generally accepted to be due to the insertion of HF species into the polarised Si–Si bonds, leading to removal of the first Si atom layer as SiH₄ and the hydrogenation of the second Si layer. The polarisation of Si–Si back-bonds, resulting from the high electronegativity difference causes the selective attack of the nucleophilic HF components.

Analogous reactions of other nucleophilic species in the solution namely OH, H₂O or O₂ we regard to be the reason for the generation of dangling bond defects back-bonded to O-atoms. The equilibrium of these reactions may be influenced by the composi-

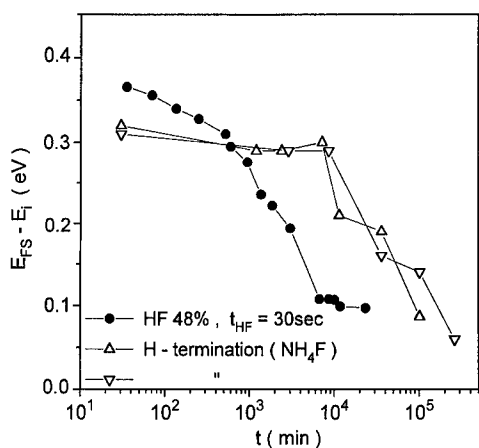


Fig. 3. Shift of surface Fermi level of HF (48%) treated (dots) and H-terminated (triangles) n-Si(111) surfaces during storage in air.

of $5 \times 10^{10} \text{ cm}^{-2} \text{ eV}^{-1}$ and about $2 \times 10^{10} \text{ cm}^{-2} \text{ eV}^{-1}$ on n-type and p-type samples, respectively (Table 1). The conventional RCA process gives in all cases a comparatively high surface state density $D_{it,min}$ of about $5 \times 10^{12} \text{ cm}^{-2} \text{ eV}^{-1}$ (Table 2).

After having studied the surface state distribution immediately after treatment we performed SPV measurements during the subsequent native oxide growth on H-terminated surfaces. In Fig. 3 the surface Fermi level positions of both, HF (48%, $t_{HF} = 30 \text{ s}$) treated and H-terminated n-type 70 $\Omega \cdot \text{cm}$ Si surfaces, are given as monitored during storage in clean-room air. In both cases after an initial phase a decrease of the positive surface charge component was observed.

Table 2

Material	$D_{it,min}$ (cm ⁻² eV ⁻¹) H-termination	$D_{it,min}$ (cm ⁻² eV ⁻¹) H-termination, SC1	$D_{it,min}$ (cm ⁻² eV ⁻¹) H-termination, SC1, SC2
p-Si 190 $\Omega \cdot \text{cm}$	4×10^{10}	4×10^{12}	7×10^{12}
n-Si 70 $\Omega \cdot \text{cm}$	5×10^{10}	5×10^{12}	1×10^{13}

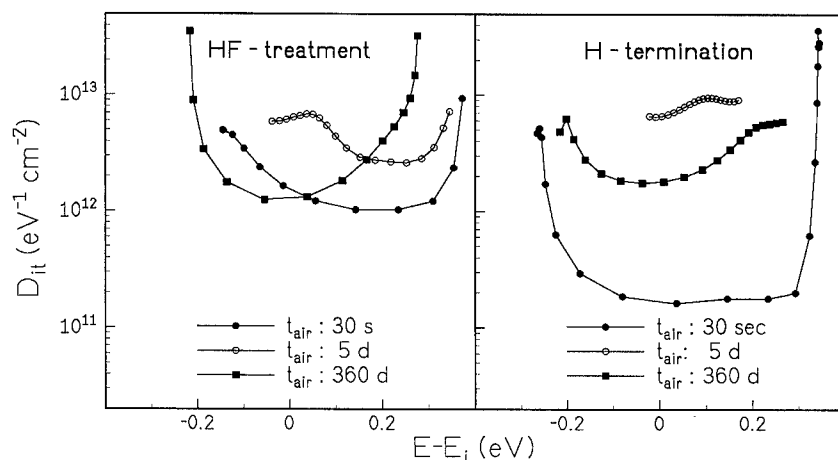


Fig. 4. $D_{it}(E)$ evolution of HF-treated and H-terminated n-Si(111) surfaces during storage in air.

tion of the HF solution and the substrate properties as well. Using X-ray photoelectron spectroscopy (XPS) and high resolution electron energy loss spectroscopy (HREELS) the resulting products of these surface reactions, for example Si–OH, were found to depend on the preparation conditions [5]. Our investigations have clearly shown that the treatment time, the concentration and the pH value of HF containing solution influences strongly and in well defined manner the concentration of extrinsic dangling bond defects [12].

Recently the influence of dissolved O_2 on the H-termination process was reported [13]. Because we obtained the best result when the preparation was carried out in N_2 atmosphere (Table 1) a reduced concentration of dissolved O_2 in the final etching solution and the rinsing water is assumed to be the reasons for these minimum surface state densities.

The micro-roughness of conventionally cleaned surfaces is mainly caused by the decomposition of H_2O_2 in alkaline RCA solutions SC1 [2], while the treatment in acid RCA solutions SC2 results in native oxide layer [1]. A longer treatment in HF (48%) solution also increases the surface micro-roughness [6]. In all cases these treatments result in a high surface state density as can be seen in Table 2. The surface roughness and the associated concentration of surface states was found to be reduced when the chemical oxidation and the final etching process were repeated (Fig. 2).

The treatment by concentrated HF (48%) solutions results in positive surface charge leading to

strong inversion for p-type and to accumulation for n-type Si surfaces. The shift of U_{ph} (U_F) curves to lower field voltage seen in Fig. 1a indicates a significant reduction of the positive surface charge on well prepared H-terminated surfaces. The remaining positive charge on ideally H-terminated Si(111) surfaces is attributed to the polarisation of the electronic-charge distribution in the back-bonds of the top-layer Si atoms saturated by hydrogen. Due to the different electronegativities surface dipoles are formed leaving the Si atoms are positively charged.

Our recently reported measurements have shown that the decrease of surface charge is related to the three phases of surface distribution changes during the native oxidation process [14]. The change of surface charge obtained by a surface charge analyzer (SCA) was also correlated to the native oxide growth detected by XPS and contact angle measurements [15]. The results presented in Fig. 3 and Fig. 4 clearly indicates that the duration of the initial phase of oxidation in air is highly sensitive to the electronic surface states induced by the H-termination treatment while the kinetics of the subsequent native oxidation process and the $D_{it}(E)$ distribution of the resulting native oxide interface are independent from the kind of HF pre-treatment.

6. Conclusion

We demonstrated that the ideally H-terminated surface is characterised by outstanding electronic

properties namely an intrinsic surface state distribution and a very low density of surface states. It is comparable to well thermally oxidised surfaces and contains only a small positive surface charge. The surface state density was found to be mainly influenced by doping, surface morphology, the kind of chemical preparation, and the clean-room conditions as well. Applying a dangling bond model surface defects have been correlated to Si surface atoms of different states of oxidation. It was shown that the SPV technique is highly sensitive to the remaining extrinsic surface states on H-terminated surfaces and can be used therefore to optimise the preparation process.

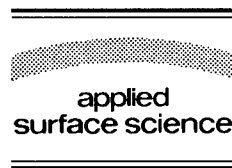
References

- [1] W. Kern, *J. Electrochem. Soc.* 137 (1990) 1887.
- [2] H.F. Schmidt et al., *Jpn. J. Appl. Phys.* 34 B (1995) 727.
- [3] G.S. Higashi, Y.J. Chabal, G.W. Trucks and K. Raghavachari, *Appl. Phys. Lett.* 56 (1990) 656.
- [4] T. Bitzer, M. Gruyters, H.J. Lewerenz and K. Jacob, *Appl. Phys. Lett.* 63 (1993) 397.
- [5] M. Grundner and R. Schulz, *Conf. Proc. No. 167, Am. Vac. Soc.* 4 (1988) 329.
- [6] Y.A. Chabal, G.S. Higashi, K. Raghavachari and V.A. Burrows, *J. Vac. Sci. Technol. A* 7 (1989) 2104.
- [7] Th. Dittrich, H. Angermann, H. Flietner, Th. Bitzer and H.J. Lewerenz, *J. Electrochem. Soc.* 141 (1994).
- [8] H. Flietner, *Surf. Sci.* 200 (1988) 463.
- [9] K.L. Brower, *Semicond. Sci. Technol.* 4 (1989) 970.
- [10] K. Heilig, H. Flietner and J. Reineke, *J. Phys. D: Appl. Phys.* 12 (1979) 927.
- [11] Y.W. Lam, *J. Phys. D: Appl. Phys.* 4 (1971) 1370.
- [12] H. Angermann, Th. Dittrich and H. Flietner, *Appl. Phys. A* 59 (1994) 193.
- [13] H. Ogawa, K. Ishikawa, M.T. Suzuki, Y. Hayami and S. Fujimura, *Jpn. J. Appl. Phys.* 34 (1995) 732.
- [14] H. Angermann, Th. Dittrich and H. Flietner, in: *Proc. 2nd Int. Symp. UCPSS* (1994) p. 3636.
- [15] A. Philipossian, *J. Electrochem. Soc.* 139 (1992) 2956.



ELSEVIER

Applied Surface Science 104/105 (1996) 113–117



Ge(111) 3×1 :K/Sn; on the influence of tin substitution in a metal induced 3×1 reconstruction

M. Göthelid^{a,*}, S. Odasso^a, G. LeLay^a, M. Björkqvist^b, E. Janin^b, U.O. Karlsson^b,
T.M. Grehk^c

^a Centre de Recherche sur les Mécanismes de la Croissance Cristalline (CRMC2), Centre National de la Recherche Scientifique (CNRS),
Campus de Luminy, F-13288 Marseille Cedex 9, France

^b Materialfysik, Kungliga Tekniska Högskolan (KTH), S-10044 Stockholm, Sweden

^c HASYLAB, Notkestrasse 85, D-22607 Hamburg, Germany

Received 28 June 1995; accepted 7 September 1995

Abstract

Co-adsorption of tin and potassium is found to induce a 3×1 reconstruction on the Ge(111) surface. A very small amount of tin influences the Ge 3d core level spectra substantially compared to the Ge(111) 3×1 :K reconstruction. This is interpreted as resulting from a relaxation of the strain in the rows Ge atoms running along the surface, as proposed for this structure.

PACS: 73.40Qv; 79.60.E

1. Introduction

A vast number of metals are known to induce 3×1 reconstructions on Si(111) (Ag, Mg, Ca, Li, Na and Cs) and Ge(111) (Li, Na, and K) (see e.g. Ref. [1]). The structural models proposed for these surfaces have also caused some debate during the past years. Fan and Ignatiev have shown, using I - V low energy electron diffraction (LEED), that the Ag, Li, Na, K and Cs induced 3×1 reconstructions on the Si(111) surface all have a similar geometry [2,3]. They further showed that the Ge(111) 3×1 :Li, Na and K systems have analogous character in terms of atomic geometry [4].

The Ge(111) 3×1 :K and Li structures were recently studied in detail by Grehk et al. [1]. Despite the similar geometries as seen with IV -LEED, marked differences between the two alkali induced surface structures were observed in the core level line shapes. The Ge(111) 3×1 :K surface was proposed to be described by a structure comprising double rows of Ge separated by single rows of potassium. A general model was proposed by Weiering et al. [5], for metal induced 3×1 reconstructions on the Si(111) surface, based on a missing top layer reconstruction with $2/3$ monolayers (ML) of Si (or Ge) atoms forming chains similar to the Si(111) 2×1 surface obtained after cleaving.

In this work we present synchrotron radiation core level photoelectron spectroscopy (PES) results from the Ge(111) 3×1 :K/Sn surface. A strong influence

* Corresponding author.

on the Ge 3d level is observed by co-evaporation of very small traces of tin, whereas the K 3p line shape is unaffected. This is interpreted as a partial Sn substitution in the top layer Ge chains which relieves the strain and inhibits the shift of the Ge 3d core level binding energy of the two topmost Ge layers.

2. Experimental

The experiments were performed at beamline 22 at the Swedish National synchrotron radiation facility MAXLAB in Lund [6]. An experimental resolution better than 0.1 eV was used for the Ge 3d and K 3p core levels and a slightly lower resolution for the Sn 4d level. All spectra were recorded at normal emission and at room temperature.

The samples were cut from a Ga-doped (0.004–0.01 Ω cm) Ge(111) wafer, prepared in situ by repeated cycles of Ar⁺ ion sputtering and resistive annealing at 700°C as measured by a pyrometer. The reconstruction was prepared by co-evaporation of the two metals and subsequent annealing. The amount of metal on the surface was estimated from wide scans including the Ge 3d, Sn 4d and K 3p core lines, where the amount of Sn was found to be around 0.05 ML by taking the different cross-sections [7] into account and the amount of K was found to be roughly 20% lower here than on the nominal Ge(111)3 \times 1:K surface [1]. However, as mentioned by Weitering et al. [5], the 3 \times 1 reconstructions are observed in a rather wide metal coverage range below 1/3 ML metal coverage.

3. Results and discussion

In Fig. 1 a set of Ge 3d core level spectra is shown, recorded at 70, 90 and 110 eV photon energy respectively as indicated in the figure. Two surface related components both shifted to lower binding energy were needed to fit the experimental spectra. This situation is the same as for the Ge(111)3 \times 1:K surface, see Fig. 2 where a Ge 3d spectrum from Ref. [1] is shown, although the binding energy shifts (E_i , $i = 1$ or 2) are slightly different for the two surfaces, $E_1 = 0.22$ eV here and 0.24 eV for the Ge(111):K surface, while the corresponding numbers

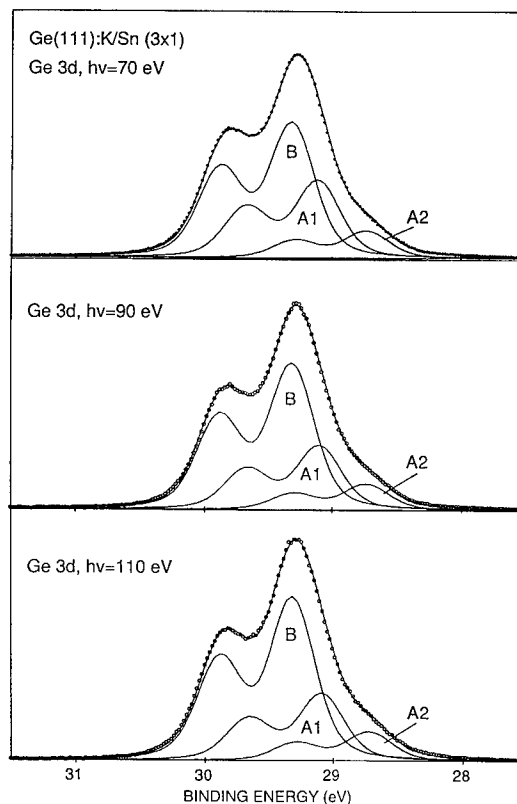


Fig. 1. A set of high resolution Ge 3d core level spectra from the Ge(111)3 \times 1:K/Sn surface reconstruction, recorded at 70, 90 and 110 eV photon energy respectively, as indicated in the figure.

for E_2 are 0.59 eV and 0.68 eV. Furthermore, the bulk peak has shifted 0.40 eV to higher binding energy compared to the Ge(111)3 \times 1:K surface,

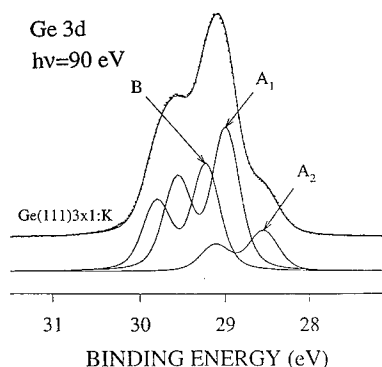


Fig. 2. Ge 3d spectrum from the Ge(111)3 \times 1:K surface (from Ref. [1]).

indicative of a change in the bandbending at the surface.

However, a more obvious difference is the relative intensity of the peaks. In the case of $\text{Ge}(111)3 \times 1:\text{K}$ the surface peak A1 was stronger than the bulk peak intensity, whereas here, the bulk peak has recovered and clearly dominates the present spectra in Fig. 1. The relative intensity of A2, which was related to second layer Ge directly below the K [1], has also decreased, about 27% as compared to the $\text{Ge}(111)3 \times 1:\text{K}$ surface where it corresponded to roughly $1/3$ ML. Thus the decrease observed here would give a corresponding coverage equal to 0.24 ML.

Fig. 3(a) presents the deconvoluted K 3p core level spectra recorded at 70 eV photon energy. The line shape and curve fitting parameters used are the same as those used to fit the $\text{Ge}(111)3 \times 1:\text{K}$ K 3p spectra [1], the only difference being that the peak as a whole has shifted 0.30 eV to higher binding energy. In Fig. 3(b) the Sn 4d spectrum recorded from this surface is shown. Two contributions must be included in the synthesis to get a good fit. The

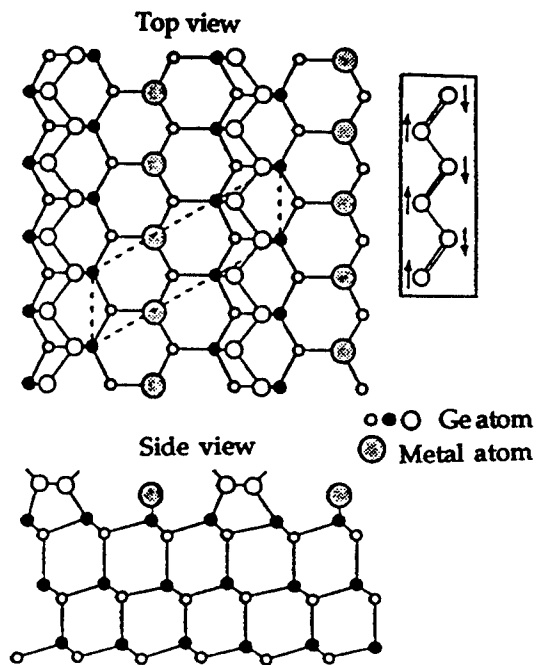


Fig. 4. Structural model from Ref. [5], proposed to be valid for metal induced 3×1 reconstructions on the $\text{Si}(111)$ surface. The assignment of the different circles are indicated in the figure.

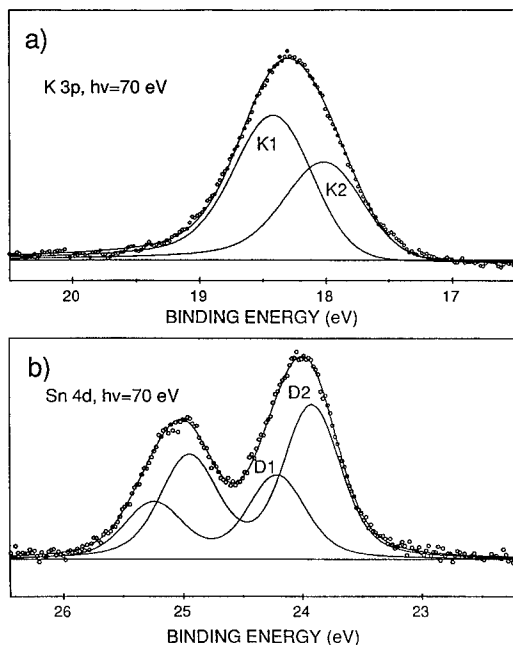


Fig. 3. K 3p (a) and Sn 4d (b) spectra from the reconstructed surface.

binding energy separation of the two Sn 4d peaks is 0.30 eV, whereas the K 3p components, K1 and K2, are 0.38 eV apart. The intensity ratios of the components are 1.47 for the K 3p line with the stronger peak being on the high binding energy side, while the ratio is 1.82 between the two Sn 4d components, but the low binding energy contribution is stronger.

The Ge 3d A1 peak, shown in Fig. 2, was assigned to a contribution from the reconstructed selvage [1]. If the structural model proposed by Weiering et al. [5], shown in Fig. 4, is supposed to be correct, this selvage may be represented by the Ge atoms in the double rows and by the Ge atoms directly below these double rows which would correspond to a total coverage of $4/3$ ML. From a comparison with results from the clean $\text{Ge}(111) c(2 \times 8)$ surface [8], assuming an electron mean free path of 4 Å in an exponential attenuation model the intensity derived for the peak A1 is in excellent agreement with the one actually obtained from the fit indeed taking into account the fact that $2/3$ ML of the intensity originates from a layer beneath the

double row. The intensity of A1 in the present case is clearly lower. By using the same argumentation as above this intensity corresponds roughly to 0.75 ML.

The potassium core level is not very much affected by the presence of tin, neither the line shape nor the relative intensities change, the binding energy shift between the two peaks is also the same. The only difference is the overall shift of the K 3p line by 0.30 eV to higher binding energy and the decrease of the total intensity as compared to the Ge(111)3 \times 1:K surface reconstruction. The decreased K 3p intensity, together with the similar decrease of the Ge 3d A2 intensity, is in good agreement with the assignment of A2 to Ge below the adsorbed K atoms. The small disagreement between the 27% Ge 3d A2 decrease and the 20% intensity drop for K 3p most probably arises from uncertainties in the cross section values.

A plausible situation would be one where tin is substituting the Ge atoms in the chains in the top surface layer. The situation is depicted in Fig. 4 where the structural model from Ref. [5] is shown. By substituting one of the Ge chain atoms, indicated by large open circles, as many as 6 Ge atoms are affected; firstly of course the one which has been substituted, but also the two neighboring chain atoms, and presumably the three Ge atoms below these two Ge and the substituting Sn atom itself. Again from the arguments used above, this would explain intensity drop for A1.

A driving force for the substitution would be to release the strain inherent in the chains, since the tin atoms are larger than Ge. A similar behavior has been observed previously on the Ge(111)–Sn surface, where two reconstructions; (7 \times 7) and (5 \times 5), are formed following tin deposition (see e.g. [9]). These structures are due to a dimer adatom stacking fault reconstruction. The substitution of tin in the dimer rows lower the strain and the elastic energy [10]. The changes seen on the Ge 3d core level line profile in the present case would then indicate that, because of the large number of atoms contributing to the shifted core level component, a substantial amount of strain is present not only in the top layer but also in the first layer below. Apparently this strain can be relaxed by introduction of a small amount of tin in the surface structure.

This scenario assumes that all tin atoms occupy

top layer chain positions, in some contradiction with the presence of two peaks in the Sn 4d spectrum, which indicates a second tin site in the structure, either subsurface or on the K sites. The K site would to some extent give an explanation to the lower K density on this surface than in the Ge(111)3 \times 1:K surface structure, and the related reduced intensity of the Ge 3d A2 peak. However, as mentioned in Ref. [5], the metal coverage may vary in the 3 \times 1 reconstructions due to metal desorption. Thus, the lower K intensity is not necessarily linked to the presence of tin on the surface, but may be an effect of slightly different annealing conditions. We thus conclude to the probable presence of tin in the Ge chains as well as in a subsurface site, by which the strain in the structure is released.

In the Ge(111)3 \times 1 K/Sn surface the Ge 3d A2 component has shifted 0.09 eV towards the bulk peak, that is to higher binding energy, whereas the K 3p peak is shifted 0.10 eV to lower binding energy, as compared to the Ge(111)3 \times 1:K surface. Thus, the presence of tin significantly influences the charge distribution in the K–Ge bond, via the relaxation of the chains.

4. Summary

We have presented core level photoelectron spectroscopy results from the Ge(111)3 \times 1: K/Sn surface reconstruction. The drastic changes observed in the Ge 3d core level line shape were interpreted as a partial substitution of tin both in the Ge rows running along the surface, as proposed in recent studies [1,5] on related surface structures, and in subsurface sites. These changes were proposed to be due to a relaxation of the strain inherent in these Ge chains. Furthermore, the results points to the importance of small traces of foreign species on the electronic properties of the interface formation during metal on semiconductor growth.

Acknowledgements

We would like to thank the MAXLAB staff for their assistance during the experiments. This work was supported by grants from the Swedish Natural

Science Foundation (NFR) and the Swedish Research Council for Engineering Sciences (TFR).

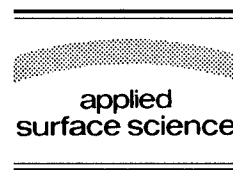
References

- [1] T.M. Grehk, M. Björkqvist, M. Göthelid, G. LeLay and U.O. Karlsson, *Phys. Rev. B*, submitted.
- [2] W.C. Fan and A. Ignatiev, *Phys. Rev. B* 41 (1990) 3592.
- [3] W.C. Fan and A. Ignatiev, *Surf. Sci.* 296 (1993) 352.
- [4] W.C. Fan and A. Ignatiev, *Phys. Rev. B* 40 (1989) 5479.
- [5] H.H. Weitering, N.J. DiNardo, R. Pérez-Sandoz, J. Chen and E.J. Mele, *Phys. Rev. B* 49 (1994) 16837.
- [6] J.N. Andersen, O. Björneholm, A. Sandell, R. Nyholm, J. Forsell, L. Thånell, A. Nilsson and N. Mårtensson, *Synchrotron Rad. Res.* 4 (1991) 15.
- [7] J.J. Yeh and I. Lindau, *Subshell Photoionization Cross Sections*, *At. Data Nucl. Data Tables* 32(1) (1985).
- [8] M. Göthelid, T.M. Grehk, M. Hammar, U.O. Karlsson and S.A. Flodström, *Phys. Rev. B* 48 (1993) 2012.
- [9] M. Göthelid, M. Hammar, C. Törnevik, U.O. Karlsson and S.A. Flodström, *Surf. Sci.* 271 (1992) L357.
- [10] J.S. Pedersen, R. Feidenhans'l, M. Nielsen, F. Grey and R.L. Johnson, *Phys. Rev. B* 38 (1988) 13210.



ELSEVIER

Applied Surface Science 104/105 (1996) 118–123



Si(110) 16×2 and Si(110) 2×3 -Sb surfaces studied by photoemission and optical spectroscopy

A. Cricenti^{a,*}, P. Perfetti^a, B. Nesterenko^b, G. LeLay^c, C. Sebenne^d

^a *Istituto di Struttura della Materia, CNR, Via Enrico Fermi 38, I-00044 Frascati, Italy*

^b *Institute of Semiconductor Physics, Prospekt Nauki 45, 252650 Kiev 28, Ukraine*

^c *CRMC2, UPR CNRS 7251, Campus de Luminy, 13288 Marseille Cedex 9, France*

^d *Laboratoire de Physique des Solides, URA CNRS 154, Université P. et M. Curie, 75252 Paris Cedex 05, France*

Received 28 June 1995; accepted 14 November 1995

Abstract

The electronic properties of clean Si(110) 16×2 and Si(110) 2×3 -Sb surfaces have been studied by angle resolved ultraviolet photoelectron spectroscopy (ARUPS) and surface differential reflectivity (SDR). For the clean 16×2 surface four surface states have been recognized by ARUPS and their dispersions have been mapped along the main symmetry lines in the surface Brillouin zone. SDR experiments revealed transitions between filled and empty surface states at ~ 1.8 , 2.4 and 2.9 eV. Antimony has been subsequently evaporated (about one monolayer) thus obtaining a 2×3 reconstruction. The surface electronic structure resulted to be strongly modified with three surface state bands observed in ARUPS along the $\bar{\Gamma}111$ direction and no optical transitions detected by SDR in our energy range (1.3–3.5 eV).

1. Introduction

As compared to the (111) and (100) face of silicon, the Si(110) face has been less studied. The first low energy electron diffraction (LEED) study [1] of the Si(110) surface has shown the presence of several reconstructions, (4×5) , (2×1) and (5×1) and several experiments [2–9] have been performed afterwards. However, with the help of auger electron spectroscopy (AES) and LEED, Ichinokawa et al. [10] proved that the Si(110)- (4×5) , (2×1) and (5×1) phases are stabilized by Ni-contamination (2–7% of a monolayer). Experiments performed in

very clean conditions have shown that the clean Si(110) face is characterized by only one superstructure, the ' 16×2 '. These conclusions were confirmed by reflection high energy electron diffraction (RHEED) [11] and scanning tunneling microscopy (STM) [12,13] and some geometrical models have been proposed [7,8] to explain the experimental data. Due to this recent discovery and the experimental difficulties of the surface preparation, the electronic properties of the clean Si(110) 16×2 phase are scarcely known. Photoemission yield spectroscopy [14] has revealed a filled band of electronic states near the valence band maximum with a width of approximately 1 eV, and field effect kinetics [15] experiments have shown that the (16×2) surface is semiconducting with a gap of 0.4 eV between filled

* Corresponding author.

and empty surface states. Further optical transitions [16] were detected at 2.4, 3.2 and 3.8 eV by means of differential reflectivity experiments.

The interaction of Sb atoms with Si(100) and Si(111) surfaces has been the subject of much research in recent years because antimony is the most commonly used donor dopant in Si-MBE. Depending on Sb coverage several reconstructions can be obtained on the Si(111) face [17] while on the Si(100) face only a Sb-induced 2×1 superstructure is observed [18,19]. In contrast just few studies are devoted to the study of the interaction of Sb atoms with the Si(110) face [20,21]. In particular Rich et al. [20] have shown that 1 ML of Sb deposited onto the Si(110) substrate held at 350°C forms a 2×3 structure. Different phases have been observed by Zotov et al. [21] as a function of Sb coverage.

In this work we present a study of the electronic properties of the clean Si(110) 16×2 and of Si(110) 2×3 -Sb surfaces with angle resolved ultraviolet photoelectron spectroscopy (ARUPS) and surface differential reflectivity (SDR). On the clean surface ARUPS spectra showed the existence of four surface state bands whose dispersions have been mapped along the main symmetry lines in the surface Brillouin zone (SBZ) showing similarities with the Si(111) 7×7 electronic properties [22]. SDR results showed, in the energy range between 1.4 and 3.3 eV, the presence of three optical transitions at 1.8, 2.4 and 2.9 eV. The Si(110) 2×3 -Sb surface shows a semiconducting behavior with the highest occupied surface-state band observed around 1.7 eV below the Fermi level (E_F) in normal emission. SDR experiments showed no optical transitions up to an energy of 3.5 eV indicating that the minimum energy position of the lowest empty band must be at least 1.8 eV above E_F .

2. Experimental set-up

ARUPS spectra were recorded in a Vacuum Generators VG-450 ultrahigh-vacuum (UHV) chamber at a pressure of less than 2×10^{-10} Torr. Unpolarized 21.2 eV radiation from a helium discharge lamp was used. The estimated total energy resolution as determined by the analyzer voltages and the width of the

He I light was 100 meV and the angular resolution of the hemispherical analyzer was $\pm 1^\circ$.

The SDR experiment consists of shining light at normal incidence onto the surface of the Si(110) in UHV conditions and measuring the intensity of the reflected light with an optical multichannel array; a dummy silicon sample is used as reference. The results are given in terms of $\Delta R/R$, i.e., the change in sample reflectivity after gas adsorption [23,24]: $\Delta R/R = (R_{\text{clean}} - R_0)/R_0$. R_{clean} corresponds to the clean surface and R_0 to the surface after atomic hydrogen adsorption. For photon energies below the silicon direct bulk gap (3.5 eV), $\Delta R/R$ gives directly the imaginary part of the surface dielectric function [25].

The samples (n-type, 10^{14} carriers/cm³) were mechanically polished and etched in the CP-type etchant [26]. They were thoroughly outgassed at 500°C in ultrahigh vacuum and the final cleaning was performed by heatings with direct current (1000–1200°C, 10 min, slow cooling) in a vacuum of less than 3×10^{-9} Torr. Quite distinct two-domain ' 16×2 ' LEED pattern was observed.

Sb was evaporated from thoroughly outgassed Knudsen cell at a rate equivalent to 0.5 ML/min, as monitored with a quartz microbalance. 1 ML of Sb is defined as the site density for the unreconstructed surface which is 9.6×10^{14} atoms/cm². Pressures during Sb deposition and sample heating did not exceed 1.0×10^{-9} Torr. The presented spectra for the Si(110) 2×3 -Sb surface were recorded from a surface obtained by evaporating 1.2 ML of Sb onto a clean 16×2 surface (prepared according to the procedure described above) held at about 650°C. This produced a surface with a sharp 2×3 LEED pattern with very low background. All temperatures were measured with an infrared pyrometer.

3. Experimental results

Fig. 1(a) is a scheme of the two-domain Si(110) 16×2 LEED pattern showing the integer-order spots (large circles) and the fractional-order spots (small circles) together with the geometry of the Si(110) surface Brillouin zone (SBZ) with the main symmetry lines. Two families of equidistant

parallel lines drawn by the spots can be easily distinguished on the diagram. This type of pattern is explained by the presence of two domains, each domain being associated to one family of parallel lines respectively oriented in the $[\bar{1}11]$ and $[\bar{1}\bar{1}\bar{1}]$ directions. It is generally admitted that this reconstruction is named '16 × 2' according to the 16 spots along the two diagonals of the unit mesh in the reciprocal lattice in the $[111]$ directions. Fig. 1(b) is a scheme of the Si(110)2 × 3-Sb LEED pattern showing the integer-order spots (large circles) and the fractional-order spots (small circles) together with the geometry of the Si(110) surface Brillouin zone (SBZ) with the main symmetry lines.

Fig. 2 shows ARUPS spectra recorded from the clean Si(110)16 × 2 surface for various angles of emission along the $[\bar{1}11]$ direction. They contained several distinct structures: the one (S_1) closest to the Fermi level has a binding energy of 0.9 eV at normal emission. The structure then moves towards E_F for larger angles of emission with maximum energy of -0.30 eV for $\Theta_e = 25^\circ$ and a total bandwidth of 0.6 eV. We point out that a similar state with a larger bandwidth (1 eV) has been observed by photoemission yield spectroscopy [14]. The structure S_2 is

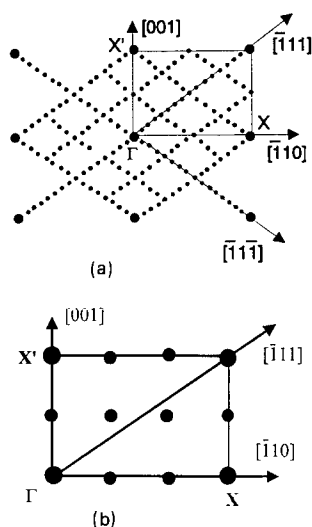


Fig. 1. Scheme of the LEED pattern showing the integer-order spots (large circles) and the fractional-order spots (small circles) together with the geometry of the Si(110) surface Brillouin zone with the main symmetry lines for the clean 16 × 2 (a) and Sb-2 × 3 (b) surfaces.

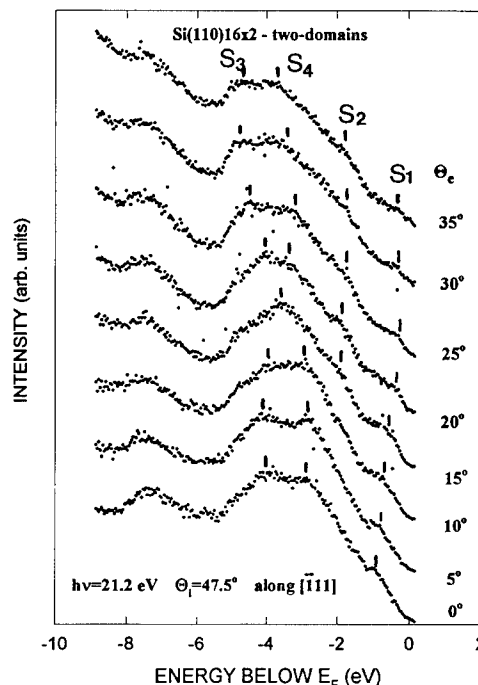


Fig. 2. Photoemission spectra recorded from Si(110)-16 × 2 for various angles of emission along the $[\bar{1}11]$ azimuthal direction. The angle of incidence is $\Theta_i = 47.5^\circ$.

observed as a weak shoulder around 1.7–1.9 eV below E_F . The feature S_3 is observed around 2.8–2.9 eV below E_F at Γ point and shows a parabolic downward dispersion for larger angles of emission with a total bandwidth of 1.8 eV. Structure S_4 is observed around 3.9–4.0 eV below E_F at Γ point, then it shows an upward dispersion of 0.75 eV with maximum energy for $\Theta_e = 25^\circ$.

The ARUPS spectra obtained along the $[\bar{1}11]$ azimuth from the Si(110)2 × 3-Sb surface are shown in Fig. 3 and present three Sb-induced structures, Sb_1 , Sb_2 and Sb_3 . Sb_1 is identified in normal emission at 1.7 eV below E_F and it shows a downward dispersion (0.4 eV) with minimum energy at $\Theta_e = 10^\circ$ and then an upward dispersion for larger angles of emission. A prominent peak (Sb_2) is present at Γ around 2.1–2.2 eV below E_F ; the peak moves downward for larger angles of emission with minimum energy of -4.9 eV for $\Theta_e = 30^\circ$ and a total bandwidth of 2.7 eV. The structure Sb_3 is observed at $\Theta_e = 25^\circ$ and disperses upwards 0.7 eV up to $\Theta_e = 40^\circ$.

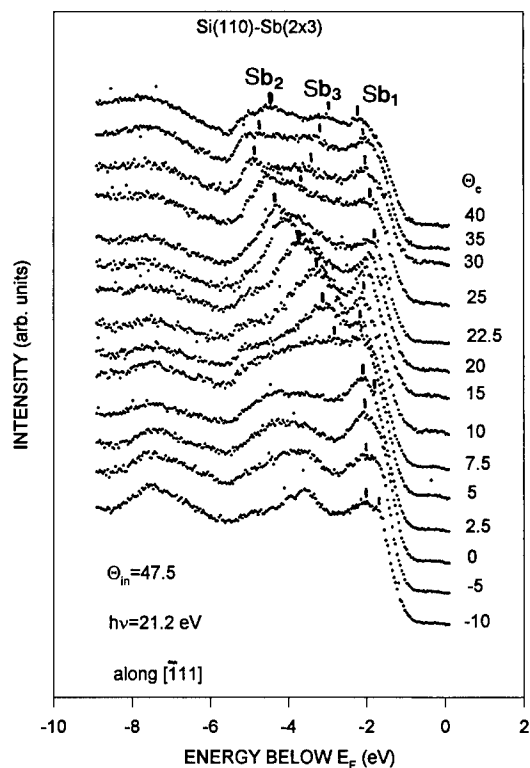


Fig. 3. Photoemission spectra recorded from Si(110)2 \times 3-Sb for various angles of emission along the $[\bar{1}11]$ azimuthal direction. The angle of incidence is $\Theta_i = 47.5^\circ$.

The surface origin of the previous features is supported by their strong sensitivity to the surface ordering and contamination. In practice on the Si(110)16 \times 2 surface ten hours at a pressure of 2×10^{-10} Torr quenched all the structures around the bulk valence band maximum. For this reason we had to refresh the surface by mild annealing at 700°C every two hours.

Similar results are obtained for the Si(110)2 \times 3-Sb surface: Fig. 4 shows ARUPS spectra taken in normal emission for a clean surface (Fig. 4(a)) and after 1000 L of excited molecular hydrogen (Fig. 4(b)).

Fig. 5 shows the experimental energy dispersions of the different structures reported in Figs. 2 and 3. Similar features with similar dispersion are observed along the $[\bar{1}10]$ direction. It can be immediately noticed that the surface states S_2 , S_3 and S_4 present on the clean surface have their corresponding ones (Sb_1 , Sb_2 and Sb_3) on the 2 \times 3-Sb surface. A

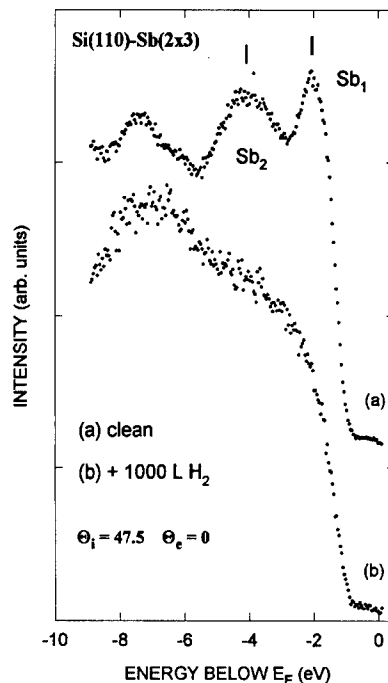


Fig. 4. Photoemission spectra for a clean (a) and contaminated (b) Si(110)2 \times 3-Sb surface.

structure corresponding to S_1 has not been observed on the 2 \times 3-Sb surface. This can be explained by the fact that S_1 is presumably due to dangling bonds

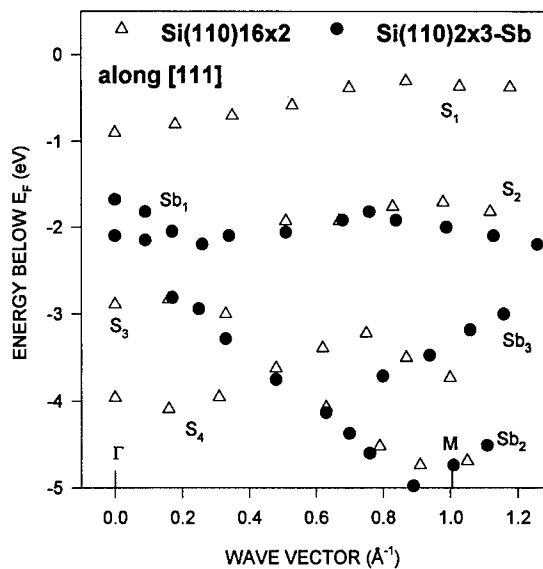


Fig. 5. The experimental energy dispersion of the structures observed in Figs. 2 and 3 along the $[\bar{1}11]$ azimuthal direction.

states on the clean 16×2 surface; on the 2×3 -Sb surface, if we take into account the trimer model by Zotov et al. [21], no dangling bonds are left unsaturated.

It is worth to note that these surface states had distributions in k -space consistent with a 1×1 SBZ, i.e. a mirror symmetry around the Brillouin zone boundary. Similarly in the photoemission studies on the Ge(111)c(2×8) [27] and Si(111) 7×7 surfaces [28], the surface state distributions have not been observed to show the periodicity of the small superstructure Brillouin zone. Rather the observed surface state bands have been found to correspond to (1×1) [27] or (2×2) [28] surface cells, indicating that the photoemission experiments, therefore, seem to be more sensitive to the short range ordering of the surface, in contrast to, e.g. LEED which reveals the long range periodicity of the surface geometry.

The SDR spectrum for the Si(110) 16×2 surface is shown in Fig. 6. It contains rather broad (~ 0.5 eV) but quite distinct peaks centered at ~ 1.8 , 2.4 and 2.9 eV. Peaks at 2.4 and 2.9 eV are in good agreement with previous data from Ref. [16] (2.4 and 3.2 eV, respectively) while the peak at ~ 1.8 eV was not observed before. The interpretation of the

SDR results needs additional information on the empty electronic states and their dispersions. On the basis of energy conservation and excluding excitonic effects we can predict from our filled bands that the transition at 1.8 eV arises between the S_1 band and an empty final state located between 0.85 and 1.5 eV above the Fermi level. The transition at 2.4 eV could involve the same S_1 initial band and a final empty band between 1.45 and 2.1 eV above E_F , or it could involve the S_2 band with an empty final state around 0.6 above E_F . The interpretation of the 2.9 eV peak is more difficult since also the S_3 band can be involved.

SDR experiments did not show any optical transition on the 2×3 -Sb surface. From the ARUPS spectra of Fig. 3 and from energy considerations the minimum energy position of the lowest empty band must be at least 1.8 eV above E_F . In this picture the empty band needs to be mapped all along the symmetry lines.

The interconnection between atomic and electronic structures of semiconductor surfaces needs information on their geometry and according to general theoretical considerations [22] the presence of features in the ARUPS spectra of semiconductor surfaces is caused by several structural peculiarities. For example, the rich ARUPS-spectrum of the Si(111)-(7×7) phase [22] is based on the variety of its structural elements (adatoms, dimers, rest atoms, stacking faults, corner holes) [29,30]. More or less detailed analysis have been performed on Si(110) 16×2 surface [8] on the ground of experimental results available and semi-empirical tight-binding total energy calculations for concrete structural elements. Structural measurements [12,13] have suggested that the 16×2 unit cell of terrace shape could be built with the help of silicon adatoms, dimers and rest atoms just as the well-known DAS-model [30] of the Si(111)-(7×7) reconstruction. For the 2×3 -Sb phase, Sb adatoms contributions based on the trimer model of Zotov et al. [21], must be taken into account.

Detailed discussion of the surface electronic spectrum of the Si(110) 16×2 and of Si(110) 2×3 -Sb phases needs to be done on the ground of modern theoretical treatment. It could clarify the participation of each structural element in the surface bands formation.

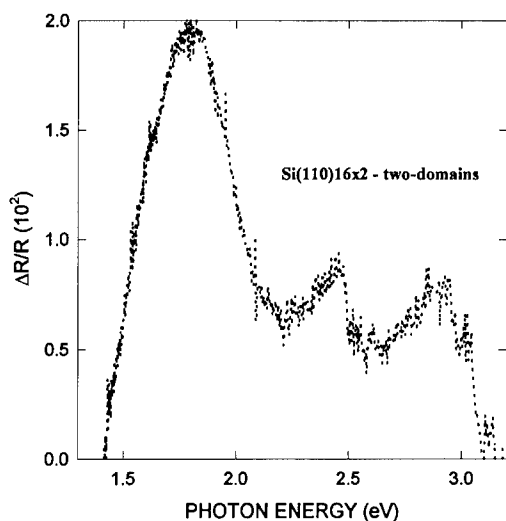


Fig. 6. Surface differential reflectivity spectrum for the clean 16×2 structure.

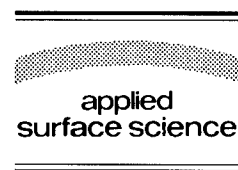
References

- [1] F. Jona, IBM J. Res. Dev. 9 (1965) 375.
- [2] B. Nesterenko, A. Brovii and A. Sorokovykh, Surf. Sci. 171 (1986) 495.
- [3] P. Martensson, G.V. Hansson and P. Chiaradia, Phys. Rev. B 31 (1985) 2581.
- [4] E.G. Keim, A. van Silfhout and L. Wolterbeek, J. Vac. Sci. Technol. A 6 (1988) 57.
- [5] B. Nesterenko, Appl. Surf. Sci. 33/34 (1988) 21.
- [6] B.Z. Olshanetsky and A.A. Shklyaev, Surf. Sci. 67 (1977) 581.
- [7] B. Nesterenko and A.I. Shkrebtii, Surf. Sci. 213 (1989) 309.
- [8] A.I. Shkrebtii, C.M. Bertoni, R. Del Sole and B. Nesterenko, Surf. Sci. 239 (1990) 227.
- [9] Y. Ishikawa, Y. Hosokawa, I. Hamaguchi and T. Ichinokawa, Surf. Sci. 187 (1987) L606.
- [10] T. Ichinokawa, H. Ampo, S. Miura and A. Tamura, Phys. Rev. B 31 (1985) 5183.
- [11] Y. Yamamoto, S. Ino and T. Ichikawa, Jpn. J. Appl. Phys. 25 (1986) L331.
- [12] E.J. van Loenen, D. Dijkamp and A.J. Hoeven, J. Microsc. 152 (1988) 487.
- [13] Y. Yamamoto, S.-i. Kitamura and M. Iwatsuki, Jpn. J. Appl. Phys. 31 (1992) L635.
- [14] N. Safta, J.-P. Lacharme and C.A. Sebenne, Surf. Sci. 287–288 (1993) 312.
- [15] B. Nesterenko, A.A. Stadnik, G. Le Lay, V.Yu. Aristov, N. Safta, J.-P. Lacharme and C.A. Sebenne, Phys. Low-Dim. Struct. 3 (1994) 1.
- [16] H. Wormeester, A.M. Molenbroek, C.M.J. Wijers and A. van Silfhout, Surf. Sci. 260 (1992) 31.
- [17] A.V. Zotov, A.A. Saranin, V.G. Lifshits and E.A. Khramtsova, Surf. Sci. 230 (1990) L147.
- [18] D.H. Rich, F.M. Leisble, A. Samsavar, E.S. Hirschorn, T. Miller and T.-C. Chiang, Phys. Rev. B 39 (1989) 12758.
- [19] A. Cricenti, S. Selci, A.C. Felici, L. Ferrari, G. Contini and G. Chiarot, Phys. Rev. B 47 (1993) 15745.
- [20] D.H. Rich, G.E. Franklin, F.M. Leisble, T. Miller and T.-C. Chiang, Phys. Rev. B 40 (1989) 11804.
- [21] A.V. Zotov, V.G. Lifshits and A.N. Demidchik, Surf. Sci. 274 (1992) L583.
- [22] H. Neddermeyer, U. Misse and P. Rupieper, Surf. Sci. 117 (1982) 405.
- [23] S. Selci, F. Ciccacci, G. Chiarotti, P. Chiaradia and A. Cricenti, J. Vac. Sci. Technol. 5 (1987) 327.
- [24] S. Selci, A. Cricenti, M. Righini, C. Petrillo, F. Sacchetti, F. Alexandre and G. Chiarotti, Appl. Surf. Sci. 56 (1992) 637.
- [25] J.D.E. McIntyre and D.E. Aspnes, Surf. Sci. 42 (1971) 417.
- [26] A. Ishizaka and Y. Shiraki, J. Electrochem. Soc. 133 (1986) 666.
- [27] F.J. Himpsel, D.E. Eastman, P. Heiman, B. Reihl, C.W. White and D.M. Zehner, Phys. Rev. B 24 (1981) 1120.
- [28] T. Yokotsuka, S. Kono, S. Suzuki and T. Sagawa, Solid State Commun. 39 (1981) 1001.
- [29] M. Fujita, H. Nagayoshi and A. Yoshimori, Surf. Sci. 208 (1989) 155.
- [30] K. Takayanagy, Y. Tanishiro, M. Takahashi and S. Takahashi, J. Vac. Sci. Technol. A 3 (1985) 1502.



ELSEVIER

Applied Surface Science 104/105 (1996) 124–129



The atomic structure of the Si(111) $(2\sqrt{3} \times 2\sqrt{3})$ R30°-Sn reconstruction

A.H. Levermann^{a,*}, P.B. Howes^a, K.A. Edwards^a, H.T. Anyele^a, C.C. Matthai^a,
J.E. Macdonald^a, R. Feidenhans'l^b, L. Lottermoser^c, L. Seehofer^c, G. Falkenberg^c,
R.L. Johnson^c

^a Department of Physics, University of Wales, Cardiff, P.O. Box 913, Cardiff CF2 3YB, UK

^b Risø National Laboratory, 4000 Roskilde, Denmark

^c Universität Hamburg, 2. Institut für Experimentalphysik, Luruper Chaussee 149, 22761 Hamburg, Germany

Received 28 June 1995; accepted 2 October 1995

Abstract

We have studied the atomic structure of the $(2\sqrt{3} \times 2\sqrt{3})$ R30° reconstruction induced by adsorption of about 1.1 monolayers of Sn on Si(111) using surface X-ray diffraction (SXRD) and scanning tunnelling microscopy (STM). The experimentally obtained structure factors in SXRD are in contradiction with existing models in the literature and we conclude the need for a new surface atomic structure model. We have been able to determine a number of properties of an appropriate surface model to allow a better fit to the experimental structure factors.

1. Introduction

One of the central aims of the surface science of semiconductors has been to understand the details of the origin of the Schottky barrier. Sn/Si(111) is an example of an abrupt metal–semiconductor interface, uncomplicated by interdiffusion or chemical reaction [1]. It can therefore be used to study the surface atomic and electronic structure of the initial stages of epitaxial Sn growth onto Si(111). Sn is of particular interest since it belongs to the same group

IV family in the periodic table as silicon and, like Si, (gray) α -Sn crystallises in the diamond structure. Also, Sn has recently been used to mediate surfactant epitaxy of Si on Si(111) [2].

When Sn is deposited onto the atomically clean Si(111)-(7 × 7) surface, three main reconstructions are formed, namely (7 × 7), $(\sqrt{3} \times \sqrt{3})$ R30° and $(2\sqrt{3} \times 2\sqrt{3})$ R30° [1] (the phase diagram of Sn/Si(111) is given in Fig. 1). Previous theoretical and experimental studies have shown that the Schottky barrier heights for the latter two reconstructions differ by 0.27 eV [3]. The atomic structure of the $(\sqrt{3} \times \sqrt{3})$ R30° phase ($\sqrt{3}$ for short), first reported by Estrup and Morrison [4], is well known from an earlier surface X-ray diffraction (SXRD) study [5]. However, the detailed atomic structure of the $(2\sqrt{3}$

* Corresponding author. Present address: Fraunhofer-Technologie Entwicklungsgruppe (TEG), Nobelstrasse 12, D-70569 Stuttgart–Vaihingen, Germany. Tel.: +49 711 970-3654; fax: +49 711 970-3998; e-mail: ahl@teg.fhg.de.

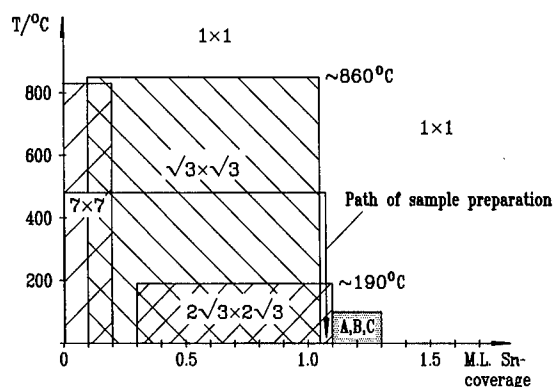


Fig. 1. Phase diagram for the Sn/Si(111)-system (after [1]). The path of sample preparation for the $2\sqrt{3}$ -reconstruction, as described in the text, is indicated.

$\times 2\sqrt{3}$)R30° phase ($2\sqrt{3}$ for short) has not been previously determined.

We have studied the atomic structure of the ($2\sqrt{3} \times 2\sqrt{3}$)R30° reconstruction induced by an adsorption of about 1.1 monolayers of Sn on Si(111) using SXRD supported by STM. We compare our data with a structural model that has been proposed earlier by Törnevik et al. [6]. This model has also been used as a starting point to perform a total energy minimisation in order to determine atomic positions more accurately in an improved structural model [3].

2. Experimental details

The experiments were performed using the surface X-ray diffraction facility of the high-intensity, wiggler X-ray beamline W1 at HASYLAB (Hamburg, Germany). The Au-coated, toroidal focusing mirror of beamline W1 collects several mrad of incoming radiation resulting in a focus size in the experimental hutch of $\sim 1.6 \times 6 \text{ mm}^2$. The monochromator box of beamline W1 contains two Ge(111) crystals with an energy resolution $\Delta E/E$ of $\sim 10^{-4}$. The incident beam was monochromated to a wavelength of 1.3777 Å. Before hitting the sample the beam is collimated with slits to $1 \times 1 \text{ mm}^2$.

The diffractometer at beamline W1 allows a vertically mounted sample surface to be oriented by means of two translations and two tilts [7]. Total external reflection of the beam is used in order to

make the position of the reflected beam independent of the sample rotation angle ω by means of arc adjustments. By fixing the angle of incidence, measurements are made using ω and the diffracted angle 2θ only.

For sample preparation Si-wafers were outgassed at $\sim 750^\circ\text{C}$ for 2 days and then flash-heated to $\sim 1100^\circ\text{C}$ for 2 min. RHEED and LEED both showed a (7×7)-reconstruction of good quality. The following sample preparation procedure to obtain a ($2\sqrt{3} \times 2\sqrt{3}$)R30°-reconstruction is indicated in the phase diagram of the Sn/Si(111) system (Fig. 1). The substrate was held at $\sim 450^\circ\text{C}$ during the deposition of Sn from a K-cell. After $\sim 90 \text{ s}$ a RHEED pattern corresponding to the $\sqrt{3}$ -reconstruction appeared, suggesting a deposition rate of ~ 0.7 monolayers per minute. After another $\sim 12 \text{ min}$ the RHEED pattern showed a disappearing $\sqrt{3}$ reconstruction finally leaving a (1×1) pattern. At this point the deposition of Sn was stopped and the substrate heater was switched off shortly after. Following the vertical line on the right side of the phase diagram of Fig. 1 the sample was found to exhibit a $2\sqrt{3}$ reconstruction (RHEED) after cooling down to a temperature below $\sim 200^\circ\text{C}$. LEED showed a small amount of at least two of the large reconstructions labelled A, B and C in Fig. 1, namely $(\sqrt{133} \times 4\sqrt{3})$, $(3\sqrt{7} \times 3\sqrt{7})$ R40.9° and $(2\sqrt{91} \times 2\sqrt{91})$ R33.0° [1]. However, they were only found near to one of the edges of the sample.

STM images of the sample, taken at bias voltages of +1.7 V and -1.7 V respectively, showed large areas of $2\sqrt{3}$ of several thousand Å² with only occasional defects.

After preparation the sample was transferred into a small UHV cell (designed by Johnson et al. [8]), which mounts on the diffractometer. Its components are a gate valve on the flange to the preparation chamber, an ion pump to keep the base pressure below 10^{-9} mbar and a beryllium window allowing the X-rays to enter and exit the sample area over the whole 360° range.

3. Data acquisition and analysis

All in-plane fractional order reflections were measured with the incident and exit angles set to 1°,

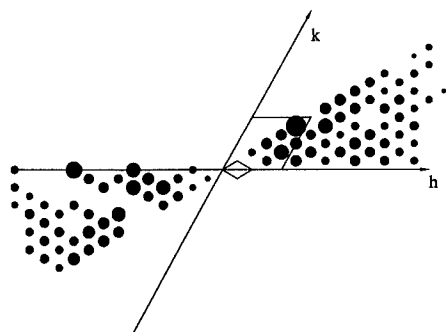


Fig. 2. Schematic diagram of the measured, in-plane structure factors. The complete pattern is obtained by application of the symmetry operations of the hexagonal lattice with space group $p3m1$. The area of each circle represents the amplitude of the equivalent structure factor. The $2\sqrt{3} \times 2\sqrt{3}$ and 1×1 unit cells are indicated.

which is well above the critical angle for total reflection of 0.20° . Refraction effects are thus avoided.

In all, 162 in-plane reflections were measured, of which 89 were inequivalent. A map of the measured reflections in reciprocal space is shown in Fig. 2. The area of each circle represents the amplitude of the equivalent structure factor. The complete pattern is obtained by application of the symmetry operations of the hexagonal lattice with space group $p3m1$. The $2\sqrt{3}$ has twofold symmetry [9] and the different orientations of this structure on the surface are responsible for a threefold symmetry in SXRD. Some reflections could not be measured due to obstructions by rods supporting the transfer chamber on the diffractometer. The integrated intensities were normalised to a beam monitor signal and determined by numerical summation. Errors attributed to each data value were derived from counting statistics and the reproducibility of equivalent reflections.

The structure factors used for calculating Patterson functions and performing fit routines were obtained after correcting the integrated intensities for the Lorentz factor and for different area sizes illuminated by the beam. For the calculation of our model Patterson maps the calculated structure factors were averaged according to the $p3m1$ symmetry of the substrate unit cell. The intensity of the (most intense) $(5/6, 5/6)$ reflection (referred to the Si(111) unit cell) was regularly monitored and used to normalise for a degradation of the sample during the experiment.

The analytical procedure involves fitting the structure factors for specific models to the experimental values using a conventional least-squares minimisation procedure. The reduced χ^2 value is used as an agreement criterion.

4. Results and discussion

In order to determine the in-plane atomic structure for the $\text{Si}(111)(2\sqrt{3} \times 2\sqrt{3})\text{R}30^\circ\text{-Sn}$ surface the models proposed earlier have been used as a starting point. The first of these models was introduced by Törnevik et al. [6] and derived from an STM study. The second model by Griffiths et al. [3] is a modification of the first one. It was obtained by minimising the total energy within a molecular dynamics framework using the Törnevik model as a starting point. A valence force field (VFF) potential model was used to determine the relaxed geometry by simulated annealing cycles. The main atomic features of both these proposed models are thus similar. Their main assumption is the existence of a (nearly) rectangular shape unit with an adatom at each corner as topmost layer, as seems to be visible in the empty state STM image. The second Sn layer mainly consists of a dimer within the rectangular arrangement and rows of atoms along the $\langle 110 \rangle$ direction.

With a large in-plane data set from a grazing incidence X-ray diffraction experiment the electron density projected onto the surface plane can be determined. Though direct Fourier inversion of the data is impossible due to lack of phase information, real space structural information can be obtained by analysing the structure factors $|F_{hk}|$ by means of the Patterson function $P(\mathbf{r})$ [10,11], which is defined as

$$P(\mathbf{r}) = \sum_h \sum_k |F_{hk}|^2 \exp\{i(\mathbf{q} \cdot \mathbf{r})\}$$

$$\propto \int \rho'(\mathbf{r}') \rho'(\mathbf{r} - \mathbf{r}') d\mathbf{r}'.$$

In a contour map of $P(\mathbf{r})$ a peak at \mathbf{r}_0 implies that at least two atoms are separated by an interatomic vector \mathbf{r}_0 , the magnitude of the peak being proportional to the product of the electron densities of the pair of atoms [11].

Such Patterson contour plots were used to compare our experimental data with the above mentioned

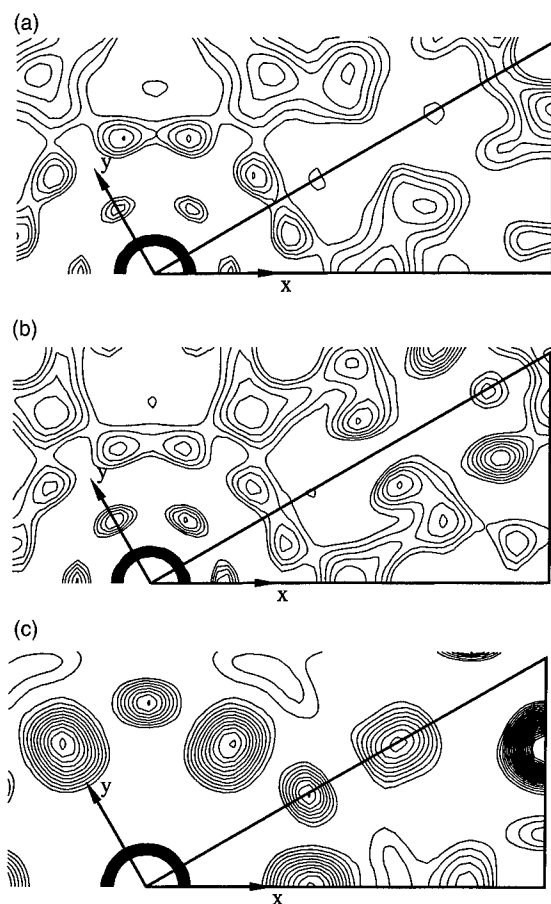


Fig. 3. Contour maps of the Patterson function in the irreducible triangle (solid lines) as calculated for (a) the model proposed by Törnevik et al. [6], (b) the model proposed by Griffiths et al. [3] and (c) the experimental data we obtained. Equally spaced positive contours are drawn.

models proposed in the literature. We can immediately recognise obvious disagreements between contour plots of the Patterson functions in the irreducible triangle as calculated for the models proposed by Törnevik et al. [6], Griffiths et al. [3] and the experimental data obtained (Fig. 3a, b and c).

Fig. 3a and b generally show the same features for the two models with minor deviations in magnitude and position. Fig. 3c however reveals a number of very strong interatomic vectors, derived from the SXRD data, for atomic difference vectors which are not at all recognisable in the Patterson functions of either of the two models. Of particular interest are strong maxima along the main crystallographic axes

in distances of $1/5$ of the unit cell length. Taking account of the surface symmetry group these peaks can be imagined to form a grid of intense spots within the unit cell on all fifth order fractional positions. Only two other strong features in the Patterson function do not correspond to the regular grid. This suggests an equally regular arrangement of Sn atoms with only few exceptions.

Furthermore, a comparison between our data and the proposed models of Törnevik et al. and Griffiths et al. reveals bad agreement factors for our fitting procedures of $\chi^2 > 20$. In particular some very high structure factors of our data set, for example that of the $(5/6, 5/6)$ peak (which is visible in Fig. 2), are not represented by these models.

Strong support for the result that both suggested models in the literature to date are not likely to give a good description of the actual atomic surface structure of the $2\sqrt{3}$ reconstruction is provided by our STM study of the sample subsequently used for the SXRD-experiment.

Fig. 4a and b show an empty (bias voltage $+1.7$ V) and filled state (bias voltage -1.7 V) image of the $2\sqrt{3}$ surface. Almost the same area of $95 \times 95 \text{ \AA}^2$ is shown in both images. The visible structure and the corrugation of $\sim 2 \text{ \AA}$ are in agreement with [6] as are the separations between the different spots.

Electronic band structure calculations using the self-consistent tight-binding method in the extended Hückel approximation have been applied to the modified surface model [3]. There is a contribution to the density of states from the topmost Sn layer at both positive and negative bias, which is small compared with the contribution from the second layer. To account for the differences observed in STM images at positive and negative bias, respectively, one would have to assume that STM imaging at positive bias (empty states, Fig. 4a) does not 'see' the topmost layer of the proposed atomic structure of the Sn-layer. The second Sn-layer on the other hand does have a large DOS contribution above E_F and should be visible at positive bias. However, the models proposed by Törnevik et al. and Griffiths et al. both derive the atomic structure of the topmost Sn layer (the rectangular shape unit mentioned above) from empty state STM images. As a result of the LDOS calculations this empty state image would be that of the second layer rather than the topmost Sn atoms.

This means that the calculated electronic structure of both models is not consistent with STM images from which the models themselves were originally deduced.

On these grounds we conclude the need for a new surface model, of which some properties have al-

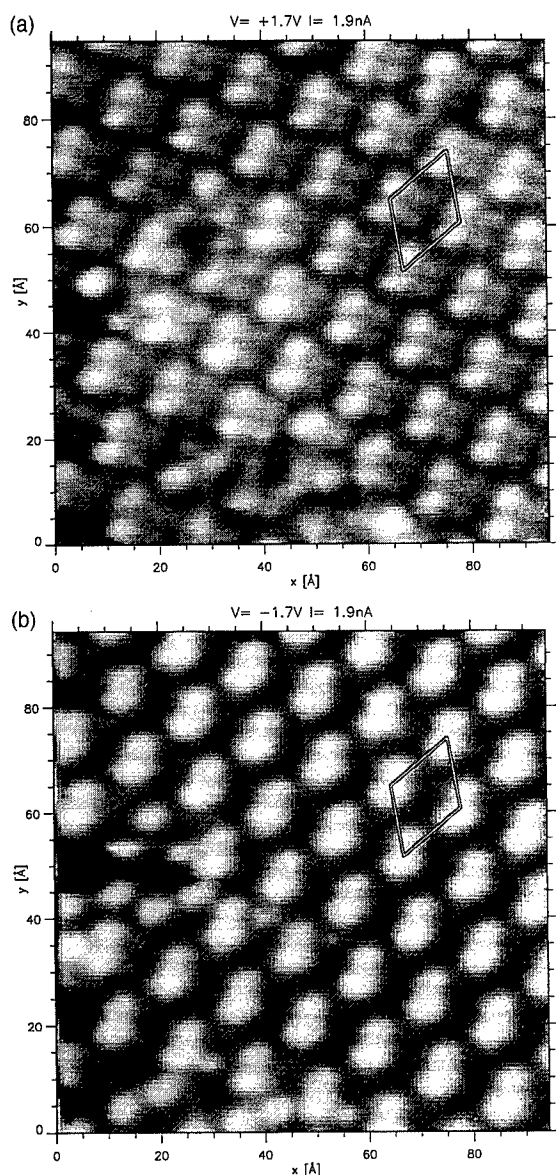


Fig. 4. $(95 \times 95) \text{ \AA}^2$ STM topographic images of roughly the same few unit cells of the $\text{Si}(111)\text{-}2\sqrt{3}\text{-Sn}$ surface, acquired with bias voltages of (a) $+1.7 \text{ V}$ and (b) -1.7 V at a constant tunnel current of 1.9 nA . Corrugation heights in both images are $\sim 2 \text{ \AA}$.

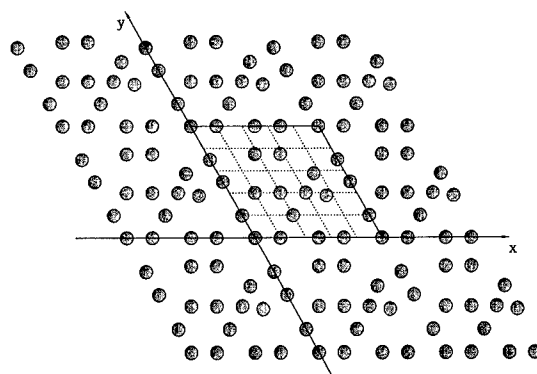


Fig. 5. $\text{Si-}2\sqrt{3}$ unit cell divided into 25 units by a superimposed grid. Possible positions of Sn atoms on mainly grid positions are indicated purely as an example of a structure having the essential features deduced from the X-ray data. The given atomic arrangement results in the Patterson function displayed in Fig. 6.

ready been determined: the strong $(5/6, 5/6)$ peak can be attributed to diffraction on a (220) plane of $\alpha\text{-Sn}$, which (like Si) crystallises in the diamond structure, giving a perfect agreement between the calculated lattice constant and the one found in literature of 6.49 \AA . We therefore infer that the structure formed of Sn-atoms for the $2\sqrt{3}$ -reconstruction has some similarities with that of bulklike $\alpha\text{-Sn}$. The problem, however, arises of how to fit an $\alpha\text{-Sn}$ structure into a $1/6$ smaller Si unit cell.

The right structural model of the $2\sqrt{3}$ has to account for the indicated interatomic vectors of Fig. 3c and at the same time the strong structure factor for the $(5/6, 5/6)$ -related reflection. This can be achieved by placing a large number of Sn atoms on positions corresponding to the intersections of a grid superimposed on the Si unit cell, which divides it into 25 units of equal size and shape (an illustration is given in Fig. 5). We assume that no intermixing takes place between bulk Si and the Sn layer [12]. For the fitting of our data, a different number of atoms (10 to 19) has been moved around grid positions only allowing for a few atoms to take non-grid positions. Atomic arrangements with interatomic distances of $1/5$ of the unit cell length along the main crystallographic axes gave the best results so far with $\chi^2 \leq 6$ (one example of such an atomic arrangement is given in Fig. 5). The corresponding Patterson function is shown in Fig. 6. Most features of the experimentally obtained contour plot of Fig. 3c can

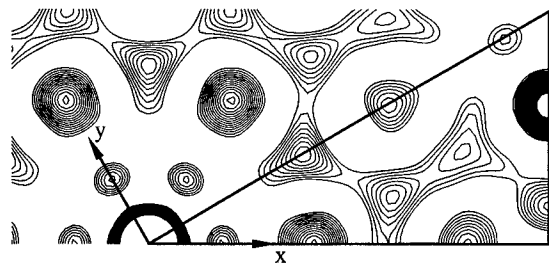


Fig. 6. Contour map of the Patterson function in the irreducible triangle (solid lines) as calculated for the atomic arrangement indicated in Fig. 5. Equally spaced positive contours are drawn.

be found, indicating a reasonable agreement between the results from our experiments and the atomic arrangement described above.

It should be emphasised that several variants of the atomic arrangement of Fig. 5 also give reasonable agreement with the experimental Patterson function. We are not in a position to deduce a conclusive unique structural model at present. The experimental data to date are at $l \sim 0$ and hence no vertical displacements can be determined. We have, however, been able to illustrate the kind of features and properties that are necessary within a new model of the surface in order to fit in with the most prominent characteristics of our experimentally obtained structure factors in SXRD.

5. Summary

We have investigated the $\text{Si}(111)(2\sqrt{3} \times 2\sqrt{3})\text{R}30^\circ$ phase after the deposition of about 1.1 monolayers of Sn onto the clean $\text{Si}(111)(7 \times 7)$ by surface X-ray diffraction (SXRD) supported by STM. Comparison of the two existing models in literature

with our experimental structure factor data set has proven conclusively the need for a new surface model. Support is provided by disagreements between the electronic structure of one of the proposed models with images obtained for STM images at different bias. Certain features and properties of a new appropriate model were determined by fitting our experimentally obtained structure factors to those derived for specific models. Although exact atomic positions are not yet known, the Sn layer is assumed to employ features of a bulklike α -Sn structure with a large number of atoms sitting on $0, 1/5, \dots, 4/5$ positions along the main crystallographic axes as illustrated.

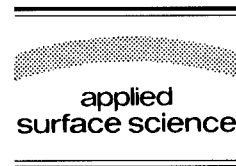
References

- [1] T. Ichikawa, *Surf. Sci.* 140 (1984) 37.
- [2] S.-I. Iwanari and K. Takayanagi, *Jpn. J. Appl. Phys.* 30 (1991) L1978.
- [3] C.L. Griffiths, H.T. Anyele, C.C. Matthai, A.A. Cafolla and R.H. Williams, *J. Vac. Sci. Technol. B* 11 (1993) 1559.
- [4] P.J. Estrup and J. Morrison, *Surf. Sci.* 2 (1964) 465.
- [5] K.M. Conway, J.E. Macdonald, C. Norris, E. Vlieg and J.F. van der Veen, *Surf. Sci.* 215 (1989) 555.
- [6] C. Törnevik, M. Hammar, N.G. Nilsson and S.A. Flodström, *Phys. Rev. B* 44 (1991) 13144.
- [7] R. Feidenhans'l, *Surf. Sci. Rep.* 10 (1989) 105.
- [8] R.L. Johnson, J.H. Fock, I.K. Robinson, J. Bohr, R. Feidenhans'l, J. Als-Nielsen, M. Nielsen and M. Toney, in: *The Structure of Surfaces*, Eds. M.A. van Hove and S.Y. Tong (Springer, Berlin, 1985) p. 313.
- [9] J. Nogami, S.-il. Park and C.F. Quate, *J. Vac. Sci. Technol. A* 7 (1989) 1919.
- [10] A.L. Patterson, *Z. Krist. A* 90 (1935) 517.
- [11] H. Lipson and W. Cochran, *The Determination of Crystal Structures* (Bell, London, 1957).
- [12] M.S. Worthington, J.L. Stevens, C.S. Chang and I.S.T. Tsong, *Nucl. Instr. Meth. Phys. Res. B* 64 (1992) 566.



ELSEVIER

Applied Surface Science 104/105 (1996) 130–136



Atomic phenomena on Si surfaces at adsorption of transition metals

B.Z. Olshanetsky

Institute of Semiconductor Physics, Russian Academy of Sciences, Siberian Branch, Novosibirsk 630090, Russian Federation

Received 28 June 1995; accepted 14 November 1995

Abstract

The effect of Ni and Co adsorption on Si surfaces with different orientations has been studied by LEED and AES. It has been established that the transport of Ni and Co atoms at Si surfaces is actually by their diffusion in the bulk of Si. There are two states of adsorbed Ni and Co atoms on Si surfaces. Nickel and cobalt adsorption may cause the reversible phase transitions on silicon surfaces at varying temperatures due to the change of their solubility in silicon and the redistribution of adsorbed atoms between the two possible states. The conditions for the existence of each of these states are different for Ni and Co atoms.

1. Introduction

The nature of atomic processes on crystal surfaces has been attracting much attention in surface science.

At the end of the nineteen-seventies and early eighties we discovered a number of reversible order–order phase transitions on germanium and silicon surfaces with different orientations by LEED in the Institute of Semiconductor Physics in Novosibirsk [1–8]. We observed several types of such reversible transitions: (1) reconstruction of one surface plane structure to another (Si(110) surface); (2) reconstruction of atomically flat surface to faceted one (Ge(110) and Si(320) surfaces); (3) reconstruction of faceted surface to stepped one (vicinal Ge(110) surfaces); (4) reconstruction of one step-terrace configuration to another (vicinal Si and Ge(111) surfaces).

Later on Ichinokawa and coauthors had shown that the phase transitions on Si(110) surfaces discovered by us were due to the presence of nickel impurity and the variations of its surface concentra-

tion with temperature [9,10]. This was one of the reasons, which prompted us to carry out a systematic study of nickel surface heterodiffusion and of the effect of nickel adsorption on the structure and phase transitions on silicon surfaces with different orientations. They were described in our papers [11–14], which contain also the references to the related studies carried out in other laboratories.

As a result we have found some interesting peculiarities of nickel behaviour on silicon surfaces, which, in turn, led us on to study the adsorption of other transition metal atoms on silicon surfaces. It was reasonable to begin such studies with Co adsorption, because the properties of Co atoms are close to those of Ni atoms.

2. Experimental

The silicon samples were of p-type with resistivities between 5–10 Ω cm and the dimensions of

$20 \times 5 \times 0.4$ mm. Samples were oriented using the Laue X-ray technique with the precision of $\pm 1^\circ$. The experiments were performed in an UHV system with the base pressure about 1×10^{-10} Torr. The surface cleaning procedure was carried out by heating in vacuum at 1200°C for 1–2 min. The sources of Ni and Co atoms consisted of a tantalum ribbon to which a piece of Ni or Co plate was welded.

The surface structure and the surface chemical composition were studied by LEED and AES in situ. To measure the Ni and Co surface concentrations the Auger Ni LMM (848 eV) and Co LMM (775 eV) electron peaks were used. The spatial resolution of the Auger spectrometer was several tens of microns.

3. Results and discussion

3.1. Surface diffusion

The unexpected outcome of our studies of the transition metals atoms adsorption on Si surfaces was the discovery of peculiarities of their transport along Si surfaces.

In order to study surface diffusion of transition metals on silicon surfaces, a metal strips several nanometers thick were deposited perpendicular to the longer side of a sample (Fig. 1). In these experiments Co was evaporated from a BeO crucible. Then samples were annealed at certain temperatures by passing an alternating current. As it is known from literature, Ni and Co layers of several nanometer thickness fully react to the disilicides at $300\text{--}350^\circ\text{C}$. At about 960°C nickel disilicide strips melted and the films became uncontinuous. The same happened with Co disilicide strips at about 1240°C .

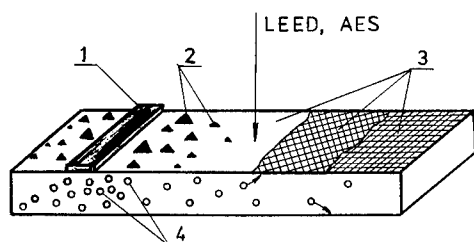


Fig. 1. Schematic of experimental setup. (1) Ni strip; (2) nickel disilicide islands; (3) Ni induced surface structures; (4) Ni atoms.

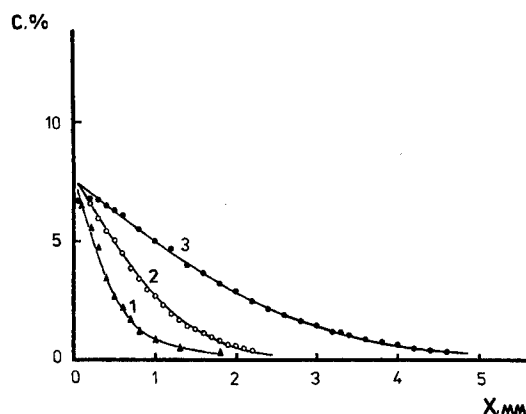


Fig. 2. Concentration distributions $C(x)$ of nickel on Si(111) surface after annealing at 860°C for: (1) 15 s, (2) 60 s, (3) 240 s.

After annealing the concentration distributions of metal atoms along Si surfaces were measured by AES. Surface structures were studied by LEED.

The examples of Ni concentration distributions measured in our experiments [11] are shown in Figs. 2 and 3.

It was commonly supposed, and we also expected, that the surface diffusion coefficients are well in excess of those in the bulk, though there is a modest number of experimental data on surface diffusion in literature at present. It is known that the process of surface diffusion may depend on the surface orientation and structure, atomic steps, concentration of adsorbed atoms and so on. However, we did not observe the relationship between the measured nickel diffusion coefficients and the features of silicon surfaces.

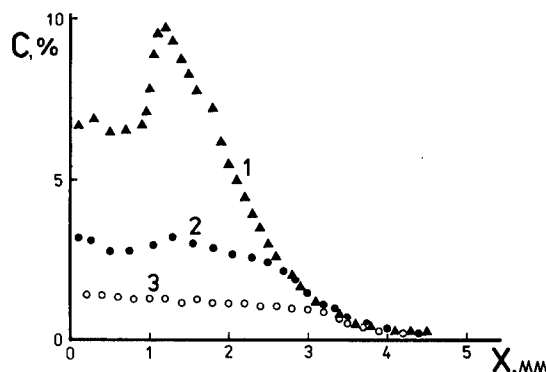


Fig. 3. Typical nickel $C(x)$ distributions on silicon surfaces after annealing at 1050°C for 80 s: (1) (111); (2) (110); (3) (100).

If nickel concentration did not exceed a certain value for given surface orientation, the concentration distributions, which we measured along the specimen, obeyed the equation

$$C(x) = C_0 \operatorname{erfc}(x/2\sqrt{Dt}),$$

where x is the distance from the edge of the disilicide strip (the Ni concentration on the strip is not shown), D the diffusion coefficient and t the annealing time (Fig. 2).

Such distributions are typical for one-dimensional surface diffusion from the source of constant strength.

At nickel concentrations exceeding certain values (different for different planes) the $C(x)$ curves deviate from those which are typical for the diffusional distributions: they become either steady-state or non-monotonous and are badly reproducible [1]. As can be seen from Fig. 3, on Si(111) surfaces it takes place with nickel concentrations above 6%, and on Si(100) and (110) surfaces it is observed with concentrations above 1% and 2.5%, respectively. These deviations are due to the formation of three-dimensional silicide islands which could be observed by scanning electron microscope. The area occupied by three-dimensional islands of nickel silicide is much lower than that occupied by uniformly distributed nickel. And this causes either a decrease or a stabilization of the Auger signal from nickel on the surface with islands.

However, the surprising thing was that nickel could not be detected at the surface by Auger spectroscopy during the sample heating. Nickel concentration distributions appeared on surfaces only after the sample cooling. So we drew the conclusion that the nickel transport along silicon surfaces is not by way of surface diffusion, but by its diffusion through the bulk with subsequent segregation to the surface at sample cooling due to the decrease of nickel solubility in silicon (Fig. 1). This conclusion agrees with the absence of correlation between the nickel diffusion coefficients and the surface orientation and structure, which was mentioned before. Besides, the diffusion coefficients deduced from our data are close to those of interstitial nickel diffusion in silicon (10^{-4} – 10^{-5} cm² s⁻¹ at 1100°C [15,16]).

The amount of Ni, diffusing through Si bulk, is limited by Ni solubility, which is 2×10^{17} – 6×10^{17} cm⁻³ in the temperature range of 1000–1300°C [17].

That is why in the distributions, presented in Figs. 2 and 3, Ni concentrations did not reach the values typical of the nickel disilicide.

However, nickel diffusion on silicon surfaces does take place. It manifests itself by the formation of ordered surface structures and epitaxial disilicide islands. But the coefficients of nickel surface diffusion are by orders of magnitude less than those of interstitial nickel diffusion in silicon.

We could not measure the temperature dependence of the Co diffusion coefficients on Si surfaces because of their small values and limited spatial resolution of the LEED and AES apparatus [18]. However, our estimates show that this coefficient is about 10^{-5} cm²/s at 1200°C. It is known from literature that the coefficients of Co diffusion in silicon bulk may range 10^{-8} – 10^{-4} cm²/s at 1000–1300°C [19], and, specifically, at 1100°C this coefficient approximates 10^{-5} cm²/s [20]. We can see that the Co diffusion coefficient deduced at Si surface is similar to that in Si bulk, like in the case of Ni diffusion. Thus, one can infer that the transport of Co atoms at Si surfaces is also by way of their diffusion through Si bulk. The solubility of Co in Si is 5×10^{14} – 3×10^{16} cm⁻³ in the temperature range of 1000–1300°C [17].

Thus, our finding is contrary to the existing notions that the activation energy of surface diffusion is much less than that of the diffusion through the body of solids and that the rate of surface atom migration is considerably greater than that in the bulk.

3.2. Two states of adsorbed atoms

Our results show that there are two states of Ni and Co atoms on Si surfaces. These states correspond to different minima of the surface system free energy. The atoms in the first state are likely to be regularly distributed on surfaces and they cause the formation of various surface structures (Fig. 1). Several structures can be formed on a Si surface of given orientation, each corresponding to a certain concentration of Ni or Co atoms. The adsorbed atoms in the second state are involved in the formation of the epitaxial disilicide islands. This state of atoms is more stable. The conditions to fall in each of these states are different for Ni and Co adsorbed atoms.

In the case of Ni adsorption the first state of adsorbed atoms could be obtained by cooling a sample at a rate above 100°C/s . However, the Ni induced structures on Si surfaces are metastable. Slow cooling or annealing at $600\text{--}700^\circ\text{C}$ of samples with adsorbed nickel causes formation of the epitaxial disilicide islands, nickel atoms diffusing to these islands from the adjacent parts of surface and leaving them free of nickel impurity. The islands can be seen using scanning electron microscope. Their density was about $5 \times 10^6 \text{ cm}^{-2}$. The first state of adsorbed atoms is associated with the shallow minima and the disilicide phase — with the deep minimum of free energy. Disilicide islands started to grow also when Ni concentration exceeded the value, which was necessary for the formation of the surface structure with the maximum nickel content for a given surface

plane. In this case on the free of islands parts of the surface the structure with the maximum nickel content remained.

Our explanation of this phenomenon is as follows. At sample cooling nickel atoms segregate to the surface. However, some time is needed for the formation of critical nuclei of the nickel disilicide phase and for their growth. During fast sample cooling (at the rates above 100°C/s) there is not enough time to do this and the outdiffused nickel atoms occupy the sites corresponding to the less deep minimum of energy. At slow sample cooling or low-temperature annealing ($600\text{--}700^\circ\text{C}$) the stable phase has time to form.

We did not observe the effect of sample cooling on the structure of cobalt adsorbed Si surfaces. In the case of Co adsorption a condition which determined

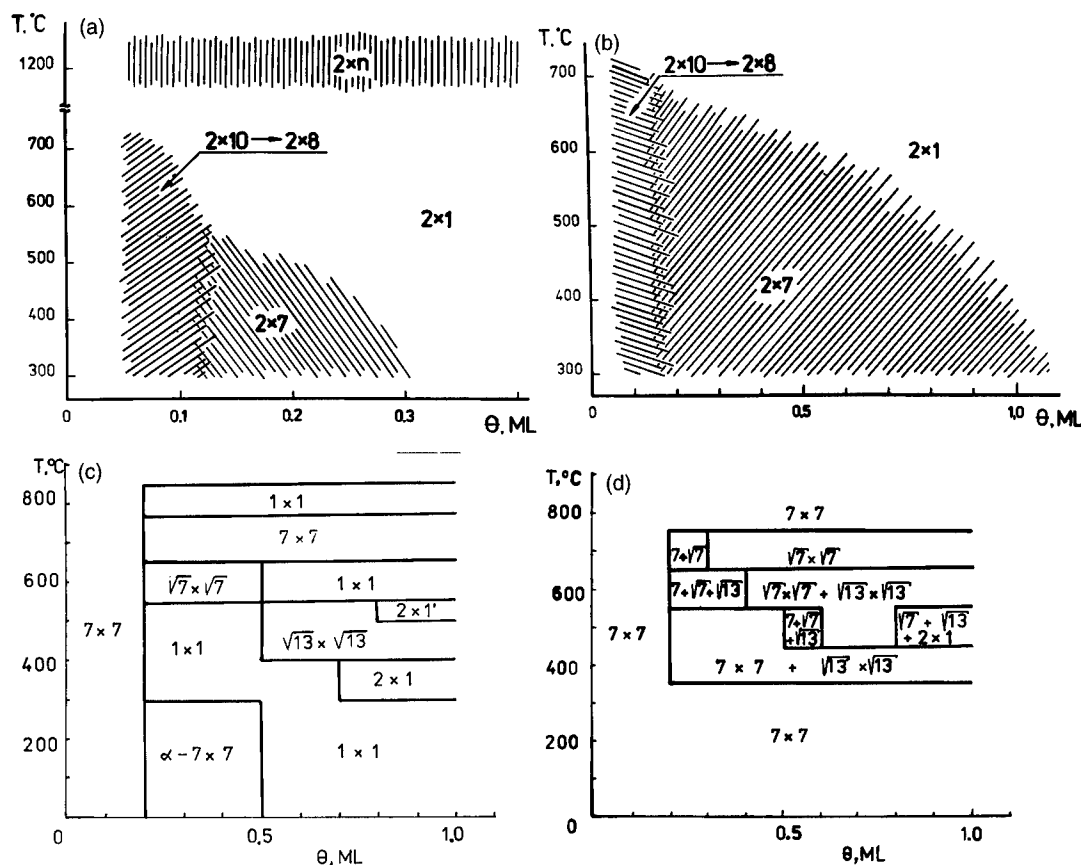


Fig. 4. Surface structures induced by Co versus Co coverage and sample temperature: (a) Si(100), SPE mode; (b) Si(100), MBE mode; (c) Si(111), SPE mode; (d) Si(111), MBE mode.

the state of adsorbed atoms was the coverage value. The epitaxial disilicide islands started to appear on Si surfaces, when Co concentrations exceeded a certain value at given temperature. For Si(100) surfaces there is a certain Co concentration for any temperature, so that if a Co concentration is below this value then a uniform and ordered distribution of Co atoms is possible. If the Co concentrations exceeded this value, only disilicide phase forms, and Co atoms outgo from the parts of Si surfaces adjacent to the epitaxial islands (Fig. 4a and b).

3.3. Surface structures

Adsorption of Ni and Co leads to the formation of many surface structures on Si surfaces with different orientations, depending on the concentration of ad-

sorbed atoms and causes the reversible order–order transitions at varying temperatures [1,12,13,18,21].

For the reasons discussed before, the Ni induced surface structures were studied at room temperature after sample cooling at the rate above 100°C/s (Table 1). One can see that Ni causes the formation of a great number of surface structures on Si and that the concentrations of Ni, at which they start to appear and form, are low.

In the case of Co adsorption [18,21] the rates of sample cooling did not influence the state of the surface. However, surface structures depended on the conditions, at which Co atoms were deposited on Si surface. Because of this, the formation of Co induced surface structures were studied under the two operating modes, which may be arbitrarily called as molecular beam epitaxy (MBE) mode and solid phase epitaxy (SPE) mode. The MBE mode means the

Table 1
Correlation between Ni concentrations and structures of Si surfaces

Miller indices	Surface structure	Nickel concentration $C_{Ni_i}^a$	Nickel concentration $C_{Ni_i}^b$	Miller indices	Surface structure	Nickel concentration $C_{Ni_i}^a$	Nickel concentration $C_{Ni_i}^b$
Singular surfaces				High index surfaces			
(100)	2×1		< 0.1%	(511)	stepped		< 0.2%
	$10 \times 2 \rightarrow 7 \times 2$	0.5%	1.0%		3×3	0.3%	0.5%
(111)	7×7		< 0.1%		3×1	0.5%	1.0%
	$\sqrt{19} \times \sqrt{19}$	0.5%	6.0%		7×1	1.3%	1.8%
(110)	$\begin{pmatrix} 11 & 5 \\ -2 & 2 \end{pmatrix}$		< 0.1%	(311)	3×1		< 0.2%
	5×8		< 0.1%		3×2	< 0.2%	0.3%
	5×1	< 0.1%	0.8%		2×2	0.3%	1.0%
	$5 \times 1 \rightarrow 2 \times 1$	0.8%	1.4%		4×2	1.5%	2.5%
	4×5	1.4%	2.0%	(211)	2×2		< 0.2%
Vicinal (111) surfaces					X	1.5%	3.0%
Inclined towards $[\bar{2}11]$:				(331)	6×2		< 0.2%
$1d_{111}$ step bands and (111) terraces					$c(13 \times 2)$	< 0.2%	0.4%
$\downarrow \uparrow 800^\circ\text{C}$					$c(17 \times 2)$	0.4%	1.5%
$1d_{111}$ regular steps					Y	1.5%	3.0%
$2d_{111}$ steps				(510)	stepped		< 0.2%
$1d_{111}$ steps					1×4	0.3%	0.5%
Inclined towards $[2\bar{1}\bar{1}]$:					1×2	0.5%	1.3%
$3d_{111}$ steps $\xrightarrow{800^\circ\text{C}}$ $1d_{111}$ steps				(210)	1×1		< 0.2%
$2d_{111}$ steps					2×2	0.4%	1.0%
		1.0%	2.8%		(320) facets	1.0%	2.0%
				(320)	(23 15 3) facets		< 0.2%
					2×1	0.2%	2.0%

^a The concentrations at which the surface structures start to appear.

^b The concentrations at which the surface structures are completely developed.

formation of surface structures during the deposition process at the sample temperatures above 300°C. By the SPE mode we mean the Co deposition on the sample at room temperature with the subsequent annealing, which brings about the formation of surface structures. The duration of sample annealing at the SPE mode was determined by the time necessary for the completion of the surface reconstruction and was in the range of tens of minutes. Surface structures induced by Co versus Co coverage and sample temperature are shown in Fig. 4.

In most cases the nickel and cobalt concentrations measured by AES were significantly less than those calculated with the assumption that there is at last one metal atom per unit cell of the surface structure. This feature is more pronounced at nickel adsorption. In some cases Si surface reconstructions occur at the nickel concentrations which are near or below the threshold sensitivity of an Auger spectrometer.

Two plausible explanations of this phenomena can be put forward: (1) the adsorbed atoms evoking surface reconstructions do not enter in the unit meshes of the induced surface structures but they are embedded at specific sites in the surface lattice and generate strains, which lead to surface reconstruction; (2) the adsorbed atoms are located not on the surface atomic plane but at certain depth in subsurface layer, which must cause the corresponding weakening of AES signal.

We believe that the second explanation is more realistic.

3.4. Phase transitions

One of the features of Si surfaces with adsorbed transition metals atoms is the possibility of reversible order–order phase transitions in surface region at temperature variations.

It is accepted that the surface region of crystals may be treated as a special phase with its own thermodynamical criterion of equilibrium and its own set of the phase transitions. Order–disorder phase transitions take place on clean Si surfaces of almost all orientations at certain temperatures. The order–order transitions at temperature variations are known on clean vicinal Si(111) surfaces [8,12,22,23].

In the case of transition metals adsorption on Si the phase transitions in surface structures are caused

by reversible variations of surface concentrations of adsorbed atoms with the temperature. In its turn, the surface concentrations of adsorbed atoms change by two reasons. First, solubility in silicon depends on temperature. Because of this, with temperature raising a certain portion of adsorbed atoms dissolves in silicon, and with the sample cooling it segregates to the surface. Second, the redistribution of the adsorbed atoms between the two possible states may take place, namely, between surface phase and the epitaxial disilicide islands.

Reversible reconstructions of surface structures with the temperature are more inherent to Ni adsorbed Si surfaces of different orientations. In most cases the transitions occur between different two-dimensional structures with the unit vectors, which lie in the same crystal plane. However, the morphologic transitions are also possible, as it takes place on Si(320) and (210) surfaces, where atomically flat surfaces reversibly reconstruct into faceted one, on Si(511) and (510) surfaces, where stepped surfaces reconstruct into flat ones, and on the vicinal Si(111) surfaces, where transitions occur between regular steps of different heights. At Co adsorption we observed only the reversible reconstructions of Si(111)- 7×7 to Si(111)- 1×1 structure at about 770°C.

4. Conclusions

Our studies have revealed some peculiarities of atomic processes on Si surfaces with adsorbed transition metals.

(1) The coefficients of nickel diffusion on Si surfaces are several orders of magnitude less than those in the bulk of silicon. Nickel transport along Si surfaces is provided by its diffusion through Si bulk. The estimated values of Co diffusion coefficients on Si surfaces do not exceed those in silicon known from literature.

(2) Ni and Co adsorbed atoms on Si surfaces may be in two states which correspond to the different minima of free energy.

(3) According to AES data Si surfaces reconstructions may take place at the Ni and Co surface concentrations which are significantly less than those calculated with the assumption that there is at last one metal atom per unit cell of the surface structure.

(4) Ni and Co atoms may cause reversible order–order phase transitions on silicon surfaces at temperature variations, due to the redistribution of adsorbed atoms between the two possible states and the temperature dependence of their solubility in silicon.

Acknowledgements

The research described in this publication was made possible in part by Grant No. JCZ100 from the International Science Foundation and Russian Government and by Grant No. 95-02-05336-a from the Russian Foundation for Fundamental Investigations.

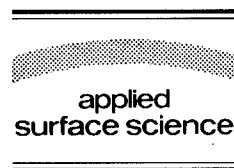
References

- [1] B.Z. Olshanetsky, S.M. Repinsky and A.A. Shklyaev, *JETP Lett.* 25 (1977) 178.
- [2] B.Z. Olshanetsky, S.M. Repinsky and A.A. Shklyaev, *Surf. Sci.* 64 (1977) 224.
- [3] B.Z. Olshanetsky and A.A. Shklyaev, *Surf. Sci.* 67 (1977) 581.
- [4] B.Z. Olshanetsky, S.M. Repinsky and A.A. Shklyaev, *Surf. Sci.* 69 (1977) 205.
- [5] B.Z. Olshanetsky and A.A. Shklyaev, *Surf. Sci.* 82 (1979) 445.
- [6] B.Z. Olshanetsky and V.I. Mashanov, *Surf. Sci.* 111 (1981) 414.
- [7] B.Z. Olshanetsky, V.I. Mashanov and A.I. Nikiforov, *Surf. Sci.* 111 (1981) 429.
- [8] V.I. Mashanov and B.Z. Olshanetsky, *JETP Lett.* 36 (1982) 355.
- [9] T. Ichinokawa and Y. Ishikawa, *Ultramicroscopy* 15 (1984) 193.
- [10] T. Ichinokawa, H. Ampo, S. Miura and A. Tamura, *Phys. Rev. B* 31 (1985) 5183.
- [11] A.E. Dolbak, B.Z. Olshanetsky, S.I. Stenin, S.A. Teys and T.A. Gavrilova, *Surf. Sci.* 218 (1989) 37.
- [12] B.Z. Olshanetsky and S.A. Teys, *Surf. Sci.* 230 (1990) 184.
- [13] B.Z. Olshanetsky, A.E. Solovyov, A.E. Dolbak and A.A. Maslov, *Surf. Sci.* 306 (1994) 327.
- [14] B.Z. Olshanetsky and A.E. Dolbak, *Phys. Low-Dim. Struct.* 2 (1994) 81.
- [15] J.H. Aalberts and M.L. Verneijke, *Appl. Phys. Lett.* 1 (1962) 19.
- [16] M. Yoshida and K. Furusho, *Jpn. J. Appl. Phys.* 3 (1964) 521.
- [17] E.R. Weber, *Appl. Phys. A* 30 (1983) 1.
- [18] A.E. Dolbak, B.Z. Olshanetsky and A.E. Solovyov, *Poverkhnost* 11 (1993) 55.
- [19] M.K. Bakhadyrkhanov, B.I. Boltaks and G.S. Kulikov, *Fiz. Tverd. Tela* 12 (1970) 181 [*Sov. Phys. Solid State* 12 (1970) 144].
- [20] H. Kitagawa and K. Hashimoto, *Jpn. J. Appl. Phys.* 16 (1977) 173.
- [21] A.E. Dolbak, A.A. Maslov and B.Z. Olshanetsky, *Phys. Low-Dim. Struct.* 8 (1994) 39.
- [22] R.J. Phaneuf and E.D. Williams, *Phys. Rev. Lett.* 58 (1987) 2563; *Phys. Rev. B* 41 (1990) 2991.
- [23] R.J. Phaneuf, E.D. Williams and N.C. Bartelt, *Phys. Rev. B* 38 (1988) 1984.



ELSEVIER

Applied Surface Science 104/105 (1996) 137–140



Hydrogenated and oxidized vicinal Si(001) surfaces investigated by reflectance-difference spectroscopy

U. Rossow^{*}, L. Mantese, T. Yasuda, D.E. Aspnes

Physics Department, North Carolina State University, Raleigh, NC 27695-8202, USA

Received 28 June 1995; accepted 14 November 1995

Abstract

We have investigated the effects of hydrogenation and oxidation on the surface-induced optical anisotropy (SIOA) of vicinal Si(001) as measured by reflectance-difference (-anisotropy) spectroscopy (RDS/RAS). By considering several vicinal Si(001) surfaces we better isolate terrace from step-induced contributions. For double-domain surfaces etched by HF or oxidized by H_2O_2 , the RD response has an energy-derivative-like shape and can be characterized by three main features, the first near 3.4 eV and a second and third around 4.3 eV. These energies are near those of the (E'_0 , E_1) and E_2 interband critical points of bulk silicon. The magnitudes of these peaks vary strongly with offcut angle suggesting that there is a strong step-induced contribution to the SIOA. Two of these features are affected by a change of the surface species, which indicates that the species bonded to the steps are changing. The RD response obtained by exposing atomic H to a double-domain surface hydrogenated by HF is similar to that obtained by exposing a clean single-domain surface to atomic hydrogen.

1. Introduction

The hydrogen-passivated Si surface is of interest because it can withstand oxidation in air for extended periods of time. Such surfaces are well suited for heteroepitaxy since the hydrogen can be desorbed at temperatures less than 530°C, which is relatively low compared to oxide desorption, which occurs at temperatures near 900°C. In addition, the need for ultrathin gate oxides (< 10 nm) has placed a demand on the determination and control of the properties of Si/SiO₂ interfaces [1].

We report RDS measurements of various Si surfaces treated by hydrofluoric acid (HF) and hydrogen peroxide (H_2O_2), which yield hydrogenated and oxi-

dized surfaces, respectively. We include the ultra-high vacuum (UHV) RDS responses of a clean vicinal (2×1) Si(001) 6° surface and an HF-etched surface exposed to atomic hydrogen.

2. Experimental

Surface-induced optical anisotropy (SIOA) measurements were made using an RDS spectrometer [2–4] that operates at near-normal incidence in the spectral range of 1.5 to 5.5 eV. The anisotropy of the complex reflectance is given by $\Delta r/r = 2(r_\alpha - r_\beta)/(r_\alpha + r_\beta) = \text{Re}(\Delta r/r) + i\Delta\theta$, where r_α and r_β are the complex reflectances along the directions α and β , respectively. Here we report the component $\text{Re}(\Delta r/r)$ with α defined to be along $[110]$ and β to be orthogonal to the α direction and to the surface

^{*} Corresponding author. Fax: +49-30-314-21769; e-mail: rossow@gift.physik.tu-berlin.de.

normal. Wafer orientations were verified using low energy electron diffraction (LEED). The chemically treated samples were measured on a rotational stage where spectra were taken at two orthogonal orientations and subtracted. This is done in order to minimize the contribution of nonidealities of the optical components to the anisotropy signal.

We have measured a broad range of Si surfaces, specifically: (a) vicinal (001) surfaces cut 4° , 6° , and 10° off (001) toward [110]; (b) the (113) surface. Wafers were lightly p-doped with resistivities from 1 to 10 Ω cm. The samples were chemically prepared by an RCA [5] (or slightly modified) clean. Further treatment included a 30 s dip in dilute HF followed by a deionized water rinse in order to obtain a hydrogenated surface or H_2O_2 to obtain an oxidized surface. Data were taken directly after treatment with the samples in air. To ensure that surfaces did not degrade during measurement, we also obtained data with a sample immersed in HF or H_2O_2 contained in a quartz beaker.

For comparison, we also measured the evolution of the SIOA response of a single-domain surface exposed to atomic H. This sample was prepared by an RCA clean, then transferred to a UHV system where the residual oxide layer was desorbed and the surface reconstructed by annealing at 950°C for 2 min. LEED patterns exhibited sharp, well-defined spots with splitting in the direction of the steps, which we define to be the [110] direction. We then measured the evolution of the RDS signal as the surface was exposed to atomic H, which was generated by dissociating H_2 in the 10^{-6} mbar range with a hot W filament. Auger spectroscopy showed minimal surface contamination by C and O.

3. Results and discussion

Fig. 1 and Fig. 2, respectively, show RD spectra obtained after HF hydrogenation and H_2O_2 oxidation. The lineshapes of the various spectra are quite similar, exhibiting three main features. The first is a derivative-type structure near 3.4 eV and the second and third form a double feature near 4.3 eV. These energies are near those of the (E'_0, E_1) and E_2 interband critical points of bulk silicon. Previous work [6–8] has shown that RD spectra can have an

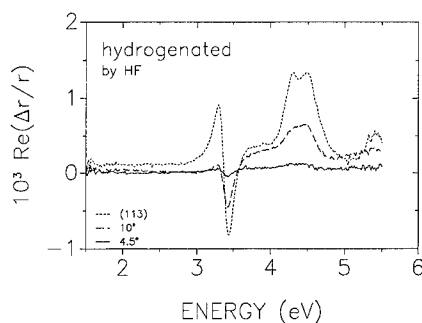


Fig. 1. RD spectra of hydrogenated vicinal Si(001) surfaces prepared by an HF dip.

energy-derivative-like shape. In those cases the signal is dominated by an energy derivative of the bulk dielectric function. For hydrogenated Si [8] it was found that the lineshape around 3.4 eV is given by the normalized energy derivative of the reflectance, $1/R(dR/dE)$ (note that $1/R(dR/dE) = 2/[\sqrt{\epsilon}(\epsilon - 1)](d\epsilon/dE)$). Interestingly, the spectra of Fig. 1 and Fig. 2 are all similar to the $1/R(dR/dE)$ spectrum obtained from a local pseudopotential calculation generated from the bulk properties of Si [9], as shown in Fig. 3. However, the spectral positions are not accurately given by theory.

It is important to note that the magnitude of the signal increases with offcut angle. Since the total area of the terraces decreases slightly with offcut angle and the areal density of steps increases, it follows that the RD signal in this case is dominated by step-induced contributions. As these surfaces were not heat treated, the surface contains double domains with single and double height steps. However, for vicinal Si(001) it is well known that one double step

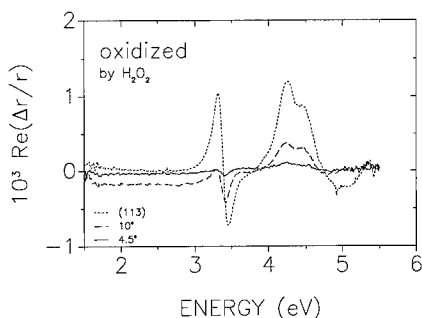


Fig. 2. RD spectra of oxidized vicinal Si(001) surfaces prepared by H_2O_2 immersion.

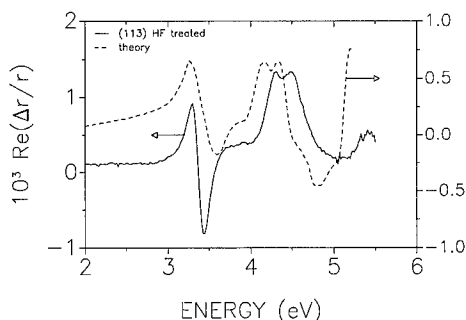


Fig. 3. Comparison between the normalized energy derivative of reflectance $1/R \, dR/dE$ derived from a theoretical local pseudopotential calculation (data taken from [9]) and a spectrum for hydrogenated Si(113).

has a lower energy than two single steps. Thus it is expected that the number of double steps increases with offcut angle while the number of single steps should not change significantly. Likewise, the signal obtained with RCA-cleaned surfaces also shows a strong dependence on offcut angle. Hence, it is likely that the signal is related to the presence of double steps on the surface.

The lineshapes of the double spectral feature located near 4.3 eV depend on surface termination. We performed a lineshape analysis of the first energy derivative of the Si(113) spectra for the hydrogenated and oxidized surfaces. For the hydrogenated surface the data indicate a slightly larger separation, 0.23 eV instead of 0.15 eV, and a 15% sharpening of both features compared to the oxidized surfaces.

The difference between the RD spectra of the HF-etched and oxidized surfaces is shown in Fig. 4. The difference is small and the surface termination

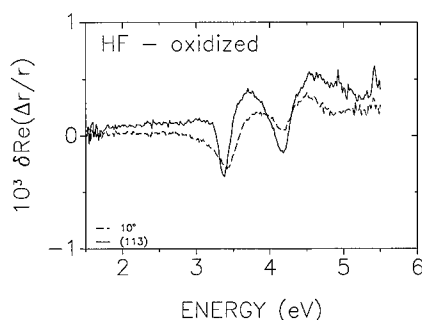


Fig. 4. Difference between RD spectra of hydrogen terminated and oxidized surfaces, taken from Figs. 1 and 2.

mainly affects only two of the three features observed in the spectra. The spectra scale with offcut angle, which indicates that an exchange of species bonded to the step atoms occurs upon treating the surface with H_2O_2 and HF. However, the magnitude of the difference is small compared to the overall anisotropy signal, which further suggests that not all step atoms are affected by this HF/ H_2O_2 treatment. As reported elsewhere, we have observed a lineshape similar to that of Fig. 4 by taking the difference between the RD spectrum for the clean (2×1) Si(001) surface and that for the same surface exposed to oxygen [8]. We have also observed this lineshape for an oxidized (113) surface that has been thermally annealed [7]. This lineshape can be modeled by assuming that the anisotropy originates from a dichroism that is step-induced and localized at the surface [8]. We have obtained this RD lineshape independently on three separate surfaces and each strongly indicates that the origin is related to surface steps.

The RD lineshape for a hydrogenated 6° vicinal Si(001) surface generated by HF etching is shown in the middle of Fig. 5. If the surface is then exposed to atomic hydrogen in a UHV environment, the signal

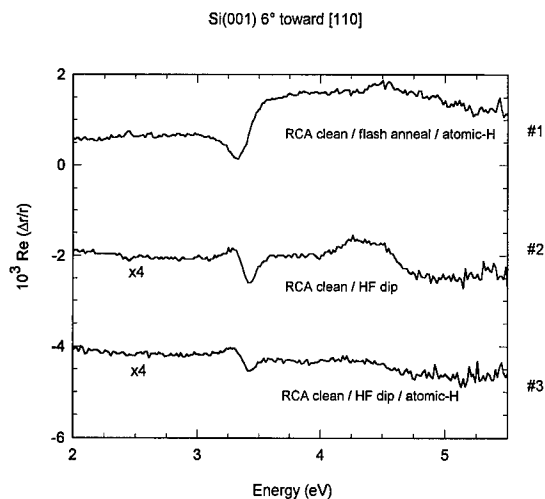


Fig. 5. #1: RD spectrum of a clean (2×1) Si(001) 6° vicinal sample after exposure to atomic hydrogen. LEED shows a (1×1) reconstruction (dihydride phase). #2: RD spectrum of a Si(001) 6° vicinal sample after RCA cleaning and final HF dip. LEED shows (1×1). #3: RD spectrum after exposing the sample of #2 to atomic hydrogen. Notice that the double structure near 4.3 eV vanishes. This feature is (partially) step induced.

evolves to that shown at the bottom of Fig. 5. After exposure to atomic hydrogen the 3.4 eV feature remains but the structure at higher energy collapses. LEED data before and after exposure show a (1×1) diffraction pattern. To determine whether the same RD signal can be obtained for a clean surface exposed to atomic hydrogen, an RCA-cleaned sample was transferred into an UHV chamber and exposed to atomic hydrogen. The RD signal evolved toward the spectrum shown at the top of Fig. 5. The resulting lineshape is surprising in that the full double feature is not observed in this case. Hence, atomic hydrogen must change the steps. The most likely explanation is that OH groups are initially bonded to the steps, which is known at least to be the case for defect sites [5,10,11]. Atomic hydrogen may break the Si–OH bond and form H_2O , which desorbs from the hydrophobic surface, and then saturates the Si dangling bond. This H replacement seems to be incomplete after the HF dip and subsequent water rinse. Another possibility is that a roughening of the steps takes place. However, the spectral lineshapes are reproducible with respect to repeated $\text{HF}/\text{H}_2\text{O}_2$ cycles, and it is unlikely that either oxidation or HF treatment results in a significant smoothening of the steps.

4. Summary and conclusion

Chemically hydrogen terminated and oxidized silicon surfaces have been analyzed using RDS. The spectra for these two different surface terminations were found to be similar and to have an energy-derivative-like lineshape. Although the origin of these spectra has not been determined, we have been able

to isolate step-induced features. Since the RD signal is sensitive to the step structure, it may be used to monitor the step evolution (roughness, bunching) during growth or surface treatment. In addition, RDS is capable of measuring surfaces in liquids or any other transparent media, which allows information about etching processes to be obtained in real time.

Acknowledgements

We gratefully acknowledge financial support from the Office of Naval Research (ONR) under contract N-00014-93-1-0255 and the Alexander von Humboldt Foundation.

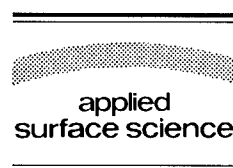
References

- [1] E. Hartmannsgruber, U. Rossow, A. Hoyer and P. Lange, *J. Non-Cryst. Solids* 187 (1995) 380.
- [2] D.E. Aspnes, *J. Vac. Sci. Technol. B* 3 (1985) 1498.
- [3] D.E. Aspnes, J.P. Harbison, A.A. Studna, L.T. Florez and M.K. Kelly, *J. Vac. Sci. Technol. A* 6 (1988) 1327.
- [4] W. Richter, *Phil. Trans. R. Soc. A* 344 (1993) 453.
- [5] W. Kern and D.A. Puotinen, *RCA Rev.* 31 (1970) 187.
- [6] D.E. Aspnes and A.A. Studna, *J. Vac. Sci. Technol. A* 5 (1987) 546.
- [7] T. Yasuda, D.E. Aspnes, D.R. Lee, C.H. Bjorkman and G. Lucovsky, *J. Vac. Sci. Technol. A* 12 (1994) 1152.
- [8] T. Yasuda, L. Mantese, U. Rossow and D.E. Aspnes, *Phys. Rev. Lett.* 75 (1995) 3431.
- [9] J.R. Chelikowsky and M.L. Cohen, *Phys. Rev.* 10 (1974) 5095.
- [10] D. Gräf, S. Bauer-Mayer and A. Schnegg, *J. Appl. Phys.* 74 (1993) 1679.
- [11] G.J. Pietsch, U. Köhler and M. Henzler, *J. Vac. Sci. Technol. B* 12 (1994) 78.



ELSEVIER

Applied Surface Science 104/105 (1996) 141–146



Se-induced 3d core-level shifts of GaAs(110)

Peter Käckell^{*}, Wolf Gero Schmidt, Friedhelm Bechstedt

Institut für Festkörpertheorie und Theoretische Optik, Friedrich-Schiller-Universität Jena, Max-Wien-Platz 1, 07743 Jena, Germany

Received 28 June 1995; accepted 25 October 1995

Abstract

We present *ab initio* pseudopotential calculations of 3d core-level shifts of the surface atoms for clean and Se-deposited GaAs(110) surfaces. We are able to explain the experimental findings for the clean GaAs(110) surface in the picture of the initial-state model. If relaxation effects are accounted for we find a distinct overestimation of the surface core-level shifts (SCLS) both for As and Ga atoms with respect to experimental results. We conclude that final-state effects play only a minor role in the dynamics of the photoemission process for the GaAs(110) surface. In order to clarify the surface chemistry of the Se/GaAs(110) system we determine the SCLS of the species involved for a series of structural models. Only one of these models gives rise to a reasonable agreement between calculated and measured SCLS. Therefore we strongly support a geometry where each surface As atom is substituted by Se and one further Se binds to the surface Ga atom.

1. Introduction

Currently there is a growing interest in the selenium and other group-VI atom deposition on the III–V compound semiconductor surfaces because of their passivating properties. Whereas the passivating action of a group-VI treatment is well known, especially for the polar GaAs(001) surface [1–3], the understanding of the actual formation process and the bonding of the adsorbate is far from being complete. The nonpolar GaAs(110) 1×1 cleavage surface represents a model face for such studies because of its smoothness on an atomic scale and is therefore discussed in the following. Tu and Kahn [4] found that upon deposition of Se the GaAs(110) 1×1 low-energy electron diffraction (LEED) pattern is

conserved, but degrades rapidly as a function of coverage. When the coverage reaches one monolayer (1 ML or $\Theta = 1$, i.e. 2 Se atoms/ 1×1 unit cell) the LEED spots are sharpened, indicating either the formation of a stable monolayer or the saturation of the Se–As exchange in the first layer or first two layers of the substrate. The strong interaction between the GaAs(110) surface and deposited Se already for low coverages ($\Theta = \frac{1}{4}$) has also been shown in electron energy loss spectroscopy (EELS) experiments [4,5]. Very recent experimental studies by Schröter et al. [6] reported the conservation of the 1×1 LEED structure after extensive Se treatment and subsequent annealing for the GaAs(110) surface. Their core level studies indicate the existence of at least two distinct bonding sites for Se on the surface and As desorption upon annealing. The thickness of the reacted layer was roughly estimated to amount to 1–2 atomic layers. By means of angle-resolved photoemission spectroscopy (ARPES) the authors found

^{*} Corresponding author. Tel.: +49-3641-635910; fax: +49-3641-635182; e-mail: kaeckell@ifo.physik.uni-jena.de.

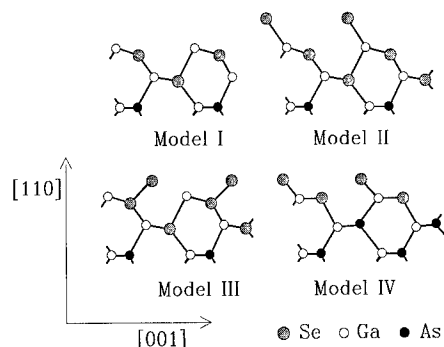


Fig. 1. Side view of four models for atomic arrangements at Se reacted GaAs(110) surfaces.

several rather dispersionless bands of surface bound states and resonances. On the basis of these experimental data Schmidt and Bechstedt [7] performed ab initio pseudopotential calculations for a variety of surface stoichiometries and structural models. For the Se-deposited and annealed GaAs(110) surface four structural models were investigated in more detail. These models can be seen in Fig. 1. On the grounds of their energetics and the agreement between calculated and measured band structures models I and IV were considered to be favourable. However, due to the existing difficulty with the correct choice of the appropriate chemical potentials and remaining discrepancies between calculated and measured band structures the question of the exact atomic surface structure could not be answered fully.

In this paper we make a different approach to gain information about structural properties of the Se-reacted GaAs(110) surface. We present ab initio calculations of the surface core-level shifts (SCLS) of the species involved in the surface reaction for the four structural models (Fig. 1). As a testing ground for the reliability of our calculations we use the free GaAs(110) surface, where a number of experiments on the SCLS have been reported [8].

2. Method

The ab initio pseudopotential approach which has been used for this work is described at some length in Ref. [7]. Therefore it may suffice to discuss here only the peculiarities which are connected with the calculation of SCLS.

In the photoemission process the photon energy is transferred to a core electron, which thereby obtains an energy above the vacuum level and can be detected as a photoelectron. The SCLS is defined as the difference in kinetic energy of an electron that has been emitted from a surface atom compared to one originating from a bulk atom. Usually, SCLS are interpreted in terms of the initial-state picture. Thereby the SCLS is explained by the energy difference of the core states localized at the surface and in the bulk, respectively. The single-particle energy eigenvalues of these core states depend on the chemical environment and therefore differ in general. The initial-state contributions to the SCLS are not directly accessible in pseudopotential theory, but can be calculated via the self-consistent potential extracted from a ground-state slab calculation [9]. The difference in the energy eigenvalues for the 3d states of surface and bulk atoms corresponds to the difference of the matrix elements of the respective Hamiltonians with the 3d orbitals localized at surface and bulk atoms. The initial-state SCLS is therefore given by:

$$\Delta E_{3d}^{\text{is}} = \langle \psi_{3d}(\mathbf{R}_s - \mathbf{r}) | V_{\text{eff}}(\mathbf{r}) | \psi_{3d}(\mathbf{R}_s - \mathbf{r}) \rangle - \langle \psi_{3d}(\mathbf{R}_b - \mathbf{r}) | V_{\text{eff}}(\mathbf{r}) | \psi_{3d}(\mathbf{R}_b - \mathbf{r}) \rangle. \quad (1)$$

The calculation of the SCLS in the initial-state picture as described above does not account for relaxation effects. In the photoemission experiment the initial state consists of a crystal in its ground state plus a photon, and the final state is a crystal with a core hole plus a photoelectron. If we assume the Fermi-level as a reservoir of electrons the crystal remains neutral. The charge of the core hole is compensated by a delocalized electron at the Fermi energy. The final-state SCLS can therefore be calculated as an energy difference between neutral slabs containing screened core holes at the surface or in a bulk-like environment of neutral slabs. Thereby the relaxation of the crystal electrons in the presence of the electron-hole pair is fully accounted for. For the explicit calculation we generated 'excited' Bachelet-Hamann-Schlüter-like pseudopotentials [10] in Kleinman-Bylander form [11,12] with a screened 3d core hole, i.e. the occupation of the 3d level is decreased by one, and the number of the 4p electrons is increased accordingly. This procedure

has been suggested by Pehlke and Scheffler [13] and more or less successfully applied to Si(100) and Ge(100) surfaces.

Our calculations were performed with periodic supercells, which contain 11 to 14 substrate(110) and adatom layers and a vacuum region equivalent in thickness to at least 6 GaAs(110) layers. For calculations of initial-state SCLS a 1×1 surface periodicity has been used whereas calculations of final-state SCLS have been done with 1×2 unit cells in order to minimize the interactions between the screened core holes in neighboured cells. In order to account for the electronic inequivalence of the two slab sides induced by the substitution of 'regular' by 'excited' atoms we apply a dipole correction to compensate for the artificial electrostatic field. All calculations were performed with an energy cutoff of 15 Ryd for the plane-wave basis set. The k -space integration was performed by a summation over 4 special points in the irreducible part of the surface Brillouin zone. We have performed a series of tests with larger unit cells, higher energy-cutoff and more k -points to make sure that our results are reliable.

3. Results and discussion

The GaAs(110) surface is probably the most intensively studied surface of binary semi-conductors. A series of experiments [8] arrived at quite similar results for the observed SCLS. The surface component of the Ga atom 3d photoelectrons is reported to have a 0.28 eV lower kinetic energy than the photoelectrons originating from bulk Ga atoms. For the As atoms a shift of about 0.37 eV in the opposite direction has been reported. In Fig. 2a we show our calculated results for the initial-state SCLS. These results were obtained for a relaxed surface geometry with geometrical details determined in perfect agreement with Ref. [14]. With respect to the innermost atoms we observe the surface components of the Ga (As) atoms to be shifted by -0.18 (0.36) eV. Thus our calculated values in the initial-state picture compare reasonably with experiment. If we consider the difference in binding energy between the first and second layer cation we observe a somewhat larger splitting of -0.22 eV which agrees slightly better with the experiment. It is interesting to note that the

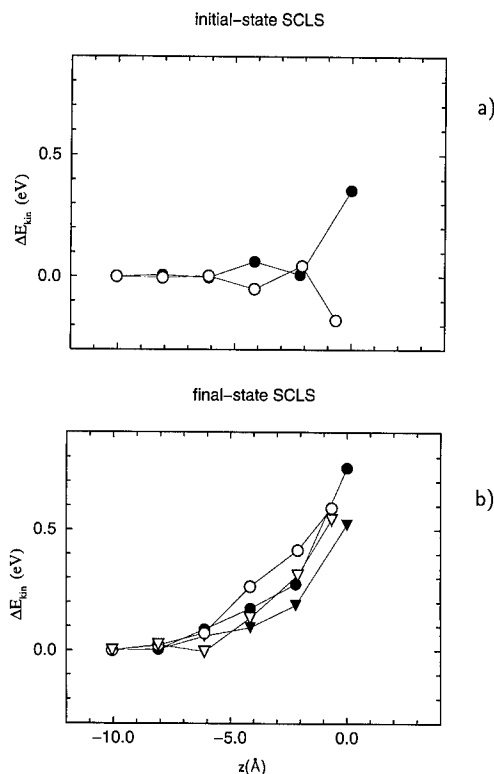


Fig. 2. Calculated SCLS for GaAs(110) in the initial and final-state picture. The energetic position of the 6th layer atoms has been chosen as energy zero. Ga (As) atoms are denoted by white (black) symbols. In case of final-state SCLS results for the electronic relaxation are denoted by circles whereas triangles are used for electronic and atomic relaxation.

core-level shifts both for anions and cations alternate in each layer. Obviously the change of the surface electronic structure due to the relaxation of the uppermost atoms influences the effective potential even several layers underneath the surface. However, the agreement between measured and calculated SCLS is not perfect. In particular the negative shift for the surface Ga atom is underestimated by about 0.1 eV.

One could assume that the remaining discrepancies are due to the complete neglect of relaxation effects. These effects are accounted for in the final-state picture. Our results for the final-state SCLS are shown in Fig. 2b. With black (white) circles the results for the SCLS of the anions (cations) in the frozen-lattice approximation are shown. In serious disagreement to experiment both surface components are now shifted to higher kinetic energies. If we

subtract the shifts due to initial-state effects we end up with the energies released upon the relaxation of the electronic wave functions. They amount to 0.40 (anion) and 0.77 eV (cation). Both the sign and the magnitude of the relaxation induced shifts can be understood in a simple physical picture. The accommodation of the screening electron is more easily done at the surface compared to the bulk, where the strong sp^3 hybridisation has to be disturbed. In particular the empty dangling bond at the surface Ga atom (the lowest unoccupied state in the GaAs(110) surface band structure, see e.g. Ref. [14]) allows a very efficient screening of the core hole in a surface cation. Therefore the relaxation of the electronic wave functions releases a particularly high amount of energy in case of surface Ga atoms. One possible reason for the complete disagreement between the calculated SCLS in the final-state picture and experiment could be that in addition to the electronic relaxation also the lattice relaxation has (at least partly) to be taken into consideration. In order to

check this possibility we also performed calculations where all atoms in the slab were allowed to relax until they occupied their equilibrium positions. The results are shown in Fig. 2b by means of black (white) triangles for the anions (cations). Obviously the overestimation of the relaxation effects with respect to the experimentally determined SCLS is somewhat smaller, but the results are still by no means comparable to the experimental findings. Summarizing the results for the SCLS in the initial and final-state picture we conclude that the initial-state effects are most important for the explanation of the experimental data, at least in case of the GaAs(110) surface. The reason seems to be the dynamics of the photoemission process. Due to the relatively large band gap the screening is less complete and the relaxation of the electronic wave functions is too slow to have substantial influence on the kinetic energy of the photoelectrons. This interpretation is also consistent with earlier model calculations which explain the SCLS for III–V(110) surfaces

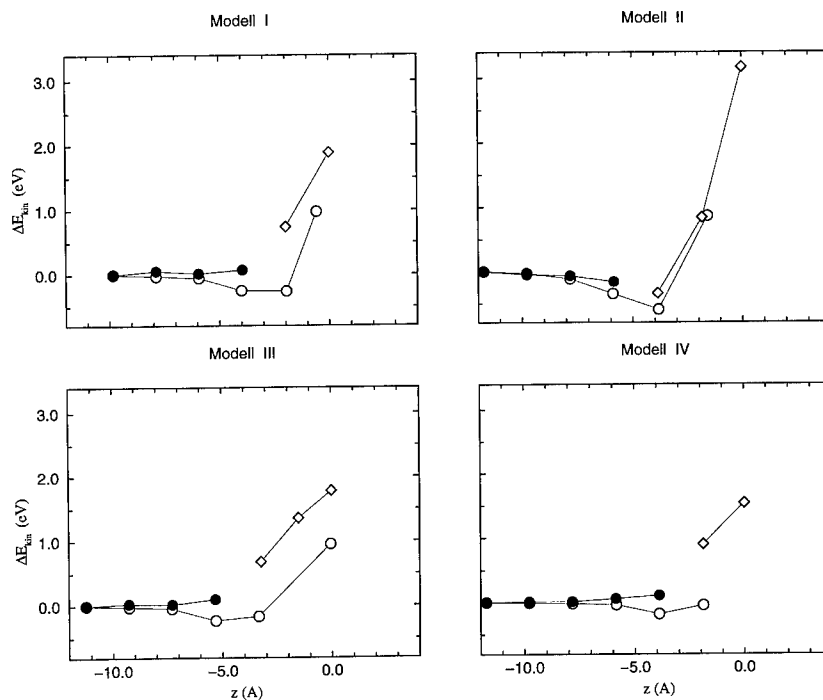


Fig. 3. Calculated initial-state SCLS for four structural models for the Se reacted GaAs(110) surface. Ga, As, and Se atoms are denoted by white circles, black circles and white diamonds. The energetic position of the innermost layer has been chosen as energy zero for Ga and As atoms. The energy zero for the Se atoms refers to a separate bulk calculation for Se in its trigonal modification.

solely on the ground of the different Madelung energies for bulk and surface [8]. It is interesting to note that Pehlke and Scheffler [13] also find a shift to higher kinetic energies for the photoelectrons originating from the surface atoms compared with the experimental findings for Si and Ge (100) surfaces. However, due to the smaller surface band gaps in these cases and the accordingly changed relaxation dynamics the explanation of the SCLS in the final-state picture is more satisfactory.

On the basis of the experience gained with the free GaAs surface we will restrict ourselves to the initial-state picture in the following discussion of SCLS for Se/GaAs(110). Characteristic features of the core level spectra for Se-deposited surfaces have been described recently by Schröter et al. [6]. Due to the Se treatment three components were reported to be necessary to fit the As component. They originate from bulk GaAs, As bound to Se, and liberated elemental As. Upon annealing to 710 K the latter two components nearly disappear and there is only the GaAs bulk component left. The Se induced change in the lineshape of the Ga 3d emission was said to be more complicated to analyze. Probably the Ga surface component is replaced by a reacted chemically shifted component at almost the same energy. Two components were needed to describe the Se signal. Using the energy position of the elemental Se as a reference they were reported to be 0.4 and 1.0 eV shifted to higher kinetic energy. As discussed above four structural models have been proposed to explain the experimental findings for the annealed Se/GaAs surface. These models are sketched in Fig. 1. For the relaxed geometries of these models [7] we calculated the initial-state SCLS. The results are shown in Fig. 3. For all four models we observe only moderate shifts for the As components which is in agreement with experimental findings. However model I, II and III have Ga surface components which are shifted to higher kinetic energies in contrast to the experimental statement. Model II and III can also be excluded since they show three Se 3d components with different energies (separated by 0.5 and 2.3 eV for model II and 0.4 and 0.7 eV for model III). Only model IV is consistent with the experimental findings. The two Se 3d components are separated by 0.6 eV. In order to approximate the chemical shift with respect to elemental Se we calcu-

lated bulk selenium in its trigonal configuration. The two Se components of model IV are shifted by about 0.9 and 1.5 eV towards higher kinetic energy. This shift is somewhat overestimated compared to the experiment. The sign of the Se shift with respect to elemental selenium agrees well with electronegativity arguments and a detailed analysis of the electronic structure [7]. Se is more electronegative than Ga and As [15] and therefore additional charge is accumulated around the Se atoms. The charge accumulation decreases the binding energy of the core electrons. The surface Ga components of model IV are placed at slightly higher energies than found experimentally. However, this overestimation should perhaps not be taken too seriously since the experimentalists had difficulty to resolve the Ga signal. In agreement with the experiment we observe nearly no shift in the As signal.

4. Conclusions

We performed ab initio calculations of the SCLS for free and Se-treated GaAs(110) surfaces. For the free GaAs(110) surface we show that the experimental results can be understood in the initial-state picture. Inclusion of relaxation effects grossly deteriorates the results, indicating the different time constants for photoemission and relaxation processes.

On the basis of our calculated SCLS for different atomic configurations for Se/GaAs we can with certainty exclude three out of four discussed models. One model shows reasonable agreement in the calculated and measured SCLS. We therefore strongly support an exchange geometry where the surface As atoms are substituted by Se and further Se atoms are bound to the surface Ga atoms.

We have shown that the comparison of calculated and measured SCLS can be used as a powerful tool to determine surface chemistry and atomic structure.

Acknowledgements

We acknowledge financial support by the Deutsche Forschungsgemeinschaft (project No. Be 1346/6-1) and the EU Programme Human Capital and Mobility (contract No. ERBCHRXCT 930337).

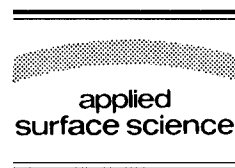
References

- [1] T. Ohno and K. Shiraishi, *Phys. Rev. B* 42 (1990) 11194.
- [2] T. Ohno, *Surf. Sci.* 255 (1991) 229.
- [3] H. Shigekawa, H. Oigawa, K. Miyake, Y. Aiso, Y. Nannichi, Y. Saito, T. Hashizume and T. Sakurai, *Appl. Surf. Sci.* 75 (1994) 169.
- [4] D.W. Tu and A. Kahn, *J. Vac. Sci. Technol. A* 3 (1985) 922.
- [5] C.R. Bonapace, D.W. Tu, K. Li and A. Kahn, *J. Vac. Sci. Technol. B* 3 (1985) 1099.
- [6] T. Schröter, A. Chassé, I. Eckardt, K. Tiedge, N. Wagner, D.R.T. Zahn, C. Nowak, A. Hempelmann and W. Richter, *Surf. Sci.* 307–309 (1994) 650.
- [7] W.G. Schmidt and F. Bechstedt, *Phys. Rev. B* 50 (1994) 17280; *Phys. Rev. B* 50 (1994) 17651.
- [8] W. Mönch, *Semiconductor Surfaces and Interfaces* (Springer, Berlin, 1993), and references therein.
- [9] J. Dabrowski, E. Pehlke and M. Scheffler, in: *Proc. 21st Int. Conf. on the Physics of Semiconductors*, Eds. P. Jiang and H.-Z. Zheng (World Scientific, Singapore, 1992) p. 389.
- [10] G.B. Bachelet, D.R. Hamann and M. Schlüter, *Phys. Rev. B* 26 (1982) 4199.
- [11] L. Kleinman and D.M. Bylander, *Phys. Rev. Lett.* 48 (1982) 1425.
- [12] X. Gonze, P. Käckell and M. Scheffler, *Phys. Rev. B* 41 (1990) 12264; X. Gonze, R. Stumpf and M. Scheffler, *Phys. Rev. B* 44 (1991) 8503.
- [13] E. Pehlke and M. Scheffler, *Phys. Rev. Lett.* 71 (1993) 2338.
- [14] J.L.A. Alves, J. Hebenstreit and M. Scheffler, *Phys. Rev. B* 44 (1991) 6188.
- [15] *Table of Periodic Properties of the Elements* (Sargent-Welch, Skokie, IL, 1980).



ELSEVIER

Applied Surface Science 104/105 (1996) 147–151



Optical study of potassium growth on the Si(100) surface

M. Roy, Y. Borensztein *

Laboratoire d'Optique des Solides, UA CNRS 781, Université Pierre et Marie Curie, Case 80, 4 place Jussieu, 75252 Paris Cedex 05, France

Received 28 June 1995; accepted 30 August 1995

Abstract

The formation of the Si(100)/potassium interface has been studied by real-time surface reflectance spectroscopy, Auger electron spectroscopy and low energy electron diffraction. The changes of the Si optical reflectance have been followed as a function of the amount of K deposited at room temperature. The first step of adsorption gave rise to a phase transition which occurs at about 0.4 SML (where 1 SML corresponds to the saturation monolayer). The corresponding optical spectra displayed peculiar features which could be due to a symmetrization of the dimers at the silicon surface. Two growth processes could be distinguished, which yielded different equilibrium states: a 'dynamic' process observed during K evaporation (with a saturation larger than 1 SML) and a 'static' one which takes place after the evaporation has been stopped (saturation at 1 SML). The optical spectrum corresponding to the saturation of the dynamic process displays an absorption band which is interpreted as due to resonances in small K clusters, as observed in free K cluster experiments.

1. Introduction

Alkali metal adsorption on the Si(100)- 2×1 surface has been widely studied for several years [1]. Among the main goals of the studies concerning the K/Si(100) are the determination of the metallic or semiconducting character of the interface, the exact mode of growth of the alkali film as a function of the experimental conditions, the saturation of the Si surface by K, etc. [2,3]. Although most of the surface sensitive techniques have been used for the investigation of the K/Si(100) interface, no or very few optical studies have been performed. We present in this paper results obtained by optical differential reflectivity spectroscopy (DRS), which has the ad-

vantage to be sensitive to changes of the surface or interface states, but also to plasmon-like resonances.

2. Experimental conditions

The Si samples were cut from intrinsic Si(100) wafers ($\rho > 200 \Omega \text{ cm}$) with no disorientation. They were cleaned by in-situ heating during 5 min at about 1000°C, then slowly cooled down, in order to get a sharp 2×1 low energy electron diffraction (LEED) pattern. The potassium was evaporated at a low rate from a SAES getter source, which has been beforehand carefully degassed, on the Si sample maintained at room temperature. The base pressure was 1×10^{-10} Torr, and the increase of pressure during the evaporation was below 4×10^{-11} Torr. The amounts of K deposits were controlled by Auger

* Corresponding author.

electron spectroscopy (AES), which was used also to check the cleanliness of the initial Si surface. The AES and LEED experiments were performed by means of a four-grid spectrometer. The energy of incident electrons in AES was fixed at 900 eV.

The differential reflectivity spectroscopy is the measurement of the relative changes of reflectivity of the Si surface upon adsorption of K atoms. The measured quantity is the differential reflectivity (DR), given by: $\Delta R/R = (R_{K/Si} - R_{Si})/R_{Si}$, where R_{Si} and $R_{K/Si}$ are the reflectivities of the clean Si(100)- 2×1 surface and of the K-covered Si surface respectively. The optical apparatus is based on a Si photodiode optical multichannel analyzer, which permits one to perform real-time measurements. The photon energy range, which was extending from 1.1 to 5.5 eV, was provided by a quartz-halogen lamp and a deuterium lamp. A more detailed description of the apparatus can be found in Ref. [4].

3. Results and discussion

Because of the high reactivity of K atoms, a low base pressure together with a low increase of pressure during K deposition are needed, in order to grow a continuous K layer on the Si surface, with no contamination and without any growth of additional K layer. When these conditions are not reached, multilayer growth is observed [5]. Fig. 1 displays the ratio of the peak-to-peak K Auger signal at 252 eV and Si Auger signal at 92 eV, as a function of evaporation

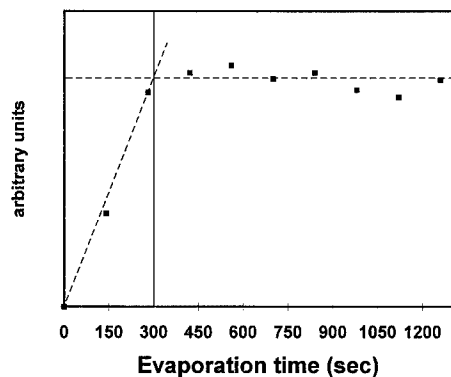


Fig. 1. Auger peak ratio K(252 eV)/Si(92 eV) as a function of evaporation time.

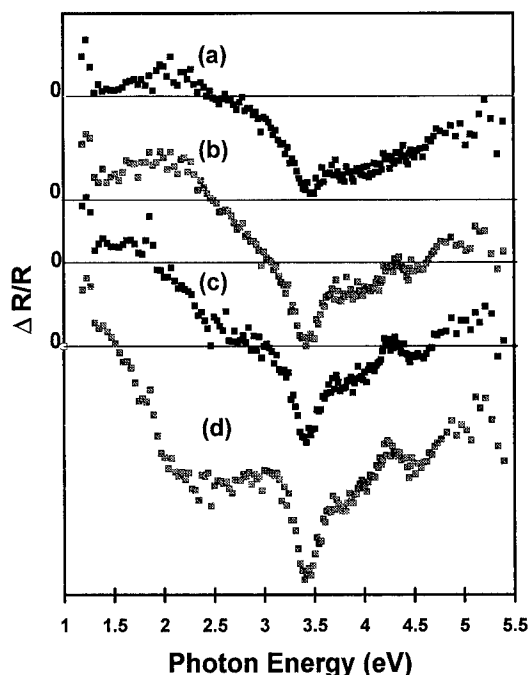


Fig. 2. $\Delta R/R$ spectra obtained on K/Si(100) at room temperature for different evaporation times: (a) 70 s; (b) 100 s; (c) 130 s; (d) 160 s.

time. Attention has to be paid to the fact that the latent period between the time when the current is set in the source and the time when evaporation begins, which can be estimated to about 30 s, has been removed from the times indicated on Fig. 1; moreover, as the points have been obtained by successive deposits on Si, the errors which are done from the estimation of the latent time are cumulative. In consequence, the absolute values for the times must be considered cautiously. Anyway, the shape of the curve is clear. The signal is first increasing up to about 300 s, then is saturating. This is the indication that only one K monolayer is formed on the Si(100) surface, without multilayer growth. The number of atoms which compose this monolayer cannot be determined from these experiments, and we will refer to it as the 'saturation monolayer' (SML).

The DR spectra were registered on-line during the K deposition. Fig. 2 displays four spectra measured before the achievement of the saturation monolayer. Contrary to the case of AES measurements, the DR spectra were registered in real-time, each 30 s, avoid-

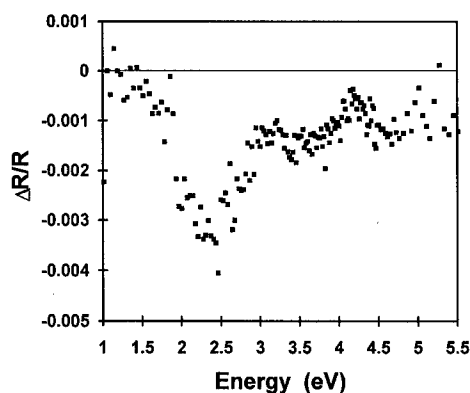


Fig. 3. Changes of $\Delta R/R$ from 100 to 130 s evaporation.

ing the uncertainty on the effective time deposition, apart from a possible initial error of a few seconds which is the same for all spectra. It will be shown later that the evaporation time where the saturation monolayer is obtained can then be more precisely measured from the optical measurements, and is about 280 s. We will consider in these spectra only two features. A sharp minimum at 3.4 eV is increasing and reaches a maximum depth for about 100 s. Then, another broader minimum is growing as a shoulder at 2.5 eV in the 130 s spectrum and becomes deeper in the 160 s spectrum. Although this is

not seen straight from the figure, the 3.4 eV minimum stops increasing at about 100 s. This comes by considering the difference between the 100 s spectrum and the 130 s one, drawn in Fig. 3. The 3.4 eV minimum is now no more visible, while the 2.5 eV shoulder appears as a clear minimum. A careful study of these spectra and of other ones obtained in experiments performed in the same conditions, show that the 3.4 eV minimum stops increasing at about 100–110 s, while the 2.5 broad minimum starts to grow at this deposition time. This intermediate coverage, reported to the one for the saturation coverage (280 s, as seen later), corresponds to 0.36 to 0.38 SML. This is precisely the coverage determined by [6] for the observation of a phase transition, from a poorly-ordered K–Si surface to a well-ordered one. The corresponding LEED patterns we obtained indicated indeed a better 2×1 ordered surface for $\theta \geq 0.4$ SML.

The 3.4 eV minimum is located at the E_1 bulk transition of Si [7]. Such a feature in the DR spectra has been observed during the adsorption of other atoms on Si(100) (H [8], Ag [9]), which indicates that it originates from the Si substrate. Theoretical calculations of the optical response of Si(100) with symmetric or asymmetric dimers [10] have shown that the corresponding spectra differ in particular by

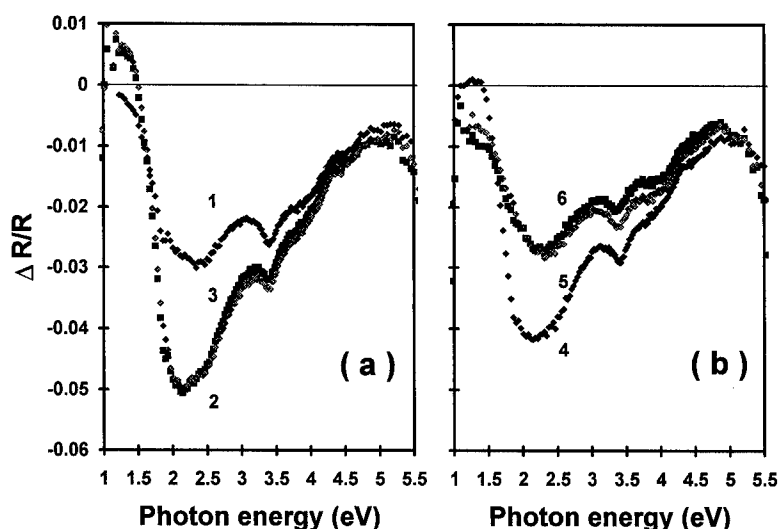


Fig. 4. $\Delta R/R$ spectra measured: during K evaporation (a), 280 s (curve 1), 370 s (curve 2) and 840 s (curve 3); after the stop of evaporation (b), 30 s (curve 4), 900 s (curve 5) and 900 s + 0.2 L of oxygen (curve 6).

a feature at this energy, and that the symmetrization of the dimers would result in a negative peak at 3.4 eV. It is now generally accepted that, at room temperature, most of the dimers on the Si(100) surface are asymmetric [11–14]. We therefore interpret the observed minimum at 3.4 eV as the symmetrization of the Si dimers on the surface induced by the presence of the K atoms. The symmetrization would be complete before the completion of the saturation monolayer, which can be explained by the long-range interaction between the dimers.

For larger amounts of K, the 2.5 eV minimum goes on becoming deeper (curve 1 of Fig. 4a, obtained at a deposition time of 280 s). Other experiments performed at higher temperature (80°C) have shown that there is no more change of the reflectance spectrum after this deposition time, which therefore corresponds to the saturation ML. On the contrary, at room temperature, the spectra continue to change after this time, but return to the 280 s spectrum in about five minutes after the evaporation has been stopped. This is illustrated in Fig. 4b, where the curve 5, registered 900 s after the stop of the deposition, has recovered the same shape and intensity as the 280 s curve. This state can be considered as a 'static equilibrium' of the saturation ML of K on the Si(100) surface. On the other hand, at room temperature, the spectra changes after the saturation ML has been formed, up to a second equilibrium state, a 'dynamic equilibrium'. This is shown by curves 2 and 3 in Fig. 4a, corresponding to 370 and 840 s of evaporation respectively. Almost no change is visible between curves 2 and 3, showing the saturation of the dynamic equilibrium. After the evaporation is stopped, a transition from the dynamic equilibrium to the static equilibrium is observed (spectra 4 and 5).

Indications on the origin of the main minimum around 2.5 eV in the saturation ML spectrum (curve 1), can be found by comparison with experiments obtained with atomic H adsorption on Si(100), which display similar features [8,15]. No specific state due to the H atoms themselves are expected, and the observed features can be interpreted as due to the changes or the removal of the Si(100) surface states because of the interaction with the H atoms. The theoretical results of Shkrebtii [10] for clean Si, which display a large feature between 1.5 eV and 3

eV, due to the dimers states and the back-bond states, reinforce this interpretation in term of the modification of the surface states of Si due to their interaction with the K atoms. The possible explanation of the 2.5 eV feature, as due to the excitation of plasmon-like resonance in the K monolayer, can be excluded. The exposure to a small amount of oxygen would indeed have destroyed this feature if due to a plasmon resonance, and curve 6 in Fig. 4b shows that almost no change is visible when exposing the K-saturated surface to 0.2 L of oxygen.

Finally, the dynamic equilibrium should correspond to extra deposits of K on the saturation ML. The investigation of this film is not easy, as it is unstable at room temperature. The equilibrium is reached when the number of K atoms which are deposited on the surface from the source is the same as the number of K atoms which are subliming from the surface. The corresponding DR curves 2 and 3 in Fig. 4a, display now a deeper and narrower minimum close to 2 eV, and also positive values below 1.5 eV. These features are typical of plasma resonances parallel and perpendicular to the surface in 3D K clusters, which have grown dynamically upon the continuous saturation ML [15,16].

Acknowledgements

We are grateful to P. Soukiassian for discussions and valuable advice.

References

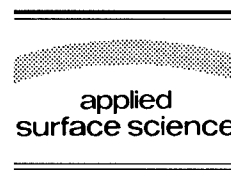
- [1] I.P. Batra, Ed., *Metallization and Metal–Semiconductor Interfaces* (Plenum, New York, 1989).
- [2] Y. Enta, T. Kinoshita, S. Suzuki and S. Kono, *Phys. Rev. B* 36 (1987) 9801.
- [3] T. Aruga, H. Tochihara and Y. Murata, *Phys. Rev. Lett.* 53 (1984) 372.
- [4] Y. Borenstein, T. Lopez Rios and G. Vuye, *Appl. Surf. Sci.* 41/42 (1989) 439.
- [5] P. Soukiassian, J.A. Kubby, P. Mangat, Z. Hurych and K.M. Schirm, *Phys. Rev. B* 46 (1992) 13471.
- [6] J.A. Kubby, X.J. Green and P. Soukiassian, *J. Vac. Sci. Technol. B* 9 (1991) 739.
- [7] S. Adachi, *Phys. Rev. B* 18 (1988) 12966.

- [8] M. Roy and Y. Borensztein, *Surf. Sci.* 331–333 (1995) 453.
- [9] Y. Borensztein and R. Alameh, *Surf. Sci.* 274 (1992) L509.
- [10] A.I. Shkrebtii and R. Del Sole, *Phys. Rev. Lett.* 70 (1993) 2645.
- [11] A.W. Munz, Ch. Ziegler and W. Göpel, *Phys. Rev. Lett.* 74 (1995) 2245.
- [12] J. Pollmann, P. Krüger and A. Mazur, *J. Vac. Sci. Technol. B* 5 (1987) 945.
- [13] F.J. Himpsel and D.E. Eastman, *J. Vac. Sci. Technol.* 16 (1979) 1297.
- [14] D.J. Chadi, *J. Vac. Sci. Technol.* 16 (1979) 1290.
- [15] M. Roy, Thèse de l'Université Paris 7 (1995).
- [16] C. Bréchnignac, Ph. Cahusac, F. Carlier and J. Leygnier, *Chem. Phys. Lett.* 164 (1989) 433; C. Bréchnignac, Ph. Cahusac, N. Kebaïli, J. Leygnier and A. Sarfati, *Phys. Rev. Lett.* 68 (1992) 3916.



ELSEVIER

Applied Surface Science 104/105 (1996) 152–157



A surface extended X-ray absorption fine structure study of tellurium adsorbed onto Si(100)

S.R. Burgess^{a,*}, B.C.C. Cowie^b, S.P. Wilks^a, P.R. Dunstan^a, C.J. Dunscombe^c,
R.H. Williams^a

^a Department of Electrical Engineering, University of Wales Swansea, Singleton park, Swansea SA2 8PP, UK

^b EPSRC Daresbury Laboratory, Warrington WA4 4AD, UK

^c Department of Physics and Astronomy, University of Wales Cardiff, P.O. Box 913, Cardiff CF2 3YB, UK

Received 28 June 1995; accepted 26 October 1995

Abstract

The adsorption of tellurium on Si(100) has been studied using surface extended X-ray adsorption fine structure (SEXAFS) and X-ray standing wave spectroscopy (XSW). This particular system is of interest due to its potential applicability in the surfactant aided growth of CdHgTe–CdTe–Si(100) based infra-red detectors. The Te/Si(100) structure was generated by depositing a thick layer (~ 100 Å) of CdTe onto a clean Si (2×1) double domain surface, and annealing the sample to 350°C. This resulted in a ~ 1 ML Te terminated surface where the (2×1) reconstruction was lost in favour of a (1×1) symmetry. X-ray absorption of the Te L_3 edge ($E = 4341$ eV), with a photon energy range of 4440–4700 eV, was probed using a total yield detection scheme. The SEXAFS results indicated that the Te atoms sat in 2-fold bridge sites directly above a fourth layer Si atom. The corresponding bond length was measured to be 2.52 ± 0.05 Å. The XSW measurements of the (400) reflection gave a coherent position of 1.63 ± 0.03 Å and a coherent fraction of 0.65. This is consistent with the breaking of the Si–Si dimers and thus could be an example of the phenomena of adsorbate-induced dereconstruction of the surface. These results are compared with those of Bennet et al. who examined a similar system using soft X-ray photoemission (SXPS) and the STM study of Yoshikawa et al.

1. Introduction

The use of tellurium as a surfactant to aid the growth of epitaxial germanium layers on Si(100) substrates is of great interest, as subsequent CdTe epilayers adopt a (100) orientation as opposed to the (111) orientation displayed when grown directly on Si(100) [1]. This system is particularly important for mercury cadmium telluride (MCT) devices on sili-

con, where the CdTe serves as a buffer layer for the growth of high quality MCT. Therefore, the technology developed for Si processing can be used for systems containing MCT devices.

The 4.2% lattice mismatch between Si and Ge leads to a Stranski–Krasanov growth mode, i.e. the first few monolayers are in layer by layer growth mode followed by the formation of Ge islands. Often, by introducing a thin layer (≤ 1 ML) of surfactant (arsenic [2,3], antimony [4,5] or tellurium [6,7]), thick epitaxial Ge layers can be grown on Si substrates. Much attention has been devoted to the As/Si and Sb/Si systems but comparatively few

* Corresponding author. Fax: +44-1792-295686; e-mail: ce-burges@swan.ac.uk.

techniques have been used to explore the Te terminated Si(100) substrates. Studies in the literature to date are (a) an STM study of various Te coverages in the range 0.25–3 ML [8], (b) an XPS study of Te on Si(100) [1].

Simple structural parameters, such as bond lengths and adsorption sites, are important prerequisites in order to understand the mechanisms of surfactant aided growth. In this work we present a structural study of the Te/Si(100) (1 × 1) phase using surface extended X-ray absorption fine structure (SEXAFS) and X-ray standing wave (XSW) spectroscopies.

The SEXAFS process is essentially the absorption of a photon by a bound electron; this electron is then ejected. The outgoing electron wave is subsequently backscattered from surrounding near-neighbour atoms. The final state is a superposition of the outgoing and backscattered waves giving rise to an interference effect, the oscillatory part of which is the EXAFS. Thus, SEXAFS is a short range order probe since this scattering is usually only confined to a few near neighbours. The variation in the X-ray absorption coefficient may be modelled theoretically yielding information on bond lengths and co-ordination numbers.

The XSW method exploits the interference between the incident X-ray wave vector E_0 and the diffracted wave E_h from the substrate diffraction planes H ; this sets up an interference wavefield inside, and to some extent, outside the crystal. This wavefield has a periodicity of the diffracting plane spacing and the nodal/antinodal planes are parallel to the diffracting planes. The phase, $\phi(\theta, E)$, between the E_h and E_0 changes from π to almost 0 as the rocking curve of the reflection is passed and in doing so the interference field moves half a layer spacing in the opposite direction to the H vector. The functional form of $\phi(\theta, E)$ can be calculated from the dynamical theory of X-ray diffraction. It is possible to predict the electric field intensity at a particular point in space. Likewise, if the electric field intensity about an emitting atom species is known, information about the local distribution of the emitting atom can be inferred. XSW measurements yield important structural parameters such as a coherent distance (D) from scattering planes, and also information on the order with respect to the scattering planes, coherent fraction (F). XSW mea-

surements are, in general, more sensitive to the adsorbate substrate registry than SEXAFS measurements, however, a combination of these two complementary techniques provides a powerful tool for structural analysis.

2. Experimental

The samples, thin Si wafers, were placed in an ultra-high vacuum (UHV) chamber having a base pressure of 5×10^{-11} mbar. The silicon samples were held in a standard UHV manipulator, which incorporated an e-beam heating facility. This allowed the sample temperature to be elevated to that required for thermal desorption of any surface contaminants. The manipulator rotation axis allows the sample to be rotated such that the sample surface can be parallel or perpendicular to the E vector of the incoming irradiating beam.

The (2 × 1) Si surface was prepared by repeated cycles of mild Ar ion sputtering ($E \approx 2$ kV and $P \approx 10^{-5}$ mbar) followed by a thermal anneal to a temperature of 900°C. The resulting surface was checked for oxygen and carbon contamination by electron induced Auger electron spectroscopy (AES). No contamination was observed to within the detection limit of the AES set up. The surface reconstruction was examined by low energy electron diffraction (LEED). On cooling below 100°C sharp (2 × 1) double domain LEED patterns were observed, indicative of a clean well ordered surface.

Cadmium telluride was evaporated from a well outgassed tantalum filament and the deposition rate monitored with a standard quartz crystal oscillator. A CdTe overlayer (~ 50 Å) was deposited onto the (2 × 1) surface at room temperature. The sample was subsequently annealed to $\approx 350^\circ\text{C}$ where the Cd was found to desorb, leaving behind ~ 1 ML of Te. The resulting overlayer formed a sharp (1 × 1) LEED pattern.

The SEXAFS and XSW experiments were carried out using the double crystal monochromator on beamline 6.3 Daresbury Laboratory, UK. For the Te L_3 edge (4341 eV) the instrumental resolution of the monochromator, using the Ge(111) crystals, was approximately $\Delta E \approx 1.2$ eV. This resolution is sufficient to perform the SEXAFS and XSW measure-

ments presented here. The full details of these techniques are published elsewhere¹ [10].

SEXAFS spectra were recorded for both near normal and grazing incidence with respect to the E vector, to give an indication of the adsorption site, using the strongly s-polarised synchrotron radiation. Normal incidence SEXAFS spectra contained a large extraneous feature due to the (400) Bragg reflection at 4565 eV, which severely shortened the usable EXAFS range available for analysis. However, by moving a few degrees off normal the signal from the (400) reflection increases in energy above that of the L_2 edge, and is thus removed from the energy range of interest containing the SEXAFS oscillations. The X-ray absorption was monitored by measuring the total yield of electrons from the sample; this was achieved by earthing the sample through a Keithly current amplifier. The resulting signal was proportional to the X-ray absorption and, hence represents the EXAFS signal. The monochromatised incident X-rays were monitored by measuring the current output of a thin Al foil which served as a reference signal. All spectra were normalised to this signal in order to eliminate any structure due to the monochromator and any fluctuations in beam intensity. The raw data was background subtracted using EXBACK, and the oscillations fitted using EXCURV92 [11]. Phase shifts were calculated within the framework of EXCURV92.

XSW lineshapes were recorded for the substrate and adsorbate (400) reflection at near normal incidence, as opposed to normal incidence, in order to avoid interference from the (220) reflection. Photoelectrons from the sample were collected with a hemispherical VSW HA100 analyser. This detector was aligned in the plane of polarisation and at 45° to the incident X-ray beam. The absolute energy corresponding to the (400) reflection was 4565 eV. This energy was determined by monitoring the drain current, due to the diffracted beam, from a screen placed directly below the beam entrance to the chamber. For the (400) measurement the Si Auger electron (1610 eV) and sample drain current served as a substrate signals while Te $2p_{3/2}$ photoelectrons

were used as an adsorbate specific signal. For the Si substrate Auger line signal to background (S/B) was 6:1. For the Te adsorbate signal S/B \approx 2:1. Theoretical XSW curves were generated by convolution of a Gaussian broadening function and calculated curves from the dynamical diffraction theory. Non structural parameters such as energy broadening and the Debye–Waller factor were obtained from the theoretical fit to the silicon substrate signal whilst constraining the coherent fraction $F \approx 1$ and the coherent distance $D = 0$. These parameters were then used to fit the adsorbate signal.

3. Results and discussion

SEXAFS spectra were recorded for both 81° and 49° grazing incidence for the (1×1) -Te/Si(100) system Fig. 1. The total yield detection scheme was utilised and an edge jump of $\sim 10\%$ was observed in the raw SEXAFS data. Shown in Fig. 2 are background subtracted and edge step normalised EXAFS $\chi(k)$ for near normal incidence, weighted by k^3 in order to emphasise higher energy data. The modulus of the corresponding Fourier transform is also shown together with the theoretical fit. In the analysis of both the grazing incidence and near normal incidence, the only parameters varied were the effective co-ordination number and the mean

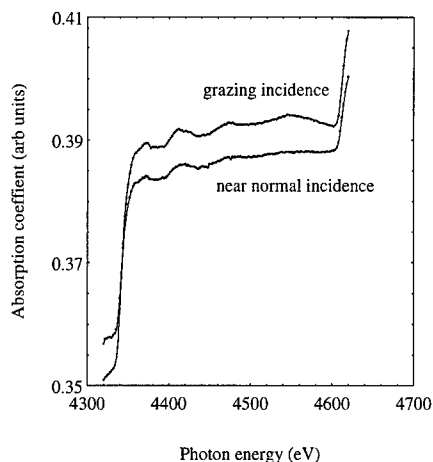


Fig. 1. Total yield SEXAFS data for the Te L_3 edge. Illustrated are both 81° and 49° grazing incidence spectra.

¹ For a complete discussion of the EXAFS/SEXAFS data analysis and formalism see [9].

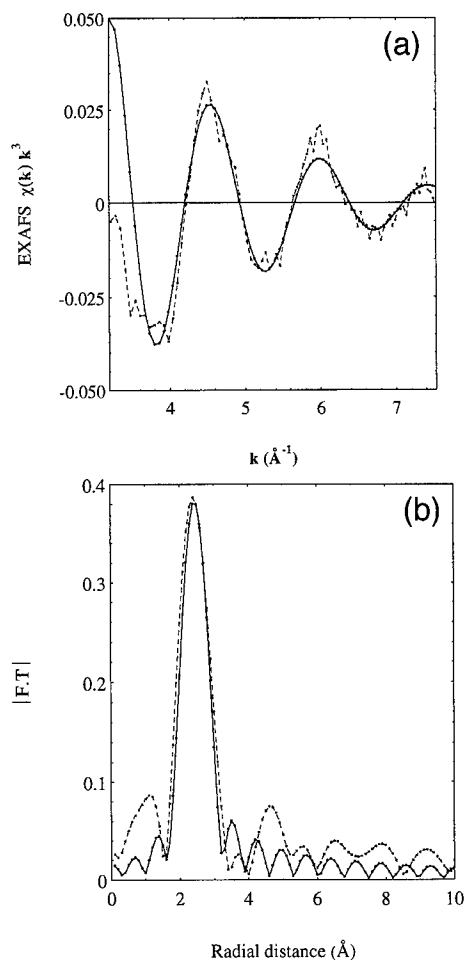


Fig. 2. (a) Total yield SEXAFS data $\chi(k)$ after background subtraction and edge step normalisation weighted by k^3 . (b) Modulus of the corresponding Fourier transform. Dash-dot lines are the experimental data and the solid-dot lines are the theoretical fits.

bond length associated with each shell of atoms. In both cases excellent fits to the data were obtained.

Distances of 2.53 ± 0.05 Å and 2.52 ± 0.05 Å were found for the first shell in near normal and grazing incidence respectively, giving an average bond length of 2.52 ± 0.05 Å. The principal contribution to the ± 0.05 Å error is the inherent uncertainty involved during the background subtraction processes. The amplitude ratio for near normal to grazing incidence was found to be 1.0 ± 0.2 . The fact that this result may indicate a disordered overlayer may be discounted due to the presence of the

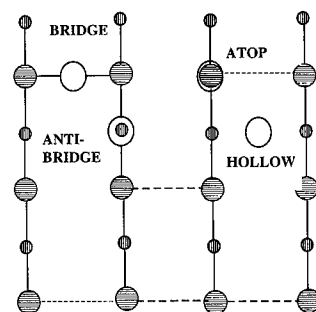


Fig. 3. Plan view of Te adsorbed on a (100) surface. Illustrated are the high symmetry sites considered in Table 1. Solid lines indicate the bond directions. White circles denote Te atoms and filled circles represent the Si substrate.

sharp (1×1) LEED pattern. To identify the adsorption site this experimental ratio is compared with the calculated ratio for several different high symmetry adsorption sites shown in Fig. 3. The effective coordination number (N^*) was calculated using the expression from [9], where θ_{ij} is the angle between a particular bond and the X-ray polarisation direction:

$$N_i^* = (0.5 + c) N_i + (1.5 - 3c) \sum_{j=1}^{N_i} \cos^2 \theta_{ij}.$$

The parameter c is the ratio of matrix elements for transitions from $l = 1$ to $l = 0$ and from $l = 1$ to $l = 2$ angular momentum states:

$$c = \left| \frac{\langle 0 | z | 1 \rangle}{\langle 2 | z | 1 \rangle} \right| = 0.2.$$

The calculated ratios for the various adsorption sites are shown in Table 1. The four-fold hollow site can be ruled out since the minimum bond length (corner atom to centre of square) is 2.71 Å and is clearly in excess of the experimentally determined bond length

Table 1

Table showing calculated versus experimental values of the effective coordination number ratio for several high symmetry adsorption sites

	Atop	Bridge	Hollow	Anti-bridge	Exp.
$N^*(81)$	0.71	0.91	ruled out	0.91	1.0 ± 0.2
$N^*(49)$					

N^* is calculated assuming $c = 0.2$ and an unreconstructed Si(100) surface.

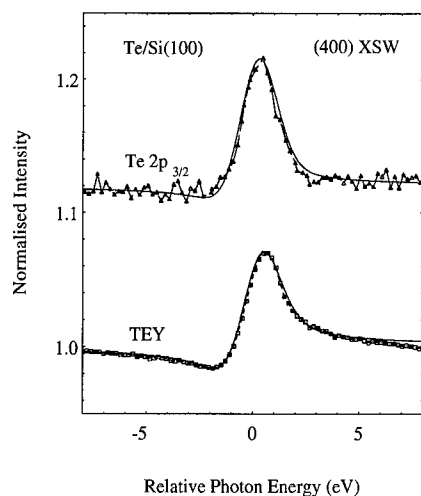


Fig. 4. Te $2p_{3/2}$ photoelectron and total electron yield (TEY) spectra of Te/Si(100) at the (400) Bragg condition. The dashed lines are the normalised experimental data and the solid lines are from the theory. The substrate profile was fitted with a broadening of 1.19 eV and a Debye–Waller factor of 0.90. The best fit to the adsorbate profile yields $D(\text{Te}) = 0.27 \pm 0.03 \text{ \AA}$ and $F(\text{Te}) = 0.65$.

$R_{\text{Si-Te}} = 2.52 \pm 0.05 \text{ \AA}$. Only the bridge and anti-bridge sites are consistent with the data. The bridge site consists of a Te atom between two Si atoms above a fourth layer Si atom and is thus parallel to the original Si–Si dimers in the (2×1) formed by clean-on silicon. This adsorption site is effectively a Si substitutional geometry. The anti-bridge site lies above a second layer Si atom, perpendicular to the dangling bond direction. Due to close proximity of the second layer Si atom, if the anti-bridge site were occupied a second shell in the data, around $\sim 2.9 \text{ \AA}$, would be observed. The SEXAFS results therefore indicate that the Te atoms are adsorbed in 2-fold bridge sites above fourth layer Si atoms with a Te–Si bond length of $2.52 \pm 0.05 \text{ \AA}$. However, although the data is of a high quality it is feasible that, in this case, the contribution to the SEXAFS signal from the second shell is not resolvable from the main Si–Te shell [9]. This point is addressed in the following section.

In Fig. 4 the results of the XSW photon energy scans for the (400) reflection from silicon are shown together with theoretical fits. The XSW lineshape for the adsorbate had a similar profile to that of the substrate signal for the same reflection. This can be interpreted as the Te atom occupying the site where

the next Si layer would have bonded, i.e. a substitutional site which in this case is the two-fold bridge site above a fourth layer Si atom. This is not consistent with the anti-bridge site postulated above. The results for the coherent fraction and coherent position are $F = 0.65$ and $D = 0.27 \pm 0.03 \text{ \AA}$ respectively. Any coherent distance measured using XSW is arbitrary to the addition of an integral number of scatter plane spacings. For the (400) direction the plane spacing is 1.36 \AA . Thus, the adsorbate atom may be displaced $0.27 \pm 0.03 + 1.36n \text{ \AA}$, where n is an integer, from the bulk extended (400) planes. Assuming a 2-fold bridge site the SEXAFS results indicate that the Te atoms are $1.63 \pm 0.05 \text{ \AA}$ above an unreconstructed Si surface. This is consistent with $n = 1$ for the XSW result which gives an coherent distance in the (400) direction of $1.63 \pm 0.03 \text{ \AA}$. In general, the coherent fraction is a measure of the overlayer order. Thus a coherent fraction close to unity is an indication that a single adsorption site is occupied in that direction. In this study, the low coherent fraction 0.65 may be interpreted in one of two ways: (a) more than one adsorption site is occupied by the Te atoms, or (b) there is in-diffusion at the interface leading to 35% of the Te atoms occupying disordered sites.

One possible model for a multiple adsorption site, consistent with the data presented here, is where the Te overlayer is slightly ‘rippled’, that is, the alternating Te atoms are displaced above and below a mean height of 1.63 \AA . In order to account for the coherent fraction of 0.65, each Te atom would need to be displaced $\pm 0.19 \text{ \AA}$ about the mean. If this were the case the two shells would be present in the SEXAFS data, the shells being separated by 0.38 \AA . However, the contribution from two or more separate shells is only resolvable if the shells are separated by a distance greater than 0.6 \AA . Indiffusion of tellurium is also a plausible model as a soft X-ray photoelectron spectroscopy (SXPS) study of this system by Bennet et al. [1] observed migration of Te into the Si(100) substrate.

Clearly the SEXAFS and XSW results presented here are, to a certain extent, in agreement with the photoemission study of Bennet et al. [1] and the STM study of Yoshikawa et al. [8] where both concluded that the Te adsorption site was the two-fold bridge site above a fourth layer Si atoms. In addition

the STM study revealed that the rows of Te lie perpendicular to the original Si–Si dimer row direction with a missing row of Te atoms every 5–6 rows. They explained the missing row as a mechanism to relieve strain due to the size difference between Si and Te (covalent radii are 1.17 Å and 1.32 Å respectively). This gives rise to a un-dimerised Si surface where the Te atoms shift position across the missing row of atoms. The XSW results presented here for the (400) reflection were only sensitive to the adsorbate position perpendicular to the surface and hence, these missing rows would not be detected. A similar XSW experiment, using the (220) or (111) Bragg reflections, would lead to the H vector having a component in the surface plane and thus give information on the missing row model. Indeed such a study is underway at present and will be published at a later date.

Yoshikawa et al. [8] also noted the presence of three dimensional Te clusters located in the missing rows which contributed to a streaky (1×1) LEED pattern. In their work elemental Te was evaporated onto clean (2×1) Si surfaces. However, a sharp (1×1) LEED pattern was always observed for the study presented here, possibly due to the different method to produce the Te overlayer using CdTe evaporation. Again it is possible that such clustering in the missing rows would also lead to a reduction in the coherent fraction perpendicular to the surface.

4. Conclusions

We have studied the 1 ML (1×1) Te/Si(100) system with SEXAFS and XSW. At this coverage the tellurium atoms were found to occupy two-fold bridge sites above fourth layer Si atoms, the rows of Te being perpendicular to the original Si–Si dimer direction. The SEXAFS results give a bond length of 2.52 ± 0.05 Å, which places the Te atoms 1.63 Å above an un-dimerised Si surface. This is in excellent agreement with the XSW result, which places

the Te layer 1.63 ± 0.03 Å above the bulk extended (400) planes. This in turn implies that there is no significant relaxation of the Si substrate and the results are thus consistent with the dereconstruction of the original (2×1) surface. The low coherent fraction of 0.65 for the (400) reflection could be due to a perfectly ordered ‘rippled’ Te overlayer. Alternatively, there may be some in-diffusion of Te into the Si substrate or there is some degree of islands formation. Further XSW experiments using the (111) and (220) reflections from Si are planned to resolve the issue of the low coherent fraction observed for the (400) reflection.

Acknowledgements

The authors gratefully acknowledge the financial support of both the Science and Research Council and Daresbury Laboratory.

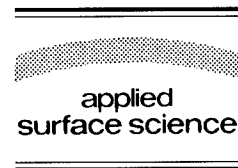
References

- [1] M.R. Bennet, J.W. Cairns, A.A. Cafolla and R.H. Williams, in: *Proc. ICFSI-4* (1993) p. 486.
- [2] R.D. Brinigans, R.I.G. Uhrberg, M.A. Olmstead and R.Z. Bachrach, *Phys. Rev. B* 34 (1986) 7447.
- [3] R.I.G. Uhrberg, R.D. Brinigans, R.Z. Bachrach and J.E. Northrup, *Phys. Rev. Lett.* 56 (1986) 520.
- [4] H.J. Osten, J. Klatt, G. Lippert, E. Bugiel and S. Hinrich, *Appl. Phys. Lett.* 60 (1992) 2252.
- [5] G. Meyer, B. Voigtlander and N.M. Amer, *Surf. Sci.* 274 (1992) 541.
- [6] S. Higuchi and Y. Nakanishi, *Surf. Sci.* 254 (1991) 1465.
- [7] H.J. Osten, J. Klatt, G. Lippert, E. Bugiel and S. Higuchi, *J. Appl. Phys.* 74 (1993) 2507.
- [8] S.A. Yoshikawa, J. Nogami, C.F. Quate and P. Pianetta, *Surf. Sci.* 321 (1994) 183.
- [9] J. Stohr, in: *Principles, Techniques and Applications of EXAFS, SEXAFS and XANES*, Eds. D. Koningsberger and R. Prins (Wiley, New York, 1984).
- [10] J. Zegenhagen, *Surf. Sci. Rep.* 18 (1993) 199.
- [11] N. Binstead, J.W. Cambell, S.J. Gurman and P.C. Stephenson, EPSRC Daresbury Laboratory EXCURV92 program (1991).



ELSEVIER

Applied Surface Science 104/105 (1996) 158–162



Optical spectroscopy study of hydrogenation of the Si(111)- 7×7 surface

M. Roy^a, C. Beitia^a, Y. Borensztein^a, A. Shkrebtii^{b,c,*}, C. Noguez^{b,d}, R. Del Sole^b

^a *Laboratoire d'Optique des Solides, Université Paris 6, 75252 Paris Cedex 05, France*

^b *Dipartimento di Fisica, Università di Roma "Tor Vergata", Roma, Italy*

^c *Institute of Semiconductors, 252028 Kiev 28, Ukraine*

^d *Instituto de Fisica, UNAM, 01000 Mexico D.F., Mexico*

Received 20 July 1995; accepted 11 September 1995

Abstract

Deposition of foreign atoms on silicon surfaces gives rise to a variety of phenomena, which are the subject of very active research. Fundamentally and technologically important, the chemisorption of hydrogen at Si(111)- 7×7 surface is still under debate due to its complex structure, the existence of different adsorption sites and the etching in the process of adsorption. We present both experimental and theoretical optical spectroscopy results on the atomic hydrogen adsorption at the Si(111)- 7×7 surface. The real-time optical, namely differential reflectivity, measurements were performed by means of an in-situ spectrometer with 60° angle of incidence. Structural changes upon H adsorption have been monitored by LEED. Microscopical calculation of the optical properties of the full scale Si(111)- 7×7 DAS structure was done within a sp^3s^* tight-binding approach. In order to model the structural changes due to H adsorption, we calculated the relative difference in reflectivity $\Delta R/R$ between the clean Si(111)- 7×7 and hydrogenated Si(111)- 1×1 :H surfaces. The surface optical response has been decomposed into the various components, due to surface-to-surface, surface-to-bulk, bulk-to-surface and bulk-to-bulk states transitions. The microscopic origin of the different contributions is discussed in detail. The comparison with the theoretical results allowed us to clarify the origin of the main optical peaks observed experimentally at the hydrogenated Si(111)- 7×7 surface.

1. Introduction

Process of hydrogen passivation and/or modification of the semiconductor surfaces is of both fundamental and applied interest.

Despite the Si(111) surface with hydrogen being an object of intensive investigation in the last decade

[1–6], a lot of structural, electronic features of the hydrogenation are not clear yet: as it is generally accepted, atomic H does not only saturate the clean surface dangling bonds (DBs), it also etches the Si(111)- 7×7 surface. The mechanisms of the Si(111)- 7×7 etching are complicated due to the variety of the dimer–adatom–stacking fault (DAS) structural units: adatoms (ADs), restatoms (RAs), stacking fault (SF), surface dimers (SD). These units are involved in the different stages of the interaction with H atoms. So, the process of the interaction

* Corresponding author. Institut für Festkörperphysik, Technische Universität Berlin, Sekr. PN 6-1, Hardenbergstr. 36, D-10623 Berlin, Germany.

between Si(111) 7×7 and H requires more careful investigation, especially in its intermediate states.

We have addressed this problem by means of optical differential reflectivity (DR) measurements in combination with microscopical calculations for the full size (7×7) DAS structure. In this paper we will discuss the origin of the optical transition at the clean Si(111) 7×7 surface, analyzing its optical response versus H-terminated (1×1) and (7×1) Si(111) surfaces. The correlation of the atomic microstructure in the process of H adsorption and the electron band structure (coming from quantum-mechanical calculations) allows us not only to clarify the origin of the observed main optical peaks, but as we will demonstrate, to gain also important structural information.

2. Experimental

The samples were cut from intrinsic Si wafers, then chemically cleaned following Shiraki procedure [7]. The oxide layer was then removed by flashing the sample at 1120 K during 5 min in the ultra-high vacuum chamber, with a base pressure of 10^{-10} Torr. The samples were then slowly cooled down in order to get a sharp 7×7 pattern observed by low-energy electron diffraction (LEED). Auger electron spectroscopy performed on samples prepared in the same way showed no, or very low, carbon contamination. Atomic hydrogen was produced by decomposition of H_2 molecules by a hot tungsten filament at 2070 K, previously heated at a higher temperature in order to eliminate any impurity. The real-time optical measurements were performed during the exposure to H, by means of an in-situ differential reflectance spectrometer, previously described [8]. The relative change of reflectance: $\Delta R/R = (R^{\text{clean Si}} - R^{\text{H/Si}})/R^{\text{clean Si}}$, is measured as a function of the photon energies. $R^{\text{clean Si}}$ and $R^{\text{H/Si}}$ are the reflectances of the clean and hydrogen-covered (7×1 and 1×1) Si surfaces respectively. The incidence of the light beam was 60° and the light was p-polarized. An important property of the $\Delta R/R$ quantity is that it is directly related to the optical absorption at the surface of the sample, and therefore provides direct information on the surface electronic transitions of Si and their changes induced by H adsorption.

Two experiments are compared here. The first one is the adsorption of a small amount of H (570 L) onto the Si sample maintained at room temperature, which resulted in a 7×1 reconstruction observed by LEED [4]. The second one consists in the adsorption of a larger amount of H (20 000 L) onto the Si sample heated at 800 K, which yielded a 1×1 reconstruction. LEED and STM experiments have proved that such an hydrogenation of the Si(111)- 7×7 leads to an ideal hydrogenated Si(111) 1×1 surface, where each dangling bond of the surface Si atoms is bound to one H atom [9].

3. Theoretical details

In order to calculate the optical response of the Si(111) 7×7 surface and of the hydrogenated 1×1 surface, we applied the well probed sp^3s^* tight-binding approach within the slab geometry (7 and 10 layers thick for the 7×7 and the 1×1 surfaces respectively). Theoretical atomic geometries (which are very close to these experimental ones) have been used in the calculation structure of 7×7 and 1×1 phases. Due to the fact that no experimental or theoretical structural data are present for the 7×1 structure, we did not calculate the optical response of this hydrogenated surface. Other technical details are similar to that of Ref. [10]. One should also stress that this theoretical treatment permits one to separate the contribution to the optical spectra coming from surface-to-surface (s-s) states transitions, bulk-to-bulk (b-b), bulk-to-surface (b-s) and surface-to-bulk (s-b) states transitions, which provides an important tool for understanding the origin of the experimental optical peaks.

The symmetry of the (7×7) DAS structure implies that the surface optical response is isotropic along the surface. Hence only differential reflectivity (DR) technique can be used to characterize experimentally the optical transitions at the Si(111) surface, while another useful optical technique as the reflectance anisotropy spectroscopy cannot succeed. For a direct comparison to the experiments, the theoretical DR has been defined as the difference of the reflectivities of the two different slabs: (7×7) versus (1×1). It is given in the following equation:

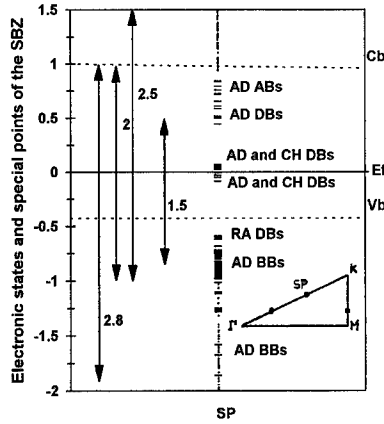


Fig. 1. The three special points in the irreducible SBZ, and the surface band structure at SP of the Si(111)-7×7. Dots and dashes denote bulk and surface states respectively. The zero energy is at the calculated Fermi level E_F , the top of the valence band and the bottom of the conduction band are indicated by Vb and Cb respectively. The main transitions between filled and empty states are indicated by arrows, and their energies are given in eV.

$$\frac{\Delta R}{R} = \frac{4\omega}{c} \cos \theta \operatorname{Im} \left\{ \left[(\epsilon_{Si}(\omega) - \sin^2 \theta) (\Delta \epsilon_{\parallel}^{7 \times 7}(\omega) - \Delta \epsilon_{\parallel}^{H-1 \times 1}(\omega)) + \epsilon_{Si}^2(\omega) \sin^2 \theta (\Delta \epsilon_{\perp}^{7 \times 7}(\omega)^{-1} - \Delta \epsilon_{\perp}^{H-1 \times 1}(\omega)^{-1}) \right] [(\epsilon_{Si}(\omega) - 1)(\epsilon_{Si}(\omega) \times \cos^2 \theta - \sin^2 \theta)]^{-1} \right\} \quad (1)$$

where θ is the angle of incidence, $\epsilon_{Si}(\omega)$ is the bulk dielectric function, and $\Delta \epsilon_{\parallel}^{7 \times 7}(\omega)$ (resp. $\Delta \epsilon_{\perp}^{7 \times 7}(\omega)$) and $\Delta \epsilon_{\parallel}^{H-1 \times 1}(\omega)$ (resp. $\Delta \epsilon_{\perp}^{H-1 \times 1}(\omega)$) are the calculated surface dielectric functions parallel (resp. perpendicular) to the surface plane, for the clean 7×7 Si surface and the hydrogenated 1×1 Si surface respectively¹. The imaginary part of the dielectric function was averaged at 3 special points [11] in the irreducible surface Brillouin zone (SBZ) (see Fig. 1). Transitions up to 13 eV were taken into account. Therefore, the calculated real part of the polarizability is accurate up to about 6 eV, after the Kramers–Kronig transform [12].

¹ The surface dielectric function is calculated subtracting the bulk dielectric constant (where the H covered layer is also included) from the slab dielectric function.

4. Results and discussion

The calculated surface band structure is shown in Fig. 1. Since it shows no significant dispersion (less than 0.1 eV) of surface states at different points in the irreducible SBZ, we will discuss the results at only one point, the special point SP shown in Fig. 1. Around E_F there are filled and empty DB-like surface states, with a predominant p_z character and mainly localized on ADs and CH atoms. In the following, the energies are referred to E_F . There are two groups of occupied surface states at -0.65 eV and from -0.75 eV to -1.25 eV. The former states (-0.65 eV) are DBs states located at RAs, while those with deeper energies are mainly backbonds (BBs) between ADs and first-layer atoms. Additional surface states are observed around -1.7 eV also with AD-first layer BBs character and a small dimer contribution. Above E_F , there are two overlapping groups of empty states. The states at 0.5 eV are mainly DBs located at ADs mixed with some back-antibonds (BAs) between ADs and second-layer atoms positioned just below them. The states at 0.7 eV are mostly AD back-antibonds with the atoms of the first layer. Further AD-first layer back-antibonding states are found at 1.3–1.5 eV. These states are not shown in Fig. 1, but they contribute to the optical response and are taken into account.

Fig. 2 gives the result of the calculation following Eq. (1). As no surface state is present on the Si(111)1×1-H surface in the investigated energy range, the features displayed by the spectrum are

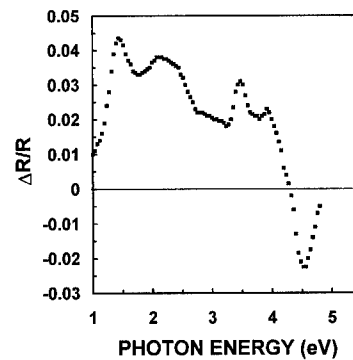


Fig. 2. $\Delta R/R$ theoretical spectrum obtained by subtracting the optical response of the Si(111)-1×1H surface to the one of the Si(111)-7×7 surface, with p-polarized light.

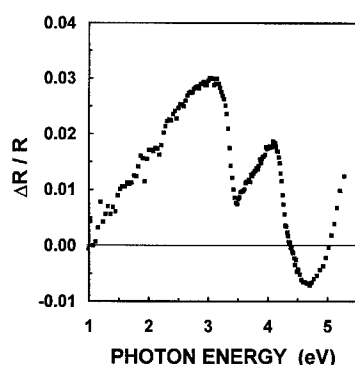


Fig. 3. $\Delta R/R$ experimental spectrum measured with p-polarized light after having exposed a Si(111)- 7×7 surface maintained at 800 K to 20000 L of atomic hydrogen.

mainly due to electronic transitions involving the surface states and the surface-modified bulk states of the clean 7×7 surface, drawn in Fig. 1. An analysis of the spectrum shows that up to 2.0 eV, the response is dominated by surface to surface (s-s) transitions, and from 2.0 to 3.0 eV by surface to bulk (s-b) transitions. The bulk to surface (b-s) transitions are small as compared with the other contributions. The states involved in the main s-s and s-b transitions are indicated by arrows in Fig. 1. The only s-s transition between 1 and 5.5 eV is a transition at 1.45 eV, from a AD-BB states to AD-DB states and AD-BA states, and from AD-DB just below E_F to AD-BA at 1.4 eV (not shown in Fig. 1). The s-b component shows a broad structure from 2.0 eV to 3.5 eV mainly due to transitions between AD-BB and bulk states in the conduction band. From 3.0 eV, the spectrum is dominated by

s-b and bulk to bulk (b-b) transitions. It shows a minimum at 3.2 eV, a structure with three maxima at 3.5 eV, 3.8 eV and 4.2 eV, and a deep minimum at 4.5 eV.

This theoretical spectrum has to be compared to the result of the experiment shown in Fig. 3, which gives the DR spectrum obtained after exposing the 7×7 Si surface to 20000 L of atomic H at high temperature, leading to the 1×1 -H surface. Apart from a general shift of 0.2 eV of the theoretical curve with respect to the experimental one, the main features previously described are present in Fig. 3, although with different relative intensities than in the calculation. In particular the s-s peak at 1.45 eV is reduced to a shoulder around 1.7 eV in the broad experiment feature between 1 and 3.4 eV. As previously shown [13], a very small H exposure permits us to clearly identify a peak at this energy, corresponding to H bound to the Si DB.

The s-b transitions between 2 and 3.2 eV are observed, with larger intensity for the transition around 3 eV than in the calculation. The s-b and b-b transitions which have a 'structural' origin, i.e. which are due to the etching of the Si ADs and to the removing of the SDs and the SF, are present above 3.2 eV: minimum at 3.5 eV, double peak at 3.7–4.1 eV, and deep minimum at 4.7 eV. The different peaks and shoulders observed in the theoretical and experimental spectra are summarized in Table 1, which demonstrates the good agreement between both curves despite the 0.2 eV shift and the different intensities.

Moreover, the effect of only structural change can be seen by comparing the DR spectrum in the Fig. 3

Table 1
Summary of the optical features observed both theoretically (Fig. 2) and experimentally (Fig. 3)

Theory		Experiment	
energy position (eV)	nature of the feature	energy position (eV)	nature of the feature
1.45	large peak	1.7	broad shoulder
2.1–2.5	double peak	2.4–3.2	large and broad structure
3	small broad peak		
3.25	minimum	3.5	minimum
3.5	large narrow peak	3.7	shoulder
3.9	peak	4.1	peak
4.3	shoulder	4.4	shoulder
4.5	negative minimum	4.7	negative minimum

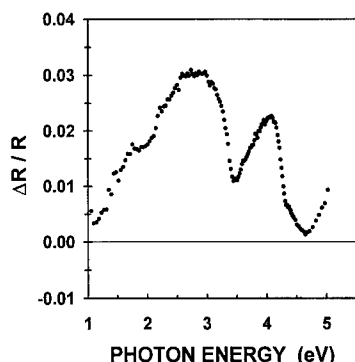


Fig. 4. $\Delta R/R$ experimental spectrum measured with p-polarized light after having exposed a Si(111)- 7×7 surface to 570 L of atomic hydrogen at room temperature.

and the one obtained for the 570 L of atomic hydrogen exposure on Si at room temperature (Fig. 4). In this second case, the temperature and the amount of hydrogen are not high enough to remove the SF. The spectrum in Fig. 4 is almost similar to the one in Fig. 3. The main difference is the absence of the negative values around 4.7 eV. The 4.7 eV minimum, well reproduced by the calculation (Fig. 2) can therefore be assigned to the bulk-to-bulk transition related to the stacking fault of the 7×7 reconstruction.

5. Conclusions

Both experimental and theoretical investigations of the hydrogen adsorption process of the Si(111)-

7×7 surface have been carried out. The process of the H saturation of the DBs leads to the evolution of the low energy part of the DR spectra, while the related structural changes have influence on the surface transition above the bulk optical continuum. At last, the negative DR at 4.5 eV is the optical signature of the removing of the SF and the restoration of the (1×1) terminated surface.

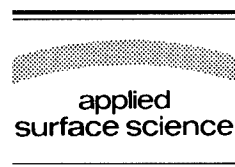
References

- [1] L. Ye, A.J. Freeman and B. Delley, *Phys. Rev. B* 48 (1993) 11107.
- [2] T. Sakurai, Y. Hasegawa, T. Hashizume, I. Kamiya, T. Ide, I. Sumita, H.W. Pickering and S. Hyodo, *J. Vac. Sci. Technol. A* 8 (1990) 259.
- [3] K. Mortensen, D.M. Chen, P.J. Bedrossian, J.A. Golovchenko and F. Besenbacher, *Phys. Rev. B* 43 (1991) 1816.
- [4] C.J. Karlsson, E. Landemark, L.S.O. Johansson, U.O. Karlsson and R.I.G. Uhrberg, *Phys. Rev. B* 41 (1990) 1521.
- [5] A. Ichimiya and S. Mizuno, *Surf. Sci.* 191 (1987) L765.
- [6] U. Jansson and K.J. Uram, *J. Chem. Phys.* 91 (1989) 7978.
- [7] A. Ishizaka and Y. Shiraki, *J. Electrochem. Soc.* 133 (1986) 666.
- [8] Y. Borensztein, T. Lopez-Rios and G. Vuye, *Appl. Surf. Sci.* 41/42 (1989) 439.
- [9] C.J. Karlsson, F. Owman, E. Landemark, Y.C. Chao, P. Martensson and R.I.G. Uhrberg, *Phys. Rev. Lett.* 72 (1994) 4145.
- [10] C. Noguez, A.I. Shkrebtii and R. Del Sole, *Surf. Sci.* 331–333 (1995) 1349.
- [11] D.J. Chadi and M.L. Cohen, *Phys. Rev. B* 8 (1973) 5745.
- [12] A. Selloni, P. Marsella and R. Del Sole, *Phys. Rev. B* 33 (1986) 8885.
- [13] M. Roy and Y. Borensztein, *Surf. Sci.* 331–333 (1995) 453.



ELSEVIER

Applied Surface Science 104/105 (1996) 163–168



Dissolution and segregation of monolayer Cu, Ni and Co atoms on the Si(111)- $\sqrt{3} \times \sqrt{3}$ -Ag surface induced by thermal annealing

J. Yuhara ^{*}, R. Ishigami, D. Ishikawa, K. Morita

Department of Crystalline Materials Science, School of Engineering, Nagoya University, Furo-cho, Chikusa-ku, Nagoya 464-01, Japan

Received 28 June 1995; accepted 2 October 1995

Abstract

Concentration changes of monolayer Cu, Ni, and Co atoms on the Si(111)- $\sqrt{3} \times \sqrt{3}$ -Ag surface by isochronal annealing at temperatures from 150 to 700°C have been studied by means of LEED-AES-RBS techniques. It is shown that Cu atoms on the Si(111)- $\sqrt{3} \times \sqrt{3}$ -Ag surface dissolve into the Si bulk at a temperature of 250°C, and segregate back to the surface when Ag atoms decay from the surface on annealing at temperatures higher than 400°C. It is also shown that Ni atoms, which have once dissolved into the bulk, segregate back to the surface on annealing above 400°C. In the case of the Co/Si(111)- $\sqrt{3} \times \sqrt{3}$ -Ag surface, Co atoms preferentially dissolve into the bulk, a situation similar to that of Cu and Ni atoms on the Si(111)- $\sqrt{3} \times \sqrt{3}$ -Ag surface; however, no segregation of Co atoms has been observed upon annealing at higher temperatures. These results are discussed in terms of the heats of mixing between the Ag atoms and the co-adsorbates and also between the co-adsorbates and the Si substrate.

1. Introduction

Recently, binary metal adsorbates on the Si(111) surface have received intensive attention from fundamental and technological points of view [1–13]. One of the reason for such studies is that the atomic interactions at the surface may take place not only between the metal adsorbates and the Si substrate but also between two different metal adsorbates. It is expected that the coexistence of binary adsorbates may modify the potential barrier height for dissolution and sublimation of individual adsorbates. The modification of the potential barrier by adding the

foreign metal atom may produce a thermally more stable intermediate layer or may promote the thermal reaction at a lower temperature. Therefore, it is interesting to study the changes of the surface concentrations and of the atomic structures of 2D binary metal adsorbates on the surface, and to look for correlations between the atomic structures of these 2D binary metal adsorbates and the corresponding 3D binary metal alloys.

So far, the thermal behaviors of the binary metal adsorbates have been studied by several authors [2,3,6,7,9,12,13]. It has been shown that Au–Cu adsorbates form a Si(111)- $\sqrt{3} \times \sqrt{3}$ -(Au, Cu) structure [2,6], which is a 2D ordered phase of Au₄Cu [6]. In the case of Au–Ag adsorbates, it has been shown that Au–Ag binary adsorbates form a 2D solid solution on the Si(111) surface [7], which reflects the

^{*} Corresponding author.

bulk phase diagram. In contrast, it has been found that Ag and Cu atoms are separated from each other on the Si(111) surface, which also reflects the bulk phase diagram [3,9]. Thus, these facts indicate that there is a similarity between the surface phases of the binary noble metals on the Si(111) surface and their bulk alloy phases.

The effects of foreign noble metals on the thermal stability of noble metal adsorbates at the Si(111) surface have also been studied by the present authors [12]. They found that the thermal stability of Au atoms at the Si(111) surface is not influenced by room temperature deposition of Ag or Cu atoms and post annealings. On the other hand, Ag atoms deposited on the Au/Si(111) surface are less stable than silver on the Si(111)- 7×7 surface upon post annealing, but the thermal stability of Ag is not influenced by the deposition of Cu atoms. Moreover, Cu atoms deposited on the Si(111)- $\sqrt{3} \times \sqrt{3}$ -Ag and $\sqrt{3} \times \sqrt{3}$ -Au surfaces become very unstable on post annealing.

During isochronal annealings of the Cu/Si(111)- $\sqrt{3} \times \sqrt{3}$ -Ag surface, it has been recently found that when a certain amount of Ag atoms leaves the surface, the same amount of Cu atoms, which had once dissolved into the bulk, segregates back to the surface [9,12]. In order to understand such a segregation phenomenon, the thermal behaviors of Ni and Co adsorbates on the Si(111)- $\sqrt{3} \times \sqrt{3}$ -Ag surface have also been studied similar to the Cu–Ag system, because the Ni–Ag and Co–Ag binary systems are mutually immiscible. We found that the Ni atoms that had once dissolved into the bulk at low temperature will segregate back to the surface at a higher temperature [13].

In this paper, we discuss experimental results on the thermal behaviors of Cu, Ni and Co adsorbates deposited on the Si(111)- $\sqrt{3} \times \sqrt{3}$ -Ag surface with the aim to correlate the atomic interactions between two kinds of metal adsorbates to those between the metal adsorbates and the Si substrate.

2. Experimental

The specimen used was a mirror-polished n-type Si(111) wafer, $3 \Omega \text{ cm}$, with a size of $25 \times 3 \times 0.5 \text{ mm}^3$. The specimen was placed on a manipulator in

a conventional UHV chamber, which was evacuated to base pressures less than 3×10^{-10} Torr. The chamber was equipped with a 4 grid optics for LEED, a double pass cylindrical mirror analyzer for AES, a water-cooled solid state detector for RBS and two evaporation sources of metals (Ag and either Cu, Ni or Co).

The specimen surface was cleaned by repeated direct current heatings, for 5 min at no less than 1050°C at pressures below 5×10^{-10} Torr. After the cleaning process, a distinct 7×7 LEED pattern was observed, and the AES spectra did not show any traces of impurities such as C and O. Specimen temperatures higher than 600°C were measured with a radiation thermometer. Lower temperatures were measured with an alumel–chromel thermocouple.

A metal film about 1 ML thick (1 ML for Si(111) face = $7.8 \times 10^{14} \text{ atoms/cm}^2$) was deposited onto the cleaned Si(111)- 7×7 surface at room temperature. Then, the binary adsorbates on the Si(111) surface were prepared by post deposition of Cu, Ni or Co at room temperature onto a $\sqrt{3} \times \sqrt{3}$ -Ag surface produced by annealing a silver film at 350°C during 5 min. Both single and binary noble metal adsorbates on the Si(111) surfaces were isochronally annealed for 15 min at temperatures from 150°C to 700°C ; the surface structures and coverages were measured by means of LEED-AES-RBS techniques at several stages of the annealing to examine the effect of Cu, Ni and Co to Ag adsorbate.

The amount of deposited metal atoms was measured by RBS with an accuracy of about $\pm 0.05 \text{ ML}$ using a 1.5 MeV He^+ ion beam. A typical He^+ ion fluence to obtain a RBS spectrum is $1 \times 10^{15} / \text{cm}^2$. The effect of He^+ beam damages on the surface coverages was carefully tested by comparing RBS spectra taken both at irradiated and non-irradiated positions after several repeated annealings. No visible change due to beam damage was observed.

3. Experimental results

Ag, Cu, Ni and Co films, about 0.6–0.8 ML thick, deposited on the Si(111)- 7×7 surface were isochronally annealed at temperatures from 200°C to 700°C . The surface structures and the coverages

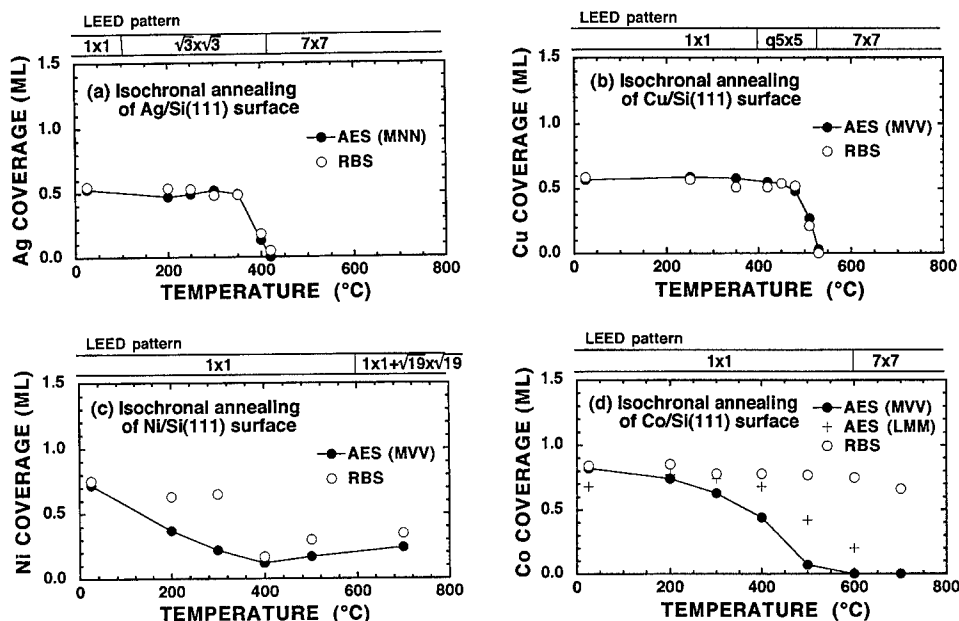


Fig. 1. Coverage changes versus temperature measured by AES and RBS on the Si(111) surface for (a) Ag; (b) Cu; (c) Ni; (d) Co.

determined by LEED, AES, and RBS at each annealing stage are shown in Fig. 1.

One notices in Fig. 1(a) and (b) that the decay curves of Ag and Cu measured by RBS are almost the same as those measured by AES. The Ag and Cu coverages decrease with annealing temperatures respectively above 350°C and 450°C. LEED observations showed a $\sqrt{3} \times \sqrt{3}$ pattern ($T \leq 400^\circ\text{C}$) for the Ag/Si(111) surface, and showed 1×1 ($T \leq 400^\circ\text{C}$) and quasi- 5×5 ($400^\circ\text{C} < T \leq 510^\circ\text{C}$) for the Cu/Si(111) surface.

Fig. 1(c) shows that the Ni coverages measured by AES decay faster than those measured by RBS. Ni coverages measured both by AES and RBS increase for annealing temperatures above 400°C. The LEED pattern changed from a 1×1 to a mixed 1×1 and $\sqrt{19} \times \sqrt{19}$ structure upon annealing at temperatures higher than 600°C.

Fig. 1(d) shows that the Co coverages measured by AES decrease at annealing temperatures above 300°C, yet the Co coverages measured by RBS almost do not change at all. The LEED patterns remained 1×1 on annealing at temperatures lower than 600°C.

The Cu/Si(111)- $\sqrt{3} \times \sqrt{3}$ -Ag surface was isochronally annealed at temperatures from 150°C to

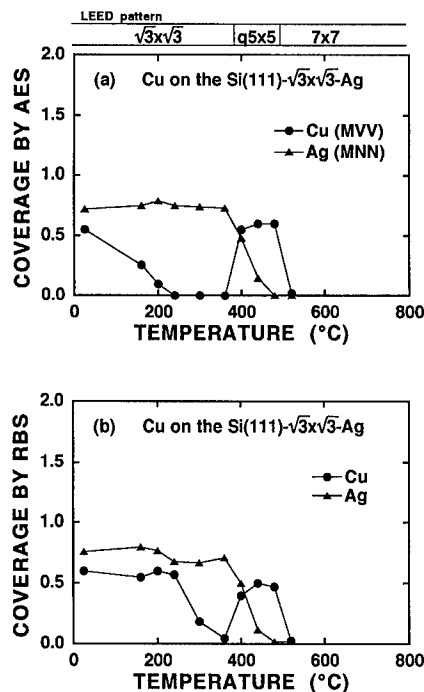


Fig. 2. Temperature variations of the Cu and Ag coverages on the Cu/Si(111)- $\sqrt{3} \times \sqrt{3}$ -Ag surface measured by AES (a) and RBS (b). The change of the LEED pattern is shown at the top of the figure.

520°C. The Cu and Ag coverages on the Cu/Si(111)- $\sqrt{3} \times \sqrt{3}$ -Ag surface measured both by AES and RBS are displayed as a function of annealing temperatures in Fig. 2. The LEED observations showed $\sqrt{3} \times \sqrt{3}$ ($T \leq 350^\circ\text{C}$), $\sqrt{3} \times \sqrt{3} + \text{quasi-}5 \times 5$ ($T = 400^\circ\text{C}$) and quasi- 5×5 ($450^\circ\text{C} \leq T \leq 480^\circ\text{C}$) structures. Clearly the Cu coverage starts to decrease at a temperature of 200°C and increases again at a temperature of 400°C. When the sample was annealed at 350°C, the intensity of Cu inside the Si crystal measured by RBS decreased to the background level, which corresponds to a Cu/Si concentration ratio of 0.02%. This result indicates that the Cu atoms migrate deeper than 3000 Å into the bulk.

Similarly, Ni and Ag coverages on the Ni/Si(111)- $\sqrt{3} \times \sqrt{3}$ -Ag surface measured by AES and RBS as a function of annealing temperature are shown in Fig. 3. The LEED patterns displayed successively $\sqrt{3} \times \sqrt{3}$ ($T \leq 350^\circ\text{C}$), $\sqrt{3} \times \sqrt{3} + 3 \times 1$ ($T = 400^\circ\text{C}$), 1×1 ($450^\circ\text{C} \leq T \leq 600^\circ\text{C}$), and $1 \times 1 + \sqrt{19} \times \sqrt{19}$ ($T \geq 600^\circ\text{C}$) structures. The Ni coverage starts to decrease at a temperature of 200°C and increases again at temperatures higher than 400°C.

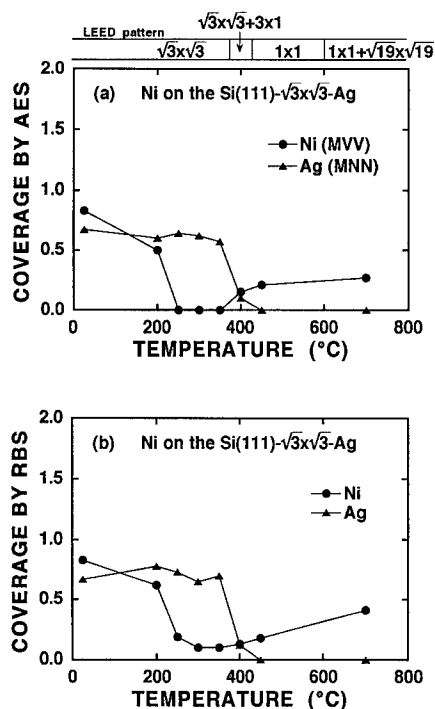


Fig. 3. Same as Fig. 2 but for Ni.

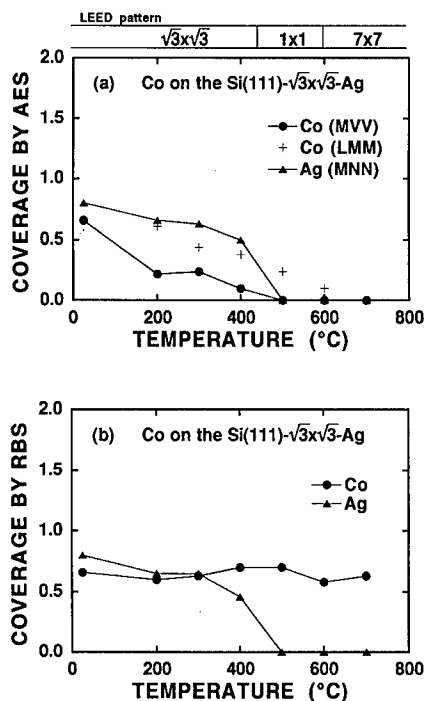


Fig. 4. Same as Fig. 2 but for Co.

The Co and Ag coverages on the Co/Si(111)- $\sqrt{3} \times \sqrt{3}$ -Ag surface measured by AES and RBS as a function of annealing temperature are also shown in Fig. 4. The LEED observation showed structures of $\sqrt{3} \times \sqrt{3}$ ($T \leq 400^\circ\text{C}$) and 1×1 ($500^\circ\text{C} \leq T \leq 600^\circ\text{C}$). The Co coverages measured by AES decrease at temperatures higher than 200°C, yet those measured by RBS do not change at all.

4. Discussion

We have seen that the variations of the Ag and Cu coverages measured by RBS are particularly the same as those measured by AES. This means that the location of the Ag and Cu adsorbates at the Si(111) surface do not change upon annealing, when the $\sqrt{3} \times \sqrt{3}$ -Ag and quasi- 5×5 structures are formed, respectively.

On the contrary, the Ni and Co coverages measured by AES decay faster than those measured by RBS. Since the coverages measured by RBS measure the total amount of atoms both at the surface and in

the sub-surface layers, the slow RBS decay curves of Ni and Co indicate that Ni and Co form the Ni- and the Co-silicides, respectively in the sub-surface layers at low temperatures. The Ni atoms diffuse rapidly into the Si bulk at a temperature of 400°C, while the Co atoms are stable in the sub-surface layers up to 700°C. This result is consistent with the fact that the Co-silicide is thermally more stable than the Ni-silicide [14]. The Co atoms do not make any superstructure at the surface but form the Co-silicide in the Si bulk, which points to a higher stability of the Co atoms in the bulk than at the surface.

Some of the Ni atoms, which have dissolved into the bulk, segregate back to the surface to form the $\sqrt{19} \times \sqrt{19}$ structure upon annealing above 600°C. The thermal behaviors of Au, Ag, Cu, Ni, and Co as single species on the Si(111)- 7×7 surface have been studied by isochronal annealing using LEED-AES-RBS techniques [12,13], and it has been observed so far that only the Ni atoms segregate back to the surface.

The Cu atoms on the Si(111)- $\sqrt{3} \times \sqrt{3}$ -Ag surface start to dissolve into the Si crystal upon annealing at a temperature of 150°C, but the Cu coverage on the clean Si(111)- 7×7 surface does not decrease on annealings up to 450°C. These facts indicate that the thermal stability of the Cu atoms is strongly influenced by the co-existence of Ag atoms. On the contrary, the thermal stability of Ag on Si(111) does not change, if Cu atoms co-exist. Further, the Cu atoms, which had once dissolved into the bulk, segregate back to the topmost surface, when the Ag atoms leave the surface upon annealings at temperatures higher than 400°C. We estimate from Fig. 2 that about 80% of the Cu atoms, which had dissolved into the bulk, have segregated back to the surface. This behavior indicates that the Cu atom location in the quasi- 5×5 structure at the surface is energetically more favorable than the solute site in the bulk.

The Ni atoms on the Si(111)- $\sqrt{3} \times \sqrt{3}$ -Ag surface start to dissolve into the bulk at 200°C and the Ni coverage measured by AES decreases to zero upon annealing at 250°C, while comparatively the Ni coverage on the Si(111)- 7×7 surface does not go down to zero for annealings up to 700°C. Hence the thermal stability of Ni atoms on the Si(111) surface is also influenced by the co-existence of Ag atoms. On the contrary, the thermal stability of Ag on

Si(111) is not influenced by the coexistence of Ni atoms. We also note that the Ni atoms segregate back to the surface for annealings above 400°C.

The Co atoms on the Si(111)- $\sqrt{3} \times \sqrt{3}$ -Ag surface start to dissolve into the Si crystal on annealing at 200°C, while the Co coverage on the Si(111)- 7×7 surface does not change at the same temperature. As for Ni, the thermal stability of Co atoms on the Si(111) surface is strongly influenced by the co-existence of Ag atoms, whereas the thermal stability of Ag on the Si(111) surface is not influenced by Co atoms. Even when the Ag coverage has decreased to zero, the Co coverages measured by RBS do not change at all up to the highest temperature of annealing; this is very similar to the case of Co/Si(111)- 7×7 . Thus, we conclude that the Co atoms do not segregate at the Si(111) surface regardless of the existence of Ag atoms.

The Ag atoms always remain on the surface, while the Cu, Ni, and Co dissolve into the Si bulk upon annealing at temperatures lower than 350°C. This common trend may be explained in terms of heats of mixing; the values of the mixed enthalpies for Cu–Ag, Ni–Ag, and Co–Ag are all positive and 0.08, 0.58, and 0.72 eV/atom respectively. This points to the presence of the repulsive forces against the mixing of these binary adsorbates. The value of the mixed enthalpy for Ag–Si is -0.15 eV/atom; it is much higher than the corresponding values of -0.35 , -0.89 , and -0.82 eV/atom for Cu–Si, Ni–Si, and Co–Si, respectively [15].

The segregation of Cu and Ni atoms in the absence of Ag at the surface may be related to the facts that Cu and Ni form thermally stable superstructures on the surface at variance with Co. When Ag leaves the surface upon annealings above 400°C, vacant sites are available for the Cu and Ni atoms diffused into the bulk to create their superstructures. As a matter of fact, more than half of the Cu atoms, which had dissolved into the bulk, segregate back to the surface.

5. Summary

The changes of the atomic structures and compositional ratios of Cu, Ni, and Co atoms on the Si(111)- $\sqrt{3} \times \sqrt{3}$ -Ag surface induced by isochronal

annealings at temperatures from 150°C to 700°C have been studied by LEED, AES and RBS. As long as the Ag atoms remain on the surface that is below 350°C, the Cu, Ni, and Co atoms dissolve into the Si bulk. The Cu and Ni atoms, which had dissolved into the Si bulk, segregate back to the surface, when the Ag atoms leave the surface upon annealing above 400°C, while no segregation of Co atoms has been observed even for annealings at higher temperatures.

The low temperature dissolution of Cu, Ni, and Co in the presence of Ag atoms at the surface has been reasonably explained in terms of heats of mixing between the Ag atom and its co-adsorbates and between the Si substrate and the co-adsorbates. The surface segregation behavior of the coadsorbates at the decay of Ag atoms at the surface is attributed to their specific surface properties.

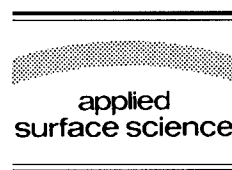
References

- [1] H. Daimon, C. Chung, S. Ino and Y. Watanabe, *Surf. Sci.* 235 (1990) 142.
- [2] I. Homma, Y. Tanishiro and K. Yagi, *Surf. Sci.* 242 (1991) 81.
- [3] I. Homma, Y. Tanishiro and K. Yagi, *The Structure of Surfaces III*, Vol. 24 (1991) 610.
- [4] A. Ichimiya, H. Nomura and Y. Horio, *Proc. 5th Topical Meeting on Crystal Growth Mechanism* (1992).
- [5] O.V. Bekhtereva, B.K. Churusov and V.G. Lifshits, *Surf. Sci.* 273 (1992) L449.
- [6] M. Sasaki, J. Yuhara, M. Inoue and K. Morita, *Surf. Sci.* 283 (1993) 327.
- [7] J. Yuhara, M. Inoue and K. Morita, *J. Vac. Sci. Technol. A* 11 (1993) 2714.
- [8] Y.L. Gavriljuk, V.G. Lifshits and N. Enebish, *Surf. Sci.* 297 (1993) 345.
- [9] J. Yuhara, R. Ishigami and K. Morita, *Control of Semiconductor Interfaces*, Eds. I. Ohdomari et al. (Elsevier, 1994) pp. 399–404.
- [10] J. Nogami, K.J. Wan and X.F. Lin, *Surf. Sci.* 306 (1994) 81.
- [11] A. Ichimiya, H. Nomura, Y. Horio, T. Sato, T. Sueyoshi and M. Iwatsuki, *Surf. Rev. Lett.* 1 (1994) 1.
- [12] J. Yuhara, R. Ishigami and K. Morita, *Surf. Sci.* 326 (1995) 133.
- [13] J. Yuhara, R. Ishigami, D. Ishikawa and K. Morita, *Surf. Sci.* 328 (1995) 269.
- [14] H.J. Goldschmidt, *Interstitial Alloys* (Butterworth, London, 1967) p. 296.
- [15] A.K. Niessen, F.R. de Boer, R. Boom, P.F. de Chatel, W.C.M. Mattens and A.R. Miedema, *CALPHAD*, Vol.7, No. 1 (Pergamon, New York, 1983) pp. 51–70.



ELSEVIER

Applied Surface Science 104/105 (1996) 169–175



Segregation of In atoms at clean and hydrogen passivated InP(100) surfaces

F. Stietz^a, Th. Allinger^a, V. Polyakov^a, J. Woll^a, A. Goldmann^a, W. Erfurth^b,
G.J. Lapeyre^c, J.A. Schaefer^{d,*}

^a *Fachbereich Physik, Universität Kassel, D-34132 Kassel, Germany*

^b *Max-Planck-Institut für Mikrostrukturphysik, D-06120 Halle, Germany*

^c *Department of Physics, Montana State University, Bozeman, MT 59717, USA*

^d *Institut für Physik, Technische Universität Ilmenau, D-98684 Ilmenau, Germany*

Received 28 June 1995; accepted 2 October 1995

Abstract

The InP(100) surfaces cleaned by ion bombardment and annealing (IBA) are known to be In-rich. Exposure to atomic hydrogen gives rise to an even higher In surface content. The nature of these In atoms at the clean and at the passivated surface was characterized by the techniques of ultraviolet and X-ray photoelectron spectroscopy (UPS, XPS) as well as low-energy electron diffraction (LEED), scanning electron microscopy (SEM), energy dispersive X-ray spectroscopy (EDX), and high-resolution electron energy-loss spectroscopy (HREELS). The heavily hydrogenated surface is dominated by metallic droplets of In. Line shape analysis can separate the contributions from these droplets and the non-metallic area in between, giving new insight into band bending at this surface. It is argued that the clean surface consists of In atoms bound in dimers. HREELS-spectra exhibit an interface plasmon at 93 meV, from which the carrier concentration can be directly determined via dielectric theory. Passivation of InP with atomic hydrogen shifts the plasmon energy to lower values. Finally, hydrogenation makes it possible to create particles from nanometer- to micrometer-size.

1. Introduction

In recent years there has been considerable interest in indium phosphide and related alloys because of their applications in many electronic and photonic devices. The progress in preparation and processing of InP-related materials, together with the development of highly reliable devices, has pushed the frontiers of the optoelectronics technology to very high levels of sophistication. Therefore, there are

greater demands on growth, processing and surface or interface characterization [1].

We prepared an In-rich InP(100) 4×2 surface by conventional cleaning procedures, i.e. ion bombardment and annealing. It is assumed that this surface consists of groups of three In dimers and one missing dimer [2]. In addition, it is possible that In is present in metallic form or not, which is crucial for the quality of an interface to be grown later. Ultraviolet photoemission spectra (UPS) will give an answer to this question [3]. Furthermore, X-ray induced photoelectron spectroscopy (XPS) in combination with low energy electron diffraction (LEED), electron energy loss spectroscopy (EELS), and scanning

* Corresponding author. Tel.: +49-3677-693609; fax: +49-3677-693205; e-mail: schaefer@phys.tu-ilmenau.de.

electron microscopy (SEM) are used to elucidate the reaction of hydrogen with the InP surface [3]. High-resolution electron energy-loss spectroscopy (HREELS) provides some direct information on the stoichiometry at the surface by using hydrogen as a local probe [4]. In addition, the space charge regime can be probed by HREELS because we are able to observe an interface plasmon before and after hydrogen interaction [5]. This communication gives a summary of our present understanding about clean and hydrogenated InP(100) surfaces.

2. Experimental

The experiments were performed in three different chambers: (1) The UPS/XPS-system consists of a preparation chamber and an analysis chamber separated by a gate valve. The analysis chamber is equipped with a hemispherical twin X-ray anode (Al/Mg, $h\nu = 1253.6$ eV/1486.6 eV) for XPS and a gas discharge lamp (He I/He II, $h\nu = 21.2/40.8$ eV) for UPS. The energy scale was referenced to the Fermi level of a clean polycrystalline indium sample. The XPS and UPS spectra were taken in normal emission. (2) The HREELS-system is equipped with LEED and XPS. In both systems the UHV cleaning of samples after bakeout consisted of Ne^+ ion bombardment at 500 eV and heating to 650 K. This treatment results in a 4×2 LEED pattern. For sample transfer to the scanning electron microscope (chamber 3) the samples were kept in a special container under inert gas. The In reference sample was etched in sulfuric acid and cleaned in vacuo by Ar^+ ion bombardment. For hydrogen exposure molecular hydrogen was admitted to the chamber through a leak valve and activated by a hot tungsten filament (2100 ± 100 K), which was in line of sight with the sample at a distance of about 5 cm. The values for the exposures are given in Langmuirs ($1 \text{ L} = 10^{-6}$ Torr s) and represent the product of the uncorrected ion gauge reading and the time the filament was heated.

3. Results and discussion

Fig. 1 shows core level spectra of the In 4d level excited by He II (40.8 eV) radiation. The In 4d level

at the clean surface (a) exhibits a doublet at 17.5/18.4 eV as well as a shoulder at 16.9 eV. The intensity of this peak is increasing with increasing hydrogen exposure, while the intensity of the doublet at 17.5/18.4 eV is diminishing. This is demonstrated in Fig. 1b–d. After exposure to 10^6 L (Fig. 1d), the spectrum resembles that of the In reference sample. For studying the intensity behavior of the In 4d line for different hydrogen exposures, we used fitting routines given elsewhere [3]. Lorentzians were convoluted by a Gaussian to take into account broadening from the analyzer and other mechanisms. This procedure results in the line shapes shown in Fig. 1

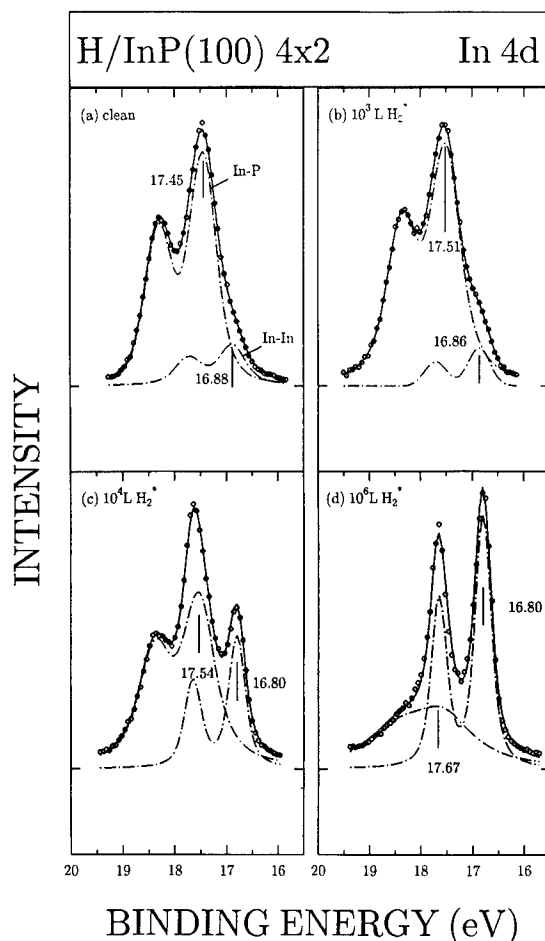


Fig. 1. UPS-spectra of the In 4d levels at the InP(100) surface: (a) clean (4×2), and after hydrogen exposure to (b) 10^3 L, (c) 10^4 L, (d) 10^6 L. Open circles are experimental data, the solid lines a fit to the experimental data, dash-dotted lines indicate the decomposition into two doublets.

with the hydrogen exposure as a parameter. The measured data are displayed as circles and the obtained model function as a solid line; the broken lines give the contribution of each doublet. Visual inspection gives direct evidence that at least two doublets have to be used. In fact, one expects an In bulk component, an In surface dimer component, and the In metal component. The latter gives an asymmetry which is rather small ($=0.02$) within the Doniach–Sunjic function [3]. Therefore the asymmetry has been neglected in our fitting routines. This reduces the number of parameters of the model function, which increased the reliability of our fit. Further, we assume the energetic positions of the In 4d line of In in a dimer configuration or In in a metallic surrounding to be degenerate, and consequently only two doublets are used. The bonding character related to this doublet can be rather different as evidenced by the full width at half maximum (FWHM), which decreases with increasing hydrogen exposure [2]. With increasing hydrogen exposure the intensity ratio of the In–In to the In–P component stays constant up to a hydrogen exposure of 10^3 L. With higher exposure the intensity ratio increases strongly. As shown in Fig. 2, the FWHM of the In–In component changes drastically from 0.76 eV at the clean surface to 0.51 eV for an exposure of 10^3 L. As

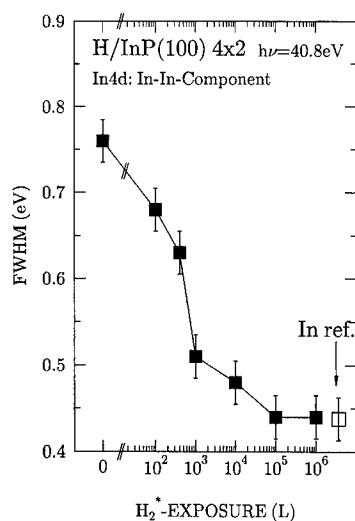


Fig. 2. Full-width at half-maximum of the In–In component as a function of hydrogen exposure, obtained from the line-shape analysis displayed in Fig. 1.

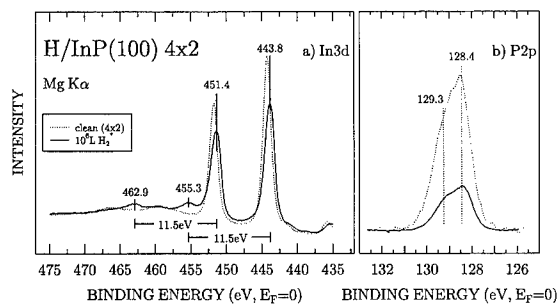


Fig. 3. XPS spectra of In 3d- and P 2p-lines for the clean (4×2) and the hydrogen treated (10^6 L) surface.

shown in the XPS-data (Fig. 4), the intensity ratio of the P 2p line to the In 3d line is almost unchanged up to this exposure as well. At this stage the surface reconstruction has already changed from a 4×2 to a 1×1 structure with a 4×1 structure in between. For higher exposure the FWHM of the In reference sample is approached. Simultaneously a strong phosphorous depletion can be observed in XPS as shown in Fig. 3, where the In 3d and the P 2p lines are displayed for the clean surface and after hydrogen exposure of 10^6 L. Furthermore, the shift of the In 3d line to lower binding energies and the appearance

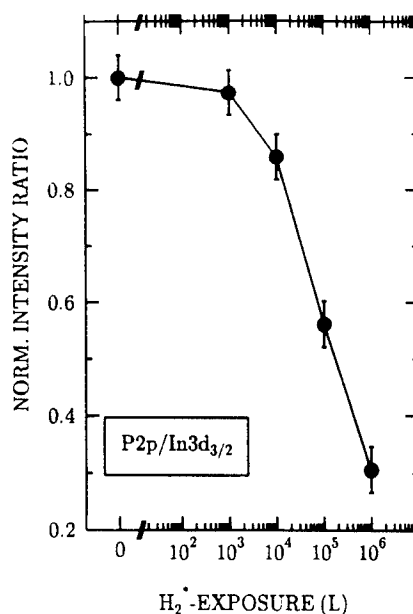


Fig. 4. Intensity ratio of the P 2p and the In $3d_{3/2}$ line, normalized to their initial values, as a function of hydrogen exposure.

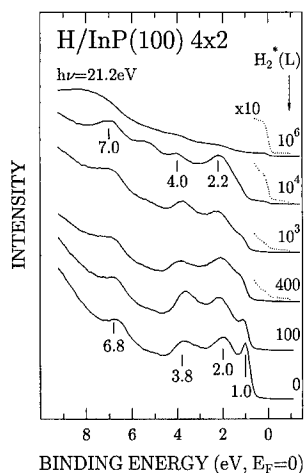


Fig. 5. Valence band spectra of the InP(100) 4×2 surface with the hydrogen exposure as a parameter ($h\nu = 21.2$ eV).

of the bulk plasmon (11.5 eV) of metallic In excited by photoelectrons from the In 3d line indicate a metallization of the sample. Fig. 4 gives the change in intensity ratio of the P 2p and the In $3d_{3/2}$ line. At higher exposure (10^3 L) there is a strong P depletion indicating an In surplus. Those changes are also reflected in the valence band spectra, as shown in Fig. 5. The peak at 1.0 eV which is attributed to a P dangling bond [6] is diminished drastically in intensity after a hydrogen exposure of 100 L. After 10^4 L exposure this peak has disappeared and a distinct Fermi edge (dotted line) is observed. Further exposure leads to an intensity reduction of the bulk features of InP and the spectral shape approaches that of the metallic In reference sample (not shown here). The peaks at 2.6 and 3.8 eV have been identified as bulk band emissions, the one at 6.8 eV as a density of states transition [6]. All of them show a shift of 0.2 eV towards higher binding energy, which is expected from the band bending shown in Fig. 5. There the change in band bending results from the shift of the In–P contribution in our In 4d-spectra (Fig. 1). If one would only evaluate the intensity maximum of the In 4d doublet and not take into account a distinction against other contributions, the band bending would actually increase drastically and not decrease, which is reasonable because of the In enrichment.

Evaluating the onset of the secondary electron emission and the position of the Fermi edge, absolute

values for the work function were determined. For the clean surface a value of 4.23 eV is obtained. Finally, after an exposure of 10^6 L the work function is 4.12 eV, a value identical to that of our metallic In reference sample. At this stage no pattern is observable anymore.

Fig. 6 shows HREELS spectra of undoped ($n = 1 \times 10^{16} \text{ cm}^{-3}$), and high level doped ($n = 1 \times 10^{19} \text{ cm}^{-3}$, sulfur) InP(100) 4×2 . Although the settings of the spectrometer were held constant, the full widths at half maximum (FWHM) are quite different: 19 meV for the undoped and 12 meV for the doped sample. Besides the commonly observed Fuchs–Kliwer phonons [7] at ± 42 meV, for the doped sample we measured a feature at 93 meV. This 93 meV feature is assigned to conduction electron surface plasmons [5,8–11] and is caused by high S-doping ($n = 1 \times 10^{19} \text{ cm}^{-3}$). Taking into account a band bending of 0.4 eV [3,12], a plasmon energy of 108 meV, would result, if measured under flat band condition. This value is obtained by using measurements at a cleaved GaAs(110) surface slightly contaminated with hydrogen [13]. Then a carrier concentration of $n_{\text{eff}} = 8.5 \times 10^{18} \text{ cm}^{-3}$ results from $(\hbar \omega_s)^2 = 4\pi n e^2 / (\epsilon_\infty + 1)$. The value determined in that way is close to the value given by the manufacturer. Therefore we have gained clear evidence that for preparing a clean and well ordered InP(100) 4×2 surface our experimental conditions play only a minor role in the creation of compensating acceptor states. For the undoped sample ($n = 10^{16} \text{ cm}^{-3}$) we measure no separate plasmon peak but a

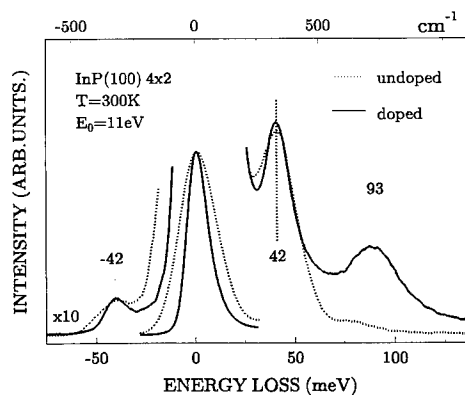


Fig. 6. HREELS-spectra for undoped ($n = 10^{16} \text{ cm}^{-3}$) and doped ($n = 10^{19} \text{ cm}^{-3}$) InP(100) 4×2 .

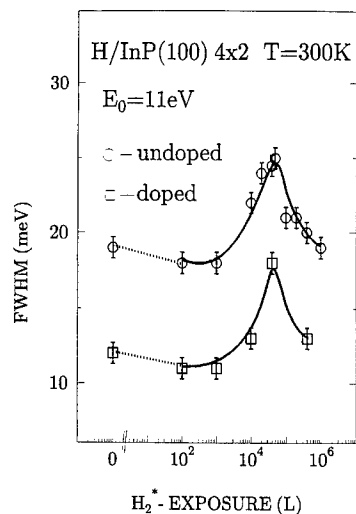


Fig. 7. Full width at half maximum (FWHM) of the quasielastically scattered electrons of InP(100) 4×2 as a function of hydrogen exposure.

broadening of the elastic peak, owing to the low carrier concentration [9]. Hydrogenation of InP shifts the plasmon energy to lower values, but in addition

there is a very strong influence on the full width at half maximum (FWHM) of the quasielastically scattered electrons, as shown in Fig. 7. After a slight drop of the FWHM, there is first a strong increase of FWHM from 12 to 19 meV and 16 to 25 meV, and then after even higher hydrogen exposure ($> 10^4$ L) a strong decrease. The increase in FWHM of the quasielastically reflected electrons can be explained by a strong carrier compensation, its decrease by the simultaneous creation of metallic indium at the InP surface, which reflects predominantly the incident electrons at this stage of hydrogenation. HREELS-calculations based on a two layer model, similar to those for GaAs(100) [5], are in progress.

Fig. 8 shows HREELS spectra for an undoped sample after gradual exposure of hydrogen up to 10^4 L. The peak of the elastically reflected electrons decreases in intensity. The stretching intensities of the indium hydride and the phosphorous hydride vibrations increase initially and then drop with hydrogen exposure. In the case of the indium hydride a complete disappearance of the signal is reached. First a passivation of dangling bonds up to an exposure of

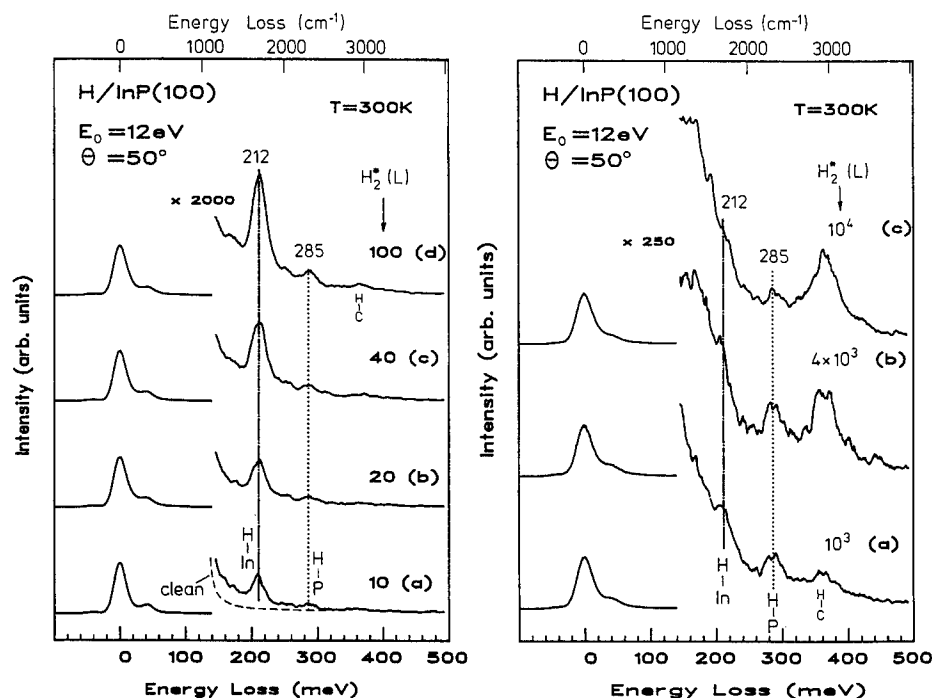


Fig. 8. HREELS-spectra of the InP(100) 4×2 surface after gradual hydrogen exposure up to 10^4 L.

100 L is observed. A ratio of about 0.2 is obtained between the intensity of the stretching vibration of the In–H and P–H. This reflects the situation of a 4×2 surface with three In dimers and one missing dimer in the 4×2 unit cell. Further hydrogenation leads to a 4×1 -surface, which is caused by a breaking of In dimers. From Fig. 8 it can be directly deduced that the P–H/In–H intensity ratio is changing from 0.2 to values higher than one. It is concluded from this result that there is a formation of indium hydrides, possibly InH_3 , which desorb into vacuum. Consequently, by the disruption of substrate surface bonds, the formation of phosphorous hydrides is increased. It is obvious from the spectra that the latter species are more stable than indium hydrides. It cannot be ruled out that phosphine also desorbs from the surface. We actually observe for an ion bombarded surface a decrease of the P–H stretching mode intensity with increasing hydrogen exposure. The structure around 360 meV is attributed to contamination by carbon hydrides, demonstrating the surface sensitivity of this method. The decrease in the indium hydride signal is also due to the formation of metallic indium clusters. Hydrogen adsorption at segregated metallic indium on InP cannot be investigated, because the surface optical phonons and their multiples cause a higher intensity than expected for the In (metallic)–H vibration in this

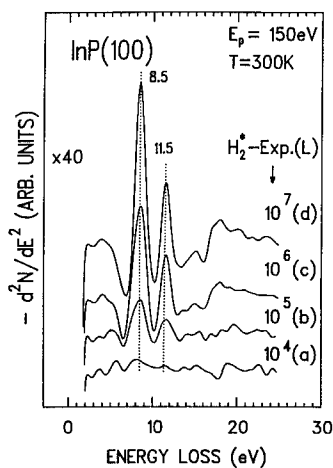


Fig. 9. EELS-spectra of InP(100) 4×2 after high hydrogen exposures (a) 10^4 L, (b) 10^5 L, (c) 10^6 L, (d) 10^7 L; primary beam energy: $E_p = 150$ eV, normal emission.

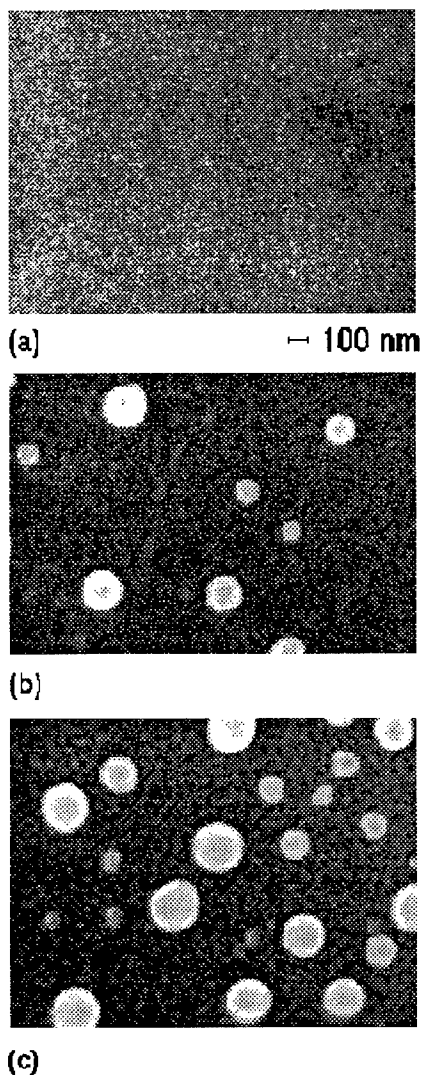


Fig. 10. SEM pictures of the InP(100) surface before (a), and after medium hydrogen exposure (10^4 L) (b), and after high hydrogen exposure (10^6 L) (c). After hydrogen exposure the samples were annealed at 650 K for 5 min. A beam energy of 20 keV and an enlargement of 25000 have been used.

case. As demonstrated before, at even higher hydrogen exposures plasmons of metallic indium become visible in XPS (Fig. 3) or in electron energy loss spectroscopy (EELS) as shown in Fig. 9. There EELS spectra are shown for a primary beam energy of $E_p = 150$ eV after different hydrogen exposures. The surface and bulk plasmons of metallic indium

are clearly resolved in the EELS-spectra after high hydrogen exposures at 8.5 eV and 11.5 eV, respectively.

The creation of metallic indium can be verified directly with scanning electron microscopy (SEM). The SEM picture of non hydrogenated InP(100) shows absolutely no contrast (Fig. 10). After an exposure of 10^4 L (b) or 10^6 L (c) and subsequent annealing, droplets with a diameter up to $0.2\ \mu\text{m}$ are seen. At a hydrogen exposure of 10^6 L the droplets of metallic In have slightly increased in size, and their number has increased drastically. Energy dispersive X-ray spectra (not shown here) clearly reveal the nature of the droplets as pure indium, whereas between the droplets there is almost no difference in the EDX spectra if compared to those of the untreated surface [3]. The thickness of these droplets for high hydrogen exposure (10^6 L) is $\geq 0.2\ \mu\text{m}$, as evidenced by cleaving the wafers and viewing the droplets in cross section (not shown here).

4. Summary

We conclude from our measurements that we have clear evidence for In dimer formation at the clean 4×2 surface. We are able to distinguish between In in a dimer configuration, In in a metallic environment and In in the InP matrix. We are able to monitor the space charge regime by the observation of carrier plasmons, which shift to lower energy by hydrogen diffusion into the bulk and subsequent carrier compensation. For low hydrogen exposures (100 L) there is first a passivation of the In–In dangling bonds and the phosphorous dangling bonds in the second layer of the 4×2 surface unit cell. Then, after further hydrogen exposures, the dimer bonds are broken and a 4×1 pattern results. Further hydrogenation leads to a 1×1 pattern, and finally to complete disorder. After higher exposures (10^3 L) the InP surface is indium rich owing to the build-up of phosphine and its subsequent desorption. By applying a line shape analysis we are able to give

results for the band bending in the areas between metallic segregations. The presence of metallic indium is directly and indirectly evidenced by different methods used in these experiments.

Acknowledgements

Financial support by the Deutsche Forschungsgemeinschaft is greatly appreciated.

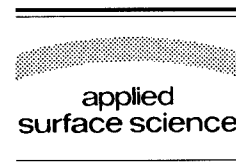
References

- [1] A. Katz, Ed., Indium Phosphide and Related Materials: Processing, Technology and Devices (Artech House, London, 1992).
- [2] J.A. Schaefer, Trends in Vacuum Science and Technology 1 (1993) 417, Eds. L.D. Brillson, R.A. Gottscho and S.J. Pearton (Swift offset Printers, Trivandrum, India); J.A. Schaefer, Appl. Phys. A (1990) 305.
- [3] J. Woll, Th. Allinger, V. Polyakov, J.A. Schaefer, A. Goldmann and W. Erfurth, Surf. Sci. 315 (1994) 293.
- [4] Th. Allinger, V. Persch, J.A. Schaefer, Y. Meng, H. De, J. Anderson and G.J. Lapeyre, Proc. SPIE, Vol. 1361, Physical Concepts of Materials for Novel Optoelectronic Device Applications I (1990) 935; J.A. Schaefer, F. Stietz, J. Woll, H.S. Wu, H. Yu and G.J. Lapeyre, J. Vac. Sci. Technol. B 11 (1993) 1497; F. Stietz, V. Persch, Th. Allinger, J.A. Schaefer and G.J. Lapeyre, J. Electron. Spectrosc. Rel. Phen. 64/65 (1993) 413.
- [5] V. Polyakov, A. Elbe and J.A. Schaefer, Appl. Phys. A 60 (1995) 567.
- [6] X. Hou, G. Dong, X. Ding and X. Wang, J. Phys. C 20 (1987) L121; F. Ladders, J. Westhof, J.A. Schaefer, H. Höpfinger, A. Goldmann and S. Witzel, Z. Phys. B 83 (1991) 263.
- [7] R. Fuchs and K.L. Kliewer, Phys. Rev. A 140 (1965) 2076.
- [8] H. Lüth, Festkörperprobleme/Advances in Solid State Physics, Vol. 21, Ed. J. Treusch (Vieweg, Braunschweig, 1981); H. Lüth, Vacuum 38 (1988) 233.
- [9] H. Ibach and D.L. Mills, Electron Energy Loss Spectroscopy and Surface Vibrations (Academic Press, New York, 1982).
- [10] Ph. Lambin, J.-P. Vigneron and A.A. Lucas, Phys. Rev. B 32 (1985) 8203.
- [11] Z.J. Cray-Crychowsk, R.A. Stradling, R.G. Egdell, P.J. Dobson, B.A. Joyce and K. Woodbridge, Solid State Commun. 59 (1986) 703.
- [12] F. Proix, Phys. B 170 (1991) 457.
- [13] Y. Chen, S. Nannarone, J.A. Schaefer, J.C. Hermanson and G.J. Lapeyre, Phys. Rev. B 39 (1989) 7653.



ELSEVIER

Applied Surface Science 104/105 (1996) 176–182



Electronic properties of antimony monolayers on III–V (110) surfaces: a comparative study by reflectance anisotropy spectroscopy and microscopic tight-binding calculations

A.I. Shkrebtii^{a,b,c}, N. Esser^{a,*}, M. Köpp^a, P. Haier^a, W. Richter^a, R. Del Sole^b

^a *Institut für Festkörperphysik der TU Berlin, Hardenbergstr. 36, D-10623 Berlin, Germany*

^b *Dipartimento di Fisica, Università di Roma “Tor Vergata”, 00133 Roma, Italy*

^c *Institute of Semiconductors Physics, 252028 Kiev 28, Ukraine*

Received 28 June 1995; accepted 4 December 1995

Abstract

A systematic investigation of the structural, electronic and optical properties (by means of Raman spectroscopy and reflectance anisotropy spectroscopy (RAS)) has been done for clean and antimony-covered (110) GaAs, InP, InAs, and GaP surfaces. We present here the theoretical interpretation of the experimental reflectance anisotropy spectra for InAs(110) and GaP(110) surfaces, both clean and Sb covered. The different contributions to the optical spectra, originating from surface-to-surface (SS), bulk-to-bulk (BB) and mixed surface-to-bulk (SB) and bulk-to-surface (BS) state transitions, are discussed in detail on the base of microscopic calculations. Good agreement of the theoretical results and experimental data allows us to clarify the origin of the surface optical modification during Sb adsorption. The appearance of strong excitonic effects for clean and Sb-covered GaP(110) surfaces is hypothesised.

1. Introduction

The ordered adsorption of foreign atoms at a semiconductor does not only modify the surface atomic and electronic band structures, but a proper adsorbate choice even allows to passivate the chemically active surface states. Antimony (Sb) is one of such interesting adsorbates at the (110) surfaces of a number of III–V compounds; a well-ordered epitaxial (1×1) monolayer forms after deposition of several monolayers of Sb and subsequent soft thermal

treatment (see e.g. [1–10] and references therein). These ideally abrupt interfaces, the so-called ‘epitaxial continued layer structure’ (ECLS), are of interest for fundamental research as well as for semiconductor surface passivation. The preparation of a well-defined Sb monolayer, however, requires to monitor both the modification of the overlayer structure and the surface electronic properties in the process of Sb adsorption and subsequent ordering on the surfaces. For this purpose we carried out a systematic experimental and theoretical investigation of the process of antimony epitaxial layer formation at the cleaved surfaces of III–V compound semiconductors, namely GaAs(110), InP(110), GaP(110), and

* Corresponding author. Fax: +49-30-31421769; e-mail: norbes@mail.physik.tu-berlin.de.

InAs(110). The deposition and thermal treatment of antimony at InSb(110) surface has also been studied, but we failed to get the well ordered Sb monolayer.

To follow the process of Sb adsorption in-situ, we have applied two modern surface-sensitive and non-destructive techniques: reflectance anisotropy spectroscopy (RAS) has been used to monitor the electronic structure genesis in the process of the antimony ordering at the surface, while the structure of Sb overlayers on the (110) surfaces was controlled in parallel by means of Raman spectroscopy. We have measured the reflectance anisotropy and the Raman phonon signal for the clean surface, for disordered Sb layers as deposited and after subsequent ordering in the process of the annealing. To fully exploit the power of such techniques, the microscopical calculations of the optical properties for the clean (110) and monolayer Sb covered surfaces have been performed within a sp^3s^* tight-binding approach. The surface optical response has been decomposed into the various components, due to surface-to-surface, surface-to-bulk, bulk-to-surface and bulk-to-bulk state transitions. Since part of the results for GaAs and InP (110) surfaces have been discussed in [6]¹, in this paper we will focus on the Sb adsorption process at the InAs(110) and GaP(110) surfaces, referring the reader for a more comprehensive discussion also to a forthcoming paper [11].

We would like to stress that the present findings are not a simple extension of the previous results. The important difference between GaP and InAs with respect to the already discussed GaAs and InP consists of: (i) GaP is an indirect and comparatively wide band-gap (2.35 eV) semiconductor, having the smallest value of the bulk static dielectric constant ϵ_s (10.0) (which is favorable for excitonic effects), while InAs is a direct and narrow gap (0.46 eV) semiconductor with the largest ϵ_s value (14.5); (ii) concerning the surface properties, atomic positions for Sb-covered GaP and InAs (110) surfaces are not known as well as for the corresponding GaAs and InP surfaces. The InAs(110)/Sb surface structure

has been only modeled theoretically [10], while experimental structural data are not available. For GaP(110)/Sb both theoretical [10] and experimental (SEXAFS) structural data [12] are available. However, they differ essentially with respect to the interatomic distances in the Sb overlayer (contrary to the case of the Sb covered GaAs and InP (110) surfaces, where both theoretical and experimental data are in good agreement).

Hence it would be important to attack this problem from the optical point of view, measuring RAS in comparison with the theoretical data. In our calculation we used the ECLS theoretical data from [10] for Sb at InAs(110), while, due to the discrepancy in the structural details, both theoretical [10] and experimental [12] atomic geometries have been used for GaP(110)/Sb. Other experimental and computational details are similar to those for GaAs and InP (110) [4–7].

2. Results and discussion

Clean (110) III–V surfaces are similar both structurally and electronically [13]. Hence one should expect an overall similarity of the observed RAS spectra due to the same nature of their reconstruction. Due to the same chemical bonding within the zig-zag Sb chains one should expect also similar optical features for the Antimony covered (110) surfaces, whereas one should expect significantly different optical features, comparing the clean and Sb passivated surfaces, due to the large polarizability of Sb and the different type of wave functions.

2.1. Preparation of the Sb monolayers

After deposition of a few monolayers of antimony on the freshly cleaved GaP and InAs (110) surfaces and subsequent soft annealing to 640 K, Raman spectra and LEED [4,7–9] indicate the formation of very well ordered Sb epitaxial monolayers.

2.2. Electron band structure

In general our calculated surface band structures are similar to those of [1] for both clean and Sb

¹ One should stress, that in [6] the RA sign convention is opposite to the present one: there we plotted RA as $(R_{[001]} - R_{[110]})/R$, while in the present paper we use the more common notation of RA as $(R_{[110]} - R_{[001]})/R$.

covered surfaces. Hence we will present here only the calculated surface band structure for clean and Sb covered InAs(110), shown in Fig. 1(a) and (b), respectively. The main surface band features for GaP(110) are similar to those of InAs(110). One should stress, however, that the gap between surface states of Sb-covered GaP(110), calculated for the experimental atomic structure, is larger than the one for the theoretical geometry by 0.2 eV [11].

The origin of the surface states of III–V compounds at the clean (110) surfaces is now well understood. The surface states (see InAs(110) in Fig. 1(a) in the vicinity of the bulk gap, mostly contributing to the optical spectra up to transition energies of $4 \div 5$ eV, arise from the empty cation (In, Ga) derived dangling bonds (DBs), C_3 , and the occupied anion (As, P) derived DBs, A_5 . (Standard notations, as in e.g. [1,13] have been used.) The filled state A_4 predominantly has As backbond character, while its antibonding partner, the empty resonance C_4 , is predominantly due to In (Ga) backbonds.

The effect of an ordered monolayer of antimony on InAs(110) (see Fig. 1(b)) is to change the origin of the surface states, their location in the gap and their symmetry with respect to the clean surface [1]. The occupied S_3 and S_4 surface states (S corresponds to the antimony-induced states), which are located at about 3 eV below the top of the valence band, are predominantly p^2 bonding states in the plane of the Sb chains. S_5 and S_6 , appearing within 1 eV below the top of the valence band, are mainly derived from the Sb double occupied dangling bonds (lone pairs). The S_7 and S_8 states, located near and just above the bottom of the conduction band, respectively, have mainly back antibond character.

Although the bulk gap of GaP is 2.3 eV, with respect to 0.46 eV for InAs(110), the energy separation between the highest occupied surface state S_6 and the lowest empty one S_7 is similar for both Sb covered surfaces. This is due to the common Sb-determined origin of these states; the type of substrate (InAs or GaP) is not so significant for that value. In a naive way one should expect, in contrast, a large difference between the surface-state gaps at the clean GaP and InAs (110) surfaces. In spite of this expectation, practically the same surface state separation occurs at clean GaP(110) and InAs(110) surfaces. In fact the surface gap at clean InAs(110) is compara-

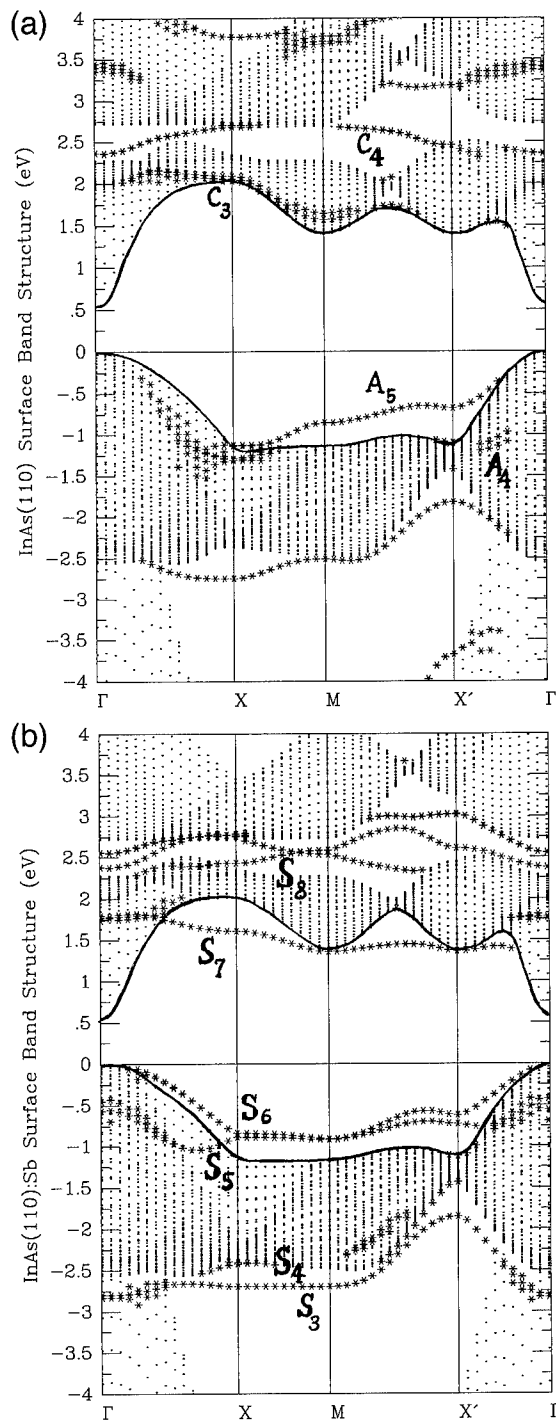


Fig. 1. Band structure of InAs(110) surfaces. Points correspond to the bulk continuum, stars to surface states; (a) clean surface, (b) surface covered by 1 ML of antimony.

tively larger due to the higher bond-rotation tilt angle with respect to the (110) surfaces of other III–V compounds [13].

2.3. Optical properties

The experimental RAS spectra of clean GaAs(110) and InP(110) [6,14,15], InAs(110) (Fig. 2(a)) and GaP(110) (Fig. 4(a)) demonstrate a few general features. (1) The reflectance of the clean surfaces for light polarized along the chains in the $[1\bar{1}0]$ direction dominates over that along the $[001]$ direction, normal to the chains. We will call the corresponding signal ‘positive’. (2) A modulation of the RAS line shape appears in the vicinity of the bulk critical points: it is stronger at low temperatures [14,15], while room temperature RA curves are generally smoother.

All these experimental features are described well in our theory. We begin with the clean InAs(110) surface. Comparing the experimental (Fig. 2(a)) and theoretical (Fig. 3(a)) spectra, the weak experimental feature at 1.6 eV correlates with the weak theoretical structure at the same energy mainly due to BB transition. The calculated peak at 2.5 eV, related to the transitions between surface states (SS), corresponds to the experimental shoulder at the same energy. One should stress that a distinct optical peak

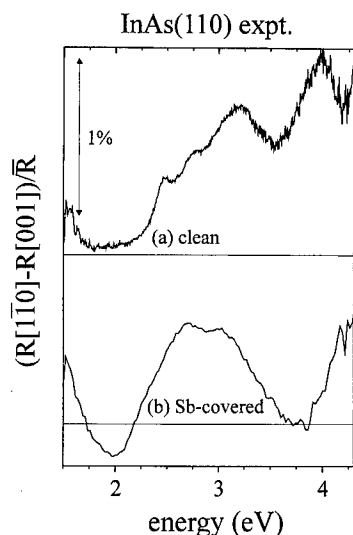


Fig. 2. Experimental reflectance anisotropy $(R_{[1\bar{1}0]} - R_{[001]})/R$ for the clean (a) and Sb covered (b) InAs(110) surfaces.

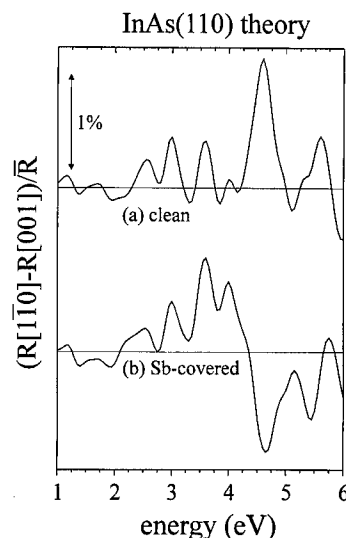


Fig. 3. Theoretical reflectance anisotropy $(R_{[1\bar{1}0]} - R_{[001]})/R$ for the clean (a) and Sb covered (b) InAs(110) surfaces.

at this energy has been observed by Berkovits et al. [14] at low temperature (4 K). As it follows from our calculations, only this peak at the clean surface is clearly related to the transition between surface states in the energy range where spectra are taken. It is due to transitions between DB-like surface states, from A_4 to C_3 , along the XM direction of the surface BZ. The initial and final wave-functions are even and odd, respectively, for reflection with respect to the $[0\bar{1}1]$ mirror plane. This fact makes transitions allowed only for $[1\bar{1}0]$ polarization. Hence the surface optical gap for all these surfaces does not correspond to the minimal gap (at Γ) from the photoemission results [16]. Transitions at higher energy have mainly bulk-to-bulk (BB) origin (together with typically weak mixed contributions from surface to bulk (SB) and bulk to surface (BS) state transitions).

The theoretical RAS minimum at 2.75 eV, due to the E_1 critical point, is seen in Fig. 3(a) as a dip at 2.6 eV. This minimum has been more clearly observed at low temperature in [15] at 2.7 eV. Since the spin–orbital splitting is not accounted for in our approach, the weaker experimental shoulder at 2.8 eV due to the $E_1 + \Delta$ critical point is out of our calculation.

The experimental peak at 3.2 eV (seen also in [14]) has the theoretical BB-related counterpart at 3.0

eV, while the calculated negative RA peak at 3.3 eV well fits the experimental minimum at 3.5 eV. (A difference of the order of few tenths of eV between theory and experiment is unavoidable due to approximations and accuracy of the calculations.) The experimental peak at 3.95 eV should be related to the theoretical BB one at 3.65 eV. The experimental minimum at 4.15 eV could be related to the broad theoretical minimum from 3.8 to 4.2 eV. The positive theoretical peak at 4.5 eV (out of the experimental range) is due to BB, SB and SS transitions. The subsequent decrease in Fig. 3(a) occurs in the vicinity of the E'_0 critical point. The theoretical peak at 5.6 eV is due mainly to SS transitions. Finally, a possible window-anisotropy effect could explain why the RAS background continuously increases with frequency. The window anisotropy causes a non-structured positive background increasing with photon energy. The features associated with optical transitions can be identified as structures added to this background. The window anisotropy is present for both clean and Sb-covered InAs(110).

As it appears from this comparison and other results [5,6,11,17], the theory is able to describe well the main optical surface features observed experimentally. It is important to note the good agreement of the calculated RAS spectra with the sharper optical peaks at 4 K [15], indicating that the structured lineshape of the theoretical spectra is not an artefact of the calculation, but reflects the physical reality at low temperatures.

Termination of the surface by a Sb epitaxial monolayer essentially changes the optical response of the (110) surfaces, as is seen in the experimental Fig. 2(b) and Fig. 4(b) for InAs(110)/Sb and GaP(110)/Sb surfaces respectively. Also in this case we have good agreement with the calculated spectra for Sb covered InAs(110), as shown in Fig. 3(b).

The first experimental negative peak around 2 eV in the calculated spectrum appears at 1.8 eV and it is due to antimony-induced surface states; it is stronger for light polarized along [001], namely perpendicular to the chain direction, that is 'negative'. These transitions are from the Sb dangling bonds to back antibonds (S_6 to S_7) near Γ (see Fig. 1(b)); because of the reflection symmetry with respect to the (110) plane, such transitions are stronger for light polarized perpendicular to the chains. This negative peak is

typical for Sb covered GaAs, InP, and InAs (110) surfaces. (Only GaP(110)/Sb demonstrates an unusual behavior at that energy, as it will be discussed below.) The broad theoretical BB peak at 2.5 eV should be related to the experimental one near 2.6 eV. It has mainly BB origin, slightly reduced due to a negative BS contribution. The weak experimental minimum at 2.8 eV (broadened by temperature effects) relates to the theoretical RAS minimum at 2.75 eV. This BB related feature is due to the E_1 critical point, like for the clean InAs(110). The next weak experimental maximum at 3 eV corresponds to the theoretical BB maximum at the same energy. To follow the comparison at higher energies, the theoretical minimum at 3.2 eV is probably not resolved experimentally, while the calculated minimum at 3.8 eV and the next increase is seen in the experimental curves at the same energy. One should keep in mind, that possible differences between the real and the theoretical Sb overlayer geometry, used for the calculation, could be responsible for a shift in the order of few tenths of eV, although leaving the RAS spectra essentially unchanged. At the other hand, possible window anisotropy effects could also influence the experimental optical features. The negative theoretical peak at 4.7 eV (outside of the experimental energy range) is due to E'_0 and E_2 bulk critical points. Finally, the change of the sign near 4–5 eV at the antimony covered surface with respect to the clean one is a characteristic signature of the Sb overlayers at III–V (110) surfaces.

Let us now consider the RAS spectra of the clean GaP(110) surface. Looking at the experimental (Fig. 4(a)) and the theoretical (Fig. 5(a)) curves for clean GaP(110) one could claim good agreement of the theoretical SS-related peak at 3.2 eV with the experimental shoulder at the same energy. The theoretical BB-related peak at 3.6 eV fits very well the experimental one at 3.5 eV. The negative theoretical structure at 3.9 eV, in the vicinity of the theoretical bulk E_1 critical point, corresponds to the experimental one at 3.7 eV, and the subsequent increase of experimental anisotropy with the peak at 3.9 eV, observed also in [15], has the calculated BB related counterpart at 4.2 eV. Supposing RT broadening, the theoretical maximum at 4.55 eV corresponds to the experimental plateau between 4.2 ÷ 4.7 eV. Finally, the strong peak of the experimental spectra at 5.2 eV has an

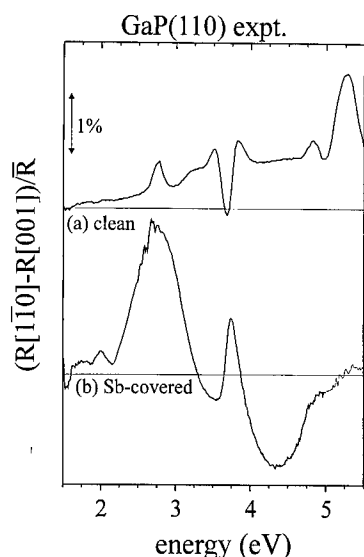


Fig. 4. Experimental reflectance anisotropy $(R_{[110]} - R_{[001]})/R$ for the clean (a) and Sb covered (b) GaP(110) surfaces.

exact theoretical analogon at the same energy. The theoretical lineshape above 3 eV also fits in an excellent way the 4 K results of [15].

However, by no means we could reproduce theoretically the experimental peak at 2.7 eV. From both theoretical and experimental [16] band structures one cannot expect strong optical transitions at 2.7 eV. If

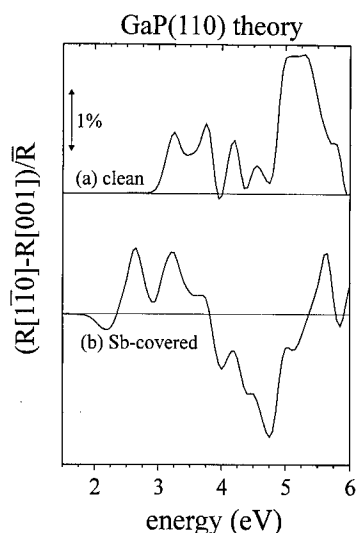


Fig. 5. Theoretical reflectance anisotropy $(R_{[110]} - R_{[001]})/R$ for the clean (a) and Sb covered (b) GaP(110) surfaces.

one will try to relate the 2.7 eV peak to transitions between surface states near the Γ point, where the surface gap is 3.0 eV (experiment) or 3.1 eV (our calculations), such an optical peak should have the opposite polarization with respect to that observed experimentally. Beside this, it should be shifted by a few tenths of eV to higher energies. As it is discussed in [17], a reasonable explanation of this peak is in terms of excitonic effects at the GaP(110) surface. In fact, the small value of the static dielectric constant of GaP (as compared with the other III–V compounds of interest) is in favor of the occurrence of strong excitonic effects.

We will discuss here the theoretical spectra (Fig. 5(b)) for GaP(110)/Sb, calculated using the theoretical [10] geometry. We will show in [11] that this geometry fits rather well the experimental spectra curve. As in the previous case of InAs (110)/Sb, the negative theoretical value at 2.2 eV is due to the transitions from the Sb dangling bonds to back antibonds (S_6 to S_7) near the Γ point.

In the calculated spectrum many surface state related transitions appear from 2.5 to 3.3 eV; those from the dangling bonds S_6 to the chain antibonds (higher in energy than S_7 and S_8) at Γ allowed for light polarized along the chains, and those from the dangling bonds S_5 to back antibonds S_7 and S_8 at Γ and X allowed for light polarized perpendicular to the chains. As a consequence, the corresponding experimental peak at 2.65 eV is positive. The theoretical minimum at 2.8 eV in the middle of a broad (mainly SS related) positive RAS structure should be due to the bulk E_0 critical point. The theoretical BB related maximum at 3.7 eV is due to the E_1 critical point. The theoretical negative RAS after 3.8 eV is due to mainly SB transitions, which are stronger for the light polarization normal to the chains.

Comparing the experimental (Fig. 4(b)) and theoretical (Fig. 5(b)) spectra for GaP(110)/Sb in the energy range below 4 eV one should admit few discrepancies. The experimental spectra do not have the typical negative peak, seen for the other III–V compounds, while it is very well defined in the theoretical curve. As we already mentioned, the predominance of the reflection of light polarized along the [001] direction at low energy is due to SS transitions near the Γ point, and there should be no reasons for the absence of such an effect at

GaP(110)/Sb. Hence, to explain the positive experimental feature at near 2 eV one should suppose the appearance of strong transitions, polarized in the opposite direction, and one could not relate them to the calculated surface band structure. Once more, the possibility of excitonic effects at Sb covered GaP(110) could be a plausible explanation of the positive experimental structure near 2 eV.

Comparing the experimental and theoretical spectra for GaP(110)/Sb, one could relate the theoretical double peak between 2.4 and 3.4 eV with the single broad experimental maximum at 2.7 eV. In the theory the minimum between the 2.65 eV and 3.3 eV peaks is due to E_0 critical point. In fact, at this critical energy one should expect also some experimental peculiarities like in the previous cases. Since in the experimental RAS such structures are not present, we would suggest the occurrence of excitonic effects, which might enhance the total response near 2.7 eV, as in the case of clean GaP(110).

At GaP(110) the typical effect of negative RA due to the Sb monolayer appears both in the experiment and in the theory. Whereas for clean GaP(110) below 4 eV a positive RAS signal appears with the strong peak near 5 eV (Fig. 4(a), Fig. 5(a)), a completely different situation is realized at GaP(110)/Sb (Fig. 4(b), Fig. 5(b)). A strong BB-related negative peak at 4.4 eV (experiment) and 4.7 eV (theory) is seen, and both theory and experiment show a subsequent sign change at higher energies.

3. Conclusions

We have interpreted the experimental reflectance anisotropy peaks at InAs(110) and GaP(110), both clean and antimony covered surfaces, on the ground of microscopic tight-binding calculations. The theory is able to reproduce the overall lineshape or the RA curves very well. This allows us to follow the changes in the surface electronic structure due to the Sb adsorption and its subsequent ordering. Discrepancies in some details are probably due to finite temperature effects, and to problems related to the accu-

racy of the structural definition of the Sb covered surfaces.

The comparison of the experimental RAS spectrum with the theoretical one based upon the structural data of Ref. [10] indicates that the theoretical atomic structure for Sb at GaP(110) gives better fits to the experimental optical results than that based upon the experimental geometry. Strong excitonic effects may be hypothesised at both clean and Sb-covered GaP(110) surfaces to account for some structures of the observed RAS spectra.

References

- [1] C. Mailhot, C.B. Duke and D.J. Chadi, *Phys. Rev. B* 31 (1985) 2213.
- [2] C. Goletti, P. Chiaradia, W. Jian and G. Chiarotti, *Solid State Commun.* 84 (1992) 421.
- [3] W. Richter, N. Esser, A. Kelnberger and M. Köpp, *Solid State Commun.* 84 (1992) 165.
- [4] N. Esser, D.R.T. Zahn, C. Müller, W. Richter, C. Stephens, R. Whittle, I.I. McGovern, S. Kulkarni and W. Braun, *Appl. Surf. Sci.* 56–58 (1992) 169.
- [5] P. Chiaradia, A.I. Shkrebtii, C. Goletti, W. Jian and R. Del Sole, *Solid State Commun.* 85 (1993) 497.
- [6] N. Esser, R. Hunger, J. Rumberg, W. Richter, R. Del Sole and A.I. Shkrebtii, *Surf. Sci.* 307–309 (1994) A1045.
- [7] N. Esser, W. Richter, U. Resch-Esser, P. Chiaradia, C. Goletti and L. Moretti, *Phil. Mag.* 70 (1994) 507.
- [8] N. Esser, M. Köpp, P. Haier and W. Richter, *Phys. Status Solidi (b)* 152 (1995) 191.
- [9] C. Nowak, J. Krujatz, A. Märkl, C. Meyne, W. Braun, W. Richter and D.R.T. Zahn, *Surf. Sci.*, to be published.
- [10] W.G. Schmidt and G.P. Srivastava, *Surf. Sci.*, to be published.
- [11] N. Esser, W. Richter, A.I. Shkrebtii and R. Del Sole, to be published.
- [12] K.E. Miyano, J.C. Woicik and T. Kendelewicz, *Phys. Rev. B* 47 (1993) 6444.
- [13] J.L.A. Alves, J. Hebenstreit and M. Scheffler, *Phys. Rev. B* 44 (1991) 6188.
- [14] V.L. Berkovits, V.A. Kiselev and V.I. Safarov, *Surf. Sci.* 211/212 (1989) 489.
- [15] V.L. Berkovits, L.F. Ivantsov, I.V. Makarenko, T.A. Minashvili and V.I. Safarov, *Solid State Commun.* 64 (1987) 767.
- [16] H. Cartensen, R. Claessen, R. Manzke and M. Skibowski, *Phys. Rev. B* 41 (1990) 9880.
- [17] A.I. Shkrebtii and R. Del Sole, to be published.



ELSEVIER

Applied Surface Science 104/105 (1996) 183–187

applied
surface science

Schottky-barrier formation at passivated surfaces: covalent and ionic semiconductors

R. Saiz-Pardo ^a, R. Rincón ^a, P.L. de Andrés ^b, F. Flores ^{a,*}

^a *Departamento de Física de la Materia Condensada (C-XII), Facultad de Ciencias, Universidad Autónoma de Madrid, E-28049 Madrid, Spain*

^b *Instituto de Ciencia de Materiales (CSIC), Facultad de Ciencias, Universidad Autónoma de Madrid, E-28049 Madrid, Spain*

Received 28 June 1995; accepted 5 October 1995

Abstract

Schottky-barrier heights can be modified by passivation of semiconductor surfaces and the resulting change in the metal-semiconductor interaction. We present theoretical calculations for two different semiconductors: Si and GaAs passivated with Sb. Passivation of GaAs(110) surfaces introduces ohmic contacts, while Si(111) presents smaller changes in its barrier height. These results are similar to the ones previously found for the same semiconductor surfaces passivated with H.

1. Introduction

Schottky-barrier heights, for free defect junctions, seem to be controlled by the local density of states induced at the interface [1,2]. As discussed in different references, when the metal is in contact with the semiconductor, interface states are induced at the energy gap around the charge neutrality level of the semiconductor, pinning the interface Fermi level at a position that only depends slightly on the metal properties [3].

It has been suggested by several authors [4,5] that the density of states at the interface can be modified by depositing an intralayer between the metal and the semiconductor. In particular, it is believed that semiconductor passivated surfaces should interact

differently with the metal forming the junction: this might alter the Fermi level pinning and the Schottky-barrier formation.

In this paper we present new theoretical results for Si(111) and GaAs(110) passivated with Sb. We analyze how the effect of passivation modifies their barrier heights for a K monolayer. We have studied in previous papers Si(111) and GaAs(110) H passivated surfaces [6]: our results show a consistent picture for the different covalent and ionic semiconductors and suggest a general pattern that will be discussed at the end of this paper.

In our theoretical approach, first of all we study the semiconductor passivated surfaces: as GaAs(110) Sb covered surfaces have been analyzed elsewhere [7,8], we present here the results for the Si(111) Sb interface. In a second step, we consider the effect of a K-monolayer deposited on both passivated semiconductor surfaces. Comparing with the ideal semi-

* Corresponding author.

conductor–K interface we deduce the effect of passivation on the Schottky-barrier height.

In Section 2 we present a brief summary of the theoretical approach used to calculate the electronic properties of the different interfaces. In Section 3, our results for the metal–semiconductor junctions are discussed and in Section 4 we present our conclusions after comparing with the H-covered case.

2. Formalism

In order to analyze the chemisorption problem we find advantageous to adopt a LCAO approach. Tight-binding methods have been introduced in the past as a convenient parametrization of the electronic properties of solids. However, these methods bump into difficulties when quantities not closely related to the ones provided by the parametrization are required. To overcome this limitation, we have in our previous work [9] introduced a self-consistent tight-binding method, extending the Hohenberg–Kohn theorem [10] for a LCAO Hamiltonian. In our formalism, we find useful to analyze separately the one-body and the many-body contributions to the Hamiltonian, so we write the following equations:

$$\hat{H} = \hat{H}^{\text{o.b.}} + \hat{H}^{\text{m.b.}} \quad (1)$$

where

$$\hat{H}^{\text{o.b.}} = \sum_{i\sigma} E_{i\sigma} n_{i\sigma} + \sum_{ij;\sigma} T_{ij\sigma} (c_{i\sigma}^\dagger c_{j\sigma} + c_{j\sigma}^\dagger c_{i\sigma}) \quad (2)$$

defines the one-electron contribution and

$$\begin{aligned} \hat{H}^{\text{m.b.}} = & \sum_i U_i^{(0)} n_{i\uparrow} n_{i\downarrow} \\ & + \frac{1}{2} \sum_{i,j \neq i;\sigma} \left[J_{ij}^{(0)} n_{i\sigma} n_{j\sigma'} + \tilde{J}_{ij}^{(0)} n_{i\sigma} n_{j\sigma} \right] \end{aligned} \quad (3)$$

defines the many-body part of the total Hamiltonian. In Eq. (2) $E_{i\sigma}^\sigma$ represent the different orbital levels and T_{ij}^σ their hoppings interactions. We obtain these values using tabulated [11] atomic wavefunctions, ψ_i , for the independent atoms forming the system (note how our self-consistent procedure allows us to use as input for our calculations the atomic number of the different elements forming our system). In Eq.

(3), $U_i^{(0)}$ and $J_{ij}^{(0)}$, $\tilde{J}_{ij}^{(0)}$ define the intrasite and intersite Coulomb interactions associated with the atomic wavefunctions, ψ_i . Solving the many-body part of the Hamiltonian is in general a difficult task, and we shall analyze it using a local density approximation within a Kohn–Sham formalism [9]. Thus, the problem can be reduced to an effective one-electron Hamiltonian where the following Hartree and exchange–correlation potentials associated with each i -orbital are introduced,

$$V_{i\sigma}^{\text{H}} = \frac{\partial E^{\text{H}}[n_{i\sigma}]}{\partial n_{i\sigma}}, \quad V_{i\sigma}^{\text{XC}} = \frac{\partial E^{\text{XC}}[n_{i\sigma}]}{\partial n_{i\sigma}}. \quad (4)$$

$E^{\text{H}}[n_{i\sigma}]$ and $E^{\text{XC}}[n_{i\sigma}]$ are the Hartree and the exchange–correlation energies related to the following Kohn–Sham Hamiltonian:

$$\hat{H} = \hat{H}^{\text{o.b.}} + \sum_{i\sigma} [V_{i\sigma}^{\text{H}} + V_{i\sigma}^{\text{XC}}] n_{i\sigma}. \quad (5)$$

This effective one-electron Hamiltonian defines the electronic properties of our system as a superposition of localized bonds. Notice that the average orbital occupation numbers, $n_{i\sigma}$, must be obtained self-consistently, as the Hartree and exchange–correlation potentials depend on these values.

The effective one-electron Hamiltonian is solved using Green function techniques [9]. In particular, the semi-infinite crystal is projected onto the last twelve layers, and the resulting film is joined to the adsorbed species. One of the advantages of using Green functions is that we can easily compute the single particle density of states associated with each orbital and their occupancies.

3. Results

In a first step, we study the chemisorption of Sb on the bulk-like terminated surfaces of Si(111) and GaAs(110) [7] (referred as the 1×1). To describe bulk properties of these two semiconductors we use well known parameters [12], and apply our formalism to compute the desired surface related properties (i.e. chemisorption). As a second step, we study the deposition of K on the Sb passivated surfaces. Results for K on the clean Si(111) surface have been reported elsewhere [6], and shall be used here to

deduce the effect of passivation on the Schottky-barrier formation by comparison of both cases.

3.1. Si(111)

Sb is known to passivate silicon surfaces. Taking as a starting point the bulk terminated (111) silicon surface we study the deposition of one monolayer of Sb (i.e., one Sb atom per one Si atoms on the top layer). It is well known from LEED and STM studies [13] that this deposition results on a $(\sqrt{3} \times \sqrt{3})R30^\circ$ overlayer, but up to the best of our knowledge there is not a reliable structural determination providing the relevant structural parameters. Therefore, we study the relative binding energies of Sb trimers located on two different points, the so-called: H3 and T4. Furthermore, STM results have suggested the existence of (2×1) chains (with the same coverage) and consequently we have studied a few different possible arrangements of these chains. In Fig. 1 we present a schematic of the geometry. Our calculations result in very similar total energy values for each of them showing the possibility of coexistence at room temperature of different arrangements. However, the T4 site is the one presenting a global marginal minimum for the total energy in our calculations, and therefore it is the position we take to analyze the Sb/Si(111) interface. We shall comment here that the approximations of our method can

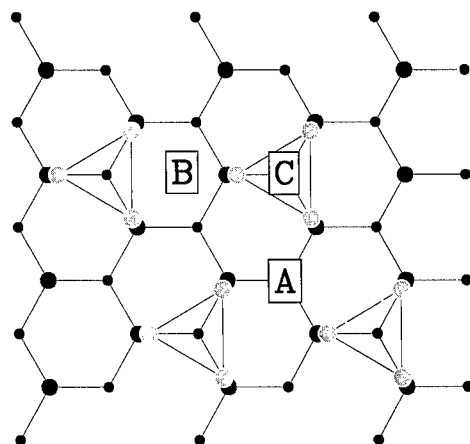


Fig. 1. Sb/Si(111) schematic geometrical arrangement: $\sqrt{3} \times \sqrt{3} R30^\circ$ trimers on T4. Black dots represent Si atoms (in two planes), light dots represent Sb trimers, and letters A, B and C represent different adsorption positions for K atoms.

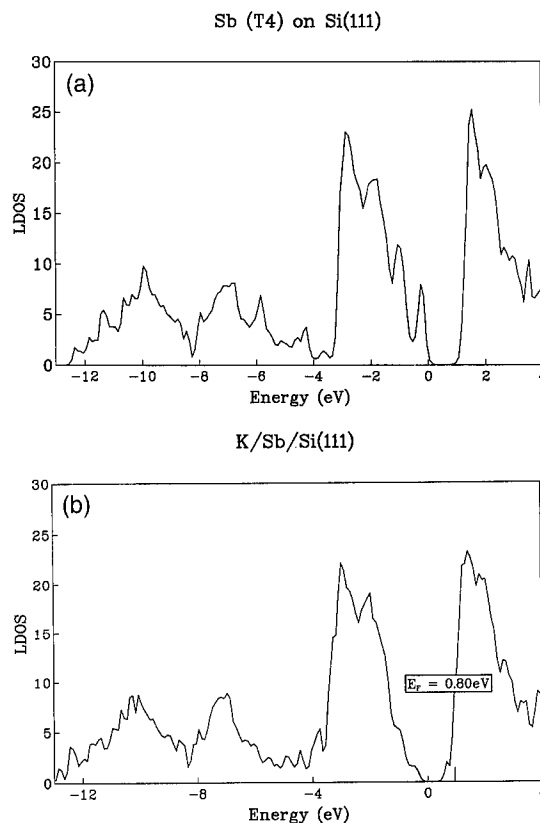


Fig. 2. Total density of states for (a) Sb/Si(111) and (b) K/Sb/Si(111).

introduce inaccuracies in our calculations that we estimate to be less than half an eV. Yet, we expect that errors in energy *differences* are around 0.1 eV, and plausible conclusions can be obtained from our approach.

In a second step we want to study the deposition of K on the passivated surface. We have calculated chemisorption energies associated with different possible sites labeled in Fig. 1 as A, B and C. The one preferred is A by ≈ 0.2 eV, so we concentrate on this position. It is interesting to notice here that the total binding energy of -0.1 eV is quite small, and it might be taken as an indication of the difficulty to grow such a K layer (although the intrinsic uncertainties in our calculations should be considered here, as we have commented before).

In Fig. 2 we present the density of states of the Sb passivated Si(111) surface (a) to be compared with the corresponding to the K/Sb/Si(111) (b). It is

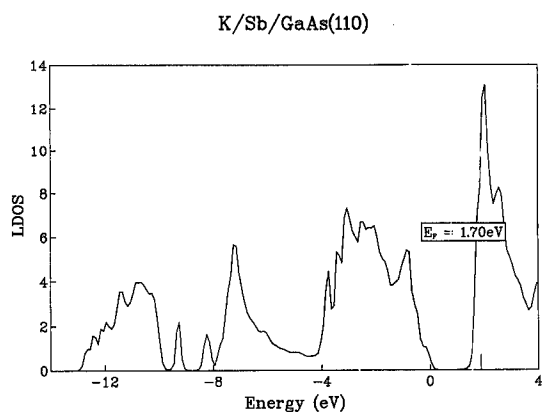


Fig. 3. Total density of states for K/Sb/GaAs(110).

observed that E_F for the K-covered interface is slightly higher by 0.28 eV than the one found for K/Si(111) [5]. This implies a corresponding reduction on the Schottky barrier height for electrons (the origin to measure the Fermi level is taken from the semiconductor valence band top).

3.2. GaAs(110)

We have already studied the deposition of Sb on GaAs(110) in an earlier work [7] (for instance, see Fig. 4 in that reference). A simple comparison of Fig. 2 and Fig. 3 already shows the similar surface band gaps of the clean and passivated surfaces (1.1 eV and 1.4 eV for silicon and gallium arsenide respectively, in good correspondence with the passivated ones: 0.7 eV and 1.0 eV respectively). However, the Fermi energy position for the K/Sb/GaAs(110) interface (Fig. 3) is very different when compared with the K/Sb/Si(111) case (1.7 eV for GaAs and 0.8 eV for Si). This creates a new situation: the Fermi level lies in the conduction band for the K/Sb/GaAs(110) interface, producing an ohmic contact upon deposition of the metallic layer.

The whole situation is rather similar to the one we have found when H is used to passivate these two surfaces [6], suggesting a general trend mainly associated with the semiconductor. This can be rationalized by realizing that, although the metal produces a noticeable change in the electronic properties of the passivated surface, the LDOS seems to be dominated by the substrate semiconductor, much in similarity

with the arguments given to explain the ideal metal–semiconductor interface.

4. Conclusions

We present a self-consistent LCAO total energy calculation within a local density approximation for the systems Sb/Si(111), K/Sb/Si(111) and K/Sb/GaAs(110). For the geometry of adsorption of Sb on the (1×1) Si(111) surface our results show that the T4-site is energetically the favourable one; however, the difference in energy with the H3-site is very small. Upon deposition of a K layer we find the K atoms creating bonds with three surroundings Sb trimers at a position we have labeled A in Fig. 1. We have analyzed the Schottky-barrier formation using the T4 site, but results for the H3-site are very similar. The Schottky-barrier height is found to be 0.28 eV smaller than the one calculated for the K/Si interface.

For GaAs we find a more dramatic change due to the Sb passivation. Our results show that the K/Sb/GaAs(110) interface forms an ohmic contact. All these results are in close agreement with the ones found for Si and GaAs–H passivated surfaces. We conclude that the Schottky-barrier formation is controlled by the density of states created at the semiconductor passivated surface.

Acknowledgements

We acknowledge financial support from the Spanish CICYT under contracts No. PB92-0168C and PB94-0053, and from the European Community, EC(CHRX-C793-0134). Iberdrola S.A. is gratefully acknowledged for help and encouragement.

References

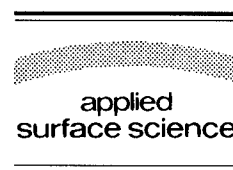
- [1] E.H. Rhoderick and R.H. Williams, *Metal–Semiconductor Contacts* (Oxford University Press, 1988); W. Mönch, *Electronic Structures of Metal–Semiconductor Contacts* (Kluwer, Dordrecht, 1990); F. Bechstedt and M. Scheffler, *Surf. Sci. Rep.* 18 (1983) 145.
- [2] C. Tejedor, F. Flores and E. Louis, *J. Phys. C* 10 (1977) 2163; J. Tersoff, *Phys. Rev. Lett.* 30 (1984) 4874.

- [3] F. Flores, R. Pérez, R. Rincón and R. Saiz-Pardo, *Phil. Trans. R. Soc. London A* 344 (1993) 567.
- [4] W. Mönch, *Europhys. Lett.* 27 (1994) 479.
- [5] F. Flores and R. Miranda, *Adv. Mater.* 6 (1994) 540.
- [6] R. Saiz-Pardo, R. Rincón and F. Flores, *Appl. Surf. Sci.* 92 (1996) 362.
- [7] F. Flores, R. Saiz-Pardo, R. Rincón, J. Ortega, R. Pérez and F.J. García-Vidal, *J. Phys. Condens. Matter* 5 (1993) A41.
- [8] C. Mailhot, C.B. Duke and D.J. Chadi, *Phys. Rev. B* 31 (1985) 2213.
- [9] F. Flores, A. Martín-Rodero, E.C. Goldberg and J.C. Durán, *Nuovo Cimento D* 10 (1988) 203; F.J. García-Vidal, A. Martín-Rodero, F. Flores, J. Ortega and R. Pérez, *Phys. Rev. B* 44 (1991) 11412; F.J. García-Vidal, J. Merino, R. Pérez, R. Rincón, J. Ortega and F. Flores, *Phys. Rev. B* 50 (1994) 10537.
- [10] P. Hohenberg and W. Kohn, *Phys. Rev.* 136 (1983) 864.
- [11] E. Clementi and C. Roetti, *At. Data Nucl. Data Tables* 14 (1974) 177.
- [12] P. Vogl, P. Hjalmarson and J.D. Dow, *J. Phys. Chem. Solids* 44 (1983) 365.
- [13] P. Martensson, G. Meyer, N.M. Amer, E. Kaxiras and K.C. Pandey, *Phys. Rev. B* 42 (1990) 7230; H.B. Elswijk, D. Dijkkamp and E.J. van Loenen, *Phys. Rev. B* 44 (1991) 3802; S. Watanabe, M. Aono and M. Tsukada, *Surf. Sci.* 287/288 (1993) 1036.



ELSEVIER

Applied Surface Science 104/105 (1996) 188–195



Midgap states observed by nonlinear optical spectroscopy of metal:GaAs junctions

J. Qi ^{a,*}, W. Angerer ^a, M.S. Yeganeh ^a, A.G. Yodh ^a, W.M. Theis ^b

^a Department of Physics, University of Pennsylvania, Philadelphia, PA 19104, USA

^b Naval Air Warfare Center, China Lake, CA 93555, USA

Received 26 June 1995; accepted 28 August 1995

Abstract

We present detailed second-order nonlinear optical spectroscopic studies of the interface electronic structure in metal:GaAs thin films and interfaces. The interface spectra from Au:GaAs, Ga-rich n-type systems exhibit two resonance features in the near infrared at 0.715 eV and 0.731 eV. A single resonance feature at 0.715 eV is observed in Au:GaAs, As-rich n-type interfaces. Similar single resonance features at 0.715 eV were observed in As:GaAs n-type samples. No resonances however were observed in oxide:GaAs and metal:GaAs p-type systems. All of the spectral features are sharp one-photon resonances. They provide compelling evidence for the existence and symmetry of atomic displacement-induced defect states just below the buried interface.

1. Introduction

The physics of buried solid/solid interfaces is of interest from both fundamental and technological viewpoints. Although new methods have been developed and used with limited success to reveal specific features about buried interfaces [1], a basic experimental problem still remains: traditional optical spectroscopies lack interface specificity and traditional surface diagnostics have a limited penetration depth. Second-order nonlinear optical spectroscopy possesses long penetration depths characteristic of most

optical methods and intrinsic interface specificity characteristic of second-order optical processes. These nonlinear optical techniques have been used recently to probe buried interfacial features associated with new bonding [2], band profiles [3], and strain [4]. The experiments have helped us to understand better the microscopic role played by interfacial excitations in affecting nonlinear optical phenomena, and their elucidation has accelerated the development of second-order nonlinear optical spectroscopy as a probe of these systems.

In this paper second-order nonlinear optical spectroscopy (second-harmonic generation (SHG) and sum-frequency generation (SFG)) was used to probe the electronic structures of different GaAs based interfaces, 80 Å Au epitaxial films on n-type and

* Corresponding author. Tel.: +1-215-8988260; fax: +1-215-8982010; e-mail: jining@sol1.lrsm.upenn.edu.

p-type GaAs(001) surfaces. We have also studied 80 Å As amorphous films on n-type and p-type GaAs(001) surfaces. In all cases the interfaces were either As-rich or Ga-rich as a result of different GaAs substrate growth conditions. Native oxide GaAs(001) samples were also studied in both n- and p-type. In Au:GaAs n-type systems, we have observed two resonance features at 0.715 eV and 0.731 eV for the Ga-rich interface, and one resonance feature at 0.715 eV for the As-rich interface. Similar single resonance features at 0.715 eV were observed in the As:GaAs n-type samples, but were not present in oxide:GaAs and metal:GaAs p-type systems. All resonance features were confirmed to be one-photon resonances. After consideration of various three-step optical processes, we suggest that the transitions originate from the midgap states. We further suggest that the interfacial resonance features are brought about by atomic displacement-induced defect states near the junction.

There are a number of experimental observations consistent with the existence of midgap states in this system, however there are very few direct spectroscopic measurements of interface energy levels. Some spectroscopic evidence for interface states has been derived from cathodoluminescence (CLS) in Au:GaAs(100) systems [5], inverse photoemission (IPS) in Ti:GaAs(110) systems [6], and ultraviolet-photoemission spectra (UPS) in Au:GaAs(110) systems [7]. These spectra however, are very broad, and the measurements are not intrinsically sensitive to the buried interface. In contrast to the CLS, IPS and UPS measurements [5–7], *sharp* resonant features were observed in our SHG and SFG experiments. The intrinsic interface sensitivity of the second-order nonlinear optical spectroscopies enable us to suppress spectral contributions from the adjoining bulk media, resulting in more specific assignments of the spectral features, and a narrowing of the features by comparison to those observed with competing spectroscopies.

The remainder of the paper is organized as follows. We first describe the experimental set-up and our samples in Section 2. In Section 3, we present measurements of the SHG and SFG spectra from different GaAs based interfaces. Then the results of measurements are discussed in Section 4. In this section we critically examine the evidence and sug-

gest that atomic displacement-induced defect states are responsible for these resonances. A brief conclusion is presented in Section 5.

2. Experiment

A schematic of the experimental apparatus is shown in Fig. 1. A 10 Hz *Q*-switched Nd:YAG pumped tunable optical parametric oscillator (OPO) or dye-laser was used as the fundamental SH generating light source for the SHG measurements. The samples were irradiated at an incidence angle of 75°. The incident light pulses had a temporal duration of 10 ns, and a fluence of ~ 1 mJ/cm². The fundamental (SH) photon energy range was from 0.68–0.78 eV (1.36–1.56 eV) (using the OPO), and from 1.29–1.40 eV (2.58–2.80 eV) (using the dye-laser). The reflected SH power was measured as a function of output light wavelength. Unfortunately continuous scanning from the visible to infrared wavelength range (0.8–1.36 eV) was impossible with our light sources. Our KTP based OPO cut off when photon energies exceeded 0.85 eV. Additionally, as the fundamental OPO photon energy was scanned towards the mid-infrared range (< 0.68 eV), we encountered several problems that made our spectroscopic measurements more difficult. For example, the very low

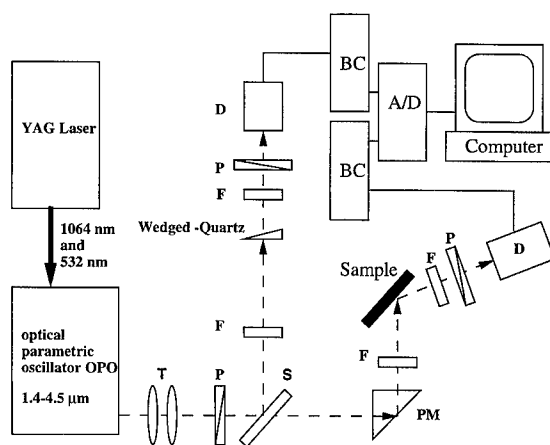


Fig. 1. Schematic diagram of experimental setup. F, spectral filter; P, polarizer; PM, prism; S, beam splitter; T, telescope; D, photo-multiplier tube and monochromator; BC, boxcar averager; A/D, analog to digital converter.

quantum efficiency of photo-multiplier tubes limited our sensitivity to SH photons in near infrared (i.e. < 1.36 eV); also the fundamental probe light was strongly absorbed by water molecules in air for energy below ~ 0.65 eV. SFG spectra were obtained by irradiating the samples with the Nd:YAG beam at 1064 nm, and the tunable infrared beam at the same incidence angle and with the same polarization. To compensate for intensity fluctuations of the input beam, SH or SF signals were simultaneously produced and measured in a parallel (reference) optical path which contained a wedged quartz plate [3]. The maximum SHG or SFG output of the reference at each frequency was obtained by translating a wedged quartz plate along a direction perpendicular to the laser beam propagation vector. Sample intensities were normalized using this reference SHG or SFG signal.

GaAs(001) has a zinc-blende crystal structure and carries a single nonzero bulk second-order susceptibility $\chi_{yxz}^{(2)}$, whose contribution to the output SH radiation is highly anisotropic. Au bulk has an isotropic structure. Therefore it does not contribute SH radiation in the dipole approximation [8]. The interface signals from the metal:GaAs(001) samples were separated from the bulk signals by proper choice of sample orientation and light polarization [3]. By setting $\phi = 0$ and employing the p-in/p-out polarization configuration, where ϕ is the angle between the [100] direction and the plane of incidence, we were able to suppress the bulk signal, $\chi_{yxz}^{(2)}$, by $\geq 10^4$, thereby greatly enhancing our sensitivity to interface features. Results obtained in the p-in/p-out configuration with $\phi = 0$ will hereafter be referred to as interface signals.

Our GaAs(001) samples were doped ($\sim 1 \times 10^{16}$ cm $^{-3}$) with Si (n-type) and Be (p-type). They were grown on an undoped GaAs substrate by molecular-beam epitaxy (MBE) at temperatures around 580°C, and with background chamber pressures of $\sim 3 \times 10^{-10}$ Torr. It is well known that GaAs(001) exhibits a wide variety of surface reconstructions. These reconstructions are often related to the relative Ga to As ratio at GaAs surface [9]. RHEED measurements were performed on all samples to determine the surface reconstructions before growth of the Au epitaxial film. GaAs(001) samples were either As-rich (2×4 RHEED surface reconstruction) or Ga-rich

(4×2 surface reconstruction) [10]. The ratio of As:Ga was 75%:25% (25%:75%) for the 2×4 reconstruction (4×2 surface reconstruction). An 80 Å epitaxial Au film was then grown on the GaAs(001) surface with a surface temperature of $\sim 400^\circ\text{C}$. We confirmed the Au film was epitaxial by RHEED. We also grew amorphous, 80 Å As metal films on GaAs. When such a sample is exposed to air, a fraction of the As film is converted into an oxide, but Auger spectroscopy confirmed that oxygen did not penetrate as far as the As:GaAs interface. Finally we studied GaAs(001) n- and p-type samples without metal films. In the air, a ~ 50 Å oxide formed on the sample surface.

3. Results

Fig. 2 exhibits the full range of SHG spectra measurements from Au:GaAs n-type samples with different GaAs surface reconstructions (As-rich 2×4 and Ga-rich 4×2). The full wavelength range used both the OPO and the dye-laser. There are no sharp resonance features within energies probed by the dye-laser. The increase in signal at higher energy occurs as the fundamental photon energy increases above the direct band-gap of GaAs. However, we see that the interface spectra possess a single sharp peak at one-photon energy 0.715 eV for the As-rich Au:GaAs n-type sample and two closely spaced peaks for the Ga-rich Au:GaAs n-type sample. Comparison measurements of interface SHG and SFG spectra from Au:GaAs n-type samples using OPO with different GaAs surface reconstructions (As-rich 2×4 and Ga-rich 4×2) are exhibited in Fig. 3. The solid lines in the spectra from the Ga-rich Au:GaAs n-type sample represent a best fit to the data using two Lorentzian lineshape functions. According to the fitting, the SH (SF) peak positions are 0.708 ± 0.014 eV (0.713 ± 0.014 eV) and 0.731 ± 0.014 eV (0.730 ± 0.014 eV) respectively. We believe that the first peak in the SHG (SFG) spectra at ~ 0.708 eV (0.713 eV), has the same origin as the single sharp peak in the As-rich Au:GaAs n-type system, while the latter peak is a new feature resulting from the different interface preparation. By comparison to SFG spectra, all resonance features were confirmed to be one-photon resonances. SHG and SFG experi-

ments were also performed on As:GaAs(001) n-type samples within the same photon energy range. A similar single resonance feature around 0.715 eV was observed (see Fig. 4(a)), and was confirmed to be a one photon resonance. Interestingly in contrast to previous spectroscopic experiments [5–7], all of the observed resonances are sharp, suggesting a narrow distribution of states at or just below the buried interface.

In Au:GaAs p-type and oxide:GaAs systems, the interface second-order nonlinear optical spectroscopies have also been performed within the same spectral region. No resonance features were observed in either system (see Fig. 4(b) and (c)). These results are surprising at first glance, since one would expect that the energy levels at the interface will not be changed by variations in bulk doping and overlayer oxidation [11]. However, the carrier occupation density in these states is modified, since the Fermi level can shift with respect to the midgap levels. In the p-type metal:GaAs system these midgap states will become empty, as the Fermi level shifts towards the valence band maximum [5]. The effects in the oxide:GaAs system are less clearly explained. However the oxide is rarely well characterized, and it is possible that the midgap levels were shifted out of our probe range.

In general the second order susceptibility for SHG, $\chi_{ijk}^{(2)}$, can be written as [8]

$$\begin{aligned} \chi_{ijk}^{(2)} &= N \frac{e^3}{\hbar^2} \sum_{n,n'} \langle g | r_i | n \rangle \langle n | r_j | n' \rangle \langle n' | r_k | g \rangle \rho_{gg} \\ &\times \left[(2\omega - \omega_{ng} + i\Gamma_{ng})^{-1} (\omega - \omega_{n'g} + i\Gamma_{n'g})^{-1} \right. \\ &+ (2\omega + \omega_{ng} + i\Gamma_{ng})^{-1} (\omega + \omega_{n'g} + i\Gamma_{n'g})^{-1} \\ &\left. + (\omega + \omega_{ng} + i\Gamma_{ng})^{-1} (\omega - \omega_{n'g} + i\Gamma_{n'g})^{-1} \right]. \end{aligned} \quad (1)$$

Here $|g\rangle$ represents the ground state, and $|n'\rangle$ and $|n\rangle$ are two excited states of the medium. ρ_{gg} is the occupied electron density of the ground states. Resonances can viewed to arise through particular terms in this sum over states. In our case, there are two probable excitation processes that can be invoked to explain the one photon resonance. In one case the three-step process starts from the top of valence band. Here the state $|g\rangle$ is at the valence band edge. In the other case the process starts from the interface midgap state. Here the state $|g\rangle$ is an interface midgap state. Our results suggest that the one photon resonances on metal:GaAs n-type samples are due to

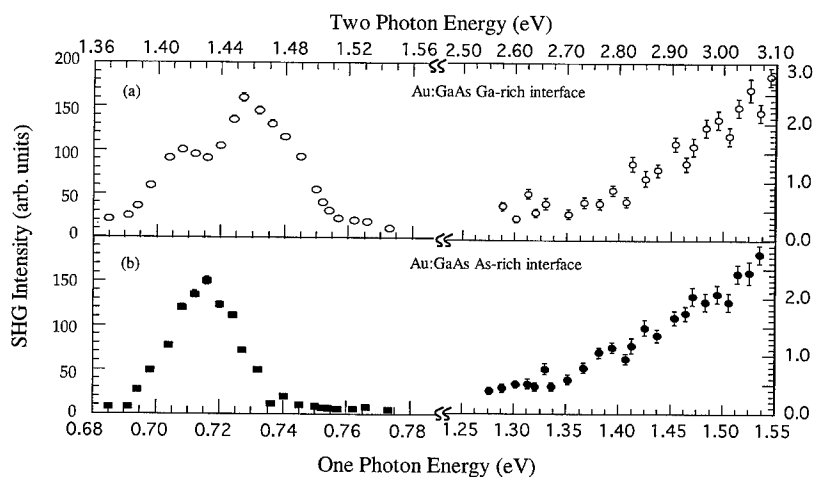


Fig. 2. Interface SHG from Au:GaAs n-type samples. The left (right) SHG intensity axis corresponds to SHG spectra from 0.68–0.78 eV (1.29–1.40 eV). Note, the horizontal axis is not continuous.

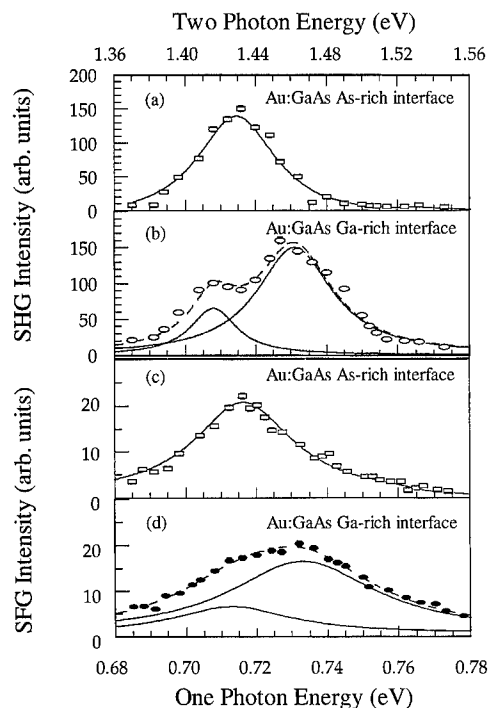


Fig. 3. Interface SHG and SFG spectra from Au:GaAs n-type samples. (a) SHG spectrum from As-rich Au:GaAs n-type sample. The solid line is a guide for the eye. (b) SHG spectrum from Ga-rich Au:GaAs n-type sample. The two solid lines are fit using two Lorentzian line shape functions, and the dashed line is the combination of the above two lines. The peak positions are estimated to be 0.708 ± 0.014 eV and 0.731 ± 0.014 eV respectively. (c) SFG spectrum from the As-rich interface sample. The solid line is a guide for the eye. (d) SFG spectrum Ga-rich Au:GaAs n-type sample. The two solid lines are fit using two Lorentzian line shape functions, and the dashed line is the combination of the above two lines. The peak positions are estimated to be 0.713 ± 0.014 eV and 0.730 ± 0.014 eV respectively.

the resonant transition from the occupied midgap states to the conduction band minimum. This follows from consideration of observations in the p-type systems. In p-type systems the resonance process originating from the midgap states would be very weak as a result of their low occupation density. Indeed no resonance was observed in these systems (see Fig. 4).

Additional measurements were performed to rule out several other possible origins for these features. Bulk SHG $\chi_{xyz}^{(2)}$ spectra measurements were performed in the p-in/s-out polarization configuration at $\phi = 0$. Using this configuration we maximized our

sensitivity to the bulk nonlinearity [3]. Fig. 4(d) reveals no resonance features in the bulk signals.

The interface signals in principle contain contributions from the front metal surface, and higher-order bulk nonlinearities. To examine the contributions from the Au surface, we measured SFG and SHG spectra from a thick Au-epitaxial film ($\sim 5 \mu\text{m}$) and found that SFG and SHG signals were below our noise level (see Fig. 4(a)). Also, since the bulk nonlinear response of the Au epitaxial layer on GaAs(001) is expected to contribute in the same way in both n- and p-type GaAs systems, the fact that no resonance features were observed in Au:GaAs p-type systems effectively rules out possible contributions

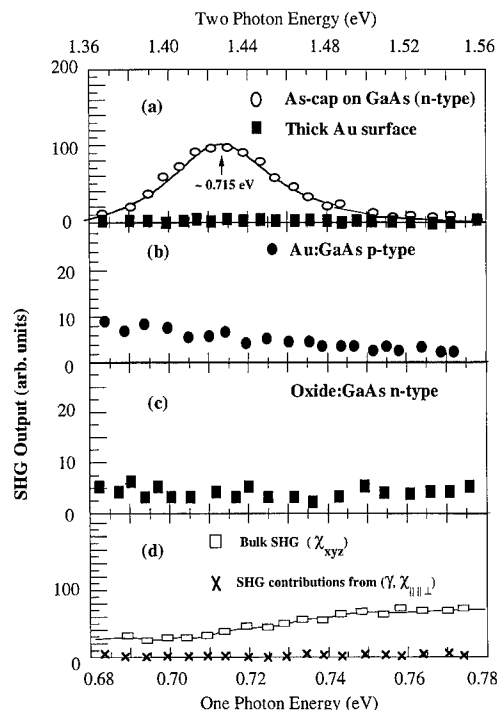


Fig. 4. (a) Interface SHG spectra from the As capped GaAs n-type sample. The solid line is a guide for the eye. The SHG from thick Au surface was at our noise level. (b) Interface SHG spectra from Au:GaAs p-type system; no resonance features were observed. (c) Interface SHG spectra from native oxide GaAs surface; no resonance features were observed. (d) Bulk SHG spectra from the Au:GaAs n-type sample; the solid line is a guide for the eye. Both As-rich and Ga-rich interface samples have the same bulk spectra. No resonance features have been observed from the bulk SHG studies. The SHG contribution from the linear combinations of γ and $\chi_{||\perp}^2$ was at least two orders of magnitude smaller than the interface signal in both n- and p-type systems.

from bulk epitaxial Au films. The possibility of higher-order GaAs bulk contributions were also examined in the s-in/s-out and s-in/p-out polarization configurations. The bulk anisotropic contribution (ξ) was below our noise level and the signal resulting from linear combinations of γ and $\chi_{||\perp}^{(2)}$ was at least two orders of magnitude smaller than the interface signal [3] (see Fig. 4(d)). In addition, the higher-order bulk terms contribute in the same way to metal:GaAs and oxide:GaAs systems, and no resonances in oxide:GaAs systems were observed. In total, these findings rule out higher-order bulk contributions as sources of the resonance features. The 0.715 and 0.731 eV resonance features most likely originate from the buried interface.

4. Discussion

Our second-order nonlinear optical spectral measurements of As-rich Au:GaAs and As:GaAs n-type samples possess a similar resonance at 0.715 eV, suggesting that the common interface state may be related to As atoms. On the other hand, the interface state at ~ 0.731 eV was only found at the Ga-rich interface in Au:GaAs n-type systems. This suggests that this latter interface state is related to the presence of excessive Ga atoms at the interface.

These observations can be understood within a simple theoretical framework. A gradient in the chemical potential for As or Ga atoms can induce the migration of these atoms from the interface into the GaAs substrate. As a result of relative concentrations of As and Ga atoms during growth, we might expect the formation of high concentrations As atom displacement-induced defect states near the As-rich interface [11]. In this case the As atom sits in a Ga atom site in the interfacial region. Such As atom displacements are the first step in the production of several primary defect states in GaAs [11–13]. Two defect-associated, strongly bound energy levels with s-like and p-like symmetries respectively, are predicted to lie near the middle of the band gap (see Fig. 5(c) and (d)) [14]. We note that the calculated states are generally more complicated than the simple atomic displacement described above; for example they may involve coupling of the antisite to a nearby vacancy [15]. Since vacancy concentrations

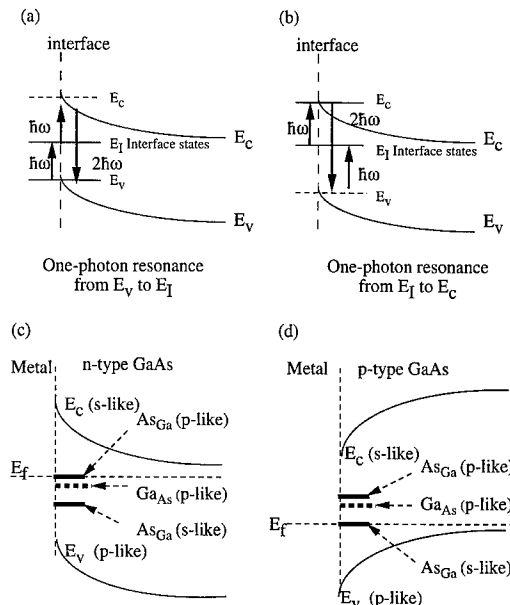


Fig. 5. Schematic of two most probable three-step optical processes giving rise to the one photon resonance. (a) Time-ordered process starts in valence band, and is represented by $E_v \xrightarrow{\hbar\omega} E_1 \xrightarrow{\hbar\omega} E_c \xrightarrow{2\hbar\omega} E_v$. (b) Time-ordered process starts from interface states, and is represented by $E_1 \xrightarrow{\hbar\omega} E_c \xrightarrow{\hbar\omega} E_v \xrightarrow{\hbar\omega} E_1$. (c) Schematic representation of As (As_{Ga}) and Ga (Ga_{As}) displacement defect state energies and symmetries in n-type GaAs:metal interfaces. (d) Same as (c) except in p-type GaAs:metal interface. E_c (E_v) denote conduction (valence) band energy minima (maxima), E_f denotes the Fermi-level in these systems, and E_1 denotes interface state energy.

may be higher near the interface, it is also plausible that a higher density of these types of defect states may exist near interfaces. We note however, that on very general grounds one would expect the As anti-site midgap state overlap strongly with bulk |s>-like and |p>-like states [15].

Similarly a high concentration of Ga displacement-induced defect states are expected for the Ga-rich interface. In this case Ga atoms sit in As atom sites. A single strongly bound Ga displacement defect state has been theoretically predicted to have an p-like symmetry and an energy level near the middle of band gap [14]. Again on general theoretical grounds one would expect this state to be pulled from p-like bulk states below the valence band edge.

Our observations can be explained quite neatly if

we assume that the theoretical assignment of defect state relative energies and symmetries is correct [14], and that Ga-rich interfaces still contain some As defect states near the interface. In this case the n-type GaAs systems will experience Fermi-level pinning by the p-like defect states, while the p-type GaAs system will experience Fermi-level pinning by the s-like defect states (see Fig. 5). (Note, in the former case it is not essential that the p-like states pin the Fermi level, only that their energy is equal to or less than the energies of states that pin the Fermi level.) The observed resonances are derived by three-step processes that progress from occupied p-like defect states, to the s-like conduction band, to the p-like valence band, and then back to the original defect state. The last step is allowed as a result of weak strain- or field-induced interfacial state symmetry breaking. In general the strain-induced symmetry breaking is strong, but is limited to a few monolayers near the interface [4]; on the other hand, the depletion field-induced symmetry breaking may occur through the depletion length range (i.e. $\sim 0.1 \mu\text{m}$ in our samples). In principle both effects could contribute to the nonlinear optical processes. The model explains the observation of two resonance peaks in the Ga-rich interface, and it predicts no transitions in p-type GaAs systems since p-like states will be unoccupied. Finally the model predicts new resonances in spectral regions not studied here, as a result of processes coupled to the s-like defect states.

By comparison to broadened interface states observed in photoemission at very low Au coverages on GaAs surfaces [7], the very sharp observed spectra suggest that overlayer metal atoms displace the As or Ga, and that the detected atomic displacement defects occur in bulk GaAs just far enough from the interface so that their interaction with the metal overlayer free electron states is weak. Since the As displacement is among the most common defects in GaAs, the resonance state at 0.715 eV was still observed in the Ga-rich interfaces, albeit more weakly [12]. Signal sizes in our experiment suggest that the interface susceptibility $\chi^{(2)} \leq 10^{-16}$ esu. Model-dependent estimates of defect number densities may be derived using this nonlinearity. In the case of strain-induced effects, we might expect $\chi^{(2)} \sim N\alpha$, here N is the surface defects density within a few monolayers of the junction and α is single defect second-

order susceptibility. If we assume $\alpha \sim 10^{-29}$ esu, then $N \sim 10^{13} \text{ cm}^{-2}$. In the case of depletion field-induced effects, there are several hundred layers within the depletion region that can contribute to the signal. We may estimate the bulk antisite defect density N within this depletion region using simple models; it is of order $N \sim 10^{18} \text{ cm}^{-3}$. In reality both effects coexist and may affect our second order nonlinear processes. Qualitatively our spectra also suggest that the ratio of the two resonance peaks (0.715 eV, 0.731 eV) can be related to the ratio of As and Ga displacements defect at the interface. For example, if we assume the single defect has the same order susceptibility coefficient, the relative peak heights ratio $I_{\text{AsGa}}/I_{\text{GaAs}} \sim N_{\text{AsGa}}^2/N_{\text{GaAs}}^2$. This may prove to be a useful methodology for in situ chemical analysis during growth.

5. Conclusion

We have used second-order nonlinear optical spectroscopies (SHG and SFG) to probe the interface states at buried metal:GaAs junctions. Sharp resonance interface spectra arise from transitions between the midgap states and the conduction band minimum. Two interface resonance states at ~ 0.715 eV and ~ 0.731 eV were observed and are associated respectively, with As and Ga atomic displacements just below the buried interface.

Acknowledgements

We are happy to acknowledge stimulating discussions with E. Burstein, M.C. Tamargo, L. Richter, and especially R.E. Allen, and E. Mele. This work was supported by the ONR through Grant No. N00014-91-J-1867. A.G.Y. also acknowledges partial support from the NSF through the PYI program Grant No. DMR-9058498 and the MRL program Grant No. DMR-8519059, and the Alfred P. Sloan Foundation.

References

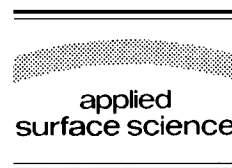
- [1] L.D. Bell and W.J. Kaiser, Phys. Rev. Lett. 61 (1988) 2368; W.J. Kaiser and L.D. Bell, Phys. Rev. Lett. 60 (1988) 1406;

- L.J. Brillson, R.E. Viturro, J.L. Shaw and H.W. Richter, *J. Vac. Sci. Technol. A* 6 (1988) 1437; D.E. Aspnes and A.A. Studra, *Phys. Rev. Lett.* 54 (1985) 1956.
- [2] T.F. Heinz, F.J. Himpsel, E. Palange and E. Burstein, *Phys. Rev. Lett.* 63 (1989) 644; U. Emmerichs, C. Meyer, H.J. Bakker, H. Kurz, C.H. Biorkman, C.E. Shearon, Y. Mao, T. Yasuda, Z. Jing, G. Lucovsky and J.L. Whitten, *Phys. Rev. B* 50 (1994) 5506; G. Lüpke, D.J. Bottomley and H.M. van Driel, *Phys. Rev. B* 47 (1993) 10389.
- [3] M.S. Yeganeh, J. Qi, A.G. Yodh and M.C. Tamargo, *Phys. Rev. Lett.* 68 (1992) 3761; 69 (1992) 3579.
- [4] W. Daum, H.J. Krause, U. Reichel and H. Ibach, *Phys. Rev. Lett.* 71 (1993) 1234; L.L. Kulyuk, D.A. Shutov, E.E. Strumban and O.A. Aktsipetrov, *J. Opt. Soc. Am. B* 8 (1991) 1766.
- [5] R.E. Viturro, J.L. Shaw, C. Mailhot, L.J. Brillson, N. Tache, J. McKinley, G. Margaritondo, J.M. Woodall, P.D. Kirchner, G.D. Pettit and S.L. Wright, *Appl. Phys. Lett.* 52 (1988) 2052.
- [6] R. Ludeke, D. Straub, F.J. Himpsel and G. Landgren, *J. Vac. Sci. Technol. A* 4 (1986) 874.
- [7] R. Haight and J. Bokor, *Phys. Rev. Lett.* 56 (1986) 2846.
- [8] Y.R. Shen, *The Principles of Nonlinear Optics* (Wiley, New York, 1984).
- [9] J.H. Neave and B.A. Joyce, *J. Cryst. Growth* 44 (1978) 387.
- [10] H.H. Farrel, M.C. Tamargo and J.L. de Miguel, *Appl. Phys. Lett.* 58 (1991) 355; M.C. Tamargo, R.E. Nahory, B.J. Skromme, S.M. Shibli, A.L. Weaver, R.J. Martin and H.H. Farrell, *J. Cryst. Growth* 111 (1991) 741.
- [11] W.E. Spicer, I. Lindau, P. Skeath and C.Y. Yu, *J. Vac. Sci. Technol.* 17 (1980) 1019.
- [12] C. Frigeri, J.L. Weyher and H.C. Alt, *Phys. Status Solidi (a)* 138 (1993) 657.
- [13] R.M. Feenstra, A. Vaterlaus, J.M. Woodall and G.D. Pettit, *Appl. Phys. Lett.* 63 (1983) 2528.
- [14] R.E. Allen and J.D. Dow, *Phys. Rev. B* 25 (1982) 1423; R.E. Allen, O.F. Sankey and J.D. Dow, *Surf. Sci.* 168 (1986) 376.
- [15] R.E. Allen, private communication.



ELSEVIER

Applied Surface Science 104/105 (1996) 196–203



Spatially resolved internal and external photoemission of Pt/n-GaP Schottky barrier

C. Coluzza^{a,b,*}, J. Almeida^b, Tiziana dell'Orto^b, F. Barbo^c, M. Bertolo^c,
A. Bianco^c, S. Cerasari^c, S. Fontana^c, O. Bergossi^d, M. Spajer^d, D. Courjon^d

^a *Dipartimento di Fisica, Università di Roma "La Sapienza", P.le A. Moro 2, 00185 Roma, Italy*

^b *Ecole Polytechnique Fédérale, PH-Ecublens, CH-1015 Lausanne, Switzerland*

^c *Sincrotrone Trieste SpA, Padriciano 99, 34012 Trieste, Italy*

^d *Laboratoire D'Optique "P.M. Duffieux", Université de Franche-Comté, 25030 Besançon, France*

Received 1 August 1995; accepted 6 October 1995

Abstract

We studied the Pt/n-GaP buried Schottky junction by several spatially resolved techniques to correlate the chemical inhomogeneities of the interface with the spatial variations of the diode transport properties. The recombination rate fluctuations and small spatial variations (3–8 meV) of the Schottky barrier height were correlated with the local stoichiometry of the bare GaP surface and of the fully formed junction. We discovered regions with local segregation of metallic gallium. In these regions we measured a Schottky barrier height only 4 meV lower than in the stoichiometric areas. On the contrary these zones presented a more important electron–hole recombination rate.

1. Introduction

We used several experimental techniques to investigate one of the major problems in today's solid-state physics: the lateral variations of buried interface properties. We performed a spatially resolved study of (80 Å)Pt/n-GaP Schottky barrier by scanning near-field optics microscopy (SNOM) [1], spatially resolved internal photoemission (SRIPE) [2], X-ray secondary photoemission electron microscope (XPEEM) [3], and X-ray photoemission spectromicroscopy (XPSM) [4]. These complementary techniques enabled us to correlate the spatial variations of the diode transport properties with the chemical

inhomogeneities of the GaP bare surface and of the buried metal–semiconductor interface.

Lateral variations of interface properties such as energy barriers and recombination rates are critical for technological applications. They also affect our fundamental understanding of this class of solid systems; for example, they can force us to re-think the very definition of parameters such as the Schottky barrier and of the corresponding interface physical properties [5,6]. In particular, it is very important to correlate these properties with the local stoichiometry of the 'clean' surface of the semiconductor substrate as well as with the local chemical properties of the fully formed interface.

The combination of internal photoemission (IPE) and of the scanning near-field optics microscopy (SNOM) enabled us to measure the interface pho-

* Corresponding author.

photocurrent with high lateral resolution. In essence, our approach consists of measuring the photocurrent induced in a circuit including the interface under investigation by a focused photon source. Interface energy barriers can be derived from thresholds in the photocurrent versus photon energy spectra, and information on the recombination rates is provided by the photocurrent intensity [2,5]. The energy barriers are measured in real devices with high energy resolution of about 1 meV, and lateral variations less than 1 μm can be detected.

Due to the escape depth of the secondary photoelectrons (around 100 Å), the X-ray secondary photoemission electron microscopy measurements are able to supply chemical information from a buried interface. The lateral resolution is similar to that of SNOM-IPE allowing a direct correlation between the local phototransport properties and the local chemical status at the interface of the same sample [3,6].

We observed large lateral variations in the photocurrent properties which do not match topographic features of shear-force microimages, and reveal fluctuations in the electron–hole recombination rate that are crucial to the interface properties and applications. With the same experimental setup we also detected equally lateral variations of the Pt/GaP Schottky barrier, of 3–8 meV on the scale of less than 1 μm . These variations correspond to local Ga segregation induced by the GaP surface preparation.

2. Experimental procedure

The specific samples studied in this experiment were obtained by electron gun evaporation of 80 Å of Pt on n-type GaP(001) sulfur doped substrates ($n = 5 \times 10^{17} \text{ cm}^{-3}$). Prior to the deposition, the substrates were cleaned with hot organic solvents and in a 5% HCl solution during 1 min and rinsed with deionized water. A 8 nm thick Pt films was deposited; the structure required for IPE measurements was completed by ohmic contacts consisting of a 62% Au–38% Sn alloy.

Before the deposition of the metallic overlayer, we performed a chemical study of the semiconductor bare surface by X-ray photoemission spectromicroscopy. Our ESCA-300 system was described in

Ref. [4]. Briefly, we worked at an operating pressure better than 3×10^{-10} mbar, with energy resolution of 0.29 eV and lateral resolution of 12 μm as determined by resolving lithographic microstructures.

On the fully formed metal–semiconductor junction, XPEEM experiments were performed at the Sincrotrone Trieste SpA by an instrument similar to that described in Ref. [3], on a beamline connected directly to an undulator. The spatial resolution was $\approx 2 \mu\text{m}$, as determined by resolving lithographic microstructures. The beamline was not equipped with a monochromator and the photon energy was tuned by changing the gap of the undulator. The photon energy resolving power was ~ 33 , sufficient to discriminate the absorption edges of Pt5p, Ga3p and P2p.

We achieved high lateral resolution in the internal photoemission measurements by illuminating the sample with a small light source. This approach is based on the SNOM technique [7–9], i.e. on pulled and aluminum coated optical fibers which concentrate the light on an open edge aperture of 50 nm. The light was injected through the tip into the 8 nm semitransparent Pt metallic layer. Piezoelectric feedback-controlled oscillators provided the vertical approach up to the near field condition as well as the X–Y scanning over an area ranging from 8–30 μm . The experiments were performed with a constant 10 nm tip-to-sample distance; this resulted in a topographic vertical resolution of about 1 nm. The tip-sample distance was controlled by a shear-force feedback system, as described in Ref. [8]. As light sources, we used a tunable dc Ti–Sapphire laser (1.35–1.5 eV) or a solid state laser diode (fixed photon energy at 1.518 eV). In the case of Ti–Sapphire laser, the photon energy was tuned in the interval 1.319–1.53 eV, with an estimated resolution of about 1 meV, as determined by the FWHM of luminescence lines of test samples.

Photocurrent microimages were obtained by detecting the photocurrent signal while scanning the beam over the sample. The photocurrent was revealed with a standard lock-in technique. Likewise, topographic images were obtained by measuring the shear-force signal with a synchronous detection including a piezoelectric oscillator and a lock-in amplifier [2,8,10]. Our present lateral resolution is already

close to, or better than, the classical limit of $\lambda/2$ as estimated by resolving lithographic structures.

3. Results and discussion

In Fig. 1, we show ESCA-300 Ga3d core level spectra taken at different positions on the 'clean' GaP surface, immediately after the chemical etching. The analyzed area was $20 \times 20 \mu\text{m}$, as determined by the magnification factor and the size of the illuminated area on the multichannel plate and of the entrance slit of the electron analyzer. The spectra were shifted by aligning the C1s peak for each position at 284.6 eV. The raw data presented a relative shift of the C1s as high as 1 eV, indicating an inhomogeneous local charging. Even after the C1s normalization, the spectra presented a non perfect alignment (see, for example, curve 200–220 μm and curve 100–120 μm), probably due to a difference in the potential energy between the carbon contaminant layer (at the surface) and the probed gallium atoms deeply located in the GaP bulk. From this figure, it is evident that in some regions (see curves 300–320 μm and 400–420 μm) the Ga3d presented a different peak shape. From a deconvolution of these peaks by Voigt functions, we observed the presence of

two doublets relatively shifted by around 0.6 eV. These results indicate the presence of a metallic gallium phase which contributes to the spectrum with a peak located at lower binding energy and shifted by the same value that we found [11]. On the contrary, the P2p core level peaks were well fitted by only one doublet in all regions, further supporting the metallic gallium segregation.

Fig. 2a shows XPEEM micrographs of a fully formed (80 Å)Pt/GaP Schottky barrier. Bright regions correspond to areas of stronger emission. The chemical information is obtained by digital subtraction of images taken at photon energies above and below the absorption edges of the elements (Pt5p, Ga3p, and P2p). Three main features are evident: (1) dark and bright areas, (2) few bright 'drops' (see squared zones in all images), (3) the presence of dark lines.

In XPEEM measurements, the contrast comes from a local difference of the surface work function and/or from a local difference in the stoichiometry of the probed thickness (around 100 Å). In our case, the surface is covered by a Pt layer of 80 Å, so we can assume that the surface work function is quite homogeneous, as demonstrated also by the Pt5p and P2p microimages. On the contrary, in the Ga3p images large bright areas are evident (see, for example, the region near the small square). These regions could be assigned to Ga segregation in good agreement with the XPSM results.

In Fig. 2b, we zoomed on the regions indicated in Fig. 2a by large squares ('drops' areas). The Ga segregation is clearly present (see in the right images the intensity plots along the dashed lines of the left images). In these zones, an increase of the Pt signal and a decrease of the P signal are also evident. This result indicates a local increase of the thicknesses of the metallic overlayer (platinum and gallium).

Fig. 3 shows a typical set of SNOM-IPE microimages taken at the photon energy of 1.518 eV (laser diode source). On the left, we see the shear-force (topographic) image over a $32 \times 32 \mu\text{m}$ area. The analyzed region presents clear lateral topographic variations on the scale of less than 1 μm . Dark-bright zones of the micrograph reveal roughness variations of the sample surface of about 140 nm. In the center, we see the scanning IPE (photocurrent) micrograph of the same area. Brightest and darkest

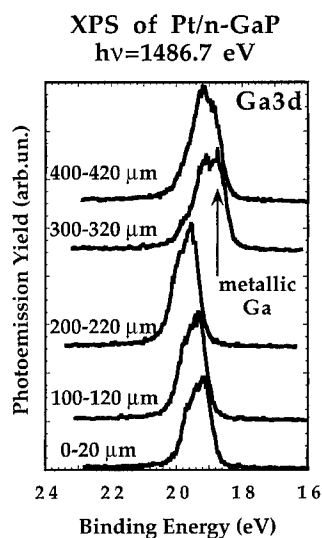


Fig. 1. ESCA-300 Ga3d core level spectra taken at different positions on the HCl chemically etched GaP surface. The metallic Ga contribution is indicated by an arrow.

XPEEM of Pt/n-GaP

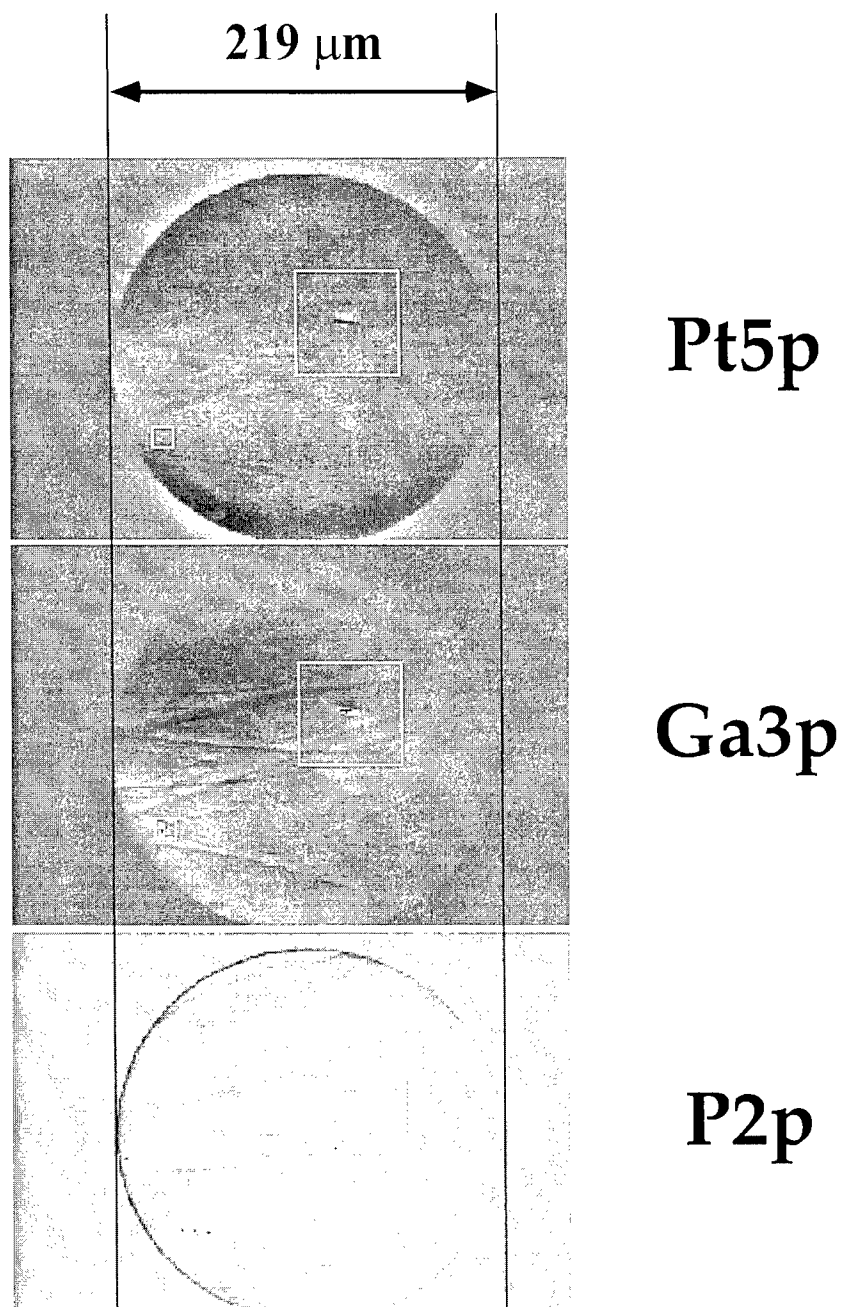


Fig. 2. (a) XPEEM micrographs of a fully formed (80 Å)Pt/GaP Schottky barrier. Bright regions correspond to areas of stronger emission. (b) Zoom of the zone marked by the large white squares in (a). On the right are reported the intensity plots along the dashed lines of the left images.

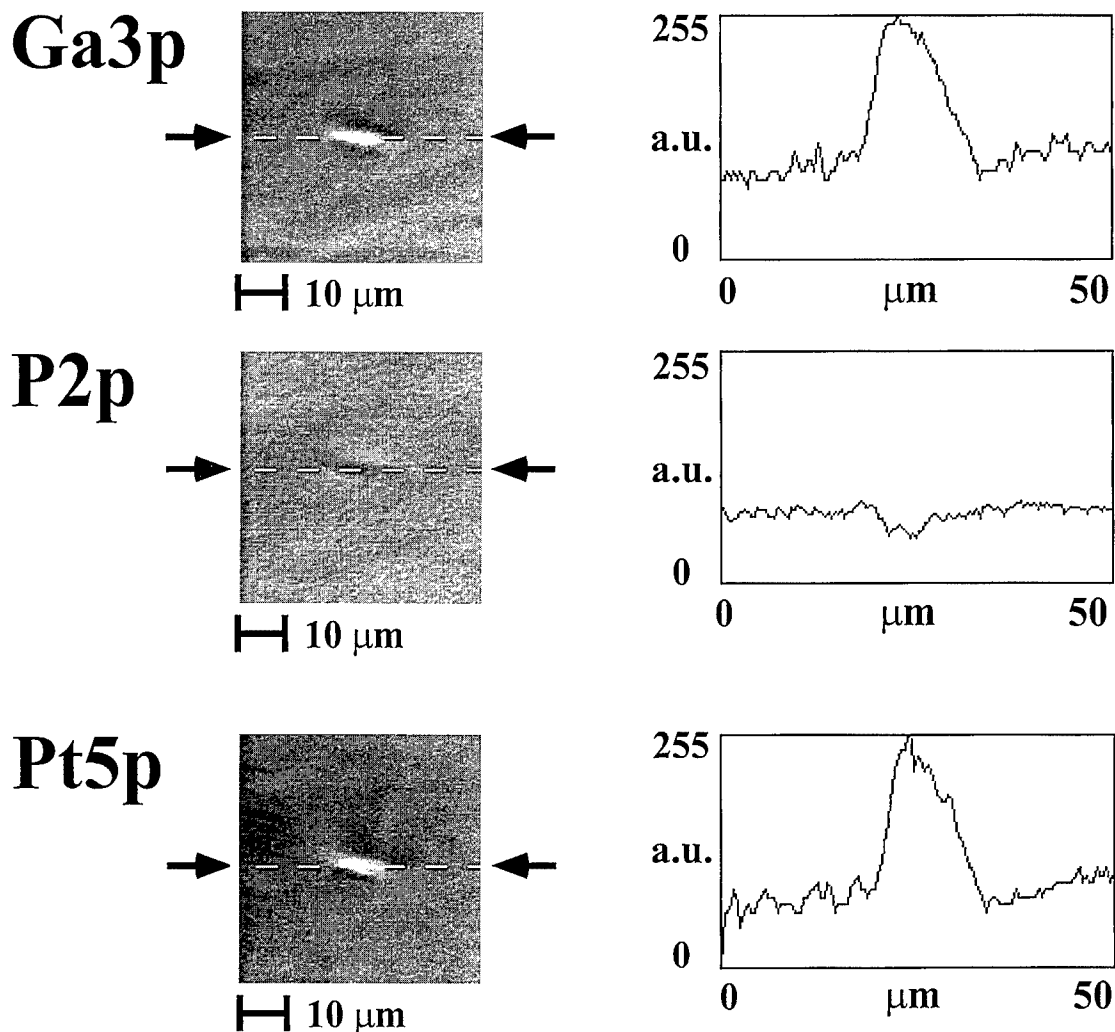


Fig. 2 (continued).

regions correspond to a photocurrent of 0.8 nA and less than 0.2 nA. On the right, we report the reflection microimage. It is important to stress that the SNOM-IPE technique gives parallel information (topography, phototransport, and optic) on the same area. The lateral resolution is similar to that of XPEEM as demonstrated by the linear features corresponding to the dark lines of Fig. 1. In the lower part of the figure, we show the intensity plots across the rectangular area indicated in the upper part. From these plots it is evident that the linear features could be explained as scratches on the GaP substrates created during the surface preparation.

A comparison of topographic and IPE photocurrent variations in Fig. 3 shows no one-to-one correspondence between them. There are dark and bright zones in the photocurrent microimage that do not correspond to any inhomogeneous area in the shear force microimage. Thus, the spatial variations in the photocurrent intensity are not — or rather not only — caused by the surface topography.

Our approach allows us to explore locally what is perhaps the most important factor for heterostructure transport properties: the interface energy barriers — the Schottky barrier height in the present case. Typical results are shown in Fig. 4. In the upper part we

SNOM-IPE of Pt/GaP

$h\nu=1.512$ eV, $32\times 32\text{ }\mu\text{m}$

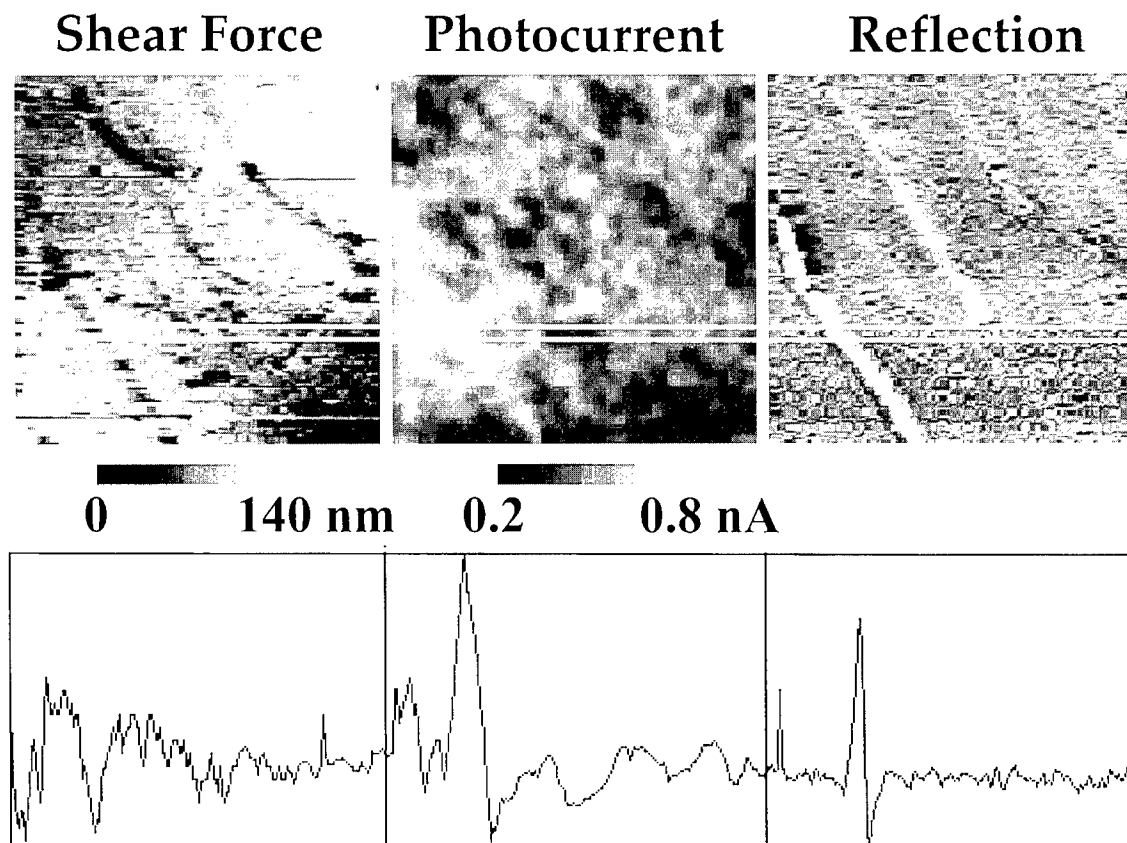


Fig. 3. Shear-force topography and corresponding photocurrent and reflection microimages of a $32 \times 32\text{ }\mu\text{m}$ region. In the lower part, we show the intensity plots across the rectangular area indicated in the upper part.

show the topographic micrograph and the corresponding photocurrent intensity image taken at $h\nu = 1.465$ eV. The correspondence between the features in both microimages is evident. These features correspond also to features indicated in Fig. 2 by small squares, where Ga segregation was found. In particular, the bright spots in the topography are not dust particles on the device surface. Such particles correspond to bright zones in the photocurrent images.

In the lower part of Fig. 4 we show the squareroot of the photocurrent versus photon energy (Fowler plot [12]) taken at points A and B of the photocurrent

image, together with the spatially integrated IPE curve. The photocurrent threshold position corresponds to the Schottky barrier height. By a linear fit of the curve edge, we obtain a Schottky barrier of 1.409 and 1.413 eV for point A and B, respectively. For the integrated case, we obtain 1.415 eV. If, as assumed, the thermoionic emission process is dominant in the I - V characteristics, a variation of 4 meV of the Schottky barrier height induces a photocurrent intensity variation of about 15%, which is too small to justify the intensity fluctuations in photocurrent microimages. The observed large intensity fluctua-

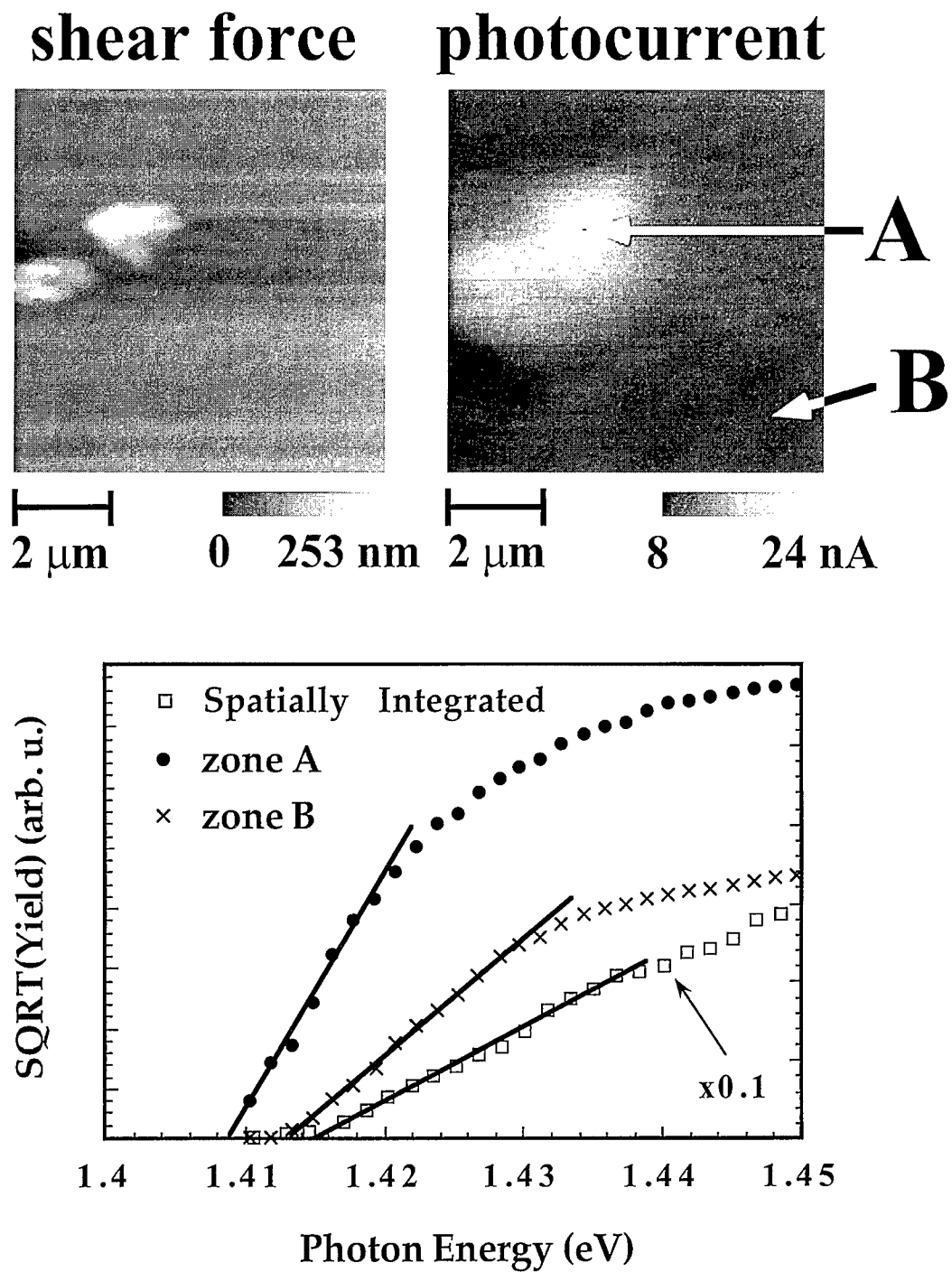


Fig. 4. (a) Shear-force topography and photocurrent microimages in a $8 \times 8 \mu\text{m}$ region taken at $h\nu = 1.465 \text{ eV}$. This zone corresponds to the areas marked by the small white squares in Fig. 2a. (b) The square-root of the internal photoemission yield versus photon energy measured at 300 K in the 'bright' (A) and 'dark' (B) zone. The scaled ($\times 0.1$) spatially integrated IPE curve is also shown.

tions could be instead assigned to lateral variations of the recombination rate or of the metal thickness.

In summary, we successfully tested a combination of different spatially resolved techniques to study different aspects of the lateral fluctuations in the properties of a buried metal–semiconductor interface. We detected four types of variations: topographic effects, chemical effects, energy barrier variations, and photocurrent intensity variations of non-topographic origin (recombination rate). In particular we found small variations of the Schottky barrier height value in zones where Ga segregation was detected.

Acknowledgements

The authors thank Professor G. Margaritondo for helpful discussions and suggestions. This work was supported by the Swiss National Science Foundation, by the Ecole Polytechnique Fédérale de Lausanne, and by the Ministère de la Recherche et de l'Enseignement Supérieur (France).

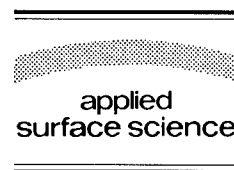
References

- [1] D.W. Pohl, *Advances in Optical and Electron Microscopy*, Vol. 12, Eds. C.J. Sheppard and T. Mulvey (Academic Press, London, 1992).
- [2] J. Almeida, T. dell'Orto, C. Coluzza, G. Margaritondo, O. Bergossi, M. Spajer and D. Courjon, *Appl. Phys. Lett.*, to be published (1995).
- [3] B.P. Tonner, G.R. Harp, S.F. Koranda and Zhang, *Rev. Sci. Instr.* 63 (1992) 564; B.P. Tonner and G.R. Harp, *J. Vac. Sci. Technol. A* 7 (1989) 1; B.P. Tonner, *Ultramicroscopy* 36 (1991) 130.
- [4] U. Gelius, B. Wannberg, P. Baltzer, H. Fellner-Feldegg, G. Carlson, C.G. Johansson, J. Larson, P. Mürger and G. Vegefors, *J. Electron Spectrosc. Rel. Phen.* 52 (1990) 747.
- [5] C. Coluzza, G. Margaritondo, A. Neglia and R. Carluccio, *J. Vac. Sci. Technol. A* 10 (1992) 744; T. dell'Orto, J. Almeida, C. Coluzza, A. Baldereschi, G. Margaritondo, M. Cantile, S. Yildirim, L. Sorba and A. Franciosi, *Appl. Phys. Lett.* 64 (1994) 16.
- [6] J. Almeida, F. Barbo, M. Bertolo, A. Bianco, A. Braem, S. Cerasari, C. Coluzza, T. dell'Orto, S. Fontana, G. Margaritondo, E. Nappi, G. Paic, F. Piuze, R. Sanjines, T. Scognetti, S. Sgobba, *Nucl. Instr. Meth. A*, to be published (1995); T. dell'Orto, J. Almeida, C. Coluzza, E. Conforto, G. De Stasio, G. Margaritondo, G. Paic, A. Braem, F. Piuze and B.P. Tonner, *J. Vac. Sci. Technol.*, to be published (1995).
- [7] E. Betzig and J.K. Trautmann, *Science* 2567 (1992) 189.
- [8] E. Betzig, P.L. Finn and J.S. Wiener, *Appl. Phys. Lett.* 60 (1994) 2484.
- [9] S.K. Buratto, J.W.P. Hsu, E. Betzig, J.T. Trautman, R.B. Bylisma, C.C. Bahr and M.J. Cardillo, *Appl. Phys. Lett.* 65 (1994) 21.
- [10] O. Bergossi and M. Spajer, *SPIE Conf. Interferometry*, Warsaw, 1994, Vol. 94.
- [11] C.D. Wagner, W.M. Riggs, L.E. Davis, J.F. Moulder and G.E. Muilenberg, Eds., *Handbook of X-ray Photoelectron Spectroscopy* (Perkin-Elmer, Eden Prairie, MN, 1979) p. 86.
- [12] R.H. Fowler, *Phys. Rev.* 38 (1931) 45.



ELSEVIER

Applied Surface Science 104/105 (1996) 204–212



Structural properties of epitaxial silicide layers on Si

H. von Känel^{*}, E. Müller, S. Goncalves-Conto, C. Schwarz, N. Onda

Laboratorium für Festkörperphysik, ETH Zürich, CH-8093 Zürich, Switzerland

Received 26 June 1995; accepted 3 October 1995

Abstract

The formation of epitaxially stabilized (pseudomorphic) Fe and Co silicides on Si(111) is reviewed. We show that, apart from the α -FeSi₂ phase, which is also stable in bulk form at high temperatures, none of the pseudomorphic phases is ever likely to be the lowest energy phase, with the exception of FeSi with the CsCl structure. For FeSi, the positive contribution of the interface to the total energy of the bulk stable phase, ϵ -FeSi, is sufficiently large to reverse the stability, i.e. (CsCl)FeSi is truly stable for thicknesses below $H_c \sim 15$ Å. From the structural point of view, Fe and Co silicides are found to be more similar than believed heretofore. In particular, we find that, at low substrate temperatures and under particular conditions, CoSi₂ may crystallize with a CsCl structure with random metal vacancies instead of the well known bulk stable CaF₂ structure.

1. Introduction

Epitaxial silicides on silicon have been of great interest, both in view of their possible applications in microelectronics [1] and for fundamental research. Most metals in contact with a clean Si surface react to form one or several silicides, depending on the temperature. Such solid state reactions have been studied in great detail during the past two decades, and excellent review articles are available [2]. Most phases formed by this procedure are not epitaxial on a large scale, however, since only few of them have simple crystal structures and are well lattice-matched to the Si substrate. The same is true for other growth techniques, such as molecular beam epitaxy (MBE),

even though in this case the problem of mass transport, i.e. the supply for Si from the substrate, does not exist. On the other hand, it is well known that, especially for bulk crystal structures characterized by a large misfit, a bulk metastable phase may be more favourable to grow epitaxially [3,4]. The physical mechanism responsible for the epitaxial stabilization of a bulk metastable phase is usually its lower elastic energy, compared to that of the bulk stable phase, when both are assumed to form coherent epitaxial interfaces. In other words, the epitaxially stabilized, or *pseudomorphic*¹ [3,5] phase is better lattice

^{*} Corresponding author. Tel.: +41-1-6332261; fax: +41-1-6331072; e-mail: kaenel@solid.phys.ethz.ch.

¹ The expression 'pseudomorphic' is not a synonym for 'coherent' here. It rather describes a situation in which an epitaxial film adopts a crystal structure which differs from that of the corresponding bulk stable phase but is determined by the underlying substrate. See also [5].

matched to the substrate than the bulk stable phase and therefore less strained. It is important to emphasize here that by epitaxial stabilization of a bulk metastable phase we refer to a situation in which this phase has the *lower* free energy when forced to the substrate lattice constant, and is therefore the thermodynamically favoured phase. It is conceivable, and in fact examples will be shown below, that a bulk metastable phase may be favoured by epitaxy for kinetic reasons alone, whence it *remains metastable* even in contact with a suitable substrate. There have been occasional reports on the occurrence of metastable epitaxial silicides in the past [6–9] but for a long time no systematic attempt was undertaken to put the observations on a quantitative basis. More recently, the study of epitaxially stabilized silicides has been stimulated by the discovery of an epitaxial FeSi₂ phase with the fluorite structure, designated with γ -FeSi₂ [10]. At first sight, the occurrence of this phase may not be very surprising, since the corresponding bulk stable phase, β -FeSi₂, may be considered to be related to it by a Jahn-Teller-like distortion, giving rise to a metal–semiconductor transition [11]. The total energy of the γ -phase turns out to be higher, however, than that of the β -phase by as much as ~ 0.5 eV per formula unit [12]. It is out of the question that the elastic energies are sufficiently different to reverse this balance. In other words, γ -FeSi₂ cannot be expected to be epitaxially stable as long as only the elastic energies associated with straining the lattices into coherency with the Si substrate are taken into account. A similar situation pertains to a FeSi phase with the CsCl structure, which is epitaxially favoured over the bulk stable ϵ -FeSi phase, even though its energy is higher by ~ 0.54 eV per formula unit [13]. A recently discovered CoSi phase with the same CsCl structure turns out to be even less stable, and yet it is preferred over the corresponding bulk stable phase when epitaxially grown on Si(111). Yet another example considered in the following are structures obtained by removing metal atoms from the CsCl lattice sites in a statistical manner [14]. The resulting CsCl defect phases are found to be surprisingly stable with respect to a phase transition to a bulk stable MSi₂ phase, where M = Fe, Co.

In all of these cases there must exist other factors contributing to the stability. As will be argued be-

low, it is the energetics of the interface that plays a decisive role.

2. Synthesis of bulk unstable epitaxial silicides

Quite a few of the silicide phases discovered in the past few years can be synthesized by simply depositing the metal onto the clean Si substrate, followed by an annealing step, resulting in solid phase epitaxy (SPE). Especially the cubic FeSi₂ phases were grown on Si(111) in this way and investigated by a variety of experimental techniques [15–26]. Since these phases are epitaxially stable only as long as the films remain very thin (typically a few monolayers), the identification of the structure becomes very difficult when the SPE technique is used for growth. In many studies the cubic phase was nevertheless ‘identified’ with γ -FeSi₂, without any real structure determination. It is therefore conceivable that at least in some of these cases the phase in question must be attributed to Fe_{1-x}Si which has the CsCl structure with randomly arranged Fe vacancies [14]. Phase identification is much simpler for MBE grown films, since they can be grown homogeneously to larger thicknesses, by making use of the kinetic barriers preventing the transition to the bulk stable phases. Before discussing in more detail the results obtained on films grown by solid source MBE, it should be emphasized that the epitaxial stabilization of silicides, notably γ -FeSi₂, has been achieved by a number of other techniques, such as gas source MBE [27], liquid phase epitaxy [28,29] and ion beam synthesis [30]. In the latter case the phase was present in the form of precipitates in Si.

As pointed out before, the great advantage of solid source MBE lies in the possibility to synthesize pseudomorphic films with thicknesses far above their stability range. This is particularly important for the pseudomorphic silicides considered here, since for all of them the true thermodynamic stability, if existent at all, is limited to very small thicknesses. It is therefore highly desirable to have a low-temperature growth technique at one’s disposal, which allows to grow films that are *metastable*.

Fortunately, it turns out that by forming an epitaxial template of the order of 10 Å in thickness on Si(111) before the actual MBE step, many of the

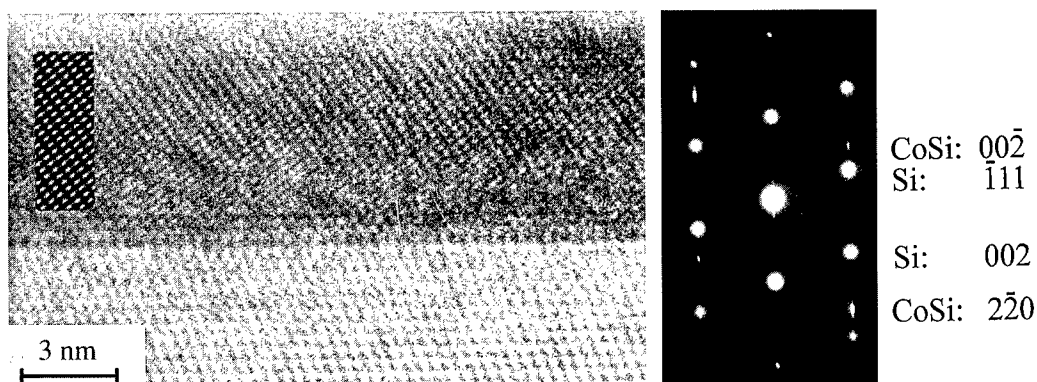


Fig. 1. HRTEM image and selected area diffraction pattern of a CoSi layer with the CsCl structure. The diffraction spots of the silicide are indexed with respect to the cubic Si unit cell. Parameters used for the image simulation: specimen thickness $d = 3.8$ nm; defocus $\Delta f = -80$ nm; high voltage = 300 kV; spherical aberration constant $C_s = 1.1$ mm; focus spread = 8 nm; semi convergence angle $\alpha = 0.6$ mrad.

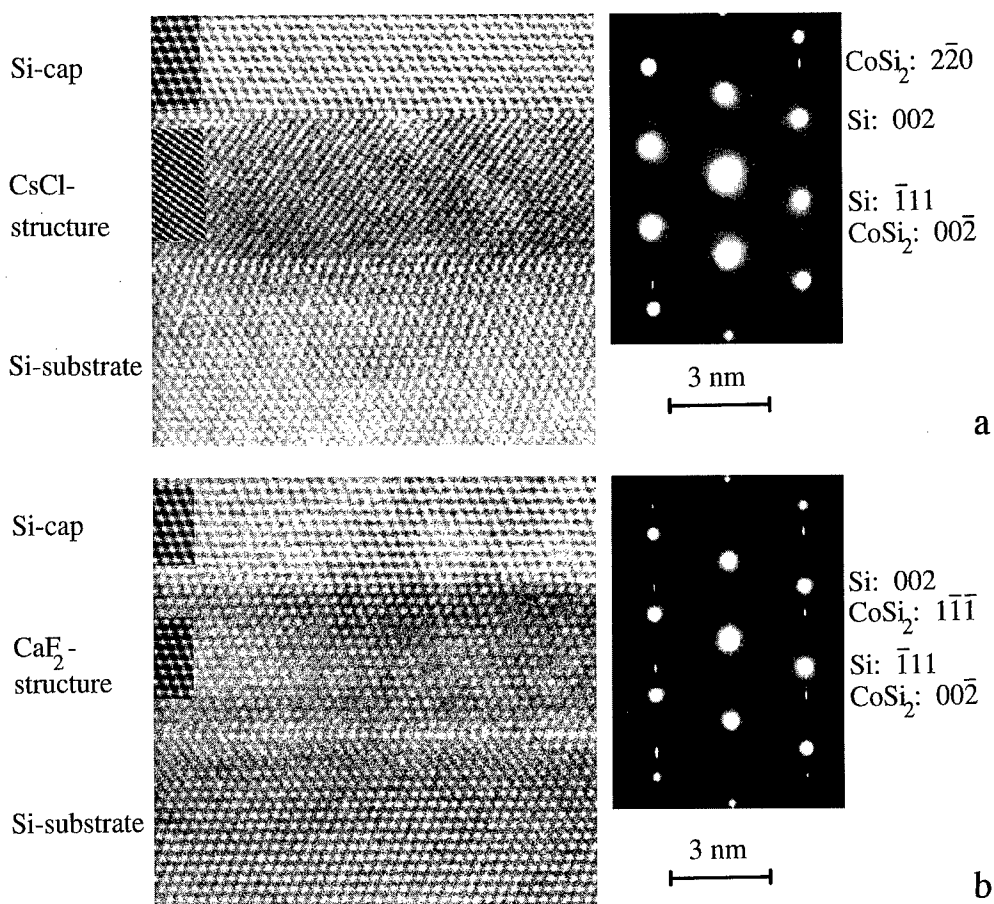


Fig. 2. HRTEM image and SAD pattern of CoSi₂ grains with the CsCl structure (a) and the CaF₂ structure (b), respectively. The SAD pattern due to the CsCl structure (indexed according to the Si unit cell) differs from that originating from the CaF₂ structure by the absence of spots with odd indices. Parameters used for the simulation: identical to those in Fig. 1, except for $d = 6.1$ nm, $\Delta f = -30$ nm (a) and $d = 4.6$ nm; $\Delta f = -37$ nm (b), respectively.

phases can be epitaxially grown at room temperature (RT). It does not seem to matter how the templates are exactly grown, since codeposition followed by annealing or deposition of the pure metal with or even without an annealing step [14] all result in epitaxial films during the subsequent codeposition. The quality of the films is, however, improved when annealed templates are used. This is exemplified by the improved ion channeling yields in Rutherford backscattering spectrometry [31]. In the case of the Fe silicides it could unambiguously be proven that the phases grown at RT are cubic in the whole stoichiometry range between FeSi_2 and pure bcc Fe [32]. Moreover, if the unit cell of the CsCl structure is taken as the basic building block, then all these phases can be derived by arranging Fe and Si atoms or vacancies on the CsCl sites in the appropriate way [33].

While the pseudomorphic Fe silicide phases have been known for a number of years, the question, to what extent similarities with other metal silicides might exist, has been raised more recently. Following a suggestion of Mäder et al. [34], a new CoSi phase with the CsCl structure could indeed be synthesized, in a manner identical to that of FeSi [13,35]. As an illustration, a high-resolution transmission electron microscopy (HRTEM) image obtained from a cross-section of a (CsCl)CoSi sample is shown in Fig. 1. An image contrast calculation and a selected area diffraction (SAD) pattern is included in the figure. The silicide reflections are indexed with respect to the unit cell of Si. Other than in the CaF_2 structure, the reflections with odd indices are absent [14]. Since the corresponding bulk stable monosilicides, $\epsilon\text{-FeSi}$ and $\epsilon\text{-CoSi}$, crystallize with the same 'FeSi' structure [36], it is interesting to compare the relative stability of the two pseudomorphic CsCl phases. This will be done in the next section.

Let us have a look first, however, at the intriguing problem of Si-rich Co silicides, such as CoSi_2 . Work on epitaxial CoSi_2 with the bulk stable fluorite structure dates back to the early eighties [37,38]. In these early studies and for many years thereafter CoSi_2 films were either grown by SPE or MBE, with annealing or substrate temperatures far above RT (typically up to 600°C). The first report on CoSi_2 grown epitaxially at RT by coevaporation onto ultra-thin templates of pure Co appeared many years later

and did not include any structure determination [39]. In view of the fact that thin pseudomorphic Fe silicides with the CsCl structure are epitaxially stable in the whole range of stoichiometries between that of FeSi and FeSi_2 , and taking into account the existence of a CoSi phase with the same structure, the question naturally arises whether perhaps the analogy might be extended to CoSi_2 . In other words, do we necessarily have to assume CoSi_2 to crystallize with the CaF_2 structure? That this may not be the case can indeed be seen in Fig. 2, displaying two HRTEM micrographs of the *same* CoSi_2 film after annealing to $\sim 550^\circ\text{C}$. The film was synthesized by using the same template technique as described above for the Fe silicides. The HRTEM image of the grain presented in Fig. 2a shows a striking similarity with the image of Fig. 1, as does the SAD pattern. The corresponding image of a CaF_2 grain is shown in Fig. 2b. Also included in Fig. 2 are the simulations of the image contrast for the two assumed structures, leaving little doubt that our assignment is correct. In particular, it has to be pointed out that the *adamantane* structure of CoSi_2 , which may occur in CoSi_2 formation from Co/Ti bilayers [40], cannot be confused with the (CsCl) $\text{Co}_{0.5}\text{Si}$ structure, where half the Co atoms have been removed from their CsCl lattice sites in a random fashion. This has been proven by calculations of the image contrast expected for the former structure.

Preliminary results obtained by X-ray diffraction indicate, that as-grown films, i.e. films grown at RT onto a preformed CoSi_2 template, may crystallize almost entirely with the proposed CsCl defect structure. This happens despite of the CaF_2 structure of the template itself. Annealed films grown *without* a template, i.e. by stoichiometric coevaporation onto the clean Si surface, rarely contain any grains of this phase, however. The growth kinetics of films codeposited on clean Si and on a template, respectively, have been known to be different for a long time [9], since in the former case the film starts out to be amorphous for substrate temperatures near RT, and becomes epitaxial only upon annealing. Our new results thus seem to indicate that CaF_2 is the favoured phase when nucleation of epitaxial grains starts from the amorphous state, whereas, in the case of MBE growth on epitaxial templates, grains of the CsCl defect phase nucleate more easily.

3. Stability of pseudomorphic phases

It has already been pointed out in the introduction that the observation of the pseudomorphic silicides discussed here can hardly be explained by simple elastic energy considerations, favouring them over their bulk stable counterparts. Let us nevertheless discuss briefly, what a behaviour should be expected, if it sufficed to take into account the elastic energy associated with straining each structure to the substrate lattice parameter [4]. We assume that for thin films the pseudomorphic phase is the one with the lowest energy. The energy per formula unit of the bulk stable and the pseudomorphic phase would then remain constant, up to a critical film thickness h_c , where that of the bulk stable phase would start to decrease because of the formation of misfit dislocations. The pseudomorphic film would tend to remain coherent because of its lower misfit, whence its energy would keep on being constant. At the critical thickness H_c , at which the two energy curves cross, a phase transition to the bulk stable phase would therefore be expected to take place, since from then on it is the lowest energy phase. A scenario of the kind described may be expected whenever there exists a metastable bulk phase whose energy is so close to the one of the stable phase, that the elastic energy increase due to the misfit strain is sufficiently large to reverse the order of the energies of the two phases. This is particularly likely for systems exhibiting a structural phase transition at some critical temperature, as is the case, e.g. for many elemental metals. There are indeed numerous reports in the literature about the epitaxial stabilization of metals in

a bulk metastable crystal structure (see, e.g. Refs. [3,4] and references therein).

A structural phase transition from the semiconducting β -phase, stable at low temperatures, to the metallic α -phase, stable above $\sim 950^\circ\text{C}$, has long been known to take place in FeSi_2 . Ion implantation, followed by a high-temperature anneal [41,42], or alternatively the more recent technique of allotaxy [43], do indeed lead to the formation of buried epitaxial α - FeSi_2 . Even more important in the present context is the fact that the α -phase can be grown at temperatures around 500°C , i.e. well below the bulk phase transition [44–46]. In these cases the α - FeSi_2 phase was found to be present in the form of small grains rather than continuous films. By annealing Fe silicide films with the CsCl defect structure around the same temperature, we have also observed the α -phase to form. Such films, despite of being characterized by extremely smooth interfaces and surfaces, always contain a mixture of α - FeSi_2 , γ - FeSi_2 and $\text{Fe}_{0.5}\text{Si}$ grains. In HRTEM images, the transition between all of these phases appears to be gradual. Fig. 3 shows such a transition region between an α - FeSi_2 grain on the left and a grain of the $\text{Fe}_{0.5}\text{Si}$ phase on the right, each one accompanied by a simulation of the image contrast. To our knowledge it has not been possible to synthesize, by any method, single crystalline films of the pure α -phase in the thickness range considered here, i.e. several nm. The closest approach to uniform α - FeSi_2 may have been 20–40 Å thick films overgrown epitaxially with Si, since they could be annealed to higher temperatures without disrupting and/or transforming into β - FeSi_2 [47]. The rhombohedral distortion ob-

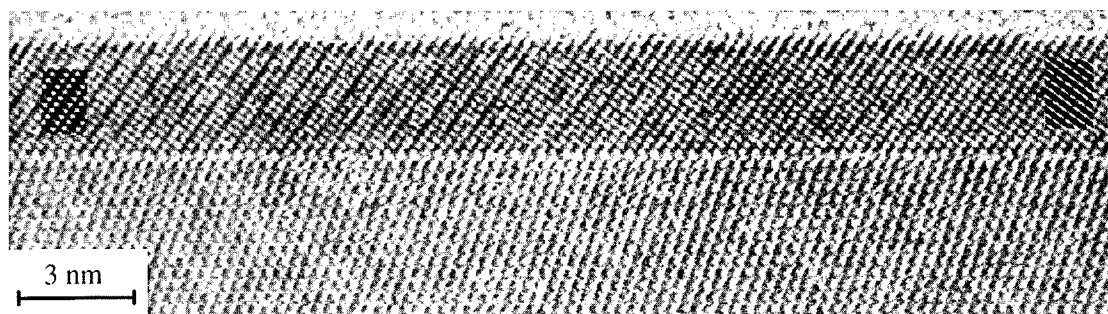


Fig. 3. HRTEM image of a Fe silicide film, showing the transition region between α - FeSi_2 (left side) and $(\text{CsCl})\text{Fe}_{0.5}\text{Si}$ (right side). Specimen thickness $d = 5.8$ nm, defocus $\Delta f = -87$ nm. For all other parameters, see Fig. 1.

served in these films is of the same sign and *larger* than that previously found for the CsCl defect phase [48], in accordance with the larger averaged misfit expected for the α -phase [46], i.e. -2.6% versus -0.55% [48]. Total energy calculations performed by Miglio and co-workers on the disordered CsCl [12] and the α -phase [49] yield a hierarchy with the β -phase lying lowest, followed by the α -phase, ~ 50 meV higher, and finally the CsCl-defect phase, ~ 120 meV above the α -phase. Although better lattice matched to Si, the CsCl-defect phase is thus high enough in energy, in order to be eventually transformed into α -FeSi₂ upon annealing.

As pointed out before, the occurrence of grains of the γ -FeSi₂ phase cannot be explained in this framework, since its energy exceeds that of the other phases by too large an amount of almost ~ 0.5 eV with respect to β -FeSi₂ [12]. The only possibility to solve this puzzle, and to explain the observation, that homogeneous γ -films are invariably very thin (~ 20 Å), is to assume an extraordinarily favourable interface. The interface structure of B-type γ -FeSi₂/Si(111) has indeed been shown to be identical with that of CoSi₂/Si(111), i.e. it is characterized by an eightfold coordination of the interfacial metal atoms [50]. The bonding configuration is certainly far simpler at this interface, resulting in less strained bonds, compared to all epitaxial interfaces of the bulk stable phases. Intuitively it seems therefore reasonable to assume the formation of such an interface to be favoured.

The contribution of the interface itself to the total energy may indeed even reverse the stability, as will now be shown for the example of the monosilicides. The atomic structure of these interfaces has not yet been determined. By looking simply at the geometry of the unit cells in the common epitaxial orientations [15], i.e.:

- (CsCl)M Si(111) \parallel Si(111) with (CsCl)MSi $[\bar{1}\bar{1}\bar{2}] \parallel$ Si $[\bar{1}\bar{1}\bar{2}]$,
- ϵ -MSi(111) \parallel Si(111) with ϵ -MSi $[0\bar{1}\bar{1}] \parallel$ Si $[\bar{1}\bar{1}\bar{2}]$,

where M = Fe, Co, and taking into account the lower site symmetry in the ϵ -phase, it becomes obvious, that the number of dangling bonds must be substantially larger for this phase. This may be seen in Fig. 4 in which the atomic projections are compared for two possible interface structures of the ϵ -phase (Fig. 4a, b) and one of the CsCl-phase (Fig. 4c). Whatever

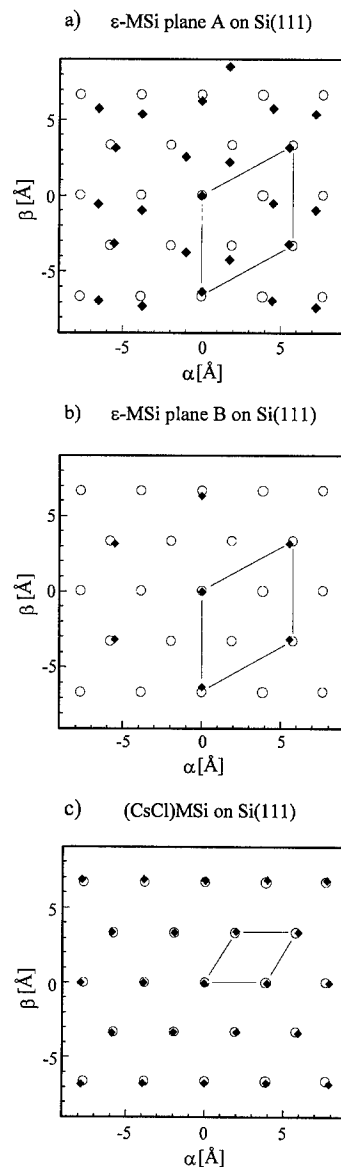


Fig. 4. Possible projections of the metal atom positions (filled diamonds) of (a) plane A of the ϵ -structure, (b) plane B of the ϵ -structure, and (c) the CsCl-structure, onto the unreconstructed Si(111) surface (open circles).

the exact arrangement is, it may be assumed that for the ϵ -phase two out of three bonds are broken while for the CsCl-phase there is a perfect match of the atomic planes with those of Si. Let us now try to obtain a rough estimate for the bond energies in FeSi and CoSi. This can be achieved by comparing the

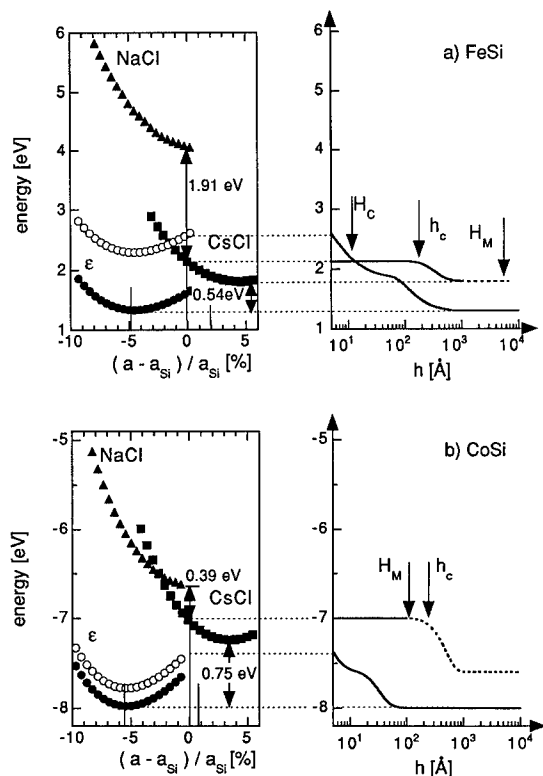


Fig. 5. (a) Left panel: total energy curves for FeSi with the NaCl, CsCl and ϵ structure as a function of the lattice parameter, expressed in terms of the relative deviation from the lattice parameter of the Si substrate. For the ϵ -phase, two curves are shown, with (open circles) and without (filled circles) taking into account the unfavourable interface contribution in the monolayer limit. Right panel: qualitative variation of the total energy per formula unit of the ϵ and CsCl phases as a function of the film thickness h . H_c indicates the stability limit of (CsCl) FeSi, h_c is the (experimental) critical thickness for strain relaxation at room temperature (RT), and H_M is the (unknown) thickness to which (CsCl) remains metastable at RT. (b) Left panel: total energy curves of the CoSi phases corresponding to those in (a). Right panel: same as in (a) for CoSi. (CsCl)CoSi is never expected to be the stable phase for any thickness. Experimentally, metastable (CsCl)CoSi films with coherent interfaces have been grown, however, up to a thickness of $H_M \sim 100$ Å (after Ref. [13]).

total energy curves for the two compounds in the CsCl and the NaCl structure [13]. They are displayed on the left hand sides of Fig. 5a and Fig. 5b, as a function of the deviation from the Si lattice parameter. Notice that the rhombohedral distortion has been neglected in this calculation [13], i.e. strictly speaking the curves in Fig. 5 apply to the hydrostatic

pressure case. We do not expect, however, this simplification to affect the qualitative conclusions drawn below. At the Si interatomic distance the NaCl curves are higher by 1.91 eV and 0.39 eV for FeSi and CoSi, respectively. Taking into account the coordination number of eight for CsCl and six for NaCl, we see that the average energy per bond is just half this number, i.e. 0.96 eV for FeSi and 0.2 eV for CoSi. With two out of three bonds broken at the ϵ -MSi/Si interface, the cohesive energy loss amounts to two thirds of these numbers, i.e. approximately 0.66 eV per formula unit in FeSi and 0.13 eV for CoSi. At the CsCl(MSi)/Si interface no bonds are broken, so we may set the cohesive energy loss to zero. The numbers just derived may be used to correct the total energy curves for the contribution of the interface in the monolayer limit. This has been done on the left panel of Fig. 5, where the lowest curves (filled circles) correspond to the energy of the ϵ -phase *without* the interface contribution, while the open circles show the energy with the interface part included. As is evident from the figure, the interface contribution is substantial in the case of FeSi. It is even large enough to reverse the order of stability of the CsCl- and the ϵ -phase, such that (CsCl)FeSi is expected to be thermodynamically stable in the monolayer limit. With increasing thickness h the contribution of the interface to the energy per formula unit will decrease as $1/h$, while the energy of the CsCl-phase remains constant as long as the corresponding interface remains coherent. The energy curves plotted as a function of h are therefore expected to cross at some critical value H_c (right hand side of Fig. 5). This is hence the thickness at which we expect the phase transition to the bulk stable phase to occur, unless it is kinetically hindered. *Experimentally*, the transition was indeed found to be absent even for the thickest films synthesized at RT (nearly 1000 Å [33]). At such a film thickness the interface contribution to the total energy can clearly no longer play a role, such that the material is definitely in a metastable state. By studying the thermal stability as a function of the film thickness, we were in fact able to deduce an experimental value of $H_c \sim 15$ Å for the stability limit [51]. When speaking about stability in this context, we mean that the (CsCl)FeSi phase is more stable than the bulk stable ϵ -phase below a thickness of H_c . In practice it

has to be born in mind of course that the silicide is always in contact with a large reservoir of Si, such that below H_c the stoichiometry evolves towards that of FeSi_2 upon annealing instead of staying constant [14]. Finally, it should be pointed out, that, according to Fig. 5, $(\text{CsCl})\text{CoSi}$ is never expected to be the lowest energy phase, even in the monolayer limit. Its occurrence must therefore be attributed to kinetic factors. This is in accordance with the lower transition temperature observed for this material, compared with the Fe silicide case. Thus close to H_c FeSi was found to transform around 300°C , whereas all CoSi films investigated seemed to undergo the phase transition around 200°C already. As the monolayer range is approached, it becomes increasingly difficult to identify the phase, however, so that we cannot tell for sure whether H_c is really zero for CoSi . The observation that the evolution of phases depends on details of the growth procedure for the more Si-rich CoSi_2 , is a clear hint that kinetics play the decisive role here as well. A more detailed understanding of the intriguing problem of nucleating either the CsCl defect phase or the CaF_2 phase will have to await further experimental and theoretical work.

4. Conclusions

Recent studies on the epitaxial growth on $\text{Si}(111)$ of those Fe and Co silicides, which are unstable or metastable in bulk form, have revealed unexpected similarities between these two material systems. Most significantly, in the stoichiometry range between MSi and MSi_2 , with $\text{M} = \text{Fe}, \text{Co}$, both may occur with the CsCl -structure or with a structure closely related to it, where vacancies are randomly formed on the metal sites. The occurrence of these epitaxial phases is found to be a pure interface phenomenon, since their total energies, neglecting the interface, are unfavourably large, compared with their bulk stable counterparts. For FeSi the contribution of the interface to the energy is even large enough to render the CsCl -phase more stable than the bulk phase, $\epsilon\text{-FeSi}$, as long as films are below a critical thickness $H_c \sim 15$ Å. In the case of the CoSi , however, the ϵ -phase remains more stable at all thicknesses, despite of its higher interfacial energy. The occurrence of CoSi_2

with the CsCl defect structure appears to be equally governed by kinetic phenomena. Here, however, the situation is less clear and will require more work, both theoretical and experimental.

Acknowledgements

The authors are grateful to L. Miglio and his co-workers for the permission to use the results of their calculations, and to the Swiss National Science Foundation for financial support. Valuable discussions with H. Sirringhaus are greatly appreciated.

References

- [1] S.P. Murarka, *Silicides for VLSI Applications* (Academic Press, New York, 1983).
- [2] F.M. d'Heurle, *J. Mater. Res.* 3 (1988) 167.
- [3] R. Bruinsma and A. Zangwill, *J. Phys. (Paris)* 47 (1986) 2055.
- [4] A. Zunger and D.M. Wood, *J. Cryst. Growth* 98 (1989) 1.
- [5] W.A. Jesser, *Mater. Sci. Eng.* 4 (1969) 279.
- [6] H. Föll, P.S. Ho and K.N. Tu, *Phil. Mag.* 45 (1982) 31.
- [7] F.M. d'Heurle, C.S. Petersson, J.E.E. Baglin, S.J. La Placa and C.Y. Wong, *J. Appl. Phys.* 55 (1984) 4208.
- [8] J.M. Gibson, J.L. Batstone, R.T. Tung and F.C. Unterwald, *Phys. Rev. Lett.* 60 (1988) 1158.
- [9] H. von Känel, *Mater. Sci. Rep.* 8 (1992) 193.
- [10] H. von Känel, R. Stalder, H. Sirringhaus, N. Onda and J. Henz, *Appl. Surf. Sci.* 53 (1991) 196.
- [11] N.E. Christensen, *Phys. Rev. B* 42 (1990) 7148.
- [12] L. Miglio and G. Malegori, *Mater. Sci. Symp. Proc.* 320 (1994) 109; *Phys. Rev. B* 52 (1995) 1448.
- [13] H. von Känel, C. Schwarz, S. Goncalves-Conto, E. Müller, L. Miglio, F. Tavazza and G. Malegori, *Phys. Rev. Lett.* 74 (1995) 1163.
- [14] H. von Känel, K.A. Mäder, E. Müller, N. Onda and H. Sirringhaus, *Phys. Rev. B* 45 (1992) 13807.
- [15] J. Chevrier, V. Le Thanh, S. Nitsche and J. Derrien, *Appl. Surf. Sci.* 56–58 (1992) 438.
- [16] Le Thanh Vinh, J. Chevrier and J. Derrien, *Phys. Rev. B* 46 (1992) 15946.
- [17] H. Moritz, B. Rösen, S. Popovic, A. Rizzi and H. Lüth, *J. Vac. Sci. Technol. B* 10 (1992) 1704.
- [18] N. Motta, A. Sgarlata, G. Gaggiotti, F. Patella, A. Balzarotti and M. De Crescenzi, *Surf. Sci.* 284 (1993) 257.
- [19] A.L. Vazquez de Parga, J. de la Figuera, C. Ocal and R. Miranda, *Ultramicroscopy* 42–44 (1992) 845.
- [20] J. Alvarez, J.J. Hinarejos, E.G. Michel and R. Miranda, *Surf. Sci.* 287/288 (1993) 490.
- [21] W. Raunau, H. Niehus, T. Schilling and G. Comsa, *Surf. Sci.* 286 (1993) 203.

- [22] T. Kobayashi, J. Dekoster, S. Degroote, M.H. Langelaar, L. Niesen and G. Langouche, in: *Formation of Semiconductor Interfaces*, Eds. B. Lengeler, H. Lüth, W. Mönch and J. Pollmann (World Scientific, Singapore, 1994) p. 455.
- [23] U. Kafader, P. Wetzel, C. Pirri and G. Gewinner, *Appl. Surf. Sci.* 70/71 (1993) 573.
- [24] U. Kafader, M.H. Tuilier, C. Pirri, P. Wetzel, G. Gewinner, D. Bolmont, O. Heckmann, D. Chandesris and H. Magnan, *Europhys. Lett.* 22 (1993) 529.
- [25] W.L. O'Brien and B.P. Tonner, *Surf. Sci.* 312 (1994) 233.
- [26] X. Wallart, J.P. Nys and C. Tételin, *Phys. Rev. B* 49 (1994) 5714.
- [27] H.Ch. Schäfer, B. Rösen, H. Moritz, A. Rizzi, B. Lengeler, H. Lüth and D. Gerthsen, *Appl. Phys. Lett.* 62 (1993) 2271.
- [28] M.G. Grimaldi, P. Baeri, C. Spinella and S. Lagomarsino, *Appl. Phys. Lett.* 60 (1992) 1132.
- [29] M.G. Grimaldi, G. Franzò, S. Ravesi, A. Terrasi, C. Spinella and A. La Mantia, *Appl. Surf. Sci.* 74 (1994) 19.
- [30] J. Desimoni, H. Bernas, M. Behar, X.W. Lin, J. Washburn and Z. Liliental-Weber, *Appl. Phys. Lett.* 62 (1993) 306.
- [31] C. Schwarz, N. Onda, S. Goncalves-Conto, H. Sirringhaus, H. von Känel and R.E. Pixley, *J. Appl. Phys.* 76 (1994) 7256.
- [32] N. Onda, H. Sirringhaus, S. Goncalves-Conto, C. Schwarz, S. Zehnder and H. von Känel, *Appl. Surf. Sci.* 73 (1993) 124.
- [33] H. von Känel, N. Onda, H. Sirringhaus, E. Müller-Gubler, S. Goncalves-Conto and C. Schwarz, *Appl. Surf. Sci.* 70/71 (1993) 559.
- [34] K.A. Mäder, H. von Känel and A. Baldereschi, *Phys. Rev. B* 48 (1993) 4364.
- [35] C. Schwarz, S. Goncalves-Conto, E. Müller-Gubler, H. Sirringhaus and H. von Känel, in: *Formation of Semiconductor Interfaces*, Eds. B. Lengeler, H. Lüth, W. Mönch and J. Pollmann (World Scientific, Singapore, 1994) p. 471.
- [36] T.B. Massalski, Ed., *Binary Alloy Phase Diagrams*, Vol. 2 (ASM International, Materials Park, OH, 1986) p. 1108.
- [37] S. Saitoh, H. Ishiwaru and S. Furukawa, *Appl. Phys. Lett.* 37 (1980) 203.
- [38] J.C. Bean and J.M. Poate, *Appl. Phys. Lett.* 37 (1980) 643.
- [39] R.T. Tung and F. Schrey, *Appl. Phys. Lett.* 54 (1989) 852.
- [40] S.-L. Zhang, J. Cardenas, F.M. d'Heurle, B.G. Svensson and C.S. Petersson, *Appl. Phys. Lett.* 66 (1995) 58.
- [41] D.J. Oostra, D.E.W. Vandenhoudt, C.W.T. Bulle-Lieuwma and E.P. Naburgh, *Appl. Phys. Lett.* 59 (1991) 1737.
- [42] K. Radermacher, S. Mantl, R. Apetz, Ch. Dieker and H. Lüth, *Mater. Sci. Eng. B* 12 (1992) 115.
- [43] O. Müller, S. Mantl, K. Radermacher, H.L. Bay, G. Crecelius, Ch. Dieker and S. Mesters, *Appl. Surf. Sci.* 73 (1993) 141.
- [44] J. Chevrier, P. Stocker, Le Thanh Vinh, J.M. Gay and J. Derrien, *Europhys. Lett.* 22 (1993) 449.
- [45] X.W. Lin, M. Behar, J. Desimoni, H. Bernas, Z. Liliental-Weber and J. Washburn, *Appl. Phys. Lett.* 63 (1993) 105.
- [46] N. Jedrecy, A. Waldhauer, M. Sauvage-Simkin, R. Pinchaux and Y. Zheng, *Phys. Rev. B* 49 (1994) 4725.
- [47] K.L. Whiteaker, I.K. Robinson, C. Benson, D.M. Smilgies, N. Onda and H. von Känel, *Phys. Rev. B* 51 (1995) 9715.
- [48] N. Onda, H. Sirringhaus, S. Goncalves-Conto, C. Schwarz, E. Müller-Gubler and H. von Känel, *Mater. Res. Soc. Symp. Proc.* 280 (1993) 581; L. Miglio, F. Tavazza and G. Malegori, *Appl. Phys. Lett.* 67 (1995) 2293.
- [49] L. Miglio, *Europhys. News* 26 (1995) 25.
- [50] E. Müller, D.P. Grindatto, H.-U. Nissen, N. Onda and H. von Känel, *Appl. Phys. Lett.* 64 (1994) 1938.
- [51] N. Onda, H. Sirringhaus, E. Müller and H. von Känel, *J. Cryst. Growth* 127 (1993) 634.



ELSEVIER

Applied Surface Science 104/105 (1996) 213–217

applied
surface science

Atomistic study of the formation process of Ni silicide on the Si(111)- 7×7 surface with scanning tunneling microscopy

Takafumi Yao^{a,b,*}, Shinji Shinabe^c, Masamichi Yoshimura^d^a Institute for Materials Research, Tohoku University Katahira, Aoba-ku, Sendai 980, Japan^b National Institute for Advanced Interdisciplinary Research, Tsukuba 305, Japan^c Department of Electrical Engineering, Hiroshima University Kagamiyama, Higashi-Hiroshima 724, Japan^d Toyota Technological Institute Hisakata, Tenpaku-ku, Nagoya 468, Japan

Received 28 June 1995; accepted 30 August 1995

Abstract

This paper reports on the surface structure of Ni-induced ' 1×1 ' on Si(111) and the dynamical nickel silicide formation observed by scanning tunneling microscopy (STM). The ' 1×1 ' surface consists of Si adatoms and two kinds of ring-clusters. The silicon adatoms form the local structure of 2×2 or $c(4 \times 2)$. One of the ring-clusters is found to form the well-known $\sqrt{19} \times \sqrt{19}$ structure. The other ring-cluster is observed to be smaller and brighter than the former ones, and forms a local $\sqrt{7} \times \sqrt{7}$ arrangement. The latter ring structure has never been reported yet. Islands of nickel silicide are formed after annealing the Ni-covered surface at elevated temperature. The surfaces of the islands show $\sqrt{3} \times \sqrt{3}$ and 2×2 periodicity for annealing temperatures of 400°C and 600°C, respectively. The transformation of the island structure seems to proceed through nickel diffusion from the surface into the bulk.

1. Introduction

It has been well known that a small amount of nickel causes a structural change to the silicon surface. One of the examples is a famous $\sqrt{19} \times \sqrt{19}$ structure [1]. Its atomic structure has been investigated by many techniques such as scanning tunneling microscopy [2] and diffraction methods [3–5], and some plausible structure models have been proposed [2,3]. However, its atomic configuration including the formation process remains unclear. According to the LEED study [3–5], a diffused ' 1×1 '

structure appears as a precursor of $\sqrt{19} \times \sqrt{19}$. Then the investigation of the ' 1×1 ' phase is indispensable in order to know precisely the atomic configuration of $\sqrt{19} \times \sqrt{19}$. However, the atomic geometry of the ' 1×1 ' structure has so far received few attention because of a lack of appropriate techniques to observe the local structure.

Nickel is also known for its high diffusion coefficient in the silicon bulk crystal. Nickel atoms on the surface diffuse into the bulk during annealing, and some of them come back on the surface during cooling [3].

In this paper, firstly, we present a structural study of nickel-induced ' 1×1 ' on the Si(111) surface by scanning tunneling microscopy (STM). It is found

* Corresponding author.

that the surface consists of Si adatoms and two types of Ni-related ring-clusters. One of the ring-cluster is related to the well-known $\sqrt{19} \times \sqrt{19}$ structure. The other ring-cluster is a precursory structure of $\sqrt{19} \times \sqrt{19}$, and forms a new structure $\sqrt{7} \times \sqrt{7}$ locally. Secondly, a dynamical formation process of the nickel silicide has been presented. At 400°C annealing, it shows $\sqrt{3} \times \sqrt{3}$ periodicity, while at 600°C, it shows 2×2 structure. The change in the periodicity might be related to the process of nickel diffusion from the surface into the bulk.

2. Experimental

The specimen we used in this study was cut from a Si(111) wafer of 0.1–1 Ω cm. After ultrasonic cleaning in acetone, it was introduced into the vacuum chamber ($< 2 \times 10^{-8}$ Pa) and prebaked at $\sim 500^\circ\text{C}$ overnight. Finally it was flashed at 1200°C to obtain a clean Si(111)- 7×7 surface. Nickel of 99.9% purity was deposited on the clean surface at room temperature. Then the sample was annealed at elevated temperatures. The STM measurements were performed in constant current mode using an electrochemically sharpened tungsten tip.

3. Results and discussion

3.1. 1×1 structure

Fig. 1 shows the surface after deposition of sub-monolayer nickel at room temperature. The sample bias is -2 V at a constant current of 0.20 nA. Brightly observed Ni atoms form clusters and adsorb preferentially on the faulted halves of the 7×7 DAS structure, and most of them are located at the rest atom sites. At this temperature and at this low coverage, the 7×7 structure seems to be fully retained. Similar preferential adsorption on the faulted halves was reported for Cu/Si(111) [6] and Ag/Si(111) [7]. This is because the faulted half has a larger charge density on the surface than the unfaulted half, and among the surface atoms the rest atom has the largest charge density because of charge transfer from neighboring adatoms [8].

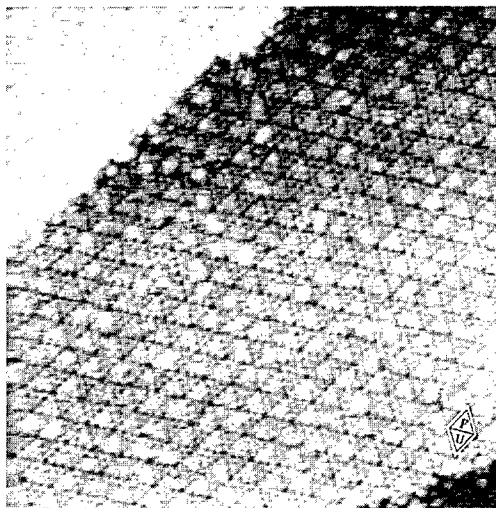


Fig. 1.

Fig. 2 shows an STM image of the surface after annealing at 800°C obtained at a sample bias of $+2$ V and a constant current of 0.20 nA. The Si- 7×7 domains and disordered regions due to Ni reaction coexist on the surface. The former and the latter are located at the higher and lower terrace of the surface step, respectively. The Ni-induced domains face the faulted halves of the 7×7 domain at the boundary, as was reported for the domain structure of Al/Si(111) [9]. The nickel-induced domain shows complicated features, consisting of two kinds of ring-like clusters (B and C) and atom-like dots (A).

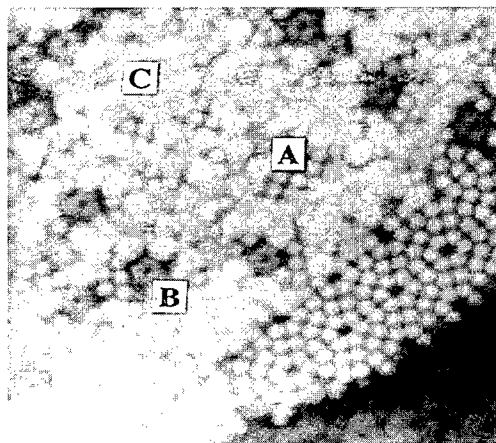


Fig. 2.

We consider this structure to be corresponding to the 1×1 structure as observed previously by LEED [3–5], since each species distributes randomly in the domain, producing the 1×1 LEED pattern diffracted from the underlying Si(111) substrate. On the assumption that the structure of the underlying silicon substrate changes from DAS to ideal 1×1 upon Ni reaction, we get insight into the local atomic arrangement of the observed structure. The atom-like dots A are located at T_4 sites and form local arrangements such as 2×2 and $c(4 \times 2)$. The same surface reconstructions have been reported for the silicon surface prepared by laser annealing [10] and higher temperature annealing at 1300°C [11]. In addition, their size, shape and the bias dependence of the image are very similar to the Si adatoms of Si(111)- 7×7 . Hence the dots A can be assigned to Si atoms adsorbed on the T_4 sites.

In contrast, the ring-clusters B and C are related to the impinging Ni atoms because the density of ring-clusters increases with the amount of evaporated Ni atoms. As shown in Fig. 2, the rings B are imaged larger in size and darker in contrast than the rings C. It is found that at both bias polarities the ring B is imaged 0.03 nm higher and the ring C is 0.07 nm lower, relative to the Si adatom A. Moreover, the centers of B and C are located at H_3 sites and ontop sites, respectively. Fig. 3 shows an STM image of another sample area of the Ni-induced

1×1 surface, obtained at a sample voltage of -0.94 V and a tunneling current of 0.2 nA. In this filled-state image, both the rings B and C split into three balls. In addition, it is found that the rings B and C form a short-range order of $\sqrt{19} \times \sqrt{19}$ -R23.4° and $\sqrt{7} \times \sqrt{7}$ -R19.1°. The ring B is responsible for the well-known $\sqrt{19}$ structure, since when we increase the amount of Ni the rings B are close-packed over all the surface and show the $\sqrt{19} \times \sqrt{19}$ structure.

Although the $\sqrt{19} \times \sqrt{19}$ structure has been extensively studied so far, the atomic geometry is still controversial. Wilson and Chiang proposed an atomic model for the $\sqrt{19} \times \sqrt{19}$ structure based on STM observations of $\sqrt{19}$ covered surfaces, where a Ni atom is located in the sixfold hollow site between the first and second Si layers and six Si adatoms are surrounding the Ni atom [2]. Another model was proposed by Ichinokawa et al. based on the LEED and AES measurements. Their model is a structure of NiSi_2 clusters composed of three Ni atoms embedded in each in the topmost layers of Si(111) [3]. In this situation, the center of the ring is located at the ontop sites. Our STM result reveals that the center position of the rings B is located at hollow sites, which supports the former model and excludes the latter model.

As for the rings C, we observe that it forms a local structure of $\sqrt{7} \times \sqrt{7}$, while some of the rings do not form complete unit cells of $\sqrt{7} \times \sqrt{7}$. This is the first observation of $\sqrt{7} \times \sqrt{7}$ on the Ni/Si(111) surface. A $\sqrt{7} \times \sqrt{7}$ reconstruction was reported for the Co/Si(111) surface [12], which system also forms a silicide. The STM observation of the Si(111)- $\sqrt{7} \times \sqrt{7}$ -Co revealed similar ring-cluster structures to the rings C, although the dependence of tunneling bias voltage on the STM image is slightly different. We didn't see ball-like structures at any tunneling voltage, as was observed on the filled state image of the Co- $\sqrt{7} \times \sqrt{7}$ structure. However, we consider that the atomic structure of the ring C can be explained by the same one as that proposed for Co- $\sqrt{7} \times \sqrt{7}$, as shown in Fig. 4. In this figure, Ni atoms are located at lattice points of the framed $\sqrt{7} \times \sqrt{7}$ unit mesh, around which 6 Si adatoms are situated. Three of the six adatoms are situated higher than the others, and produce threefold maxima in the filled-state image. The Ni atom lies deeper than the silicon

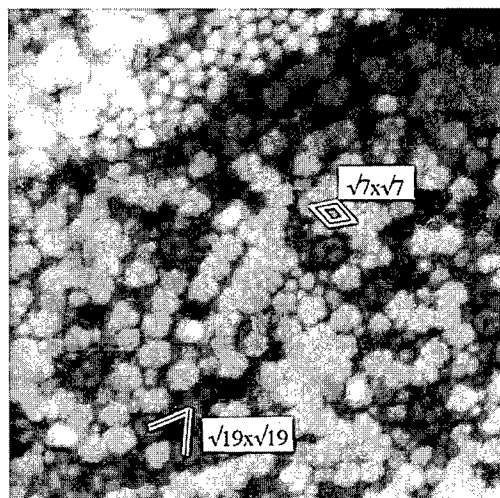


Fig. 3.

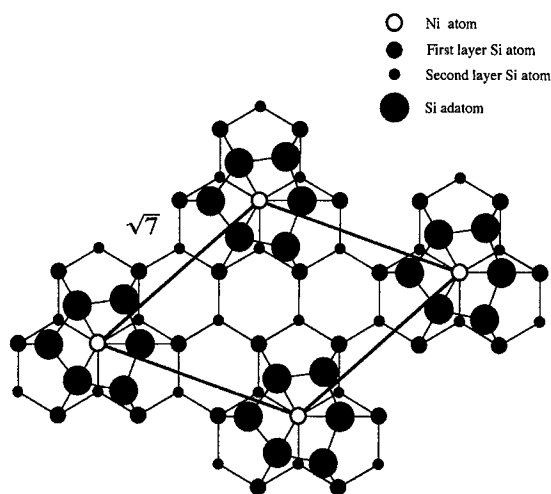


Fig. 4.

adatoms and seems difficult to be probed by the STM tip.

3.2. Formation of nickel islands

Fig. 5 shows an STM image after deposition above 1 ML at room temperature. The tunneling bias is +2 V and the current is 0.20 nA. Ni clusters adsorb preferentially on the center part of the half units of Si- 7×7 . Although the 7×7 units are still

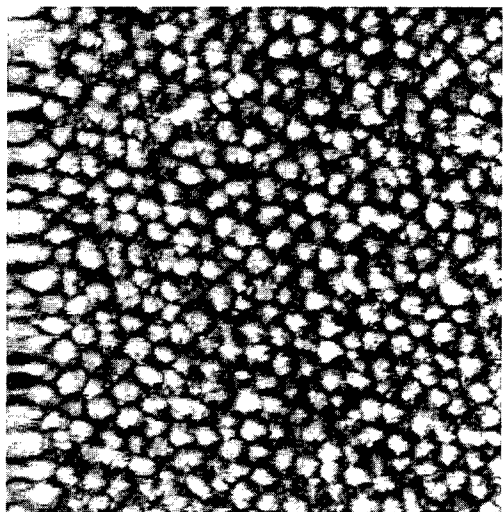


Fig. 5.

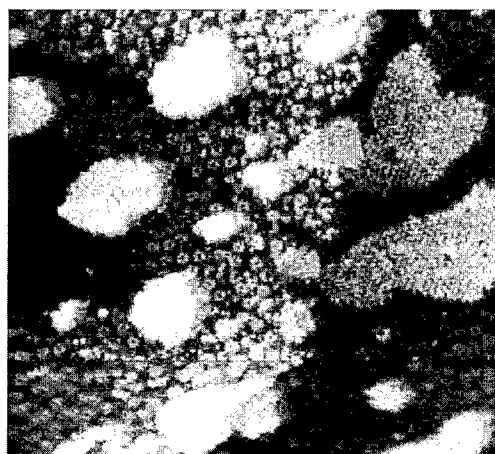


Fig. 6.

observed, a few of them are somewhat destroyed. This suggests that, at this coverage, Ni reaction already causes some structural change to the Si substrate even at room temperature.

When the surface is annealed at elevated temperature, the reaction proceeds to create the unique island structures. Fig. 6 shows an STM image after annealing at 400°C. The sample voltage is -2 V and the current is 0.20 nA. The islands are observed here and there, surrounded by the disordered $\sqrt{19} \times \sqrt{19}$ domains (ring B). The islands have no distinct shape but the atom-like dots are clearly observed inside it, showing $\sqrt{3} \times \sqrt{3}$ -R30 structure. Higher temperature annealing to 600°C causes dynamical transformation of the island structures. The size of the island becomes bigger, and the surface shows the 2×2 structure. Neither surface structure has been reported so far. When the surface is annealed at 1000°C, the islands disappear and the 7×7 structure appears again showing the surface like Fig. 2. This indicates that in the process of annealing Ni atoms diffuse from the surface into the bulk. Then the transformation of the island is considered to be related with Ni diffusion from the surface. Detailed analysis on the atomic models is in progress.

4. Conclusion

We have investigated the surface structure of Ni-induced ' 1×1 ' on the Si(111) by scanning tun-

neling microscopy. STM images of the Ni-induced '1 × 1' shows complicated features consisting of Si adatoms and two types of ring-clusters including Ni atoms. One ring-cluster (B) is imaged larger in size and darker in contrast than the other one (C). Further investigation of the coexisting area of '1 × 1' and Si-7 × 7 shows that the centers of the ring-clusters B and C are located at H₃ and ontop sites of the underlying Si substrate, respectively. In addition, the rings B and C are observed to form $\sqrt{19} \times \sqrt{19}$ and $\sqrt{7} \times \sqrt{7}$ structure, respectively. The latter superstructure is observed for the first time. A possible structural model for the $\sqrt{7} \times \sqrt{7}$ is proposed.

Annealing the Ni-covered surface causes the formation of the islands. The surface shows the $\sqrt{3} \times \sqrt{3}$ and 2 × 2 structure for annealing temperatures of 400°C and 600°C, respectively. The transformation of the surface structure can be related to the Ni diffusion from the surface into the bulk upon annealing.

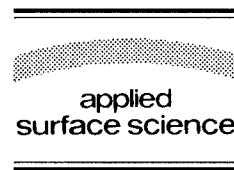
References

- [1] R.E. Schlier and H.E. Farnsworth, *J. Chem. Phys.* 30 (1959) 917.
- [2] R.J. Wilson and S. Chiang, *Phys. Rev. Lett.* 58 (1987) 2575.
- [3] T. Ichinokawa, T. Tani and A. Sayama, *Surf. Sci.* 219 (1989) 395.
- [4] P.A. Bennett, A.P. Johnson and B.N. Halawith, *Phys. Rev. B* 37 (1988) 4268.
- [5] A.E. Dolbak, B.Z. Olshanetsky, S.I. Stenin and S.A. Teys, *Surf. Sci.* 247 (1991) 32.
- [6] St. Tosch and H. Neddermeyer, *Surf. Sci.* 211/212 (1989) 133.
- [7] St. Tosch and H. Neddermeyer, *Phys. Rev. Lett.* 61 (1988) 349.
- [8] Ph. Avouris and R. Wolkow, *Phys. Rev. B* 39 (1989) 5091.
- [9] K. Takaoka, M. Yoshimura, T. Yao, T. Sato, T. Sueyoshi and M. Iwatsuki, *Phys. Rev. B* 48 (1993) 5657.
- [10] R.S. Becker, J.A. Golovchenko, G.S. Higashi and B.S. Swartzentruber, *Phys. Rev. Lett.* 57 (1986) 1020.
- [11] M. Tomitori, F. Iwawaki, N. Hirano, F. Katsuki and O. Nishikawa, *J. Vac. Sci. Technol. A* 8 (1990) 222.
- [12] S.C. Wu, Z.Q. Wang, Y.S. Li, F. Jona and P.M. Marcus, *Phys. Rev. B* 33 (1986) 2900.



ELSEVIER

Applied Surface Science 104/105 (1996) 218–222



Analytical studies of nickel silicide formation through a thin Ti layer

F. Fenske^{a,*}, A. Schöpke^a, S. Schulze^b, B. Selle^a

^a Department AP, Hahn-Meitner-Institut Berlin, Rudower Chaussee 5, D-12489 Berlin, Germany

^b Solid Surfaces Analysis Group, Department of Physics, Technical University of Chemnitz–Zwickau, D-09107 Chemnitz, Germany

Received 28 June 1995; accepted 2 October 1995

Abstract

Interfacial reaction sequences of a Ti/Ni diffusion couple on Si were studied by cross-sectional TEM. At all stages of temperature treatment an amorphous interlayer was observed. There is a small window of annealing parameters where epitaxial growth of disconnected NiSi₂ islands can be obtained. By further annealing NiSi forms. Principal component analysis (PCA) based AES depth profiling confirms these findings. High energy RBS with ¹⁵N⁴⁺ ions was successfully applied to study the interdiffusion processes taking place in the whole Ag/Ni/Ti metal multilayer system.

1. Introduction

Metallization schemes involving the formation of uniform submicron-size contact layers on silicon are of increasing significance for future silicon technology. So, epitaxially growing metal and silicide layers could be the ideal structure [1,2]. However, conventional formation of epitaxial silicides requires MBE preparation or implantation techniques. The key points are low deposition rate and ultraclean conditions. These layers have been intensively investigated since 1980 (e.g. [3] and references therein).

It is of fundamental interest to predict and control material reactions. Obviously, by proper selection of

the reacting components, reaction paths and products can be influenced when modifying atomic diffusivities and interface reactivities. By exploring for alternative growing methods for silicides promising results have been obtained with bilayer systems, recently [4–8]. These methods use an intercalated thin Ti layer which controls the reaction between the silicide forming upper layer and Si. Similar results were reported for the NiCr/Si system, where a thin diffusion controlling amorphous interlayer forms during the reaction heat treatment [9]. Silicon reactions with alloys or multisandwich structures are also under discussion for producing shallow contacts [10,2].

This work describes detailed microstructural investigations of the interfacial reactions in a Ni/Ti bilayer system on c-Si. The purpose is to clarify the solid-state reaction chain by analytical methods.

* Corresponding author. Tel.: +49-30-67053360; fax: +49-30-67053333; e-mail: fenske@hmi.de.

2. Experimental

The phosphorus doped Si(111) samples were cleaned by a standard wet process, immediately before they were loaded into the sputter deposition chamber, an HF dip was performed. The sequential deposition of first 50 nm Ti, then at least 200 nm Ni and, finally, an Ag top layer of more than 200 nm onto the unheated substrates was carried out by dc magnetron sputtering with 15 W cm^{-2} target power density in a commercial bell jar system. After evacuating to the base pressure of 2×10^{-4} Pa the chamber was backfilled with Ar to 0.5 Pa and the targets were presputter cleaned. Isochronal annealings were performed between 300 and 550°C in a conventional quartz tube furnace under forming gas atmosphere.

Cross-sectional transmission electron microscopy (XTEM) was performed with a Philips CM 20 FEG to get microstructural information of interfacial reactions after etching away the upper Ag layer and the remaining unreacted Ni layer [11]. EDX analysis was carried out by means of a Voyager EDX system from Tracor Europa with an Explorer Ge-detector. AES depth profiles on the same samples were recorded on a PHI 590 spectrometer with the analyzer running in the differentiated mode. 19 MeV high energy $^{15}\text{N}^{4+}$ Rutherford backscattering was carried out with the beam of the CN injector at the Hahn-Meitner-Institut Berlin ion beam facilities.

3. Results and discussion

3.1. High energy RBS measurements

Ion beam backscattering spectra of the as-deposited and annealed samples are shown in Fig. 1. These investigations give evidence of the interactions in the Ag/Ni/Ti multilayer metal system. For the as-sputtered sample the component peaks are clearly separated and permit the determination of the metal single layer thickness to be 350 nm Ag, 190 nm Ni and 50 nm Ti. After the temperature treatment (450°C, 30 min), the interaction in the Ni–Ti diffusion couple is indicated, whereas the Ag layer does not change the shape, as expected [11]. The weak tail is due to a small degree of interface roughness, possibly caused by recrystallization processes in the

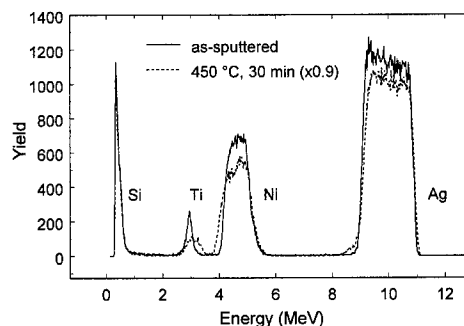


Fig. 1. High energy RBS spectra of the as-sputtered system and after annealing at 450°C for 30 min, recorded with 19 MeV $^{15}\text{N}^{4+}$ ions (backscattering angle 165°).

Ag film during the annealing. Interface reactions with the Si substrate are not so well resolved by RBS with the higher mass projectile N^{4+} . A detailed description of our findings will be published elsewhere.

3.2. Cross-sectional TEM investigations

Cross-sectional micrographs are made of the silicon interface region to reveal interfacial reactions of silicide growth. For the as-deposited sample we also find an amorphous interlayer between the Ti layer and the c-Si substrate, in accordance with [14]. The detection of a-interlayers in solid-state reacted systems has created much interest. Overviews on metal/a-Si and metal/c-Si reactions have been given in [15,16]. From the HRTEM lattice image in Fig. 2 we estimated the a-interlayer thickness to be in the order of 1–2 nm, which corresponds to 3–6 atomic

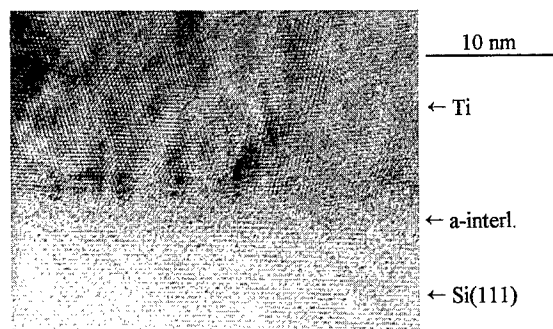


Fig. 2. High resolution lattice image from the Ti/Si interface of the as-sputtered system.

planes with a lattice constant of 0.313 nm for the Si(111). It has been shown, that the thickness of the built-up a-interlayers in as-deposited systems depends on the free energy of mixing, particularly on the electronegativity of the constituents, on their crystallinity and on the substrate surface preparation [15–17]. Following the argumentation of Clemens [15] for layer growth one has also to consider the type of deposition method, because in systems with a negative heat of mixing layer growth by species with high surface mobility will result in improved interface sharpness. Therefore, for sputtered Ti layers on Si, being systems with a relatively high heat of mixing [18], one would expect thinner a-interlayers than for thermally evaporated films. Additionally, interface contamination will probably influence this process of a-interlayer formation. By AES we detected in our samples at the Ti/Si interface small levels of C and O, which originate from residues of the chemical cleaning procedure and air adsorbates [11]. From these results and from published data [14–16] we conclude that this a-interlayer contains mainly Ti and Si with small amounts of oxygen and carbon, whereas Si is the dominant diffusion species at this time. Because of the difference in heat of formation for TiO_2 (–87.2 kcal/mol) and for SiO_2 (–68.5 kcal/mol) [19] the oxygen in the a-layer is bonded to Ti. For increasing annealing temperature our studies revealed an a-interlayer growth asymptotically to a thickness of about 10–15 nm.

There are small intervals of the annealing parameters temperature and time, where epitaxial silicide growth can be obtained. Depending on the temperature, in the range between 450–500°C for an annealing time of 15 min or longer, Ni has penetrated both the Ti layer and the a-interlayer and starts to react with the underlying Si(111) to form silicide. From Fig. 3 epitaxial growth of disconnected silicide islands with atomically sharp interfaces can be observed. By EDX analysis we revealed the existence of NiSi_2 (large grain) and of NiSi (dark spots). By means of XTEM studies on different samples it was verified, that NiSi starts to grow probably inside the NiSi_2 grains. At this stage of interface reaction NiSi is not detected in all NiSi_2 grains. Further annealing leads to the formation of a continuous NiSi layer with an undulated interface to Si (see Fig. 4). This figure of a SiO_2 contact window also clearly demon-

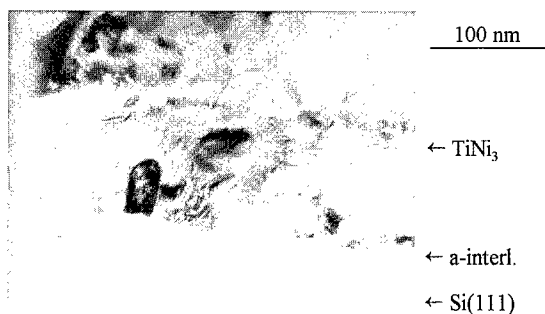


Fig. 3. XTEM image of the Si interface region after annealing at 475°C for 15 min.

strates the lateral NiSi growth. In this temperature range Ni becomes the dominant moving species, whereas the a-interlayer has been preserved. At temperatures higher than 525°C Si starts to penetrate the metal system [11].

AES depth profiling was performed on 2 selected samples. To avoid uncertainties caused by the matrix dependence of Auger sensitivity factors, principal component analysis (PCA) [12] rather than conventional quantitative AES was applied to detect the silicon compounds near the Si substrate up to the a-interlayer. This method has been modified to get more reliable results with respect to the number of chemical compounds and their depth distribution [13]. Fig. 5(a) and Fig. 6(a) show the AES peak height profiles (broken lines) and the depth distribution of silicon compounds obtained by PCA (solid lines) of the samples annealed at 450°C for 30 min and 45 min, respectively. The AES spectra evaluation by the modified PCA method confirms our results from

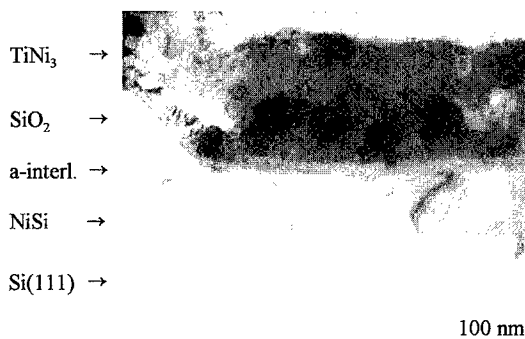


Fig. 4. XTEM micrograph of a SiO_2 contact window after annealing the system at 475°C for 60 min.

XTEM investigations, where first NiSi_2 forms and then NiSi starts to grow. For comparison, XTEM micrographs of the same samples are shown in Fig. 5(b) and Fig. 6(b). A compound analysis by this method of the a-interlayer and of the Ni–Ti intermetallics is in progress.

Published data on silicide growth with different systems suggest that the kinetic effects mainly determine the sequence of compound formation [20]. For a Ni–Ti alloy there is no driving force to react with Si [21] until, at higher temperatures Si starts to diffuse into the alloy forming ternary silicides [22]. Therefore, in our case of a Ni/Ti bilayer system with Ni excess we assume a Ni diffusion from the Ni layer (source) through the intermetallic and the a-interlayer to the silicon. The velocity of Ni diffusion front motion previously determined to be about 0.5 Å/s [11] is as low as the Ni deposition rate by MBE techniques for preparing NiSi_2 by direct reaction [23]. The results concerning epitaxial silicide islands

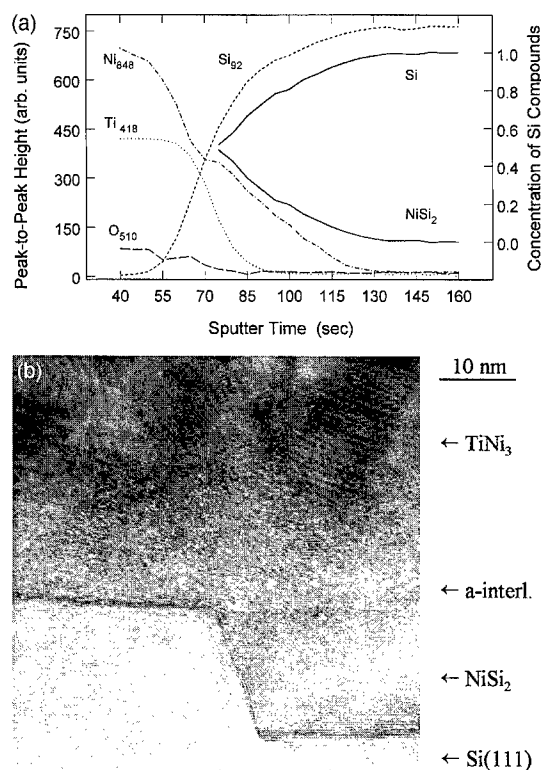


Fig. 5. (a) AES depth profile after annealing at 450°C for 30 min. Silicon compound distribution from the PCA analysis is shown by the continuous lines. (b) XTEM image.

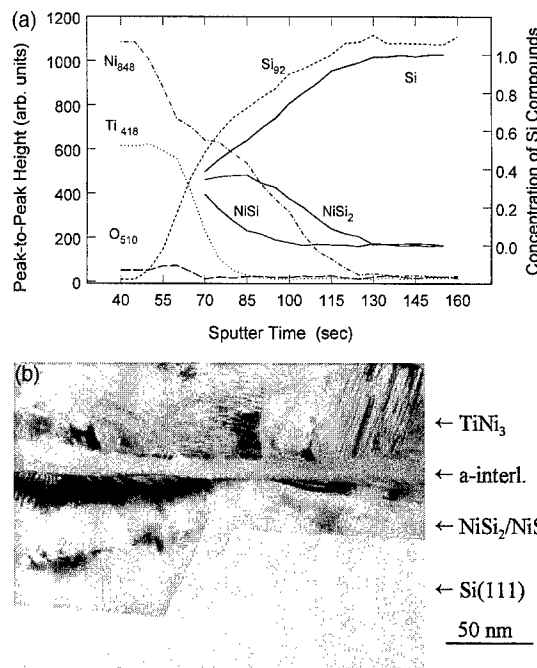


Fig. 6. (a) AES depth profile after annealing at 450°C for 45 min. Silicon compound distribution is shown by the continuous lines. (b) XTEM image.

growth are strikingly similar. Instead of forming first metal rich nickel silicide phases as it is the rule for conventional Ni thin film interaction with Si [24] NiSi_2 starts to grow. First data of investigations on the cause of silicide nucleation sites have been reported recently [23,25]. The nature of the NiSi_2 nucleation mechanism cannot be deduced from our data. The NiSi probably starts to grow inside the NiSi_2 grains by subsequent delivery of Ni and probably will consume all the disilicide at high annealing temperatures. The process of thermally induced NiSi_2 dissociation in contact with Ni was studied by Hung et al. in a Ni–Si system without an intercalated Ti layer [26]. Further slowing down of the Ni delivery rate will probably promote the NiSi_2 growth and suppress the beginning of the undesirable metal rich NiSi phase.

4. Conclusions

High energy RBS, cross-sectional TEM and PCA based AES resulted in a more detailed description of

the interdiffusion and solid-state reaction processes in metal multilayer systems on Si. Our results on a Ni/Ti bilayer system on Si illustrate the significance of kinetics as the limiting factor for the compound formation sequence. On the other hand, the ultimate complexity of interaction processes in this multicomponent system has been demonstrated. Further work has to be done to clarify the initial stages of silicide growth. This will contribute to improve laterally homogeneous epitaxial silicide contacts which can be created in a simple manner by metal bilayer systems on Si.

Acknowledgements

The use of the RBS facility at the Ion Beam Laboratory in the Hahn-Meitner-Institut Berlin and of the EDX equipment at the IFW Dresden is gratefully acknowledged. The authors thank Dr. H. Lange for helpful discussions and critical reading the manuscript. This work was partly supported by the Bundesministerium für Bildung und Forschung of the FRG under contract No. 0329 230 A.

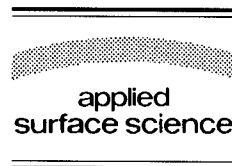
References

- [1] S.P. Murarka, *Metallization: Theory and Practice for VLSI and ULSI*, 1st ed. (Butterworth-Heinemann, Boston, MA, 1993).
- [2] K.N. Tu, *Thin Solid Films* 140 (1986) 71.
- [3] L.J. Chen, W. Lur and J.Y. Cheng, *Thin Solid Films* 191 (1990) 221.
- [4] F. Fenske et al., Patent DD 277 602 (21 December 1987).
- [5] M.L.A. Dass, D.B. Fraser and C.-S. Wei, *Appl. Phys. Lett.* 58 (1991) 1308.
- [6] B.-H. Tseng, C.-K. Lee and M.-F. Tseng, *Mater. Res. Soc. Symp. Proc.* 260 (1992) 685.
- [7] S. Ogawa, J.A. Fair, M.L.A. Dass, E.C. Jones, T. Konzaki, N.W. Cheung and D.B. Fraser, in: *Ext. Abstr. 1993 Int. Conf. Solid State Devices*, p. 195.
- [8] A. Lauwers, A. Vercaemst, M. Van Hove, K. Kylesbech Larsen, R. Verbeeck, R. Van Meirhaeghe, K. Maex and M. Van Rossum, *Mater. Res. Soc. Symp. Proc.* 320 (1994) 59.
- [9] J.-H. Lee, G.A. Rozgonyi, B.K. Patnaik, D. Knoesen, D. Adams, P. Balducci and A.S. Salih, *J. Appl. Phys.* 73 (1993) 4023.
- [10] K.N. Tu, W.N. Hammer and J.O. Olowolafe, *J. Appl. Phys.* 51 (1980) 1663.
- [11] F. Fenske, S. Schulze, B. Selle, H. Lange and W. Wolke, *Mater. Res. Soc. Symp. Proc.* 320 (1994) 427.
- [12] S. Gaarenstrom, *Appl. Surf. Sci.* 7 (1981) 1.
- [13] S. Kelling, Diploma Work, Technical University Berlin, June 1995.
- [14] R. Sinclair, K. Holloway, K.B. Kim, D.H. Ko, A.S. Bhansali, A.F. Schwartzman and S. Ogawa, *Inst. Phys. Conf. Ser. No.* 100, Sect. 8 (1989) 599.
- [15] B.M. Clemens and R. Sinclair, *MRS Bull.* (1990) 19.
- [16] L.J. Chen, W.Y. Hsieh, J.H. Lin, T.L. Lee, J.F. Chen, J.M. Liang and M.H. Wang, *Mater. Res. Soc. Symp. Proc.* 320 (1994) 343.
- [17] I. Kondo, T. Yoneyama, K. Kondo, O. Takenaka and A. Kinbara, *J. Vac. Sci. Technol. A* 10 (1992) 3166.
- [18] R.W. Béne, *J. Appl. Phys.* 61 (1987) 1826.
- [19] M.A. Nicolet and S.S. Lau, in: *VLSI Electronics*, Eds. N.G. Einspach and G.B. Larrabee, Vol. 6 (Academic Press, New York, 1983) p. 453.
- [20] C. Calandra, O. Bisi and G. Ottaviani, *Surf. Sci. Rep.* 4 (1985) 271.
- [21] L.S. Hung, S.Q. Wang, J.W. Mayer and F.W. Saris, *Mater. Res. Soc. Symp. Proc.* 54 (1986) 161.
- [22] M. Setton, J. van der Spiegel, J.J. Santiago and C.S. Wei, *Vide Couches Minces* 42 (1987) 145.
- [23] D. Hesse, P. Werner, J. Heydenreich and R. Mattheis, *Mater. Res. Soc. Proc.* 320 (1994) 221.
- [24] G. Ottaviani, *Thin Solid Films* 140 (1986) 3.
- [25] W.Y. Hsieh, J.H. Lin, M.H. Wang and L.J. Chen, *Mater. Res. Soc. Symp. Proc.* 311 (1993) 323.
- [26] L.S. Hung and J.W. Mayer, *Thin Solid Films* 109 (1983) 85.



ELSEVIER

Applied Surface Science 104/105 (1996) 223–227



Scanning tunneling spectroscopy examination of surface electronic structures of $\text{Si}(111)(2\sqrt{3} \times 2\sqrt{3})30^\circ\text{-Sn}$ surface

X.F. Lin, I. Chizhov, H.A. Mai, R.F. Willis

Department of Physics, Pennsylvania State University, University Park, PA 16802, USA

Received 26 June 1995; accepted 11 December 1995

Abstract

Scanning tunneling spectroscopy (STS) measurements have been performed on $\text{Si}(111)(2\sqrt{3} \times 2\sqrt{3})30^\circ\text{-Sn}$ surface. Tunneling spectral analysis of the energy of the surface states around the Fermi-level (E_f) indicates two filled and two empty states straddling E_f , showing a ~ 1.6 eV surface bandgap. As part of the identification of these surface states, STS spectra were also taken on a coexisting well-known $\sqrt{3} \times \sqrt{3}$ surface, and the intrinsic nature of these surface states is discussed.

1. Introduction

The $(2\sqrt{3} \times 2\sqrt{3})30^\circ$ structure is one of two major surface reconstructions group-IV Sn displays on $\text{Si}(111)$ [1]. (Hereafter, we simply denote this structure as $2\sqrt{3}$.) The atomic geometry and electronic structure of this surface reconstruction have been previously studied by various surface science tools [1–9]. However, there is still lot of controversy. Typically, photoemission studies by Kinoshita et al. [3] show that this surface exhibits a semiconductor character with at least two filled and one empty surface states located about the Fermi-level (E_f); while the results from the same studies by Griffiths et al. [8] show uncertainties of this nonmetallic aspect. As to the atomic geometries of this $2\sqrt{3}$ phase, several different atomic structural models have been proposed based on different theoretical and experimental approaches. Using scanning tunneling microscopy (STM) results [4–6], Tornevik et al. have introduced the first three-dimensional structural

model for this phase. Later, Griffiths et al. [8] have calculated this model using the self-consistent tight-binding method in the extended Huckel approximation, and a slight disagreement has led them to modify this model. Recently, Levermann et al. [9] have conducted surface X-ray diffraction (SXRD) studies on the $2\sqrt{3}$ surface and the results are in contradiction with these previous two models.

In this paper, we report our scanning tunneling spectroscopy (STS) results on the $2\sqrt{3}$ surface reconstruction. Leaving out the more controversial atomic structural models, we focus on the surface electronic states and the Fermi-level position in the surface-state band structure which are not well addressed in previous studies. We also compare the $2\sqrt{3}$ STS spectra with these taken on a coexisting well-known $\sqrt{3} \times \sqrt{3}$ surface so as to possibly explore the origins of the $2\sqrt{3}$ surface electronic states. This will be helpful in the understanding of the atomic geometric structures of this $2\sqrt{3}$ surface. (Hereafter, we simply denote the $\sqrt{3} \times \sqrt{3}$ structure as $\sqrt{3}$.)

2. Experimental

All experiments were performed in an ultrahigh vacuum chamber with a base pressure 2×10^{-10} Torr and equipped with an STM. Commercial n-type Si(111) samples were used, which have been cleaned and checked with STM. Keeping the sample at either $\sim 400^\circ\text{C}$ or room-temperature (RT), tin was resistively evaporated from an evaporator. The metal flux was monitored by a crystal thickness monitor. The typical rate was 0.1 ML/min, where one monolayer (ML) is defined as $7.84 \times 10^{14}/\text{cm}^2$. A $2\sqrt{3}$ and $\sqrt{3}$ surface was obtained by annealing 0.5–1.3 ML of Sn to 350 – 500°C . STS measurements on several samples with different tips were averaged to eliminate tip-induced effects. All STM and STS measurements were taken at RT.

3. Results and discussion

Fig. 1(a) is an empty-state topographic image ($240 \times 240 \text{ \AA}$), showing a $2\sqrt{3}$ and a $\sqrt{3}$ structural domain separated by a curved step-edge. The bottom section of this image shows the $\sqrt{3}$ structure on a lower terrace; while the rest section is the $2\sqrt{3}$ phase on a higher terrace, as they are labeled, respectively. In this empty-state image, on $2\sqrt{3}$ terrace two types

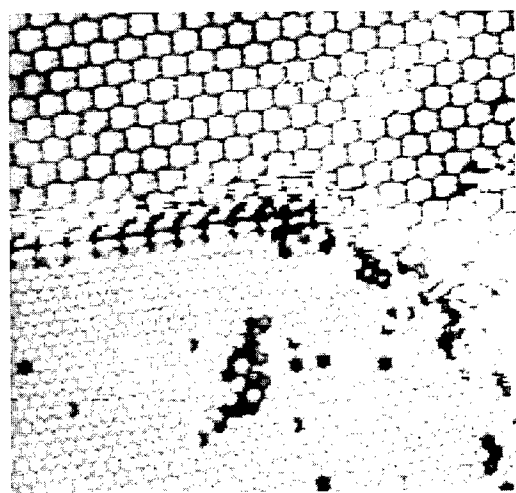


Fig. 1. An empty-state image shows $2\sqrt{3} \times 2\sqrt{3}$ area and an adjacent $\sqrt{3} \times \sqrt{3}$ area separated by a curved step-edge ($I = 1.1 \text{ nA}$, $V = 1.0 \text{ V}$).

of features are seen, with each of them having pairing structures. This is the same as that observed previously [5,6]. On the $\sqrt{3}$ area, a small amount of surface defects (black areas) induced by missing Sn atoms are observed.

Along $[\bar{1}\bar{1}2]$ direction at a partial step-edge, a distinctly structured domain-boundary separates the $\sqrt{3}$ and $2\sqrt{3}$ terraces; while roughly along a 45° angle away from $[\bar{1}\bar{1}2]$ direction, a domain-boundary at the step-edge separating these two terraces is not seen with any ordered structure. The height of the step-edge in this empty-state image is measured to be 1.2 Å. The structured domain boundary only seen along $[\bar{1}\bar{1}2]$ direction separating the $\sqrt{3}$ and the $2\sqrt{3}$ terraces might function as to relieve the stronger surface strain arising from these two surface structures especially along $[1\bar{1}0]$ direction. The same effects of the domain boundary on the surface have been reported in several other studies [10,11].

To understand well the electronic properties of $2\sqrt{3}$ surface, we measure the electronic structures of the $2\sqrt{3}$ and the adjacent $\sqrt{3}$ domain with STS. Fig. 2 shows two sets of I – V curves (solid lines), differential I – V curves (dI/dV) (dash-dot lines), and normalized differential I – V curves ($dI/dV \cdot V/I$) (dashed lines), averaged on both structural areas, respectively, where we normalize the differential I – V curves in a mode as suggested by Feenstra [12]. Curves in Fig. 2(a) are associated with the $\sqrt{3}$ area and curves in (b) with the $2\sqrt{3}$ area. The STS I – V measurements were taken with the feedback loop stabilized around $\pm 2.0 \text{ V}$. In the normalized I – V curves, the energy of the surface states is measured by the sample voltage relative to the Fermi level at 0 V.

We start with the well-known $\sqrt{3}$ surface. Normalized curve in (a) shows four surface states on filled-state and two on empty-state side. Like the Si(111)-simple metal (Al, Ga, In), the Si(111) $\sqrt{3}$ -Sn surface has been shown to be simply composed of Sn atoms preferentially residing at the T_4 sites on the ideal Si(111) surface [3–8,13–15]. Fig. 3 shows $\sqrt{3}$ surface atomic structural model of T_4 sites, with (a) top view and (b) cross-section view. Each Sn adatom covalently bonds to the underlying Si three half-filled p_z -like sp^3 hybridized dangling bonds, producing two occupied surface states S_2 (at $\sim -1.2 \text{ eV}$) and S_3 (at $\sim -1.8 \text{ eV}$) due to the Sn adatom $p_{x,y}$ -like

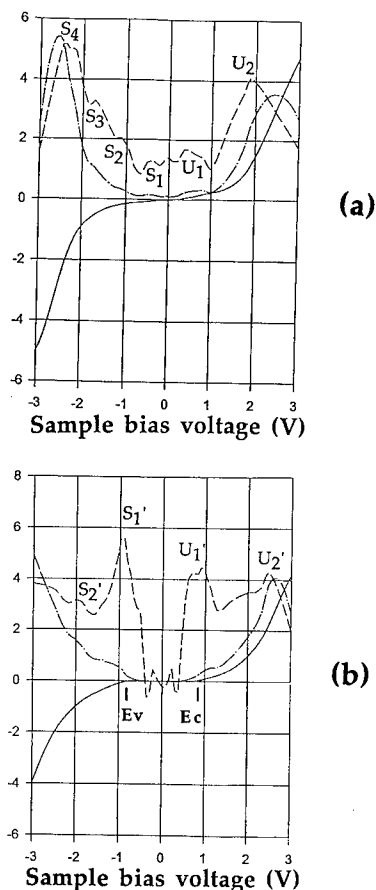


Fig. 2. STS $I-V$ spectra taken on (a) $\sqrt{3} \times \sqrt{3}$ and (b) $2\sqrt{3} \times 2\sqrt{3}$ surface area (see text for details).

sp^3 hybridized orbitals interacting with the Si adatom p_z -like orbitals. It's not quite clear about the origins of a surface state (S_4) located at ~ -2.5 eV. A surface state with the same energetic position has been reported by Becker et al. [16] on the clean

Si(111) 7×7 surface, and it is assigned to be derived from the stacking-fault structures on the surface.

Unlike the empty p_z -like orbitals on the simple metal atoms, one more valence electron located in the p_z -like sp^3 hybridized orbital on the Sn adatoms at the T_4 sites shows an unbonded dangling-bond state, and this half-filled bond produces the metallic surface states S_1 (at ~ -0.5 eV) and U_1 (at ~ 0.4 eV) crossing the Fermi-level (E_f) [3,7,13], just like those on the clean Si(111) 7×7 surface [17] and the Si(111) $\sqrt{3}$ -Si surface [18]. A small peak seen at 0 eV position, we think, is due to the specific normalization procedure we used, representing a typical character of metallic surface.

One unoccupied surface state U_2 (at ~ 1.9 eV) above the E_f represents an intrinsic contribution from the $\sqrt{3}$ -Sn surface, and this intrinsic contribution also overlaps with the surface states S_2 and S_3 . The positions of these intrinsic surface states are consistent with those reported in photoemission studies [3,8,13].

However, one issue we need to address is that, as previous STM studies shown [5], the surface behavior of Si(111) $\sqrt{3}$ -Sn structure is quite dependent on both the metal coverage and the annealing temperature. Specifically, annealing surface to higher temperature will produce a mosaic surface of Si atoms replacing the Sn surface atoms. This will significantly change the surface electronic properties. We will report the details of our STM and STS measurements on the changes of the surface electronic properties with Sn coverage and the annealing temperature in another publication.

In curves Fig. 2(b) taken on the $2\sqrt{3}$ -Sn area, on either side of the Fermi-level (E_f) we see two occupied surface states and two unoccupied surface states, and these states are located about E_f , producing a surface bandgap. As marked by the surface valence-band maximum (E_v) and conduction-band minimum (E_c), the surface band gap is measured to be ~ 1.6 eV. This indicates that the $2\sqrt{3}$ structures exhibit a semiconducting α -Sn character. For comparison, in Fig. 4 we show schematic diagram of positions of surface states from photoemission results of Kinoshita et al performed on Si(111) $2\sqrt{3}$ -Sn surface [3]. As one can see, the energetic positions of the surface states S_1' , S_2' , U_1' and U_2' about the E_f seen in

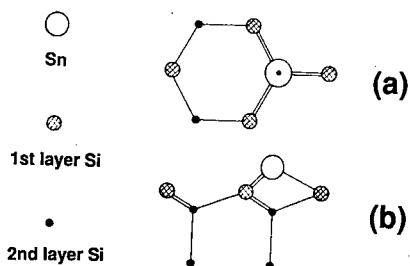


Fig. 3. A $\sqrt{3} \times \sqrt{3}$ atomic structural model, with (a) top-view and (b) cross-section view.

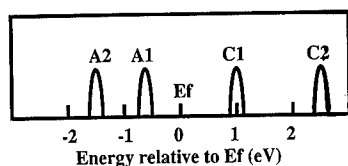


Fig. 4. Schematics of photoemission results of Kinoshita et al. on a $2\sqrt{3} \times 2\sqrt{3}$ surface.

our STS I - V spectra are consistent with these of A_1 , A_2 , C_1 , and C_2 observed in the photoemission studies, except small shifts of the two filled surface states. Kinoshita et al. have not assigned these surface states to any particular origins in their studies.

The surface states S'_1 (at ~ -1.0 eV) and U'_1 (at ~ 1.0 eV), we think, reflect the bonding and antibonding states arising from the Sn surface atoms themselves, since the same surface states are observed for Sn adatoms growing on a 7×7 reconstructed substrate Si surface at relatively high metal coverage [19], where covalent-like bonding formed within the 7×7 ordered Sn clusters maintains the surface nonmetallic character which is initially induced by Sn half-filled p_z -like sp^3 hybridized orbitals covalently bonding to the underlying Si partially filled p_z -like sp^3 hybrids and saturating these Si dangling-bonds.

There is no convincing evidence to assign the surface states S'_2 (at ~ -2.0 eV) and U'_2 (at ~ 2.5 eV) to the specific origins. As seen from the STS spectral curves in Fig. 2(a) and 2(b) taken respectively on the $\sqrt{3}$ -Sn and the $2\sqrt{3}$ -Sn surface, the surface state S'_2 has the similar energetic positions as the surface state S_3 and the state S_3 is contributed from the interactions between the Sn and Si atoms as we mentioned above. So it might be reasonable that the bonding between the interfacial Sn atoms and the underlying Si atoms plays a major role in the appearance of the surface state S'_2 , assuming that there is no intermixing between Sn and Si atoms [2,7] and that at least two layers of Sn atoms exist on the substrate Si surface for the $2\sqrt{3}$ structure. A small energy shift from S_3 to S'_2 possibly associates with the Sn atoms locating on different positions of the substrate Si atoms within $\sqrt{3}$ and $2\sqrt{3}$ surfaces. The surface state U'_2 might be derived from the substrate Si bulk structure.

One more point we want to mention is that, as

seen in the curve in Fig. 2(b), on the $2\sqrt{3}$ surface the Fermi-level position is located within a wide surface bandgap between the occupied and unoccupied surface states, which is ~ 0.8 eV above the top of surface valence band. These surface states derived from the ordered $2\sqrt{3}$ -Sn overlayer themselves are not sufficient to pin the surface Fermi-level [20]. We find that the surface states arising from the edges of $2\sqrt{3}$ terrace or the surface defects induced by missing Sn atoms possibly serve to determine the surface Fermi-level position, as will be discussed elsewhere.

4. Conclusion

In summary, scanning tunneling spectroscopy (STS) is used to examine the $\text{Si}(111)(2\sqrt{3} \times 2\sqrt{3})\text{R}30^\circ\text{-Sn}$ surface. STS measurements show two occupied and two unoccupied surface states located about the Fermi-level (E_f), producing a ~ 1.6 eV surface bandgap. An analysis indicates that the covalent-like bonding within the Sn atoms determines the top and bottom positions of surface valence and conduction bands. Compared with the STS spectra taken on a coexisting $(\sqrt{3} \times \sqrt{3})\text{R}30^\circ\text{-Sn}$ surface, the intrinsic nature of the other $2\sqrt{3} \times 2\sqrt{3}$ surface states is possibly explored.

Acknowledgements

We acknowledge support from the Office of Naval Research, Grant No. N00044-92-J-1479.

References

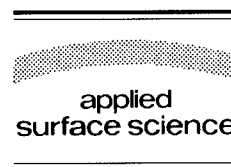
- [1] P.J. Estrup and J. Morrison, *Surf. Sci.* 2 (1964) 466.
- [2] T. Ichikawa, *Surf. Sci.* 140 (1984) 37.
- [3] T. Kinoshita et al., *J. Phys. Soc. Jpn.* 56 (1987) 4015.
- [4] J. Nogami, S.I. Park and C.F. Quate, *J. Vac. Sci. Technol. A* 7 (1989) 1919.
- [5] C. Tornevik, M. Hammar, N.G. Nilsson and S.A. Flodstrom, *Phys. Rev. B* 44 (1991) 13144; C. Tornevik et al., *Surf. Sci.* 314 (1994) 179.
- [6] M.S. Worthington, J.L. Stevens, C.S. Chang and I.S.T. Tsong, *J. Vac. Sci. Technol. A* 10 (1992) 657; *Nucl. Instr. Meth.* 64 (1992) 566.
- [7] A. Taleb-Ibrahimi, C.A. Sebenne, F. Proix and P. Maigne, *Surf. Sci.* 163 (1985) 478.

- [8] C.L. Griffiths, H.T. Anyele, C.C. Matthai, A.A. Cofolla and R.H. Williams, *J. Vac. Sci. Technol. B* 11 (1993) 1559.
- [9] A.H. Levermann et al., *Appl. Surf. Sci.* 104/105 (1996) 124.
- [10] R.S. Becker, T. Klitsner and J.S. Vickers, *J. Microsc.* 152 (1988) 157.
- [11] X.F. Lin, K.J. Wan and J. Nogami, *Phys. Rev. B* 49 (1994) 7385.
- [12] P. Martensson and R.M. Feenstra, *Phys. Rev. B* 39 (1989) 7744.
- [13] T. Kinoshita, S. Kono and T. Sagawa, *Phys. Rev. B* 34 (1986) 3011.
- [14] K.M. Conway et al., *Surf. Sci.* 215 (1989) 555.
- [15] S.K. Ramchurn, D.M. Bird and D.W. Bullett, *J. Phys. Condens. Matter* 2 (1990) 7435.
- [16] R.S. Becker, J.A. Golovchenko, D.R. Hamann and B.S. Swartzentruber, *Phys. Rev. Lett.* 55 (1985) 2032.
- [17] R.J. Hamers, R.M. Tromp and J.E. Demuth, *Phys. Rev. Lett.* 56 (1986) 1972.
- [18] J.E. Northrup, *Phys. Rev. Lett.* 53 (1984) 683.
- [19] X.F. Lin, I. Chizhov, H.A. Mai and R.F. Willis, submitted.
- [20] R.M. Feenstra, *Appl. Surf. Sci.* 56–58 (1992) 104.



ELSEVIER

Applied Surface Science 104/105 (1996) 228–233



Unpinned behavior of the Fermi level and photovoltage on p-(100)GaAs surface facilitated by deposition of cesium

V.L. Alperovich^{a,b,*}, A.G. Paulish^a, H.E. Scheibler^a, V.I. Tynnyi^{a,b},
A.S. Terekhov^{a,b}

^a Institute of Semiconductor Physics, 630090 Novosibirsk, Russian Federation

^b Novosibirsk State University, 630090 Novosibirsk, Russian Federation

Received 26 June 1995; accepted 30 August 1995

Abstract

The preparation technique of (100)GaAs surface with unpinned electronic properties is further developed in this work. It was proved that the unpinned behavior of the Fermi level and surface photovoltage on p-(100)GaAs surface was facilitated by the deposition of cesium. The surface preparation technique included removal of oxides in the solution of HCl in isopropanol and transfer to a UHV set-up in nitrogen atmosphere. The variations of band bending and surface photovoltage were measured by means of photoreflectance spectroscopy after anneals at successively increasing temperatures. Without Cs deposition, the band bending varied only by 50–100 meV as the annealing temperature increased from 300 to 600°C. Deposition of a monolayer of Cs, followed by annealing at 400°C, caused a pronounced decrease of band bending. The evolution of surface photovoltage, which depends both on band bending and on the rates of capture and recombination of the photogenerated carriers on the surface, was more diverse and sensitive to the details of surface treatment. Possible mechanisms of cesium influence on the electronic properties of the surface are discussed.

1. Introduction

Control of band bending and other electronic properties of clean and adsorbate-covered surfaces of (100)GaAs is a challenging problem both for fundamental surface science and applications. Results of recent studies show that the behavior of electronic properties of (100)GaAs surface may be diverse and depend on the type and level of doping, surface preparation technique and chemical nature of adsorbates [1–8]. It was found by Chen et al. [1] and Vitomirov et al. [2] that the Fermi level on the

surface of (100)GaAs grown by molecular beam epitaxy and protected by arsenic cap layer was close to the midgap and almost independent of the decapping temperature. On the other hand, a possibility to obtain the surface of p-(100)GaAs with the Fermi level close to the valence-band maximum (corresponding to small values of band bending of about 0.15–0.3 eV) was demonstrated by Yin et al. [3], Pashley et al. [4], and Glembocki et al. [5]. Deposition of various metals on decapped GaAs surface led to considerable variations of the band bending, which correlate with adsorbate electronegativity [6].

Large reversible variations of the band bending and surface photovoltage were observed recently on p-(100)GaAs(Cs, O) interface under alternate deposi-

* Corresponding author. E-mail: alper@ispht.nsk.su.

tion of Cs and O₂ at room temperature [7]. This interface is of particular interest because of widespread usage of GaAs(Cs,O) negative electron affinity photocathodes. In Ref. [7] the surface of GaAs was prepared by removal of oxides in alcohol solution of HCl and transfer to UHV chamber under nitrogen atmosphere, followed by annealing in UHV at relatively low temperature $T = 400^\circ\text{C}$. Moreover, even without annealing one could observe substantial variations of band bending after a few cycles of Cs–O deposition [8]. This indicates that some kind of ‘cleaning’ of the surface from residual products of chemical treatment takes place during the first Cs–O cycles.

The aim of the present paper is further development of the technique, which is based on the HCl chemical treatment under nitrogen atmosphere [9,10], for the preparation of clean p-(100)GaAs surface with desired electronic properties. First, by means of photorefectance spectroscopy [3,5,7,8,11–13] we measured the band bending and surface photovoltage on p-(100)GaAs surface as a function of annealing temperature. The band bending varied with annealing temperature within a narrow range of 0.33–0.42 eV. Second, it was shown that the deposition of a monolayer of Cs followed by further anneals facilitated a substantial decrease of the band bending down to 0.22 eV. Along with the variations of the band bending, the variations of the surface photovoltage by about one order of magnitude were observed. Possible mechanisms of the Cs-facilitated unpinning behavior of surface electronic properties are discussed.

2. Experimental technique

MBE-grown undoped/p⁺-GaAs structures (the so-called UP⁺ structures) used in this study are designed specially for precise determination of the surface electric field and band bending by photorelectance spectroscopy [12,13]. A UP⁺ structure consists of a Be-doped ($N = 2 \times 10^{18} \text{ cm}^{-3}$) 1000 nm thick p⁺-GaAs layer grown on a p⁺-(100)GaAs substrate and a thin ($d_c = 100 \text{ nm}$) undoped i-GaAs cap layer with uniform electric field.

The surface preparation technique [9,10] included removal of oxides in isopropyl-alcohol solution of

HCl and transfer to UHV chamber under nitrogen atmosphere without air contact. It was shown earlier by Auger electron spectroscopy [10] that after such treatment the surface was enriched with 1–2 monolayers (ML) of arsenic and covered by submonolayer amount of chlorine and carbon-contained species, which could be removed by the heat cleaning of the sample in UHV at relatively low temperature $T \approx 400^\circ\text{C}$. In this study 10 min or one hour anneals of the samples at successively increasing temperatures were performed by passing electric current through the sample. The dependence of sample temperature versus heating power was calibrated using the near-bandgap features in reflectance spectra [14].

A chopped pump beam of a He–Ne laser with the wavelength of 632.8 nm and a monochromatic probe beam produced by a halogen lamp and a grating monochromator were used for the measurements of photorelectance (PR) spectra [11]. PR measurements were done at room temperature. Surface electric field F_s was determined by the Fourier analysis of Franz–Keldysh oscillations observed in PR spectra, with the random error being less than 1% [15]. The systematic error in F_s related to surface photovoltage [13] was estimated to be about 10% in the present experiments. The band bending ϕ_s was calculated from the measured values of the surface field. The effect of penetration of free carriers from the buffer into cap layer was treated rigorously by numerically solving the Poisson equation. The result is presented in Fig. 1. It is seen that for small surface fields $F_s < 2 \times 10^4 \text{ V/cm}$ this effect yields a diffusion potential step of about 0.1 V at the abrupt buffer cap interface and, therefore, should be taken into account. The magnitude of the step also increases with increasing doping level of the p⁺ buffer layer.

Among various electronic properties of semiconductor surfaces, the Fermi level position (or surface band bending), which is determined by the charge of equilibrium (majority) carriers captured on the surface, is studied most extensively. To create a complete picture of surface electronic processes, it is important also to study capture and recombination of nonequilibrium charged carriers. To this end, together with the band bending we studied the evolution of the modulated surface photovoltage (SPV), which reflects these nonequilibrium processes and determines the amplitude of photorelectance signal

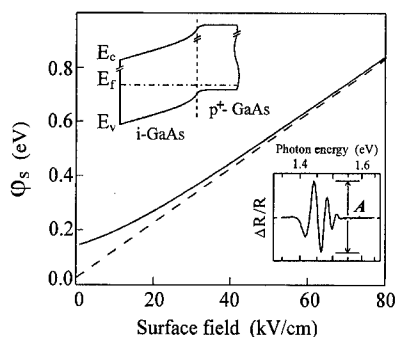


Fig. 1. Calculated band bending ϕ_s versus surface electric field F_s for the UP^+ structure. Dashed line shows a simple linear dependence $\phi_s = F_s d + kT$ that neglects a diffusion potential step at the cap layer–buffer layer interface. Solid curve is calculated rigorously according to Poisson equation and includes the potential step at the interface. The diffusion potential step is seen on the energy band diagram shown in the upper left insert. This diagram corresponds to $\phi_s = 0.22$ eV. The lower right insert shows a typical measured PR spectrum of a UP^+ structure.

A [16]. On a clean or adsorbate-covered surface of a semiconductor, SPV originates from the screening of surface field by free photoexcited charged carriers and from the charge of nonequilibrium (minority) carriers captured by the surface states. The magnitude of the former contribution to SPV depends mainly on the band bending. The latter contribution to SPV depends also on the concentration and capture cross-sections of the respective surface states. Little is known about the evolution of these states during surface preparation. Experimental data presented in this paper show considerable variations of SPV and, thus, the parameters of surface states during surface preparation. However, further work should be done to analyze the data on surface photovoltage quantitatively.

3. Results and discussion

3.1. The influence of annealing temperature on the band bending

In Fig. 2 the dependences of the band bending and amplitude of photoreflectance on the temperature of anneals of a UP^+ structure are shown for two experiments with different duration of the anneals. For 10 min anneals the band bending ϕ_s varied

nonmonotonically within a narrow range of 0.33–0.42 eV, with a trend for the increase of ϕ_s at annealing temperature $T > 500^\circ\text{C}$. For one hour anneals the variations of ϕ_s were even smaller (within the range of 0.37–0.42 eV). It should be noted that the observed variations are well above the random error, which is below 10 meV for PR spectroscopy of UP^+ structures.

Small (within 0.1 eV) variation of ϕ_s with annealing temperature is in accordance with the results obtained by Chen et al. [1] and Vitomirov et al. [2] on MBE-grown GaAs layers decapped from protective As overlayer. However, we observed smaller mean values of the band bending of approximately 0.4 eV, as compared to 0.65 eV observed in [1] and 0.55 eV observed in [2].

In the same two experiments the amplitude A of photoreflectance varied by one order of magnitude (see the bottom of Fig. 2). One can see the temperature regions where SPV and band bending variations correlate (at $T < 500^\circ\text{C}$) and anti-correlate (at $T > 500^\circ\text{C}$) with each other. This shows complicated nature of the surface photovoltage. Despite the increase of band bending as T rises from 500 to 600°C , surface photovoltage decreases in this temperature region. This decrease of SPV may be due to the variations of the concentrations or cross-sections of electron and hole surface traps, or due to the increase of surface recombination velocity.

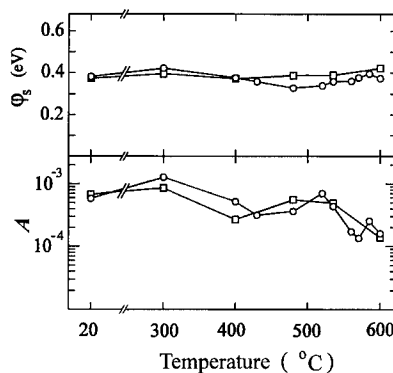


Fig. 2. The dependence of surface band bending ϕ_s (top) and amplitude of photoreflectance A (bottom) on the successively increasing temperature of 10 min (circles) and one hour (squares) anneals of a UP^+ structure in UHV. The position of a point on the temperature scale denotes the temperature of the preceding anneal.

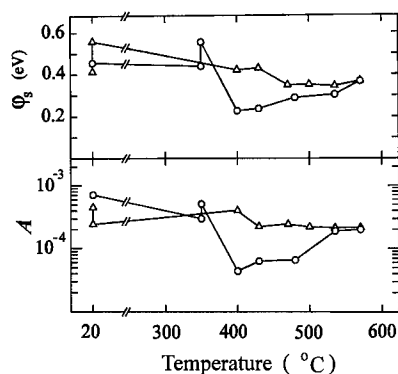


Fig. 3. The evolution of surface band bending ϕ_s (top) and amplitude of photoreflectance A (bottom) measured under the experimental conditions similar to those used in the previous experiment (see Fig. 2), but with the deposition of a monolayer of Cs after preliminary anneal at 350°C (As-rich surface, circles) or 550°C (Ga-rich surface, triangles). The evolution of ϕ_s under the deposition of Cs is shown by vertical segments of the lines. For convenience of comparison the dependences for Ga-rich surface start from room temperature, although the surface was preliminary annealed at $T = 550^\circ\text{C}$.

3.2. Unpinned behavior of band bending facilitated by Cs deposition

In the next experiment we tried to find out whether it is possible to enlarge the band bending excursions on HCl-prepared p-GaAs surface by combining anneals and deposition of cesium adsorbate layers. After preliminary anneal at $T = 350^\circ\text{C}$, a monolayer of cesium was deposited at room temperature. Then the surface was annealed for 10 min at successively increasing temperatures. The evolution of the band bending and photoreflectance amplitude is shown by circles in Fig. 3. In this experiment the initial value of band bending after HCl treatment was larger by approximately 70 meV than the values presented in Fig. 2. It should be noted that before annealing the initial value of band bending on chemically prepared surfaces of p-doped GaAs varied from one experiment to another in the range of 0.30–0.45 eV due to some possible variations of the surface composition and stoichiometry.

The deposition of Cs led to an increase of the band bending up to 0.56 eV, while subsequent anneal at 400°C yielded substantial decrease of ϕ_s

down to 0.22 eV. Comparing Fig. 2 and Fig. 3, one can see that such a low value of ϕ_s could not be achieved by simple annealing. Further anneals at elevated temperatures led to $\phi_s = 0.38$ eV for $T = 600^\circ\text{C}$. It is seen from the bottom of Fig. 3 that in the experiment with Cs deposition, PR amplitude varied by more than one order of magnitude and correlated with the band bending.

The increase of ϕ_s under Cs deposition agrees well with a donorlike character of Cs-induced surface states [7,17–20]. However, the effect of Cs-induced decrease of ϕ_s after annealing is not yet fully understood. Similar effect was observed on MBE-grown p-(100)GaAs surface and explained by Cs-induced desorption of arsenic [21]. One can also suggest that cesium atoms are bonded to chlorine, oxygen and other species, which may be present on the surface after chemical treatment. Thus, the residual contaminations are either neutralized, or more easily removed under low temperature annealing. This ‘cesium cleaning’ results in the surface with lower concentration of donor-like surface states, which are responsible for the band bending on p-type semiconductor surfaces.

Cesium-facilitated decrease of the band bending observed in the present study is in accordance with the results obtained in Refs. [7,8]. In particular, in Ref. [7] we observed large reversible variations of band bending from half-bandgap values to almost flat bands under alternate deposition of cesium and oxygen on clean p-(100)GaAs surfaces. The minimal values of band bending decreased with the increasing number of Cs–O deposition cycle. Similar variations were observed on chemically prepared but unheated surface after a few cycles of Cs–O deposition [8]. Therefore, together with earlier studies, the results of the present paper prove that adsorbate-facilitated unpinned behavior of electronic properties is a general feature of carefully prepared p-GaAs surface.

3.3. The influence of surface stoichiometry

To check the mechanisms of Cs-facilitated unpinned behavior of band bending and SPV, we performed experiments with Cs deposition on a p-GaAs surface that was preliminary subjected to a heat cleaning at 550°C for five minutes. As a result, the surface was enriched with gallium [1], in contrast to

the initial chemically prepared As-rich surface. Then PR spectra were measured before and after the deposition of a monolayer of Cs, and after 10 min anneals at successively increasing temperatures. The results are shown in Fig. 3 by triangles. The initial band bending on Ga-rich surface was equal to 0.41 eV and increased up to 0.56 eV after deposition of Cs due to creation of Cs-induced donorlike surface states. It is seen, however, that in contrast to As-rich surface, further anneals of Ga-rich surface did not lead to a substantial decrease of ϕ_s below its initial value. The variation of PR amplitude for Ga-rich surface was also relatively small (see the bottom of Fig. 3). Note, however, that for this surface the variation of PR amplitude anti-correlate with that of the band bending after the deposition of Cs and anneal at 400°C. This behavior shows again that the mechanisms of SPV are complicated and its magnitude is sensitive to details of surface treatment.

The result for Ga-rich surface are compatible with the explanations of Cs-facilitated unpinning behavior discussed above. However, these experiments do not allow to distinguish between the effects of Cs-facilitated desorption of excessive arsenic and ‘cesium cleaning’ from residual contaminations due to formation of electrically inactive species.

4. Conclusions

In conclusion, the variations of the band bending with annealing temperature are found to be small (within 0.1 eV) on the surface of p-doped (100)GaAs prepared by HCl-treatment in nitrogen atmosphere. This observation agrees with the results of earlier studies, although the mean value of band bending is lower than for decapped MBE-grown surfaces. The deposition and subsequent desorption of a monolayer of cesium on the As-rich surface enlarge substantially the variations of the band bending. The reduction of band bending down to 0.22 eV is observed after annealing the Cs-covered surface at 400°C. Cs-facilitated reduction of band bending is not observed for Ga-rich surface. The evolution of surface photovoltage is diverse, showing sensitivity to the variations of capture and recombination rates of nonequilibrium charged carriers on the surface. Possible mechanisms of Cs-facilitated variations of the

surface electronic properties are the effect of ‘cesium cleaning’ of the surface, or cesium-induced desorption of excessive arsenic.

Acknowledgements

The authors are grateful to A.I. Toropov and N.T. Moshegov for supplying the epitaxial GaAs structures. This work was partly supported by the Russian Foundation for Fundamental Research under grant No. 93-02-15177 and by the Scientific Program ‘Russian Universities’ under grant 3H-354.

References

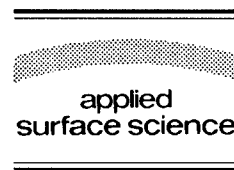
- [1] W. Chen, M. Dumas, D. Mao and A. Kahn, *J. Vac. Sci. Technol. B* 10 (1992) 1886.
- [2] I.M. Vitomirov, A. Raisanen, A.C. Finnefrock, R.E. Viturro, L.J. Brillson, P.D. Kirchner, G.D. Pettit and J.M. Woodall, *Phys. Rev. B* 46 (1992) 13293.
- [3] X. Yin, H.-M. Chen, F.H. Pollak, Y. Cao, P.A. Montano, P.D. Kirchner, G.D. Pettit and J.M. Woodall, *J. Vac. Sci. Technol. A* 10 (1992) 131.
- [4] M.D. Pashley, K.W. Haberern, R.M. Feenstra and P.D. Kirchner, *Phys. Rev. B* 48 (1993) 4612.
- [5] O.J. Glembocki, A.J. Tuchman, K.K. Ko, S.W. Pang, A. Giordana and C.E. Stutz, *Mater. Res. Soc. Symp. Proc.* 324 (1994) 153.
- [6] R.E. Viturro, J.L. Shaw, C. Mailhot, L.J. Brillson, N. Tache, J. McKinley, G. Margaritondo, J.M. Woodall, P.D. Kirchner, G.D. Pettit and S.L. Wright, *Appl. Phys. Lett.* 52 (1988) 2052.
- [7] V.L. Alperovich, A.G. Paulish and A.S. Terekhov, *Phys. Rev. B* 50 (1994) 5480.
- [8] V.L. Alperovich, A.S. Jaroshevich, V.N. Kuzaev, S.V. Shevelov, A.G. Paulish and A.S. Terekhov, *Phys. Low-Dim. Struct.* 1 (1994) 45.
- [9] R.P. Vasquez, B.F. Lewis and F.J. Grunthaner, *J. Vac. Sci. Technol. B* 1 (1983) 791.
- [10] Yu.G. Galitsin, V.I. Poshevnev, V.G. Mansurov and A.S. Terekhov, *Prib. Tekhn. Eksp.* 4 (1989) 191 [*Instr. Exp. Tech.* 31 (1989) 1057].
- [11] D.E. Aspnes, in: *Handbook of Semiconductors*, Vol. 2, Ed. T.S. Moss (North-Holland, Amsterdam, 1980) p. 109.
- [12] C. Van Hoof, K. Deneffe, J. De Boeck, D.J. Arent and G. Borghs, *Appl. Phys. Lett.* 54 (1989) 608.
- [13] X. Yin, H.-M. Chen, F.H. Pollack, Y. Chan, P.A. Montano, P.D. Kirchner, G.D. Pettit and J.M. Woodall, *Appl. Phys. Lett.* 58 (1991) 260.
- [14] M.K. Weilmeyer, K.M. Colbow, T. Tiedje, T. Van Buuren and L. Xu, *Can. J. Phys.* 69 (1991) 422.

- [15] V.L. Alperovich, A.S. Jaroshevich, H.E. Scheibler and A.S. Terekhov, *Solid-State Electron.* 37 (1994) 657.
- [16] T. Kanata, M. Matsunaga, H. Takakura, Y. Hamakawa and T. Nishino, *J. Appl. Phys.* 68 (1990) 5309.
- [17] R. Cao, K. Miyano, T. Kendelewicz, I. Lindau and W.E. Spicer, *Appl. Phys. Lett.* 54 (1989) 1250; *Phys. Scr.* 41 (1990) 887.
- [18] W. Mönch, *Europhys. Lett.* 7 (1988) 275.
- [19] J.E. Klepeis and W.A. Harrison, *J. Vac. Sci. Technol. B* 7 (1989) 964.
- [20] F. Bechstedt and M. Scheffler, *Surf. Sci. Rep.* 18 (1993) 145.
- [21] X. Yang, R. Cao, J. Terry, P. Pianetta and R. Mariella, Jr., private communication.



ELSEVIER

Applied Surface Science 104/105 (1996) 234–239



Development of the Na/GaAs(111)A-(2 × 2) interface at room and low temperature

J.M.C. Thornton ^{a,*}, P. Weightman ^a, P. Bailey ^b, D.A. Woolf ^c, A.D. Laine ^d,
D.A. Evans ^e

^a IRC in Surface Science, University of Liverpool, Liverpool L69 3BX, UK

^b EPSRC Daresbury Laboratory, Warrington WA4 4AD, UK

^c Department of Physics, U.W.C.C., Cardiff CF2 3YB, UK

^d Istituto di Struttura della Materia, Università di Messina, Messina, Sicilia, Italy

^e AMRL, Athrofa Gogledd Ddwyrain Cymru, Wrexham, Clwyd, UK

Received 28 June 1995; accepted 20 November 1995

Abstract

The alkali-metal/III–V semiconductor interface is a model system with which to study overlayer metallization and Schottky barrier development. Until now, typically the cleaved (110) surfaces of the semiconductor have been utilized in this respect, though in this work we have used the Ga-vacancy (2 × 2) reconstructed surface of GaAs(111)A as the starting surface. This surface is known to exhibit many similarities with the cleaved (110) surface, due to the separation of empty and filled dangling bonds onto the Ga and As surface atoms respectively. We have found through using soft X-ray photoemission from both core-level and valence-band features that the interface is remarkably unreactive, with almost no change in the Ga 3d lineshape with Na deposition at low temperatures. With regard to the growth-mode, work-function variation and band-bending however, the behaviour is close to that found for the cleaved surface. The onset of the Na LVV Auger transition only occurs after metallization begins and is consistent with ionic bonding to the substrate, though the substrate core-level development points to a reduced charge transfer with respect to the (110) surface.

1. Introduction

In studies of Schottky barrier development at the metal/semiconductor interface considerable attention has been focused on alkali-metal/semiconductor interfacial systems [1]. This is because they offer the best approximation to an ideal system, where chemical reaction and interfacial interdiffusion have been found to be limited, especially in the case of Cs

on GaAs [2–4]. The Na/GaAs(110) system is particularly interesting since its electronic structure is sufficiently simple to allow meaningful comparison with theoretical models [5] and a temperature dependent interface reactivity has been observed [2]. Theoretical predictions have been made for the transfer of charge from the metal into the previously empty Ga surface state [5], which have been supported by experimental results [6].

Recent scanning tunnelling microscopy (STM) and photoemission studies have shown that the GaAs(111)A Ga-vacancy (2 × 2) surface reconstruc-

* Corresponding author.

tion bears many similarities with the cleaved (110) surface [7]. In the (111)A surface bilayer, the Ga atoms are outermost, and with an annealing procedure it is possible to desorb 1/4 of the Ga, leaving vacancies with a (2×2) surface periodicity. Both theory and experiment agree that the surface rehybridizes, forming completely filled and completely empty dangling bonds on the As and Ga atoms respectively [7,8]. Another aspect of this rehybridization is that the surface bilayer collapses with the top-most Ga atoms relaxing downwards, becoming almost in-plane with the As atoms. In this condition, the surface closely resembles that from a cleaved (110) surface, with zig-zag chains of As and Ga atoms, each with a filled or empty dangling bond accordingly. Such a surface makes an interesting comparison with the (110) orientation, since no other GaAs surface is known to exhibit a similar spatial distinction of filled and empty states. This reconstruction therefore provides a useful alternative starting surface for a Schottky barrier investigation.

This study investigates for the first time the development of a Na overlayer on a GaAs(111)A Ga-vacancy (2×2) surface at both room and low temperatures using soft X-ray photoemission and makes comparison with that found for the cleaved (110) orientation. In particular, consideration is given to the variation in work function, the onset of both metallization and the LVV Auger transition, from which some insight into the nature of the initial Na-surface bond is gained.

2. Experimental

The samples used in this work were Zn-doped ($P \sim 10^{19} \text{ cm}^{-3}$) on-axis GaAs(111)A, prepared by molecular beam epitaxy (MBE). Following the thermal desorption of the oxide layer, a $0.1 \mu\text{m}$ thick GaAs buffer layer was grown, which was doped p-type with Si to a concentration of $\sim 10^{18} \text{ cm}^{-3}$. Throughout growth, a sharp, clear (2×2) electron diffraction pattern (RHEED) was visible. At the cessation of growth each sample was cooled in the reactor growth chamber to a temperature between -40°C and -50°C , whereupon the surface was capped with a protective layer (several microns thick) of amorphous As. This preparation allowed the sam-

ples to be transferred between laboratories in air, and then be loaded into the experimental UHV systems through fast entry load-locks. The samples were mounted on previously outgassed Mo holders using In. Decapping was achieved by gently electron-beam heating the sample to $\sim 315^\circ\text{C}$, at which the As desorbed as seen using a mass spectrometer. When the As_2 partial pressure dropped after about 10 min, and normal UHV was regained, the As cap could be seen to have desorbed as the mirror polish of the GaAs crystal surface was again visible. The sample was then ramped to 350°C and finally allowed to cool before examination with low energy electron diffraction (LEED) which revealed a sharp, low background (2×2) pattern. Some samples were then cooled using liquid nitrogen to a temperature of 100 K, which was maintained throughout the remainder of the experiment.

The photoemission experiments were performed at the synchrotron radiation source at Daresbury Laboratory (UK) using both the grazing incidence monochromator on beamline 6.1 and the 'Dragon' monochromator on the IRC beamline 4.1. These provided a photon flux in the energy range 50–170 eV, with measurements made using 90–105 eV radiation. An HA 100 hemispherical analyzer (CHA) from VSW was used on the beamline 6.1 experiments, and a 54 mm radius hemispherical angle-resolving analyzer on beamline 4.1. These provided a total instrumental resolution of $\sim 150 \text{ meV}$ and $\sim 100 \text{ meV}$ respectively. Overlayers of Na were deposited using well outgassed getter sources (SAES) such that the UHV pressure never exceeded $2 \times 10^{-10} \text{ mbar}$ during deposition.

3. Results and discussion

Both the Ga and As 3d core-levels are shown as a function of Na coverage at low temperature in Fig. 1, and from the lack of change in peakshapes it is immediately clear that there is no large scale chemical disruption of the surface. The peaks in Fig. 1 have all been normalized to the same count-rate to assist comparison of their peakshape. The clean surface core-level peakshape is known to be very similar to those found from the (110) surface due to the similarity of the surface bonding arrangements [7]. Each core-level may be decomposed into a peak

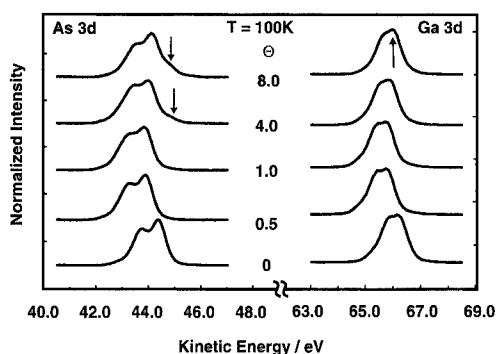


Fig. 1. The Ga and As 3d core-levels as a function of Na coverage in monolayers. Note the absence of satellite peaks on the Ga 3d, which would be expected to high kinetic energy on the (110) surface. An arrow marks the first signs of an extra component on the Ga 3d at 8 ML. Arrows also mark the Na–As reacted component from 4 ML on the As 3d.

from the bulk emission, and a single satellite peak from the surface layer, where the Ga 3d satellite peak is to lower kinetic energy than the bulk peak, and that on the As 3d is to higher kinetic energy. In comparison with these data, further high kinetic energy components are clearly seen on both core-levels on the (110) surface of GaAs under similar conditions, in particular on the Ga 3d indicating an interaction between the Na adatom and the empty Ga dangling bond of the clean, relaxed surface at low coverages [6]. No such component appears in the Ga 3d emission in this case, though at a coverage of 8 ML the lineshape alters, appearing with a more distinct peak at high kinetic energy rather than a 'flat-top' lineshape (Fig. 1). This suggests the onset of a small high kinetic energy component commensurate with the high coverage Na–Ga bonding seen on the (110) surface [2,6]. With increased coverage, no significant change in the Ga 3d lineshape is seen, the bulk component dominating throughout. A high energy shoulder appears on the As 3d at coverages greater than 4 monolayers (ML) indicating the onset of Na–As interfacial bonding (Fig. 1). Prior to this coverage, the lack of change in lineshape is probably best explained by coincidence in energy of the clean surface SCLS and that from the initial surface As bonding with Na [2]. The intensity of this shoulder relative to that of the bulk increases with further coverage only slightly beyond the that of the clean surface core-level shift and then stabilizes, which

confirms the limited nature of the interfacial disruption. The onset of the shoulder only occurs after distinct emission at the Fermi energy is seen from the Na overlayer, which is suggestive that a minimum metal coverage needs to be attained prior to any reaction taking place. The onset also coincides with the first deviation of the core-level attenuation away from exponential, indicating a link between the metallization of the layer with interfacial reaction and three-dimensional growth. The lack of change in the lineshape of the Ga 3d is particularly interesting, in that a decrease in the clean surface core level shift, with the resulting overall peakshape change, might be expected regardless of the bonding scheme of the overlayer. Nevertheless, the observed behaviour does show the lineshape to be almost invariant, which might be explained by any reacted interfacial components being low in intensity, and/or of identical energy shift to that of the clean SCLS. This is in variance to previous studies on the alkali/GaAs(110) interface, where some change is seen in the Ga 3d lineshape regardless of substrate temperature or alkali-metal used [2–4,6].

The intensity of both Ga and As 3d core-levels initially decreases exponentially with Na coverage at a sample temperature of 100 K, implying a uniform growth mode as shown in Fig. 2. A departure from this is seen above a coverage of 1 ML, which coincides with the onset of the As 3d lineshape change, linking the reaction with limited interface disruption. The change in attenuation rate is not dramatic, however, suggesting that the growth mode beyond this point is not significantly removed from

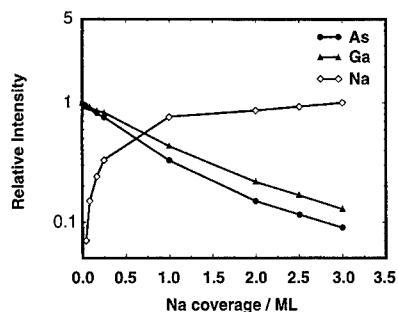


Fig. 2. A semi-logarithmic plot showing the decay of Ga and As core-level intensity relative to their clean surface values as a function of Na coverage. The growth is layer-by-layer until 1 ML when the attenuation departs from the exponential.

layer-by-layer and that large scale metal clustering is not occurring, though the Na 2p does begin to appear asymmetric at this point. This is due to the reduced surface mobility of the Na at low temperatures, which results in a growth mode sometimes described as 'statistical layered' once a critical surface roughness has been reached. This regime continued up the maximum Na coverage of ~ 16 ML, after which the substrate signal was almost undetectable. The linear region up until 1 ML is consistent with an electron escape depth of ~ 4.5 Å (1 ML of Na) and is also consistent with the variation in the sample work function, which shows a minimum at this point.

At room temperature, the intensity of the Ga and As core-levels remain almost constant as that for the Na 2p increases, showing that the Na is clustering strongly, leaving the GaAs largely uncovered, exactly as found for the cleaved (110) surface. In contrast with this, the peakshapes of the Ga and As core-levels also remain virtually unchanged, signifying a lack of any significant chemical reaction between the Na clusters and the GaAs substrate. This is in marked contrast to the situation found on the cleaved (110) surface, where large Ga and As peakshape changes occur after only ~ 1.5 ML Na coverage [2,6]. This may be due to enhanced mobility of the Na on the (111)A-(2×2) surface, leading to stronger clustering, thereby minimizing the Na-surface interaction.

The Na 2p core-level displays a number of changes with the development of the overlayer. At low coverages (~ 0.04 ML) the peak is clearly asymmetric due to the presence of two components separated by about 0.7 eV (Fig. 3). At this stage the component at lower kinetic energy dominates, but by 0.1 ML both are approximately equal in intensity. This appears very similar to the (110) case, where the two components have also been observed at low Na coverage. From this point on, the higher energy peak increases, appearing symmetric at a coverage of ~ 0.25 ML, and showing the initiation of an asymmetric Doniach–Sunjic metallic lineshape at 1.0 ML. This is the coverage at which strictly uniform growth is departed from i.e. the onset of large scale Na clustering. With further coverage, this shape becomes more asymmetric, characteristic of a fully metallic layer. This coincides with the onset of a distinct Fermi-edge in the Na valence band, which is not apparent at 1.0

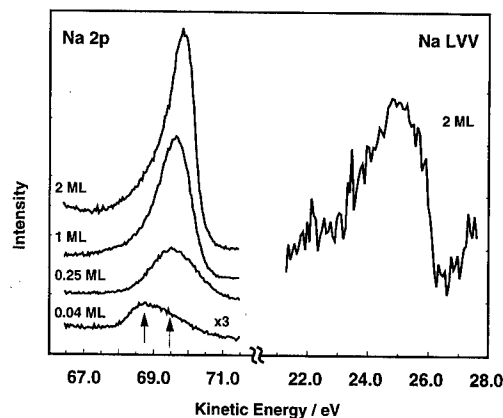


Fig. 3. A set of normalized Na 2p spectra with increasing Na coverage. Initially two components are present (arrowed) which merge and develop into an asymmetric lineshape indicative of metallic Na. The Na LVV Auger transition is also shown at its onset at a coverage of 2 ML with an arbitrary intensity.

ML, when the peakshape is asymmetric, but not fully 'metallic'. The two components found at low coverage can be one of a number of possibilities. The most obvious would seem to be Na–Ga and Na–As bonding at the surface, though it is also possible that one could be due to Na–Na bonds in clusters [2,6]. It is possible however, that a similar situation to that reported in an STM study of Na/GaAs(110) may be occurring, where chains of Na form at low coverage [9]. In the case of Na–As and Na–Ga bonding, however, chemically shifted components on the substrate core-levels might also be expected, and yet we see no evidence for this at this low coverage. One possible explanation is that the shifts induced by the overlayer are small and occur coincident in energy with the surface core level shifts for the clean surface. This is a departure from the obvious and large shift seen on the (110) Ga 3d core-level [6] and suggests that no large charge transfer associated with ionic bonding is taking place. A smaller charge transfer cannot be ruled out on this evidence, though it does allow a covalent bonding scheme to warrant serious consideration. It must be remembered that the starting surface is only similar to the cleaved (110) due to significant rehybridization following the loss of 1/4 of the surface Ga. The introduction of Na to this surface could be responsible for a new (de)relaxation or reconstruction which would make the core-levels appear quite different when compared

with previous studies on the (110) orientation. Against this, it seems unlikely that a large scale reconstruction could occur at the low temperatures used in these experiments since some surface mobility would be required. Unfortunately, it was not possible to monitor the reconstruction using LEED during the experiments, as the electron beam would have caused contamination of the sample. A low temperature STM study of this interface would be most revealing and helpful in answering this question.

At room temperature, the Na 2p peakshape is a symmetric Gaussian throughout the overlayer development, though it does increase in full-width half-maximum (FWHM) from 0.95 eV to 1.4 eV in the deposition range equivalent to 1–8 ML (layer-by-layer). This is to be expected considering the degree of oxidation of the surface, as seen by the presence of oxygen in the valence band. The Ga and As core-levels did not display any signs of oxidation however, and so it is believed that at room temperature the Na clusters oxidize, not the surface as a whole at this initial stage of interface development. The clean GaAs(111)A-(2 × 2) surface was found to be remarkably unreactive in a normal UHV environment at room temperature, with no significant quantity of oxygen apparent in the valence band after a period of more than 12 h.

The substrate material used was highly doped ($\sim 10^{18} \text{ cm}^{-3}$) and p-type, so the finding that the Fermi-level was 0.6 eV above the valence band maximum (VBM) for the starting surface at low temperature indicates the existence of band-bending and pinning of the Fermi-level in the starting surface, unlike that found on well cleaved (110) oriented material [2]. At room temperature, the Fermi-level was found to be pinned 0.18 eV higher than this in the band-gap. This is thought to be largely due to disorder on the de-capped surface rather than a surface-photovoltage (SPV) effect, since the doping level is high, and the SPV is known to be small in p-type material at low temperatures [10]. Furthermore, no difference in the Fermi-energies of the Na overlayer at higher coverages and spectra from the metal sample holder was found. Cooling the sample was also found to sharpen the Ga and As core-levels slightly, as the inhomogeneity of the pinning became reduced at low temperature. With the initial Na

coverage, the Fermi-level rose sharply by ~ 0.5 eV, and then returned to a final pinning position of VBM + 0.84 eV after a coverage of 1 ML i.e. the Fermi-level is pinned by a large density of interface states at mid-gap, as found for the (110) orientation [2,6,10]. No further change in the position was seen beyond this coverage. This rise in the Fermi-level position, or overshoot, has been recorded on a number of material systems, including alkali-metals on GaAs [6,10]. The final pinning position is also very similar to the cleaved (110) surface, where the Fermi-level is found to pin close to mid-gap under similar conditions due to the development of interfacial gap states [6,10]. It would be most instructive to perform similar experiments on n-type substrates in order to make comparison with the (110) surface, where the Na acts as a donor, causing markedly different Fermi-level movements between n- and p-type material [2,10]. Unfortunately, n-type (111)A layers grown by MBE are not yet available, and so these experiments were not possible.

Throughout the experiments, the change in work-function of the sample was measured with respect to the clean starting surface. This may be seen in Fig. 4, which shows a dramatic drop followed by a minimum and a stable region beyond. This behaviour is indicative of the growth of metallic Na, since a minimum is not seen when a reaction occurs at room temperature. It is useful here to highlight the correlation between the observed behaviour of the work-function and the rest of the dataset. The initial sharp drop in work-function coincides with the Na adatom adsorption stage, when the two components in the Na 2p emission merge and develop into a single

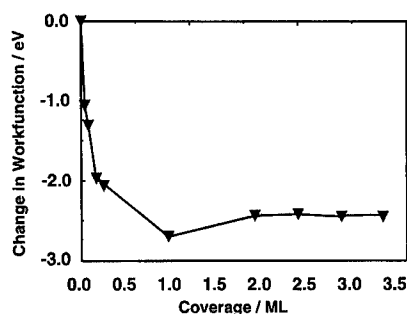


Fig. 4. Variation of the work-function as a function of coverage, showing the sharp drop over the initial coverages, a minimum at 1 ML, and a stabilization from 2 ML.

symmetric peak. No satellite peaks are seen on the Ga and As 3d core-levels at this stage. The minimum in the work-function occurs at 1 ML Na coverage, when the Na 2p first develops an initial asymmetric (metallic) lineshape, the growth mode departs from layer-by-layer and the As 3d displays a component due to Na–As bonding. From 1 ML the work-function rises due to the mutual depolarization of dipoles in the Na overlayer, and from 2 ML is essentially constant, with the change reflecting the difference in the work-functions of the two materials. Some Na–Ga interaction is present here, the Na 2p has become more asymmetric and the onset of both the Na Fermi-edge and LVV Auger transition occurs (Fig. 3).

The onset of the LVV Auger peak is sudden, with no evidence for a gradual increase in intensity (transition-rate) prior to this. In the Na atom, the 3s valence level is occupied by a single electron, and so the many-electron LVV Auger transition cannot take place. When Na is in a condensed environment, off-site screening can occur, where electron hopping involving neighbours allows the Auger transition to take place. It is interesting that the transition cannot occur earlier in the overlayer development, for instance when the depolarization of the overlayer results in the increase of the work-function. At that stage, there is clear in-plane interaction between the Na atoms, which might be expected to prove sufficiently intimate for hopping to occur. Moreover, the degree of Na–Na interaction is emphasized by the initiation of an asymmetric metallic Na 2p lineshape at the same coverage. It would appear therefore, that the interaction between the substrate and the Na overlayer is the most important factor, rather than that in-plane between Na atoms, and that there must be significant localization of the charge away from the Na atom to reduce the hopping transition rate. This is consistent with an ionic bonding scheme, similar to that proposed for the Na/GaAs(110) interface [6].

4. Conclusions

The adsorption of Na on the GaAs(111)A Ga-vacancy (2×2) reconstructed surface has been investigated both at room and low temperatures. In

general, the comparison with similar experiments on the cleaved (110) surface is very close, with similarities in growth-mode, work-function, Fermi-level pinning and limited reaction at the interface. These studies have revealed, however, that the chemical reactivity of this interface is much lower than that on cleaved GaAs, with no large energy shifts observed on the Ga and As core-level emission during the initial stages of overlayer development. The LVV Auger transition is not seen to occur until a Na coverage of ~ 2 ML has been deposited which is suggestive of initially ionic bonding of the Na to the surface. The limited changes in the core-level lineshapes, however, suggests that any such charge transfer must be small, unlike the significant interaction between Na and the empty Ga dangling bond on the (110) surface.

Acknowledgements

We would like to thank A.W. Robinson, D. Collier and M.D. Jackson for their assistance in these experiments, T.P. Morrison and A.A. Cafolla for their development of analysis software and the EPSRC for supporting these investigations.

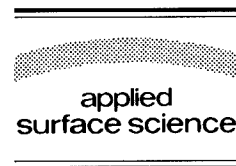
References

- [1] P. Soukiassian and H.I. Starnberg, *Physics and Chemistry of Alkali Metal Adsorption*, Eds. H.P. Bonzel, A.M. Bradshaw and G. Ertl (Elsevier, Amsterdam, 1989).
- [2] M. Prietsch, M. Domke, C. Laubschat, T. Mandel, C. Xue and G. Kaindl, *Z. Phys. B* 74 (1989) 21.
- [3] T. Kendelewicz, P. Soukiassian, M.H. Bakshi, Z. Hurych, I. Lindau and W.E. Spicer, *Phys. Rev. B* 38 (1988) 7568.
- [4] R. Cao, K. Miyano, T. Kendelewicz, I. Lindau and W.E. Spicer, *J. Vac. Sci. Technol. B* 7 (1989) 919.
- [5] J. Hebenstreit, M. Heinemann and M. Scheffler, *Phys. Rev. Lett.* 67 (1991) 1031.
- [6] D.A. Evans, G.J. Lapeyre and K. Horn, *J. Vac. Sci. Technol. B* 11 (1993) 1492.
- [7] J.M.C. Thornton, P. Weightman, D.A. Woolf and C.J. Dunscombe, *Phys. Rev. B* 51 (1995) 14459.
- [8] E. Kaxiras, Y. Bar-Yam, J.D. Joannopoulos and K.C. Pandey, *Phys. Rev. B* 35 (1987) 9625.
- [9] C.L. Bai, T. Hashizume, D.R. Jeon and T. Sakurai, *J. Vac. Sci. Technol. A* 11 (1993) 525.
- [10] A. Bauer, M. Prietsch, S. Molodtsov, C. Laubschat and G. Kaindl, *J. Vac. Sci. Technol. B* 9 (1991) 2108.



ELSEVIER

Applied Surface Science 104/105 (1996) 240–247



Metal overlayers on the MBE-grown ZnSe(001) surface

D.A. Evans^{a,*}, D. Wolfframm^a, D. Gnoth^a, J. Cairns^{a,1}, A.C. Wright^a, M. Evans^b,
J. Riley^c, D. Westwood^d, D.A. Woolf^d

^a AMRL, Athrofa Gogledd Ddwyrain Cymru (NEWI), Wrexham LL11 2AW, UK

^b Sincrotrone Trieste, Trieste, Italy

^c La Trobe University, Bundoora, Australia

^d University of Wales College of Cardiff, Cardiff, UK

Received 26 June 1995; accepted 21 November 1995

Abstract

N-type ZnSe thin films have been grown by MBE on GaAs (001) surfaces and capped with an amorphous selenium layer. The Se cap was thermally desorbed under ultrahigh vacuum to recover the (2×1) and $c(2 \times 2)$ reconstructed surfaces. Selected metal contact formation was monitored using core and valence level photoelectron emission spectroscopy by *in-situ* exposure of the surface to heated sources of Au, Ag and Pb. In each case, lineshape analysis of emission spectra indicated a low level of interfacial mixing and provided an insight into the metal layer growth mode. Both Au and Ag were found to grow in closely spaced islands of approximately equal height. The morphology of Au and Ag layers was confirmed by cross-sectional transmission electron microscopy. Monitoring of core and valence level emission peak positions allowed the determination of the metal–n-ZnSe Schottky barrier height, for a sufficiently thick metallic layer. Measurements on this wide-gap semiconductor, even at 300 K, were influenced by the presence of a surface photovoltage, which could be identified and subtracted for a fully-formed metallic layer. The n-type ZnSe Schottky barrier heights inferred from the relative Fermi level shifts ($\Phi_{\text{BN}}(\text{Au}) = 1.74$ eV, $\Phi_{\text{BN}}(\text{Ag}) = 1.47$ eV and $\Phi_{\text{BN}}(\text{Pb}) = 1.25$ eV), were found to scale with the metal work function for these three unreactive interfaces.

1. Introduction

The use of wide band gap II–VI semiconductor thin films in the fabrication of opto-electronic devices operating at the low wavelength end of the electromagnetic spectrum has fuelled the extensive study of this class of material. Most attention has

been focussed on ZnSe films grown on GaAs substrates for which the lattice mismatch is low [1]. However, realisation of practical devices has been hindered by the difficulty in controlling the conductivity of the bulk material and metal contacts to the p-type material. Early electrical studies of metals on ZnSe suggested that rectifying Schottky contacts are normally formed with common metals at room temperature (RT) [2], as for group IV and III–V semiconductors. With the larger band gap of this material, the formation of ohmic contacts is more difficult, and is a particular problem for p-ZnSe [3]. Low

* Corresponding author. Tel.: +44-1978-293161; e-mail: a.evans@newi.ac.uk.

¹ present address: DRA Malvern, Worcs, UK.

resistance contacts on n-ZnSe have been obtained using methods similar to GaAs involving annealing of In-alloys [4], but the corresponding method for p-GaAs using annealed Au-alloys has not been successful. For p-ZnSe, the highest quality low resistance contacts have required the growth of graded semiconductor structures [5] which adds considerably to the complexity of the fabrication process. Some success has however been reported using metallic layers based on high work function metals [4] and this is due to the observation that the Schottky barrier heights for II–VI semiconductors are much more strongly dependent on the metal work function [2]. In order to eliminate fabrication influences, intrinsic barrier heights have been determined for III–V semiconductors, such as GaAs, InP and GaP [6–8], by growing intimate metal contacts under controlled ultrahigh vacuum (UHV) conditions. In each case, a very weak work function dependence has been observed. For GaAs [6], most metals conform to a Fermi level pinning position near mid-gap. For GaP [7], all metal contacts yield barrier heights determined by an intrinsic level near mid-gap and a weak work function dependence. For InP [8], the precise interface chemistry is important, with low n-type barrier heights observed for contacts where interface reactivity leads to the presence of elemental indium [8]. This means that for p-type III–V semiconductors, low resistance contacts can only be made using annealing methods involving the formation of highly doped near-surface layers and/or chemically graded interfaces [4]. In the current study, we have monitored the formation of the intimate ZnSe–metal interface under UHV conditions to provide further insights into the factors affecting the position of the interfacial Fermi level and hence the barrier height. The technique of soft X-ray photoelectron emission spectroscopy (PES) is chosen to provide a parallel probe of the development of the Fermi level and distribution of chemical species as the contact is grown on a known surface in a controlled environment. The structure of the metal contact was further investigated using high resolution transmission electron microscopy (TEM). As part of a wider programme, this initial study reports on three selected metals, Au, Ag and Pb which are chosen to give a range of metal work function, and are expected to be relatively inert, avoiding strong interfacial reactions.

2. Experimental

In order to achieve the high energy resolution and surface sensitivity required in such a study, synchrotron radiation was used to excite photoelectrons from the solid. Photon energies in the range (40–100) eV were used to probe valence band and shallow core level densities of states, and experiments were performed at the surface science beamline 6.2 at the Daresbury Laboratory. Photoelectrons were collected at normal emission in an angle-resolved hemispherical analyser. ZnSe thin films ($\sim 2 \mu\text{m}$, $N_D \sim 10^{16} \text{ cm}^{-3}$) were grown using molecular beam epitaxy (MBE) and capped with Se to protect the surface during transportation to the synchrotron source. The crystal structure of these layers was monitored during growth by reflection high energy electron diffraction (RHEED) and examined after growth using high resolution transmission electron microscopy (HRTEM). The clean ZnSe (001) surfaces were recovered in UHV by thermal desorption of the Se cap and the surface reconstructions were confirmed using low energy electron diffraction (LEED). Metal layers were deposited in stages from W-filament sources at submonolayer level and up to a thickness corresponding to the bulk metal.

Transmission electron microscopy operated at a voltage of 300 kV was used to examine [110] cross-sectional samples. All specimens were prepared by mechanical polishing followed by low energy (4 kV) ion-milling using argon gas. A final ion-milling stage used iodine to reduce the ion-related damage that normally occurs with argon milling of II–VI compounds.

3. Results and discussion

3.1. The ZnSe surface

Due to its technological relevance, the surface chosen for study is the polar (001) surface of the zincblende semiconductor, ZnSe. The surface reconstructions observed by RHEED during MBE growth indicate the dominance of a Se-rich 2×1 surface under conditions of high Se/Zn flux ratio and low surface temperature and a Zn-rich $c(2 \times 2)$ surface under conditions of low Se/Zn flux ratio and high

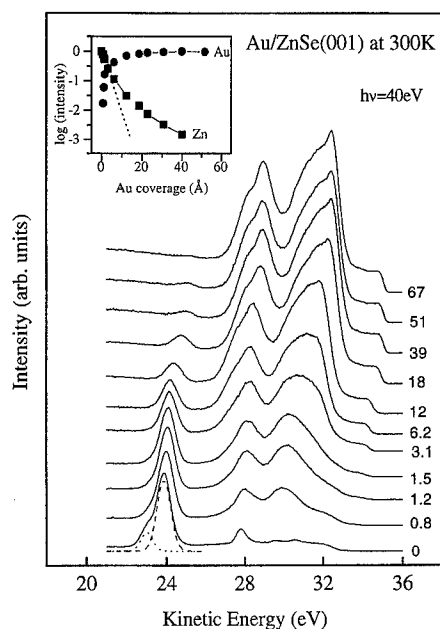


Fig. 1. Photoelectron emission spectra for the ZnSe(001) surface as a function of Au exposure shown at the right hand side in Å. The relative changes in the intensities of the Zn 3d (at KE = 24 eV) and Au 5d (at KE = 27–33 eV) peaks are represented in a semi-logarithmic plot in the inset. The evolving metallic nature of the overlayer above 1.5 Å is accompanied by a broadening of the metal d-bands and the appearance of a Fermi edge. The surface and bulk components are shown for the clean surface Zn peak (bottom).

surface temperature [9,10]. The samples used in the current study were grown under Se-rich conditions leading to high quality 2×1 RHEED patterns [10]. On mounting in the PES analysis chambers, the surface spectra for capped samples showed the absence of a Zn signal and the dominance of a Se 3d split peak at a binding energy (BE) of around +1 eV with respect to Se in ZnSe, in agreement with previously reported data [11]. On heating to 170°C, the Se cap was desorbed and a Zn 3d emission peak appeared. Further annealing to 350°C resulted in a 2×1 LEED pattern, and annealing above this temperature resulted in a more Zn-rich $c(2 \times 2)$ surface.

The clean surface spectra shown at the bottom of Fig. 1 and Fig. 3 are deconvolved into two zinc components corresponding to surface and bulk atoms in the reconstructed ZnSe film. The bulk peak (dashed) appears at a binding energy of -9.2 eV with respect to the valence band maximum (VBM)

in agreement with previous work [12] and the surface peak (dotted) was found to lie at a binding energy of -0.87 eV (Fig. 1) and -0.83 eV (Fig. 3) with respect to the bulk peak. The surface component is particularly clear in the clean surface spectrum in Fig. 1, and the relative magnitude of this component is indicative of a Zn-rich $c(2 \times 2)$ surface. The fitting of these band-like levels involves a higher degree of inaccuracy than the core-like 3d levels in GaAs and this leads to a spread in values for all surfaces studied of (0.8–0.9 eV), where the mean value of 0.84 eV is slightly larger than that reported elsewhere [11]. However, this is believed to reflect the reliability of the fitting procedure rather than the quality of the ZnSe surface.

3.2. Metal overlayer morphology

Changes in the substrate electronic levels as a function of Au coverage at 300 K are illustrated in the series of spectra shown in Fig. 1. The photon energy of 40 eV ensures surface sensitivity and access to the substrate Zn 3d (at kinetic energy (KE) = 24 eV) and overlayer Au 5d levels (at KE = 28–32 eV) as well as the remainder of the valence band. The clean surface spectrum (bottom) is dominated by the Zn 3d peak and the valence band structure is due to direct transitions consistent with the region of the bulk Brillouin zone studied at this energy at normal emission. The valence band maximum can be determined from this data, and by comparison with a reference metal Fermi level, the initial surface Fermi level is found to lie around 2.0 eV above the VBM. As the surface is exposed to Au, the substrate Zn peak is attenuated and the spectrum is dominated by the Au 5d emission intensity.

The surface component (shown dotted for the clean surface) is rapidly attenuated relative to the bulk peak (shown dashed for the clean surface) and is completely absent at a coverage of 1.5 Å. Since this corresponds to a coverage < 1 monolayer (ML), this provides confirmation that the initial surface Zn atom concentration is low and that the surface Zn atoms are covered by the Au film at this point. No further components are required to fit the Zn peak at higher coverage, although the increasing Au d-band emission may obscure small peaks at high kinetic

energy. However, the bulk peak is the dominant component of the Zn 3d emission throughout, confirming the absence of large scale disruption of the ZnSe surface. Although the experimental set-up did not allow access to the Se 3d core levels, similar lineshape changes were observed for the Zn 3d level during Pb exposure [13] and in this case the absence of large chemically shifted components in the Se 3d emission confirms the inert nature of the interface. The intensity of the bulk peak can then be used to monitor the metal film growth mode and the integrated peak areas as a function of Au coverage are illustrated in the inset of Fig. 1 for Zn and Au peaks. The data are plotted semi-logarithmically and the attenuation predicted by a layered growth mode is shown as the broken line. The departure of the Zn 3d attenuation from this line indicates island formation, although the small departure from linearity indicates that strong clustering does not occur.

In order to investigate the final metal layer morphology, samples were retained for study by high-resolution transmission electron microscopy. The cross-sectional image shown in Fig. 2 corresponds to an Au layer grown at room temperature on the ZnSe surface. This gives an insight into the metal film growth and interface diffusion as well as providing an estimate of film thickness. In this high resolution image, the ZnSe (111) planes and Au (002) planes can be resolved and the former are used to determine the distance scale. The coverages given for the PES spectra in Fig. 1 and Fig. 3 are estimated by comparing the total exposure time with the thickness estimated from the HRTEM data. It is clear from the

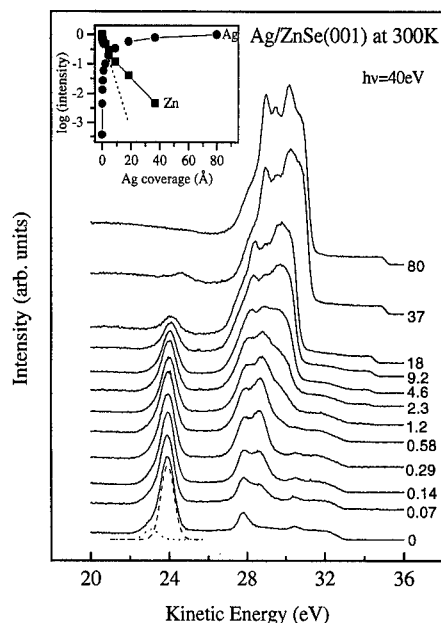


Fig. 3. Photoelectron emission spectra for the ZnSe(001) surface as a function of Ag exposure shown at the right-hand side in Å. The relative changes in the intensities of the Zn 3d (at KE = 24 eV) and Ag 4d (at KE = 26–31 eV) peaks are represented in a semi-logarithmic plot in the inset. The surface Zn component (dotted) is small for the Se-rich surface prior to metal exposure.

cross-sectional image of Fig. 2 that the gold layer does not 'wet' the ZnSe surface and does not appear to have reacted with this surface. This is evidenced by the observation of amorphous material from the surrounding epoxy within the interfacial region. The absence of interface reaction is consistent with the

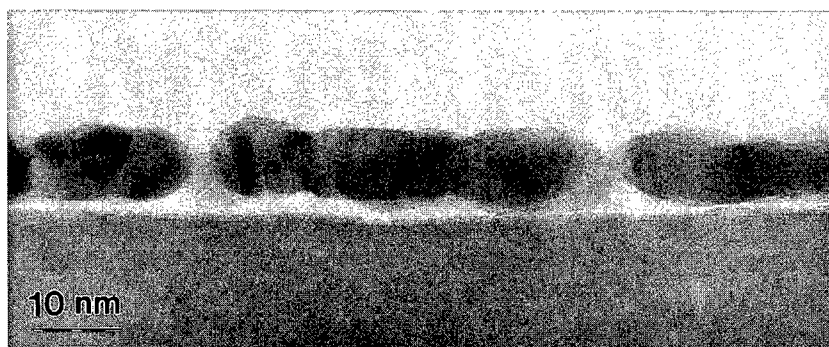


Fig. 2. Cross-sectional transmission electron micrograph of the Au/ZnSe interface grown at 300 K. The polycrystalline metal layer is made up of large, closely-packed irregular islands of approximately equal height. Note the lack of reaction between Au and the ZnSe.

absence of extra components in the Zn emission spectra shown in Fig. 1. From this image and from an oblique view of the same surface (not shown) it can be concluded that the Au film is made up of closely-spaced polycrystalline Au islands of approximately equal height which make up a broken, quasi-uniform film.

The developing metallic character of the Au layer can be monitored by noting the broadening of the d-bands and the onset of emission at the Fermi level as previously reported for uniform Ag films grown on GaAs at 100 K [14]. The broadening of the Au d-bands (Fig. 1) commences at around 1.5 Å coverage and is complete at 6.2 Å coverage. This corresponds to a coverage of 1–2 monolayers, and the point at which the Au intensity reaches its maximum value corresponds to around 4 monolayers. The broadening of the d-bands is accompanied by the appearance of a metallic Fermi edge which is fully established at 6.2 Å.

The combined PES and TEM data thus suggest that the growth of Au on ZnSe (001) is not strongly 3D, in agreement with previous studies of this interface [11,15] and in contrast to Au on GaAs [16] and InP [17] where significant intermixing and metal clustering are observed at RT. The emission of photoelectrons from the Zn 3d and valence levels of ZnSe (001) as a function of Ag coverage is represented in Fig. 3, and the overall development is similar to the growth of Au. The coverages shown were again estimated from the HRTEM images, although the latter were more difficult to obtain due to the even lower cohesion of the Ag film to the ZnSe substrate. In this case, the degree of clustering was however increased with a larger proportion of the surface exposed for a given coverage. The Zn 3d peak for the starting surface shown at the bottom of Fig. 3 has a lower intensity surface component at a binding energy -0.83 eV relative to the bulk peak. This is consistent with the observed 2×1 reconstruction which is Se-rich. Both of these components are attenuated with increasing coverage, but the surface peak is completely attenuated above 2.3 Å coverage whereas the bulk peak persists up to 37 Å. This suggests that although the surface Zn atoms are covered by the thin Ag film, there is evidence for overlayer island formation. As the surface is covered by Ag, no further components are needed to fit the

Zn 3d peak, and this suggests that the substrate is not chemically reacted with Ag. The attenuation of the bulk Zn 3d peak, shown in the inset of Fig. 3, is similar to Au deposition and the departure from linearity is again not pronounced (although somewhat greater than for Au on ZnSe). The growth does not therefore involve the formation of large 3D islands. The inert nature of the Ag/ZnSe interface is confirmed by the undisrupted ZnSe surface and loosely bound Ag film observed by HRTEM. The PES data of Fig. 3 again show the developing metallic character of the metal film, with the onset of high KE broadening of the 4d bands accompanied by the emergence of a Fermi level emission. This occurs between 1.2 and 4.6 Å, and this suggests that a coverage of around 1–2 monolayers marks the onset of metallicity. Above 9.2 Å coverage, the emission spectrum is representative of bulk Ag, with a well-defined metallic edge at the Fermi level. Ag layers are thus morphologically similar to Au layers grown under the same conditions, although the degree of metal clustering for this inert interface is larger.

The Pb/ZnSe(001) interface is also unreactive as inferred from the absence of dominant extra components in the Zn 3d and Se 3d spectra [13]. However, the metal layer is more clustered than both Au and Ag in this case.

3.3. Schottky barriers on ZnSe (001)

The Schottky barrier height for the Au/ZnSe(001) contact can be determined from the initial pinning position and the band bending during metal contact formation. The change in relative position of the surface Fermi level with respect to the band edges is shown in Fig. 4 for Au and Ag contacts. This band bending is inferred from the bulk Zn 3d data of Fig. 1 and Fig. 3, and it appears that the Fermi level is fixed close to the pinned surface position up to a coverage of 6 Å for Au and 18 Å for Ag.

Above these coverages, the Fermi level moves towards the VBM, which results in a different final pinning position, and hence Schottky barrier height, for Au and Ag. Such a step-like behaviour for metals on III–V semiconductors has been interpreted in terms of a coverage-dependent Fermi level pinning position [18], but an alternative explanation in terms of surface charging [19] is believed to be valid in this

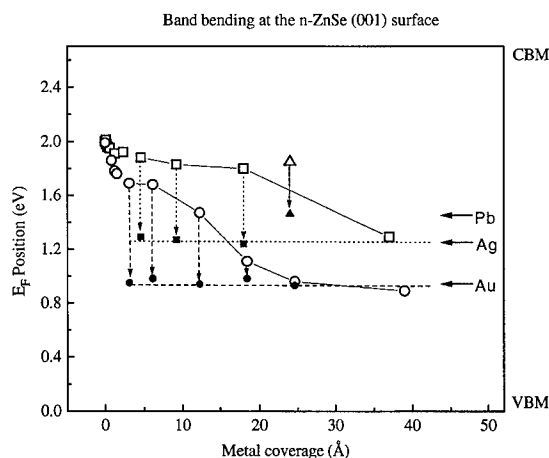


Fig. 4. Movement of the surface Fermi level with respect to the band edges as a function of metal coverage at 300 K. Au (circles) and Ag (squares) data are subject to a surface photovoltage (SPV) which breaks down above 6 Å coverage for Au and 18 Å for Ag, where the metal layer is fully formed. SPV corrections are shown as solid symbols, and the final barrier heights are indicated by the arrows (see Table 1 for values). Data for a Pb coverage of 24 Å (triangles) are also shown.

case. The photocurrent generated in the emission process can lead to the accumulation of charge at the surface, which results in a surface photovoltage (SPV). The magnitude of this SPV is determined by the efficiency of the charge flow from the semiconductor bulk to the surface to compensate the surface charging. At low doping levels ($< 10^{18} \text{ cm}^{-3}$), this compensating current is due to thermionic emission over the surface barrier which is reduced at high barriers and low temperatures [19]. In the absence of a SPV, the Fermi level at the clean surface ZnSe has been reported to lie within the band gap at VBM + 1.45 eV [11]. This implies that the ZnSe surfaces in the current study are subject to surface charging although this is not sufficient to produce completely flat bands. Under the present conditions, a surface voltage of around 0.55 V is implied, and this value is in agreement with Chen et al. [11]. Flat band conditions for low coverages of metals on GaAs [19] are observed only at reduced temperatures, and so the partial unpinning at RT for ZnSe is a consequence of the larger barrier heights in this case. The SPV effect has however been observed at RT for the larger band gap semiconductor, GaP [20]. The step-like change

in Fermi level position is a commonly observed phenomenon, especially in metals on III–V's [19,20], and is a consequence of the breakdown of surface charging by conduction through the metal film [20]. This requires a relatively uniform metal film to provide the parallel leakage path and, above 6 Å coverage, the conductivity of the gold film is sufficient to remove the surface charging. This is consistent with the absence of large 3D islands inferred from the peak intensity analysis. The situation is somewhat different for Ag which requires a higher exposure after the onset of metallicity to provide a parallel leakage path. This reflects the increased island separation in this case. For Pb layers [13], the stronger clustering results in a persistence of the SPV at higher coverages since the metal film is even less uniform and conducting in the surface plane. At Au and Ag coverages above 3 Å, a metal Fermi level can be measured even though the conductivity is too low to compensate the surface charging. This Fermi level position is shifted from the equilibrium reference Fermi level by an amount equal to the SPV, and hence the band bending can be corrected for SPV in this range. Corrected values are shown as solid symbols in Fig. 4, and it is seen that the step-like behaviour is removed. Therefore, the final pinning position for Au and Ag are attained for coverages above 3 Å, and these values are used to derive the n-type barrier heights given in Table 1. Also shown in Fig. 4 and Table 1 is the value for the Pb contact corrected for SPV. The value for Au, $\Phi_{\text{BN}}(\text{Au}) = 1.74 \pm 0.12 \text{ eV}$, was obtained even where the initial surface composition corresponded to a different reconstruction (more Se-rich). Since the Se 3d core level could not be accessed the error in this barrier height determination is large. However, these measurements were consistent during repetition of experiments and the likely errors do not affect the observed trend in values for the three metals. For Pb layers, where the Se 3d levels were accessible, the

Table 1

Metal	Work function (eV)	Schottky barrier (eV)
Au	5.10	1.74
Ag	4.41	1.47
Pb	4.25	1.25

Zn and Se levels showed a similar shift of the bulk peaks [13].

The barrier height for the Au/ZnSe interface has been studied by several groups using a range of techniques under various conditions. Previous PES measurements, under similar conditions [11], report a lower value of 1.55 eV for n-ZnSe; *I*–*V* and *C*–*V* measurements on etched samples give values of 1.67 eV [21] and around 1.5 eV [2]. These values are consistently lower than the present value, although the error margins for such measurements from photoemission data are large. Also, measurements on etched surfaces using ballistic electron emission spectroscopy [21] has revealed a range of barrier heights from 1.53 eV to 2.15 eV. It therefore appears that although the barrier height for Au/ZnSe appears to be linked to the metal work function, and is higher than that for the other metals, the precise fabrication method can lead to a small but significant variation in this value. The corrected Schottky barrier height for the Ag contact in the present study, $\Phi_{\text{BN}}(\text{Ag}) = 1.47 \pm 0.12$ eV, is also insensitive to the starting composition of the surface. The barrier height is again larger than that measured on etched surfaces by electrical methods [2]. Data for the formation of Schottky contacts to II–VI semiconductors is more limited than for III–V semiconductors and early studies [2] suggested a dependence on metal work function for these materials. Although the values measured here for Au and Ag are larger than the *I*–*V* values [2], the difference between the two metals is similar (~ 0.3 eV). Since the two interfaces are morphologically similar, it appears that the barrier height increases with work function for these two metals (Table 1). For metal contacts grown under controlled UHV conditions on III–V semiconductors, the low coverage values measured by PES agree with the *I*–*V* values, although for GaP [7], the n-type values measured by PES are consistently higher. However, unlike ZnSe, the barrier heights are insensitive to metal work function. The trend for Au and Ag on ZnSe appears to extend to the other unreactive metal Pb, where the lower work function metal yields a lower barrier height (Table 1), and also to the reactive metal, Al [11]. However, these values do not scale exactly with work function. In addition, as previously discussed, a wide range of values have been reported for Au/ZnSe by different

techniques suggesting that preparation-induced factors can influence the barrier height. For other II–VI materials such as CdTe [22], it has been reported that the surface stoichiometry has a large influence on the barrier height and that the observed values are determined by Fermi level pinning due to semiconductor defect levels. It has been reported in a study of the Sb–ZnSe [23] interface using chemically etched surfaces that the barrier height can be strongly influenced by surface preparation, and a study of the Au interface using PES [11] has also illustrated the influence of significant amounts (several ML) of elemental Se at the interface. However, the latter has been interpreted in terms of the electronegativity of the Se interlayer rather than the generation of semiconductor defect states. It thus appears that for metals on the untreated surface, the Schottky barrier heights show a clear work function dependence, although surface modification can induce changes in these values. Further studies are therefore needed to determine the overall behaviour of metal contacts on the clean surface and to understand the factors influencing changes in barrier heights for different surface preparation.

4. Conclusion

In conclusion, the growth and Schottky barrier heights for Au, Ag and Pb contacts to the ZnSe(001) surface have been investigated at room temperature using photoelectron emission spectroscopy and transmission electron microscopy. All three interfaces are chemically abrupt and, for Au and Ag, the metal islands are of uniform height and closely packed. The data are influenced by a surface photovoltage, and the corrected Schottky barrier heights are significantly different for each metal. The highest n-type barrier height is measured for the highest work function metal, Au.

Acknowledgements

This work was in part facilitated by the EU-HCM network, Chalcogen Modification of Semiconductor Interfaces, and one of us (D.A.E) would also like to acknowledge the support of the Nuffield Foundation.

The EPSRC are also thanked for the provision of access to the Synchrotron Radiation Source at the Daresbury Laboratory.

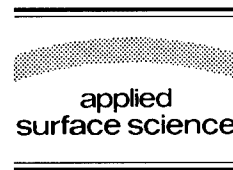
References

- [1] J. Qiu, H. Cheng, J.M. DePuydt and M.A. Haase, *J. Cryst. Growth* 127 (1993) 279.
- [2] R.K. Swank, M. Aven and J.Z. Devine, *J. Appl. Phys.* 40 (1969) 89.
- [3] J. Han, Y. Fan, M.D. Ringle, L. He, D.C. Grillo, R.L. Gunshor, G.C. Hua and N. Otsuka, *J. Cryst. Growth* 138 (1994) 464.
- [4] A.G. Milnes and D.L. Feucht, *Heterojunctions and Metal–Semiconductor Junctions* (Academic Press, New York, 1972).
- [5] Y. Lansari, J. Ren, B. Sneed, K.A. Bowers, J.W. Cook, Jr. and J.F. Schetzina, *Appl. Phys. Lett.* 61 (1992) 2554.
- [6] A.B. Maclean and R.H. Williams, *J. Phys. C: Solid State Phys.* 21 (1988) 783.
- [7] M. von der Emde, D.R.T. Zahn, Ch. Schultz, D.A. Evans and K. Horn, *Appl. Surf. Sci.* 70/71 (1993) 507.
- [8] N. Newman, M. van Schilfgaarde and W.E. Spicer, *Phys. Rev. B* 35 (1987) 6298; D.A. Evans, T.P. Chen, Th. Chasse, K. Horn, M. von der Emde and D.R.T. Zahn, *Surf. Sci.* 269/270 (1992) 979.
- [9] J.M. DePuydt, H. Cheng, J.E. Potts, T.L. Smith and S.K. Mohapatra, *J. Appl. Phys.* 62 (1987) 4756.
- [10] J. Riley, D. Wolfframm, D. Westwood and D.A. Evans, in press.
- [11] W. Chen, A. Kahn, P. Soukiassian, P.S. Mangat, J. Gaines, C. Ponzoni and D. Olego, *J. Vac. Sci. Technol. B* 12 (1994) 2639.
- [12] A. Ebina, T. Unno, Y. Suda, H. Koinuma and T. Takahashi, *J. Vac. Sci. Technol.* 19 (1981) 301.
- [13] D. Wolfframm, D. Gnoth, D. Westwood, M. Evans, A.C. Wright and D.A. Evans, to be published.
- [14] D.A. Evans and K. Horn, *J. Electron Spectrosc. Rel. Phen.* 62 (1993) 59.
- [15] M. Vos, F. Xu, S.G. Anderson, J.H. Weaver and H. Cheng, *Phys. Rev. B* 39 (1989) 10744.
- [16] R.M. Feenstra, *J. Vac. Sci. Technol. B* 7 (1989) 925; W.E. Spicer, N. Newman, T. Kendelewicz, W.G. Petro, M.D. Williams, C.E. McCants and I. Lindau, *J. Vac. Sci. Technol. B* 3 (1985) 11778.
- [17] G.D. Waddill, C.M. Aldao, I.M. Vitomirov, Y. Gao and J.H. Weaver, *J. Vac. Sci. Technol. A* 7 (1989) 865; R. Ludeke, T.-C. Chiang and T. Miller, *J. Vac. Sci. Technol. B* 1 (1983) 581.
- [18] C.M. Aldao, I.M. Vitomirov, G.D. Waddill, S.G. Anderson and J.H. Weaver, *Phys. Rev. B* 41 (1990) 2800.
- [19] M. Alonso, R. Cimino and K. Horn, *Phys. Rev. Lett.* 64 (1990) 1947; M. Hecht, *Phys. Rev. B* 41 (1990) 7918.
- [20] D.A. Evans, T.P. Chen, T. Chasse and K. Horn, *Appl. Surf. Sci.* 56–58 (1992) 233.
- [21] R. Cortager, F. Ajustron, J. Beauvillain, I.M. Dharmadasa, C.J. Bloomfield, K.A. Prior, J. Simpson and B.C. Cavenett, *Phys. Rev. B* 51 (1995) 2357.
- [22] I.M. Dharmadasa, J.M. Thornton and R.H. Williams, *Appl. Phys. Lett.* 54 (1989) 137.
- [23] I.M. Dharmadasa, C.J. Bloomfield, G.E. Gregory, B.C. Cavenett, K.A. Prior and J. Simpson, *Surf. Interf. Anal.* 21 (1994) 718.



ELSEVIER

Applied Surface Science 104/105 (1996) 248–252



Metal–insulator transition for K on GaAs(100) –As rich surfaces

A. Levy Yeyati, A. Martín-Rodero, F. Flores^{*}, J. Ortega, R. Rincón

Departamento de Física de la Materia Condensada C-XII, Facultad de Ciencias, Universidad Autónoma de Madrid, E-28049 Madrid, Spain

Received 28 June 1995; accepted 1 September 1995

Abstract

Recent LD-LCAO (local density-linear combination of atomic orbitals) calculations show that atoms deposited on the As-rich GaAs(100)- 2×4 reconstructed surface tend to form quasi one-dimensional structures along the missing rows of the semiconductor surface. We show that the ‘conduction’ band associated with the K-orbitals may be described by an effective extended Hubbard Hamiltonian. Using Green functions techniques we study the metal–insulator transition within this model, which allows us to establish the metallic or insulating character of a given one-dimensional structure. We find that the transition into the metallic phase takes place when going from $5/8$ to $7/8$ monolayers.

PACS: 68.35.Bs; 73.20.-r; 73.30.+y

1. Introduction

The metal–semiconductor interface formation and its properties are intimately related to the chemical bonds formed between the metal adatoms and the semiconductor surface. A great deal of the research in this area has been performed for the deposition of alkali atoms on GaAs(110), a system where the interplay between the experimental and theoretical information is enhanced due to the low reactivity of the interface and the simplicity of growth of the metal layer. In these interfaces the alkali atoms interact mainly with Ga-dangling bonds of the semiconductor surface, forming 1D and 2D structures that exhibit an insulating behavior in the low coverage regime [1]. For larger depositions, around 1 ML, a Mott metal–insulating transition appears [2]; then,

the Fermi level is pinned by the metallic density of states induced around the semiconductor charge neutrality level [3].

Metal–GaAs(100) interfaces have not been analyzed so thoroughly as the previously mentioned cases [4], the main reason being the complication introduced by the geometry of the GaAs(100) surface. In a recent work [5], we have analyzed the K/GaAs(100) interface formation, taking the As-rich GaAs(100)- 2×4 surface reconstruction with three As-dimers [6] as our prototype system. In that work, the geometrical and electronic properties of the K–GaAs(100) interface have been analyzed using a selfconsistent LD-LCAO method [7,8], and considering different metal coverages up to 1 ML. It was found that the alkali atoms interact strongly with the Ga-dangling bonds of the semiconductor second layer and form quasi 1D chains along the missing rows of the semiconductor surface. For the specific recon-

^{*} Corresponding author.

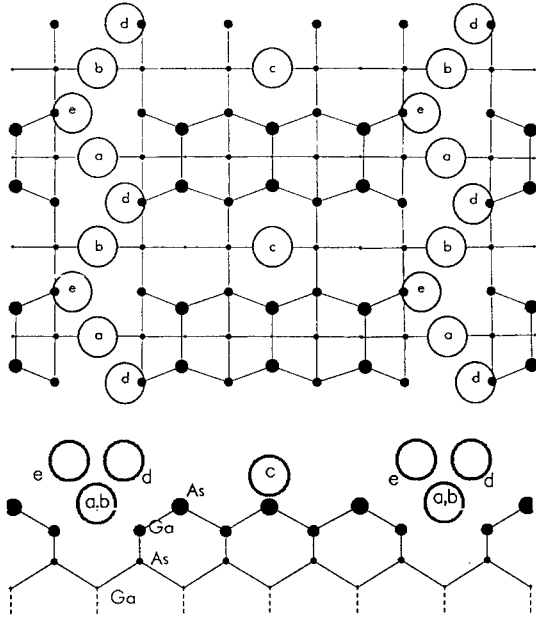


Fig. 1. Surface geometry (top and side view) for an unrelaxed As-rich GaAs(100) 2×4 reconstruction. Different sites of adsorption for progressive deposition of K-atoms are shown by labels (a), (b), (c) and (d) and (e). Notice that atoms (d) and (e) form a 1D chain along the missing rows.

struction we have analyzed, we also find an isolated K-atom linking the 1D chains.

Fig. 1 shows the geometry of deposition that we have obtained for a K-coverage of $\theta = 5/8$. The K-atoms located on the (a) and (b) sites form strong bonds with the Ga-dangling bonds, giving rise to two new occupied bands filled by 4 electrons. Then, we find a 'conduction' band (around 0.5 eV wide) associated with the atoms (d) and (e) having a $1/4$ occupancy (1 electron per unit cell). Increasing the alkali metal coverage completes the formation of the 1D structures along the missing rows. On the other hand, for a larger coverage of $\theta = 7/8$, the additional K-atoms are placed besides sites (d) and (e) thus forming a double chain along the missing rows. The conduction band associated with these double chains is filled up to $3/8$.

2. Effective Hamiltonian for the K-1D structures

In this paper, our aim is addressed to understanding the metallic properties associated with the quasi

linear chains created by the K-deposition on the GaAs(100) surface. We have analyzed these quasi-1D chains by means of the following Hamiltonian:

$$\hat{H} = \sum_{\alpha, \sigma} E_{\alpha} \hat{n}_{\alpha \sigma} + \sum_{\alpha, \sigma} t (c_{\alpha \sigma}^{\dagger} c_{\alpha+1 \sigma} + c_{\alpha+1 \sigma}^{\dagger} c_{\alpha \sigma}) + \sum_{\alpha} U \hat{n}_{\alpha \uparrow} \hat{n}_{\alpha \downarrow} + \frac{1}{2} \sum_{\alpha \neq \beta, \sigma \sigma'} J_{\alpha \beta} \hat{n}_{\alpha \sigma} \hat{n}_{\beta \sigma'}, \quad (1)$$

where α and β refer to the Wannier-wavefunctions associated with the K-atoms forming the conduction band having a one-quarter band-filling; E_{α} is the energy level of each Wannier functions that, in our calculations appear as practically equivalent; t is the effective hopping between nearest neighbors that gives rise to a band-width of 0.5 eV ($t \approx 0.12$ eV); and U and $J_{\alpha \beta}$ are the intrasite and the intersite Coulomb interactions. In our calculations, using the Wannier functions of Hamiltonian (1), we have obtained $U = 3.4$ eV and $J_{i, i+1} = 2.6$ eV (this is the interaction between nearest neighbors); the intersite Coulomb interaction $J_{i, i+n}$ for $n > 1$ is close to $e^2/(\epsilon_1 d_{i, i+n})$, where $d_{i, i+n}$ is the distance between sites i and $i+n$ and ϵ_1 an effective interface dielectric constant ($\epsilon_1 \approx 5$).

It is important to notice that in our model Hamiltonian (1), we have introduced the off-diagonal Coulomb interactions $J_{\alpha \beta}$; this is essential to describe the metal–insulator transition. It is well known that the simplest 1D-Hubbard model, with $J_{\alpha \beta} = 0$, does not exhibit a Mott transition at a one-quarter band filling.

We show below that in order to analyze the metal–insulator transition for a one-quarter band filling, we can replace the complete Hamiltonian (1) by an effective short-range one:

$$\hat{H}^{\text{eff}} = \sum_{\alpha, \sigma} E_{\alpha} \hat{n}_{\alpha \sigma} + \sum_{\alpha, \sigma} t (c_{\alpha \sigma}^{\dagger} c_{\alpha+1 \sigma} + c_{\alpha+1 \sigma}^{\dagger} c_{\alpha \sigma}) + \sum_{\alpha} U^{\text{eff}} \hat{n}_{\alpha \uparrow} \hat{n}_{\alpha \downarrow} + \sum_{\alpha, \sigma, \sigma'} J^{\text{eff}} \hat{n}_{\alpha \sigma} \hat{n}_{\alpha+1 \sigma'}, \quad (2)$$

where U^{eff} defines an effective intrasite Coulomb interaction and J^{eff} the one corresponding only to nearest-neighbor sites.

The first point to notice is that we expect the insulating phase for a one-quarter band filling to show an electron localized every two K-sites. Then, we can establish the equivalence between Hamiltoni-

ans (1) and (2), by imposing that any kind of charge fluctuations between nearest-neighbor sites yield the same solution for both cases. This has been achieved by considering the local density solution presented in Ref. [8] for LCAO-Hamiltonians.

In this regard, notice that the many-body terms of Hamiltonian (1) and (2), $U\hat{n}_{\uparrow}\hat{n}_{\downarrow} + \sum J\hat{n}_{\alpha\sigma}\hat{n}_{\alpha'\sigma'}$, can be replaced in the LD-approximation we are considering by the following local potential:

$$V^{\text{mb}}(n_{\alpha\uparrow}) = Un_{\alpha\downarrow} + \sum_{\beta} J_{\alpha\beta} n_{\beta} + V^{\text{xc}}(n_{\alpha\uparrow}), \quad (3)$$

where $V^{\text{xc}}(n_{\alpha\uparrow})$ can be taken as:

$$V^{\text{xc}}(n_{\alpha\uparrow}) = -J_{\alpha,\alpha+1}\left(\frac{1}{2} - n_{\alpha\uparrow}\right). \quad (4)$$

Eq. (4) is defined using the equation $V^{\text{xc}}(n_{\alpha\uparrow}) = \partial E^{\text{xc}}(n_{\alpha\uparrow}) / \partial n_{\alpha\uparrow}$ and $E^{\text{xc}}(n_{\alpha\uparrow}) = -\frac{1}{2}J_{\alpha,\alpha+1}n_{\alpha\uparrow}(1 - n_{\alpha\uparrow})$. This exchange–correlation energy represents the interaction between the charge $n_{\alpha\uparrow}$ and its hole, $1 - n_{\alpha\uparrow}$, that is assumed to be localized in the nearest-neighbor sites. For Hamiltonian (1)

$$V_1^{\text{mb}}(n_{\alpha\uparrow}) = Un_{\alpha\downarrow} + \sum_{\beta} J_{\alpha\beta} n_{\beta} - J_{\alpha,\alpha+1}\left(\frac{1}{2} - n_{\alpha\uparrow}\right), \quad (5)$$

while for Hamiltonian (2)

$$V_2^{\text{mb}}(n_{\alpha\uparrow}) = U^{\text{eff}}n_{\alpha\downarrow} + J^{\text{eff}}(n_{\alpha+1} + n_{\alpha}) - J^{\text{eff}}\left(\frac{1}{2} - n_{\alpha\uparrow}\right). \quad (6)$$

The equivalence between the LD-solutions of both Hamiltonians is established by considering charge fluctuations such that

$$n_{\alpha} + n_{\alpha+1} = \frac{1}{2}, \quad (7)$$

or equivalently

$$n_{\alpha\uparrow} = \frac{1}{2} - n_{\alpha\downarrow} - n_{\alpha+1}. \quad (8)$$

Eqs. (5) and (6) yield the following condition for the equivalence between the solutions of Hamiltonians (1) and (2):

$$(U - J_{\alpha,\alpha+1})n_{\alpha\downarrow} + \left[\sum_{\beta} J_{\alpha\beta} n_{\beta} - J_{\alpha,\alpha+1}n_{\alpha+1} \right] = (U^{\text{eff}} - J^{\text{eff}})n_{\alpha\downarrow} + [J^{\text{eff}}n_{\alpha+1}], \quad (9)$$

then

$$U - J_{\alpha,\alpha+1} = U^{\text{eff}} - J^{\text{eff}}, \quad (10)$$

$$\gamma J_{\alpha,\alpha+1} = J^{\text{eff}}, \quad (11)$$

where $(1 + \gamma)J_{\alpha,\alpha+1} = \sum_{\beta} J_{\alpha\beta} n_{\beta}$ defines for $n_{\alpha} + n_{\alpha+1} = 0$ the Madelung potential crated on the α -site.

Using for U and J the values given above, we obtain the effective Hamiltonian (2) with $U^{\text{eff}} \simeq 1.19$ eV and $J^{\text{eff}} \simeq 0.39$ eV.

3. Analysis of the metal–insulator transition

The extended Hubbard model (Eq. (2)) at quarter filling is known to exhibit a metal–insulator transition for sufficiently large interatomic Coulomb interaction J^{eff} (for the following discussion we shall omit the superscript ‘eff’ in U and J). This transition has been analyzed by means of small cluster diagonalization in Ref. [9], which predicts a critical J value of $2t$ almost independent of U (provided that $U \gg t$).

In order to analyze the transition with more detail we have used a Green functions approach based on the introduction of an appropriate self-energy for describing correlation effects in Hamiltonian (2). In our solution, we allow for charge transfer between nearest-neighbors, with the condition $n_i + n_{i+1} = \frac{1}{2}$. As $U \gg J$ for the relevant parameter range we are interested in, the effect of the interatomic Coulomb repulsion is included within a mean field approximation, while the correlation effects associated with the intraatomic repulsion are included in a local self-energy.

This self-energy is calculated as follows: first, we evaluate the second-order proper self-energy diagram, $\Sigma_{ii}^{(2)}(\omega)$, given by

$$\Sigma_{ii}^{(2)}(\omega) = U^2 \int_{-\infty}^{\infty} d\omega_1 \int_{-\infty}^{\infty} d\omega_2 G_{ii}^{(0)}(\omega - \omega_1) \times G_{ii}^{(0)}(\omega_1 + \omega_2) G_{ii}^{(0)}(\omega_2). \quad (12)$$

In this diagram the one-electron propagators, $G_{ii}^{(0)}(\omega)$, are determined in a self-consistent way following a procedure introduced in Ref. [10] to study the metal–insulator transition in the half-filled

Hubbard model. In this procedure $G_{ii}^{(0)}(\omega)$ is calculated from

$$\frac{1}{G_{ii}^{(0)}(\omega)} = \frac{1}{G_{ii}(\omega)} + \Sigma_{ii}^{(2)}(\omega), \quad (13)$$

where $G_{ii}(\omega)$ is the completely dressed one-electron propagator given by

$$G_{ii}(\omega) = \int d\omega' \frac{\rho_i(\omega')}{\omega - \epsilon_i - \Sigma_{ii}^{(2)}(\omega) - \omega'}, \quad (14)$$

ρ_i being the noninteracting local density of states and ϵ_i is the mean field local level.

In the half-filled case the second-order self-energy is known to describe correctly both the $U \rightarrow 0$ and $U \rightarrow \infty$ limits providing an adequate approximation for the intermediate region [11]. However, for the case of a partially filled band the second-order self-energy does not yield the correct $U \rightarrow \infty$ limit. This failure can be corrected using an interpolative scheme as described in Refs. [11,12], in which $\Sigma_{ii}^{(2)}$ is replaced by

$$\Sigma_{ii}(\omega) = \frac{\Sigma_{ii}^{(2)}(\omega)}{1 - \alpha \Sigma_{ii}^{(2)}(\omega)}, \quad (15)$$

with

$$\alpha = \frac{(1 - n_i/2)U - \Sigma_{ii}(\mu)}{n_i/2(1 - n_i/2)U^2}.$$

The metal–insulator transition that takes place for increasing values of J is illustrated in Fig. 2 where the spectral density is plotted for a fixed value of U ($U = 9t$, which is close to the value estimated in section II) and three different values of J around the transition. As can be observed, when approaching the transition, the metallic phase is characterized by the appearance of a Kondo-like resonance around the Fermi energy. The transition is signaled by the weight of this resonance going to zero together with the opening of an energy gap of width $\sim J$. We obtain a critical value $J \sim 2t$ in agreement with the small cluster results [9].

4. Conclusions

We therefore conclude that for the parameters estimated above for the 5K-atom case (which corre-

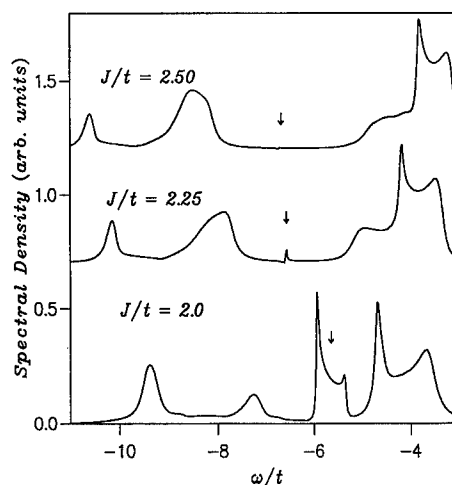


Fig. 2. Spectral density for the effective extended Hubbard model at quarter filling describing the K-1D chains. Results for three values of J around the metal–insulator transition are shown. The arrows indicate the position of the Fermi energy.

spond to $J = 3t$), the system is clearly on the insulating phase. On the other hand, when increasing the metal deposition we expect the transition into the metallic phase to take place. The reason for this is twofold: on the one hand there is an increase in the effective band-width due to the larger coordination number (for a coverage of $7/8$ monolayers the K atoms form double chains along the missing rows of the (100) surface [5]); on the other hand for a band filling larger than $1/4$ the charge density wave phase becomes energetically unfavorable.

In conclusion we have presented a theoretical study for K deposited on the Ga–As (100) surface which suggests the appearance of a metal–insulator transition for coverages between $5/8$ and $7/8$ monolayers.

References

- [1] W.E. Spicer, Appl. Surf. Sci. 41/42 (1989) 1; M. Prietsch et al., Phys. Rev. Lett. 60 (1988) 436; L.J. Whitman et al., Phys. Rev. Lett. 66 (1991) 1338.
- [2] N.J. DiNardo et al., Phys. Rev. Lett. 64 (1990) 2177; O. Pankratov et al., Phys. Rev. Lett. 70 (1993) 351; F. Flores et al., Phys. Low-Dim. Struct. 1 (1994) 23.
- [3] F. Flores and C. Tejedor, J. Phys. C 20 (1987) 145; J. Tersoff, Phys. Rev. Lett. 52 (1984) 465.

- [4] D. Mao et al., Phys. Rev. B 45 (1992) 1273; R.E. Viturro et al., J. Vac. Sci. Technol. B 7 (1989) 1007; C.J. Spindt et al., J. Vac. Sci. Technol. B 9 (1991) 2090; S.P. Wilks et al., J. Vac. Sci. Technol. B 9 (1991) 2118.
- [5] R. Rincón et al., Phys. Rev. B 52 (1995) 16345.
- [6] D.J. Chadi, J. Vac. Sci. Technol. A 5 (1987) 834.
- [7] F.J. García-Vidal et al., Phys. Rev. B 44 (1991) 11412.
- [8] F.J. García-Vidal et al., Phys. Rev. B 50 (1994) 10537.
- [9] F. Mila and X. Zotos, Europhys. Lett. 24 (1993) 133.
- [10] M. Rozemberg et al., Phys. Rev. Lett. 69 (1992) 1236.
- [11] A. Martín-Rodero et al., Solid State Commun. 44 (1982) 911.
- [12] A. Levy Yeyati et al., Phys. Rev. Lett. 71 (1993) 2991.

Quantitative analysis of degradation in Schottky diode characteristics induced by single ion implantation

M. Koyama^{a,c}, Y. Akita^a, C. Cheong^a, M. Koh^a, T. Matsukawa^a, K. Horita^a,
B. Shigeta^a, I. Ohdomari^{a,b,*}

^a School of Science and Engineering, Waseda University, 3-4-1 Ohkubo, Shinjuku-ku, Tokyo 169, Japan

^b Kagami Memorial Laboratory for Materials Science and Technology, Waseda University, 2-8-26 Nishiwaseda, Shinjuku-ku, Tokyo 169, Japan

^c ULSI Research Laboratory, Toshiba Corporation, Komukai Toshiba-cho, Saiwai-ku, Kawasaki 210, Japan

Received 28 June 1995; accepted 14 November 1995

Abstract

In order to characterize the isolated defect clusters in Si crystal induced by single ion implantation (SII), a quantitative analysis of forward I – V characteristics of ion irradiated Schottky diodes was performed. A very good linearity was found between the number of single ions and the number of recombination centers. By a careful choice of SII condition, in order to get a linear response of a device function to the single ion dose, this quantitative analysis could be applied to the test of device immunity against ion irradiation and to the diagnosis of the process integrity.

1. Introduction

As the size of semiconductor devices is reduced to less than 0.1 μm , fluctuation in the number of dopant atoms will seriously affect the device characteristics. In order to suppress the fluctuation, we are developing a novel ion implantation technique designated as ‘single ion implantation (SII)’ [1]. Since, in the SII technology, we implant dopant ions one by one, the interval of single ion incidence in target materials is much longer than the conventional ion implantation and the crystal defects after SII would be much less in number and smaller in size than the ones after the conventional ion implantation. Hence

the track of each ion would be isolated and the isolated defect clusters must be formed. For the electrical activation of implanted single ions heat treatment is essential, but the behavior of these ‘isolated defect clusters’ after the SII is not known yet.

It is expected that the isolated defect clusters would act as recombination centers for carriers and may affect the carrier lifetime in target materials [2]. The change in minority carrier lifetime in semiconductor substrate would change the I – V characteristics of Schottky diodes (SD’s), because the generation–recombination current is directly affected by the carrier lifetime. In this work, as a probe to detect a small number of isolated defect clusters, we have analyzed I – V characteristics of SD’s implanted with MeV He single ions and clarified a relationship

* Corresponding author.

between the exact number of implanted single ions and the amount of isolated defect clusters.

2. Experimental

The experimental procedure consists of three steps: (1) Schottky diodes (SD's) fabrication; (2) MeV He single ion irradiation and in-situ I – V measurement of SD's; (3) curve fitting of the measured I – V data. In order to fabricate SD's, we have used a thermally oxidized n-type Si(100) wafer with circular openings of 50 μm in diameter. The sample was degreased and etched in diluted HF solution for a few seconds to remove the native oxide on the specimens. After short rinsing in deionized water and brown drying with air, the sample was immediately placed into an UHV evaporation chamber for metal deposition. Platinum thin films were deposited to a thickness of 300 nm through the metal mask to define circular spots with a diameter of 800 μm over the oxide openings under a working pressure of 10^{-7} Torr. The wafer was then annealed in a N_2 ambient at 400°C to form PtSi.

In order to find a quantitative relationship between the number of implanted single ions and the amount of isolated defect clusters, it is important to implant a well defined number of ions into a well defined Schottky junction. For the precise control of the number of implanted ions, we took full advantage of the single ion microprobe (SIMP) at Waseda university [3] which enabled us to implant He single ions one by one until the necessary number was reached. For the high precision aiming of the defined area to be hit by the ions, the single ion beam induced charge (SIBIC) imaging [4] was used. The SIBIC imaging method which is based on the two-dimensional mapping of collected charges induced by single ion irradiation uses inherently non-destructive only a few ions per pixel. A typical SIBIC image of the SD is shown in Fig. 1. 2 MeV He single ions were irradiated to the SD's at ion doses ranging from 10^2 to 10^5 ions. During ion irradiation and I – V measurement the sample temperature was kept at room temperature.

After ion irradiation we have quantitatively analyzed the I – V characteristics by the curve fitting. In the curve fitting we assumed that the forward current

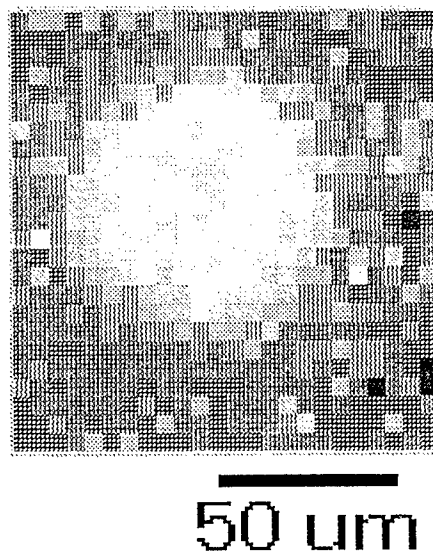


Fig. 1. A typical SIBIC image of a PtSi/n-Si Schottky diode. The scanned area is $120 \times 120 \mu\text{m}^2$ and the diameter of the diode is 50 μm . The bright area in this image corresponds to the SD depletion region.

of a SD consists of two components: thermionic emission current and recombination current [5]. In fitting a theoretical I – V curve to an experimental one, the program finds by iteration a set of three parameters of real barrier height (ϕ_{b0}), recombination current density (J_{r0}), and series resistance (R_s).

3. Results and discussions

Fig. 2 shows I – V characteristics of an SD with a diameter of 50 μm irradiated with 1.2×10^5 He single ions. After ion irradiation, the current increased for both the reverse and the forward characteristics. This result clearly shows that ion irradiation induced defect clusters in which a number of generation–recombination centers are accommodated. In order to perform a quantitative analysis of the results, the curve fitting was carried out for the forward characteristics of the SD's. The set of parameters determined by the curve fitting is summarized in Table 1. The reproducibility of the real Schottky barrier height is excellent.

In order to estimate the number of recombination centers in the SD induced by single ion irradiation

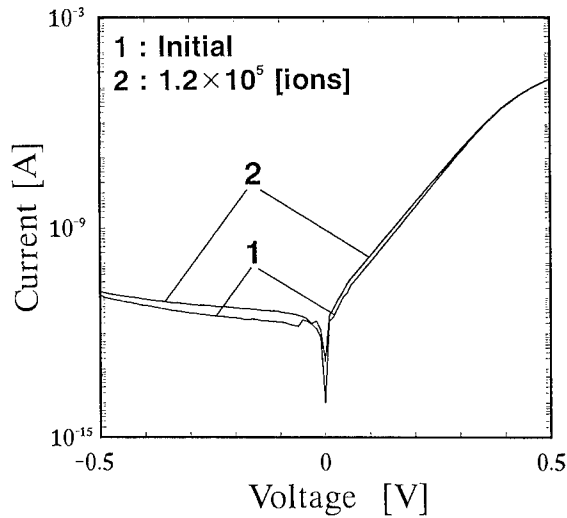


Fig. 2. The I - V characteristics of a PtSi/n-Si Schottky diode before and after ion irradiation. He single ions were irradiated at an acceleration energy of 2 MeV to a dose of 1.2×10^5 ions.

on the basis of the experimental results and the curve fitting, we derive the relation between the recombination center density (N_r) and the recombination current density (J_{ro}). The recombination current (J_r) of forward biased SD's can be written approximately as [6]

$$J_r = J_{ro} \exp(qV/2kT) \{1 - \exp(-qV/kT)\}, \quad (1)$$

where V is the applied voltage to SD's. In this equation, the recombination current density (J_{ro}) is correlated with the recombination lifetime of carriers (τ_r):

$$J_{ro} = qn_i w / 2\tau_r, \quad (2)$$

Table 1

The results of curve fitting for I - V curves of ion irradiated Schottky diodes. The recombination current density gradually increased with the increase in ion dose

Ion dose (ions)	J_{ro} (A/cm ²)	ϕ_{bo} (eV)	R_s (Ω)
initial	2.6×10^{-7}	0.84	5.4×10^3
1.5×10^2	2.7×10^{-7}	0.84	5.7×10^3
2.6×10^3	2.9×10^{-7}	0.84	5.6×10^3
2.3×10^4	3.0×10^{-7}	0.84	7.1×10^3
7.2×10^4	4.2×10^{-7}	0.84	7.9×10^3
1.2×10^5	5.5×10^{-7}	0.84	6.1×10^3

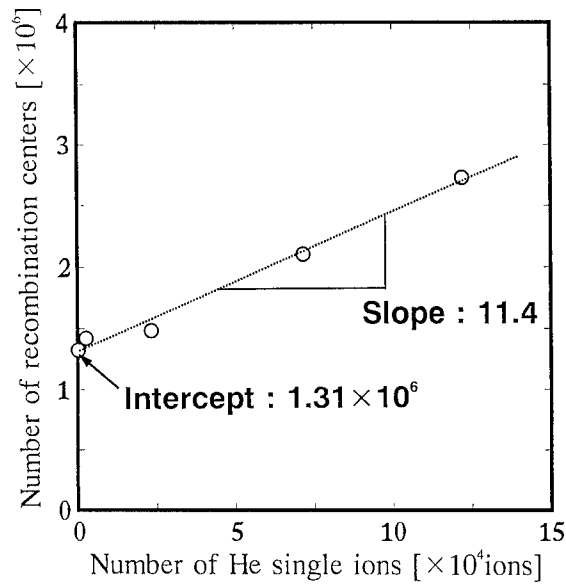


Fig. 3. The relation between the number of He single ions and the number of recombination centers.

where n_i is the intrinsic carrier density and w the depletion region width, respectively. On the other hand, the recombination lifetime (τ_r) can be represented by the recombination center density (N_r) as follows [7]:

$$\tau_r = 1/v_{th} \sigma N_r, \quad (3)$$

where v_{th} is the thermal velocity of carriers and σ the carrier capture cross section of recombination centers, respectively. It should be noted that Eq. (3) is valid only under the following two assumptions: firstly, the electron density in n-type Si is much larger than the hole density; secondly, the recombination center is at the midgap of Si. Substituting Eq. (3) in Eq. (2) we obtain the next equation for correlating J_{ro} with N_r :

$$N_r = 2 J_{ro} / v_{th} \sigma q n_i w. \quad (4)$$

In the calculation of N_r from J_{ro} , we have assumed v_{th} to be 10^7 cm/s and σ 10^{-15} cm².

Fig. 3 shows a relation between the number of implanted He single ions and the number of recombination centers (N_n) in the depletion region of the SD. The dotted line in this figure is the least square fit to the experimental plots. It is obvious that there

is a very good linearity between N_n and the number of He single ions. The slope of the dotted line, 11.4, means an average number of recombination centers induced by a He single ion at an energy of 2 MeV at room temperature. This value would depend on ion species, acceleration energies, and irradiation temperature. Especially the irradiation temperature must have played an important role in the relaxation process during and after the ion collision cascade. Therefore it is expected that by a careful choice of experimental conditions and by taking advantage of the simulation of ion collision cascade, we could shed a light on the behavior of recombination centers. A more important aspect of Fig. 3 is that if we plot a quantity related to a process or device function, the slope of the dotted line in Fig. 3 can be regarded as an index of the device immunity against ion irradiation, e.g. the slope would be high for a 'fragile' device.

The intercept, 1.31×10^6 , found by extrapolating experimental plots in Fig. 3 to zero ions yields the number of recombination centers which exist at the initial M/S interface. The initial number was obtained directly from the I - V characteristic of the SD before ion irradiation was to be 1.27×10^6 . The coincidence of the two values is quite good. This suggests that, even if the initial value is below the detection limit, the extrapolation to zero ions gives an alternative method to evaluate the initial value. Thus the slope and the intercept at the vertical axis in the linear relationship as shown in Fig. 3 can be a powerful tool for process and device diagnoses.

Assumptions made in evaluating N_n might cause some ambiguity because of a not well defined carrier capture cross section (σ) and defect energy levels (E_t). In addition, when the relatively heavy single ions such as As^+ are to be implanted at lower energies, the nature of isolated defect clusters would be altered significantly, thus a simple assumption of a single E_t and σ may not hold. Therefore, for a

more quantitative analysis the measurement of these quantities by DLTS or other independent analytical means would be necessary.

4. Conclusion

In order to develop the single ion implantation (SII) technique, we have tried to probe the nature of isolated defect clusters induced by the SII. A change in forward I - V characteristics of Schottky diodes before and after the SII has been analyzed quantitatively. We found a very good linear correlation between the number of implanted He single ions and the number of recombination centers. This approach has turned out to be a powerful tool for process and device diagnoses.

Acknowledgements

This work is supported by a Grant-in-Aid for Specially Promoted Research, the Ministry of Education, Science and Culture.

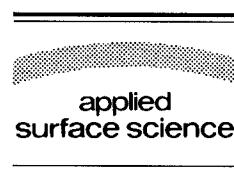
References

- [1] I. Ohdomari, in: Proc. 1st Int. Symp. on Control of Semiconductor Interfaces, Karuizawa, 1993, p. 233.
- [2] A. Holmes-Siedle and L. Adams, *Handbook of Radiation Effects* (Oxford University Press, 1993) ch. 3.
- [3] I. Ohdomari, M. Sugimori, M. Koh, K. Noritake, Y. Takiguchi and H. Shimizu, *Nucl. Instr. Meth. B* 72 (1992) 436.
- [4] M. Koh, K. Hara, K. Horita, B. Shigeta, T. Matsukawa, A. Kishida, T. Tanii, M. Gotoh and I. Ohdomari, *Nucl. Instr. Meth. B* 93 (1994) 82.
- [5] I. Ohdomari, T.S. Kuan and K.N. Tu, *J. Appl. Phys.* 50 (1979) 7020.
- [6] E.H. Rhoderick and R.H. Williams, *Metal-Semiconductor Contacts* (Oxford Science Publications, 1988) p. 118.
- [7] S.M. Sze, *Semiconductor Devices* (Wiley, New York, 1985) p. 51.



ELSEVIER

Applied Surface Science 104/105 (1996) 257–261



A normal incidence X-ray standing wave study of sulphur adsorption on InP(110)

T.K. Johal^a, P. Finetti^a, V.R. Dhanak^a, A.W. Robinson^a, A. Patchett^b,
D.R.T. Zahn^b, R. McGrath^{a,*,1}

^a *Interdisciplinary Research Centre in Surface Science, The University of Liverpool, P.O. Box 147, Liverpool L69 3BX, UK*

^b *Fachbereich Physik, TU Chemnitz–Zwickau, Reichenhainer Str. 70, 9022 Chemnitz, Germany*

Received 23 July 1995; accepted 10 October 1995

Abstract

A normal incidence X-ray standing wave (NIXSW) study of room temperature in-situ S adsorption on InP(110) is described. The S atom XSW profile was measured by detecting S 1s photoemission yield for the (220) Bragg reflection. The average perpendicular distance of the S atoms from the InP(110) surface was determined to be 1.95 ± 0.02 Å. The coherent fraction f_c was found to be 0.67 ± 0.02 , which upon annealing to 270°C increased to 0.82 ± 0.02 . A (1×1) low energy diffraction (LEED) pattern was observed in all cases. Models for the adsorption geometry are discussed.

1. Introduction

The ability of chalcogens to modify III–V semiconductor heterojunction behaviour has been the subject of scientific and technological interest in recent years. Improvements in electronic and optical characteristics of III–V semiconductor devices treated with sulphides has been extensively reported and attributed to the reduction in the density of interface states [1]. Surfactant behaviour of chalcogens on GaAs(001) substrates has enabled improvements in the growth mode of both metal [2] and semiconductor [3] thin films and Schottky barrier heights of

metal–semiconductor systems exhibit a greater sensitivity to the metal work functions when a chalcogen interlayer is incorporated [4].

Sulphur passivation of the III–V semiconductor surfaces arises from the modification of the surface electronic structure and can be explained in terms of the S/III–V semiconductor bonding geometry [5]. In this work the bonding geometry of the S/InP(110) system is investigated.

A number of different approaches to the formation of S/III–V overlayer systems have been taken. The S/InP(001) system, where the sulphur treatment has been achieved by a variety of ex-situ wet chemical sulphide etchants [5–11] or by the in-situ exposure to H₂S [12,13], has been studied extensively. Photoemission studies have shown that after room temperature treatment using a $(\text{NH}_4)_2\text{S}_x$ solution S bonds only to In [9] and a (1×1) low energy

* Corresponding author. Fax: +44-151-7080662; e-mail: mcgrath@ssci.liv.ac.uk.

¹ Also at the Department of Physics, The University of Liverpool, P.O. Box 147, Liverpool L69 3BX, UK.

electron diffraction (LEED) pattern is observed [14]. Annealing in the temperature range 350°C–500°C leads to the formation of a (2×1) LEED pattern [11,14,15]. The $\text{H}_2\text{S}/\text{InP}(110)$ system has been studied for low exposure of H_2S (2 L) resulting in a weakly bound adsorbate which readily desorbs when annealed to 50°C [16] and for high exposures which upon annealing to temperatures in the range 200°C–300°C results in the formation of In–S bonding [17].

In this work the interaction of S emanating from a solid-state source in ultra high vacuum (UHV) conditions with the in-situ cleaved (110) surface of InP is studied. The advantages of studying the cleavage surface are that it is well-understood, has a known stoichiometry and is easily reproducible.

The structural aspects of this system are investigated using NIXSW [18,19] and low energy electron diffraction (LEED). The NIXSW technique is based on the fact that when an X-ray impinges on a crystalline substrate near a Bragg condition the incident beam is strongly reflected. The superposition of the incident and reflected beam forms an XSW which possesses the periodicity of the reflecting Bragg planes of the crystal. The electric field intensity of the XSW therefore exhibits a spatial modulation over an interplanar distance, and this makes the XSW technique sensitive to the atomic positions since the photoexcitation of the atoms is proportional to this spatial modulation. The pertinent task is to monitor the photoexcitation process and this can be achieved by detecting the emitted photoelectrons or the products of the subsequent decay processes such as Auger electrons or fluorescent photons. Analysis of the absorption yield as a function of the photon energy over the range of a Bragg reflection allows a precise determination of the vertical height of the adsorbate atom with respect to the reflecting Bragg plane. The structures of Sb/GaP(110) [20], Sb/GaAs(110) [21,22] and $\text{H}_2\text{S}/\text{InP}(110)$ [16] have been investigated using this technique.

2. Experimental details

NIXSW experiments were conducted at the IRC beamline 4.2 of the synchrotron radiation source (SRS) at the Daresbury Laboratory, UK. A Ge(111) double-crystal monochromator provides monochro-

matic light in the energy range ~ 1950 – 5000 eV [23]. A chromium-quartz mirror combination allows high-energy cut-off preventing contamination of the incident beam with third-order radiation. The UHV chamber was equipped with a concentric hemispherical electron analyser (Vacuum Generators AX100) and Omicron LEED optics.

XSW profiles of the adsorbate and substrate atoms were measured using photoemission yield (S 1s, P 1s and In $3p_{3/2}$ core levels). The photoemission yield sits on a background consisting of inelastically scattered secondary electrons. This background was corrected for by subtracting XSW profiles measured at a kinetic energy ~ 10 eV above the photoemission peaks.

The variation as a function of photon energy (E) in the total electron yield $\text{TEY}(E)$ and the sample reflectivity $R(E)$ were measured simultaneously with the photoemission yield $Y(E)$ from the adsorbate atoms in the region of the Bragg reflection. These measurements provide information on the energy resolution and calibration of the incident beam. The $\text{TEY}(E)$ was measured using the drain current of the sample. $R(E)$ was measured *via* photocurrent yield using a 90% transmission copper grid. The measured photocurrent is composed of two signals, that of the back-reflected beam $R(E)$ and that of the transmitted incident beam. $R(E)$ is extracted from the total signal by subtracting a polynomial background representing the transmitted signal.

Undoped InP samples (MCP Wafer Technology, UK) in the form of (110) orientated single crystal bars were used. These bars were notched and subsequently cleaved in-situ. Sulphur deposition was achieved by decomposition of tin(IV)sulphide (SnS_2) in a Knudsen-type evaporator.

3. Results

The emission yield $Y(E)$ in the XSW field where extinction effects are negligible is given by [20]

$$Y(E)/Y_0 = 1 + R(E) + 2\sqrt{R(E)} f_c \cos(\theta(E) - 2\pi\Phi_c) \quad (1)$$

where Y_0 is the average yield away from the region of strong reflection, $R(E)$ is the sample reflectivity,

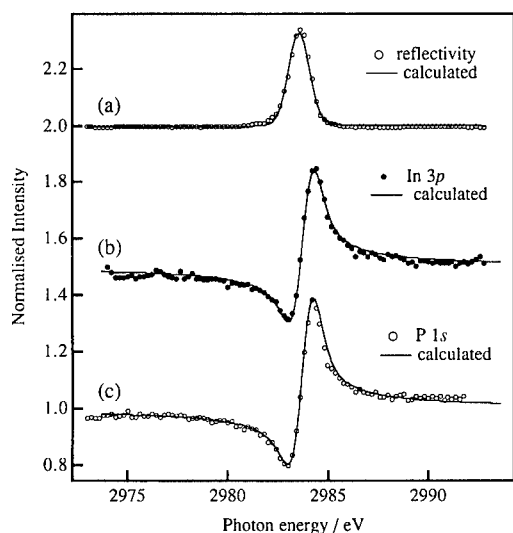


Fig. 1. (a) The (220) Bragg reflection of InP(110) as a function of photon energy. The data are fitted to the Darwin–Prins curve for reflectivity convoluted with a Gaussian of full width half maximum (FWHM) = 0.64 ± 0.01 eV. (b, c) The substrate In $3p_{3/2}$ and P 1s core level photoemission signals monitored as a function of photon energy in the region of the (220) Bragg reflection together with fits to Eq. (1).

$\theta(E)$ is the phase factor relating the incident beam electric field to the reflected beam electric field, Φ_c is the coherent distance, i.e. the adsorbate–substrate distance in units of the reflecting plane spacing (modulo nd , where d is the bulk interplanar spacing and n an integer), and f_c is the coherent fraction which corresponds to the fraction of total contributing atoms at Φ_c . f_c and Φ_c are the fitting parameters.

The measured $R(E)$ at the (220) Bragg reflection is shown in Fig. 1(a). By fitting this curve to the Darwin–Prins curve for reflectivity [24] convoluted with a Gaussian approximating the instrumental broadening, a value of 0.64 ± 0.01 eV was obtained which is an indication of the photon energy resolution. The photon energy calibration and broadening obtained from the reflectivity were then used in the subsequent analysis of the XSW profiles. Fig. 1(b) and (c) show the substrate In $3p_{3/2}$ and P 1s core level photoemission signals monitored as a function of photon energy in the region of the (220) Bragg reflection together with fits to Eq. (1) using this procedure. The coherent fractions and distances obtained from the fits for the In $3p_{3/2}$ and P 1s core

level photoemission yields are $f_c = 0.93$, $\Phi_c = 1.0$ and $f_c = 0.93$, $\Phi_c = 1.0$ respectively. The departure of the values for f_c from the expected value of unity may be due to the fact that the Debye–Waller factor is not independently determined and is therefore chosen to be unity in all fits.

Fig. 2(a) shows the S 1s XSW profile for the (220) Bragg reflection for a room temperature exposure of 0.5 L, together with the fit to the data using Eq. (1). A sharp 1×1 LEED pattern was observed before dosing, which exhibited only a reduction in spot intensity after dosing. The coherent fraction is $f_c = 0.67 \pm 0.02$ and the coherent position is $\Phi_c = 0.94 \pm 0.01$. The sample was then annealed. The annealing temperature was measured using a thermocouple on the sample holder to be 270°C . This is therefore a maximum value for the sample surface temperature. The subsequent XSW profile for the S atoms is shown in Fig. 2(b). The fitting parameters are $f_c = 0.82 \pm 0.02$ and $\Phi_c = 0.94 \pm 0.01$. The increase in f_c indicates that the annealing procedure

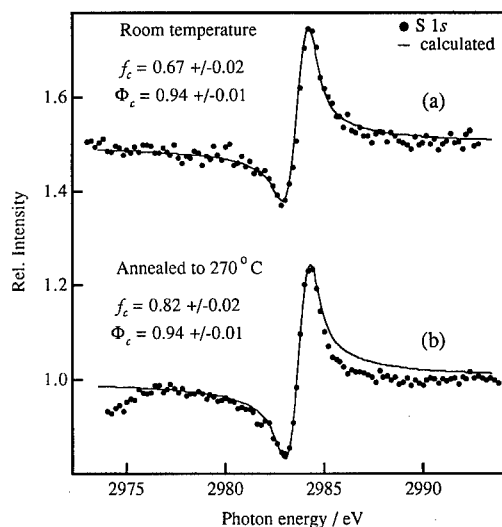


Fig. 2. (a) Photon energy dependence of the background-subtracted and normalised S 1s photoemission yield from approximately 1 ML of S on InP(110) in the region of the (220) Bragg reflection. The fit to Eq. (1) yields $f_c = 0.65 \pm 0.05$ and $\Phi_c = 0.93 \pm 0.02$. (b) Photon energy dependence of the background-subtracted and normalised S 1s photoemission yield from approximately 1 ML of S on InP(110) in the region of the (220) Bragg reflection after annealing the surface to 270°C . The fit to Eq. (1) yields $f_c = 0.84 \pm 0.05$ and $\Phi_c = 0.93 \pm 0.02$.

increases the fraction of the S atoms at $\Phi_c = 0.94 \pm 0.01$.

4. Discussion

Room temperature S adsorption results in a measured coherent fraction of 0.67 ± 0.02 . This value is low in comparison to a typical value of 0.8 obtained for a highly ordered S overlayer [18]; this may be explained in terms of the S adsorption occurring at multiple sites [25] or by the presence of disordered S.

Annealing results in an increase in the coherent fraction (to 0.82 ± 0.02) and no change in the coherent position. Annealing may cause an exchange reaction to occur between S and P atoms in the first atomic layers: S and P exchange has been observed by photoelectron diffraction from an $(\text{NH}_4)_2\text{S}_x$ -treated InP(001) surface annealed to 350°C [15]. The exchange reaction is favoured thermodynamically and by the similarity of the P and S atomic sizes [15]. However S atoms diffused into the bulk would assume substitutional sites and since the position of the S atoms determined here is not that of the actual bulk lattice positions and there is no change in the coherent position upon annealing this is unlikely. The fact that the coherent fraction increases without a change in coherent position is consistent with a single adsorption site and the removal of kinetically limited disorder. Similar behaviour has been observed in an XSW study of S adsorption on GaAs(001) [26]. It seems probable that annealing to the higher temperature of 350°C is necessary to activate the exchange reaction.

As a starting point for our discussion of possible adsorption geometries, we assume that the clean surface relaxation [27,28] is removed by the adsorption process². Four possible high symmetry adsorption sites (Fig. 3) are considered. These sites were chosen to be consistent with the observed absence of exchange reaction, the near bulk-like S distance from the surface and the observed (1×1) periodicity of

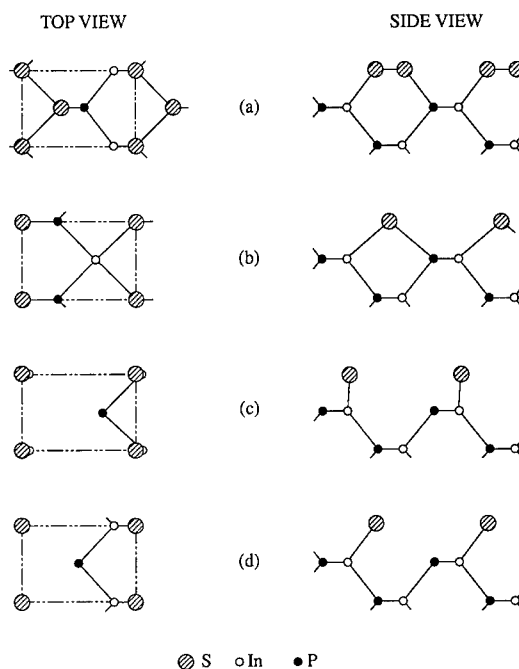


Fig. 3. Schematic diagrams of possible surface geometries for a (1×1) overlayer of S on InP(110). (a) Epitaxial continued layer structure (ECLS), (b) interchain bridging structure, (c) modified epitaxial on-top structure (EOTS) with bonding only to In, (d) so-called 'defect' model.

the overlayer. The sites are, following the notation of Refs. [30] and [31], the epitaxial continued layer structure (ECLS), Fig. 3(a), $\Theta = 1$ ML; the interchain bridging structure, Fig. 3(b), $\Theta = 0.5$ ML; a modified epitaxial on-top structure (EOTS) with bonding only to In, Fig. 3(c), $\Theta = 0.5$ ML; and the so-called 'defect' model, Fig. 3(d), $\Theta = 0.5$ ML, where the S atoms adopt the positions of P atoms in the next atomic layer.

Since previous work on the InP(001) surface showed that S bonds only to In [9] and only the In–S bond persists after annealing the $\text{H}_2\text{S}/\text{InP}(110)$ system in the temperature range 200°C – 300°C [17], the ECLS site and the interlayer bridging site which involve bonding to both In and P (Fig. 3(a) and (b)) can be ruled out. Assuming removal of the clean surface relaxation, the measured coherent position of 0.94 ± 0.01 corresponds to an average vertical distance of 1.95 ± 0.02 Å for the S atoms from the InP surface. Within this context the In–S bond length for the modified EOTS would be 1.95 Å which is very

² Although there is no direct evidence for this in our study, complete or partial removal of the clean surface relaxation has been observed for other adsorbates, e.g. $\text{Cs}/\text{InP}(110)$ [29], $\text{H}_2\text{S}/\text{InP}(110)$ [16].

much less than the sum of the covalent radii (2.48 \AA) [32] so this adsorption site can also be eliminated. Finally, the S atoms may assume P sites of the ideal bulk termination, Fig. 3(d). If the bond-length is assumed to be the sum of the covalent radii then the In–S–In bond angle would be $104 \pm 1^\circ$ which is close to the bulk tetrahedral bond angle (109.6°) implying In–S bonding of covalent sp^3 character. Our work points to this site as the most likely.

5. Conclusions

Room temperature in-situ adsorption of 0.5 L of S on the cleaved InP(110) surface results in a less than perfect overlayer. Subsequent annealing to $\leq 270^\circ\text{C}$ removes the kinetically limited disorder resulting in a high coherent fraction (0.82 ± 0.02) which indicates a high degree of order and a single adsorption site. The S atoms are a vertical distance of $1.95 \pm 0.02 \text{ \AA}$ from the surface. A model for the adsorption geometry is suggested where the S atoms assume positions close to the ideal bulk-termination P sites.

Acknowledgements

P. Weightman is thanked for the use of a UHV chamber and F.M. Leibsle for the loan of an electron analyser. D. Collister is thanked for technical assistance, B.C.C. Cowie, J.M.C. Thornton and R.I. Blyth for helpful discussions and D.A. Evans for a critical reading of the manuscript. This work was funded in part by EC HCM grant No. ERBCHRXCT930317.

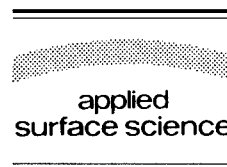
References

- [1] C.J. Sandroff, R.N. Nottenburg, T.C. Bischoff and R. Baht, *Appl. Phys. Lett.* 51 (1987) 33.
- [2] G.W. Anderson, M.C. Hanf and P.R. Norton, *Phys. Rev. Lett.* 74 (1995) 2764.
- [3] N. Grandjean, J. Massies and V.H. Etgens, *Phys. Rev. Lett.* 69 (1992) 796.
- [4] J.R. Waldrop, *Appl. Phys. Lett.* 47 (1985) 1301.
- [5] T. Ohno, *Phys. Rev. B* 44 (1991) 6306.
- [6] C.W. Wilmsen, K.M. Geib, J. Shin, R. Iyer, D.L. Lile and J.J. Pouch, *J. Vac. Sci. Technol. B* 7 (1989) 851.
- [7] F. Maeda, Y. Watanabe and M. Oshida, *Appl. Phys. Lett.* 62 (1993) 297.
- [8] R.W.M. Kwok and W.M. Lau, *J. Vac. Sci. Technol. A* 10 (1992) 2515.
- [9] Y. Tao, A. Yelon, E. Sacher, Z.H. Lu and M.J. Graham, *Appl. Phys. Lett.* 60 (1992) 2669.
- [10] A. Kapila and V. Malhotra, *Appl. Phys. Lett.* 62 (1993) 1009.
- [11] Y. Fukada, Y. Suzuki, N. Sanada, S. Sasaki and T. Ohsawa, *J. Appl. Phys.* 76 (1994) 3059.
- [12] A.J. Nelson, S. Frigo and R. Rosenberg, *J. Appl. Phys.* 71 (1992) 6086.
- [13] A.J. Nelson, S. Frigo and R. Rosenberg, *J. Vac. Sci. Technol. A* 11 (1993) 1022.
- [14] O.L. Warren, G.W. Anderson, M.C. Hanf, K. Griffiths and P.R. Norton, *Phys. Rev. B* 52 (1995) 2959.
- [15] D. Gallet and G. Hollinger, *Appl. Phys. Lett.* 62 (1993) 982.
- [16] E. Dudzik, PhD Thesis, Dublin University (1995).
- [17] T. Chassé, private communication.
- [18] D.P. Woodruff, D.L. Seymour, C.F. McConville, C.E. Riley, M.D. Crapper, N.P. Prince and R.G. Jones, *Phys. Rev. Lett.* 58 (1987) 1460.
- [19] D.P. Woodruff, D.L. Seymour, C.F. McConville, C.E. Riley, M.D. Crapper, N.P. Prince and R.G. Jones, *Surf. Sci.* 195 (1988) 237.
- [20] K.E. Miyano, T. Kendelwicz, J.C. Woicik, P.L. Cowan, C.E. Bouldin, B.A. Karlin, P. Pianetta and W.E. Spicer, *Phys. Rev. B* 46 (1992) 6869.
- [21] T. Kendelwicz, J.C. Woicik, K.E. Miyano, A. Herrera-Gomez, P.L. Cowan, B.A. Karlin, C.E. Bouldin, P. Pianetta and W.E. Spicer, *Phys. Rev. B* 46 (1992) 7276.
- [22] T. Kendelwicz, J.C. Woicik, A. Herrera-Gomez, K.E. Miyano, P.L. Cowan, B.A. Karlin, P. Pianetta and W.E. Spicer, *J. Vac. Sci. Technol. A* 11 (1993) 2351.
- [23] A.W. Robinson, S. d'Addato, V.R. Dhanak, P. Finetti and G. Thornton, *Rev. Sci. Instr.* 66 (1995) 1762.
- [24] B.W. Batterman and H. Cole, *Rev. Mod. Phys.* 36 (1964) 681.
- [25] N. Hertel, G. Materlik and J. Zegenhagen, *J. Phys. B Condens. Matter* 58 (1985) 199.
- [26] M. Sugiyama, S. Maeyama, S. Heun and M. Oshima, *Phys. Rev. B* 51 (1995) 14778.
- [27] W.K. Ford, T. Guo, K.-J. Wan and C.B. Duke, *Phys. Rev. B* 45 (1992) 11896.
- [28] G.P. Srivastava, *Surf. Sci.* 307–309 (1994) 328.
- [29] Th. Chassé, G. Neuhold, J.J. Pagel and K. Horn, *Surf. Sci.* 331–333 (1995) 528.
- [30] C.B. Duke, A. Paton, W.K. Ford, A. Kahn and J. Carelli, *Phys. Rev. B* 26 (1982) 803.
- [31] W.G. Schmidt and F. Bechstedt, *Phys. Rev. B* 50 (1994) 17280.
- [32] L.C. Pauling, *The Nature of the Chemical Bond and the Structure of Molecules and Crystals* (Cornell University Press, Ithaca, NY, 1960).



ELSEVIER

Applied Surface Science 104/105 (1996) 262–266



The Schottky barrier of Co on strained and unstrained $\text{Si}_x\text{Ge}_{1-x}$ alloys

Ja-Hum Ku^{*}, R.J. Nemanich

Department of Physics, North Carolina State University, Raleigh, NC 27695-8202, USA

Received 28 June 1995; accepted 7 September 1995

Abstract

In this study, metal films of Co were deposited in situ on strained and unstrained $\text{Si}_x\text{Ge}_{1-x}$ alloys, and the Schottky barrier ($E_F - E_V$) was determined by angle resolved ultraviolet photoemission spectroscopy (ARUPS). Measurements were obtained as a function of Ge composition. Strained and unstrained epitaxial $\text{Si}_x\text{Ge}_{1-x}$ alloys were grown on Si(100) wafers using electron beam evaporation in an ultra-high vacuum molecular beam epitaxy (UHV MBE) chamber. The ARUPS experiments were performed to measure the Schottky barrier heights of Co on a series of $\text{Si}_x\text{Ge}_{1-x}$ alloys, and to observe the surface states. The surface states of clean $\text{Si}_x\text{Ge}_{1-x}$ alloys were observed and were extinguished as Co thickness increased to ~ 0.4 Å. The p-type Schottky barrier of Co on Si was found to be 0.52 eV. The measured barrier heights of Co on strained $\text{Si}_x\text{Ge}_{1-x}$ alloys ranged from 0.33 eV to 0.46 eV as x increased from 0.40 to 0.80. The Schottky barrier of Co on unstrained $\text{Si}_x\text{Ge}_{1-x}$ alloys ranged from 0.23 eV to 0.41 eV as x increased from 0 to 0.60. In fact, the p-type Schottky barrier was essentially identical for strained and unstrained $\text{Si}_x\text{Ge}_{1-x}$ alloys of the same concentration. This indicates that the n-type Schottky barrier is substantially different for strained and unstrained alloys. ARUPS was also conducted to measure the electron affinities of the series of $\text{Si}_x\text{Ge}_{1-x}$ alloys and the work function of Co. The results show that the barrier does not follow the work function model.

1. Introduction

Recently, there has been interest in $\text{Si}_x\text{Ge}_{1-x}$ alloys because of the potential applications in high-speed heterojunction devices [1–5] and in optoelectronics [6,7]. Metal/ $\text{Si}_x\text{Ge}_{1-x}$ contacts, however, have not been investigated extensively despite of the importance for device applications. Silicon and germanium are completely miscible over the entire

compositional range and give rise to alloys with the diamond crystal structure. Due to the lattice mismatch (4.17%) between silicon and germanium, two types of epitaxial growth of $\text{Si}_x\text{Ge}_{1-x}$ alloys are possible on a bulk substrate, usually Si; strained or pseudomorphic, and unstrained or relaxed. The band gap of the $\text{Si}_x\text{Ge}_{1-x}$ alloys decreases as the Ge content increases, and the strained $\text{Si}_x\text{Ge}_{1-x}$ alloys exhibit a greater reduction in the band gap than unstrained $\text{Si}_x\text{Ge}_{1-x}$ alloy [8]. To date, several attempts have been made to investigate the Schottky barrier of metals on $\text{Si}_x\text{Ge}_{1-x}$ alloys. Kanaya et al. [9] studied the Schottky barrier heights of Pt(Pd)

^{*} Corresponding author. Tel.: +1-919-5153225; fax: +1-919-5157331; e-mail: robert_nemanich@ncsu.edu.

silicide/p-Si_xGe_{1-x} using *I*-*V* techniques and found that the Schottky barrier heights decrease as the Ge content increases and that the Schottky barrier height of the strained Si_xGe_{1-x} sample is smaller than that of the relaxed one. Liou et al. [10] also performed an experiment about the interfacial reactions and Schottky barriers of Pt/n-Si_{0.8}Ge_{0.2} and Pd/n-Si_{0.8}Ge_{0.2} with *I*-*V* measurements. They found that the Schottky barrier heights are much smaller than those of n-Si.

In this work, the Schottky barrier heights of cobalt (Co) on Si, strained Si_xGe_{1-x} alloys ($x = 0.40, 0.60$, and 0.80) and unstrained Si_xGe_{1-x} alloys ($x = 0, 0.20, 0.40$, and 0.60) were measured using angle resolved ultraviolet photoemission spectroscopy (ARUPS). With this technique, the barrier height not only can be measured for a submonolayer film but also can be directly deduced by determining the valence band edge and the Fermi level position. Surface reconstruction and contamination were monitored by means of in situ low energy electron diffraction (LEED) and Auger electron spectroscopy (AES). The purpose of this study is to examine the Schottky barrier heights of Co on a series of Si_xGe_{1-x} alloys as a function of Ge composition and the effects of strained and unstrained Si_xGe_{1-x} alloys on the Schottky barrier heights. The Schottky barrier formation will also be discussed in comparison with existing models.

2. Experimental procedures

The samples were prepared and measured using an integrated ultra-high vacuum (UHV) system, which consists of molecular beam epitaxy (MBE), ARUPS, LEED, AES, and loadlock chambers linked by a UHV transfer line. The Si_xGe_{1-x} film growth, the Co deposition and the surface measurements were all made in UHV without exposure to ambient.

The substrates used in this study were 25 mm diameter n-type Si(100) wafers with a resistivity of $0.8\text{--}1.2\ \Omega\ \text{cm}$. The wafers were cleaned by exposure to UV/ozone for 5 min to remove hydrocarbon contaminants, an HF based spin etch (HF:H₂O:ethanol = 1:1:10) to remove the native oxide, and followed by in situ heat cleaning to 850°C for 10 min in the UHV MBE chamber to eliminate

the residual contamination. The wafers were mounted with tantalum (Ta) wire on a molybdenum (Mo) sample holder. A 200 Å homoepitaxial silicon buffer layer was deposited on the atomically clean Si(100) substrate to ensure a contamination free interface. A series of Si_xGe_{1-x} alloys were epitaxially grown on top of the silicon buffer layers using electron beam evaporation in the UHV MBE chamber. The base pressure of the MBE chamber was better than 1×10^{-10} Torr. The substrate temperature was held at 550°C during all depositions. The parameters of samples used in this experiment were 300 Å for pure Si and pure Ge, and 200 Å, 120 Å, and 40 Å, which are far below the critical thicknesses [11], for strained Si_{0.8}Ge_{0.2}, Si_{0.6}Ge_{0.4} and Si_{0.4}Ge_{0.6} alloys, respectively. For unstrained Si_{0.6}Ge_{0.4}, Si_{0.4}Ge_{0.6}, and Si_{0.2}Ge_{0.8} samples, 8000 Å, 5000 Å, and 3000 Å were chosen respectively, which are far above the critical thicknesses [11]. LEED images of these samples exhibited a sharp double domain 2×1 surface reconstruction, and AES data indicated no detectable carbon or oxygen on the surface before or after Si_xGe_{1-x} alloy depositions. The Co was evaporated at a rate $\sim 0.05\ \text{\AA/s}$ using a tungsten filament under a pressure in the 10^{-9} Torr with the sample kept at room temperature in the UHV ARUPS chamber. The thickness of the Co layer was monitored by a quartz oscillator.

ARUPS was employed to measure the Schottky barrier heights and to observe the surface states of the clean surface. The base pressure of the ARUPS chamber was less than 2×10^{-10} Torr with an operating pressure of $< 1 \times 10^{-9}$ Torr. The ARUPS spectra were obtained with a differentially pumped He discharge lamp delivering the HeI (21.2 eV) radiation. The UV light is incident on the sample at $\sim 45^\circ$ from the surface normal in the analyzer rotation plane and at $\sim 15^\circ$ from the surface in the perpendicular plane to the analyzer rotation plane. The photoemitted electrons were analyzed with a 50 mm mean radius hemispherical analyzer with an energy resolution of 0.25 eV and an angular resolution of 2° . The analyzer is mounted on a two stage goniometer which allows angle dependent measurement and can be rotated in the plane which is perpendicular to the surface of the sample. All ARUPS experiments presented in this paper were performed at emission angles, Θ_e , along the [010]

crystal direction, since along the [010] direction, the surface Brillouin zones of the two domains are equivalent according to the crystal symmetry. The selection of angle for comparison in the spectra was chosen to emphasize features associated with the bulk states of Si, Ge, or $\text{Si}_x\text{Ge}_{1-x}$ alloys. Each spectrum was acquired using a 0.005 eV step size and an integration time of 1 s at each energy. To improve the signal-to-noise ratio, each sample was scanned five times and the five spectra were summed. After summing, the spectra were subjected to a five point smooth to further distinguish the data from the random noise. The position of the Fermi level was determined by measuring either a spectrum of a thick Co layer on the semiconductor or a spectrum of the metallic (Mo) sample holder. Both techniques yielded the same values.

3. Results and discussion

The Schottky barrier height of a metal on a p-type semiconductor is defined as the energy difference between the valence band edge of the semiconductor and the Fermi level of the metal at the interface. In order to determine the Schottky barrier height from ARUPS data, it is necessary to establish the position of the valence band edge in the spectra. The valence band position, which is distinguished by the onset of the spectra, can also be expressed relative to the bulk peaks. Experiments are therefore limited to thin metal films because photoemission from the metal overlayer tends to mask that from the underlayer, and it obscures features necessary to determine the valence band edge at higher metal coverage.

An emission angle of 35° was chosen for the pure Si sample and the strained $\text{Si}_x\text{Ge}_{1-x}$ samples, while a 30° emission angle was chosen for the unstrained $\text{Si}_x\text{Ge}_{1-x}$ samples, because the bulk state features are prominent at these angles. ARUPS spectra of Co on the strained $\text{Si}_{0.8}\text{Ge}_{0.2}$ and the unstrained $\text{Si}_{0.2}\text{Ge}_{0.8}$ for different Co coverage are shown in Fig. 1 and Fig. 2. The spectra of the clean strained $\text{Si}_{0.8}\text{Ge}_{0.2}$ at a 35° emission angle and the clean unstrained $\text{Si}_{0.2}\text{Ge}_{0.8}$ at a 30° emission angle look similar, but there is a substantial difference in the spectra obtained at normal emission for the same samples. The feature (S) associated with the dangling

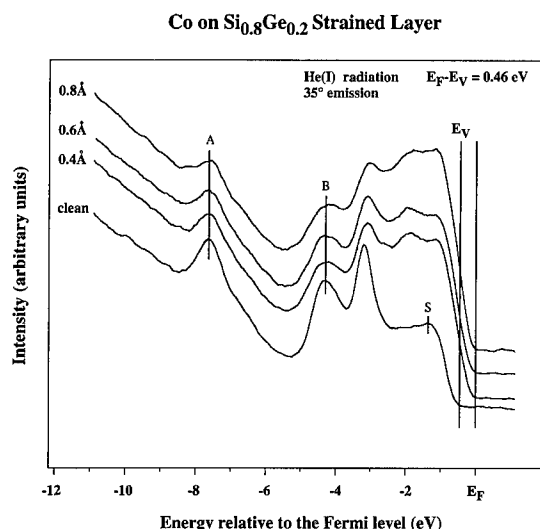


Fig. 1. The ARUPS spectra of clean strained $\text{Si}_{0.8}\text{Ge}_{0.2}$ alloy, and Co on strained $\text{Si}_{0.8}\text{Ge}_{0.2}$ alloy obtained as a function of Co coverages. A and B indicate states due to bulk transition and S indicates a surface state attributed to dangling bond states.

bond surface state located at 1.37 eV below the Fermi level was observed from the clean strained $\text{Si}_{0.8}\text{Ge}_{0.2}$ spectrum and was extinguished with Co evaporation. The features (A, B) due to the bulk transition at 7.64 eV and at 4.33 eV below the Fermi

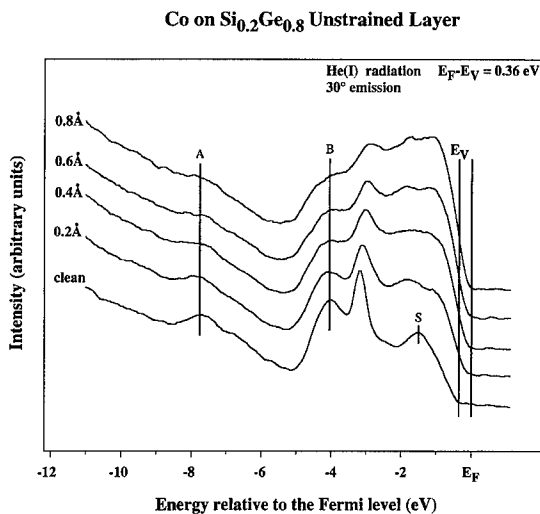


Fig. 2. The ARUPS spectra of clean unstrained $\text{Si}_{0.2}\text{Ge}_{0.8}$ alloy, and Co on unstrained $\text{Si}_{0.2}\text{Ge}_{0.8}$ alloy obtained as a function of Co coverages. A and B indicate states due to bulk transition and S indicates a surface state attributed to dangling bond states.

Table 1

The measured Schottky barrier heights ($E_F - E_V$) of Co on Si, strained $\text{Si}_x\text{Ge}_{1-x}$ alloys, and unstrained $\text{Si}_x\text{Ge}_{1-x}$ alloys. The value for Si is also shown in the strained column for comparison

Strained	$E_F - E_V$ (eV)	Unstrained	$E_F - E_V$ (eV)
Si (cubic)	0.52 ± 0.03	Si (cubic)	0.52 ± 0.03
$\text{Si}_{0.8}\text{Ge}_{0.2}$	0.46 ± 0.03		
$\text{Si}_{0.6}\text{Ge}_{0.4}$	0.39 ± 0.03	$\text{Si}_{0.6}\text{Ge}_{0.4}$	0.41 ± 0.03
$\text{Si}_{0.4}\text{Ge}_{0.6}$	0.33 ± 0.03	$\text{Si}_{0.4}\text{Ge}_{0.6}$	0.36 ± 0.03
		$\text{Si}_{0.2}\text{Ge}_{0.8}$	0.36 ± 0.03
		Ge	0.23 ± 0.03

level were used as reference peaks for deducing the valence band edge after Co deposition. The valence band edge, which was found to be 7.18 eV above the reference peak A, was determined by the onset of emission at ~ 0.46 eV below the Fermi level from the clean $\text{Si}_{0.8}\text{Ge}_{0.2}$ spectrum. No shifts in the kinetic energies of the peak originating from bulk transition were observed for all measured samples and for all Co coverages. The Schottky barrier height ($E_F - E_V$) of 0.46 eV and 0.36 eV were deduced for Co on the strained $\text{Si}_{0.8}\text{Ge}_{0.2}$ and the unstrained $\text{Si}_{0.2}\text{Ge}_{0.8}$, respectively. The measured Schottky barrier heights for all of the samples are summarized in Table 1.

Fig. 3 shows a schematic drawing of the band alignment with the $E_F - E_V$ for the strained $\text{Si}_x\text{Ge}_{1-x}$ alloys with Co overlayer. The band align-

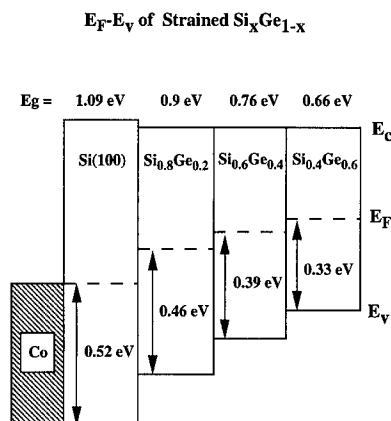


Fig. 3. A schematic drawing of the band alignment of the $E_F - E_V$ for strained $\text{Si}_x\text{Ge}_{1-x}$ alloys with a Co overlayer. The band alignment for strained $\text{Si}_x\text{Ge}_{1-x}$ alloys on a Si(100) substrate is type I [12].

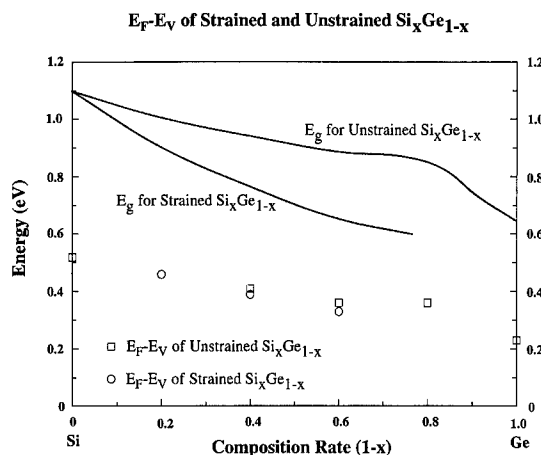


Fig. 4. The p-type Schottky barrier heights of Co on strained and unstrained $\text{Si}_x\text{Ge}_{1-x}$ alloys with the band gap reported by People [8].

ment for strained $\text{Si}_x\text{Ge}_{1-x}$ alloys on Si(100) substrates is type I with a band discontinuity of 0.020 eV at the conduction band [12]. The Schottky barrier heights of Co on the series of strained $\text{Si}_x\text{Ge}_{1-x}$ alloys are pinned at around the middle of the band gap.

The Schottky barrier heights of Co on the strained and the unstrained $\text{Si}_x\text{Ge}_{1-x}$ alloys in Table 1 are plotted in Fig. 4 together with the band gap obtained by People [8]. It is noted that the Schottky barrier height of Co on strained and unstrained $\text{Si}_x\text{Ge}_{1-x}$ alloys decreases with increasing Ge content, which is similar to the results for Pt(Pd) in contact with the $\text{Si}_x\text{Ge}_{1-x}$ alloys obtained by Kanaya et al. [9]. The Schottky barrier heights, however, were identical for Co on strained and unstrained $\text{Si}_x\text{Ge}_{1-x}$ alloys with the same Ge content despite the fact that the strained and unstrained $\text{Si}_x\text{Ge}_{1-x}$ alloys exhibit substantial differences in the band gap for identical alloy concentrations. In other words, the n-type Schottky barrier heights of unstrained $\text{Si}_x\text{Ge}_{1-x}$ alloys are remarkably larger than those of strained $\text{Si}_x\text{Ge}_{1-x}$ alloys since the n-type barrier height can be obtained by subtracting p-type Schottky barrier height from the energy band gap of the semiconductor.

The ARUPS spectra of the alloys were extended to measure the electron affinity of the semiconductor and the work function of metal. The electron affinity of the semiconductor and the metal work function are given by

$\chi = h\nu - D - E_g$ for the electron affinity of the semiconductor, and

$\phi = h\nu - D$ for the metal work function,

where $h\nu$ is the incident energy (21.21 eV for He I radiation), E_g is the band gap of the semiconductor, and D is the width of the ARUPS spectrum. To obtain the width it is necessary to bias the sample to overcome the work function of the analyzer. The Co work function was found to be 4.98 eV which is in close agreement with the reported work function (5 eV) of bulk Co [13]. The measured electron affinities of Si, strained $\text{Si}_x\text{Ge}_{1-x}$ alloys and unstrained $\text{Si}_x\text{Ge}_{1-x}$ alloys ranged from 3.83 eV to 4.05 eV ($\chi_{\text{Si}} < \chi_{\text{Ge}}$) and showed a slight difference between measured values of the electron affinities of Si and Ge and previously reported values ($\chi_{\text{Si}} = 4.01$ eV, $\chi_{\text{Ge}} = 4.13$ eV) [14]. The calculated values of the p-type Schottky barrier using the measured electron affinities and the Co work function resulted in negative values for all alloys. This indicates that the Schottky barrier of Co on a series of strained and unstrained $\text{Si}_x\text{Ge}_{1-x}$ alloys is not consistent with the work function model. The results suggest that the Fermi level has been pinned by interface states [15].

4. Conclusions

It was shown that the measured Schottky barrier height of Co on a series of $\text{Si}_x\text{Ge}_{1-x}$ alloys decreased as the Ge content increased. No significant difference, however, was observed between the measured p-type Schottky barrier heights of Co on strained $\text{Si}_x\text{Ge}_{1-x}$ alloys and those of Co on unstrained $\text{Si}_x\text{Ge}_{1-x}$ alloys of the same Ge concentration. Since the band gap of the strained and unstrained alloys are significantly different, this indicates that the n-type barrier differs for the strained and unstrained alloys. It was also shown that the barrier heights of Co on strained $\text{Si}_x\text{Ge}_{1-x}$ alloys

and unstrained $\text{Si}_x\text{Ge}_{1-x}$ alloys do not follow the work function model, which suggests that the Fermi level has been pinned by interface states.

Acknowledgements

The authors would like to thank Z. Wang, D. Yuan and D.B. Aldrich for their invaluable help. This work is supported in part by the NSF under grant #DMR9204285.

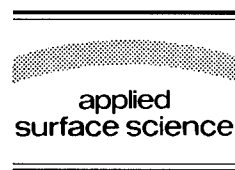
References

- [1] R. People, *IEEE J. Quantum Electron.* QE-22 (1986) 1696.
- [2] E. Kasper and J.C. Bean, Eds., *Silicon Molecular Beam Epitaxy* (CRC Press, Boca Raton, FL, 1988).
- [3] J.N. Burghartz, J.H. Comfort, G.L. Patton, B.S. Meyerson, J.Y.-C. Sun, J.M.C. Stork, S.R. Mader, C.L. Stanes, G.J. Scilla and B.J. Ginsberg, *IEEE Electron Device Lett.* EDL-11 (1990) 288.
- [4] G.L. Patton, J.H. Comfort, B.S. Meyerson, E.F. Crabbé, G.J. Scilla, E.D. Frésart, J.M.C. Stork, J.Y.-C. Sun, D.L. Harame and J.N. Burghartz, *IEEE Electron Device Lett.* EDL-11 (1990) 171.
- [5] J.C. Sturm, E.J. Prinz and C.W. Magee, *IEEE Electron Device Lett.* EDL-12 (1991) 303.
- [6] R.D. Thompson, K.N. Tu, J. Angillelo, S. Delage and S.S. Iyer, *J. Electrochem. Soc.* 135 (1988) 3161.
- [7] T.L. Lin, T. George, E.W. Jones, A. Ksendozov and M.L. Huberman, *Appl. Phys. Lett.* 60 (1988) 380.
- [8] R. People, *Phys. Rev. B* 32 (1985) 1405.
- [9] H. Kanaya, F. Hasegawa, E. Yamaka, T. Moriyama and M. Nakajima, *Jpn. J. Appl. Phys.* 28 (1989) L544.
- [10] H.K. Liou, X. Wu, U. Gennser, V.P. Kesan, S.S. Iyer, K.N. Tu and E.S. Yang, *Appl. Phys. Lett.* 60 (1992).
- [11] R. People and J.C. Bean, *Appl. Phys. Lett.* 47 (1985) 322.
- [12] R. People and J.C. Bean, *Appl. Phys. Lett.* 48 (1986) 538.
- [13] D.R. Lide, *Handbook of Chemistry and Physics*, 72nd ed. (CRC Press, Boca Raton, FL) pp. 12–97.
- [14] T.S. Moss, *Handbook on Semiconductors*, Vol. 4 (North-Holland, Amsterdam) p. 5.
- [15] E.H. Rhoderick and R.H. Williams, *Metal–Semiconductor Contacts*, 2nd ed. (Oxford Science Publications) p. 15.



ELSEVIER

Applied Surface Science 104/105 (1996) 267–273



Characterization of cobalt–diamond (100) interfaces: electron affinity and Schottky barrier

P.K. Baumann^{*}, R.J. Nemanich

Department of Physics, North Carolina State University, Raleigh, NC 27695-8202, USA

Received 28 June 1995; accepted 5 October 1995

Abstract

UV photoemission measurements were used to relate the electron affinity and Schottky barrier of thin Co layers on diamond (100) surfaces. Cobalt films of 2 Å thickness were deposited on natural single crystal diamond (100) substrates by hot filament evaporation in ultra-high vacuum (UHV). The surfaces were characterized with auger electron spectroscopy and atomic force microscopy. The study explores the properties of the cobalt–diamond interface as a function of different surface cleaning procedures. Prior to deposition the diamond samples have been cleaned by UHV anneals at either 500°C or 1150°C. Following either of these anneals a positive electron affinity was deduced from the ultraviolet photoemission measurements. The measurements indicate that the surface annealed at 500°C is terminated with oxygen while the surface annealed at high temperature is free of adsorbates. Upon deposition of Co on the surface heated to 1150°C, a negative electron affinity (NEA) was detected, and a Schottky barrier height of 0.35 eV was measured. However, for Co films deposited on substrates annealed to 500°C a positive electron affinity and a Schottky barrier height of 1.45 eV were observed. The results are discussed in terms of a model that relates the electron affinity to the metal workfunction and the Schottky barrier.

1. Introduction

The electron affinity of a semiconductor surface is defined as the energy difference between the vacuum level and the conduction band minimum. For most materials the conduction band minimum lies below the vacuum level resulting in a positive electron affinity surface. For wide bandgap semiconductors like diamond the conduction band minimum is likely to be close to the vacuum level. Different surface treatments can induce or inhibit a NEA on diamond

surfaces [1–4]. Such treatments include annealing in UHV or plasma cleaning. Following a chemical etch the diamond (100) surface is terminated by oxygen. Chemisorbed oxygen forms a dipole layer on the surface that tends to increase the workfunction. Such a surface exhibits, therefore, a positive electron affinity. In addition it has been found that annealing the oxygen terminated diamond (100) crystals to 900–1050°C resulted in the removal of the oxygen which coincided with the appearance of a NEA and a 2×1 reconstructed surface [1,3,4]. We have found that different wet chemical pre-treatments raised or lowered the annealing temperature at which the chemisorbed oxygen was removed from the diamond (100) surface [1]. However heating these samples to

^{*} Corresponding author. Tel.: +1-919-5157530; fax: +1-919-5157331; e-mail: peter_baumann@ncsu.edu.

1150°C resulted in a positive electron affinity while the surface remained 2×1 reconstructed [4]. It has been proposed that the diamond surfaces are terminated by a monohydride following a 900–1050°C anneal. A monohydride on the diamond (100) surface changes the surface dipole such that the workfunction of the surface is lowered. Whereas the removal of hydrogen leads to a clean surface and an increase in the workfunction. Indeed, *ab initio* calculations for the 2×1 reconstructed surface indicate a NEA for the monohydride terminated surface and a positive electron affinity for the clean surface [3].

The deposition of a few Å of metals like Ti, Ni or Cu on diamond has also been shown to induce a NEA [5,6,1]. The presence of a NEA or positive electron affinity has been correlated with different structures of the metal–diamond interface. Indeed, metal–diamond interfaces exhibiting a NEA have been found to have lower Schottky barrier heights than those exhibiting a positive electron affinity [6]. Depositing a few Å of Ni on an Ar-plasma cleaned diamond (111) surface resulted in a NEA. A Schottky barrier height of 0.5 eV was measured for this interface. However, a positive electron affinity and a Schottky barrier height of 1.0 eV were found after growing a Ni layer of the same thickness on a hydrogen terminated diamond (111) surface.

A number of studies have dealt with Schottky barrier height measurements of metals deposited on (100) and (111) oriented diamond surfaces as well as polycrystalline diamond films [1,5–16]. It has been found that the Schottky barrier height of metals on diamond is virtually independent of the workfunction of the metal. But it has been reported that the Schottky barrier height clearly depends on the surface treatment of the diamond before metal deposition. In general, cleaning the diamond surfaces chemically in air results in a higher value for the Schottky barrier height than cleaning in vacuum.

Photoemission spectroscopy is very sensitive to determine whether a surface exhibits a NEA. Electrons from the valence band are photoexcited into states in the conduction band and some will quasi thermalize to the conduction band minimum. Indeed, these secondary electrons can escape freely from a NEA surface. The spectra then exhibit a sharp feature at the low kinetic energy end of photoemission [10,17].

In this study diamond (100) surfaces were cleaned by two different in vacuo heat treatments. Subsequent to Co deposition on these diamond substrates the effects of the different surface treatments on the Co–diamond interface were examined.

2. Experimental details

Several natural type IIb semiconducting diamond (100) crystals ($3.0 \times 3.0 \times 0.25$ mm) were used in this study. To remove non-diamond carbon and metal contaminants an electrochemical etch has been employed [18]. This cleaning step involved placing the diamond samples between two Pt electrodes in deionized (DI) water as an electrolyte. A dc voltage of 350 V was applied between the electrodes. A typical value for the current was 0.5 mA. The crystals were then exposed to UV/ozone and rinsed in a HF solution to clean the surface from SiO_2 contaminants. It has previously been reported that SiO_2 was present on the surface after an electrochemical etch [1]. Following this wet chemical cleaning step the samples were blown dry with N_2 . The wafers were mounted on a Mo holder and then transferred into the loadlock of the UHV system. This UHV system consists of several interconnected chambers including capabilities for annealing, metal deposition, UPS, AES and LEED.

Two different in vacuo cleaning processes were employed to assess the influence of surface preparation on the properties of the cobalt–diamond interface. One procedure involved annealing the samples to 500°C for 10 min. And the other involved a 1150°C anneal for 10 min. During the anneals the pressure increased to $\sim 8 \times 10^{-10}$ Torr and $\sim 7 \times 10^{-9}$ Torr, respectively. Before deposition on the substrate, 10 Å of Co was evaporated from the hot filament to clean surface contaminants from the source material. Then 2 Å of Co was deposited on the diamond substrates. The thickness was monitored by a quartz crystal oscillator. The pressure during deposition was typically $\sim 2 \times 10^{-9}$ Torr. The samples have been characterized by means of UPS, AES and LEED subsequent to the annealing and the deposition steps.

The presence of a cobalt layer was confirmed by AES. AFM images of the diamond wafers used in

this study clearly showed arrays of linear grooves parallel to each other. Typical depths of about 20 Å were observed for these grooves. This surface structure is due to the commercial surface polishing of the diamond samples. For both cases of growing Co on diamond samples annealed to 1150°C and on those heated to 500°C, the cobalt layers replicated the surface morphology of the underlying diamond substrates. Indeed Co grew as uniform films on the polishing grooves of the diamond surfaces (Fig. 1). A 1×1 unreconstructed LEED pattern was observed for the diamond samples subsequent to the 500°C anneal. Upon heating to 1150°C a 2×1 reconstruction was obtained.

The photoemission spectra were excited by HeI (21.21 eV) radiation. A 50 mm hemispherical analyzer was employed to measure the emitted electrons. In this study the energy resolution was 0.15 eV and the acceptance angle was 2° . To overcome the workfunction of the analyzer a bias of 1 V was applied to the sample. It was therefore possible to detect the low energy electrons emitted from the NEA surface. These electrons appear as a sharp peak at the low energy end of UPS spectra. The position of this feature corresponds to the energy position of

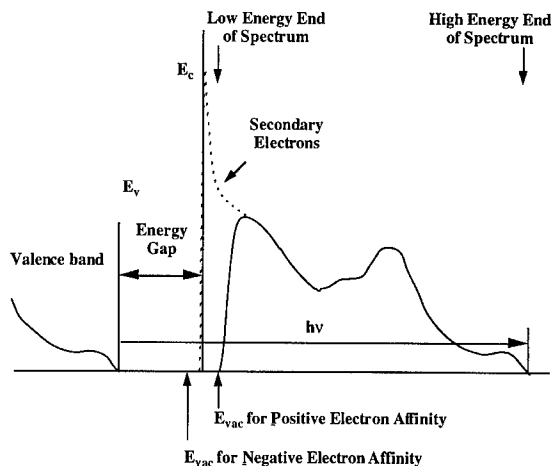


Fig. 2. Schematic diagram of photoemission spectra for a negative electron affinity surface (dotted line) and a positive electron affinity surface (solid line).

the conduction band minimum, E_c (Fig. 2). Electrons emitted from E_c appear at $E_v + E_G$ in the spectra, where E_v is the energy of the valence band maximum and E_G the bandgap energy. Furthermore, electrons from E_v get photoexcited to an energy level at $E_v + h\nu$ in the conduction band and are

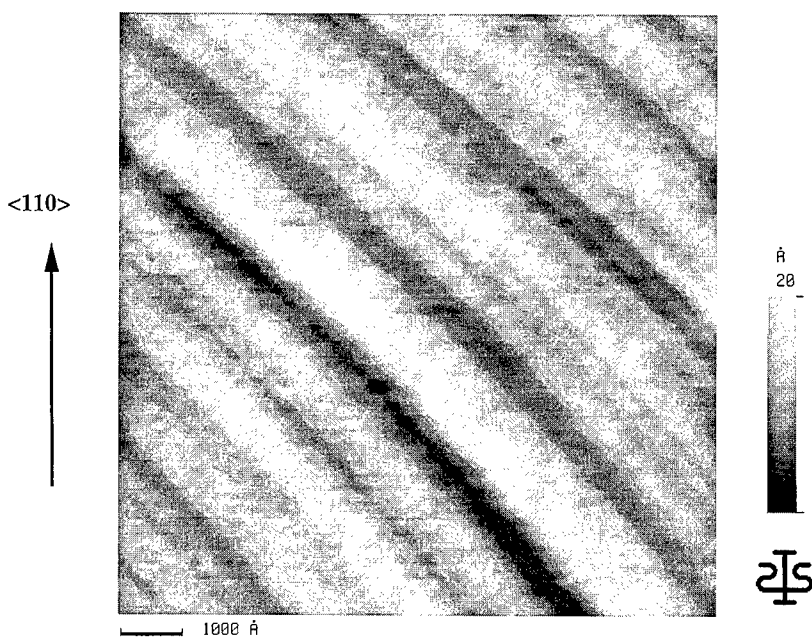


Fig. 1. AFM micrograph of 2 Å of Co deposited on diamond (100).

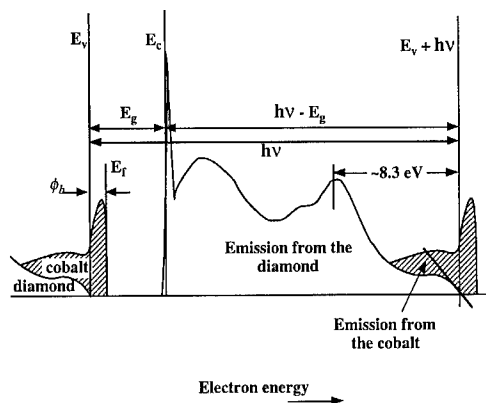


Fig. 3. Schematic diagram of photoemission spectra for cobalt deposited on diamond. The Schottky barrier height Φ_B is determined from the difference between the position of the valence band edge of diamond E_v and the metal Fermi level E_F .

obviously detected at $E_v + h\nu$ in UPS spectra. This corresponds to the high kinetic energy end of the spectra. Therefore the spectral width for a NEA surface is $h\nu - E_G$. Using the value of $h\nu = 21.21$ eV for HeI radiation and $E_G = 5.47$ eV for the bandgap of diamond, a spectral width of ~ 15.7 eV is obtained. For a surface with a positive electron affinity the low energy cutoff is determined by the vacuum level and will therefore be shifted to higher energies in the spectra compared to the case of a NEA surface. This results in a smaller value for the spectral width.

Photoemission spectra can also be used to determine the Schottky barrier height Φ_B . For p-type semiconductors like diamond, Φ_B corresponds to the difference between the position of the valence band edge, E_v , of the semiconductor and the Fermi level of the metal, E_F (Fig. 3). Since features from both the semiconductor and the metal need to be visible this method is only suitable for metal films with thicknesses equal to or less than the electron mean free path (≤ 5 Å). The relatively weak onset of emission at E_v may, however, be obscured by the metal Fermi level even for metal layers thinner than the mean free path. As an independent method E_v can be referenced to some strong features in the diamond spectrum before metal deposition. These features can still be detected following the overgrowth of a thin metal layer. Here we have chosen a peak positioned 8.3 eV below E_v . In case of a NEA

the position of the low energy turnon (which corresponds to E_c) can also be used as a reference point to find E_v (which is the high energy turnon of the spectrum). The distance between E_c and E_v has to be $h\nu - E_G$ (Fig. 3).

3. Results and discussion

Consider first the termination of the surfaces prior to Co deposition. The AES spectra of the as-loaded diamond samples showed peaks indicative of the presence of oxygen (Fig. 4). Upon heating the crystals to 500°C the oxygen features were only slightly reduced. However as a result of the 1150°C anneal the amount of oxygen on the diamond surface dropped below the detection limit of the AES instrument. Crystals annealed to 1150°C as well as those heated to 500°C exhibited a positive electron affinity as evidenced by UPS (Fig. 5 and Fig. 6). By referencing the low energy turnon to a bulk feature in the spectrum (feature A in Fig. 5 and Fig. 6) an electron affinity of $\chi \cong 0.65$ eV was determined for the surfaces free of adsorbates and an electron affinity of $\chi \cong 1.50$ eV for the oxygen terminated surfaces. Indeed, oxygen chemisorbed to the diamond surface is expected to induce a stronger surface dipole and therefore cause an increase in the workfunction in

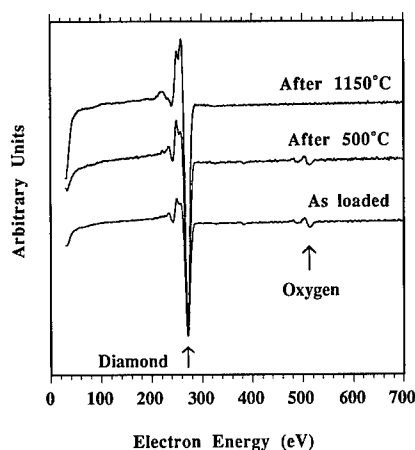


Fig. 4. AES spectra of diamond as a function of different surface cleaning processes. The as-loaded surface exhibits features indicative of oxygen which get only slightly reduced following a 500°C anneal. Subsequent to a 1150°C anneal the oxygen peak is removed.

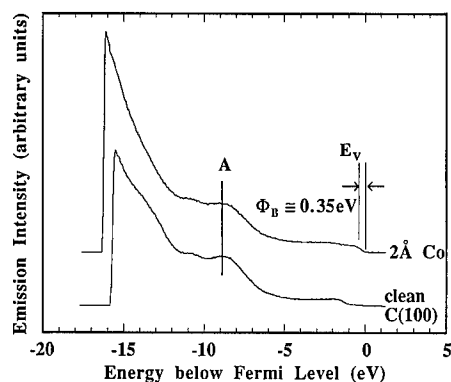


Fig. 5. UV photoemission spectra of diamond (100) following a 1150°C anneal and of Co deposited on diamond. A metal induced NEA is observed upon deposition of Co.

comparison with a clean surface. Our results are consistent with this.

Deposition of 2 Å of Co on the diamond samples heated to 1150°C induces a NEA. Indeed, the width of the UPS spectrum increased following the Co deposition (Fig. 4). Furthermore, a Schottky barrier height of $\Phi_B \approx 0.35$ eV was measured by means of UPS. The electron affinity of a p-type semiconductor subsequent to the formation of a Schottky barrier is given by [19]

$$\chi = (\Phi_M + \Phi_B) - E_G. \quad (1)$$

In our study $\Phi_M = 5.00$ eV is the workfunction of cobalt and $E_G = 5.47$ eV the bandgap of diamond.

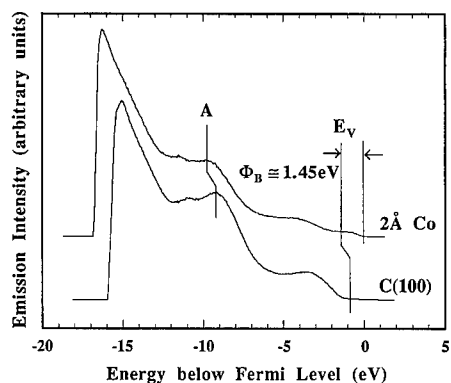


Fig. 6. UV photoemission spectra of diamond (100) following a 500°C anneal and of Co deposited on diamond. The diamond sample exhibits a positive electron affinity both after the 500°C anneal as well as the deposition of Co.

Using these values and the measured Schottky barrier height one can calculate an electron affinity of $\chi \approx -0.1$ eV. Indeed this is consistent with the experimental result of the formation of a NEA. In comparison, depositing 2 Å of Co on the diamond crystals annealed at 500°C resulted in a positive electron affinity, and the spectrum shifted ~ 0.6 V to lower energies (Fig. 6). Furthermore, a Schottky barrier height of $\Phi_B \approx 1.45$ eV was determined from the UPS spectra. By referencing the low energy turnon to a bulk peak in the spectrum an electron affinity of $\chi \approx 0.90$ eV was deduced for the cobalt diamond interface. Due to Co deposition the electron affinity was reduced by about 0.60 eV. From Eq. (1) an electron affinity of $\chi \approx 0.95$ eV is obtained for Co grown on oxygen terminated diamond surfaces. Again this result is in agreement with the experimental data.

The simple workfunction model described above (Eq. (1)) has been employed in previous studies to explain NEA or positive electron affinity effects of Ti or Ni deposited on diamond (111) surfaces [5,6]. Indeed it has been found that Ni grown on Ar plasma cleaned diamond (111) crystals induces a NEA, and a Schottky barrier height of 0.5 eV was measured. It has been demonstrated that an Ar plasma or a 950°C anneal can remove a NEA from a H plasma treated diamond (111) surface [2]. Therefore it has been proposed that an Ar plasma removes chemisorbed hydrogen and thus leads to a clean surface. However, depositing Ni on a hydrogen terminated diamond (111) surface resulted in a positive electron affinity. And a larger value for the Schottky barrier height ($\Phi_B \approx 1.0$ eV) was measured. Theoretical studies of the Ni–diamond interface have been performed by Erwin and Pickett [20–23] and Pickett et al. [24]. For the adsorbate free diamond (100) and (111) surfaces a Schottky barrier height of less than 0.1 eV was calculated for the most stable configurations. Lambrecht calculated the Schottky barrier height for copper on diamond (111) surfaces depending on the interface structure [25]. A Schottky barrier of less than 0.1 eV was determined for the clean surface and ≥ 1.0 eV for the hydrogen terminated surface. The values obtained for both Ni and Cu on clean surfaces are indeed similar. And these results indicate that the Schottky barrier depends on the interface termination.

We suggest that a 1150°C anneal removes chemisorbed atoms from sufficiently large portions of the diamond (100) surface, that a positive electron affinity is induced on the diamond surface itself, and that the Schottky barrier height due to metal deposition on this surface is significantly smaller than for metal deposition on a hydrogen or oxygen terminated surface. In fact the Schottky barrier height is small enough to result in a NEA from the metal–diamond interface. Furthermore, we note that an Ar plasma exposure or an anneal at 950°C of the diamond (111) surface has similar effects on the properties of the diamond surface and metal–diamond interface as a 1150°C anneal does pertaining to the diamond (100) surface [2,6]. In particular, the results on Co reported in this paper and the previous study on Ni clearly suggests that the value of the electron affinity is correlated with the Schottky barrier height. Metal–diamond interfaces with a lower Schottky barrier height also exhibit a lower electron affinity, and no clear dependence of the Schottky barrier height on the metal workfunction has been found. But the type of surface treatment of the diamond substrate prior to metal deposition is critical for the properties of the metal–diamond interface. It can be said that choosing an appropriate surface cleaning procedure is therefore crucial for obtaining a NEA. Treatments capable of removing chemisorbed atoms from diamond surfaces are necessary to obtain a minimum for both the Schottky barrier height and the electron affinity. Apparently a surface sufficiently free of adsorbates is necessary to minimize the Schottky barrier height enough to induce a NEA for most metals. Only metal–diamond interfaces with low workfunction metals such as Cs have been reported to exhibit a NEA for non adsorbate free diamond surfaces [26]. Overall, different types of surface treatments have been shown to influence the Schottky barrier height and the electron affinity significantly.

4. Conclusions

Thin cobalt films have been deposited on clean (after a 1150°C anneal) and oxygen terminated (following a 500°C anneal) diamond (100) substrates. Both the clean and oxygen terminated surfaces ex-

hibited a positive electron affinity as evidenced by UPS. A metal induced NEA has been detected and a Schottky barrier height of 0.35 eV was measured by means of UPS for the clean diamond samples. Cobalt deposited on oxygen terminated surfaces resulted in a positive electron affinity and a Schottky barrier height of 1.45 eV. Furthermore, the Co films were shown to be uniform. The results discussed here indicate that surface cleaning can have a significant impact on the properties of the metal–diamond interface.

Acknowledgements

This work was supported in part by the Office of Naval Research (Contract No. N00014-92-J-1477).

References

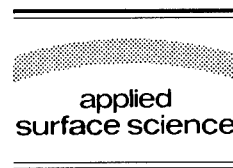
- [1] P.K. Baumann, T.P. Humphreys and R.J. Nemanich, in: *Diamond, SiC and Nitride Wide Bandgap Semiconductors*, Eds. C.H. Carter, G. Gildenblat, S. Nakamura and R.J. Nemanich, Mater. Res. Soc. Proc. 339 (MRS, Pittsburgh, PA, 1994) p. 69.
- [2] J. van der Weide and R.J. Nemanich, *Appl. Phys. Lett.* 62 (1993) 1878.
- [3] J. van der Weide, Z. Zhang, P.K. Baumann, M.G. Wensell, J. Bernholc and R.J. Nemanich, *Phys. Rev. B* 50 (1994) 5803.
- [4] P.K. Baumann and R.J. Nemanich, in: *Proc. 5th Eur. Conf. on Diamond, Diamond-like and Related Materials*, Eds. P.K. Bachmann, I.M. Buckley-Golder, J.T. Glass and M. Kamo, *J. Diamond Rel. Mater.* 4 (1995) 802.
- [5] J. van der Weide and R.J. Nemanich, *J. Vac. Sci. Technol. B* 10 (1992) 1940.
- [6] J. van der Weide and R.J. Nemanich, *Phys. Rev. B* 49 (1994) 13629.
- [7] P.K. Baumann, T.P. Humphreys, R.J. Nemanich, K. Ishibashi, N.R. Parikh, L.M. Porter and R.F. Davis, in: *Proc. 4th Eur. Conf. on Diamond, Diamond-like and Related Materials*, Eds. P.K. Bachmann, I.M. Buckley-Golder, J.T. Glass and M. Kamo, *J. Diamond Rel. Mater.* 3 (1994) 883.
- [8] C.A. Mead and T.C. McGill, *Phys. Lett. A* 58 (1976) 149.
- [9] F.J. Himpsel, D.E. Eastman and J.F. van der Veen, *J. Vac. Sci. Technol.* 17 (1980) 1085.
- [10] F.J. Himpsel, P. Heimann and D.E. Eastman, *Solid State Commun.* 36 (1980) 631.
- [11] J.W. Glesener, A.A. Morrish and K.A. Snail, *J. Appl. Phys.* 70 (1991) 5144.
- [12] M.W. Geis, D.D. Rathman, D.J. Ehrlich, R.A. Murphy and W.T. Lindley, *IEEE Electron Device Lett.* EDL-8 (1987) 341.

- [13] H. Shiomi, H. Nakahata, T. Imai, Y. Nishibayashi and N. Fujimori, *Jpn. J. Appl. Phys.* 28 (1989) 758.
- [14] T. Tachibachi, B.E. Williams and J.T. Glass, *Phys. Rev. B* 45 (1992) 11975.
- [15] M.C. Hicks, C.R. Wronski, S.A. Grot, G.S. Gildenblat, A.R. Badzian, T. Badzian and R. Messier, *J. Appl. Phys.* 65 (1989) 2139.
- [16] S.A. Grot, S. Lee, G.S. Gildenblat, C.W. Hatfield, C.R. Wronski, A.R. Badzian, T. Badzian and R. Messier, *J. Mater. Res.* 5 (1990) 2497.
- [17] B.B. Pate, W.E. Spicer, T. Ohta and I. Lindau, *J. Vac. Sci. Technol.* 17 (1980) 1087.
- [18] M. Marchywka, P.E. Pehrsson, S.C. Binari and D. Moses, *J. Electrochem. Soc.* 140(2) (1993) L19.
- [19] E.H. Rhoderick and R.H. Williams, *Metal–Semiconductor Contacts* (Clarendon, Oxford, 1988).
- [20] S.C. Erwin and W.E. Pickett, *Surf. Coat. Technol.* 47 (1991) 487.
- [21] S.C. Erwin and W.E. Pickett, *Solid State Commun.* 81 (1992) 891.
- [22] W.E. Pickett and S.C. Erwin, *Phys. Rev. B* 41 (1990) 9756.
- [23] W.E. Pickett and S.C. Erwin, *Superlatt. Microstruct.* 7 (1990) 335.
- [24] W.E. Pickett, M.R. Pederson and S.C. Erwin, *Mater. Sci. Eng. B* 14 (1992) 87.
- [25] W.R.L. Lambrecht, *Physica B* 185 (1993) 512.
- [26] M.W. Geis, personal communication.



ELSEVIER

Applied Surface Science 104/105 (1996) 274–281



Hot-electron scattering at Au/Si(100) Schottky interfaces measured by temperature dependent ballistic electron emission microscopy

C.A. Ventrice Jr., V.P. LaBella, G. Ramaswamy¹, H.-P. Yu, L.J. Schowalter^{*}

Department of Physics, Rensselaer Polytechnic Institute, Troy, NY 12180, USA

Received 28 June 1995; accepted 1 September 1995

Abstract

Ballistic electron emission microscopy (BEEM) measurements have been performed on n-type Au/Si(100) interfaces as a function of STM tip bias, Au film thickness, and temperature. From these measurements, the attenuation length, λ_a , of the BEEM electrons in the metal overlayer has been determined to be $133 \pm 2 \text{ \AA}$ at room temperature (RT) and $147 \pm 6 \text{ \AA}$ at 77 K for tip biases from -1.20 V to -0.92 V . The ratio of the zero thickness BEEM transmittances at 77 K to that at RT, $I_0(77 \text{ K})/I_0(\text{RT})$, was determined to be 1.79 ± 0.09 . Within the experimental uncertainties of these measurements, no energy dependence of λ_a or $I_0(77 \text{ K})/I_0(\text{RT})$ was observed. The large increase in the BEEM transmittance and the relatively small increase in λ_a at 77 K indicate that the primary temperature dependent scattering mode affecting BEEM electron transport is phonon absorption in the Si substrate. Images with large reductions in the BEEM current at topographic locations which have a large surface gradient have been obtained at RT. Our calculations, which assume that the probability of transmission across the interface is independent of the electron's transverse momentum, correlate well with the experimentally observed reductions. This result indicates that the BEEM electrons remain forward focused with very little broadening as they pass through the Au overlayer, and also implies that strong scattering must occur at the Au/Si interface to explain the previously documented non-conservation of transverse momentum at Au/Si interfaces.

1. Introduction

The growth of Au/Si interfaces has been studied extensively for more than 20 years. The initial interest in these interfaces was for the production of metal/Si contacts for integrated circuits. Although

Au has proven to be an unsuitable candidate for device fabrication since it is a fast diffuser in Si at room temperature (RT), the growth morphology and electronic properties of Au/Si interfaces are still a topic of current interest within the scientific community for many fundamental reasons. For instance, Au has a relatively simple electronic structure, a lone 6s electron in its outer shell and a filled inner 5d shell, which makes it an ideal candidate for modeling metal–semiconductor (M-S) Schottky barrier formation and hot-electron transport properties. Since Au

^{*} Corresponding author. Tel.: +1-518-2766435; fax: +1-518-2768761; e-mail: schowalt@unix.cie.rpi.edu.

¹ Present address: Department of Physics, Indian Institute of Science, Bangalore 560012, India.

is a noble metal, it also provides an advantage over most metals in that it can be characterized under ambient conditions.

In this paper, we report ballistic electron emission microscopy (BEEM) measurements which were performed to determine the relative importance of temperature dependent scattering mechanisms on hot-electron transport across Au/Si(100) interfaces. BEEM is a scanning tunneling microscopy (STM) based technique where the STM tip is used as a very narrow, tunable, forward-focused electron source for injection into the metal overlayer [1]. By collecting the current which passes through the metal into the semiconductor as a function of tip position and tip bias, information about the local Schottky barrier height and the hot-electron transport properties can be obtained on a nanometer scale. However, to properly interpret the interfacial images obtained with BEEM, a fundamental understanding of the scattering processes within the metal overlayer, at the metallurgical interface, and within the Si substrate is essential.

Although Au/Si has been the most thoroughly studied interface with the BEEM technique, it has also proved to be one of the most controversial interfaces. In the first BEEM studies of Au/Si(100) by Bell and Kaiser [1], excellent agreement was obtained between their spectroscopy data and calculated curves which were derived assuming ballistic transport through the metal overlayer and transverse momentum conservation at the interface. However, Schowalter and Lee [2] made the observation that the BEEM spectra for both the Si(100) and Si(111) substrates have similar line shapes and current onsets which was unexpected since transport into the Si(111) surface requires a large transverse crystal momentum component while transport into the Si(100) surface does not. Monte Carlo simulations of the BEEM spectra were performed which indicated that strong elastic scattering in the Au overlayers resulted in a near isotropic momentum distribution at the M-S interface and an inherent loss of spatial resolution at the interface. A subsequent microscopy study by Lee et al. [3], which found no correlation between surface gradients and the measured BEEM current, gave support to their previous Monte Carlo calculations. In contrast to these results, a microscopy study of Au overlayers deposited on patterned SiO₂ structures

grown on Si observed transitions in the BEEM current over spatial distances of ~ 10 Å which indicated that the transport through the metal overlayer is essentially ballistic [4]. To complicate matters further, a microscopy study by Fernandez et al. [5] found that for Au/Si interfaces grown under ultra-high vacuum (UHV) conditions on bare Si and imaged in air, no BEEM current could be detected. They interpreted the lack of BEEM current to the formation of a disordered Au–Si alloy at the interface which resulted in strong scattering of the BEEM electrons. However, a recent BEEM study by Cuberes et al. [6] of Au/Si(111) samples prepared and imaged under UHV conditions found that BEEM currents could be obtained at tip biases as large as 8 eV with no apparent modification of the interface. Their photoemission results also indicated that the Au/Si interface formed at RT is an abrupt interface with a silicide-like surface segregation layer.

Although the experimental evidence for non-conservation of transverse momentum is quite strong for Au/Si [2] and Pd/Si [7] interfaces, the precise nature of the scattering mechanism is not well understood. It would seem that symmetry breaking parallel to the interface would be a sufficient condition for violation of transverse momentum conservation since these are non-epitaxial systems. On the other hand, microscopy and spectroscopy studies of Au/GaP(110) [8] and Mg/GaP(110) [8,9] which are non-epitaxial and also non-abrupt interfaces have obtained good agreement between curves fitted with a transverse momentum conserving model and their experimental data.

To better understand the scattering mechanisms at Au/Si interfaces, we have performed a temperature dependent BEEM spectroscopy and RT BEEM microscopy study on the Au/Si(100) interface. Our spectroscopy data indicate that there is a large temperature dependence to the measured BEEM transmittance yet only a small temperature dependent change in the attenuation length, λ_a , of the hot-electrons in the Au overlayers which indicates that the primary temperature dependent scattering mechanism is phonon scattering in the Si substrate. Within the uncertainty of the measurement of λ_a , no energy dependence was observed at RT or 77 K. This result and the aforementioned relatively small temperature dependence of λ_a indicate that the mean free path

for scattering from defects in the Au overlayer is much smaller than that for inelastic electron–electron scattering or for quasi-elastic electron–phonon scattering. Evidence for reductions in the BEEM current for large surface gradients has been obtained for microscopy images taken with sufficiently sharp STM tips and correlated with the increase in path length to the interface, assuming that the probability of transmission is independent of incident angle. This result provides strong evidence that the electron transport through the Au overlayer is essentially ballistic and that violation of transverse momentum conservation occurs at the interfacial region.

2. Hot-electron scattering processes

A schematic of BEEM electron transport across a M-S Schottky interface is shown in Fig. 1. Electrons injected into the metal overlayer from the STM tip will have an energy distribution which decays exponentially from a maximum value of eV_T . All electrons which approach the semiconductor region with an energy which is less than the Schottky barrier

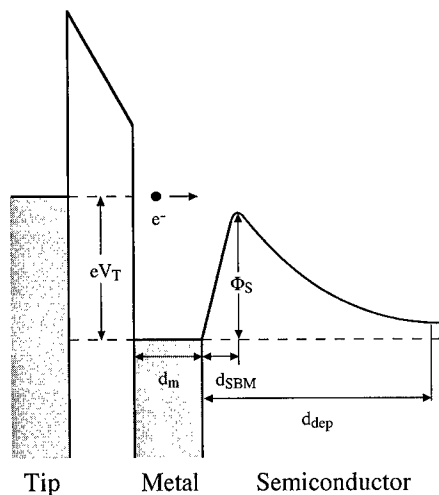


Fig. 1. Schematic of BEEM electron transport across a metal–semiconductor Schottky interface (not drawn to scale). For electrons injected into the metal overlayer with a tip bias, V_T , greater than the Schottky barrier, Φ_S , a fraction of the injected electrons will travel across the barrier and be detected as a BEEM electron. The magnitude of the BEEM current is strongly influenced by scattering processes in the metal overlayer, at the metallurgical interface, and within the semiconducting substrate.

height, Φ_S , will be scattered back into the metal. A fraction of the electrons which approach the semiconductor region with an energy greater than Φ_S will travel across the barrier and be detected as a BEEM electron. The magnitude of the collected BEEM current is strongly influenced by scattering mechanisms in the metal overlayer, at the metallurgical interface, and within the semiconducting substrate. In the metal overlayer, electrons can scatter elastically off defect sites or quasi-elastically from acoustic phonons. Electrons can also undergo inelastic electron–electron collisions with electrons near the Fermi level which results in an energy loss of approximately half of their original kinetic energy. At the M-S interface, a fraction of the incident electrons will backscatter into the metal overlayer due to quantum mechanical reflection. For non-epitaxial systems and non-abrupt interfaces, there will also be a break in symmetry parallel to the interface which will result in additional scattering at the interface. Within the Si substrate, electrons can scatter off both acoustic and optical phonons back towards the M-S interface. As shown in Fig. 1, the position of the Schottky barrier maximum is not at the metallurgical M-S interface but shifted into the semiconducting region. This effect is due to the image force. For the 2–4 Ω cm samples used in this experiment, the distance to the Schottky barrier maximum, d_{SBM} , is calculated to be ~ 50 Å, and the depletion depth, d_{dep} , is calculated to be 0.84 μ m. Electrons just over the energy threshold for transmission which excite a phonon in the region before d_{SBM} will have a high probability of reentering the metal region since this excitation is an energy loss process for the electron. However, for phonon excitation and absorption beyond d_{SBM} the electron may travel either towards or away from the metallurgical interface since the position dependence of the conduction band minimum is very gradual for the doping density of the samples used in this experiment.

For metal overlayers more than a few monolayers thick, Φ_S , d_{dep} , and d_{SBM} are expected to be coverage independent. Therefore, the BEEM current can be expressed as a product of the transmissivities through the metal overlayer, across the metallurgical interface, and through the semiconductor depletion region. The proportion of electrons with energy, E , which traverse the metal region will decay exponen-

tially with the path length to the metallurgical interface, $d_m/\cos(\theta)$, where θ defines the injection angle from the surface normal. This results in the following expression for the measured BEEM current,

$$I_B(E, T, d_m) = I_{\text{tip}} A(E) B(E, T) \times \exp[-d_m/\lambda_a(E, T) \cos(\theta)], \quad (1)$$

where $A(E)$ is a kinematic transmission factor for electron transport from the metal overlayer into the semiconductor lattice, $B(E, T)$ is the transmission factor for electron through the semiconductor depletion region, and I_{tip} is the tunnel current into the metal overlayer. The factor $A(E)$ is assumed to be independent of incident angle, which results from the assumption of non-conservation of transverse momentum at the interface [2]. Both $B(E, T)$ and $\lambda_a(E, T)$ should be temperature dependent since the path length for phonon absorption will depend strongly on the phonon populations in the metal and semiconductor regions.

3. Experimental

The BEEM measurements were performed with a modified Kaiser–Jaklevic STM design [10] which has three, separate, orthogonal, planar piezo drives for tip control and uses a stepper motor for the fine approach of the sample. The STM is housed in a liquid nitrogen (LN_2) dewar which is incorporated into a glove box. To perform low temperature BEEM, the dewar is purged with high-purity N_2 before backfilling with LN_2 . Since the performance characteristics of the operational amplifiers and the feedback resistors of the tip and BEEM current amplifiers can be affected by immersion in LN_2 , the amplifiers are mounted outside of the dewar on the STM support flange. Low temperature compatible ultra-thin coax [11] is used to carry the signals to the amplifiers. The outer insulating sheath of the coax was also removed to improve the flexibility of the coax at low temperatures.

The Au/Si(100) Schottky diodes were prepared from n-type 2–4 Ω cm Si. An Ohmic contact was applied to the back of each sample by melting indium onto an area of the sample which had been

roughened with a diamond scribe. The oxide of the Si was removed by dipping the samples in a solution of 10:1 ethanol:HF solution for 1–2 min. After removal from the etching solution, the samples were dried with high-purity N_2 before insertion into a cryopumped evaporation unit. The Au was evaporated from a tungsten thermal boat source through a shadow mask to form a rectangular 2.5 mm \times 10 mm diode. The nominal deposition rate was ~ 0.5 Å/s and was monitored with a quartz crystal microbalance. The base pressure of the evaporation unit is $\sim 10^{-8}$ Torr with a typical evaporation pressure of $\sim 5 \times 10^{-7}$ Torr. Calibration of the Au overlayer coverages measured with the quartz crystal microbalance was performed periodically using Rutherford backscattering at a separate facility.

Au and Pt–Ir (90:10) STM tips were chosen for the BEEM measurements since they do not form a native oxide under ambient conditions. The Au tips were prepared from 0.25 mm diameter wire either by DC electrochemical etching in a 50:50 HCl:ethanol solution or by cleaving at a very sharp angle with a razor blade. Etching produced very sharp whisker-like tips, as examined under an optical microscope. However, instabilities in the tunnel current during the fine sample approach were often observed for etched tips which we correlated to the poor mechanical rigidity of the whisker-like tip structures. Since cleaved tips did not exhibit instabilities during the fine approach, this was the primary method used for making Au tips. The STM images from both etched and cleaved Au tips produced similar topographies. The Pt–Ir tips were prepared from 0.50 mm diameter wire by cutting the wire at a very sharp angle with ordinary wire snippers.

4. Results

4.1. Temperature dependent BEEM spectroscopy

Ballistic electron emission spectroscopy (BEES) spectra were obtained at both RT and 77 K over a range of Au overlayer thicknesses from ~ 66 Å to ~ 339 Å. A semilog plot of the percent transmittance ($I_B/I_T \times 100$) as a function of Au overlayer thickness at a tip bias of -1.2 V is shown in Fig. 2. A minimum of 100 spectra were collected over a

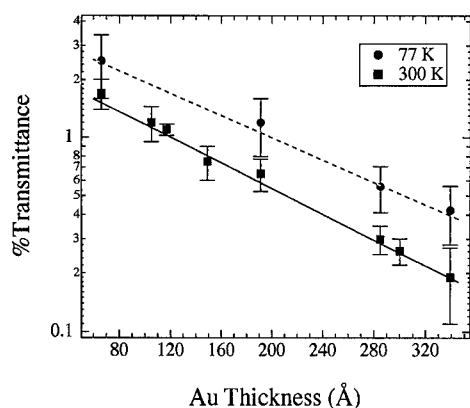


Fig. 2. Semilog plot of BEEM transmittances ($I_B/I_T \times 100$) at a tip bias of -1.2 V measured on several Au/Si(100) samples at 77 K (circles) and RT (squares). A minimum of 100 spectra were collected at each coverage and temperature. The linear curves through the data sets represent least-squares fits applied to the data. From the slope and intercept of these curves, the attenuation length of the electrons in the Au overlayer, λ_a , and the zero thickness transmittance, I_0 , are determined.

surface area of $\sim 2000 \text{ Å} \times \sim 2000 \text{ Å}$ for each coverage and temperature. A histogram of the transmittances was plotted for each data set, and the value of the average transmittance was derived by fitting a Gaussian to each histogram with the error bars representing the FWHM. For coverages with both a 77 K and RT transmittance, both data sets were collected from the same sample within 6 h of each other (RT data collected first). The linear curves through the data sets represents least-squares fits applied to the data. Since averaging over such large data sets should eliminate any effects of surface gradient on the transmissivity, λ_a can be obtained from the inverse of the slope of the least squares fit, and the zero length transmittance, $I_0(E, T)$, which is the product of $A(E)$ and $B(E, T)$, are obtained from the intercept.

The absolute value of $A(E)$ and $B(E, T)$ cannot be determined independently from our measurements. However, the temperature dependence of $B(E, T)$ can be determined by calculating $I_0(E, 77 \text{ K})/I_0(E, \text{RT})$ since $A(E)$ is expected to be independent of temperature. A 50 meV increase in Φ_s is measured at 77 K due to the increase in the band gap of Si at low temperatures; therefore, the ratio $I_0(E, 77 \text{ K})/I_0(E, \text{RT})$ was calculated for constant kinetic energy in the Si conduction band and resulted in a

value of 1.79 ± 0.09 over a kinetic energy range of 140 meV to 380 meV. A plot of the energy dependence of λ_a measured at both RT and 77 K is shown in Fig. 3. With our instrumentation, λ_a could only be measured accurately to a value of ~ 100 meV above Φ_s . A value of $133 \pm 2 \text{ Å}$ and $147 \pm 6 \text{ Å}$ were measured for λ_a at RT and 77 K, respectively, which agrees qualitatively with the previously measured value for λ_a at RT of 125 Å [12]. No energy dependence for λ_a was observed within the uncertainty of the measurements at either temperature.

4.2. Room temperature BEEM imaging

Although our spectroscopy data, which measured only an $\sim 11\%$ increase in λ_a at 77 K, indicate that quasi-elastic scattering from acoustic phonons in the Au overlayer has a negligible effect on the temperature dependent transmission probability, this does not preclude the possibility that elastic scattering will affect the trajectory of the electrons in the metal overlayer. Therefore, a detailed BEEM microscopy analysis of several Au/Si(100) samples was performed with both Au and Pt–Ir STM tips in an attempt to correlate surface topographic features with changes in the BEEM current. Since electron injection over a surface topographic feature with a non-zero gradient will increase the path length to the M–S

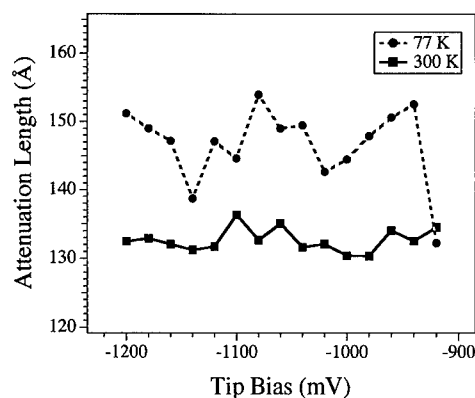


Fig. 3. Plot of the attenuation length of the BEEM electrons in the Au overlayer at both 77 K (circles) and RT (squares) as a function of tip bias. Only a slight temperature dependence to λ_a is observed, $\lambda_a(300 \text{ K}) = 133 \pm 2 \text{ Å}$ and $\lambda_a(77 \text{ K}) = 147 \pm 6 \text{ Å}$. Within the experimental uncertainties of these measurements, no energy dependence of λ_a is observed.

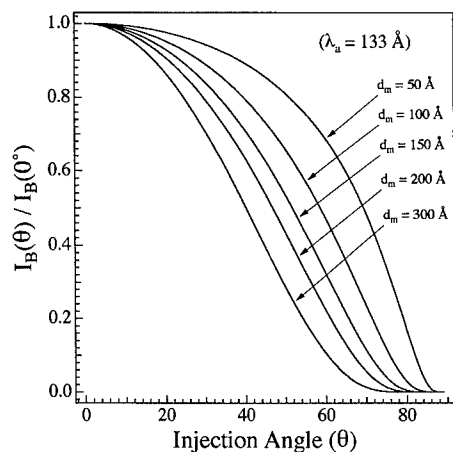


Fig. 4. Calculation of the reduction of BEEM current (I_B) that results from the increase in path length to the M-S interface for non-zero injection angles. This calculation assumes that any electron reaching the M-S interface is equally likely to cross it regardless of its momentum parallel to the interface.

interface, it is expected that reductions in the BEEM current should be observed at large surface gradients. This effect is often called the 'search-light effect'. A calculation of the expected reduction in the BEEM current as a function of injection angle is shown in Fig. 4. This calculation assumes that the probability of transmission across the Schottky barrier is independent of the incident angle, i.e. transverse momentum is not conserved at the interface. For thin Au overlayers, a very large surface gradient is needed to observe appreciable decreases in I_B (for a 50 Å overlayer, a gradient of $\sim 70^\circ$ is needed to observe a 50% reduction in I_B). At larger Au overlayer thicknesses, I_B is more sensitive to surface gradient (for a 300 Å overlayer, a gradient of $\sim 40^\circ$ is needed to observe a 50% reduction in I_B), but the magnitude of I_B is near the limit of detection.

From analysis of our BEEM data measured with Au tips and Pt–Ir tips, it was determined that the tip apex geometry is the primary factor which influences the spatial resolution of BEEM. For imaging with Au tips, tip geometry changes were often observed during STM scans and often resulted in featureless images which we correlate to an extremely blunt tip apex. Imaging with Pt–Ir tips produced much more consistent STM topographies. For the range of Au overlayer thickness in this study, rounded surface features with a spatial extent of ~ 50 Å to ~ 200 Å

and heights from ~ 30 Å to ~ 80 Å were observed. Since surface gradients large enough to observe appreciable changes in the BEEM current exist only near the bottom of the crevices between these rounded

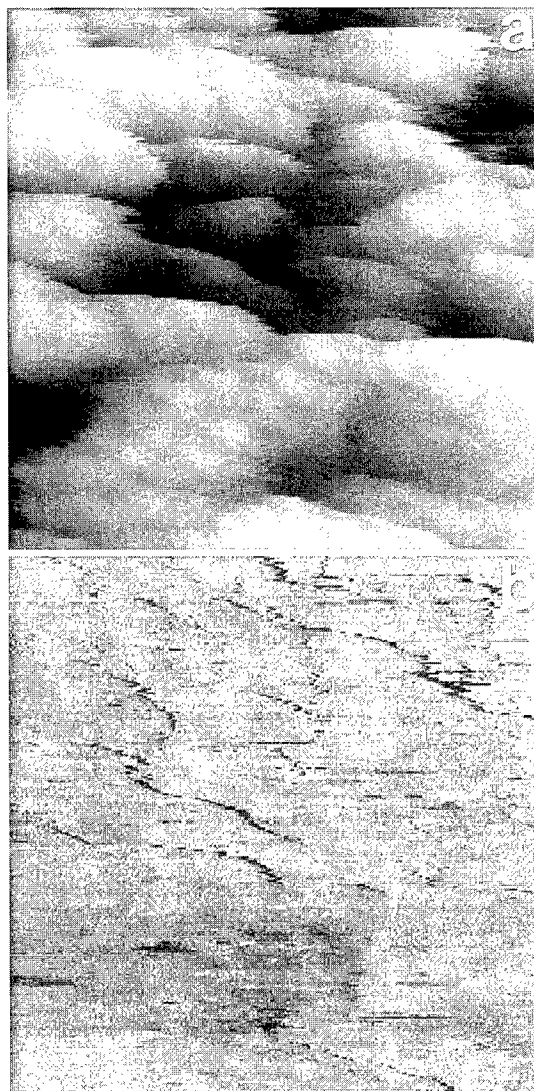


Fig. 5. (a) STM topographic image of a ~ 500 Å \times ~ 500 Å area of a 103 Å Au/Si(100) sample ($V_T = -1.2$ V and $I_T = 5$ nA). (b) BEEM image taken simultaneously with the topography image shown in (a). The grey scale range for the BEEM image is 0–120 pA with dark areas representing low BEEM current. The grey scale range for the STM image is 120 Å with light areas representing high surface features. Surface gradients as high as $\sim 75^\circ$ are observed in the STM image and correlate to regions of the BEEM image with an $\sim 85\%$ reduction in the BEEM current.

structures, a sharp tip protrusion which is longer than the average height of the rounded surface structures is needed to probe these regions. A BEEM image of a $\sim 500 \text{ \AA} \times \sim 500 \text{ \AA}$ area of a 103 \AA Au/Si(100) sample imaged with a Pt–Ir tip is shown in Fig. 5. Asymmetric surface features are observed in the STM topography shown in Fig. 5a with surface gradients as large as $\sim 75^\circ$ being measured. The corresponding BEEM image shown in Fig. 5b shows regions of reduced BEEM current of up to $\sim 85\%$ which correlate with the regions of the STM topography where high surface gradients were measured. During collection of the data, the reductions in the BEEM current were observed for both scan directions which indicates that this effect does not result from the tracking of the feedback control system. Images performed below the Schottky barrier height were also featureless which precludes the possibility that the features observed are due to a coupling of the BEEM current with the signals from the piezo-electric drives.

5. Discussions

The exponential dependence of the transmissivity plots at both 77 K and RT shown in Fig. 2 gives strong evidence that the attenuation length model, Eq. (1), is valid for Au overlayers over the range of $\sim 66 \text{ \AA}$ to $\sim 339 \text{ \AA}$. The observation that the attenuation length in the metal and the transmissivity through the semiconductor depletion region are temperature dependent is expected since the phonon populations in both regions should decrease as a function of temperature. To estimate the relative interaction lengths of both elastic and inelastic scattering events in the metal overlayer, both the temperature and the energy dependence of λ_a must be taken into account. Assuming that an electron is scattered isotropically for an elastic scattering event, the attenuation length of the BEEM electrons in the metal overlayer can be expressed as $1/\lambda_a = 1/\lambda_i + 1/\lambda_c$. Since the probability of electron–electron scattering is theoretically predicted to have a $1/E^2$ dependence [13], the lack of energy dependence for λ_a indicates that the path length for inelastic scattering is much larger than that for elastic scattering. The relatively

small $\sim 11\%$ increase in λ_a at 77 K also gives indication that the path length for elastic scattering from defect sites is considerably smaller than the path length for quasi-elastic phonon scattering. Since RT-grown Au/Si(100) is a non-epitaxial system with a very large lattice mismatch ($\sim 25\%$), it is expected that the metal overlayer will have a very large defect density during the first several layers of growth which, indeed, has been observed in a previous low energy electron diffraction (LEED) study of RT-grown Au/Si interfaces [14].

The measurement of almost double the transmissivity through the depletion region of the Si at 77 K is in direct contradiction with previous calculations which have predicted only an $\sim 15\%$ increase in the transmissivity for Au/Si at 77 K [15,16]. Both studies modeled the temperature dependent collection efficiency in the depletion region as due to electron interactions only with the optical phonon modes in Si. Although it is expected that the coupling of electrons to the optical phonon modes should be stronger than that for the acoustic modes in this energy range, the population of acoustic phonons is significantly higher than the population of optical phonons at room temperature ($E_{TO} \sim 57 \text{ meV}$, $E_{TA} \sim 20 \text{ meV}$). Therefore, neglecting the acoustic phonon scattering modes in these calculations is the most probable origin of the large discrepancy.

The observation of nearly featureless BEEM images of Au/Si(100) by several groups is most certainly an effect of tip apex geometry. Although we have obtained images which show clear evidence for the search-light effect, the great majority of images taken with both Au and Pt–Ir tips also do not show this effect. In addition, the lifetime of the tips with an apex that allows imaging of the ‘search-light effect’ are typically limited to a fraction of a BEEM scan (a typical BEEM scan takes $\sim 15 \text{ min}$ for our microscope). This is presumably due to the delicate nature of such a sharp protrusion. Although, the quality of Au tips for imaging was found to be inferior to Pt–Ir tips, the contrary was true for spectroscopy. Tip contamination problems were not encountered very often for either Au or Pt–Ir tips at RT; however, large instabilities in the tunneling current were often observed when using Pt–Ir tips at 77 K. Therefore, all of the spectroscopy data reported in this paper were taken using Au STM tips.

6. Conclusions

The approximately two-fold increase in the zero length BEEM transmittance at 77 K that has been measured indicates that previous analytical calculations [15,16] of this effect have underestimated the importance of acoustic phonon scattering in the semiconductor region. In addition, the lack of energy dependence of λ_a at both RT and 77 K and the relatively small 11% increase in λ_a at 77 K indicate that the predominant hot-electron scattering mode in the Au overlayer is from defect scattering for the range of thicknesses measured in this study.

The observation of the 'search-light effect' for Au/Si(100) gives very strong evidence that BEEM electron transport through the metal overlayer is essentially ballistic at energies up to 1.2 eV. The good agreement between the experimentally observed and the calculated reductions in the BEEM current using a model which assumes the transmission probability across the metal/semiconductor interface is independent of incident angle also gives strong indications that violation of transverse momentum conservation results from scattering at the metallurgical interface.

Acknowledgements

The technical support provided by Wolf Nadler in the design of the BEEM electronics is gratefully acknowledged. We would also like to thank Hitesh

Dholakia and Anthony Chan for the assistance that they provided in the development of our BEEM imaging software. This work is supported in part by the U.S. Air Force through Rome Laboratories at Hanscom AFB and the Office of Naval Research (ONR).

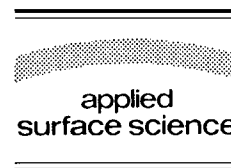
References

- [1] L.D. Bell and W.J. Kaiser, *Phys. Rev. Lett.* 61 (1988) 2368.
- [2] L.J. Schowalter and E.Y. Lee, *Phys. Rev. B* 43 (1991) 9308.
- [3] E.Y. Lee, B.R. Turner, L.J. Schowalter and J.R. Jimenez, *J. Vac. Sci. Technol. B* 11 (1993) 1579.
- [4] A.M. Milliken, S.J. Manion, W.J. Kaiser, L.D. Bell and M.H. Hecht, *Phys. Rev. B* 46 (1992) 12826.
- [5] A. Fernandez, H.D. Hallen, T. Huang, R.A. Buhrman and J. Silcox, *Appl. Phys. Lett.* 69 (1990) 2679.
- [6] M.T. Cuberes, A. Bauer, H.J. Wen, D. Vandr , M. Prietsch and G. Kaindl, *J. Vac. Sci. Technol. B* 12 (1994) 2422.
- [7] R. Ludeke and A. Bauer, *Phys. Rev. Lett.* 71 (1993) 1760.
- [8] A. Bauer, M.T. Cuberes, M. Prietsch and G. Kaindl, *Phys. Rev. Lett.* 71 (1993) 149.
- [9] M. Prietsch and R. Ludeke, *Phys. Rev. Lett.* 66 (1991) 2511.
- [10] W.J. Kaiser and R.C. Jaklevic, *Surf. Sci.* 181 (1987) 55.
- [11] Lake Shore Cryotronics, C-1 coax cable, part No. 9002-002-025.
- [12] L.D. Bell, W.J. Kaiser, M.H. Hecht and L.C. Davies, in: *Scanning Tunneling Microscopy*, Eds. J.A. Stroscio and W.J. Kaiser (Academic Press, Boston, MA, 1993) ch. 7.
- [13] S.M. Sze, J.L. Moll and T. Sugano, *Solid State Electron.* 7 (1964) 509.
- [14] K. Oura and T. Hanawa, *Surf. Sci.* 82 (1979) 202.
- [15] C.R. Crowell and S.M. Sze, *Solid State Electron.* 8 (1965) 979.
- [16] E.Y. Lee and L.J. Schowalter, *J. Appl. Phys.* 70 (1991) 2156.



ELSEVIER

Applied Surface Science 104/105 (1996) 282–285



Valence band of $\text{Cd}_{1-x}\text{Fe}_x\text{Se}/\text{Fe}$ in resonant photoemission spectra

B.A. Orlowski ^{a,*}, B.J. Kowalski ^a, N. Barrett ^b, D. Martinotti ^b, C. Guillot ^b,
J.-P. Lacharme ^c, C.A. Sébenne ^c

^a Institute of Physics, Polish Academy of Sciences, Al. Lotnikow 32 / 46, 02668 Warszawa, Poland

^b Laboratoire pour l'Utilisation du Rayonnement Electromagnétique, Bât. 209 D, Centre Universitaire Paris-Sud, 91405 Orsay Cédex, France

^c Laboratoire de Physique des Solides, ERS 113 au CNRS, Case 79, Université Pierre et Marie Curie, 75252 Paris Cédex 05, France

Received 26 June 1995; accepted 5 December 1995

Abstract

Resonant photoemission spectra of Fe atoms (3p–3d) were measured for freshly cleaved $\text{Cd}_{0.86}\text{Fe}_{0.14}\text{Se}$ crystal (110) surface and for the same surface with sequentially deposited Fe atoms in the range 0.3–80 ML. The synchrotron radiation (LURE, Orsay, France) was used to measure valence band density of state distributions and Cd 4d core level for the radiation energy range 50–60 eV, which includes the Fe 3p–3d resonant energy equal to 56 eV. At the lowest stages of Fe atom deposition (up to about 3 ML), Fe atoms replace Cd atoms in the crystal, making a $\text{Cd}_{1-x}\text{Fe}_x\text{Se}$ alloy with a higher x and leaving extra Cd as small islands or clusters. For the next stages of Fe deposition (about 3–10 ML) the dissociated Cd atoms create a Cd–Fe alloy. At higher stages of Fe deposition (above about 10 ML) a Fe thin film is formed.

1. Introduction

Semimagnetic semiconductors (SMSC) or diluted magnetic semiconductors (DMS) have attracted a great deal of attention as a new group of semiconducting materials mainly due to their abnormally high magneto–optical and magneto–transport effects [1].

These materials are obtained by the substitution of a cation in II–VI or IV–VI semiconductor compounds by transition metal cations ($\text{M}3\text{d}^n$) like $\text{Mn}(3\text{d}^5)$, $\text{Fe}(3\text{d}^6)$, or by rare earth metals like Eu or

Gd. Such a change of cation introduces disorders: crystalline (local structure), magnetic (introduction of magnetic ions) and chemical (a foreign ion, with its core levels and valence electrons) and brings a strong interaction between the d electrons and the valence electrons of II–VI or IV–VI semiconductor crystal.

The present work is strongly stimulated by the recent efforts done to obtain and understand the electronic properties of the interfaces and superstructures with semimagnetic semiconductors (SMSC). A special interest can be found in the difference in the contribution of 3d electrons to the valence band of the ternary crystal either in the bulk or along the surface. In the present experiments, either the iron

* Corresponding author.

atoms were introduced into the bulk of the crystal, either through a growth at thermodynamic equilibrium of Cd, Fe and Se, or Fe atoms were deposited on the freshly cleaved surface of the ternary crystal $\text{Cd}_{0.86}\text{Fe}_{0.14}\text{Se}$.

The previous investigation of the Schottky barrier formation process occurring during deposition of Fe atoms on CdSe (110) surface showed that the Fe atoms induce a local dissociation of the CdSe compound [2]. Auger spectra measured for Fe, Cd and Se atoms under sequentially deposited Fe atoms showed remarkable decrease of the Auger peaks measured for Cd atoms in comparison to the Se atoms peaks. It was assumed that the dissociation of CdSe crystal occurs at the crystal surface and leads to the appearance of a Fe_xSe_y compound. At the early stages of the Fe atom deposition, the ordered character of the crystalline surface was favorable to the epitaxial growth of a crystal with a new Fe-rich composition: the Fe atoms lead to the creation of $\text{Cd}_{1-x}\text{Fe}_x\text{Se}$ crystal with an increasing amount of Fe atoms (increase of the parameter x) along the surface.

A new approach in the study of the Fe/CdFeSe interface formation is proposed in the present paper which reports experiments performed using photoemission under resonant conditions for the Fe 3p–3d transition.

2. Experimental conditions and results

The $\text{Cd}_{1-x}\text{Fe}_x\text{Se}$ samples were grown by the modified Bridgman method [3] at the Institute of Physics, Polish Academy of Sciences. The clean surface of the parallelepipedic sample was obtained by cleavage using a knife–anvil technique under UHV conditions ($p = 1 \times 10^{-10}$ Torr). It gave a $4 \times 4 \text{ mm}^2$ (110) clean and smooth surface, with a small density of steps, directly in the photoemission chamber. Once the photoemission measurements performed for the freshly cleaved surface, the sample was exposed to the Fe flux obtained by sublimation from a Joule-heated pure Fe wire. The Fe sublimator was calibrated using a quartz balance and the Fe coverage upon the CdFeSe surface will be expressed in monolayer units (ML) where 1 monolayer has 7.7×10^{14} Fe atoms per cm^2 . The sample temperature during Fe deposition did not rise more than 30

degrees. After each step of Fe deposition the photoemission spectra were measured.

The experiment was performed using vacuum ultraviolet radiation with available photon energy in the range 20–130 eV, obtained from the line SA71 (TGM 2.5 m) of the synchrotron ring SUPER-ACO in LURE, Orsay, France. The radiation impinges the sample surface at a 45° angle with respect to the normal. The sets of photoemission spectra were measured in the $h\nu$ energy range close to the resonant Fe 3p–3d transition ($h\nu = 56 \text{ eV}$). The energy distribution curves (EDC) spectra were taken with an energy resolution comprised between 150 and 300 meV.

Recently a large effort has been devoted to a better understanding of the contribution of the 3d electrons of iron to the valence band using the resonant photoemission experiment for Fe_xO_y [4] and $\text{Cd}_{1-x}\text{Fe}_x\text{Se}$ [5,6]. In the resonant photoemission experiment the photon energy is tuned relatively to the energy of the optical absorption edge corresponding to the 3p–3d transition [7]. For the $h\nu$ energy region of the resonant energy, the Fe ions are excited selectively and locally. The relaxation of the excited Fe ions leads to the emission of additional electrons according to the formula

$$3p^6 3d^6 + h\nu = [3p^5 3d^7]^* = 3p^6 3d^5 + e^-$$

(* – excited state).

Both effects contribute to the measured photoemission energy distribution curves (EDC's) in the region of the resonant $h\nu$ energies. The contribution of the resonant photoemission can be described by the Fano formula introduced for atomic systems and illustrated by the Fano line shape with the resonant maximum followed by the antiresonant minimum [7]. For transition metal compounds the profiles of the line can be more complex.

In Fig. 1 the set of measured EDC's for a $\text{Cd}_{0.86}\text{Fe}_{0.14}\text{Se}$ freshly cleaved surface (110) and for the same surface after Fe deposition is presented. For the clean surface of the crystal a small maximum appears at the edge of the valence band at -0.5 eV (A). This maximum is due to a contribution of Fe 3d (e-spin up) electron and it corresponds to an electron with spin opposite to the rest of Fe3d5 electrons [5]. The states visible at binding energy about -3.7 eV (B), corresponds to the Fe 3d (e-spin down) electrons

[5]. The maxima obtained at -0.5 and -3.7 eV can be treated as fingerprints of $\text{Cd}_{1-x}\text{Fe}_x\text{Se}$ crystal existence. A and B intensity are then proportional to the amount of 4 ML, the increase of B is visible in Fig. 1 and it can be treated as corresponding to the increase of x in the $\text{Cd}_{1-x}\text{Fe}_x\text{Se}$ crystal. At this stage of deposition the edge of the EDC's is build as a sum of the electrons emitted from the increasing height of A corresponding to the $\text{Cd}_{1-x}\text{Fe}_x\text{Se}$ crystal band edge and the Fe islands starting to grow. At the Fe deposition equal to 4 ML the edge of the curves shifts up by about 0.3 eV and it can be treated as resulting from the increase of x in $\text{Cd}_{1-x}\text{Fe}_x\text{Se}$. The islands of Fe which started to grow at this stage of Fe deposition can only slightly contribute at the edge of the valence band.

For the next range of Fe depositions, higher than 4 ML, the crystal coverage by Fe islands increases and the peak B is well visible for depositions 8 and 13 ML: it then decreases for 40 ML of Fe. The edge of EDC's shifts steply with Fe deposition by about

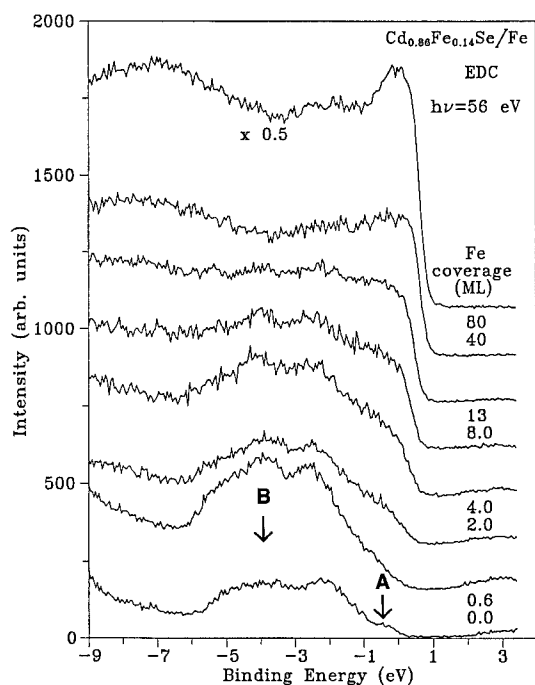


Fig. 1. The set of EDC's obtained for the $\text{Cd}_{0.86}\text{Fe}_{0.14}\text{Se}$ crystal (1210) clean surface and for various Fe coverages in monolayer units (ML), measured at the Fe 3p–3d resonant photon energy (56 eV).

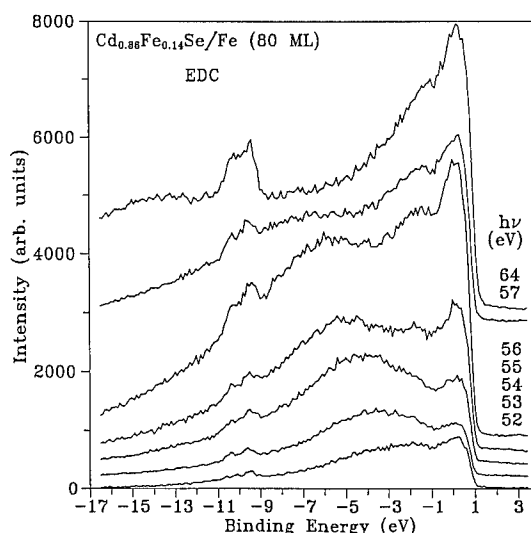


Fig. 2. The set of EDC's obtained for the $\text{Cd}_{0.86}\text{Fe}_{0.14}\text{Se}$ crystal covered by 80 ML Fe measured at different photon energies close to 56 eV, the Fe 3p–3d resonant energy.

0.7 eV for 40 ML of deposition. This edge does not change anymore for deposition of 80 ML and its position can be treated as corresponding to the edge of Fe metal. The surface is not uniformly covered by the Fe atoms and the EDC's obtained at 80 ML of Fe deposition can be still treated as the sum of a large contribution of electrons emitted from the islands of Fe and a smaller contribution from the alloy which remains visible.

At high Fe coverage (80 ML), the set of EDC's presented in Fig. 2 was measured for radiation energies in the range between 52 and 64 eV. The highest contribution of the Fe electrons to the measured EDC's corresponds to the resonant radiation energy $h\nu = 56$ eV and the lowest contribution of Fe corresponds to the antiresonant energy of $h\nu = 54$ eV. In the range of high energies (see curve for 64 eV) the cross section of localized electrons (Cd 4d and Fe 3d) increases and the relative increase of the peaks is visible. The resonant curve corresponds well to the Fe crystal spectra [8].

In Fig. 3, the set of EDC's is presented for the Cd 4d band obtained after different amounts of deposited Fe. For the clean $\text{Cd}_{0.86}\text{Fe}_{0.14}\text{Se}$ sample, the Cd 4d level does not show clearly the spin–orbit splitting usually present in Cd metal, in the isolated atom or even in CdSe [9]. This must be due to the

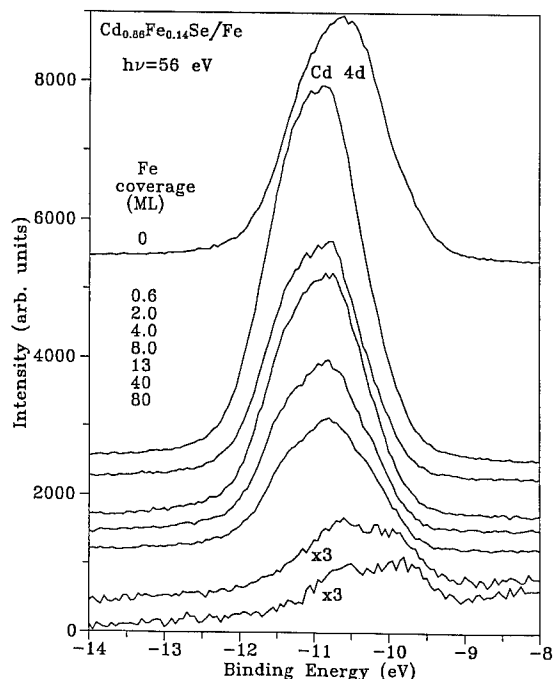


Fig. 3. The photoemitted Cd 4d core level band measured in cleaved $\text{Cd}_{0.86}\text{Fe}_{0.14}\text{Se}$ after increasing amount of deposited Fe atoms (expressed in monolayer units (ML)) upon 56 eV photon excitation.

presence of Fe which creates various surroundings for each Cd atom in the alloyed crystal, giving to the Cd 4d band a multi-component character.

After the very first stages of Fe deposition, the binding energy of Cd 4d increases by 0.33 eV which may be explained at least partly by a band bending change at the surface. During the next steps of Fe deposition, the shape of the Cd 4d peaks only slightly changes as a result of the change of the Cd nearest neighbours from Se to Fe or even Cd, but the energy position of the Cd 4d band is still located at around -10.8 eV and the intensity decrease remains moderate.

For Fe deposited at coverages of 40 or 80 ML, the measured peak is the same time affected by a neat intensity reduction and a reduction in intensity shift towards lower binding energies. At this stage of Fe deposition, the Cd 4d band has lost its previous

specifications attributed to CdFeSe alloy and must rather correspond to the Cd 4d band of the metal diluted in Fe.

3. Conclusion

The reaction between Fe and a clean (110) surface of a ternary $\text{Cd}_{0.86}\text{Fe}_{0.14}\text{Se}$ crystal starts at the first stages of the Fe atoms deposition leaving an Fe-enriched and Cd-depleted layer in the surface region. Photoemission measurements have been performed at photon energies close to the resonant energy for Fe 3p–3d transition in order to enhance the contribution of the Fe 3d electrons to the valence band. The character of this contribution does not change in comparison to the contribution in ternary crystal up to a 3–5 ML Fe coverage range.

When the amount of deposited Fe is increased, the Cd 4d band spectra changes have been attributed to the formation of Fe–Cd alloy islands.

At higher Fe coverages (40–80 ML), the photoemission resonant spectrum becomes more and more similar to the Fe metal one with a vanishing contribution of the ternary crystal substrate.

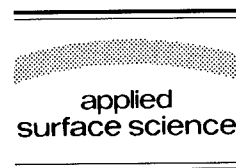
References

- [1] J.K. Furdyna, *J. Appl. Phys.* 64 (1988) R29.
- [2] B.A. Orlowski, J.-P. Lacharme, N. Safta and C.A. Sébenne, in: *Proc. 4th Int. Conf. on the Formation of Semiconductor Interfaces*, Eds. Lengeler, H. Lüth, W. Mönch and J. Pollmann (1993) p. 235.
- [3] R.R. Galazka, in: *Proc. XIV Int. Conf. on the Physics of Semiconductors*, Inst. Phys. Conf., Edinburgh, Vol. 43 (1979) p. 133.
- [4] R.J. Lad and V.E. Henrich, *Phys. Rev. B* 39 (1984) 13478.
- [5] M. Taniguchi, Y. Ueda, I. Morisada, Y. Muashita, T. Ohta, I. Souma and Y. Oka, *Phys. Rev. B* 41 (1990) 3069.
- [6] R. Denecke, L. Ley and J. Fraxedas, *Phys. Rev.* 47 (1993) 13197.
- [7] B. Sonntag and P. Zimmermann, *Rep. Prog. Phys.* 55 (1992) 911.
- [8] L. Ley, O.B. Dabbousi, S.P. Kowalczyk, F.R. McFeey and D.A. Shirley, *Phys. Rev. B* 16 (1977).
- [9] N.J. Shevchik, J. Tejeda, M. Cardona and D.W. Langer, *Phys. Status Solidi (b)* 59 (1973) 87.



ELSEVIER

Applied Surface Science 104/105 (1996) 286–290



Intrinsic surface atom manipulations in STM and AFM

K. Cho^{*}, J.D. Joannopoulos

Department of Physics, Massachusetts Institute of Technology, Cambridge, MA 02139, USA

Received 28 June 1995; accepted 10 August 1995

Abstract

State-of-the-art first-principles simulations are performed to investigate the possibility of using a tungsten tip in atomic force microscopy (AFM) as a mechanical tool to manipulate the surface atoms of Si(100). Calculations of total energy and electronic structure are used to study the energetics and bonding properties associated with the tip and surface for a variety of atomic configurations. The results predict that under certain protocols the tip can be used effectively to flip dimers on the surface, from one buckled configuration to another, reversibly, and without inducing damage to either the intrinsic surface or the tip. This leads directly to the exciting possibility of using the intrinsic (100) surface of silicon as an ultra-high memory storage device approaching the ultimate limit of one bit of data per atom.

Atomic force microscopy (AFM) [1] and scanning tunneling microscopy (STM) [2] have revolutionized experimental studies of the properties of surfaces of solids. Both techniques utilize very sharp metallic tips (typically tungsten) to probe the surface and obtain resolution on an atomic scale. In an AFM experiment one typically measures the force on the tip due to the elastic deformation of the surface atoms. By scanning the surface at constant force one can obtain a detailed topograph of the surface atomic structure. This procedure is an extension and derivative of STM except that in STM it is the induced electric current between tip and surface that is held fixed. For both techniques, however, the interpretation of scanned images may not always be straightforward because of possible induced structural

changes of the surface or tip during the measurement process [3–5]. Moreover, theoretical insight in the form of first-principles calculations which include tip-surface interactions has been quite limited because of inherent complexity of modeling the tip and surface system together [3–6].

In this paper we present the results of theoretical calculations which include both tip and surface atom relaxations to simulate an atomic force microscope (AFM) experiment on the surface of a semiconductor. Our motivation is to determine the extent to which the tip in an AFM experiment can be used to reversibly rearrange atoms on a clean surface of a semiconductor. This potential ability is similar to that of rearranging adsorbed impurities on a surface using pulsed STM [7]. However, it differs in that the present surface system has no adsorbed atoms so that one is investigating the intrinsic surface itself, and in that the procedure for inducing coupling between tip and surface atoms is mechanical in nature rather than electrical.

^{*} Corresponding author. Fax: +1-617-253-2562; e-mail: kj-cho@mit.edu.

The specific system of interest is the (100) surface of silicon in the presence of a sharp tungsten tip. Our choice of system is dictated by the widely studied nature of this surface, its relative simplicity in terms of reconstruction, and its significant technological importance (see for example [8]). The results of our calculations will show that an AFM tip can indeed be used as a microscopic tool to mechanically and reversibly rearrange the silicon atoms that form the outermost layer of the intrinsic surface. Moreover, an exciting bonus of these results is that this prediction can be used for the novel design of an ultra-high density memory device capable of storing over six orders of magnitude more data than conventional devices.

Typical STM images of the Si(100) surface reveal that every two atoms on the outermost layer bond together to form a dimer and that these dimers lie side by side in rows running perpendicular to the dimer bonds [9–11]. At low temperatures the dimers are buckled in alternating configurations along each row [5,11–14] as shown schematically in Fig. 1. Our focus will be on the introduction of a sharp tungsten tip above and close to the surface and on the determination of how the position, proximity, and motion of the tip can be used to rearrange the dimers on the surface in a reversible fashion. We present here a very brief description of our calculations. The technical details are discussed in depth elsewhere [5,15]. Quantum mechanical electronic structure and total energy calculations are performed using local density functional theory to describe the electron–electron

interactions [15,16], separable pseudopotential theory to deal with the strong electron–nuclei potential [15,17], supercells to model the aperiodic atomic surface geometry [15], and conjugate gradient minimization to relax the electronic and nuclear degrees of freedom [15]. A typical calculation proceeds as follows: for a given position of all the nuclei, electrons are introduced and allowed to self-consistently relax to their ground state, the total energy of the system is then recorded and quantum mechanical forces on the nuclei calculated. These forces are then used to slightly displace the nuclei to lower energy positions, at which point the electrons are allowed to relax once again. This process is repeated until all the atoms have reached their equilibrium geometry.

The supercell geometry chosen to model the basic structure of the AFM system (tungsten tip plus silicon surface) consists of the following: a four layer slab of silicon, a passivating layer of hydrogen atoms on one surface, and 10 Å of vacuum on either side. This represents the bare Si(100) surface system. To model the AFM tip we note that only the atoms at the very edge of the tip need to be adequately represented in order to address the questions raised in this work. Since tungsten atoms on the surface form a close packed structure, we have opted to represent the apex of the AFM tip simply as a tetrahedron of four atoms. The tungsten cluster is placed in the vacuum region with an apex atom pointing down towards the non-passivated surface. This choice of supercell geometry provides accurate and reliable results for the interatomic forces and

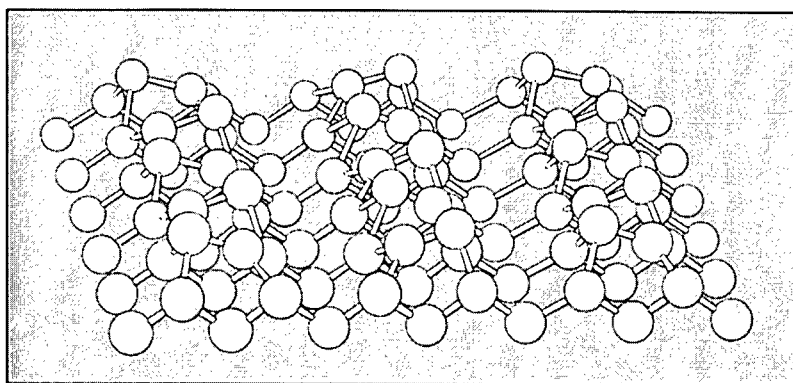
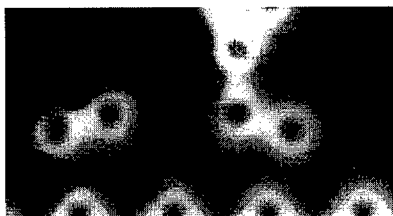


Fig. 1. Ball-and-stick model illustrating three rows of buckled dimers of the Si(100) surface.

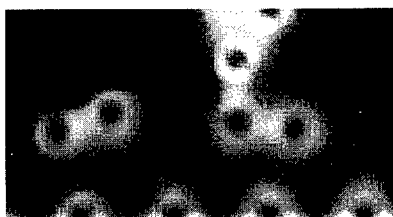
electronic structure of the system [5,15]. For any given position of the tip above the surface, all the atoms (except the three tungsten atoms at the top of the tip and the silicon and hydrogen atoms comprising the passivated side of the slab) are allowed to relax to their equilibrium configurations.

The results of our calculations at very low tem-

$h = 2.5$



$h = 2.25$



$h = 2.0$



$h = 1.75$

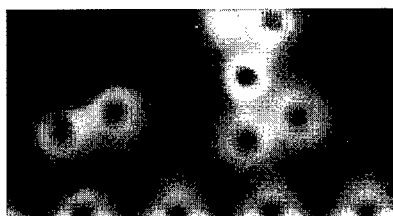


Fig. 2. A sequence of total valence electron charge densities (proceeding from top to bottom) depicting an attempt to flip a dimer by pushing on it with the tip. The equilibrium dimer angle changes gradually until the third panel. From the third to the fourth panel there is a discontinuous change in equilibrium dimer angle which corresponds to a flip of the dimer to its other buckled configuration. However, raising the tip back up (not shown here) will restore the dimer to its original buckled configuration. This is a consequence of the formation of a covalent bond which appears as a small white cloud between the edgemost tungsten tip atom and one of the silicon atoms of the dimer.

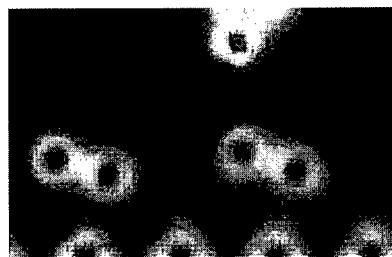
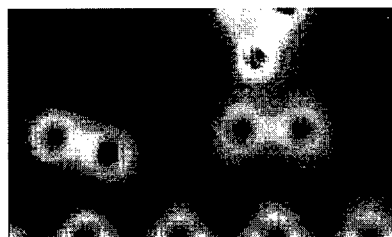
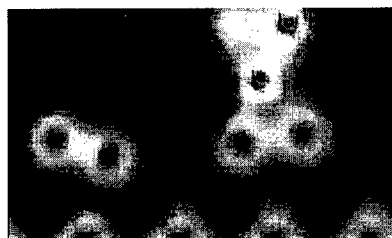
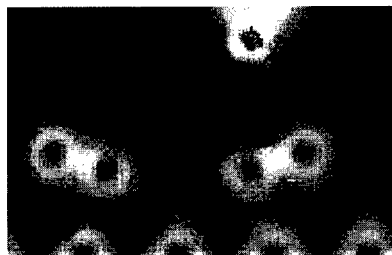


Fig. 3. A sequence of total valence electron charge densities depicting how a tip can be used to flip a dimer by pulling on it. In the top two panels the tip is brought down onto the lower dimer atom. Once a covalent bond is formed, the tip is raised back up as shown in the bottom two panels. With this approach the tip is able to flip the dimer and detach itself without inducing damage to the system.

perature (e.g. liquid helium) are displayed in Fig. 2 and Fig. 3. In each case, electronic charge densities associated with the valence electrons of the system are shown in a crosssectional plane perpendicular to the (100) surface. At the top of each panel is the

lower portion of the tungsten tip. At very low temperatures, the fluctuations of the dimers become frozen-in, and a typical AFM scan over the surface will not disturb the dimers. But might it not be possible to somehow increase the interaction between the tip and a dimer so that the tip would flip a dimer and leave it flipped even after the tip has moved away?

We first attempt to flip a dimer by moving the tip down onto the upper atom of the dimer and essentially pushing on it. This is illustrated in Fig. 2. As we proceed from the top panel to the bottom panel, the tip is moved closer and closer to the surface, inducing the dimer to rotate, until the dimer reaches a horizontal configuration, after which there occurs a discontinuous change in the equilibrium value of the dimer buckling angle. At this point the dimer has flipped to its other buckled configuration. Moreover, the discontinuity in equilibrium angle would appear to suggest that the dimer would remain in this state even after the tip was removed. But this is not the case in general. For example, if we were to pull the tip back up, we would find that the tip drags the dimer back to its original configuration. This is a consequence of the rather strong covalent bond that is formed between the dimer atom and the edge-most tungsten atom of the tip. This bond can be seen as a small white region between the corresponding nuclei in Fig. 2.

Nevertheless, a dimer on the surface can be flipped so that it remains flipped even after the tip is removed by using the approach shown in Fig. 3. Here the process of flipping is performed by having the tip pull on a dimer atom rather than push on it. Proceeding from top to bottom, the first two panels represent a tip being brought down to a surface dimer, while the next two panels correspond to the tip being pulled back up. By bringing the tip down to the lower atom of a dimer, the tip can capture it by forming a covalent bond as before. A subsequent raising of the tip drags the dimer to its other buckled state. The bond between the tip and dimer eventually breaks without harming the dimer or the tip. This is because the silicon–tungsten bond is weaker than both the silicon–silicon and tungsten–tungsten bonds. The net effect of this procedure is the flipping of a dimer on the surface that remains flipped after the tip is removed.

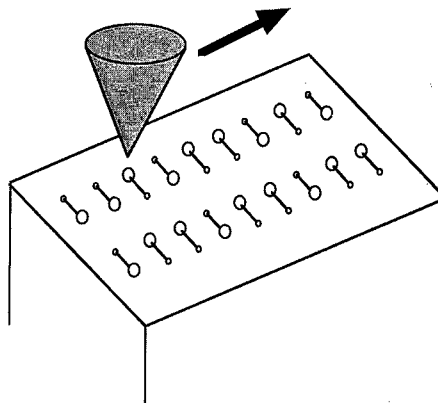


Fig. 4. Schematic representation of a high-density memory reading and writing device using STM and/or AFM tip on the Si(100) surface.

This predicted capability of the AFM tip to reversibly rearrange atoms without damage to the system leads at once to the notion of a novel memory device as illustrated in Fig. 4. A memory storage device has two basic components: a writing/reading device and a storage medium. The storage density of a storage device is determined by the size of the basic storage unit which can store one bit of data. This size is determined by the resolution of the writing and reading device which modifies the storage medium and retrieves the stored data. One can easily imagine that the ultimate limit of a surface storage device is one bit of data per surface atom, and this limit provides an enormously higher storage density than any conventional storage device. The realization of this limit requires both a writing and reading device with atomic resolution and a storage medium with a storage unit of atomic scale.

Since each dimer on Si(100) can be made to exist in one of two possible buckled configurations, each dimer can conceivably store one bit of data of information. One simply assigns a 0 and a 1, respectively, to each dimer configuration. The recording of information would be accomplished by flipping dimers using the AFM technique illustrated in Fig. 3. Information retrieval would be accomplished by simply performing a conventional AFM (or for that matter STM) horizontal scan at higher distance from the surface. This would enable one to swiftly image large portions of the surface without perturbing the existing dimer configurations. The entire intrinsic

Si(100) surface now becomes a potentially massive storage bin. One bit of information for every dimer corresponds to 1 bit per 30 \AA^2 or 420 Gbytes per mm^2 . This corresponds to a *six orders of magnitude* increase in storage capability compared to conventional devices.

Since the time scale for an AFM/STM scan, however, is still slow compared to modern memory devices, perhaps the most useful application for this device might be archival memory storage. Of course, many engineering obstacles will need to be overcome before such a device could be made operational. Ultra-high vacuum conditions would be necessary to keep the surface from being contaminated and very low temperatures would be needed to freeze out thermal fluctuations of the dimers. Interestingly, both of these requirements are easily satisfied in satellites.

Acknowledgements

We would like to thank Dr. K. Dunussi and Dr. P. Villeneuve for a critical reading of the manuscript. This work was supported in part by ONR Grant N0014-94-1-0591 and JSEP Grant DAA4-04-95-1-0038.

References

- [1] G. Binnig, C.F. Quate and Ch. Gerber, *Phys. Rev. Lett.* 56 (1986) 930.
- [2] G. Binnig and H. Rohrer, *Phys. Rev. Lett.* 49 (1982) 57.
- [3] H.J. Kreuzer, L.C. Wang and N.D. Lang, *Phys. Rev. B* 45 (1992) 12050.
- [4] Z.H. Huang, M. Weimer, R.E. Allen and H. Lim, *J. Vac. Sci. Technol. A* 10 (1992) 974.
- [5] K. Cho and J.D. Joannopoulos, *Phys. Rev. Lett.* 71 (1993) 1387.
- [6] D. Tomanek, G. Overney, H. Miyazaki, S.D. Mahanti and H.J. Güntherodt, *Phys. Rev. Lett.* 63 (1989) 876.
- [7] Y.W. Mo, *Science* 261 (1993) 886.
- [8] D. Haneman, *Rep. Prog. Phys.* 50 (1987) 1045, and references therein.
- [9] R.M. Tromp, R.J. Hamers and J.E. Demuth, *Phys. Rev. Lett.* 55 (1985) 1303.
- [10] R.J. Hamers, R.M. Tromp and J.E. Demuth, *Phys. Rev. B* 34 (1986) 5343.
- [11] R.A. Wolkow, *Phys. Rev. Lett.* 68 (1992) 2636.
- [12] D.J. Chadi, *Phys. Rev. Lett.* 43 (1979) 43.
- [13] J. Ihm, D.H. Lee, J.D. Joannopoulos and J.J. Xiong, *Phys. Rev. Lett.* 51 (1983) 1872.
- [14] J. Dabrowski and M. Scheffler, *Appl. Surf. Sci.* 56–58 (1992) 15.
- [15] M.C. Payne, M.P. Teter, D.C. Allan, T.A. Arias and J.D. Joannopoulos, *Rev. Mod. Phys.* 64 (1992) 1045, and references therein.
- [16] J.P. Perdew and A. Zunger, *Phys. Rev. B* 23 (1981) 5048.
- [17] L. Kleinman and D.M. Bylander, *Phys. Rev. Lett.* 48 (1982) 1425.



ELSEVIER

Applied Surface Science 104/105 (1996) 291–296

applied
surface science

Surface diffusion limitation in laser focused atomic deposition

R.E. Behringer, Vasant Natarajan, G. Timp *

AT&T Bell Laboratories, ID-431, P.O. Box 636, Murray Hill, NJ 07974-0636, USA

Received 28 June 1995; accepted 7 September 1995

Abstract

We have previously demonstrated that an optical standing wave can be used to focus a neutral atomic beam into a structure which is deposited on a substrate, under conditions that are compatible with molecular beam epitaxy. We have made structures in sodium with linewidths of $\delta \approx 45$ nm and contrast better than 10:1. Here, we observe that the condition of the surface prior to deposition is critical in producing these features. With certain surface conditions, apparently the mobility of the atoms on the surface reduces the contrast of the grating to approximately 1:1. We discuss the condition necessary during deposition to insure that the resolution of the deposited features is retained.

PACS: 42.50.Vk; 32.80.-t; 42.82.Cr

Recently, light pressure forces have been used to focus the atoms in a neutral atomic beam into a pattern which is deposited on a substrate [1,2]. This technique represents a fundamentally new method for surface modification where a pattern is transferred directly to the substrate, without the need of resists, high energy charged particle or photon beams. Since the forces used to focus the atomic beam are atom-specific, it is conceivable that the position of particular atomic elements could be controlled during the deposition of multiple elements or molecular species. And so, when used as part of a material growth system, this technique could provide the opportunity to create three dimensional structures within a material while it is being deposited. To laterally control the deposition of a material effectively, the patterning technique should: (1) produce

nanometer-scale structures, and provide high contrast, to distinguish between the feature and the adjacent unpatterned areas; (2) maintain the fidelity of the pattern against surface diffusion after the atoms have been deposited.

We have already shown that light can be used to focus a sodium beam into a grating with linewidths as narrow as $\delta \approx 45$ nm with contrast (the ratio of the average height of the deposited feature to the thickness of the material between the features), of about 10:1 [3]. We used an optical standing wave (SW) to focus a thermal sodium beam into grating structure. The period of the gratings (294.5 nm = $\lambda/2$) is determined by the sodium D_2 atomic resonance at $\lambda = 589.0$ nm. The interaction of the optical field of the SW with this atomic resonance provides the force used to focus atoms. We examined the deposited structures in an ultra-high vacuum (UHV) scanning tunneling microscope (STM), to characterize the linewidth and contrast [3–5].

* Corresponding author.

Here, we will examine the limitations imposed by the surface conditions on the integrity of the deposited pattern. We show that for depositions under conditions similar to our previous work but on nominally cleaner substrates, the contrast of the grating is reduced to approximately 1 : 1.

Fig. 1 shows a schematic of our laser-focused deposition system. In UHV, an atomic source is directed along \hat{z} at a room temperature substrate, and a SW along \hat{x} intersects the atomic beam parallel to the substrate surface. The atomic beam deposits on the substrate at a rate of about 0.01 nm/s. The SW acts like an array of cylindrical lenses that focuses the atomic beam into a grating structure on the sample surface. The SW in our experiments has a Gaussian power profile along \hat{z} , i.e. $P = P_0 e^{-z^2/2L_z^2}$ where P_0 is the integrated power and the sample is placed along the centerline of this beam. While sodium atoms are focused in our experiments, the same technique can be used with

other elements given a suitable laser source. For example, McClelland et al. [2] have demonstrated the focusing of chromium with a standing wave at $\lambda = 425$ nm and McGowen and Lee [6] have likewise focused aluminum with a 300 nm SW.

The Si substrates used in all these experiments are 5 mm \times 7 mm pieces cleaved from $\langle 100 \rangle$ 10 Ω cm n-type wafers. After cleaving to size, the substrates are cleaned and the surface is prepared following Higashi et al. [7]. The substrates are solvent cleaned and the as-delivered 200 nm thermal oxide is removed in a buffered HF solution (BOE). The pieces are then etched in a 1 : 1 : 4 solution of $\text{NH}_3\text{OH}:\text{H}_2\text{O}_2:\text{H}_2\text{O}$ at 80°C for 10 min, which leaves an oxide on the surface. The Si substrates are rinsed in deionized water and the chemically grown oxide is then removed by etching in a 5% solution of HF for 30 s. This is supposed to produce a hydrogen-terminated silicon surface that is stable in air [7]. The pieces are then clamped to a Mo sample holder appropriate for the STM and placed above a Mo heater in a vacuum load-lock to the UHV chamber. The substrates are heated in vacuum to $T > 550^\circ\text{C}$ for 13 min to remove the hydrogen from the surface [8].

The force used to focus the atoms during the deposition of sodium is proportional to the gradient of the optical intensity [9,10]. The depth of the optical potential that produces this force can be controlled by adjusting: (1) the power in the incoming beam; (2) the interaction length between the light and the atoms, L_z ; and (3) the detuning between the light forming the SW and the atomic resonance, Δ . For $\Delta > 0$ the atoms are forced to the regions of low intensity. Simulations based on the classical equations of motion of atoms in a conservative potential [11] show, that under ideal conditions, an atomic beam can be focused to a linewidth $\delta < 1$ nm. We have examined the focusing achieved for a wide range of power, interaction length and detuning both experimentally and theoretically in our system. These results are presented elsewhere [3–5].

Fig. 2 shows STM images obtained from two Na films deposited at room temperature under different surface conditions. Both of the films shown diffracted light, indicating regions of long range order with a period of 294.5 nm. The substrates shown in Fig. 2 received the cleaning procedure outlined above, al-

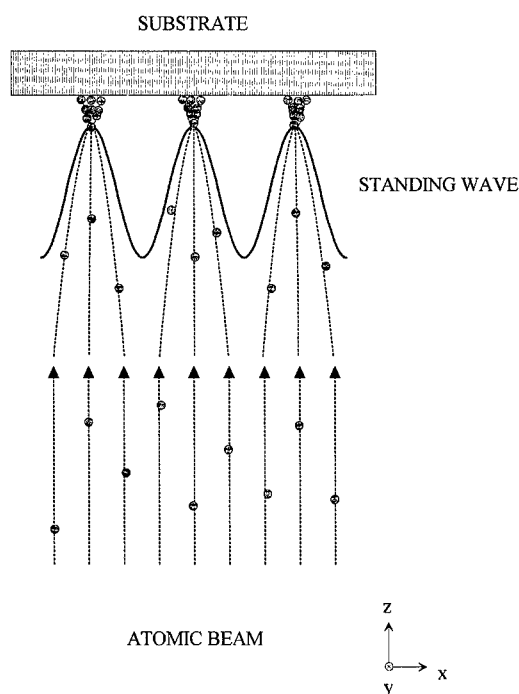


Fig. 1. Schematic of our laser focused deposition system. A collimated atomic beam is directed at a substrate held at room temperature. The beam passes through an optical standing wave which acts as an array of lenses to focus the atomic beam into a grating on the surface.

though the substrate in Fig. 2b was heated with a higher residual hydrocarbon background in the load-lock. We speculate that the heat treatment results in residual hydrocarbon defects on the Si surface [8]. Fig. 2a is typical of a Na film deposited after heating in a lower residual hydrocarbon background. No lines can be discerned in the STM image, and the grains observed are approximately 100 nm in diameter.

This is in stark contrast to the STM image shown in Fig. 2b. In Fig. 2b we observe lines $\delta = 45$ nm wide, consisting of grains approximately 10 nm in diameter. The regions between the lines show only a few isolated Na grains, indicative of the high contrast. The SW parameters used to form this grating were $\Delta = +1.7$ GHz, $L_i = 60$ μm , with an integrated power of 12 mW in the incoming beam. The atomic beam has an angular divergence of $\Theta \approx 0.5$

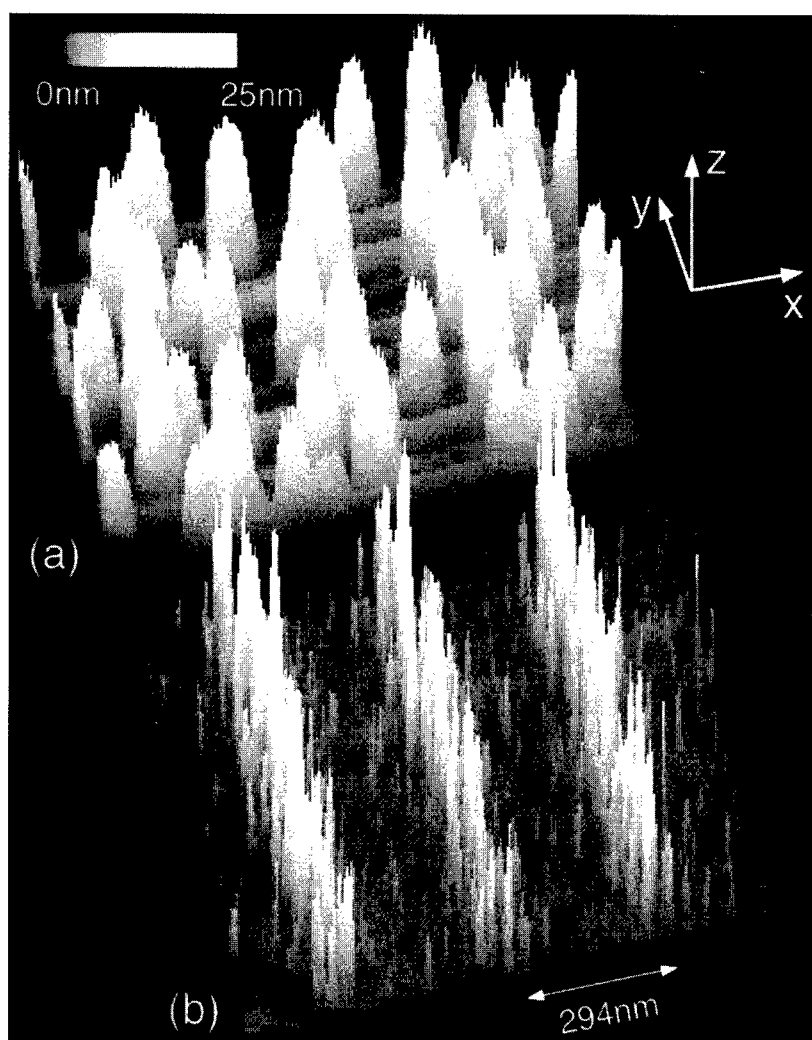


Fig. 2. Two STM images of as-deposited Na gratings using a SW with $\Delta = +1.7$ GHz and $L_i = 60$ μm to focus the atomic beam. The residual hydrocarbon background was different during pre-deposition heating for the two samples. (a) is an image of a grating deposited with a lower hydrocarbon background. Although the sample diffracted light, no lines are visible, and the Na grain size is approximately 100 nm. (b) was deposited with a higher residual hydrocarbon background. The lines in (b) have $\delta \approx 45$ nm, the grains that form the lines are approximately 10 nm in diameter, and the contrast of this grating is better than 10:1.

mrads and we assume a Boltzmann distribution of longitudinal velocities with an estimated rms velocity of $\bar{V} = 860$ m/s, corresponding to a measured oven temperature of $T = 420^\circ\text{C}$.

We speculate that the surface in Fig. 2a has fewer defects than the surface in Fig. 2b. Higher sodium surface mobility after deposition would account for the larger grains and poor grating quality observed in Fig. 2a. So, it is apparent from the images in Fig. 2 that the surface diffusion coefficient of the focused atoms must be small enough to guarantee that the lateral resolution of the pattern is maintained once the atoms have been deposited.

After Flynn [12] and using Fig. 2, we can estimate the surface and bulk diffusion coefficients required for three dimensional materials engineering. The surface diffusion coefficient, D_s , is given approximately by

$$D_s = (L^3/a^3)(a^2N/t_0),$$

where L is the maximum distance that the atom can travel on the surface, a is the lattice spacing of the substrate, N is the number of layers deposited and t_0 is the deposition time. In general, the surface diffusion coefficient must be small enough to maintain the fidelity of the deposited feature, so we must have $L < \lambda/4$ at most. In particular, from Fig. 2b, $L \approx \delta$. Similarly, the bulk diffusion coefficient must be small enough to avoid intermixing of the focused atoms and the Si substrate. The bulk diffusion coefficient, D_b , is given by [12]

$$D_b = a^2/t_0.$$

Using these expressions, with $L \approx \delta$ and a deposition rate of 0.01 nm/s, we estimate that $D_s < 10^{-9}$ cm²/s and $D_b < 10^{-19}$ cm²/s are necessary to retain the fidelity of the grating in Fig. 2b during deposition.

Instead of using contamination, the diffusion could be reduced by lowering the substrate temperature during deposition. The distance an atom diffuses during deposition can also be reduced by increasing the deposition rate. Simulations of crystal growth show that the ratio of diffusion rate to deposition rate is influential in determining the width of grown interfaces [13]. In our particular case, the width of the interface translates to the deposited linewidth. Decreasing this ratio by increasing the deposition

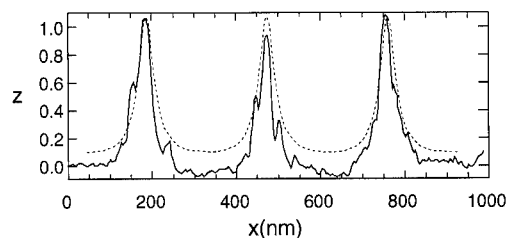


Fig. 3. Comparison of a classical simulation (dotted line) to an averaged line scan (solid line) of the image shown in Fig. 2b. While there is good agreement in the linewidth, the observed contrast of the deposited structure is better than predicted.

rate decreases the distance an atom can diffuse, but decreasing this ratio has the same effect as reducing the growth temperature: i.e. increased variation in linewidth, so that the grating fidelity is compromised. High atomic fluxes associated with large deposition rates during growth can also degrade the focusing of the atom lens. If there is significant absorption in the SW, then an additional global force component along the SW pushes the atoms parallel to the substrate, potentially reducing the contrast, and broadening or skewing the deposited features. The effect of absorption can be mitigated if large detunings are used in the SW, however.

Another requirement for three-dimensional material engineering is that the SW focus the atoms into a pattern with high contrast and narrow linewidth. In our system, the beam divergence and longitudinal velocity spread, combined with aberrations in our atom lens, broaden the deposited linewidth in Fig. 2b from the ideal case. Fig. 3 represents a comparison between the classical simulation of the atom lens and the averaged profile derived from Fig. 2b. The dotted line in Fig. 3 is the result of a simulation for the lens conditions used in the image in Fig. 2b, assuming a Boltzmann distribution of longitudinal velocities at $T = 420^\circ\text{C}$, and an angular divergence of $\Theta = 0.5$ mrad. The FWHM of the lines found in the simulation is $\delta = 53$ nm. The solid line in Fig. 3 is the averaged profile derived from the data in Fig. 2b. This profile is calculated by averaging in the \hat{y} direction over all the line scans that form the image of Fig. 2b, and subtracting the background estimated for similar measurements on a clean Si surface [4]. From this we estimate that the deposited lines have $\delta \approx 45$ nm and that the contrast is approximately

10:1. While there is good agreement between the calculated and measured estimate of the linewidth, the measured contrast of the deposited sodium grating is better than would be expected on the basis of these simulations. We do not know the origin of the difference in contrast, but there are many effects in the SW that are not accounted for in these naive simulations, such as velocity-dependent forces in the standing wave, or the evaporation of sodium from the silicon substrate.

The parameters of the atomic beam also play an important role in the linewidth and contrast of the deposited features. Fig. 4 shows another Na grating deposited under similar SW conditions to those of Fig. 2, with the divergence of the Na beam increased to $\theta \approx 3$ mrad. The substrate in this image was prepared with the same procedures as the sample in Fig. 2b. As expected from geometric optics, [14] the increased beam divergence increases the deposited linewidth and degrades the contrast according to $\delta \approx \theta L_i$ [14], to about the same level found in Fig. 2a. However, unlike the grating shown in Fig. 2a, the sodium grains are only about 10 nm in diameter and the lines which comprise the grating can still be discerned. We infer that, in order to produce

nanometer-scale structures with high contrast, it is not only necessary to control the diffusion of the atoms on the surface, but also optimize the conditions in the SW and the atomic beam [3,4].

In conclusion, we have shown that light can be used as a lens to focus a neutral atomic beam into nanometer-scale structures. Apparently, the mobility of the atoms on the surface is critical in preserving the pattern on the substrate. This technique could be used to three-dimensionally engineer materials, if the atom lens can provide high resolution features with high contrast; and if the diffusion of the focused atoms on the substrate is small enough that the resolution of the pattern is maintained. The sensitivity of the deposited pattern to the surface conditions also introduces the possibility of using this technique as a probe of diffusion on surfaces. For example, in the GaAs system surface diffusion lengths have been measured on different facets of etched structures by examining the period of reflection high-energy electron diffraction (RHEED) intensity oscillations [15,16], or the thickness of grown layers on different facets [17]. Alternatively, using the techniques described here, a surface could be characterized in the STM before deposition, then a well-controlled pat-

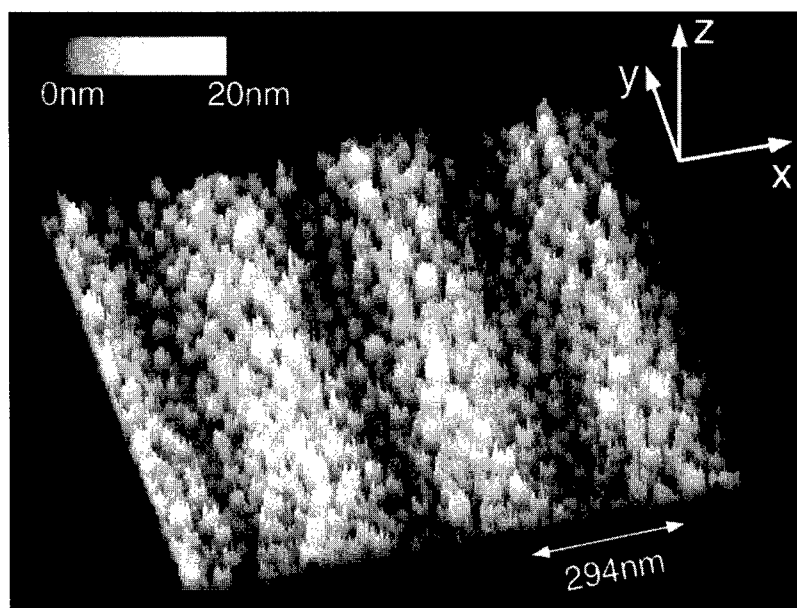


Fig. 4. STM image of a Na grating deposited with the same conditions as the grating in Fig. 2b, but with an atomic beam divergence of $\theta \approx 3$ mrad. While the contrast and linewidth are similar to the image in Fig. 2a, the grain size is about the same as in Fig. 2b.

tern of atoms could be deposited on the surface, and subsequently the distribution of the deposited feature could be measured.

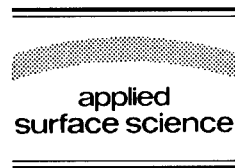
References

- [1] G. Timp, R.E. Behringer, D.M. Tennant, J.E. Cunningham, M. Prentiss and K.K. Berggren, *Phys. Rev. Lett.* 69 (1989) 1636.
- [2] J.J. McClelland, R.E. Sholten, E.C. Palm and R.J. Cellotta, *Science* 262 (1993) 877.
- [3] V. Natarajan, R.E. Behringer and G. Timp, *Phys. Rev. Lett.*, submitted.
- [4] V. Natarajan, R.E. Behringer and G. Timp, *J. Vac. Sci. Technol. B.*, submitted.
- [5] R.E. Behringer, V. Natarajan and G. Timp, *Phys. Rev. Lett.*, submitted.
- [6] R. McGowen and S. Lee, private communication.
- [7] G.S. Higashi, Y.J. Chabal, G.W. Trucks and K. Raghavachari, *Appl. Phys. Lett.* 56 (1990) 656.
- [8] D.J. Eaglesham, G.S. Higashi and M. Cerullo, *Appl. Phys. Lett.* 59 (1991) 685.
- [9] J.P. Gordon and A. Ashkin, *Phys. Rev. A* 21 (1980) 1601.
- [10] J. Dalibard and C. Cohen-Tannoudji, *J. Opt. Soc. Am. B* 2 (1985) 1707.
- [11] K.K. Berggren, M. Prentiss, G.L. Timp and R.E. Behringer, *J. Opt. Soc. Am. B* 11 (1994) 1166.
- [12] C.P. Flynn, *J. Phys. F* 18 (1988) L195.
- [13] P.I. Tamborena and S. Das Sarma, *Phys. Rev. E* 48 (1993) 2575.
- [14] J.J. McClelland, private communication.
- [15] M. Hata, T. Isu, A. Watanabe and Y. Katayama, *J. Vac. Sci. Technol. B* 8 (1990) 692.
- [16] Y. Nomura, Y. Morishita, S. Goto, Y. Katayama and T. Isu, *Appl. Phys. Lett.* 64 (1994) 1123.
- [17] S. Koshiba, Y. Nakamura, M. Tsuchiya, H. Noge, H. Kano, Y. Nagamune, T. Noda and H. Sakaki, *J. Appl. Phys.* 76 (1994) 4138.



ELSEVIER

Applied Surface Science 104/105 (1996) 297–303



Graphitization of diamond (111) studied by first principles molecular dynamics

Alessandro De Vita^{a,*}, Giulia Galli^a, Andrew Canning^b, Roberto Car^a

^a *Institute Romand de Recherche Numérique en Physique des Matériaux (IRRMA), IN-Ecublens, CH-1015 Lausanne, Switzerland*

^b *CRAY Research, CH-1015 Lausanne, Switzerland*

Received 28 August 1995; accepted 7 September 1995

Abstract

Large scale first principles numerical simulations, performed on modern massively parallel computers, can be usefully applied to study the physics of semiconductor surface and interface systems. We report on a recent study of the surface-initiated diamond to graphite structural transition of crystalline carbon. Our investigation consisted of a series of fully ab initio molecular dynamic simulations of the diamond C(111)-(2 × 1) surface, with cells containing from 200 to 300 atoms. We observed a spontaneous graphitization of the surface, followed by a fast graphitization of the entire diamond slab, at temperatures above 2500 K. We find that the transition starts at the reconstructed surface layer and rapidly proceeds into the bulk region by highly correlated breaking of z-oriented diamond bonds. We identify a precursor seed to the structural transformation, and in particular we obtain a non abrupt graphite–diamond interface forming prior to the transition. This interface is characterised by a regular alternation of three- and four-fold coordinated atoms along the [110] direction at the convex corner of the phase boundary. Local density of states (LDOS) analysis reveals the presence of chemically active sites at the interface region. Our results are in agreement with experiments on the thermal behaviour of diamond (111), confirm early measurements about surface induced graphitization of diamond, and bear important implications to the formation process of graphite islands in chemical vapor deposited (CVD) diamond films. In particular, we discuss the role of surface dangling bonds as chemisorption sites for atomic hydrogen, in relation to the stabilisation of CVD-grown diamond films by selective etching.

The simulation of surface dynamical and chemical processes has largely benefitted in recent times from the advent of parallel computers [1–3]. A detailed account of the computational techniques underlying these applications is beyond the purpose of the present work, and can be found in the specialized literature [4,5]. The unprecedented computational power obtained by porting and optimising serial

codes on the current-generation parallel supercomputers allows as a routine dynamical simulation of physical systems constituted of hundreds or sometimes thousands of atoms, the precision of the modelling being the typical one of electronic structure calculations of the first principles or tight-binding type.

The present work consists of a series of fully ab initio molecular dynamics (MD) simulations of the diamond C(111)-(2 × 1) surface, with cells containing between 200 and 300 atoms. The main purpose

* Corresponding author.

of the investigation is to study the structural transition from the diamond (D) to the graphite (G) phase. The advantage of first principles MD simulations over more modellistic approaches is in the high accuracy and robustness of the technique, which requires no fitting to experimental data and thus generates unbiased results even in situations which are far from the experimental conditions providing the input for more crude models. While a range of techniques exists to parametrise interatomic forces into model potentials, so that a phase space region exists for which each model potential is correct, the extent of such region of validity is in general not known. A first principle calculation, whenever affordable, is the elective mathematical tool for simulating a given physical system if little is a priori known of this range of validity (variations of coordination, bond lengths, chemical environment) [6].

Carbon displays a rich variety of allotropes whose structural transitions into each other is considerably complex. Diamond surfaces have a unique thermal behaviour (e.g. no surface dynamical disordering is observed, as opposed to the case of other elemental semiconductor surfaces like Si(111)-(7 × 7) and Ge(111) [7]) whose features in turn determine their properties as growth planes for technologically relevant processes (e.g. growth of diamond films by chemical vapor deposition). Diamond is, at normal pressure, a metastable phase of carbon, the stable one being graphite. Due to the ~1.5 volume ratio between graphite and diamond, graphitization is forbidden in bulk diamond, where the growth of graphitic inclusions is limited by the compressive reaction of the diamond matrix. Graphitization is, on the other hand, observed as a surface initiated process [8,9] and a variety of studies is available about surface related D to G transformations.

Most of these studies are experimental investigations, and the theoretical research has mainly dealt with simple model systems. The earliest experimental studies on the structural phase transitions of diamond upon thermal treatment date back to the mid-nineteenth century [10,11]. After the structure of graphite was clarified [12], experiments on graphitization were performed in the nineteen-twenties [13–15], which revealed low pressure graphitization at temperatures above 1500 K.

A theoretical model for the D to G phase transi-

tion was originally put forward by Nath in 1935 [16]. According to Nath's model, the (111) puckered double layers of diamond flatten to form graphitic sheets of hexagonal carbon rings, which subsequently glide in pairs to give the Bernal graphite stacking (i.e. A, B, hexagonal stacking) from the original diamond stacking (A, B, C, rhombohedral stacking). There is no transport of isolated atoms or groups of atoms in this model of the phase transition, according to which the relative atomic positions in the (111) planes remain unchanged throughout the reaction. From the point of view of chemical bonding of individual atoms, the model has the character of a sp^3 to sp^2 hybridization change of the C atoms, uniformly throughout the system.

Later experimental work [8,9] focused on the surface-induced nature of the transition. As stated above, the D to G phase transformation is only possible at the surface of the samples, where the graphitic sheets nucleated in the transition can adjust their spacing by moving into the vacuum region. Evans and Davies ruled out Nath's direct transition model, on the basis of the great differences in electronic structure between D and G; in addition the percentage of rhombohedrally stacked graphite found in the treated samples was considered insufficient to support this model. These authors proposed instead a two-stage mechanism of graphite nucleation, in which grain growth of graphite would occur after an initial first step of debonding and transport of one [8] or more [9] C atoms. Although some experimental work supporting this view was available [17–19], the exact nature of the first stage of the transition could, however, not be clarified by the experiments. In the present work we present a theoretical study of the reconstructed diamond (111) surface as a function of temperature (T), based on a series of first principles molecular dynamics (MD) simulation [20]. A surface initiated graphitization process was obtained in the course of the simulations, and an interface between the D and G phases was identified and characterised. The LDOS analysis on the interface system revealed the presence of Fermi energy-pinning electronic states which might play a relevant role in the selective etching of the G phase by atomic H in CVD diamond film synthesis techniques [21].

In our calculations the C(111) surface in the reconstructed (2 × 1) geometry was represented by

periodically repeated slabs of C atoms, separated by a vacuum region of ≈ 9 Å. Both sides of the diamond slab were (2×1) reconstructed, and all atoms were allowed to move. The interaction between C ionic cores and valence electrons was described by a fully nonlocal pseudopotential [22] represented in

separable form [23] with s-only nonlocality. Single particle orbitals and charge density were expanded in plane waves with kinetic energy cutoffs of 33 and 99 Ry, respectively. Only Bloch functions at the Γ point of the supercell Brillouin zone (BZ) were included in the calculations. We performed computa-

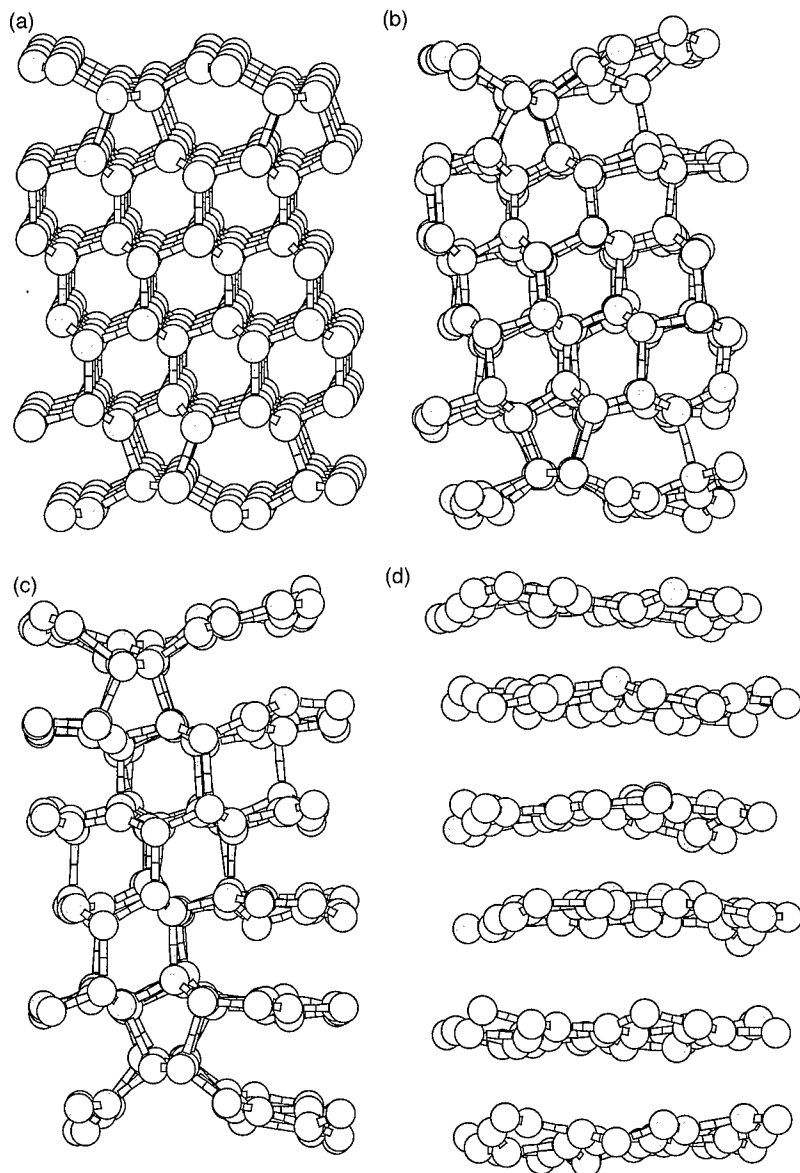


Fig. 1. Graphitization of the diamond slab at $T \approx 2500$ K. (a) The relaxed 192 atom system at 0 K. (b) Graphitization starts at the surface ($t = 0$). Almost all bonds between the first and the second double layers are broken, and the first double layers flatten to form strained graphite seeds on both sides of the slab. (c) Graphitization has progressed throughout the slab by a correlated z-oriented bond-breaking mechanism ($t \approx 0.2$ ps; see text). A D/G interface orthogonal to the surface is formed. (d) All bonds between double layers are broken ($t \approx 0.4$ ps).

tions on supercells containing 16 atoms per layer (192 atom slab) or 24 atoms per layer (288 atom slab). These *ab initio* simulations, adding up to a total simulated time of about 12 ps, have been made possible by the use of a massively parallel computer (a CRAY T3D at the EPFL, Lausanne) and of a newly designed code LAUTREC, optimised for this machine [5].

In the first part of our study, the system represented by the 192 atom slab was heated up to about 2500 K, starting from the (2×1) reconstructed geometry, which is the stable structure at 0 K (Fig. 1a). A constant temperature (CT) simulations was then carried out at $T \approx 2500$ K, and a surface induced graphitization of the diamond slab was observed to occur spontaneously. The CT simulations were performed using Nosé thermostats [24]. The sensitivity of the results with respect to the effective mass of the thermostat was carefully monitored. Diamond graphitization with unchanged features was obtained with different values of the thermostat mass parameter [24] varying within two orders of magnitude, giving us complete confidence into the thermal treatment used. Graphitization was also obtained for a system similar to that of Fig. 1, in which one of the slab surfaces was a diamond (111) cleaved surface saturated with H atoms and kept fixed throughout the simulations.

The graphitization process starts at the surface. The bonds between the first and the second double layer break (in the reconstructed geometry at 0 K they are about 8% longer than those of bulk diamond [25]) and the first two surface layers flatten to form a strained graphite seed (Fig. 1b; the projected intra-layer bond distance of diamond is 1.45 Å, to be compared to the equilibrium bond length of graphite, 1.42 Å). Once the graphitic seed is formed, a fast graphitization of the whole slab takes place, without any intermediate reconstruction of the ideal layers underneath. The slab graphitization proceeds through a correlated sp^3 to sp^2 hybridisation change of the nearest neighbour atoms in the (111) diamond double layers. Every bond of the subsurface region oriented in the (*z*) direction perpendicular to the surface connects two (111) double layers. Starting from the surface and proceeding into the slab, for each of these bonds there are three similar nearest neighbour *z*-oriented bonds, connecting the next cou-

ple of (111) double layers further into the bulk region. Thus, the correlated hybridisation change from diamond to graphite bonding of pairs of neighbouring atoms in the (111) double layers involves the breaking of nearest neighbour *z*-oriented bonds in the system. This in turn results in penetration of the graphite phase into the diamond phase before complete graphite planes can form, and therefore implies the formation of D/G interfaces which are not parallel to the surface. We notice that the observed correlated sp^3 to sp^2 hybridisation change of neighbouring atoms in the (111) diamond double layers may take place due to the energy gain of forming π -bonded C-atom couples (or closed rings, see Fig. 1c) in the (111) diamond double layers on their way to transforming into graphite sheets.

After ~ 0.5 ps of simulation the graphitization process is completed (Fig. 1d). The stacking of the graphitic slab obtained at the end of the transition is (A, B, C), i.e. the same as that of the starting diamond slab. The size of our simulation cell prevents the study of a possible stacking change during the transition. Nath's direct transition mechanism [16] is strongly supported by our results, while we have no evidence to support a two stages transition mechanism of the kind proposed in later work [8,9]. (A mechanism involving transport of carbon atoms at the surface cannot, however, be conclusively ruled out by our calculations, since such a mechanism could still in principle take place on a timescale not accessible to our simulations.) The diamond to graphite transition was also obtained at *T* lower than 2500 K, starting a CT run from a quenched atomic configuration (Fig. 1b) which corresponds to the onset of the transition found at $T \approx 2500$ K. The transition is found to proceed in the same way as at higher *T*. In particular, induced graphitization was observed at $T \approx 1900$ K. On the time scale of our simulations, the transition no longer occurred at $T \approx 1000$ K, from which a metastable interface geometry was instead obtained after ~ 1.5 ps of simulation time.

In the second part of our study we investigated the coexistence of the diamond and graphite phases, prior to the completion of the graphitization transition. To this purpose, we performed CT simulations starting from atomic configurations which contained a frozen seed of the structural transformation. The

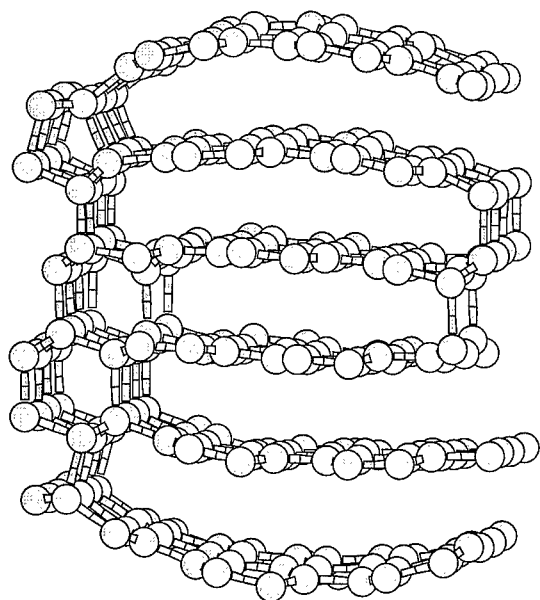


Fig. 2. D/G interface in the 288 atom slab system after 1 ps at $T = 300$ K. Notice the alternation of 3-fold and 4-fold coordinated atoms in the $[110]$ rows on both phase boundary convex edges (center of the slab).

last simulation mentioned above, which was performed at 1000 K on the 192 atom system, clearly showed the formation of an interface between the D and G phases which was stable over the time span of the simulation. To substantiate our findings, we repeated CT-MD runs with the 288 atom slab starting from an interface geometry obtained from the results of the 1000 K run. Namely, we structurally relaxed the 288 atom system and then heated it up to 300 K, at which temperature we performed a CT-MD simulation for a time $t \approx 1$ ps. We found that the interface remained stable, indicating that the potential energy surface of the system does not have local minima close in energy to that of the interface. The onset of the graphite into the diamond phase is found to take place via a sharp merging, occurring over one bond length. This interface between the two phases, shown in Fig. 2, is characterised by the alternation of three-fold and four-fold coordinated atoms along the $[110]$ direction at the convex corner of the phase boundary (center of the slab, on both sides of the graphite region) without any defect. This reconstruction can be easily seen to maximise the number of

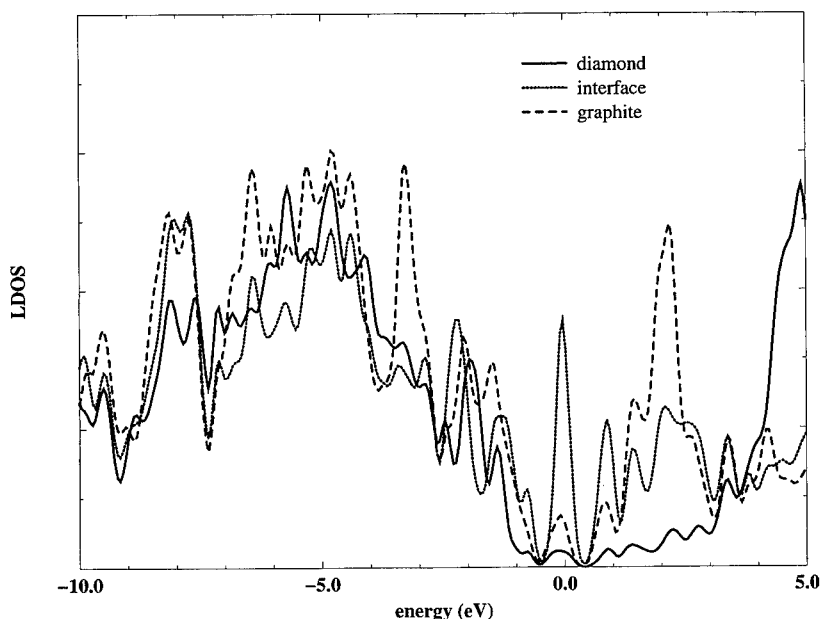


Fig. 3. Local density of electronic states for the 288 atom surface slab system. The three curves refer to the electronic density of states projected onto (110) planes orthogonal to the slab and parallel to the D/G interface. The planes are located in the diamond, graphite and D/G interface regions of the system. Notice the peak at the Fermi level in the LDOS at the interface, arising from localized electronic states with a predominantly p_z character. Such states may give rise to semimetallic or metallic conduction along the interface [27].

energetically stable closed hexagonal rings at the phase interface. At the same time, the sign change in the local stress field from the region of graphite (under compression in the z direction) to that of diamond (under tension in the z direction) is non abrupt, which may help to reduce the elastic contribution to the interface formation energy. (Stress relieving mechanisms such as nucleation of dislocations are not directly addressed by the present work, although our calculations provide no indications that such mechanisms take place.)

The termination of the graphite sheets into diamond in the interface system is characterised by the presence of unsaturated 'dangling' bonds. These bonds are responsible for the sharp peak in the LDOS in the region of the interface, and give rise to localised chemically active sites. The LDOS for the system of Fig. 2 is reported in Fig. 3. The three curves refer to the electronic density of states, projected onto (110) planes orthogonal to the slab and parallel to the D/G interface. The eigenvalue spectrum is convoluted with a Gaussian of width $\sigma = 0.1$

eV; the zero energy corresponds to the Fermi energy. The solid, dashed and dotted plots are the LDOS corresponding to planes located in the diamond, graphite and D/G interface regions of the system, respectively. The peak at the Fermi level in the LDOS at the interface arises from localized electronic states. Interface states of this kind may give rise to semimetallic or metallic conduction along the interface [26,27]. Further analysis reveals that these states are not entirely localised into the subsurface region, since some of them can be characterised as surface dangling bonds of predominantly p-character, located at the phase boundary (Fig. 4). These states could be the ideal binding sites for hydrogen atoms in chemisorption processes, in agreement with the band structure results in Ref. [28] on hydrogenated {10 $\bar{1}$ 0} graphite edges.

Atomic H is used as a selective etching agent [21] in CVD technique. Graphitic formations can nucleate within the diamond phase in low pressure synthetically grown diamond, depending on the CVD growth conditions [31]. It is likely that electronic states

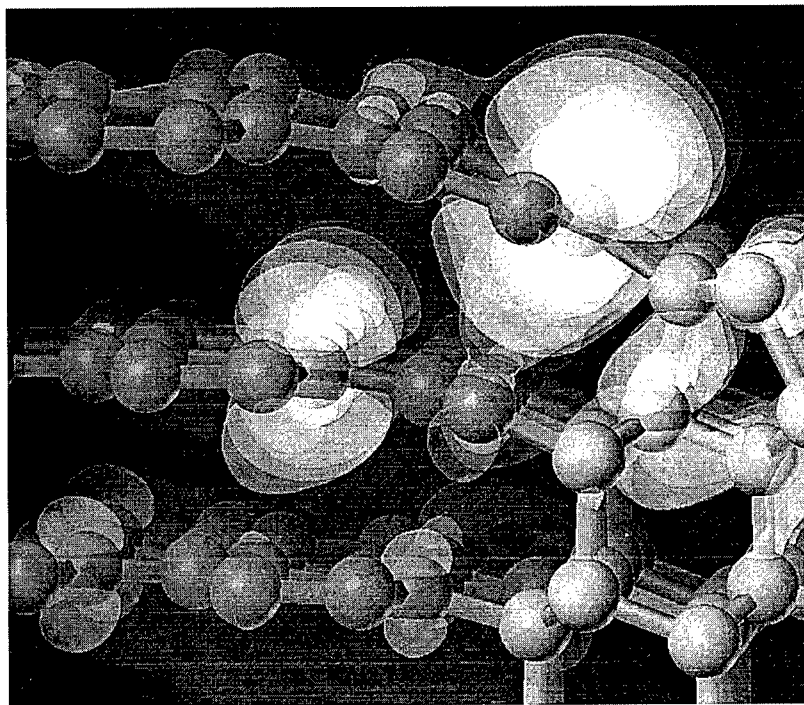


Fig. 4. Isovalue surfaces of the electronic particle density corresponding to the lowest unoccupied orbital of the system in Fig. 2, and to the peak at the Fermi energy in the D/G interface LDOS of Fig. 3. This and similar states are found at the insertion of the graphite plane in the diamond region and are expected to act as chemically active sites in processes like, e.g. hydrogen chemisorption.

similar to the Fermi energy-pinning interface states we observe are also present at the surface insertion of the graphitic phase into diamond in any graphitic nuclei which may form in CVD grown diamond films. The existence of chemically active sites at the surface phase boundary can play a significant role in the H etching processes. Firstly, preferential hydrogenation sites at the coherent insertion of the (stable) graphitic phase into the (metastable) diamond phase clearly substantiate the role of H in inhibiting graphite growth. Secondly, once a coherent D/G interface similar to the one illustrated in Fig. 2 is formed by spontaneous surface-initiated graphitization, the saturation of dangling bonds by hydrogen adsorption at the boundary between the two phases may conceivably initiate a dislocation generation mechanism, to relieve the z -oriented stress present at the interface. A possible picture is one in which the graphitic planes 'cut' from the diamond by hydrogenation relax into the vacuum to achieve their normal inter-layer spacing and form a graphitic extrusion on the surface of the film, laterally terminated by an hydrogenated prism plane. Hydrogenation of graphitic precursors is believed to play an important role in diamond nucleation and growth in diamond films obtained by CVD [30]. In particular, a well established model [29] for the growth of CVD diamond involves nucleation at the hydrogenated prism plane of graphitic formations somehow generated in the films [29]. Work is in progress on H/C systems to investigate the graphite formation process outlined above as a possible mechanism to generate diamond nucleation sites.

Acknowledgements

This work was partially supported through the Parallel Application Technology Program (PATP) between EPFL and Cray Research, Inc., and by Swiss NSF under grant No. 20-39528.93.

References

- [1] M.C. Payne, I. Stich, R.D. King-Smith, J.S. Lin, A. De Vita and M.J. Gillan, *Ab initio Simulations on Parallel Computers*, in: *Computer Aided Innovation of New Materials II*, Eds. M. Doyama, J. Kihara, M. Tanaka and R. Yamamoto (Elsevier, Amsterdam, 1993).
- [2] I. Stich, M.C. Payne, R.D. King-Smith, J.-S. Lin and L.J. Clarke, *Phys. Rev. Lett.* 68 (1992) 1351.
- [3] A. De Vita, I. Stich, M.J. Gillan, M.C. Payne and L.J. Clarke, *Phys. Rev. Lett.* 71 (1993) 1276.
- [4] L.J. Clarke, I. Stich and M.C. Payne, *Comput. Phys. Commun.* 72 (1992) 14.
- [5] A. Canning, A. De Vita and R. Car, in preparation; A. De Vita, A. Canning, G. Galli, F. Gygi, F. Mauri and R. Car, *Supercomputing Rev. (EPFL)* 6 (1994) 22.
- [6] M.C. Payne, I. Stich, A. De Vita, M.J. Gillan and L.J. Clarke, *Faraday Disc.* 96 (1993) 151.
- [7] N. Takeuchi, A. Selloni and E. Tosatti, *Phys. Rev. Lett.* 72 (1994) 2227, and references therein.
- [8] T. Evans and P.F. James, *Proc. R. Soc. London A* 277 (1964) 260.
- [9] G. Davies and T. Evans, *Proc. R. Soc. London A* 328 (1972) 413.
- [10] Jacquelin, *Ann. Chim. Phys.* 20 (1847) 468.
- [11] A.R. v. Schrötter, *Sitzungsber. Akad. Wiss. (Wien)* 63 (1871) 465.
- [12] J.D. Bernal, *Proc. R. Soc. A* 106 (1924) 749.
- [13] M. de Kay Thompson and P.K. Frölich, *Trans. Am. Electrochem. Soc.* 43 (1923) 161.
- [14] G. Friedel and G. Ribaud, *C.R. Acad. Sci.* 178 (1924) 1126.
- [15] P. Libeau and M. Picon, *C.R. Acad. Sci.* 179 (1924) 1059.
- [16] N.S.N. Nath, *Proc. Indian Acad. Sci. A* 2 (1935) 143.
- [17] H.P. Bovenkerk, F.P. Bundy, H.T. Hall, H.M. Strong and R.H. Wentorf, *Nature (London)* 184 (1959) 1094.
- [18] H.J. Rodewald, *Helv. Chim. Acta* 43 (1960) 1657.
- [19] F.P. Bundy, H.T. Hall, H.M. Strong and R.H. Wentorf, *J. Chem. Phys.* 15 (1961) 192.
- [20] R. Car and M. Parrinello, *Phys. Rev. Lett.* 55 (1985) 2471.
- [21] J.C. Angus, H.A. Will and W.S. Stanko, *J. Appl. Phys.* 39 (1968) 2915.
- [22] G.B. Bachelet, D. Hamman and M. Schluter, *Phys. Rev. B* 26 (1982) 4199.
- [23] L. Kleinman and D.M. Bylander, *Phys. Rev. Lett.* 48 (1982) 1425.
- [24] S. Nosé, *Mol. Phys.* 52 (1984) 255; W. Hoover, *Phys. Rev. A* 31 (1985) 1695.
- [25] S. Iarlori, G. Galli, F. Gygi, M. Parrinello and E. Tosatti, *Phys. Rev. Lett.* 69 (1992) 2947.
- [26] D.J. Klein, *Chem. Phys. Lett.* 217 (1993) 261.
- [27] A.T. Balaban, D.J. Klein and C.A. Folden, *Chem. Phys. Lett.* 217 (1993) 266.
- [28] S.P. Mehandru, A.B. Anderson and J.C. Angus, *J. Phys. Chem.* 96 (1992) 10978.
- [29] W.R.L. Lambrecht, C.H. Lee, B. Segall, J.C. Angus, Z. Li and M. Sunkara, *Nature* 364 (1993) 607.
- [30] J.C. Angus and C.C. Hayman, *Science* 241 (1988) 913, and references therein.
- [31] W. Zhu, C.A. Rendall, A.R. Badzian and R. Messier, *J. Vac. Sci. Technol. A* 7 (1989) 2315.



ELSEVIER

Applied Surface Science 104/105 (1996) 304–311

applied
surface science

A comparative study of the adsorption and thermal decomposition of triethylgallium and trimethylgallium at GaAs(100) surfaces studied by electron energy loss spectroscopy

A.A. Aquino^a, T.S. Jones^{b,*}

^a Department of Chemistry, Imperial College, London SW7 2AY, UK

^b Department of Chemistry and Interdisciplinary Research Centre for Semiconductor Materials, Imperial College, London SW7 2AY, UK

Received 1 July 1995; accepted 2 October 1995

Abstract

High resolution electron energy loss spectroscopy (HREELS) has been used to study the adsorption and thermal decomposition of triethylgallium (TEGa) and trimethylgallium (TMGa) at Ga-terminated GaAs(100) surfaces. HREEL spectra recorded for adsorption of TEGa at room temperature show that the dominant surface species is based on intact ethyl (C_2H_5) groups. The surface species, which is likely to be diethylgallium (DEGa), is stable up to 250°C. Heating to 400°C results in the complete decomposition of the molecule via the facile β -elimination mechanism. For TMGa adsorption, HREEL spectra indicate that the stable surface species at room temperature is based on intact methyl (CH_3) groups, and is likely to be a dimethylgallium (DMGa) species. Decomposition of this species occurs with increasing temperature and involves the loss of CH_3 groups from the surface. In contrast to the clean decomposition of TEGa, a surface methylene (CH_2) species is also identified for TMGa at elevated temperatures and suggests an additional decomposition pathway involving loss of hydrogen from adsorbed CH_3 groups. The presence of this stable species in the case of TMGa, and not TEGa, is a possible explanation for the high carbon incorporation levels found in GaAs grown by chemical beam epitaxy (CBE) from this precursor.

1. Introduction

Trimethylgallium (TMGa) and triethylgallium (TEGa) are widely used as precursors in the epitaxial growth of GaAs from organometallic sources [1]. TMGa is commonly employed in the high pressure metalorganic vapour phase epitaxy (MOVPE) growth

process with low carbon incorporation levels resulting from the grown material [2]. In contrast, the use of TMGa in ultra high vacuum (UHV) growth techniques, such as chemical beam epitaxy (CBE) and metalorganic molecular beam epitaxy (MOMBE), leads to very high levels of carbon incorporation, with acceptor concentrations ranging typically from 10^{19} to 10^{21} cm^{-3} [3,4]. Whilst such high acceptor levels are useful for certain specific applications, it is generally more desirable to grow GaAs based material with low impurity levels. Consequently, TEGa is the more commonly used precursor for both CBE

* Corresponding author. Tel.: +44-171-5945794; fax: +44-171-5945801; e-mail: t.jones@ic.ac.uk.

and MOMBE growth as it leads to significantly lower carbon incorporation levels ($\sim 10^{14} \text{ cm}^{-3}$) [5].

Being UHV based growth techniques, the epitaxial process in both CBE and MOMBE is determined entirely by surface reactions. It is generally accepted that the high carbon levels obtained in GaAs growth from TMGa reflect a very different surface decomposition process compared with TEGa. It has been suggested that TEGa decomposes with the release of ethylene (C_2H_4) groups via a β -hydride elimination mechanism [6]. This facile process cannot occur with TMGa. In addition, the growth behaviour with TMGa has a much stronger dependence on the growth conditions, including the substrate temperature [7], the group V/III flux ratio [8,9] and the atomic nature of different step terminations [7]. This chemical specificity has resulted in TMGa being used as the main precursor in atomic layer epitaxy (ALE), a growth process which involves the Ga and As sources being supplied in an alternating sequence, and depends on the ability of the precursor to deposit a self-limiting monolayer of Ga [10].

There have been a number of studies concerned with understanding the adsorption and thermal decomposition of TMGa and TEGa on both Ga- and As-terminated GaAs(100) surfaces [11–27]. The majority have involved thermal desorption (TPD) and mass spectrometric detection of the desorbing products (e.g. modulated beam mass spectroscopy, MBMS). However, the details of the reaction mechanisms are still unknown, in particular the identification of the surface intermediates in the thermal decomposition process. Surface vibrational spectroscopy is one of the most powerful methods for identifying molecular fragments adsorbed on surfaces. In this paper, we present a high resolution electron energy loss spectroscopy (HREELS) study of the vibrational properties of TMGa and TEGa adsorbed on Ga-rich GaAs(100) surfaces. Since the CBE and MOMBE growth processes are generally carried out under As-rich conditions, the Ga-terminated surface is not an ideal representation of the growing surface. However, our measurements have been carried out with a far higher resolution than previous HREELS studies and enable a more rigorous study of the vibrational properties of the adsorbate to be made.

2. Experimental

The experiments were carried out in an UHV system (base pressure $< 2 \times 10^{-10}$ Torr) equipped with HREELS, Auger electron spectroscopy (AES) and low energy electron diffraction (LEED). The n-type (Si doped, $n \sim 2 \times 10^{17} \text{ cm}^{-3}$) GaAs(100) substrates were cleaned in situ by cycles of argon ion bombardment (2 keV, 5 μA sample current, 10 min, 400°C) and annealing (400°C, 10 min). This resulted in a clean surface as determined by AES and a (4×1) LEED pattern corresponding to a Ga-terminated surface. The samples were then exposed to TMGa or TEGa (Epichem, UK) at room temperature until saturation coverage was obtained, as evidenced by no further changes in the intensity of the vibrational loss peaks with increasing precursor exposure.

The HREEL spectrometer (HIB 1000) consists of a double pass cylindrical monochromator and analyser assembly, with the analyser fixed and the monochromator rotatable [28]. Measurements were carried out in specular ($\theta_i = 45^\circ$, $\theta_s = 45^\circ$) and off-specular scattering geometries and with incident electron energies less than 10 eV [29]. The resolution of the spectrometer (FWHM) in the 'straight through' beam was $16\text{--}24 \text{ cm}^{-1}$, while a resolution of $28\text{--}56 \text{ cm}^{-1}$ was routinely obtained both from the clean and adsorbate covered GaAs surface. Specular HREELS studies of the clean GaAs(100) surface are characterised by two intense losses (and the corresponding gains) at 285 and 570 cm^{-1} (Fig. 1). These are the strongly dipole active surface optical phonon excitations which dominate specular HREELS studies of III–V semiconductor surfaces [30].

HREELS spectra of the adsorbate covered surface were always recorded at room temperature. The effects of substrate temperature on the decomposition of the adsorbate were monitored in two different ways. Firstly, by adsorbing at room temperature and recording HREELS spectra after annealing for a few minutes at several different elevated temperatures. Alternatively, the sample was exposed to the precursor at various substrate temperatures and the HREELS spectra were subsequently recorded after cooling to room temperature. There was no discernable difference in the HREELS spectra recorded using these two approaches.

3. Results

3.1. TEGa / GaAs(100)

A specular HREEL spectrum, recorded at a primary electron beam energy of 8 eV, for a GaAs(100) surface exposed to TEGa at room temperature, is shown in Fig. 1. Similar spectra have been observed with much lower resolution in previous HREELS studies of the adsorption of TEGa on GaAs(100) at 300 K [26]. Apart from the intense phonon losses at 285 and 570 cm^{-1} , the spectrum shows a series of loss peaks at 860, 950, 990, 1170, 1220, 1370, 1450 and 2910 cm^{-1} . These can be assigned by comparison with infrared (IR) and Raman studies of liquid

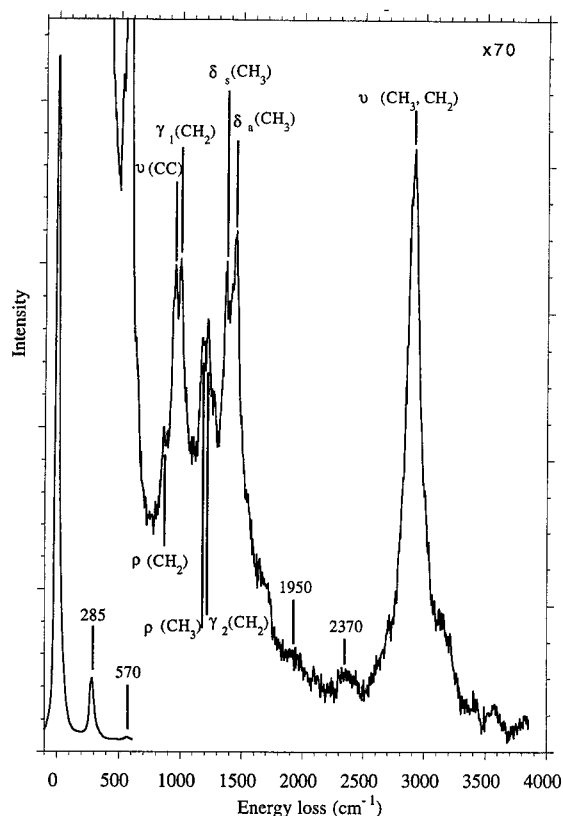


Fig. 1. Specular ($\theta_i = \theta_r = 45^\circ$) HREEL spectrum for TEGa adsorbed on GaAs(100) at room temperature. The spectrum was recorded with an incident electron energy of 8 eV and the loss region has been multiplied by a factor of 70 with respect to the elastic peak. A spectrum recorded at 8 eV for the clean GaAs(100) surface is also shown with two intense phonon losses at 285 and 570 cm^{-1} .

Table 1

The vibrational frequencies (cm^{-1}) obtained from specular HREELS spectra, recorded with an incident electron energy of 8 eV, for TEGa adsorbed on GaAs(100) at room temperature (Fig. 1)

Assignment	TEGa/GaAs(100)	Liquid TEGa [31]
phonon	570	—
$\rho(\text{CH}_2)$	860	890
$\nu(\text{CC})$	950	960
$\gamma(\text{CH}_2)$	990, 1220	1000, 1060, 1230
$\rho(\text{CH}_3)$	1170	1100
$\delta_s(\text{CH}_3)$	1370	1380, 1390
$\delta_a(\text{CH}_3)$	1450	1460
$\nu(\text{CH}_3, \text{CH}_2)$	2910	2870, 2900, 2950

The assignments are made by comparison with IR spectra obtained from liquid TEGa [31].

TEGa [31] (Table 1). The bands at 860 and 1170 cm^{-1} correspond to CH_2 and CH_3 rocking modes ($\rho(\text{CH}_2)$ and $\rho(\text{CH}_3)$), the band at 950 cm^{-1} to a C–C stretch ($\nu(\text{CC})$), the bands at 990 and 1220 cm^{-1} to twists of the CH_2 groups ($\gamma(\text{CH}_2)$), the bands at 1370 and 1450 cm^{-1} to the symmetric and asymmetric deformations of the CH_3 groups ($\delta_s(\text{CH}_3)$ and $\delta_a(\text{CH}_3)$) and the band at 2910 cm^{-1} to C–H stretching vibrations of the CH_3 and CH_2 groups ($\nu(\text{CH}_3)$ and $\nu(\text{CH}_2)$). These frequencies suggest that intact ethyl groups are present at the surface, although it is not possible even with this resolution to determine precisely the nature of the adsorbed species. The origin of the two weak bands at 1950 and 2370 cm^{-1} , which cannot be attributed to fundamental vibrations of adsorbed ethyl groups, will be discussed in Section 4.1.

The effects of temperature on the HREELS spectra for the TEGa covered GaAs(100) surface are shown in Fig. 2. There is very little change in the spectra as the temperature is raised to 250°C. However, upon heating to 350°C, there is a significant decrease in the intensities of all the bands, indicating the removal of ethyl groups from the surface. Further heating to 450°C results in the disappearance of all the vibrational bands, suggesting that the ethyl groups have been completely removed from the surface and the decomposition of TEGa is complete.

3.2. TMGa / GaAs(100)

A specular HREEL spectrum, recorded at a primary beam electron energy of 5 eV, for a GaAs(100)

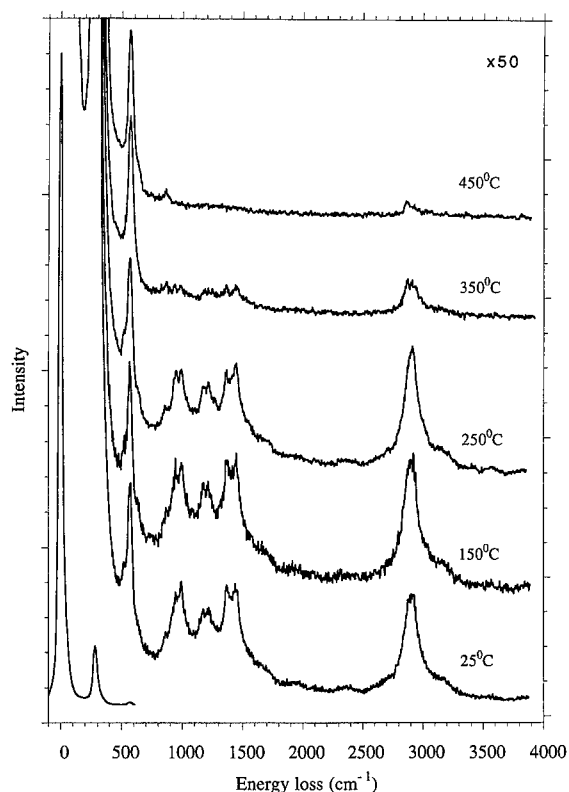


Fig. 2. Specular ($\theta_i = \theta_s = 45^\circ$) HREEL spectra recorded at 8 eV for TEGa adsorbed on GaAs(100) at room temperature and then annealed to 150, 250, 350 and 450°C, respectively. All the spectra were recorded at room temperature and the loss regions have been multiplied by a factor of 50 with respect to the elastic peak.

surface exposed to TMGa at room temperature, is shown in Fig. 3. A series of loss peaks can be seen at 700, 1200, 1450 and 2930 cm^{-1} . Assignments can be made by comparison with bulk IR and Raman data for solid TMGa [32] (Table 2). The band at 700 cm^{-1} corresponds to a CH_3 rocking mode ($\rho(\text{CH}_3)$), the bands at 1200 and 1450 cm^{-1} to the symmetric and asymmetric deformations of the CH_3 groups ($\delta_s(\text{CH}_3)$ and $\delta_a(\text{CH}_3)$) and the band at 2930 cm^{-1} to C–H stretching vibrations of the CH_3 groups ($\nu(\text{CH}_3)$). Similar loss features were observed in off-specular scattering although there were no significant changes in the relative intensities of the bands. Similar spectra have been observed in other HREELS studies of the adsorption of TMGa on GaAs(100) at room temperature [20–22] and the frequencies obtained suggest that intact methyl groups are present at the surface, although again it is not possible even

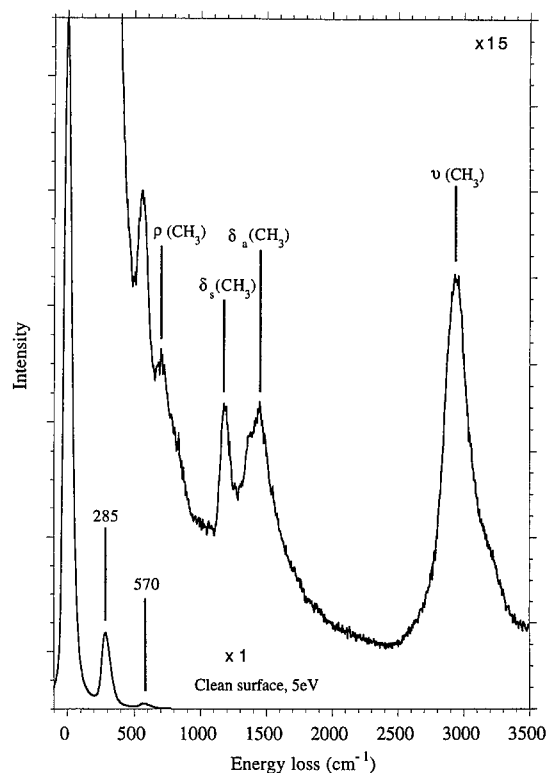


Fig. 3. Specular ($\theta_i = \theta_s = 45^\circ$) HREEL spectrum for TMGa adsorbed on GaAs(100) at room temperature. The spectrum was recorded with an incident electron energy of 5 eV and the loss region has been multiplied by a factor of 15 with respect to the elastic peak. A spectrum recorded at 5 eV for the clean GaAs(100) surface is also shown with two intense phonon losses at 285 and 570 cm^{-1} .

with this improved resolution to determine whether the adsorbed species is TMGa, dimethylgallium (DMGa) or monomethylgallium (MMGa).

Table 2

The vibrational frequencies (cm^{-1}) obtained from specular HREELS spectra, recorded with an incident electron energy of 5 eV, for TMGa adsorbed on GaAs(100) at room temperature (Fig. 3)

Assignment	TMGa/GaAs(100)	Solid TMGa [32]
phonon	570	—
$\rho(\text{CH}_3)$	700	673, 745
$\delta_s(\text{CH}_3)$	1200	1168
$\delta_a(\text{CH}_3)$	1450	1425
$\nu(\text{CH}_3)$	2930	2898, 2955

The assignments are made by comparison with IR and Raman spectra obtained from solid TMGa [32].

The effects of temperature on the HREELS spectra for the TMGa covered GaAs(100) surface are shown in Fig. 4. As the temperature is raised to 200°C, the intensities of $\delta_s(\text{CH}_3)$ and $\delta_a(\text{CH}_3)$ both decrease whilst a new band appears at 1330 cm^{-1} . There is also a significant reduction in the intensity of $\nu(\text{CH}_3)$ and a new band appears at 860 cm^{-1} . These changes become more pronounced upon annealing to 400°C and there is a small down shift in the C–H stretching frequency from $\sim 2930 \text{ cm}^{-1}$ at 25°C to 2900 cm^{-1} at 400°C. Further heating to 500°C results in a significant decrease in the intensity of all the bands indicating that the decomposition of TMGa is almost complete.

The three losses at 860, 1330 and 2900 cm^{-1} , which dominate the spectra at elevated temperatures, do not derive from a surface species based on methyl

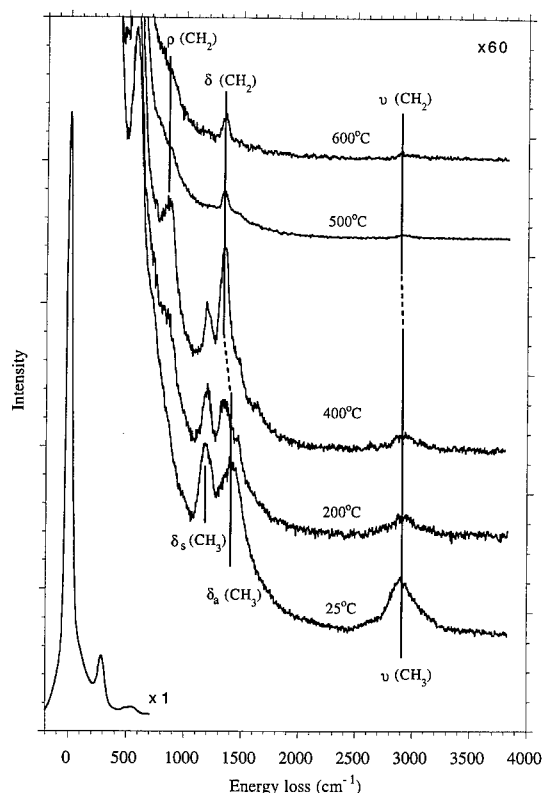


Fig. 4. Specular ($\theta_i = \theta_s = 45^\circ$) HREEL spectra recorded at 6 eV for TMGa adsorbed on GaAs(100) at room temperature and then annealed to 200, 400, 500 and 600°C, respectively. All the spectra were recorded at room temperature and the loss regions have been multiplied by a factor of 60 with respect to the elastic peaks.

Table 3

The vibrational frequencies (cm^{-1}) obtained from HREELS spectra of TMGa adsorbed on GaAs(100) at room temperature and subsequently annealed to 400°C (Fig. 2)

	Ref.	$\delta(\text{CH}_2)$	$\nu(\text{CH}_2)$	$\rho(\text{CH}_2)$
TMGa/GaAs(100)		1330	2900	860
$\text{SiH}_3\text{CH}_2\text{SiH}_3$	[33]	1363	2902, 2941	776
$\text{GeH}_3\text{CH}_2\text{SiH}_3$	[34]	1362–1382	2900	745
$\text{CH}_2/\text{Ni}(111)$	[35]	1300	2980	790
$\text{CH}_2/\text{Ru}(001)$	[36]	1295	2870, 2945	890

Comparisons are made with vibrational spectra obtained from two organometallic compounds [33,34] and also with previous HREELS studies of the adsorption of CH_2 on transition metal surfaces [35,36].

groups. They can be assigned by comparison with IR and Raman studies of several organometallic compounds containing methylene (CH_2) groups, e.g. $\text{SiH}_3\text{CH}_2\text{SiH}_3$ [33] and $\text{GeH}_3\text{CH}_2\text{SiH}_3$ [34] (Table 3). The band at 860 cm^{-1} is the rocking mode of a CH_2 group, $\rho(\text{CH}_2)$, the band at 1330 cm^{-1} is the in-plane bending mode of a CH_2 species, $\delta(\text{CH}_2)$, and the band at 2900 cm^{-1} is the stretching vibration of CH_2 ($\nu(\text{CH}_2)$). Similar frequencies and assignments have been made in previous HREELS studies of the methylene species formed on transition metal surfaces [35,36] and also in recent studies of the adsorption of both trimethylaluminium (TMAI) [37] and trimethylindium (TMIn) [38] on GaAs(100) surfaces.

4. Discussion

4.1. TEGa decomposition

The vibrational frequencies in the HREEL spectrum shown in Fig. 1 for room temperature adsorption are consistent with an adsorbed species based on intact ethyl groups. Since adsorption takes place on a Ga-terminated surface, it is highly probable that one ethyl group detaches itself from the TEGa molecule leading to an adsorbed DEGAs and ethyl species (Fig. 5). This process occurs for substrate temperatures up to 250°C as there are no changes of any consequence

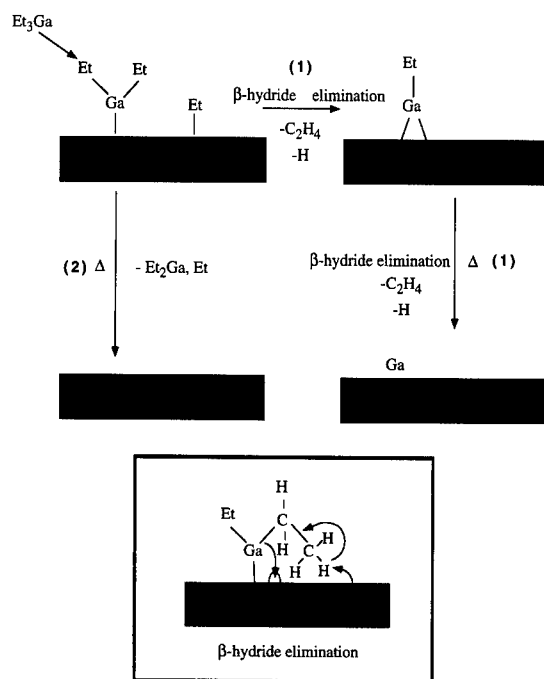


Fig. 5. A schematic diagram illustrating the possible decomposition pathways for TEGa adsorbed on GaAs(100). At room temperature, TEGa dissociatively adsorbs on the Ga-terminated surface to form DEGa and an adsorbed ethyl species. On heating, decomposition can occur via two routes: (1) a β -hydride elimination reaction resulting in the desorption of C₂H₄ and (2) desorption of Et₂Ga and ethyl groups. Note that hydrogen atoms released in the β -elimination process combine and desorb as molecular hydrogen.

in the HREEL spectra recorded over this temperature range (Fig. 2).

Previous desorption studies (both TPD methods and in situ MBMS growth studies) of the decomposition of TEGa at GaAs(100) surfaces indicate that diethylgallium (DEGa), C₂H₄ and to a lesser extent ethyl groups, are the primary desorbing products [6,18,27]. Two different decomposition mechanisms (labelled route (1) and (2)) are shown in Fig. 5. Route (1) involves loss of ethyl groups via a facile β -hydride elimination reaction with the production of C₂H₄ as a desorption product. In principle, this concerted process should also result in atomic hydrogen bonded to the surface. Previous HREELS studies of hydrogen adsorbed on GaAs(100) showed that stretching frequencies of 1875 and 2110 cm⁻¹ are characteristic of Ga-H and As-H surface bonds respectively [39]. Although the HREEL spectrum for

room temperature adsorption of TEGa shows two weak bands at 1950 and 2370 cm⁻¹ (Fig. 1), the significantly higher frequency of these bands suggests that they do not correspond to vibrations of adsorbed hydrogen atoms, but instead are likely to be combination bands involving $\nu(\text{CC}) + \gamma(\text{CH}_2)$ and $\gamma(\text{CH}_2) + \rho(\text{CH}_3)$. Furthermore, no bands were seen in this frequency range in the spectra recorded at elevated temperatures. The implication is either that the concentration of surface hydrogen is too low to be detected by HREELS, or more likely, that surface hydrogen atoms produced from different ethyl groups by the β -elimination mechanism recombine and lead to the desorption of molecular hydrogen; H₂ desorption has been detected in previous TPD studies of TEGa adsorbed on GaAs(100) [27]. Route (2) simply involves the loss of DEGa and ethyl groups from the surface, resulting in little gallium being deposited on the surface.

It has previously been shown that there is a significant decrease in the amount of products formed by the β -hydride elimination reaction (H₂ and C₂H₄) for adsorption of TEGa on As-rich GaAs(001) surfaces [27]. This suggests that surface Ga atoms play an important role in this concerted reaction and the results are consistent with our HREELS data, which shows that all adsorbed species are removed from the surface after heating to temperatures in excess of 400°C (Fig. 2).

4.2. TMGa decomposition

TMGa cannot undergo the facile β -hydride elimination reaction which occurs in the case of TEGa. The vibrational spectrum shown in Fig. 3, for adsorption of TMGa at room temperature, is consistent with an adsorbed species based on intact methyl groups. There has been some debate as to whether the adsorbed species is molecular TMGa or involves loss of CH₃ groups and the formation of either dimethylgallium (DMGa) or monomethylgallium (MMGa). Molecular beam scattering studies on both As- and Ga-terminated surfaces have shown that at room temperature, TMGa adsorbs molecularly intact on the As-rich surface, whereas dissociation to a DMGa species occurs on the less electron rich Ga-terminated surface [15]. The HREELS data for room temperature adsorption in Fig. 3 are therefore consis-

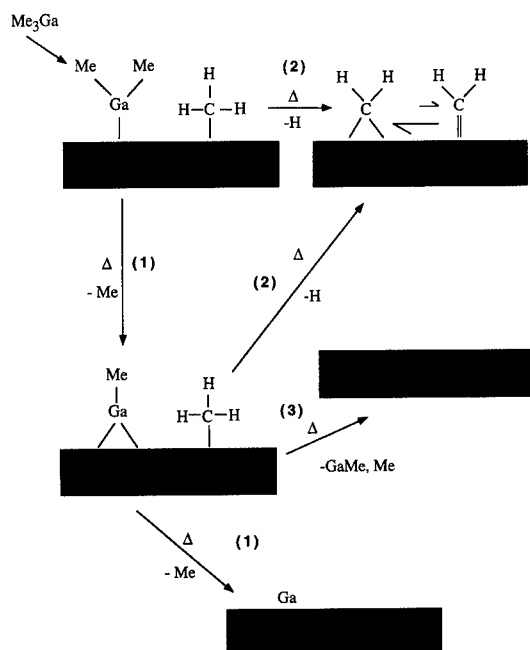


Fig. 6. A schematic diagram illustrating the possible decomposition pathways for TMGa adsorbed on GaAs(100). At room temperature, TMGa dissociatively adsorbs on the Ga-terminated surface to form DMGa and an adsorbed CH₃ species. On heating, decomposition can occur via three routes: (1) the sequential loss of CH₃ groups, (3) the loss of GaCH₃ and CH₃ groups and (2) loss of H from adsorbed CH₃ groups, leading to the formation of a surface CH₂ species. Note that hydrogen atoms released in the formation of the surface CH₂ species combine and desorb as molecular hydrogen.

tent with an adsorbed DMGa and CH₃ species (Fig. 6).

The possible decomposition routes are summarised in Fig. 6. Previous desorption experiments [15] have shown that the dominant decomposition route for TMGa at GaAs(100) surfaces involves the sequential loss of CH₃ groups from the surface (route (1)), although some CH₃ groups also desorb as MMGa species (route (3)). A similar decomposition process is also well known for TMGa in the gas phase [40]. The formation of the CH₂ species at elevated temperature indicates an additional decomposition pathway involving hydrogen abstraction from CH₃ groups bonded to the surface (route (2)) [23]. Similar to the situation with adsorbed TEGa, there is no evidence in the HREEL spectra (both on- and off-specular) for adsorbed hydrogen atoms. We

again assume that recombination and desorption of H₂ occurs consistent with previous TPD studies [23]. The low frequency of $\nu(\text{CH}_2)$ indicates that the likely bonding arrangement of this species involves the carbon atom bridging two surface gallium atoms, as opposed to an arrangement involving a Ga–C double bond which would result in a correspondingly higher frequency for $\nu(\text{CH}_2)$ (Fig. 6). Further heating to temperatures in excess of 500°C leads to the complete decomposition of all adsorbed species.

It has recently been suggested on the basis of local vibrational mode (LVM) IR measurements that the identification of C–H pairs in GaAs grown by MOMBE using TMGa is consistent with a mechanism for carbon incorporation involving a surface CH₂ species [41]. The observation of C–H pairs in the bulk crystal was explained by the formation of a CH₂ species on the surface during growth and its subsequent decomposition. The high concentration of carbon impurities in the bulk material (typically $> 10^{19} \text{ cm}^{-3}$) indicate that the concentration of the surface species is sufficiently high to be detected by surface sensitive techniques such as HREELS.

5. Conclusions

HREELS has been used to study the vibrational properties of TEGa and TMGa adsorbed on Ga-terminated GaAs(100) surfaces. Adsorption at room temperature shows that the dominant surface species are based on intact ethyl or methyl groups respectively. With increasing temperature the intensities of the characteristic ethyl and methyl vibrational bands are significantly reduced. These results are consistent with TEGa and TMGa decomposing with increasing temperature via the release of ethyl and methyl groups, respectively.

Significant differences are apparent in the HREEL spectra recorded at higher temperatures. For TEGa adsorption, thermal decomposition is essentially complete at $\sim 400^\circ\text{C}$, consistent with the dominant decomposition route occurring via the facile β -elimination mechanism leading to the desorption of C₂H₄. However, for TMGa adsorption, a surface methylene (CH₂) species is clearly identified at higher temperatures which suggests a second minority decomposition route involving the dehydrogena-

tion of CH_3 groups. The stability of the CH_2 species at high substrate temperatures and its absence in the thermal decomposition of TEGa, indicates that this species is the most likely source of the high carbon incorporation levels observed in the CBE/MOMBE growth of GaAs based material from TMGa.

Acknowledgements

This work was supported by the Engineering and Physical Sciences Research Council (EPSRC), UK under grant number GRIH66662. A.A.A. is grateful to the British Vacuum Council for financial assistance.

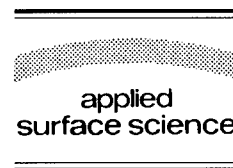
References

- [1] A.C. Jones, *J. Cryst. Growth* 129 (1993) 728, and references therein.
- [2] P.D. Dapkus, H.M. Manasevit, K.L. Hess, T.S. Low and G.E. Stillman, *J. Cryst. Growth* 55 (1981) 10.
- [3] N. Putz, H. Heinecke, M. Heyen, P. Balk, M. Weyers and H. Lüth, *J. Cryst. Growth* 74 (1986) 292.
- [4] T.F. Kuech, M.A. Tischler, P.J. Wang, G. Scilla, R. Potemski and F. Cardone, *Appl. Phys. Lett.* 53 (1988) 1317.
- [5] B.J. Lee, Y.M. Hwang and J.N. Miller, *J. Cryst. Growth* 105 (1990) 168.
- [6] T. Martin and C.R. Whitehouse, *J. Cryst. Growth* 105 (1990) 57.
- [7] T. Kaneko, O. Naji, T.S. Jones and B.A. Joyce, *J. Cryst. Growth* 127 (1993) 1059.
- [8] T. Kaneko, O. Naji, T.S. Jones and B.A. Joyce, *J. Cryst. Growth* 136 (1994) 99.
- [9] T. Kaneko, B.A. Joyce, O. Naji and T.S. Jones, *Appl. Phys. Lett.* 67 (1995) 998.
- [10] M.L. Yu, *J. Appl. Phys.* 73 (1993) 716.
- [11] M.L. Yu, U. Memmert and T.F. Kuech, *Appl. Phys. Lett.* 55 (1989) 1011.
- [12] U. Memmert and M.L. Yu, *Appl. Phys. Lett.* 56 (1990) 1883.
- [13] J.R. Creighton, K.R. Lykke, V.A. Shamamian and B.D. Kay, *Appl. Phys. Lett.* 57 (1990) 279.
- [14] J.R. Creighton, *Surf. Sci.* 234 (1990) 287.
- [15] M. Sasaki and S. Yoshida, *Surf. Sci.* 315 (1991) L964.
- [16] V.M. Donnelly and J.A. McCaulley, *Surf. Sci.* 238 (1990) 34.
- [17] J.R. Creighton, *J. Vac. Sci. Technol. A* 9 (1991) 2895.
- [18] A.J. Murrell, A.T.S. Wee, D.H. Fairbrother, N.K. Singh, J.S. Foord, G.J. Davies and D.A. Andrews, *J. Appl. Phys.* 68 (1990) 4053.
- [19] R. Souda and M.L. Yu, *Surf. Sci.* 280 (1993) 115.
- [20] X.Y. Zhu, J.M. White and J.R. Creighton, *J. Vac. Sci. Technol. A* 10 (1992) 316.
- [21] J. Stienstra, B.S. Lewis and J.F.M. Aarts, *J. Vac. Sci. Technol. A* 10 (1992) 920.
- [22] A. Nörmann and M.L. Yu, *Surf. Sci.* 269/270 (1992) 1041.
- [23] J.R. Creighton, B.A. Bansenauer, T. Huett and J.M. White, *J. Vac. Sci. Technol. A* 11 (1993) 876.
- [24] A.V. Annapragada, S. Salim and K.F. Jensen, *Mater. Res. Soc. Symp. Proc.* 222 (1991) 81.
- [25] A.A. Aquino, J.J. Hill and T.S. Jones, *Surf. Sci.* 327 (1995) 74.
- [26] E.T. Fitzgerald and J.S. Foord, *Surf. Sci.* 279 (1992) 121.
- [27] B.A. Banse and J.R. Creighton, *Science* 257 (1991) 221.
- [28] H. Ibach, *Electron Energy Loss Spectroscopy: The Technology of High Performance*, Springer Series in Optical Sciences, Vol. 63 (Springer, Berlin, 1991).
- [29] A.A. Aquino, C.P.A. Mulcahy and T.S. Jones, *Chem. Phys. Lett.* 252 (1996) 159.
- [30] L.H. Dubois and G.P. Schwartz, *Phys. Rev. B* 26 (1982) 794.
- [31] A.P. Kurbakova, L.A. Leimes, V.T. Alesanyan, L.M. Golubinsaya, E.N. Zorina and V.I. Bregadze, *Zh. Strukt. Khim.* 15 (1974) 1083.
- [32] S. Kvisle and E. Rytter, *Spectrochim. Acta A* 40 (1984) 939.
- [33] D.C. McKean, G. Davidson and L.A. Woodward, *Spectrochim. Acta A* 26 (1970) 1815.
- [34] C.H. van Dyke, E.W. Kifer and G.A. Gibbon, *Inorg. Chem.* 11 (1972) 408.
- [35] J.E. Demuth and H. Ibach, *Surf. Sci.* 78 (1978) L238.
- [36] M.A. Henderson, P.L. Radloff, J.M. White and C.A. Mims, *J. Phys. Chem.* 92 (1988) 4111.
- [37] J.J. Hill, A.A. Aquino, C.P.A. Mulcahy, N. Harwood, A.C. Jones and T.S. Jones, *Surf. Sci.* 340 (1995) 49.
- [38] A.A. Aquino, C.P.A. Mulcahy and T.S. Jones, *Surf. Sci.* 344 (1995) L1231.
- [39] D.J. Frankel, C. Yu, J.P. Harbison and H.H. Farrell, *J. Vac. Sci. Technol. B* 5 (1987) 1113.
- [40] O. Naji, J. Zhang, T. Kaneko, T.S. Jones, J.H. Neave and B.A. Joyce, *J. Cryst. Growth*, in press.
- [41] B.R. Davidson, R.C. Newman, T. Kaneko and O. Naji, *Phys. Rev. B* 50 (1994) 12250.



ELSEVIER

Applied Surface Science 104/105 (1996) 312–316



Smoothing of crystal surfaces during growth interruption

A.Yu. Kaminski ^{*}, R.A. Suris

A.F. Ioffe Physico-Technical Institute, 194021 St. Petersburg, Russia

Received 28 June 1995; accepted 28 August 1995

Abstract

The evolution of a crystal surface during growth interruption when adatom diffusion along the surface is the prevailing smoothing process is studied both theoretically and numerically. During this process, 2D islands and holes interact via adatom diffusion changing their sizes and making the surface smoother. Surface smoothing is described in terms of two main processes that determine mode and rate of surface smoothing: Ostwald ripening of islands and capturing of adatoms wandering on the surface by the holes. This description offers to determine reflection high-energy electron diffraction (RHEED) specular intensity in a step-density approximation.

1. Introduction

Nowadays, thicknesses of films grown by molecular beam epitaxy (MBE) can be controlled at the level of single monolayers. Nevertheless, these films do not have atomically smooth interfaces because formation of a new layer on flat substrates begins before the previous one is complete. So an interface of a growing film shows two-dimensional (2D) islands, nuclei of new monolayers, and 2D holes, incompleting regions of previous ones. Growth interruption (GI) is widely applied to smooth interfaces. After GI, an interface becomes significantly smoother than before, but not absolutely smooth [1]. We consider the evolution of crystal surfaces during GI when adatom diffusion along the surface is the prevailing smoothing process. 2D islands and holes exchange with adatoms changing their sizes. It is

well known from the experiment that it leads to smoothing of the surface.

Interaction of clusters of solid phase via diffusing atoms was considered by Lifshitz and Slezov for 3D cases [2] and by Chakraverty for quasi-2D cases (spherical caps on the substrate) [3]. During this process, concentration of free atoms gradually decreases. Larger clusters grow mainly due to absorption of atoms extracted by smaller ones which dissolve. This process, called Ostwald ripening, goes on because the oversaturation level decreases further, and more and more clusters begin to dissolve and 'die' giving 'food' for growth of bigger ones. MBE provides some modifications to such a system and changes the laws of its evolution. One of these modifications is due to an external source of condensing atoms (molecular beam) during the growth process. In this case, Ostwald ripening is suppressed and there is no 'struggle for life' between islands [4]. Another feature is the existence of 'anti-islands' i.e. holes. Interaction of islands and holes plays a crucial role in smoothing of crystal surfaces during growth interruption.

^{*} Corresponding author.

2. Theoretical model

We consider a three-level surface that is formed by an almost filled upper monolayer, its incomplete regions (holes), and nuclei of the next monolayer on it. Additional levels are excluded from our consideration because the transformation of the multi-level surface to the three-level state is much faster than its subsequent evolution.

During the growth process, 2D islands nucleate, grow and coalesce, forming quaint dendritic forms that result from kinetics of growth. When GI begins, these 2D dendritic structures transform to 2D islands and holes with more plain edges. This process is responsible for the significant increase of RHEED specular intensity in the beginning of GI [5]. Since it involves adatom diffusion at the distances of the order of distances between islands/holes, it is much faster than processes involving adatom exchange between islands/holes. The latter stage, that is responsible for the final state of an interface, is the subject of our consideration.

Based on the Burton et al. approach [6] we consider adatom diffusion along the surface. A diffusing adatom can be captured either by an island or by a hole. Let τ_c be the adatom lifetime with respect to this process. Reevaporation from the surface is neglected. In our model [4,7], we assume the adatom diffusion length $L_D = \sqrt{2D\tau_c}$ to be greater than the average distance between islands/holes. It means that a wandering adatom passes by some other islands/holes before being captured by an island/hole. In this case, the adatom diffusional flux to/from an island/hole depends not on positions of neighboring islands/holes but on average characteristics of the surface, and we can calculate this flux taking into account only averaged distribution of other islands/holes instead of their exact positions. For the sake of simplicity we consider round islands and holes. In this case, adatom distribution around an island/hole is axially symmetrical. If we consider non-round islands/holes, the equation for adatom 2D concentration in the vicinity of a nucleus/hole would include terms with spherical functions that decay the faster the more their order. So adatom concentration at some distance from an island/hole and, consequently, full adatom flux to it is defined by the axially symmetrical term.

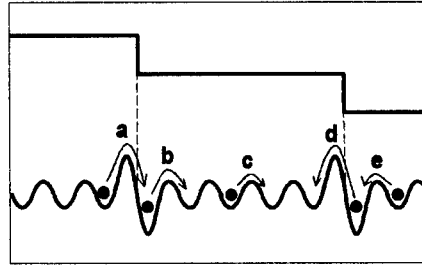


Fig. 1. The typical picture of adatom potential energy on the substrate and possible types of hopping: (a) down-step hopping; (b) detaching from a step edge; (c) diffusion along the surface; (d) up-step hopping (forbidden); and (e) attaching to a step edge.

Setting the boundary conditions at islands/holes step edges we start from the standard picture of adatom potential energy near a step edge (Fig. 1). Since an adatom can detach from an island, the equilibrium concentration at its boundary has non-zero value and its dependence on the radius of an island, R_i , is given by the equation [8]

$$n|_{R_i} = n_\infty \exp\left(\frac{\alpha S}{TR_i}\right), \quad (1)$$

where S is area taken up by an adatom in the surface monolayer, α is the 2D surface (more accurately, linear) tension constant, T is the temperature and n_∞ is the equilibrium 2D concentration of adatoms at the boundary of an island of infinite radius. One can see that the less the radius of an island the more its equilibrium boundary concentration. Therefore, less islands require larger adatom concentration in vicinity for growing. Up-step jumps are neglected so that the equilibrium concentration at the boundary of a hole is equal to zero. Due to the additional energy barrier of height ε_s for down-step jumps the boundary condition for adatom concentration outside a hole of radius R_h ,

$$\left.\frac{dn}{dr}\right|_{R_h} = \frac{1}{\sqrt{S}} \exp\left(-\frac{\varepsilon_s}{T}\right) n|_{R_h}, \quad (2)$$

is derived from the equation for adatom flux to a hole

$$D \left.\frac{dn}{dr}\right|_{R_h} = \nu n|_{R_h}, \quad (3)$$

where $\nu = D \exp(\varepsilon_s/T)/\sqrt{S}$ is the rate of down-step capture, D is the 2D diffusion constant.

The boundary conditions (Eqs. (1), (2)) determine the following equations for islands/holes evolution

$$\frac{d}{dt} \left(\frac{\pi R_i^2}{S} \right) = \frac{4\pi D}{\ln(1/\pi \mathcal{N} R_i^2)} \left\{ \tilde{n} - n_\infty \exp \left(\frac{\alpha S}{TR_i} \right) \right\}, \quad (4)$$

$$\begin{aligned} \frac{d}{dt} \left(\frac{\pi R_h^2}{S} \right) &= \frac{-4\pi D}{\ln(1/\pi \mathcal{N} R_h^2) + \exp(-\varepsilon_s/T)/\sqrt{\pi R_h^2/S}} \tilde{n}, \\ & \end{aligned} \quad (5)$$

where \tilde{n} is 2D adatom concentration,

$$\mathcal{N} = N_i + N_h \frac{1}{1 + \exp(-\varepsilon_s/T)/\sqrt{\pi R_h^2/S}} \quad (6)$$

is the effective concentration of sinks on the surface, $\langle \dots \rangle$ denote averaging over the surface. Together with the matter conservation law,

$$N_i \left\langle \frac{\pi R_i^2}{S} \right\rangle + N_h \left\langle \frac{\pi R_h^2}{S} \right\rangle + \tilde{n} = \text{const.}, \quad (7)$$

they describe completely the evolution of crystal surfaces during GI in the context of our model. For calculating RHEED specular intensity, I , we use the step-density approximation [5]. In the framework of this approximation the surface steps are the dominant feature that determines the deviation of RHEED specular intensity from its value for the smooth surface. This deviation is proportional to the step density that for the simple cubic lattice is given by

$$\begin{aligned} \sigma(\phi) &= L^{-1} \sum_{i,j} \left\{ [1 - \delta(h_{i,j}, h_{i+1,j})] \cos \phi \right. \\ & \quad \left. + [1 - \delta(h_{i,j}, h_{i,j+1})] \sin \phi \right\}, \end{aligned} \quad (8)$$

where ϕ is the azimuthal angle between the electron beam and the i axis, $\delta(i, j)$ is the Kronecker delta function, $h_{i,j}$ is the height of the column of atoms at the lattice cite (i, j) and L is the number of lattice sites. One can see that the contribution of an island or a hole to the step density is proportional to its radius so that

$$\sigma = N_i \langle R_i \rangle + N_h \langle R_h \rangle \quad (9)$$

and

$$I \propto 1 - C\sigma = 1 - C[N_i \langle R_i \rangle + N_h \langle R_h \rangle], \quad (10)$$

where C is the parameter depending on the diffraction conditions.

3. Results and discussion

If 2D concentration and sizes of holes are small in comparison to those of the islands, holes have no effect on the processes going on the surface. In this case, we deal with usual Ostwald ripening. In the opposite case an adatom having detached from an island has almost no chance to attach to another island because it will most probably be captured by a hole, and there is no Ostwald ripening. Thus the mode of GI is determined by the relation between the probability of a wandering adatom capturing by islands, W_i , and that by holes, W_h , that are proportional to the two terms in the right side of Eq. (6). To begin with, we consider two limiting cases.

3.1. $W_i \gg W_h$

We deal with such a situation when the step-edge barrier is high enough or when the number of deposited monolayers slightly exceeds an integer number. This mode also is realized when the kinetic barrier for island nucleation is low enough and some little islands can nucleate on the top of a bigger island (that can take its origin from some coalesced islands). In this case, holes do not have strong effect on the processes going on the surface.

Eq. (4) describing islands evolution can easily be transformed to the form

$$\begin{aligned} \frac{dR_i}{dt} &= \frac{2DSn_\infty\sigma}{\ln(1/\pi \mathcal{N} R_{iC}^2) + 2\ln(R_{iC}/R_i)} \frac{1}{R_i} \\ & \quad \times \left(\frac{1}{R_{iC}} - \frac{1}{R_i} \right), \end{aligned} \quad (11)$$

where $\sigma = \alpha S/T$, exponent (1) is expanded into a Taylor series up to the first term, the critical radius, R_{iC} , is defined by the equation

$$R_{iC} = \frac{n_\infty \sigma}{\tilde{n} - n_\infty}. \quad (12)$$

Assuming that

$$\ln(1/\pi\mathcal{N}R_{iC}^2) \gg 2\ln(R_{iC}/R_i) \quad (13)$$

we obtain the equation that is similar to the equation describing 3D Ostwald ripening [2]. This means that the results of the Lifshitz–Slezov theory are quite applicable for our case. These results are:

(i) The critical radius, R_{iC} , is equal to the average radius of islands and their time evolution is described by the equation

$$R_{iC} = \langle R_i \rangle = \left(\langle R_{iC} \rangle_0^3 + \frac{2Dn_\infty\sigma S}{\ln(\theta^{-1})} t \right)^{1/3}, \quad (14)$$

where $\theta = \pi N_i \langle R_i^2 \rangle$ is the surface coverage in the layer of the islands that can be set to be a constant in the course of GI under the assumption $W_i \gg W_h$. The subscript '0' denotes the initial value of quantities.

(ii) The islands size distribution function has a rather sharp maximum at $R_i = R_{iC}$ so our assumption (13) is justified.

Since the total quantity of adatoms, θ , remains constant,

$$N_i \approx \theta \left(\frac{2Dn_\infty\sigma S}{\ln(\theta^{-1})} t \right)^{-2/3}, \quad (15)$$

RHEED specular intensity evolution is given by

$$I \propto 1 - C\theta \left(\frac{2Dn_\infty\sigma S}{\ln(\theta^{-1})} t \right)^{-1/3}. \quad (16)$$

At the same time the contribution of evolution of holes to surface smoothing is small. The results of this subsection are shown in Fig. 2.

3.2. $W_i \ll W_h$

This mode of GI is realized when the number of deposited monolayers is slightly less than an integer number. It can also result from the mode previously described when, due to Ostwald ripening, the 2D concentration of islands decrease enough for W_i to be much less than W_h . In this case, Ostwald ripening is suppressed because of capturing of wandering adatoms by holes and the essential process is 2D evaporation of islands and absorption of 2D adatom vapor by holes.

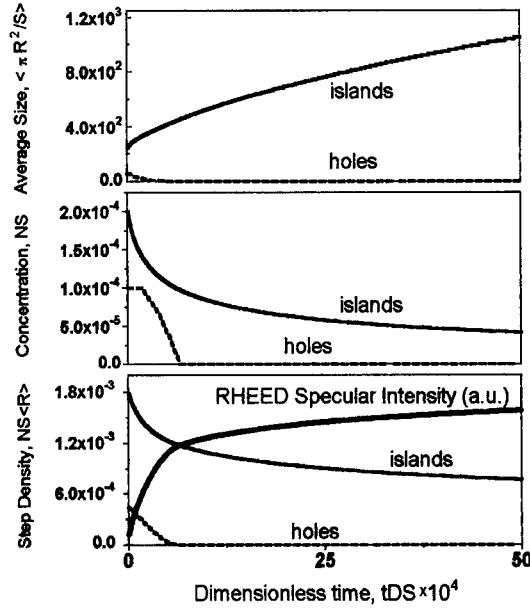


Fig. 2. The evolution of the main characteristics of the surface during GI. The upper part — average number of atoms in an island/hole; the middle part — dimensionless 2D concentration of islands/holes; the lower part — dimensionless step density (Eq. (9)) and RHEED specular intensity (Eq. (10)). The parameters used are $\exp(-\varepsilon_s/T) = 100$, $N_{i0}S = 2 \times 10^{-4}$, $N_{h0}S = 10^{-4}$, $\alpha\sqrt{\pi S}/T = 6.1$, $n_\infty S = 10^{-4}$. Initially island sizes $\pi R_i^2/S$ were homogeneously distributed within the interval $50 \leq \pi R_i^2/S \leq 450$, that of the holes $12 \leq \pi R_h^2/S \leq 112$.

Eq. (4) gives us the estimation

$$\langle R_i \rangle \approx \sqrt{\langle R_i^2 \rangle_0 - \frac{4DSn_\infty}{\ln(1/\pi\mathcal{N}R_i^2)} t}. \quad (17)$$

One can see that islands disappear in a finite time. At the same time holes evolution is given by

$$\langle R_h \rangle \approx \langle R_h \rangle_0 - \frac{2DSn_\infty}{\langle R_h \rangle_0 \ln(1/\pi\mathcal{N}\langle R_i^2 \rangle_0)} t \quad (18)$$

under the assumption that $\langle R_h \rangle \gg \langle R_i \rangle$. The process stops at $t = \langle R_i^2 \rangle_0 \ln(\theta^{-1})/(4DSn_\infty)$. RHEED specular intensity

$$I \propto 1 - C \left[N_{i0} \sqrt{\langle R_i^2 \rangle_0 - \frac{4DSn_\infty}{\ln(1/\pi\mathcal{N}\langle R_i^2 \rangle_0)} t} + N_{h0} \langle R_h \rangle_0 - N_{h0} \left(\frac{2DSn_\infty}{\langle R_i^2 \rangle_0 \ln(1/\pi\mathcal{N}\langle R_i^2 \rangle_0)} t \right) \right]. \quad (19)$$

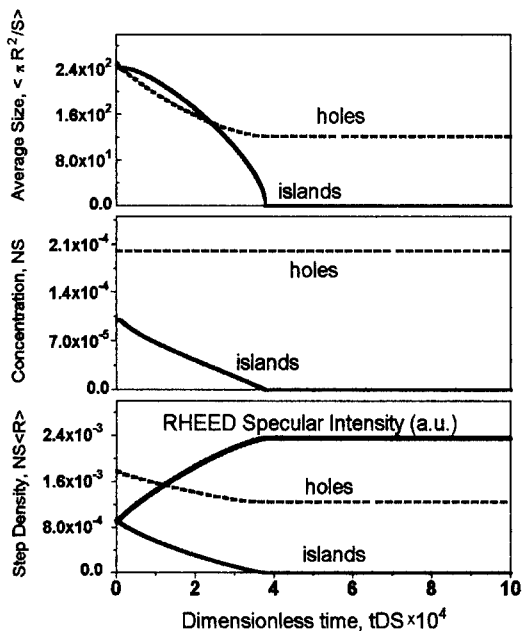


Fig. 3. The same as Fig. 2, but $N_{i0}S = 10^{-4}$, $N_{h0}S = 2 \times 10^{-4}$, $\exp(-\varepsilon_s/T) = 33$, $50 \leq \pi R_i^2/S \leq 450$, $50 \leq \pi R_h^2/S \leq 450$.

Here the contribution of the second time-dependent term is much less than the contribution of the first one if $\langle R_h \rangle \gg \langle R_i \rangle$. The results of this subsection are shown in Fig. 3.

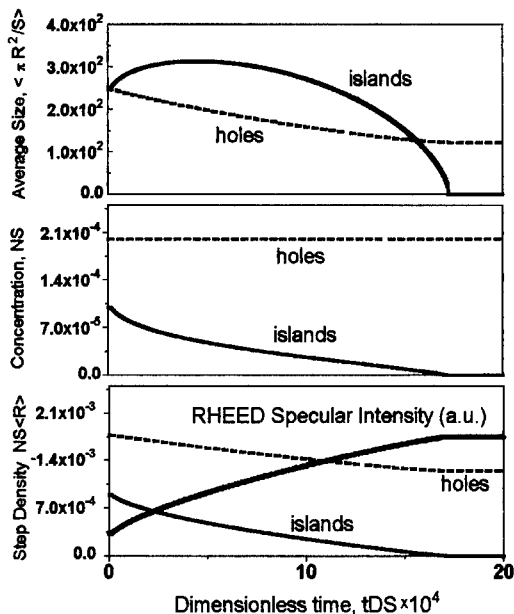


Fig. 4. The same as Fig. 3, but $\exp(-\varepsilon_s/T) = 450$.

3.3. $W_i \sim W_h$

The intermediate case is complicated for analytical consideration. Nevertheless, the numerical results shown in Fig. 4 can be easily interpreted. If in the beginning of GI $W_i > W_h$, the islands exchange with adatoms and the process similar to Ostwald ripening begins. Then concentration of islands gradually decreases and W_h becomes larger than W_i . Ostwald ripening ceases by the reason described in the previous subsection and all the islands begin to dissolve filling the holes.

4. Conclusion

Thus we have shown that during growth interruption surface evolution can go in various ways depending on the initial state of the surface. If 2D islands dominate, the prevailing process is Ostwald ripening and RHEED specular intensity in the step-density approximation is

$$I \propto 1 - Ca_1 t^{-1/3}. \quad (20)$$

The equation for the parameter a_1 can be taken from Eq. (16). If holes dominate, they suppress Ostwald ripening of islands and surface evolution during GI consists in absorption by holes adatoms extracted by dissolving islands. In this case

$$I \propto 1 - Ca_2 \sqrt{t_0 - t}. \quad (21)$$

The parameters a_2 and t_0 can be taken from Eq. (19). The intermediate case presents the superposition of both of these processes.

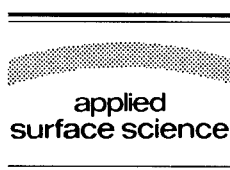
References

- [1] A. Yoshinaga, P. Mookherjee, R. Murray, J.H. Neave and B.A. Joyce, *J. Cryst. Growth* 127 (1993) 788.
- [2] I.M. Lifshitz and V.V. Slezov, *Sov. JETP* 35 (1958) 479; *J. Phys. Chem. Solids* 19 (1961) 35.
- [3] B.K. Chakraverty, *J. Phys. Chem. Solids* 28 (1967) 2401.
- [4] A.Yu. Kaminski and R.A. Suris, *Solid State Commun.* 8 (1994) 609.
- [5] S. Clarke and D.D. Vvedensky, *J. Appl. Phys.* 63 (1988) 2272.
- [6] W.K. Burton, N. Cabrera and F.C. Frank, *Phil. Trans. R. Soc. London Ser. A* 243 (1951) 299.
- [7] A.Yu. Kaminski and R.A. Suris, *Superlatt. Microstruct.* 16 (1994) 221.
- [8] L.D. Landau and E.M. Lifshitz, *Statistical Physics*, Vol. 1, 3rd ed. (Pergamon, Oxford, 1980).



ELSEVIER

Applied Surface Science 104/105 (1996) 317–322



Comparison of structurally relaxed models of the Si(001)–SiO₂ interface based on different crystalline oxide forms

Alfredo Pasquarello^{a,b,*}, Mark S. Hybertsen^b, Roberto Car^{a,c}

^a *Institut Romand de Recherche Numérique en Physique des Matériaux (IRRMA), IN-Ecublens, CH-1015 Lausanne, Switzerland*

^b *AT & T Bell Laboratories, 600 Mountain Avenue, Murray Hill, NJ 07974, USA*

^c *Department of Condensed Matter Physics, University of Geneva, CH-1211 Geneva, Switzerland*

Received 28 June 1995; accepted 2 October 1995

Abstract

We present a comparative study of the structural properties of three different models for the Si(001)–SiO₂ interface. The models are obtained by attaching different crystalline forms of SiO₂, such as tridymite and beta-cristobalite, to Si(001). In the case of tridymite, the Si bond-density reduction is accounted for by introducing either dimers or oxygen bridges at the interface, whereas the construction proposed by Ohdomari et al. has been used in the case of beta-cristobalite. The models have been allowed to fully relax within density functional theory. None of the models shows electronic states in the Si gap. Compared to the tridymite models, the longer Si–O bonds found at the interface of the beta-cristobalite derived model suggests that the latter is a higher energy structure.

In spite of the use of many experimental techniques [1], the microscopic bond pattern at the Si(001)–SiO₂ interface has not yet been elucidated. This uncertainty is a consequence of the interplay of several factors. Because of the difficulty of accessing a buried interface, application of a single experimental technique only provides an indirect and partial piece of information on the structure. Consequently, models of the interface structure must be shown to be consistent with several experimental results of different origin. This process is further hindered by the dependence of the interface structure on the sample preparation. Finally the amorphous nature of

the SiO₂ component suggests the existence of a variety of structural moieties at the interface.

The continued reduction in size of electronic devices, with the attendant reduction in the thickness of the SiO₂ insulating regions, requires a better understanding of the structure of the Si(001)–SiO₂ interface at the microscopic level. In the absence of a complete picture, the availability of models of the local interface structure becomes essential to study processes such as the growth mechanism, the effect of structural defects, or the incorporation of nitrogen at the interface.

Though the Si(001)–SiO₂ interface is one between a crystalline and an amorphous material, electrical measurements show that there is only one interface defect state for every 10⁴ interface atoms [2]. On the other hand bulk terminated Si(001) pre-

* Corresponding author.

sents an areal density of bonds at the interface which is roughly a factor of two higher than that of SiO_2 . Furthermore, valuable information on the structure can be extracted from core-level photoelectron spectroscopy (PES) [3–5]. We have recently established [6] that a consistent interpretation of photoelectron spectra requires that all three partial oxidation states of silicon be present at the interface in comparable amounts. These properties put severe limitations on the choice of models.

The general purpose of this work is to provide insight in the structural properties at the $\text{Si}(001)$ – SiO_2 interface. In particular, we would like to understand the structural differences that occur when different models for the interface are used. To this end, we have generated model interfaces by attaching different forms of crystalline SiO_2 to $\text{Si}(001)$. In all the models the bond-density mismatch is fixed so that all the bonds at the interface are saturated. The atomic positions in our model interfaces have been fully relaxed within the local density approximation to density functional theory. An analysis of the electronic states shows that none of the models presents states in the fundamental gap of silicon, in

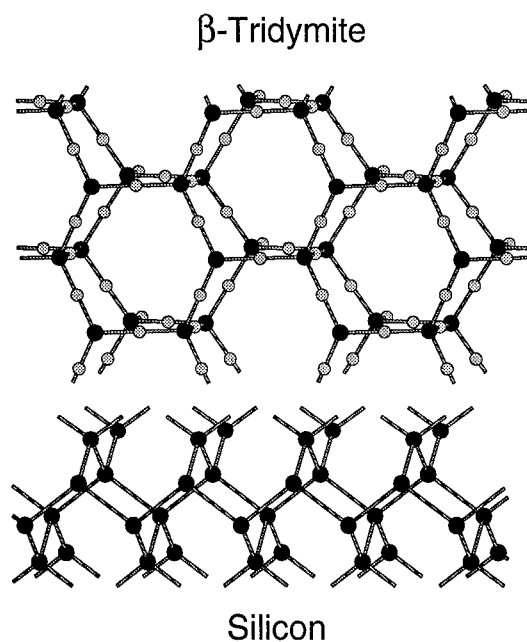


Fig. 1. Schematic view of the match between tridymite and $\text{Si}(001)$. Note that this construction leaves one extra dangling bond per Si atom which must be saturated.

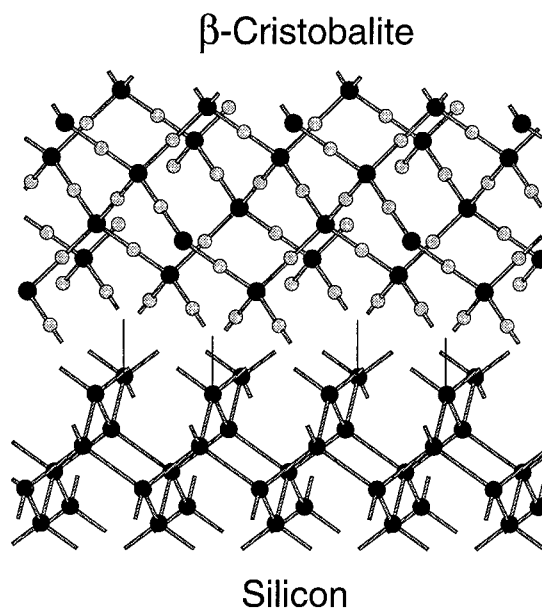


Fig. 2. Schematic view of the match between beta-cristobalite and $\text{Si}(001)$. Note that if this construction was directly attached to $\text{Si}(001)$, half of the silicon interface atoms would have saturated bonds whereas the other half would have two dangling bonds each.

agreement with electrical experiments [2]. In one of the present models, the distribution of partial oxidation states of silicon is consistent with PES experiments. Through a comparative analysis of bond-length and bond-angle distributions in these models we attempt to identify general structural features of the $\text{Si}(001)$ – SiO_2 interface.

We have considered three different configurations as starting points of the relaxation process. Two of these configurations (model I and II) correspond to the structures we have used in a previous study [6]. In these models, tridymite has been attached to bulk terminated $\text{Si}(001)$ as shown in Fig. 1. In this way, half of the dangling bonds of the bulk terminated $\text{Si}(001)$ interface atoms are saturated by forming bonds to the tridymite, leaving one dangling bond per silicon interface atom. The saturation of these remaining bonds occurs either by dimerization of the Si atoms (model I) or by the presence of oxygen bridges (model II). Finally, the third initial configuration (model III) has been obtained in a rather different way. In this case, we attached beta-cristobalite to $\text{Si}(001)$ as shown in Fig. 2, following an early idea [7,8]. Since direct attachment of beta-cris-

tobalite to Si(001) would saturate all the dangling bonds of *half* of the interface silicon atoms, but would leave the other half with two dangling bonds, we have used an intermediate construction proposed by Ohdomari et al. [9] to fix the bond density mismatch. In practice this construction halves the number of silicon interface atoms which have two dangling bonds. In this way beta-crystobalite can be attached saturating all the bonds.

The actual models I, II and III (shown in Fig. 3(a), Fig. 4(a), and Fig. 5(a), respectively) are obtained by fully relaxing the atomic coordinates of these initial configurations. This is done by minimizing the total energy using the Car–Parrinello method [10], which provides the electronic structure as well as the forces that act on the ions. Only valence electrons are explicitly considered using pseudopotentials (PP's) to account for the core–valence interactions. A norm-conserving PP is used for Si [11], whereas the O atoms are described by an ultrasoft Vanderbilt PP [12]. The electronic states were expanded on a plane-wave basis set. Exchange and correlation were included using Perdew and Zunger's interpolation formulae [13]. A description of the method is given in Ref. [14].

In order to achieve good convergence in the electronic properties, we have used a plane-wave cutoff of 16 Ry for the wave functions and of 150 Ry for the augmented electron density. Our system contains a 2×2 interface unit of side $L = 7.65$ Å (based on the theoretical equilibrium lattice constant of Si). The dimension of the cell in the direction orthogonal to the interface is 31.7 Å containing 10 layers of Si (≈ 13 Å). In the models in which the oxide is derived from tridymite (models I and II) we considered 7 monolayers of oxide (9 Å), whereas 8 monolayers of beta-crystobalite were retained in model III (7 Å). The extremities have been saturated with hydrogen atoms. In the minimization process, all the atoms of the oxide as well as the first 6 Si layers are allowed to relax. The Brillouin zone of our simulation cell is sampled using only the Γ -point.

By analyzing the electronic wave functions, we find that the highest occupied state as well as the lowest unoccupied state are both Si related and do not present any significant weight at the interface. We therefore conclude that there are no states in the fundamental gap of Si.

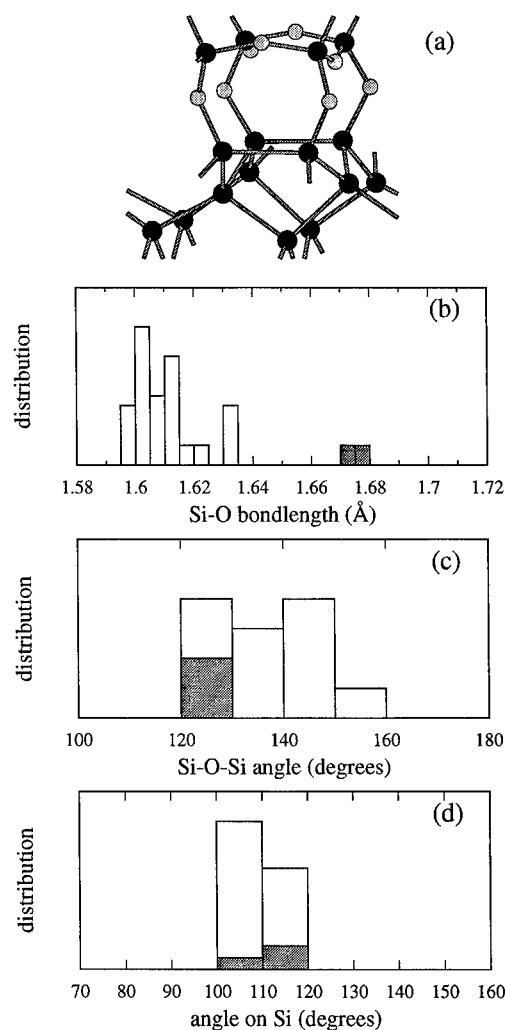


Fig. 3. Structural properties of model I derived by matching tridymite to Si(001) as illustrated in Fig. 1 where the extra interface dangling bonds are saturated by dimer formation. (a) Ball and stick model showing the relaxed atomic positions near the interface; (b) Si–O bond-angle distribution; (c) Si–O–Si bond-angle distribution; (d) distribution of bond-angles on silicon atoms. The shaded portion of the histograms indicates the contribution of partially oxidized Si atoms.

In model III, the three intermediate oxidation states of Si are equally represented and their total number amounts to 1.5 monolayers. Thus this model is consistent with the data from PES experiments [5] as far as for both the relative intensities as well as the total amount of partial oxidation states are concerned. In model I and II, only one partial oxidation

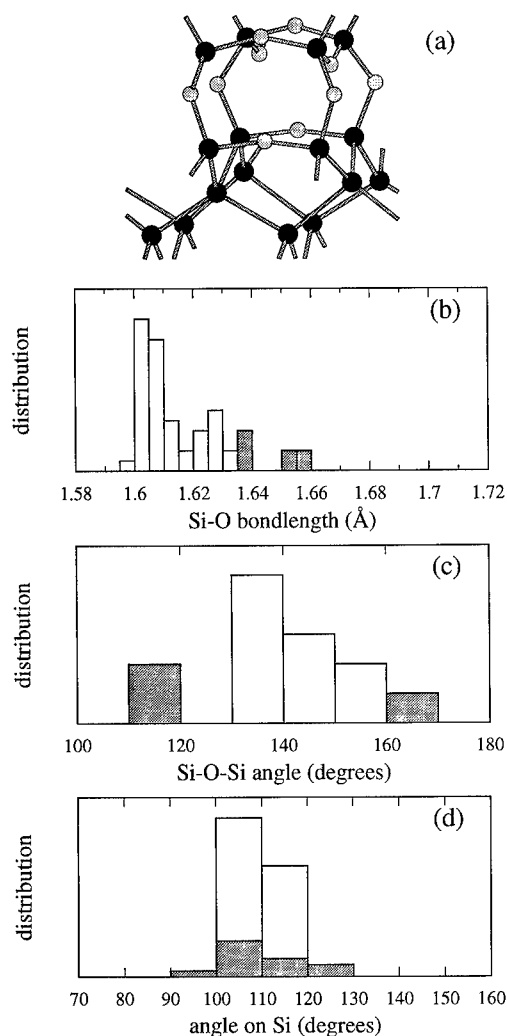


Fig. 4. Same as in Fig. 1 for interface model II where the bond-density mismatch is fixed by the presence of oxygen bridges.

state is found, namely Si^{+1} and Si^{+2} , respectively. Although these structures do not satisfy the requirements imposed by PES experiments, it is of interest to consider their structural properties in view of a comparison with those of model III.

Distributions of structural parameters as found at the end of the relaxation process for the interface models are given in Figs. 3–5. We show distributions of Si–O bond-lengths, of Si–O–Si bond-angles and of the bond angles on the silicon atoms. The contribution due to silicon atoms in partial oxidation states have been highlighted. The initial oxide struc-

tures (Fig. 1 and Fig. 2) are high symmetry idealized structures derived from high temperature diffraction measurements with 180° Si–O–Si bond angles. However, the relaxed structures show a more realistic distribution of bond lengths and bond angles.

The Si–O bond-length distribution of the three models shows common features. Bond lengths in the oxide are centered around 1.62 \AA within $\pm 0.02 \text{ \AA}$ in all the models. However, bond lengths which involve partially oxidized silicon atoms show a systematic

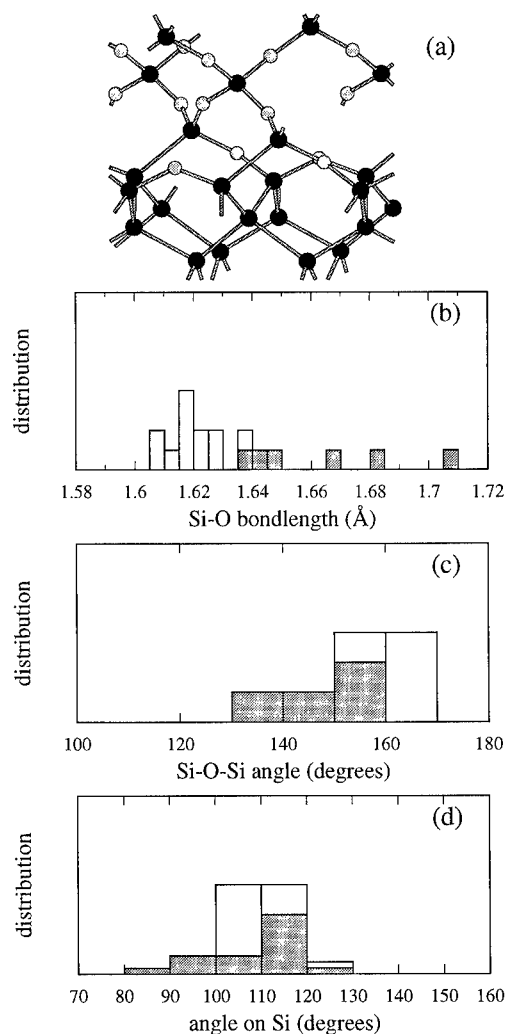


Fig. 5. Same as in Fig. 1 for interface model III, derived by matching beta-cristobalite to Si(001). The construction proposed by Ohdomari et al. [9] has been used to fix the bond-density mismatch.

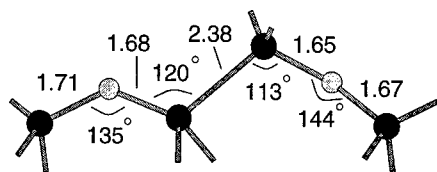


Fig. 6. Detail of the interface region shown in Fig. 5(a), representing the structure proposed by Ohdomari et al. [9] to fix the bond-density mismatch. The calculated relaxed bond lengths and bond angles are indicated.

preference for slightly larger values. Bond lengths as large as ≈ 1.68 Å are found in models I, and some even range up to ≈ 1.71 Å in model III. An increase of the Si–O bond length at the interface can be understood as a consequence of the reduced ionic charge on the silicon atoms. The rather large bond-lengths in model III occur as a consequence of the bond configuration proposed by Ohdomari et al. [9], as shown in detail in Fig. 6. Comparison with the bond lengths in model I and II suggests that this configuration corresponds to a higher energy structure.

The Si–O–Si bond-angle distribution is extremely broad ranging from 110° to 170° . In models I and II, the oxide angles range from 120° to 160° , which are typical values for amorphous SiO_2 [15]. In model III, the oxide angles are concentrated towards the high-values side. We believe the large angles in model III to be a consequence of the mismatch between the beta-cristobalite structure and the silicon substrate. Twisting the Si–O–Si bond angles involves a low energy cost. Its distribution is expected to be affected significantly by the strain conditions. The distribution may also be sensitive to other steric constraints such as the interface periodicity of our model systems.

The distribution of angles on the Si atoms in the oxide is sharply peaked at the tetrahedral angle in all three models, in close agreement with results for amorphous SiO_2 [15]. The width of the distribution involving partially oxidized atoms is generally larger. In model III, it extends from 80° to 130° . In model I and II, the distribution of partially oxidized silicon atoms is less broad. Since larger distortions from the tetrahedral angles on the silicon atoms are expected to indicate larger deviations from the local minimal

energy configuration, this provides further support for the good structural properties of the models based on the tridymite construction.

In conclusion, we have studied the structural properties of three different interface models of the $\text{Si}(001)\text{--SiO}_2$ interface. The models differ by the choice of the oxide forms, e.g. tridymite versus beta-cristobalite and by the way the bond-density mismatch is fixed. We have considered bond-density reductions as induced by dimerization, by the presence of oxygen atoms and by the use of the construction proposed by Ohdomari et al. [9]. A comparative study between the three models has allowed us to recognize that the Si–O bond-lengths at the interface are found to be larger than typical values in the oxide. We found unusually long Si–O bonds at the Ohdomari construction, which lead us to suggest that the latter might be a higher energy structure.

Acknowledgements

Two of us (A.P. and R.C.) acknowledge support from the Swiss National Science Foundation under grant No. 20-39528.93. Part of the calculations were performed on the NEC-SX3 of the Swiss Center for Scientific Computing (CSCS) in Manno.

References

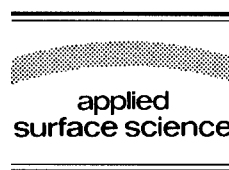
- [1] S. Pantelides, Ed., *The Physics of SiO_2 and its Interfaces* (Pergamon, New York, 1978); C.R. Helms and B.E. Deal, Eds., *The Physics and Chemistry of SiO_2 and the Si– SiO_2 Interface* (Plenum, New York, 1988).
- [2] S.C. Witzak, J.S. Suehle and M. Gaitan, *Solid-State Electron.* 35 (1992) 345.
- [3] P.J. Grunthaner, M.H. Hecht, F.J. Grunthaner and N.M. Johnson, *J. Appl. Phys.* 61 (1987) 629.
- [4] F.J. Himpsel, F.R. McFeely, A. Taleb-Ibrahimi and J.A. Yarmoff, *Phys. Rev. B* 38 (1988) 6084.
- [5] Z.H. Lu, M.J. Graham, D.T. Jiang and K.H. Tan, *Appl. Phys. Lett.* 63 (1993) 2941.
- [6] A. Pasquarello, M.S. Hybertsen and R. Car, *Phys. Rev. Lett.* 74 (1995) 1024.
- [7] F. Herman and R.V. Kasowski, *J. Vac. Sci. Technol.* 19 (1981) 395.
- [8] M. Hane, Y. Miyamoto and A. Oshiyama, *Phys. Rev. B* 41 (1990) 12637.
- [9] I. Ohdomari, H. Akatsu, Y. Yamakoshi and K. Kishimoto, *J. Non-Cryst. Solids* 89 (1987) 239; I. Ohdomari, H. Akatsu, Y.

- Yamakoshi and K. Kishimoto, *J. Appl. Phys.* 62 (1987) 3751.
- [10] R. Car and M. Parrinello, *Phys. Rev. Lett.* 55 (1985) 2471.
- [11] G.B. Bachelet, D.R. Hamann and M. Schlüter, *Phys. Rev. B* 26 (1982) 4199.
- [12] D. Vanderbilt, *Phys. Rev. B* 41 (1990) 7892.
- [13] J.P. Perdew and A. Zunger, *Phys. Rev. B* 23 (1981) 5048.
- [14] A. Pasquarello, K. Laasonen, R. Car, C. Lee and D. Vanderbilt, *Phys. Rev. Lett.* 69 (1992) 1982; K. Laasonen, A. Pasquarello, R. Car, C. Lee and D. Vanderbilt, *Phys. Rev. B* 47 (1993) 10142.
- [15] J. Sarnthein, A. Pasquarello and R. Car, *Phys. Rev. Lett.* 74 (1995) 4682.



ELSEVIER

Applied Surface Science 104/105 (1996) 323–328



Initial stage of oxidation of hydrogen-terminated silicon surfaces

Takeo Hattori ^{a,*}, Takeshi Aiba ^a, Etsuo Iijima ^a, Yohichi Okube ^a, Hiroshi Nohira ^a,
Naoto Tate ^b, Masatake Katayama ^b

^a Department of Electrical and Electronic Engineering, Musashi Institute of Technology, 1-28-1 Tamazutsumi, Setagaya-ku, Tokyo 158, Japan

^b Shin-Etu Handotai Co. Ltd., 2-13-1 Isobe, Annaka, Gumma 379-01, Japan

Received 28 June 1995; accepted 5 December 1995

Abstract

Structural changes produced by the oxidation of hydrogen-terminated Si(111)-1 × 1 and Si(100)-2 × 1 surfaces at 300°C in dry oxygen under a pressure of 1 Torr were investigated by X-ray photoelectron spectroscopy (XPS) and multiple internal reflection infrared absorption spectroscopy (MIR-IRAS). Following results are obtained from the analysis and simulation of the experimental results: (1) the layer-by-layer oxidation reaction occurs locally at SiO₂/Si(111) interface, while that does not occur at SiO₂/Si(100) interface, however, (2) the oxidation on Si(100) surface proceeds more uniformly in atomic scale than that on Si(111) surface.

1. Introduction

As a result of continuing progress in microfabrication technology metal-oxide-semiconductor field-effect transistor (MOSFET) with gate oxide film thickness of 1.5 nm was shown to operate at room temperature [1] and the fabrication of 1 Gbit dynamic random access memory (DRAM) was reported [2,3]. The mass production of 1 Gbit DRAM using MOSFET with gate oxide film thickness of about 5 nm must be realized by the end of this century [4]. In this case the thickness of one-molecular-layer of SiO₂ corresponds to 6% of gate oxide film thickness. Therefore, it is necessary to control the formation of SiO₂/Si interface in atomic scale. Because the formation of native oxide can be sup-

pressed by terminating Si surface with hydrogen atoms [5–7], the hydrogen-terminated Si surface (abbreviated as H-Si surface hereafter) must be used instead of a clean Si surface for this purpose. Furthermore, an atomically flat H-Si(111)-1 × 1 surface can be obtained by the treatment [8,9] in 40% NH₄F solution or that [10–12] in boiling water, while an atomically flat H-Si(100)-2 × 1 surface can be obtained by the annealing [13] in hydrogen atmosphere under pressures higher than 0.2 Torr at 700°C or by the annealing [14] at high temperature (> 1100°C) in hydrogen atmosphere at 1 bar. The thermal oxidation of H-Si(111)-1 × 1 and H-Si(100)-2 × 1 surfaces has been studied by measuring oxidation-induced changes in Si 2p photoelectron spectra, [15–19] while native oxide growth in moist air has been studied by scanning tunneling microscopy [20].

The initial stage of oxidation of H-Si(111)-1 × 1 surface was investigated in dry oxygen under a

* Corresponding author. Tel.: +81-3-37033111/2768; fax: +81-3-57072173; e-mail: hattori@ipc.musashi-tech.ac.jp.

pressure of 1 Torr [15–18]. The following results were obtained from the analysis of Si 2p spectra: (1) the oxidation at 300°C does not proceed uniformly, however, the oxidation proceeds more uniformly at 200°C, (2) by the oxidation at 300°C the interface layer becomes continuous at the oxide film thickness of 0.5 nm, and (3) at thickness greater than this the oxidation reaction at the interface occurs layer-by-layer at 600–800°C. The initial stage of oxidation of H-Si(100)-2 × 1 surface was also investigated in the same oxidation atmosphere [19]. Following results were obtained from the analysis of Si 2p spectra: (1) the initial stage of interface formation at 300°C does not depend on the initial surface morphology, (2) by the oxidation at 300°C the interface layer becomes continuous at the oxide film thickness of 0.5 nm, and (3) at thickness greater than this the deviation from an atomically flat interface increases with the progress of oxidation, however, an abrupt compositional transition occurs.

In the analysis of Si 2p spectral changes produced by the oxidation at 300°C most of the spectra arising from Si-H bonds were neglected, because it was difficult to separate the hydrogenation-induced changes from oxidation-induced changes in Si 2p spectra. However, according to the infrared absorption study described in the following, the desorption of hydrogen does not occur by the oxidation in 1 Torr dry oxygen at 300°C. In the present study the oxidation process of surface Si was investigated from the measurement of oxidation-induced changes in infrared absorption spectra arising from stretching vibration of Si-H bonds. Consequently, the initial stage of oxidation process on H-Si(111)-1 × 1 surface determined previously only from the measurement of oxidation-induced changes in Si 2p spectra is modified by the oxidation process of surface Si determined by MIR-IRAS studies. The initial stage of oxidation process on H-Si(100)-2 × 1 surface was also investigated and the difference in the distribution of bridging oxygen atoms for two kinds of surfaces are discussed.

2. Experimental details

The silicon surfaces used for XPS and MIR-IRAS studies were prepared as follows. First, 200 nm thick oxide films were formed in dry oxygen at 1000°C on

2–6 Ω cm n-type Si(111) and 5–8 Ω cm n-type Si(100) wafers for XPS studies and on 10–20 Ω cm n-type Si(111) and 10–20 Ω cm n-type Si(100) wafers for MIR-IRAS studies. The wafers used for MIR-IRAS studies have dimensions of 0.5 × 52 × 127 mm and have 45-degree bevels on each of the long sides. The H-Si(111)-1 × 1 surfaces used for XPS studies were prepared by the treatment in 40% NH₄F solution at 20°C for 6 min after removing 200 nm thick oxide films. The H-Si(100)-2 × 1 surfaces were prepared by the epitaxial growth of silicon in hydrogen atmosphere at 1100°C for 10 min after removing 200 nm thick thermal oxide films by the treatment in 1% hydrofluoric acid solution. Here, silicon is epitaxially grown using SiHCl₃ and cooled to below 400°C in hydrogen atmosphere. MIR-IRAS was used as a sensitive tool to determine the microscopic arrangement of the H-Si(100) surface. For XPS studies a part of the silicon surfaces, whose area is 20 mm in diameter and central part of which were used for XPS studies, were heated optically, while for MIR-IRAS studies the silicon surfaces, central part of which were used for MIR-IRAS studies, were heated uniformly by flowing current along the long sides of the wafers. Oxidation was performed in dry oxygen under a pressure of 1 Torr at 300°C. The dew point of oxygen gas used in the present oxidation process is below -93°C. The oxidation-induced changes in SiO₂/Si interface structures were studied by measuring Si 2p spectra excited by monochromatic Al Kα radiation at photoelectron take-off angles of 15°, 30° and 90° with an energy resolution of 0.37 eV and an acceptance angle of 3.3° using ESCA-300 manufactured by Scienta Instruments [21]. The area used for XPS studies is 6 × 0.5 mm for the photoelectron take-off angle of 90°. Infrared absorption spectra were measured based on MIR-IRAS using JIR-5500 manufactured by JEOL with a resolution of 1 cm⁻¹. The infrared radiation from the interferometer is focused at normal incidence onto the input bevel, and is internally reflected nearly 100 times, making the output bevel to be collected and refocused onto the photodetector. Here, the infrared absorption spectrum measured for native oxide formed in a mixed solution of H₂SO₄ and H₂O₂ (H₂SO₄:H₂O₂ = 4:1) is used as a reference spectrum. Other experimental details were described elsewhere [16].

3. Initial stage of oxidation of H-Si(111)-1 × 1 surface

The oxidation-induced changes in infrared absorption spectra for H-Si(111)-1 × 1 surface were measured, and are shown in Fig. 1. The infrared absorption spectra of M1, M2 and M3, whose bonding configurations are illustrated in Fig. 1, appear not only for p-polarized infrared, but also for s-polarized infrared. This implies that the insertion of oxygen atoms in the bridging positions between Si atoms in the first and second layer produces the inclination of Si-H bonds from the direction perpendicular to the H-Si surface. Fig. 2 is obtained from the spectral analysis of Fig. 1 and shows the amounts of bonding states of surface Si as a function of areal density of bridging oxygen atoms bonded with surface Si. Here, the horizontal scales are calculated by considering bonding configurations of oxidized surface Si atoms and the oscillator strengths are assumed to be the same for all kinds of stretching vibrations of Si-H

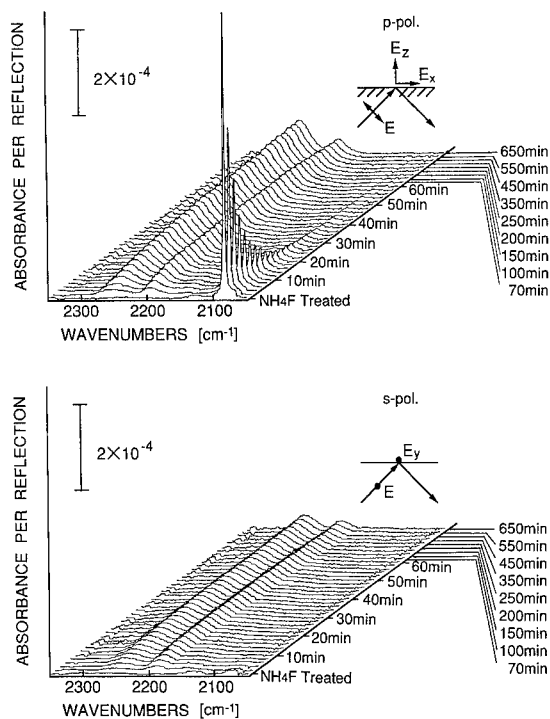


Fig. 1. Oxidation-induced changes in infrared absorption spectra for p- and s-polarized infrared measured for H-Si(111)-1 × 1 surface with oxidation time as a parameter.

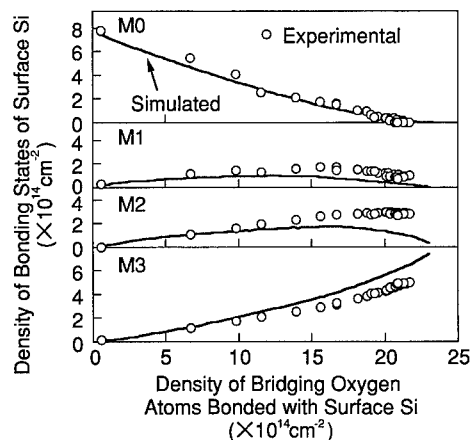


Fig. 2. Amounts of bonding states of surface Si on Si(111) surface as a function of areal density of bridging oxygen atoms bonded to surface Si. The simulated results are shown by the solid curves.

bonds appearing in Fig. 1. This assumption seems to be verified because it can be seen from Fig. 2 that the total spectral intensity of M0, M1, M2 and M3 is not affected by the backbond oxidation. Here, the bonding configuration of M0 is illustrated in Fig. 1. Therefore, it can be seen from Fig. 1 that the frequency of stretching vibration of Si-H bond is only affected by the backbond oxidation. The validity of the assumption should be verified theoretically in the near future.

The oxidation-induced changes in Si 2p spectra for H-Si(111)-1 × 1 surface were measured until nearly one-molecular layer thick oxide is formed, as is shown in Fig. 3. Because Si³⁺, M3 and Si⁴⁺

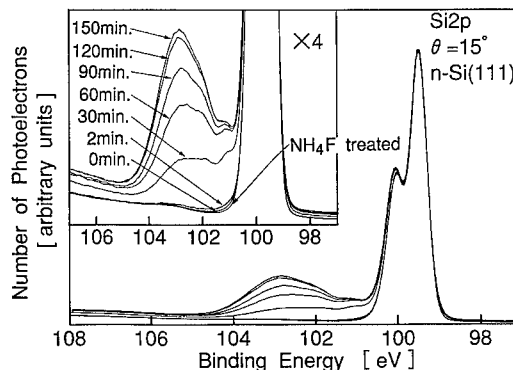


Fig. 3. Oxidation-induced changes in Si 2p spectra on H-Si(111)-1 × 1 surface with oxidation time as a parameter.

spectra can be separated from Si 2p spectra with rather small ambiguity, these spectra are used for the following studies of oxidation process. Here, Si^{3+} , M3 and Si^{4+} denote the Si atom bonded with one Si atom and three oxygen atoms, the Si atom bonded with one hydrogen atom and three oxygen atoms [22] and the Si atom bonded with four oxygen atoms, respectively. Fig. 4 shows the amounts of Si^{3+} , M3 and Si^{4+} as a function of areal density of bridging oxygen atoms obtained from the analysis of Fig. 3. If the oxidation reaction proceeds uniformly, the oxide consists only of Si^{4+} at the areal density of bridging oxygen atoms of $7.8 \times 10^{14} \times 4 \text{ cm}^{-2}$, which corresponds to one molecular layer of SiO_2 . However, according to this figure, this is not the case. This implies the non-uniform oxidation reaction at the early stage.

The oxidation processes shown in Fig. 2 and Fig. 4 are simulated as follows: The three dimensional Si lattice consisting of 52 atoms \times 52 atoms in each layer on Si(111) plane is used for the simulation of oxidation. The bonding probabilities of Si atoms with oxygen atoms are adjusted until almost the same figures as shown in Fig. 2 and Fig. 4 are obtained. For example, the Si atom bonded with an oxygen atom is assumed to have higher bonding probability with another oxygen atom as compared to the Si atom, which is not bonded with an oxygen atom. The solid curves in Fig. 2 and Fig. 4 are obtained from optimized simulation. The distribution of bridging oxygen atoms on each Si layer thus determined is shown in Fig. 5. From the top to the

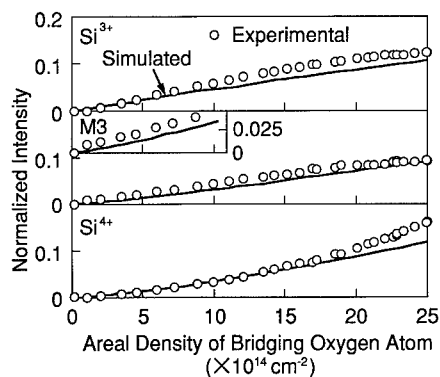


Fig. 4. Amounts of intermediate oxidation states on Si(111) surface as a function of areal density of bridging oxygen atoms. The simulated results are shown by the solid curves.

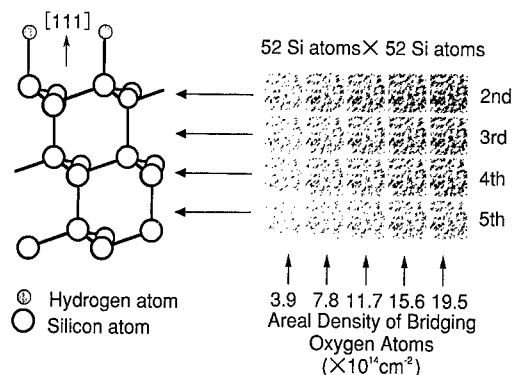


Fig. 5. Distribution of bridging oxygen atoms in each layer with areal density of bridging oxygen atoms as a parameter.

bottom of this figure, the topmost layer, the second layer from the top, the third layer and so on, are shown in this order. From the left to the right the amount of bridging oxygen atoms increases. This figure indicates that once the isolated bridging oxygen atoms are produced the oxidation proceeds in lateral direction around these oxygen atoms. With oxidizing further the oxidation proceeds in vertical direction and results in the non-uniform oxidation. The discrepancies observed between experimental results and simulated result in Fig. 2 and Fig. 4 must be partly attributed to the change in formation probabilities of bridging oxygen atoms produced by the oxidation-induced stress.

4. Initial stage of oxidation of H-Si(100)- 2×1 surface

As in the case of H-Si(111)- 1×1 surface, the MIR-IRAS and XPS studies on the initial stage of oxidation were performed on H-Si(100)- 2×1 surface until nearly one-molecular layer thick oxide is formed, shown in Fig. 6 and Fig. 7, respectively. According to Fig. 6, the oxidation produces not only M1 and M2, but also M3. Therefore, the dimer bonds are bridged by oxygen atoms to form Si-O-Si bonds at the early stage of oxidation. Such bonds are considered in the simulation of changes in Si 2p spectral intensities with the progress of oxidation. Fig. 8 shows the amounts of bonding states of surface Si as a function of areal density of bridging

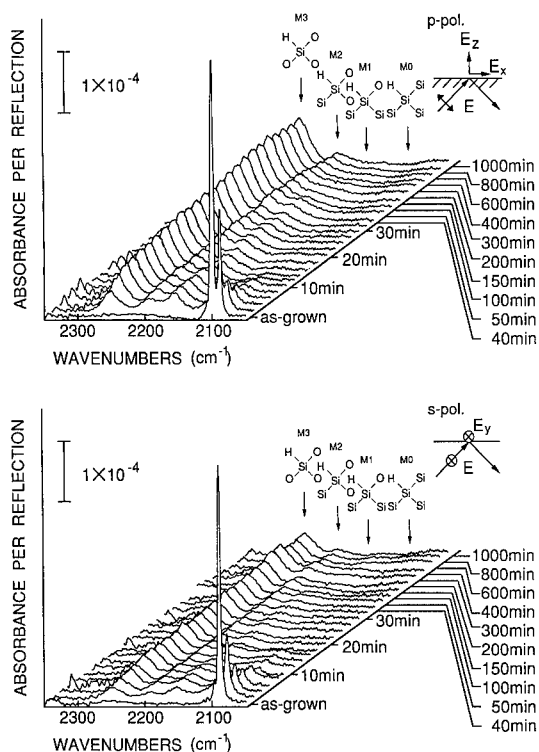


Fig. 6. Oxidation-induced changes in infrared absorption spectra for p- and s-polarized infrared measured for H-Si(100)-2×1 surface with oxidation time as a parameter.

oxygen atoms bonded with surface Si obtained from the analysis of Fig. 6. Fig. 9 shows the amounts of Si^{3+} , M3 and Si^{4+} as a function of areal densities of bridging oxygen atoms obtained from the analysis of Fig. 7. The solid curves in Fig. 8 and Fig. 9 exhibit

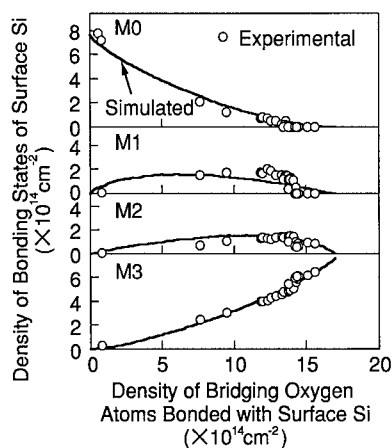


Fig. 8. Amounts of intermediate oxidation states on Si(100) surface as a function of areal density of bridging oxygen atoms bonded to surface Si. The simulated results are shown by the solid curves.

simulated results. The distribution of bridging oxygen atoms on each Si layer thus determined is shown in Fig. 10 with areal density of bridging oxygen atoms as a parameter. Bridging dimer bonds with oxygen atoms observed in Fig. 6 are considered in the simulation. According to this figure, the bridging oxygen atoms on Si(100) surface are distributed more uniformly than that on Si(111) surface. In other words, the sizes of oxide-clusters on Si(100) surface are smaller in average than those on Si(111) surface. Therefore, the oxidation-induced stress on Si(100) surface must be large. This must be the reason why the discrepancies observed between experimental re-

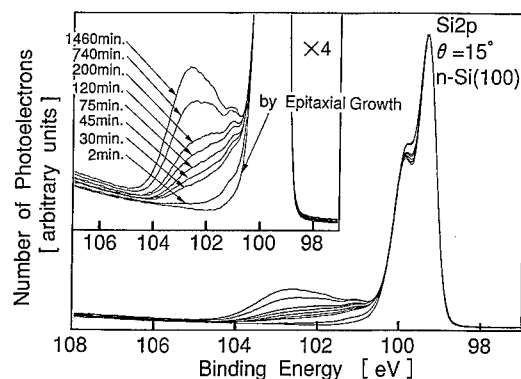


Fig. 7. Oxidation-induced changes in Si 2p spectra measured for H-Si(100)-2×1 surface with oxidation time as a parameter.

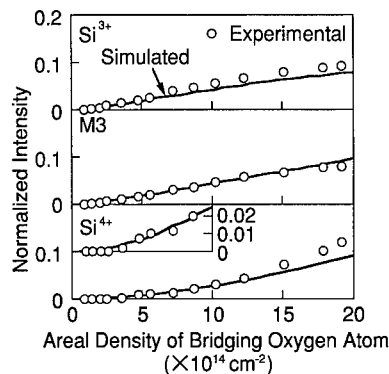


Fig. 9. Amounts of intermediate oxidation states on Si(111) surface as a function of areal density of bridging oxygen atoms. The simulated results are shown by the solid curves.

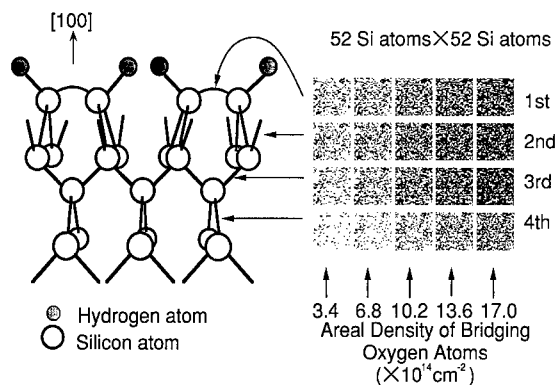


Fig. 10. Distribution of bridging oxygen atoms in each layer with areal density of bridging oxygen atoms as a parameter.

sults and simulated result in Fig. 8 and Fig. 9 are small for Si(100) surface.

5. Summary

Structural changes produced by the oxidation of H-Si(111)- 1×1 and H-Si(100)- 2×1 surfaces at 300°C in dry oxygen under a pressure of 1 Torr were investigated by MIR-IRAS and XPS. The oxidation-induced changes in infrared absorption spectra arising from stretching vibration of Si-H bonds were measured for the determination of oxidation processes of surface Si on H-Si(111)- 1×1 and H-Si(100)- 2×1 surfaces. These are combined with the oxidation processes determined by the oxidation-induced changes in Si 2p photoelectron spectra. Following results are obtained from the analysis and simulation of experimental results: (1) the layer-by-layer oxidation reaction occurs locally at SiO₂/Si(111) interface, while that does not occur at SiO₂/Si(100) interface, however, (2) the oxidation on Si(100) surface proceeds more uniformly in atomic scale than that on Si(111) surface. Therefore, in the present oxidation condition the layer-by-layer oxidation reaction at SiO₂/Si(111) interface seems to result in the non-uniform oxidation on Si(111) surface in atomic scale.

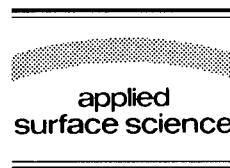
References

- [1] H. Sasaki Momose, M. Ono, T. Yoshitomi, T. Ohguro, S. Nakamura, M. Saito and H. Iwai, IEDM 94-593 (1994).
- [2] M. Horiguchi, T. Sakata, T. Sekiguchi, S. Ueda, H. Tanaka, E. Yamasaki, Y. Nakagome, M. Aoki, T. Kaga, M. Ohkura, R. Nagai, F. Murai, T. Tanaka, S. Iijima, N. Yokoyama, Y. Gotoh, K. Shoji, T. Kisu, H. Yamashita, T. Nishida and E. Takeda, Conf. on Int. Solid-State Circuits, Dig. Tech. Pap., 1995, p. 252.
- [3] T. Sugibayashi, I. Naritake, S. Utsugi, K. Shibahara, R. Oikawa, H. Mori, S. Iwao, T. Murotani, K. Koyama, S. Fukazawa, T. Itani, K. Kasama, T. Okuda, S. Ohya and M. Ogawa, Conf. on Int. Solid-State Circuits, Dig. Tech. Pap., 1995, p. 254.
- [4] T.E. Seidel, 1994 Int. Symp. on Semiconductor Manufacturing, Tokyo, 1994, p. 14.
- [5] T. Takahagi, I. Nagai, A. Ishitani and H. Kuroda, J. Appl. Phys. 64 (1988) 3516.
- [6] T. Takahagi, A. Ishitani, H. Kuroda, Y. Nagasawa, H. Ito and S. Wako, J. Appl. Phys. 68 (1990) 2187.
- [7] M. Sakuraba, J. Murota and S. Ono, J. Appl. Phys. 75 (1994) 3701.
- [8] G.S. Higashi, R.S. Becker, Y.J. Chabal and A.J. Becker, Appl. Phys. Lett. 58 (1991) 1656.
- [9] P. Jakob, P. Dumas and Y.J. Chabal, Appl. Phys. Lett. 59 (1991) 2968.
- [10] S. Watanabe, N. Nakayama and T. Ito, Appl. Phys. Lett. 59 (1991) 1458.
- [11] S. Watanabe, M. Shigeno, N. Nakayama and T. Ito, Jpn. J. Appl. Phys. 30 (1991) 3575.
- [12] S. Watanabe and Y. Sugita, Surf. Sci. 327 (1995) 1.
- [13] K. Goto, T. Aoyama, T. Yamazaki and T. Ito, IEICE SDM 92-49 (1992) 33.
- [14] H. Bender, S. Verhaverbeke, M. Caymax, O. Vatel and M.M. Hynes, J. Appl. Phys. 75 (1994) 1207.
- [15] T. Hattori, H. Nohira, Y. Tamura and H. Ogawa, Jpn. J. Appl. Phys. 31 (1992) L638.
- [16] H. Nohira, Y. Tamura, H. Ogawa and T. Hattori, IEICE Trans. Electron. E 75-C (1992) 757.
- [17] T. Hattori, J. Vac. Sci. Technol. B 11 (1993) 528.
- [18] K. Ohishi and T. Hattori, Jpn. J. Appl. Phys. 33 (1994) L675.
- [19] T. Aiba, K. Yamauchi, Y. Shimizu, N. Tate, M. Katayama and T. Hattori, Jpn. J. Appl. Phys. 34 (1995) 707.
- [20] U. Neuwald, H.E. Hessel, A. Feltz, U. Memmert and R.J. Behm, Appl. Phys. Lett. 60 (1992) 1307.
- [21] U. Gelius, B. Wannberg, P. Baltzer, H. Fellner-Feldegg, G. Carlsson, C.-G. Johansson, J. Larsson, P. Munger and G. Vergerfos, J. Electron Spectrosc. Rel. Phen. 52 (1990) 327.
- [22] H. Ogawa and T. Hattori, Appl. Phys. Lett. 61 (1992) 577.



ELSEVIER

Applied Surface Science 104/105 (1996) 329–334



The initial oxidation of silicon: new ion scattering results in the ultra-thin regime

E.P. Gusev, H.C. Lu, T. Gustafsson, E. Garfunkel *

Departments of Chemistry and Physics, and Laboratory for Surface Modification, Rutgers University, Piscataway, NJ 08855, USA

Received 28 June 1995; accepted 21 November 1995

Abstract

We present new results on the SiO_2/Si system obtained by high resolution medium energy ion scattering. Isotopic labeling experiments demonstrate that the traditional Deal Grove and related models fail for sub-10 nm films. Any realistic model in this ultra-thin film region should include near-interfacial and surface exchange reactions. We also observed that the surface can be roughened during oxidation. Simple models explaining the genesis of roughness during active oxidation and in a transition regime between active and passive oxidation are given, based on relative rates of various surface processes.

1. Introduction

The oxidation of silicon remains of critical importance because SiO_2 is the dominant dielectric of the microelectronics industry. However, despite over thirty years of research, a variety of questions remain unanswered [1–4]. In this paper we review our recent results using predominantly medium energy ion scattering (MEIS) that address some of the key questions concerning the oxidation of silicon in the ultrathin film regime. We discuss new results that can help us better understand the oxide growth mechanism [5], and roughness of the SiO_2/Si system. In particular, we show how roughness is greatly exacerbated by oxidizing in certain regions of P–T phase space [6].

The dominant growth mechanistic model was provided by Deal and Grove in 1965 [7]. They argued,

based on kinetic data of oxygen uptake, that the oxidation was accomplished by the diffusion of oxygen through a growing oxide film followed by the reaction of oxygen with silicon at the interface. Their ‘linear–parabolic’ phenomenological model has for the most part survived the test of time, although variants of the model now permit layered structures, enhanced diffusion or other features to exist in the region close to the interface, helping to rationalize anomalous growth behavior [1–4,8]. In this paper we present results that demonstrate that there are not only *interface* channels of oxidation, but a broad *near-interface* growth throughout a transition region of the near-interfacial oxide, and outer *surface exchange* reactions which become important in understanding oxidation in the ultrathin film regime.

2. Experimental

MEIS is a high resolution variant of RBS in which the incident energy of the probing ion (pro-

* Corresponding author. Tel.: +1-908-4452747; fax: +1-908-4455312; e-mail: garf@rutchem.rutgers.edu.

tons in our case) is on the order of 100 keV [9]. The kinetic energy of the backscattered ion gives information about the mass and depth of the atom in the solid from which the ion scatters. We usually use channeling and blocking techniques, in which one directs the incident and detected ion beam along bulk crystallographic axes, enhancing surface sensitivity. For an amorphous SiO_2 overlayer, all the silicon and oxygen in the overlayer are observed, along with one or two layers of the bulk Si (see Fig. 1a). The width of the oxygen peak reflects the thickness of the oxide film. We take further advantage of the high mass and depth resolution of MEIS by performing sequential oxidation in $^{16}\text{O}_2$ and $^{18}\text{O}_2$ [5,10]. This permits us to determine where oxygen incorporates into a growing oxide film, thus helping to confirm which mechanistic model, if any, is correct. In Fig. 1b we present a model spectrum of a conventional SiO_2 film (grown with ^{16}O) which has been reoxidized in $^{18}\text{O}_2$. If, upon reoxidation, the ^{18}O incorporates at the top surface and at the interface, then two separate peaks should be observed in the spectrum (Fig. 1b). The total amount of each isotope and their relative distributions in the SiO_2 film are indicated by the size and shape of the two spectral regions.

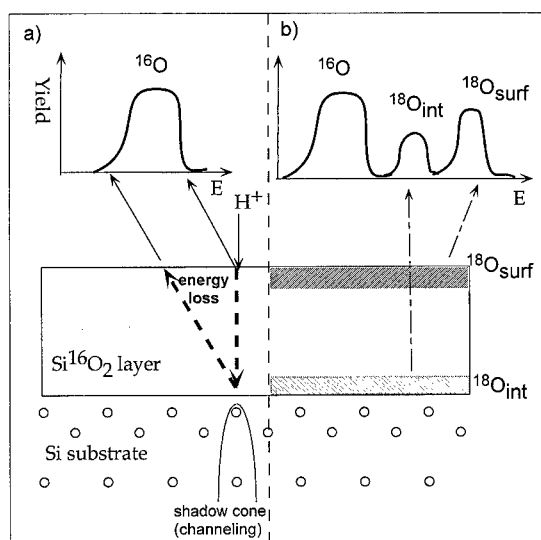


Fig. 1. An illustration of the use of MEIS for examining the isotopic oxidation of silicon. The lower panel shows oxygen isotope distribution in the film before and after reoxidation in $^{18}\text{O}_2$ (not drawn to scale); the upper panel shows the anticipated energy spectra in the oxygen region.

$\text{Si}(100)$ substrates were used for isotopic oxidation experiments. Both $^{18}\text{O}_2/^{16}\text{O}_2$ and $^{16}\text{O}_2/^{18}\text{O}_2$ sequential exposures were employed. The oxygen pressure was varied from 10^{-6} to 20 Torr, and the oxidation temperature from 700 to 1000°C. Some wafers were first oxidized using state-of-the art fab facilities at IBM or AT&T Bell Laboratories. Surface roughening studies were performed on $\text{Si}(111)$. Si pads were put between the sample and sample holder to reduce metal contaminations during oxidation. More details about sample preparation, oxidation, experimental set-up and data analysis can be found elsewhere [5,10].

3. Results

3.1. Isotopic labeling experiments

First we introduce results of isotope oxidation studies that are clearly inconsistent with classical (thick film) models of oxidation. In Fig. 2 we present MEIS results for the reoxidation of a 60 Å oxide (^{16}O) film in $^{18}\text{O}_2$ at 800°C and 1 Torr. Spectrum a is observed for the as-delivered 60 Å oxide (from IBM), following a brief flash to ca. 400°C to remove adsorbates. The shape of the scattering signal in the initial Si^{16}O_2 is discussed below. Following reoxidation in $^{18}\text{O}_2$, we see two features develop in the ^{18}O region of the backscattering spectrum. The first is at the high energy edge, 80 keV (spectrum b), indicating ^{18}O incorporation in the outer surface layers. This feature is not expected from any of the classical models of oxide growth, as all assume that oxidation takes place at or near the SiO_2 -Si interface. Concomitant with the growth of this peak is a decrease in the yield at the high energy edge of the ^{16}O peak. Further oxidation under the same conditions for 21 h (spectrum c) results in growth of the surface peak and pronounced growth of the second broad feature at 78.7 keV. This feature, representing growth from well below the surface, is more consistent with classical growth models.

Quantitative information about the oxygen and silicon depth profiles in the films can be obtained through energy spectral simulations, as shown in Ref. [5]. The purpose of the simulation is to deter-

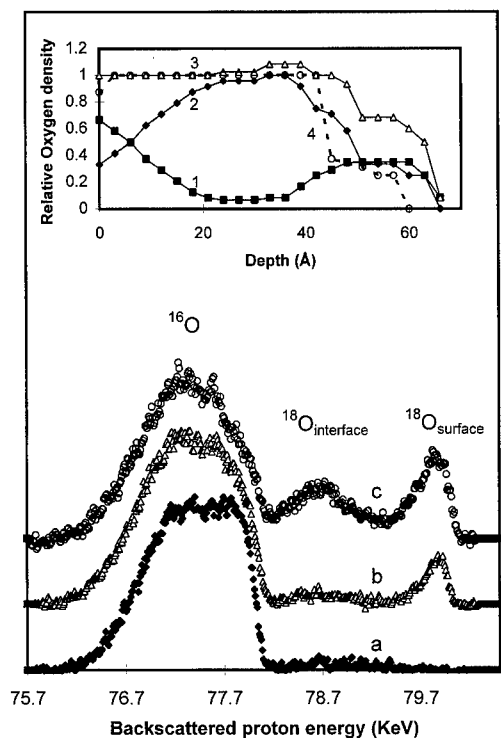


Fig. 2. Oxygen spectra for (a) a 60 Å oxide grown on Si(100), (b) the same sample reoxidized in $^{18}\text{O}_2$ at 1 Torr, 800°C for 3 h, and (c) following further reoxidation for 21 h. The insert shows oxygen depth profiles in the oxide that determined by model simulation of the spectrum (c).

mine the absolute oxygen density as a function of depth, the relative ^{16}O to ^{18}O distributions, and the O and Si concentration gradients. Results of the modeling simulations are presented in the inset in Fig. 2, in which we plot the normalized oxygen yield as a function of depth (where 1 corresponds to stoichiometric SiO_2). The ^{18}O incorporated (curve 1), ^{16}O following reoxidation (2), and total O profiles (3) are included, along with the original ^{16}O profile (4).

What is apparent is that there are two main regions of oxygen incorporation during oxidation, one at or near the interface, and the other at the outer oxide surface. Close inspection actually reveals that the profiles of both oxygen isotopes overlap in the interface region; in this case it appears that the overlap region is about 20 Å wide. That the oxidation reaction takes place over a wide region is neither discussed nor accounted for in the kinetic models; however the concept of a transition region has

been extensively discussed. Although it may not significantly effect oxidation kinetic behavior for thicker films, an accurate description of oxide growth must include the surface, interface and near-interface reactions that we observe. This is especially the case in the ultrathin film regime (as we discuss in more detail elsewhere [5]) where the layer thicknesses and separations are almost the same size as the total thickness of the oxide. It is perhaps even more important now to understand the kinetics of reactions and interdiffusion, and the spacial distribution of all species, such as H, N, halides and other impurities that are purposely added for a variety of reasons during complex multistep oxidation processing.

We have also observed that the surface exchange reaction is enhanced by impurities. In Fig. 3 we present spectra demonstrating the enhancement in the surface reaction rate when metal impurities are present. For this experiment, one of the samples was reoxidized without the Si pads and metal from the holder diffused onto the Si (~ 0.01 ML of Ta and 0.25 ML of Mo, 1 ML = 6.8×10^{14} at/cm², were observed in the surface after the reoxidation). Comparing this sample with one oxidized under the same conditions with Si pads, we observed the area under the ^{18}O surface peak to be about 3 times larger. This result emphasizes the importance of a metal-free environment during the oxidation of silicon [11].

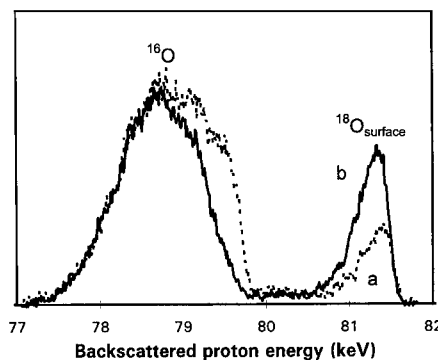


Fig. 3. Oxygen spectra after oxidation at 800°C with (a) and without (b) silicon pads between the sample and sample holder. The growth of the ^{18}O peak and depletion of the high energy part of the ^{16}O peak demonstrate the effect of metal impurities on the oxidation.

3.2. Transition region near the Si / SiO₂ interface

As mentioned above, the isotopic labeling experiments demonstrate that, in addition to the traditional reaction at the interface, oxidation also occurs in the near-interfacial oxide. This observation stimulated us to further understand the structure of the oxide near the interface and its role in silicon oxidation. Our studies of this specific region of the oxide are also driven by the important role of the interface in device performance.

It has been shown that there is a transition region between the crystalline Si and stoichiometric a-SiO₂. The transition region has been observed by a variety of techniques (e.g. photoemission, HRTEM, ellipsometry, RBS, etc.) [2,12–14]. One should keep in mind, however, that different techniques probe different properties of the transition region (chemical, structural, optical etc.). Different oxidation conditions may also result in variations in the width of the transition region [15]. For these reasons, the thickness of the transition region ranges from 5 to 50 Å.

MEIS is a technique that can be used to determine compositional variations of the transition region since energy distributions of protons scattered from targets with different compositional gradients are different. A typical simulation of the oxygen energy peak is shown in Fig. 4. The parameters of the energy loss ('stopping power') and straggling which are input into the simulation, are checked by changing the scattering angle (hence the total average travel length of the protons in the solid). The very good fit of the two sets of data for both angles lends further credence to the model. We also use XPS, and spectroscopic ellipsometry to determine oxide thickness and cross-correlate it with the MEIS results. The procedure of energy spectral modeling is discussed in more detail elsewhere [5].

We note that the region between the oxide and the silicon substrate is not sharp (insert in Fig. 4). Oxygen density in the transition region gradually decreases from the 'bulk' oxide value and vanishes at the silicon substrate, while, the silicon density is higher than in the oxide (see Fig. 12 in Ref. [5]). The thickness of the (compositional) transition region is about 12 ± 4 Å. Our profiles collect all compositional inhomogeneities in the oxide, e.g. suboxides and surface roughness. Roughness, which could be

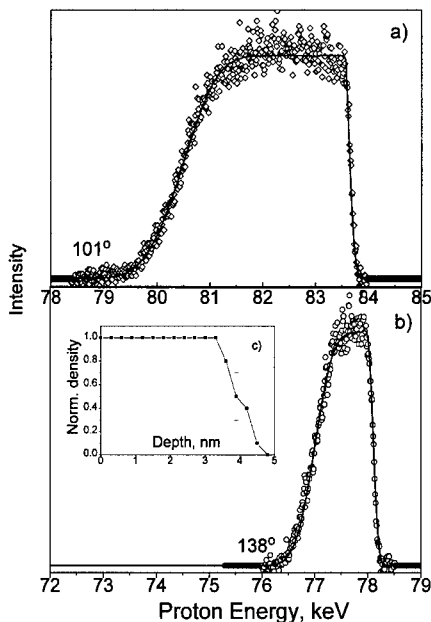


Fig. 4. Oxygen spectra for a 45 Å oxide on Si(100) taken at two different scattering angles: (a) 101° (with an exit angle of 11°), and (b) 138° (an exit angle of 48°). Solid lines show the result of the modeling. The oxygen depth profile for this sample is shown in the insert.

confused with a compositional gradient, when measured by XRD on the samples grown in the same laboratory under similar conditions was on the order of $\text{rms} = 2\text{--}3$ Å [15]. Suboxides (or incompletely oxidized silicon atoms) are the other major contributor to the depth distribution gradients observed in our experiments. Suboxide states are also routinely observed in photoemission experiments [5,12].

We believe that the suboxides are the key species in a near-interfacial reaction in which diffusing oxygen reacts with incompletely oxidized silicon atoms throughout the transition region. The incompletely oxidized silicon is likely to be supplied by the oxidation reaction at the interface; some silicon atoms may be released from the substrate due to the large molecular volume mismatch between crystalline silicon and the oxide, and the stress near the interface created during the oxidation process [2]. Silicon interstitials and SiO diffusion into the oxide have been discussed in some recent models [16,17]. We also note that the existence of a transition region was the departure point of the reactive layer model [4,18].

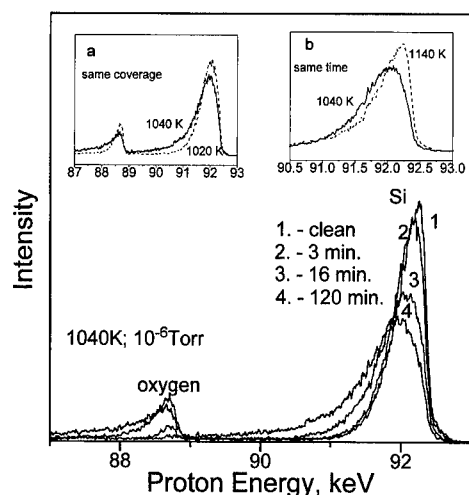


Fig. 5. Initial oxidation of Si(111) at 770°C and 10^{-6} Torr as a function of exposure time. Both oxygen and silicon regions of the spectra are displayed. The inserts shows a comparison of the spectrum in the transition oxidation regime (solid line) with the (dashed) spectra in the passive (lower temperature) (a) and active (higher temperature) (b) oxidation regimes.

However, this model considers the reaction as taking place only on-top of the reactive layer, inconsistent with our results.

3.3. Surface roughening

In addition to the compositional gradient in the transition region, another interfacial issue which reportedly affects device properties is the roughness. Although we do not report at length here on interface roughness, we do wish to elucidate two poorly understood and appreciated mechanisms by which the SiO_2/Si system roughens during oxidation [19]. In Fig. 5 we present results demonstrating that surface roughness can be enhanced during oxidation under certain conditions. For a roughened surface, the average ion travel length in the solid is increased relative to the uniform film case, especially when the incident or exit angles are glancing. A spectrum of a roughened film should show a decrease in the yield at the high energy edge and a broader low-energy tail relative to the flat film case. Fig. 5 shows spectra in both the Si and O regions that result from oxidizing very close to the boundary between active (etching) and passive (growth) oxidation [8]. Both peaks

demonstrate a broad low energy tail, a fingerprint of roughness in this case. Both peaks are qualitatively different from ones taken in the passive and active oxidation regimes (as it follows from the comparison shown in the inserts) implying a separate region with specific oxidation behavior.

This region of phase space is called the transition oxidation regime, following the suggestion of [20,21]. Under certain conditions, the quasi-steady state surface oxygen concentration is high enough to have two dimensional oxide nuclei form, but not high enough to have the nuclei fully cover the surface. The areas that are covered by the oxide are relatively unreactive, while the clean Si areas are continuously being etched by the incident oxygen. We and others [22] have obtained a roughness over 30 Å when intentionally trying to roughen the surface during oxidation in the transition regime.

We have also observed roughening of the surface during active oxidation (etching). In this case the surface roughens, as noted in Fig. 5b, however, no oxygen is observed in the spectrum. We believe that in this case, the roughening is caused by continuous etching of the Si by O_2 , but at a temperature too low to allow for significant smoothing of the surface by diffusion. The etching occurs randomly, but limited vacancy diffusion only leads to void formation without step flow. We thus have two different sets of processes which occur in two different parts of the P–T oxidation phase space, both of which lead to roughening of the surface. As any form of roughening could be detrimental to state of the art devices, care must be taken during processing to avoid these regions of oxidation phase space.

Acknowledgements

The authors acknowledge valuable discussions with D. Buchanan, L.C. Feldman, and M.L. Green and their help in sample preparation. The work is supported by NSF (DMR-9408578), PRF (28788-AC5) and NJ AIMS grants.

References

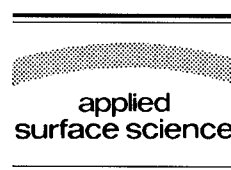
- [1] C.R. Helms and E.H. Poindexter, *Rep. Prog. Phys.* 57 (1994) 791.

- [2] E. Irene, *Crit. Rev. Solid State Mater. Sci.* 14 (1988) 175.
- [3] B.E. Deal, in: *The Physics and Chemistry of SiO₂ and the Si–SiO₂ Interface*, Eds. C.R. Helms and D.E. Deal (Plenum, New York, 1988) p. 5.
- [4] C.J. Sofield and A.M. Stoneham, *Semicond. Sci. Technol.* 10 (1995) 215.
- [5] E.P. Gusev, H.C. Lu, T. Gustafsson and E. Garfunkel, *Phys. Rev. B* 52 (1995) 1759; *Appl. Phys. Lett.* 67 (1995) 1742.
- [6] F.W. Smith and G. Ghidini, *J. Electrochem. Soc.* 129 (1982) 1300.
- [7] B.E. Deal and A.S. Grove, *J. Appl. Phys.* 36 (1965) 3770.
- [8] J.M. Delarious, C.R. Helms, D.B. Kao and B.E. Deal, *Appl. Surf. Sci.* 39 (1989) 89.
- [9] J.F. van der Veen, *Surf. Sci. Rep.* 5 (1985) 199.
- [10] E.P. Gusev, H.C. Lu, T. Gustafsson and E. Garfunkel, in: *Interface Control of Electrical, Chemical and Mechanical Properties*, Eds. S.P. Murarka, K. Rose, T. Ohmi and T. Seidel (MRS, Pittsburgh, PA, 1994) p. 69.
- [11] H. Dallaporta, M. Liehr and J.E. Lewis, *Phys. Rev. B* 41 (1990) 5075.
- [12] F.J. Himpsel, F.R.M. Feely, A. Taleb-Ibrahimi, J.A. Yarmoff and G. Hollinger, *Phys. Rev. B* 38 (1988) 6084.
- [13] J.M. Gibson and M.Y. Lanzerotti, *Nature* 340 (1989) 128.
- [14] R. Haight and L.C. Feldman, *J. Appl. Phys.* 53 (1982) 4884.
- [15] M.L. Green, D. Brasen, K.W. Evans-Lutterodt, L.C. Feldman, K. Krisch, W. Lennard, H.T. Tang, L. Manchanda and M.T. Tang, *Appl. Phys. Lett.* 65 (1994) 848.
- [16] S.I. Raider, in: *The Physics and Chemistry of SiO₂ and the Si–SiO₂ Interface*, Eds. C.R. Helms and D.E. Deal (Plenum, New York, 1988) p. 35.
- [17] S.T. Dunham, in: *The Physics and Chemistry of SiO₂ and the Si–SiO₂ Interface*, Eds. C.R. Helms and D.E. Deal (Plenum New York, 1988) p. 477.
- [18] A.M. Stoneham, C.R.M. Grovenor and A. Cerezo, *Phil. Mag. B* 55 (1987) 201.
- [19] H.C. Lu, E.P. Gusev, E. Garfunkel and T. Gustafsson, *Surf. Sci.* 351 (1996) 111.
- [20] F.M. Ross, J.M. Gibson and R.D. Twisten, *Surf. Sci.* 310 (1994) 243.
- [21] A. Feltz, U. Memmert and R.J. Behm, *Surf. Sci.* 314 (1994) 34.
- [22] J. Seiple and J.P. Pelz, *J. Vac. Sci. Technol. A* 13 (1995) 772.



ELSEVIER

Applied Surface Science 104/105 (1996) 335–341



Local atomic structure and electrical properties of nitrided Si–SiO₂ interfaces produced by low-temperature plasma processing and rapid thermal annealing, and explained by ab-initio quantum chemistry calculations

G. Lucovsky^{*}, D.R. Lee, S.V. Hattangady, H. Niimi, S. Gandhi, C. Parker, Z. Jing, J.L. Whitten, J.R. Hauser

Departments of Physics, Materials Science and Engineering, Electrical and Computer Engineering, and Chemistry, North Carolina State University, Raleigh, NC 27695-8202, USA

Received 28 June 1995; accepted 13 December 1995

Abstract

This paper discusses the effectiveness of nitrogen (N-) atom incorporation at Si–SiO₂ interfaces in improving device reliability. N-atoms are introduced by a low thermal budget process that includes: (i) a 300°C plasma-assisted oxidation/nitridation; (ii) a 300°C plasma-assisted deposition of the dielectric layer; and (iii) a 900°C post-deposition anneal, either as a separate 30 s rapid thermal annealing (RTA) step, or during dopant activation of the gate electrode. The amount of incorporated-N has been varied at the monolayer range by using N₂O/O₂ mixtures for the oxidation step, and has been measured by Auger electron spectroscopy (AES), secondary ion mass spectrometry (SIMS), and optical second harmonic generation (OSHG). A model, based on ab-initio calculations, is used to explain the role of N-atoms in improving device reliability, e.g. in reducing H-atom induced generation of positively-charged defects, the so-called anomalous positive charge (APC).

1. Introduction

As field effect transistor, FET, device dimensions are scaled down into the deep submicron (≤ 0.25 μm) for ULSI circuits, there must be corresponding decreases in the oxide equivalent thickness (t_{OX}) of gate dielectrics into a regime below about 5 nm. At these thicknesses, defect generation mechanisms under stress bias conditions are determined mostly by

local bonding at the Si–SiO₂ interface rather than by properties of the bulk oxide films [1]. Much attention has been focused on benefits of incorporating small amounts of N at, or in the immediate vicinity the Si–SiO₂ interface of these ultra-thin dielectrics [2,3]. Reported benefits of N-atom incorporation include (i) increased resistance to defect generation and (ii) effective barriers to boron (B-) atom diffusion from boron-doped polycrystalline-silicon gate electrodes [4–7]. In addition, use of nitrided oxide films with higher dielectric constants than SiO₂ allows increases in thickness of dielectric film while maintain-

^{*} Corresponding author. Tel.: +1-919-5153301; fax: +1-919-5157331.

ing capacitances corresponding to those of thinner oxides. It is not obvious that these increases will be beneficial in reducing direct tunneling currents since increases in the dielectric constant are usually coupled with decreases in the bandgap of the dielectric thereby mitigating some of the potential advantages of increased film thicknesses.

In previous studies we have used NH_3 as the N-atom source gas for low-temperature (300°C) plasma-assisted deposition of oxynitrides and nitrides, and this has lead to incorporation of large amounts (~ 20 at%) of H (mostly as NH) in the bulk of these films [8,9]. In addition, N-atoms were also incorporated as NH groups at the Si–SiO₂ interface of composite film structures, e.g. in oxide–nitride–oxide (ONO) stacked dielectrics. Infrared (IR) studies showed H-atoms are released from NH groups in these nitrated dielectrics during post metallization annealing (PMA) at ~ 400 – 450°C yielding interface trap (D_{it}) levels of about $5 \times 10^{11} \text{ cm}^{-2} \text{ eV}^{-1}$. However, the D_{it} concentrations could be reduced to levels comparable to those of thermal oxides ($\sim 10^{10} \text{ cm}^{-2} \text{ eV}^{-1}$) by a 30 s RTA at 900°C . IR studies showed that this reduction in D_{it} resulted from an additional and significant release of H-atoms during the higher temperature RTA process, followed by formation of Si–N bonds between near-neighbor Si- and N-atoms that had lost H-atoms during the high temperature RTA.

Conventional methods used by other groups for incorporating N-atoms at Si–SiO₂ interfaces include furnace oxidation, and rapid thermal oxidation, RTO, in N_2O and NO, and/or annealing in either N_2O or NH_3 at temperatures in the range of 850°C to 1200°C [2–7]. As noted above, these high temperature processes have yielded improved device reliability. This paper reports on a newly developed low-temperature/low-thermal budget process that achieves comparable levels of N-atom incorporation at Si–SiO₂ interfaces with low H-atom incorporation through 300°C plasma processes using N-atom source gases other than NH_3 ; e.g. N_2O . Defect levels in devices subjected to 400°C PMAs, but without 900°C RTAs, are comparable to what has been achieved with plasma-deposited and furnace-grown oxides [10], whilst device performance and reliability after a 30 s 900°C RTA are comparable to what is obtained using the high-temperature/high-thermal budget ni-

triding processes indicated above [2–7]. We explain the improved reliability that results from N-atom incorporation at the Si–SiO₂ interface in the context of a microscopic model that is based on H-atom induced defect generation resulting in the creation of the so-called anomalous positive charge (APC) centers [11].

2. Interface formation and device fabrication

We have separated fabrication of the Si–SiO₂ heterostructures into three independently controlled process steps [12,13]: (i) Si–SiO₂ interface formation by plasma-assisted oxidation/nitridation at 300°C ; (ii) deposition of dielectrics by remote PECVD at 300°C ; and (iii) chemical and/or structural relaxation of Si–SiO₂ interfaces and dielectric films by rapid thermal annealing at 900°C . For the experiments described below, these steps were used in the fabrication of two different device structures: (i) metal-oxide-semiconductor (MOS) capacitors with Al-gate electrodes, and (ii) field effect transistors (FETs) with phosphorus doped polycrystalline-silicon gate electrodes. For the MOS capacitors, the substrates were p/p⁺ Si(100) wafers with an epilayer resistivity of $\sim 10 \Omega \text{ cm}$; lower resistivity wafers with hole concentrations, $p \sim 4 \times 10^{17} \text{ cm}^{-3}$ were used for the FETs. In both instances the in situ processing began with a 300°C plasma-assisted oxidation step in either O_2 , N_2O or $\text{N}_2\text{O}/\text{O}_2$ mixtures. For MOS capacitors, the pre-oxidation treatment was a standard, high temperature, RCA clean terminated by an HF-rinse. For the FETs, the Si surface used for the gate dielectric was not subjected to an RCA clean; instead, a field oxide about 200 nm thick was grown on the entire wafer, and the gate oxide region was defined by a combination of low-pH and dilute HF oxide removal processes. This results in smoother interfaces for Si(100) than an RCA clean, and hence yields a reduced fall-off of the channel mobility as a function of the electric field at the Si surface [14]. For the MOS capacitors, 15 nm of SiO₂ was then deposited by remote PECVD at a pressure of 300 mTorr and a temperature of 300°C by excitation of He (200 sccm) and N_2O (20 sccm) in a rf plasma upstream from the Si wafer; 2 sccm of 10% SiH_4 in He was introduced through a dispersal ring down-

stream from the plasma. For the FETs, both N_2O and O_2 were used in the deposition of 5.5 nm of SiO_2 by a similar 300°C remote PECVD process. MOS capacitors were fabricated using Al-gate electrodes and patterning was standard photolithographic techniques. The maximum processing temperature for the MOS capacitors was 400°C , the temperature of the PMA. The FET structures incorporated phosphorus-doped polycrystalline Si gate electrodes. These were processed at 900°C for about 30 min using a conventional POCl_3 doping process that also formed the source and drain junctions in a self-aligned device structure.

3. Interface characterization

The AES and SIMS measurements reported below were restricted to wafers used for MOS capacitor studies. Additional SIMS measurements have been performed on the interfaces and films used in the FETs, and these give substantially the same results as discussed below for the MOS capacitor wafers. The AES measurements (Fig. 1(a)) were performed on-line in a surface analysis chamber immediately after the plasma oxidations; the SIMS depth profiles (Fig. 1(b)) were made after the oxide depositions. The AES Si_{LVV} peak at 92 eV is due to Si–Si bonds and is identical in all spectra of Fig. 1(a). For comparison, we have included data for the remote H_2 plasma cleaning/passivation process, as well as the pre-deposition oxidation/nitridation processes described above. After an ex-situ RCA clean and HF rinse, the H-terminated Si surface displayed readily detectable C and O contamination. After a 2 min exposure to a remote H_2 plasma, C contamination was reduced below the AES detection limit of ~ 1 at%, and the amount of O was also reduced. C was also reduced below detection by a 15 s exposure to an O_2 plasma, or by a 30 s exposure to an N_2O plasma with a concurrent plasma-assisted growth of ~ 0.5 – 0.6 nm of SiO_2 [12,14]. Exposure to the N_2O plasma also produced a detectable N AES signal; the relative 92 eV Si_{LVV} signal level demonstrated that the N feature was due to N–Si bonds within at most two–three molecular layers of the Si– SiO_2 interface.

Areal densities of the N, C and F at the Si– SiO_2 interfaces were determined by integration of the

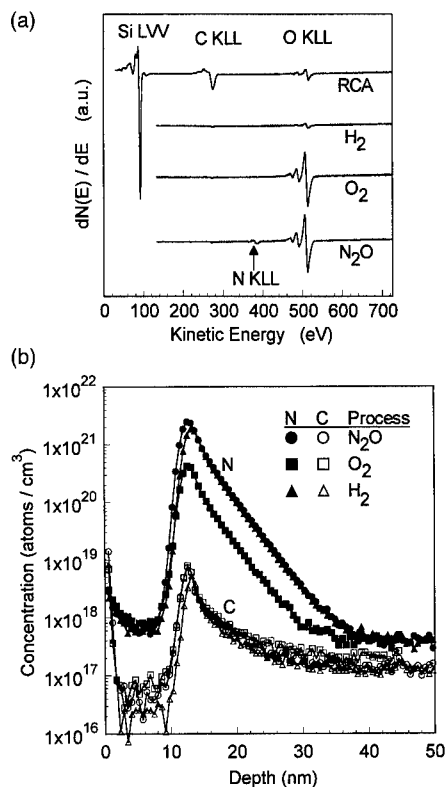


Fig. 1. (a) AES measurements for different surface treatments: (i) RCA clean with HF rinse, (ii) 2 min plasma- H_2 , (iii) 15 s plasma- O_2 , and (iv) 30 s plasma N_2O . (b) SIMS profiles for N and C after 15 s plasma- O_2 and 30 s plasma- N_2 treatments. Also included in (b) is the SIMS profile for N after the plasma- H_2 treatment.

respective mass signals, and by using sensitivity factors appropriate to these elements in a Si host material. This technique is based on an observation that interfacial N, C and F are driven into the Si substrate by the sputtering process used in the SIMS analysis. Reduction of SIMS data in Fig. 1(b) showed that each of three plasma treatments reduced residual C-contamination to about the same level of $(2 \pm 0.5) \times 10^{12} \text{ cm}^{-2}$; F-atom concentrations were also in the 10^{12} cm^{-2} range for all three treatments. The 15 and 30 s exposures to the N_2O plasma gave N concentrations, $[\text{N}]$ of $(9 \pm 0.5) \times 10^{14} \text{ cm}^{-2}$, whilst 5 s and 15 s exposures to the O_2 plasma yielded $[\text{N}] \approx (2 \pm 0.5) \times 10^{14} \text{ cm}^{-2}$. The sample exposed to the H_2 plasma had $[\text{N}] \approx 6 \times 10^{14} \text{ cm}^{-2}$. Interfacial N after H_2 and O_2 treatments was derived from the

N_2O source gas used in SiO_2 depositions. Combining the SIMS and AES measurements with studies of optical second harmonic generation (OSHG), we have been able to show that the N atoms discussed above are at the Si– SiO_2 interface [15]. The key aspect of the OSHG measurements is that resonance energies are different O-atom and N-atom coverage of the crystalline Si component of the Si– SiO_2 interface.

SIMS and AES measurements were also performed on samples in which the oxidation step was performed using $\text{N}_2\text{O}/\text{O}_2$ mixtures. In all instances, C and F levels were comparable to those described above. In addition, levels of N at the Si– SiO_2 interface scaled with the fraction of N_2O in the $\text{N}_2\text{O}/\text{O}_2$ mixture. The observed scaling was also consistent with on-line AES measurements made on the same samples.

4. Device studies: MOS capacitors and field effect transistors

Table 1 includes results of electrical measurements performed on (i) MOS capacitors with Al electrodes, and (ii) FETs with polycrystalline Si gates. MOS capacitors were analyzed by conventional high-frequency/quasi-static (HF/QS) capacitance–voltage (C – V) techniques which gave the mid-gap D_{it} values, and also values for the flat-band voltage, V_{fb} . The HF C – V measurements were done

at 100 kHz whilst the QS C – V characteristics were obtained with a voltage ramp of 35 mV/s. The mid-gap D_{it} values did not correlate with the N concentration at the Si– SiO_2 interfaces. Interfaces formed by 2 min exposure of an H_2 remote plasma resulted in values of mid-gap $D_{it} \sim 2 \times 10^{11} \text{ eV}^{-1} \text{ cm}^{-2}$. Exposure to an O_2 remote plasma for 5 s give a mid-gap D_{it} of $\sim 7 \times 10^{10} \text{ eV}^{-1} \text{ cm}^{-2}$; this value decreased to $\sim 1 \times 10^{10} \text{ eV}^{-1} \text{ cm}^{-2}$ after a 15 s exposure. A similar trend was found for the remote N_2O plasma: a mid-gap D_{it} of $\sim 5 \times 10^{10} \text{ eV}^{-1} \text{ cm}^{-2}$ for a 15 s exposure decreasing to $\sim 1 \times 10^{10} \text{ eV}^{-1} \text{ cm}^{-2}$ after a 30 s exposure. From these measurements we conclude that: (i) comparable levels of D_{it} can be obtained by predeposition oxidation in either O_2 or N_2O , and (ii) these low D_{it} values are obtained provided that the oxidation step is performed at sufficiently long times, i.e. 15 s for the O_2 , and 30 s for the N_2O treatments. In addition, comparisons with MOS capacitors with oxide layers formed by conventional thermal oxidation in dry O_2 at 900°C have demonstrated that D_{it} levels in the optimized MOS capacitors with plasma-oxides and N-atom or O-atom terminated interfaces are comparable to those of the thermal oxides. Based on the results for the H_2 plasma treatment, wherein oxidation proceeds in parallel with the initial stages of film deposition, we conclude that the oxidation treatment must be sufficiently complete to prevent oxidation during deposition that has been shown to lead to comparatively high values of D_{it} , (i.e. $\sim 10^{11} \text{ eV}^{-1} \text{ cm}^{-2}$). In addition, the comparisons cited above, combined with the studies we have performed on devices with nitride and oxynitride composite dielectrics indicate that N-atoms, as introduced above, and NH-groups, as introduced using NH_3 source gases, behave very differently at Si– SiO_2 interfaces; (i) the N-atom terminations can promote defect densities as low as thermal oxides, whilst (ii) NH-groups promote significantly higher levels of D_{it} , that can only be reduced after high temperature RTAs (typically 30 at 900°C) in which the H-atoms are eliminated from the NH groups [13].

The beneficial effects of N-atom incorporation with respect to reliability at Si– SiO_2 interfaces are clearly evident from stress bias studies on FETs. Before discussing reliability measurements, it is important to understand the effects of N-atom incorpo-

Table 1
Electrical measurements on MOS and FET devices

(a) MOS capacitors		
Interface treatment	$D_{it} (\times 10^{10} \text{ cm}^{-2} \text{ eV}^{-1})$	
O-atom terminated	1.0 ± 0.5	
N-atom terminated	1.0 ± 0.5	
NH-terminated (400°C)	20 ± 5	
NH-terminated (900°C)	1.0 ± 0.5	
Thermally-grown oxide	1.0 ± 0.5	
(b) FETs		
Interface treatment with plasma-oxide	Effective mobility ($\text{cm}^2/\text{V s}$)	Threshold voltage (V)
O-atom terminated	460 ± 5	0.41 ± 0.03
N-atom terminated	460 ± 5	0.38 ± 0.03
Thermally-grown oxide	450 ± 5	0.33 ± 0.03

ration on the transistors current-drive characteristics. This is illustrated in Fig. 2(a) and (b), (i) where we show FET characteristics of devices with plasma-oxides, and both nitrided and non-nitrided interfaces, and (ii) where these properties are compared with the properties of devices with conventional thermally-grown oxides, (i.e. dry oxidation at 900°C). The oxide thicknesses and transistor geometries are essentially the same, and the data in the figure are normalized to take account of any small quantitative differences in oxide thickness and/or channel length and width. There are two observations: (i) the highest drive currents were obtained in devices with the thermally-grown oxides, and (ii) devices with deposited oxides and nitrided interfaces displayed higher drive currents than devices without interfacenitridation. The data in Fig. 2(b), in the context of the Tasch model [16], provides a basis for understanding

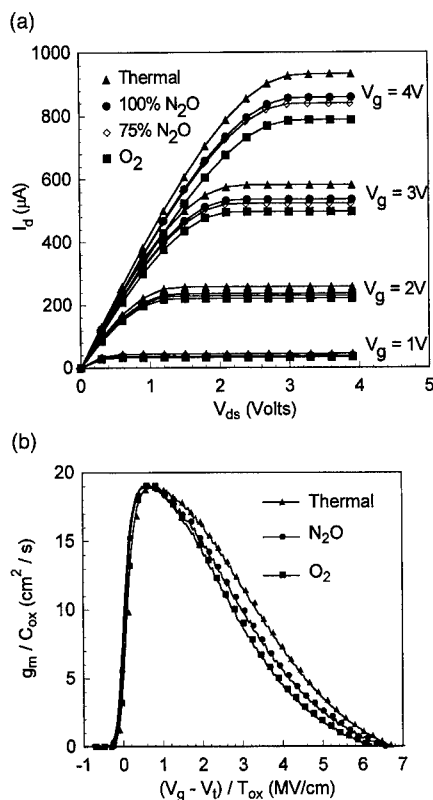


Fig. 2. (a) Current-voltage and (b) g_m characteristics of FETs for (i) plasma-deposited oxides with O-atom and N-atom terminated Si-SiO₂ interfaces, and (ii) thermally-grown oxides.

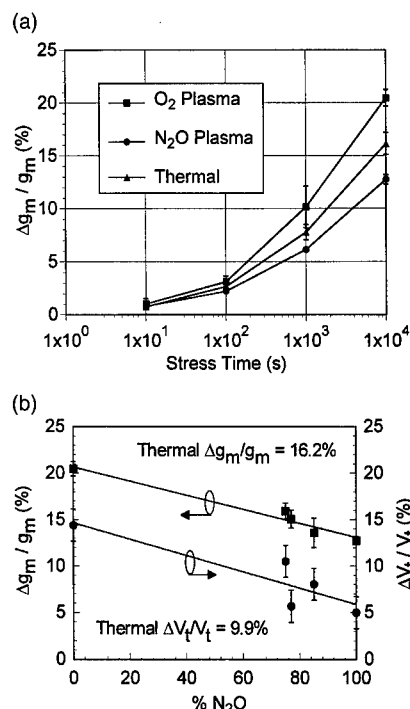


Fig. 3. (a) $\Delta g_m / g_{m,max}$ versus stress time, and (b) $\Delta g_m / g_{m,max}$ and $\Delta V_t / V_t$ versus interfacial N-atom concentration after a 10⁴ s stress.

the differences in drive currents in Fig. 2(a). The peak values of the transconductance, g_m , are about the same for all three processing techniques. This is consistent with there being no significant differences in D_{it} as noted in the MOS capacitors studies. The increasing rate of g_m fall-off as we go from the FET with the thermal oxide to the devices with the plasma oxides and nitrided and non-nitrided interfaces is interpreted in terms of surface roughness scattering. The microscopic basis for the observed differences in behavior in Fig. 2(b) is still an open issue, but it is believed that chemical and mechanical strain at the Si-SiO₂ interface can be contributing factors to the observed differences.

Fig. 3(a) and (b) illustrate improved reliability that comes with interface nitridation. Fig. 3(a) compares values of $\Delta g_m / g_{m,max}$ as a function of stress time for same three devices as shown in Fig. 2(b). In this case, the best performance is for device with the plasma oxide and the nitrided interface. Fig. 3(b) presents reliability data for stress-induced changes in

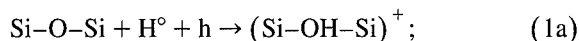
the peak transconductance and the threshold voltage, $\Delta g_m/g_{m,\max}$ and $\Delta V_t/V_t$, respectively as functions of the amount of nitrogen at the Si–SiO₂ interface. In both instances, reliability for FETs with O-terminated interfaces with plasma oxides is poorer than for FETs with thermal oxides; however, in both instances reliability for devices with plasma oxides and N-terminated interfaces is improved with respect to FETs with thermal oxides. To the best of our knowledge, there is not as yet any published data on similar stress testing of devices with nitrided interfaces produced by high temperature processing as Refs. [2–7]. Most of the stress testing reported has been time and charge to breakdown for capacitors structures.

5. Defects in devices with ultra-thin gate dielectrics

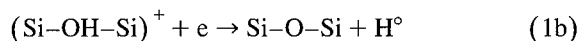
In devices with gate oxide dielectrics less than about 6 nm, the DiMaria [1] has shown that the dominant defect generation mechanisms are associated with H-atom motion. Experiments performed by DiMaria, and others [1,11,17] have established that H-atom migration to Si–SiO₂ interfaces plays a significant role in creation of (i) positively charged defect centers, the so-called APC defects, as well as (ii) interfacial defects that contribute to D_{it} . In addition, studies referenced above have shown that APC defects can be neutralized by trapping of electrons,

and this trapping event and defect neutralization is accompanied by H-atom release and motion as well. To date, no microscopic model has been proposed for the APC defect center, or the way in which H-atoms participate in defect generation and neutralization.

Based on quantum chemistry calculations published elsewhere [18], we propose a microscopic basis for APC generation and neutralization. This model also explains (i) the increased reliability of nitrided interfaces, and (ii) the marked differences between N and NH interfacial terminations. The essence of the model is shown in Fig. 4, and is presented through the two equations given below:



and



We suggest that the positively-charged, over-coordinated, hydrogenated oxonium group, $(\text{Si-OH-Si})^+$, is an APC center. Note, that this type of defect bonding arrangement has been previously proposed by one of the authors (GL) [19]. Due the *chemical equivalence* of O and NH, the same type of defect mechanism as given in Eqs. (1a) and (1b) can take place when NH groups are substituted for O at the Si–SiO₂ interface as in the ONO and oxynitride devices prepared from NH₃, but not subjected to RTAs. In this instance the APC center is a fourfold coordinated, positively-charged ammonium center $(\text{Si-NH}_2\text{-Si})^+$. On the other hand, N-atoms can bond only to Si atoms at the Si–SiO₂ interface in a planar geometry, in which reactions analogous to those represented in Eqs. (1a) and (1b) are not energetically favored to occur; e.g. to the structural relaxations necessary to distort the planar configuration N–Si₃, to a distorted tetrahedral configuration, $(\text{H-N-Si}_3)^+$ will present a significant energy barrier to a defect generation reaction. The experimental difference in behavior between N and NH has also been observed in other studies conducted by our research group in which nitride and oxynitride dielectrics were prepared using N₂ and N₂O sources gases to replace NH₃. These devices displayed low values of D_{it} in the absence of 900°C RTAs, consistent with significantly reduced levels of NH groups at the Si–SiO₂ interface [10].

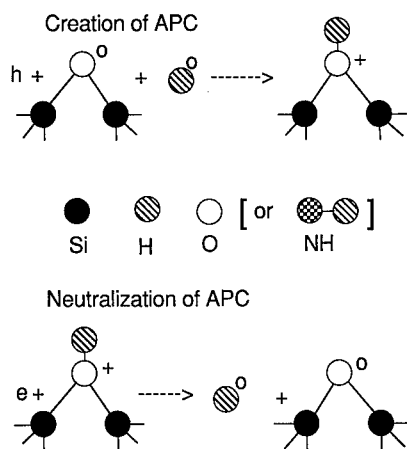


Fig. 4. Schematic representation of reactions for defect generation and neutralization as presented in Eqs. (1a) and (1b).

6. Summary

The comparisons presented in this paper demonstrate that improvements in device performance and reliability are obtained for controlled incorporation of N at Si–SiO₂ interfaces, and in bulk oxynitride alloys by using N₂ and N₂O and N source gases to replace NH₃. This is readily accomplished in plasma-assisted processes, but will be much more difficult to achieve at low-temperatures and with low-thermal budgets in thermal processes, including furnace and RTO oxidations, RTCVD and post-deposition anneals. We have demonstrated that plasma and rapid thermal processing can be combined in relatively simple processing equipment [13]. We are currently exploring combinations of low-temperature, low-thermal budget plasma and rapid thermal processes to optimize N atom incorporation at Si–SiO₂ interfaces and in bulk dielectrics.

Acknowledgements

Supported by ONR, the NSF and SEMATECH. We acknowledge a research collaboration with the group of Professor H. Kurz at RWTH-Aachen, Germany in studying optical second harmonic generation at Si–SiO₂ interfaces.

References

- [1] D.J. DiMaria, *Microelectron. Eng.* 28 (1995) 63.
- [2] L.K. Han, M. Bhat, D. Wristers, H.H. Wang and D.L. Kwong, *Microelectron. Eng.* 28 (1995) 89.
- [3] M. Green, D. Brasen, K.W. Evans-Lutterodt, L.C. Feldman, K. Krisch, W. Lennard, H.-T. Tang, L. Manchanda and M.-T. Tang, *Appl. Phys. Lett.* 65 (1994) 848.
- [4] T. Ito, T. Nakamura and H. Ishikawa, *IEEE Trans. Electron Devices* ED-29 (1982) 498.
- [5] T. Hori and H. Iwasaki, *IEEE Electron Device Lett.* EDL-10 (1989) 195.
- [6] G.Q. Lo and D.L. Kwong, *IEEE Electron Device Lett.* EDL-12 (1991) 175.
- [7] Y. Okada et al., *IEEE Trans. Electron Devices* EDL-41 (1994) 191.
- [8] Y. Ma, T. Yasuda, S. Habermehl and G. Lucovsky, *J. Vac. Sci. Technol. B* 11 (1993) 1533.
- [9] Y. Ma, T. Yasuda and G. Lucovsky, *Appl. Phys. Lett.* 64 (1994) 2226.
- [10] S.V. Hattangady, PhD Thesis, North Carolina State University (1995).
- [11] R.E. Stahlbush, E. Cartier and D.A. Buchanan, *Microelectron. Eng.* 28 (1995) 15.
- [12] T. Yasuda, Y. Ma, S. Habermehl and G. Lucovsky, *Appl. Phys. Lett.* 60 (1992) 434.
- [13] G. Lucovsky, J.J. Wortman, T. Yasuda, X.-L. Xu, V. Misra, S.V. Hattangady, Y. Ma and B. Hornung, *J. Vac. Sci. Technol. B* 12 (1994) 2839.
- [14] D.R. Lee and G. Lucovsky, *J. Vac. Sci. Technol. A* 13 (1995) 607; D.R. Lee, C. Parker, J.R. Hauser and G. Lucovsky, *J. Vac. Sci. Technol. B* 13 (1995) 607; D.R. Lee, PhD Thesis, North Carolina State University (1995).
- [15] C. Meyer, G. Lüpke, U. Emmerichs, F. Wolter, H. Kurz, C.H. Bjorkman and G. Lucovsky, *Phys. Rev. Lett.* 74 (1995) 3001.
- [16] H. Shin, G.M. Yeric, A.F. Tasch and C.M. Mazier, *Solid State Electron.* 34 (1991) 545.
- [17] E. Cartier and J.H. Stathis, *Microelectron. Eng.* 28 (1995) 3.
- [18] Z. Jing and G. Lucovsky, *J. Vac. Sci. Technol. B* 13 (1995) 1613.
- [19] G. Lucovsky, *Phil. Mag.* B 39 (1979) 513; G. Lucovsky and D.J. Chadi, in: *Physics of MOS Insulators*, Eds. G. Lucovsky, S.T. Pantelides and F.L. Galeener (Pergamon, New York, 1980) p. 301.



ELSEVIER

Applied Surface Science 104/105 (1996) 342–348

applied
surface science

Density of states and relaxation spectra of etched, H-terminated and naturally oxidized Si-surfaces and the accompanied defects

H. Flietner^{*}, W. Füssel, N.D. Sinh, H. Angermann

Dept. Photovoltaic, Hahn-Meitner-Institut, D-12489 Berlin, Germany

Received 28 June 1995; accepted 25 October 1995

Abstract

A new contactless method, the modulation CV-technique, is described which allows a very sensitive determination of surface and interface state densities as well as the complete dispersion behaviour of these states. With chemical H-termination surface state distributions may be achieved which are comparable to the best thermally oxidized surfaces. The comparison of these two surfaces shows: Though these surfaces have the same distribution of interface traps D_{it} , they have a remarkable difference in the relaxation behaviour. The characteristic relaxation times are one to two orders of magnitude lower for thermally oxidized surfaces than for H-terminated ones. This is a hint that the matrix elements which determine the interaction with the bands are different in the two different cases. The natural oxidation of H-terminated surfaces shows a quite different behaviour than thermal oxidation: Peaked defect groups which are related to O-back-bonded Si-dangling-bonds grow and disappear during the first stages of oxidation. This is a hint to ordering processes during oxidation in addition to defect creation during growth. These results supplement the general understanding of growth mechanisms. The appearing defects during all treatments may be put into three categories: (1) normally distributed defects (Gaussian distribution); (2) reconstruction defects; (3) Boltzmann-distributed defects.

1. Introduction

Etching, H-termination and natural oxidation are typical low temperature processes which have become of topical interest in high-technology [1–4]. Therefore methods of monitoring the electronic properties are needed and the physical understanding must be improved (for the Si–SiO₂-system, see [5]). Since the pretreatment of samples before oxidation, epitaxial growth (especially MBE) and layer deposition (for example CVD) plays an important role for the electronic properties, contactless methods were

developed which enable the characterization at any stage of preparation. The large signal surface photovoltage method was the best way to perform a good characterization, especially of etched surfaces, from 1979 [7] up to now [8–10]. But with the development of H-terminated surfaces [11–14] this method allows only a rough estimate of the best prepared surfaces with midgap densities of states about $10^{10} \text{ eV}^{-1} \text{ cm}^{-2}$ [8–10]. For further study of the kinetic behaviour (electronic relaxation and recombination phenomena) this method allows only to determine the pulse response of the surface system, but with little sensitivity (no sensitive determination of the relaxation spectrum). In search for a better tool a very sensitive CV-method was introduced,

^{*} Corresponding author. Tel.: +49-30-67053388; fax: +49-30-67053333; e-mail: flietner@hmi.de.

which earlier had been used to determine interface state distributions near the band edges [15], where a high sensitivity is needed. First results and the general outline of the new setup were reported at the 4th ICFSI [16]. The relaxation spectrum given by the imaginary part of the surface impedance reveals new features of surface and interface states. The next section will describe the new improved setup of the modulation-CV (MCV)-technique which allows a sensitive and contactless determination of surface and interface state distributions as well as their relaxation behaviour.

2. The modulation-CV (MCV)-setup

The general scheme of the setup is shown in Fig. 1. The measuring chamber is designed to allow HV (high vacuum) and no dielectric between sample surface and counter electrode. The sample is sucked to a metallic base the temperature of which may be varied from 90 to 300 K. Sometimes it is important to avoid the dielectric between electrode and sample

surface because the polarization of the dielectric may cause mismeasurements. A high breakdown stability allows induced charges of 10^{13} e/cm². One main point of the construction of the measuring capacitor is the very accurate positioning of the electrode up to a distance of 2–3 μm from the surface. In earlier field effect measurements for the determination of surface properties [17] one could only use the total induced charge because the surface capacitance was too large compared to the total capacitance of the electrode/surface. So no discrimination between total charge and the charge in the surface states was possible. To get the charge in surface states one had to know the surface conductance which includes many uncertainties. This equipment now allows to discriminate these two capacitances and thus one may get information about surface mobilities even at ordinary surfaces by combining this method with field effect measurements. This is an interesting and still open opportunity. But these remarks serve only to demonstrate the experimental progress. This paper is concerned with the surface and interface states and their relaxation spectra.

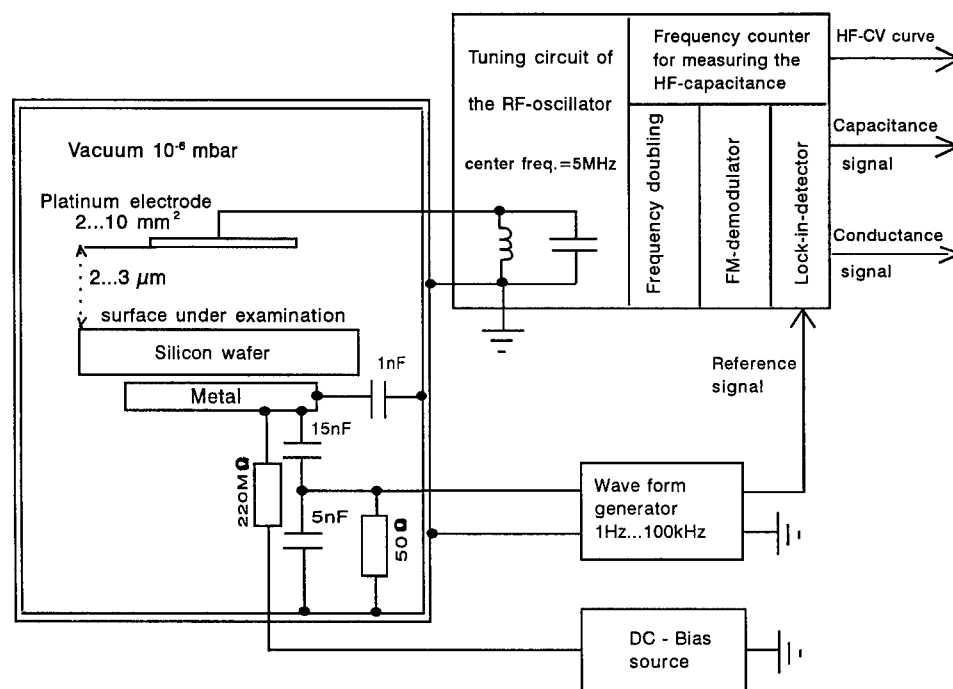


Fig. 1. Scheme of the modulation-CV (MCV)-method.

The electronic part of the setup contains:

(1) A dc-bias source which allows to vary the induced charge and either to choose a certain position of the Fermi-level (FL) at the surface or to act as a ramp for CV-measurements.

(2) A wave form generator which allows sinusoidal as well as rectangular low-frequency (LF) modulation of the electrode voltage in the range of 1 Hz to 100 kHz. Within this range all interesting relaxation phenomena may be observed using the frequency dispersion of the surface or interface impedance, if one includes a wide variation of the specimen temperature.

(3) The signal detection part of the setup takes advantage of both the possibilities of the commercially well developed frequency-modulation-technique and the lock-in principle. While the total capacitance of the electrode/sample is of the order 30 pF, the changes of the surface and interface capacitance may be well detected with a sensitivity of 10^{-4} pF. Surface state distributions down to $10^{10} \text{ eV}^{-1} \text{ cm}^{-2}$ may clearly be determined. Moreover, the frequency dispersion of the impedance may be determined to get full information throughout the total frequency range of 1 Hz to 100 kHz. In this case the lock-in serves for separating the two 90° -components of the surface impedance, the capacitance and the conductance.

3. Experimental results and discussion

3.1. Comparison of thermally oxidized and H-terminated surfaces

Our first results concerning the dispersion behaviour of surfaces and interfaces [15] showed that the imaginary part of the surface and interface impedance is much more sensitive to technological treatments than the real part or the surface and interface state distribution is. The dispersion curves hint to different kinds of electronic processes at etched and oxidized surfaces. This was mainly seen by the appearance of relaxation spectra at a wide separation of relaxation times. To examine this statement most clearly we prepared to different samples with the same distribution of interface states D_{it} , one thermally oxidized, the other H-terminated. We suc-

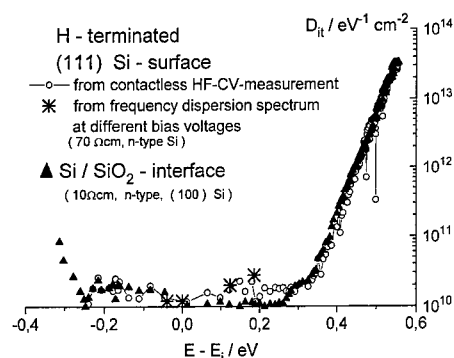


Fig. 2. Interface state distributions for thermally oxidized and H-terminated Si-surfaces.

ceeded for the first time to prepare as good H-terminated surfaces as the best thermally oxidized ones, seen from the viewpoint of the D_{it} -distribution. Fig. 2 demonstrates it for two different samples. Though these samples are of different orientation and different doping level and different surface coverage, the common understanding is that this is not of influence on the character of the isolated defects at the interface respectively surface. The character of the isolated defects is only determined by their immediate neighbours [6]. So it may be stated that both samples have the same defects. Fig. 3 shows the dispersion behaviour of these samples at midgap. This means the Fermi-level (FL) is set by the bias to E_i (intrinsic level) or E_0 (the neutral point of the U-shaped distribution [6]) and the small signal modulation is varied from 1 Hz to 100 kHz. This gives the variation of the low-frequency (LF)-capacitance to the high-frequency (HF)-capacitance of the interface or surface. Because of the fact that the capacitances of the interface or surface states C_{it} and of the space charge layer C_{sc} are in parallel — $C_{tot} = C_{it} + C_{sc}$ — the difference of LF- and HF-capacitance gives directly C_{it} or D_{it} . This is the most reliable and sensitive method of determination of D_{it} . In both cases of Fig. 3a and b $D_{it}(\text{midgap})$ for both samples is determined after determination of the scaling factor from the capacitance at surface accumulation. $D_{it}(\text{midgap, ox}) = 1.5\text{--}2 \times 10^{10} \text{ eV}^{-1} \text{ cm}^{-2}$, $D_{it}(\text{midgap, H-term}) = 1.2\text{--}1.5 \times 10^{10} \text{ eV}^{-1} \text{ cm}^{-2}$. The conductance behaviour of the two samples exhibits two differences:

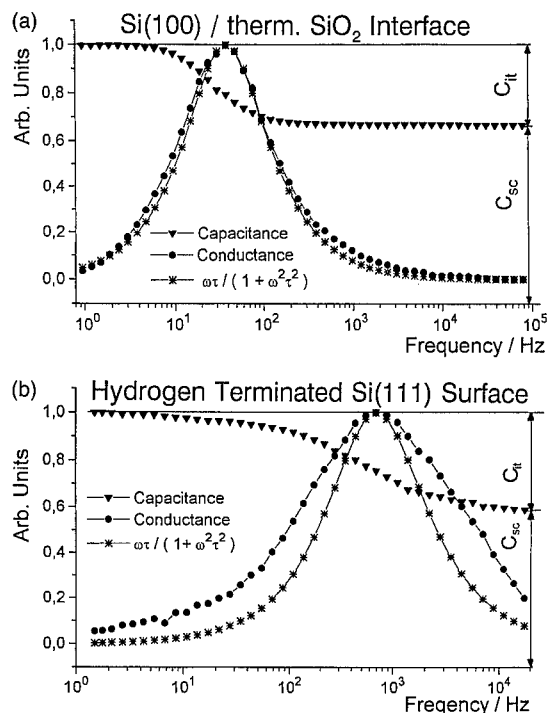


Fig. 3. Frequency dispersion of the interface impedance (capacitance and conductance) for the thermally oxidized (a) and H-terminated (b) surface of Fig. 2. $\tau = 1/40$ s (a), $\tau = 1/750$ s (b) for the single relaxation time approximation $\omega\tau/(1 + \omega^2\tau^2)$.

1. the dispersion regions differ by about orders of magnitude on the frequency scale (and respectively on the relaxation scale);
2. while the dispersion spectrum of the oxidized sample corresponds very good to a single relaxation time (proportional to $\omega\tau/(1 + \omega^2\tau^2)$), the H-terminated sample exhibits a remarkable broader relaxation spectrum.

Though interface or surface states have the same energetic distribution D_{it} they may differ markedly in electronic interaction with the bands. If we remember, that the energetic position of the defects is determined by their immediate atomic neighbourhood, this statement means that the defects may have different interaction potentials which determine their interaction with the bands and the relaxation and recombination behaviour.

These interaction potentials include also the long range potentials which are relevant for the boundary

conditions with the crystal wave functions. Obviously the Si/SiO₂-barrier is different from the H-terminated surface and the electronic wave functions (Bloch waves) have different boundary conditions.

Though there are certain differences in band bending and space charge layer thickness between the two samples (ox: 10 Ω cm, H-term: 70 Ω cm, both n-type) these properties cannot account for those differences. These two samples are chosen from a larger group of experiments to demonstrate most strikingly the effect that the same distribution of interface states may show a different interaction behaviour with the bands.

Besides the low density of interface/surface states, both samples show a low concentration of positive interface- respectively surface-fixed charge. In the case of the oxidized sample this charge is attributed to the fixed oxide charge originating in defects of the SiO₄-tetrahedral bond. The occupied level of this defect lies above the conduction band and loses its electron by tunnelling when being close enough to the interface. The positive surface charge of a good H-terminated surface as it is given here with about 10^{10} unsaturated bonds per cm² cannot be attributed to these defects. Its origin must be the polarity of the SiH-bond. According to Pauling [18] the electronegativity difference between Si and H is 0.3 which corresponds to an ion-character of the bond of about 2%. If the H-terminated surface atom is thought to be H-Si≡Si₃ the negative charge at the H-atom 'induces' a negative charge at the back bonds. A rough estimate with the image charge picture would give a charge between 0.1 and 0.5 elementary charges per bond. This corresponds to some 10^{11} e/cm² in the space charge layer which again corresponds to an equal positive fixed charge. By experiment a value of $1-2 \times 10^{11}$ e/cm² is obtained, independent of doping for all good H-terminated surfaces. This tendency of the band bending corresponds to an increase in work function which was observed in [19].

Another interesting and surprising result of Fig. 2 is the complete congruence of the group of tail states U_T for both samples. In earlier papers [6,14] it was supposed that this group of strained bonds was originated by the stress exerted by the cover layer onto the interface. Now it is seen that this group is due to bonding relaxation effects. The exponential Boltz-

mann-distribution says that there is a complete statistical distribution of bonds in the range from the ideal to the broken bond with no preferential configuration (superstructure) seen in this group.

3.2. Naturally oxidized surfaces

Natural oxidation starting with H-terminated surfaces has become a promising step for getting good gate insulators for highly-integrated MOS-FETs [1–5,20,21]. The success of this oxidation step relies on the reproducibility of the starting point. It turned out that the electronic control described above allows to state that the low surface state density and in any case the U-shaped surface state distribution is the most accurate and reliable description of this starting point. Fig. 4 describes the natural oxidation in deionized water. The oxidation process may be described in terms of the well proved defect model [6]: The U-shaped group in the middle of the gap U_M consists of Si-dangling-bonds with pure Si-back-bonds. The Gauss-distributed peaked groups are Si-dangling-bonds with one O-back-bond (P_L in the lower part of the gap) or with two O-back-bonds (P_H in the upper part of the gap). During the first stage of oxidation the P_L -group grows. It disappears later and P_H arises. Also this group disappears and again a pure U-shaped distribution is seen with almost the same density of states. For room temperature (30°C) this process is rather slow and the final U-shaped distribution of the

oxidized surface is reached after more than two hours. The same result may be achieved with a temperature of 90°C at 10 min. This is a completely different oxidation process than observed during thermal oxidation. While thermal oxidation is clearly determined by diffusion processes and reactions with defect creation at the interface [22–25] this process is governed, in addition to the creation and disappearance of defects by ordering processes at lower temperatures. The transition between these two processes appears at about 400°C which may be estimated from the annealing behaviour. The change of the fixed charge is as follows: $1-2 \times 10^{11}$ e/cm² for the H-terminated surface, slightly decreasing to $2-6 \times 10^{10}$ e/cm² for the intermediate stages of oxidation, increasing slightly to $1-1.5 \times 10^{11}$ e/cm² for the final curve.

Thus these defects, the dangling bonds of different stages of oxidation, may clearly be related to the formation of layers in that stage of oxidation [26–28]. The beginning of oxidation is with a layer where the surface atoms are bonded to one O. The formation of this layer is accompanied by the P_L -defect. During the next stage of oxidation the surface atoms are attacked by the next O and become bonded to two O. The formation of this layer is accompanied by the P_H -defect. As may be seen from the disappearance of this defect, further oxidation completes the oxidation state of the cover layer. This may be regarded in some sense as a kind of layer by layer growth. The studies of oxidation kinetics are in general agreement with these results [29], but they are mostly performed with optical and spectroscopical methods and the defect situation was followed only on completed MOS-structures. So these results fill just that gap of knowledge left by normal MOS-measurements by the described sensitive contactless MCV-method.

3.3. The general character of the defects

Though the physico-chemical nature of each group is known [6], it is interesting that there are more general physical aspects for describing these groups and to understand more deeply their character and the differences between the different kinds of distributions. These general characteristics are:

1. normally distributed defects (Gaussian distribution);

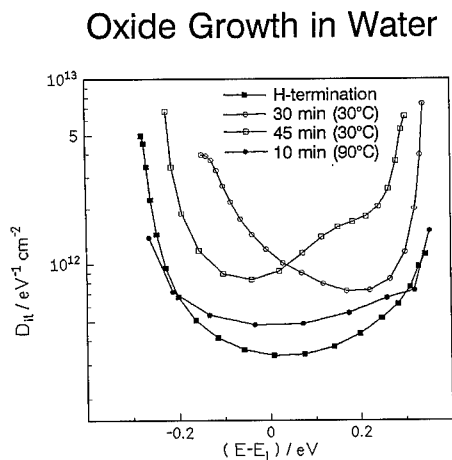


Fig. 4. Natural oxidation of a H-terminated Si(111)-surface in deionized water.

2. defects related to reconstruction centres;
3. Boltzmann-distributed defects.

The normal distribution of the first category (i.e. P_L, P_H) comes about in the following way: The total energy of any defect may be given by $E_{\text{tot}} = E_{\text{min}} + cx^2$ for a local deviation x from the position of E_{min} , while c being an elastic constant reflecting the bonding situation of the defect. The position of the corresponding electronic level may be given by $E = E_h + hx$, E_h being the value at E_{min} and h is determined by the bonding or hybrid structure of the defect. The main point is that E is a *linear* function of x . Thus the density of states is given by $D_{\text{it}} = D_0 \exp(-E_{\text{tot}}/kT) = D_0 \exp(-(E - E_h)^2/2\sigma^2)$ with $E_{\text{min}} = 0$ arbitrarily. The width of the Gauss-distribution σ is determined by the elastic properties and the hybrid structure of the defect, $\sigma^2 = kTh^2/2c$.

Reconstruction centres are characterized by the fact that the total energy of the defect is strongly influenced by the reconstruction or the dehybridization of the defect which depends on the electron occupancy [30]. It may even occur that the occupation by a second electron does not change its level indicating that the total amount of electron–electron-interaction energy is absorbed by the lattice (seen near midgap). U_M is an example of this kind of defects, the distribution of which can be calculated to a first approximation by the assumption $E_{\text{tot}} = \text{const.}$ for all defects of this group and a certain (disorder) assumption in k -space [6].

Boltzmann-distributed states are characterized by an exponential distribution $D_{\text{it}} = D_0 \exp(-E_{\text{tot}}/kT)$. As long as this exponential distribution holds also for the electronic levels as seen by the behaviour of the tail states U_T (the exponential part of the U-shaped distribution at the band edges), it may be concluded that $E_{\text{tot}} = \alpha E$. With $E_{\text{tot}} = 0$ at the band edges and $E_{\text{tot}} = E_{\text{Si-Si}}$ at about midgap $\alpha = 2E_{\text{Si-Si}}/E_g$ as a first estimate.

4. Conclusion

The surprising new results concerning

- the electronic kinetics of the interaction between bands and surface states, as described by their relaxation spectra;
- the congruence of the strained bond group U_T for

high temperature oxidation and room temperature H-termination;

- the defect arising and decreasing during natural oxidation,
- open new insights into the mechanisms which govern the formation of semiconductor interfaces during technological processes and show that new ideas are needed. For relaxation and recombination processes a more elaborated theory, which includes also barrier properties in addition to the defect properties, is needed.

References

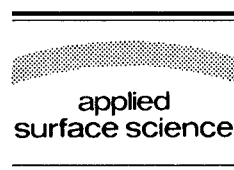
- [1] P. Balk and J.J.M. de Nijs, Eds., *Insulating Films on Semiconductors (INFOS '93)*, Proc. 8th Conf., Delft, June 1993 (Elsevier, 1993).
- [2] B. Lengeler, H. Lüth, W. Mönch and J. Pollmann, Eds., *Formation of Semiconductor Interfaces*, Proc. 4th Int. Conf., Jülich, June 1993 (World Scientific, Singapore, 1994).
- [3] *Passivation of Metals and Semiconductors*, Proc. 7th Int. Symp. on Passivity, Clausthal, August 1994, Mater. Sci. Forum 185–188 (1995).
- [4] S. Christovoleanu and N. Gillemot, Eds., *Insulating Films on Semiconductors (INFOS '95)*, Proc. 8th Conf., Villard de Lans, June 1995, Microelectron. Eng. 28 (1995) Nos. 1–4.
- [5] P. Balk, Ed., *Mater. Sci. Monogr.* 32 (1988).
- [6] H. Flietner, *Phys. Status Solidi (a)* 91 (1985) 153; *Surf. Sci.* 200 (1988) 463; W. Eccleston and M. Uren, Eds., *INFOS '91* (Hilger, Bristol, 1991) p. 151; *Passivation of Metals and Semiconductors*, Proc. 7th Int. Symp. on Passivity, Clausthal, August 1994, Mater. Sci. Forum 185–188 (1995) 73.
- [7] K. Heilig, H. Flietner and J. Reineke, *J. Phys. D: Appl. Phys.* 12 (1979) 927.
- [8] Th. Dittrich, H. Angermann, W. Füssel and H. Flietner, *Phys. Status Solidi (a)* 140 (1993) 463; Th. Dittrich, H. Angermann, H. Flietner, Th. Bitzer and H.J. Lewerenz, *J. Electrochem. Soc.* 141 (1994) 3595.
- [9] H. Angermann, Th. Dittrich and H. Flietner, *Appl. Phys. A* 59 (1994) 193; H. Angermann, Th. Dittrich and H. Flietner, in: *Ultra-clean Processing of Silicon Surfaces*, Eds. M. Heyns, M. Meuris and P. Mertens (Acco, Leuven, 1994) p. 363; H. Angermann, W. Füssel, K. Kliefth and H. Flietner, in: *Insulating Films on Semiconductors (INFOS '95)*, Proc. 8th Conf., Villard de Lans, June 1995, Eds. S. Christovoleanu and N. Gillemot, Microelectron. Eng. 28 (Nos. 1–4) (1995) 51; H. Angermann, K. Kliefth and H. Flietner, *Appl. Surf. Sci.* 104/105 (1996) 107.
- [10] L. Elstner, H. Eschrich, K. Kliefth and H. Flietner, in: *Proc. 12th Eur. Photovoltaic Solar Energy Conf., Vol. II*, Eds. R. Hill, W. Palz and P. Helm (Stephens, Bedford, 1994) p. 1800.

- [11] Y.Y. Chabal, G.S. Higashi and K. Raghavachari, *J. Vac. Sci. Technol. A* 7 (1989) 2104.
- [12] G.S. Higashi, Y.J. Chabal, G.W. Trucks and K. Raghavachari, *Appl. Phys. Lett.* 56 (1990) 656; G.S. Higashi, R.S. Becker, Y.J. Chabal and A.J. Becker, *Appl. Phys. Lett.* 58 (1991) 1656.
- [13] M. Meuris et al., in: *Insulating Films on Semiconductors (INFOS '93)*, Proc. 8th Conf., Delft, June 1993, Eds. P. Balk and J.J.M. de Nijs (Elsevier, Amsterdam, 1993) p. 21.
- [14] T. Bitzer, M. Gruyters, H.J. Lewerenz and K. Jakob, *Appl. Phys. Lett.* 63 (1993) 397.
- [15] H. Flietner and N.D. Sinh, *Phys. Status Solidi (a)* 37 (1976) 533.
- [16] N.D. Sinh and H. Flietner, in: *Formation of Semiconductor Interfaces*, Proc. 4th Int. Conf., Jülich, June 1993, Eds. B. Lengeler, H. Lüth, W. Mönch and J. Pollmann (World Scientific, Singapore, 1994) p. 369.
- [17] H. Flietner, *Phys. Status Solidi* 2 (1962) 221.
- [18] L. Pauling, *Natur d. Chem. Bindung* (Chemie Verlag, Weinheim, 1968) pp. 87–95.
- [19] A. Stockhausen, T.U. Kampen, H. Nienhaus and W. Mönch, in: *Formation of Semiconductor Interfaces*, Proc. 4th Int. Conf., Jülich, June 1993, Eds. B. Lengeler, H. Lüth, W. Mönch and J. Pollmann (World Scientific, Singapore, 1994) p. 150.
- [20] M. Morita et al., *Appl. Phys. Lett.* 55 (1989) 562; *J. Appl. Phys.* 68 (1990) 1272; 29 (1990) L2392; 33 (1994) 370.
- [21] M. Hirose, M. Hiroshima, T. Yasaka, M. Takakura and S. Miyazaki, in: *Insulating Films on Semiconductors (INFOS '93)*, Proc. 8th Conf., Delft, June 1993, Eds. P. Balk and J.J.M. de Nijs (Elsevier, Amsterdam, 1993) p. 3.
- [22] B.E. Deal and A.S. Grove, *J. Appl. Phys.* 36 (1965) 3770.
- [23] A.G. Revesz and K.H. Zaininger, *RCA Rev.* 29 (1968) 22.
- [24] E.A. Irene, *J. Electrochem. Soc.* 125 (1978) 1708.
- [25] D.R. Wolters and A.T.A. Zegers-van Duynhoven, *Phil. Mag. B* 55 (1987) 669.
- [26] N. Lieske and R. Hezel, *Thin Solid Films* 61 (1979) 197.
- [27] F.J. Himpsel, F.R. McFeely, A. Taleb-Ibrahimi and J.A. Yarmoff, *Phys. Rev. B* 38 (1988) 6084.
- [28] T. Hattori, H. Nohira, K. Ohishi, Y. Shimizu and Y. Tamura, in: *Formation of Semiconductor Interfaces*, Proc. 4th Int. Conf., Jülich, June 1993, Eds. B. Lengeler, H. Lüth, W. Mönch and J. Pollmann (World Scientific, Singapore, 1994) p. 385.
- [29] H.Z. Massoud, in: *Insulating Films on Semiconductors (INFOS '95)*, Proc. 8th Conf., Villard de Lans, June 1995, Eds. S. Christovoleanu and N. Gillemot, *Microelectron. Eng.* 28 (Nos. 1–4) (1995) p. 109.
- [30] K.L. Ngai and C.T. White, *J. Appl. Phys.* 52 (1981) 320.



ELSEVIER

Applied Surface Science 104/105 (1996) 349–353



Synchrotron radiation photoelectron spectroscopy of the O(2s) core level as a tool for monitoring the reducing effects of ion bombardment on SnO₂ thin films

P. De Padova^{a,*}, R. Larciprete^b, C. Ottaviani^a, C. Quaresima^a, P. Perfetti^a,
E. Borsella^b, C. Astaldi^c, C. Comicioli^c, C. Crotti^d, M. Matteucci^d,
M. Zacchigna^c, K. Prince^c

^a CNR-ISM, via E. Fermi 38, 00044 Frascati (RM), Italy

^b ENEA, Dip. INN / FIS, via E. Fermi 27, 00044 Frascati (RM), Italy

^c Sincrotrone Trieste, Padriciano 99, Trieste, Italy

^d CNR-ISM, sez. Trieste, Padriciano 99, Trieste, Italy

Received 28 June 1995; accepted 6 October 1995

Abstract

Synchrotron radiation ultraviolet photoemission spectroscopy (UPS) of O(2s) core levels, valence band (VB) and Sn(4d) spectroscopy was used to monitor the effect of Ar⁺ sputtering on SnO₂ films. The decrease of the O(2s) peak intensity and the increase of the Sn²⁺ component in the Sn(4d) peak could be satisfactorily correlated with the enhancement of the band gap feature, occurring at 2.9 eV in the VB spectrum, never been due to the formation of Sn(5s–5p) states.

1. Introduction

The reducing effect of Ar⁺ sputtering on both SnO₂ films and single crystals, has often been investigated [1–6]. The occurrence of a significant oxygen loss leading to a Sn²⁺ phase has been evidenced by the modification of the Sn core level line shape [5,6] or by the increase of the band gap emission [1–6], associated to the Sn(5s–5p) states in SnO [6,7].

A more straightforward way for monitoring the oxygen removal, namely O(2s) spectroscopy, has rarely been exploited, since the O(2s) peak, occur-

ring at binding energy (BE) of about 22 eV, is almost hidden by the nearby more intense Sn(4d) peak (BE about 27 eV). This problem is overcome when working with synchrotron radiation (SR), since the photon energy can be tuned to the Cooper minimum for the tin core level, where the weak O(2s) becomes visible.

In this work, O(2s) photoemission spectroscopy was combined with valence band (VB) and Sn(4d) spectroscopy in order to investigate the effects of Ar⁺ sputtering on SnO₂ films. The oxygen decrease, evidenced by monitoring the O(2s) peak and by deconvoluting the Sn(4d) peak in Sn²⁺ and Sn⁴⁺ components, could be satisfactorily correlated with the enhancement of the band gap feature occurring at 2.9 eV in the VB spectrum.

* Corresponding author.

2. Experimental

UPS measurements were performed in a UHV chamber (base pressure 1×10^{-10} mbar) attached to the VUV beam line of Elettra (Trieste). Spectra were recorded with a VSW electron analyser (mean average radius 150 mm with an acceptance cone of approximately 16°). The SGM (mod. Dragon) monochromator of the beam line allowed an average resolving power greater than 10,000 over the whole energy range. A SnO_2 film deposited by spray pyrolysis on a glass substrate was sputtered for increasing periods of time with Ar^+ ions (500 eV, 30 μA , 2×10^{-5} mbar of Ar). After each Ar^+ sputtering cycle VB, $\text{Sn}(4d)$ and $\text{O}(2s)$ core level spectra were recorded using, respectively, photon energies of 44, 88 and 129.5 eV and pass energies of 5, 10 and 15 eV. The total resolution is of 60, 120 and 180 meV respectively.

3. Results and discussion

Fig. 1 shows the $\text{Sn}(4d)$ core levels measured at photon energy of 88 eV after 60, 360 and 3600 s of Ar^+ sputtering. The $\text{Sn}(4d)$ spectra measured on the 'as received' SnO_2 films were not reported because the surface was covered by air-induced contaminants. It is well-known [5,8] that in SnO_2 the $\text{Sn}(4d)$ components lie at BE of 27.3 (3/2) and 26.2 (5/2) eV, with the center of gravity at 26.7 eV. On the other hand, several authors measured a chemical shift of about 0.7 eV between the peaks associated with Sn^{2+} and Sn^{4+} species, either for $\text{Sn}(3d)$ [6,9] or for $\text{Sn}(4d)$ [8] core levels. In a previous work [8], the present authors have demonstrated that when both Sn^{2+} and Sn^{4+} oxides are present (shifted by 0.7 eV with respect to each other), the position of the centre of gravity of the whole peak $\text{Sn}(4d)$ scales with the variation in the relative concentrations of the two phases. The energy position of the center of gravity (about 26 eV), and the modification of the line shape of the peaks of Fig. 1 thus indicate the reduction of the SnO_2 to a SnO phase, which concentration increased with sputtering time [5,6]. Therefore, following the indication given by the shift of the center of gravity, the spectra of Fig. 1 were fitted in terms of Sn^{2+} and Sn^{4+} components. The

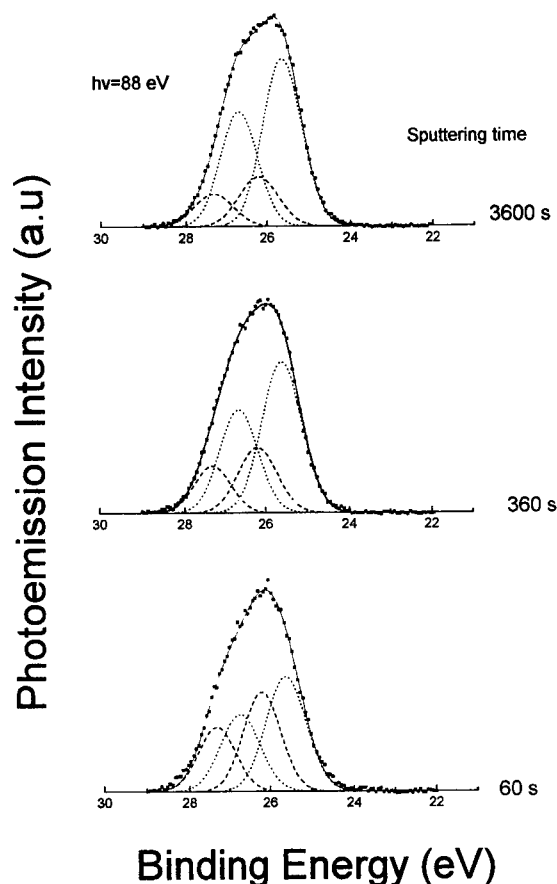


Fig. 1. $\text{Sn}(4d)$ core levels measured at photon energy of 88 eV at increasing sputtering time (indicated on the right side). The solid lines represent the best fit curves, whereas Sn^{2+} and Sn^{4+} Gaussians are indicated respectively with dotted and dashed lines.

fit procedure was tested, in the first spectrum, using Voigt functions with a background subtraction included in the fit parameters. It was then decided to fit the data with Gaussian functions since the Lorentzian contribution to the line shape was negligible, and the choice of the background subtraction function was not influential on the quality of the fits. This choice is justified by the disordered nature of the polycrystalline surface examined. The $4d_{3/2}$ and $4d_{5/2}$ peaks of Sn^{2+} and Sn^{4+} were considered as two doublets of Gaussians, having a spin orbit splitting of 1.10 ± 0.05 eV, and an intensity ratio of 1.50 ± 0.05 between the 3/2 and 5/2 components which is the statistically expected value. The best-fit curves, indicated by the solid lines, are shown in Fig.

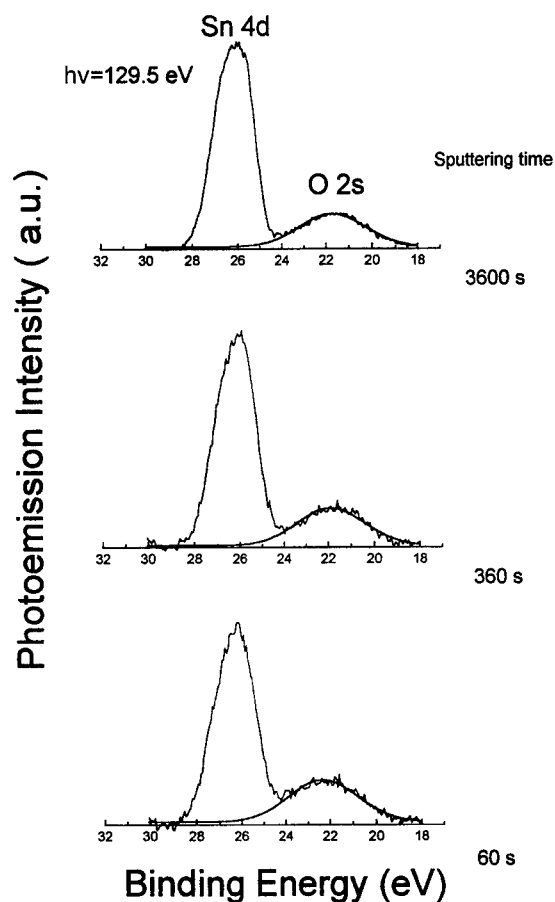


Fig. 2. O(2s) and Sn(4d) core level peaks measured at photon energy of 129.5 eV at increasing Ar^+ sputtering times (indicated on the right side).

1 together with the Sn^{2+} and Sn^{4+} components. The residuals of the fits, not reported in Fig. 1, were structureless. The corresponding fit parameters are reported in Table 1.

The Ar^+ bombardment induced oxide reduction,

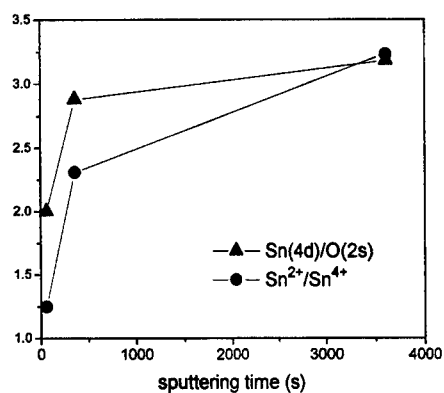


Fig. 3. $\text{Sn}^{2+}/\text{Sn}^{4+}$ (see Fig. 1) and Sn(4d)/O(2p) (see Fig. 2) peak area ratios versus the Ar^+ sputtering time.

manifested by the enhancement of the Sn^{2+} component in the Sn(4d) peaks, can be evidenced also by monitoring the O(2s) peak, occurring at BE of 22 eV. This peak, which is undetectable in Fig. 1, becomes visible when working at the Cooper minimum for Sn(4d) levels. In fact Fig. 2 shows the O(2s) peak, measured at photon energy of 129.5 eV. The fit parameters reported in Table 1 were used to subtract the Sn(4d) contribution from the spectra in order to isolate the O(2s) peak. The ratio between the Sn(4d) and the O(2s) areas is plotted versus the sputtering time in Fig. 3. The same figure also shows the ratio between the areas of the Sn^{2+} and Sn^{4+} components obtained from the curve-fitting of the Sn(4d) peaks.

The SnO_2 VB exhibits three main peaks centered at BE of 5, 7.8 and 11 eV [5,10], attributed respectively to O(2p) lone pair non-bonding states and to states originated from the Sn(5s)–O(2p) and Sn(5p)–O(2p) interacting orbitals [5,11,12]. It has been shown that these spectral features are fingerprints of stannic oxide. In fact the VB of SnO appears quite different,

Table 1
Parameters of the best fit curves for the Sn(4d) core level spectra of Fig. 1

Sputtering time (s)	Sn^{2+}						Sn^{4+}					
	BE (eV)		HWHM (eV)		area (a.u.)		BE (eV)		HWHM (eV)		area (a.u.)	
	$4d_{5/2}$	$4d_{3/2}$	$4d_{5/2}$	$4d_{3/2}$	$4d_{5/2}$	$4d_{3/2}$	$4d_{5/2}$	$4d_{3/2}$	$4d_{5/2}$	$4d_{3/2}$	$4d_{5/2}$	$4d_{3/2}$
60	25.62	26.74	0.49	0.49	0.66	0.44	26.21	27.32	0.46	0.46	0.54	0.35
360	25.61	26.67	0.49	0.48	0.87	0.58	26.21	27.32	0.48	0.45	0.38	0.25
3600	25.62	26.69	0.48	0.46	0.95	0.63	26.21	27.32	0.48	0.48	0.29	0.19

showing three structures at BE of 3, 6.5 and 9.7 eV [10]. In this case the peak appearing at around 3 eV has been attributed to Sn(5p) states hybridized with Sn(5s) states [6,7].

The VBs measured on the SnO₂ films at increasing sputtering time are shown in Fig. 4. It is evident that, although the Sn(4d) core levels reported in Fig. 1 show a large Sn²⁺ component, the VB keeps essentially the Sn⁴⁺ features. Evidently, at the Sn²⁺ concentration reached after the ion bombardment, the contribution of the SnO structures is not effective to shape the measured VB, but only to provoke slight modifications of the profile of the SnO₂ VB. However the formation of the Sn²⁺ phase is manifested by the presence of the band gap emission which

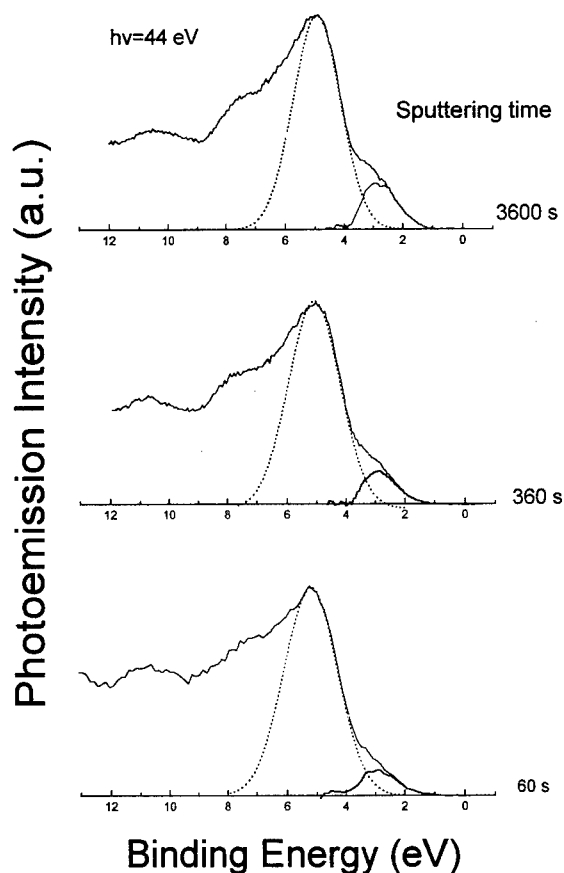


Fig. 4. VB photoemission spectra measured at 44 eV at increasing sputtering times. The O(2p) at 5 eV fitted with a Gaussian (dashed line) has been subtracted from the VB in order to isolate the band gap emission peak at 2.9 eV.

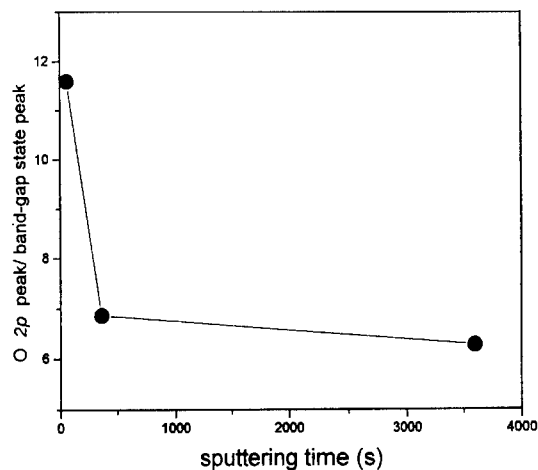


Fig. 5. Ratio between the O(2p) and Sn(5s–5p) peak areas (see Fig. 4) as a function of the Ar⁺ sputtering time.

increases with sputtering time. After having subtracted the O(2p) peak as a Gaussian from the VBs, the Sn(5s–5p) band gap peak is centred at 2.9 eV. The ratio between the O(2p) and the Sn(5s–5p) peak areas is plotted in Fig. 5 as a function of sputtering time.

A direct comparison between the areas of the Sn(5s–5p) peaks and the Sn²⁺ components of the Sn(4d) core level is not possible with our data, since the intensities of the VB spectra (as well as of the core level components) are not calibrated with respect to each other. However the two quantities can be related by writing

$$\frac{A_{O(2p)}}{A_{Sn(5s-5p)}} \propto \frac{A_{O(2s)}}{A_{Sn(4d)}} \frac{A_{Sn(4d)}}{A_{Sn(5s-5p)}},$$

where A_{Xy} indicates the area of the photoemission peak relative to the y level of the X element. In this way the ratio between the Sn(4d) and Sn(5s–5p) peak areas results proportional to the product of measured values

$$\frac{A_{Sn(4d)}}{A_{Sn(5s-5p)}} \propto \frac{A_{O(2p)}}{A_{Sn(5s-5p)}} \frac{A_{Sn(4d)}}{A_{O(2s)}}. \quad (1)$$

On the other hand, if we assume that the intensity of the band gap emission is proportional to the concentration of the Sn²⁺ sites, the left term of relation (1) can be written as

$$\frac{A_{Sn(4d)}}{A_{Sn(5s-5p)}} \propto \frac{[Sn^{2+}] + [Sn^{4+}]}{[Sn^{2+}]} = 1 + \frac{1}{R}. \quad (2)$$

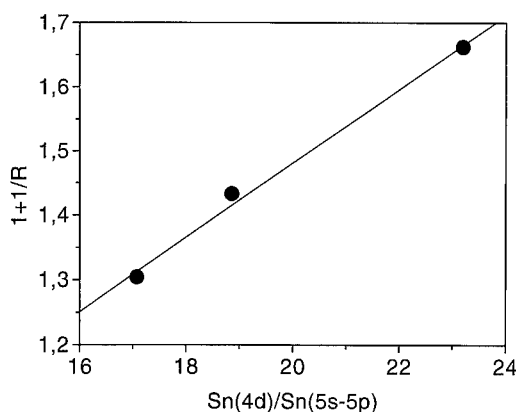


Fig. 6. $1 + 1/R$ (see text) plotted versus $\text{Sn}(4d)/\text{Sn}(5p-5s)$ peak area ratio.

The right terms of relations (1) and (2) are plotted one versus the other in Fig. 6. The linearity of the resulting curve confirms that the $\text{Sn}(5s-5p)$ peak follows the formation of the Sn^{2+} phase. Therefore this peak is the most sensitive among the VB structures to the occurrence of SnO_2 reduction and its intensity directly monitors the abundance of the Sn^{2+} phase.

It is worth noting that the VB measured at photon energy of 129.5 eV after 60 s of ion bombardment and reported in Fig. 7 presents the feature at 11 eV more pronounced than in the corresponding VB taken at photon energy of 44 eV. This structure tends to

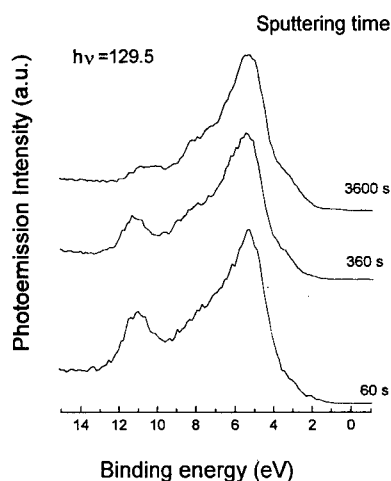


Fig. 7. VB photoemission spectra measured at 129.5 eV at increasing sputtering times.

decline with sputtering time, whereas the residual portion of the band originally located at 11 eV moves toward lower BE. We suggest that this behaviour is correlated with the simultaneous enhancement of the $\text{Sn}(5s-5p)$ states.

4. Conclusions

O(2s) photoemission spectroscopy, performed at the Cooper minimum for tin, combined with VB and $\text{Sn}(4d)$ spectroscopy, was used to monitor the effect of Ar^+ sputtering of SnO_2 films. The oxygen decrease, evidenced by monitoring the O(2s) peak and deconvoluting the $\text{Sn}(4d)$ peak in Sn^{2+} and Sn^{4+} components, could be satisfactorily correlated with the increase of the VB feature occurring at 2.9 eV, due to the formation of $\text{Sn}(5s-5p)$ states.

Acknowledgements

The authors wish to thank M. Capozzi, S. Priori, S. Rinaldi and L. Romanzin for their precious technical assistance. The work was done at the facility Elettra of Trieste and the assistance of the Sincrotrone Trieste personnel was greatly appreciated.

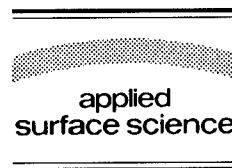
References

- [1] R.G. Egdell, S. Eriksen and W.R. Flawell, *Solid State Commun.* 60 (1986) 835.
- [2] R.G. Egdell, S. Eriksen and W.R. Flawell, *Surf. Sci.* 192 (1987) 266.
- [3] D.F. Cox, T.B. Fryberger and S. Semancik, *Surf. Sci.* 224 (1989) 221.
- [4] C.S. Fang, F.M. Pan, W.S. Tse and S.R. Orng, *Surf. Sci.* 211 (1989) 279.
- [5] J.M. Themlin, R. Sporken, J. Darville, N. Caudano and J.M. Gilles, *Phys. Rev. B* 42 (1990) 11914.
- [6] J.M. Themlin, M. Ctaib, L. Henrard, Ph. Lambin, J. Darville and J.M. Gilles, *Phys. Rev. B* 46 (1992) 2460.
- [7] J. Terra and D. Gwenzburger, *Phys. Rev. B* 44 (1991) 8584.
- [8] P. De Padova, M. Fanfoni, R. Larciprete, M. Mangiantini, S. Priori and P. Perfetti, *Surf. Sci.* 313 (1994) 379.
- [9] G.M. Ingo, L. Giorgi, N. Zacchetti and N. Azzeri, *Corros. Sci.* 20 (1991) 361.
- [10] C.L. Lau and G.K. Wertheim, *J. Vac. Sci. Technol.* 15 (1979) 622.
- [11] J. Robertson, *J. Phys. C* 12 (1979) 4767.
- [12] S. Munnix and M. Schmeits, *Phys. Rev. B* 27 (1983) 7624.



ELSEVIER

Applied Surface Science 104/105 (1996) 354–358



Influences of hydrogen on initial oxidation processes of H-terminated Si(100) surfaces

H. Ikeda^{*}, K. Hotta, S. Furuta, S. Zaima, Y. Yasuda

Department of Crystalline Materials Science, School of Engineering, Nagoya University, Furo-cho, Chikusa-ku, Nagoya 464-01, Japan

Received 28 June 1995; accepted 26 September 1995

Abstract

The initial oxidation of H-terminated Si(100) surfaces by atomic oxygen at room temperature has been investigated by using high-resolution electron energy loss spectroscopy (HREELS). It has been found on H-terminated Si(100) surfaces with a 1×1 (dihydride) structure that there are two oxidation steps in the range of oxygen coverage, θ , less than unity. The adsorption of oxygen atoms on the Si–Si back bond with a constant vibrational energy of about 128 meV for the Si–O–Si asymmetric stretching mode occurs in the first step of $\theta < 0.4$, and an increase in the Si–O–Si vibrational energy can be observed in the second step $\theta > 0.4$. Moreover, in the case of oxidation of clean surfaces, the Si–O–Si vibrational energy is monotonously increased with increasing oxygen coverage and is identical with that on H-terminated surfaces at $\theta > 0.4$. It is considered that the structural relaxation of Si–O–Si bonds is promoted by a charge transfer from back bonds to surface Si–H bonds.

1. Introduction

With a decrease in the thickness of gate oxide films in ultra-large scale integrated circuit (ULSI) devices, the influence of atomic bonding structures at SiO₂/Si interfaces on the device characteristics such as leakage current and breakdown voltage, becomes larger. How the growth of thin oxide films is precisely controlled has become significantly important. Hence, it is necessary to clarify reaction processes in the formation of oxide films on an atomic scale. Surface-passivation techniques using hydrogen have been widely noticed from the viewpoint of control-

ling the growth of thin oxide films, since HF treatments are effective for the realization of an atomically flat Si surface [1] and H-terminated Si surfaces are stable against the native oxidation [2]. The oxidation of H-terminated Si(100) surfaces in the air at room temperature was reported to be layer-by-layer oxidation, being studied by X-ray photoelectron spectroscopy [3]. Moreover, in the oxidation above 300°C, the layer-by-layer oxidation reaction at the interface does not occur at oxide film thicknesses above 5 Å [4]. However, influences of hydrogen on the initial oxidation process of H-terminated Si surfaces have not been made clear yet.

We have investigated surface reactions of H-terminated Si(100) surfaces with oxygen by high-resolution electron energy loss spectroscopy (HREELS) to clarify the initial oxidation process of H-terminated

^{*} Corresponding author. Tel.: +81-52-7893819; fax: +81-52-7893818; e-mail: ikeda@alice.xtal.nagoya-u.ac.jp.

Si surfaces. We reported that the adsorption of molecular oxygen is limited by the desorption of hydrogen atoms and that the dangling bonds on Si surfaces are essential to the dissociative adsorption of molecular oxygen [5]. In the present work, influences of hydrogen atoms on the initial oxidation has been investigated on H- and D-terminated Si(100) surfaces by HREELS.

2. Experiments

Experiments in the present study were carried out in an ultra-high vacuum (UHV) chamber with a base pressure of 3×10^{-10} Torr, equipped with apparatuses of HREELS, low-energy electron diffraction (LEED) and Auger electron spectroscopy (AES). Reaction gases were introduced into the chamber through a variable leak valve.

P-type Si(100) substrates cut to 10 mm \times 10 mm were chemically cleaned and then introduced into the UHV chamber. Clean surfaces were obtained by thermal cleaning at 1000°C in vacuum. The AES peak intensity ratio of C-KLL to Si-LVV for clean surfaces was less than 1%. Atomic hydrogen, deuterium and oxygen were produced by thermal cracking of the molecules using a tungsten filament heated at 1500°C. H- and D-saturated surfaces were formed by exposing to atomic hydrogen or deuterium at room temperature after the substrates were thermally cleaned. H- and D-terminated Si(100) surfaces are very stable for exposure to molecular oxygen [5,6]. Therefore, atomic oxygen was used for oxidizing H- and D-terminated surfaces at room temperature. The amount of atomic oxygen exposure was indicated by using the partial pressure of molecular oxygen, since the exact fraction of oxygen atoms dissociated by this method was not known. HREELS measurements were performed at room temperature under a specular reflection condition, in which the incident energy and angle of electron beams were 7.8 eV and 55° with respect to the surface normal.

3. Results and discussions

HREELS spectra of H-terminated Si(100) surfaces with and without exposing to atomic oxygen at

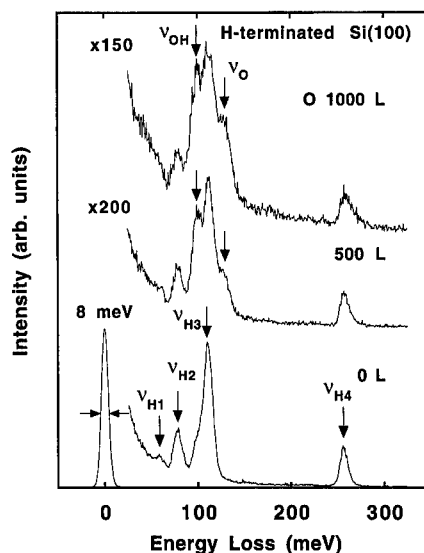


Fig. 1. Changes in HREELS spectra of H-terminated Si(100) surfaces without and with atomic oxygen exposure of 500 and 1000 L at room temperature. The exposure amount of atomic oxygen is indicated by that of molecular oxygen.

room temperature are shown in Fig. 1. In the spectrum of the H-terminated Si(100) surface without atomic oxygen exposure, there exist loss peaks of a rocking (ν_{H1}), wagging (ν_{H2}), scissors (ν_{H3}) and stretching mode (ν_{H4}) of Si–2H species at loss energies of 61, 78, 112 and 259 meV [7], respectively. The LEED pattern of this surface showed a 1×1 structure. These results indicate that the H-terminated Si(100) surface has a dihydride structure. After exposing to atomic oxygen, the loss peaks for a stretching mode (ν_{OH}) of Si–OH [8] and for an asymmetric stretching mode (ν_O) of Si–O–Si species [9] are found at 100 and about 128 meV, respectively. The intensities of these peaks are increased with increasing exposure to atomic oxygen. The appearance of the asymmetric stretching mode of Si–O–Si means that oxygen atoms adsorb on the back bonds of surface Si atoms because only the component of vibrational modes normal to a surface can be detected in HREELS measurements [10]. In contrast, a symmetric stretching mode with a vibrational energy of about 50 meV and/or a symmetric bending mode with about 90 meV of Si–O–Si species are scarcely observed, which indicates no existence

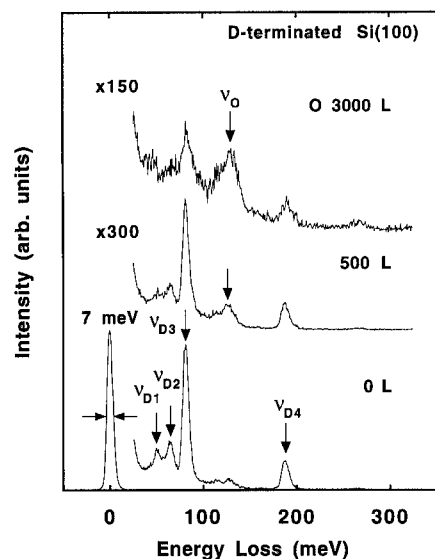


Fig. 2. Changes in HREELS spectra of D-terminated Si(100) surfaces without and with atomic oxygen exposure of 500 and 3000 L at room temperature. The exposure amount of atomic oxygen is indicated by that of molecular oxygen.

of the adsorption of oxygen into the top-bridge sites. Consequently, the initial adsorption sites of oxygen atoms are Si–Si back bonds and Si–H bonds for the oxidation on H-terminated Si(100) [5]. In the oxidation of H-terminated Si(100) surfaces in air, the Si–H bonds are reported to be much more stable against oxidation than the Si–Si back bonds [11]. These differences in the initial adsorption site are considered to arise from the chemical activity of atomic oxygen.

Fig. 2 shows HREELS spectra of D-terminated Si(100) surfaces with and without exposing to atomic oxygen at room temperature. The spectrum of the as-terminated Si(100) surface has loss peaks due to a scissors (ν_{D3}) and stretching mode (ν_{D4}) of Si–2D species at 81 and 188 meV, respectively. The loss peaks at 51 and 65 meV correspond to a wagging mode (ν_{D1} , ν_{D2}) of Si–2D. The split in this mode is reported to be due to bulk phonon coupling [12]. A dideuteride structure is also formed on the D-terminated surface, since a 1×1 structure was confirmed from LEED observation. As well as the oxidation of H-terminated Si surfaces, the loss peaks for an asymmetric stretching mode (ν_0) of Si–O–Si

species at about 128 meV are observed with increasing oxygen exposure, which leads to the same conclusion that oxygen atoms adsorb on Si–Si back bonds. Although a vibrational energy of a Si–OD stretching mode is reported to be 80 meV [8], the separation of the Si–OD peak from a peak of a Si–2D scissors mode could not be done. However, the adsorption of oxygen on Si–D bonds is considered to also occur, since a peak of an O–D stretching mode was found at about 360 meV.

In the result, there are no significant differences between the adsorption of oxygen atoms on H- and D-terminated surfaces except the vibrational energy of the species containing hydrogen and deuterium atoms. It should be noted that the loss peak of the Si–O–Si asymmetric stretching mode is apart from other loss peaks in the case of D-terminated Si(100) surfaces, while it overlaps with the peak of the Si–2H scissors mode in the case of H-terminated ones. Therefore, the use of D-terminated Si surfaces is very effective for oxidation studies by HREELS. In the following results, the oxidation process of D-terminated surfaces has been mainly examined and the expression of H-terminated Si(100) surfaces is used without any distinction between H- and D-terminated Si(100) surfaces.

Fig. 3 shows a change in the energy loss due to an asymmetric stretching vibrational mode of Si–O–Si species with increasing oxygen coverage. The oxy-

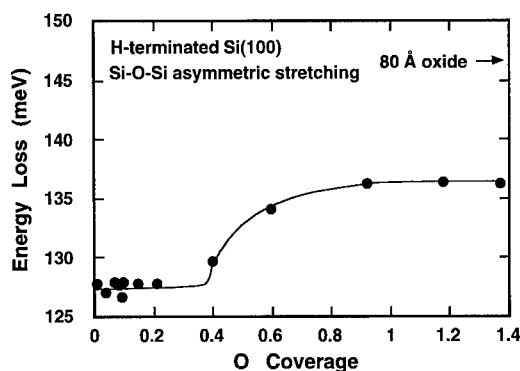


Fig. 3. Changes in the vibration energy loss of the Si–O–Si asymmetric stretching mode with increasing oxygen coverage in the oxidation on H-terminated Si(100) surfaces at room temperature. The measured energy loss for an 80 Å thick oxide film formed by dry oxidation at 850°C is also indicated by an arrow.

gen coverage, θ , is defined as the ratio of the number of oxygen atoms to that of the back bonds of surface Si atoms, which is determined from AES measurements. In Fig. 3, the measured energy loss for an 80 Å thick oxide film formed by dry oxidation at 850°C is indicated by the arrow. The change in the vibrational energy is related to the structural relaxation of Si–O–Si bonds, such as changes in the force constant and the bond angle. It is clearly found in Fig. 3 that the vibrational energy of the Si–O–Si species is constant at oxygen coverages below 0.4 and monotonously increases and then saturates in the range above 0.4. The Si–O–Si bonds of the 80 Å thick oxide film have a vibrational energy higher than that in the oxidation at room temperature. These facts mean that the Si–O–Si structure approaches that of oxide formed at a high temperature with increasing oxygen coverage. Schaefer et al. [9] reported that the vibrational energy of a Si–O–Si asymmetric stretching mode approach that for vitreous silica with an increase in film thickness and oxidation temperature. Therefore, it can be considered that the first oxidation step on H-terminated Si(100) surfaces is a simple adsorption and that the second step is an adsorption accompanied with

changes in the Si–O–Si structure, in which the structure approaches gradually that formed at a high temperature.

Next, we pay attention to the oxidation in the first step. Fig. 4 shows changes in the energy loss of the asymmetric stretching mode of Si–O–Si bonds as a function of oxygen coverage for oxidation at room temperature on H-terminated Si(100) surfaces with a 1×1 (dihydride) and a 2×1 (monohydride) structure and a 2×1 Si(100) clean surfaces. The Si–O–Si structure formed depends strongly on the initial surface structure in the first oxidation step below $\theta = 0.4$. As seen in Fig. 4, a marked increase in the vibrational energy of Si–O–Si bonds takes place with proceeding oxidation on the clean surfaces and the Si–O–Si vibrational energies are much lower than those on H-terminated surfaces. This result indicates that the existence of surface Si–H bonds makes the Si–O–Si structure approach a high-temperature structure. It is thought that the bond strength of Si–Si back bonds is weakened by a charge transfer from Si back bonds to Si–H bonds, which increases the flexibility in Si–O–Si geometric structures. Comparing H-terminated surfaces with a 1×1 and a 2×1 structure, the vibrational energies for 2×1 surfaces seem to be slightly lower than those for 1×1 surfaces. The differences between the 1×1 and 2×1 surfaces are the number of adsorbed hydrogen atoms per surface Si atom and the existence of dimer bonds, which may lead to the lowering of the vibrational energy. The essential differences between the influences of a 1×1 and a 2×1 surface on the oxidation are not clear yet and further investigation is necessary.

On the other hand, no difference in the initial surface structures is observed at $\theta > 0.4$. Considering that the number of adsorbed oxygen atoms at $\theta = 0.4$ corresponds to half the number of the total back bonds of surface Si atoms, it is suggested that the structural relaxation of Si–O–Si bonds at $\theta > 0.4$ is governed by the adsorption of oxygen atoms on the other back bond of a surface Si atom. Detailed results and discussions will be reported elsewhere.

In conclusion, hydrogen atoms adsorbed on Si(100) surfaces relax the Si–O–Si geometric structure formed by oxidation at room temperature at oxygen coverages below 0.4. In the sequential oxidation process, there is no difference between the

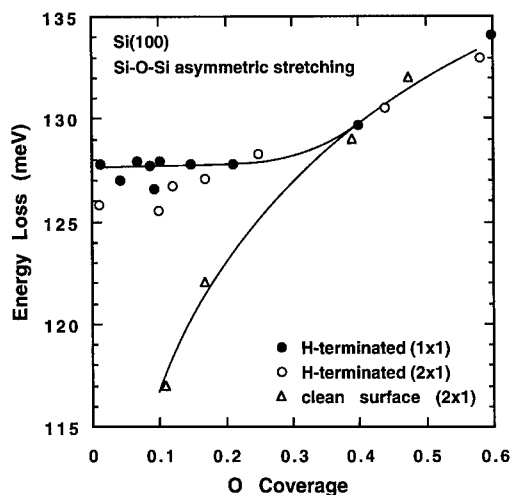


Fig. 4. Changes in the energy loss due to the vibrational energy for an asymmetric stretching mode of Si–O–Si bonds as a function of oxygen coverage for oxidation at room temperature on H-terminated Si(100) surfaces with a 1×1 (dihydride) and a 2×1 (monohydride) structure and a 2×1 Si(100) clean surface.

Si–O–Si structures on H-terminated and clean Si surfaces.

4. Conclusions

The oxidation on H- and D-terminated Si(100) surfaces at room temperature by atomic oxygen has been investigated by using high-resolution electron energy loss spectroscopy (HREELS). There are two steps in the oxidation process at oxygen coverages below 1.4. The adsorption of oxygen atoms with a constant vibrational energy of the Si–O–Si asymmetric stretching mode, that is without structural changes, occurs on H-terminated 1×1 surfaces at the oxygen coverages below 0.4, which is contrary to the oxidation of Si(100) clean surfaces with a marked change in the vibrational energy. This result is interpreted as due to the weakening of the bond strength of Si back bonds by a charge transfer from Si–Si back bonds to Si–H bonds arising from adsorbed hydrogen atoms. The presence of surface Si–H bonds leads to the flexibility in Si–O–Si geometric structures and an approach to the SiO₂ structure formed at a high temperature. On the other hand, in the second step at oxygen coverages above 0.4, the formation of Si–O–Si bonds is accompanied with changes in the Si–O–Si structure. In this step, there

is no difference in the Si–O–Si geometric structure between H-terminated Si surfaces and clean Si surfaces.

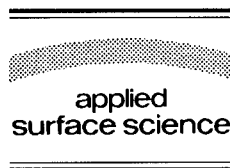
References

- [1] G.S. Higashi, Y.J. Chabal, G.W. Trucks and K. Raghavachari, *Appl. Phys. Lett.* 56 (1990) 656.
- [2] N. Hirashita, M. Kinoshita, I. Aikawa and T. Ajioka, *Appl. Phys. Lett.* 56 (1990) 451.
- [3] T. Sunada, T. Yasaka, M. Takakura, T. Sugiyama, S. Miyazaki and M. Hirose, *Jpn. J. Appl. Phys.* 29 (1990) L2408.
- [4] T. Aiba, K. Yamauchi, Y. Shimizu, N. Tate, M. Katayama and T. Hattori, *Jpn. J. Appl. Phys.* 34 (1995) 707.
- [5] H. Ikeda, K. Hotta, T. Yamada, S. Zaima, H. Iwano and Y. Yasuda, *J. Appl. Phys.* 77 (1995) 5125.
- [6] N. Yabumoto, K. Saito, M. Morita and T. Ohmi, *Jpn. J. Appl. Phys.* 30 (1991) L419.
- [7] W.B. Pollard and G. Lucovsky, *Phys. Rev. B* 26 (1982) 3172.
- [8] H. Ibach, H. Wagner and D. Bruchmann, *Solid State Commun.* 42 (1982) 457.
- [9] J.A. Schaefer and W. Göpel, *Surf. Sci.* 155 (1985) 535.
- [10] H. Ibach and D.L. Mills, *Electron Energy Loss Spectroscopy and Surface Vibrations* (Academic Press, New York, 1982).
- [11] T. Takahagi, A. Ishitani and H. Kuroda, *J. Appl. Phys.* 68 (1990) 2187.
- [12] H. Froitzheim, U. Köhler and H. Lammering, *Surf. Sci.* 149 (1985) 537.



ELSEVIER

Applied Surface Science 104/105 (1996) 359–363



Effect of chemical preoxidation treatment on the structure of SiO_2/Si interfaces

Hiroshi Nohira ^{*}, Hiroaki Sekikawa, Masanori Matsuda, Takeo Hattori

Department of Electrical and Electronic Engineering, Musashi Institute of Technology, 1-28-1 Tamazutsumi, Setagaya-ku, Tokyo 158, Japan

Received 28 June 1995; accepted 25 October 1995

Abstract

The effects of chemical preoxidation treatments on the oxidation reaction at $\text{SiO}_2/\text{Si}(111)$ interfaces were investigated using XPS. In the case of preoxidation treatment in a mixed solution of H_2SO_4 and H_2O_2 the layer-by-layer oxidation reaction occurs at the interface as in the case of the preoxidation treatment in dry oxygen at 300°C . The effect of chemical preoxidation treatment in a hot solution of HNO_3 and that in a mixed solution of HCl and H_2O_2 on the oxidation reaction at the interface were also investigated.

1. Introduction

Recently the fabrication of 1 Gbit dynamic random access memory (DRAM) chips was reported [1,2]. Furthermore, the mass production of 1 Gbit DRAMs using metal–oxide–semiconductor field-effect-transistors (MOSFETs) with gate oxide film thickness of about 5 nm must be realized by the end of this century [3]. In this case the thickness of one monolayer of silicon dioxide corresponds to approximately 6% of gate oxide thickness. It is then necessary to minimize the effect of native oxides, present at the Si surface prior to oxidation, on the final SiO_2/Si interface structure. This can be realized for example either by modifying the native oxide structure by a UV/ O_3 treatment [4] or by backbond

oxidation of H-terminated Si surface without breaking Si–H bonds [5].

It was found from the measurement of infrared absorption spectra and Si 2p photoelectron spectra that the amount of Si–H bonds in native oxide formed in chemical solution depends on the kind of chemical treatment [6,7] and is below the detection limit for native oxide formed in a mixed solution of H_2SO_4 and H_2O_2 [7]. It was also found from the X-ray reflectivity measurement [8] that the density of the native oxide formed in a mixed solution of H_2SO_4 and H_2O_2 is close to that of thermal oxide. Furthermore, it was found from the measurement of cumulative failure of MOS diodes that the chemical oxide formed in a mixed solution of H_2SO_4 and H_2O_2 can function as a passivating film and suppress the increase in surface microroughness, which is caused by the heating of Si substrate to thermal oxidation temperature in inert gas ambient [9]. It was also found from a study on the initial stage of

^{*} Corresponding author. Tel.: +81-3-37033111 ext. 2788; fax: +81-3-57072172.

oxidation of atomically flat hydrogen-terminated Si(111)- 1×1 surfaces [10] that the oxidation proceeds non-uniformly until a one atomic layer thick interface is formed. However, once the interface is formed, a layer-by-layer oxidation reaction occurs at the SiO₂/Si(111) metallurgical interface [11]. This result was obtained by thermal oxidation at 600–800°C, following preoxidation in dry O₂ at 300°C. This initial oxide is designated as a low temperature oxide in the rest of this paper.

It is the purpose of present paper to clarify the effect of preoxidation treatment in chemical solution on the oxidation reaction at the SiO₂/Si(111) interface and to compare with the effect of preoxidation treatment in dry oxygen at 300°C on the oxidation reaction at the interface.

2. Experimental details

Wafers used in the present study were Czochralski-grown p-Si(111) with a resistivity of 10–20 Ω cm. In order to decrease atomic step densities on initial silicon surfaces [12], approximately 200-nm-thick thermal oxide films were formed in dry O₂ at 1000°C on Si(111) surfaces. After the chemical cleaning, the thermal oxide films were removed by the treatment in a buffered HF solution (HF 0.17 wt%, NH₄F 17 wt%) followed by a rinse in deionized water for 10 min. The atomically flat hydrogen-terminated Si(111)- 1×1 surfaces were prepared by the treatment in 40% NH₄F solution [13]. Following this three kinds of native oxides and a low temperature oxide were formed. The native oxides formed are that in a mixed solution of H₂SO₄ and H₂O₂ (H₂SO₄:H₂O₂ = 4:1, designated as the H₂SO₄ oxide) at 85–90°C for 10 min, that in a mixed solution of HCl, H₂O₂ and H₂O (HCl:H₂O₂:H₂O = 1:1:4, designated as the HCl oxide) at 48–51°C for 10 min, and that in a hot solution of 70% HNO₃ (designated as the HNO₃ oxide) at 45–55°C for 5 min. The low temperature oxide was formed at 300°C in dry O₂ at a pressure of 1 Torr and was used as a reference. Following these preoxidation treatments the oxidation was performed at 600–830°C in dry O₂ with a pressure of 1 Torr. The dew points of both nitrogen and oxygen gases used for the oxidation are below –95°C. Therefore, the relative amount of H₂O in

these gases is equal to 37 ppb. The changes in chemical structures of SiO₂/Si interface with the progress of oxidation were studied from the measurement of Si 2p photoelectron spectra by X-ray photoelectron spectroscopy (XPS). By connecting the oxidation chamber and the sample analysis chamber with a gate valve, the oxidation and XPS measurement could be performed without breaking vacuum. Photoelectron spectra, excited by monochromatic AlK α radiation, were measured at a photoelectron take-off angle of 15° with an energy resolution of 0.37 eV and an acceptance angle of 3.3°, using an ESCA-300 manufactured by Scienta Instruments AB [14]. The surface morphologies of three kinds of chemical oxides were measured by atomic force microscope SPI3700/SPA300 manufactured by Seiko Instruments, Inc. Other experimental details are described elsewhere [15,16].

3. Experimental results and discussions

The surface morphologies of three kinds of chemical oxides were measured by atomic force microscope (AFM) are shown in Fig. 1. The surface microroughnesses Ra of the H₂SO₄ oxide, the HNO₃ oxide and the HCl oxide is 0.08 nm, 0.08 nm and 0.09 nm, respectively. After removing the relatively small background signal by Tougaard's method [17] from the observed spectrum, the spectrum was decomposed into Si 2p_{1/2} and Si 2p_{3/2} spin-orbit partner lines. In this decomposition, it is assumed that the spin-orbit splitting of Si 2p photoelectron spectrum is 0.61 eV, and the Si 2p_{1/2} to Si 2p_{3/2} intensity ratio is 0.5 [18]. It is also assumed that the intermediate oxidation states consist only of Si¹⁺, Si²⁺ and Si³⁺ as defined by Hollinger et al. [19]. The thicknesses of present oxide films are calculated from the analysis of Si 2p photoelectron spectra by assuming that the electron escape depth in silicon and that in silicon dioxide are 2.6 nm and 3.4 nm, respectively [20]. Here, the electron escape depth in the intermediate oxidation state is assumed to be the same as that in silicon dioxide.

Fig. 2 compares the dependences of spectral intensity of Si⁴⁺ and the summed spectral intensities of Si¹⁺, Si²⁺ and Si³⁺ normalized by the Si 2p spectral intensity of silicon substrate on the oxide

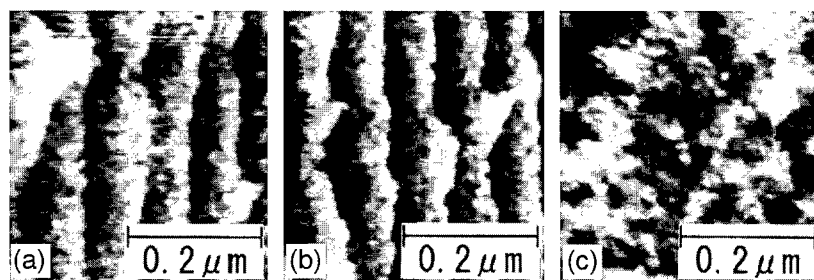


Fig. 1. Surface morphologies of three kinds of chemical oxides: (a) that for the H_2SO_4 oxide; (b) that for HNO_3 oxide; (c) that for the HCl oxide.

film thickness for thermal oxidation through the H_2SO_4 oxide with those for thermal oxidation through the low temperature oxide. Here, Si^{4+} denotes a silicon atom bonded with four oxygen atoms. According to Fig. 2, the normalized spectral intensity of the intermediate oxidation states saturates at a thickness of nearly 0.5 nm, while the normalized spectral intensity of Si^{4+} does not saturate at this thickness. Furthermore, the saturated normalized spectral intensity of the intermediate oxidation states is in good agreement with that [15,16] calculated for an abrupt interface, which is shown by the dashed line in Fig. 2. Therefore, once the interface is formed,

the thickness of silicon dioxide only increases with further oxidation [11]. It can be seen from this figure that the H_2SO_4 oxide gives almost the same result with the low temperature oxide.

Fig. 3 compares the dependences of areal densities of Si^{1+} , Si^{2+} and Si^{3+} spectra on the oxide film thickness for thermal oxidation through the H_2SO_4 oxide with those for thermal oxidation through the low temperature oxide. Although the total amount of intermediate oxidation states does not change above the oxide film thickness of 0.5 nm as shown in Fig. 1 the each component of intermediate oxidation states

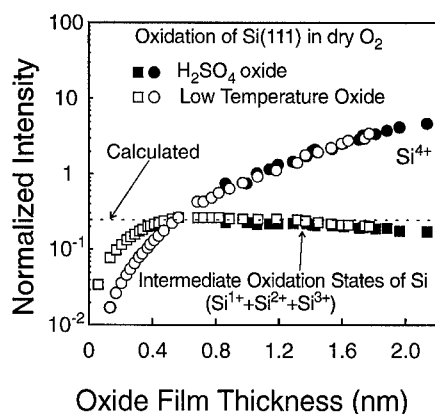


Fig. 2. Normalized spectral intensity of Si^{4+} and summation of intensities for all intermediate oxidation states are shown as a function of oxide film thickness for thermal oxidation through the H_2SO_4 oxide and that through low temperature oxide. The dashed line shows the normalized spectral intensity calculated for an abrupt interface.

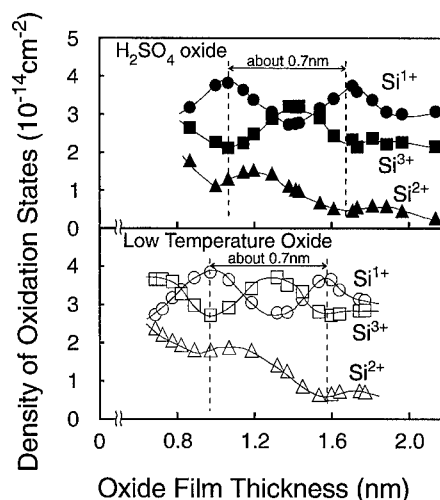


Fig. 3. Dependence of areal densities of Si^{1+} , Si^{2+} and Si^{3+} on thickness for thermal oxidation through the H_2SO_4 oxide and that through low temperature oxide.

exhibits changes as shown in Fig. 3. Namely, the areal density of Si^{1+} and that of Si^{3+} repeatedly increase and decrease with a period in thickness of approximately 0.7 nm for thickness of less than about 1.8 nm. Therefore, the periodic change in the interface structures with progress of oxidation, which indicates oxidation reaction at metallurgical interface, appears for thermal oxidation through the H_2SO_4 oxide as in the case of thermal oxidation through the low temperature oxide reported previously [11]. This implies that the quality of H_2SO_4 oxide, i.e., the surface smoothness etc., is comparable to that of the low temperature oxide.

Fig. 4 compares the dependence of areal densities of Si^{1+} , Si^{2+} and Si^{3+} on the oxide film thickness for thermal oxidation through the HNO_3 oxide with those for thermal oxidation through the H_2SO_4 oxide. In the case of thermal oxidation through the HNO_3 oxide, the periodic change in interface structure is not as well defined as in the case of thermal oxidation through the H_2SO_4 oxide for oxide film thickness of less than about 1.3 nm. For the difference between these two cases the following two causes can be considered: One is the difference in the surface microroughness of these two kinds of chemical oxides and the other is the difference in the amount of Si–H bonds in two kinds of chemical oxides. Because the surface microroughness R_a of the HNO_3 oxide measured by atomic force microscopy is 0.08 nm and is the same with that of the

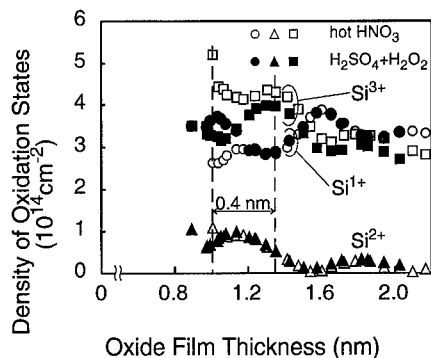


Fig. 4. Dependence of areal densities of Si^{1+} , Si^{2+} and Si^{3+} on thickness for thermal oxidation through the HNO_3 oxide and that through the H_2SO_4 oxide.

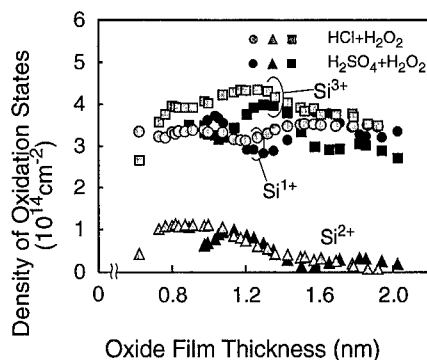


Fig. 5. Dependence of areal densities of Si^{1+} , Si^{2+} and Si^{3+} on thickness for thermal oxidation through the HCl oxide and that through the H_2SO_4 oxide.

H_2SO_4 oxide and the amount of Si–H bonds in the HNO_3 oxide determined by infrared absorption spectroscopy is larger than that in the H_2SO_4 oxide [9], the difference in the amount of Si–H bonds can be the cause for the difference between thermal oxidation through these two kinds of chemical preoxidation treatment. On the other hand, in the case of thermal oxidation through the HNO_3 oxide, periodic changes in interface structure appear for oxide film thickness of greater than about 1.3 nm and coincide with those for thermal oxidation through the H_2SO_4 oxide. This implies that after about 0.4 nm thick thermal oxide is formed beneath the HNO_3 oxide, the interface becomes smooth and similar to that formed through the H_2SO_4 oxide. This gives the lowest oxide film thickness for the smoothing effect of thermal oxidation on the interface microroughness [12]. This is additional confirmation that the oxidation reaction occurs at metallurgical interface.

Fig. 5 compares the dependence of areal densities of Si^{1+} , Si^{2+} and Si^{3+} on the oxide film thickness for thermal oxidation through the HCl oxide with those for thermal oxidation through the H_2SO_4 oxide. Periodic changes in interface structure appears only weakly with the progress of oxidation in the case of thermal oxidation through the HCl oxide implying that the oxidation proceeds non-uniformly because the initial surface was roughened by the HCl process to produce surface morphology shown in Fig. 1 whose surface microroughness R_a is 0.09 nm.

4. Conclusion

The effects of three kinds of chemical preoxidation treatments on the $\text{SiO}_2/\text{Si}(111)$ interface formation in dry oxygen at 600–830°C were investigated by XPS. In the case of preoxidation treatment in a mixed solution of H_2SO_4 and H_2O_2 , the periodic change in interface structure with progress of oxidation, which indicates the oxidation reaction at metallurgical interface, appears. Furthermore, the amplitude of this periodic change is almost the same as that for the low temperature oxide. This implies that the quality of the H_2SO_4 oxide, i.e., the surface smoothness etc., is comparable to that of the low temperature oxide. In the case of thermal oxidation through the HNO_3 oxide, the periodic change in interface structure is not as well defined as that in the case of thermal oxidation through the H_2SO_4 oxide for oxide film thickness of less than about 1.3 nm. This can be attributed to the existence of Si–H bonds in the HNO_3 oxide. After about 0.4 nm thick thermal oxide is formed beneath the chemical oxide, the interface becomes smooth and similar to that formed through the H_2SO_4 oxide. This gives additional confirmation that the oxidation reaction occurs at metallurgical interface. Finally, the periodic change in interface structure appears only weakly with process of oxidation through the HCl oxide implying that the oxidation proceeds non-uniformly because the surface microroughness measured by AFM of the HCl oxide is larger than that of the H_2SO_4 oxide.

Acknowledgements

One of the authors (T.H.) expresses his hearty thanks to Dr. Masatake Katayama of SEH Isobe R and D Center for supplying the silicon wafers used in the present study. Part of this work was supported by a 1994–1995 Grand-in-Aid for General Scientific Research from the Ministry of Education, Science and Culture of Japan.

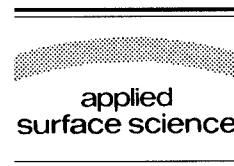
References

- [1] M. Horiguchi, T. Sakata, T. Sekiguchi, S. Ueda, H. Tanaka, E. Yamasaki, Y. Nakagome, M. Aoki, T. Kaga, M. Ohkura, R. Nagai, F. Murai, T. Tanaka, S. Iijima, N. Yokoyama, Y. Gotoh, K. Shoji, T. Kisu, H. Yamashita, T. Nishida and E. Takeda, Conf. on Int. Solid-State Circuits, Dig. Tech. Pap. (1995) p. 252.
- [2] T. Sugibayashi, I. Naritake, S. Utsugi, K. Shibahara, R. Oikawa, H. Mori, S. Iwao, T. Murotani, K. Koyama, S. Fukazawa, T. Itani, K. Kasama, T. Okuda, S. Ohya and M. Ogawa, Conf. on Int. Solid-State Circuits, Dig. Tech. Pap. (1995) p. 254.
- [3] T.E. Seidel, 1994 Int. Symp. on Semiconductor Manufacturing, Tokyo, 1994, p. 14.
- [4] S. Ohkubo, Y. Tamura, R. Sugino, T. Nakanishi and K. Takasaki, reported at Symp. VLSI Tech. 1995, p. 116.
- [5] Y. Nagasawa, H. Ishida, T. Takahagi and H. Ishitani, Solid-State Electron. 33 Suppl. (1990) 123.
- [6] H. Ogawa and T. Hattori, Appl. Phys. Lett. 61 (1992) 577, and references therein.
- [7] H. Ogawa and T. Hattori, IEICE Trans. Electron. E 75-C (1992) 774.
- [8] N. Awaji, Y. Sugita, S. Ohkubo, T. Nakanishi, K. Takasaki and S. Komiya, Jpn. J. Appl. Phys. 34 (1995) L1013.
- [9] J. Takano, K. Makihara and T. Ohmi, Mater. Res. Soc. Symp. Proc. 315 (1993) 381.
- [10] T. Hattori, H. Nohira, K. Ohishi, Y. Shimizu and Y. Tamura, Mater. Res. Soc. Symp. Proc. 315 (1993) 387.
- [11] K. Ohishi and T. Hattori, Jpn. J. Appl. Phys. 33 (1994) L675.
- [12] P.O. Hahn and M. Henzler, J. Vac. Sci. Technol. A 2 (1984) 574.
- [13] G.S. Higashi, R.S. Becker, Y.J. Chabal and A.J. Becker, Appl. Phys. Lett. 58 (1991) 1656.
- [14] U. Gelius, B. Wannberg, P. Baltzer, H. Fellner-Feldegg, G. Carlsson, C.-G. Johansson, J. Larsson, P. Munger and G. Vergerfos, J. Electron Spectrosc. Rel. Phen. 52 (1990) 327.
- [15] H. Nohira, Y. Tamura, H. Ogawa and T. Hattori, IEICE Trans. Electron. E 75-C (1992) 757.
- [16] T. Hattori, H. Nohira, Y. Tamura and H. Ogawa, Jpn. J. Appl. Phys. 31 (1992) L638.
- [17] S. Tougaard, Surf. Sci. 216 (1989) 343.
- [18] F.J. Himpsel, F.R. McFeely, A. Talev-Ibarahimi, J.A. Yarmoff and G. Hollinger, Phys. Rev. B 38 (1988) 6084.
- [19] G. Hollinger and F.J. Himpsel, Appl. Phys. Lett. 44 (1984) 93.
- [20] T. Suzuki, M. Muto, M. Hara, K. Yamabe and T. Hattori, Jpn. J. Appl. Phys. 25 (1986) 544.



ELSEVIER

Applied Surface Science 104/105 (1996) 364–368



Radiation immunity of pMOSFETs and nMOSFETs examined by means of MeV He single ion microprobe

M. Koh ^{a,*}, K. Horita ^a, B. Shigeta ^a, T. Matsukawa ^a, A. Kishida ^a, T. Tanii ^a,
S. Mori ^a, I. Ohdomari ^{a,b}

^a School of Science and Engineering, Waseda University, 3-4-1 Ohkubo, Shinjuku-ku, Tokyo 169, Japan

^b Kagami Memorial Laboratory for Material Science and Technology, Waseda University, 2-8-6 Nishi-waseda, Shinjuku-ku, Tokyo 169, Japan

Received 28 June 1995; accepted 11 September 1995

Abstract

Radiation effects induced by MeV He single ions in pMOSFETs and nMOSFETs in commercially available CMOS4007 have been studied extensively. The key results from this study are: (1) pMOSFETs are more fragile than nMOSFETs in terms of threshold voltage shift, (2) nMOSFETs are more susceptible than pMOSFETs to the degradation of subthreshold swing. The different features in the radiation effects have been discussed comprehensively.

1. Introduction

In order to optimize device structures or processes for radiation hardness of CMOS devices it is inevitable to investigate radiation effects in both pMOSFETs and nMOSFETs fabricated in a same chip quantitatively. So far radiation hardening has been done based on the data obtained by irradiating a whole IC chip with energetic particles randomly [1–5]. However, the information obtained in this way has not been quantitative in the sense that identifying a site dependence of radiation immunity has never been possible. Random irradiation with energetic particles would induce also the so-called lateral

non-uniformity effects, i.e., the influence of non-uniform distribution of trapped charges on device characteristics, which will obscure the proper interpretation of radiation effects [6,7].

So far we have succeeded in developing the single ion beam induced charge (SIBIC) imaging by using the single ion microprobe (SIMP) system which has made it possible to hit a local area of less than 3 μm square in a target with MeV He single ions one by one [8–11]. The SIBIC imaging enables us to ‘observe’ the feature of MOSFET without degradation of device characteristics. The sample feature observation before any tests is very important for the quantitative analysis of site-dependent radiation effects in MOSFETs. In this study, we have investigated site dependent radiation effects in CMOS devices induced by high energy He single ions and comparing the difference in pMOSFETs and nMOS-

* Corresponding author. Tel.: +81-3-52863380; fax: +81-3-52725749; e-mail: meishoku@cfi.waseda.ac.jp.

FETs. We first introduce an experimental setup and the method of sample positioning. Then we describe the difference in ion irradiation effects in the characteristics of pMOSFETs and nMOSFETs in a test CMOS chip.

2. Experimental

A schematic diagram of the SIMP system is illustrated in Fig. 1. The beam line is connected to a tandem accelerator (NEC 5SDH) with a terminal voltage of 1.0 MV. As shown in Fig. 1, each single ion is extracted one by one from a continuous ion beam by chopping. If the ion current, the slit opening and the switching velocity are set that after chopping several times only one ion may pass through the slit, single ion can be successfully extracted. Extracted single ion is focused with a high precision quadrupole magnet and irradiated within an area corresponding to the micro beam spot size. Number of the incident ions is controlled by an electron multiplier tube (EMT) by detecting secondary electrons (SEs) emitted upon ion incidence. Signals from the EMT are fed to the chopper controller which keeps on sending the beam chopping signals to the deflector until the desired number of single ions are detected. A device to be irradiated is mounted on a high precision goniometer, which is movable in three directions under the control of a host computer. I - V character-

istics of MOSFETs can be measured in situ by combining HP4140B system with the SIMP. In this study, I - V characteristics were recorded before exposure and after irradiation of a certain number of ions.

Throughout this work, 2.0 MeV He single ions have been used. The number of irradiated ions has been varied from 0 to $10^2/\mu\text{m}^2$. The irradiated area was $240 \times 240 \mu\text{m}^2$. During irradiation all pins were grounded.

A commercial inverter CMOS TC4007UBP produced by Toshiba, which contains three pMOSFETs and three nMOSFETs, was used as a test target in this study. Fig. 2 shows an optical micrograph of the CMOS4007 after removal of plastic package with heated fuming acid. Since this sample is made for commercial purpose, detailed information on device structure, e.g. oxide thickness and doping concentration are not clear. The radiation tests have been performed on each FET.

Sample positioning was performed by using the SIBIC imaging method. Fig. 3 shows a coarse SIBIC image of the entire chip which consists of 16×16 pixel array. The scanned area was $800 \times 800 \mu\text{m}^2$ and the number of incident ions per pixel was only two. The image clearly reveals each MOSFET. After the coarse imaging, much clearer SIBIC image of the desired transistor was taken for higher precision sample positioning. The radiation damage during these SIBIC imaging is negligible for the subsequent

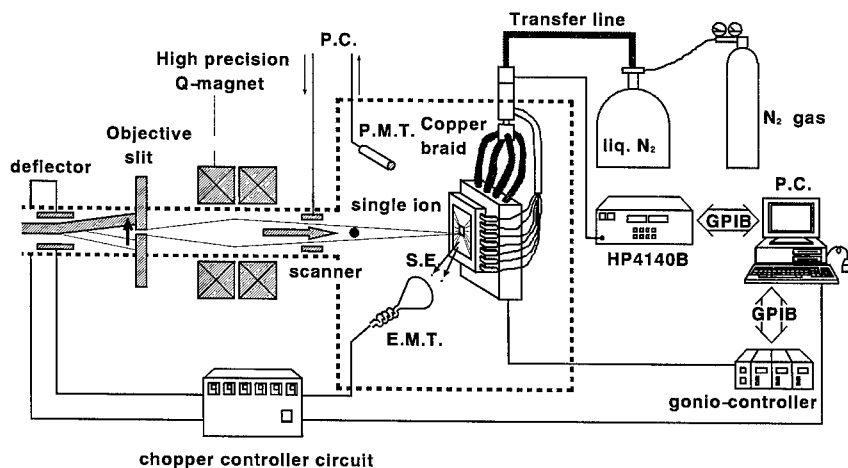


Fig. 1. Schematic drawing of the experimental system.

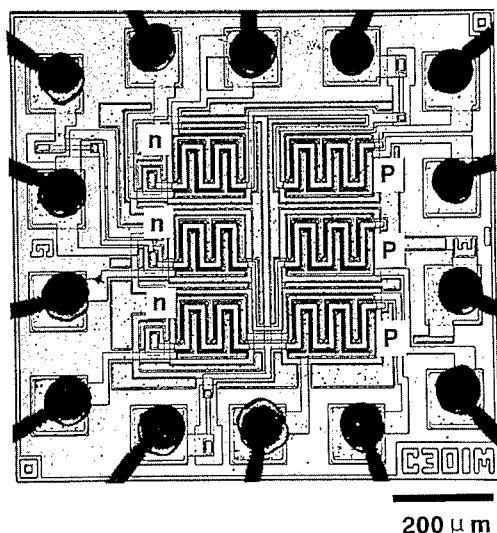


Fig. 2. Optical micrograph of the test device.

analyses. The analysis of the ion irradiation effects in the MOSFETs has been done by repeatedly taking the SIBIC images. Details of sample positioning using the SIBIC imaging are introduced in the other literatures [10,11].

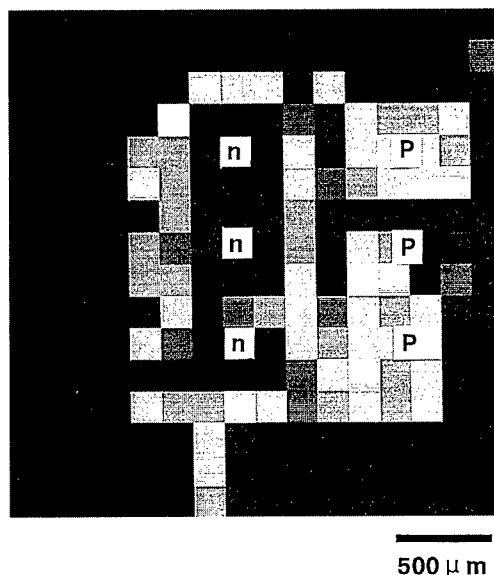


Fig. 3. SIBIC image of the entire chip which is composed of 16×16 pixels. The scanned area is $800 \times 800 \mu\text{m}^2$.

3. Results and discussion

In this section, we describe the different responses of pMOSFETs and nMOSFETs in the test CMOS4007 (Toshiba) against ion irradiation. Fig. 4 shows the threshold voltage shift ΔV_{th} for both pMOSFETs and nMOSFETs as a function of ion dose at room temperature. The threshold voltage was defined as the zero current intercept of square root of the I_d versus V_g curves in the saturation mode. The threshold voltage V_{th} shifted to the negative direction for both pMOSFETs and nMOSFETs proportional to the number of He ions. There are two major causes in generation of radiation induced interface charges which are responsible for V_{th} shift. They are oxide trapped holes and trapped charges by interface states [12]. The slope represents fragility of the target devices against ion irradiation. Since the slope for pMOSFETs is steeper than that for nMOSFETs, pMOSFETs are more fragile than nMOSFETs in the threshold voltage shift at room temperature.

The reason for the steeper slope, i.e., larger ΔV_{th} for pMOSFETs, can be explained as follows. It is known that the net ΔV_{th} is the algebraic sum of voltage shifts due to the trapped holes ΔV_{Noi} and the trapped charges by the interface states ΔV_{Nit} [13]. It also should be noted that the Pb-centers responsible for the interface states have amphoteric nature. They are donors in the lower part of the bandgap and acceptors in the upper part of the bandgap. Their occupancy depends on the value of the surface potential. The donor-like interface states are responsi-

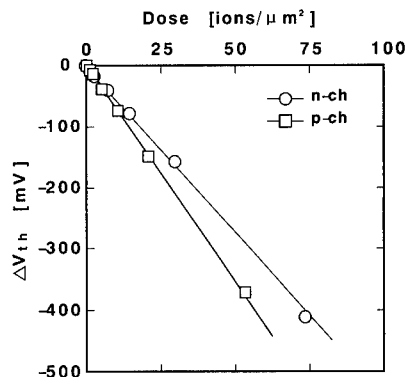


Fig. 4. Threshold voltage shift ΔV_{th} for both pMOSFETs and nMOSFETs induced by ion irradiation.

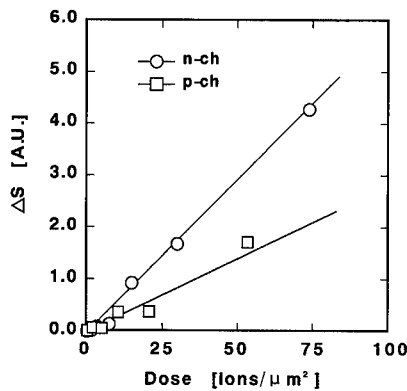


Fig. 5. Subthreshold swing shift ΔS for both pMOSFETs and nMOSFETs induced by ion irradiation.

ble for the V_{Nit} shift of pMOSFETs, while the acceptor-like interface states are responsible for the V_{Nit} shift of nMOSFETs. Therefore ΔV_{Nit} is negative for pMOSFETs and positive for nMOSFETs, while ΔV_{Not} induced by trapped holes is always negative [14]. For pMOSFETs, sign of ΔV_{Nit} is the same as ΔV_{Not} , which causes larger ΔV_{th} . For nMOSFETs, however, it is expected that the opposite signs of ΔV_{Nit} and ΔV_{Not} result in a relatively small shift in V_{th} . Thus pMOSFETs are more fragile than nMOSFETs in the threshold voltage shift.

Fig. 5 shows the subthreshold swing shift ΔS for both pMOSFETs and nMOSFETs as a function of ion dose. The subthreshold swing is defined as the change in gate voltage necessary to reduce transistor current by one decade. It is well known that the subthreshold swing S is proportional to the average interface state density, D_{it} , in the weak inversion region. The change in interface state density induced by an ion irradiation ΔD_{it} is given by

$$\Delta D_{\text{it}} = [C_{\text{ox}} / (kT \ln(10))] \Delta S, \quad (1)$$

where C_{ox} is the oxide capacitance, and k the Boltzmann constant [15]. Although the exact amount of interface state density cannot be estimated because of the lack of information on the precise sample structure, a tendency of the change in mean interface state density can be understood by evaluating the change in the subthreshold swing before and after the ion irradiation. As shown in Fig. 5, the subthreshold swing S became larger for both pMOSFETs and nMOSFETs, as the number of He ions was increased, and ΔS for nMOSFETs was higher than

that for pMOSFETs. This suggests that a larger number of interface states were induced by high energy ions in nMOSFETs than pMOSFETs.

The difference in ΔS between nMOSFETs and pMOSFETs can be attributed to the asymmetrical distribution of radiation induced interface states in the midgap, which was found by Ma [16,17]. According to his work, the density of electron beam induced interface states in the upper half of the band gap is higher than that in the lower half of the band gap and the peak is located at 0.2–0.3 eV above midgap. Similar distribution has been recognized for γ -ray induced interface states [18–20]. Since the interface states in the upper half of the bandgap are responsible for the degradation of S in nMOSFETs and the one in the lower half for the degradation in pMOSFETs, it is clearly concluded that nMOSFETs are more susceptible than pMOSFETs to the degradation of the subthreshold swing S .

4. Summary

We have investigated the radiation effects induced by MeV He single ions in pMOSFETs and nMOSFETs in commercially available CMOS4007 using the SIMP. It has been concluded that, (1) pMOSFETs are more fragile than nMOSFETs in threshold voltage shift and (2) nMOSFETs are more susceptible than pMOSFETs to the degradation of subthreshold swing S . These effects have been fully explained on the basis of different contribution of oxide trapped charges and the charges at interface states depending on the channel conduction type.

Acknowledgements

This work is partly supported by a Grant-in-Aid for Specially Promoted Research, the Ministry of Education, Science and Culture.

References

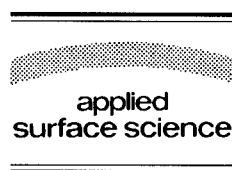
- [1] R.W. Tallon, M.R. Ackermann, W.T. Kemp, M.H. Owen and D.P. Saunders, IEEE Trans. Nucl. Sci. NS-32 (1985) 4393.

- [2] G.J. Brucker, E.G. Stassinopoulos, O. Van Gunten, L.S. August and T.M. Jordan, *IEEE Trans. Nucl. Sci.* NS-29 (1982) 1966.
- [3] E.G. Stassinopoulos, G.J. Brucker and O. Van Gunten, *IEEE Trans. Nucl. Sci.* NS-31 (1984) 1444.
- [4] W.J. Stapor, L.S. August, D.H. Wilson, T.R. Oldham and K.M. Murray, *IEEE Trans. Nucl. Sci.* NS-32 (1985) 4399.
- [5] T.R. Oldham and J.M. McGarrity, *IEEE Trans. Nucl. Sci.* NS-28 (1981) 3975.
- [6] N.S. Saks and M.G. Ancona, *IEEE Trans. Nucl. Sci.* NS-34 (1987) 1348.
- [7] M.A. Xapsos, R.K. Freitag, C.M. Dozier, D.B. Brown, G.P. Summers, E.A. Bruke and P. Shapiro, *IEEE Trans. Nucl. Sci.* NS-37 (1990) 1677.
- [8] I. Ohdomari, M. Sugimori, M. Koh, K. Noritake, Y. Takiguchi and H. Shimizu, *Nucl. Instr. Meth. B* 72 (1992) 436.
- [9] I. Ohdomari, M. Sugimori, M. Koh, K. Noritake, M. Ishikawa and H. Shimizu, *Nucl. Instr. Meth. B* 54 (1991) 71.
- [10] M. Koh, K. Hara, K. Horita, B. Shigeta, T. Matsukawa, A. Kishida, T. Tanii, M. Goto and I. Ohdomari, *Nucl. Instr. Meth. B* 93 (1994) 82.
- [11] M. Koh, K. Hara, K. Horita, B. Shigeta, T. Matsukawa, A. Kishida, T. Tanii, M. Goto and I. Ohdomari, *Jpn. J. Appl. Phys.* 33 (1994) L962.
- [12] E.H. Nicollian and J.R. Brews, *MOS Physics and Technology* (Wiley, New York, 1982) p. 549.
- [13] P.J. McWhorter and P.S. Winokur, *Appl. Phys. Lett.* 48 (1986) 133.
- [14] P.M. Lenahan and P.V. Dressendorfer, *J. Appl. Phys.* 55 (1984) 3495.
- [15] H. Gesch, J.-P. Leburton and G.E. Dorda, *IEEE Trans. Electron Devices* ED-29 (1982) 913.
- [16] T.P. Ma, G.A. Scoggan and R. Leone, *Appl. Phys. Lett.* 27 (1975) 61.
- [17] G.A. Scoggan and T.P. Ma, *J. Appl. Phys.* 48 (1977) 294.
- [18] J.M. Benedetto and H.E. Boesch, Jr., *IEEE Trans. Nucl. Sci.* NS-31 (1984) 1461.
- [19] M. Gaitan and T.J. Russell, *IEEE Trans. Nucl. Sci.* NS-31 (1984) 1256.
- [20] K. Naruke, M. Yoshida, K. Maeguchi and H. Tango, *IEEE Trans. Nucl. Sci.* NS-30 (1983) 4054.



ELSEVIER

Applied Surface Science 104/105 (1996) 369–372



Weak fluence dependence of charge generation in ultra-thin oxides on silicon

K.R. Farmer^{a,*}, C.P. Debauche^{a,b}, A.R. Giordano^a, P. Lundgren^c,
M.O. Andersson^c, D.A. Buchanan^d

^a Department of Physics, New Jersey Institute of Technology, University Heights, Newark, NJ 07102, USA

^b U.S. Army Electronics Technology and Devices Laboratory, Ft. Monmouth, NJ 07703, USA

^c Department of Solid State Electronics, Chalmers University of Technology, S-412 96 Gothenburg, Sweden

^d IBM Research Division, T.J. Watson Research Center, P.O. Box 218, Yorktown Heights, NY 10598, USA

Received 28 June 1995; accepted 11 December 1995

Abstract

We examined charge generation in metal/tunnel-oxide/n-silicon diodes fabricated with polycrystalline silicon (poly-Si) gates. In these devices, electron injection from the substrate in the direct tunnel regime leads to charge generation which evolves with *time* rather than electron fluence, as has been previously reported for injection in the Fowler–Nordheim tunnel regime. Our findings complete the picture proving the existence of a distinct degradation mode in the direct tunnel regime for devices fabricated at different facilities, using both aluminum and polycrystalline silicon gates, and stressed via either gate or substrate injection. This work directly impacts the prediction of the lifetimes of devices in which direct tunneling is measurable.

The continued scaling of metal–insulator–silicon devices has brought about the need to understand electrical degradation effects in structures with insulating layers so thin ($< \sim 3.5$ nm) that direct tunneling (DT) is observable at bias levels below the onset of Fowler–Nordheim (FN) electron injection into the insulator conduction band. The study of such thin films is of current interest to the semiconductor industry for memory and ≤ 0.1 μm logic applications [1]. In metal/tunnel-oxide/p-silicon diodes fabricated with either aluminum (Al) or polycrys-

talline silicon (poly-Si) gates, the principle degradation effect for DT electron injection from the gate has been shown to be a gradually increasing tunnel current over time [2]. This degradation is bias dependent, but as revealed by studying samples of different oxide thickness, it is not strictly dependent on the fluence of tunneling electrons through the oxide. In contrast to the DT results, defect generation for both gate and substrate injection in the FN regime in 4.5 to 5.5 nm oxides has been found to scale with electron fluence, independent of oxide thickness [3]. In these thicker samples, DT degradation was not observed. The kinetics of FN degradation have been interpreted in terms of incident electron energy and defect generation rates per tunneling electron [3]. DT

* Corresponding author.

degradation, on the other hand, is less straightforward to interpret, and requires that defect generation be at least a two-step process that involves both the deposition or release of electronic energy and a time evolution step controlled by the applied bias, with the electron interaction not being the rate-limiting step [2]. The remaining unexplored area of fluence dependence during either DT or FN device degradation is DT electron injection from the substrate. We note that DT substrate injection degradation has recently been reported for Al gate samples of a single thickness, but fluence dependence for different oxide thicknesses, and the use of poly-Si gates have not been studied for this injection mode [4]. Because of the different chemical nature of the gate/oxide and substrate/oxide interfaces, there is no clear reason to suspect that DT defect generation from both gate and substrate injection should be the same. However, in this work we show that DT defect generation for substrate injection, as a function of both time and temperature, is remarkably similar to that for gate injection, in support of the results on Al gate devices [4]. In addition, we present evidence that the DT degradation effect may die out as the oxide thickness increases above 3.5 nm, consistent with the results for the 4.5 to 5.5 nm oxides where DT degradation was not seen.

Devices for this study have been fabricated on the silicon line at IBM, Yorktown Heights. Active tunnel oxides of four different nominal thicknesses, 2.0, 2.4, 2.8 and 3.4 nm, are formed at 700°C in dry O_2 in windows opened in a field oxide grown on $\langle 100 \rangle$ oriented, $\sim 0.005\text{--}0.02\ \Omega\text{ cm}$, n-type silicon wafers. After the gate oxidation, the active oxide is immediately covered by poly-Si deposition. Although windows of various sizes ranging from $1\ \mu\text{m}^2$ to 1 mm^2 are available on each chip, measurements for this work have been carried out using mainly $250\ \mu\text{m} \times 250\ \mu\text{m}$ devices. As shown in Fig. 1, measurements of current density versus positive gate bias (J - V) reveal that the current density scales with oxide thickness. J increases by a factor of ~ 100 for each 0.4 nm decrease in thickness, in good agreement with first principles tunneling theory [5].

We find that just as for gate injection, substrate injection at constant bias gives rise to degradation which is measured as a gradually increasing tunnel current over time. This is illustrated in Fig. 2 which

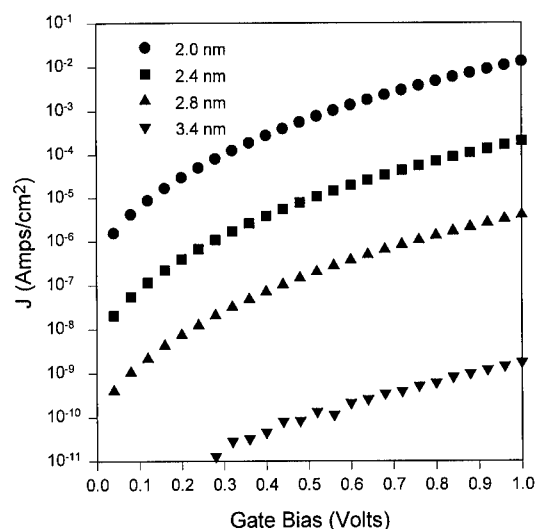


Fig. 1. Current density versus positive gate voltage bias for 2.0, 2.4, 2.8 and 3.4 nm oxides.

plots a typical DT degradation curve in the usual way, as the fractional increase in tunnel current versus time. This device was electrically stressed at an applied gate voltage of 2.0 V, at room temperature. Electron fluence is also noted in the figure for comparison with previously published results. Our minimum resolution to fluence is $\sim 2 \times 10^{-9}$

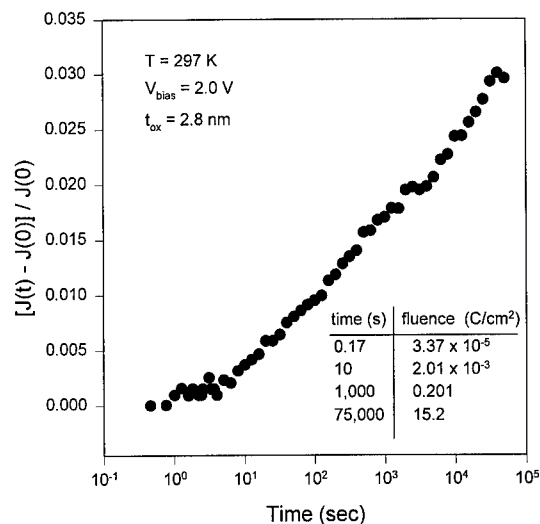


Fig. 2. The fractional increase in the current density, $\Delta J/J_0$, through 2.8 nm oxide versus time, measured at room temperature at 2.0 V.

C/cm² in the thickest oxides. The fractional increase in current is a sensitive measure of the net charge associated with degradation-related defects [4]. In these devices, constant shifts in high frequency capacitance–voltage (HFCV) curves are too small to be measured accurately, even for a 10% fractional increase in current, the largest which we observe. The limit of our sensitivity to charge using HFCV's is $\sim 10^{11}$ charges/cm² in a 2.8 nm oxide, corresponding to a ~ 10 mV HFCV shift. Thus the maximum amount of charge which we create is below this level. In the figure, notice that the charge creation does not seem to saturate, as has been reported for FN degradation of slightly thicker oxides [3].

Fig. 3 explores the thickness and bias dependence of DT defect generation resulting from substrate injection in our poly-Si gate devices. The figure plots the fractional increase in tunnel current measured after 1000 s of stress, versus the gate voltage at which the stress was applied. Data is shown for the three oxide thicknesses. Similar graphs can be obtained for any amount of stress time less than $\sim 10^4$ s. Analogous to charge generation observed in the DT gate injection studies, we find that substrate injection degradation is bias dependent, increasing with increasing gate voltage, but not strictly dependent on the tunnel electron fluence. To highlight the

Table 1

Initial values of current density, J_0 , for some of the data shown in Fig. 3

t_{ox} (nm)	J_0 (A/cm ²)	
	$V_{\text{bias}} = 1.7$ V	$V_{\text{bias}} = 2.0$ V
3.4 nm	2.4×10^{-8}	6.4×10^{-8}
2.8 nm	6.4×10^{-5}	1.6×10^{-4}
2.4 nm	3.2×10^{-3}	8.0×10^{-3}

weak dependence on fluence, the initial current density, J_0 , for some of the data in Fig. 3 is given in Table 1. In the table, notice that J_0 at a given stress voltage, and hence the fluence through the oxides of different thickness differs by nearly five orders of magnitude, but in Fig. 3, the corresponding fractional increase in current at that stress voltage varies by no more than a factor of two. In fact, the amount of charge generated seems to be identical in the 2.4 and 2.8 nm oxides, and decreases only slightly in the 3.4 nm oxides. Clearly, damage arising from substrate injection is at best weakly dependent on electron fluence. This similarity to gate injection damage is remarkable. It implies that a similar, multi-step mechanism may underlie degradation in direct tunnel devices, regardless of injection mode. We interpret the decrease in charge generation for the thickest oxide as possible evidence that the DT degradation effect may die out as the oxide thickness increases above 3.5 nm, consistent with the results for the 4.5 to 5.5 nm oxides where DT degradation was not seen. Because the charge generation evolves in time, the plot in Fig. 3 can be interpreted as the rate of charge generation versus gate bias.

A further study of the similarity between gate and substrate injection damage can be made by measuring the temperature dependence of charge generation. For gate injection, it has been shown that the charge generation exhibits a transition from thermally activated kinetics at temperatures above ~ 150 K to relatively temperature-independent behavior below this value [2]. The temperature dependence of the DT charging for substrate injection is presented in Fig. 4 and Fig. 5. In Fig. 4 we plot the fractional increase in tunnel current measured after 1000 s of stress, versus the gate voltage at which the stress was applied. Data is shown for the 2.8 nm oxide for various temperatures between 300 K and 77 K.

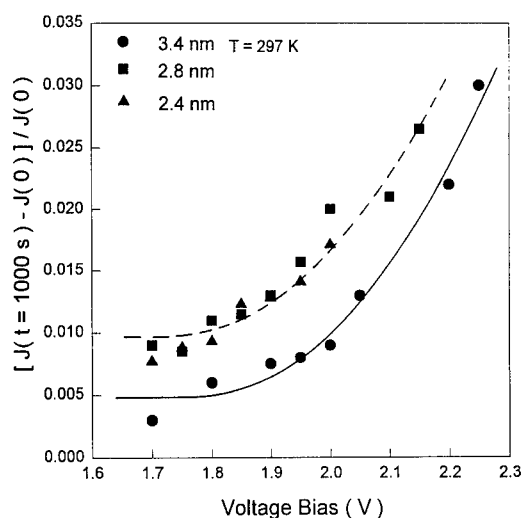


Fig. 3. Bias and oxide thickness dependence of poly-Si gate device degradation at room temperature.

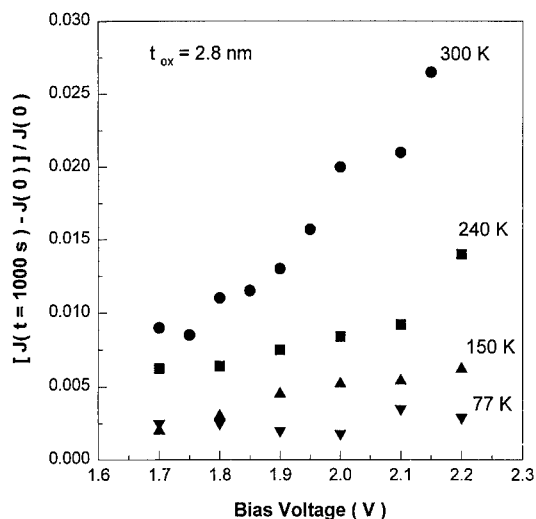


Fig. 4. The temperature dependence of the initial rate of charging, defined as $\Delta J/J_0$, measured at $t = 1000$ s for 2.8 nm oxide versus positive gate voltage bias.

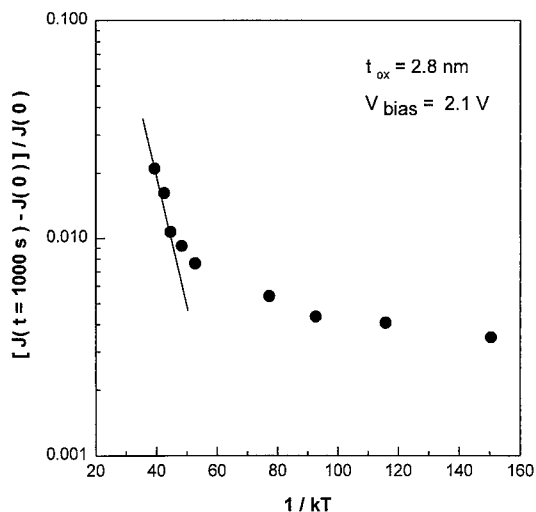


Fig. 5. The temperature dependence of the initial rate of charging, defined as $\Delta J/J_0$, measured at $t = 1000$ s for 2.8 nm oxide at $V_g = 2.1$ V.

Observe that the charge generation rate decreases strongly with temperature. In Fig. 5, we show an Arrhenius plot of the charge generation measured at $V_{gate} = 2.1$ V after 1000 s of stress. Again, similar to the DT gate injection results, DT substrate injection

degradation shows what appears to be thermally activated kinetics above $T \sim 150$ K, and weak temperature dependence below this value. Curve fitting suggests that at low temperatures, the charge generation rate may vary proportional to $\sim T^2$, but more measurements are needed to confirm this possibility. The behavior illustrated in Fig. 5 is similar to that reported for both interface state generation [6] and trap creation [7] in thicker oxides which undergo FN degradation, suggesting the possibility that while the DT defect generation mode is distinctly different from the FN mode, the nature of the defects created may be similar in both cases.

In conclusion, this work completes the picture proving the existence of a distinct degradation mode in the DT regime for devices fabricated at different facilities, using both Al and poly-Si gates, and stressed via either gate or substrate injection. This mode is characterized by charge generation which evolves with time, rather than injected fluence. The current findings refute the claim that oxide charge creation 'disappears' with the transition from FN to DT injection [8], and directly impact the prediction of the lifetimes of devices in which direct tunneling is measurable.

Acknowledgements

This work was funded in part by NSF award No. ECS-9313937.

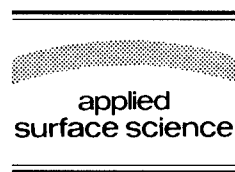
References

- [1] Y. Taur et al., IEDM Tech. Dig. (1992) 35.6.1.
- [2] K.R. Farmer, M.O. Andersson and O. Engstrom, Appl. Phys. Lett. 60 (1992) 730.
- [3] D.A. Buchanan, D.J. DiMaria, C.A. Chang and Y. Taur, Appl. Phys. Lett. 65 (1994) 1820.
- [4] P. Lundgren, M.O. Andersson, K.R. Farmer and O. Engstrom, in: Proc. Insulating Films on Semiconductors, 1995, to be published.
- [5] P.V. Dressendorfer, PhD Thesis, Yale University (1978).
- [6] D. Vuillaume, Appl. Phys. Lett. 59 (1991) 3118.
- [7] D.J. DiMaria, J. Appl. Phys. 68 (1990) 5234.
- [8] M. Depas, B. Vermeire, P.W. Mertens, M. Meuris and M.M. Heyns, Semicond. Sci. Technol. 10 (1995) 753.



ELSEVIER

Applied Surface Science 104/105 (1996) 373–378



Studies on low temperature silicon grain growth on SiO_2 by electron cyclotron resonance chemical vapor deposition

K.C. Wang^a, H.L. Hwang^{a,*}, J.J. Loferski^a, T.R. Yew^b

^a Department of Electrical Engineering, National Tsing Hua University, Hsinchu, Taiwan, ROC

^b Materials Science Center, National Tsing Hua University, Hsinchu, Taiwan, ROC

Received 28 June 1995; accepted 11 December 1995

Abstract

Electron cyclotron resonance chemical vapor deposition has resulted in poly-Si films with grains of one micron dimension by using the hydrogen dilution method. The crystalline fraction of the poly-Si film is almost 100% as determined from analysis of Raman spectra. The poly-Si films have preferred $\langle 111 \rangle$ and $\langle 110 \rangle$ orientations according to their XRD spectra. The hydrogen content of the poly-Si films is less than 0.8%. A simple model of grain formation is proposed to explain grain growth in the electron cyclotron resonance chemical vapor deposition deposited poly-Si films.

1. Introduction

Hydrogenated silicon films deposited by the hydrogen-dilution and the hydrogenatom-treatment methods exhibit $\mu\text{-Si:H}$ characteristics when they incorporate a large amount of hydrogen. This suggests that such films have a more compact structure than conventional a-Si:H films. By incorporating various amounts of hydrogen, and utilizing an atomic hydrogen treatment during the deposition, the degree of crystallinity in the hydrogenated silicon films can be systematically adjusted [1]. A recent publication reported a new method for producing poly-Si films at a low temperature (250°C). The SiO_2 was subjected to a sulfurization treatment before deposition of the hydrogenated Si film. This eliminated the

amorphous transition layer which usually forms between the SiO_2 and the poly-Si film. The influence of sulfurization is quite distinct once the hydrogen dilution ratio reached 92%. The grain size in the resulting poly-Si was estimated to be around 200–500 Å [2]. In this paper we report a new low temperature poly-Si film deposition in which electron cyclotron resonance chemical vapor deposition (ECR-CVD) is combined with hydrogen dilution. The largest grain poly-Si films (grain dimensions of one micron) occurred when the dilution ratio was 98%. These large grains have a special ‘leaf-like’ shape. The surfaces of these poly-Si films are shown to be very rough by AFM, with the mean value of roughness of the films increasing as the grain size increases. The Raman spectra of the poly-Si films showed the characteristics of single crystal with no evidence of the amorphous silicon band. Therefore, the crystalline fraction of poly-Si films was nearly 100%. XRD spectra

* Corresponding author.

showed that the poly-Si films have $\langle 111 \rangle$ and $\langle 110 \rangle$ preferred orientations. As the grain size increased, the $\langle 110 \rangle$ orientation becomes more dominant. The orientation and grain size are strongly dependent on the hydrogen dilution ratio. The hydrogen content of these poly-Si films is less than 0.8 at% and decreases as the hydrogen dilution ratio increases [3–5].

2. Poly-Si grain formation experiments

Three conditions are necessary to produce large grained films. The first is a high H_2/SiH_4 dilution ratio. The second is the presence of a magnetic field since plasma enhanced CVD even with high dilution ratios does not lead to large grains. The third condition is a high microwave power in the ECR-CVD process. The magnetic field increases the efficiency of ionization of H_2 and SiH_4 ions. The large ionized hydrogen content of the gas in the chamber suggests that ionized hydrogen coverage of the growth surface somehow increases the diffusion length of the adsorbed Si precursors. Increasing dilution increases

hydrogen coverage and increases the probability of Si nucleation on the surface and the construction of a dense Si–Si network structure. The Raman spectra show that there is no amorphous silicon phase present in the poly-Si films deposited by the ECR-CVD method. The crystalline fraction of the poly-Si films identified by Raman scattering spectra is nearly 100%. From the X-ray diffraction patterns, the preferred orientations of poly-Si films are $\langle 110 \rangle$ and $\langle 111 \rangle$ [3–5].

The largest grain poly-Si films were deposited with 1200 W of microwave power, a 250°C substrate temperature, and 20 mTorr deposition pressure. Fig. 1 shows the plan view TEM images of samples with different thicknesses (a) T-18, (b) T-55, (c) T-90, and (d) T-120 whose thicknesses were 0.18, 0.55, 0.9, and 1.2 microns, respectively. These TEM images show that the grain size increases as the film thickness increases. The three-dimensional AFM images of these four samples of Fig. 2 show that the grain size in these films is strongly dependent on film thickness. The TEM and AFM images show that poly-Si films have cone-shape grains.

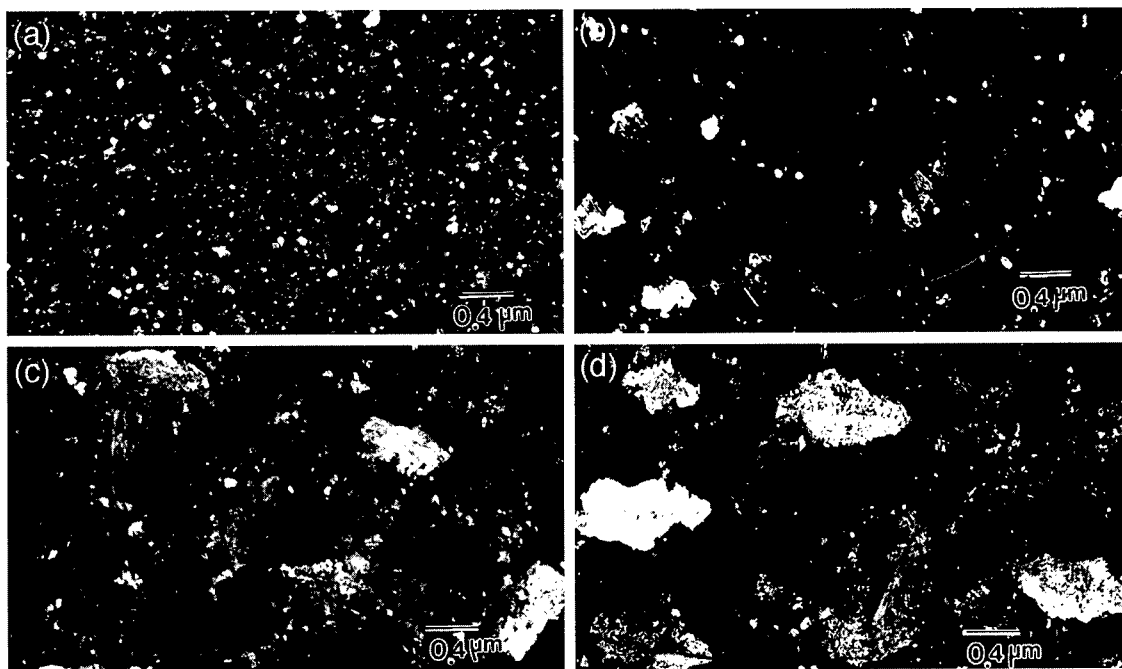


Fig. 1. Plan view TEM dark field images of samples: (a) T-18, (b) T-55, (c) T-90, and (d) T-120.

3. A qualitative picture of grain formation

The following simple qualitative model is advanced to account for the main features of grain formation in our films.

When the hydrogen dilution ratio is low, the vertical growth rate of the grains in the silicon film is much larger than the lateral growth rate. Therefore, the grains grow vertically and result in columnar poly-Si grains. When hydrogen dilution ratio is increased, the vertical growth rate decreases while the lateral growth increases. This enhances the lateral growth of the poly-Si grains. For the $\langle 110 \rangle$ vertical

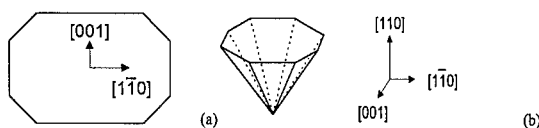


Fig. 3. Grain expanding with an effective lateral growth rate: (a) plan view and (b) three-dimensional view.

direction, the lateral axes can be $\langle 1\bar{1}0 \rangle$ and $\langle 100 \rangle$. The $\langle 1\bar{1}0 \rangle$ and $\langle 110 \rangle$ planes are equivalent. From the plan view of the expanding grain, the $\langle 1\bar{1}0 \rangle$ plane will expand faster than the $\langle 100 \rangle$ plane. This results in grains with an octagonal shape, as shown

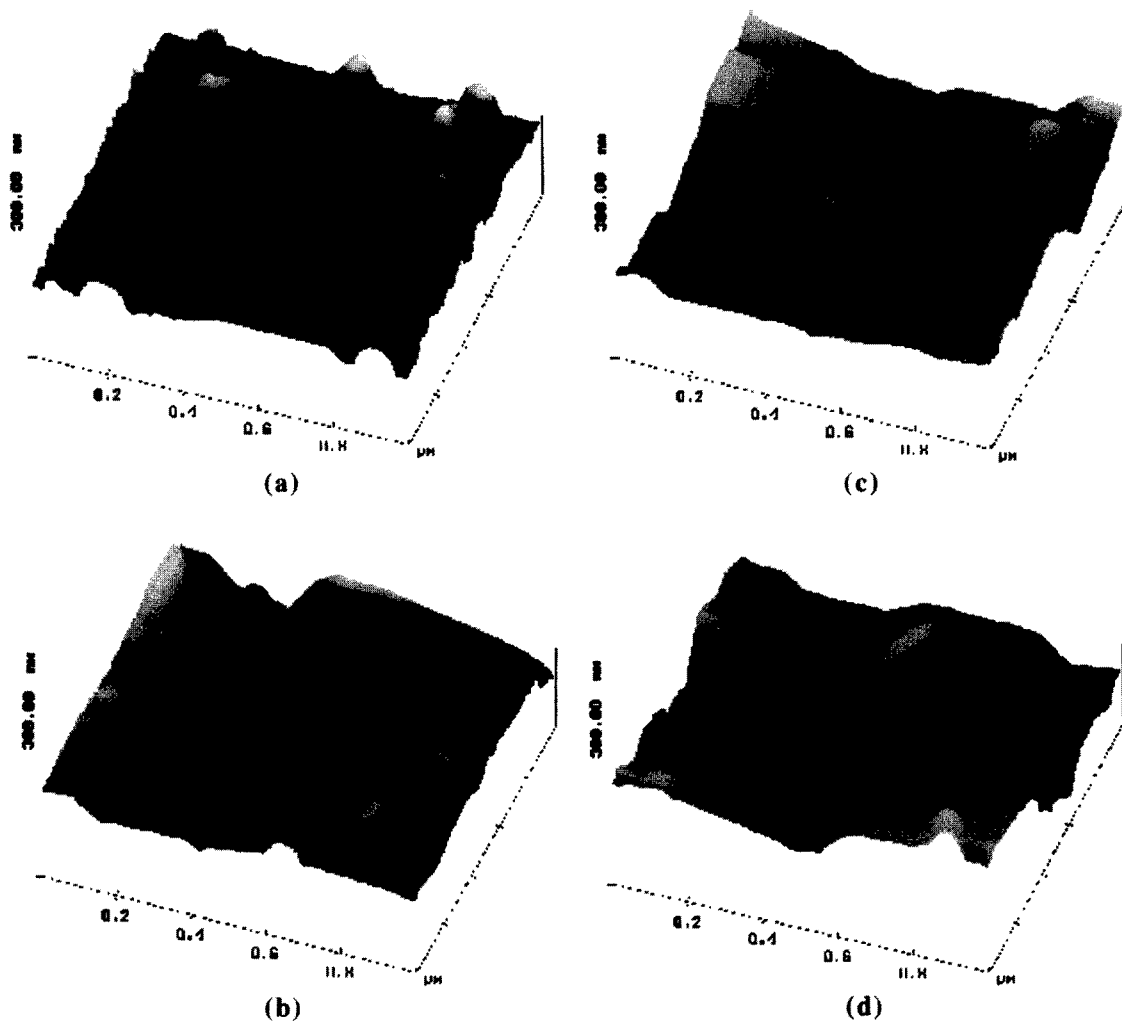


Fig. 2. Three-dimensional AFM images of samples: (a) T-18, (b) T-55, (c) T-90, and (d) T-120.

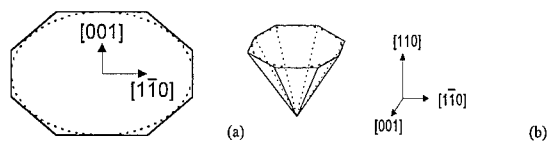


Fig. 4. Grain shape changed by the etching effect: (a) plan view and (b) three-dimensional view (solid line for the original grain shape and dash line for the new one).

in Fig. 3(a). A three-dimensional view of poly-Si grain which is an octagonal cone is shown in Fig. 3(b). The silicon atoms at corners of the octagon [Fig. 3(a)] react easily with hydrogen radicals and are removed from their sites ('etching' effect). This phenomenon is displayed in Fig. 4(a). The corners of the octagon are curved and the grain shape becomes elliptical, as shown in Fig. 4 (a). The solid line presents the original grain shape and the dashed line, the final shape. The three-dimensional grain shape transformation is shown in Fig. 4(b). The final shape of the poly-Si grain produced by the 'etching' effect is shown in Fig. 5. The plan view of grain shape in Fig. 5(a) is consistent with the leaf-like grains of plan view TEM images. The cone-shaped grain in Fig. 5(b) is consistent with the grain shape in the XTEM image. This grain formation model explains the results of our experiments qualitatively and provides an explanation for the peculiar grain geometries observed in our poly-Si film.

Hydrogen dilution is necessary but not sufficient to deposit large-grain poly-Si at low temperatures. In our poly-Si deposition, several factors contributed to the grain formation. First, the hydrogen dilution produces an 'etching' effect [6] which eliminates the energetically unfavorable configurations and prevents formation of an amorphous network. The grain size in these poly-Si film is mainly limited by the lateral growth rate and the distance between two neighbor preferentially oriented grains. In the beginning stage of deposition, the nucleation center density is high and the growing grains are small. The

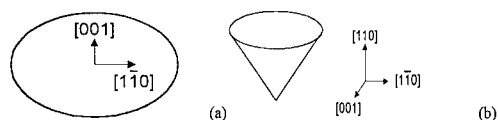


Fig. 5. The new grain shape: (a) plan view and (b) three-dimensional view.

small grains expand in competition with each others. A more rapidly expanding grain grows faster than its neighbors and stunts their growth. An enhanced lateral growth rate helps the grain expand laterally, while the grains continue to grow. The lateral growth rate is probably determined by the ion energy of radicals and their surface mobility on the growth surface.

Hydrogen dilution will prevent the formation of an amorphous network and eliminates the energetically unfavorable configurations by 'etching'. Furthermore, the hydrogen passivation of silicon surface increases the surface mobility of the silicon precursor on the growth surface and helps the poly grains expanding laterally.

Hydrogen radicals in the heavily hydrogen diluted silane plasma sustain the 'etching' operations on the energetically unfavorable configurations and provide hydrogen passivation of the dangling bonds of the silicon atoms on the growth. This increases the surface mobility of the silicon-hydride radicals.

In the ECR-CVD system, the gases are ionized by the resonance electrons and coupled microwave power into the plasma. The ECR-CVD is electrodeless and can have a high ionization efficiency and reduced level of plasma damage.

The dependence of grain size on microwave power is shown in Fig. 6. For microwave power of 300 W, the deposited silicon film is microcrystalline with a maximum grain size of 300 Å. For microwave power of 800 W, the poly-Si film is polycrystalline with a maximum grain size of 5000 Å. The microwave power transfers energy to the silicon radicals in the

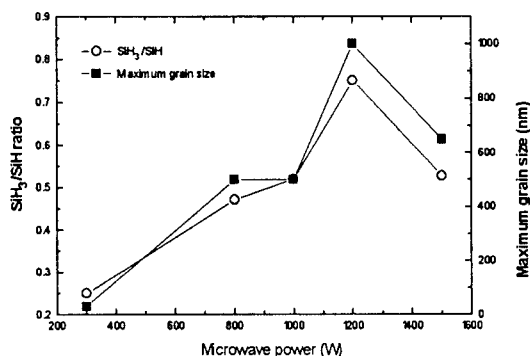


Fig. 6. Effects of microwave power on maximum grain size and SiH₃/SiH₄ ratio.

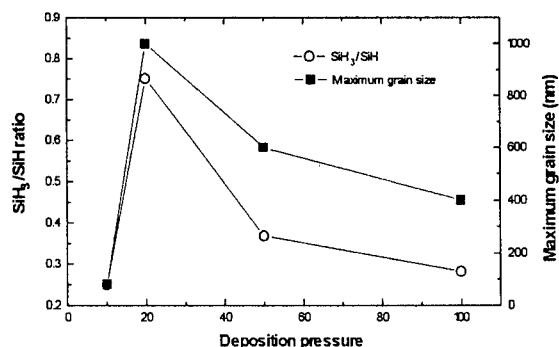


Fig. 7. Effects of deposition pressure on maximum grain size and SiH₃/SiH ratio.

plasma and helps the radicals to travel energetically on the growing surface. If the microwave power is low, the silicon radicals do not have enough energy, and their migration on the growing surface is inhibited, which would prevent lateral expansion of the grain. This results in a fine-grain silicon film deposition. A high power source for plasma generation is necessary for the large-grain poly-Si film deposition. This explains why large-grain poly-Si film can only be deposited by ECR-CVD with 1200 W microwave power. The grain size increases as the microwave power increases and then decreases as the microwave power was increased beyond 1200 W to 1500 W. Note that dependence of grain size on the SiH₃/SiH ratio is similar to its dependence on the microwave power as shown in Fig. 6.

The dependence of grain size on deposition pressure is shown in Fig. 7. For a pressure of 10 mTorr, the maximum grain size was 800 Å. The largest grains were obtained at a deposition pressure of 20 mTorr. Increasing the pressure beyond 20 mTorr led to a decrease in grain size. Again, the dependence of the SiH₃/SiH on deposition pressure is similar to that of the maximum grain size, as shown in Fig. 7.

Fig. 8 shows that maximum grain size changes somewhat as the substrate temperature changes. The grain size increased as the temperature was increased from 100 to 250°C. Higher substrate temperature reduces the grain size. The difference in surface mobility of the radicals over the temperature range is very small. Again, as shown in Fig. 8, the dependence of grain size on the SiH₃/SiH ratio and on the substrate temperature are similar.

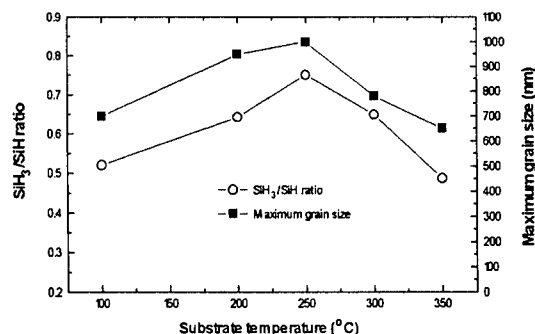


Fig. 8. Effects of substrate temperature on maximum grain size and SiH₃/SiH ratio.

From these experiments we are led to conclude that SiH₃ radicals play an important role in producing large grains. This probably means that they have low reactivity on the hydrogen-terminated silicon surface. They move on the surface until they find a suitable site where they are incorporated into the film [7,8].

The grain size increased as the film thickness increased. To explore whether the grain size keeps on increasing as the film thickness is increased, a poly-Si film was deposited to a greater total thick-



Fig. 9. Cross-sectional TEM images of a 4-μm thick poly-Si film deposited by 98% hydrogen dilution.

ness using the conditions for sample S-98. Fig. 9 shows the cross-sectional TEM images of this thicker film. The maximum grain size was about $1.2\ \mu\text{m}$. The grain was not a perfect cone shape. The edges of the cone side seem to be distorted. When the grains are expanding freely, without any side obstructions, they should grow in a cone shape. After they expand laterally for some distance, neighboring grains intersect with each others. If the growth rates of two intersecting grains differ substantially, the one with the higher growth rate survives and the other stops growing. Based on our XRD observations, it appears that grains in the $\langle 110 \rangle$ and $\langle 111 \rangle$ orientations, will keep on expanding, while others stop growing and remain small. When coalescence occurs between two grains having the preferred orientation, the competition for grain expansion results in the distortion of the side-edge of the cone-shaped grains. Grain boundaries are also determined by the coalescence between the two preferentially oriented grains. Therefore, the distance between the two closest preferentially oriented grains limits the grain expansion and also determines the maximum grain size of the deposited poly-Si films.

4. Conclusions

The formation of large grained poly-Si films is facilitated by the hydrogen 'etching' effect which is more efficient when the hydrogen dilution ratio is high. The etching eliminates energetically unfavorable configurations. The grain size increase is related to the ability of grains to expand laterally. The grain

size ultimately limited by the maximum spacing between two nearest neighbor grains having a preferred orientation. The lateral growth rate is determined by the energy of the ions, the ion species (SiH_3 or SiH etc.), and the trap states of growing surface of the silicon films. Heavy hydrogen dilution provides hydrogen passivations of the dangling bonds of silicon atoms on the growing surface and thus increases the surface mobility of the silicon-hydride radicals on the growth surface. The SiH_3 species have a high surface mobility on the growth surface. The dependence of grain size on the SiH_3/SiH ratio and on the microwave power, deposition pressure, and substrate temperature are similar. A simple model based on our experimental data is proposed to explain the poly-Si film formation and the growth of grains in the films.

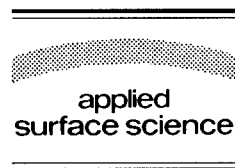
References

- [1] K.C. Hsu, PhD Thesis, Dept. of Electrical Engineering, Natl. Tsing Hua University (1993).
- [2] K.C. Wang, H.L. Hwang and T.R. Yew, *Appl. Phys. Lett.* 64 (1994) 1204.
- [3] K.C. Wang, K.L. Cheng, Y.L. Jiang, T.R. Yew and H.L. Hwang, *Jpn. J. Appl. Phys.* 34 (1995) 28.
- [4] K.C. Wang, H.L. Hwang, P.T. Leong and T.R. Yew, *J. Appl. Phys.*, in press (1995).
- [5] K.C. Wang, T.R. Yew and H.L. Hwang, *Appl. Surf. Sci.* 92 (1996) 99.
- [6] C.C. Tsai, R. Thompson, C. Doland, F.A. Ponce, G.B. Anderson and B. Wacker, *Mater. Res. Soc. Symp. Proc.* 118 (1988) 49.
- [7] K. Tanaka and A. Matsuda, *Mater. Sci. Rep.* 2 (1987) 139.
- [8] T. Kamei, G. Ganguly, N. Hata and A. Matsuda, *J. Non-Cryst. Solids* 43 (1993) 164.



ELSEVIER

Applied Surface Science 104/105 (1996) 379–384



Characterization of nitrided SiO₂ thin films using secondary ion mass spectrometry

M.R. Frost^{*}, C.W. Magee

Evans East, 666 Plainsboro Road, Suite 1236, Plainsboro, NJ 08536, USA

Received 28 June 1995; accepted 11 September 1995

Abstract

For the fabrication of MOS devices, the incorporation of nitrogen into thin SiO₂ dielectric films has been shown to improve the electrical and structural integrity of the films. For example, nitrogen present at the SiO₂/Si interface acts to enhance the charge-trapping properties of the oxide. Furthermore, nitrided oxides are more resistant to impurity and dopant diffusion and further oxidation than non-nitrided films. The understanding of the nitriding process has progressed to the point where the distribution and concentration of the nitrogen (the N depth profile) can be controlled, to some extent. The final N depth profile in these films is a critical piece of information to the process engineer. By using different nitriding agents and growing the films using varying temperatures and times, the nitrogen can be 'concentrated' at virtually any depth in a very thin oxide (< 100 Å). We have successfully employed secondary ion mass spectrometry (SIMS) for determining the nitrogen distributions in such films. Using an SiO₂ standard, calibrated both in terms of concentration and film thickness, accurate quantification of unknown samples has become straightforward. Through the extensive development of the instrumental protocol, the long-term reproducibility of this measurement has been shown to be better than 9%. The N detection limit using this protocol is approximately 0.001% atomic. We will present recent examples of results using SIMS on dielectric films processed using a variety of oxidation and nitridation conditions.

1. Introduction

There has been ample research conducted that outlines the beneficial aspects of the use of nitrided gate oxides in current generation metal-oxide-semiconductor (MOS) devices. One of the critical ways in which these films build in reliability is when used as a diffusion barrier for dopants from both the gate to the channel and vice versa. The characterization of

nitrided oxides, in terms of understanding where the N is located within the layer and obtaining an accurate concentration determination, has proven to be a challenge. Given that current MOS technology utilizes gate oxides having thicknesses of less than 100 Å, depth resolution has been the major limiting factor. In this paper, the use of secondary ion mass spectrometry (SIMS) for the depth profile characterization of nitrided oxide films is demonstrated, where the depth resolution, sensitivity, accuracy and precision are high. Other analytical techniques have been utilized in an effort to characterize the N profile in such films, e.g. Auger electron spectroscopy (AES)

^{*} Corresponding author.

[1,2], X-ray photoelectron spectroscopy (XPS) [3], nuclear reaction analysis (NRA) [4] and neutron depth profiling (NDP) [5]. Also, various approaches to the SIMS technique have been applied to the analysis of nitrided oxide films [6]. However, in this study, the use of Cs bombardment and CsX^+ detection ($\text{X} = \text{N}, \text{O}, \text{Si}, \text{etc.}$) [7] has been exploited. The merit of using this technique will be discussed, and examples will be illustrated showing how this technique has been used to better understand nitrided oxide thin films.

2. Cesium cluster ion spectrometry

In SIMS, a focussed, energetic beam of ions is accelerated towards a sample surface, and the collisions between the ion beam and the sample results in sputtering. During sputtering, many types of secondary particles form. In the more conventional analytical schemes, Cs ion bombardment is used to enhance negative secondary ion emission. This is especially the case for electronegative species, such as N, O and Si. However, in this work, Cs bombardment was used to form cesium cluster ions, CsX^+ (where $\text{X} = \text{analyte atom}$).

Cesium cluster ion SIMS has been used successfully in the past by others [7,8]. Although the ion yields (and thus sensitivity) are lower using this mode of SIMS compared to using negative ion detection, many benefits are realized. One distinct advantage of CsX^+ detection is the reduced matrix effect encountered between SiO_2 and Si. Compared to using negative ion detection, where the change in ion yield can be as much as 2 orders of magnitude, CsX^+ detection experiences a mere 6X change. As a result, the data interpretation becomes much more straightforward, since the Si and O profiles are flat in the oxide layer, and their raw signals closely represent their true change in concentration.

3. Quantification

Our experiments were conducted using a PHI Model 6600 SIMS instrument, on which the mass spectrometer is quadrupole-based. Low energy (1 kV) Cs primary ion bombardment at 25 nA of beam

current, rastered over a $500 \times 500 \mu\text{m}$ area, was used to obtain a low sputter rate. Through an extensive development of the remaining instrument conditions, an optimized analytical protocol is now in place. Strict adherence to the protocol is necessary to obtain high accuracy and precision in the measurement.

One of the important aspects in the measurement of the N in nitrided oxide films is the accuracy of the quantification. In SIMS, quantification is typically achieved using relative sensitivity factors (RSF's) generated from the analysis of ion implanted standards, for which the dose of the implanted species is well-known. If, for example, the analysis is for N in SiO_2 , then an ion implanted standard of N into SiO_2 must be used to generate the RSF to obtain the highest level of accuracy. This quantitative strategy results in a level of accuracy primarily limited by the accuracy of the dose of the implanted standard, typically around 10%.

Although the use of Cs cluster ion SIMS reduces the matrix effect significantly relative to other modes of SIMS, it does not remove it completely. The extent to which CsN^+ forms in bulk SiO_2 is approximately $5.7 \times$ higher than that in bulk Si. This was determined by comparing the RSF's from ion implanted standards of N in Si and SiO_2 . Knowing this, it might be expected that there would also be a measurable change in ion yield from N (as CsN^+) in the transition region of the SiO_2/Si interface than in the bulk of either matrix. It is imperative for accurate quantification that the extent of this matrix effect be well-understood.

An experiment was conducted to investigate the interface matrix effect. Three wafers, each containing a nitrided oxide film, were reoxidized, each receiving different oxidation times. During the process of the reoxidation, which is a reaction between oxygen that has diffused to the substrate interface and the Si from the substrate, the interfacial nitrogen was 'pushed' away from the interface by the newly formed SiO_2 . Depth profiles obtained using SIMS on these four samples are shown in Fig. 1. In effect, the amount of nitrogen originally present at the interface was now present in the 'bulk' of the oxide, making it perfectly amenable to quantification by the conventional approach of using an ion implanted standard of N in SiO_2 . By doing so, the amount of N origi-

nally at the interface (stated in terms of an areal density in units of atoms/cm²) was back-calibrated using the areal density determined in the bulk of the oxide layer. It was observed that this matrix effect was approximately $3 \times$. Subsequently, the original nitrided oxide film (not reoxidized) had a calibrated amount of N, and could be used as a standard for quantifying the N in unknown gate oxide films in which the N is located at the interface. A fully quantified depth profile of the calibrated nitrided oxide standard is shown in Fig. 2.

Using this instrumental protocol for N analysis, a nitrided oxide film was chosen as a 'statistical process control' (SPC) sample, for use in determining the long-term precision of the measurement. For every set of analyses, the calibrated nitrided oxide standard would be analyzed, and the RSF generated

from this analysis was used to obtain the peak concentration of the N located at the SiO₂/Si interface of the SPC sample. This measurement was repeated on a regular basis for a time period of 18 months. An SPC chart was generated, and is shown in Fig. 3. It was determined that the precision of this measurement, as expressed in terms of the relative standard deviation (1σ), was better than 9%. The precision of a single set of measurements made in one day would be expected to be in the 1–2% range.

4. Applications

Cesium cluster ion SIMS has been utilized for the measurement of N in nitrided oxide films fabricated using a variety of oxide growth and nitridation con-

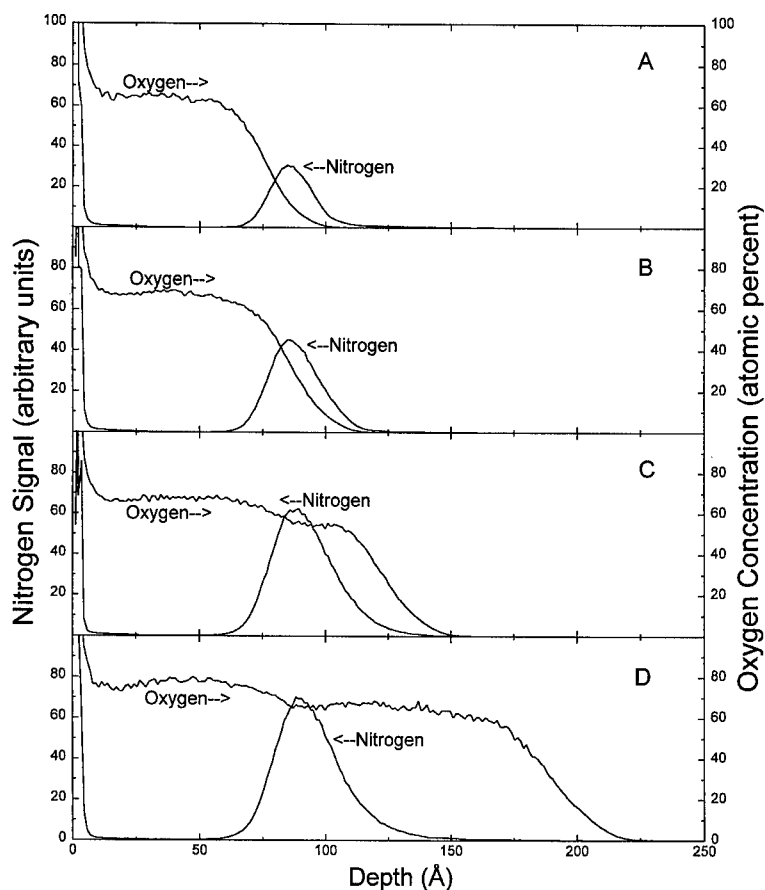


Fig. 1.

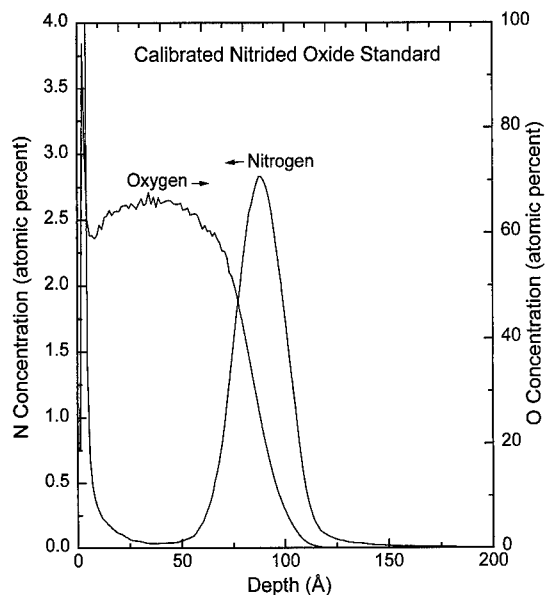


Fig. 2.

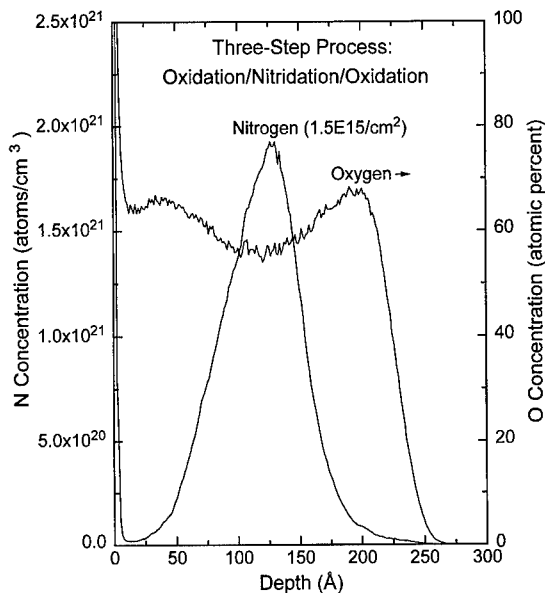


Fig. 4.

ditions. These studies proved useful for the researchers and engineers involved by allowing them to better understand these processes. A few of the studies are discussed below.

In Fig. 4, the depth profile for N shows, much like that shown above for the example showing the matrix effect, that during reoxidation, the N that originally accumulated at or near SiO_2/Si interface was removed from the interface and finally resides

near midfilm. This type of layer structure has excellent interpoly silicon dielectric characteristics, when used in an EPROM application. From a characterization standpoint, this SIMS technique provided the high depth resolution necessary to observe the location of the N.

Due to the depth resolving capability of this method, it was also possible to learn that the final position of N incorporated using different process sequences can differ slightly. Fig. 5 is a comparison of the N depth profiles resulting from (i) growth in N_2O followed by an anneal in O_2 and (ii) oxide growth in O_2 followed by N_2O anneal. The final oxide thickness of these two films was approximately equivalent. The location of the N resulting from (i) is shallower by the thickness of the oxide grown in the O_2 annealing step.

The minimum SiO_2 film thickness that can be measured using Cs cluster ion SIMS is limited by the depth resolution of this technique, which is in the 15–20 Å range. Another potential problem is that the signal from adventitious N on the surface can overlap the N from nitridation. In Fig. 6, an overlay of five N profiles is presented. These samples each received the same nitridation treatment, but the preceding oxidation steps involved varying oxidation

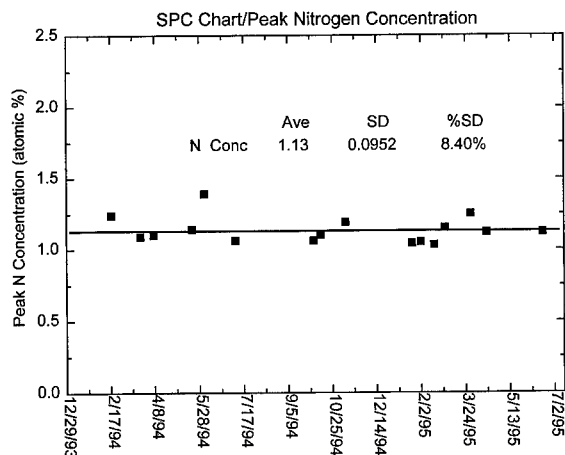


Fig. 3.

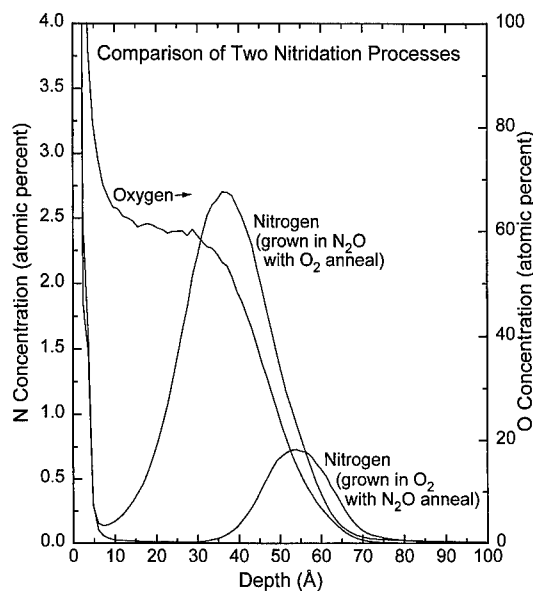


Fig. 5.

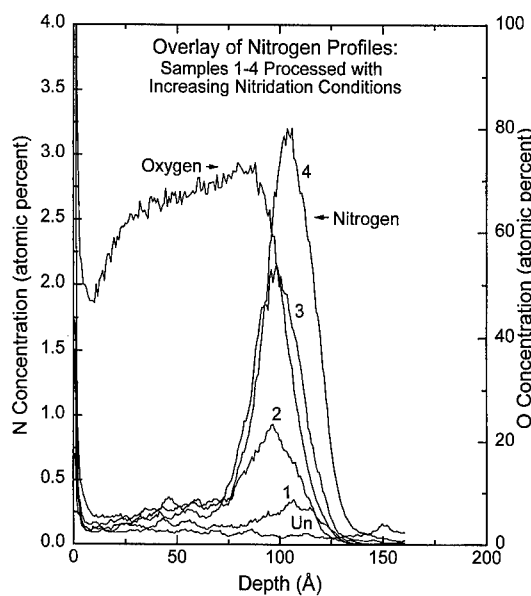


Fig. 7.

times, resulting in different oxide film thicknesses. The N in sample 1, which has an oxide thickness in the range of the depth resolution of the technique, is not well resolved from N surface contamination.

However, the oxides for samples 2–5 are thicker, allowing for adequate resolution of the N profile.

For process optimization in MOS technology, it is imperative that there be empirical understanding of the chemical composition of the gate dielectric layer. By correlating the electrical performance of the gate oxides with the variation in N resulting from iterative nitridation treatments, one can draw substantive conclusions concerning the optimum process, as well as document the process itself. A range of nitridation processing conditions was used to produce the N profiles shown in Fig. 7. From these data, the manufacturing engineer was able to determine the ideal process flow.

5. Conclusions

Secondary ion mass spectrometry can be used to obtain high-depth-resolution depth profiles of N in nitrided oxide layers. Under low energy Cs bombardment, secondary sputtered species clustered with Cs provide high sensitivity for N. Using a carefully developed instrument protocol, including the use of a specially-calibrated standard, high accuracy and precision are also obtained.

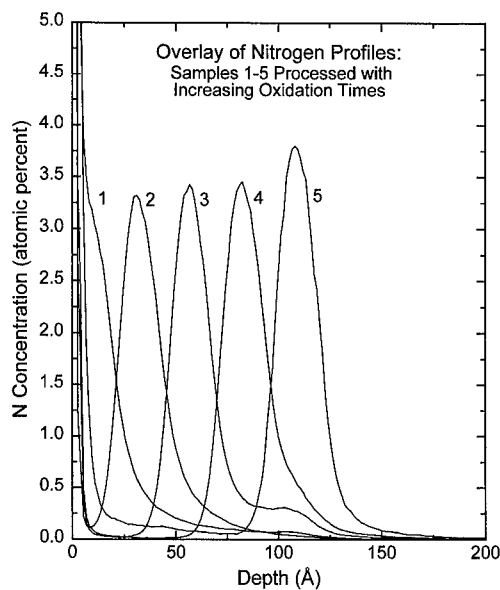


Fig. 6.

Acknowledgements

The authors would like to thank R. Hegde of Motorola and B. Harrington and S. Novak of Evans East for many helpful discussions.

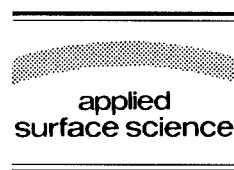
References

- [1] S.V. Hattangady, H. Niimi and G. Lucovsky, *Appl. Phys. Lett.* 66 (1995) 3495.
- [2] J. Ahn, W. Ting, T. Chu, S. Lin and D.L. Kwong, *Appl. Phys. Lett.* 59 (1991) 283.
- [3] E.C. Carr and R.A. Buhrman, *Appl. Phys. Lett.* 63 (1993) 54.
- [4] H.T. Tang, W.N. Lennard, M. Zinke-Allmang, I.V. Mitchell, L.C. Feldman, M.L. Green and D. Brasen, *Appl. Phys. Lett.* 64 (1994) 3473.
- [5] I. Banerjee, M.R. Frost, P.W. Davies, J.N. Cox and R.G. Downing, in: *Proc. SIMS VII* (Wiley, New York, 1990) p. 235.
- [6] A.T. Wu, V. Murali, N. Cox, M.R. Frost, B. Triplett and T.Y. Chan, *Appl. Phys. Lett.* 55 (1989) 1665.
- [7] C.W. Magee, W.L. Harrington and E.M. Botnick, *Int. J. Mass Spectrosc. Ion Proc.* 103 (1990) 45.
- [8] Y. Gao, *J. Appl. Phys.* 64 (1988) 3760.



ELSEVIER

Applied Surface Science 104/105 (1996) 385–391



Plasma assisted oxidation of SiGe layers at 500°C: interface characterization

C. Tételin ^{a,1}, X. Wallart ^{a,*}, L. Vescan ^b, J.P. Nys ^a

^a Institut d'Electronique et de Microélectronique du Nord, U.M.R. C.N.R.S. 9929, Département I.S.E.N., B.P. 69, 59652 Villeneuve d'Ascq Cédex, France

^b Institut Für Schicht und Ionentechnik, Forschungszentrum, Jülich GmbH, D-52425 Jülich, Germany

Received 28 June 1995; accepted 20 November 1995

Abstract

In this paper, we investigate the germanium behaviour during the low temperature plasma assisted oxidation of strained epitaxial $\text{Si}_{1-x}\text{Ge}_x$ ($x = 0.05, 0.1$ and 0.2) layers. For an oxidation temperature of 500°C and an oxide thickness between 80 and 350 Å, using Auger depth profiling, we find that the oxidation process leads to the formation of a pure SiO_2 top layer and the rejection of Ge at the oxide/alloy interface. Taking into account in a suitable way the broadening effects affecting the Auger profiles, we show that a pure Ge layer is formed at the interface. For longer oxidation times, this interfacial layer reaches a 'critical' thickness which is found to be independent of the germanium concentration of the SiGe substrate. Then, some germanium atoms begin to be embedded in the SiO_2 layer before starting to be oxidized.

1. Introduction

SiGe alloys offer the opportunity to grow new heterostructure based devices such as the heterojunction base transistor (HBT) [1,2], as well as to improve existing ones such as pMOS transistors [3,4] in silicon technology. However, in order to use SiGe alloys in Si-based devices, it is of primary importance to study the oxidation of these alloys since it is a major step in Si technology. Moreover, since silicon oxidation has been studied for a long time, it is of physical interest to compare the basic physical

phenomena involved in both silicon and SiGe oxidation.

Investigations performed so far on SiGe oxidation have been mainly concerned with thermal oxidation and have shown different behaviours depending on the oxidation conditions and alloy composition. In the case of wet oxidation, for Ge concentrations below 50%, a pure SiO_2 layer is formed and a Ge pileup occurs at the SiO_2 /SiGe interface [5]. For Ge concentrations above 50%, both Si and Ge are first oxidized. Then, when the oxide layer reaches a given thickness, the oxygen concentration at the reactive interface becomes so low that only Si is oxidized and Ge starts to pile up in a mechanism similar to the low Ge content case [6,7]. As a more general rule, the nature of the oxide formed depends on whether thermodynamic or kinetic factors dominate. The thermodynamic factors lead to SiO_2 formation with

* Corresponding author.

¹ Present address: Institut Supérieur d'Electronique de la Méditerranée, ISEM Maison des Technologies, Place G. Pompidou, 83000 Toulon, France.

a rejection of Ge while when the kinetic dominates, the oxide formed is a mixture containing both SiO_2 and GeO_2 [8]. In case a SiO_2 layer is formed, an increase by a factor of about 2 of the oxidation rate in the linear regime of SiGe compared to Si is observed. This increase has been explained by the presence of the Ge rich layer at the interface [5,9–11].

As regards dry oxidation, the formation of a SiO_2 top layer with a Ge pile up at the interface has been reported too [7,11,12]. However, no increase of the oxidation rate of SiGe alloys with respect to Si has been noted although a Ge rich layer is present at the interface. LeGoues et al. [5] have tentatively explained this discrepancy by considering the important difference in oxidation rates between dry and wet oxidation. Following them, the Ge rich interfacial layer would prevent interstitials formation, which is the limiting factor in wet oxidation but not in dry oxidation which is much slower. On the other hand, electrical $C(V)$ measurements reveal that this Ge rich interfacial layer probably accounts for the rather high interfacial defects densities measured [5,13–15]. However, up to now, little interest has been devoted to accurately describe the precise composition and structure of this interfacial layer although its role seems prominent on oxidation kinetics as well as on the electrical properties of the oxides formed.

Finally, thermal oxidation processes implying high temperatures (700–1000°C) are quite questionable when applied to strained SiGe layers since they can undergo dislocations formation and degradation of electrical characteristics under such high temperature treatments. Clearly, low thermal budgets are highly desirable for processing such strained layers. That is why, in this paper, we report on the low temperature plasma-assisted-oxidation of strained SiGe alloys, which has not been much investigated so far [14,19]. Using mainly Auger electron spectroscopy (AES) and Auger depth profiling (ADP), we describe the nature of the oxides formed under such plasma conditions and we focus on the composition of the interfacial layer.

2. Experimental

In this work, we use strained n-type $\text{Si}_{1-x}\text{Ge}_x$ ($x = 0.05, 0.1$ and 0.2) layers grown by chemical

vapour deposition (CVD) at 700°C on n-type Si(100) substrates. The thicknesses of these layers are 360 nm for $\text{Si}_{0.95}\text{Ge}_{0.05}$, 250 nm for $\text{Si}_{0.9}\text{Ge}_{0.1}$ and 73 nm for $\text{Si}_{0.8}\text{Ge}_{0.2}$ [20]. Oxidation is performed at 500°C using an oxygen plasma source (OPS). This OPS consists of a curved quartz tube fitted on an UHV flange in order to allow its introduction in an UHV system (base pressure 3×10^{-10} Torr). A dc plasma is formed in this tube at an oxygen pressure less than 1 Torr and oxidant species can effuse through a submillimeter hole. Auger measurements are carried out using an electron beam energy of 5 keV and a current of 900 nA. Auger Si LVV, Si KLL, Ge LMM and O KLL spectra are acquired in the undifferentiated mode and the peak heights are taken as the signal intensity. For Auger depth profiling, the samples are sputtered by using an ion gun working at 1 keV and $0.1 \mu\text{A}/\text{cm}^2$. During the sputtering and simultaneous AES measurements, the argon pressure is 5×10^{-8} Torr in the analysis chamber. The incidence angles of electron and ion beams are 45° and 60° respectively, referred to the normal in the sample. Before loading in the UHV system, the samples are prepared with a 30 s dip in a $\text{H}_2\text{O}:\text{HF}$ solution with 9:1 volume ratio, rinsed in de-ionized water and blown dry with N_2 . In order to avoid the relaxation of the strained layers, the native oxide is removed by a light ion bombardment instead of high temperature thermal desorption. The samples are then heated at temperatures that do not exceed 600°C until a (2 × 1) surface reconstruction is visible in LEED.

In this study, we make use of Auger depth profiling in order to determine the thickness and composition of the interfacial layer. However, due to broadening effects and variations of the sputtering rate with materials, Auger profiles do not generally give the 'true' in depth concentration profiles. The most visible effect is an apparent broadening, generally described by a resolution function [16] $g(z)$ which affects the shape of the true in depth concentration distribution, $c(z)$. We have chosen a Gaussian resolution function which seems a reasonable approximation in most cases and which is described by only one parameter σ (the standard deviation). The main factors contributing to the total depth resolution $\Delta z_T = 2\sigma$ are: the Auger electron escape depth λ , the atomic mixing, the primary ion implantation and

sputtering erosion processes. Each factor gives rise to its own depth resolution which can be evaluated in the case we know all the parameters involved. The total depth resolution Δz_T associated with the depth z could then be taken as the sum of all the squared uncertainties due to the factors mentioned above. In this work, considering the depth range we are going to work (between 80 and 350 Å), the energy and angle of ion beam, we have taken into account only two types of broadening effects: the Auger electron escape depth and the atomic mixing. Then, the total depth resolution can be approximated by [16]:

$$\Delta z_T = 2\sigma = \sqrt{(1.6\lambda)^2 + kz} \quad (1)$$

In Eq. (1), λ is the Auger electron escape depth and z is the depth. Since the atomic mixing is approximately the same in the SiO_2 and SiGe [16], we have determined the parameter k using a sample consisting of 73 nm $\text{Si}_{0.8}\text{Ge}_{0.2}$ on Si. This sample is known to present a sharp interface so that we can measure the total depth resolution associated with a 73 nm depth. Calculating the electron escape depth for Ge in SiGe with the Seah and Dench formula [17], we have then determined the value of k ($k = 16$ Å). Taking into account this value and the depth range under study in this work (80–350 Å), the contributions to the depth resolution due to the escape depth and the atomic mixing are then of the same order of magnitude. This reinforces the choice we make of a Gaussian resolution function [16].

Once a good approximation of the total depth resolution is obtained, an estimated model for the true concentration profile is built. The validity of the model is then tested by making the convolution with the appropriate gaussian function. The result is then compared with the measured profile. In order to compare the experimental and simulated Ge Auger profiles, the experimental Ge Auger intensity is normalized to that in pure Ge. We choose this simple procedure since for SiGe alloys, it gives the right Ge content when compared to RBS or XRD measurements.

Finally, we have tested the whole procedure on a test sample consisting of a 10 Å pure Ge epitaxially grown layer on Si(100) and covered with a 100 Å thick epitaxial Si layer. The best fit we find (Fig. 1) in this case is for a Ge content of 100% and a

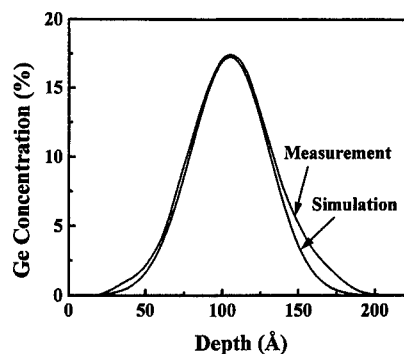


Fig. 1. Comparison between measured Auger profile and simulated one for the following structure: 100 Å Si/10 Å Ge/Si substrate.

thickness of 11 Å which validates our fitting procedure. Complementary details on the fitting procedure can be found elsewhere [21].

3. Results and discussion

In this section, we present results relative to oxidized strained SiGe layers on Si(100) with three Ge contents (5, 10 and 20 at% Ge) and for different oxidation times at 500°C. Fig. 2 shows a typical Auger profile recorded after short oxidation time (< 1 h) of a $\text{Si}_{0.8}\text{Ge}_{0.2}$ layer. The general trends observed on this profile are similar for all samples discussed here. More precisely, we can note the formation of a top oxide layer. The associated Si KLL Auger line exhibits a chemical shift (~ 10 eV

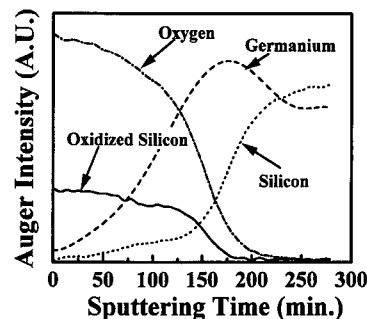


Fig. 2. Typical Auger depth profile measured after plasma oxidation of $\text{Si}_{0.8}\text{Ge}_{0.2}$ layer at 500°C. The Auger lines represented are O KLL, Ge LMM and Si LVV in the oxidized and non-oxidized state.

towards lower kinetic energies with respect to pure silicon), corresponding to silicon dioxide, and no evidence of the presence of germanium has been detected. Below this SiO_2 layer, the profile of Fig. 1 evidences the presence of a Ge rich interface layer. The germanium oxidation state will be determined using the energy shift of the Ge LMM Auger line recorded at this interface with respect to pure germanium. The following is concerned with the precise determination of the composition and width of this interface layer.

In order to compare the experimental Auger profile measured on these samples with reconstructed ones, we have first transformed the time scale into a thickness one. In this work, the samples studied consist of three distinct composition layers. The top layer is pure SiO_2 where the concentrations of the elements are constant. The next layer is a 'transition' region where all the concentrations change. Lastly, the third region represents the bulk SiGe layer. As the compositions do not vary in the first and third regions, the sputtering rates are constant in these regions. We have measured them using reference samples: one with 50 nm of thermally grown SiO_2 layer on Si and an other with 73 nm $\text{Si}_{0.8}\text{Ge}_{0.2}$ layer grown on Si. Concerning the transition region, as its extension is not very large and as the two measured sputtering rates are close together ($V_{\text{SiO}_2} = 0.64$ Å/min and $V_{\text{SiGe}} = 0.71$ Å/min), we have chosen a linear variation of the sputtering rate from V_{SiO_2} at the beginning of this region to V_{SiGe} at the end of this region. After this scale transformation is done, we determine the oxide thickness, d_{oxm} , for each sample. In order to do this, we estimate the interface position at the thickness for which the oxygen Auger intensity is half its value in pure SiO_2 . Then, we fit these experimental profiles with simulated ones us-

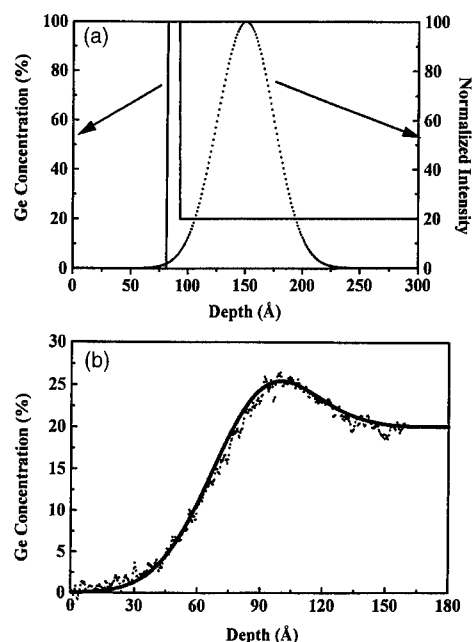


Fig. 3. (a) Representation of the Gaussian resolution function and Ge profile used for the convolution in the model. (b) Comparison between the experimental Ge profile (dotted line) and the simulated one (full line).

ing the method detailed in the previous section. In Table 1, we have summarized the parameters used in our fitting procedure.

For instance, we consider the case of an 80 Å thick oxide layer on SiGe 20%. Fig. 3a shows the step function corresponding to the Ge concentration profile and the broadening Gaussian function used to obtain the best fit presented on Fig. 3b. The excellent agreement between the experimental and simulated Ge profile observed in Fig. 3b is common for all the samples obtained after short oxidation times at 500°C. This strongly supports the assumption of a step like

Table 1

Parameters used in the fitting procedure together with the independently estimated ones

Notation	Signification
C_{GeT}	germanium concentration at the SiO_2/SiGe interface (calculated by the simulation code)
L	Ge-rich interface width (calculated by the simulation code)
d_{oxf}	oxide thickness (calculated by the simulation code)
σ_f	standard deviation of the Gaussian resolution function (calculated by the simulation code)
σ	standard deviation of the Gaussian resolution function (independently estimated using Eq. (1))
d_{oxm}	oxide thickness experimentally measured using Auger intensities

function for the Ge profile that we make. Applying the same method to other samples leads to the results presented in Table 2. In this table, d_{oxm} is the oxide thickness measured on the profile whereas d_{oxf} is the oxide thickness, C_{GeT} is the Ge concentration in the interface layer, L is the width of this layer and σ_f the standard deviation of the Gaussian resolution function determined by the fit.

From these results, a point to be discussed is the value of the standard deviation of the Gaussian function σ . For increasing oxide thickness, the σ_f value found by the fit increases too as expected from Eq. (1). Moreover, we can note that for two different samples with different Ge content and the same oxide thickness, the two corresponding values of σ_f are very close. As the values of σ_f found by the fit are close to the calculated ones (Eq. (1)), it shows that the broadening effect is rather well estimated in our treatment. This in turn validates the values of C_{GeT} and L found within our model. Indeed, a significant variation of C_{GeT} with respect to those reported in Table 2, would lead to very different values of σ_f which would no more be in agreement with the calculated ones.

As regards the first step of oxidation of SiGe layers, the most important result in Table 2 are the C_{GeT} values. Indeed, whatever the samples studied here, this concentration lies always above 95%. It means that when a pure SiO_2 layer is formed, the rejection of Ge from the growing oxide leads first to the formation of a pure Ge layer at the interface. This conclusion is of primary interest in order to explain the difference observed in the oxidation kinetics between Si and SiGe in the linear regime.

Table 2

Results obtained by fitting the simulated Ge profiles to the experimental ones for three Ge contents and different oxidation times at 500°C

Sample composition	d_{oxm} (Å)	d_{oxf} (Å)	C_{GeT}	L (Å)	σ (Å)	σ_f (Å)
$\text{Si}_{0.9}\text{Ge}_{0.1}$	81	78	1	4.5	24.5	24.2
$\text{Si}_{0.95}\text{Ge}_{0.05}$	81	84	1	2	24.5	24.6
$\text{Si}_{0.8}\text{Ge}_{0.2}$	79	81	1	11	24.3	24.5
$\text{Si}_{0.8}\text{Ge}_{0.2}$	100	98	1	13	26	26
$\text{Si}_{0.9}\text{Ge}_{0.1}$	124	120	1	6.5	27.8	26.5
$\text{Si}_{0.95}\text{Ge}_{0.05}$	174	176	1	4	31.2	31
$\text{Si}_{0.9}\text{Ge}_{0.1}$	201	193	1	10.5	32.9	33.5

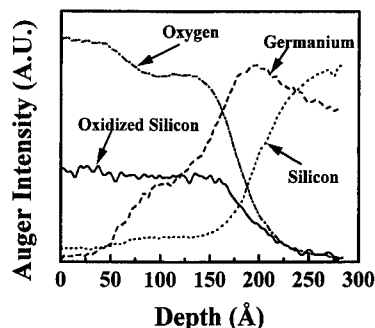


Fig. 4. Auger depth profile measured after plasma oxidation of a $\text{Si}_{0.8}\text{Ge}_{0.2}$ layer at 500°C. The interfacial region can be divided in two parts. The first part, near the substrate, is a pure Ge layer. The second part shows the Ge incorporation in the SiO_2 layer.

Indeed, in this regime, the oxidation rate is mainly limited by the interface reactions. One can expect the presence of a pure Ge layer at the interface to strongly modify these reactions with respect to the case of pure Si.

Fig. 4 shows the Auger profile obtained after one hour oxidation of a SiGe 20% sample at 500°C. As in the previous cases, for shorter oxidation times, the top layer consists of a pure SiO_2 layer with no evidence of the presence of Ge. There is always a transition region between this layer and the underlying SiGe substrate. The difference is that in this case, our profile simulation code does not succeed to provide a good fit. Indeed, as we can see in Fig. 4, it is quite evident that the germanium profile can no more be fitted by the convolution between a Gaussian function and a simple step like concentration profile. The interface region can be divided in two parts. The first part, adjacent to the SiO_2 layer, is made of silicon dioxide containing some germanium ($\sim 10\%$). The Ge LMM Auger line recorded in this region shows that the germanium is in its elemental state (not oxidized). The second part, next to the SiGe substrate exhibits the same Auger profile characteristics than the interface layer formed after shorter oxidation time. We can then suppose that this region is a layer containing almost pure germanium. The same interface behaviour (i.e. incorporation of elemental Ge in the silicon dioxide) has been observed with the $\text{Si}_{0.9}\text{Ge}_{0.1}$ and $\text{Si}_{0.95}\text{Ge}_{0.05}$ substrates but after 2 and 4 h oxidation respectively. This tends to demonstrate that the incorporation of germanium in

SiO_2 occurs once the pure Ge interfacial layer reaches a 'critical' thickness. This thickness corresponding to the transition between formation of a pure SiO_2 layer with complete rejection of Ge at the interface and the beginning of Ge incorporation in the oxide has been measured. Its value is around 10 or 11 Å and is independent of the concentration of Ge in the SiGe substrates used in this study. In a paper dealing with thermal oxidation of SiGe layers with SiO_2 formation [5], LeGoues et al. have demonstrated by TEM measurements that the Ge rich interfacial layer could be for thin SiO_2 layers perfectly commensurate with underlying SiGe. As the thickness of this enriched layer increases, they supposed that it would become energetically more favorable to generate dislocations between the enriched layer and the SiGe substrate. In a more recent work, Cracium et al. [18] have studied the low temperature (550°C) UV-assisted oxidation of SiGe (20% Ge) leading to the formation of SiO_2 with rejection of Ge at the oxide/substrate interface. TEM measurements have been performed concluding that even at such a low oxidation temperature the interface layer is crystalline and completely commensurate with the SiGe substrate. Using Auger depth profile, they observed that, for long oxidation time, a small amount of Ge was incorporated in the silicon dioxide layer. They performed high-resolution X-TEM measurements and they concluded that this Ge forms Ge or Ge-rich SiGe microcrystals. From these two studies, we can suppose that in our oxidation configuration the pure Ge interface layer formed in a first time has a crystalline structure and is commensurate with the SiGe substrate. If it were actually the case, the dislocation formation observed by LeGoues et al. or the formation of microcrystals embedded in the SiO_2 layer described by Cracium et al. could be related to the incorporation of Ge in the oxide we have observed in our study. The fact that this incorporation occurs always when the same amount of Ge is segregated at the interface seems to act along the same lines. Such formation of microcrystalline Ge inclusions in SiO_2 has also been reported by Liu et al. upon the reduction of a mixed oxide SiGeO_2 [22].

Fig. 5 shows the Auger depth profile obtained after two hours oxidation of $\text{Si}_{0.8}\text{Ge}_{0.2}$ at 500°C. As in the profile shown in Fig. 4, we form a pure SiO_2 top layer with rejection of Ge at the oxide/substrate

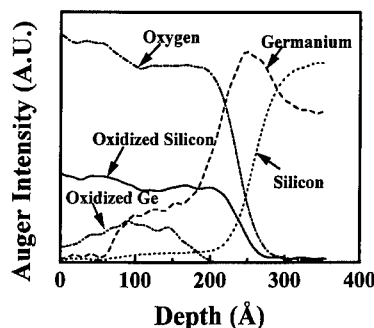


Fig. 5. Auger depth profile measured after plasma oxidation of a $\text{Si}_{0.8}\text{Ge}_{0.2}$ layer at 500°C. The Ge LMM in an oxidized state is represented indicating that the Ge embedded in the SiO_2 layer starts to be oxidized.

interface. This interface can be again divided in two parts. A first part close to the SiGe substrate is made of pure Ge and its extension is around 10 or 11 Å. The second part consists of a SiO_2 layer with some Ge embedded in. The main difference with the profile presented in Fig. 4 is that according to the Ge LMM Auger line, the germanium found in the SiO_2 layer begins to be oxidized. The presence of an energy shift (~ 9 eV towards lower kinetic energies) indicates the presence of some germanium atoms in a fully oxidized state. The fact that we do not start to oxidize the germanium right at the beginning of the oxidation process (when the oxygen flux is maximum), but only after a 'critical' amount of Ge has been segregated at the interface can be explained as follow. In the first step of the SiGe oxidation, the oxidant species can react with silicon and/or germanium atoms. As it is energetically more favorable to form SiO_2 than GeO_2 (-234.5 kcal/mol for SiO_2 and -153.2 kcal/mol for GeO_2 [12]), the oxide formed is pure SiO_2 and the germanium atoms are rejected at the interface. However, after long oxidation time, there are some germanium atoms embedded in SiO_2 . The oxidant species diffusing across the SiO_2 layer then react with these Ge atoms before they reach the reactive interface and the silicon atoms.

4. Conclusion

In this study, we have shown that during plasma-assisted-oxidation of $\text{Si}_{1-x}\text{Ge}_x$ ($x = 0.05, 0.1, 0.2$)

at 500°C, a pure SiO₂ layer is formed with rejection of Ge at the interface. Using reference samples and proper treatments, we have estimated quite precisely the influence of broadening effects on Auger profiles. Taking then these effects into account, we have been able to recover the 'true' germanium profile in our layers. This allows us to conclude that Ge from the alloy piles up forming a pure Ge layer at the oxide/alloy interface during oxidation. After longer oxidation time, the interfacial Ge pure layer reaches a 'critical' width (between 10 and 11 Å). This width is found to be independent of the substrate germanium concentration (within the range under study here). Once this interfacial thickness is reached, Ge starts to be embedded in the SiO₂ layer when the thickness of the Ge pure layer remains constant. Then, the germanium atoms embedded in the SiO₂ layer start to be oxidized.

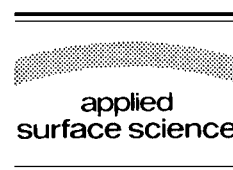
References

- [1] R. People, *IEEE J. Quantum Electron.* QE-22 (1986) 1696.
- [2] S.S. Iyer, G.L. Patton, J.M.C. Stork, B.S. Meyerson and D.L. Harame, *IEEE Trans. Electron Devices* ED-36 (1989) 2043.
- [3] Y.H. Xie, E.A. Fitzgerald, D. Monroe, G.P. Watson and P.J. Silverman, *Jpn. J. Appl. Phys.* 33 (1994) 2372.
- [4] S.S. Iyer, P.M. Solomon, V.P. Kesan, A.A. Bright, J.L. Freeouf, T.N. Nguyen and A.C. Warren *IEEE Electron Device Lett.* EDL-12 (1991) 246.
- [5] F.K. LeGoues, R. Rosenberg, T.N. Nguyen, F. Himpsel and B.S. Meyerson, *J. Appl. Phys.* 65 (1989) 1724.
- [6] J. Eugène, F.K. LeGoues, V.P. Kesan, S.S. Iyer and F.M. d'Heurle, *Appl. Phys. Lett.* 59 (1991) 78.
- [7] H.K. Liou, P. Mei, V. Gennser and E.S. Yang, *Appl. Phys. Lett.* 59 (1991) 1200.
- [8] E.C. Frey, N. Yu, B. Patnaik, N.R. Parikh, M.L. Swanson and W.K. Chu, *J. Appl. Phys.* 74 (1993) 4750.
- [9] D. Fathy, O.W. Holland and C.W. White, *Appl. Phys. Lett.* 51 (1987) 1337.
- [10] O.W. Holland, C.W. White and D. Fathy, *Appl. Phys. Lett.* 51 (1987) 520.
- [11] F.K. LeGoues, R. Rosenberg and B.S. Meyerson, *Appl. Phys. Lett.* 54 (1989) 644.
- [12] D.C. Paine, C. Caragianis and A.F. Schwartzman, *J. Appl. Phys.* 70 (1991) 5076.
- [13] D.K. Nayak, K. Kamjoo, J.S. Park, J.C.S. Woo and K.L. Wang, *Appl. Phys. Lett.* 57 (1990) 369.
- [14] P.W. Li and E.S. Yang, *Appl. Phys. Lett.* 63 (1993) 2938.
- [15] C. Caragianis, Y. Shigesato and D.C. Paine, *J. Electron. Mater.* 25 (1994) 883.
- [16] S. Hofman, *Prog. Surf. Sci.* 36 (1991) 35.
- [17] M.P. Seah and W.A. Dench, *Surf. Interf. Anal.* 1 (1979) 2.
- [18] V. Craciun, I.W. Boyd, A.H. Reader, W.J. Kersten, F.J.G. Hakkens, P.H. Oosting and D.E.W. Vandenhoudt, *J. Appl. Phys.* 75 (1994) 1972.
- [19] M. Mukhopadhyay, S.K. Ray, C.K. Maiti, D.K. Nayak and Y. Shiraki, *Appl. Phys. Lett.* 65 (1994) 895.
- [20] L. Vescan, W. Jäger, C. Dieker, K. Schmidt, A. Hartmann and H. Lüth, *Mater. Res. Soc. Symp.* 263 (1992) 23.
- [21] C. Tételin, X. Wallart, J.P. Nys and L. Vescan, *Surf. Interf. Anal.* 23 (1995) 363.
- [22] W.S. Liu, J.S. Chen, M.A. Nicolet, V. Arbet-Engels and K.L. Wang, *Appl. Phys. Lett.* 62 (1993) 3321.



ELSEVIER

Applied Surface Science 104/105 (1996) 392–401



Diffraction spot profile analysis for heteroepitaxial surfaces applied to the initial growth stages of CaF_2 adlayers on $\text{Si}(111)$

Joachim Wollschläger^{*}, Andreas Meier

Institut für Festkörperphysik, Universität Hannover, Appelstrasse 2, D-30167 Hannover, Germany

Received 28 June 1995; accepted 25 October 1995

Abstract

We have studied the heteroepitaxial growth of CaF_2 on $\text{Si}(111)$ by high resolution low energy electron diffraction. Analysing spot profiles recorded during CaF_2 deposition (SPA-LEED) we obtained information about the film morphology. The spots show a central spike and diffuse shoulder caused by atomic steps of the CaF_2 film. In order to evaluate quantitatively the layer distribution from the intensity oscillations of the central spike at the out-of-phase condition we included the interference between substrate and adlayer in our analysis. Depositing CaF_2 at 300°C we conclude from the central spike intensity that the nucleation of the second CaF_2 layer starts immediately. We attribute this behaviour to the poor binding of the CaF_2 molecules to the 7×7 substrate so that obviously the nucleation at surface defects (atomic steps, anti-phase boundaries) is favoured. The analysis of the central spike oscillations also reveals that the film grows in the multi layer growth mode at higher coverages.

1. Introduction

The epitaxial growth of insulating films on semiconductors receives more and more attention because these films are well suited to design electronic devices, for instance to fabricate three dimensional integrated circuits. First, one has to grow insulating films of good quality before one can deposit metallic or semiconducting material on top of it. On the other hand growing multi layers on a nanometer scale also opens the possibility to build electronic devices with new properties. Here quantum effects (e.g. discrete spectrum of energy levels, electron tunneling) will play a very important role. Of course, one also needs epitaxial defect free insulating layers to obtain well

working quantum devices. For instance pin holes for insulating layers could short circuit two adjacent metallic or semiconduction layers so that quantum effects would be immediately destroyed.

For epitaxial insulating adlayers on silicon CaF_2 is a very good candidate since the misfit between CaF_2 and Si is less than 0.5% at room temperature. CaF_2 grows with the (111) surface because this is the non-polar surface of the fluorite structure. Therefore $\text{Si}(111)$ is the best suited substrate for the epitaxial growth of CaF_2 . On the other hand, if one deposits CaF_2 on $\text{Si}(100)$ one obtains a grooved morphology for thin films [1] so that these films may not be closed in the regime of very few atomic layers necessary for quantum devices.

Up to now most morphology studies have been carried out for thin films of some 100 nm thickness [2]. On the other hand recent STM studies focussed

^{*} Corresponding author. Tel.: +49-511-7624830; fax: +49-511-7624877; e-mail: wollj@dynamic.fkp.uni-hannover.de.

their interest on the structure of submonolayer CaF_2 films grown at high substrate temperature [3,4]. From early RBS measurements [5] it is well known that the interface between CaF_2 and Si substrate has the best quality if the CaF_2 is deposited at 700°C. On the other hand, this high process temperature is often disadvantageous to producing electronic devices. Therefore we present here our investigation of the morphology of ultrathin CaF_2 films grown at low temperature.

For this purpose we used a high resolution SPA-LEED instrument because this experimental method has the advantage that one can record the diffraction pattern of the CaF_2 during deposition using an external electron beam gun. From the analysis of the spot profiles one may obtain information about the morphology of the growing film. This method is well established to characterise the growth of homoepitaxial films. On the other hand, there are some complications for heteroepitaxial films because of the different scattering amplitudes of the adlayer and the substrate.

It is well known that for submonolayer heteroepitaxial films the additional diffuse shoulders of the fundamental spots can be used to evaluate the adlayer island size distribution and the adlayer scattering amplitude [6,7]. Previously we reported about the effect of statistically distributed inhomogeneities on rough surfaces [8]. Up to now, no spot analysis for heteroepitaxial films with atomic steps is available. These effects, however, have to be included in the spot profile analysis to evaluate quantitatively the layer distribution of heteroepitaxial films. Therefore we extended the spot profile analysis to include also the nucleation of higher adlayers often observed for low temperature epitaxy.

2. Electron diffraction at heteroepitaxial adlayers

2.1. Basics

For a diffracted electron beam the intensity can be calculated from

$$I(\mathbf{K}, \mathbf{k}_i) = \sum_{n,m} f_n f_m^* e^{i\mathbf{K}(\mathbf{r}_n - \mathbf{r}_m)} \quad (1)$$

where \mathbf{k}_i denotes the wave vector of the incoming

electron wave and \mathbf{K} the scattering vector while f_n is the scattering amplitude of the n th surface atom and all underlying atoms (column approximation) and \mathbf{r}_n denotes its position [9]. Thus, generally, the intensity of a diffracted electron beam depends on both the kind of surface atoms and their positions.

In the following we suppose that heteroepitaxial adlayers grow pseudomorphically so that both the adlayer and the substrate have the same regular lattice for all atoms. On the other hand it is immediately clear that the scattering amplitudes of the substrate and the heteroepitaxial adlayer are different. Furthermore, considering the small penetration depth for low energy electrons, the scattering amplitude of the adlayer depends on the local coverage only during the very first stages of the adlayer deposition supposing the column approximation. For films thicker than some angstroms, however, this coverage dependence vanishes. Overall we conclude that the scattering amplitude depends only on the vertical position of the surface atoms, namely the layer distribution.

Since the specular spot is not very sensitive to the lateral positions of surface atoms it is not affected if the adlayer is laterally non-pseudomorphic [10]. Thus the following spot profile evaluation is also valid for the (00) spot for incommensurate adlayers. On the other hand, there are drastic effects on the higher order spots since, for instance, they are strongly influenced by the lattice constant and lateral defects.

For pseudomorphic adlayers with atomic steps Eq. (1) can be simplified to

$$I(\mathbf{K}, \mathbf{k}_i) = \sum_{\mathbf{r}} \Phi(\mathbf{r}, \mathbf{K}_{\perp}) e^{i\mathbf{K}_{\parallel}\mathbf{r}}, \quad (2)$$

introducing the scattering correlation function

$$\Phi(\mathbf{r}, \mathbf{K}_{\perp}) = \sum_{lh} f_l f_{l+h}^* C_{l,l+h}(\mathbf{r}) e^{id\mathbf{K}_{\perp}h} \quad (3)$$

where d denotes the level distance and \mathbf{r} the lateral distance between atoms while \mathbf{K}_{\perp} and \mathbf{K}_{\parallel} are the scattering vectors perpendicular and parallel to the surface, respectively. The pair correlation $C_{lh}(\mathbf{r})$ is the probability to find one atom at level l and a second atom at level h separated laterally by the distance \mathbf{r} .

Following the spot profile evaluation introduced by Lent and Cohen for stepped homogeneous sur-

faces [11], the pair correlation $C_{lh}(\mathbf{r})$ can be separated into

$$C_{lh}(\mathbf{r}) = p_l p_h [1 - \phi_{lh}(\mathbf{r})] \quad \text{for } l \neq h \quad (4)$$

with $\phi_{lh}(0) = 1$ and $\phi_{lh}(\infty) = 0$. Here

$$p_l = \Theta_l - \Theta_{l+1}$$

denotes the exposed coverage of the l th level. Except for the two fixed values for vanishing and infinity distance the function $\phi_{lh}(\mathbf{r})$ depends only on the details of the surface morphology. Finally, the missing pair correlation $C_{ll}(\mathbf{r})$ can be obtained from

$$C_{ll}(\mathbf{r}) = p_l - \sum_{h \neq l} C_{lh}(\mathbf{r}) \quad (5)$$

because the summation over all possible levels h for the second atom involved in the pair correlation equals the probability p_l to find the first atom at the level l .

Inserting Eqs. (4) and (5) into Eqs. (2) and (3) we obtain the intensity

$$I(\mathbf{K}, \mathbf{k}_i) = I_0(K_{\perp}, \Theta) \sum_{\mathbf{G}_{\parallel}} \delta(\mathbf{K}_{\parallel} - \mathbf{G}_{\parallel}) + I_{\text{diff}}(\mathbf{K}, \Theta). \quad (6)$$

Here \mathbf{G}_{\parallel} denotes the lateral reciprocal scattering vector. The intensity of the delta function like central spikes

$$I_0(K_{\perp}, \Theta) = \left| \langle f_h e^{i d K_{\perp} h} \rangle \right|^2 \quad (7)$$

depends on the average scattering amplitude

$$\langle f_h e^{i d K_{\perp} h} \rangle = \sum_h p_h f_h e^{i d K_{\perp} h}$$

including the scattering condition dK_{\perp} and the layer distribution. On the other hand, the diffuse shoulder

$$I_{\text{diff}}(\mathbf{K}, \Theta) = \sum_{l, h \neq 0} f_l (f_l^* - f_{l+h}^* e^{i d K_{\perp} h}) \times p_l p_{l+h} \Phi_{l, l+h}(\mathbf{K}_{\parallel})$$

contains additionally information about the distribution of atomic adlayer steps. Here $\Phi_{l, l+h}(\mathbf{K}_{\parallel})$ denotes the two dimensional lateral Fourier transform of $\phi_{l, l+h}(\mathbf{r})$. Finally, the total spot intensity

$$I_{\text{total}}(\Theta) = \langle |f_h|^2 \rangle = \sum_h p_h \langle |f_h|^2 \rangle \quad (8)$$

can be evaluated by integrating Eq. (6) over the Brillouin zone.

Experimentally, one can obtain the ratio ρ of the absolute values of the adlayer and the substrate scattering amplitudes

$$\rho = \frac{|f_{\text{ad}}|}{|f_{\text{sub}}|} = \sqrt{\frac{I_{\text{total}}(\Theta \gg 1 \text{ ML})}{I_{\text{total}}(\Theta = 0 \text{ ML})}} \quad (9)$$

by comparing the total intensity before depositing any admaterial and after depositing several adlayers because scattered electrons cannot escape from the buried substrate after growing thick adlayers. Here f_{ad} and f_{sub} denote the scattering amplitudes of the adlayer and the substrate, respectively.

In the following we suppose that the penetration depth is so short that backscattering from the second layer can be neglected. Therefore all exposed adlayer atoms have the same scattering amplitude. Eq. (7) reveals that the intensity of the central spike depends on both the scattering vector K_{\perp} and the scattering amplitudes including the phase shift φ between adlayer and substrate defined by

$$\rho e^{i\varphi} = f_{\text{ad}}/f_{\text{sub}}.$$

Fig. 1 illustrates that the phase difference φ drastically influences the central spike oscillations even

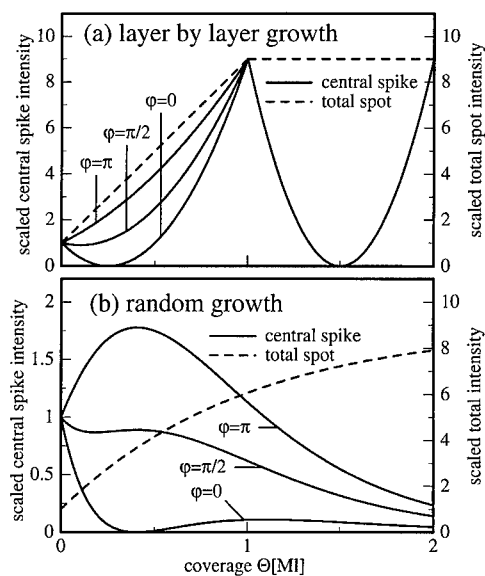


Fig. 1. Intensity oscillation of the central spike for (a) the perfect layer by layer and (b) the random growth mode. Please, note the different scaling used for the central spike intensity evaluated for the random growth mode.

for identical growth conditions. Since we like to obtain information about the morphology from the central spike oscillations we have to check in detail how the intensity is influenced additionally by the inherent scattering amplitude superimposed to the experimentally used out-of-phase scattering condition

$$dK_{\perp}/2\pi = n + \frac{1}{2}$$

where adjacent layers interfere destructively.

2.2. Analysis of the initial central spike oscillation

For the layer by layer growth mode (cf. Fig. 1(a)) parabolic intensity oscillations are observed for the out-of-phase condition. On the one hand, one obtains minima at half covered top layers after depositing more than one monolayer. For homoepitaxial growth conditions this behaviour is also expected during deposition of the first layer. On the other hand, Fig. 1(a) shows that for the heteroepitaxial layer by layer growth the first minimum is shifted to coverages smaller than 0.5 ML if the adlayer scattering amplitude is larger than the substrate scattering amplitude. The minimum shifts into the opposite direction if the adlayer scattering amplitude is smaller than that of the substrate. The parabolic oscillation is caused by the linear dependence of the exposed coverages

$$p_0(\Theta) = 1 - \Theta \quad \text{and} \quad p_1(\Theta) = \Theta \quad (10)$$

on the deposited coverage Θ .

This analysis has been used to evaluate the scattering phase during deposition of the first adlayer [7]. Of course one can apply this analysis only for perfect growth of the first layer. However, it can be checked whether the analysis is correct because there is a one to one relationship between the critical coverage Θ^* where the minimum appears and the intensity expected for this coverage (cf. Fig. 2). Thus after obtaining the ratio ρ of the absolute scattering amplitudes one has to check the minimum intensity for the phase shift evaluated from the critical coverage Θ^* . Fig. 2 reveals that the intensity vanishes only for the critical coverage

$$\Theta^* = 1/(1 + \rho)$$

and vanishing phase shift $\varphi = 0$.

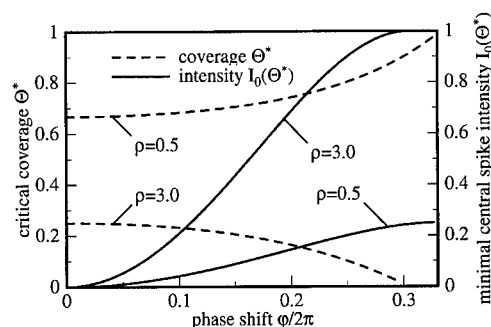


Fig. 2. Phase shift dependence of the critical coverage Θ^* for minimal central spike intensity and the minimal intensity. Generally, with increasing phase shift the critical coverage shifts to lower values for $\rho > 1$ while the minimal intensity increases. On the other hand, the critical coverage increases for $\rho < 1$.

Supposing that the adlayer grows in the random growth mode with Poisson distributed exposed layers Fig. 1(b) illustrates that the intensity is influenced drastically even while depositing the first monolayer because of the nucleation of the higher levels before the first layer is closed. While for $\varphi = 0$ the coverage for the intensity minimum shifts, the curvature of the intensity switches even for $\varphi = \pi$. Additionally, Fig. 1 shows that the total spot intensity depends on the growth mode. The total intensity increases more smoothly if the adlayer does not grow in the layer by layer growth mode because the substrate is less perfectly covered by the adlayer with the larger scattering amplitude.

On the one hand, in experiments one often observes a parabolic behaviour of the central spike at the very beginning of the adlayer deposition as reported recently for perfect substrate wetting. On the other hand the position and the intensity of the minimum does not fit to the perfect layer by layer growth. Thus, one has to include that the second layer is populated before closing of the first layer. The parabolic behaviour shows that both the exposed coverages of the first and the second layer increase almost linearly with deposited coverage. Therefore we extend Eq. (10) to

$$\Theta_1(\Theta) = (1 - \alpha)\Theta \quad \text{and} \quad \Theta_2(\Theta) = \alpha\Theta \quad (11)$$

where $\alpha = \Theta_2/\Theta$ denotes the relative second layer coverage.

Fig. 3 shows that for vanishing phase shift between substrate and adlayer ($\varphi = 0$), the minimum

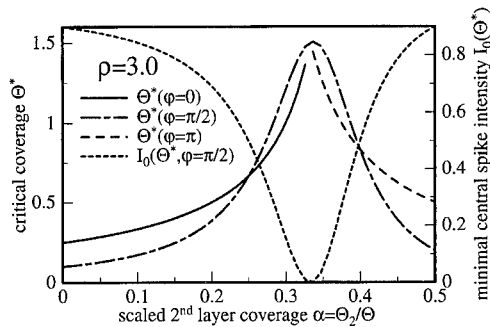


Fig. 3. Dependence of the critical coverage Θ^* for minimal central spike intensity if the second layer grows in competition to the first. For $\varphi = 0$ the constructive interference between second layer and substrate increases the critical coverage Θ^* necessary to obtain minimal intensity. For $\varphi = \pi$ the situation is vice versa. For $\varphi = \pi/2$ the intensity is shown in addition to the critical coverage.

shifts to larger critical coverages Θ^* with increasing scaled second layer coverage α . The second layer nucleation α , however, cannot exceed the value $\alpha = \frac{1}{3}$ to obtain a minimum because for larger values the *constructive* interference of the second layer and the substrate overwhelm the *destructive* interference of both with the first adlayer. The opposite is true for $\varphi = \pi$ where the substrate and the first adlayer interfere constructively. In this case the second layer coverage has to be large to cancel this constructive interference effect. For both scattering phases, however, the intensity at the minimum always vanishes because of the total destructive interference.

If the phase shift is neither constructive nor destructive one observes also a minimum. Generally, however, the intensity at the minimum does not vanish because one cannot obtain total destructive interference from *all* layers. For $\varphi = \pi/2$ Fig. 3 shows that the minimum intensity vanishes only for $\alpha = \frac{1}{3}$ and $\Theta^* = 1.5$ ML so that half a monolayer is grown on top of the closed first layer. Also, for all other scattering phases (except in- and out-of-phase) and all absolute amplitudes we find that this is the only layer distribution where total interference can be obtained since for different layer distributions the substrate scattering disturbs seriously the destructive diffraction effects.

Thus from both the critical coverage Θ^* for minimal intensity and the central spike intensity at this coverage one can obtain the adlayer phase shift

and the second layer coverage. At first sight this seems to be a drastic limitation to confine the analysis to two simultaneously growing adlayers. Therefore, we checked our simple model by analysing the central spike oscillations for the random growth mode shown in Fig. 1(b). Intensity minima appear at $\Theta^* = 0.40$ with $I_0(\Theta^*) = 0$ and $\Theta^* = 0.18$ with $I_0(\Theta^*) = 0.87$ implying scaled second layer coverages $\alpha = 0.15$ and $\alpha = 0.10$ for scattering phases $\varphi = 0$ and $\varphi = \pi/2$, respectively. Already the coverage dependence of α shows that the second layer does not increase linearly with the total coverage as supposed for our simple model. Nevertheless, our analysis shows almost the exact values of $\alpha = 0.15$ and $\alpha = 0.08$ with $I_0(\Theta^*) = 0.84$ for the scaled second layer coverage and the intensity (cf. Fig. 1).

2.3. Analysis of the full central spike oscillation

Because of this excellent agreement we extend our 3-level-model to evaluate the layer distribution directly from the intensity oscillations. Supposing that two adlayers grow simultaneously from the beginning of the adlayer deposition, Eq. (7) can be modified to

$$\frac{I_0(\Theta)}{I_0(0)} = |p_0(\Theta) - [p_1(\Theta) - p_2(\Theta)] \rho e^{i\varphi}|^2. \quad (12)$$

As discussed earlier, one obtains the absolute value of the relative scattering amplitude ρ by comparing the initial intensity and the total intensity after depositing several layers. A more serious problem is to determine the scattering phase φ . For this purpose one may apply the analysis of the intensity minimum just presented. Thereafter the evaluated central spike intensity depends only on the layer coverage. Furthermore, since the layer distribution depends on the deposited total coverage via

$$\Theta = \sum_h \Theta_h(\Theta) = \sum_h h p_h(\Theta)$$

and we may apply the summation rule

$$\sum_h p_h(\Theta) = 1,$$

we are able to calculate the full layer distribution after inserting the additional equations into Eq. (12).

Obviously the situation changes after the substrate is covered totally by the first adlayer since the interference of the adlayer with the substrate vanishes. From hereon the electron beam is diffracted at a homogeneous stepped surface so that one may apply the oscillation analysis of the central spike restricted to three exposed layers introduced earlier for homoepitaxy [12].

3. Experimental

The experiments were performed in a UHV chamber (base pressure 10^{-8} Pa) equipped with a SPA-LEED system and an external electron beam gun at an angle of 135° with respect to the channeltron detector so that diffraction patterns could be recorded during CaF_2 evaporation. CaF_2 has been evaporated from a electron beam evaporator containing a graphite crucible and a quartz balance to control the evaporation rate. A second quartz monitor close to the sample position was used for calibration reasons. We used an evaporation rate of 0.1 ML/min to deposit less than 1% of a ML CaF_2 during recording one spot profile.

4. Results

After preparation of the clean surface the scans show the specular (00) spot and the first order superstructure $(\frac{1}{7}0)$ spot due to the 7×7 reconstruction. The $(\frac{1}{7}0)$ spot vanishes very quickly after depositing only very little CaF_2 on the substrate at 300°C . Already for $\Theta = 0.5$ ML one cannot observe any superstructure spots since the CaF_2 grows with 1×1 structure at this temperature. Our investigation about the effect of the deposited CaF_2 on the 7×7 reconstruction will be presented elsewhere [13].

Here, however, we will focus our interest on the analysis of the (00) spot to obtain information about the morphology of the CaF_2 film during the initial growth stages. Fig. 4 shows that the (00) spot profiles recorded at the out-of-phase condition

$$S = dK_{\perp}/2\pi = 1.5$$

for the $[2\bar{1}1]$ direction split into a central spike and a broad diffuse shoulder due to forming of CaF_2 is-

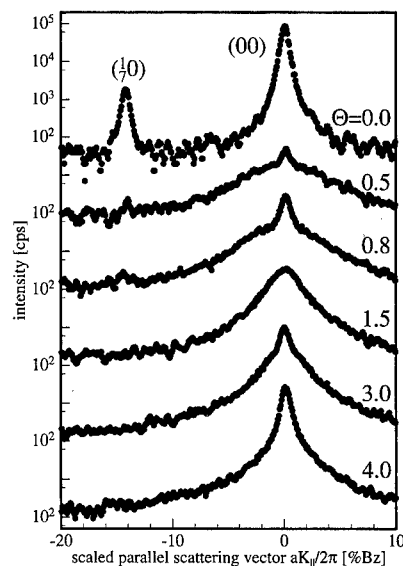


Fig. 4. Coverage dependence of line scans in the $[2\bar{1}1]$ direction at the out-of-phase condition $S = 2.5$. Please, note the logarithmic abscissa and that the profiles are shifted with respect to each other for clarity. While the $(\frac{1}{7}0)$ spot vanishes already after depositing a small amount of CaF_2 , the (00) spot splits into a central spike and a diffuse shoulder due to CaF_2 islands.

lands. Both the intensity of the central spike and the halfwidth of the shoulder depend oscillatory on the coverage. For instance, the central spike vanishes for $\Theta = 1.5$ ML and reappears for $\Theta = 3.0$ ML.

The (00) spot has been analysed by fitting the profiles to a sharp and a broad 2D Lorentzian

$$\frac{\kappa^3}{(\kappa^2 + K_{\parallel}^2)^{3/2}},$$

implying a geometric distribution of terraces [14] with average terrace length $\langle L \rangle = 2/\kappa$. Fig. 5 shows the central spike and the total intensity obtained from analysing all scans recorded during growth of the CaF_2 adlayer. The total intensity of the closed CaF_2 layer ($\Theta > 1.5$ ML) is roughly 10 times larger than for the Si substrate. Thus we obtain the scattering amplitude ratio $\rho = 3.15$ for the scattering condition used here.

In order to analyse the layer distribution from the central spike oscillations, additionally, we have to determine the phase shift. Supposing perfect growth of the first CaF_2 layer we expect that the first

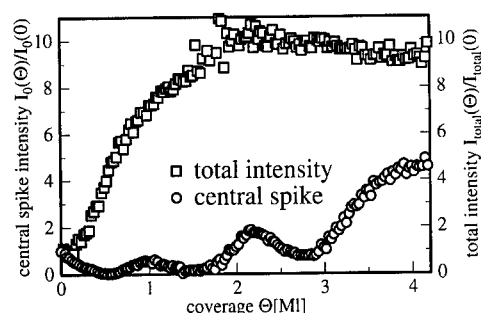


Fig. 5. Analysis of the (00) spot. The total intensity increases with CaF_2 deposition because the CaF_2 scattering amplitude is larger than the Si scattering amplitude. The central spike intensity oscillates until 4 ML CaF_2 are deposited. Since the diffuse shoulder does not vanish for any coverage the CaF_2 film growth in the multi layer growth.

intensity minimum appears for critical coverages $\Theta^* < 0.25$ ML because of the scattering amplitude ratio $\rho = 3.15$ (cf. Fig. 2). Obviously the minimum appears at $\Theta^* = 0.5$ ML so that we conclude that CaF_2 grows simultaneously in the second layer. Combining this result with the experimental finding that the central spike intensity at the minimum vanishes the phase shift of the CaF_2 can only be completely constructive ($\varphi = 0$) or destructive ($\varphi = \pi$). Fig. 3 demonstrates that on the one hand for constructive interference ($\varphi = 0$) 20% of the total coverage are grown in the second layer. On the other hand, for destructive interference ($\varphi = \pi$) the portion of second layer growth is even 50% implying perfect double layer growth. Since this seems to be very unlikely we conclude that the phase shift of the CaF_2 adlayer is constructive. This result is supported by the analysis of the total spot intensity discussed later.

The intensity of the central spike oscillates until $\Theta \approx 4$ ML are deposited with distinct minima at almost half order and maxima at integral order total coverages as expected for homoepitaxial growth. The diffuse shoulder, however, does not vanish for any CaF_2 coverage so that perfectly closed CaF_2 adlayers without atomic steps are never formed (multi layer growth). Additionally, this result is supported by the smooth increase of the total intensity. After depositing 1 ML CaF_2 the total intensity has not the value observed after depositing many monolayers CaF_2 . Therefore, the diffraction experiment is still influ-

enced from the Si substrate with much smaller scattering amplitude and some CaF_2 must have been deposited in the second level. On the other hand, comparing this behaviour with the calculated behaviour for the random growth mode we see immediately that the CaF_2 does not grow in the latter mode because we observed more than one oscillation. Thus the additionally deposited CaF_2 molecules are able to cross steps (inter layer diffusion).

For the coverages where we observed the central spike minima during growth ($\Theta = 1.6$ ML and $\Theta = 2.6$ ML) we interrupted the deposition process to measure the adlayer morphology more quantitatively. For this purpose we recorded spot profiles at different scattering conditions ($S = 2.5$ to $S = 3.5$). The scaled central spike intensity

$$G_0(S, \Theta) = \frac{I_0(S, \Theta)}{I_{\text{total}}(S, \Theta)} = \left| \sum_h p_h e^{2\pi i S h} \right|^2 \quad (13)$$

depends only on the layer distribution for a homogeneous surface with identical scattering amplitudes ($f_h = f$) obtained from Eqs. (7) and (8). From these data one can evaluate the layer distribution of the homogeneously stepped adlayer [15]. The layer distributions for both of these coverages reveal that always more than 0.1 ML CaF_2 are grown already on top of the non-closed layers.

Fig. 6 shows the experimental data and the fitted scaled central spike intensity $G_0(S)$ from which the layer distribution has been evaluated. From the layer distribution we calculated also the rms-roughness of the adlayers. Comparison of both values $\Delta = 0.86d$ for $\Theta = 1.6$ ML and $\Delta = 0.71d$ for $\Theta = 2.6$ ML shows again that CaF_2 grows in the multi layer growth mode since the rms-roughness is larger than expected for the perfect layer by layer growth ($\Delta_{\text{bl}} = 0.49d$). On the other hand, the rms-roughness is smaller than for adlayers grown in the random growth mode (cf. Fig. 7).

The experimental finding that rms-roughness Δ is larger for $\Theta = 1.6$ ML than for $\Theta = 2.6$ ML (demonstrated by the sharper $G_0(S)$ curve and supported by the lower value at the out-of-phase conditions) is caused by the fact that even the first layer is not perfectly closed when the third level starts to grow. This is also the reason why the total intensity at this

coverage $\Theta = 1.6$ ML is still slightly smaller than the finally obtained value after depositing more CaF_2 .

Fig. 7 shows the coverage dependence of the layer distribution obtained from the analysis of the intensity oscillations. Additionally, also the data from the phase dependence for $\Theta = 1.6$ ML and $\Theta = 2.6$ ML and from the total intensity analysis for $\Theta = 1.0$ ML are included. For $\Theta = 1$ ML and $\Theta = 2.6$ ML the 3-exposed-layer analysis agrees very well with these data so that we conclude that our analysis within the 3-level model is correct.

Small differences are observed at $\Theta = 1.6$ ML which may be on one hand due to the morphology of the CaF_2 adlayer at the initial growth stage. On the other hand, this may also be attributed to the assumption of our analysis that the penetration depth of the electron beam is so small that only scattering at the first layer has to be considered. We rule out this reason because for the scattering condition used the perpendicular penetration depth is approximately 2 \AA including the electron energy 140 eV (revealing 5 \AA penetration depth approximately) and the inclination angle of 67.5° while the layer spacing for both silicon and CaF_2 is 3.14 \AA .

Furthermore, effects by second layer scattering can be analysed from the total spot intensity. Fig. 5 shows that the total intensity for $\Theta \approx 2$ ML slightly overshoots the finally obtained intensity for $\Theta \approx 4$

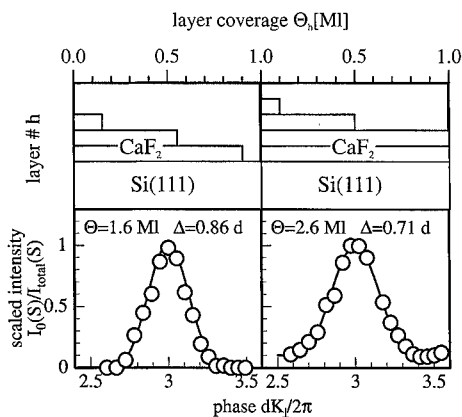


Fig. 6. Layer distribution from the scattering phase dependence of the central spike intensity for $\Theta = 1.6$ ML and $\Theta = 2.6$ ML where the central spike has minimal intensity at the out-of-phase condition. While the rms-roughness of these layers is larger than predicted for both the perfect layer by layer growth ($\Delta = 0.49 d$), the films are smoother than expected for the random growth mode ($\Delta = d\sqrt{\Theta}$).

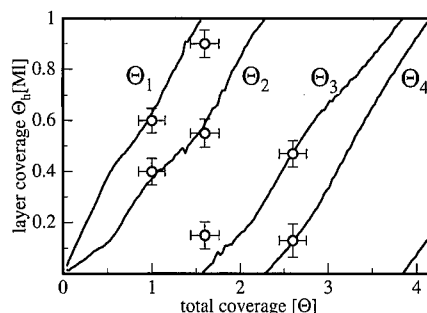


Fig. 7. Layer analysis of the central spike oscillations applying the 3-level model. For comparison, the layer distribution from the scattering phase analysis for $\Theta = 1.6$ ML and $\Theta = 2.6$ ML and from the analysis of the total intensity for $\Theta = 1.0$ ML are presented. The 3-level analysis describes excellently the layer distribution except for $\Theta = 1.6$ ML. We attribute this to the diffusion of the CaF_2 molecules. The diffusion length of the CaF_2 molecules is too small to arrive at the remaining holes of an almost closed layer so that more than three exposed layers exist.

ML. This effect may be attributed to a stronger scattering for 1 ML $\text{CaF}_2/\text{Si}(111)$ compared to thicker CaF_2 coverages. On the other hand, we have proven that the effect of layer depending scattering amplitudes (varying the scattering amplitude in the range $\rho = 3.0$ – 3.3 implying that the total intensity for the CaF_2 adlayer is 9–11 times larger than the intensity of the Si substrate) on our layer distribution analysis is quite small. Additionally, we checked our analysis with the more simple 3-layer analysis for homoepitaxial surfaces which is valid after closing of the first CaF_2 layer. Both analysis agree very well for $\Theta > 1.5$ ML so that our analysis seems to be correct.

Thus we attribute the discrepancy for $\Theta = 1.6$ ML between the 3-layer analysis and the layer distribution obtained from the phase dependence (revealing four exposed layers) solely to the film morphology: the first layer is almost closed while the third layer starts to nucleate. Therefore we conclude that our 3-level analysis describes correctly the growth of the CaF_2 layers but cannot characterize the closing and nucleation of layers in full detail.

5. Discussion

Obviously, the CaF_2 shows a strong tendency to grow during the initial nucleation stage with double

layer islands. After deposition of 0.5 ML CaF_2 (first minimum of the central spike) the second CaF_2 layer has a coverage of $\Theta_2 = 0.1$ ML. This effect of double layer growth has also been observed for the homoepitaxial growth of silicon with SPA-LEED [12] and STM [16]. For the silicon homoepitaxy the double layer growth has been attributed to nucleation at defects (anti-phase boundaries of the 7×7 reconstructed substrate and of even more complicated anti-phase boundaries of the growing islands including 5×5 and 9×9 unit cells). For the heteroepitaxial growth of insulators on silicon the complication of the ad-molecule binding to the Si substrate is even worse. It is difficult for the CaF_2 molecules to form nuclei on the plain 7×7 surface since there are not many Si atoms with dangling bonds. Thus nucleation at defects is preferred. Furthermore, from RBS [5] and XPS [17] studies it is well known that the interface between the CaF_2 adlayer and the Si substrate shows a lot of defects because of the poor binding between the fluorine and silicon.

Also, LEEM investigations performed at higher deposition temperatures reveal that the first monolayer CaF_2 does not close before the nucleation of the second layer starts [18]. For the temperature range reported by these authors (600–700°C), however, the nucleation of the second layer starts very late compared to the deposition at 300°C which we studied. This strong temperature dependence can be attributed to the very fast diffusion of the CaF_2 molecules so that the probability to form a new nucleus is very small at higher deposition temperatures. Nevertheless the LEEM studies also show that the nucleation of the second layer shifts to higher coverages with increasing temperature.

Our analysis of the layer distribution (Fig. 7) reveals that the CaF_2 adlayer is quite rough during the very initial growth stages because of the early nucleation of higher adlayers. This situation changes for $\Theta \approx 4$ ML. For the 4 ML thick CaF_2 adlayer we find that only very little CaF_2 is grown in the 5th layer. Here the central spike shows a strong maximum from which we conclude that less than 0.1 ML are on top of the 4th layer. At this coverage, however, also the growth mode changes since we do not find any oscillations depositing more CaF_2 . Neither the central spike intensity nor the halfwidth of the diffuse shoulder are influenced by the growing CaF_2

adlayer. Since this behaviour is typical for three dimensional island growth with increasing rms-roughness we cannot apply our 3-level model to this coverage range.

6. Conclusion

In conclusion, we have shown that the analysis of spot profiles recorded during growth of heteroepitaxial adlayers is a powerful tool to obtain a lot of information about the morphology of the growing adlayer. The analysis is complicated by the different scattering amplitudes of adlayer and substrate. This complication can be overcome if one analyses carefully the initial coverage dependence of the central spike intensity. From the intensity and the critical coverage Θ^* at the first minimum one can extract the phase shift of the adlayer (compared to the substrate) while the ratio of the total values is obtained from the total spot intensity in the large coverage limit.

Applying this spot profile analysis to the initial growth stages of CaF_2 on Si(111) we found that the CaF_2 tends strongly to nucleate in the second layer before closing the first. We attribute this tendency to the interplay of the very fast diffusion of CaF_2 molecules and their difficulties to form a strong binding to the Si 7×7 substrate. Also after closing of the first layer the CaF_2 adlayers grow in the multi layer growth mode with larger rms-roughness than for the perfect layer by layer growth mode. The closing of the lower levels is hindered by kinetic effects. The diffusion of the CaF_2 molecules is too small to fill the remaining holes before nucleation of the next layer. The multi layer growth switches to three dimensional island growth at $\Theta \approx 4$ ML since for larger CaF_2 coverages the intensity oscillations die out.

References

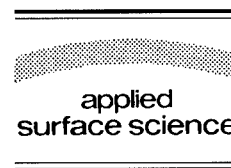
- [1] L.J. Schowalter and R.W. Fathauer, *CRC Crit. Rev. Solid State Mater. Sci.* 15 (1989) 367.
- [2] R.W. Fathauer and L.J. Schowalter, *Appl. Phys. Lett.* 45 (1984) 519.
- [3] Ph. Avouris and R. Wolkow, *Appl. Phys. Lett.* 55 (1989) 1074.

- [4] T. Nakayama, M. Katayama, G. Selva and M. Aono, *Phys. Rev. Lett.* 72 (1994) 1718.
- [5] T. Asano, H. Ishiwara and N. Kaifu, *Jpn. J. Appl. Phys.* 22 (1983) 1474.
- [6] D. Saloner and M.G. Lagally, in: *The Structure of Surfaces*, Eds. M.A. Van Hove and S.Y. Tong, Springer Series in Surface Science 2 (Springer, Berlin, 1985) p. 366.
- [7] M. Henzler, H. Busch and G. Friese, in: *Kinetics of Ordering and Growth at Surfaces*, Ed. M.G. Lagally (Plenum, New York, 1990) p. 101.
- [8] J. Wollschläger, J. Falta and M. Henzler, *Appl. Phys. A* 50 (1990) 57, 101.
- [9] M. Henzler, *Appl. Phys. A* 34 (1984) 205.
- [10] J. Wollschläger, D. Thielking and M. Henzler, in preparation.
- [11] C.S. Lent and P.I. Cohen, *Surf. Sci.* 139 (1984) 121.
- [12] M. Horn-von Hoegen, J. Falta and M. Henzler, *Thin Solid Films* 183 (1989) 213.
- [13] J. Wollschläger and A. Meier, *J. Appl. Phys.* 79 (1996) 7373.
- [14] J. Wollschläger, E.Z. Luo and M. Henzler, *Phys. Rev. B* 44 (1991) 13031.
- [15] R. Altsinger, H. Busch, M. Horn and M. Henzler, *Surf. Sci.* 200 (1988) 235.
- [16] U. Köhler, R.J. Hamers and J. Demuth, *J. Vac. Sci. Technol. A* 7 (1989) 2860.
- [17] M.A. Olmstead and R.D. Bringans, *J. Electron. Spectrosc. Rel. Phen.* 51 (1990) 599.
- [18] R.M. Tromp and M.C. Reuter, *Phys. Rev. Lett.* 73 (1994) 110.



ELSEVIER

Applied Surface Science 104/105 (1996) 402–408



Structural transformations at $\text{CaF}_2/\text{Si}(111)$ interfaces

N.S. Sokolov^{a,*}, J.C. Alvarez^a, Yu.V. Shusterman^a, N.L. Yakovlev^a,
R.M. Overney^b, Y. Itoh^c, I. Takahashi^c, J. Harada^d

^a Solid State Optics Department, Ioffe Physico-Technical Institute, Politechnicheskaya St., 194021 St. Petersburg, Russia

^b Exxon Research and Engineering Company, Annandale, NJ, USA

^c Department of Applied Physics, Nagoya University, Nagoya, Japan

^d University of the Electro-Communications, Tokyo, Japan

Received 28 June 1995; accepted 14 November 1995

Abstract

Transformations of the atomic structure of the $\text{CaF}_2/\text{Si}(111)$ interface during annealing have been studied by reflection high energy electron diffraction (RHEED) and X-ray crystal truncation rod (CTR) scattering. The surface morphology after annealing has been studied by atomic force microscopy (AFM). A conversion of the epitaxial relation of the film with respect to the substrate, from type-A (nonrotated) to type-B (with the axes of the film rotated by 180° around the interface normal), is monitored by RHEED during annealing of the films. On the basis of RHEED, CTR and AFM data, a model of the conversion is suggested. In addition, a spontaneous transition of the type-B interface formed during the growth to the interface with another atomic arrangement has been studied with CTR. The possible role of point defect motion in the CaF_2 film during this transition is discussed.

1. Introduction

Single crystal fluoride layers grown on semiconductor substrates by molecular beam epitaxy (MBE) have recently received much attention owing to various potential applications in micro- and optoelectronics. Among different epitaxial insulator/semiconductor heterocouples, $\text{CaF}_2/\text{Si}(111)$ structures have a relatively small lattice mismatch (0.6% at RT), and it is easy to grow them by MBE. They appear to be very attractive for fundamental studies of processes of heteroepitaxial growth [1–6], as well as of the atomic and electronic structure of an inter-

face between an ionic insulator and a covalent semiconductor [3,5,7–11].

One intriguing problem is the existence of two types of epitaxial relations at the interface between CaF_2 and $\text{Si}(111)$. In type-A structures, the film and the substrate have the same orientation, while in type-B structures, the film is rotated by 180° around the surface normal with respect to the substrate, as shown in Fig. 1. It was shown [12] that CaF_2 films grown at 200°C have the type-A epitaxial relation and that, during annealing at 600°C , these films can be converted into the type-B orientation. In this paper, we report the first in situ observation of type-A to type-B interface conversion, an analysis of the surface morphology before and after annealing using atomic force microscopy (AFM), and an X-ray crystal truncation rod (CTR) scattering study of the

* Corresponding author. Tel.: +7-812-2479911; fax: +7-812-2471963; e-mail: nsokolov@fl.ioffe.rssi.ru.

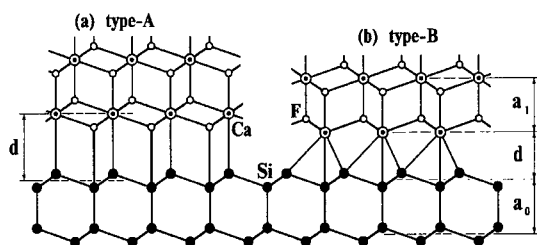


Fig. 1. Scheme of type-A (a) and type-B (b) epitaxial relations at a $\text{CaF}_2/\text{Si}(111)$ interface and notations of interlayer distances.

structure of as-grown and annealed interfaces. On the basis of the results of all these investigations, we suggest a mechanism for A to B conversion.

Atomic arrangements at $\text{CaF}_2/\text{Si}(111)$ interfaces were extensively studied by middle energy ion scattering [7], X-ray standing waves measurements [8,13] and, until recently, the structure of at least the type-B interface seemed to be determined. However it was lately found [5] that, in the structures grown under certain conditions, the interface which is formed just after growth is not stable and that a spontaneous transition to an interface with another structure occurs. Confirmation of this finding is appropriate since this result is meaningful, not only for investigations of fluoride heterostructures, but also for a deeper understanding of the behavior of other buried interfaces. Here we present new evidence for this transition and an X-ray CTR study of the stability of the just grown interface.

2. Conversion of type-A to type-B interface

2.1. MBE growth and RHEED studies

Fluoride heterostructures studied in this work were grown at the Physico-Technical Institute by MBE. The surface structure analysis was performed by reflection high energy electron diffraction (RHEED). The electron energy was 14 keV and the diffracted intensity was detected by a sensitive CCD camera with an electron-optical amplifier which makes it possible to decrease the beam current to 0.05 nA. A typical electron dose during each run of RHEED monitoring was $0.5 \mu\text{C}/\text{cm}^2$ which is much smaller than the value $500 \mu\text{C}/\text{cm}^2$ required to desorb a monolayer of fluorine [14]. Silicon substrates had a

miscut of less than 6 arcmin from the (111) plane. After a standard chemical treatment, they were loaded into the growth chamber, cleaned thermally at 1250°C during 1 min and had a distinct 7×7 superstructure typical for $\text{Si}(111)$ clean surface after cooling below 830°C .

Type-A heterostructures were grown at 200°C and RHEED patterns indicated that CaF_2 films were single-crystal. During a gradual increase of the substrate temperature to 850°C in 15 min, we monitored the intensities of RHEED specular (00) and side (01 and $0\bar{1}$) beams. In Fig. 2, the dependence of specular beam intensity I_{00} on the annealing temperature for CaF_2 layers of 3, 4 and 6 monolayers (ML) thick is presented. Two steps, marked by the arrows, can be seen on each of the curves. For thicker layers, both steps shift to higher temperatures and the height of the second one decreases. The steps should be connected with some morphological changes on the surface. Monitoring the RHEED intensity around the specular beam, we found that the second step is accompanied by a drastic decrease in the intensity of diffuse scattering. This means that the surface of the annealed layer has become considerably smoother.

Based only on the temperature dependence of specular beam intensity, it is difficult to attribute each step to some certain processes in the film, but knowing the temperatures at which the steps occur, one can apply other methods to study the structures grown at just those temperatures. In such a way, we

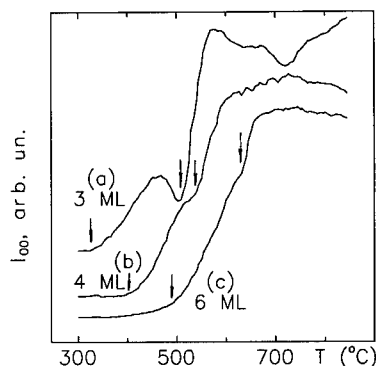


Fig. 2. Dependence of RHEED specular beam intensity from CaF_2 layers on annealing temperature. Heating rate $40^\circ\text{C}/\text{min}$, electron energy 14 keV, beam azimuth $[110]$, incidence angle 0.5° . The layer thickness is: (a) 3 ML, sample #597; (b) 4 ML, sample #625; (c) 6 ML, sample #624.

obtained the information about the surface morphology at 450°C and 600°C by using AFM (see below), and an advanced RHEED study enabled us to connect the second step with the conversion of the type of epitaxial relation at the interface.

In order to distinguish type-A and type-B epitaxy, we analyzed RHEED along the $[1\bar{1}0]$ azimuth where the side beams are not equivalent and rotation of the film by 180° around the $[111]$ axis swaps their positions and hence their intensities. At 14 keV and 2.5° incidence angle, the $(0\bar{1})$ beam intensity ($I_{0,-1}$) is close to zero, while the opposite (01) beam has significant intensity ($I_{0,1}$) [15]. At this incidence angle, the intensity of one of the side beams is proportional to the area of the type-A domains and the intensity of the other side beam is proportional to the area of the type-B domains. Thus, the component of the film which has the type-B epitaxial relation can be derived as

$$B_{\text{fraction}} = I_{0,-1} / (I_{0,-1} + I_{0,1}). \quad (1)$$

The fraction of type-B component of the layer was determined and plotted versus the annealing temperature in Fig. 3. It is seen that the A to B conversion of a 4 ML thick CaF_2 film occurs in two steps with the thresholds at 530°C and 650°C. One can notice that the first step of the conversion coincides with the high temperature step observed in Fig. 2. This demonstrates the close connection between structural transformations in the film and morphological transformations on the surface. However the second step

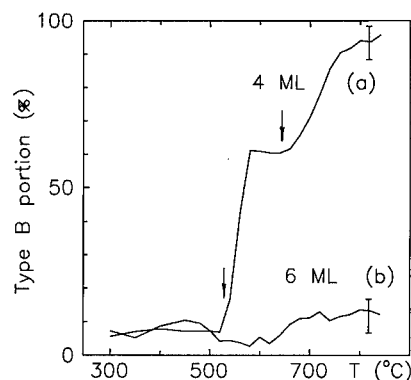


Fig. 3. Dependence of the type-B fraction in CaF_2 layer on Si(111) on annealing temperature. The beam incidence angle is 2.5°, the other conditions are like in Fig. 2. The layer thickness is: (a) 4 ML, sample #625; (b) 6 ML, sample #624.

in Fig. 3a does not change I_{00} , as it is seen from Fig. 2b. We suppose that this is because the surface is smoothed mostly during the first conversion step at 530°C, so further smoothing at higher temperatures is negligible.

The type-A epitaxial relation remains in the structures with 6 ML or more of CaF_2 ; the type-B fraction in them does not exceed the 10% experimental error, as shown in Fig. 3b. We also found that the conversion is time dependent; at other annealing conditions, when the substrate temperature was fixed at 600°C for 30 min, RHEED showed a pure type-B orientation of a 4 ML thick film, i.e. all the conversion occurred at a temperature lower than that of the second step in Fig. 3a.

2.2. Atomic force microscopy measurements

The AFM technique has already been applied successfully for investigations of the epitaxial growth of CaF_2 and BaF_2 on Si(111) [16]. In this work, the AFM measurements were carried out at the Exxon Research and Engineering Company to study the morphological transformations in annealed CaF_2 layers. All AFM scans were performed using commercially available microscopes with 1, 20 and 150 μm scanners and a beam-reflection detection scheme. A wide range of Si_3N_4 and Si cantilevers with spring constants of 0.03 up to 0.8 N/m have been used. Typically the applied force was of the order of 10 nN even though the application of higher forces had no apparent effect on the recorded images. The samples were transferred to the microscope in a sealed box filled with dry air. Owing to the stability of the CaF_2 (111) surface demonstrated earlier [17], it was possible to conduct the measurements in an ambient atmosphere at room temperature. Fig. 4 shows the AFM images taken from different samples with a CaF_2 layer grown at 200°C without annealing (a) or annealed in situ at different temperatures (b, c and d). The scanning area for all the images is 1.5 $\mu\text{m} \times 1.5 \mu\text{m}$ and the range of the height deviation is shown in nanometers near the gray scale for each image.

In Fig. 4a, one can see that the surface of the layer grown at 200°C is covered with islands 1 or 2 ML high and about 50 nm wide. The small sizes of the islands are due to the relatively short CaF_2

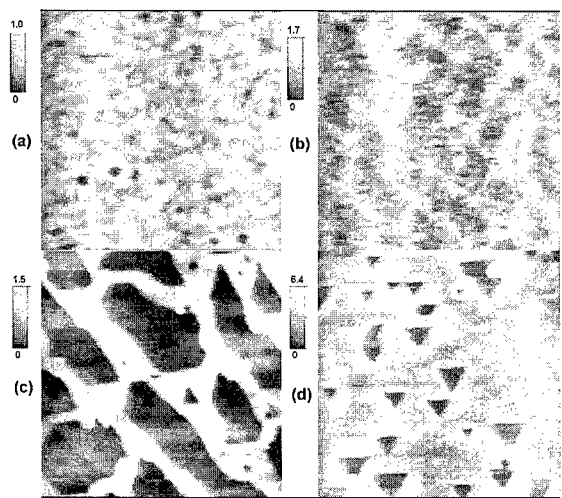


Fig. 4. AFM images from CaF_2 layers grown on Si(111) (a) at 200°C without annealing (6 ML, #658) and annealed: (b) to 450°C for 60 min (4 ML, #659), (c) to 600°C for 30 min (4 ML, #661), (d) to 850°C for 2 min (6 ML, #657). The scan area is $1.5 \times 1.5 \mu\text{m}^2$ for each image.

molecule migration length under the given growth conditions. A layer annealed at 450°C for 1 h is shown in Fig. 4b. As it is indicated by RHEED (see Fig. 2b), the surface morphology changes at this temperature; the islands form some row-like structures. It may be interpreted as being due to the islands concentrating along the terrace edges.

Atomically flat terraces larger than 200 nm dominate in the AFM image of the 4 ML thick CaF_2 layer annealed at 600°C for 30 min, as shown in Fig. 4c. The islands have the shape of stripes aligned in the direction of the steps on the substrate. The same orientation of triangular pits indicates that the epitaxial relation is uniform over the area of this layer. This film had type-B orientation after the annealing, as determined by RHEED.

At 850°C, a re-evaporation of CaF_2 film occurs [2]. It is seen from Fig. 4d that the evaporation proceeds through the appearance and enlargement of triangle pits as deep as the layer thickness of 6 ML. The same orientation of all the pits indicates the identical epitaxial relation throughout the studied area, which is type-A as revealed by RHEED. The 20 ML high borders around the pits can be explained, if one assumes that the bottom of the pit is covered with a single CaF layer. Because of weaker

adhesion of CaF_2 to it [18], the molecules, driven by surface tension, diffuse from the perimeter of the pit and spread out onto the film. The border recedes due to fluoride re-evaporation and accompanies the expanding pits.

2.3. X-ray crystal truncation rod scattering studies

The atomic arrangement at the $\text{CaF}_2/\text{Si}(111)$ interface was studied by the X-ray CTR technique [6,19]. It uses measurements of X-ray scattering intensity along reciprocal lattice rods normal to the crystal surface. For this purpose, 20 ML CaF_2 films were grown at 200°C on top of the layers studied by RHEED. This thickness corresponds to the best sensitivity of the CTR profiles to the film-substrate interface distance. The low temperature at the last stage allowed us to keep the films coherent with the substrate. X-ray diffraction from them was measured at the synchrotron radiation source, beam line 6A₂, Photon Factory, Tsukuba, Japan. The samples were transported in dry air and measured in He to reduce atmosphere scattering. The radiation wavelength was 1.0 Å and the scattered intensity was detected using an imaging plate [6]. All experimental points, shown as open circles in Fig. 5 and Fig. 6, represent the

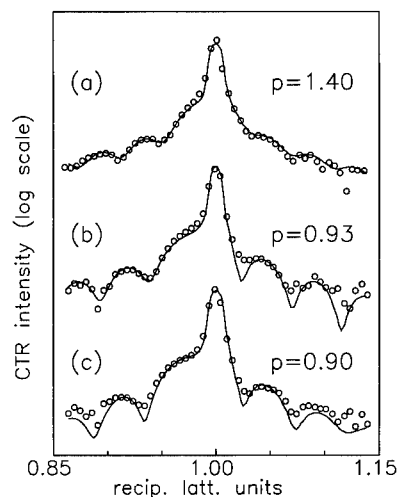


Fig. 5. CTR profiles of $\text{CaF}_2/\text{Si}(111)$ heterostructures with the interface formed at 200°C (a) without annealing, type-A (#623); (b) annealed 6 ML, type-A (#624); (c) annealed 4 ML, type-B (#625). Circles are experimental points, the solid line is the best fit.

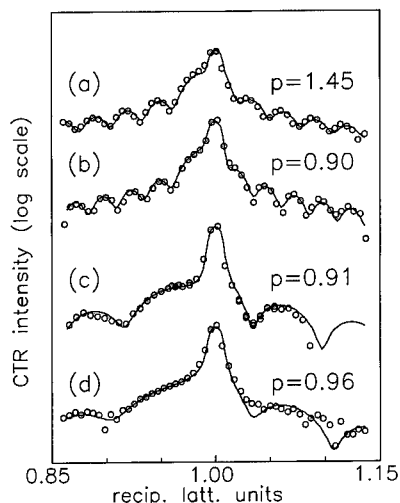


Fig. 6. CTR profiles of $\text{CaF}_2/\text{Si}(111)$ type-B heterostructures: (a) and (b) on a clean 7×7 reconstructed surface (#671 and #672), (c) and (d) on H-terminated surface (#629). See the text for details.

CTR scattering intensity integrated across the specular rod. They are plotted versus the length of the diffraction vector X measured in reciprocal lattice units, where $X = 1$ corresponds to the (111) Bragg reflection.

The data were fitted using a one-dimensional scattering model:

$$I = |A_{\text{sub}} + QA_{\text{film}} \exp(2\pi i Xp)|^2, \quad (2)$$

where I is the reflected intensity, A_{sub} and A_{film} are the Si substrate and CaF_2 film contributions to the scattering amplitude correspondingly, $p = d/a_0$ is the ratio of the interface distance d to $\text{Si}(111)$ inter-layer spacing $a_0 = 0.315$ nm (d and a_0 are defined in Fig. 1) and Q is the factor representing the crystal quality of the film. Surface roughness was taken into account in accordance with Ref. [20].

Fig. 5 presents three experimental CTR profiles together with their best fits; the corresponding values of p are also indicated. We found that in type-A structures, grown without annealing, the interface distance p has the value 1.40, which is close to that measured in Ref. [9]. The structures, where the initial thin layer was annealed prior to the subsequent growth, have $p = 0.93$ at the interface which has remained type-A, and $p = 0.90$ at the interface converted to type-B. These values correspond to the

interface where Si is bonded to Ca [7]. It is known from XPS measurements [2] that there are Si–F bonds at the interface formed at low temperature, and depletion of interfacial fluorine occurs when the CaF_2 layer is annealed. This correlates with the changes of the interface distance on annealing measured here. Therefore one can expect that the larger p value at the as-grown interface is due to the presence of F ions between Si and Ca atoms. Both type-A and type-B annealed interfaces have the shorter interface distance. Thus we conclude that they have the same sequence of atomic layers, Si–Ca–F, and that the F depletion itself does not cause the type-A to B conversion.

The higher amplitude of thickness oscillations in the CTR profiles shows a higher crystal quality of the films having an initial layer annealed, as compared to those grown without annealing. Still there were no polycrystalline features in imaging plate patterns taken, even from the samples with $Q \approx 0.3$.

2.4. Possible mechanism of A to B conversion

On the basis of RHEED, AFM, and CTR data, we can suggest a mechanism for the conversion of the epitaxial relation from A to B. In the layers grown at 200°C to an average thickness of 4 ML, the amplitude of height deviation is about 3 ML (see gradation bar for Fig. 4a). Hence there can be small pits where the local thickness is 2 ML or even 1 ML. At the second step in the dependence of the RHEED specular beam intensity on annealing temperature, shown in Fig. 2, the surface becomes much flatter. This process can be attributed to the activation of surface diffusion, when small islands fall apart and the molecules move along the terraces to form larger islands. They can also fill the pits. However at this temperature (600°C and higher), irreversible fluorine depletion is expected to occur, forming a CaF layer bonded to Si in those pits where only one CaF_2 ML was at the bottom. A single CaF layer is known to have the type-B epitaxial relation, interface distance $p = 0.9$ [7] and weaker wetting by CaF_2 [18]. Thus, when the molecules diffuse, the pits having a single CaF monolayer at the bottom are not totally filled, but migrate along the terraces. Sooner or later they pass over each part of the surface, making type-B film over the whole area.

Thicker layers should have far fewer pits with a single CaF ML at the bottom. Thus there are no points for the conversion to start during the annealing. However the interface distance very close to $p = 0.9$ was measured in such films, the example is shown in Fig. 5b. In this case, the depletion of the interfacial fluorine may go through the volume diffusion in the film or in the substrate.

3. Stability of type-B 'short' interface

It was shown [11,21] that pseudomorphic (coherent with the substrate) CaF_2 layers on Si(111) with type-B epitaxial relation can be grown by depositing several monolayers at a higher temperature ($\sim 700^\circ\text{C}$), and then the main part of the film at a lower temperature. Initially these structures have the 'short' interface ($p = 0.9$), however this interface is metastable and transforms to the 'long' interface ($p = 1.45$) [5,9,11]. The transition time was observed to be shorter for thinner films [11]: in the case of a 15 ML thick film, the transition occurred in a day, but for a 27 ML film, it occurred about a month after the growth.

In this work, we found conditions for which the 'short' to 'long' interface transition is delayed. The influence of the growth temperature of the main part of the film was studied. For this purpose, two structures were prepared, each starting with 5 ML grown at 700°C , but the main part with 32 ML grown at 20°C in one of them and at 500°C in the other. Three weeks after the growth, CTR measurements showed that the former had the 'long' interface already, but the latter still had the 'short' one, as indicated in Fig. 6a and Fig. 6b. The value $p = 0.9$ was also observed in the film with the overlayer grown at 200°C . These facts confirm the supposition that this structural transition is connected with motion of some growth defects to the interface. Due to the lower temperature, the film grown at 20°C is expected to have more point defects. These point defects can diffuse to the interface and change its atomic arrangement. The higher their concentration, the faster the rate of change of the interface. A lower concentration of point defects can explain why the 'short' interface is stable for a longer time in the films grown at 200°C and higher.

We have also studied MBE growth of CaF_2 layers on H-terminated Si(111) surface prepared by etching in NH_4F aqueous solution [22]. Here, RHEED patterns indicated that the H-Si(111) surface had a 1×1 structure and was quite flat with only some small scale roughness due to terraces about 30 nm wide. It may be similar to single ML triangular pits found on H-terminated Si(111) surface prepared by similar processing [23]. After passivation of the surface with hydrogen, the first three CaF_2 monolayers were grown at 200°C and annealed at 850°C and then 12 ML were overgrown at 200°C . The short ($p = 0.9$) type-B interface was found in these structures, as shown in Fig. 6c. There was no difference between this interface and the 'short' one discussed so far. Thus we suppose that the H atoms diffused away from the interface during annealing, like the F atoms did.

Even for films as thin as 15 ML, the 'short' interface, obtained on H-terminated substrates, remained stable over four months (compare Fig. 6c and Fig. 6d). The reason of this effect is still unclear, however one can suppose that it can be connected in some way with higher concentration of interface steps (terrace edges at the interface) than on the thermally cleaned substrates. In type-B structures, each step along the interface results in a coreless dislocation which can attract defects, not allowing them to diffuse along the interface and change its structure.

4. Conclusion

We showed, using in situ RHEED measurements, that $\text{CaF}_2/\text{Si}(111)$ type-A structures with layer thicknesses less than 5 ML are converted to type-B during a temperature ramp ($40^\circ\text{C}/\text{min}$) from 200°C to 850°C . Two steps in the conversion were found with thresholds at 530°C and 650°C . Measurements by the X-ray CTR method revealed that the interface distance in type-A structures is 4.2 \AA as-grown and is 2.9 \AA after annealing. This decrease was attributed to depletion of fluorine from the interface. A mechanism of A to B conversion connected with changes of the surface morphology was suggested.

For type-B CaF_2 films grown on Si(111) 7×7 , it was found that the transition from the so called

Table 1

Parameters of $\text{CaF}_2/\text{Si}(111)$ structures studied by RHEED and CTR

Sample No.	CaF_2 growth regimes	Type of epitaxy	Interval from growth to CTR measurements	p	Q
623	25 ML 200°C/Si(111)	A	3 weeks	1.40	0.3
624	* 20 ML 200°C/850°C/6 ML 200°C/Si(111)	A	3 weeks	0.93	1
625	* 20 ML 200°C/850°C/4 ML 200°C/Si(111)	B	3 weeks	0.90	1
671	32 ML 20°C/5 ML 700°C/Si(111)	B	3 weeks	1.45	0.95
672	32 ML 500°C/5 ML 700°C/Si(111)	B	3 weeks	0.90	1
629	* 12 ML 200°C/850°C/3 ML 200°C/Si(111)–H	B	2 weeks	0.90	1
629	the same sample	B	4 months	0.95	0.95

The typical error bar is ± 0.03 for p and ± 0.05 for Q values.

* * means annealing with temperature ramp (40°C/min) from 200°C to 850°C.

‘short’ interface (2.9 Å) to the ‘long’ one (4.6 Å) is delayed in the film grown at 500°C with respect to one grown at 20°C. It was explained by the expected reduction in the concentration of point defects in the layers grown at higher temperature. We found also that the ‘short’ interface remains stable for at least 4 months in the structures grown on hydrogen-terminated Si(111).

Structural parameters of $\text{CaF}_2/\text{Si}(111)$ films and interfaces are summarized in Table 1.

Acknowledgements

The authors appreciate the support of this work by the Swiss National Science Foundation, the Photon Factory, KEK, under proposal No. 93G268; the International Science Foundation grants Nos. NUL000 and NUL300; the grant of the Russian Foundation for Fundamental Studies No. 95-02-04141-a. The authors are sincerely grateful to Professor L.J. Schowalter for critical reading of the manuscript and valuable comments during his visit to St. Petersburg in September 1995, supported by the NATO Linkage Grant HTECH.LG 950926.

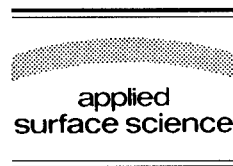
References

- [1] L.J. Schowalter and R.W. Fathauer, *CRC Crit. Rev. Solid State Mater. Sci.* 15 (1989) 367.
- [2] M.A. Olmstead, R.I.G. Uhrberg, R.D. Bringans and R.Z. Bachrach, *Phys. Rev. B* 35 (1987) 7526.
- [3] J.D. Denlinger, E. Rotenberg, U. Hessinger, M. Leskovar and M.A. Olmstead, *Appl. Phys. Lett.* 62 (1993) 2057.
- [4] R.M. Tromp and M.C. Reuter, *Phys. Rev. Lett.* 73 (1994) 110.
- [5] C.A. Lucas, G.C.L. Wong and D. Loretto, *Phys. Rev. Lett.* 70 (1993) 1826.
- [6] T. Shimura and J. Harada, *J. Appl. Cryst.* 26 (1993) 151.
- [7] R.M. Tromp and M.C. Reuter, *Phys. Rev. Lett.* 61 (1988) 1756.
- [8] J. Zegenhagen and J.R. Patel, *Phys. Rev. B* 41 (1990) 5315.
- [9] N.S. Sokolov, T. Hirai, K. Kawasaki, S. Ohmi, K. Tsutsui, S. Furukawa, I. Takahashi, Y. Itoh and J. Harada, *Jpn. J. Appl. Phys.* 33 (1994) 2395.
- [10] T.F. Heinz, F.J. Himpsel, E. Palange and E. Burstein, *Phys. Rev. Lett.* 63 (1989) 644.
- [11] C.A. Lucas, D. Loretto and G.C.L. Wong, *Phys. Rev. B* 50 (1994) 14340.
- [12] S. Ohmi, K. Tsutsui and S. Furukawa, *Jpn. J. Appl. Phys.* 33 (1994) 1121.
- [13] J.C. Alvarez, K. Hirano, A.Yu. Kazimirov, M.V. Kovalchuk, A.Ya. Kreines, N.S. Sokolov and N.L. Yakovlev, *Semicond. Sci. Technol.* 7 (1992) 1431.
- [14] H.C. Lee, T. Asano, H. Ishiwara and S. Furukawa, *Jpn. J. Appl. Phys.* 27 (1988) 1616.
- [15] N.L. Yakovlev, J.L. Beeby and P.A. Maksym, *Surf. Sci.* 342 (1995) L1121.
- [16] S. Blunier, H. Zogg, C. Maissen, A.N. Tiwari, R.M. Overney, H. Haefke, P.A. Buffat and G. Kostorz, *Phys. Rev. Lett.* 68 (1992) 3599.
- [17] R.M. Overney, H. Haefke, E. Meyer and H.-J. Güntherodt, *Surf. Sci.* 277 (1992) L29.
- [18] G.C.L. Wong, D. Loretto, E. Rotenberg, M.A. Olmstead and C.A. Lucas, *Phys. Rev. B* 48 (1993) 571.
- [19] I.K. Robinson and D.J. Tweet, *Rep. Progr. Phys.* 55 (1992) 599.
- [20] J. Harada, *Ultramicroscopy* 52 (1993) 233.
- [21] N.S. Sokolov, N.L. Yakovlev and J. Almeida, *Solid State Commun.* 76 (1990) 883.
- [22] G.S. Higashi, R.S. Becker, Y.J. Chabal and A.J. Becker, *Appl. Phys. Lett.* 58 (1991) 1656.
- [23] G.J. Pietsch, U. Kohler and M. Henzler, *J. Appl. Phys.* 73 (1993) 4797.



ELSEVIER

Applied Surface Science 104/105 (1996) 409–416



Molecular beam epitaxial growth of thin CaF_2 films on vicinal $\text{Si}(111)$ surfaces

B.M. Kim^a, C.A. Ventrice, Jr.^a, T. Mercer^b, R. Overney^c, L.J. Schowalter^{a,*}

^a Department of Physics, Rensselaer Polytechnic Institute, Troy, NY 12180, USA

^b Department of Physics, Drexel University, Philadelphia, PA 19104, USA

^c Exxon Research and Engineering Company, Exxon, Annandale, NJ 08801, USA

Received 28 June 1995; accepted 26 September 1995

Abstract

The growth of CaF_2 on $\text{Si}(111) 7 \times 7$ surface at $\sim 770^\circ\text{C}$ and $\sim 250^\circ\text{C}$ on both $\sim 2^\circ$ and $\sim 0.5^\circ$ off-normal, vicinal substrates (titled towards the $[11-2]$ azimuth) has been studied using RHEED, AFM and SEM. For growth at $\sim 770^\circ\text{C}$ on both substrates, the CaF_2 grows in a layer-by-layer fashion for the first two monolayers which gives rise to RHEED intensity oscillations. Beyond two monolayers, relatively thick CaF_2 islands nucleate at the Si step edges (which are bunched into step bands) and grow laterally with constant height (~ 5 nm for $\sim 2^\circ$ and ~ 2 nm for $\sim 0.5^\circ$ miscut substrates) along the Si step edges and eventually form a flat overlayer. The height of the CaF_2 islands appears to be determined by the height of the Si step bunches which, in turn, is determined by the substrate miscut angle. For growth at $\sim 250^\circ\text{C}$, the integral diffraction spot RHEED intensity decreases exponentially for the first ~ 2 monolayers of growth and then oscillates for ~ 6 periods. In addition, the non-integral diffraction spots, corresponding to the $\text{Si}(111) 7 \times 7$ pattern, are not fully removed until the integral diffraction spot intensity starts to oscillate at ~ 3 monolayers. These results indicate that the CaF_2 initially grows by nucleation and coalescence of 2D islands which are 2 to 3 monolayers high, followed by a multilayer-by-multilayer mode which leads to a featureless, flat surface morphology.

1. Introduction

The epitaxial growth of insulator–semiconductor structures, such as CaF_2/Si , has received considerable attention due to both fundamental interests and potential technological applications such as the use of CaF_2 as a plastic buffer layer in substrate engineering or as a gate dielectric in metal insulator semiconductor (MIS) field-effect transistor structures and resonant tunneling diodes [1,2]. Since the lattice

mismatch of CaF_2 and $\text{Si}(111)$ is only 0.6% at room temperature and CaF_2 has a large relative dc dielectric constant of 6.8, and band gap of 12 eV, this system shows a promise for future applications in insulator–semiconductor technology. However, high quality, epitaxial growth is crucial for the proper electrical performance of these devices.

Traditionally, the growth mechanism of CaF_2 on the $\text{Si}(111)$ surface was assumed to be in a layer-by-layer mode from the formation of interfacial layer to the subsequently grown thicker films. However, recently published works [3–8] have shown that CaF_2 chemisorption on to a $\text{Si}(111)$ surface is fundamen-

* Corresponding author. Tel.: +1-518-2766435; fax: 518-2768761; e-mail: schowalt@unix.cie.rpi.edu.

tally different from subsequent CaF_2 – CaF_2 homoepitaxy. In particular, Lucas et al. [7] and Wong et al. [8] have reported a (7×7) to (3×1) reflection high energy electron diffraction (RHEED) pattern transition at $\sim 500^\circ\text{C}$. Below this temperature, the submonolayer growth mode is Volmer–Weber with CaF_2 growing directly on the Si surface, and above $\sim 500^\circ\text{C}$ the initial growth mode is Stranski–Krastanov with CaF_2 islands forming on a CaF wetting layer. In addition, three growth regimes for the initial overlayer growth of CaF_2 have been reported by Denlinger et al. [9,10] using X-ray photoelectron diffraction: at $T \geq 600^\circ\text{C}$ with low flux, CaF_2 forms thick islands on a reacted Si– CaF interfacial layer; while at higher flux, subsequent growth on this interfacial layer proceeds as 2 layer high islands that coalesce, followed by layer-by-layer growth; and, at $T \sim 450^\circ\text{C}$ with all fluxes, the interface becomes an incompletely occupied Si– CaF_x ($x \sim 2$) layer that does not fully cover the substrate before nucleation of subsequent layers in an approximately layer-by-layer mode. On the other hand, Tromp et al. [11] reported step-flow growth after the initial growth of 2 monolayers of CaF_2 at 770°C .

In this paper, we present our reflection high energy electron diffraction (RHEED), atomic force microscopy (AFM), and scanning electron microscopy (SEM) studies of CaF_2 grown epitaxially on $\sim 2^\circ$ and $\sim 0.5^\circ$ miscut Si(111) 7×7 surfaces. For growth at $\sim 770^\circ\text{C}$, a ~ 2 monolayers thick interfacial wetting layer is first formed in a layer-by-layer fashion followed by a subsequent nucleation/propagation of thick islands (multilayer) along the Si atomic step edges which are bunched into step bands. The average height of the thick islands is a function of the substrate miscut angle which, apparently, is determined by the height of the original Si step bunches. The islands grow laterally, with subsequent deposition, to eventually form a flat overlayer. We have also performed a quantitative analysis of the CaF_2 islanding behavior observed at $\sim 770^\circ\text{C}$ and discuss the origin of the rough interfacial wetting layer as well as the role of the bunched step edges of the Si substrate which act as a preferential nucleation sites for CaF_2 molecules.

Epitaxial growth of CaF_2 at $\sim 250^\circ\text{C}$ on $\sim 0.5^\circ$ miscut Si(111) 7×7 surfaces has also been characterized. Initially, the CaF_2 forms 2 to 3 monolayers

high isolated islands on the Si terraces followed by growth primarily in a multilayer-by-multilayer mode. It is also noted that the rate at which the Si(111) 7×7 RHEED pattern is removed is much slower at $\sim 250^\circ\text{C}$ than at $\sim 770^\circ\text{C}$ which may indicate a weaker chemical reaction at the overlayer–substrate interface.

2. Experimental method

Samples were prepared in a Fisons V90S molecular beam epitaxy (MBE) system equipped with a high temperature graphite Knudsen cell [12] for CaF_2 evaporation, an e-beam evaporator for Si evaporation, and a RHEED apparatus for in-situ monitoring of the growth morphology. Vicinal Si(111) substrates (4" diameter, $0.006 \Omega \text{ cm}$ arsenic doped) with their surface normal tilted at either $\sim 2^\circ$ or $\sim 0.5^\circ$ (both towards the $[11-2]$ azimuth) were used in this experiment. After a standard RCA chemical cleaning, the Si substrate was loaded into the deposition chamber where it was heated to a temperature of $\sim 975^\circ\text{C}$ for 30 min to remove the thin native oxide. During the cooling process, the transition from the (1×1) to (7×7) RHEED pattern was observed at $850 \pm 20^\circ\text{C}$ for each wafer preparation. This was then followed by the growth of an 20 nm Si buffer layer at $\sim 700^\circ\text{C}$ with a deposition rate of 0.1 nm/s to eliminate any initial surface roughness and to bury any impurities left on the original Si substrate surface. The CaF_2 films were then grown on the Si buffer layer at either $\sim 770^\circ\text{C}$ or $\sim 250^\circ\text{C}$. The RHEED spot intensity variation was monitored during CaF_2 growth using a charge-coupled device (CCD) video camera and a digital image processing system. For CaF_2 evaporation, high purity CaF_2 was thermally heated to $\sim 1400^\circ\text{C}$ in the K-cell. The CaF_2 flux was measured by an ion gauge at the sample position which indicated a typical pressure of $\sim 1 \times 10^{-7}$ mbar (deposition rate of 0.01 to 0.03 nm/s during growth). The typical base vacuum pressure of the deposition chamber was in the mid 10^{-11} mbar range and the pressure increased to the mid 10^{-10} mbar range during CaF_2 deposition and to the high 10^{-9} mbar range during Si deposition. Substrate temperatures were measured with a thermocouple placed behind the substrate and calibrated

with an optical pyrometer (assuming an emissivity of 0.6 for the Si surface). The thickness of the CaF_2 films were measured ex-situ with Rutherford backscattering spectroscopy (RBS) using 2 MeV He^{1+} ions. These measurements were used to calibrate the deposition rate. The electron beam energy used for the RHEED analysis was 14 keV. After the growth, the surface morphology of the films were characterized ex-situ with AFM and/or SEM.

3. Results and discussion

3.1. The growth of CaF_2 at 770°C on 2° miscut Si(111) substrates

Typical RHEED intensity temporal profiles, monitored during CaF_2 growth, are shown in Fig. 1. The integral diffraction spot RHEED intensity initially shows almost two complete oscillations which correspond to ~ 2 monolayers of layer-by-layer CaF_2 growth as determined by RBS. The intensity then gradually decays to a constant level which indicates that the CaF_2 nucleates and then grows by step flow mode on the interfacial wetting layer. The RHEED pattern of the bare Si(111) 7×7 was observed to convert to a sharp 1×1 streaked pattern well before the first monolayer of CaF_2 growth. An AFM image of 0.5 ± 0.1 nm thick CaF_2 grown at 770°C is shown in Fig. 2(a). The surface morphology of this sample exhibits random corrugations which have an average height of 0.45 ± 0.10 nm and a diameter of 30 ± 15 nm. This result is consistent with oscillating RHEED intensity observed at the very early stage of the epitaxy and indicates that the interfacial wetting layer grows by formation and coalescence of isolated islands of atomic height on the Si terraces. Similar findings under these growth conditions have also been reported by Tromp et al. [11] using in-situ low energy electron microscopy (LEEM) and by Avouris et al. [4] using ultra high vacuum scanning tunneling microscopy (UHV-STM), although Cuberes et al. [13] have not observed such atomic-step corrugations in their UHV-STM work. The consistency in our measurement between RHEED intensity variations and the AFM topographies allows us to believe that the corrugations are not artifacts. However, the significantly larger substrate misorientation used in our

experiment with respect to the Cuberes' work may have resulted in the different surface morphologies observed. In particular, complete coverage of the wetting layer may already have been achieved in the Cuberes' work by the time that 4 monolayers of CaF_2 has been deposited.

The atomic-step corrugations which appear on the interfacial wetting layer may be due to excess Si atoms on the Si terraces which are unable to diffuse to the Si steps. Since the CaF_2 atoms react with the Si substrate to form an F–Ca–Si interfacial layer and SiF_4 molecules which evaporate, there will remain an excess of Si atoms on the terrace above the next Si layer. This must lead to roughening between steps unless the excess Si atoms can all migrate to the step edges.

Beyond ~ 2 monolayers, island nucleation (in a triangular shape with an average height of ~ 5 nm) is initiated at the Si step edges which are bunched into step bands with an average height of ~ 3 nm (Fig. 2(b)). These islands grow laterally (in a trapezoidal shape) along the step bunches (Fig. 2(c)) and eventually form a flat overlayer when ~ 5.2 nm of CaF_2 deposited (Fig. 2(d)). The origin of the unusual island nucleation and lateral growth mode observed here will be discussed in Section 3.4.

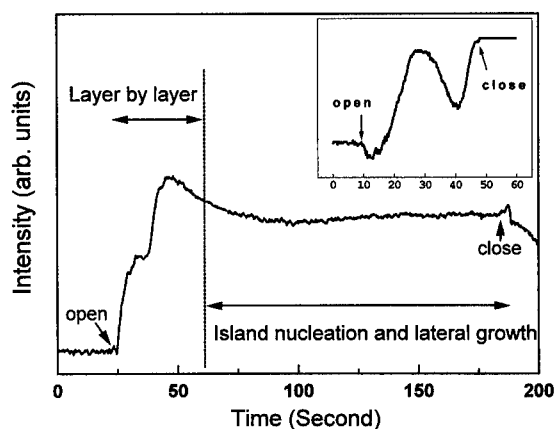


Fig. 1. The integral diffraction spot RHEED intensity temporal profiles monitored during 2.5 ± 0.1 nm and 0.5 ± 0.1 nm (shown in the inset figure) thick CaF_2 epitaxy on 2° miscut Si(111) substrates at 770°C. The RHEED intensity initially shows almost two complete oscillations which correspond to ~ 2 monolayers (monolayer = 0.315 nm) of layer-by-layer CaF_2 growth. The intensity then gradually decays to a constant level which indicates that the CaF_2 islands nucleate and then grow by step flow.

3.2. The growth of CaF_2 at 770°C on 0.5° miscut $\text{Si}(111)$ substrates

In Fig. 3, a typical time dependence of the RHEED intensity during CaF_2 growth is shown. Similar to

the behavior shown in Fig. 1, the integral diffraction spot intensity initially oscillates up to ~ 2 monolayers and then it gradually decays to a constant level with subsequent CaF_2 deposition. Also, the $1/7$ fractional order diffraction spots in the RHEED pat-

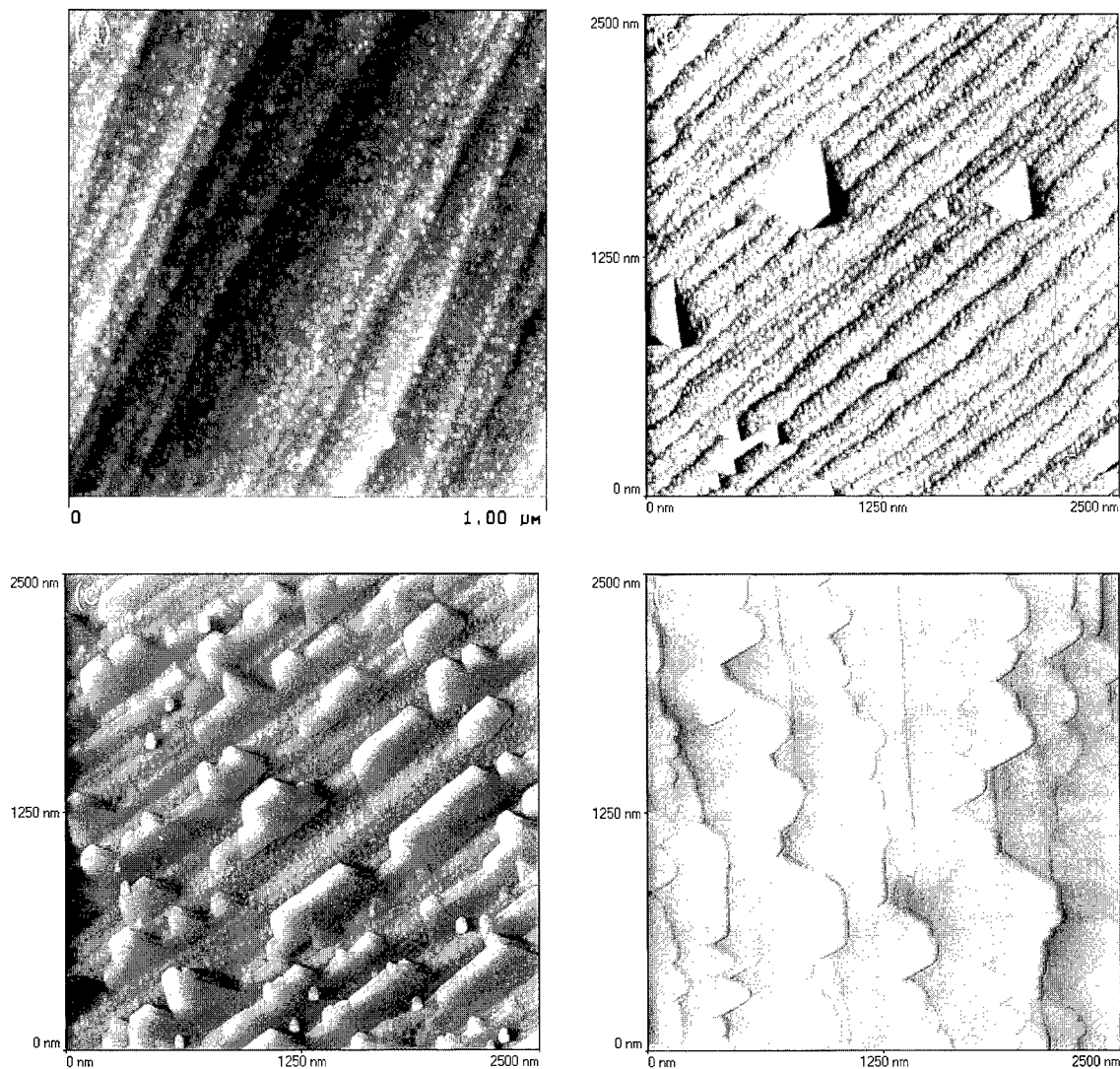


Fig. 2. (a) An AFM topography of a 0.5 ± 0.1 nm thick CaF_2 film grown on vicinal $\text{Si}(111)$ 2° miscut substrate at 770°C which shows that the surface of the interfacial wetting layer exhibits a roughness with an average corrugation height of 0.45 ± 0.10 nm and a diameter of 30 ± 15 nm. The total height range is 10 nm. (b) An AFM topography of a 0.8 ± 0.1 nm thick CaF_2 film grown on vicinal $\text{Si}(111)$ 2° miscut substrate at 770°C which shows that thick island (~ 5 nm in height) nucleation in a triangular shape is initiated at the Si step edges which are bunched into step bands with an average height of ~ 3 nm. The total height range is 16 nm. (c) An AFM topography of a 2.5 ± 0.1 nm thick CaF_2 film grown on vicinal $\text{Si}(111)$ 2° miscut substrate at 770°C which shows that triangular islands grow laterally (in a trapezoidal shape) along the step bunches. The total height range is 14 nm. (d) An AFM topography of a 5.2 ± 0.1 nm thick CaF_2 film grown on vicinal $\text{Si}(111)$ 2° miscut substrate at 770°C which shows that the thick islands eventually connect to form a complete overlayer with a very smooth surface. The total height range is 29 nm.

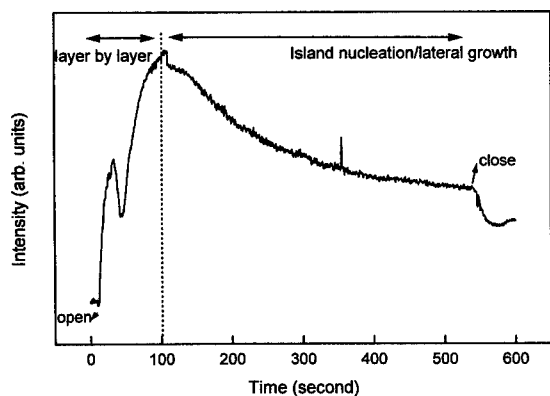


Fig. 3. The integral diffraction spot RHEED intensity temporal profile monitored during 5.3 ± 0.1 nm thick CaF_2 epitaxy on 0.5° miscut $\text{Si}(111)$ substrate at 770°C . The RHEED intensity profile initially shows almost two oscillations which correspond to ~ 2 monolayers of layer-by-layer CaF_2 growth. The intensity then gradually decays to a constant level which indicates that the CaF_2 islands nucleate and then grow by step flow mode.

tern, characteristic of the 7×7 reconstruction on the bare $\text{Si}(111)$ surface, completely disappeared and were replaced by a well defined streaked 1×1 pattern, characteristic of $\text{CaF}_2(111)$, well before the

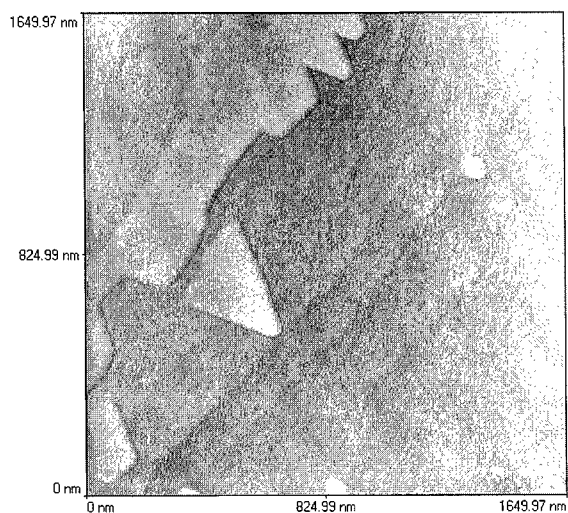


Fig. 4. An AFM topography of a 0.7 ± 0.1 nm thick CaF_2 film grown at 770°C on a 0.5° miscut $\text{Si}(111)$ substrate which shows that the nucleation of triangular and trapezoidal islands (~ 2 nm in height) is initiated at the Si step edges which are bunched into step bands of ~ 1.5 nm in height. The total height range is 6.99 nm.

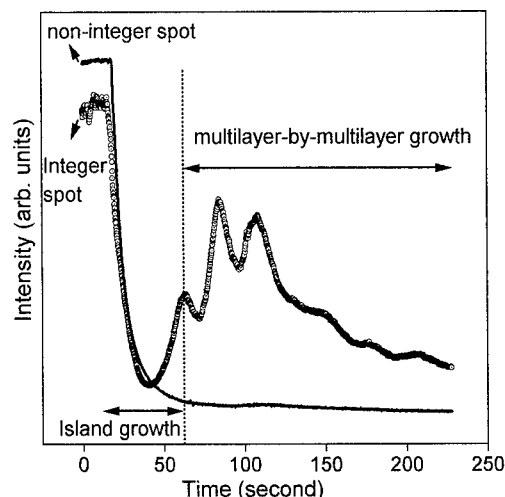


Fig. 5. The intensity temporal profiles of an integral and of a non-integral diffraction RHEED spots were monitored during epitaxy of an 2.8 ± 0.3 nm thick CaF_2 layer on a 0.5° miscut $\text{Si}(111)$ 7×7 surface at 250°C . The integral diffraction spot RHEED intensity decreases exponentially up to ~ 2 monolayers and then oscillates for about 6 periods afterwards with the first peak at ~ 3 monolayers. The intensity of the non-integral diffraction spot decreases exponentially up to ~ 3 monolayers and has disappeared completely beyond this point.

first monolayer of CaF_2 was grown. Fig. 4 illustrates a surface morphology after 0.7 ± 0.1 nm CaF_2 growth. It shows that the nucleation of triangular and trapezoidal islands (~ 2 nm in height) is initiated at the step bunches (~ 1.5 nm in height). These islands grow laterally along the step bunches and eventually form a flat overlayer when ~ 2.1 nm of CaF_2 is deposited.

3.3. The growth of CaF_2 at 250°C on 0.5° miscut $\text{Si}(111)$ substrates

The typical RHEED intensity temporal profiles monitored during CaF_2 growth are shown in Fig. 5. The integral diffraction spot RHEED intensity initially decreases exponentially up to ~ 2 monolayer and oscillates for about 6 periods afterwards with the first peak at ~ 3 monolayers. The intensity of a non-integral diffraction spot decreases exponentially up to ~ 3 monolayers and is completely removed beyond this point. The slower removal of the reconstructed RHEED pattern, characteristic of the bare

7×7 Si(111) surface, indicates that the interaction at the overlayer-substrate interface is much weaker at 250°C than at 770°C . Published RHEED work by Lucas et al. [7] also indicates the slower conversion of the 7×7 pattern into a 1×1 pattern during submonolayer CaF_2 growth for $T < 450^\circ\text{C}$ than for $T > 550^\circ\text{C}$. These results imply that the growth of the interfacial wetting layer is by formation of bi/tri-layer high isolated islands nucleation and coalescence on the Si terraces, and subsequent layers are grown primarily in a multilayer-by-multilayer growth mode (i.e., flat layer growth by formation of mono/bi-layer high isolated islands nucleation and coalescence on the terraces). This kind of bi-layer formation has been seen by other workers [7,14]. The SEM topography of the CaF_2 films grown at 250°C illustrates a featureless, flat surface morphology at ~ 4 , 7 and 9 monolayers, while the SEM topography of the CaF_2 films grown at 770°C shows a island nucleation/propagation morphology that is consistent with the AFM images.

3.4. Quantitative analysis of CaF_2 growth at 770°C on 2° and 0.5° miscut Si(111) substrates

The plot shown in Fig. 6 summarizes the early stages of CaF_2 epitaxy at $\sim 770^\circ\text{C}$ on both $\sim 2^\circ$ and $\sim 0.5^\circ$ miscut Si(111) substrates. By linearly fitting the data points in the plot, we have extracted a simple equation of the form

$$d_B = d_C + d_I f, \quad (1)$$

where d_B corresponds to the average CaF_2 thickness (measured by RBS), f corresponds to the fraction of area covered by CaF_2 islands (determined by AFM), d_C and d_I are fitting parameters corresponding to the interfacial wetting layer thickness and the average island height, respectively. Quantitatively, it illustrates that f increases linearly with d_B at the best-fitted values of $d_I = 5.19$ nm and $d_C = 0.54$ nm for 2° miscut substrate. Corresponding fit values on the 0.5° miscut substrates are: $d_I = 1.91$ nm and $d_C = 0.21$ nm. Qualitatively, it summarizes the CaF_2 growth behavior observed by RHEED and AFM in the following model. Island nucleation is not initiated until interfacial wetting layer (d_C) is formed. Island nucleation then occurs in triangular shapes at the step bunches. Once nucleated, these islands grow

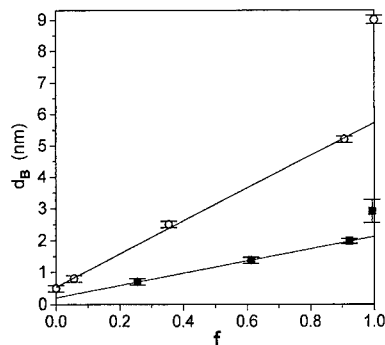


Fig. 6. Quantitative analysis of CaF_2 growth at 770°C on vicinal Si(111) 7×7 surfaces miscut by 2° (open circle) and 0.5° (solid square): f represents the fraction of the area covered by CaF_2 islands determined by AFM and d_B represents the average CaF_2 film thickness measured by RBS. It shows that island coverage increases linearly with the film thickness at a constant island height of ~ 5 nm for 2° miscut Si substrate and ~ 2 nm for 0.5° miscut Si substrate. It should be noted that there is no data below 0.5 nm for 0.5° miscut Si substrate, and that the straight line is only a linear extrapolation.

laterally along the step bunches with a constant island height (d_I) to eventually form a flat overlayer (i.e., $d_B = d_C + d_I$ at $f = 1$). The model predicts that CaF_2 islands will completely cover the entire interfacial wetting layer to form a flat layer when $d_B = 5.73$ nm or 2.12 nm is deposited on vicinal substrates miscut by 2° or 0.5° , respectively. The lowering in d_I , d_C and therefore d_B for $f = 1$ with decreasing in substrate miscut angle suggests that we may be able to control the CaF_2 growth modes from the very thick islanded structures to the extremely thin flat-layer structures by going from highly vicinal substrates to very well oriented substrates.

There are two questions to be answered about CaF_2 growth behavior on the interfacial wetting layer. First, why do CaF_2 molecules prefer to nucleate at the step bunches? Second, once island nucleation is initiated, why do islands form in a triangular shape and then propagate laterally along the step bunches in a trapezoidal shape? These questions may be answered if we make an assumption that CaF_2 molecules interact weakly with surface bonding sites on the interfacial wetting layer and move around until they find stronger bonding sites which are along the step bunches. Once nucleation of CaF_2 molecule along the step bunch is initiated, in order to

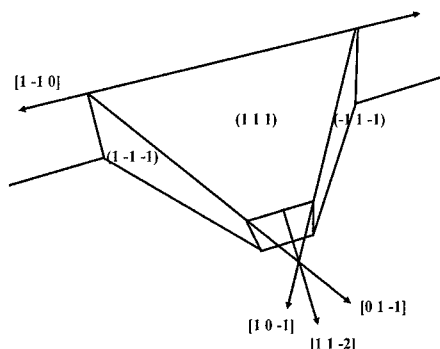


Fig. 7. A schematic of the observed thick CaF_2 islands is shown. This shape is expected from surface energy considerations. The Si step edge runs along a $[1\bar{1}0]$ (or $[\bar{1}10]$) direction, and $[1\bar{1}2]$ represents the direction which is perpendicular to the Si step edge.

minimize the total surface energy of the growing system, subsequent CaF_2 molecules will try to nucleate in a most stable configuration. This would be a terrace edge nucleation in a triangular shape as shown in Fig. 7. As indicated in this figure, island nucleation and propagation along $[1\bar{1}2]$ will eventually saturate with the decrease in the exposed aerial density of preferential bonding sites. The preferential bonding sites lying in $(\bar{1}1\bar{1})$ and $(1\bar{1}\bar{1})$ surfaces remain essentially the same as islands grow laterally along the $[1\bar{1}0]$ and $[\bar{1}10]$ directions to eventually cover the entire interfacial wetting layer. This model also applies to CaF_2 molecules impinging on the flat surfaces of the growing islands where the terrace edges will act as sinks until the fractional island coverage over the interfacial wetting layer becomes unity.

To get a feel for the relative bond strength between CaF_2 adatoms and sites on the thick CaF_2 islands versus sites on the interfacial surface, we have estimated the surface diffusion coefficient D and the energy barrier to the diffusion E of CaF_2 molecules moving on the interfacial wetting layer. First, we treat the CaF_2 diffusion length on the interfacial wetting layer to be the average separation, $S \sim 955 \pm 317$ nm, between the triangular islands observed in Fig. 2(b). Assuming that the sticking coefficient is unity, the diffusion time t of 21 s is taken from the time to deposit a monolayer of CaF_2 .

We evaluate D from the Einstein relation for surface diffusion given by [15]:

$$D = S^2/2t, \quad (2)$$

and E is evaluated from a hopping model given by [10,16]:

$$E = k_B T \ln(\nu a^2/D), \quad (3)$$

where ν is an atomic vibration frequency (approximated with $k_B T/h = 2.3 \times 10^{13}$ Hz), a is the nearest neighbor spacing of 0.386 nm for $\text{CaF}_2(111)$ surface, and $k_B T = 0.089$ eV. The calculated values of D and E for the CaF_2 diffusion on the interfacial wetting layer are $2.33 \pm 1.18 \times 10^{-10}$ cm²/s and 1.68 ± 0.05 eV, respectively. Denlinger et al. [10] and Mathet et al. [17] have separately evaluated the diffusion barrier energy to be 1.33 ± 0.06 eV and 1.1 eV, respectively. The same authors in Ref. [10] have also calculated a CaF_2 binding energy of 1.6 eV, based on the surface corrugation due to the Madelung potential. Our estimation of energy barrier to CaF_2 diffusion is in closer agreement with the CaF_2 binding energy calculation.

4. Conclusion

We have shown that at 770°C on vicinal Si(111) 7×7 surface, CaF_2 first forms an interfacial wetting layer, which exhibits a rough surface, in a layer-by-layer mode. The surface roughening between the steps may be caused by the absence of sufficient Si atoms in the terraces between step bands to form a complete Si monolayer after the reaction (and evaporation of SiF_4) of CaF_2 molecules with the bare Si surface. Beyond this point, CaF_2 weakly interacts with atomic sites on the interfacial wetting layer and finds it energetically favorable to nucleate as a triangular island and grow laterally in a trapezoidal shape along the bunched step edges to eventually form a flat overlayer. A simple model has been presented to explain the effect of substrate miscut angle on the CaF_2 growth at 770°C. It shows that the average island height which is function of substrate miscut angle is determined by step bunch height and predicts that the monoatomic steps on starting Si surface will yield flat CaF_2 layer without the introduction of

the thicker island nucleation/propagation growth regime. At 250°C, the CaF₂ initially grows by formation of 2 to 3 monolayers high isolated islands on the Si terraces and subsequent layers grow dominantly in a multilayer-by-multilayer mode. The relatively slow disappearance of the fractional-order diffraction spots corresponding to the Si(111) 7×7 RHEED pattern at 250°C compared to the almost instantaneous disappearance at 770°C indicates the weaker interaction at the overlayer–substrate interface when CaF₂ is deposited at lower temperatures.

Acknowledgements

This work was partially supported by the AFOSR, Rome Laboratory at Hanscom AFB, the NY State Science and Technology Foundation through the Thin Film and Coating CAT, and the National Science Foundation. Support for RO from the Exxon Research and Engineering Company is also gratefully acknowledged.

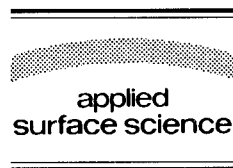
References

- [1] L.J. Schowalter and R.W. Fathauer, *CRC Crit. Rev.* 15 (1989) 367.
- [2] T. Suemasu, M. Watanabe, J. Suzuki, Y. Kohno, M. Asada and N. Suzuki, *J. Appl. Phys.* 33 (1994) 57.
- [3] R.M. Tromp and M.C. Reuter, *Phys. Rev. Lett.* 61 (1988) 1756.
- [4] Ph. Avouris and R. Wolkow, *Appl. Phys. Lett.* 55 (1989) 1074.
- [5] K.G. Huang, J. Zegenhagen, J.M. Philips and J.R. Patel, *Phys. Rev. Lett.* 72 (1994) 2440.
- [6] M.A. Olmstead, R.I. Uhrberg, R.D. Bringans and R.Z. Bachrach, *Phys. Rev. B* 35 (1987) 7526.
- [7] C.A. Lucas, D. Loretto and G.C.L. Wong, *Phys. Rev. B* 50 (1994) 14340.
- [8] G.C.L. Wong, D. Loretto, E. Rotenberg, M.A. Olmstead and C.A. Lucas, *Phys. Rev. B* 48 (1993) 5716.
- [9] J. Denlinger, E. Rotenberg, U. Hessinger, M. Leskovar and M.A. Olmstead, *Appl. Phys. Lett.* 62 (1993) 2057.
- [10] J.D. Denlinger, E. Rotenberg, U. Hessinger, M. Leskovar and M.A. Olmstead, *Phys. Rev. B* 51 (1995) 5352.
- [11] R.M. Tromp, F.K. LeGoues and M.C. Reuter, *Phys. Rev. Lett.* 74 (1995) 2706.
- [12] A.P. Taylor, K. Yang and L.J. Schowalter, *J. Vac. Sci. Technol. A* 9 (1991) 3181.
- [13] M.T. Cuberes, A. Bauer, H.J. Wen, M. Prietsch and G. Kaindl, *J. Vac. Sci. Technol. B* 12 (1994) 2646.
- [14] R.M. Tromp and M.C. Reuter, *Phys. Rev. Lett.* 73 (1994) 110.
- [15] J.H. Neave, P.J. Dodson and B.A. Joyce, *Appl. Phys. Lett.* 47 (1985) 100.
- [16] A.K. Myers-Beaghton and D.D. Vedensky, *Phys. Rev. B* 42 (1990) 5544.
- [17] V. Mathet, F. Nguyen-Van-Dau, J. Oliver and P. Galtier, *J. Cryst. Growth* 148 (1995) 133.



ELSEVIER

Applied Surface Science 104/105 (1996) 417–421



Growth of $\text{CdF}_2/\text{CaF}_2/\text{Si}(111)$ heterostructure with abrupt interfaces by using thin CaF_2 buffer layer

A. Izumi^{a,*}, K. Kawabata^a, K. Tsutsui^a, N.S. Sokolov^b, S.V. Novikov^b,
A.Yu. Khilko^b

^a Department of Applied Electronics, Tokyo Institute of Technology, 4259 Nagatsuta, Midori-ku, Yokohama 226, Japan

^b Ioffe Physico-Technical Institute, Russian Academy of Sciences, 26 Polytechnicheskaya, 194021 St. Petersburg, Russian Federation

Received 28 June 1995; accepted 14 November 1995

Abstract

The minimum thickness of CaF_2 buffer layer in $\text{CdF}_2/\text{CaF}_2/\text{Si}(111)$ heterostructure to grow CdF_2 epitaxially on $\text{Si}(111)$ under less stringent vacuum conditions ($\sim 10^{-8}$ Torr) was found to be 0.9 nm. Chemical reaction and growth mode at the initial stage of growth of CdF_2 layer on $\text{Si}(111)$ and on $\text{CaF}_2/\text{Si}(111)$ were studied with the in-situ X-ray photoelectron spectroscopy method. It was found that oxygen-related, chemical reaction of the CdF_2 occurred on the $\text{Si}(111)$ surface, but not on the $\text{CaF}_2(111)$ surface. Two-dimensional growth of CdF_2 layer from the initial stage was observed on the CaF_2 buffer layer. These results indicate that the CaF_2 buffer layer plays a role as a barrier layer to chemical reaction between the CdF_2 and the Si substrates. A short-period $\text{CdF}_2/\text{CaF}_2$ superlattice was grown on $\text{CaF}_2/\text{Si}(111)$ and the XRD showed satellite peaks which is consistent with the growth rate. This result shows that the structure has abrupt interfaces with less than a few monolayers.

1. Introduction

Epitaxial alkaline-earth fluorides such as CaF_2 , SrF_2 , BaF_2 have been investigated extensively since they are very attractive as insulators in future devices, e.g., high-speed and high-density three-dimensional integrated circuits, optoelectronic devices and intelligent sensors [1]. Cadmium fluoride (CdF_2) has the same crystalline structure as that of these alkaline-earth fluorides, and has been shown to have peculiar electrical and optical properties. In spite of a

large energy gap (8 eV) [2], doping by trivalent impurities followed by annealing allows the CdF_2 to be converted into a semiconducting material with shallow donor levels of about 0.1 eV and free electron concentration up to $4 \times 10^{18} \text{ cm}^{-3}$ at room temperature [3]. Another remarkable property of the doped CdF_2 is its efficient electroluminescence, where it is possible to change the emission wavelength from infrared to ultraviolet by choosing the dopant [4]. All these features will make epitaxial CdF_2 layers to be attractive especially on Si substrates. We have recently succeeded in the high quality epitaxial growth of CdF_2 on $\text{Si}(111)$ using the CaF_2 buffer layer [5]. It was also found that the direct growth of CdF_2 on $\text{Si}(111)$ without the CaF_2 buffer layer was difficult, even though the lattice

* Corresponding author.

¹ Research fellow of the Japan Society for the Promotion of Science.

constant of CdF_2 (5.39 Å) is closer to that of Si (5.41 Å) than that of CaF_2 (5.46 Å). From the viewpoint of device applications, it is necessary to make the thickness of the CaF_2 buffer layer so thin that electrons can tunnel through it between the CdF_2 layer and Si substrate for applications using vertical transport of electrons and for well defined superlattice (SL) structures which are desirable for such applications as unipolar optical devices [6], quantum effect devices [7], etc., by utilizing the large conduction band discontinuity of the $\text{CdF}_2/\text{CaF}_2$ interface [8]. Thus, the control of interfaces of the $\text{CdF}_2\text{--CaF}_2\text{--Si}$ system is very important.

In this paper, we investigated the minimum thickness of the CaF_2 buffer layer to grow CdF_2 epitaxially well on Si(111) and the role of the buffer layer by X-ray diffractometry (XRD) and in-situ X-ray photoelectron spectroscopy (XPS) method. A short-period $\text{CdF}_2/\text{CaF}_2$ SL was also grown on Si(111) to examine the formation of abrupt interfaces.

2. Experimental

In these experiments, we used two molecular beam epitaxy (MBE) systems. One of them, MBE-A, has three chambers consisting of a loading chamber, XPS analysis chamber ($< 10^{-9}$ Torr), and growth chamber ($\sim 10^{-8}$ Torr). It is possible to grow and analyze the samples in-situ in this system. X-ray photoelectron spectroscopy measurements were performed using the Al $K\alpha$ X-ray line (1486.6 eV) to examine the growth mode of CdF_2 layers and chemical reactions on the surface. The angle between the surface normal and the take-off direction of the photoelectrons was 0° . The binding energy scale was calibrated on the basis of 284.6 eV of C1s. CaF_2 layers were grown at 600°C on n-type Si(111) substrates whose resistivity is $4000\ \Omega\ \text{cm}$. On the other hand, CdF_2 layers were grown on the Si(111) or $\text{CaF}_2/\text{Si}(111)$ at 50°C . The thickness of CdF_2 overlayers was measured by the Rutherford backscattering spectroscopy (RBS) method after the characterizations by XPS. The other system, MBE-B, was composed of two chambers consisting of a loading chamber and a growth chamber ($< 10^{-10}$ Torr) which was used for growth of a short period SL of $[\text{CdF}_2\text{--}3\text{ML}/\text{CaF}_2\text{--}3\text{ML}]_{10}$ on a $\text{CaF}_2/\text{Si}(111)$ to

investigate interdiffusion between CdF_2 and CaF_2 . The SL was grown at 100°C on the 13 nm thick CaF_2 buffer layer. This CaF_2 buffer layer was grown coherently on the Si(111) substrate by using the two-step growth technique [9] where several monolayers (ML) were first grown at 700°C followed by succeeding growth at 100°C until the total thickness reached approximately 13 nm. The growth chamber of MBE-B was equipped with reflection high-energy electron diffraction (RHEED), where the growth rate of the fluorides was calibrated by RHEED intensity oscillations. Double crystal XRD ($\text{Cu K}\alpha_1$ radiation) was used to characterize the epitaxial growth of CdF_2 layers and the abruptness of interfaces of the $\text{CdF}_2\text{--CaF}_2$ SL.

3. Results and discussion

3.1. The minimum thickness of the CaF_2 buffer layer

Fig. 1 shows several $\theta\text{--}2\theta$ scans of the double crystal XRD patterns of $\text{CdF}_2/\text{CaF}_2/\text{Si}(111)$ structures using different thickness (0.6 nm, 0.9 nm and 1.2 nm) of the CaF_2 buffer layers. The structures were fabricated by the MBE-A system. The thicknesses of the CdF_2 overlayers were 185 nm, 35 nm and 155 nm on the 0.6 nm, 0.9 nm, and 1.2 nm CaF_2 buffer layers, respectively. The XRD revealed that CdF_2 grew well epitaxially on the 0.9 nm CaF_2 buffer layer, whereas, CdF_2 cannot grow epitaxially on the 0.6 nm CaF_2 buffer layer. So, the minimum

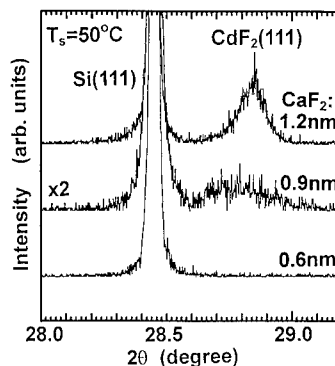


Fig. 1. Several $\theta\text{--}2\theta$ scans of the double-crystal, XRD patterns of $\text{CdF}_2/\text{CaF}_2/\text{Si}(111)$ structures with different thickness (0.6 nm, 0.9 nm and 1.2 nm) of CaF_2 buffer layers.

thickness of the CaF_2 buffer layer to obtain epitaxial CdF_2 layer under less stringent vacuum conditions ($\sim 10^{-8}$ Torr) was found to be 0.9 nm (~ 3 ML). This value of the thickness is considered to be so thin that significant electron tunneling through it should be expected.

3.2. Role of the CaF_2 buffer layer on the growth of $\text{CdF}_2/\text{CaF}_2/\text{Si}(111)$

Overview XPS spectra of F1s, O1s, Cd3d and Si2p for different thickness of CdF_2 overlayers, which were grown on the Si(111) substrates or on the CaF_2 (111) buffer layers, are shown in Fig. 2. An apparent peak is recognized in the O1s spectrum after 0.3 nm of CdF_2 , which corresponds to about 1 ML of CdF_2 , has been grown on Si(111) without a CaF_2 buffer layer, and its intensity stays constant even as the thickness of CdF_2 is increased beyond 1.2 nm. The quantity of these oxygen atoms can be estimated to be about 2 ML. On the other hand, in the case of growth on the CaF_2 buffer layers, no O1s peak could be observed at all after the growth of the

CdF_2 overlayers. For Cd3d spectra, no chemical shift was observed in the case of growth on the CaF_2 buffer layer. The different binding energy of F1s of CaF_2 and CdF_2 was observed before and after the growth of the CdF_2 layer in the case of growth on the CaF_2 buffer layer. The value of the difference between them is 0.6 eV which is in agreement with the reported value [10]. However, distinct chemical shifts of the F1s and Cd3d spectrum were observed in the case of direct growth on Si(111) as the thickness of CdF_2 layer increased from 0.3 nm. The peak of Cd3d has shifted 0.75 eV to lower binding energy. This value is found to be close to that of $\text{Cd}(\text{OH})_2$ [11]. The chemical shift on F1s spectra also can be considered to show a different chemical state from that of CdF_2 . In the Si2p spectra, however, no significant change was observed for growth both on the Si(111) and on the CaF_2 buffer layer except for their intensity. In addition, about half of the F ions seems to be desorbed from the first CdF_2 layer (0.3 nm), which is estimated from the integral intensity and the peak separation of the F1s spectra. These results suggest that the CdF_2 reacted with residual

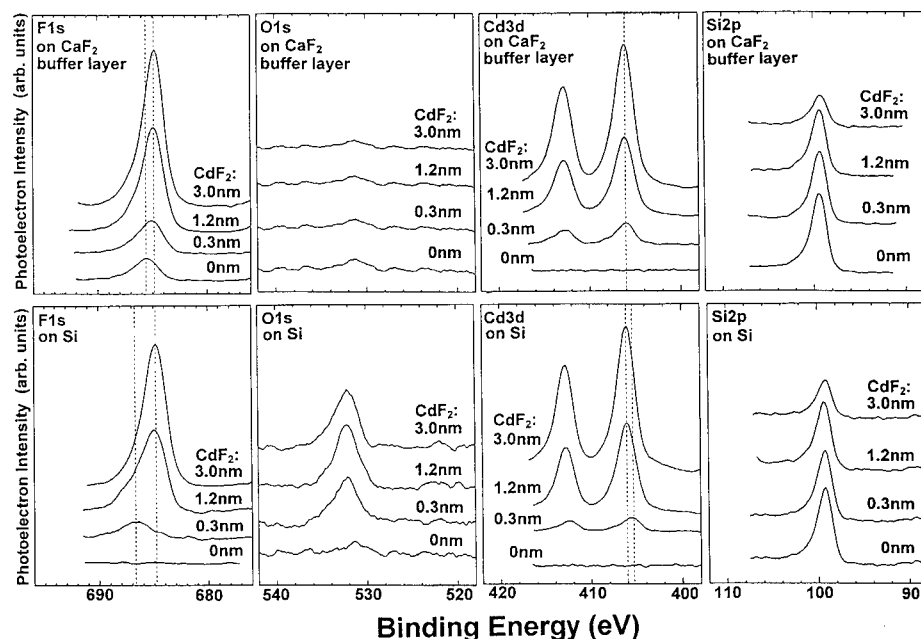


Fig. 2. Overview XPS spectra of F1s, O1s, Cd3d and Si2p for different thickness of CdF_2 overlayers which were grown on the Si(111) (lower column) or on the $\text{CaF}_2/\text{Si}(111)$ (upper column).

gasses containing oxygen in the atmosphere when CdF_2 molecules reached on the $\text{Si}(111)$ surface. But no such reaction occurred on the $\text{CaF}_2(111)$ surface. In other words, the $\text{Si}(111)$ surface appeared to act as a catalyzer. Indeed, using the MBE-B system, whose base pressure ($< 10^{-10}$ Torr) is better than that of the MBE-A system, we could succeed in the epitaxial growth of CdF_2 on $\text{Si}(111)$ although its crystallinity was not so good as that grown on the CaF_2 buffer layer [5]. The CaF_2 buffer layer whose thickness is over 0.9 nm considered to play a role for barrier layer to prevent chemical reactions from occurring and, thus, allowing a well ordered hetero-interface in the CdF_2 – CaF_2 – Si heterostructure to form even under less stringent vacuum conditions.

3.3. Growth mode of the initial stage of CdF_2 growth

The growth mode of the initial stage of growth of CdF_2 on $\text{Si}(111)$ and on $\text{CaF}_2/\text{Si}(111)$ was studied by observation of the decrease in the intensity of the $\text{Si}2p$ peak with increasing thickness of the overgrown CdF_2 . The photoelectron intensity I from the Si substrate can be expressed simply as indicated in the following equation when another uniform film is grown on the Si substrate,

$$I = I_0 \exp(-d/\lambda),$$

where I_0 represents the initial intensity before overgrowth, d represents the thickness of the overlayer, and λ represents the escape depth of photoelectrons penetrating the CdF_2 overlayer. So, if the CdF_2 overlayer grows two dimensionally to form a uniform layer, the photoelectron intensity from the Si should decrease exponentially as the thickness of the CdF_2 overlayer is increased. It was found that, in the case of growth on the $\text{CaF}_2/\text{Si}(111)$ substrates, the intensity of the $\text{Si}2p$ peak decreased exponentially with the thickness of the CdF_2 overlayer as shown in Fig. 3. The solid line in Fig. 3 shows a calculated curve by assuming $\lambda = 2.54$ nm which was obtained from Penn's equation [12]. As can be seen, the experiment agrees well with the calculation. So it can be said that CdF_2 grew two dimensionally to form a uniform layer from the initial stage on the CaF_2 buffer layer. On the other hand, in the case of growth on the bare $\text{Si}(111)$ substrates, the intensity

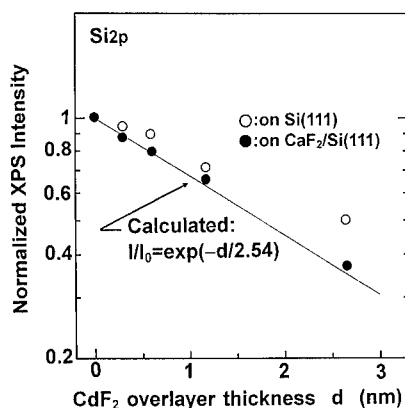


Fig. 3. Normalized XPS intensities of $\text{Si}2p$ as a function of CdF_2 overlayer thickness. Closed (●) and open (○) circles show the growth of the CdF_2 on the $\text{CaF}_2/\text{Si}(111)$ and on the $\text{Si}(111)$, respectively. The solid line indicates the calculated intensity assuming a uniform two dimensional growth of CdF_2 .

of $\text{Si}2p$ was observed not to decrease exponentially as shown in Fig. 3. This result suggests that CdF_2 grows with island formation on the bare $\text{Si}(111)$, which is considered to be related to the chemical reaction discussed above.

3.4. Formation of a CdF_2 – CaF_2 SL on $\text{CaF}_2/\text{Si}(111)$

Fig. 4 shows θ – 2θ , double crystal XRD patterns obtained from a short-period SL of $[\text{CdF}_2$ –3 ML/ CaF_2 –3 ML] $_{10}$. A well pronounced oscillating structure, which shows the well flatness of the SL,

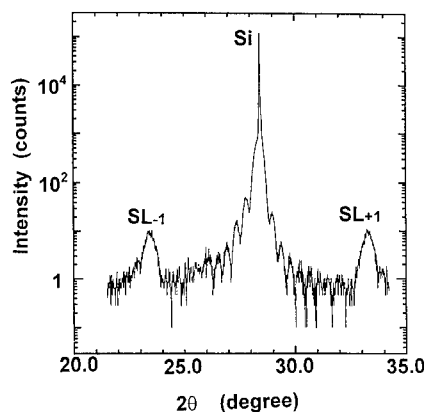


Fig. 4. Double crystal XRD pattern of $[\text{CdF}_2$ –3 ML/ CaF_2 –3 ML] $_{10}$ SL.

can be observed. The positions of the satellite peaks show that the period of the SL is 6 ML which is consistent with the growth rate. This result shows that the layered heterostructure has remained without being smeared at all by interdiffusion and/or chemical reaction. Thus, we considered that the structure has abrupt interfaces with less than a few ML at most.

4. Conclusion

The minimum thickness of CaF_2 buffer layer to grow CdF_2 epitaxially on $\text{Si}(111)$ was investigated. It was found that 0.9 nm CaF_2 is necessary for CdF_2 to grow epitaxially on $\text{Si}(111)$ under the less stringent vacuum conditions. Chemical reaction and growth mode at the initial stage of growth of CdF_2 layer on $\text{Si}(111)$ and $\text{CaF}_2/\text{Si}(111)$ were studied by in-situ XPS method. It was found that an oxygen-related chemical reaction of the CdF_2 occurred on the $\text{Si}(111)$ surface, but not on the $\text{CaF}_2(111)$ surface. Two-dimensional growth of CdF_2 layer at the initial stage was observed on the CaF_2 buffer layer. These results indicate that the CaF_2 buffer layer plays a role as a barrier layer to prevent chemical reaction during CdF_2 growth on Si substrates. A short-period $\text{CdF}_2/\text{CaF}_2$ SL was grown on $\text{CaF}_2/\text{Si}(111)$, and the XRD showed the structure had abrupt interfaces with less than a few ML.

Acknowledgements

This work was partially supported by Research fellowships of the Japan Society for the Promotion of Science for young scientists, and Kanagawa Academy of Science and Technology Research Grants.

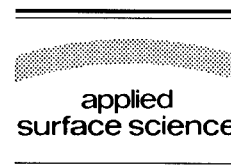
References

- [1] L.J. Schowalter and R.W. Fathauer, *CRC Crit. Rev.* 15 (1989) 367.
- [2] J.W. Hodby, in: *Crystals with the Fluorite Structure*, Ed. W. Hayes (Clarendon, Oxford, 1974) ch. 1.
- [3] R.P. Khosla, *Phys. Rev.* 183 (1969) 695.
- [4] J.M. Langer, T. Langer and B. Krukowska-Fulde, *J. Phys. D* 12 (1979) L95.
- [5] N.S. Sokolov, N.N. Faleev, S.V. Gastev, N.L. Yakovlev, A. Izumi and K. Tsutsui, *J. Vac. Sci. Technol. A* 13 (1995).
- [6] R.F. Kazarinov and R.A. Suris, *Fiz. Tekh. Poluprov.* 5 (1971) 797 [*Sov. Phys. Semicond.* 5 (1971) 707].
- [7] F. Capasso, K. Mohammed and A.Y. Cho, *IEEE J. Quantum Electron.* QE-22 (1986) 1853.
- [8] A. Izumi, T. Hirai, K. Tsutsui and N.S. Sokolov, *Appl. Phys. Lett.* 67 (1995).
- [9] N.S. Sokolov, T. Hirai, K. Kawasaki, S. Ohmi, K. Tsutsui, S. Furukawa, I. Takahashi, Y. Itoh and J. Harada, *Jpn. J. Appl. Phys.* 4 B (1994) 2395.
- [10] C.K. Jorgensen, H. Berthou and L. Balsenc, *J. Fluorine Chem.* 1 (1971–1972) 327.
- [11] C.D. Wagner, L.H. Gale and R.H. Raymond, *Anal. Chem.* 51 (1979) 466.
- [12] D.R. Penn, *J. Electron Spectrosc.* 9 (1976) 29.



ELSEVIER

Applied Surface Science 104/105 (1996) 422–427



Hydrogen ion treatments of oxidized GaAs(100) and AlGaAs(100) surfaces: surface stoichiometry and electronic properties

Ying-Lan Chang ^{a,*}, Sang I. Yi ^a, Song Shi ^a, Evelyn Hu ^a, W.H. Weinberg ^a,
James Merz ^b

^a Center for Quantized Electronic Structures (QUEST), University of California, Santa Barbara, CA 93106, USA

^b Department of Electrical Engineering, University of Notre Dame, Notre Dame, IN 46556-5602, USA

Received 28 June 1995; accepted 2 October 1995

Abstract

Near-surface GaAs/AlGaAs quantum wells, with and without a GaAs cap, have been used as effective probes of the electronic properties of oxidized GaAs surfaces and AlGaAs surfaces. We find that the variation of surface stoichiometry due to hydrogen ion treatments appears to be similar for both oxidized AlGaAs and GaAs surfaces, as examined by Auger electron spectroscopy. However, the composition of the oxide significantly affects both hydrogenation process and the efficacy of surface passivation.

1. Introduction

There is a great need for surface passivation treatments that result in enhanced electronic device properties, and which are both reproducible and of long-term durability. We have used the photoluminescence (PL) of a near-surface GaAs quantum well, clad by Al_{0.3}Ga_{0.7}As barrier layers, to gauge the effectiveness of surface passivation treatments on an oxidized AlGaAs surface [1]. The PL measurements revealed that irradiation by low energy (100 eV) hydrogen ion resulted in increased luminescence of the near-surface quantum wells, which persisted for more than two years [2]. Auger electron spectroscopy (AES) measurements indicate that the surface oxygen concentration remains unchanged after hydrogen

ion treatments with low exposures [3]. This oxide may serve as an over-passivation layer and, hence, preserve the passivated oxide–semiconductor interface. If this is true, then the composition of the oxide should be important in determining the quality and/or stability of the hydrogen passivation.

In this work, we have carried out a systematic set of experiments with a near-surface GaAs/AlGaAs quantum well, which had an additional 30 Å GaAs cap overlying the AlGaAs barrier layer. The luminescence efficiency of the near-surface GaAs/AlGaAs QW in this case should depend on the electronic properties of the oxidized GaAs surface. By comparing with our results on an oxidized AlGaAs surface, we can study the effect of oxide components on hydrogenation processes.

To offer insight into the chemical changes during the reaction, we have utilized AES to monitor in situ the changes in composition resulting from exposure

* Corresponding author. Now at Hewlett-Packard Co., Hewlett-Packard Laboratory, Palo Alto, CA 94304, USA.

of native oxide-covered GaAs to hydrogen ions. Ex situ PL measurements were then made to evaluate the modification of surface electronic properties, achieved after 100 eV hydrogen ion irradiation with different exposures.

2. Experimental procedures

The material structures used for the study of oxidized GaAs surface are shown in Fig. 1(a) and (b), and each consists of both a near-surface and a deep GaAs/Al_{0.3}Ga_{0.7}As QW grown on a semi-insulating GaAs(100) substrate by molecular beam epitaxy. All layers are non-intentionally doped. For both structures, the upper QW, denoted by Q1, is capped by an AlGaAs barrier layer (designated as a 'surface barrier layer, d' '), and the surface barrier layer is covered by a 30 Å thick GaAs cap. In structures (a), and (b), the surface barrier thickness, d , is 350 Å and 90 Å, respectively. The deeper QW, denoted by Q2, is separated by a 3500 Å barrier layer from the upper QW. The deeply embedded QW is insensitive to surface states and can thus serve as a reference for normalization of luminescence intensity. The material structure used for the study of oxidized AlGaAs surface is shown in Fig. 1(c). In this case, the upper QW is only capped by 80 Å thick AlGaAs barrier layer.

The samples were cleaned by a buffered HF solution, and then immediately introduced, via an external load lock, into an ultra-high vacuum (UHV) chamber with a base pressure of 5×10^{-11} Torr. The chamber is equipped with a four-grid rear-view low-energy electron diffraction (LEED) optics, an Auger electron spectrometer with a single-pass cylindrical mirror energy analyzer, an ion sputter gun, a pin-hole gas doser, and a tungsten filament. The chamber is pumped by a 1000 l/s turbomolecular pump.

Hydrogen ions were generated by using an ion sputter gun with differential gas inlet, operated at an ion energy of 100 eV. The flux was measured using the ion current collected on the sample. A typical ion current density of $\sim 2 \mu\text{A}/\text{cm}^2$ was used. To minimize the diffusion of hydrogen during the hydrogen treatment, the samples were cooled to 200 K during the experiments using liquid nitrogen.

AES measurements were made to provide information on the composition of the native oxide-covered GaAs and AlGaAs surface before and after different hydrogen treatments. The thickness of the native oxide has been estimated to be between 5 and 10 Å [4]. For AES measurements, the compositions of Ga, As, and Al were probed by the high kinetic energy peaks, i.e. 1070 eV, 1228 eV, and 1396 eV, respectively. This allows us to monitor the variation of composition of both the native oxide and the semiconductor surface (see, for example, Ref. [5]).

The variation of normalized luminescence efficiency (η), which is defined as $[I_{Q1}/I_{Q2}]^d/[I_{Q1}/I_{Q2}]^{d=350\text{Å}}$, before and after different hydrogenation treatments was determined by ex situ PL measurements. The near-surface QW sample was held at a temperature of 1.4 K and was excited by an Ar ion laser with a power density of $\sim 1 \text{ W}/\text{cm}^2$. The PL spectra were measured with a GaAs photomultiplier detector.

3. Results

3.1. In situ AES measurements

Our earlier AES measurements of the hydrogenated AlGaAs-barrier samples (structure in Fig. 1(c)) showed that low energy hydrogen ion irradiation

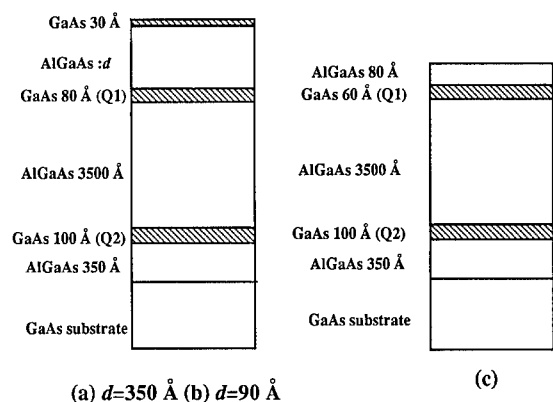


Fig. 1. Sample structures of GaAs/AlGaAs QW. The Al fractional composition is 0.3. The upper QW is denoted by Q1, and the deeper QW is denoted by Q2. The AlGaAs surface barrier layer thickness is 350 Å for structure (a), and 90 Å for structure (b). In structure (c), the upper QW is only capped by 80 Å thick AlGaAs layer.

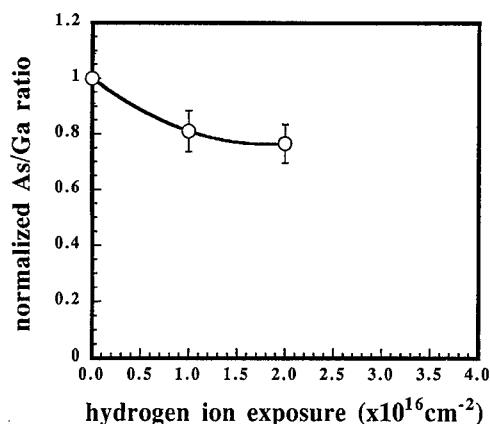


Fig. 2. The variation of normalized As(1228 eV)/Ga(1070 eV) AES peak height ratio with hydrogen ion exposure. The solid curves are guides for the eyes.

tion causes the reduction of the As/Ga ratio without changing the surface oxygen concentration [3]. Similar results can be observed on an oxidized GaAs surface, as shown in Fig. 2. In this figure, the AES peak height ratio has been normalized to the initial value of the untreated substrate, i.e. we are plotting $[I_{\text{As}}/I_{\text{Ga}}]^{\text{hydrogen treatments}}/[I_{\text{As}}/I_{\text{Ga}}]^{\text{as received}}$. As can be seen from the experimental results, low exposures ($\sim 10^{16} \text{ cm}^{-2}$) of hydrogen ions produce a modified, Ga-rich surface. The departure from the initial As/Ga stoichiometry increases with the ion exposure. At an exposure of $2 \times 10^{16} \text{ cm}^{-2}$, the As/Ga peak height ratio is reduced to ~ 0.75 . However, the surface oxygen concentration remains the same in these cases.

After hydrogen ion treatment and AES measurements, the samples were allowed to warm to room temperature, and the AES spectra were measured again. In all cases, no significant difference in the AES composition profiles was found.

3.2. Ex situ PL measurements

Fig. 3 shows the PL spectra for structures (a) and (b) with different surface barrier thicknesses. Curve (a) of Fig. 3 displays the PL spectrum obtained from an as-grown sample with $d = 350 \text{ \AA}$, where the higher energy peak denoted as Q1 at $\sim 1.57 \text{ eV}$ is from the near-surface QW and the other one denoted as Q2 at $\sim 1.555 \text{ eV}$ is from the deep QW. Each

excitonic peak corresponds to the fundamental transition between electron and hole states (e1-hh1). The PL spectrum for the sample with a reduced barrier thickness of 90 \AA is shown in curve (b). As expected, the PL intensity for the near-surface QW with reduced barrier thickness is itself greatly reduced. Since we believe that the nonradiative carrier recombination at the GaAs/AlGaAs interface is negligible [6], we assume that the luminescence reduction is primarily through interactions with the oxidized GaAs surface. Structure (b), with strongly reduced luminescence efficiency without passivation, was then used to study the passivation effects of oxidized GaAs surface achieved under different hydrogen treatments.

The hydrogen ion exposures were varied from $5 \times 10^{14} \text{ cm}^{-2}$ to $5 \times 10^{16} \text{ cm}^{-2}$. In these cases, the O/Ga peak height ratios were unchanged after the hydrogen ion treatments. Therefore, we will assume that the nature of the interface between the oxide layer and the GaAs barrier is not significantly altered during the transfer necessary for ex situ PL measurements.

The observed variation of η is summarized in Fig. 4. For comparison, the data taken on structure (c) are also shown [3]. This set of data demonstrates the electronic properties of an oxidized AlGaAs surface before and after different hydrogen treatments.

As mentioned above, we observed a reduction of

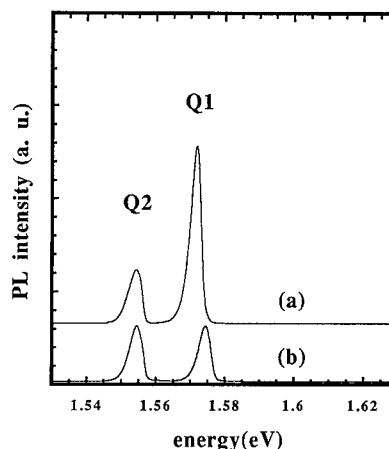


Fig. 3. The PL spectra for structures (a) and (b) before hydrogen ion treatments. The emission denoted by Q1 is from the upper QW, and the emission denoted by Q2 is from the deep QW.

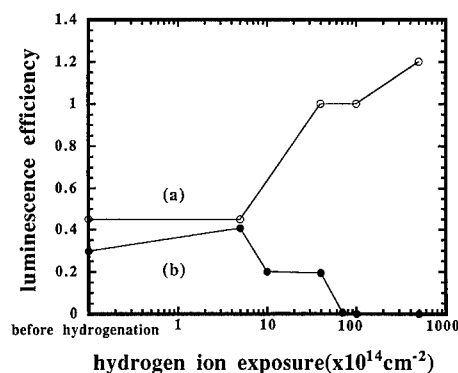


Fig. 4. The variation of luminescence efficiency, $[I_{Q1}/I_{Q2}]^d/[I_{Q1}/I_{Q2}]^d_{d=350\text{\AA}}$, of the near-surface QW with and without a GaAs cap before and after different surface treatments. (a) AlGaAs surface (without GaAs cap); (b) GaAs surface (with GaAs cap).

the As/Ga peak height ratios for both oxidized AlGaAs and GaAs surfaces. However, the variation of the luminescence efficiency of the QW is quite different for these two structures. For a near-surface QW with an oxidized AlGaAs surface, as shown in Fig. 4(a), we observed enhanced luminescence above a threshold exposure of $\sim 10^{15} \text{ cm}^{-2}$. For a hydrogen ion exposure of $5 \times 10^{16} \text{ cm}^{-2}$, η is greater than unity, which is presumably due to the diffusion of hydrogen into the material and the passivation of defects in the bulk [3]. On the contrary, for a near-surface QW covered by a GaAs cap, a slight enhancement in the luminescence efficiency ($\sim 40\%$)

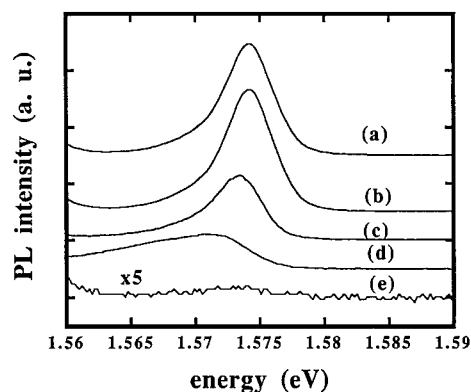


Fig. 5. The PL spectra of the free exciton transition line of Q1 in structure (b) before and after different hydrogen ion treatments. (a) Before treatment, (b) $5 \times 10^{14} \text{ cm}^{-2}$, (c) 10^{15} cm^{-2} , (d) $4 \times 10^{15} \text{ cm}^{-2}$, (e) $7 \times 10^{15} \text{ cm}^{-2}$. A significant broadening was observed with increasing hydrogen ion exposures.

was already observed with a hydrogen ion exposure of $5 \times 10^{14} \text{ cm}^{-2}$. Increasing hydrogen ion exposures resulted in *degradation*, rather than enhancement, of the luminescence efficiency, with a significant broadening of the free exciton transition line, as shown in Fig. 5.

Curve (a) of Fig. 5 displays the PL spectrum of the free exciton transition line of Q1 in structure (b) before any hydrogen ion treatment. An increased exposure of hydrogen ions produced a broadening of Q1, accompanied by a slight red-shift, relative to the energy peak position of the as-grown sample. Both the peak intensity and the energy position of Q2 remain the same as in the as-grown sample.

4. Discussion

The understanding of hydrogen ion passivation we had established from previous studies on the near-surface GaAs/AlGaAs QW structures, having AlGaAs at the surface, is as follows. Hydrogen ions interact with the AlGaAs surface through the native oxide layer, forming volatile arsine (AsH_3), which was observed by temperature-programmed desorption (TPD) measurements [2]. This results in a Ga/Al-rich oxide–semiconductor interface, the presence of which was verified by in situ AES measurements. AES also shows no significant change of the oxygen concentration due to hydrogen ion treatment with low exposures, relative to the reference (non-hydrogenated) sample. The removal of arsenic from the oxide/substrate interface reduces the number of As-antisite defects, which are near-midgap states, and can be responsible for a high surface recombination velocity [7]. This passivation mechanism also provides an appropriate interpretation of our experimental observations on InGaAs/InP surface QW structures after different hydrogen ion treatments [8].

For an oxidized GaAs surface, the AES measurements also show the reduction of the As/Ga peak height ratio. However, the PL spectra of the near-surface QW clearly show a general degradation in surface quality, in direct proportion to the hydrogen ion exposure. The enhancement of PL intensity was observed for InGaAs/InP QW, situated directly at the surface, under the similar operation conditions [8]. We therefore conclude that the degradation we

observe at the present structure is not related to ion bombardment effects. A detailed comparison of exposure-dependent behavior, as shown in Fig. 4, provides some insight into the different hydrogenation processes in the two materials.

For the GaAs-capped samples, there is a slight enhancement of PL intensity of Q1 at a hydrogen ion exposure of $5 \times 10^{14} \text{ cm}^{-2}$. This is much smaller than the threshold value for effective passivation of the AlGaAs-capped samples, as shown in Fig. 4. For the same external exposure, there appears to be a larger concentration of hydrogen ions reaching the oxide–semiconductor interface in the GaAs-capped material. Hence, the luminescence enhancement can be observed at a much lower external exposure than for the AlGaAs-capped material.

We have previously reported that extensive hydrogen-ion exposure can lead to hydrogen agglomeration at defect sites in the material [9,10], which results in the appearance of broad peaks in the luminescence spectrum and degradation of the luminescence efficiency. We similarly expect this threshold in hydrogen exposure producing material damage will be reached at a lower exposure for the GaAs-capped material, which is actually what is experimentally observed. The change of shape of the free exciton transition line for the near-surface QW, as observed at high exposure (Fig. 5), might be an indication of the formation of hydrogen-related defects in the near-surface region.

An alternative explanation for the broadening of the free exciton transition line could be associated with the increased surface roughness due to the effect of ion impact. It has been reported that a clear metallic threshold can be observed on a clean GaAs(110) surface treated by a high exposure of H_2^+ [11]. Although we do not have direct evidence of the clustering of Ga atoms in the present case, we expect that the oxidized AlGaAs surface is more robust than oxidized GaAs, under the irradiation of 100 eV hydrogen ions. Examination of the heats of formation of the different oxides shows that the Al-oxide is more stable than the oxides of Ga or As [12]. As a result, the broadening of the free exciton transition line of a near-surface QW with an oxidized AlGaAs surface was only observed after hydrogen ion treatments at very high exposures ($\sim 5 \times 10^{16} \text{ cm}^{-2}$) [3]. The high durability of Al-oxide can also explain the

long-term stability of hydrogen passivation from an oxidized AlGaAs surface.

5. Conclusions

In summary, we have reported in situ monitoring of the chemical changes that take place on a native oxide-covered GaAs surface treated by hydrogen ions. Although the change of surface stoichiometry is similar for oxidized GaAs and AlGaAs surfaces, the variation of luminescence efficiency of the near-surface QW with and without a GaAs cap are quite different under 100 eV hydrogen ion irradiation.

Our experiments demonstrate that the hydrogen ion treatment is able to modify the oxide–GaAs interface even at low exposures. The threshold in hydrogen exposure that produces material damage is also lower for the GaAs-capped material. The net effect is as if the GaAs-oxide allows greater penetration of the hydrogen ions than does the AlGaAs-oxide. This may be due to differences in the thickness of the two native oxides or in the quality of the oxides.

A systematic determination of the optimal hydrogenation parameters, including ion energies and ion exposures, will be carried out for $\text{Al}_x\text{Ga}_{1-x}\text{As}$ surfaces with different Al compositions. Such information is essential for further application of this technique to GaAs-based devices and will lead to further understanding of hydrogen passivation.

Acknowledgements

We are grateful to Professor William E. Spicer, and Dr. Renyu Cao of Stanford University for helpful discussions. Primary support for this work was provided by the NSF Science and Technology Center for Quantized Electronic Structures (QUEST), Grant #DMR 91-20007, with additional support from the W.M. Keck Foundation.

References

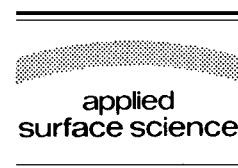
- [1] Y.-L. Chang, I.-H. Tan, Y.H. Zhang, J. Merz, E. Hu, A. Prova and V. Emiliani, *Appl. Phys. Lett.* 62 (1993) 2697.

- [2] Y.-L. Chang, S.I. Yi, S. Shi, E. Hu, W.H. Weinberg and J. Merz, *J. Vac. Sci. Technol. B* 13 (1995) 1801.
- [3] Y.-L. Chang, W. Widdra, S.I. Yi, J. Merz, W.H. Weinberg and E. Hu, *J. Vac. Sci. Technol. B* 12 (1994) 2605.
- [4] P. Friedel, J.-P. Landesman, P. Boher and J. Schneider, *J. Vac. Sci. Technol. B* 5 (1987) 1129.
- [5] D.R. Penn, *J. Vac. Sci. Technol.* 13 (1976) 221, and references therein.
- [6] E. Yablonovitch, C.J. Sandroff, R. Bhat and T. Gmitter, *Appl. Phys. Lett.* 51 (1987) 439.
- [7] W.E. Spicer, T. Kendelewicz, N. Newman, R. Cao and E.R. Weber, *J. Vac. Sci. Technol. B* 6 (1988) 1245.
- [8] Y.-L. Chang, I.-H. Tan, C. Reaves, E. Hu, J. Merz and S. DenBaars, *J. Vac. Sci. Technol. B* 12 (1994) 3704.
- [9] Y.-L. Chang, M. Krishnamurthy, I.-H. Tan, E. Hu, J. Merz, P.M. Petroff, A. Frova and V. Emiliani, *J. Vac. Sci. Technol. B* 11 (1993) 1702.
- [10] Y.-L. Chang, I.-H. Tan, E. Hu, J. Merz, V. Emiliani and A. Frova, *J. Appl. Phys.* 75 (1994) 3040.
- [11] F. Proix, *Physica B* 170 (1991) 457.
- [12] O. Kubaschewski and C.B. Alcock, *Metallurgical Thermochemistry*, 5th ed. (Permagon, New York, 1979).



ELSEVIER

Applied Surface Science 104/105 (1996) 428–433



Interface properties of PN_x/InP structures by in-situ remote plasma processes

Takashi Sugino, Yoshifumi Sakamoto, Takashi Miyazaki, Junji Shirafuji *

Department of Electrical Engineering, Faculty of Engineering, Osaka University, 2-1 Yamadaoka, Suita, Osaka 565, Japan

Received 28 June 1995; accepted 6 October 1995

Abstract

Interfacial properties of $\text{Au}/\text{PN}_x/\text{n-InP}$ Schottky junctions and metal–insulator–semiconductor (MIS) diodes formed by a series of in-situ remote plasma processes have been evaluated by measuring electrical characteristics. The in-situ processes consist of removal of native oxide by a H_2 plasma, surface modification by a PH_3 plasma, deposition of a PN_x layer by the use of PH_3 and N_2 plasma, and subsequent metal evaporation. An effective barrier height of 0.83 eV and a true barrier height of 0.57 eV are observed for the tunnel MIS Schottky junction. An interface state density as low as $1.4 \times 10^{11} \text{ eV}^{-1} \text{ cm}^{-2}$ is obtained for the MIS diodes. From the behavior of the true barrier height and the low interface state density, it is suggested that a novel in-situ process is effective in forming an interface of PN_x/InP structure.

1. Introduction

The fabrication process of Schottky and metal–insulator–semiconductor (MIS) contacts with a low interface state density is a key technology for InP and GaAs-based electronic and optoelectronic devices. It is well known that the surface Fermi level pinning occurs for Schottky contacts formed on InP and GaAs [1,2]. For conventional Schottky contacts formed on chemically etched n-InP surfaces, the barrier height is nearly fixed at about 0.4 eV irrespective of the type of metal and its work functions [3].

A conventional way for enhancing the effective barrier height of the Schottky contact is to introduce a tunnel metal–insulator–semiconductor (MIS) structure [4]. Attempts to form tunnel MIS Schottky

structures have been carried out by deposition of an insulating layer by applying various processes [5,6]. The effective barrier heights higher than 0.8 eV were achieved for tunnel MIS junctions employing a thin insulating layer of P_xO_y or $\text{PO}_x\text{N}_y\text{H}_z$ deposited by pyrolytic CVD [5,6]. However, in these cases the surface Fermi level is still pinned around 0.4 eV below the conduction band edge. The apparent enhancement of the barrier height is only due to the existence of the insulating tunnel barrier layer.

Another and orthodox way is to unpin the surface Fermi level and to use a Schottky metal with a large work function. It has recently been reported that the true barrier height is increased to 0.59 eV for Au/InP tunnel MIS Schottky junctions formed on the surface modified with photodecomposed phosphine (PH_3) or PH_3 plasma [7,8].

The photodecomposed PH_3 or PH_3 plasma process can cause the following combined effects on the

* Corresponding author.

substrate surface: removal of native oxide, surface modification including defect passivation and deposition of a phosphorus-related insulating layer. However, it is important to reveal the effect of an individual processing step on the surface properties of semiconductors in order to improve properties of InP-based Schottky and MIS diodes.

We have tried an in-situ multi-step plasma process consisting of a series of removal of native oxide by H_2 plasma, surface modification by a PH_3 plasma, plasma-enhanced deposition of a PN_x insulating layer by PH_3 and N_2 , and Schottky metal evaporation. Each plasma process is carried out using a remote plasma to minimize plasma damage. However, when InP surfaces are treated with a H_2 plasma, even if the plasma is remote, phosphorus dissociation from the surface is not avoidable [9]. Subsequent PH_3 plasma treatment is required to improve the surface exposed to H_2 plasma. Synthesis of PN_x as an insulating film can suppress phosphorus dissociation from the InP surface during film deposition because it is carried out in an excess phosphorus environment.

In this paper electrical characteristics are examined for Au/ PN_x /InP tunnel MIS Schottky junctions and MIS diodes fabricated by using the in-situ remote plasma process. It is demonstrated that the in-situ remote plasma process is effective in forming PN_x /InP interfaces.

2. Experimental

The experiments were carried out on the (100)-oriented surface of undoped n-type InP substrates of which the electron concentration was $5 \times 10^{15} \text{ cm}^{-3}$. Prior to plasma treatment, an ohmic contact was provided on the back side of the InP substrate with AuGeNi. The samples were chemically etched with a solution consisting of $H_2SO_4 : H_2O_2 : H_2O = 5 : 1 : 1$ for 3 min and then with a solution of $HF : H_2O = 1 : 1$ for 1 min to remove the native oxide. A reaction chamber was specially designed for carrying out in-situ processes of remote H_2 and PH_3 plasma treatments, PN_x deposition due to decomposition of PH_3 by a N_2 plasma, and vacuum evaporation of various metals [10]. The remote plasma was excited in a horizontally equipped quartz tube by supplying

an rf (13.56 MHz) power (30 W) to an inductive coil 10 cm away from the substrates in the reaction chamber. After the substrates were loaded on the holder, the chamber was evacuated to the base pressure of 3×10^{-6} Torr. H_2 or 10% PH_3 diluted with Ar was introduced into the horizontal quartz tube located on the side of the reaction chamber at a flow rate of 15 sccm. The gas pressure was regulated at 0.2 Torr. At first H_2 plasma treatment was carried out at 95°C for 10 min in order to remove the native oxide at the surface of InP. The InP substrate was then treated with PH_3 plasma at 250°C for 5 min. After that, PN_x thin films were synthesized at 250°C by decomposing PH_3 by a N_2 remote plasma. It has been reported previously that the bandgap of PN_x films is estimated to be 5.3 eV by optical absorption measurement [10]. Finally Schottky contacts were formed at room temperature by in-situ Au evaporation. The contact area was 1 mm in diameter.

X-ray photoelectron spectroscopy (XPS) was carried out to analyze the interfacial region between Au and InP. Current–voltage (I – V) characteristics of Schottky junctions were measured at various temperatures to estimate both apparent and true Schottky barrier heights. I – V characteristics were also measured for PN_x films at room temperature to estimate the electrical resistivity. Capacitance–voltage (C – V) characteristics were measured at 1 MHz for Au/ PN_x /InP MIS diodes. The interface state density was evaluated by Terman's method [11].

3. Results and discussion

In order to examine the existence of a surface layer on the InP treated with PH_3 plasma after removal of native oxide due to H_2 plasma treatment, the cross section of the sample was observed by transmission electron microscopy (TEM). The sample for TEM observation was covered by an Au layer after the successive plasma treatments with H_2 (10 min) and with PH_3 (5 min). This Au coating was necessary to avoid oxidation of the plasma treated surface due to air exposure. Fig. 1 shows the cross sectional TEM micrograph of the Au/InP structure. The presence of an interfacial layer of 4 nm in thickness between Au and InP is clearly seen.

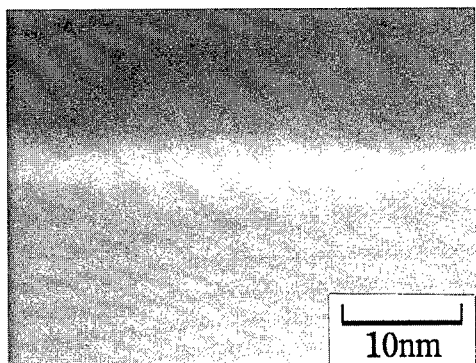


Fig. 1. Cross sectional TEM micrograph of modified the Au/InP Schottky junction.

The interfacial region confirmed by TEM observation was analyzed by XPS on the same sample. XPS measurement and Ar sputtering for 0.1 min were made alternately. The sputtering rate was estimated to be at most 20–30 nm/min. It was considered that the XPS signal was obtained in the region of about 1 nm deep from the surface, taking account of the escape depth of photoelectrons. Fig. 2 (a) and (b) show the XPS spectra of the In 3d_{5/2} core level and the P 2p core level, respectively, measured in the interfacial layer near the InP substrate. For comparison, the XPS spectra from the InP bulk obtained after further Ar sputtering was examined. The XPS spectrum of the In 3d_{5/2} core level measured in the interfacial layer was quite comparable to that of the bulk. The main peak at 444.2 eV is due to In–P bonding as confirmed from the spectrum of the bulk. On the other hand, the P 2p core level spectrum of the bulk at 128.8 eV was very symmetrical, while that measured in the interfacial layer (Fig. 2(b)) widens asymmetrically in the higher energy region. After deconvolution of the XPS signal from the interfacial layer, the coexistence of a weak signal at 130.2 eV due to elemental phosphorus [12] is revealed. This suggests a pile-up of elemental phosphorus in the interfacial region. It should be noted here that no oxide layer is detected at and near the interface due to the effect of H₂ plasma treatment.

Three categories of Schottky junctions were prepared as follows:

(1) Au/PN_x/InP MIS Schottky junctions: The in-situ H₂ and subsequent PH₃ plasma treatments were performed for 10 min and 5 min, respectively.

A PN_x film was then deposited for 1 min followed by in-situ Au evaporation. The thickness of the PN_x film was 3.3 nm as estimated from the deposition rate of 0.055 nm/s.

(2) Modified Au/InP Schottky junctions: The surface of the InP substrates was treated with H₂ and subsequent PH₃ plasmas in the same manner as in case 1. The Au Schottky contact was then evaporated immediately after PH₃ plasma treatment.

(3) Au/InP Schottky junctions: The Au Schottky contact was evaporated on a conventionally wet etched surface.

Fig. 3 shows the room temperature *I*–*V* characteristics of Au/InP, modified Au/InP and Au/PN_x/InP Schottky junctions. On the basis of a thermionic emission model [12], the effective barrier height of the Au/InP Schottky junction is 0.45 eV, assuming the effective Richardson constant is 9.2 A cm⁻² K⁻² for the electron effective mass ($m^* = 0.077m_0$) [13]. On the other hand, it is seen that the effective barrier heights are increased to 0.74 and 0.83 eV for the modified Au/InP and Au/PN_x/InP Schottky junctions, respectively.

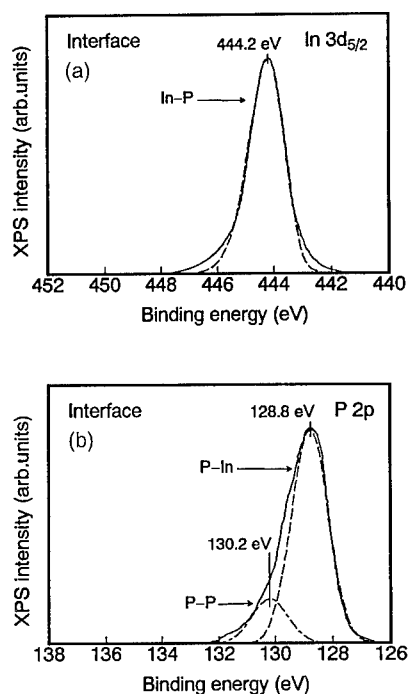


Fig. 2. XPS spectra of In 3d_{5/2} and P 2p core levels from the interfacial region of the modified Au/InP Schottky junction.

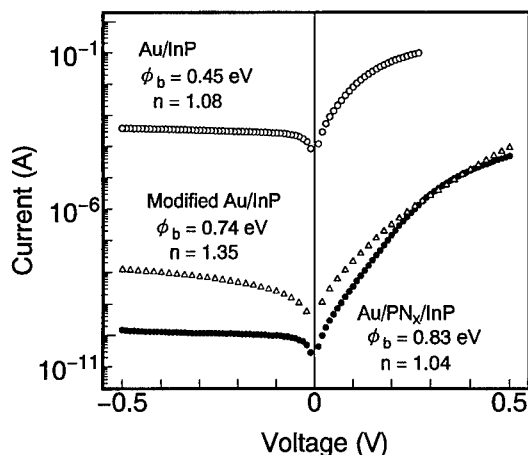


Fig. 3. Room-temperature I - V characteristics for conventional Au/InP, modified Au/InP and Au/PN_x/InP Schottky junctions.

The true barrier height corresponding to the surface Fermi level measured from the conduction band edge was evaluated from the slope of the Richardson plot as depicted in Fig. 4. The true barrier height is 0.39 eV for the conventional Au/InP junction, while it is increased to 0.52 and 0.57 eV for the modified Au/InP and Au/PN_x/InP junctions, respectively. The difference between effective and true barrier heights observed for these three Schottky junctions is due to the effect of tunnel MIS Schottky structure. Tunnel barriers are possibly due to native oxide for

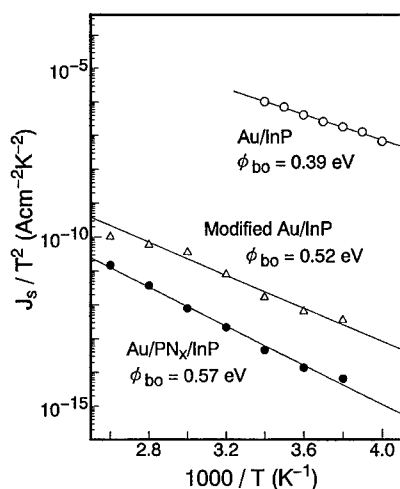


Fig. 4. Richardson plot for conventional Au/InP, modified Au/InP and Au/PN_x/InP Schottky junctions.

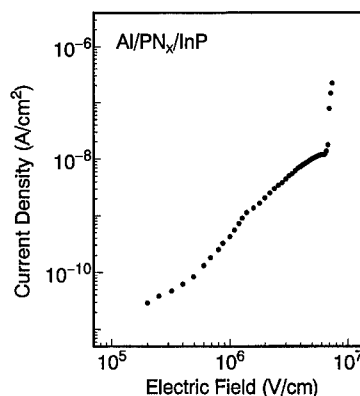


Fig. 5. Room-temperature I - V characteristic for PN_x film.

Au/InP, elemental phosphorus for modified Au/InP and PN_x for Au/PN_x/InP junctions.

Au/PN_x/InP MIS diodes were fabricated by depositing a PN_x film with a thickness of 50 nm immediately after plasma treatments with H₂ (10 min) and PH₃ (5 min). Prior to C - V measurements, an I - V characteristic was measured for the MIS diode. Fig. 5 indicates the current density as a function of the electric field. The electrical resistivity of the PN_x film is estimated to be $3.7 \times 10^{14} \Omega \text{ cm}$ from the slope in the ohmic region. The resistivity of the InP substrate ($2 \times 10^{-3} \Omega \text{ cm}$) was negligibly small in comparison with that of the PN_x film. A deviation from the ohmic conduction with increasing applied voltage is due to the Frenkel-Poole emission [13]. The conduction mechanism of the PN_x film will be shown in detail elsewhere.

Fig. 6 shows the C - V characteristics at 1 MHz. The counterclockwise hysteresis loop with a width of

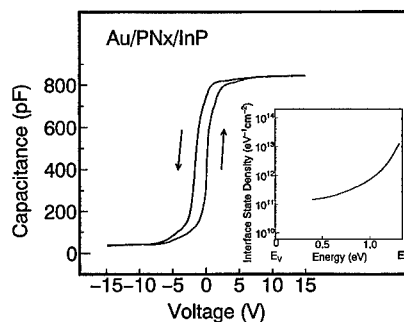


Fig. 6. C - V characteristics for the Au/PN_x/InP MIS diode. The inset shows the interface state density profile estimated by Terman's method.

1.6 V is observed and the flat band shift is 0.7 V when the bias voltage is swept up from -15 to 15 V. The dielectric constant of the PN_x layer was evaluated to be $6.1\epsilon_0$ from the capacitance of the accumulation region and the thickness of the PN_x film (50 nm), assuming no frequency dispersion of PN_x films. The inset of Fig. 6 indicates the interface state density profile evaluated from the C - V characteristic by using Terman's method [11]. The interface state density at the lowest level is $1.4 \times 10^{11} \text{ eV}^{-1} \text{ cm}^{-2}$.

From the standpoints of physical interests and device applications of Schottky contacts, it is important to understand the underlying mechanism of the surface Fermi level pinning which causes a Schottky barrier height independent of the metal work function. In order to explain the surface Fermi level pinning of Schottky junctions, a metal-induced gap states (MIGS) model [14], an advanced unified defect model [15] and other models [16,17] have been proposed so far. MIGS would become the main origin of the surface Fermi level pinning only when an intimate contact between metal and semiconductor without interfacial chemical reaction is realized. However, in the case of the present Schottky junctions, there exists a thin interfacial layer which prevents metal-semiconductor intimate contact and can block sufficient penetration of the metal electron wave function into the semiconductor gap, suppressing the occurrence of MIGS.

An enhancement of the true barrier heights is observed for the modified Au/InP^1 and $\text{Au/PN}_x/\text{InP}$ Schottky junctions in the present experiment. The value of the true barrier height is quite similar to that of the Au Schottky junction formed on H_2 -plasma treated InP as previously reported [9]. In the case of treating InP with H_2 plasma, the surface Fermi level pinning occurred, the position of which is around 0.53 eV below the conduction band edge. From the experimental facts of the C - V characteristic being close to the ideal one and the interface state density as low as $1.4 \times 10^{11} \text{ eV}^{-1} \text{ cm}^{-2}$, on the other hand, the enhancement of the true barrier

heights of the modified Au/InP and $\text{Au/PN}_x/\text{InP}$ Schottky junctions are not due to the surface Fermi level pinning, but to approaching the Schottky limit of 0.7 eV determined by the work function of Au (5.1 eV) [18] and the electron affinity of InP (4.4 eV) [19]. The behavior of Schottky junctions prepared by the present in-situ process is related to a remarkable reduction in surface defects which should be effective in the surface Fermi level pinning. The H_2 plasma process is also useful for eliminating native oxide and contaminations from the InP surface. However, surface defects are introduced simultaneously, causing the surface Fermi level pinning [9]. Therefore, it is our conviction that in the present experiment PH_3 plasma treatment subsequent to H_2 plasma process is vital to form an improved defect-free surface of InP.

4. Summary

Modified Au/n-InP and $\text{Au/PN}_x/\text{n-InP}$ Schottky junctions have been constructed by an in-situ sequential remote plasma process including H_2 and PH_3 plasma treatments. The presence of an interfacial layer of 4 nm in thickness is found by cross-sectional TEM observation in the modified Au/InP contact. The existence of elemental phosphorus is detected in the interfacial region by XPS measurement. The true and effective barrier heights of the $\text{Au/PN}_x/\text{InP}$ Schottky junction are 0.57 and 0.83 eV, respectively. The interface state density as low as $1.4 \times 10^{11} \text{ eV}^{-1} \text{ cm}^{-2}$ is achieved for the $\text{Au/PN}_x/\text{InP}$ MIS diode. The true barrier height approaching the Schottky limit of 0.7 eV suggests that the surface Fermi level pinning is weakened due to reduced surface defects by PH_3 plasma treatment.

Acknowledgements

The authors are much indebted to Dr. T. Shirakawa of Sumitomo Electric Industries Inc. for supplying InP wafers, and to Dr. Z. Ueda of Nitto Denko Corp. and Mr. H. Tsuchiya of Nitto Technical Information Center Co., Ltd. for their supporting transmission electron microscopic observation. They

¹ For modified Au/InP Schottky junctions after the optimized PH_3 plasma treatment, the true barrier height of 0.62 eV was achieved.

also thank Mr. H. Ono for offering mass flow controllers in the experimental apparatus.

References

- [1] L.J. Brillson and C.F. Brucker, *J. Vac. Sci. Technol.* 21 (1982) 564.
- [2] W.G. Spitzer and C.A. Mead, *J. Appl. Phys.* 34 (1963) 3061.
- [3] E. Hokelek and G.Y. Robinson, *Appl. Phys. Lett.* 40 (1982) 426.
- [4] H. Card and E.H. Rhoderick, *J. Phys. D* 4 (1971) 1589.
- [5] K. Hattori and Y. Torii, *Solid State Electron.* 34 (1991) 527.
- [6] D.T. Quan and H. Hbib, *Solid State Electron.* 36 (1993) 339.
- [7] T. Sugino, H. Ito and J. Shirafuji, *Electron. Lett.* 26 (1990) 1750.
- [8] T. Sugino, Y. Sakamoto, T. Sumiguchi, K. Nomoto and J. Shirafuji, *Jpn. J. Appl. Phys.* 32 (1993) L1196.
- [9] Y. Sakamoto, T. Sugino, H. Ninomiya, K. Matsuda and J. Shirafuji, *Jpn. J. Appl. Phys.* 34 (1995) 1417.
- [10] Y. Sakamoto, T. Sugino, T. Miyazaki and J. Shirafuji, in: *Proc. 7th Int. Conf. on Indium Phosphide and Related materials*, May 1995, Sapporo, p. 605.
- [11] L.M. Terman, *Solid State Electron.* 5 (1962) 285.
- [12] G. Hollinger, E. Bergignat, J. Joseph and Y. Robach, *J. Vac. Sci. Technol. A* 3 (1985) 2028.
- [13] S.M. Sze, *Physics of Semiconductor Devices*, 2nd ed. (Wiley-Interscience, New York, 1981) pp. 245, 403.
- [14] M. Neuberger, *III–V Semiconducting Compounds* (Plenum, New York, 1971) pp. 110, 111.
- [15] J. Tersoff, *Phys. Rev. Lett.* 52 (1984) 465.
- [16] W.E. Spicer, T. Kendelewicz, N. Newman, R. Cao, C. Mccants, K. Miyano, I. Lindau, Z. Liliental-Weber and E.R. Weber, *Appl. Surf. Sci.* 33 (1988) 1009.
- [17] J. Bardeen, *Phys. Rev.* 71 (1947) 717.
- [18] J.L. Freeouf and J.M. Woodall, *Appl. Phys. Lett.* 39 (1981) 727.
- [19] H.B. Michaelson, *J. Appl. Phys.* 48 (1977) 4729.



ELSEVIER

Applied Surface Science 104/105 (1996) 434–440

applied
surface science

Sulfur passivated InP(100): surface gaps and electron counting

C.E.J. Mitchell ^{a,*}, I.G. Hill ^a, A.B. McLean ^a, Z.H. Lu ^b

^a Department of Physics, Queen's University, Kingston, Canada K7L 3N6

^b Institute for Microstructural Sciences, National Research Council of Canada, Ottawa, Canada K1A 0R6

Received 28 June 1995; accepted 30 September 1995

Abstract

The atomic and electronic structures of the sulfur passivated InP(100) surface have been studied with electron diffraction, photoemission and inverse photoemission spectroscopies. The InP(100) surfaces were passivated using a wet chemical treatment. In agreement with previous studies, we find that the unannealed surface has the 1×1 symmetry of the bulk lattice, which transforms to a 2×1 pattern upon annealing to temperatures in the range 350–500°C. Photoemission and inverse photoemission studies of the electronic states in the vicinity of the valence band maximum and conduction band minimum demonstrate that the passivation process removes states from the region of the fundamental gap of InP. No bands cross the Fermi level. The dispersion of several two-dimensional states has been measured. These states show a strong similarity to surface states of the Ge(100)-S(1 ML)(1×1) system. By applying electron counting rules, we demonstrate that several of the surface structural models that have been proposed to date are inconsistent with our experimental results, since they should result in partially filled surface bands crossing the Fermi level.

1. Introduction

Within the last few years attempts have been made to formulate a small number of physical principles that have general utility in identifying equilibrium semiconductor surface structures [1,2]. This field has recently been reviewed by Duke [3]. Considerable progress has been made and this is due, in part, to the fact that many semiconductor surface structures have been solved [4]. The motivation has been to look beyond individual surface structures to find the common principles that govern their formation. Although it is clear that the main driving force for semiconductor surface reconstruction is the formation of surface bonds that saturate the valence of

the surface atoms, other factors are also important. For example, because the surface atoms terminate a three dimensional lattice the bonding constraints are quite different from the constraints imposed by either bulk or small molecule coordination. Surface relaxation often places the substrate under elastic stress and consequently the surface layer may be considered to be epitaxially constrained.

In this paper we have examined the atomic and electronic structure of the S-passivated InP(100) surface. The passivation process is interesting in itself because it reduces the density of gap states on the InP(100) surface and consequently this allows a greater degree of Fermi level movement [5]. As would be expected, the reduction in the density of gap states also improves the quality of Schottky contacts to InP [6], and the Schottky barrier height extracted from diodes fabricated on the S-passivated

* Corresponding author. Fax: +1-613-5456463; e-mail: katie@hecate.phy.queensu.ca.

surface exhibits a stronger dependence upon the work function of the metal overlayer [7]. In this paper we will discuss the atomic and electronic structure of the monolayer system. From a fundamental point of view the system is sufficiently simple to allow us to apply the general principles described above, and demonstrate that several of the structural models that have been proposed for this system are inconsistent with our experimental finding that there are no partially filled electronic bands at the Fermi energy.

2. Experimental

The experiments were performed in an ultra high vacuum (UHV) chamber which has a base pressure of 8×10^{-11} Torr. All photoemission and inverse photoemission measurements are angle-resolved. The photoemission experiments were performed with a differentially pumped resonance lamp and a hemispherical electron energy analyzer with a 50 mm mean radius. The inverse photoemission experiments were performed with a home-built electron gun [8] and a bandpass photon detector consisting of a CaF_2 window and a Cu–Be electron multiplier [9,10]. The photoemission and inverse photoemission energy scales can be aligned by using the hemispherical analyzer to measure the kinetic energy of electrons produced by the electron gun [11]. This allows us to accurately measure gaps between occupied and unoccupied states without resorting to a secondary reference. The low-energy electron diffraction (LEED) studies were performed using a Princeton Research Instruments RVL 8-120 reverse view LEED system. The samples were mounted on Mo sample holders and transferred from atmosphere into UHV through a custom load lock system which is evacuated using a turbomolecular pump.

Epiready n-type InP(100) wafers (Crystacomm), both unintentionally doped with a carrier density of $5.6 \times 10^{15} \text{ cm}^{-3}$ and Sn doped with a carrier density of $1.2 \times 10^{18} \text{ cm}^{-3}$, were used in the experiments. The wafers were immersed in ammonium sulfide solution (20.1% $(\text{NH}_4)_2\text{S}$) for 15 min at a temperature of 65°C. They were then dipped in ammonium sulfide solution (20.1% $(\text{NH}_4)_2\text{S}$) at room temperature and blown dry with Ar. Sample mounting was

also performed while blowing Ar over the sample. The samples were transferred directly into UHV and annealed at 350°C in order to remove physisorbed gases and to order the overlayers. The principal gases found to be desorbing from the samples were H_2O , SO_2 , and NH_3 . The samples were brought up to the annealing temperature slowly and left at that temperature for 5–10 min. The photoemission results were found to be reproducible after multiple annealing cycles. No differences were observed in the results for the unintentionally n doped and Sn doped samples.

The photoemission results reported here were obtained after annealing at 350°C as described above. LEED studies were performed as a function of annealing temperature. In each case the sample was annealed at the specified temperature for approximately ten minutes. The sample was allowed to cool to room temperature before taking the LEED data.

Photoemission and inverse photoemission studies were also performed on clean InP(100) surfaces. Sn doped (n-type, carrier density $1.2 \times 10^{18} \text{ cm}^{-3}$) epiready InP(100) wafers (Crystacomm) were inserted into the vacuum untreated, and cleaned by Ne ion bombardment (20 min at $1 \mu\text{A}/\text{cm}^2$, 500 eV) and subsequent 10 min anneal at 350°C.

3. Results

In Fig. 1 we show some representative LEED patterns that were collected from the S-passivated InP(100) surface. The orientation of the wafer is indicated on the figure. After annealing to temperatures below 350°C the surface layer has the 1×1 symmetry of the bulk lattice. This transforms to a 2×1 pattern if the system is annealed in the temperature range 350–500°C. The lowest temperature at which the 2×1 pattern was observed and the quality of the pattern varied from sample to sample, probably as a result of slight differences in the preparation procedure. It should be noted that, on most of the samples studied and in order to reduce the possibility of contamination, LEED measurements were not performed until after the sample had been annealed to 350°C and the photoemission data had been obtained. It is therefore possible that the 2×1 reconstruction occurs also after annealing to lower temper-

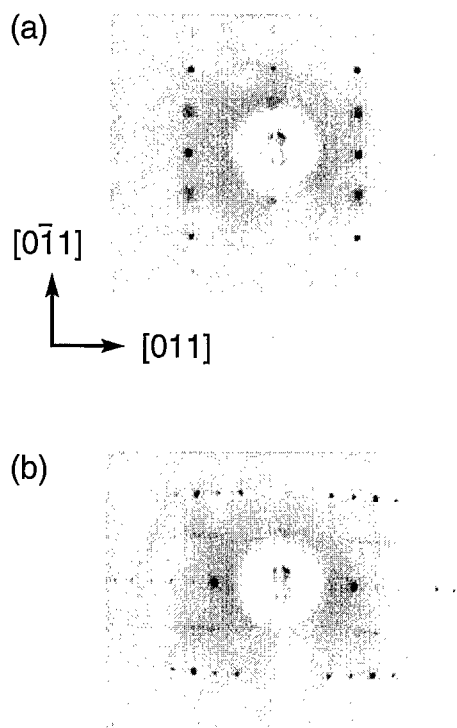


Fig. 1. LEED patterns obtained on InP(100)-S after annealing to (a) 450°C and (b) 500°C. The gun energies are (a) 85 eV and (b) 75 eV. As discussed in the text, the 2×1 pattern was observed after annealing to temperatures in the range 350–500°C. The patterns show a progression in surface symmetry from $2 \times 1 \rightarrow 2 \times 4$. This transition has previously been associated with the desorption of S from the surface, although it is also possible that the S diffuses into the bulk. The orientation of the patterns is as illustrated.

atures, but that we simply did not observe it on the few samples that were studied after annealing to these temperatures. The 2×1 pattern corresponds to a doubling of the direct lattice spacing along the $[0\bar{1}1]$ direction. Annealing to a temperature of approximately 500°C produced a 2×4 pattern which is the characteristic phosphorous rich reconstruction seen on InP(100) [12]. Note that the notation used here corresponds to the $\frac{1}{2}$ order spots lying along the $[0\bar{1}1]$ direction and the $\frac{1}{4}$ order spots lying along the $[011]$ direction. The appearance of the 2×4 pattern after annealing to a temperature near 500°C is consistent with previous work indicating that the S-terminated surface is stable up to this temperature [7,13]. One group [5] reports a stable 2×1 reconstruction up to 560°C. The difference may lie in the

annealing procedure, since the system is expected to be very sensitive to annealing time once preferential P desorption starts to occur [12]. A 2×4 pattern was also obtained on the clean InP(100) surfaces prepared by ion bombardment and annealing to 350°C.

The electronic states near the valence band maximum and conduction band minimum on both the clean 2×4 and S-passivated 2×1 surfaces were probed at the zone center, $\bar{\Gamma}$, with photoemission and inverse photoemission. In Fig. 2, the results obtained for the two surfaces are compared. The features of the clean surface photoemission spectrum and its position relative to the Fermi level are consistent with results obtained by previous authors [14,15]. The valence band features of the S-passivated surface are shifted to higher binding energy. This indicates a smaller degree of band bending on the S-passivated surface, consistent with the removal of surface states from the gap region. The sharp feature seen at ≈ 1 eV below the Fermi level on the clean

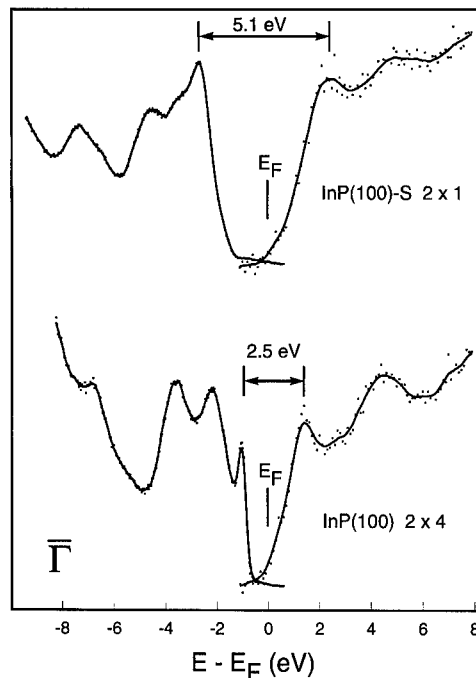


Fig. 2. Photoemission and inverse photoemission spectra obtained in normal emission are shown for InP(100)-S 2×1 and InP(100) 2×4 . The alignment of the spectra is discussed in the text. The Fermi level is marked in the figure, but was not used to align the spectra. The surface bandgap is marked in both cases.

surface has been attributed to P dangling bonds [14]. This feature is absent on the S-passivated surface. An unoccupied state near the bottom of the conduction band is also removed by the S-passivation. The unoccupied state is identified as a surface feature since it does not appear on the S-passivated surface. Using a calibration obtained by previous authors [15] of the position of the valence band maximum on the clean 2×4 surface, we find that this unoccupied state lies 2.2 eV above the valence band maximum. This is close to the energy position of an unoccupied state seen on sputter/annealed GaAs(100) 4×2 , which has been assigned to Ga dangling bonds [16] (note that the crystallographic directions given by the authors indicate that their 4×2 pattern is equivalent to our 2×4 pattern). It is therefore reasonable that

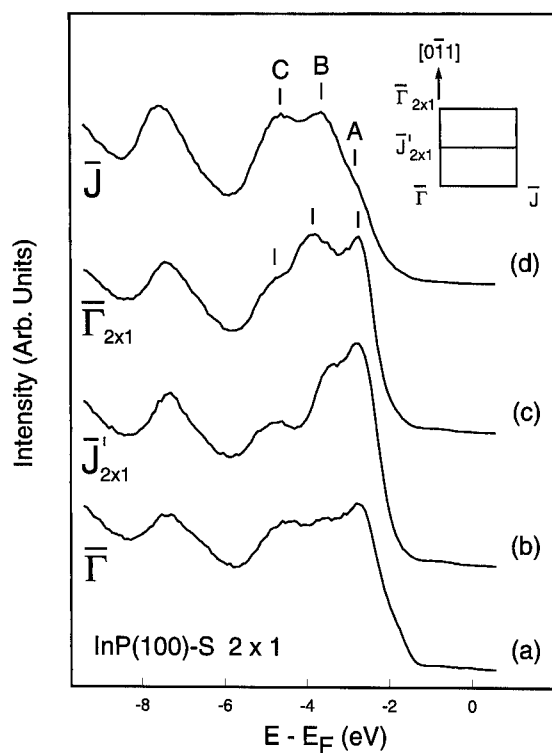


Fig. 3. Photoemission obtained on InP(100)-S 2×1 is shown for several high symmetry points in the surface Brillouin zone. The photon energy is 21.2 eV and the take-off angles are 0° , 12° and 24° respectively along $[0\bar{1}1]$ for (a), (b) and (c). For (d), the take-off angle is 24° along $[011]$. The angles were chosen such that in each case k_{\parallel} is at the indicated symmetry point for the feature labelled A.

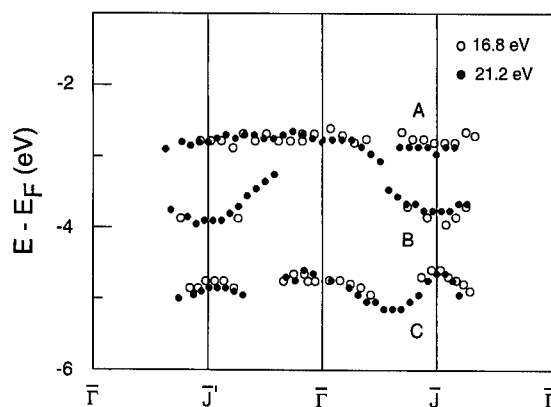


Fig. 4. The dispersion of surface-related features seen on both the 1×1 and 2×1 surfaces of InP(100)-S is plotted along the $\bar{\Gamma}\bar{J}$ and $\bar{\Gamma}\bar{J}'$ directions. The energy is referenced to the Fermi level. The labelling of the features corresponds to the labels used in Fig. 3.

the feature seen on InP(100) 2×4 corresponds to an empty In dangling bond.

On InP(100) 2×4 , the surface bandgap at $\bar{\Gamma}$ was found to be 2.5 eV (see Fig. 2), while on InP(100)-S 2×1 , it was found to be 5.1 eV. The same results were obtained on a surface of predominantly 1×1 symmetry. It should be noted that we are not measuring the bulk bandgap. Since the photoemission and inverse photoemission experiments were performed at fixed photon energies and not necessarily at an energy where emission from the critical points is observed, the measured gap may be larger than the room temperature bulk bandgap of 1.35 eV [17].

Photoemission measurements were performed on surfaces of both predominantly 1×1 and 2×1 symmetry, along the $\bar{\Gamma}\bar{J}$ and $\bar{\Gamma}\bar{J}'$ directions of the surface Brillouin zone, at photon energies of 21.2 eV (He I) and 16.8 eV (Ne I). No significant differences were noted in the photoemission from the two surfaces, and it has not yet been possible to identify features specifically related to the 2×1 reconstruction. This is perhaps not surprising, since if the 2×1 reconstruction is related to a weak dimerisation, no strong differences are expected [18]. In Fig. 3, spectra obtained at $\bar{\Gamma}$, $\bar{J}'_{2 \times 1}$, \bar{J} ($\bar{\Gamma}_{2 \times 1}$), and \bar{J} are presented. The features marked have been tentatively identified as surface related. These features are seen at the same binding energy with both photon energies, and exhibit the symmetry of the 1×1 surface Brillouin

zone. The dispersion of the surface related features is shown in Fig. 4. The labelling of the states corresponds to the labels used in Fig. 3. Measurements were also performed along the zone edges [19]. No evidence was found for any bands crossing the Fermi level, indicating that there are no partially filled surface bands.

Assignment of the surface features to particular states awaits a calculation of the surface bands for S-passivated InP(100). The relevant calculations are currently being performed [20]. Qualitatively, one would expect the lower binding energy features to be dangling-bond related, while back bond features should occur at higher binding energies. S dangling-bond features would be expected to occur at a higher binding energy than the P dangling bond feature seen on the clean surface [21].

An interesting similarity is noted between the dispersion of the surface related features reported here and the dispersion of surface features reported for the Ge(100)-S 1×1 system [22]. While no assignment of the surface features has been made for

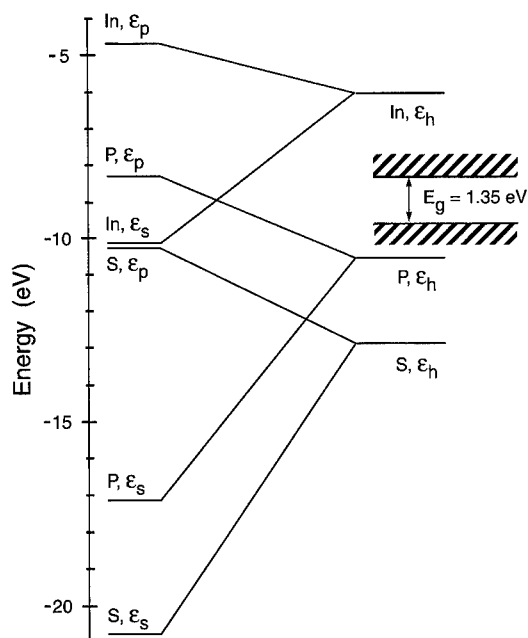


Fig. 5. The energy positions of the In, P and S sp^3 hybrid orbitals are plotted with respect to the valence band maximum and fundamental gap of InP. Hybrid energies were calculated as linear combinations of the energies of the s and p orbitals. The data are from Harrison [21].

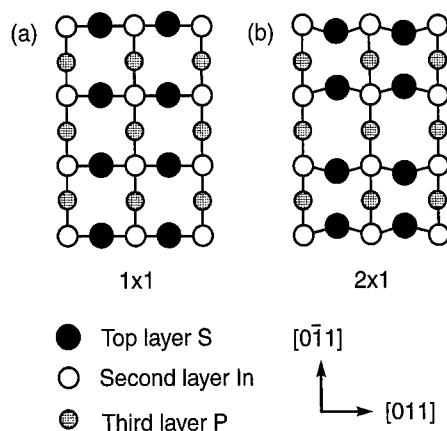


Fig. 6. Simple structural models are shown for (a) InP(100)-S 1×1 and (b) InP(100)-S 2×1 . As is discussed in the text, neither of these models satisfies electron counting.

either the Ge or InP systems, the comparison is worthy of note. In both cases, a monolayer of S is bonded to the (100) surface of a tetrahedrally coordinated semiconductor, and the lattice constants are similar. The differences in the two systems should be directly related to the difference in valence of the substrate species.

4. Discussion

As noted above, no evidence was found with photoemission for any surface bands crossing the Fermi level. Therefore the surface is semiconducting and the electron counting model must be satisfied. The electron counting model [23,24] requires that the number of electrons in a semiconductor surface layer is such that all valence band dangling bond states are filled and all conduction band dangling bond states are empty. For the III–V semiconductors, the cation sp^3 dangling bonds lie in the conduction band and the anion sp^3 dangling bonds lie in the valence band. The relative energy positions of the relevant states are shown in Fig. 5 for S, In and P. For the InP(100)-S surface, any S and P dangling bonds should be completely occupied, and any In dangling bonds should be completely empty.

Total energy minimization calculations for S on GaAs(100) [18] and for S on InP(100) [25] have shown that the most energetically favorable adsorp-

tion configuration is one in which the S is bridge-bonded to two In atoms. X-ray photoelectron spectroscopy and Auger electron spectroscopy results indicate that the S coverage on the passivated surface is 1 ML [5,7,26]. Both 1×1 [26] and 2×1 [5,7] patterns have been observed with LEED and RHEED. The simplest models that might account for these observations are shown in Fig. 6. These models are consistent with the diffraction data, and dimer formation, as postulated for the 2×1 reconstruction, is common on the (100) surfaces of tetrahedrally coordinated semiconductors (see e.g. [27]). However, neither of these structures satisfies electron counting.

In order to apply the electron counting model to the InP(100) surface, we assume that an In atom (valence 3) contributes $\frac{3}{4}$ of an electron to each of its four sp^3 hybrids, and that a P atom (valence 5) contributes $\frac{5}{4}$ of an electron to each of its four sp^3 hybrids. One is then able to count up the number of electrons available per surface unit cell and to compare this number with the number required to fill the appropriate dangling bond orbitals.

We will first consider the case of 1 ML of S bridge-bonded to In, corresponding to the postulated 1×1 structure [26]. The electron counting model requires that all of the S dangling bonds be completely occupied. There is one S atom per surface unit cell. $2\frac{1}{2}$ of its six electrons are required for bonding to the top layer of In atoms. There are $3\frac{1}{2}$ electrons left over to fill the two dangling bonds per unit cell. However, four electrons are needed to saturate the dangling bonds. Consequently, the electron counting model is not satisfied.

A similar argument can be applied to the 2×1 model, in which the S atoms are assumed to form dimers along the $[0\bar{1}1]$ direction. Again, the electron counting model requires that all of the S dangling bonds be completely occupied. There are now two S atoms per surface unit cell. Five electrons are required for bonding the two S atoms to the top layer of In atoms. There are seven electrons left over to fill the dimer bond and the two remaining S dangling bonds. Only six are required. Again, the electron counting model is not satisfied.

In order to satisfy the electron counting model for a 1 ML coverage of S atoms bridge bonded to In (whether dimerized or not), either P or In vacancies must be introduced in subsurface layers. If the S

coverage is greater than 1 ML, structures satisfying the electron counting model can be found by replacing some of the third layer P atoms by S. A structure of this type has been proposed for the system GaAs(001)-Se 2×1 , in which the electron counting considerations are the same as for sulfur on InP(100) [28].

We note that the electron counting model can be naturally satisfied if the surface layer comprises only half a monolayer of P atoms and half a monolayer of S atoms. In this case the formation of S–P dimers saturates the S and P dangling bond orbitals. As before, the S contributes $2\frac{1}{2}$ electrons to surface bonds and has $3\frac{1}{2}$ left over. The P contributes $2\frac{1}{2}$ electrons to surface bonds and has $2\frac{1}{2}$ left over. The S–P dimer then has a full complement of six electrons with which to fill the dimer bond and the two dangling bonds. Attractive as this possibility is, there is little experimental evidence that the overlayer comprises 0.5 ML of S, at least for surfaces annealed at temperatures less than 500°C. However, a previous study [5] found 0.5 ML S remaining on a well-ordered 2×1 surface after annealing to 560°C, and the S–P dimer structure was suggested as a possible surface model.

Several experiments on S-passivated InP(100) (for example Ref. [5]), indicate that at least after annealing to 350°C, S is present in the third layer, in bulk P positions. Thermodynamically, the P–S exchange is favored [5]. Thus, there are good reasons for incorporating some subsurface S in any proposed structural model. If the S coverage is close to 1 ML as suggested by the experiments performed to date, then a structure satisfying electron counting would naturally include both subsurface vacancies and subsurface S.

As noted above, the surface electronic features on S-passivated Ge(100) and InP(100) are strikingly similar. An obvious difference between the two systems is that in the case of Ge(100), the tetravalent Ge atoms allow the simple bridge-bonded 1×1 S overlayer to satisfy the electron counting model. On InP(100)-S, a more complicated reconstruction is required to satisfy this model. Since the substrate structure and adsorption sites are the same, however, it is not surprising that the resulting electronic structures are similar. One of the features that makes the InP(100)-S system especially interesting is the 1×1

→ 2×1 transition. This transition indicates the existence of an activation barrier [3] which may be related to S incorporation in subsurface layers and/or to the formation of subsurface vacancies.

Acknowledgements

This research was supported by the Natural Sciences and Engineering Research Council of Canada.

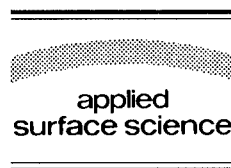
References

- [1] C.B. Duke, *J. Vac. Sci. Technol. B* 11 (1993) 1336.
- [2] C.B. Duke, *J. Vac. Sci. Technol. A* 10 (1992) 2032.
- [3] C.B. Duke, *Appl. Surf. Sci.* 65 (1993) 543.
- [4] J.P. LaFemina, *Surf. Sci. Rep.* 16 (1992) 133.
- [5] D. Gallet and G. Hollinger, *Appl. Phys. Lett.* 62 (1993) 982.
- [6] G. Eftekhari, *J. Vac. Sci. Technol. B* 12 (1994) 3214.
- [7] H. Oigawa, J. Fan, Y. Nannichi, H. Sugahara and M. Oshima, *Jpn. J. Appl. Phys.* 30(3A) (1991) L322.
- [8] P.W. Erdman and E.C. Zipf, *Rev. Sci. Instr.* 53 (1982) 225.
- [9] N. Babbe, W. Drube, I. Schaefer and M. Skibowski, *J. Phys. E* 18 (1985) 158.
- [10] I. Schaefer, W. Drube, M. Schlueter and G. Plagemann, *Rev. Sci. Instr.* 58 (1987) 710.
- [11] H. Carstensen, R. Claessen, R. Manzke and M. Skibowski, *Phys. Rev. B* 41 (1990) 9880.
- [12] C.R. Stanley, R.F.C. Farrow and P.W. Sullivan, MBE of InP and Other P-Containing Compounds, in: *The Technology and Physics of Molecular Beam Epitaxy*, Ed. E.H.C. Parker (Plenum, New York, 1985).
- [13] G.W. Anderson, M.C. Hanf, P.R. Norton, Z.H. Lu and M.J. Graham, *Appl. Phys. Lett.* 65 (1994) 171.
- [14] X. Hou, G. Dong, X. Ding and X. Wang, *J. Phys. C* 20 (1987) L121.
- [15] J. Woll, Th. Allinger, V. Polyakov, J.A. Schaefer, A. Goldmann and W. Erfurth, *Surf. Sci.* 315 (1994) 293.
- [16] J.E. Ortega and F.J. Himpsel, *Phys. Rev. B* 47 (1993) 2130.
- [17] S.M. Sze, *Physics of Semiconductor Devices* (Wiley, New York, 1981).
- [18] T. Ohno, *Surf. Sci.* 255 (1991) 229.
- [19] C.E.J. Mitchell, I.G. Hill and A.B. McLean, to be published.
- [20] V. Smelyansky, D.D. Klug and J.S. Tse, to be published.
- [21] W.A. Harrison, *Electronic Structure and the Properties of Solids* (Freeman, San Francisco, CA, 1980).
- [22] T. Weser, A. Bogen, B. Konrad, R.D. Schnell, C.A. Schug, W. Moritz and W. Steinmann, *Surf. Sci.* 201 (1988) 245.
- [23] H.H. Farrell, J.P. Harbison and L.D. Peterson, *J. Vac. Sci. Technol. B* 5 (1987) 1482.
- [24] M.D. Pashley, *Phys. Rev. B* 40 (1989) 10481.
- [25] J.-M. Jin, M.W.C. Dharma-Wardana, D.J. Lockwood, G.C. Aers, Z.H. Lu and L.J. Lewis, *Phys. Rev. Lett.* 75 (1995) 878.
- [26] Y. Tao, A. Yelon, E. Sacher, Z.H. Lu and M.J. Graham, *Appl. Phys. Lett.* 60 (1992) 2669.
- [27] P.K. Larsen, J.F. van der Veen, A. Mazur, J. Pollmann, J.H. Neave and B.A. Joyce, *Phys. Rev. B* 26 (1982) 3222.
- [28] M.D. Pashley and D. Li., *J. Vac. Sci. Technol. A* 12 (1994) 1848.



ELSEVIER

Applied Surface Science 104/105 (1996) 441–447



GaAs surface passivation using in-situ oxide deposition

M. Passlack¹, M. Hong^{*}, R.L. Opila, J.P. Mannaerts, J.R. Kwo

AT&T Bell Laboratories, 600 Mountain Avenue, Murray Hill, NJ 07974-0636, USA

Received 28 June 1995; accepted 14 November 1995

Abstract

In-situ deposition of Ga₂O₃, SiO₂, and MgO films on clean, atomically ordered (100) GaAs surfaces grown by molecular beam epitaxy using a multiple-chamber ultra high vacuum system has been investigated. Using this technique, direct bonding of oxide molecules to GaAs surface atoms revealing *intrinsic* oxide–GaAs interface properties has been achieved. The GaAs surface reconstruction prior to deposition as observed by reflection high energy electron diffraction and the chemical shift of the interfacial As 3d core level acquired by X-ray photoelectron spectroscopy depth profiling are clearly correlated. As_xO_y or elemental As were not detectable at in-situ fabricated oxide–GaAs interfaces. In sharp contrast to SiO₂– and MgO–GaAs interfaces which are characterized by a Fermi level intrinsically pinned at midgap, Ga₂O₃–GaAs interfaces exhibit unique *intrinsic* electronic properties including an interface state density and recombination velocity in the mid 10¹⁰ cm^{−2} eV^{−1} range and of 4500 cm/s, respectively.

1. Introduction

Since the emergence of GaAs technology, the development of GaAs electronic and optoelectronic devices has been hampered by the lack of dielectric films providing low interface state density [1]. Recent efforts have been mainly focused on a variety of dry and wet surface treatments prior to deposition of dielectric films [2–6]. Interface state densities are still high, typically around 10¹² cm^{−2} eV^{−1} or above. Apparently, these techniques inadequately ad-

dress major sources of interface states such as surface exposure and defects [7–11] as well as surface nonstoichiometry [12].

An interface state density comparable to that typically obtained in the SiO₂–Si system of 10¹⁰ cm^{−2} requires a defect density of less than one defect per 10⁵ surface atoms (the GaAs (100) surface has 1.6 × 10¹⁵ atoms/cm²). Therefore, prior to deposition (i) extremely low GaAs surface exposure to impurity gases and (ii) preservation of surface stoichiometry are prerequisites. The effects of exposing a clean GaAs surface to impurity gases, in particular to oxygen, are well established; an oxygen exposure of e.g., 10 langmuir (1 L = 10^{−6} Torr s) results in a surface impurity coverage of 10^{−5} to 10^{−3}% of a monolayer or 10⁸ to 10¹⁰ surface impurities/cm² depending on sticking coefficient [7,8,13]. An oxygen exposure ≥ 10⁴ L causes strong Fermi level pinning [7]. Other species such as metals and carbon

^{*} Corresponding author.

¹ Motorola Inc., Phoenix Corporate Research Laboratories, 2100 E. Elliot Road, Tempe, AZ 85284, USA. Tel.: +1-602-4134962; fax: +1-602-4135934; e-mail: a646aa@email.mot.com.

give rise to similar effects [7,14,15]. Subsequently, molecules or atoms of insulating materials intentionally deposited on a clean surface must provide a local interfacial atomic structure such that no gap states are induced in GaAs. Thermodynamic stability requires the exclusion of chemical reactions between GaAs surface atoms and the deposited species.

This paper investigates *intrinsic* insulator–GaAs interface properties obtained by in-situ oxide deposition on clean and atomically ordered (100) GaAs surfaces.

2. Sample preparation

The samples were fabricated using a multiple-chamber ultra-high vacuum (UHV) system described in Ref. [16]. Fig. 1 shows the pressure regime after completion of GaAs growth at time t_c (solid line) and the GaAs surface exposure occurring prior to oxide deposition for $t_c < t < t_s$ (dashed line) for in-situ fabrication of oxide–GaAs structures. The sample fabrication comprised 1.5 μm thick GaAs n-type ($1.6 \times 10^{16} \text{ cm}^{-3}$) or p-type ($4.4 \times 10^{16} \text{ cm}^{-3}$) layers grown at 650°C on n^+ or p^+ doped (100) GaAs substrate, respectively, in a solid-source III–V chamber at a background pressure of 2×10^{-11} Torr. Subsequently, the wafer with an As-stabilized (2×4) surface was transferred (background pressure

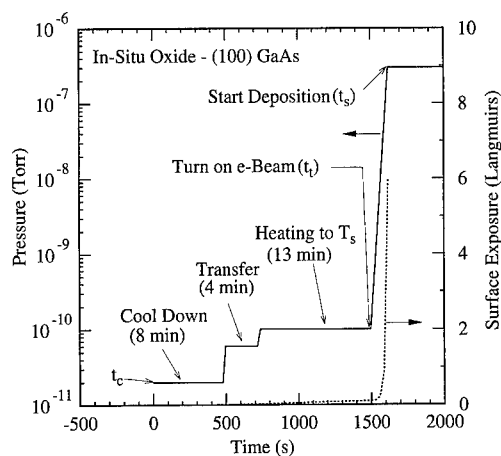


Fig. 1. Pressure (solid line) and surface exposure (dashed line) measured between completion of GaAs epitaxial growth (t_c) and start of oxide deposition (t_s).

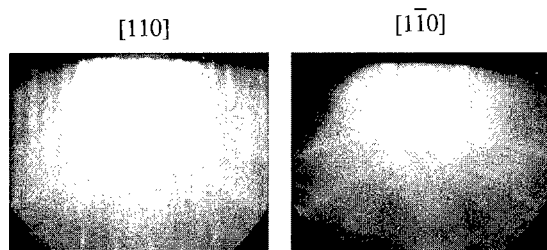


Fig. 2. RHEED picture taken after completion of GaAs growth (t_c) and at start of oxide deposition (t_s). The identical RHEED picture shows a (2×4) As stabilized surface and indicates preservation of surface stoichiometry.

= 6×10^{-11} Torr) from the MBE growth chamber into an oxide deposition chamber (1×10^{-10} Torr). Note that the typical GaAs surface exposure (predominantly oxygen) prior to oxide deposition ($t_c < t < t_s$) is ≤ 10 L (Fig. 1). Finally, Ga_2O_3 , SiO_2 , or MgO films were deposited by electron-beam evaporation from a single-crystal $\text{Gd}_3\text{Ga}_5\text{O}_{12}$ [17], SiO_2 , or MgO source at substrate temperatures ranging from 0°C to 620°C. While Ga_2O_3 and SiO_2 films are amorphous, MgO films are epitaxially grown on GaAs or randomly oriented polycrystalline depending on substrate temperature.

Reference samples with identical GaAs epitaxial structure and substrate were also fabricated in the same solid-source III–V chamber using (i) no oxide deposition (bare samples) and (ii) $\text{Al}_{0.45}\text{Ga}_{0.55}\text{As}$ –GaAs interfaces.

3. Sample characterization

3.1. Structural surface and interface properties

GaAs surface and oxide–GaAs interface properties were investigated using reflection high energy electron diffraction (RHEED) and X-ray photoelectron spectroscopy (XPS), respectively.

The GaAs surface was characterized in situ by RHEED at time of (i) completion of GaAs growth (t_c), (ii) reaching the substrate temperature T_s for oxide deposition (t_i), (iii) opening the shutter for oxide deposition (t_s), (iv) completion of the first oxide monolayer, and (v) completion of oxide deposition. RHEED pictures taken from a (100) GaAs

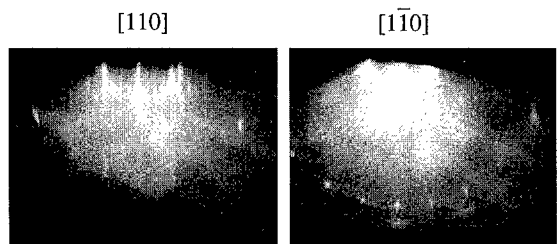


Fig. 3. RHEED picture taken prior to turn on of e-beam (t_c) and at the start of oxide deposition (t_s). The RHEED picture shows a (4×6) reconstructed surface and indicates preservation of surface stoichiometry.

surface after completion of GaAs epitaxial growth (t_c) and at start of oxide deposition at a substrate temperature T_s of 350°C (t_s) are identical, showing a (2×4) reconstructed, As stabilized surface (Fig. 2). This indicates preservation of an atomically ordered, stoichiometric GaAs surface prior to oxide deposition ($t_c < t < t_s$). The estimated As coverage of a (2×4) reconstructed surface is $> 60\%$ [18,19]. Lower As coverage is typically obtained when the wafer is heated to temperatures above 500°C prior to oxide deposition. This is demonstrated in Fig. 3

showing a (4×6) GaAs surface reconstruction with an estimated As coverage of $\approx 30\%$ [18] at a substrate temperature $T_s = 600^\circ\text{C}$ (time t_t). Note that the subsequent surface exposure to impurity gases of less than 10 L ($t_t < t < t_s$) does not affect the RHEED pattern and the (4×6) GaAs surface reconstruction is completely preserved prior to opening the shutter for oxide deposition (t_s). Thus, prior to oxide deposition, (i) the surface stoichiometry is maintained as observed by RHEED and (ii) extremely low GaAs surface exposure of typically less than 10 L has been accomplished. Therefore, the estimated GaAs surface impurity coverage is $\approx 10^{-4}\%$ of a monolayer or $\approx 10^9 \text{ cm}^{-2}$ assuming a typical initial oxygen sticking coefficient of 10^{-6} .

As 3d and Ga 3d core level spectra were acquired from XPS depth profiles on fabricated oxide–GaAs structures. A Perkin Elmer 5600 series XPS spectrometer equipped with a monochromatic Al K α X-ray source was used. The photon energy was 1486.6 eV. Depth profiling was done in situ in an UHV chamber (background pressure = 5×10^{-10} Torr) by Ar sputtering using an ion gun at 4 keV. The XPS spectra were acquired using an energy step width of 0.2 eV.

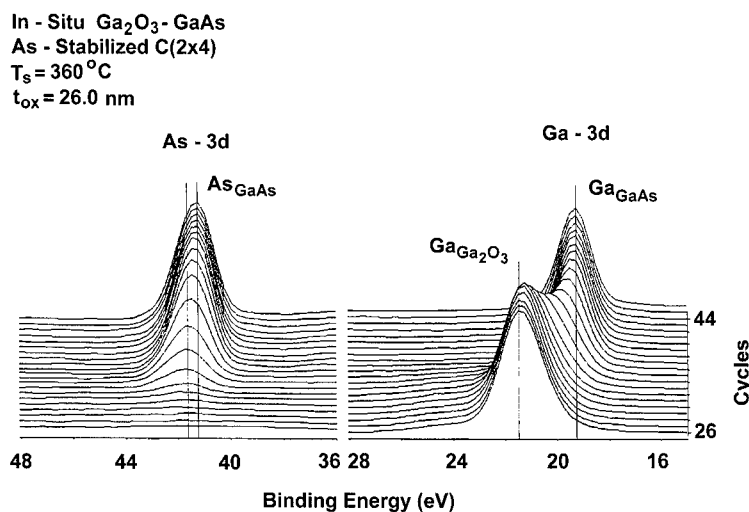


Fig. 4. Ga and As 3d core levels of a Ga_2O_3 –GaAs interface measured by XPS. Energy positions and full line width at half-maximum (FWHM) of $\text{Ga}_{\text{Ga}_2\text{O}_3}$, Ga_{GaAs} and As_{GaAs} peaks are 21.3 ± 0.1 , 19.2 ± 0.1 , and 41.2 ± 0.1 eV, respectively, and 1.80, 1.34, and 1.60 eV, respectively. The As 3d level exhibits a shift of 0.44 ± 0.2 eV at the interface.

Table 1
Observed binding energies of Ga and As 3d core levels

GaAs surface reconstruction	Oxide		Observed binding energy (eV)				
	estimated As coverage (%)	substrate deposition temperature (°C)	type	Ga 3d		As 3d	
				GaAs bulk	Ga ₂ O ₃ bulk shift	interface shift	GaAs bulk interface shift
(published binding energies [7–9,21–23])							
(2×4)	> 60	0	Ga ₂ O ₃	19.2	+1.2	—	41.2
(2×4)	> 60	360	Ga ₂ O ₃	19.2±0.1	+(2.0±0.2)	—	41.2±0.1
(2×4)	> 60	400	SiO ₂	19.2±0.1	+(2.1±0.2)	—	41.2±0.1
(4×6)	≈ 30	550	Ga ₂ O ₃	19.3±0.1	—	+(0.36±0.2)	41.2±0.1
(4×2) ^a	< 20	500	Ga ₂ O ₃	19.2±0.1	+(2.0±0.2)	—	41.2±0.1
					+(2.0±0.2)	—	0±0.2

^a (4×2) surface reconstruction was obtained by heating the sample to 620°C for a few seconds.

Fig. 4 and Fig. 5 show typical depth profiles of Ga and As 3d core levels of in-situ fabricated Ga_2O_3 -GaAs structures as a function of depth, at depths near the Ga_2O_3 -GaAs interface. These spectra are shown for structures fabricated using a (2×4) As and a (4×2) Ga stabilized GaAs surface with an estimated As surface coverage prior to deposition of $> 60\%$ and $< 20\%$, respectively [18,19]. A sputtering rate of 7.4 \AA/cycle (Fig. 4) and 1.5 \AA/cycle (Fig. 5) provided a depth resolution considerably better than an estimated escape depth of $\approx 25 \text{ \AA}$ [20]. In the following, (i) the binding energy (BE) of Ga 3d levels in bulk Ga_2O_3 and GaAs, (ii) the BE of the As 3d level in bulk GaAs, and (iii) the interfacial chemical shifts of As and Ga 3d peaks will be discussed. Table 1 compares Ga and As 3d BEs of $\text{Ga}_{\text{Ga}_2\text{O}_3}$, Ga_{GaAs} and As_{GaAs} peaks to previously reported results [7–9,21–23]. The BEs of Ga_{GaAs} and As_{GaAs} are identical to standard XPS lines reported earlier (19.2 and 41.2 eV, respectively).

The chemical shift of the Ga 3d peak in our bulk Ga_2O_3 films is $0.8 \pm 0.2 \text{ eV}$ larger than a shift of 1.2 eV typically obtained from XPS surface analysis during the initial stage of GaAs oxidation [8,9,21,24]. The $2.0 \pm 0.2 \text{ eV}$ shift reported here is based on bulk values; as sputtering proceeds the peak appears to

gradually shift from the bulk Ga_2O_3 to the GaAs on a length scale consistent with the electron escape depth. The intermediate peak can easily be fitted as a sum of two components; band bending is not excluded, but is not necessary to explain these results. Furthermore, oxide-GaAs structures with different band bending of $\approx 0 \text{ eV}$ for Ga_2O_3 -GaAs and $\approx 0.7 \text{ eV}$ for SiO_2 -GaAs (see discussion of electronic interface properties) exhibit a virtually identical interfacial As 3d core level shift. Previously reported smaller shifts of Ga 3d level during initial oxidation of GaAs is complicated by the fact that these shifts in the Ga 3d level may represent Ga-suboxide formation and/or formation of As oxides [9,10].

The chemical shift of the interfacial As 3d core levels acquired by XPS depth profiling are clearly correlated to As surface coverage prior to deposition and thus, to surface reconstruction (Table 1). The chemical shift is $0.44 \pm 0.2 \text{ eV}$ for an As stabilized surface ($> 60\%$ As coverage), however, no shift is detectable at a Ga stabilized surface ($< 20\%$ As coverage). The increase in As 3d binding energy can be explained by (i) an increasing As/Ga atomic surface ratio and/or (ii) the existence of As-O bonds. No quantitative analysis is possible at this

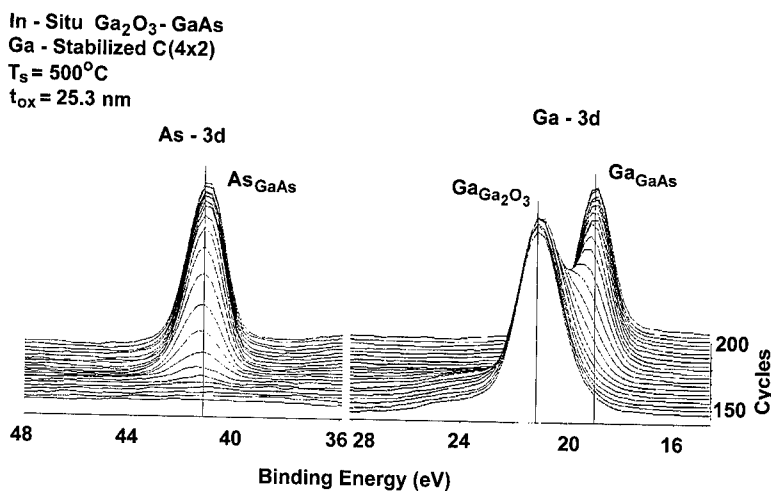


Fig. 5. Ga and As 3d core levels of a Ga_2O_3 -GaAs interface measured by XPS. Energy positions and FWHM of $\text{Ga}_{\text{Ga}_2\text{O}_3}$, Ga_{GaAs} and As_{GaAs} peaks are 21.2 ± 0.1 , 19.2 ± 0.1 , and $41.2 \pm 0.1 \text{ eV}$, respectively, and 1.83, 1.39, and 1.63 eV, respectively. No chemical shift of the As 3d peak is detectable at the interface.

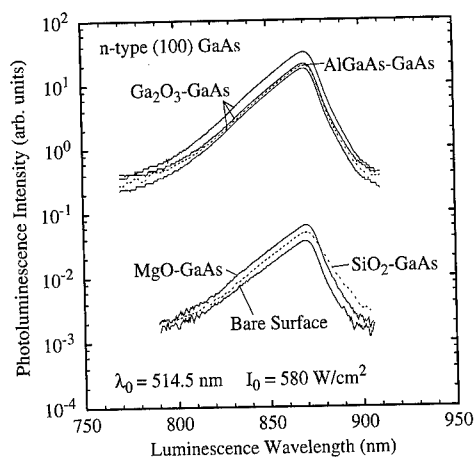


Fig. 6. Measured PL spectra of Ga_2O_3 -, $\text{Al}_{0.45}\text{Ga}_{0.55}\text{As}$ -, SiO_2 -, and MgO -GaAs structures as well as of a corresponding bare surface. The deposition temperatures for Ga_2O_3 are 620, 360, and 550°C from the highest to the lowest measured spectrum, respectively. The other results were typically obtained for $T_s = 690^\circ\text{C}$ ($\text{Al}_{0.45}\text{Ga}_{0.55}\text{As}$), and $0^\circ\text{C} \leq T_s \leq 500^\circ\text{C}$ (SiO_2 , MgO).

time and further work is required to clarify the specific bonding mechanisms of oxide molecules on a clean and atomically ordered (100) GaAs surface.

3.2. Electronic interface properties

Electronic interface properties including interface recombination velocity and interface state density have been investigated by steady-state photoluminescence (PL) and capacitance-voltage (C - V) measurements, respectively. Although the results will be briefly outlined in the following, the reader is referred to other reports for details [25,26].

Typical PL spectra of Ga_2O_3 -, $\text{Al}_{0.45}\text{Ga}_{0.55}\text{As}$ -, SiO_2 -, and MgO -GaAs structures as well as of a corresponding bare surface (Fig. 6) have been measured using an argon ion laser ($\lambda_0 = 514.5$ nm). While Ga_2O_3 -GaAs structures exhibit PL spectra comparable to that of excellent $\text{Al}_{0.45}\text{Ga}_{0.55}\text{As}$ -GaAs interfaces, SiO_2 - and MgO -GaAs structures show PL similar to that of a bare surface. The interface recombination velocity S has been derived from the nonlinear dependence of the steady state PL on incident light intensity I_0 measured for $20 < I_0 < 5000$ W/cm^2 . In the case of Ga_2O_3 -GaAs struc-

tures, the best fit to the measured data using a model solving Poisson's and current continuity equations self-consistently (see for example [27]), has been obtained for $4500 \leq S \leq 7000$ cm/s [26]. The interface state density D_{it} has been determined by quasi-static and high frequency C - V measurements. A midgap interface state density in the mid 10^{10} cm^{-2} eV^{-1} range has been inferred for Ga_2O_3 -GaAs structures [25] using the quasi-static/high frequency technique [28]. For SiO_2 - and MgO -GaAs structures, interface state densities and recombination velocities of $\approx 5 \times 10^{13}$ cm^{-2} eV^{-1} and $\approx 10^7$ cm/s have been inferred, respectively. The results clearly indicate fundamental differences in electronic interface properties.

4. Conclusions

The analysis of structural and electronic interface properties of Ga_2O_3 , SiO_2 , and MgO films deposited in-situ on clean and atomically ordered (100) GaAs surfaces allows the following conclusions. (i) Chemical reaction products, in particular As_2O_3 (44.6 eV) and As_2O_5 (45.7 eV) are not detectable at in-situ fabricated oxide-GaAs interfaces. (ii) Consequently, thermodynamic stability is obtained as predicted by thermodynamic phase diagrams [29]. In particular, the chemical reaction $\text{As}_2\text{O}_3 + 2 \text{GaAs} \rightarrow \text{Ga}_2\text{O}_3 + 4 \text{As}$ ($\Delta G = -62$ kcal/mol) resulting As formation and degradation of electronic interface properties [2,12] is excluded. (iii) Interfacial As 3d and Ga 3d lines are essentially identical for all considered in-situ fabricated oxide-GaAs structures. (iv) Electronic interface properties, however, are fundamentally different. While Ga_2O_3 -GaAs interfaces exhibit unique *intrinsic* electronic properties with interface state densities in the mid 10^{10} cm^{-2} eV^{-1} range, SiO_2 - and MgO -GaAs interfaces are characterized by an intrinsically pinned Fermi level at midgap.

Acknowledgements

M.P. gratefully acknowledges support by the Deutsche Forschungsgemeinschaft.

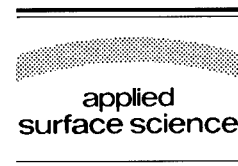
References

- [1] C.W. Wilmsen, Ed., *Physics and Chemistry of III–V Compound Semiconductor Interfaces* (Plenum Press, New York, 1985) chs. 1, 3, 4, 6.
- [2] F. Capasso and G.F. Williams, *J. Electrochem. Soc.* 129 (1982) 821.
- [3] S.D. Offsey, J.M. Woodall, A.C. Warren, P.D. Kirchner, T.I. Chapell and G.D. Pettit, *Appl. Phys. Lett.* 48 (1986) 477.
- [4] C.J. Sandroff, R.N. Nottenburg, J.-C. Bischoff and R. Bhat, *Appl. Phys. Lett.* 51 (1987) 33.
- [5] A. Callegari, P.D. Hoh, D.A. Buchanan and D. Lacey, *Appl. Phys. Lett.* 54 (1989) 332.
- [6] J.S. Herman and F.L. Terry, *Appl. Phys. Lett.* 60 (1992) 716.
- [7] W.E. Spicer, I. Lindau, P. Skeath, C.Y. Su and P. Chye, *J. Vac. Sci. Technol.* 17 (1980) 1019.
- [8] P. Pianetta, I. Lindau, C. Garner and W.E. Spicer, *Phys. Rev. Lett.* 35 (1975) 1356.
- [9] C.R. Brundle and D. Seybold, *J. Vac. Sci. Technol.* 16 (1979) 1186.
- [10] J.J. Barton, W.A. Goddard III and T.C. McGill, *J. Vac. Sci. Technol.* 16 (1979) 1178.
- [11] P. Pianetta, I. Lindau, C.M. Garner and W.E. Spicer, *Phys. Rev. B* 18 (1978) 2792.
- [12] J.M. Woodall and J.L. Freeouf, *J. Vac. Sci. Technol.* 19 (1981) 794.
- [13] R. Ludeke and A. Koma, *CRC Crit. Rev. Solid State Mater. Sci.* 5 (1975) 259.
- [14] A.Y. Cho and F.K. Reinhart, *J. Appl. Phys.* 45 (1974) 1812.
- [15] J. Saito and K. Kondo, *J. Appl. Phys.* 67 (1990) 6274.
- [16] M. Hong, K.D. Choquette, J.P. Mannaerts, L.H. Grober, R.S. Freund, D. Vakhshoori, S.N.G. Chu, H.S. Luftman and R.C. Wetzel, *J. Electron. Mater.* 23 (1994) 625.
- [17] M. Passlack, E.F. Schubert, W.S. Hobson, M. Hong, N. Moriya, S.N.G. Chu, K. Konstadinidis, J.P. Mannaerts, M.L. Schnoes and G.J. Zyzdik, *J. Appl. Phys.* 77 (1995) 688.
- [18] P. Drathen, W. Ranke and K. Jacobi, *Surf. Sci.* 77 (1978) L162.
- [19] J.R. Arthur, *Surf. Sci.* 43 (1974) 449.
- [20] S. Tanuma, C.J. Powell and D.R. Pen, *Surf. Interf. Anal.* 17 (1991) 911.
- [21] Y. Mizokawa, H. Iwasaki, R. Nishitani and S. Nakamura, *J. Electrochem. Soc.: Solid State Sci. Technol.* 126 (1979) 1370.
- [22] Y. Mizokawa, H. Iwasaki, R. Nishitani and S. Nakamura, *J. Electron Spectrosc. Rel. Phen.* 14 (1978) 129.
- [23] G. Schön, *J. Electron Spectrosc. Rel. Phen.* 2 (1973) 75.
- [24] E.S. Aydil, K.P. Giapis, R.A. Gottscho, V.M. Donnelly and E. Yoon, *J. Vac. Sci. Technol. B* 11 (1993) 195.
- [25] M. Passlack, M. Hong and J.P. Mannaerts, *Appl. Phys. Lett.*, submitted.
- [26] M. Passlack, M. Hong, J.P. Mannaerts, J.R. Kwo and L.W. Tu, *Appl. Phys. Lett.*, submitted.
- [27] M.S. Lundstrom and R.J. Schuelke, *IEEE Trans. Electron Devices* ED-30 (1983) 1151.
- [28] E.H. Nicollian and J.R. Brews, *MOS (Metal Oxide Semiconductor) Physics and Technology* (Wiley, New York, 1982) p. 331.
- [29] G.P. Schwartz, *Thin Solid Films* 103 (1983) 3.



ELSEVIER

Applied Surface Science 104/105 (1996) 448–454



Influence of physisorbed arsenic on RHEED intensity oscillations during low-temperature GaAs molecular beam epitaxy

R. Venkatasubramanian^{a,*}, Vamsee K. Pamula^a, Donald L. Dorsey^b

^a Department of Electrical and Computer Engineering, University of Nevada, Las Vegas, NV 89154, USA

^b Wright Laboratory (WL / MLPO), 3005 P Street, Materials Directorate, Wright-Patterson Air Force Base, OH 45433, USA

Received 28 June 1995; accepted 19 December 1995

Abstract

In a recent work, RHEED specular spot intensity oscillations were obtained during low-temperature molecular beam epitaxy (MBE) growth of GaAs when near stoichiometric V/III flux ratios ($\leq 2:1$) were used. The cause of these oscillations has not been fully explained. In this work, we have developed a stochastic model of growth which correctly describes the RHEED intensity dynamics over a wide range of growth conditions. A critical and novel improvement to the stochastic model is the inclusion of a physisorbed state. The experimental RHEED responses for various growth conditions were matched by taking into account the build-up of a physisorbed As layer and its effect on the specular spot RHEED intensity. The dynamics of the physisorbed As layer were introduced into the stochastic model by including the thermally activated processes of chemisorption and evaporation of the As physisorbed state. Model results indicate that for typical low- T GaAs growth temperatures (200°C), the steady-state coverage of physisorbed As ranged from 0.72 at a V/III flux ratio of 2:1 to 0.24 at a flux ratio of 1:1. Increased scattering of the RHEED beam due to the higher physisorbed As coverage at 2:1 leads to a factor of 5 decrease in the steady-state amplitude of the RHEED oscillations compared to the 1:1 case. This is in excellent agreement with the experimental results of Ibbetson et al. The RHEED intensity oscillates under these conditions due to layer-by-layer growth and a periodic variation in the coverage of physisorbed As, even though the surface migration rates are small. A factor in maintaining this growth mode is that arsenic stays in the physisorbed state with lifetimes in the range of 10^{-3} to 10^{-5} s and incorporates only when an appropriate configuration of Ga atoms forms on the surface. The temperature dependence of the evaporation and chemisorption time constants of physisorbed As yield activation energies of 0.24 eV and 0.39 eV, respectively, which are in excellent agreement with the experimental data.

1. Introduction

Reflection high energy electron diffraction intensity oscillations (RO) observed during molecular beam epitaxy (MBE) growth of semiconductors are indicative of layer-by-layer growth [1,2]. It has been

proposed that the ROs correspond directly to the step density oscillations during growth [1–3]. This has been validated by the scanning tunneling microscopy observations of Sudijono et al. [4]. For these reasons ROs have been accepted as an in-situ growth quality monitoring tool during MBE of both elemental and compound semiconductors.

Until the recent work of Ibbetson et al. [5], the observation of ROs during GaAs MBE had been

* Corresponding author. Tel.: +1-702-8951094; fax: +1-702-8954075; e-mail: venkat@unlv.edu.

limited to the high temperature growth regime (500–700°C) with an As₄ to Ga flux ratio of at least 5:1. Recently, non-stoichiometric GaAs thin films grown by low temperature MBE have become an important technological material due to their semi-insulating property [6–8]. During low temperature growth (200°C), ROs have been observed under close to stoichiometric flux ratios [5]. The severely limited adatom surface migration at these low temperatures suggests that ROs are a result of some other physical mechanism. At higher flux ratios the ROs are absent, even though films with good crystallinity can be grown. The purpose of this work is to study these issues theoretically using the stochastic growth model, which has proven successful in previous theoretical MBE growth studies [9–12].

The model for the physisorbed state of As and its kinetics are presented in Section 2. In Section 3, results of numerical simulations using the modified stochastic model are presented and compared with experimental results. This is followed by a discussion on the validity and limitations of the model. Conclusions are presented in Section 4.

2. The modified stochastic model

The stochastic model of growth developed by Venkatasubramanian [9,10] is based on a rigid lattice gas of a zincblende structure in which the atoms occupy only the lattice sites within their sublattice. Anti-site defects are not allowed. The surface kinetic processes considered for the model are: adsorption, evaporation and interlayer and intralayer surface migrations. The rate of adsorption is dictated by the flux rate and the availability of proper surface site with surface covalent bonds satisfied. The rate of evaporation and migrations are modeled based on Arrhenius type rate equations with frequency factors and activation energies. The atom interactions are assumed pairwise and only up to second nearest neighbor interactions are considered. The stochastic model develops a set of time evolution equations of macro-variables of growth such as concentration of adatoms in a layer n , $C(n)$ and atom-vacancy pair concentration in layer n , $Q(n)$. The time evolution equations are written in terms of the rates of individual surface processes and their quantitative influence

on the macro-variables. These equations are coupled first order nonlinear differential equations in the macro-variables with activation energies, frequency factors and pair interaction energies as model parameters. Solving these equations numerically on a computer provides one with time evolution of macro-variables from which one can obtain various surface data such as surface roughness, surface coverage as a function of time, growth rate, etc.

The stochastic model is suitable for growth of a quaternary semiconductor compound such as $A_x B_{1-x} C_y D_{1-y}$ where A and B belong to the cation sublattice and C and D belong to the anion sublattice. Unlike the Monte Carlo simulation and the molecular dynamics, the stochastic model is not size-limited and therefore, is suitable for doping kinetics studies.

The kinetic model proposed by Foxon et al. [13] includes a weakly bound physisorbed state for As₂ from which As₂ can either chemisorb onto the crystal surface and become part of it or evaporate into vacuum. Physical evidence of this layer was found by Ibbetson et al. [5] for growths below 350°C. They observed an increase in the diffuse background and attributed this to the presence of an amorphous physisorbed As layer. Preliminary desorption mass spectroscopy experiments are in agreement with this interpretation [14].

The kinetic processes of the physisorbed state play a critical role in the overall growth kinetics, especially during low temperature MBE growth of compound semiconductors. Under these conditions, thermally activated surface processes may become rate limiting and therefore dominate the growth of the film. In addition to their intrinsic control of the growth processes, the presence of surface species may influence the in-situ monitoring of the growth rate and surface quality by RHEED. For example, in the presence of physisorbed As (PA), the RHEED electron beam will interact with both the crystalline surface and the amorphous surface species. Thus, the amplitude of ROs is dictated not only by the step density variation, but also by the physisorbed species coverage variation with time. Even if the step density is constant, a periodic variation of the surface coverage of physisorbed As will cause periodic variation in the crystalline surface exposed to the RHEED beam and may therefore result in ROs. Based on the

above reasoning, the presence of physisorbed As was included in the stochastic model. The dynamic processes of chemisorption and evaporation from the physisorbed state were modeled using the following Arrhenius rate form:

$$\tau_i = \tau_{0,i} e^{E_i/kT}, \quad (1)$$

where $\tau_{0,i}$ is the inverse of the frequency factor for the process ' i ', E_i is the activation energy, k is the Boltzmann constant and T is the temperature in K. Processes $i = 1$ and $i = 2$ correspond to evaporation and chemisorption respectively.

The details of the stochastic model are presented in Ref. [9–12]. In these works, the stochastic model only includes processes occurring on the crystalline surface. For the present study, as the growth temperature is low, the dynamics of the physisorbed As layer is important. The time evolution of the concentration of the physisorbed layer, $c_{\text{phy,As}}$, is described by the following differential equation:

$$\frac{dc_{\text{phy,As}}}{dt} = \left(J_{\text{As}} - \frac{dc_{\text{As}}}{dt} \right) - \frac{c_{\text{phy,As}}}{\tau_1} - \frac{c_{\text{phy,As}} f_{\text{Ga}}}{\tau_2}, \quad (2)$$

where J_{As} is the molecular flux of As into the physisorbed state and dc_{As}/dt is the rate of incorporation of As into the epilayer, with C_{As} describing the total As incorporation into crystalline epilayer. The first term represents the net flux into the physisorbed state. The second and third terms in Eq. (2) represent the loss of physisorbed As due to evaporation and chemisorption, with the chemisorption rate proportional to the fraction of available Ga sites, f_{Ga} . Since there is no systematic experimental data available for the time constants τ_i , these values were obtained by fitting the simulated RHEED data to the experimental RHEED results of Ref. [5], as detailed in Section 3.

In contrast to the original stochastic model [9], the solid-on-solid restriction was relaxed. Specifically, both Ga and As_2 can incorporate on the surface, even when only one of the surface covalent bonds is satisfied.

3. Results and discussion

The coupled nonlinear first order differential equations were integrated using a fourth order Runge–Kutta method with time steps of 10^{-4} s or less. The growth time was kept 10 s. The growths were simulated on Cray YMP 2/216. Due to unavailability of sufficient systematic data of MBE growth of GaAs at low temperatures, the following approach for obtaining the model parameters was employed. With a judicious choice of the life times for evaporation and chemisorption from the physisorbed state, growths were simulated at flux ratios 1:1, 1.5:1 and 2:1 (As:Ga) with a fixed temperature of 200°C and at temperatures 200°C to 350°C with a fixed flux ratio of 2:1.

Since As_2 molecular beam is employed for this study, the flux ratios in terms of atomic fluxes is twice the molecular flux ratios mentioned above. The individual fluxes were chosen to be same as the experiments [5]. Specular beam RHEED intensity was obtained using kinematic theory of electron diffraction as a function of time and the relative amplitudes of ROs were compared with the experimental data [5]. The model parameters which yielded agreement between theory and experiments to within a factor of two were accepted. Using these time constants and Eq. (1), the $\tau_{0,i}$ and the activation energies, E_i were obtained and are reported in Table 1. These values for the model parameters were used for rest of the simulations.

Simulations were performed for various flux ratios at 200°C. The RHEED intensity versus time and physisorbed arsenic (PA) coverage versus time are shown in Fig. 1 and Fig. 2, respectively. The relative amplitudes of the ROs obtained agree with the experimental results within a factor of two [5]. Higher the flux ratio, lower was the amplitude of ROs with weak or no ROs present for flux ratios greater than 2:1 which is consistent with the experimental observations [5]. For higher flux ratios, there is a proportionally higher coverage of PA as evidenced in Fig. 2. It is noted that the physisorbed coverage builds up almost exponentially within the first second and reaches a steady state value. The steady state coverage of PA depends on the flux ratio with higher flux ratio yielding larger coverage. The lesser amplitude of the ROs at higher flux is due to lesser effective

Table 1
Model parameters such as frequency factors and activation energies for various surface kinetic processes *

Parameter	Symbol	Value used
Frequency factor for migration in crystalline state	R_{do}	$k_B T/h \text{ s}^{-1}$
Activation energy for migration in crystalline state	E_d	1.0 eV
Prefactor lifetime for evaporation from physisorbed state	$\tau_{0,1}$	$6 \times 10^{-4} \text{ s}$
Activation energy for evaporation from the physisorbed state	E_1	0.24 eV
Prefactor lifetime for chemisorption from physisorbed state	$\tau_{0,2}$	$1 \times 10^{-6} \text{ s}$
Activation energy for chemisorption from the physisorbed state	E_2	0.39 eV

* h is the Planck constant and k_B is the Boltzmann constant.

migration of the adatoms and higher coverage of PA whereas the larger amplitude of ROs at lower flux is due to greater effective migration and lower PA coverage. It should be noted that as the PA coverage is varying, the area of the crystalline surface exposed to the RHEED is also varying, which also contributes to the oscillations in the intensity in addition to step density variation. An approximate solution to Eq. (2) assuming that the first term which represents the net flux into the physisorbed state is a constant (in reality, it can be oscillatory due to time varying direct chemisorption of As from the molecular beam dictated by time varying availability of surface Ga concentration), can be obtained as

$$c_{\text{phy,As}}(t) = J_{\text{phy,As}} \tau_1 (1 - e^{-t/\tau_1}), \quad (3)$$

where $J_{\text{phy,As}}$ is the net flux entering the physisorbed state. Eq. (3) yields that the steady state PA coverage is a product of the net As flux and the time constant, τ_1 . Since τ_1 decreases with temperature as given by

Eq. (1), the steady state coverage will decrease with temperature. The estimated steady state coverage agrees well with the simulation results. An additional feature observed during the steady state period is that the PA coverage oscillates with time. During the growth of a Ga layer, the surface coverage of available Ga peaks and at the same time the chemisorption of As also peaks. Thus, the loss of As from the physisorbed state peaks periodically during the steady state period.

Correlating the time evolutions of the PA coverage and the RHEED intensity, it is observed that PA coverage inversely relates to the RHEED intensity. In other words, valleys and peaks in the PA coverage profiles correspond exactly to the peaks and valleys in the RHEED intensity, respectively. As the PA coverage is varying, the crystalline surface exposed to the RHEED will also be varying inversely with it. So, this periodical nature of the exposure of the crystalline layer to the incident beam will give rise to

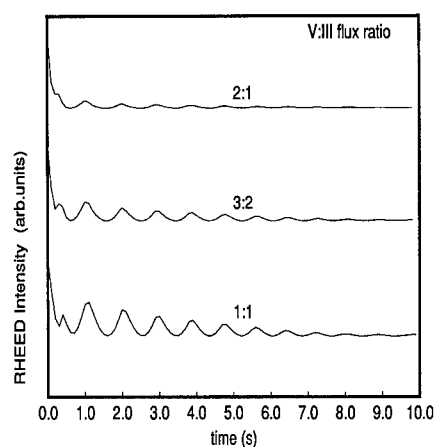


Fig. 1. RHEED intensity versus time for various flux ratios at 200°C.

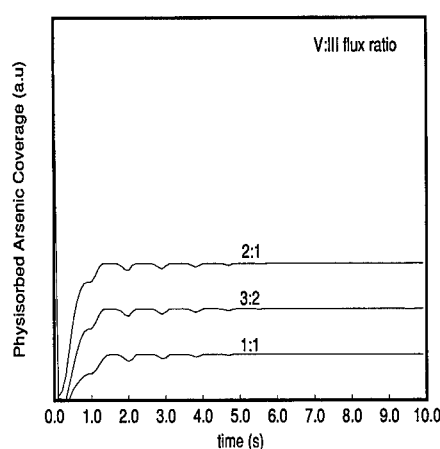


Fig. 2. Coverage of the physisorbed As versus time for various flux ratios at 200°C.

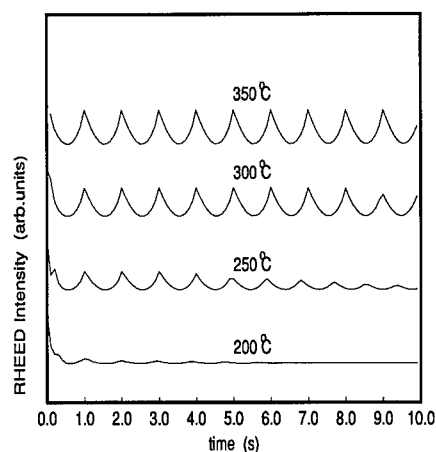


Fig. 3. RHEED intensity versus time for various temperatures at flux ratio 2:1.

the oscillations in the specular beam intensity. Therefore, this periodical exposure of the crystalline surface due to periodical change in the PA coverage should also be considered. Thus, the traditional notion that the ROs are due to step density changes on the surface requires to be modified to include the influence of the presence and time evolution of the PA coverage.

Results of RHEED intensity versus time and PA coverage versus time for simulations with flux ratio 2:1 and temperatures in the range 200–350°C are shown in Fig. 3 and Fig. 4, respectively. The relative amplitudes of ROs shown in Fig. 3 are in excellent

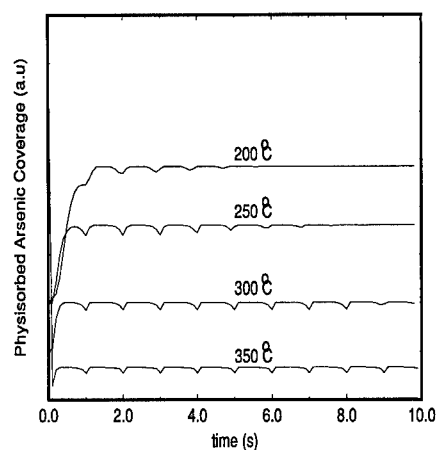


Fig. 4. Coverage of physisorbed As versus time for various temperatures at flux ratio 2:1.

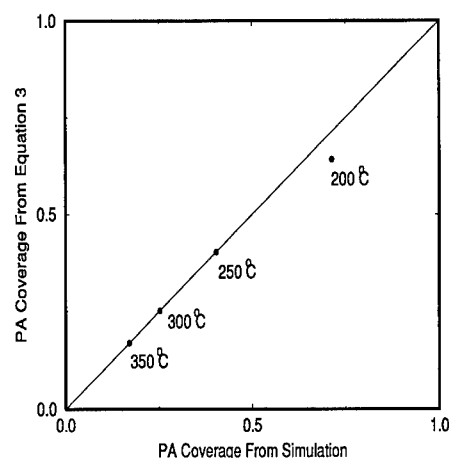


Fig. 5. Comparison of the physisorbed As obtained from simulations and Eq. (3) for various temperatures at flux ratio 2:1. The diagonal line represents the case of equal PA coverage from the simulation and Eq. (3).

agreement with the experiments [5]. As the temperature increases, the PA coverage decreases and the ROs are predominantly due to the increase in the effective migration rates resulting in step density variations. At around 350°C, the steady state PA coverage decreases to 17% which is consistent with the experimental observation that the RHEED streaks reappear around 350°C [5]. This is also consistent with the low energy electron diffraction results of Bachrach et al. [15] in which they report a temperature of 300°C for evaporating the surface PA state completely. The steady state PA coverage obtained using Eq. (3) agrees well with the simulation results as shown in Fig. 5 validating the approximate solution. It is noted that the exponential decay behavior of RHEED intensity as a function of time observed in actual experiment is not pronounced in our data. This discrepancy may be due a possible difference in the starting substrate surface condition such as roughness. Thus, even though our model does not quantitatively match all details of the experimental RHEED oscillations, it does reproduce some of the broad features such as the variation of the amplitude with flux ratio and temperature.

The evaporation time constant, τ_1 , is found to be in the range of 0.2 to 0.05 s and the corresponding activation energy is found to be 0.24 eV. The results of activation energy is in good agreement with value

of 0.36 eV of Foxon et al. [16], whereas the absolute evaporation life times are at least an order of magnitude different. This discrepancy may be attributed to the fact that life time measured by Foxon et al. [16] has a chemisorption life time component built in to it. Noting that the chemisorption life times are at least an order of magnitude smaller than the evaporation life time as shown by Eq. (1) and Table 1, this argument is valid. It is noted that the data of Foxon et al. [16] is for the temperature range of 300–450 K which is slightly lower than the range of this study. The chemisorption activation energy of 0.39 eV is also in good agreement with the sticking coefficient versus temperature data of Foxon et al. [16] for the temperature range of 400–900 K which yields activation energies in the range of 0.35 to 0.9 eV for high and low fluxes of Ga, respectively. It is noted here that the sticking coefficient data may include evaporation component and therefore, comparison between theory and experiments should be made with caution. Thus, the results of this work are in good agreement with various independent experimental works validating [5,13,14,16,15] the consistency of the model.

In spite of the many strengths of the present studies in terms of agreement with various experimental works in the literature [5,13,14,16,15], there are a few limitations which need to be discussed. Firstly, the stochastic model does not provide and/or use the microstructural details of the surface atomic configurations beyond the second nearest neighbor which may be important for surface reconstruction which, in turn, may influence the surface processes such as adsorption, chemisorption and evaporation. Secondly, the presence of surface reconstructions and their dependence on temperature and flux ratio is completely ignored. Thirdly, the RHEED intensity calculations are based on kinematical theory of electron diffraction without regard to multiple reflections. The RHEED intensity contribution from the amorphous physisorbed layer and the crystalline layer underneath, are excluded as the amorphous layer is expected to result in a diffused background as observed in experiments [5]. Finally, it is noted that even though we have reproduced the relative RO amplitudes for various experimental conditions, the theoretical ROs are not identical to the experimental ones in terms of individual oscillations. In particular,

our ROs have broader troughs and sharper peaks unlike the experimental ones. This discrepancy may be due to a variety of reasons including the contribution to the RHEED intensity from crystalline material under the physisorbed As and neglecting of the multiple scattering effect in our calculations.

4. Conclusion

In this work, we have developed a stochastic model of growth which correctly describes the RHEED intensity dynamics over a wide range of growth conditions. By the inclusion of a physisorbed state with amorphous As to the stochastic model and its surface dynamics, we were able to match the RHEED responses for various growth conditions, by taking into account the influence of time evolving physisorbed As layer and its effect on the RHEED intensity. The RHEED intensity versus time behavior for various growth conditions in the temperature range of 200–350°C and flux ratio range of 1:1 to 1:2.0 are in excellent agreement with the experimental results of Ibbetson et al. [5]. The RHEED intensity oscillates under these conditions due to layer-by-layer growth and a periodic variation of the surface coverage of physisorbed As. An important factor in maintaining this growth mode is that arsenic can only incorporate when appropriate configurations of Ga atoms form on the surface. The temperature dependence of the evaporation and chemisorption time constants of physisorbed As yield activation energies of 0.24 eV and 0.39 eV, respectively, which are in excellent agreement with the experimental data [13,14,16,15]. Even though, the present model was developed and employed for the low temperature and low flux ratio regime, since the model is general enough, it can be adopted for high temperature and high flux ratio regimes and also for other compound semiconductors.

References

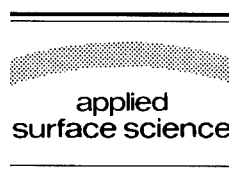
- [1] J.H. Neave, B.A. Joyce, P.J. Dobson and N. Norton, *Appl. Phys. A* 31 (1983) 1.
- [2] J.M. Van Hove, C.S. Lent, P.R. Pukite and P.I. Cohen, *J. Vac. Sci. Technol. B* 1 (1983) 741.

- [3] M. Henzler, *Surf. Sci.* 73 (1978) 240.
- [4] J. Sudijono, M.D. Johnson, C.W. Snyder, M.B. Elowitz and B.G. Orr, *Phys. Rev. Lett.* 69 (1992) 2811.
- [5] J.P. Ibbetson, R.P. Mirin, U.K. Mishra and A.C. Gossard, *J. Vac. Sci. Technol. B* 12 (1994) 1050.
- [6] F.W. Smith, A.R. Calawa, C.L. Chen, M.J. Manfra and L.J. Mahoney, *IEEE Trans. Electron Device Lett.* EDL-11 (1990) 561.
- [7] A.C. Warren, J.M. Woodall, J.L. Freeouf, D. Grischowsky, M.R. Melloch and N. Otsuka, *Appl. Phys. Lett.* 57 (1990) 1331.
- [8] M.R. Melloch, N. Otsuka, J.M. Woodall, A.C. Warren and J.L. Freeouf, *Appl. Phys. Lett.* 57 (1990) 1531.
- [9] R. Venkatasubramanian, *J. Mater. Res.* 7 (1992) 1221.
- [10] R. Venkatasubramanian, *J. Mater. Res.* 7 (1992) 1235.
- [11] R. Venkatasubramanian and D.L. Dorsey, *J. Vac. Sci. Technol. B* 11 (1993) 253.
- [12] R. Venkatasubramanian and S. Bendi, *Int. J. Comput. Math. Phys. Electr. Eng.* 12 (1993) 423.
- [13] C.T. Foxon and B.A. Joyce, *Surf. Sci.* 64 (1977) 293.
- [14] K. Evans, private communication, 1994.
- [15] R.Z. Bachrach, R.S. Bauer, P. Chiaradia and G.V. Hansson, *J. Vac. Sci. Technol.* 19 (1981) 335.
- [16] C.T. Foxon and B.A. Joyce, *Surf. Sci.* 50 (1975) 434.



ELSEVIER

Applied Surface Science 104/105 (1996) 455–460



UV photoemission study of heteroepitaxial AlGa_N films grown on 6H-SiC

M.C. Benjamin, M.D. Bremser, T.W. Weeks, Jr., S.W. King, R.F. Davis,
R.J. Nemanich^{*}

Department of Physics and Department of Materials Science and Engineering, North Carolina State University, Raleigh, NC 27695-8202, USA

Received 28 June 1995; accepted 10 October 1995

Abstract

This study presents results of UV photoemission measurements of the surface and interface properties of heteroepitaxial AlGa_N on 6H-SiC. Previous results have demonstrated a negative electron affinity of AlN on 6H-SiC. In this study Al_xGa_{1-x}N alloy films were grown by organometallic vapor phase epitaxy (OMVPE) and doped with silicon. The analytical techniques included UPS, Auger electron spectroscopy, and LEED. All analysis took place in an integrated UHV transfer system which included the analysis techniques, a surface processing chamber and a gas source MBE. The OMVPE alloy samples were transported in air to the surface characterization system while the AlN and GaN investigations were prepared in situ. The surface electronic states were characterized by surface normal UV photoemission to determine whether the electron affinity was positive or negative. Two aspects of the photoemission distinguish a surface that exhibits a NEA: (1) the spectrum exhibits a sharp peak in the low kinetic energy region, and (2) the width of the spectrum is $h\nu - E_g$. The in situ prepared AlN samples exhibited the characteristics of a NEA while the GaN and Al_{0.13}Ga_{0.87}N samples did not. The Al_{0.55}Ga_{0.45}N sample shows a low positive electron affinity. Annealing of the sample to $> 400^\circ\text{C}$ resulted in the disappearance of the sharp emission features, and this effect was related to contaminant effects on the surface. The results suggest the potential of nitride based cold cathode electron emitters.

1. Introduction

There is increasing interest in electronic devices composed of III-nitride materials for opto-electronic applications in the blue and UV region [1]. An alternative application of these semiconductors is in electron emission devices. Recent studies have demonstrated that diamond surfaces can exhibit a negative electron affinity (NEA). NEA surfaces may

prove to be critical elements for cold cathode devices, vacuum microelectronics, and photodetectors [2,3]. In addition to diamond, thin films of AlN grown on 6H-SiC have been shown to exhibit a negative electron affinity (NEA) [4,5]. The AlN NEA surfaces were obtained from air exposed surfaces, and do not appear to be readily poisoned. In contrast to diamond, AlGa_N materials exhibit the wurtzite crystal structure. One of the most significant limitations in the application of diamond is that reliable n-type doping has not been achieved. In contrast, n-type doping has been obtained for GaN and some

^{*} Corresponding author. Tel.: +1-919-5153225; fax: +1-919-5157331; e-mail: robert_nemanich@ncsu.edu.

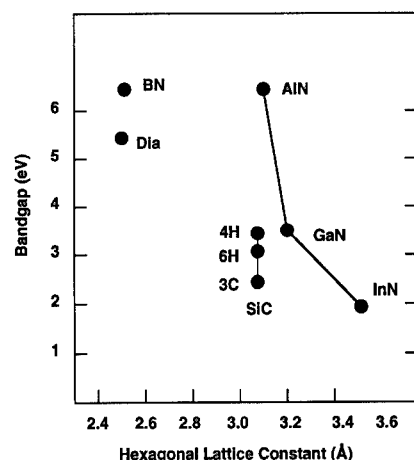


Fig. 1. The bandgap versus hexagonal lattice constant (a) for a variety of wide bandgap semiconductors. The lattice constant for the cubic materials has been determined from the (111) plane.

AlGaN alloys. This study explores further the electron affinity of epitaxial AlGaN films on 6H-SiC.

The wurtzite AlN and GaN form a continuous solid solution of $\text{Al}_x\text{Ga}_{1-x}\text{N}$ for $0 \leq x \leq 1$ with bandgaps that range from 3.4 eV (GaN) to 6.2 eV (AlN). Fig. 1 displays the bandgap of several materials as a function of the equivalent hexagonal lattice constant. The alloys are also miscible with In, hence the inclusion of InN could extend the range to 1.9 eV. The electron affinity of a semiconductor is related to the surface dipole and to the fundamental energy levels of the materials. Because the valence and conduction bands of the semiconductors have origin in the sp^3 bonding and antibonding levels, it may be suggested that the larger bandgap materials will exhibit a smaller or negative electron affinity. In comparison with diamond, it might be assumed that AlGaN alloys with a bandgap greater than 5.4 eV could exhibit a NEA. In this paper we report studies of AlGaN with x values of 0.55 and 0.13 as well as preliminary studies of GaN.

The AlGaN and GaN films used in this study were grown on vicinal 6H-SiC substrates. The n-type SiC substrates used have a small lattice mismatch with AlN (3.08 Å versus 3.11 Å) and GaN ($a = 3.19$ Å). The small lattice mismatch enables heteroepitaxial growth of the wurtzite (2H) structure. Furthermore, the fact that the substrates are conducting avoids charging problems associated with photoemission from large bandgap and insulating materials.

The electron affinity of a semiconductor or the presence of a NEA can be determined by ultraviolet photoemission spectroscopy (UPS) [6–8]. The experiments described here involve directing 21.2 eV light (the He I resonance line) to the surface of the sample and detecting the spectrum of the emitted photoexcited electrons as a function of electron kinetic energy. Typically, UPS is used to obtain a profile of the valence band (VB) electronic states. As such, most studies of UPS of semiconductors present data of the most energetic electrons emitted from the surface. Electrons scattered to lower energy and secondary electrons will be displayed in the spectrum at lower kinetic energies. In addition, for a semiconductor which exhibits a NEA surface, a distinctive peak may be observed at the low kinetic energy (highest binding energy) end of the photoemission spectra. Fig. 2 depicts a schematic representation of the photoemission spectra from a semiconductor with a negative or positive electron affinity. The low kinetic energy feature is due to secondary electrons which (quasi) thermalize to the conduction band minimum. Note that the solid line indicates a material with a positive electron affinity while the dashed line is a feature indicative of a NEA. In this paper we discuss samples with both positive and negative affinity surfaces.

The sharp features typical of a NEA have been observed from spectra of (111) and (100) diamond surfaces [6–10]. In the studies of diamond, a correlation was made between the presence of hydrogen and the NEA peak [9,10]. In addition, it was also

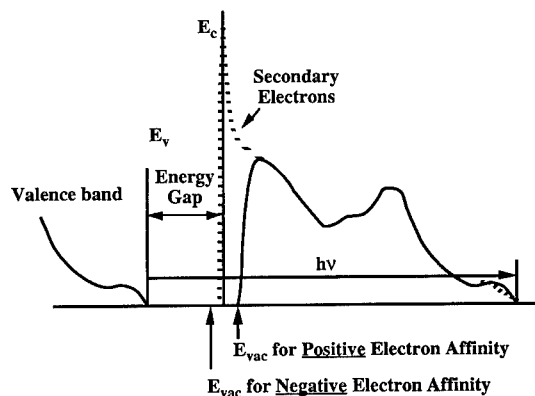


Fig. 2. A schematic of the difference in the photoemission spectra of a semiconductor with a positive or negative electron affinity.

shown that thin metal layers such as Ti or other moderate work function metals could induce a NEA on the diamond surface [10,11]. These measurements verify that the surface dipole can be influenced by surface processing and that the effects contribute to the observation of a NEA.

2. Experimental procedure

The 6H-SiC substrates used in this study were supplied by Cree Research, Inc. The samples were n-type with doping concentrations of 10^{16} to 10^{18} cm^{-3} . The AlGaIn samples were grown by CVD in a remote location and transported in ambient to the analysis system. To avoid surface contamination AlN and GaN samples were also grown in the integrated UHV transfer system by gas source molecular beam epitaxy (GSMBE). This system includes the UPS system, LEED, Auger, hydrogen and argon plasma processing chamber, and XPS as well as the GSMBE. The system is described elsewhere [9,11]. Recently added is the capability of gas source MBE (GSMBE) to grow undoped AlN and GaN films.

The AlGaIn thin films were grown on vicinal n-type, Si-face α (6H)-SiC(0001) substrates at 1100°C. Vicinal wafers were SiC(0001) 3° – 4° off-axis toward the $\langle 11\bar{2}0 \rangle$. The as-received SiC wafers were cut into 7.1 mm squares. The SiC pieces were degreased, dipped into a 10% HF solution for 10 min to remove the thermally grown oxide layer, and blown dry with N_2 before being loaded onto the SiC-coated graphite susceptor. The reactor was evacuated to less than 3×10^{-5} Torr prior to initiating growth. The continuously rotating susceptor was rf inductively heated to the AlGaIn deposition temperature of 1100°C in 3 SLM of flowing H_2 diluent. Hydrogen was also used as the carrier gas for the various metalorganic precursors. Once this growth temperature was reached and stabilized, AlGaIn deposition was started by flowing triethylaluminum (TEA), triethylgallium (TEG) and ammonia (NH_3) into the reactor at 23.6 $\mu\text{mol}/\text{min}$, 10.5 $\mu\text{mol}/\text{min}$ and 1.5 SLM, respectively. The approximate solid solution alloy concentration using these growth parameters was estimated to be $\text{Al}_{0.55}\text{Ga}_{0.45}\text{N}$ from cathodoluminescence measurements. The AlGaIn films were doped with Si from a SiH_4 source (8.2

ppm in N_2 balance) at flow rates between 2.89 and 5 nmol/min to minimize charging problems. The system pressure during AlGaIn growth was 45 Torr. The AlGaIn layer was grown for 90 min resulting in an approximate thickness of 1.5 μm . AlGaIn samples were transported in air to the analysis system. Film concentrations were determined from the bandgap values of cathodoluminescence. Auger electron spectroscopy was also used to characterize the surface.

The GaN growth took place in a GSMBE. The cleaning procedure is similar to the above described process but differs in that once in vacuum the substrate is annealed in a silane flux [12]. The GaN samples were not intentionally doped, but since very thin films were employed, charging problems were avoided.

The UPS measurements were excited with 21.21 eV radiation (He I resonance line), and emitted electrons are collected with a hemispherical energy analyzer. The base pressure of the UPS system is 2×10^{-10} Torr, and operating conditions involve pressures up to 1×10^{-9} Torr, but the higher pressure is due to the helium inflow and does not contaminate the sample. The 50 mm mean radius hemispherical electron analyzer was operated at a 0.15 eV energy resolution and a 2° angular resolution. The analyzer (VSW HA50) is mounted on a double goniometer and can be tilted with respect to the sample in two independent directions. The samples were fastened with tantalum wire to a molybdenum sample holder. The sample holder is biased by up to 3 V to allow low energy electrons to overcome the work function of the analyzer. The Fermi level of the system (sample and analyzer) is determined by UPS measurement of the sample holder with no sample bias (i.e., grounded). The sample holder can be heated to 1150°C, and the temperature is measured by a thermocouple.

3. Results and discussion

The UV photoemission spectra of all four samples studied here are shown in Fig. 3. The AlN and GaN films were prepared by gas source MBE and transferred under UHV to the photoemission system. The two alloy samples were prepared by CVD and suffered ambient exposure. Samples were biased with

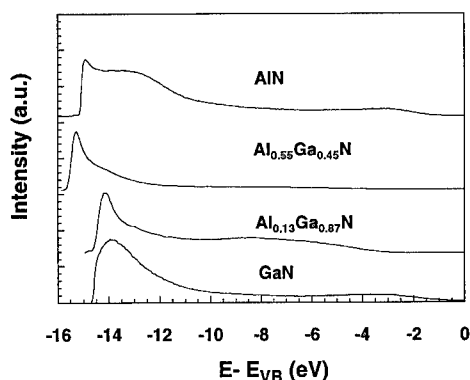


Fig. 3. The UV photoemission spectra of $\text{Al}_x\text{Ga}_{1-x}\text{N}$ for $x = 0, 0.13, 0.55, 1.0$. Spectra were aligned at the valence band maximum.

2–3 V to overcome the work function of the analyzer, and all spectra were shifted to be aligned at the valence band maximum. The spectra were scaled such that the strongest emission was the same for all curves.

The first aspect to be noted is that the spectra of the 55% aluminum alloy and AlN exhibit sharp strong features at the highest binding energy, which corresponds to the lowest kinetic energy. These features are possibly indicative of a negative electron affinity. As noted in the introduction, the feature is attributed to emission from electrons quasi-thermalized to the conduction band minimum. The emission from the $\text{Al}_{0.13}\text{Ga}_{0.87}\text{N}$ sample is significantly weaker, and the GaN emission does not show the sharp peak at all.

A second indication of the change in electron affinity with alloy concentration is the extension of the $\text{Al}_x\text{Ga}_{1-x}\text{N}$ spectra to lower energy as x is decreased. A more precise description of the relation of the NEA is obtained from the spectral width. The spectral width is obtained from a linear extrapolation of the emission onset edge to zero intensity at both the low kinetic energy cutoff and at the high kinetic energy end (reflecting the valence band maximum). For a material with a positive electron affinity, Fig. 2 shows that $\chi = h\nu - E_g - W$, and for a material with a negative electron affinity Fig. 2 indicates that $0 = h\nu - E_g - W$, or rewriting, $h\nu = E_g + W$. This analysis indicates that the 55% aluminum sample does not have a negative affinity but rather a low positive affinity value, as discussed below. We note

that the photoemission measurements cannot be used to determine the energy position of the electron affinity for the NEA case.

To determine the energy position of the valence band maximum, the spectral gain was increased, and the intensity was extrapolated to 0 emission. The spectra are aligned in Fig. 3 at the deduced valence band maximum. The spectral widths obtained from the $\text{Al}_x\text{Ga}_{1-x}\text{N}$ samples were 14.5, 14.5, 15.5, and 15 eV for $x = 0, 0.13, 0.55$, and 1.0, respectively. In applying the relations noted above, the bandgaps of the bulk AlN and GaN must also be known. The literature values of the AlN and GaN bandgaps are 6.2 and 3.4 eV respectively. Assuming a linear extrapolation for the bandgap of the alloys, we deduce $x = 0.55$ for $E_g = 4.70$ eV and $x = 0.13$ for $E_g = 3.80$ eV. Using the relations described above, the AlN surface satisfies the relations for a NEA within ± 0.2 eV, while the GaN, $\text{Al}_{0.55}\text{Ga}_{0.45}\text{N}$, and the $\text{Al}_{0.13}\text{Ga}_{0.87}\text{N}$ surfaces do not satisfy the relations for a NEA. We can, however, determine the value of the electron affinity of these materials and find that $\chi = 3.3$ eV, 2.9 eV, and 1.0 eV for $x = 0, 0.13$, and 0.55, respectively.

Another aspect that is evident from the photoemission spectra is the position of the surface Fermi level relative to the valence band maximum. It was found that E_F ranges from 2 to 3.5 eV above the valence band maximum for each sample. For the GaN and $\text{Al}_{0.13}\text{Ga}_{0.87}\text{N}$ surfaces, these values position E_F in the upper part of the gap while for the AlN and 55% Al samples, the values indicate that the surface Fermi level is pinned near midgap. The pinning at midgap may be an indication of increased impurity incorporation. In particular, the strong affinity of Al with oxygen often results in increased oxygen incorporation for these films.

To further explore the surface affinity, the effect of annealing in vacuum was explored for the $x = 0.55$ sample. The results are shown in Fig. 4. After annealing to 475°C and 580°C for 10 min the photoemission spectra showed a decrease in the relative intensity of the NEA related peak. Furthermore, the width of the spectra also decreases. As these temperatures are much less than the temperatures involved in growth, it is unlikely that a component present during growth is removed. It is possible that we introduced some type of contamination which af-

affected the emission. We suggest hydrocarbon contaminants as a likely possibility. No LEED pattern was visible for the $\text{Al}_{0.55}\text{Ga}_{0.45}\text{N}$ sample, and the lack of a LEED pattern for the as-loaded samples is possibly related to carbon and oxygen on the surface (attributed to the transport in air). The annealing may result in more complete bonding of the surface adsorbed hydrocarbon layer which results in a change in the surface dipole. Another possibility is that the electron affinity has been affected by adsorbed molecules such as hydrogen. While previous results have shown that hydrogen can induce a negative electron affinity surface on diamond [7,10], the Al-GaN surfaces have not been intentionally exposed to H. It is evident that further studies are necessary to characterize the surfaces more completely.

The deduced electron affinities versus alloy concentration are shown in Fig. 5. Again we note that the photoemission measurements cannot be used to determine the position of the vacuum level for a NEA surface so this point is indicated at $x = 0$ with an arrow to larger negative values. The results suggest that the electron affinity depends on the alloy concentration as originally suggested. Unfortunately, we do not have sufficient data at this time to more completely describe the effect. Additionally, we have made no effort to control the surface termination for these samples. For diamond, it was found that the observation of a NEA is critically dependent on the surface termination. Future studies will explore

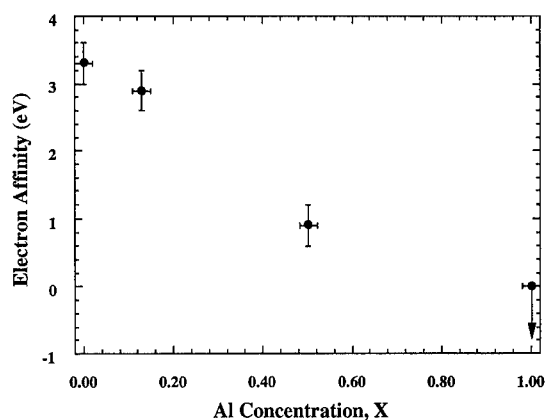


Fig. 5. Electron affinities of $\text{Al}_x\text{Ga}_{1-x}\text{N}$ alloys versus Al concentration. The arrow indicates that the electron affinity is less than (or equal to) 0, but the value cannot be determined from the UV photoemission measurements.

whether the electron affinity of AlGaN materials is also affected by different surface preparations.

4. Conclusions

In summary, we have observed features in the UPS spectra indicative of a NEA surface on AlN and a low positive electron affinity for $\text{Al}_{0.55}\text{Ga}_{0.45}\text{N}$. The AlN spectra exhibited both the sharp features at low kinetic energy that have been found to be characteristic of a NEA, and the width of the spectra was also consistent with the observed effect. The UPS spectra of AlGaN alloys did not show an NEA, but the measurements have been used to determine the electron affinity of GaN, $\text{Al}_{0.13}\text{Ga}_{0.87}\text{N}$, and $\text{Al}_{0.55}\text{Ga}_{0.45}\text{N}$ yielding values of 3.3, 2.9, and 1.0 eV, respectively.

The surface Fermi level was found to shift towards the middle of the band gap for the Al rich samples, and this may indicate an increase in oxygen impurities.

The NEA surfaces were robust showing the effect even after transfer through ambient. AlN samples grown in situ have shown NEA surfaces without the presence of oxygen. The positive affinity surfaces when annealed result in a change of the electron affinity. This effect was attributed to a change in the surface layer that affected the surface dipole.

Future work will involve examining samples to fill in the gaps in the solid solution of AlGaN alloys.

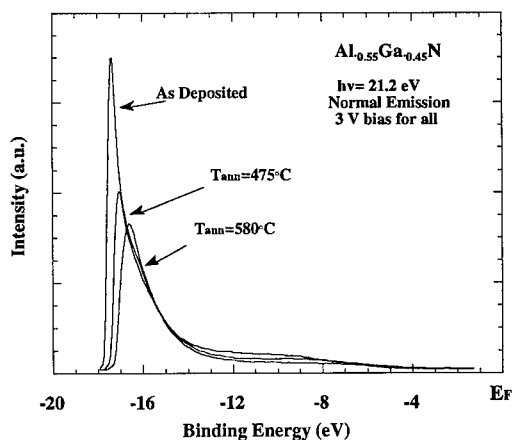


Fig. 4. The UV photoemission from $\text{Al}_{0.55}\text{Ga}_{0.45}\text{N}$ on 6H-SiC versus annealing temperature.

Furthermore, we will explore whether surface treatments can be employed on the AlGaIn alloys to form stable NEA surfaces.

Acknowledgements

This work was supported in part by the Office of Naval Research through grants N0014-92-J-1477 and N0014-92-J-1604. The SiC substrates used were supplied by Cree Research. We thank Bill Perry for performing the cathodoluminescence measurements.

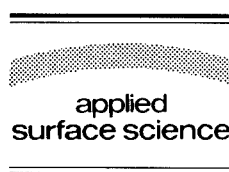
References

- [1] S. Strite and H. Morkoç, *J. Vac. Sci. Technol. B* 10 (1992) 1237.
- [2] J.H. Edgar, *J. Mater. Res.* 7 (1992) 235.
- [3] M.D. Williams, M.D. Feuer, S.C. Shunk, N.J. Sauer and T.Y. Chang, *J. Appl. Phys.* 71 (1992) 3042.
- [4] M.C. Benjamin, C. Wang, R.F. Davis and R.J. Nemanich, *Appl. Phys. Lett.* 64 (1994).
- [5] M.C. Benjamin, C. Wang, R.S. Kern, R.F. Davis and R.J. Nemanich, *Mater. Res. Soc. Symp.* 339 (1994) 81.
- [6] F.J. Himpsel, J.A. Knapp, J.A. van Vechten and D.E. Eastman, *Phys. Rev. B* 20 (1979) 624.
- [7] B.B. Pate, *Surf. Sci.* 165 (1986) 83.
- [8] B.B. Pate, M.H. Hecht, C. Binns, I. Lindau and W.E. Spicer, *J. Vac. Sci. Technol.* 21 (1982) 364.
- [9] J. van der Weide and R.J. Nemanich, *J. Vac. Sci. Technol. B* 10 (1992) 1940.
- [10] J. van der Weide and R.J. Nemanich, *Appl. Phys. Lett.* 62 (1993) 1878.
- [11] J. van der Weide and R.J. Nemanich, *Phys. Rev. B* 15 (1994) 49, 13629.
- [12] R. Kaplan, *Surf. Sci.* 215 (1989) 111.



ELSEVIER

Applied Surface Science 104/105 (1996) 461–467



Initial stage of growth of GaN/GaAs(001) in plasma-assisted molecular beam epitaxy

H. Yang^{a,*}, O. Brandt^a, A. Trampert^b, K.H. Ploog^a

^a Paul-Drude-Institut für Festkörperelektronik, Hausvogteiplatz 5–7, 10117 Berlin, Germany

^b Max-Planck-Institut für Festkörperforschung, Heisenbergstrasse 1, 70569 Stuttgart, Germany

Received 28 June 1995; accepted 29 August 1995

Abstract

The nucleation and subsequent growth of cubic GaN on GaAs(001) in molecular beam epitaxy are studied by reflection high-energy electron diffraction (RHEED), transmission electron microscopy (TEM), and X-ray diffraction. We find that the layer finish is strongly dependent on the conditions chosen for the nucleation of the first monolayers of GaN on GaAs. For optimized growth conditions, TEM demonstrates 10 nm thick GaN films to be epitaxial and connected layers regardless of the 20% lattice mismatch. Furthermore, RHEED reveals an increasing lateral domain size in the course of growth for this case. This approach towards two-dimensional growth manifests itself in a steady improvement of the crystal quality with increasing thickness as determined by X-ray diffraction. However, this improvement does not take place for non-optimum conditions in the initial stage of growth regardless the conditions chosen in the later stage of growth, from which we conclude that control over nucleation is a necessity for the successful fabrication of GaN-based heterostructures.

1. Introduction

Group III-nitrides are attractive for opto-electronic devices emitting in the blue and UV spectral ranges. For the growth of such devices, AlGaIn/GaN/InGaIn double-heterostructures are required. A key parameter for the performance of these structures is the interface quality, which is, first of all, determined by the growth front of the GaN epilayer. This prerequisite of a smooth growth front encounters, however, the fundamental problem of the huge lattice mismatch between GaN and all available

substrates. For obtaining connected and epitaxial films, the concept of an amorphous low temperature buffer layer is commonly employed [1–4]. The epilayers obtained by this recipe consist of columnar, nonepitaxial grains [5–7], and thick buffer layers have to be grown in order to obtain connected films. Here, we report the synthesis of exceptionally smooth, epitaxial cubic GaN films on GaAs(001) substrates without the use of this low temperature buffer layer. The influence of growth conditions at the hetero-nucleation stage are studied by in-situ reflection high-energy electron diffraction (RHEED), transmission electron microscopy (TEM) and X-ray diffraction. We discuss our findings in terms of the surface diffusion length of Ga adatoms.

* Corresponding author. Tel.: +49-30-20377327; fax: +49-30-20377201; e-mail: yang@pdi.wias-berlin.de.

2. Experimental

Our GaN samples are grown in a plasma-assisted molecular beam epitaxy (MBE) system on GaAs(001) substrates. A N_2 plasma is generated by a dc glow-discharge at a power of 30 W and a pressure of 5×10^{-4} Torr in the growth chamber. The effective Ga flux used in this study ranges from 2.0×10^{13} to 1.2×10^{14} atom/cm² s, corresponding to nominal growth rates of 0.02–0.12 ML/s. Prior to GaN growth, a GaAs buffer layer is deposited under growth conditions optimized such that to obtain an as clean and ordered surface as possible. Substrate temperature was set to 580°C at the beginning of GaN growth and increased after deposition of a few monolayers to 650°C.

The initial nucleation and subsequent growth of GaN are monitored by RHEED operating at an electron beam energy of 15 keV and incidence angles of 1°–4°. RHEED images are recorded by a CCD camera and analyzed by an image processing system. TEM images are taken on a JEOL 4000FX operating at 400 kV. Cross-sections of the samples are prepared by conventional ion milling to a thickness of about 15–20 nm. X-ray diffraction profiles are measured on a double-crystal diffractometer using Cu $K\alpha_1$ emission and a Ge (004) monochromator. The X-ray rocking curves (XRC) are measured with wide open detector while a 50 μ m detector slit is used for the θ –2 θ scans.

3. Results

Fig. 1 shows TEM micrographs of two samples nucleated under (a) high and (b) low V/III ratios, respectively, together with the corresponding RHEED patterns. The growth of the two samples was continued after the deposition of the first 5 ML under otherwise identical conditions. The comparison of the two low resolution images evidences drastic differences between the samples' structural quality in terms of grain orientation, as well as interface and surface roughness. The high-resolution micrographs reveal the structural details. For sample A (Fig. 1a), the grains clearly have an epitaxial relationship to the substrate in spite of the large amount of stacking faults, misfit dislocations and grain boundaries. On

the other hand, sample B (Fig. 1b) consists of grains with widely differing crystal orientations both with respect to the substrate and with each other. The corresponding RHEED patterns of the two samples taken during the initial stage of the growth are consistent with these observations. The diffuse GaN transmission reflections observed in the case of sample A demonstrate the formation of comparatively small, well-oriented epitaxial nuclei. In this case, GaN starts to grow on GaAs(001) in the Volmer–Weber mode [8], i.e., by the immediate nucleation of 3-dimensional islands¹. For sample B, in contrast, sharp and intense GaN transmission reflections are observed from the very beginning of the growth along the [110] azimuth, while a ring-like pattern evolves along the [110] azimuth (not shown here). These patterns reflect the formation of comparatively large, textured grains, meaning that the grains are rotated with respect to the same axis. We find that the orientation distributions of the grains does not improve as growth proceeds regardless of the final thickness of the film.

Fig. 2 shows a sequence of RHEED patterns recorded during the growth of a GaN film nucleated under a high V/III ratio. The separation of the GaN and GaAs reflections evidences that the GaN lattice establishes its bulk lattice constant already in the nucleation stage. As growth proceeds, the lateral size of the islands increases as shown by the fact that the GaN spots become considerably sharper. After growth of about 120 ML GaN the surface becomes sufficiently flat for a surface reconstruction to take place. For optimum growth conditions [10] this surface reconstruction appears after growth of 10 nm of GaN.

For a quantitative determination of the surface domain size [11] we analyze line scans of the RHEED intensity profiles in both horizontal and vertical directions. Fig. 3 shows such a line scan together with

¹ Prior to the completion of the first GaN monolayer, there is a (3×3) reconstruction appearing which is commensurate to GaAs. This reconstruction also appears upon supply of 0.3 ML of active nitrogen onto the GaAs(001) surface without incident Ga flux. The atomic structure of this reconstruction is still an open question. We think, however, that in view of the huge lattice misfit it is unlikely to originate from the formation of a coherently strained GaN monolayer as proposed recently [9].

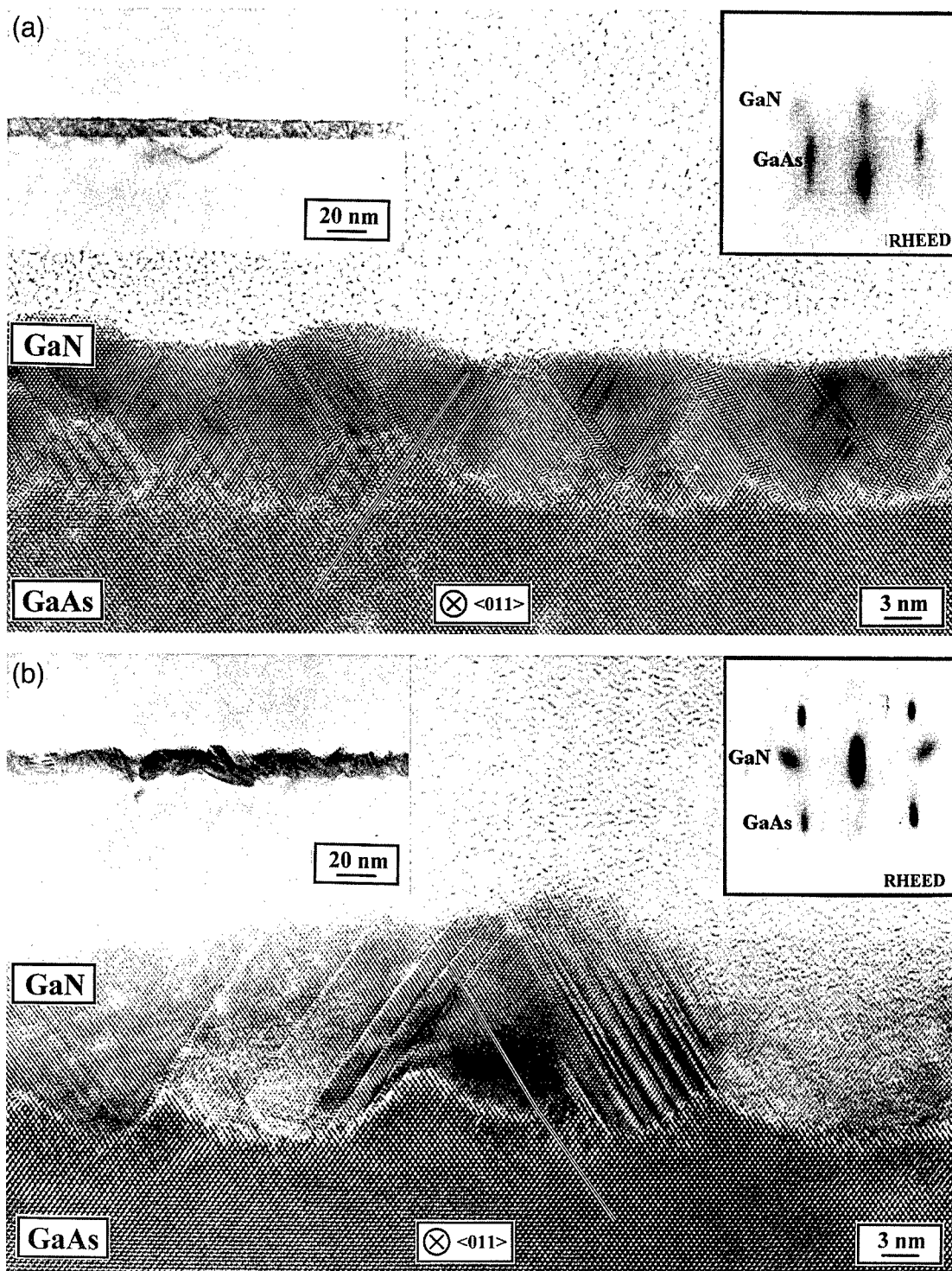


Fig. 1. Cross-section TEM images of samples grown by starting with high V/III ratio (a) and low V/III ratio (b), and the corresponding RHEED patterns (upper-right corners) at the initial stage. Well-oriented grains are visible in (a) in contrast to grains with different orientations in (b).

a Lorentzian fit to the experimental data. The lattice constant of GaN determined in this way is 0.453 nm at temperature of 650°C, which is in good agreement with previous reports [12]. The linewidth determined in the course of the growth is plotted in Fig. 4. The linewidth decreases with increasing film thickness according to a power law. The linewidths of the XRC from samples of different thickness are also shown in Fig. 4. Although the linewidth of RHEED and that of XRC are different in absolute value, it is interesting to see that they follow the same trend with thickness. This identical dependence of the

linewidths of RHEED and XRC profiles on film thickness clearly suggest a relationship between surface island size during growth as measured by RHEED and mosaicity/bulk grain size as measured by XRC. Note that the linewidth of our XRC measurements includes broadening not only from the finite bulk domain size and mosaicity, but also from the lattice constant distribution. In order to separate the latter contribution, some of the samples were also measured in the θ - 2θ mode. Typical linewidths of θ - 2θ scans are in the range of 5–10 arcmin, much smaller than those of XRC, which show that the

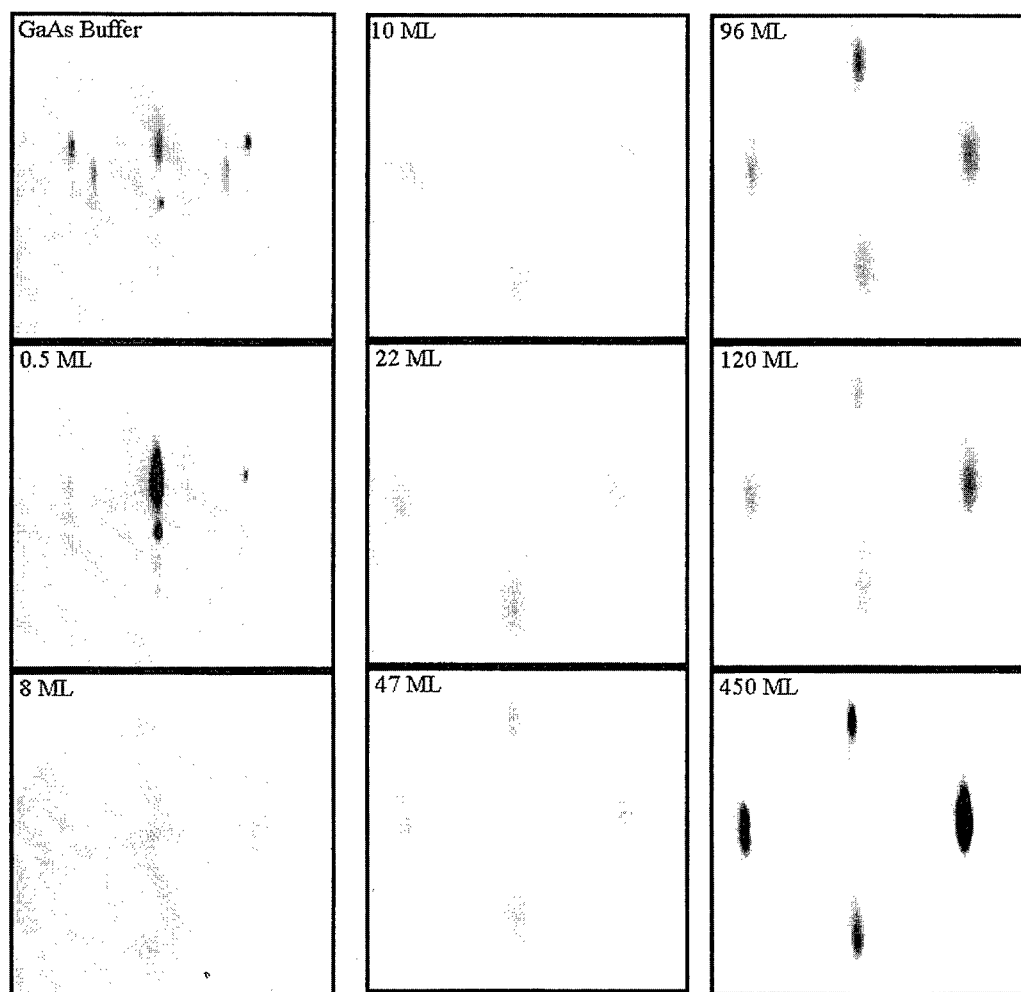


Fig. 2. RHEED images in $[110]$ azimuth recorded at various stages of growth of GaN on GaAs(001). The thickness of the growing GaN film is given in MLs in the upper-left corner of each image. The spotty patterns of GaN in the initial stage reveal nucleation of strain-relieved three-dimensional islands, while the reconstructed patterns at later stages evidence that two-dimensional growth is approached.

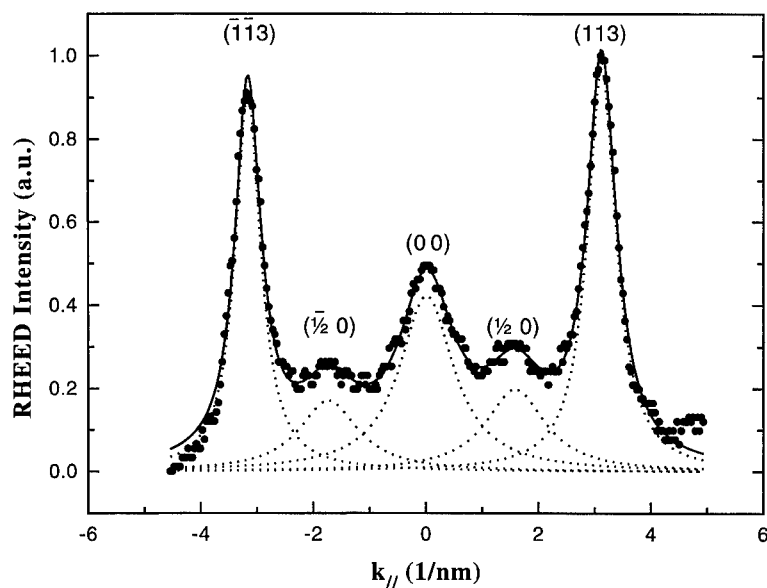


Fig. 3. RHEED intensity profile along a line going through the (113) bulk reflection spot and parallel to the shadow edge. The solid line shows a fit of the data by Lorentzians, whereas the dashed lines depict the individual contributions.

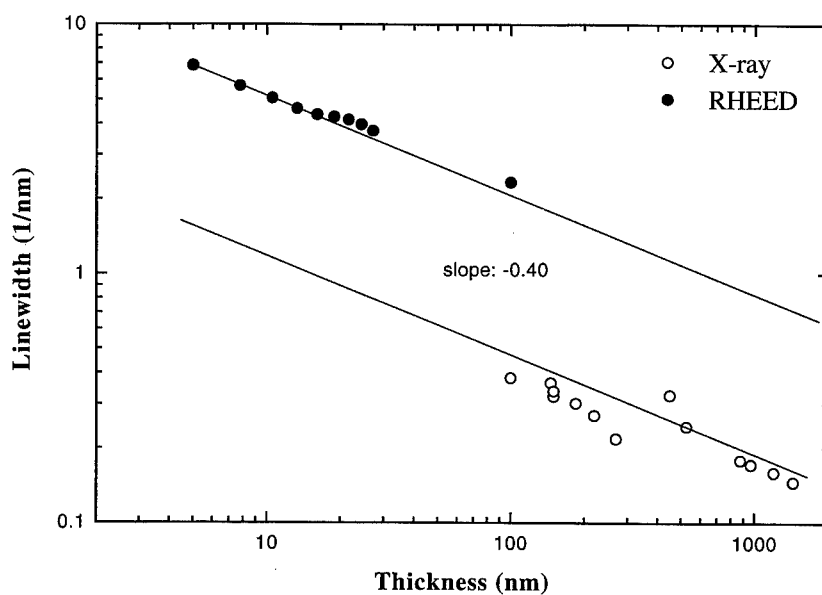


Fig. 4. Linewidth of the (113) and (002) reflections in RHEED and XRC, respectively, as a function of film thickness. The XRC data are taken from samples with different thickness.

XRC linewidth depicted in Fig. 4 is dominated by mosaicity and finite lateral domain sizes.

4. Discussion

The dramatic influence of the nucleation stage can be understood based on the different size of GaN nuclei on GaAs as revealed by RHEED patterns at the initial stage of growth. Since, in both cases, the initial GaN nuclei do exhibit the GaN bulk lattice constant, they relax during nucleation. In this stage, relaxation will proceed by the generation of 90° or 60° dislocations. 60° dislocations will tilt the nuclei with respect to the orientation of the substrate. This tilt depends on the number of dislocations introduced and may be quite large because of the high mismatch. Furthermore, nuclei relaxed by 60° dislocations gliding on opposed $\{111\}$ planes are severely misoriented with respect to each other. However, if the nuclei are sufficiently small, their coalescence will tend to annihilate the tilt either by compensation of the two opposite 60° dislocations or by their reaction resulting in a 90° dislocation [13]. As a result, a well-oriented epitaxial film is established after the deposition of a few monolayers. On the other hand, if a tilted grain grows by the incorporation of new atoms, new misfit dislocations will be formed at the edge of the grain [14]. The preexisting tilt will favor the same dislocation type, and thus a regular array of dislocations having the same type will form resulting in a misoriented grain. Clearly, the larger these grains grow the more difficult it will be for them to rearrange by coalescence. The resulting layer will then consist of grains exhibiting a large orientational spread which upon further growth develops into a textured polycrystalline film.

The importance of a high V/III ratio at the nucleation stage may simply result from the kinetic limitation imposed on the migration length of Ga adatoms by the group V species, thus favoring the formation of a high density of small nuclei. In contrast, a low V/III ratio enhances the migration of Ga adatoms and reduces the density of nuclei, which allows them to grow quickly by incorporation of adatoms. Similarly, it has been reported [15] that a high arsenic pressure during growth helps to obtain purely cubic GaN on GaAs(001) and GaP(001) sub-

strates. We believe this phenomenon to also result from the kinetic limitation imposed onto adatom migration during nucleation.

5. Conclusions

RHEED shows that GaN nucleates on GaAs(001) substrates in the Volmer–Weber mode. Only for GaN nucleated under a high V/III ratio, the following growth approaches the two-dimensional mode. TEM shows that such films of 10 nm thickness to be connected and epitaxial. With increasing thickness, X-ray measurements reveal a steady improvement of the crystal quality in terms of increasing grain sizes and decreasing mosaicity. However, the layer finish is found to be strongly dependent on the conditions chosen for the nucleation of the first monolayers of GaN on GaAs. The initial stage of growth apparently largely determines the destiny of the crystal regardless of its final thickness, from which we conclude that control over nucleation is a necessity for the successful fabrication of GaN-based heterostructures. We explain this finding by considering the nucleation kinetics. Both low temperature and high V/III ratio kinetically hinder Ga adatom migration and thus reduce the size of the individual nuclei. The coalescence of these small nuclei finally rearranges the grains resulting in well-oriented epitaxial films.

Acknowledgements

We would like to thank B. Jenichen for help with the X-ray measurements, and Hans-Peter Schönherr and Peter Schützendübe for their technical assistance with the set-up of our MBE system.

References

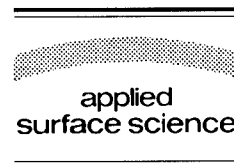
- [1] S. Yoshida, S. Misawa and S. Gonda, *Appl. Phys. Lett.* 42 (1983) 427.
- [2] H. Amano, N. Sawaki, I. Akasaki and Y. Toyoda, *Appl. Phys. Lett.* 48 (1986) 353.
- [3] M.J. Paisley and R.F. Davis, *J. Cryst. Growth* 127 (1993) 136.
- [4] J.N. Kuznia, M. Asif Khan, D.T. Olson, R. Kaplan and J. Freitas, *J. Appl. Phys.* 73 (1993) 4700.

- [5] K. Hiramatsu, S. Itoh, H. Amano, I. Akasaki, N. Kuwano, T. Shiraishi and K. Oki, *J. Cryst. Growth* 115 (1991) 628.
- [6] S.D. Lester, F.A. Ponce, M.G. Craford and D.A. Steigerwald, *Appl. Phys. Lett.* 66 (1995) 1249.
- [7] W. Qian, M. Skowronski, M. De Graef, K. Doverspike, L.B. Rowland and D.K. Gaskill, *Appl. Phys. Lett.* 66 (1995) 1252.
- [8] E. Bauer, *Z. Krist.* 10 (1958) 372.
- [9] R.J. Hauenstein, D.A. Collins, X.P. Cai, M.L. O'Steen and T.C. McGill, *Appl. Phys. Lett.* 66 (1995) 2861.
- [10] H. Yang, O. Brandt and K. Ploog, presented at EMC-37 Conf., June 1995, Charlottesville, USA.
- [11] M.G. Lagally, D.E. Savage and M.C. Tringides, in: *Reflection High-Energy Electron Diffraction and Reflection Electron Imaging of Surfaces*, Eds. P.K. Larson and P.J. Dobson (Plenum, New York, 1989) p. 139.
- [12] S. Strite and H. Morkog, *J. Vac. Sci. Technol. B* 10 (1992) 1237.
- [13] D. Gerthsen, D.K. Biegelsen, F.A. Ponce and J.C. Tramontana, *J. Cryst. Growth* 106 (1990) 157.
- [14] H.L. Tsai and R.J. Matyi, *Appl. Phys. Lett.* 55 (1989) 265.
- [15] T.S. Cheng, L.C. Jenkins, S.E. Hooper, C.T. Foxon, J.W. Orton and D.E. Lacklison, *Appl. Phys. Lett.* 66 (1995) 1509.



ELSEVIER

Applied Surface Science 104/105 (1996) 468–471



Nitridation of GaAs surfaces stimulated by nitrogen glow discharge

Q.J. Xu, X.M. Ding^{*}, X.Y. Hou, Xun Wang

Surface Physics Laboratory and Fudan T.D. Lee Laboratory, Fudan University, Shanghai 200433, China

Received 28 June 1995; accepted 14 December 1995

Abstract

Nitridation of a GaAs surface can be realized simply by exposing the substrate to a windowless-connected nitrogen glow discharge light source. The photoemission data measured in situ show that both GaN and AsN species have been formed during the exposure process. In addition, it is found that nitridation can result in a 0.3 eV reduction of surface band bending.

1. Introduction

Nitridation of GaAs surfaces is of great interest to the device technology of III–V semiconductors. For GaAs-based devices, the existence of a thin nitride layer can effectively reduce the high surface state density and hence improve surface quality and device performance. A thin GaN film may also be used as an in situ mask for selective-area epitaxy of GaAs [1]. Furthermore, III–V nitrides themselves are promising optoelectronic materials and GaAs is one of the substrates often used for their heteroepitaxy [2–4].

Recent studies show that thin nitride layers can be formed on GaAs surfaces by simultaneous exposure of the substrate to ammonia [5] (or hydrazoic acid [6]) and UV photons in an ultrahigh vacuum environment. While photodissociation of the N-containing

species plays a key role in the nitride formation process, to keep the substrate at low temperatures during the exposure seems important to ensure a high coverage of the adsorbate.

In this paper, we report that photodissociation-induced nitridation can also be achieved with the GaAs substrate kept at room temperature. The key feature here is the use of a windowless-connected nitrogen glow discharge light source, acting both as a nitrogen plasma beam directed to the GaAs surface and as a stimulus to the dissociation of pure nitrogen near the surface. Besides its simplicity, the present approach has the potential to be further developed as a technique for the growth of a thick GaN film if a gallium source is attached.

2. Experimental

The experiment was carried out in a home-made sample preparation chamber attached to a VG ADES-400 electron spectrometer, as has been de-

^{*} Corresponding author. Fax: +86-21-65493232; e-mail: xmding@fudan.ihep.ac.cn.

scribed elsewhere [4]. The base pressure of the chamber was 5×10^{-10} Torr. The substrate used was an n-type GaAs(100) single crystal wafer with the carrier concentration of 10^{17} cm^{-3} . After routine chemical treatment, the substrate surface was first bombarded by 1 keV argon ions and then annealed at above 500°C for 30 min. Several cycles of such an ion bombardment and annealing (IBA) process would result in the appearance of a (4×1) low-energy electron diffraction (LEED) pattern, indicating that the surface was an ordered Ga-rich one [7,8].

Nitrogen glow discharge was set in a differentially pumped, standard UV lamp. Under the conditions for maintaining a steady discharge, the nitrogen pressure in the sample preparation chamber was on the order of 10^{-8} Torr. Nitrogen exposure times in the present study were typically a few hours.

Both X-ray and ultraviolet photoelectron spectroscopies (XPS and UPS) were used to examine the variations in composition and electronic state of the GaAs surface upon the nitrogen exposures. An Al X-ray source ($h\nu = 1486.6 \text{ eV}$) was chosen for XPS measurements. The 2p peaks instead of the 3d peaks of Ga and As were measured to raise the relative intensities of the surface components. For UPS, He I ($h\nu = 21.2 \text{ eV}$) was adopted. The photoelectron exit angle is 45° for XPS and 0° for UPS with respect to the surface normal.

3. Results and discussion

During the nitrogen exposure process, the LEED pattern changed gradually from (4×1) to (1×1) , accompanied by a considerable increase in background intensity. This is evidence that nitrogen molecules do dissociate and adsorb on the GaAs surface when the glow discharge light source is on. It is generally accepted that there exist both Ga and As dangling bonds on the GaAs(100) (4×1) surface [7,9]. So a gradual LEED pattern change means that the photodissociated nitrogen atoms may bond randomly to the surface Ga and As atoms. Such an explanation is consistent with the previous results that both surface GaN and AsN species are present after a Ga-rich GaAs(100) surface has been exposed to N-containing species and photons at low temperatures [5,6]. More direct support of the above deduc-

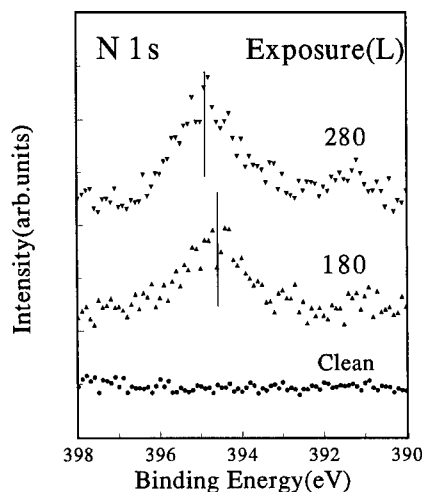


Fig. 1. N 1s XPS spectra taken after the GaAs(100) (4×1) surface was exposed to a windowless-connected nitrogen glow discharge light source. The sample was kept at room temperature during the exposure.

tion is of course from the photoemission measurements.

Fig. 1 shows the N 1s XPS spectra measured following different nitrogen-photon exposures (in units of L, $1 \text{ L} = 10^{-6} \text{ Torr} \cdot \text{s}$). Since the N 1s peak is close to the Ga LMM Auger peaks and hence difficult to distinguish from the latter, the spectra given in the figure are not those originally measured but the difference curves between the N-exposed and clean ones. As is immediately evident, increase in nitrogen exposure results not only in an intensity increase but also in a position shift of the N 1s peak. Meanwhile, the full width at half maximum (FWHM) of the peak remains unchanged. This is a strong hint that the surface Fermi level, E_F , which is always pinned in the band gap for non-cleaved III–V semiconductors, may change its position to some extent during the N-exposure process. If this is the case, the substrate core-level spectra should show the same rigid shift. Shown in Fig. 2 and Fig. 3 are Ga 2p and As 2p spectra, respectively. Now both FWHM and peak position are changed. Each Ga and As peak, which has been broadened upon exposure, can be fitted by two components, as shown in the figures. Obviously, the main component here corresponds to Ga or As in GaAs and the minor one corresponds to surface Ga or As bonded to N. The shift of the main

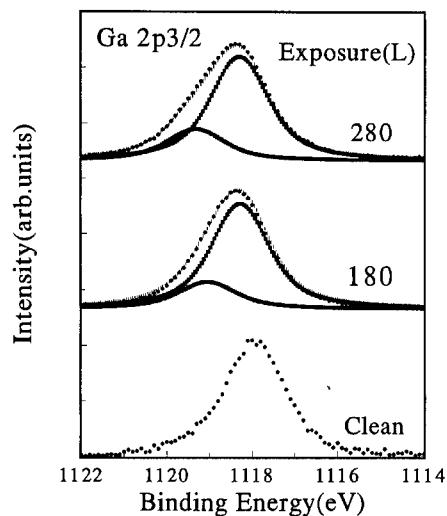


Fig. 2. Ga 2p XPS spectra taken after the same treatments as in Fig. 1.

component following a 280 L exposure is 0.3 eV towards the higher binding energy side, independent of whether it is Ga or As. In other words, the shift is rigid and surface band bending is reduced by 0.3 eV during the process. The maximum shifts of the minor components in the present experiment, which can be read directly from the 280 L spectra, are 0.9 eV for Ga 2p and 1.5 eV for As 2p, consistent with those previously observed [6]. It is thus clear that exposing

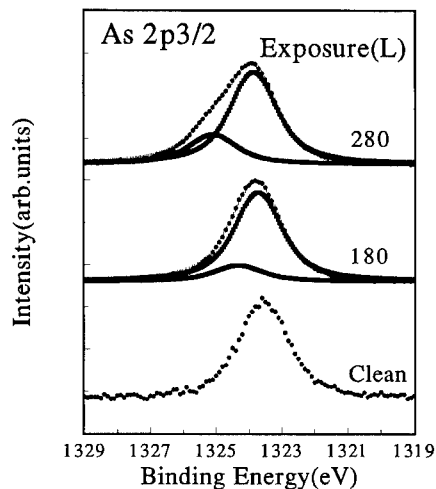


Fig. 3. As 2p XPS spectra taken after the same treatments as in Fig. 1.

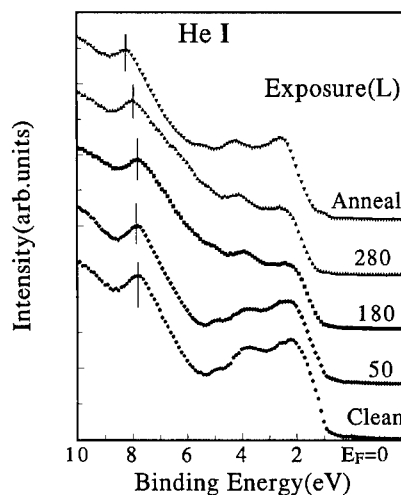


Fig. 4. UPS spectra of clean and N-covered GaAs(100) surfaces.

a GaAs surface to N_2 -photon can result in nitridation of the surface and a shift of E_F .

From the variation of valence band spectra upon N-exposure one can come to the same conclusion. Fig. 4 shows the UPS spectra measured from various N-covered GaAs surfaces as noted. The top spectrum was taken after the 280 L exposed surface had been annealed at 500°C for 10 min. The common energy reference for all the spectra here is E_F ($= 0$ eV), which is 0.8 eV above the valence band maximum (VBM) of the clean surface. The strong peak at 6.9 eV below VBM is a well-known bulk structure, related to the transition from the X_3 critical point [10]. Similar to what observed in XPS, this peak, and the VBM as well, shift to higher binding energies during the N-exposure process. It is thus further confirmed that band bending is reduced in the process of nitridation.

Besides the shift of the bulk-related band structures, uptake of nitrogen on the GaAs surface leads to a quenching of surface peaks, and to the emergence of a broad N-induced peak. To show this effect in a more straight manner, we plot in Fig. 5 the difference spectra between the clean and N-covered surfaces taken by aligning and normalizing their X_3 peaks. It is well established that the peaks in a difference spectrum obtained so can unambiguously be attributed to surface-originating effects. In other words, a positive peak in the spectrum must result from a complete or partial quenching of a

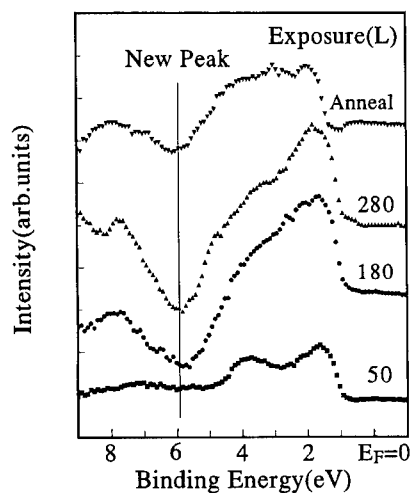


Fig. 5. Difference spectra between clean and N-covered GaAs(100) surfaces taken by aligning and normalizing their X_3 bulk structures.

surface state which existed initially at the clean surface, while a negative peak should be due to the emergence of a new state associated with uptake of foreign atoms or molecules on the surface. Thus, the positive and negative peaks in the present case should originate from the Ga- and/or As-related surface states and the N 2p valence states respectively. One can also see from the figure that although annealing can make the surface recover from nitridation to some extent, a relatively strong N 2p peak remains. This is understandable as the GaN species should still be on the surface after annealing.

Both XPS and UPS spectra also reveal that only limited Ga and As atoms are involved in the nitridation process under the experimental conditions we use. That means what happens on the surface is probably the saturation of the Ga and As dangling bonds by N atoms. It is likely that the process continues if extra Ga and/or As is supplied. We

hope therefore that, with a gallium source attached, the present method can be used for the growth of thick GaN films.

4. Conclusion

A GaAs surface can be nitrided by using a nitrogen glow discharge light source to dissociate nitrogen molecules near the surface. As a result of nitridation, surface band bending can be reduced to some extent.

Acknowledgements

This work was supported by the National Natural Science Foundation of China.

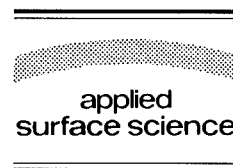
References

- [1] S. Yoshida, M. Sasaki and H. Kawanishi, *J. Cryst. Growth* 136 (1994) 37.
- [2] S. Strite, J. Ruan, Z. Li, A. Salvador, H. Chen, D.J. Smith, W.J. Choyke and H. Morkoc, *J. Vac. Sci. Technol. B* 9 (1991) 1924.
- [3] H. Okumura, S. Misawa and S. Yoshida, *Appl. Phys. Lett.* 59 (1991) 1058.
- [4] Z.Q. He, X.M. Ding, X.Y. Hou and X. Wang, *Appl. Phys. Lett.* 64 (1994) 315.
- [5] X.Y. Zhou, M. Wolf and J.M. White, *J. Vac. Sci. Technol. A* 11 (1993) 838.
- [6] Y. Bu and M.C. Lin, *Surf. Sci.* 317 (1994) 152.
- [7] Y.B. Xu, G.S. Dong, X.M. Ding, S. Yang and X. Wang, *Chin. Phys.* 4 (1984) 189.
- [8] N.K. Singh, A.T. Murrell and J.S. Foord, *Surf. Sci.* 274 (1992) 341.
- [9] D.K. Biegelsen, R.D. Bringans, J.E. Northrup and L.E. Swartz, *Phys. Rev. B* 41 (1990) 5701.
- [10] T.C. Chiang, J.A. Knapp, M. Aono and D.E. Eastman, *Phys. Rev. B* 21 (1980) 3513.



ELSEVIER

Applied Surface Science 104/105 (1996) 472–478



Growth and characterization of ZnSe/GaAs single quantum well structures

J.L. House ^a, D.J. Dougherty ^a, G.S. Petrich ^a, L.A. Kolodziejski ^{a,*}, E.P. Ippen ^a,
G.-C. Hua ^b

^a Department of Electrical Engineering and Computer Science, Research Laboratory of Electronics, Massachusetts Institute of Technology, Cambridge, MA 02139, USA

^b School of Electrical Engineering, Purdue University, West Lafayette, IN 47907, USA

Received 28 June 1995; accepted 8 December 1995

Abstract

The integration of II–VI and III–V semiconductors into a single II–VI/III–V heterojunction device enables the exploitation of the many similarities, as well as the many differences, in material properties (energy bandgap, lattice constant, dielectric constant, etc.) to create new devices exhibiting unique optical and electronic properties. The epitaxial growth of dielectric quantum wells (QWs) composed of ZnSe and GaAs is under investigation. One of the critical factors affecting the properties of the ZnSe/GaAs QW structure is the formation of the heterovalent interfaces, particularly the formation of the inverted interface formed by GaAs nucleated onto a ZnSe epitaxial surface. The stoichiometry of each interface is engineered by using various growth techniques. Due to the severe mismatch in optimal growth temperatures for the two material systems (600°C for GaAs and 300°C for ZnSe), additional emphasis has been placed on the reduced temperature growth of GaAs on ZnSe. The effects of the growth parameters and nucleation methodology are examined by in situ surface reconstruction analysis using reflection high energy electron diffraction and ex situ using transmission electron microscopy. The optical properties of the reduced temperature GaAs and ZnSe/GaAs QWs are further investigated with photoluminescence.

1. Introduction

A comparison of the different types of technologically important compound semiconductors highlights the many similarities and the many differences between the II–VIs and the III–Vs. In a variety of examples the lattice constants are very closely matched, such as for CdTe and InSb, although the

energy bandgaps can be significantly different. Similar contrasts exist regarding optical constants, such as the dielectric constant and thus refractive index, and therefore offers the opportunity to exploit II–VI/III–V combinations for photonic devices, including waveguides, cladding layers, and unique dielectric quantum wells [1]. Additional degrees of freedom in device design are offered by the integration of the II–VI and III–V compound semiconductor families. As one example, GaAs clad by wide bandgap barrier layers of ZnSe possesses a large

* Corresponding author. Tel.: +1-617-2536868; fax: +1-617-2586640; e-mail: lak@mtl.mit.edu.

valence-band offset (~ 1 eV) with a substantial dielectric constant discontinuity, suggesting the possibility of enhanced excitonic nonlinearities in the optical properties of ZnSe/GaAs quantum well (QW) structures [1]. The presence of a deep potential well for holes also provides an opportunity to explore intersubband transitions at long wavelengths near $1.55 \mu\text{m}$ for use in photonic switching devices for fiber optic applications. However, to demonstrate the existence of a II–VI/III–V quantum well structure is a significant challenge since each separate interface is unique in its formation. For example, the II–VI community is currently exploring various techniques aimed at optimizing the growth of ZnSe on GaAs to achieve layer-by-layer nucleation, thus minimizing defect formation in ZnSe. On the other hand, the nucleation of GaAs on a ZnSe surface represents a new environment for Ga and As species, completely distinct from the formation of a GaAs layer on a III–V surface, i.e. the formation of a homovalent interface.

The growth and characterization of ZnSe/GaAs quantum wells have been previously reported using migration-enhanced epitaxy [2] in a single molecular beam epitaxy (MBE) growth reactor, and by Funata et al. [3,4] grown by metalorganic chemical vapor deposition, also in a single reactor. The growth is complicated by several factors including widely varying optimal growth temperatures for each layer (300°C for ZnSe and 600°C for GaAs), the necessity to stoichiometrically control the formation of the II–VI/III–V heterovalent interface to minimize interface state density [5,6] and to correctly produce the desired valence band offset [7–10]. In addition, for the growth of GaAs occurring at a growth temperature [11,12] limited by the ZnSe surface decomposition (~ 300 – 350°C), the As-to-Ga flux ratio must be carefully controlled to enable the growth of high optical quality GaAs quantum wells. The nucleation conditions for forming the inverted GaAs on ZnSe interface must be established.

In this paper, the fabrication of ZnSe/GaAs quantum wells has been divided into two areas of emphasis as schematically illustrated in Fig. 1. The quantum well is clad by the wide bandgap barrier layers of ZnSe, typically maintained at a thickness of 500 \AA . An investigation into the formation of the inverted interface of GaAs on a ZnSe epitaxial surface

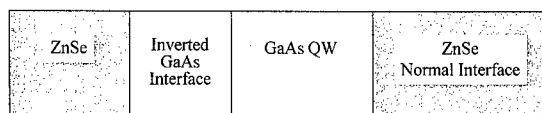


Fig. 1. Schematic illustration of a ZnSe/GaAs quantum well containing the nucleating layer for formation of the inverted GaAs on ZnSe interface, the reduced temperature GaAs quantum well, and the wide bandgap barrier layers of ZnSe.

employed in situ analysis of reflection high energy electron diffraction (RHEED) patterns and cross-sectional transmission electron microscopy (TEM). Following the formation of the inverted interface, the remainder of the GaAs quantum well was grown at reduced temperatures ($\sim 350^\circ\text{C}$). To understand the optical properties of the reduced temperature GaAs material, and to remove the affects of the presence of the II–VI/III–V heterointerface, a III–V barrier layer of (In, Ga)P was employed in a multiple quantum well structure specifically designed to optically probe the reduced temperature GaAs growth approach. Finally, a series of ZnSe/GaAs quantum wells and double heterostructures have been fabricated on both ZnSe and GaAs bulk substrates, and have been characterized by cross-sectional TEM, photoluminescence, and photoreflectance.

2. Experimental approach

The epitaxial growth of the various layers was achieved using molecular beam epitaxy for ZnSe layers and gas source molecular beam epitaxy (GSMBE) for the III–V-based compounds. The separate growth of the II–VI and III–V layers was carried out in dedicated ultrahigh vacuum reactors that are connected to one another via an ultrahigh vacuum transfer chamber having a typical background pressure of 1×10^{-9} Torr. Two types of (100)-oriented bulk substrates, GaAs and ZnSe, have been employed for the growth of the ZnSe/GaAs quantum well structures to clearly distinguish optical features originating from the GaAs well versus the substrate. Our initial studies show comparable results for GaAs/ZnSe double heterostructures grown on either substrate material. For the growth of GaAs QWs on ZnSe bulk substrates, the substrates were degassed prior to insertion into the ultrahigh vac-

uum chamber, and then cleaned in situ by the use of a radio frequency-generated hydrogen/argon (10% Ar) plasma inside the II–VI reactor. The cleaning conditions that were utilized included a ramp from 150–300°C in substrate temperature, a plasma power of 350 W, and a period of 30 min. This procedure was employed to remove contaminants such as carbon and oxygen from the surface without the need to resort to high temperature thermal cleaning techniques. An epitaxial ZnSe buffer layer (1–1.5 μm in thickness) was then grown on the bulk ZnSe substrates. The GaAs bulk substrates were epi-ready wafers that were immediately loaded into the reactor for growth of an epitaxial GaAs buffer layer; the GaAs is grown at the standard substrate temperature of 580°C, an arsenic-to-gallium flux ratio of 1.3, and a growth rate of 1 $\mu\text{m}/\text{h}$. Group III-limited and group V-limited RHEED intensity oscillations were used to establish incorporation rates for the individual species, and thus to determine exact group V-to-

III flux ratios. When an (In, Ga)P buffer layer was employed, the growth was carried out on the GaAs buffer layer grown on the epi-ready bulk substrate. Using GSMBE, elemental In and Ga, and thermally decomposed phosphine (at 900°C) were used. The approximate composition was 50% In to provide lattice-matched growth to the GaAs buffer layer, and the growth temperature was maintained at 470°C.

The growth of all of the ZnSe layers was carried out at temperatures near 300°C, with elemental fluxes of Zn and Se. The flux ratio of the group VI to group II species was maintained at 1.3–1.5 and measured by a quartz crystal oscillator placed at the location of the substrate. Additional confirmation of the surface stoichiometry was provided by in situ observations of RHEED patterns, which indicated a (2×1) Se-stabilized reconstructed surface during growth.

The growth of the GaAs quantum wells was carried out using elemental Ga and thermally decomposed arsine (at 900°C). As mentioned previously

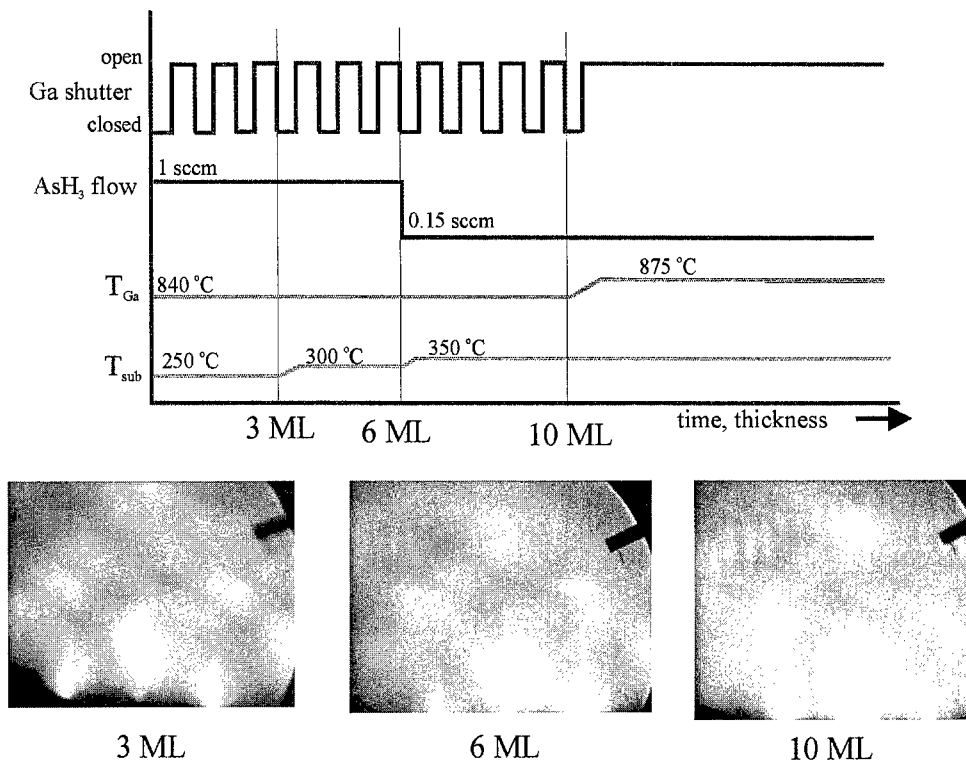


Fig. 2. Sequence of growth parameters employed to form the inverted GaAs interface and the quantum wells. Also shown are the (001) RHEED diffraction patterns observed at 3 monolayers (ML), 6 ML, and 10 ML of GaAs growth.

(and schematically illustrated in Fig. 1), the GaAs quantum well can be considered as two separate types of material due to the fabrication conditions that we explored. A variety of nucleating conditions were investigated for the formation of the inverted GaAs on ZnSe interface. The typical approach to forming an interface involves MBE-like nucleating conditions [13], where the ZnSe surface is first exposed to an arsenic species, in this case As_2 , followed by impingement of a Ga flux (V-to-III ratio of 5 and a growth rate of $0.2 \mu\text{m/h}$) at a 370°C reduced growth temperature. With a Zn-stabilized $c(2 \times 2)$ surface, the RHEED pattern was seen to immediately become spotty and bulk-like indicating very poor nucleation and a rough GaAs surface morphology (also confirmed by Nomarski microscopy). The growth temperature was then increased to 470°C in an attempt to reduce the surface roughness, but the bulk RHEED diffraction pattern persisted for the remainder of the $0.25 \mu\text{m}$ GaAs growth. The use of migration-enhanced epitaxy, which is the alternate exposure of the Se-stabilized (2×1) ZnSe surface to Ga and As_2 species (parameters consistent with the MBE-like nucleating conditions), again at the starting growth temperature of 370°C , was also found to result in the same bulk and fishnet-like RHEED pattern; Nomarski microscopy indicated a poor surface morphology. Similar to the growth using MBE-like nucleating conditions, after 10 monolayers the growth temperature was raised to 470°C for the remainder of the growth, but the RHEED pattern did not show any improvement. The

most successful technique found to form the inverted interface nucleated individual layers of GaAs, while simultaneously varying the V-to-III ratio and the substrate temperature. Fig. 2 shows a flow chart of the growth parameters used for the formation of a high quality nucleating layer that forms the inverted GaAs on ZnSe interface, and corresponding RHEED diffraction patterns. For the first three monolayers (ML), the Ga shutter is sequenced with a constant flux of As_2 at a high arsine flow rate (V-to-III ratio of 12) and a substrate temperature of 250°C . The streaky $c(2 \times 2)$ RHEED pattern of the Zn-stabilized ZnSe surface is replaced by a bulk-like unreconstructed diffraction pattern from the GaAs layer. After 3 MLs, the substrate temperature is raised to 300°C for an additional 3 MLs of growth, and the RHEED patterns begin to show sharp streaks and the expected $c(4 \times 4)$ reconstructed GaAs surface. The next four MLs are grown at 350°C at a reduced arsine flow to provide a V-to-III ratio of 3. After 10 MLs, the Ga oven temperature is raised to increase the growth rate and to provide a V-to-III ratio of approximately one-to-one at a substrate temperature of 350°C . The RHEED patterns continue to remain bulk-like and elongated, exhibiting the $c(4 \times 4)$ reconstructed GaAs surface that was initially observed at 6 MLs. The $c(4 \times 4)$ reconstructed surface persists until the end of the GaAs growth (see Fig. 2). Subsequent Nomarski microscopy indicates a very smooth GaAs surface morphology.

For the growth of the ZnSe/GaAs quantum wells and double heterostructures, the aforementioned nu-

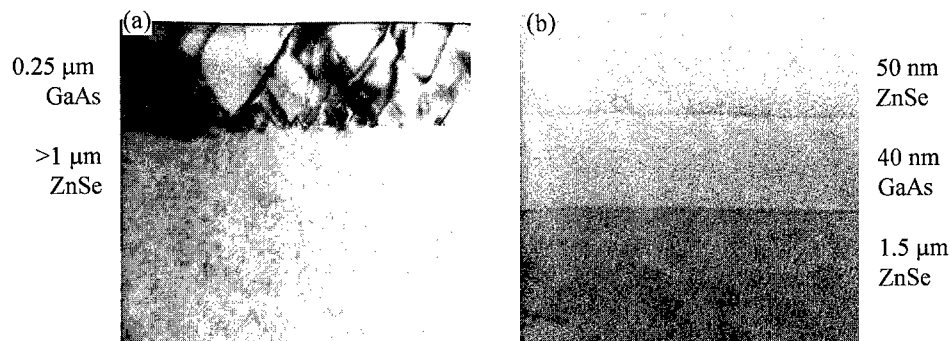


Fig. 3. Cross-sectional transmission electron micrographs of GaAs nucleated on an epitaxial ZnSe surface. In (a) the GaAs layer was nucleated using typical MBE growth techniques. In (b) the GaAs inverted interface was formed using the growth parameter sequence described in Fig. 2. A ZnSe/GaAs/ZnSe double heterostructure is shown and is grown on a ZnSe bulk substrate.

cleation layer (described in Fig. 2), which forms the inverted GaAs on ZnSe interface, was employed for all cases. The growth procedure was as follows. The desired substrate, either II–VI or III–V bulk, was inserted into the appropriate reactor for the growth of the homoepitaxial buffer layer. A secondary buffer layer of (In, Ga)P was used for some samples as indicated. The sample was transferred in vacuum to the II–VI reactor for the growth of the bottom ZnSe barrier, again transferred into the III–V reactor for the GaAs quantum well growth, and then returned to the II–VI reactor for the final ZnSe barrier layer growth. The nucleating conditions for the normal ZnSe/GaAs interface consisted of starting with an As-rich $c(4 \times 4)$ GaAs surface, a pretreatment of Zn flux, followed by typical MBE growth where the surface is exposed simultaneously to the fluxes of Zn and Se.

Fig. 3 shows the cross-sectional transmission electron micrographs obtained when nucleating GaAs on ZnSe using (a) typical MBE-like conditions and (b) by using the nucleating conditions described in Fig. 2. As can be clearly seen in Fig. 3(a), the MBE growth of $0.25 \mu\text{m}$ GaAs on one μm ZnSe results in a heterostructure containing a high density of stacking faults and dislocations apparently nucleated at the inverted interface and is similar to that reported previously [13]. In contrast, Fig. 3(b) shows that an interface formed by growth under more optimal conditions does not induce the same heavily defective GaAs layer. Additional samples having GaAs layer thicknesses up to 100 nm formed in a similar fashion as for the case of Fig. 3(b) show the same interfacial microstructure.

3. Characterization of ZnSe/GaAs single quantum well structures

An additional emphasis was placed on the quality of the GaAs well material grown at reduced temperatures (see Fig. 1). The optical properties of the reduced temperature GaAs material were investigated using an all III–V heterostructure composed of (In, Ga)P and GaAs. A single multiple quantum well structure containing four GaAs QWs having widths of 9, 6, 3, and 1.5 nm, with 20 nm (In, Ga)P barriers, was grown. For the growth of each subsequent quan-

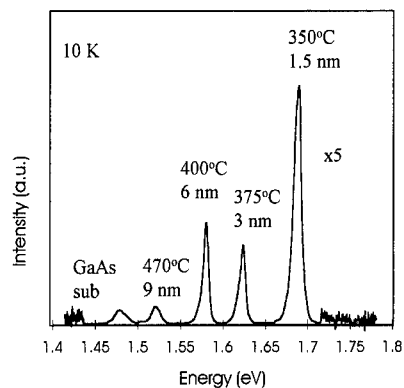


Fig. 4. Low temperature (10 K) photoluminescence spectrum obtained from a multiple quantum well structure composed of GaAs wells embedded within (In, Ga)P barrier layers. As each GaAs quantum well was grown, the growth temperature was gradually reduced. The well dimensions and growth temperatures were 9 nm at 470°C, 6 nm at 400°C, 3 nm at 375°C, and 1.5 nm at 350°C. The 514.5 nm line of an Ar ion laser was used in the PL measurement with a power density of $\sim 1 \text{ W/cm}^2$.

tum well, the substrate temperature was reduced according to the following schedule in steps: 470°C, 400°C, 375°C, and 350°C, respectively. The highest temperature of 470°C for the 9 nm GaAs QW is constrained by the optimum growth temperature of the (In, Ga)P, which we have found in our experiments to be 470°C. In this manner, the optical properties for the various GaAs quantum well materials were examined simultaneously. In all quantum wells that were grown, the As-to-Ga flux ratio was kept at one-to-one. Fig. 4 shows the low temperature (10 K) photoluminescence (PL) collected from the (In, Ga)P/GaAs quantum well structure. Band-edge luminescence from the GaAs substrate can be seen along with emission corresponding to the first confined state of each quantum well [14]. The presence of luminescence from the 1.5 nm quantum well grown at a substrate temperature of 350°C is an example of the optical quality of the reduced temperature GaAs.

Low temperature PL originating from the ZnSe/GaAs double heterostructures has been measured for GaAs layers, having thicknesses ranging from 100 nm to 0.3 nm sandwiched between 50 nm ZnSe barrier layers. In the case of GaAs thicknesses of 100 nm and 40 nm, the ZnSe/GaAs double heterostructure was grown on a $1.5 \mu\text{m}$ thick (In,

Ga)P buffer layer (on a GaAs substrate) to ensure that the PL measurement was probing the GaAs 'well' layer as opposed to the substrate material. The 10 K PL of each double heterostructure shows band-edge luminescence corresponding to the (In, Ga)P barrier layer and to GaAs material. However, further investigation of test structures has shown that luminescence from the (In, Ga)P buffer layer has the capability of exciting the GaAs substrate and causing a detectable level of GaAs bandedge PL. It is difficult to discern the origination of the detected GaAs bandedge PL for these ZnSe/GaAs double heterostructures grown on (In, Ga)P buffer layers. Furthermore, as the GaAs well dimension is further reduced, no blue-shifted low temperature PL is detected from the GaAs well material. We speculate that for an excitonic radius of 16 nm, as the GaAs well dimension is reduced such that the exciton will begin to probe the interfaces, that the nucleating layer may be playing a role in prohibiting the observation of PL for the narrow ZnSe/GaAs quantum wells. The nonstoichiometric conditions used during the formation of the nucleation layer may be a factor in contributing to a reduced GaAs carrier lifetime [11,12,15]. The presence of the mixed II–VI/III–V heterovalent interface, and its effect on the band offsets, interface state density, and interface roughness, potentially causes a local charge imbalance that may also affect the optical properties of thin GaAs QWs. Additional investigations are required to isolate these two effects. Photorefectance (PR) measurements of GaAs quantum wells grown on both GaAs and ZnSe substrates exhibit oscillations corresponding to the GaAs well material for well widths of 40 nm and 20 nm. Similar to the PL measurements, however, no PR features from the narrower GaAs quantum wells were observed.

4. Summary

In summary, the growth and characterization of ZnSe/GaAs single quantum well heterostructures have been investigated. The nucleation of GaAs on ZnSe, forming the inverted heterovalent interface, has been established using single layer MBE at a reduced growth temperature; microstructural analysis shows defect-free material at the heterointerfaces.

Low temperature photoluminescence of the (In, Ga)P/GaAs heterostructure has been observed from the GaAs grown at the reduced temperature of 350°C. However, the ZnSe/GaAs single quantum well structures only exhibit low temperature PL when wide GaAs 'wells' are fabricated. At the present time, we believe that the nucleation layer may contribute to inhibiting the luminescence from narrow ZnSe/GaAs single quantum wells. A more intensive investigation of the ZnSe/GaAs optical properties is underway. In particular, pump–probe measurements to determine the carrier lifetime in various ZnSe/GaAs quantum wells and heterostructures will provide additional insight regarding the optical properties and the roles of the nucleating layer and the heterovalent interfaces.

Acknowledgements

We would like to thank E. Ho and J. Ahadian for their contributions in the growth of the ZnSe and (In, Ga)P, respectively. M. Frongillo of MIT is appreciated for his help in the transmission electron microscopy. The authors would like to acknowledge the support of the Joint Services Electronic Program (JSEP) sponsored by the Army Research Office Grant No. DAAH04-95-1-0038. This work was supported in part by the MRSEC Program of the National Science Foundation under Award Number DMR 92-02957.

References

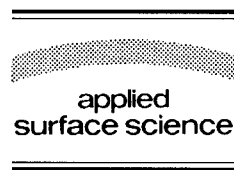
- [1] M. Kumagai and T. Takagahara, *Phys. Rev. B* 40 (1989) 12359.
- [2] S. Zhang and N. Kobayashi, *Appl. Phys. Lett.* 60 (1992) 883; S. Ramesh, N. Kobayashi and Y. Horikoshi, *Appl. Phys. Lett.* 57 (1990) 1102.
- [3] M. Funato, M. Ishii, P.A. Murawala, O. Tsuji, S. Fujita and S. Fujita, *J. Cryst. Growth* 117 (1992) 543.
- [4] M. Funato, S. Fujita and S. Fujita, *Jpn. J. Appl. Phys.* 32 (1993) 3396.
- [5] J. Qui, D.R. Menke, M. Kobayashi, R.L. Gunshor, D. Li, Y. Nakamura and N. Otsuka, *Appl. Phys. Lett.* 58 (1991) 2788.
- [6] W. Chen, A. Kahn, P. Soukiasian, P.S. Mangat, J. Gaines, C. Ponzoni and D. Olego, *Phys. Rev. B* 49 (1994) 10790.
- [7] G. Bratina, L. Vanzetti, R. Nicolini, L. Sorba, X. Yu, A. Franciosi, G. Mula and A. Mura, *Physica B* 185 (1993) 557.

- [8] R. Nicolini et al., *Phys. Rev. Lett.* 72 (1994) 294.
- [9] R. Eppenga, *Phys. Rev. B* 40 (1989) 10402.
- [10] A. Kley and J. Neugebauer, *Phys. Rev. B* 50 (1994) 8616.
- [11] R.P. Mirin, J.P. Ibbetson, U.K. Mishra and A.C. Gossard, *Appl. Phys. Lett.* 65 (1994) 2335.
- [12] M. Missous and S. O'Hagan, *J. Appl. Phys.* 75 (1994) 3396.
- [13] M.C. Tamargo, J.L. de Miguel, F.S. Turco, B.J. Skromme, M.H. Meynadier, R.E. Nahory, D.M. Hwang and H.H. Farrell, *Proc. SPIE*, Vol. 10, Los Angeles, December 1988, p. 1037.
- [14] X. He and M. Razeghi, *Appl. Phys. Lett.* 61 (1992) 1703.
- [15] S. Gupta, M.Y. Frankel, J.A. Valdmanis, J.F. Whitaker, G.A. Mourou, F.W. Smith and A.R. Calawa, *Appl. Phys. Lett.* 59 (1991) 3276.



ELSEVIER

Applied Surface Science 104/105 (1996) 479–484



Photomodulation Raman scattering spectroscopy of ZnSe/GaAs heterostructure interface

H. Talaat^{a,*}, L. Elissa^a, S. Negm^a, E. Burstein^b

^a Department of Physics, Faculty of Science, Ain Shams University, Cairo, Egypt

^b Department of Physics, University of Pennsylvania, Philadelphia, PA 1910, USA

Received 28 June 1995; accepted 22 December 1995

Abstract

Photomodulation Raman spectroscopy is employed to affect and to measure the band bending at the interface of the heterostructure system ZnSe/GaAs. Our samples are pseudomorphic layers of undoped ZnSe (001) grown by molecular beam epitaxy (MBE) on undoped GaAs (001) films terminated with a 2×4 surface reconstruction. The interdiffusion of Zn (Ga) into GaAs (ZnSe) during growth produces an intrinsic band bending at the interface. The ZnSe overlayer with energy band gap $E_{\text{Zn-Se}} = 2.67$ eV offers a transparent window for the photomodulating pumping beam of photon energy E_{PM} to reach the heterojunction while the Raman measurements are in progress. We observed a decrease in the Raman scattering intensity of $\text{LO}_{\text{Zn-Se}}$ and an increase in the scattering intensity of $\text{LO}_{\text{Ga-As}}$ for $E_{\text{PM}} > E_{\text{Zn-Se}}$ while almost the reverse behaviour occurred for $E_{\text{PM}} < E_{\text{Zn-Se}}$. These observations are explained in terms of the presence of hole traps at this 2×4 reconstructed interface.

1. Introduction

Conventional Raman scattering (RS) has been used extensively to study heterostructure interfaces of II–VI/III–V compound semiconductor systems [1–9]. In particular, the system ZnSe/GaAs has recently attracted considerable attention due to its exciting optoelectronic properties, most important among these is the blue laser action achieved in ZnSe [10]. The MBE epitaxial growth of thin layers of ZnSe (energy band gap $E_{\text{Zn-Se}} = 2.67$ eV) on GaAs ($E_{\text{Ga-As}} = 1.40$ eV) results in new charge distribu-

tions at the interface due to interdiffusion during growth and defects at the interface. The interdiffusion results in interfacial band bending both in GaAs and ZnSe [11]. RS is traditionally used to probe the resulting electric fields (E_s) at the interfaces (Franz–Keldysh effect) employing the intensity of the Fröhlich LO-phonon scattering as a measure of such fields [3–6,9]. In these electric fields induced Raman scattering (EIRS), the intensity is proportional to the square of the strength of the interfacial electric field (E_s^2), and is a direct measure of the change in the potential energy or band bending. Olego [6] used this conventional RS to determine the variation of the band bendings at the interface of doped (001) ZnSe/GaAs as a function of the thickness of the ZnSe overlayer. RS studies of the un-

* Corresponding author.

doped heterostructure of (001) ZnSe/GaAs was also carried out by Talaat et al. [9] using the allowed and the forbidden LO Fröhlich interactions for the bulk and the interface investigations respectively.

In this work, a newly developed photomodulation Raman scattering (PRS) is introduced to characterize, and to affect the interfacial field E_s . In this technique, a pump photomodulating beam E_{PM} is incident on the sample while the RS experiment is in progress. The underlying mechanism of the technique can be described as follows. The photogenerating light beam with photon energy E_{PM} greater than the band gap of the material produces electron–hole pairs. Some of these free carriers move towards the junction and are captured by the interfacial trap centres, thereby altering the interface charge density. The new interface charges will modify the band bending. For the heterostructure system of undoped ZnSe/GaAs under study, the interfacial trapped holes decrease the negative charge of the interface and decrease (increase) the band bending on the ZnSe (GaAs) side of the junction. Alternatively, interfacial trapped electrons would decrease the positive charge at the interfaces with a corresponding change in the band bending in each material, the scattering will be changed accordingly. This combined PRS technique is quite attractive since it provides a dynamic non-contact, non-destructive method to vary the interfacial fields. Furthermore, the method has been used in this work to determine the type of interfacial traps as will be discussed later. Experiments that combine photomodulation with second harmonic generation (SHG) were performed by Yeganeh et al. [12]. They employed the cross-over resonance state between the valence band of the ZnSe and the quantum well state in the GaAs as their sensitive probe of the interfacial parameters. The present work employs the EIRS intensity by the forbidden LO-phonon as the sensitive probe for these parameters.

For our particular system of undoped ZnSe and undoped GaAs, it was established that Zn and Ga diffuse across the buried interface during the MBE growth processes [13]. Because Zn is an acceptor in GaAs and Ga is a donor in ZnSe, their diffusion produces an intrinsic band bending at the interface [14]. As a result of this band bending, an interfacial quantum well forms in the GaAs conduction band. In other words, the interdiffusion of Zn in GaAs and Ga

in ZnSe will induce an interfacial electric field which results in allowing Raman scattering by the above mentioned forbidden LO-phonon at the interface. Furthermore, the thin ZnSe overlayer suffers internal strains due to the small lattice mismatch (0.27%) in the (001) ZnSe/GaAs system [15]. Typically the lattice strain relaxes when the overlayer thickness becomes greater than some critical value, $h_c \approx 1500$ Å for our samples [9]. The corresponding deformation potential due to this small lattice mismatch of the heterojunction produces a small field at the interface. Careful computation of the shift in the band energy of ZnSe (due to the tetragonal distortion and the resulting biaxial compressive strain in the layer), gives maximum energy shifts of the order of 13 meV. Hence the interfacial fields due to this lattice mismatch deformation potential were ignored in our work.

In the PRS technique introduced here, the photoexcited electron–hole pairs generated in the depletion layer are separated by the strong interfacial fields. They tend to neutralize the space charge and thus flatten the band bending near the interface. Photons of energy E_{PM} less than the band gap of ZnSe but larger than the band gap of GaAs, will produce electron–hole pairs in GaAs only with the electrons migrating towards the interface. On the other hand, photons with energies close to ZnSe band gap will generate electron–hole pairs in both ZnSe and GaAs with holes (electrons) in ZnSe (GaAs) migrating towards the interface. Some of these carriers will be trapped by charged interfacial defects near the junction and will modify the band bending. Accordingly, the change in the PRS intensity of the LO-Fröhlich interaction may indicate the presence as well as the character of the interfacial charge traps at the interface.

2. Experimental

The samples were grown at Bellcore, New Jersey, USA by molecular beam epitaxy (MBE) in a dual chamber Riber MBE system. Our samples consist of an epitaxial layer of undoped ZnSe (001) grown in a dual chamber MBE system [16] on a $0.5 \mu\text{m}$ undoped GaAs (001) epitaxially film terminated with 2×4 surface reconstructed layer. The thickness of

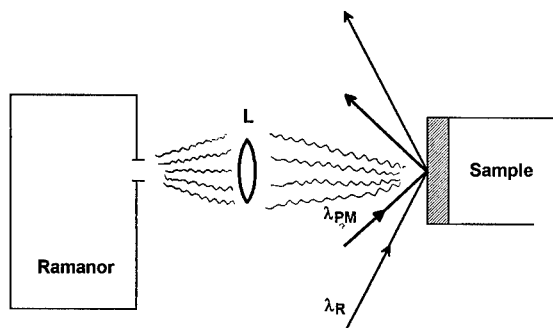


Fig. 1. Schematic of PRS experiment: Sample was illuminated by light (λ_{PM}) from an argon laser while the Raman experiment (λ_R) was in progress.

the ZnSe overlayer was between 215 to 1330 Å. Our photomodulating beam was kept in the lower limits ($\leq 20 \text{ W/cm}^2$) to avoid generating plasmons [17]. This relatively weak PM beam results in generating

electron–hole pairs in the system. In the work reported here, we concerned ourselves with samples in the pseudomorphic region ($d_{\text{Zn-Se}} \leq h_c$) where we were able to measure the effect at such a relatively low photomodulation intensity. The forbidden LO-phonon scattered intensities were measured in the parallel configuration with the polarizations of the incoming and scattered photons along the (010) direction. The schematic of the incident PM and RS beams are shown in Fig. 1. Photoexcited electron–hole pairs were generated in GaAs only when using the PM wavelength $\lambda_{PM} = 5145 \text{ Å}$ (2.41 eV) while photoexcited carriers were generated in ZnSe and GaAs when using the $\lambda_{PM} = 4579 \text{ Å}$ (2.71 eV). The PM beam was incident on the samples at the same time that the Raman measurements with $\lambda_R = 4880 \text{ Å}$ beam (2.54 eV), were in progress. All measurements were taken at room temperature. The intensity of the Raman excitation beam was kept at 20 W/cm^2

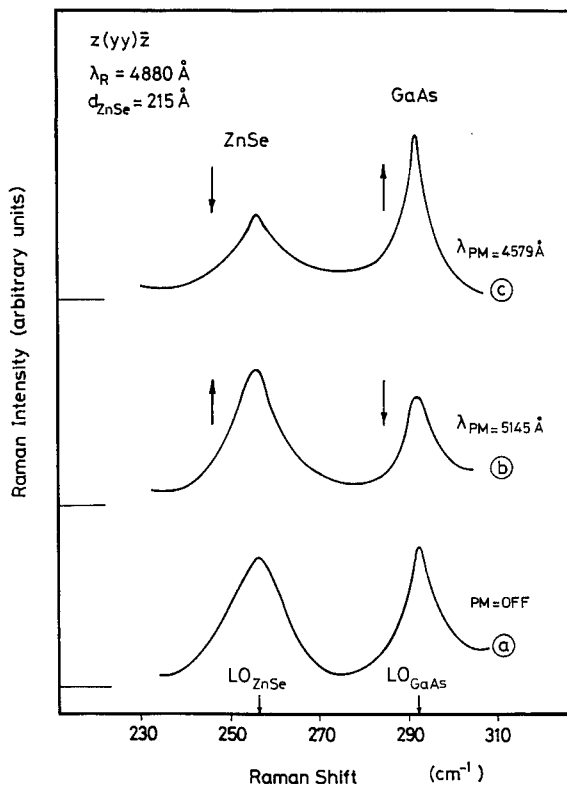


Fig. 2. First order Raman spectra for undoped ZnSe/GaAs (001) heterostructure obtained at $\lambda_R = 4880 \text{ Å}$ for ZnSe layer thickness $d_{\text{Zn-Se}} = 215 \text{ Å}$ in the $z(yy)\bar{z}$ forbidden configuration: (a) PM beam is OFF; (b) PM beam is ON ($\lambda_{PM} = 514 \text{ Å}$); (c) PM beam is ON ($\lambda_{PM} = 4579 \text{ Å}$). The horizontal lines indicate the background levels.

in all the experiments and the photoexciting beam λ_{PM} was carefully aligned on the same scattering spot. This arrangement gave us the best experimental conditions to observe the modulation of the band bending.

3. Results and discussion

Fig. 2a shows the regular Raman spectrum obtained for the overlayer thickness of ZnSe, $d_{\text{Zn-Se}} = 215 \text{ \AA}$ at $\lambda_{\text{R}} = 4880 \text{ \AA}$. In Fig. 2b, the PRS results are shown for the same sample when using the PM beam of $\lambda_{\text{PM}} = 5145 \text{ \AA}$, while the case for PM beam with $\lambda_{\text{PM}} = 4579 \text{ \AA}$ is shown in Fig. 2c. It can be seen from Fig. 2b that in case of $\lambda_{\text{PM}} = 5145 \text{ \AA}$, there is a decrease in the forbidden LO-phonon Raman scattering intensity in GaAs by almost 32% when compared to its intensity in the absence of the PM beam. At the same time, there is an increase in the scattering intensity of ZnSe by an order of 6% compared to its intensity in the absence of the PM beam. Such spectra were only obtained when the intensity of the PM beam was of the same order as the intensity of the incident Raman beam. PRS spectra obtained using the He–Ne laser ($\lambda_{\text{PM}} = 6328 \text{ \AA}$ of 0.5 mW) did not show any measurable change. In these two cases, both the PM beams as well as the Raman beam generate electron–hole pairs only on the GaAs side of the interface since they have an energy larger than the energy gap of GaAs. The generated electrons in GaAs move towards the interface whereas the generated holes move away decreasing the band bending in the GaAs side. Accordingly, the forbidden LO-GaAs scattering intensity also decreases. As observed on the ZnSe side, the same effect results in the increase of the LO-ZnSe scattering intensity. It seems that in the case of the He–Ne measurements the relative increase of the photoexcited electron hole pairs are extremely small to be observed within the accuracy of our measurements.

On the other hand, when using a PM beam with energy larger than the band gap of the ZnSe, $\lambda_{\text{PM}} = 4579 \text{ \AA}$, the obtained spectra shown in Fig. 2c indicates a decrease in the forbidden LO-phonon Raman scattering intensity in ZnSe by 36%, accompanied by an increase in the forbidden LO-phonon

Raman scattering intensity in GaAs by 18% relative to their intensities in the absence of the PM beam. In this case, PM beam is responsible for generation of electron–hole pairs in both ZnSe and GaAs. So, in addition to the electrons moving towards the interface in the GaAs side, the photogenerated holes in ZnSe side move towards the buried interface also. This normally would have resulted in flattening the band bending and a drop in both ZnSe and GaAs signals would have been expected. The observation that there is an increase in LO-GaAs scattering intensity and a decrease in LO-ZnSe, can be explained in terms of the presence of hole traps at the interface. The presence of these traps allows the motion of the holes in the ZnSe side towards the buried interface (resulting in the net decrease in the LO_{Zn-Se}-phonon RS intensity as observed in Fig. 2c), and reduces the

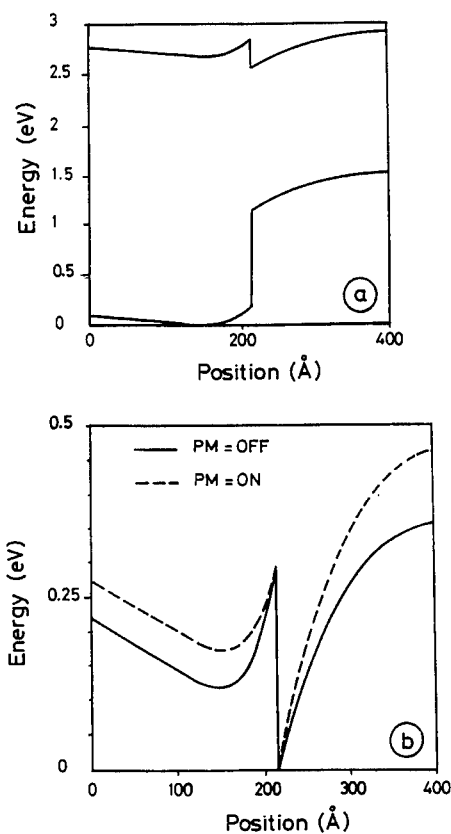


Fig. 3. (a) Energy-band profile as a function of the depth for the ZnSe/GaAs (001) system for $d_{\text{Zn-Se}} = 215 \text{ \AA}$. (b) Variation of the energy-band profile with photomodulation for the same sample $d_{\text{Zn-Se}} = 215 \text{ \AA}$.

flow of electrons towards the buried interface (resulting in a net increase in the $\text{LO}_{\text{Ga-As}}$ -phonon RS intensity).

The band profile of the ZnSe/GaAs was constructed by solving Poisson's equation $-\nabla^2\phi = \rho(z)/\epsilon$, where $\phi = -V(z)/e$ and $\phi(z)$ is a given charge distribution described by a Gaussian function in the z direction perpendicular to the interface. On substituting in this equation the number density of the charge N_{Ga} ($8.5 \times 10^{12} \text{ cm}^{-2}$) and N_{Zn} ($5.1 \times 10^{12} \text{ cm}^{-2}$) and the diffusion lengths λ_{Ga} (40 Å) and λ_{Zn} (100 Å) [11], the potential $V(z)$ for the valence band and the conduction band is shown in Fig. (3a) with $d_{\text{Zn-Se}} = 215 \text{ Å}$. The potential barriers of ZnSe and GaAs at the buried interface of this system are found to be $\phi_{\text{Zn-Se}} = 0.18 \text{ eV}$ and $\phi_{\text{Ga-As}} = 0.365 \text{ eV}$, respectively. Poisson's equation was resolved after adding a positive charge to the interface to simulate the photomodulation effect. The resulting band profile is shown in Fig. 3b. There is a decrease

in the band bending of the ZnSe and an increase in the band bending of the GaAs in agreement with the presence of hole traps at the interface.

The Raman scattering as well as the PM Raman scattering spectra, where $\lambda_{\text{PM}} = 4579 \text{ Å}$, are shown in Fig. 4, for the samples with varying overlayer thicknesses of ZnSe. The spectra follows the same behaviour discussed above. A complete analysis of the dependence of the PRS on the thickness variation is complicated by the oscillatory variation of the LO-phonon intensity resulting from the interference effects in the ZnSe overlayer [9]. Hence a comparison of the ratio of the change in intensity of the $\text{LO}_{\text{Ga-As}}$ and $\text{LO}_{\text{Zn-Se}}$ for the same overlayer thickness were carried out when the PM beam is ON to the ratio when the PM beam is OFF for each thickness. Our results indicate that this ratio varied slightly between $(1.9 \text{ to } 2.3) \pm 0.2$. This relatively constant ratio leads conclusion that the number of holes traps is independent of the thickness of the overlayer. This

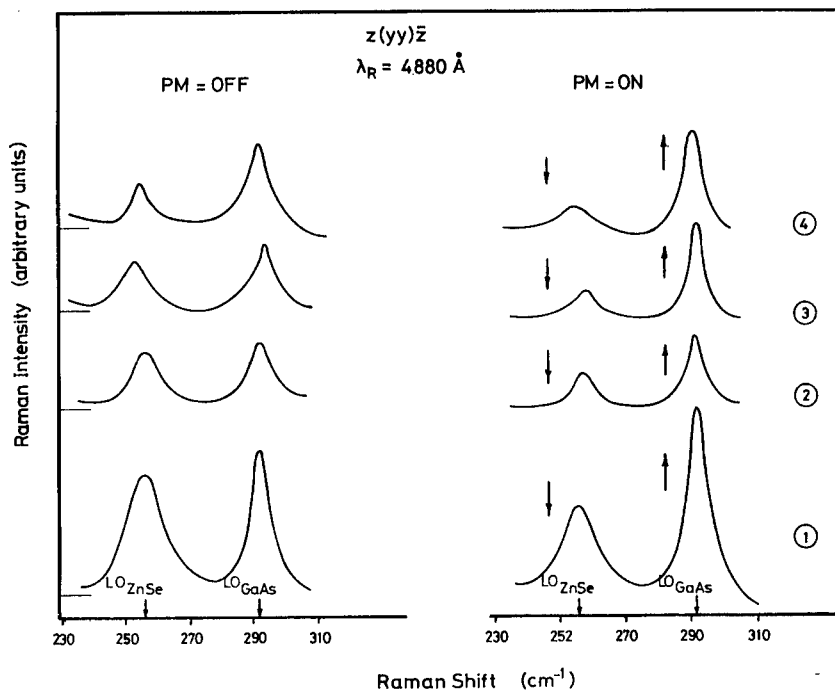


Fig. 4. First order Raman spectra for undoped ZnSe/GaAs(001) heterostructure obtained at $\lambda_{\text{R}} = 4880 \text{ Å}$ for different ZnSe thicknesses (1) $d_{\text{Zn-Se}} = 215 \text{ Å}$, (2) $d_{\text{Zn-Se}} = 650 \text{ Å}$, (3) $d_{\text{Zn-Se}} = 1000 \text{ Å}$ and (4) $d_{\text{Zn-Se}} = 1330 \text{ Å}$. The horizontal lines indicate the background levels. (L.H.S. \Rightarrow PM beam is OFF and R.H.S. \Rightarrow PM beam is ON ($\lambda_{\text{PM}} = 4579 \text{ Å}$)).

conclusion is consistent with the fact that these hole traps are formed in the first few layers of the epitaxial growth of the ZnSe overlayer.

4. Conclusion

Photomodulation Raman scattering spectroscopy is introduced as a new technique to modulate the band bending and to affect the interfacial fields at the heterostructure interfaces. Using this technique, we were able to detect the presence of traps at the interface and to identify them as hole traps. Working with different samples of varying overlayer thicknesses of ZnSe, our results indicate that the hole traps density is independent of the thickness of the ZnSe overlayer since they are mostly formed during the initial growth process of the first few layers.

Acknowledgements

We gratefully acknowledge A.G. Yodh and M.S. Yeganeh for providing the samples for this study.

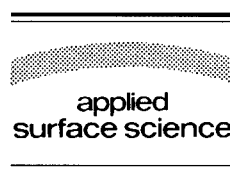
References

- [1] E. Burstein and A. Pinczuk, in: *The Physics of Opto-Electronic Materials*, Ed. W.A. Albers, Jr. (Plenum, New York) p. 33.
- [2] J.G. Gay, J.D. Dow, E. Burstein and A. Pinczuk, in: *Proc. 2nd Int. Conf. on Light Scattering in Solids*, Ed. M. Balkanski (Flammarion, Paris, 1971) p. 33.
- [3] G. Abstreiter, E. Bauser, A. Fisher and K. Ploog, *Appl. Phys.* 16 (1978) 345.
- [4] D.J. Olego, *Appl. Phys. Lett.* 51 (1987) 18.
- [5] D.J. Olego, *J. Vac. Sci. Technol. B* 6 (1988) 4.
- [6] D.J. Olego, *Phys. Rev. B* 39 (1989) N17.
- [7] O. Brafman, *J. Vac. Sci. Technol. B* 10 (1992) 4.
- [8] A. Krost, W. Richter, D.R.T. Zahn, K. Hingert and H. Sitter, *Appl. Phys. Lett.* 57 (1990) 19.
- [9] H. Talaat, L. Elissa, S. Negm, E. Burstein, M.S. Yeganeh and A.G. Yodh, *J. Vac. Sci. Technol. B* 12 (1994) 2598.
- [10] M.A. Haase, J. Qiu, J.M. Depuydt and H. Chng, *Appl. Phys. Lett.* 59 (1991) 1272.
- [11] L. Kassel, H. Abad, J.W. Garland, P.M. Raccach, J.E. Potts, M.A. Haase and H. Cheng, *Appl. Phys. Lett.* 56 (1990) 42.
- [12] M.S. Yeganeh, J. Qi, A.G. Yodh and M.C. Tamargo, *Phys. Rev. Lett.* 68 (1992) 3761.
- [13] R.M. Park, H.A. Mar and N.M. Salansky, *J. Vac. Sci. Technol. B* 3 (1985) 676; R.L. Longini, *Solid State Electron.* 5 (1962) 127.
- [14] M. Altarelli, in: *Heterojunctions and Superlattices*, Eds. G. Allan, G. Bastard, N. Boccara, M. Lannoo and M. Voos (Springer, New York, 1986).
- [15] T. Yao, in: *Technology and Physics of Molecular Beam Epitaxy*, Eds. M.G. Dowsett and E.H.C. Parker (Plenum, New York, 1985) p. 313.
- [16] See, for example, M.C. Tamargo, J.L. de Miguel, D.M. Hwang and H.H. Farrell, *J. Vac. Sci. Technol. B* 6 (1988) 784, and references therein.
- [17] A. Krost, W. Richter and D.R.T. Zahn, *Appl. Surf. Sci.* 56 (1992) 691.



ELSEVIER

Applied Surface Science 104/105 (1996) 485–489



Raman monitoring of selenium decapping and subsequent antimony deposition on MBE-grown ZnSe(100)

D. Drews^{a,*}, A. Schneider^a, D.R.T. Zahn^a, D. Wolfframm^b, D.A. Evans^b

^a Professur für Halbleiterphysik der TU-Chemnitz, D-09107 Chemnitz, Germany

^b North East Wales Institute, Connar's Quay, Clwyd CH5 4BR, Wales, UK

Received 28 June 1995; accepted 26 September 1995

Abstract

Epitaxial layers of ZnSe were grown on GaAs(100) substrates using molecular beam epitaxy at a substrate temperature of 300°C. Immediately after growth the samples were capped with thick layers of amorphous Se as a protection against contamination of the ZnSe surface during the exposure to air, e.g. during transport. Such samples were then investigated using Raman monitoring. This new technique is realised by the combination of a specially designed ultrahigh vacuum (UHV) chamber with a triple Raman spectrometer equipped with multichannel detection. As a result, Raman spectra can be taken *on-line* and *in situ* from the sample surface during desorption or deposition processes. While Raman spectra from the capped samples taken at room temperature show only a broad structure centred around 255 cm⁻¹, which is characteristic for amorphous Se, the evolution of Raman spectra during the annealing of the samples indicates the formation of crystalline Se for temperatures above 100°C, as can be judged from the appearance of the well known phonon features of trigonal Se. Further annealing results in the complete desorption of the Se cap. Thereafter Sb was deposited on such clean ZnSe(100) surfaces. The formation of the Sb overlayer was investigated for the first time using Raman monitoring. In this case the *on-line* technique allows the so called explosive phase transition in the overlayer, i.e. from the amorphous to the crystalline state of Sb, to be observed without interrupting the deposition process.

1. Introduction

Raman spectroscopy has been demonstrated to be a powerful tool for the characterisation of semiconductor bulk material as well as thin films and layered structures [1,2]. Raman scattering is also often used to investigate the effect of surface modifications, e.g. deposition or desorption of material. This is usually done by taking Raman spectra from the sample at

various stages of the process, which is normally interrupted for this purpose. Furthermore, such interruptions are very often accompanied by a change of external parameters, e.g. sample temperature. Obviously it is desirable to avoid such interruptions and take spectra *on-line*.

In this paper Raman measurements were carried out *on-line* and *in situ* during the thermal desorption of selenium from ZnSe(100) without any interruption of the annealing process and subsequent antimony deposition. ZnSe is one of the most promising II–VI materials for an application in opto-electronic devices operating in the green–blue part of the visible

* Corresponding author. Tel.: +49-371-5313036; fax: +49-371-5313060; e-mail: drews@physik.tu-chemnitz.de.

spectrum [3,4]. Se had been deposited onto the ZnSe(100) surface immediately after the molecular beam epitaxial (MBE) growth of the ZnSe layer on GaAs(100) as a protective layer against surface contamination during exposure to air. Analogous procedures are carried out e.g. for GaAs MBE grown layers using As capping [6]. This first Raman monitoring study of the Se decapping process reveals the transition of the initially amorphous Se cap to a crystalline state at about 100°C followed by the complete desorption of the cap.

Thereafter the deposition of antimony on such clean ZnSe(100) surfaces was monitored. This study is thus complementing previous investigations of Sb adsorption on clean III–V surfaces [5]. The evolution of Raman spectra indicates, that the Sb layer stays amorphous up to a layer thickness of 13.5 nm but then undergoes an explosive, i.e. abrupt, crystallization process to the trigonal phase.

2. Experimental

ZnSe layers of typical thickness 1 μm were grown at the Physics department of the University of Wales College of Cardiff on GaAs(100) by molecular beam epitaxy (MBE) at a substrate temperature of 300°C using an atomic flux (VI/II)-ratio of 1.25:1. At the end of the ZnSe growth the substrate heater was turned off and both the Zn and the Se sources were closed. After about 10 min the Se source was opened again for the deposition of the Se cap, and the sample was cooled down to room temperature (RT) under the continuous Se flux. As judged from cross-sectional transmission electron microscope images and Dektac measurements a Se capping layer of approximately 0.5 to 1 μm was found to be present on the surface.

After transport to Chemnitz the samples were placed in an UHV chamber. For the desorption of the Se cap the sample holder was heated by a resistive heater assembly, and its temperature was measured by a thermocouple. The true temperature of the sample surface, however, was derived from the shift of the GaAs longitudinal optical (LO) phonon peak position in the Raman spectra. Previous calibration measurements had revealed a constant shift of 1.8 $\text{cm}^{-1}/100^\circ\text{C}$ between RT and 500°C.

Sb was evaporated from a Knudsen cell as oven. The Sb evaporation rate was controlled by means of a quartz crystal microbalance.

The 1.83 eV (676.5 nm) emission line of a Kr^+ ion laser or the 2.41 eV (514.5 nm) emission line of an Ar^+ ion laser was used for excitation, the monochromator slits were set for a resolution of 2.4 cm^{-1} and 4.6 cm^{-1} , respectively. The laser beam ($P < 20 \text{ mW}$) was focused to a spot of about 100 μm in diameter on the sample surface. All Raman spectra were recorded in a backscattering geometry, the polarization of the incident light was always parallel to the [011] direction of the substrate. No analyzer was employed for the scattered light. A triple monochromator Raman system (Dilor XY) equipped with a CCD camera for multichannel detection was used in combination with the specially designed UHV chamber. A detailed description of this set-up is given elsewhere [8].

3. Results and discussion

Fig. 1 shows the evolution of Raman spectra taken from the Se capped sample during the annealing process. In this case the 1.83 eV line was used for excitation in order to take advantage from resonant Raman scattering [7]. The spectrum in front taken at RT displays mainly a broad structure centred around 250 cm^{-1} , which is caused by scattering from amorphous Se and basically representing the phonon density of states [9]. The appearance of the shoulder at the lower energy side of the broad structure indicates that a certain amount of crystalline Se

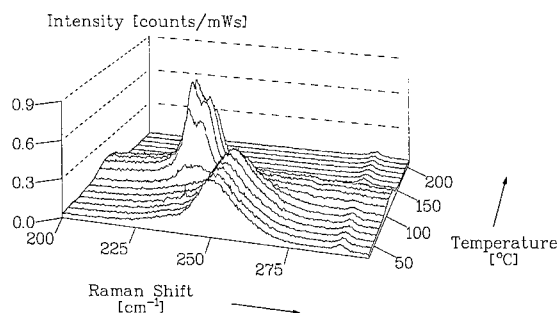


Fig. 1. Series of Raman spectra taken successively during the annealing of Se on ZnSe(100) up to 200°C; incident polarization parallel to [011] direction of the substrate. $E_{\text{ex}} = 1.83 \text{ eV}$.

is likely to be present within the analyzed area of the cap. The small peak at 291 cm^{-1} is assigned to scattering from the longitudinal optical (LO) mode of the GaAs substrate. This structure is observable despite the ZnSe layer, since the excitation energy (1.83 eV) is far below the bandgap of ZnSe (2.7 eV at RT), therefore the ZnSe is completely transparent while GaAs substrate is opaque. Raman scattering of ZnSe is thus extremely out of resonance and no ZnSe LO peak at about 250 cm^{-1} is observable.

While the sample temperature is slowly increased, the Raman spectrum does not change significantly up to about 80°C . Further increase of the temperature changes the spectra drastically as can more clearly be seen from Fig. 2. The broad structure vanishes rapidly and a new feature consisting of two peaks at 233 cm^{-1} and 237 cm^{-1} appears. These peaks can be assigned to scattering from the E and A_1 mode, respectively, of trigonal Se [9]. They are shifted with respect to the broad feature at around 250 cm^{-1} owing to the nature of the phonon dispersion of Se [9]. Thus the Raman spectra reveal the phase transi-

tion of the amorphous Se cap to a crystalline state in the temperature range $80\text{--}100^\circ\text{C}$. Upon further annealing the features of the trigonal Se also decrease in intensity and vanish at a temperature of 150°C indicating the complete desorption of the Se cap. In this region the GaAs LO feature is hardly visible. Due to linear dependence of the thermal frequency shift the sample temperature can still be determined by an extrapolation of lower and higher temperature spectra.

The phase transition of Se is accompanied by an increase of the background in the Raman spectra (see Fig. 1) caused by elastically scattered light from the sample surface. This is interpreted as a surface roughening during the crystallization. After Se desorption, however, the background decreases to a level lower than in the initial spectrum at RT, indicating a very smooth surface.

After the sample had cooled down to room temperature again, Sb was deposited onto the ZnSe surface and now the deposition process was monitored by Raman scattering. In this case the 2.41 eV emission line of an Ar^+ laser was used for excitation, since this energy is close to the electron interband transition of Sb [7], so again signal enhancement due to resonant Raman scattering is anticipated. Fig. 3 shows the evolution of Raman spectra as a function of deposition time. The spectrum in the front corresponds to the clean ZnSe surface and is featureless in the displayed range. However, scattering from the LO modes of ZnSe and GaAs can be observed at 252 cm^{-1} and 291 cm^{-1} , respectively. During the Sb deposition a broad structure centred around 145 cm^{-1} appears in the Raman spectra which is characteristic for amorphous Sb. Simultaneously the intensity of the ZnSe and GaAs peaks decreases due to the absorption of light in the Sb layer. The dependence of the intensities of the GaAs and the ZnSe LO mode on deposition time was fitted to an exponential decay as shown in the insert in Fig. 3. From this decay the deposition rate of the Sb layer was determined to be about 3.0 nm/h using an absorption coefficient of $8.97 \times 10^5\text{ cm}^{-1}$, which was calculated from the optical data given by Aspnes and Studna for polycrystalline Sb [10].

As can be seen from Fig. 3, only amorphous Sb is formed on the ZnSe during the first stage of the deposition process, but at a certain layer thickness

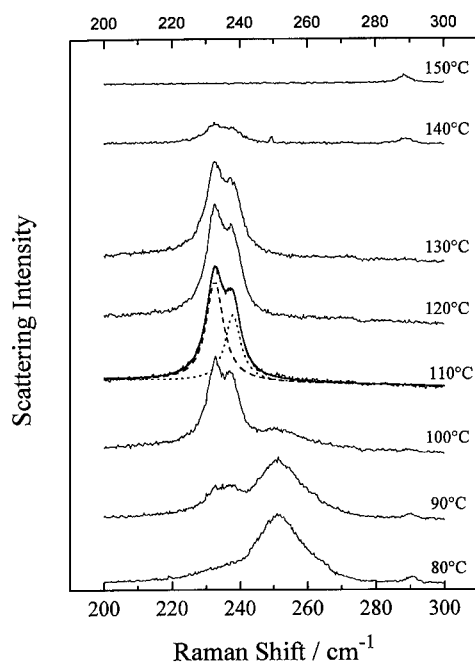


Fig. 2. Individual Raman spectra of Fig. 1 at different temperatures showing the phase transition from the amorphous to the crystalline state and the subsequent desorption. For the spectrum at 110°C the curve fitting of the A_1 , E modes are inserted.

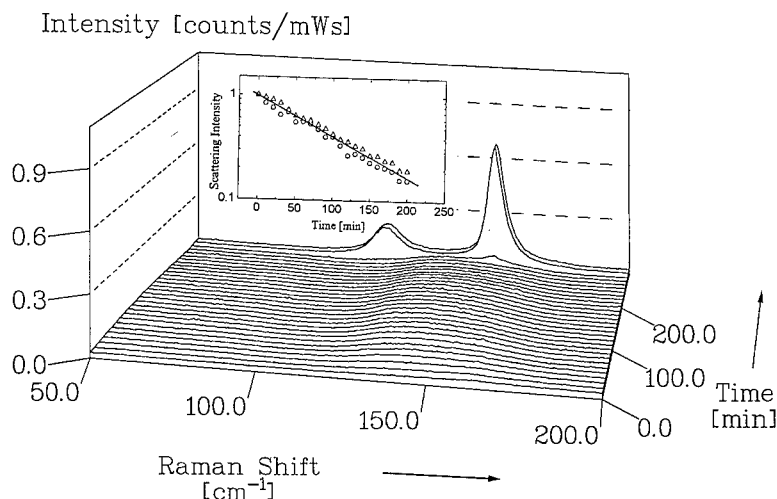


Fig. 3. Series of Raman spectra taken successively during the deposition of Sb on ZnSe(100) at room temperature. The insert shows the exponential decrease of the scattering intensity of the LO modes of the GaAs substrate and the ZnSe layer, from which the Sb growth rate was calculated to be 3.0 nm/h.

the Raman spectra change suddenly. Two new peaks appear at 117 cm^{-1} and 155 cm^{-1} , which are assigned to scattering by the E_g and A_{1g} phonon modes of trigonal Sb [11]. The critical thickness for this crystallization is 13.5 nm as calculated using the growth rate mentioned above. This critical thickness is larger than for Sb on GaAs(110) [12] but it is in a good agreement with the crystallisation of Sb at 15 nm on different other amorphous and crystalline substrates [13,14]. The slight deviation from the

critical thickness mentioned above could be explainable by a minor influence of the laser during Raman monitoring as judged from Raman spectra taken from spots which were not continuously irradiated during deposition. There the crystallisation was found to be delayed. The transition from the amorphous to the trigonal phase happens on a much shorter timescale than the deposition process as can be seen from Fig. 4. Here Raman spectra successively taken during the deposition near the critical thickness are displayed. The integration time for each spectrum is 60 s, so the spectra cover a time interval of three minutes. This corresponds to a change of thickness about 0.15 nm during the crystallization. To our knowledge this is the first time that this explosive phase transition during the deposition of Sb on ZnSe is observed on-line using Raman spectroscopy.

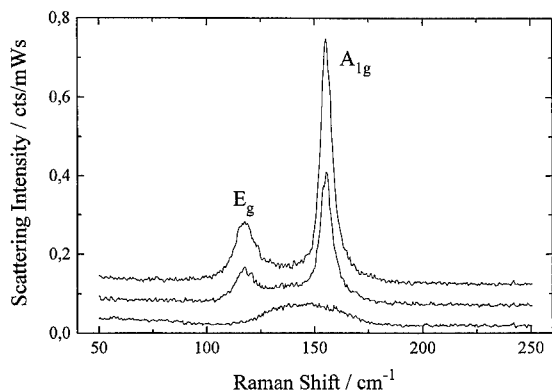


Fig. 4. Individual Raman spectra of Sb on ZnSe(100) at a layer thicknesses near 13.5 nm showing the explosive phase transition from the initially amorphous (lowest curve) to the crystalline state. The three spectra cover a time interval of three minutes and a thickness variation of 0.15 nm.

4. Summary

Raman spectroscopy was used to investigate the thermal desorption of an amorphous Se capping layer on MBE-grown ZnSe/GaAs(100). For this purpose Raman spectra were recorded continuously from the sample surface during the annealing process. The spectra reveal the crystallization of the initially amorphous Se at temperatures above 80°C and the

complete desorption of the cap at 150°C. Sb was deposited onto such a clean ZnSe surface at room temperature. The Sb layer was found to be amorphous up to a layer thickness of 13.5 nm, where the explosive phase transition to the trigonal phase was observed.

Acknowledgements

Financial support by the Deutsche Forschungsgemeinschaft (Za146/2-3) and the DAAD-British Council ARC programme is gratefully acknowledged.

References

- [1] J. Geurts, *Surf. Sci. Rep.* 18 (1–3) (1993).
- [2] D.R.T. Zahn, *Surf. Rev. Lett.* 1 (1994) 421.
- [3] R. Gunshor, A. Nurmikko and M. Kobayashi, *Phys. World* (March 1992) 46.
- [4] M. Heuken, *J. Cryst. Growth* 146 (1995) 570.
- [5] R.H. Williams, D.R.T. Zahn, N. Esser and W. Richter, *J. Vac. Sci. Technol. B* 7 (1989) 997.
- [6] U. Resch, N. Esser, Y.S. Raptis, W. Richter, J. Wasserfall, A. Förster and D.I. Westwood, *Surf. Sci.* 269/270 (1992) 797.
- [7] W. Richter, in: *Resonant Raman Scattering in Semiconductors*, Springer Tracts in Modern Physics, Vol. 78, Ed. G. Höhler (Springer, Berlin, 1976).
- [8] V. Wagner, D. Drews, N. Esser, D.R.T. Zahn, J. Geurts and W. Richter, *J. Appl. Phys.* 75 (1994) 7330.
- [9] A. Mooradian and G.B. Wright, in: *The Physics of Selenium and Tellurium* (Pergamon, Oxford, 1969) p. 269.
- [10] D.E. Aspnes and A.A. Studna, *Appl. Opt.* 14 (1975) 220.
- [11] R.I. Sharp and E. Warming, *J. Phys. F* 1 (1971) 570.
- [12] W. Pletschen, N. Esser, H. Münder, D. Zahn, J. Geurts and W. Richter, *Surf. Sci.* 178 (1986) 140.
- [13] G. Fuchs, P. Melinon, F. Santos Aires, M. Treilleux, B. Cabaud and A. Hoareau, *Phys. Rev. B* 44 (1991) 3926.
- [14] M. Hashimoto, T. Niiziki and K. Kambe, *Jpn. J. Appl. Phys.* 19 (1980) 21.



ELSEVIER

Applied Surface Science 104/105 (1996) 490–494

applied
surface science

Heterocrystalline SiC: *ab initio* calculations for the interface structure of combinations of cubic and hexagonal SiC

P. Käckell^{*}, F. Bechstedt

Institut für Festkörpertheorie, Friedrich-Schiller-Universität, Max-Wien-Platz 1, 07743 Jena, Germany

Received 28 June 1995; accepted 25 October 1995

Abstract

We present the results of *ab initio* DFT-LDA pseudopotential calculations of structural and electronic properties of heterocrystalline combinations of cubic and hexagonal SiC, which are chemically identical but structurally different materials. The structural rearrangement of atoms along the hexagonal axis at the interface is taken into account. The resulting superlattices possess indirect gaps which are smaller than the presently known smallest one of 3C-SiC. The relationship of electron or hole confinement and polytype arrangement is explicitly derived for a zinc-blende/wurtzite combination. The existence of electronic interface states is carefully studied.

1. Introduction

One of the most fascinating properties of the group IV compound silicon carbide (SiC) is its polytypism. Up to now, more than 200 different crystalline modifications are known. The two most extreme polytypes are zinc blende (3C) with pure cubic stacking of the Si–C double layers in [111] direction and wurtzite (2H) with pure hexagonal stacking in [0001] direction. The stacking of bilayers in a unit cell is commonly described by ABC for zinc-blende and AB for wurtzite. The other polytypes represent combinations of these stacking sequences. The pure polytypes lie very close together in energy and possess similar lattice constants. For example, the most

common polytypes 3C, 6H, 4H, and 2H differ only by about 3 mÅ in the lattice constant *a*. On the other hand, the electronic structures of the polytypes are rather different. Zinc-blende 3C-SiC is characterized by the smallest indirect energy gap of 2.390 eV, whereas the hexagonal polytypes exhibit gaps between 3.023 eV (6H) and 3.330 eV (2H) [1].

Meanwhile, it seems to be possible to grow crystalline SiC layers of different polytypes by means of molecular-beam epitaxy (MBE) applying different gas or solid sources [2–4]. As theoretical and experimental studies of semiconductor heterosystems consisting of two chemically inequivalent components have shown, the electronic structure changes drastically in comparison with that of the pure materials. Therefore the question arises, how structural symmetry changes will affect the electronic properties of such heterocrystalline SiC-systems. As a consequence the localization of electrons and holes at the

^{*} Corresponding author. Tel.: +49-3641-635910; fax: +49-3641-635182; e-mail: kaeckell@ifo.physik.unijena.de.

interfaces and in different space regions of the heterocrystalline compound has to be discussed.

2. Computational details

We study heterocrystalline combinations of zinc-blende 3C and hexagonal 2H. The self-consistent calculations are performed using density functional theory (DFT) in the local density approximation (LDA) and norm-conserving *ab initio* pseudopotentials. A more detailed description can be found in Refs. [5,6]. As basis set we use plane waves with a relatively small energy cutoff of 34 Ry. For that purpose we have derived a softened carbon pseudopotential. In a previous paper [7], we have clearly shown that an energy cutoff of 34 Ry is sufficient for the convergence of the physical quantities we are

interested in. The k -integration is replaced by a summation over six Chadi–Cohen special points in the irreducible part of the BZ. The self-consistent numerical calculations are performed by means of the computer code *fh93cp* [8]. Explicitly the superlattices $(3C)_4(2H)_3$ and $(3C)_2(2H)_6$ — each containing 18 bilayers and therefore represented in an 18H supercell — are studied, and additionally a test calculation with a larger $(3C)_6(2H)_6$ structure (in a 30H superlattice) has been performed. The stacking patterns of the smaller structures are represented in Fig. 1.

The calculations for the pure polytypes [6,9] have shown that the different polytypes match rather perfectly in the $[111-0001]$ direction within values smaller than 0.1%. As a first step we therefore replace the hexagonal lattice constants a and c by their weighted average values ($a = 3.033$ Å, $c = 31.553$ Å for $(3C)_4(2H)_3$ and $a = 3.032$ Å, $c = 31.565$ Å for $(3C)_2(2H)_6$). The starting atomic positions are taken from the ideal polytype geometries, and the atomic coordinates are optimized until the Hellmann–Feynman forces resulting in the heterocrystalline interfaces parallel to the c -axis vanish.

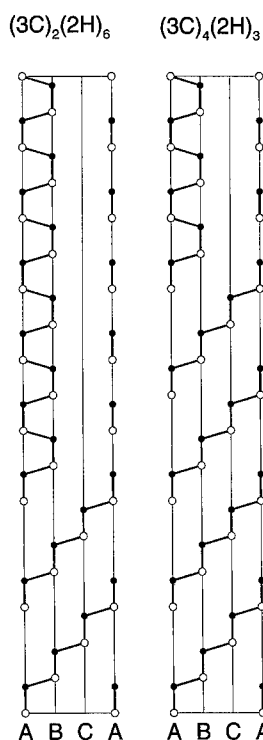


Fig. 1. Schematic representation of the 18H unit cells of the superlattices under consideration. The zig-zag chain structures indicate the positions of Si (open circles) and C (filled circles) atoms. All atoms are located in the (1120) plane. The different (1100) planes within the unit cells are denoted by A, B, and C to make obvious the stacking sequences.

3. Results

The relative energetic stability of the superlattices is derived from their total energies. The energetically more favourable superlattice structure is $(3C)_4(2H)_3$. However, the energy variations are extremely small as known from the natural polytypes [6,9]. Comparing with a zinc-blende structure, for calculating purposes represented also within the 18H unit cell ($a = 3.034$ Å, $c = 31.541$ Å) we find energy differences per Si–C pair of -5.2 meV ($(3C)_2(2H)_6$) and -6.6 meV ($(3C)_4(2H)_3$). Despite the interface relaxation effects the relative distances between the total energy differences follow directly the results for the individual polytypes. The energies of the heterocrystalline structures are somewhat lower than the results expected from those for the polytypes [6]. These findings are not yet understood. Two reasons might be the increased number of atomic degrees of freedom due to the reduced symmetry and interface relaxation effects.

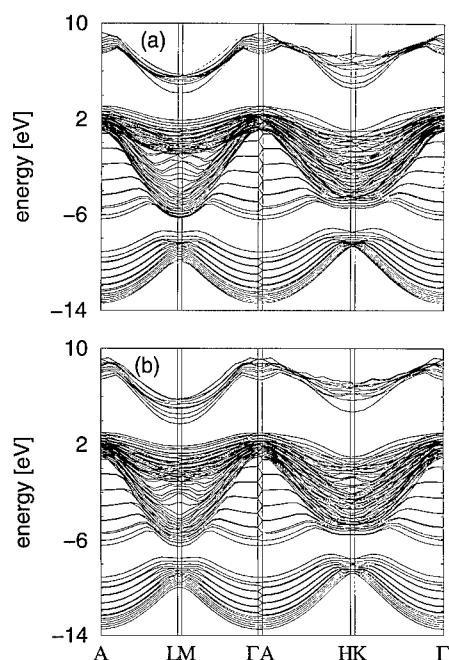


Fig. 2. DFT-LDA band structures of the considered superlattices versus high-symmetry lines in the 18H Brillouin zone (a) $(3C)_2(2H)_6$, and (b) $(3C)_4(2H)_3$.

Instead of the space group C_{6v}^4 ($P6_3mc$) of the hexagonal polytypes only C_{3v}^1 is relevant. The actual atomic displacements depend on the stacking sequence, the interfaces are inequivalent: The two Si–C bonds around the interface $3C \rightarrow 2H$ (cf. upper part of Fig. 1) possess lengths increased by 10 to 20 mÅ. On the other hand, the bonds in the interface $2H \rightarrow 3C$ (cf. lower part of Fig. 1) remain rather unchanged due to the continuation of the Si–C bond chains within the lateral extent of the unit cell. Inside the material layers, the atomic displacements parallel to the c -axis are negligible.

We have also calculated the DFT-LDA bandstructures of the two smaller combinations. They are represented in Fig. 2 versus high-symmetry lines within the hexagonal BZ. The top of the valence band (bottom of the conduction band) is located at the Γ (M) point. The same holds for the $(3C)_6(2H)_6$ combination, not displayed here.

The location of the band extrema may be understood in terms of the underlying bulk band structures. The valence-band maximum in all polytypes is located at the Γ point. The lowest conduction band

minimum occurs in the 3C band structure at the M point when it is represented within the BZ of a 3H structure [5,10]. In the wurtzite 2H case the conduction band minimum appears at K. The lowest conduction band minimum in 2H is by about 1 eV higher in energy than that in 3C [5,10]. Consequently, the M minima of the superlattices should mainly arise from states localized in the cubic polytype.

From our previous work [5] we would expect the combinations to behave as type-II heterostructures, i.e. a reduction of the gap energy compared to the zinc-blende structure, a localization of electrons and holes in different space regions of the structure, and possibly the appearance of interface states. The indirect energy gaps of 1.09 eV ($(3C)_2(2H)_6$), 0.75 eV ($(3C)_4(2H)_3$) and 0.86 eV ($(3C)_6(2H)_6$) are in any case smaller than the smallest energy gap in a naturally occurring polytype, the zinc blende 3C-SiC, where the DFT-LDA value amounts to 1.27 eV. The reduction is much larger than the valence-band offset of 0.13 eV estimated for 3C/2H [5,10] taking into account only the asymptotics of the pseudopotentials. Therefore the valence-band portion of the total-gap discontinuity is larger in real structures. This can be explained in terms of a charge transfer from 3C to 2H at the interfaces during the self-consistency procedure. The resulting interface dipole is accompanied by a step-like potential, which changes the position of the electrostatic potential and therefore the ratio of the conduction-band and valence-band discontinuities. Comparing the average values of these potentials in the corresponding parts of the heterostructure, we find the average value for the 3C-part to be lower by approximately 0.56 eV ($(3C)_4(2H)_3$), 0.25 eV ($(3C)_2(2H)_6$) and 0.03 eV ($(3C)_6(2H)_6$) than the average for the 2H-part. In the first two cases, this matches mainly the diminuation of the band gap, whereas it could not be the explanation for the small gap in the larger structure. In the latter case the averaged electrostatic potential behaves more sawtooth-like and the interface-state character of the band edges increases. Such a behaviour is expected due to the different polarizations of the components (where 3C shows no polarization, by symmetry, and 2H possesses a static dipole moment).

Finally, we study the localization of the Bloch wave functions for the lowest conduction band and

the highest valence band. In Fig. 3 the localization for the lowest conduction band at M as well as the highest valence band at Γ is represented for the two smaller structures along the extent of a unit cell parallel to the c -axis. In Fig. 4 the same is shown for the $(3C)_6(2H)_6$ structure. Fig. 3 clearly confirms the type-II character of the structure resulting for the $(3C)_4(2H)_3$ combination. The lowest conduction-band state at M is actually essentially localized in the 3C material with pure cubic stacking. The electrons are confined to the cubic part of the supercell. On the other hand, the highest valence state at Γ is localized in the hexagonally stacked 2H-like region of the unit cell. Consequently holes should appear in the hexagonal layers. We have to mention that after increase of the hexagonal character of the heterocrystalline structure in the $(3C)_2(2H)_6$, the lowest conduction band state is localized within 2H-like layers as a consequence of the particle-in-the-box effect in the 3C material, which pushes the 3C-like layers towards higher energies. If we enlarge the regions of each

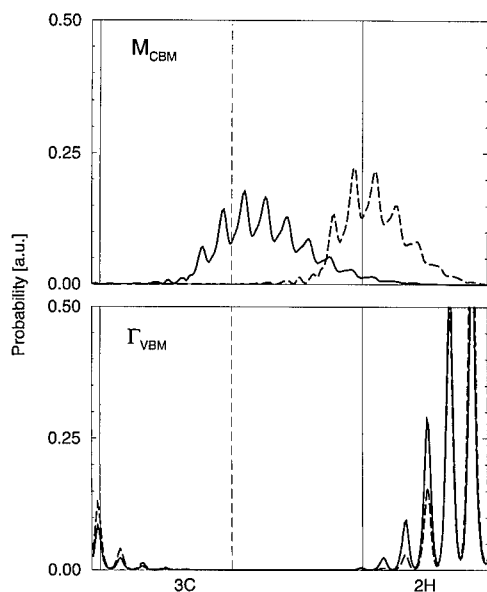


Fig. 3. Squared wave functions of the lowest conduction band state at M as well as of the highest valence band at Γ for $(3C)_4(2H)_3$ (solid line) and $(3C)_2(2H)_6$ (dashed line) superlattices. In order to have an impression of the localization of electrons and holes, the probabilities are integrated over the plane perpendicular to the growth direction. The position of Si and C atoms are indicated by vertical ticks. The vertical lines separate the 3C and 2H regions.

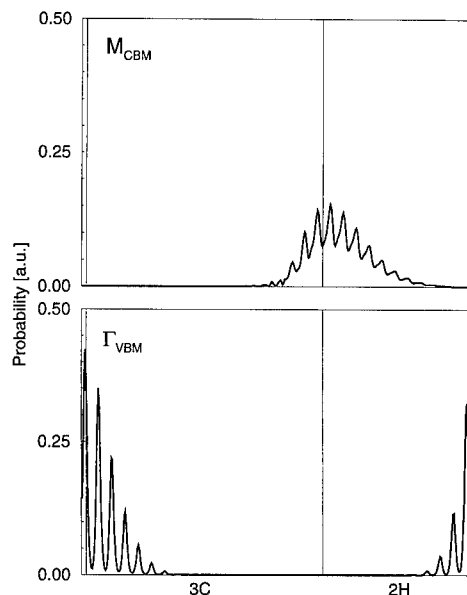


Fig. 4. Squared wave functions of the lowest conduction band state at M as well as of the highest valence band at Γ for a $(3C)_6(2H)_6$ superlattice.

polytype, as done in the $(3C)_6(2H)_6$ combination, this effect vanishes and the type-II character is again stabilized. Moreover, the states at CBM and VBM can be interpreted as interface states, since they are mainly localized in one of the two interfaces and decay towards the bulk polytype regions. Fig. 4 exhibits clearly the localization of the highest occupied (lowest unoccupied) Γ_{VBM} (M_{CBM}) state in the interface $2H \rightarrow 3C$ ($3C \rightarrow 2H$). This corresponds to the maximum (minimum) of the saw-tooth-like potential.

4. Conclusions

In summary, we have found that the arrangement of different natural polytypes gives 'heterostructure-like' materials with novel properties. We predict them to have electronic properties of type-II heterostructures: The gap is not only indirect in k -space but also in real space. For the larger 30H-superlattice, the existence of interface states could be derived. Because of the present dramatic progress in the homoepitaxial growth of SiC far from the equilibrium we expect an experimental realization of the

predicted heterocrystalline SiC structures made by different polytypes. Owing to resulting perfect interfaces without any alloying effect, interesting physical and technological applications are possible.

Acknowledgements

We like to acknowledge fruitful discussions with W.G. Schmidt. This work was supported by the Sonderforschungsbereich 196 (project A08) of the Deutsche Forschungsgemeinschaft and the EC Programme Human Capital and Mobility under Contract No. ERBCHRXCT 930337.

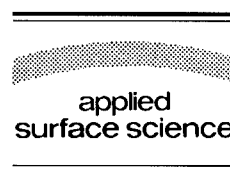
References

- [1] O. Madelung, Ed., Numerical Data and Functional Relationships in Science and Technology, Landolt-Börnstein, New Series, Group III, Vols. 17a, 22a (Springer, Berlin, 1982, 1986).
- [2] T. Sugii, T. Aoyama and T. Ito, *J. Electrochem. Soc.* 137 (1990) 989.
- [3] H. Matsunami, *Physica B* 185 (1993) 65.
- [4] A. Fissel, B. Schröter and W. Richter, *Appl. Phys. Lett.* 66 (5 June 1995).
- [5] P. Käckell, B. Wenzien and F. Bechstedt, *Phys. Rev. B* 50 (1994) 10761.
- [6] P. Käckell, B. Wenzien and F. Bechstedt, *Phys. Rev. B* 50 (1994) 17037.
- [7] B. Wenzien, P. Käckell and F. Bechstedt, *Surf. Sci.* 307–309 (1994) 989.
- [8] R. Stumpf and M. Scheffler, *Comput. Phys. Commun.* 79 (1994) 447.
- [9] C. Cheng, V. Heine and R.J. Needs, *J. Phys.: Condens. Matter* 2 (1990) 5115.
- [10] B. Wenzien, P. Käckell, F. Bechstedt and G. Cappellini, *Phys. Rev. B.*, in press.



ELSEVIER

Applied Surface Science 104/105 (1996) 495–501



Highly mismatched heteroepitaxy: 2D platelets assisted nucleation of self-assembled 3D quantum dots

C. Priester^{*}, M. Lannoo

Département ISEN, IEMN, BP 69, 59652 Villeneuve D'Ascq Cedex, France

Received 28 June 1995; accepted 28 August 1995

Abstract

In the early stages of highly mismatched heteroepitaxy (e.g. for InAs deposited on GaAs) self assembled dots (SAD) with a sharp distribution in sizes appear as soon as the coverage exceeds a critical value. We show that this phenomenon is determined by the preliminary growth of 2D platelets which act as precursors for the formation of 3D coherent islands. The argumentation is based on a total energy calculation using a valence force field approach for the elastic part (including dimers), the residual surface contribution (dangling bonds) being added separately. It is demonstrated that the existence of a critical coverage is related to the interaction between platelets. The proposed mechanism provides an appealing explanation for the fairly good calibration of the observed 3D islands. Moreover, our description appears to give the right order of magnitude for the 2D platelets size, the early quantum dots size, the width of the Gaussian distribution, the magnitude of the critical coverage, and finally the fact that such a phenomenon is not observed at lower values of the mismatch.

1. Introduction

Highly mismatched heteroepitaxy can lead, in its early stages, to the formation of SAD [1,2]. Such objects are very attractive and recent studies of their physical properties have been reported [3–5]. For several III–V highly mismatched systems [1,2] such as InAs/GaAs, but also in case of intermediate mismatches [6,7] these islands appear to be dislocation free (coherent islands) similarly to what has been earlier established by Eaglesham and Cerullo for the growth of Ge on Si [8]. The nucleation of these SAD is governed by a few main features:

- existence of a critical coverage below which growth is purely 2D and beyond which one observes islands;
- abrupt 2D–3D transition as the observed islands directly have a minimal size (one does not observe very small islands which would slowly grow up to reach an optimal size);
- at the very early stages of 3D islands formation, they appear to be well calibrated in size (and shape).

Here we want to address two questions: (i) the physical origin of the critical coverage, and how it is defined, (ii) what nucleation process can produce such a sharp calibration.

Up to now the theoretical attempts to describe the 2D–3D transition mainly consider pure 3D growth [9–13]. Such studies have shown that large enough

^{*} Corresponding author. Tel.: +33-20197911; fax: +33-20197884; e-mail: priester@isen.fr.

coherent islands are more stable than a purely 2D pseudomorphic layer and that, for a given amount of deposited material, the most stable islands are the largest ones. As will be shown below, this situation should lead to an island size distribution much larger than what has been recently observed [2,14]. In the following, we want to emphasize the role played by 2D platelets which occur in the early stage of the deposition of the second layer for InAs on GaAs. We shall see that these platelets can reach an equilibrium distribution governed by Boltzmann statistics. For this, we assume that the surface diffusion is fast enough for these platelets to reach an equilibrium distribution and we show from total energy calculations that this distribution is narrow, in agreement with experiment.

2. Distribution law at thermal equilibrium

Let us first discuss the characteristics of such an equilibrium distribution for a given constant coverage θ . We then consider quite generally an ensemble of non-interacting platelets. We take them to have an identical shape and label D_n the platelet containing n atoms, with total energy $E(n)$. We assume that thermal equilibrium can be reached and want to determine the corresponding distribution in sizes. We can get it, for instance, from the reaction:



In the limit where the platelets are distant and non-interacting, one can apply the law of mass action to get the concentration $c_n = N_n/N_s$ (where N_n is the number of platelets D_n , and N_s is the number of surface sites):

$$c_n = c_{n-1} c_1 \exp - \frac{(E(n) - E(n-1) - E(1))}{kT} \quad (2)$$

or, equivalently, defining the chemical potential μ as $E(1) + kT \ln(c_1)$,

$$c_n = \exp \left(\frac{n(\mu - \varepsilon(n))}{kT} \right) \quad (3)$$

where $\varepsilon(n) = E(n)/n$ is the energy per atom in the platelet which is the basic quantity determining the

equilibrium, and in the following referred to as the reduced energy. It is important to emphasize that physically meaningful values are obtained from Eq. (3) only if $\mu < \varepsilon(n)$ for any value of n . In fact, the physically interesting case where one can reach equilibrium is when $\varepsilon(n)$ has an absolute minimum ε_m at the value $n = n_m$. In this case the physical condition $c_n \ll 1$ requires $\mu < \varepsilon_m$. Then, in the limit $T \rightarrow 0$ one will get $\mu \rightarrow \varepsilon_m$ and the system is characterized by an infinitely sharp distribution of identical platelets of size n_m . If T increases then μ is lowered and the distribution is broadened. As long as it remains sufficiently narrow we can expand $n(\mu - \varepsilon(n))$ in Eq. (3) to second order around its maximum at $n = n_M$ which differs from n_m . This leads, for c_n , to a Gaussian distribution:

$$c_n = \exp \left(\frac{f_M}{kT} \right) \exp - \left(\frac{|f''|}{2kT} n_M^2 \left(\frac{n}{n_M} - 1 \right)^2 \right) \quad (4)$$

where f'' is the second derivative of $n(\mu - \varepsilon(n))$ taken at $n = n_M$ and

$$f_M = n_M(\mu - \varepsilon(n_M)). \quad (5)$$

The value of the chemical potential μ (and consequently of f_M), is determined by the total number of particles, i.e. by writing that the coverage θ is equal to the number of wetting layers w plus the integral over n of nc_n . This gives

$$\theta_c - w = n_M \sqrt{\frac{2\pi kT}{|f''|}} \exp \left(\frac{f_M}{kT} \right). \quad (6)$$

Of course the validity of this formulation depends on the fact that the Gaussian is narrow. The relevant quantity for this is the halfwidth at half maximum Δn which is given by

$$\Delta n = \left(\frac{1.4 kT}{|f''|} \right)^{1/2}. \quad (7)$$

If $\Delta n/n_M \ll 1$, then the above expansion is meaningful.

3. Pure 3D growth

Before applying this to platelets, let us consider first the case of separated 3D islands. The competing phenomenons which govern the coherent 3D growth

mechanisms are (i) extra surface energy and (ii) a better elastic relaxation when the island grows. From this balance results an optimal shape for the islands. The reduced energy for a system made of a periodic array of pyramidal islands deposited on a substrate, with eventually a wetting layer can be split into 3 parts: the purely elastic reduced energy of the corresponding isolated islands, the reduced interaction between the islands spaced by d , and the surface reduced energy. A careful study of the interaction between islands versus their spacing shows that it decreases as d^{-3} .

For large enough islands we can make use of arguments derived from continuous elasticity theory which allows us to write quite generally

$$\varepsilon(n) = \varepsilon_{ps} - A_r + A_s n^{-1/3} + B_i n/d^3 \quad (8)$$

or, equivalently, as the ratio n/d^2 is fixed by the coverage

$$\varepsilon(n) = \varepsilon_{ps} - A_r + A_s n^{-1/3} + A_i n^{-1/2} \quad (9)$$

where ε_{ps} is the energy per atom of the corresponding pseudomorphic layer, the last three terms describing respectively the relaxation, surface and interaction energies, A_r , A_s and A_i being three positive constants, only A_i depending on the coverage. $\varepsilon(n)$ is a continuously decreasing function and, if one neglects interactions between islands, one recovers the function encountered in the usual form of nucleation theory [16]. The corresponding total energy $n\varepsilon(n)$ reaches a maximum at a critical size $n^* = (3A_s/2A_r)^3$. The evolution of the system is that the islands which have reached this critical size tend to grow indefinitely since their energy continuously decreases. However, at constant θ this tendency is limited by the depletion in the concentration c_1 of the monomers, a phenomenon called Oswald ripening [15]. The corresponding time evolution of the size distribution has been calculated for epitaxial growth in Ref. [12] extending the bulk theory of Ref. [15]. The distribution in sizes is found to be broader than the experimental one for InAs on GaAs [2,14] and is also strongly asymmetric, contrary to what is observed.

To check the applicability of Eq. (9), we have performed a microscopic calculation of the total energy of these islands. We have studied a periodic array of pyramidal islands, limited by [104] planes,

over a one monolayer thick wetting layer deposited on GaAs. The microscopic elastic energy is treated within a valence force field approach, more precisely the Keating model for the present calculation. As regards the surface contribution, the [104] planes are treated as [100] terraces separated by steps. We then allow for dimerization and treat the dimers bonds as distorted normal bonds, again by the Keating model (which we have adjusted to reproduce the As–As natural bond length equal to 2.5 Å, the experimental value in elemental As). We are then left with surface atoms possessing one dangling bond to which we assign a positive formation energy ε_{db} . In the following $\varepsilon_{db} \sim 0.3$ eV which is a reasonable value for reasons discussed elsewhere [17].

The method described above (details can be found in Ref. [18]) can thus be applied to the calculation of the relaxation energy. Its advantage is that it allows to treat up to 10^6 atoms in the periodic cell. The stable atomic positions are computed via a conjugate gradients method. We have calculated the reduced energy $\varepsilon(n)$ versus the size of the islands for a coverage θ between 1 and 2 monolayers (where the first monolayer corresponds to the wetting layer, the useful coverage for building the islands being thus $\theta - 1$). We have found that, at n greater than 1000 atoms, $\varepsilon(n)$ does not depend on the coverage. This means that the islands become distant enough for their interaction to become negligible and also that the classical elasticity expression given by Eq. (9) becomes valid. Deviations for smaller islands are observed, with the eventual existence of a barrier, but this occurs only when the islands begin to overlap. We can thus safely conclude that these calculations confirm our previous conclusion that direct formation of 3D islands cannot explain the observed narrow distribution in sizes and the existence of a critical coverage. This leads us to consider now the formation of 2D platelets.

4. 2D platelets

Obviously the beginning of the formation of the first monolayer following the wetting layer corresponds to the growth of 1 ML high platelets. The interesting issue is to see if these platelets can reach a stable equilibrium distribution and if this is stable

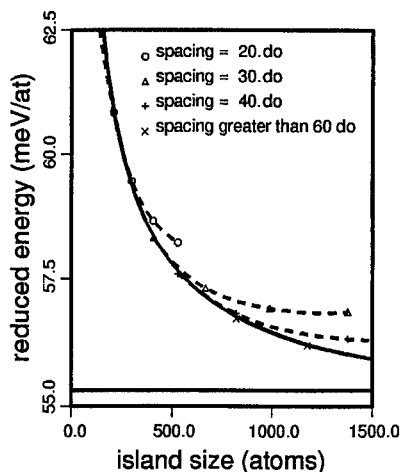


Fig. 1. Evidence for interactions between platelets: reduced energy variations (in meV per atom) for an InAs square platelet deposited on a GaAs substrate versus the platelet size (in atoms), for varying spacing between platelets, referred to the corresponding ideally flat reduced energy (horizontal full line). 'do' is the distance between two substrate atoms along the 110 and $\bar{1}\bar{1}0$ directions parallel to the square sides. The dangling bond energy cost is 0.3 eV. Within this range of island sizes, all curves corresponding to platelets separated by more than 60 'do' are identical.

against formation of 3D islands. As a preliminary analysis, let us again present the result of classical elasticity theory. As shown by Tersoff and Tromp [10], the reduced energy $\varepsilon(n)$ of non-interacting square platelets can be written in this limit:

$$\varepsilon(n) = \varepsilon_{ps} - B_r n^{-1/2} \ln(n^{1/2}) + B_s n^{-1/2} \quad (10)$$

where, again, the last two terms represent the relaxation and linear tension energies, B_r and B_s being positive.

Such an expression has a minimum and one is in the interesting situation where, if equilibrium can be reached, then the size distribution of the platelets will take the Gaussian form of Eq. (4). However several factors can modify $\varepsilon(n)$ from its ideal form (Eq. (10)) like deviations from continuous elasticity and interactions between islands. Furthermore the constants B_r and B_s have to be determined. For these reasons, we have performed a microscopic calculation for square platelets as described above. Fig. 1 shows the results of such a computation for the reduced energy $\varepsilon(n)$ per atom in each platelet versus platelet size (i.e. n), and this for different distances between the platelets, i.e. varying cover-

ages. It is seen that the full line corresponding to Eq. (10) provides the correct behavior for large distances between neighboring platelets and that the interactions between platelets become important at small distances. One major result of these calculations is that when $\theta < 1.4$ ML the interactions between platelets can be neglected.

When varying the cost in dangling bond energy ε_{db} we find, as anticipated from Eq. (10), that there is always a minimum at $n = n_m$ which is displaced towards larger n_m when ε_{db} is increased since this corresponds to larger values of the constant B_s . On the other hand an increase in coverage results in a repulsive interaction between the platelets which corresponds to adding a repulsive term in Eq. (10), thereby displacing n_m to larger values as found numerically. For coverages $\theta < 1.4$ this repulsive interaction is negligible so that Eq. (10) becomes valid, our calculation providing a unique value of B_r equal to 60 meV, B_s depending linearly on ε_{db} . For $\varepsilon_{db} = 0.3$ eV, the minimum of $\varepsilon(n)$ occurs at $n_m \sim 26000$ atoms. One can thus make use of Eq. (6) to get n_M , f'' and Δn as a function of the temperature. At a typical growth temperature (i.e. 500°C) one gets a Gaussian centered around 10500 atoms and a value of $\Delta n/n_M = 33\%$. For lower temperatures n_M shifts towards n_m and, as can be seen on Eq. (4), the distribution sharpens. These values are very sensitive to the dangling bond energy: when it increases, the maximum of the Gaussian is shifted towards larger n_M , and the distribution is also sharpened. Let us now consider the relation of this result to the growth of 3D islands. This can be done by consideration of the curves plotted on Fig. 2 which shows the reduced energy $\varepsilon(n)$ versus n both for 2D and 3D islands. We have considered two values of the coverage: $\theta = 1.4$ for which the 2D platelets do not interact, and $\theta = 1.8$ for which their interaction becomes important, which shifts n_m to larger values. We have also reported on Fig. 2 the distribution of 2D platelets for a temperature of 500°C. We do not treat here in detail the deposition of the first monolayer since this is a wetting layer whose origin can be explained in terms of surface and interface energies. After completion of this layer the first atoms which are deposited tend to form 2D platelets whose size is determined by the number of atoms deposited in an area defined by the diffusion length. This can be

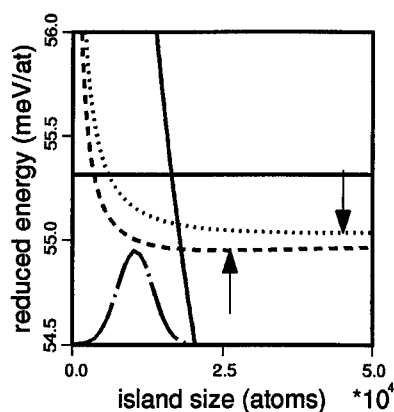


Fig. 2. Representation of the relative variations of 3D (full line) and 2D (dotted and dashed lines) reduced energy curves versus the number of atoms in the island, referred to the corresponding ideally flat reduced energy (horizontal full line). The 2D dashed line corresponds to a coverage lower than the critical coverage, and the 2D dotted line to a coverage greater than the critical coverage (see text). The 3D curve does not depend on the coverage. The chain-dotted curve gives the size distribution for 2D platelets at 500°C.

deduced from Fig. 2 which shows that, for small sizes, the 2D platelets are more stable than the 3D islands in such a way that the first 'objects' on the surface are small platelets like those observed in homoepitaxy. As the coverage increases, these platelets grow as they keep more stable than 3D islands until they reach their optimal distribution centered on n_M (which depends on the temperature, contrarily to n_m which is indicated by an arrow in Fig. 2). As long as n_M is smaller than the crossing point where 3D islands become more stable than the platelets, the growth mode keeps 2D, and one gets a Gaussian distribution of platelets centered on n_M . This will remain true as long as the platelets do not interact, i.e. when $1.0 < \theta < 1.4$. In this regime, the density of such platelets will then simply increase. However when θ becomes larger than 1.4, the average distance between platelets becomes small enough for them to interact with the consequence that $\varepsilon(n)$ becomes less stable and its minimum n_m is displaced to larger values as shown on Fig. 2 for $\theta = 1.8$. As the slope of $\varepsilon(n)$ for 3D islands is much larger, there exists a critical coverage θ_c at which the 3D islands become more stable than the platelets. In the case of Fig. 2, this critical coverage will occur at $\theta_c \sim 1.7$, i.e. close to the experimental value.

5. Discussion and conclusion

Our understanding of the 2D \rightarrow 3D transition is that at $\theta = \theta_c$ the 2D platelets spontaneously transform into 3D islands at practically constant number of atoms in each island. The resulting size distribution of these 3D islands thus reflects the platelets' one and one gets a pretty narrow Gaussian curve as observed experimentally. The platelets can thus be viewed as 'precursors' for the formation of the 3D islands. Once this transformation is achieved, a further increase in coverage results in a subsequent growth of these islands which, at some critical size, can lead to the creation of misfit dislocations (as also demonstrated experimentally) and finally to coalescence. Of course such a mechanism requires that the atoms at the edge of the platelet can easily overcome the Schwoebel barrier, i.e. the energy corresponding to the jump on the top of the platelet [19]. This implies that this barrier is not much larger than the barrier for surface diffusion which is pretty small for these systems. There is at present no clear cut proof that this is really so, but recent experiments in the vicinity of the transition point have shown the coexistence of platelets and 2D islands [20] which is naturally explained in the framework of our interpretation. Another criterion which needs to be satisfied is that growth conditions allow the migration of the atoms from the edges of the platelets to its center, otherwise kinetic limitations would prevent the formation of 3D islands from the platelets. This can be checked by comparing the size of the optimal platelets to the diffusion length. For InAs on GaAs these platelets contain typically 40000 atoms, leading to a size of about 600 Å which is much lower than the diffusion length under typical growth conditions.

Defining n_{3D} as the size at which $\varepsilon(n)$ for 3D islands changes sign, the critical parameter in our calculation is n_M/n_{3D} . Only when it is smaller than unity can one get a narrow distribution of self organized 3D islands. It is interesting to note that, as both B_r and A_r decrease quadratically with the mismatch, when the lattice mismatch decreases, n_{3D} increases as a power function of the inverse of the lattice mismatch, whereas n_M exponentially increases with the inverse of the lattice mismatch. This explains why such a narrow distribution of self organized 3D islands is not observed for a small lattice mismatch

[20–22]. In this case n_M/n_{3D} rapidly becomes larger than unity in which case the growth of 3D islands is only delayed by kinetic limitations and one can get surface roughening during the 2D growth mode. This also points out the extreme sensitivity of the n_M/n_{3D} ratio to the parameter B_s/B_r , B_s varying linearly with the dangling bond energy ε_{db} .

Our predicted size (~ 16000 atoms) for the early 3D islands compares reasonably well with the experimental values (roughly 50 000 atoms per dot in Ref. [1] whereas in Ref. [2], the early dots contain about 20000 atoms). Our result can be considered as pretty close in view of the sensitivity of the predicted value and the fact that we have not performed any optimization of the cluster shapes. Our calculated width for the Gaussian distribution (33% for $\Delta n/n$ at 500°C) has to be compared with $\Delta h/h + 2\Delta d/d$ (h for the height, d for the diameter — or half base — of the quantum dots) which has been reported equal to $(10 + 2 \times 7) = 24\%$ in Ref. [1] and to $(20 + 2 \times 10) = 40\%$ in Ref. [2].

In any case the values determined here for the relevant parameters appear to give the right order of magnitude for n_M , n_{3D} , the width of the Gaussian distribution, the magnitude of theoretical coverage, and finally the fact that such a phenomenon is not observed at lower values of the mismatch. Our description also implies that whenever 2D platelets assist SAD nucleation, the 2D–3D critical coverage is bound to be lower than 1 ML beyond the wetting layer. This is verified by recent observations for the system InAs/InP [7].

In conclusion we have shown here that the existence of a narrow distribution of self assembled 3D islands for highly mismatched heteroepitaxy can be explained by the preliminary formation of stable 2D platelets. These reach their equilibrium distribution and, at the critical coverage, their repulsive interaction induces a spontaneous transformation into 3D islands which keep the same distribution. Our calculation allows to correlate in a consistent way the different experimental information on this phenomenon.

For describing this mechanism, we only considered the ideal case of square platelets and perfect square base pyramids. Obviously, depending on the lattice mismatch, on surface anisotropy (mainly bound to reconstruction), and also on statistical dis-

tribution, realistic platelets are more irregular, islands may be lengthened and their crest lowered. A further study which takes into account these considerations is on current investigation, but it will not alter the validity of the basic mechanism presented here.

Acknowledgements

The “Institut d’Electronique et de Microélectronique du Nord” (IEMN) is “Unité mixte n°9929 du Centre National de la recherche Scientifique”. This work has been partly supported by EEC (contracts CHRX-CT930134 and CHRX-CT940428), PIRMAT(CNRS/DRET/DRED) and France Telecom (contract No. 94 6B 007).

References

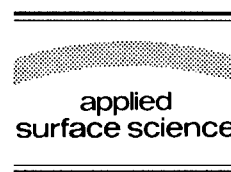
- [1] D. Leonard, M. Krishnamurthy, C.M. Reaves, S.P. DenBaars and P.M. Petroff, *Appl. Phys. Lett.* 63 (1993) 3203.
- [2] J.M. Moison, F. Houzay, F. Barthe, L. Leprince, E. André and O. Vatel, *Appl. Phys. Lett.* 64 (1994) 196.
- [3] G. Wang, S. Fafard, D. Leonard, J.E. Bowers, J.L. Merz and P.M. Petroff, *Appl. Phys. Lett.* 64 (1994) 2815.
- [4] J.Y. Marzin, J.M. Gérard, A. Izrael and D. Barrier, *Phys. Rev. Lett.* 73 (1994) 716.
- [5] D. Leonard, S. Fafard, K. Pond, Y.H. Zhang, J.L. Merz and P.M. Petroff, *J. Vac. Sci. Technol. B* 12 (1994) 2516.
- [6] A. Rudra, R. Houdré, J.F. Carlin and M. Ilegems, *J. Cryst. Growth* 136 (1994) 278.
- [7] A. Ponchet, A. Le Corre, H. L’Haridon, B. Lambert and S. Salaün, *Appl. Phys. Lett.* 67 (1995) 1850; A. Le Corre, H. L’Haridon, B. Lambert, S. Salaün and A. Ponchet, *Proc. Euro-MBE VIII*, Sierra Nevada, Grenada, Spain, March 1995.
- [8] D.J. Eaglesham and M. Cerullo, *Phys. Rev. Lett.* 64 (1990) 1943.
- [9] K.E. Khor and S. das Sarma, *Phys. Rev. B* 49 (1994) 13657.
- [10] J. Tersoff and R.M. Tromp, *Phys. Rev. Lett.* 70 (1993) 2782.
- [11] J. Tersoff and F.K. Le Goues, *Phys. Rev. Lett.* 72 (1994) 3570.
- [12] B.K. Chakraverty, *J. Phys. Chem. Solids* 28 (1967) 2401, 2413.
- [13] J. Drucker, *Phys. Rev. B* 48 (1993) 18203.
- [14] D. Leonard, K. Pond and P.M. Petroff, *Phys. Rev. B* 50 (1994) 11687.
- [15] I.M. Lifshitz and V.V. Slyozov, *J. Phys. Chem. Solids* 19 (1961) 35.
- [16] J.W. Christian, in: *The Theory of Transformations in Metal and Alloys* (Pergamon, New York, 1981); E.M. Lifshitz and L.P. Pitaevski, *Physical Kinetics*, Eds. Landau and Lifshitz,

- Course of Theoretical Physics, Vol. 10 (Pergamon, New York, 1981).
- [17] C. Priester and M. Lannoo, *Phys. Rev. Lett.* 75 (1995) 95.
- [18] C. Priester, I. Lefebvre, G. Allan and M. Lannoo, *MRS Symp. Proc.* 317 (1993) 131.
- [19] R.L. Schwoebel, *J. Appl. Phys.* 40 (1969) 614.
- [20] J.M. Moison and N. Lebouché, *Appl. Surf. Sci.*, presented at this conference; private communication.
- [21] M. Gendry, V. Drouot, C. Santinelli, G. Hollinger, C. Miossi and M. Pitaval, *J. Vac. Sci. Technol. B* 10 (1992) 1829.
- [22] N. Grandjean and J. Massies, *J. Cryst. Growth* 134 (1993) 51; N. Grandjean, J. Massies and F. Raymond, *Jpn. J. Appl. Phys.* 33 (1994) L1427.



ELSEVIER

Applied Surface Science 104/105 (1996) 502–509



Photoluminescence and transmission electron microscopy investigation of SiGe quantum wires grown on patterned Si substrates

Arno Hartmann^{a,*}, Christel Dieker^a, Uschi Bangert^b, Roger Loo^a, Lili Vescan^a,
Hans Lüth^a

^a *Institut für Schicht- und Ionentechnik (ISI), Forschungszentrum Jülich GmbH, D-52425 Jülich, Germany*

^b *Department of Pure and Applied Physics, UMIST, Manchester M60 1QD, UK*

Received 28 June 1995; accepted 25 October 1995

Abstract

Growth of SiGe by low pressure chemical vapor deposition on nonplanar Si substrates is studied for nominal Ge concentrations of $0.4 \leq x_{\text{Ge}}^{\text{nom.}} \leq 1$. Self-organized growth leads to the formation of approx. 30 nm wide SiGe quantum wires at convex corners of the substrate. In photoluminescence (PL) spectra of samples with $x_{\text{Ge}}^{\text{nom.}} = 0.4$ we identify transitions from quantum wells on the flat parts of the substrate and from quantum wires. The energetic positions of the quantum wire transitions are in good agreement with Ge concentrations measured by spatially resolved energy dispersive X-ray spectroscopy, using a scanning transmission electron microscope (TEM). We find that the Ge concentration inside the wire is considerably lower than the nominal value for growth on planar parts of the substrate. Even for wires grown with $x_{\text{Ge}}^{\text{nom.}} = 1$, where only GeH_4 and H_2 are present during growth, PL and TEM indicate a Ge concentration as low as 32% for the wires. In such growth experiments we observe different regimes of strain relaxation. While quantum wires and wells are heavily decorated with Stranski–Krastanov islands in larger structures, smaller structures ($\leq 5 \mu\text{m}$) exhibit homogeneous thickness.

1. Introduction

The physical properties of semiconductor quantum wires (QWR) are a subject of current research because of the possible benefits for applications arising from two-dimensional quantum confinement effects [1]. Unusually high carrier mobility in such wires has been predicted [2] and low threshold laser

structures have already been built. One successful method to fabricate quantum wires for laser structures in the GaAs/AlAs/InAs system has been the selfordered growth on V-groove patterned substrates (for a review see Ref. [3]). The advantages of this method are firstly that the size of the wires is controlled not by lithography but rather by the growth itself and secondly all wire interfaces are defined in one growth step. This leads to a low density of interfacial defects. Recently, Usami et al. [4] showed that V-groove patterned substrates can also be used in the SiGe/Si system to fabricate QWRs. They

* Corresponding author. Tel.: +49-2461-613781; fax: +49-2461-612940; Internet: a.hartmann@kfa-juelich.de.

investigated these wire structures using photoluminescence (PL) and electroluminescence spectroscopy [5]. That not only a V-groove, but more generally, any convex corner of a patterned Si substrate leads to the formation of a SiGe QWR was shown recently by our group [6,7].

In the first part of this paper we present a correlation between the PL properties of SiGe QWRs grown in (001)–(111) corners (L-corners) and their microstructure as investigated by transmission electron microscopy (TEM) and scanning TEM (STEM) in connection with energy dispersive X-ray analysis (EDX). We find that the Ge concentration inside the wire is $x_{\text{Ge}}^{\text{wire}} \leq 21\%$, a value which is considerably lower than the nominal concentration $x_{\text{Ge}}^{\text{nom}} = 0.4$ for layers on planar parts of the substrate. In the second part of this paper we investigate the possibility of obtaining wires with higher Ge content by deposition of layers with nominally $x_{\text{Ge}}^{\text{nom}} = 0.7$ –1. While the wires in larger structures are found to relax by forming pseudomorphic and/or dislocated islands, smaller structures ($\leq 5 \mu\text{m}$) exhibit homogenous wires. From PL and TEM results we deduce that even wires grown in the absence of Si in the gas phase contain approx. 70% Si.

2. Experimental

Samples were prepared as follows (for more details see Ref. [7]): The substrates were patterned using standard optical lithography, subsequent reactive ion etching and wet chemical etching. The patterns investigated are rectangular and square structures arranged along $\langle 110 \rangle$ directions. In a cross-sectional view, the rectangular structures (lines) consist of a (001) bottom facet bounded by two {111} facets on each side as shown in Fig. 1. (Squares exhibit such cross-sections in both orthogonal $\langle 110 \rangle$ directions.) The width of the (001) bottom facet is varied from $0.5 \mu\text{m}$ to $100 \mu\text{m}$ for different structures. Onto these substrate patterns a Si/SiGe/Si quantum well (QWL) layer sequence was deposited by low pressure chemical vapor deposition. As source gases SiCl_2H_2 and GeH_4 diluted in H_2 as carrier gas were used. The deposition pressure was 120 mTorr at a temperature of 700°C . PL spectra were taken between 4 K and 50 K using a Fourier transform

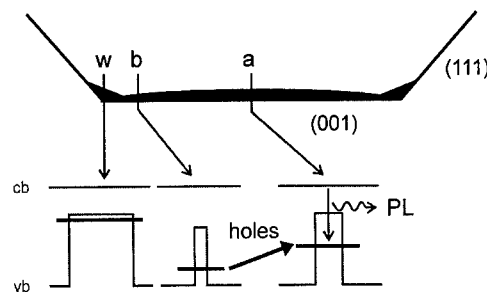


Fig. 1. Schematic of a line structure cross-section. The incorporated amount of Ge in the (001) QWL is illustrated by the thickness of the black line. The resulting potential wells in the valence band are sketched for different positions below the cross-section drawing.

spectrometer (BIO RAD FTS40) and an argon ion laser emitting 50 mW at 488 nm. The microstructure of the samples was investigated by means of a JEOL 4000 FX microscope for cross-section TEM images while a Fison VG HB601 UX STEM as well as a Philips CM20 FEG was used for spatially resolved EDX measurements.

3. PL and microstructure of quantum wires

The samples studied in this section were grown with the following layer sequence: 20 nm Si buffer, 1 nm $\text{Si}_{0.6}\text{Ge}_{0.4}$ quantum well and 50 nm Si cap. For clarity reasons we will shortly review the discussion of the QWL PL given in Refs. [6,7]. Fig. 2 shows a

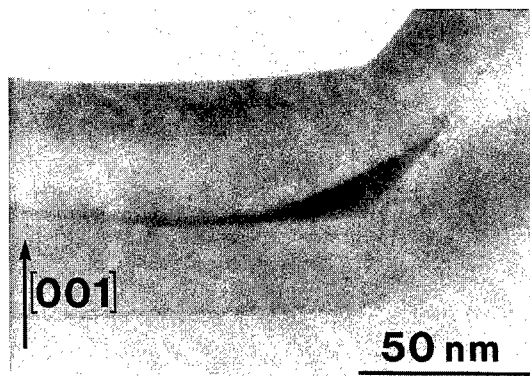


Fig. 2. Bright field cross-section TEM image of a L-corner QWR. The SiGe QWL and QWR are visible as dark areas. Some substrate-epi interface contamination is also visible as black spots.

cross-sectional (CS) TEM image of a SiGe QWR grown in an L-corner structure. The growth rate of Si is not affected by the presence of the corner. The SiGe growth rate, on the contrary, is strongly enhanced by a factor of up to 10 right at the corner. This leads to the formation of an approx. 30 nm wide and 10 nm thick SiGe QWR. The large amount of Ge incorporated into the wire is supplied by surface diffusion of Ge adatoms or Ge precursor ad-molecules from the adjacent (001) and (111) QWLs to the wire. Therefore, less Ge is incorporated into the QWL in the vicinity of the wire: a Ge depleted zone extends from the wire into the QWL. This is illustrated in Fig. 1 where the incorporated amount of Ge on the (001) facet is represented by the thickness of the corresponding black line. The spatial variation of the amount of incorporated Ge results in a variation of the binding energy of holes, as sketched in the lower part of Fig. 1.

In a PL experiment at low temperatures, photo-generated holes follow the gradient in binding energy and accumulate in the midst of the (001) QWL. As a result, the observed PL peaks stem from this middle part of the (001) QWL. This opens up the possibility for measuring the spatial extent of the Ge depleted zone and therefore the Ge adatom or ad-molecule diffusion length [6,7]: When the width of the (001) QWL is reduced, the Ge depleted zones begin to overlap at a certain width. As a result the Ge content of the QWL decreases even in the middle of the structure and a blue shift of the QWL related PL transitions is observed. This behavior is shown in Fig. 3(a). PL spectra taken at 4 K from line structures of different width are compared to a large area (001) QWL reference sample. Proceeding from high to low energies one finds excitonic recombinations in the Si substrate, and no phonon (NP), transverse acoustical (TA) and transverse optical (TO) phonon assisted transitions. These transitions can easily be attributed to the (001) SiGe QWL since they also appear in the large area reference sample. As the width of the line structures is reduced below 8 μm , the blue shift of the QWL transitions arising from the overlap of the Ge depleted zones is clearly visible.

One question arising in this context is why we do not observe any PL from the QWRs in the spectra of Fig. 3(a). Because of the large thickness of 10 nm

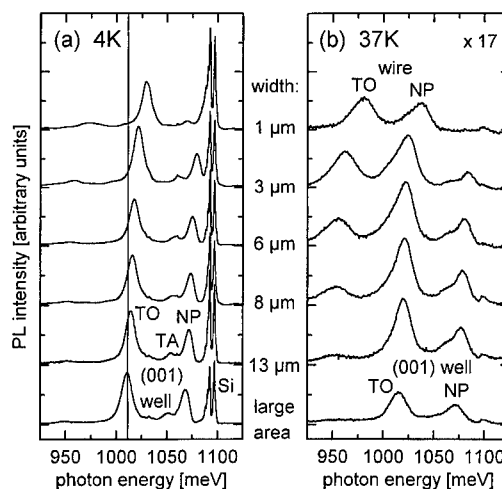


Fig. 3. PL spectra of line structures of different width taken (a) at 4 K and (b) at 37 K. The width of the (001) bottom facet equivalent to the wire spacing is indicated in the figure.

for the QWR compared to 1 nm for the QWL, we would expect such QWR related PL at lower energy than the QWL PL. A possible explanation for the missing QWR PL at low temperatures might be as follows. Almost all photogenerated holes are captured by the QWL which covers a much larger area in comparison to the QWR. At low temperatures, these holes follow the potential gradient and accumulate in the midst of the (001) facet, at the thickest point of the QWL (point 'a' in Fig. 1). At higher temperatures, on the contrary, the thermal energy of the holes is sufficient to overcome the energetic barrier imposed by the Ge depleted zones (point 'b'). Hence they accumulate in the much deeper potential well of the wire (point 'w'). We therefore expect to see recombination processes in the QWRs at higher temperatures. Fig. 3(b) shows PL spectra of the same samples as in Fig. 3(a) taken at 37 K. The spectrum of the large area reference sample did not change except for thermal broadening of the (001) QWL PL lines. The PL spectra of the patterned samples, in contrast, changed considerably upon the increase of temperature. From the 13 μm to the 1 μm sample, the well NP peak disappears slowly, while a new peak appears on the low energy side of the spectra. For the 1 μm sample, it becomes clear that the new, low energy peak is in fact the TO-phonon replica of a NP peak near 1040 meV. We attribute these two

peaks to the quantum wires. Since the NP wire peak coincides with the TO well peak the sum intensity at this energetic position stays almost constant for all different structure widths. The disappearing well TO peak, whose intensity is linked to the well NP peak is slowly replaced by the wire NP peak upon reduction of the structure width. Considering the small relative area coverage of the wires which increases from approx. 0.7% for the 13 μm structure to 3% for the 1 μm structure, it is quite astonishing that these QWR transitions are visible so clearly. This high PL efficiency implies a low defect density so that enough excitons can diffuse towards and be captured by the QWR.

The following arguments suggest an assignment of the observed low energy transitions to recombinations in the QWRs: (1) The intensity of the transitions is clearly related to the structure width and therefore to the area density of wires. (2) The QWR transitions are shifted to higher energy as the width of the structures is decreased. This is expected, since for small structures the Ge depleted zones near the wires, which are nothing else but Ge supply zones, for the wires, will begin to overlap. The two wires are competing for the same Ge adatoms adsorbed on the (001) facet between them. As a result, those closely spaced wires will contain less Ge than a 'lonely' wire. This causes the observed blue shift. (3) The temperature dependence of the well and wire PL peaks as expected for our structures of quite low wire density (see explanation given above). (4) For samples containing square — instead of line — structures, the QWR PL is even more intense and the blue shift is more pronounced because of the higher wire density in those structures.

One important point, namely the absolute energetic position of the QWR PL peaks, has not yet been discussed. If we assume a wire thickness of 10 nm, as observed in cross-sectional TEM, and a Ge concentration of 40%, which is the nominal value of the epitaxy, we would expect to find the QWR NP peak somewhere near 890 meV. The observed peak positions are above 1000 meV which suggests a Ge concentration of $\leq 20\%$. A similar observation was made by Usami et al. for V-groove QWRs grown by gas source molecular beam epitaxy [5]. A nominal composition of 17.7% Ge resulted in a QWR which contains only 10% Ge if we apply our simple calcu-

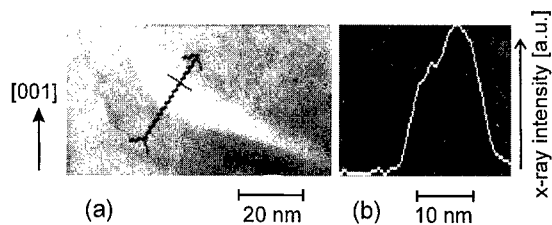


Fig. 4. Large angle dark-field STEM image of an L-corner QWR (a) in which the position and direction of the EDX line scan is marked by an arrow (length = 32 nm). The resulting GeK_{α} X-ray intensity is shown in (b).

lation to the observed PL peak positions in their publication.

In order to clarify these issues, we performed spatially resolved EDX measurements using a scanning TEM. Fig. 4 shows a cross-sectional image of a L-QWR. An EDX line scan was taken along the line marked by the arrow. The resulting GeK_{α} X-ray intensity is plotted right next to the TEM picture. It is obvious from Fig. 4 that there is a gradient in the Ge concentration of the QWR. The Ge concentration increases in the growth direction. In order to obtain quantitative results, reference samples containing thick SiGe layers of known composition were studied. The influence of the beam probe size of approximately 1.5 nm as well as the beam broadening to about 5 nm caused by the finite sample thickness were corrected by a deconvolution procedure [8–10]. Table 1 compares the Ge concentrations obtained from EDX and the concentrations calculated from the NP PL peak positions. In order to obtain Ge concentrations from the PL results we had to assume a thickness of 10 nm for the QWR, a homogenous Ge distribution and a strain state equal to a strained (001) QWL, neglecting effects of elastic strain relaxation that can be important in such small structures. According to Table 1 the EDX results do confirm

Table 1

Ge concentrations of QWRs in line structures of different width as inferred from spatially resolved EDX and PL. For EDX measurements the concentration values at the lower and upper interface of the QWR are given

Width	8 μm	1 μm
x_{Ge} (EDX)	15–21% \pm 2%	11–16.5% \pm 2%
x_{Ge} (PL)	20%	16%

that the Ge concentration in the QWRs is much lower than the nominal one. They even agree quantitatively with the results obtained from PL. Therefore this is another independent proof that the observed PL peaks in Fig. 3(b) actually do stem from the QWRs. The EDX results also confirm the lower Ge concentration in more closely spaced wires of smaller structures with overlapping 'Ge supply zones'. Since the calculated Ge concentrations, based on the results from PL and on the assumption that the SiGe wire is completely strained, agree with the EDX measurements within the error limits we conclude that elastic strain relaxation of the wire does not play an important role in the determination of the PL transition energy.

4. Samples of high nominal Ge concentration

An epitaxy of nominal $x_{\text{Ge}}^{\text{nom}} = 0.4$ resulted in quantum wires containing only $\leq 21\%$ Ge. Two questions arise in this context: (1) Is it possible to fabricate wires of higher Ge content? (2) What is the origin of the surplus Si in the wire? Is it supplied by the gas phase SiCl_2H_2 or does it stem from the Si layers below or above the SiGe layer? To answer these questions we prepared samples with a nominal Ge concentration of $x_{\text{Ge}}^{\text{nom}} = 0.7$ (939) and $x_{\text{Ge}}^{\text{nom}} = 1$ (938). The growth conditions (700°C, 120 mTorr) and layer sequences (25 nm Si buffer, ~ 1 nm SiGe quantum well, 35 nm Si barrier and the same SiGe quantum well layer as capping layer) were exactly the same for both samples. Only for the SiGe layers the gas mixture was changed by adding 0.11% of SiCl_2H_2 for epi 939 to the 0.26% of GeH_4 in H_2 used for epi 938. For both samples, the deposited SiGe thickness is above the critical limit for Stranski–Krastanov island growth [11,12].

The CS-TEM image of Fig. 5 shows a L-corner region of a 1 μm wide structure of epi 938 (100% Ge). The buried as well as the top quantum wire is clearly visible in this picture. This implies that neither the Si capping layer nor the presence of SiCl_2H_2 in the gas phase during Ge growth influences the selforganized growth process leading to the wire formation. The observation that top and buried wire look very similar should, in principle, allow us to judge the homogeneity of wires by looking at sec-

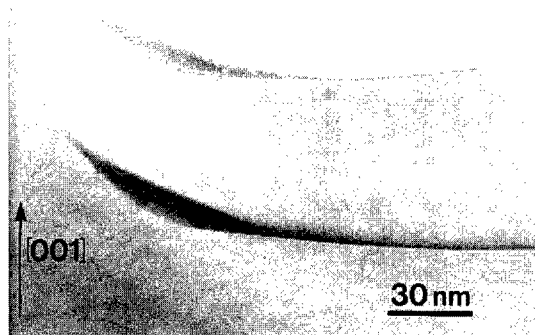


Fig. 5. Bright field CS TEM picture showing an L-corner region of a line structure with 1 μm wire spacing of sample 938 (pure Ge QWL). Uncapped and buried QWR are clearly visible and of similar shape and size.

ondary electron microscopy (SEM) images of the sample surface.

Fig. 6 shows a compilation of such SEM images of different wide square structures comparing samples 939 and 938. On the right-hand side the corresponding PL spectra (4 K, 50 mW) are also shown. In Fig. 6(a) 100 μm wide squares of epi 939 (70% Ge, top) and 938 (100% Ge, bottom) are compared. In both SEM pictures we see the etched (111) facet on the left and the (001) bottom plane. Three main differences in the SEM pictures of epi 939 and 938 are evident: (1) The density of Stranski–Krastanov islands on the (001) plane is *lower* in the pure Ge sample 938 than in 939. (2) A corridor of reduced island population is visible near the corner which is considerably *wider* in the case of the pure Ge sample. (3) The wire at the interfacet corner consists of islands in both cases, but they are considerably *larger* in the case of the pure Ge sample. All three observations lead to the conclusion that surface diffusion is *enhanced* for growth with GeH_4 alone compared to the case where also SiCl_2H_2 is present. Closer inspection of the wires at the corners by TEM reveals that the wire-islands are of similar size and pseudomorphic in the case of epi 939 while they are coagulated and dislocated in the pure Ge sample 938. The high island density ($18 \mu\text{m}^{-2}$) of epi 939 manifests itself in strong island related PL transitions and only very weak transitions from the Stranski–Krastanov wetting layer ('Qwell' in Fig. 6(a)) be-

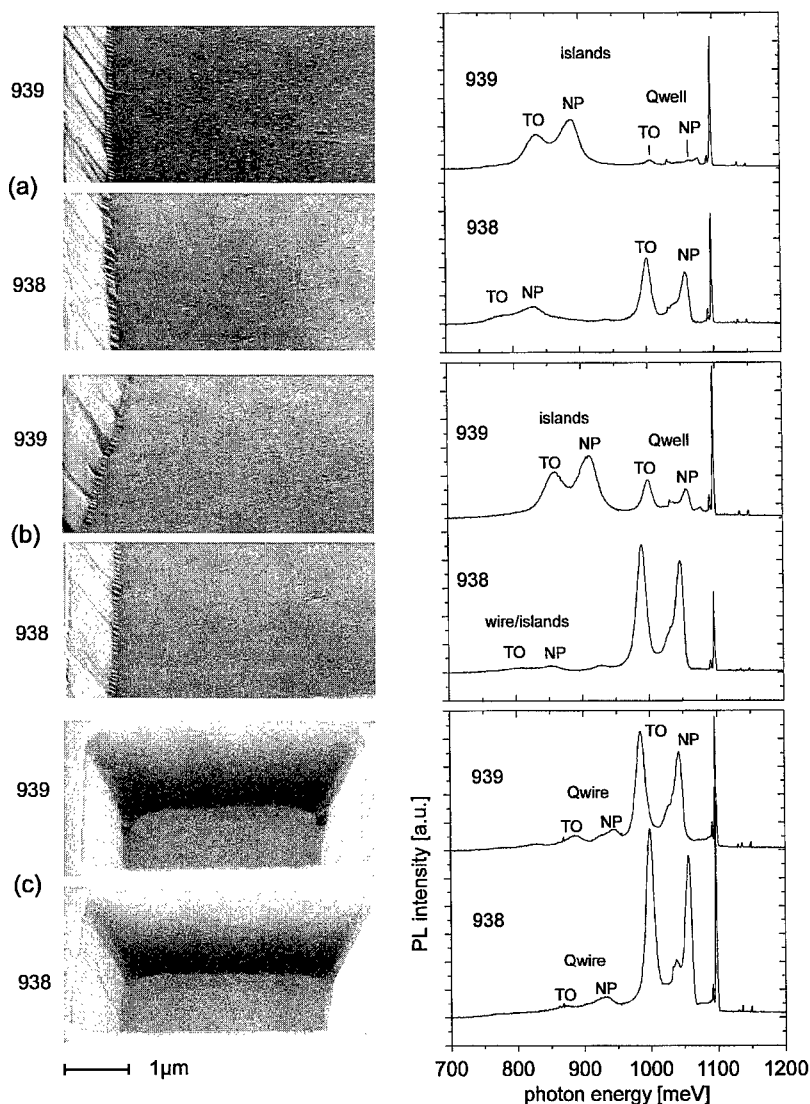


Fig. 6. Compilation of SEM pictures and PL spectra of (a) 100 μm , (b) 13 μm , and (c) 3 μm square structures comparing samples 939 (70% Ge, top) and 938 (100% Ge, bottom). SEM pictures have been taken at an angle of 70° for (a) and (b) and 60° for (c). PL spectra are recorded at 4 K and 50 mW laser power and drawn to the same scale.

tween the islands. The PL spectrum of sample 938, in contrast, shows quite prominent wetting layer transitions. The island transitions are found at lower energy compared to those of sample 939, implying a higher Ge content and/or thickness. Their intensity is lower due to the lower island density ($5.5 \mu\text{m}^{-2}$).

The differences in surface diffusion between pure and 70% Ge become most important in the case of the 13 μm square structures shown in Fig. 6(b).

While the (001) plane of sample 939 is still covered by a dense island population, sample 938 exhibits nearly no islands at all. This implies that the Ge depleted zones caused by the outdiffusion of Ge into the wire are already overlapping at a distance of 13 μm in the case of sample 938. The wires at the interfacet corners are still covered with islands. The size of the wire-islands in sample 938 is reduced in Fig. 6(b) compared to (a) due to the fact, that the Ge

supply zones of the four wires are overlapping. Once again, the difference in island coverage of the two samples is well represented by the PL intensities of the island related and the wetting layer related transitions.

Complete absence of islands can be observed in the 3 μm square structures of Fig. 6(c): neither the (001) plane nor the quantum wires exhibit islands. On this basis we can attribute the PL transitions on the lower energy side of the quantum well transitions to these homogenous wires. The absence of islands in small structures like those of Fig. 6(c) is also confirmed by CS-TEM pictures (e.g. Fig. 5). We estimate the wire thickness from such CS-TEM pictures to be approximately 10 nm.

Assuming a thickness of 10 nm and a homogeneous Ge distribution, a NP-PL energy of 930 meV for sample 938 results in a wire-Ge composition of only 31%. (This result is in agreement with recent EDX/STEM measurements.) Hence, the quantum wires contain a considerable amount of Si, even though Si was not supplied during growth. Since the top and the buried wire in Fig. 5 are of similar size and shape, we believe that also the top wire contains a considerable amount of Si. (Also this assumption is confirmed by EDX/STEM measurements.) Therefore a possible source for the Si incorporated into the wire can be the Si buffer underneath. The total amount of Si in the wire is approx. equal to the amount present in a one monolayer (ML) thick and 2 μm wide slab of Si. Such a small amount of Si could be supplied by segregation or intermixing from the Si layer underneath the Ge, considering the small quantity of Ge (~ 7 ML) deposited. Such a mechanism could explain the pronounced gradient in Ge content throughout the wire cross-section as observed by EDX (Fig. 4): as the wire grows thicker, less Si will be present at the growth front and the Si concentration incorporated into the wire decreases.

5. Conclusions

SiGe QWRs of approximately 30 nm lateral width have been fabricated by selfordered growth on non-planar substrates. They show strong PL at 37 K in spite of their low area coverage due to the efficient transport of excitons from the adjacent QWLs. The

energetic positions of the QWR PL transitions are in good agreement with results obtained from TEM and spatially resolved EDX. Both PL and EDX, therefore, lead to the astonishing result, that the Ge concentration in the wires is much lower than the nominal value from the epitaxy parameters. Even in experiments where only Ge was supplied during growth we find a Ge concentration as low as 31% in the quantum wire. This is in contrast to the fact that Si alone doesn't have the tendency to accumulate in convex corners. Comparison of growth experiments using 70% and pure Ge as quantum well material leads to the conclusion that the addition of a small amount of SiCl_2H_2 to the gas phase effectively reduces Ge surface diffusion. In these experiments it was possible to produce homogenous quantum wires of 10 nm thickness containing approximately 31% of Ge, as deduced from PL and TEM. This is a remarkable result since the critical thickness for island growth on 2D layers was found to be only 1.5–2 nm for 30% Ge and our growth conditions [12].

Acknowledgements

The authors would like to thank H.P. Bochem for the preparation of SEM pictures and K. Wambach for technical assistance.

References

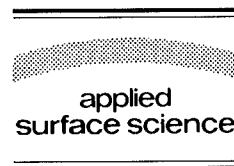
- [1] C. Weisbuch and B. Vinter, *Quantum Semiconductor Structures: Fundamentals and Applications* (Academic Press, San Diego, CA, 1991).
- [2] H. Sakaki, *Jpn. J. Appl. Phys.* 19 (1980) L735.
- [3] E. Kapon, in: *Semiconductors and Semimetals*, Vol. 40 (Academic Press, San Diego, CA, 1994) p. 259.
- [4] N. Usami, T. Mine, S. Fukatsu and Y. Shiraki, *Appl. Phys. Lett.* 63 (1993) 2789.
- [5] N. Usami, T. Mine, S. Fukatsu and Y. Shiraki, *Appl. Phys. Lett.* 64 (1994) 1126.
- [6] A. Hartmann, L. Vescan, C. Dieker and H. Lüth, *J. Appl. Phys.* 77 (1995) 1959.
- [7] A. Hartmann, L. Vescan, C. Dieker and H. Lüth, *Mater. Sci. Technol.* 11 (1995) 410.
- [8] U. Bangert, A.J. Harvey, R.J. Keyse, C. Dieker and A. Hartmann, *Proc. Royal Microscopical Society Conference on Microscopy of Semiconducting Materials*, to be published (1995).
- [9] C. Dieker, A. Hartmann, U. Bangert, W. Jäger, L. Vescan

- and H. Lüth, Proc. Royal Microscopical Society Conference on Microscopy of Semiconducting Materials, to be published (1995).
- [10] A. Hartmann, C. Dieker, R. Loo, L. Vescan, H. Lüth and U. Bangert, Appl. Phys. Lett. 67 (1995) 1888.
- [11] D.J. Eaglesham and M. Cerullo, Phys. Rev. Lett. 64 (1990) 1943.
- [12] L. Vescan, W. Jäger, C. Dieker, K. Schmidt, A. Hartmann and H. Lüth, Mater. Res. Soc. Symp. Proc. 263 (1992) 23.



ELSEVIER

Applied Surface Science 104/105 (1996) 510–515



AFM and RHEED study of Ge islanding on Si(111) and Si(100)

Peter W. Deelman^a, Thomas Thundat^b, Leo J. Schowalter^{a,*}

^a Department of Physics and Center for Integrated Electronics and Electronics Manufacturing, Rensselaer Polytechnic Institute, Troy, NY 12180, USA

^b Oak Ridge National Laboratory, P.O. Box 2008, Oak Ridge, TN 37831, USA

Received 28 June 1995; accepted 26 September 1995

Abstract

Strain relaxation and clustering of Ge thin films grown on Si(111) and Si(100) by molecular beam epitaxy (MBE) have been studied in situ with reflection high energy electron diffraction (RHEED) and analyzed by atomic force microscopy (AFM) and Rutherford backscattering spectrometry (RBS). At low temperature, growth is dominated by island nucleation and by strain relief through island formation. The cluster size distribution (measured by AFM) just after the 2D–3D growth mode transition is broader than that for ‘late-stage’ growth (when diffusion gradients dominate cluster growth) and is well fit by a model in which the surface diffusion of adatoms is described by a random walk. At high temperature, growth is dominated by dislocation formation and the aspect ratio of the islands changes. The barrier to dislocation formation is reduced at step bunches; thus, islands nucleate preferentially at the step bunches and grow along them. By understanding Ge island nucleation and evolution, we hope to grow a population of uniformly-sized nanocrystals exhibiting quantum confinement effects.

1. Introduction

The growth of Ge on Si, primarily Si(100), has been widely studied over the last few years, and the growth mode is known to be Stranski–Krastanov [1–3]. That is, initially, Ge wets Si (we will consider only the (111) and (100) surfaces). However, due to the 4% lattice mismatch between Ge and Si, the Ge film is subjected to a bilateral, compressive stress, and the resulting strain energy grows linearly with the thickness of the Ge film. At some ‘critical thickness’, it is energetically favorable for the film to

relieve strain by roughening and/or by creating dislocations [4–6]. Impinging adatoms attach preferentially to these strain-relieved locations and subsequent growth will proceed with the evolution of these islands. The spontaneous formation of these islands, requiring no artificial patterning or lithography, is termed ‘self-assembly’. Our goal is to exploit the self-assembly of Ge islands during MBE growth to form nanocrystals exhibiting three-dimensional, quantum-confinement effects, as other researchers have done for InGaAs/GaAs [7]. The challenge is to use thermodynamics and kinetics to control the nanocrystal sizes and size distributions. Toward that end, we have studied strain relaxation as a function of film thickness for Ge/Si(111) and Ge/Si(100) at different temperatures. We have also attempted to

* Corresponding author. Tel.: +1-518-2766435; fax: +1-518-2768761; e-mail: schowalt@unix.cie.rpi.edu.

understand the island size distributions of those films within the context of a cluster growth theory.

2. Experiment

Samples were grown on 100 mm Si(111) and Si(100) wafers in a VG V90S MBE system with a base pressure less than 5×10^{-11} mbar. The system was equipped with electron-beam-heated hearths for Si and Ge evaporation. Deposition rates were controlled by Inficon rate monitors (calibrated using RBS measurements) [8]. RHEED was used for in situ studies of growth and RHEED images were captured using a PC-controlled CCD camera [9].

The wafers used were on-axis $\pm 0.5^\circ$. We also used Si(111) wafers intentionally misoriented $2.85^\circ \pm 0.05^\circ$ toward the (110) direction, as determined from RBS channeling measurements [8]. Prior to growth, the wafers were subjected to a standard RCA chemical clean to remove any residual organic impurities or metal contaminants and were immediately loaded into the MBE system [10]. They were then heat-cleaned at a substrate temperature of 900°C to desorb the relatively volatile SiO_x surface layer and exhibited sharp 7×7 or 2×1 RHEED patterns at the subsequent growth temperatures. Si buffer layers, approximately 200 Å to 300 Å thick, were grown at 700°C at a rate of 1.0 Å/s just prior to Ge deposition. Ge was deposited at rates between 0.02 Å/s and 0.05 Å/s (rates were controlled within $\pm 0.005 \text{ Å/s}$) and at substrate temperatures between 400°C and 700°C while the RHEED pattern of the growth front was monitored.

3. Lattice relaxation at high and low temperatures

Apparent changes in the in-plane lattice constant were determined by measuring changes in the distance between the $(\bar{1}1)$ and $(1\bar{1})$ RHEED spots of the Ge lattice during the epitaxial Ge growth. Initially, the Ge epitaxy is expected to be pseudomorphic and the Ge film to be compressively strained (in the plane parallel to the surface) in order to match the Si lattice constant. Thus, one would expect to see no change in surface lattice constant (from that of Si) during the initial stages of growth. When islands

begin to form, however, the material near the tops of the islands will begin to relax toward the bulk Ge lattice parameter. The RHEED beam, which has an effective penetration depth of 10 Å, samples this material [9]. The contribution to the RHEED pattern of the unrelaxed, Stranski–Krastanov layer between the islands is difficult to quantify; however, we expect that layer to be substantially ‘shadowed’ by the islands, which are already 30–40 Å taller than the wetting layer after 3.4 ML of deposition.

Thus, as the islands begin to relax, the corresponding diffraction pattern will begin to indicate an increase in the in-plane lattice constant, because the spacing between diffraction spots will decrease. In addition, transmission electron diffraction spots should appear as a portion of the RHEED beam passes through the bodies of the islands. Eventually, the material sampled by the RHEED beam will have fully relaxed, and the RHEED pattern will be 4% narrower than that for the bare Si substrate.

For growth of Ge/Si(111) at 450°C , we observe the in-plane lattice constant to remain essentially that of the underlying Si substrate until a ‘critical thickness’ of $2.5 \text{ ML} \pm 0.1 \text{ ML}$, when the apparent lattice constant begins to increase (see Fig. 1). This thickness corresponds to a critical thickness for islanding and we observe the appearance of transmission electron diffraction features in the RHEED pattern. After

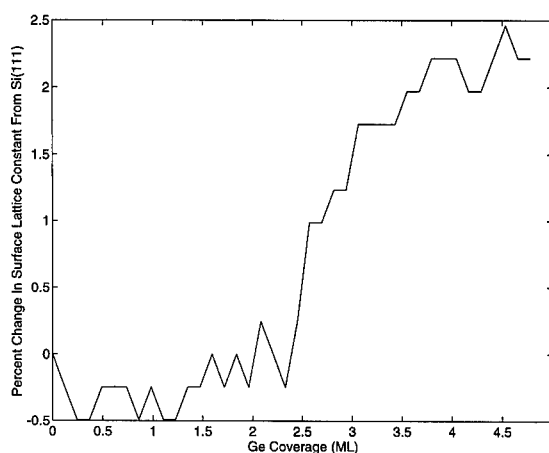


Fig. 1. Apparent relaxation of the surface lattice constant of Ge/Si(111) at 450°C as determined from the decrease in spacing between $(\bar{1}1)$ and $(1\bar{1})$ RHEED spots. Appreciable strain remains after 5 ML.

deposition of 5 ML of Ge, the material sampled by the RHEED beam is still somewhat strained, having an apparent lattice parameter only $2.3 \pm 0.5\%$ greater than that of Si. For growth of Ge/Si(111) at 700°C , however, transmission diffraction features did not appear even after the deposition of 109 Å of Ge, despite the fact that atomic force microscope images show broad ($\sim 1 \mu\text{m}$), flat islands. A RHEED study of the evolution of the in-plane lattice parameter suggests no relaxation (to within $\pm 0.5\%$) occurs even after 6 ML of growth.

We interpret these RHEED results in the context of a model in which the aspect ratio (height/width) of the Ge islands is different for the two temperature regimes. At low temperatures, dislocations have difficulty forming, and, once islanding begins, impinging adatoms will attach preferentially to the tops of the islands to minimize strain energy. Atomic force microscope images of samples, which were quenched soon after the islanding transition, confirm that the island aspect ratios are as high as ~ 0.07 in this regime, with at least 30% of the material in the islands more than 7 ML above the two-dimensional wetting layer.

For a comparable Ge coverage grown at 350°C , Voigtländer et al. measured island aspect ratios on the order of 0.13 using STM [6]. With increasing coverage, they found the aspect ratio decreased, which they interpreted in terms of a transition from coherent to dislocated 3D islands. That we see lower-aspect-ratio islands for a comparable coverage may result from a decreased barrier for dislocation formation at our somewhat higher growth temperatures. Finally, we note that other studies have found Ge islands grown on Si(111) to have (113) facets [3,6]. Although many of the AFM images of the islands seemed to suggest that they were faceted, we were not able to confirm that the facets were (113) or, perhaps, some shallower-angle facet.

A recent STM study of Ge island relaxation on Si(111) (Theiss et al.) found a three-stage relaxation of the surface lattice constant: as islands grew from 0 to 50 ML tall, the lattice constant increased from the bulk Si value to the bulk Ge value (sometimes even exceeding it); as the islands grew from 50 to 80 ML tall, the lattice constant decreased by 2%; afterwards, the lattice constant gradually relaxed to the bulk Ge value [11]. The islands in our growths were typically

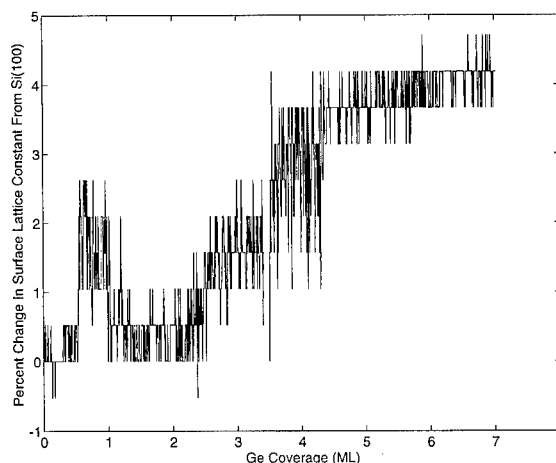


Fig. 2. Apparent relaxation of the surface lattice constant of Ge/Si(100) at 450°C as determined from the decrease in spacing between $(\bar{1}1)$ and $(1\bar{1})$ RHEED spots. The film appears relaxed after ~ 6 ML.

10 ML tall, so we are unable to confirm the existence of a three-stage relaxation. However, for islands 10 ML tall, Theiss et al. found a 2% relaxation of the surface lattice constant, in agreement with our RHEED measurements.

At high temperatures, dislocations may form much more easily and islands grow very rapidly in width as adatoms attach preferentially to their sides [12]. The islands are broad and flat so the 14 keV electrons continue to reflect and diffract off the surface of these islands. Moreover, the strain in the islands is apparently more uniformly distributed over the height of the islands. The material near their tops, which the RHEED beam samples, approaches the bulk Ge lattice constant much more slowly than the Ge near tops of the large-aspect-ratio islands which are observed at the lower growth temperatures.

For growth of Ge/Si(100) at (450°C), we observed similar results to those of Ge/Si(111) at the same temperature, except that the in-plane lattice constant appears to have relaxed to that of bulk Ge after deposition of the equivalent of only ~ 6 ML of Ge (see Fig. 2). Unlike the case of Ge/Si(111), for Ge/Si(100) growth at 700°C transmission diffraction features appear after only 1.7 ± 0.1 ML of Ge growth, suggesting that the critical thickness for islanding is smaller in this temperature regime than at 450°C . RHEED measurements of the in-plane lattice param-

eter, however, indicate no relaxation occurs even after 3 ML of growth. These results tend to suggest that, although strain-relieving islands with relatively large aspect ratios have formed, the majority of the material which the RHEED beam is sampling remains highly strained. However, a detailed model of this behavior is not available at present.

Finally, the role of the barrier to dislocation formation in the nucleation and evolution of islands is exemplified by growth on vicinal substrates. On Si(111) wafers misoriented toward the (110) direction, Si tends to form step bunches, at which Ge islands nucleate and along which the islands grow. Therefore, the density of nucleation is much higher than on exactly-oriented substrates, and coalescence occurs at lower surface coverages. Even at moderate temperatures (500°C), AFM images show islands coalesced before they produced transmission diffraction spots in RHEED (after deposition of ~ 7 ML).

4. Cluster size distributions

We have analyzed the island size distribution which resulted during the deposition of 3.4 ML of Ge on Si(111) at 450°C (Fig. 3) within the context of the Ostwald ripening of clusters [13]. Within that model, which, strictly speaking, only describes mass-conserved systems, the average cluster radius grows as

$$r_c(t) = r_c(0)(1 + t/\tau_c)^{1/(m+2)}, \quad (1)$$

where τ_c is a characteristic time and m depends on the dimensionality of the system (that is two-dimensional or three-dimensional islands — based on AFM images, we need only consider the latter here) and the process limiting the mass transport (for example, surface diffusion or the kinetic barrier for atoms to detach from islands). For ‘late-stage’ growth, when surface diffusion gradients have developed and dominate cluster growth, $m = 2$. However, in the transient, ‘non-steady-state’ regime, prior to the establishment of gradients, surface diffusion is properly modeled as a random walk and $m = 1$. Theoretically, $m = 1$ is also appropriate for a system in which the rate of mass transport is limited by the kinetic barrier for atoms to detach from islands. For the systems under consideration here, however, surface diffusion has been shown to be the process limiting mass transport [14].

For both $m = 1$ and $m = 2$, the distribution of cluster sizes has been calculated [13]. As shown in Fig. 4, our data is well-fit by the distribution predicted for the $m = 1$ regime, indicating diffusion gradients had not yet been established before sample growth was stopped (and the sample quenched to room temperature). In this case ($m = 1$), the theoretical distribution $n(\rho)$ is given by

$$n(\rho) = \rho^2 \left(\frac{3}{3 + \rho} \right)^{7/3} \left(\frac{-3/2}{\rho - 3/2} \right)^{11/3} e^{(\rho/(\rho - 3/2))}, \quad (2)$$

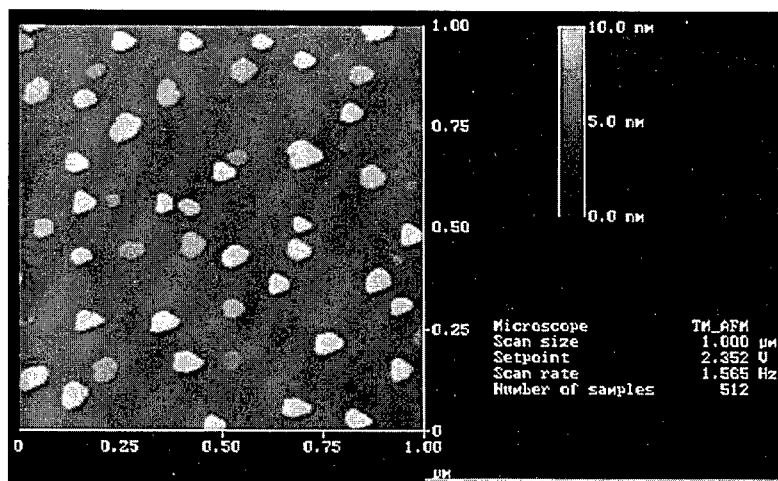


Fig. 3. Atomic force microscope image of 3.4 ± 0.1 ML of Ge/Si(111) grown at 450°C at 0.02 \AA/s .

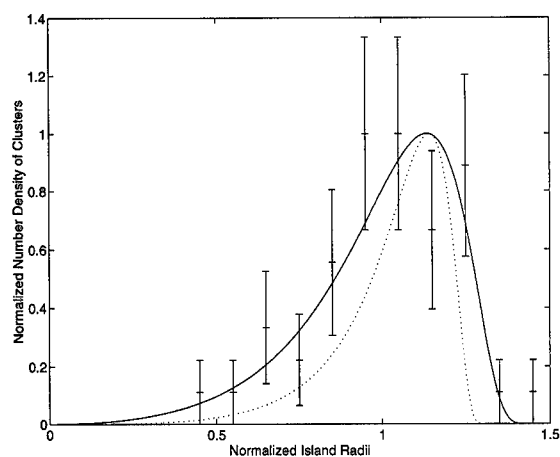


Fig. 4. Island size distribution for 3.4 ± 0.1 ML of Ge/Si(111) grown at 450°C at 0.02 \AA/s . The solid line is a theoretical prediction for a regime in which surface diffusion is described by a random walk ($m=1$); the dotted line is the prediction for a regime in which cluster growth is dominated by surface diffusion gradients ($m=2$). The island radii are normalized to the mean island radius (245 \AA), and the number densities are normalized to the maximum density (9 islands in the observation area of $1 \mu\text{m}^2$).

for ρ less than or equal to $3/2$, where ρ is the actual cluster radius normalized to the average cluster radius ρ_c . Even in mass-conserved systems, for which the Ostwald ripening model was developed, diffusion gradients develop only after a period of island nucleation and initial growth. The deposition rate in our experiment may have been large enough such that diffusion gradients would not develop and that a regime in which surface diffusion is described as a random walk indeed represents the ‘steady state’, or, at least, that such gradients would require a longer period to develop. A recent estimate of the limit of applicability of the Ostwald-ripening model to non-zero deposition rates for Ge/Si(100) at 650°C suggests the model is appropriate for deposition rates on the order of $5 \times 10^{-13} \text{ cm}^{-2} \text{ min}^{-1}$ [15]. This estimate is approximately an order of magnitude less than the rates used in our experiments. Nevertheless, the island size distribution predicted for the $m=1$ regime seems to fit our data well, which may indicate that the Ostwald ripening model is extendible to higher deposition rates.

5. Conclusions

We observe a transition in the islanding behavior of Ge thin films from low temperature to high temperature regimes. At low temperature, the islands have a relatively high aspect ratio which permits transmission diffraction and strain is non-uniformly distributed over the height of the island — highly strained at the base and relatively relaxed at the top. Ge films seem to relax more quickly on Si(100) than on Si(111), although, on both surfaces, transmission diffraction features appear after 2.5 ML coverage with a simultaneous initiation of relaxation. At high temperatures (more than 600°C), Ge grown on Si(111) forms flat, low-aspect-ratio islands that permit no transmission electron diffraction. Strain appears to be more uniformly distributed throughout the thin island’s height, which results in a slower apparent relaxation rate as a function of thickness when measured by RHEED. On the other hand, Ge grown on Si(100) at high temperature produces islands that permit transmission diffraction at a smaller ‘critical thickness’ than that at low temperature, but without a simultaneous relaxation of the surface lattice constant.

The island size distribution we measure for low temperature growth is accurately fit by the Ostwald theory of cluster growth, although that model was developed for mass-conserved systems. The model indicates that we are in a ‘non-steady-state regime’ in Ostwald ripening, where surface diffusion is described as a random walk, rather than a ‘late-stage’ regime, in which diffusion gradients would dominate cluster growth. Perhaps the deposition rate of Ge prevents surface diffusion gradients from developing. Finally, when grown on vicinal substrates with step bunches, Ge islands nucleate at the bunches, where the barrier to dislocation formation is lower, and grow along them. This process keeps the island aspect ratio rather small and the islands coalesce even before producing transmission diffraction features in RHEED.

Acknowledgements

The National Science Foundation is acknowledged for support of this work.

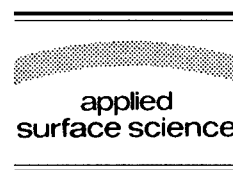
References

- [1] H.-J. Gossmann and L.C. Feldman, *Appl. Phys. A* 38 (1985) 171.
- [2] P.W. Deelman, T. Thundat and L.J. Schowalter, *Mater. Res. Soc. Symp. Proc.* 358 (1995).
- [3] P.M.J. Maree, K. Nakagawa, F.M. Mulders and J.F. van der Veen, *Surf. Sci.* 191 (1987) 305.
- [4] D.J. Eaglesham and M. Cerullo, *Phys. Rev. Lett.* 64 (1990) 1943.
- [5] C.W. Snyder, B.G. Orr, D. Kessler and L.M. Sander, *Phys. Rev. Lett.* 66(23) (1991) 3032.
- [6] B. Voigtlander and A. Zinner, *Appl. Phys. Lett.* 63 (1993) 3055.
- [7] D. Leonard, M. Krishnamurthy, C.M. Reaves, S.P. Denbars and P.M. Petroff, *Appl. Phys. Lett.* 63 (1993) 3203.
- [8] W.K. Chu, J.W. Mayer and M.A. Nicolet, *Backscattering Spectrometry* (Academic Press, New York, 1978).
- [9] E. Bauer, in: *Techniques for the Direct Observation of Structure and Imperfections*, Ed. R.F. Bunshah, *Techniques of Metals Research*, Vol. 2 (Interscience, New York, 1969) ch. 15, pp. 501–558.
- [10] W. Kern, *RCA Eng.* 28 (1983) 99.
- [11] S.K. Theiss, D.M. Chen and J.A. Golovchenko, *Appl. Phys. Lett.* 66 (1995) 448.
- [12] F.K. LeGoues, M.C. Reuter, J. Tersoff, M. Hammar and R.M. Tromp, *Phys. Rev. Lett.* 73 (1994) 300.
- [13] M. Zinke-Allmang, L.C. Feldman and M.H. Grabow, *Surf. Sci. Rep.* 16 (1992) 377.
- [14] L.C. Feldman and M. Zinke-Allmang, *J. Vac. Sci. Technol. A* 8 (1990) 3033.
- [15] M. Zinke-Allmang, L.C. Feldman, S. Nakahara and B.A. Davidson, *Phys. Rev. B* 39 (1989) 7848.



ELSEVIER

Applied Surface Science 104/105 (1996) 516–521



Surface and subsurface imaging of indium in InGaAs by scanning tunneling microscopy

M. Pfister^{a,b,*}, M.B. Johnson^{a,1}, S.F. Alvarado^a, H.W.M. Salemink^a, U. Marti^b,
D. Martin^b, F. Morier-Genoud^b, F.K. Reinhart^b

^a IBM Research Division, Zurich Research Laboratory, 8803 Rüschlikon, Switzerland

^b Institut de Micro- et Optoélectronique, Ecole Polytechnique Fédérale, 1015 Lausanne, Switzerland

Received 28 June 1995; accepted 10 October 1995

Abstract

Investigating the ternary $\text{In}_x\text{Ga}_{1-x}\text{As}$ alloy ($x \sim 12\%$) by cross-sectional scanning tunneling microscopy, we find that on the UHV-cleaved (110) surface the In distribution in both the surface and the first subsurface layer can be atomically resolved in the empty- and filled-state images, respectively. This is found to be mostly a geometric effect due to the larger size of the In. We apply this method to study the incorporation of In during the growth of $\text{In}_{0.12}\text{Ga}_{0.88}\text{As}$ quantum wires on nonplanar substrates. Strong In segregation in the growth direction is seen in the structure, and we compare the incorporation profiles across the quantum wire and a planar quantum well. No In clustering beyond the statistical expectation is observed.

1. Introduction

Cross-sectional scanning tunneling microscopy (XSTM) on (110)-cleaved III–V heterostructures has been demonstrated in recent years to be a powerful characterization tool for the atomic-scale investigation of such structures [1a] (for a review see [1b]). In this contribution we use XSTM to characterize InGaAs quantum wires (QWR) embedded in AlAs/GaAs short-period superlattices (SL). Dense arrays of such QWRs can be used as the active material in a variety of future optoelectronic devices,

where the 1D density of states of the QWR is expected to lead to improved device performance. The growth by molecular beam epitaxy (MBE) on prepatterned substrates is a successful method to obtain defect-free wires [2]. It relies on the different mobilities and incorporation rates on the nonplanar growth surface of the group-III species. Certain consequences, such as the formation of a vertical quantum well (QW) due to lateral variations of the Ga concentration in an AlGaAs barrier, might not be desired. On the other hand, lateral variation of the In incorporation in an InGaAs QWR, notably a higher In concentration at the center of the QWR at the bottom of the V-groove, would result in a higher 2D confinement potential. This quantitative information is difficult to obtain by conventional means such as transmission electron microscopy or secondary ion mass spectroscopy.

* Corresponding author. Present address: Beckman Institute, University of Illinois, Urbana, IL 61801, USA.

¹ Present address: Department of Physics and Astronomy, University of Oklahoma, Norman, OK 73072, USA.

In this work, the incorporation of In during the growth of InGaAs QWRs is studied by imaging individual In atoms in the cross-sectional surface [3]. We show that In atoms can be atomically resolved not only in the cross-sectional surface layer, but also in the *first subsurface layer*. The contrast mechanism, which we argue is predominantly geometric here, will be discussed. The measured In distribution clearly reveals In segregation in the growth direction observed as a delayed incorporation at the GaAs/InGaAs bottom interface as well as In atoms segregating into the barrier material at the top interface. Finally, the substitutional In is found to be randomly distributed on the group-III sublattice, i.e. no short-range In clustering beyond the statistical expectation is observed.

2. Experiment

The sample discussed here consists of a series of InGaAs QWRs and planar control QWs. They are fabricated by MBE growth at a substrate temperature of 540°C over a V-groove-patterned GaAs n-type substrate. The substrate is patterned by holographic lithography and wet etching [4], resulting in V-grooves having side wall facets close to {311}B planes and a periodicity of 250 nm. The InGaAs layers are undoped because we wanted to avoid the imaging of dopant atoms [5], which would complicate the interpretation of the results. The InGaAs layers are embedded in 16 monolayers (ML) of GaAs and 8.5 periods of a Si-doped ($n = 5 \times 10^{17} \text{ cm}^{-3}$) (AlAs)₄(GaAs)₈ SL barrier. The QWR and QW layers nominally consist of 18 ML of In_xGa_{1-x}As, where $x = 12\%$. Growth was interrupted every 3 ML for 20 s to promote the formation of the crescent-shaped wire and to enhance the In concentration within the wire.

STM measurements were performed in ultrahigh vacuum (1×10^{-11} mbar) using electrochemically etched W tips. The sample is cleaved in situ to expose an atomically flat, electronically unpinned (110) surface. Images recorded with positive and with negative sample bias (sensitive to empty and filled surface states, respectively [6]) were acquired in a constant current mode.

3. Results and discussion

3.1. Contrast mechanisms

We start with a discussion of the contrast mechanisms in cross-sectional STM imaging of InGaAs and AlAs/GaAs structures. On the (110) surface of III–V semiconductors, the surface dangling bond states are located energetically outside the bulk band gap [7]. The tunneling current is therefore dominated by the bulk states to which a contribution from the surface states is superimposed [8].

Fig. 1a and b show empty-state (group-III-related) STM images of the cross section of an InGaAs QW and QWR, respectively, acquired with a positive sample bias of $V_s = +1.9$ V. Linecuts along the [001]-oriented atomic columns indicated are displayed in Fig. 1c. They show a slowly varying contribution from tunneling into the bulk states that are related to the electronic band structure of the subsurface heterostructure. The atomically resolved part from the empty surface states contains chemical information on a true atomic scale, as discussed in detail below [9].

The QWRs are formed by accumulation of the lower band-gap material at the bottom of the V-groove. They consist of sections of QWs having different thicknesses. The middle of the QWRs is thicker than the tapered QWs on the sidewalls of the structure and the planar reference QW. Therefore the lowest accessible state for electrons tunneling into the conduction band is *lower* in energy than that of the QWs, and more states are available for tunneling. This leads to the brighter appearance of the center of the QWR in a constant-current image such as the one shown in Fig. 1 and makes the lateral confinement of the QWR visible in the STM image. An enhanced In concentration in the InGaAs material would also reduce the band gap and make the QWR appear brighter, but such an enhancement is not present as discussed below.

The chemical information is contained in the atomically resolved contrast arising from the surface dangling bonds. Empty-state and filled-state images directly probe the energy and spatial extent of dangling bonds associated with group-III sites and of the As dangling bonds, respectively.

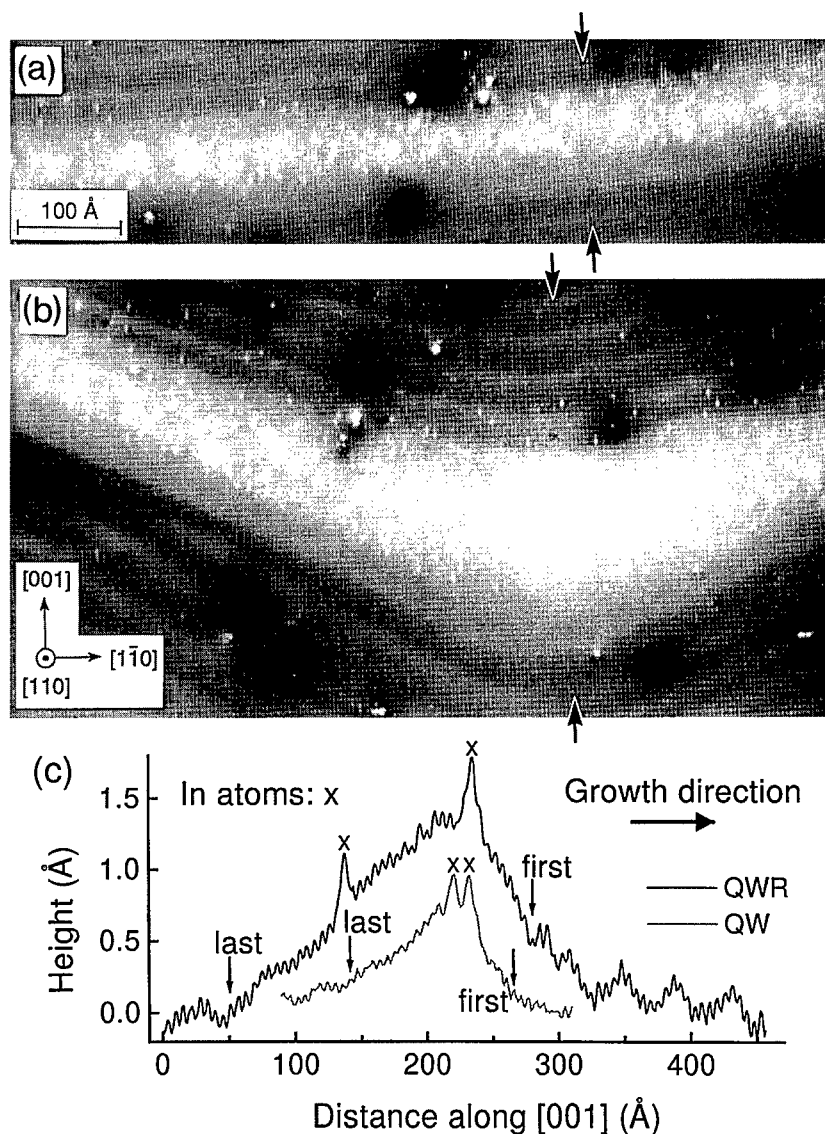


Fig. 1. Cross-sectional STM images of (a) an $\text{In}_{0.12}\text{Ga}_{0.88}\text{As}$ QW and (b) a QWR. Tunneling conditions: sample bias +1.9 V and tunneling current 40 pA. Individual In atoms appear as atomically sharp white dots. (c) Linecuts across the QWR and the QW along the [001] columns indicated in (a) and (b). 'First' and 'last' mark the start and end of the SL barriers.

Fig. 2a is an enlarged empty-state view of the center of the QWR for which the slowly varying background contrast has been removed, and Fig. 2b is the corresponding filled-state image (group-V-related) of the exact same area acquired with $V_s = -2.3$ V. (Although the two images were not taken simultaneously, it is possible to align them by adjusting the position of defects in the surface). In the empty-state image the atomically localized white

features correspond directly to In atoms in the surface layer. The filled-state image also shows atomically localized white features² having a density

² In the filled-state image in Fig. 2b, the white features appear slightly elongated due to the lack of atomic resolution in the [110] direction. In other filled-state images they clearly occupy only a single lattice site.

close to the nominal In concentration, but surprisingly the positions of the white features in the two images *do not correlate*. Only faint filled-state features correlate with the empty-state In positions as shown, for example, at 'A' in Fig. 2c, which displays linecuts along the same [110]-oriented zig-zag line. Inversely, faint empty-state double-site features also correlate with the filled-state white features as shown at 'B'. This observation suggests that the filled-state white features must themselves be independent In atoms, not in the surface, but in the first subsurface layer, where In is in the back-bond position below the imaged As sites. These In atoms are

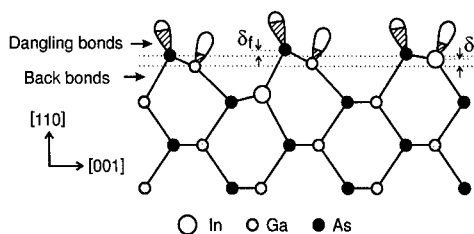


Fig. 3. Cross-sectional view of the InGaAs(110) surface. The larger In atoms induce the vertical displacements δ_e and δ_f seen in empty- and filled-state images, respectively.

located in the (001) ML that is normally not imaged when scanning on the (110) surface.

The situation is displayed in the schematic cross-sectional view of the surface in Fig. 3. The (110) surface of III–V semiconductors crystallizing in the zincblende structure relaxes by a bond rotation of the surface atoms known as 'buckling' [10]. Charge transfer from the group-III (Ga) dangling bond towards the group-V (As) dangling bonds leads to this energetically favorable configuration. As mentioned above, this shifts the empty and filled surface states into the conduction and the valence bands, respectively. There is consensus that the bond lengths are conserved during relaxation of this surface. More generally it is known that the Pauling covalent radii are a better parameter than ionicities to describe the surface structure [11]. Consequently we suggest the following picture of a place where an In atom is situated in the surface layer: The In atom has a covalent radius $\sim 0.2 \text{ \AA}$ larger than that of Ga and its position is slightly higher (δ_e) than the plane of the Ga surface atoms. Intimately connected to this geometric relaxation will be an electronic rearrangement that shifts the empty and filled dangling bonds in energy. This electronic change of the surface dangling bonds, however, seems to be small, as seen by the weak influence of a surface In on its two neighboring As atoms (label 'A' in Fig. 2). When an In atom is located in the back-bond position, the surface As above it is pushed out of its regular position by δ_f . Additionally the two Ga neighbors of the As also move slightly out of the surface (resulting in the double feature at label 'B'). At label 'C' in Fig. 2 there is an In atom in the surface layer about 1.5 lattice sites to the left of an In atom in the first subsurface layer. The resulting empty- and filled-state

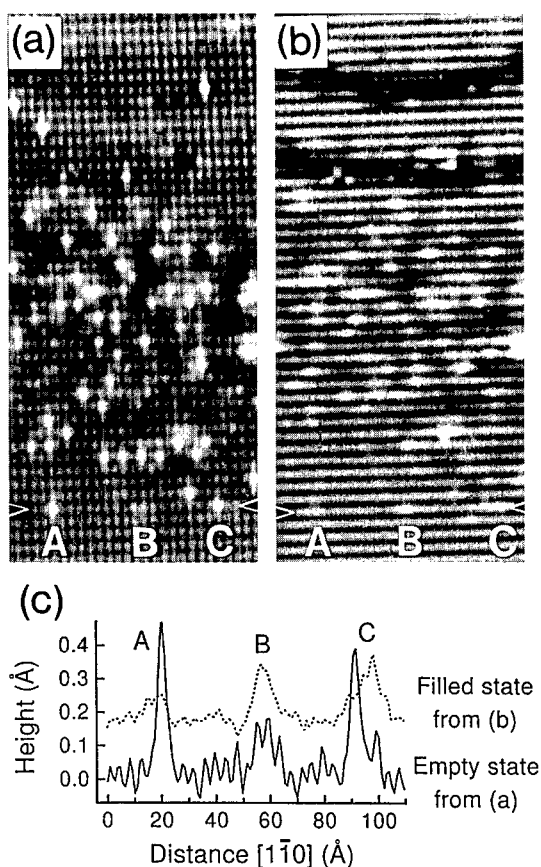


Fig. 2. In atoms in the surface and subsurface (110) layers, seen in (a) empty- and (b) filled-state images of exactly the same $112 \times 250 \text{ \AA}^2$ region of the QWR. The In distributions are random and uncorrelated. (c) Linecuts through the same atomic row (indicated in the images) showing a surface In, a subsurface In, and adjacent surface and subsurface In atoms, labeled A, B and C, respectively.

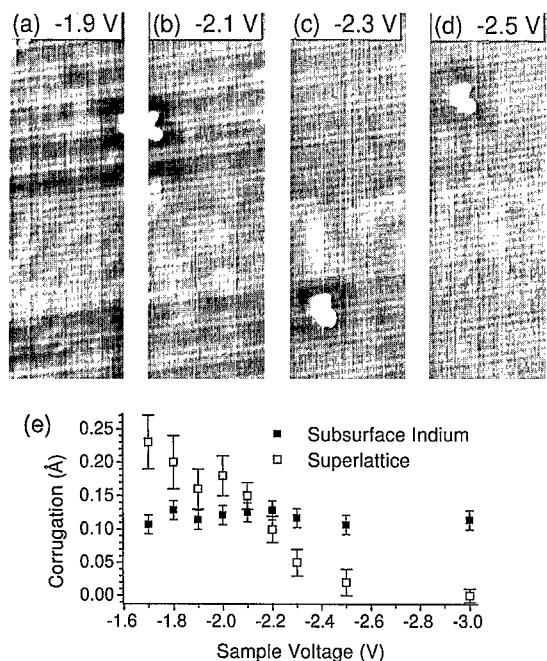


Fig. 4. (a–d) Spectroscopic imaging of an InGaAs QW and an AlAs/GaAs SL with the sample voltages indicated. (e) Corrugation versus sample voltage for the In atoms and for the SL. The In contrast is voltage independent.

traces are a superposition of the features observed at 'A' and 'B'.

Further evidence that the imaging of individual In atoms relies predominantly on the geometric effect comes from spectroscopic filled-state images. Fig. 4a–d are four such images taken from a different sample over a region having $(\text{AlAs})_4(\text{GaAs})_4$ SL barriers and a planar $\text{In}_{0.18}\text{Ga}_{0.82}\text{Al}$ QW acquired with sample voltages V_s between -1.9 and -2.5 V. Again, the slowly varying background of these images has been removed. Despite the slight noise in the data, one can make the following observation: The appearance of the white features corresponding to In atoms in the back-bond position below the imaged As atoms is quite independent of the tunnel voltage. If the contrast arose primarily because of the locally disturbed electronic configuration (changed As surface dangling and/or back bond), one would expect large changes in the corrugation of the features. As this is not the case (see also the data for a wider voltage range plotted in Fig. 4e) we conclude that this contrast is mostly geometric in nature. (Note that the changes in the tip-sample separation induced

by the different voltages are not expected to have a large effect on the geometric imaging.)

The appearance of the SL, on the other hand, changes strongly with increasing voltage. There the contrast between the two darker rows corresponding to 4 ML of AlAs and the two brighter rows corresponding to 4 ML of GaAs decreases rapidly with increasing sample bias. This is the expected spectroscopic behavior for an electronic contrast, because the energy difference between the two states matters less when it is small compared to the tip Fermi energy. It is difficult to say to what extent the SL contrast arises from surface states or from the 'bulk' (subsurface) energy bands. Note, however, that the appearance of the $(\text{AlAs})_4(\text{GaAs})_8$ SL in the empty-state images (Fig. 1 and top of Fig. 2a) is different from that observed in filled-state images (at the top of Fig. 2b and Fig. 4). Surprisingly, the layer contrast is much less distinct in the case where the surface Ga and Al atoms are imaged directly (empty-state images). We attribute this behavior to the fact that empty-state imaging involves the tunneling of electrons into conduction-band states having a much lower effective mass than the hole states in the valence band involved in filled-state imaging. These conduction-band states are therefore more delocalized in such a short-period SL and result in less distinct contrast.

3.2. In incorporation in InGaAs QWR

Having the ability to count In atoms in the group-III sublattice in the *first two (110)-oriented layers*, we can examine the incorporation of In with improved statistics. Here we show as an example the In concentration across the center of the QWR and across the QW plotted in Fig. 5 [12]. The histograms are the result of counting In atoms over a width of 20.0 nm (50 lattice sites) in the case of the QWR — a width over which the QWR does not 'bend' much — and over 40.0 nm (100 lattice sites) in the case of the QW. The darker shading indicates the ratio of In atoms counted in the filled-state images. A running average over five rows is also plotted. A comparison of the histograms of In incorporation reveals the following: (i) For both the planar reference QW and the (311)-V-groove QWR there is a maximum In concentration of $11.5 \pm 1.4\%$. The statistical error is

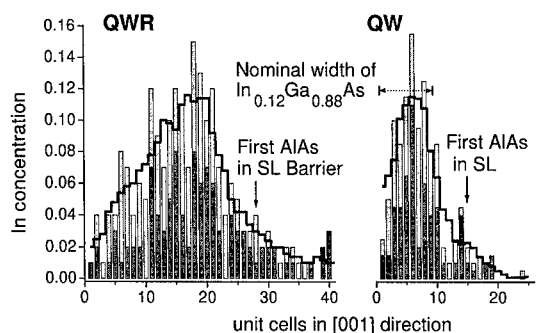


Fig. 5. Indium concentration profiles of the QWR and QW. Light and dark shading indicates the ratio of In atoms counted in the surface (empty-state data) and the first subsurface layer (filled-state data), respectively. The bold line is a running average over five rows. One unit cell in [001] direction is equal to 2 ML. From [12].

calculated for the averaged data, and systematic counting errors are assumed to be the same for the QW and the QWR regions. (ii) There is a marked difference in the buildup of the nominal In concentration in the planar and the nonplanar situations. This buildup occurs over about 6 ML, in the planar case (three imaged rows), but is significantly slower for the QWR. This difference is only partly due to the averaging over the slightly bent center of the QWR. The remaining difference means that, under the present growth conditions, there is initially more Ga incorporation at the bottom of the V-groove than in the planar case. Several explanations are possible for this observation, but they are beyond the scope of this paper. (iii) At the InGaAs/GaAs interface the In segregation continues after the In flow has been stopped [13]. For the data presented here, the growth of the (AlAs)₄ layers in the overlying SL shows no significant influence on In segregation.

The In is not clustered beyond statistical expectations [12]. This is in contrast to the data of Zheng et al. [3], who reported that the In in a GaAs/In_{0.2}Ga_{0.8}As/GaAs sample grown by MBE at the same growth temperature as here, but without the 20 s growth interruptions, exhibited strong preferential clustering in the [001] growth direction. We find a few larger clusters only in the filled-state measurement and for the horizontal [110] direction, which we attribute to the missing atomic resolution in this direction in the filled-state image. This sometimes makes it difficult to distinguish between, say, two In atoms and a cluster of three In atoms.

4. Conclusions

We have shown that, in the case of the ternary InGaAs material, STM empty- and filled-state images show the In distribution in the (110) surface and the first subsurface layer, respectively. Spectroscopic imaging revealed that the contrast mechanism is predominantly geometric. To within statistical error, we observe no preferential In incorporation in the crescent-shaped quantum wire at the bottom of the V-groove compared to a planar quantum well reference. Strong In segregation is seen into the superlattice barriers. The cluster size distribution shows that In is randomly distributed on the group-III sublattice.

Acknowledgements

We thank P. Silva and Y. Magnenat for assistance in sample preparation, as well as P. Blöchl and A. Baldereschi for valuable discussions. This work was supported in part by the Swiss Priority Program in Optics and the Swiss National Science Foundation, contract No. 21/34317.92.

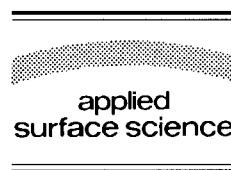
References

- [1a] O. Albrektsen, D.J. Arent, H.P. Meier and H.W.M. Salemink, *Appl. Phys. Lett.* 57 (1990) 31.
- [1b] R.M. Feenstra, *Semicond. Sci. Technol.* 9 (1994) 2157.
- [2] E. Kapon, *Optoelectronics* 8 (1993) 429.
- [3] J.F. Zheng, J.D. Walker, M.B. Salmeron and E.R. Weber, *Phys. Rev. Lett.* 72 (1994) 2414.
- [4] U. Marti, M. Proctor, D. Martin, F. Morier-Genoud, B. Senior and F.K. Reinhart, *Microelectron. Eng.* 13 (1991) 391.
- [5] M.B. Johnson, O. Albrektsen, R.M. Feenstra and H.W.M. Salemink, *Appl. Phys. Lett.* 63 (1993) 2923.
- [6] R.M. Feenstra, J.A. Stroscio, J. Tersoff and A.P. Fein, *Phys. Rev. Lett.* 58 (1987) 1192.
- [7] H. Carstensen, R. Claessen, R. Mancke and M. Skibowski, *Phys. Rev. B* 41 (1990) 9880.
- [8] R.M. Feenstra, *Phys. Rev. B* 50 (1994) 4561.
- [9] H.W.M. Salemink and O. Albrektsen, *Phys. Rev. B* 47 (1993) 16044.
- [10] A.R. Lubinsky, C.B. Duke, B.W. Lee and P. Mark, *Phys. Rev. Lett.* 36 (1976) 1058.
- [11] C.B. Duke, *J. Vac. Sci. Technol. B* 1 (1983) 732.
- [12] M. Pfister, M.B. Johnson, S.F. Alvarado, H.W.M. Salemink, U. Marti, D. Martin, F. Morier-Genoud and F.K. Reinhart, *Appl. Phys. Lett.* 67 (1995) 1459.
- [13] J. Massies, F. Turco, A. Salates and J.P. Contour, *J. Cryst. Growth* 80 (1987) 307.



ELSEVIER

Applied Surface Science 104/105 (1996) 522–528



Characterization of arsenide/phosphide heterostructure interfaces by scanning tunneling microscopy

A.Y. Lew, C.H. Yan, C.W. Tu, E.T. Yu *

Department of Electrical and Computer Engineering, University of California, San Diego, La Jolla, CA 92093-0407, USA

Abstract

We have used cross-sectional scanning tunneling microscopy (STM) to study interface structure in arsenide/phosphide heterostructures grown by gas-source molecular beam epitaxy. High-resolution images of a sample grown at 550°C and consisting of GaAs interrupted at 200 Å intervals with a 40 s P₂ flux reveal phosphide interlayers as wide as 30 Å and exhibiting lateral variations in structure over nanometer length scales. A similar sample grown at 450°C exhibits narrower interlayers and a lower level of phosphorus incorporation. Data obtained by STM have been corroborated by data from high-resolution X-ray diffraction (HRXRD) and reflection high-energy electron diffraction (RHEED) studies. Together, these studies provide direct information about nanometer-scale grading and lateral nonuniformity of interfaces that can occur under these growth conditions.

Arsenide/phosphide-based heterostructures have attracted wide interest for use in opto-electronic device applications. For example, InGaAs/InP structures lattice-matched to InP are of great importance for applications in photodiodes, modulators, and lasers operating at optical wavelengths near 1.55 μm [1–4]. However, arsenide/phosphide hetero-interfaces are extremely susceptible to atomic cross-incorporation and diffusion processes, particularly at higher growth temperatures. During growth of InGaP/GaAs heterostructures, for example, it has been shown that growth interrupts needed to switch the group V molecular beams at the hetero-interfaces can cause intermixing within the group V sublattice

and lead to surface roughness [5,6]. Arsenide/phosphide interface roughening has been observed in structures grown by a number of techniques including gas-source molecular beam epitaxy (GSMBE), [5–8] metalorganic molecular beam epitaxy (MOMBE), [9–11] and metalorganic vapor phase epitaxy (MOVPE) [12,13]. A detailed understanding of the atomic-scale structural and electronic properties of these interfaces is therefore essential in optimizing growth parameters for arsenide/phosphide heterostructure devices.

Scanning tunneling microscopy (STM) has emerged as a powerful tool for investigating the structural and electronic properties of semiconductor materials and devices at or near the atomic level because of its extremely high spatial resolution and its sensitivity to electronic properties of materials. Cross-sectional STM in particular has been used to study structural and electronic properties of epitaxi-

* Corresponding author. Tel.: +1-619-5346619; fax: +1-619-5342486; e-mail: ety@ece.ucsd.edu.

ally grown material and device structures in many different heterostructure material systems [14–23].

In this paper we describe cross-sectional STM studies of the dependence of interface structure on growth temperature in samples grown by GSMBE using AsH_3 and PH_3 sources cracked at 1000°C . Nominally identical samples were grown at substrate temperatures of 450°C and 550°C on exactly oriented (001) n-type GaAs substrates. After growing a 2000 Å GaAs buffer layer, a 25 period superlattice region was created by interrupting the growth of GaAs at 200 Å intervals with a 40 s P_2 flux, resulting in the formation of interlayers containing phosphorus. Specifically, after growth of GaAs, the Ga shutter was closed and the As shutter left open for 5 s to form a smooth growth surface. The As shutter was then closed, and a 3 s pause was introduced to evacuate the residual gas. The 40 s P_2 flux was then introduced to the system. After another 3 s pause to evacuate residual gas, As was reintroduced to the growth chamber. After 5 s, the Ga shutter was opened and GaAs growth resumed. Study of the compositional and structural properties of the interlayers should provide insight into the quality of arsenide/phosphide hetero-interfaces grown under similar conditions.

Samples grown for these STM studies were cleaved in an ultrahigh-vacuum STM system at a base pressure of $<2 \times 10^{-10}$ Torr to expose an atomically flat (110) cross-sectional surface of the epitaxial layers, on which STM measurements were performed. Commercially available Pt–Ir tips cleaned in situ by electron bombardment were used for these studies. STM data have been corroborated by high-resolution X-ray diffraction (HRXRD) and reflection high-energy electron diffraction (RHEED) studies. HRXRD was carried out with a double-crystal diffractometer using $\text{Cu K}\alpha_1$ radiation monochromated by four Ge (220) crystals. X-ray rocking curves were obtained from the (004) reflection of (001)-oriented samples.

Fig. 1(a) shows a high-resolution constant-current STM image of the sample grown at 550°C , obtained at a sample bias voltage of -2 V and a tunneling current of 0.1 nA. Since the image was obtained at negative sample bias, the features seen correspond to the group V sublattice on the cleaved (110) surface. [24] The uniform corrugations visible in the image

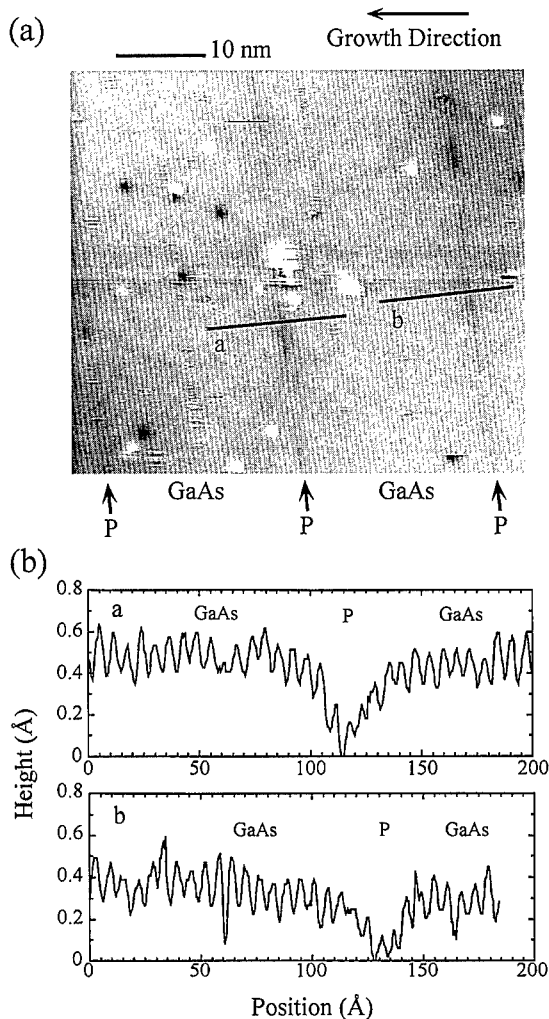


Fig. 1. (a) Constant-current image of the arsenide/phosphide heterostructure sample grown at 550°C , obtained at a sample bias of -2 V and a tunneling current of 0.1 nA. Phosphide interlayers appear as irregularly shaped regions between the GaAs layers. (b) Corrugation height profiles taken along the corresponding lines 'a' and 'b' are indicated in the image.

correspond to bilayers on the (110) surface. Contrast between the GaAs layers and the darker, irregularly shaped phosphide interlayers can clearly be seen. Such contrast is induced by differences in electronic features such as band offsets and carrier concentrations, rather than resulting from actual features in the physical topography of the cleaved sample. Specifically, the higher valence band edge energy of the phosphide layer compared to the GaAs layer results

in the darker appearance of the phosphide interlayers in the filled-state images. At the arsenide/phosphide interfaces, lateral variations in interface structure over nanometer length scales can be seen. Fig. 1(b) shows corrugation amplitude profiles obtained from the STM data, at the locations indicated by the corresponding lines in Fig. 1(a). The image and profiles show that the phosphide interlayers formed at 550°C can be as wide as 30 Å with an apparent difference in height, induced by changes in electronic structure, of up to 0.5 Å between the phosphide interlayers and the GaAs layers.

Fig. 2 shows a high-resolution constant-current image of a different portion of the sample grown at 550°C, obtained using a different Pt–Ir tip at a sample bias voltage of -2.5 V and a tunneling current of 0.1 nA. Though the image in Fig. 2 was obtained at a slightly different bias voltage than the image in Fig. 1(a), negligible differences in contrast were observed in images obtained from a given sample over this range of bias voltages. With this particular STM tip, individual GaAs bilayers are not as clearly seen as they are in Fig. 1(a); however, electronically induced contrast between the brighter GaAs layers and the darker phosphide interlayers is

still visible in the image. The growth direction of the sample is indicated in the figure. Closer inspection of Fig. 2 shows that the interfaces between GaAs layers and phosphide interlayers appear sharper at the top of the phosphide growth fronts (i.e., at the left-hand side of the interlayers shown in the image), and more diffuse at the bottom of the phosphide growth fronts. This suggests that at the locations of the P_2 growth interrupts, phosphorus at the surface diffuses downward into previously grown GaAs layers. If the phosphorus at the surface were to carry over into subsequently grown GaAs, then the tops of the phosphide growth fronts would be expected to appear diffuse as well. However, the STM images suggest that this process of phosphorus carry-over appears much weaker than the process of phosphorus diffusion into the material below.

Fig. 3(a) shows a constant-current image of the sample grown at 450°C, obtained at a sample bias voltage of -2.5 V and a tunneling current of 0.1 nA. As was the case in the comparison between Fig. 1(a) and Fig. 2, negligible differences in contrast were observed in images obtained from a given sample over bias voltages ranging from -2.5 V to -2.0 V. Electronically induced contrast between the

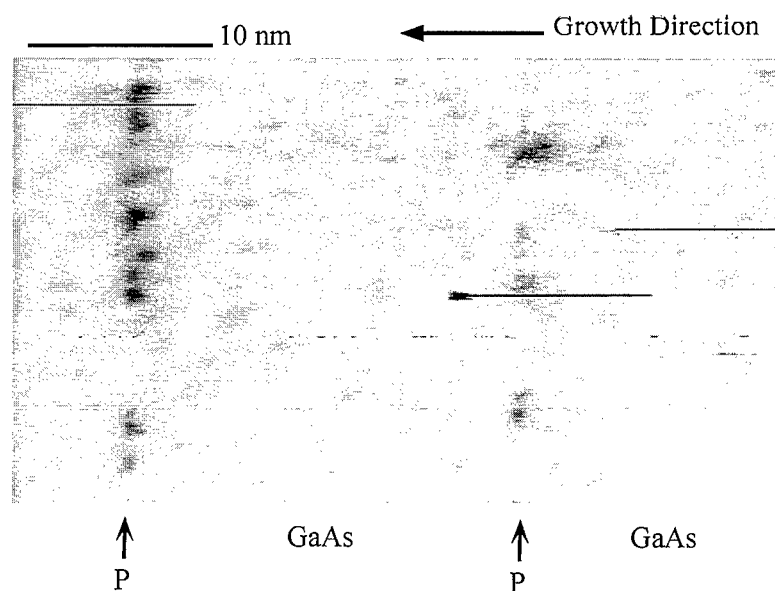


Fig. 2. Constant-current image of the arsenide/phosphide heterostructure sample grown at 550°C, obtained at a sample bias of -2.5 V and a tunneling current of 0.1 nA. Phosphorus at the growth surface appears to diffuse down into previously grown GaAs layers rather than carrying over into subsequently grown GaAs layers.

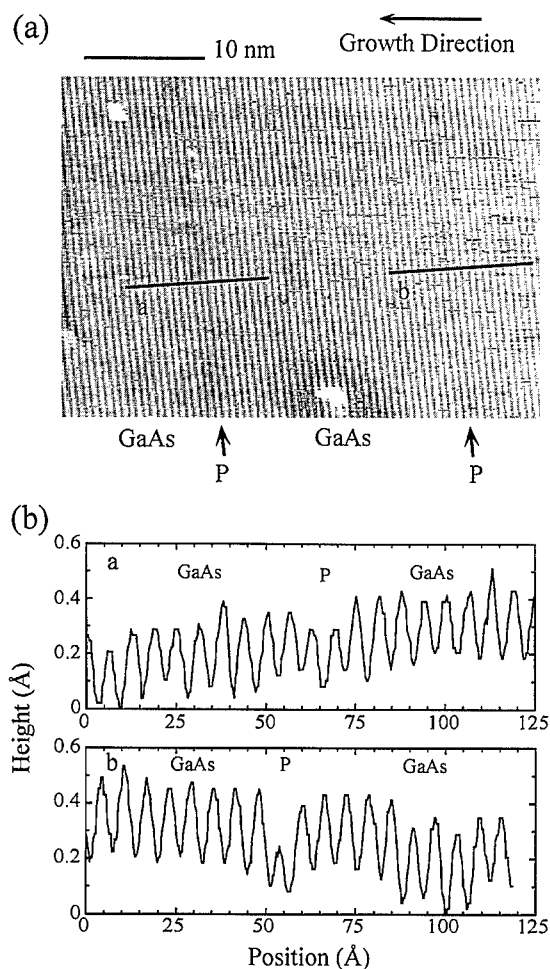


Fig. 3. (a) Constant-current image of the arsenide/phosphide heterostructure sample grown at 450°C, obtained at a sample bias of -2.5 V and a tunneling current of 0.1 nA. Phosphide interlayers are clearly narrower than those found in the sample grown at 550°C. (b) Corrugation height profiles taken along the corresponding lines 'a' and 'b' are indicated in the image.

GaAs layers and the phosphide interlayers is still visible in the image. This contrast is smaller than that observed in images of the sample grown at 550°C, suggesting differences in electronic structure of the phosphide interlayers between the two samples. The image shows that the interlayers are clearly narrower in width than those found in the sample grown at 550°C. Fig. 3(b) shows corrugation amplitude profiles obtained from the STM data at the locations indicated by the corresponding lines in Fig. 3(a). The profiles confirm that at 450°C the phos-

phide interlayers are narrower in width and exhibit smaller corrugation amplitudes, reflecting a lower level of phosphorus incorporation.

Data obtained by STM have been corroborated by high-resolution X-ray diffraction and reflection high-energy electron diffraction experiments. Fig. 4 shows X-ray rocking curves obtained from the samples. The large peak to the right of the substrate peak in both plots is attributed to a combination of the zeroth-order superlattice peak and a peak corresponding to the initially grown buffer layer. Since both arsine and phosphine are injected into the same cracker during growth, there is a background incorporation in the buffer and superlattice regions of residual phosphorus from previous growth runs [25]. Closer analysis of this peak leads to a determination

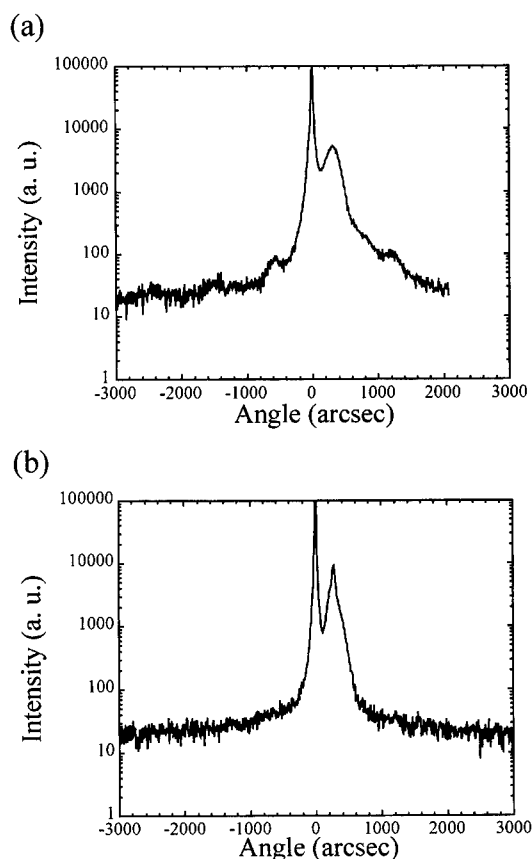


Fig. 4. High-resolution X-ray diffraction (HRXRD) spectra of the sample grown: (a) at 550°C and (b) at 450°C. The spectrum for the sample grown at 550°C shows stronger satellite peaks, indicating the presence of a more pronounced periodic structure.

of a background phosphorus level of approximately 3%. Superlattice peaks arising from the periodic interlayer structure are also visible in the spectra. The rocking curve from the sample grown at 550°C, shown in Fig. 4(a), shows stronger satellite peaks than the rocking curve from the sample grown at 450°C, shown in Fig. 4(b), indicating the presence of a more pronounced periodic interlayer structure in the sample grown at higher temperature. By measuring the spacing between the satellite peaks visible in the spectrum of the sample grown at 550°C, the period of the superlattice structure is calculated to be approximately 210 Å. For the sample grown at 450°C, the presence of only very weak satellite peaks in the X-ray diffraction spectrum is indicative of a lower level of phosphorus incorporation in the interlayers, which is consistent with the data obtained by STM.

RHEED patterns obtained during the growth of both samples show changes in the surface reconstruction immediately after the growth of GaAs is halted and the surface exposed to a P_2 flux. At 550°C the reconstruction changes from 2×4 to 2×3 , indicating the presence of a phosphorus-stabilized surface. The 2×3 surface reconstruction remains stable under the subsequent group V change from P_2 to As_2 , and changes back to the 2×4 state only when the growth of GaAs is resumed. The change in reconstruction from the 2×3 to the 2×4 state occurs over an interval of 1–2 s. At 450°C the surface reconstruction changes from 2×2 to 2×3 after the surface is exposed to a P_2 flux, again indicating the presence of a phosphorus-stabilized surface. The surface reconstruction then changes back to the 2×2 state immediately upon resumption of the As_2 flux, but before GaAs is grown. The longer switching time from a phosphorus-stabilized surface to an arsenic-stabilized surface at higher substrate temperatures has significant implications for arsenide/phosphide heterostructure materials and devices grown under similar growth conditions.

RHEED patterns at both temperatures under the 40 s P_2 flux remained streaky throughout sample growth, indicating that a flat growth surface is maintained. Fig. 5 shows RHEED patterns observed in samples grown with longer P_2 growth interruptions. All patterns were obtained for the $[1\bar{1}0]$ scattering direction. Fig. 5(a) shows the RHEED pattern of the sample surface at 550°C during GaAs growth (i.e.,

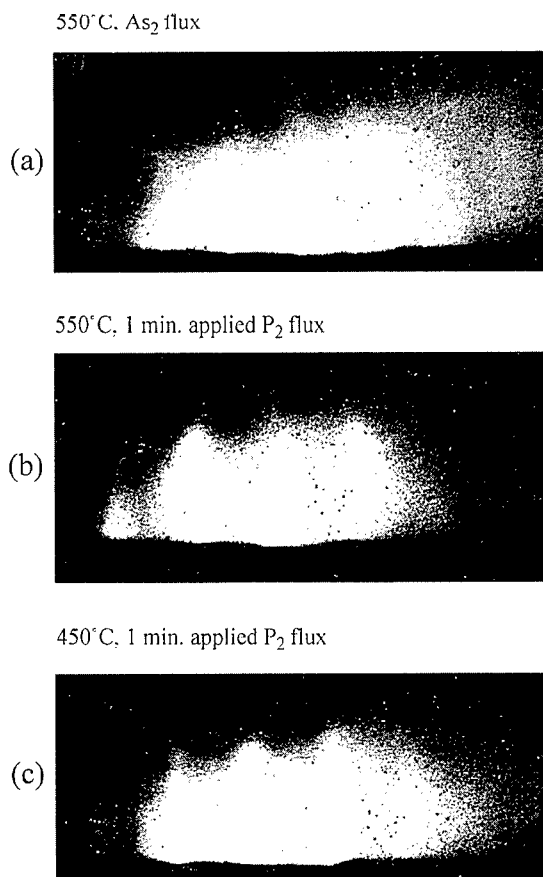


Fig. 5. (a) Streaky RHEED pattern indicating a flat growth surface at 550°C. (b) Spotty RHEED pattern indicating the presence of island growth at the surface at 550°C after a 60 s P_2 flux. (c) Streaky RHEED pattern indicating a flat growth surface at 450°C after a 60 s P_2 flux.

under applied As_2 flux). The streaky pattern that is observed indicates planar growth. Fig. 5(b) shows the RHEED pattern of the surface after an applied P_2 flux of 60 s duration. The pattern changed from streaky to spotty in appearance, indicating the presence of island growth. Fig. 5(c) shows the RHEED pattern of the surface at 450°C after an applied P_2 flux of 60 s duration. In contrast to the pattern seen in Fig. 5(b), the pattern seen at 450°C remained streaky not only at the end of the 60 s P_2 flux, but even after several minutes of applied P_2 flux. These results suggest a roughening of the growth front under applied P_2 flux at higher substrate temperatures.

These results are consistent with other studies of arsenide/phosphide growth fronts exposed to phosphorus and arsenic beams. Nagao et al. [8] used X-ray photoelectron spectroscopy (XPS) and Auger electron spectroscopy (AES) to characterize GaAs surfaces exposed to a cracked phosphorus beam for 60 s at surface temperatures ranging from 490 to 590°C. They report the formation of a 20 to 30 Å thick P-rich/As-poor layer at the surface, with the thickness of this layer increasing at higher substrate temperature. The surface roughening of an arsenide growth front upon exposure to a P₂ flux has also been reported by other groups [6,7]. Our studies confirm these results and provide more direct and detailed information about the local nanometer-scale lateral variations and asymmetry present in arsenide/phosphide interlayer structure.

In summary, we have used cross-sectional scanning tunneling microscopy to characterize interface structure in arsenide/phosphide heterostructures grown by gas-source molecular beam epitaxy. High-resolution constant-current images of samples consisting of GaAs interrupted at 200 Å intervals with a 40 s P₂ flux show electronically induced contrast between the GaAs layers and the phosphide interlayers. STM data obtained from the sample grown at 550°C show lateral variations in interface structure over nanometer length scales. Corrugation profiles obtained from constant-current images indicate that at 550°C phosphide interlayers up to 30 Å in width are formed, with an apparent difference in height, induced by changes in electronic structure, of up to 0.5 Å between the phosphide interlayers and GaAs layers. The images also suggest that during P₂ growth interrupts at 550°C, phosphorus at the surface diffuses into previously grown GaAs layers rather than carrying over into subsequently grown GaAs layers. STM data obtained from the sample grown at 450°C reveal phosphide interlayers which are narrower in width and exhibit lower topographic contrast, reflecting a lower level of phosphorus incorporation. The X-ray diffraction spectrum from the sample grown at 550°C shows a more pronounced periodic structure than the spectrum obtained from the sample grown at 450°C, consistent with STM data. RHEED data obtained during sample growth show that a longer time is needed to switch from a phosphorus-stabilized surface to an arsenic-stabilized surface at higher

substrate temperatures. Together these studies demonstrate that there is a strong dependence of interfacial abruptness on growth temperature, and also show that cross-sectional STM can provide direct information about nanometer-scale grading and lateral nonuniformity of interfaces that can occur under these growth conditions.

Acknowledgements

A.Y.L. and E.T.Y. would like to acknowledge the support of the National Science Foundation (Award No. ECS 93-07986) and ARPA (Optoelectronics Technology Center). C.H.Y. and C.W.T. would like to acknowledge the support of the Hughes Aircraft Co. through the University of California MICRO program, and the Air Force Wright Laboratory.

References

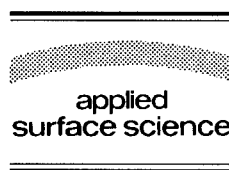
- [1] S. Kagawa, K. Inoue, I. Ogawa, Y. Takada and T. Shibata, *Jpn. J. Appl. Phys.* 28 (1989) 1843.
- [2] A. Tomita, Y. Kohga, A. Suzuki, T. Terakado and A. Ajisawa, *Appl. Phys. Lett.* 55 (1989) 1817.
- [3] A. Lidgard, T. Tanbun-Ek, R.A. Logan, H. Temkin, K.W. Wecht and N.A. Olsson, *Appl. Phys. Lett.* 56 (1990) 816.
- [4] H. Temkin, T. Tanbun-Ek and R.A. Logan, *Appl. Phys. Lett.* 56 (1990) 1210.
- [5] H.Y. Lee, M.J. Hafich and G.Y. Robinson, *J. Cryst. Growth* 105 (1990) 244.
- [6] K. Mahalingam, Y. Nakamura, N. Otsuka, H.Y. Lee, M.J. Hafich and G.Y. Robinson, *J. Electron. Mater.* 21 (1992) 129.
- [7] T. Anan, S. Sugou, K. Nishi and T. Ichihashi, *Appl. Phys. Lett.* 63 (1993) 1047.
- [8] S. Nagao, M. Takashima, Y. Inoue, M. Katoh and H. Gotoh, *J. Cryst. Growth* 111 (1991) 521.
- [9] M.J.S.P. Brasil, R.E. Nahory, W.E. Quinn, M.C. Tamargo and H.H. Farrell, *Appl. Phys. Lett.* 60 (1992) 1981.
- [10] M.J.S.P. Brasil, R.E. Nahory, M.C. Tamargo and S.A. Schwarz, *Appl. Phys. Lett.* 63 (1993) 2688.
- [11] D.E. Aspnes, M.C. Tamargo, M.J.S.P. Brasil, R.E. Nahory and S.A. Schwarz, *Appl. Phys. Lett.* 64 (1994) 3279.
- [12] R. Meyer, M. Hollfelder, H. Hardtdegen, B. Lengeler and H. Lüth, *J. Cryst. Growth* 124 (1992) 583.
- [13] M. Takemi, T. Kimura, K. Mori, K. Goto, Y. Mihashi and S. Takamiya, *Appl. Surf. Sci.* 82/83 (1994) 115.
- [14] P. Murali, H. Meier, D.W. Pohl and H.W.M. Salemink, *Appl. Phys. Lett.* 50 (1987) 1352.
- [15] H.W.M. Salemink, H.P. Meier, R. Ellialtıoglu, J.W. Gerritsen and P.R.M. Murali, *Appl. Phys. Lett.* 54 (1989) 1112.

- [16] O. Albrechtsen, D.J. Arent, H.P. Meier and H.W.M. Salemink, *Appl. Phys. Lett.* 57 (1990) 31.
- [17] R.M. Feenstra, E.T. Yu, J.M. Woodall, P.D. Kirchner, C.L. Lin and G.D. Pettit, *Appl. Phys. Lett.* 61 (1992) 795.
- [18] E.T. Yu, J.-M. Halbout, A.R. Powell and S.S. Iyer, *Appl. Phys. Lett.* 61 (1992) 3166.
- [19] H.W.M. Salemink and O. Albrechtsen, *Phys. Rev. B* 47 (1993) 16044.
- [20] S. Gwo, K.-J. Chao, C.K. Shih, K. Sadra and B.G. Streetman, *Phys. Rev. Lett.* 71 (1993) 1883.
- [21] J.F. Zheng, J.D. Walker, M.B. Salmeron and E.R. Weber, *Phys. Rev. Lett.* 72 (1994) 2414.
- [22] R.M. Feenstra, D.A. Collins, D.Z.-Y. Ting, M.W. Wang and T.C. McGill, *Phys. Rev. Lett.* 72 (1994) 2749.
- [23] A.Y. Lew, E.T. Yu, D.H. Chow and R.H. Miles, *Appl. Phys. Lett.* 65 (1994) 201.
- [24] R.M. Feenstra, J.A. Stroscio, J. Tersoff and A.P. Fein, *Phys. Rev. Lett.* 58 (1987) 1192.
- [25] C.H. Yan and C.W. Tu, unpublished.



ELSEVIER

Applied Surface Science 104/105 (1996) 529–538



Atomic force microscopy of III–V nanostructures in air

F. Reinhardt, B. Dwir, G. Biasiol, E. Kapon *

Institute de Micro- et Optoelectronique, Departement de Physique, Ecole Polytechnique Federal de Lausanne, CH-1015 Lausanne, Switzerland

Received 28 June 1995; accepted 10 October 1995

Abstract

Atomic force microscopy (AFM) in air was used to study the $\bar{1}10$ and (001) surfaces of III–V-heterostructures, grown by organometallic chemical vapor deposition (OMCVD) on planar or patterned (001) substrates. Topographies of the grown (001) surfaces as well as of $\bar{1}10$ cleaved cross-sections were examined. Although contamination and oxidation processes in air are expected to modify the structure of the surfaces in both cases, the AFM height profile, taken at constant force, yields structural information down to the monolayer level. On a cleaved surface of a III–V-heterostructure exposed to air, a natural oxide layer starts to grow immediately after cleaving. The growth rate of the oxide depends on the material composition and thus the topography can be used to map the composition within the scanned area. We used the AFM to characterize the growth of oxide on $\text{Al}_x\text{Ga}_{1-x}\text{As}$ - and GaAs-layers, and performed imaging of $\text{Al}_x\text{Ga}_{1-x}\text{As}/\text{GaAs}$ heterostructures utilizing the topography for composition identification. On the (001) surface of GaAs and InP, exposed to air, we observed terraces, separated by steps of monolayer height, and exhibiting a staircase-like morphology. Average terrace size and direction depend on the misorientation of the substrate. Formation of isolated growth islands, probably due to spontaneous nucleation, was also observed.

1. Introduction

Modern epitaxial growth of semiconductor heterostructures requires efficient methods for characterizing the grown layers, capable of yielding rapid and accurate information on the layer thickness, composition, growth direction and surface morphology on an atomic scale. Traditionally, scanning and transmission electron microscopy (SEM and TEM) of cross-sections or surfaces has been used for high-resolution (nm or sub-nm) imaging. Unfortunately,

these methods suffer from several drawbacks, particularly complicated and time-consuming sample preparation in the case of TEM, and relatively low resolution and poor contrast in the case of SEM.

Scanning probe microscopy (SPM), especially scanning tunneling microscopy (STM) and atomic force microscopy (AFM), has been developed as a versatile technique combining simple operation and the capability for achieving atomic resolution on the (001) and on cleaved $\bar{1}10$ or (110) surfaces of III–V-semiconductors [1–4]. STM of samples cleaved under ultra-high vacuum (UHV) conditions have been employed to perform imaging of GaAs/AlGaAs heterostructures with atomic resolution [2], including identification of single oxygen

* Corresponding author. Tel.: +41-216933388; fax: +41-21-6934525.

atoms on the surface [5]. These techniques necessitate expensive UHV-equipment and require more careful SPM techniques as compared with SPM in air.

In the case of SPM in air the exposure of the surface to air leads to chemical reactions, especially with molecular oxygen, which complicates the interpretation of tunneling spectroscopy [6]. Although the reaction of oxygen with clean III–V-semiconductor surfaces has been extensively studied using surface sensitive techniques [7–9], there is only little knowledge about the structure of these surfaces under ambient conditions and the nature of the oxide growth in reactive AlGaAs compounds. The generalization of SPM to these non ideal surfaces is important for applications in device fabrication processes. AFM under ambient conditions is the ideal tool for such studies, because of its insensitivity to the detailed electronic structure of the scanned surface and its rapid application, without complicated sample preparation steps.

We studied the growth of native oxides on the cleaved ($\bar{1}10$) surface of GaAs and $\text{Al}_x\text{Ga}_{1-x}\text{As}$ -layers with known Al mole fractions x , using the AFM to measure the height profiles at constant force. Using the difference in oxide height to distinguish between various heterostructure layers, we then performed AFM imaging of semiconductor nanostructures, particularly quantum wells (QWs) and quantum wires (QWRs). We also find that the formation of oxide on the (001) surface of GaAs and InP does not impede the use of AFM to visualize the morphology on an atomic scale [10–12], showing one monolayer terraces. We analyzed the step height and terrace size on GaAs and InP surfaces grown at different temperatures. Assuming that the oxidized morphology reflects the morphology during growth, we find that AFM in air is a useful technique for analyzing the mechanisms of epitaxial growth.

2. Experimental

The semiconductor layers and structures investigated in the present work were grown by organometallic chemical vapor deposition (OMCVD) either on planar, exactly oriented (etch pit density $< 1000 \text{ cm}^{-2}$) (001) GaAs ($\pm 0.1^\circ$) or on (001) InP

($\pm 0.03^\circ$) substrates. Only the $\text{Ga}_{0.5}\text{In}_{0.5}\text{P}/\text{GaAs}$ heterostructure, used for calibration of GaAs oxide growth, was grown by chemical beam epitaxy (CBE) on exactly oriented GaAs (001). For OMCVD growth we used trimethylaluminium TMAI (0.006–0.156 Pa), trimethylgallium TMGa (0.152 Pa), trimethylindium TMIIn, arsine AsH_3 (33 Pa), phosphine and H_2 as carrier gas in a standard low-pressure (20 hPa) horizontal reactor with a rotating susceptor plate at a total flux of 6 l/min. The substrate temperature was between 600 and 750°C, depending on the grown structure. OMCVD growth on substrates corrugated with $\sim 0.25 \mu\text{m}$ deep V-grooves, oriented along the $[\bar{1}10]$ -direction, made by holographic-lithography and wet chemical etching, was utilized for nonplanar and QWR growth studies. The details of the nonplanar growth as well as TEM studies of such QWR structures are described in detail elsewhere [13,14].

For cross-sectional studies the samples were cleaved in air and at room temperature, then mounted vertically in a specially designed AFM holder. The edge region of the cleaved surface was scanned with a silicon tip in contact or tapping mode at a constant force in the range of 0.1 nN. SEM images indicate a radius of curvature of $r \sim 15 \text{ nm}$ for the tips used. Accurate z -calibration of the piezoscanner were achieved by measuring the height of steps on a (001) graphite surface, which were found to be multiples of the thickness of a monoatomic layer. From this we deduced that the systematic error in our height measurements is smaller than 0.05 nm. On the graphite crystallographic planes atomic resolution was obtained and the average noise was 0.03 nm. For studies on the (001) oriented surface the samples were glued directly on the scanning piezo crystal. The surface was exposed to air for a period varying between several minutes and several weeks prior to investigation by AFM. Tapping mode AFM was found to lead qualitatively to the same results as obtained with contact mode, but with a lower noise level.

3. Results and discussion

3.1. AFM of the cleaved ($\bar{1}10$) surface

Two calibration samples were grown on planar (001) GaAs-substrates for the purpose of studying

the oxide growth on the cleaved edge. The first consisted of a stack of 20 pairs of 65 nm thick GaAs-layer and 69 nm thick $\text{Ga}_{0.5}\text{In}_{0.5}\text{P}$ -layer. The second was composed of nine layers of $\text{Al}_x\text{Ga}_{1-x}\text{As}$, with composition x ranging from 0.12 to 0.72 and thickness of 85–260 nm, separated by 75 nm thick GaAs-spacers. The Al mole fractions were inferred from growth rate calibration and verified by X-ray diffraction measurements. We used the AFM to image the cross-section of the cleaved samples in air at room temperature.

AFM images of both samples after 18 h of oxidation are shown in Fig. 1 and Fig. 2. The oxidized GaAs-layers appear as lighter (higher) than the intermediate $\text{Ga}_{0.5}\text{In}_{0.5}\text{P}$ -layers in the image of the $\text{Ga}_{0.5}\text{In}_{0.5}\text{P}/\text{GaAs}$ heterostructures (Fig. 1). Fig. 2 shows that the oxidized $\text{Al}_x\text{Ga}_{1-x}\text{As}$ -layers stick higher than the neighboring GaAs-layers, by an amount which increases with mole fraction x . For high Al mole fractions and large exposure times the height profiles show fluctuations which could be due

to inhomogeneities in the oxidation process for the corresponding Al-concentrations.

We studied the evolution of the height profile for both samples as a function of exposure time in air. In Fig. 3 we plot the mean height difference between GaAs and $\text{Ga}_{0.5}\text{In}_{0.5}\text{P}$ as a function of time after cleavage. The height difference increases quickly from an initial value of 0.2 nm four minutes after the cleave up to a nearly saturated difference of about 0.5 nm. The same results were obtained for dark as well for normal light conditions. The effect of oxidation of $\text{Ga}_{0.5}\text{In}_{0.5}\text{P}$ can be neglected; the oxidation rate of InP was reported to be much smaller than that of GaAs [7,8]. The measured height difference can thus be assigned to the thickness of the oxidized GaAs.

The mechanism of oxidation of a $(\bar{1}10)$ GaAs surface was extensively investigated [7–9] and was explained by the formation of a protective layer on top of the cleaved surface, consisting of elemental arsenic and Ga_2O_3 [15], which acts as a diffusion

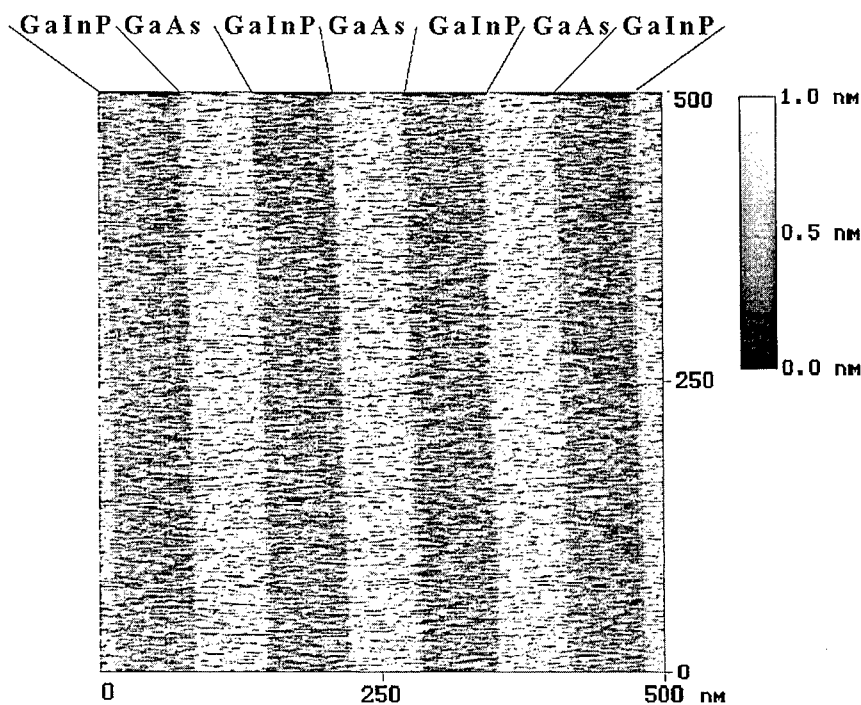


Fig. 1. AFM topographical image of the cleaved $(\bar{1}10)$ surface of a GaAs/ $\text{Ga}_{0.5}\text{In}_{0.5}\text{P}$ (65 nm/69 nm) heterostructure after 18 h of oxidation, taken at constant force in contact mode.

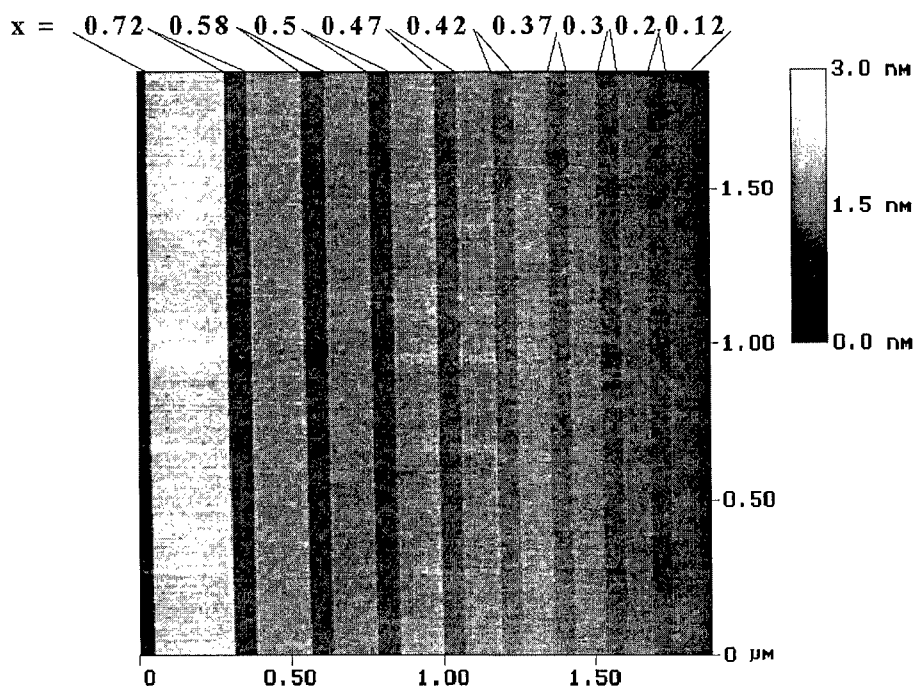


Fig. 2. AFM height image of the cleaved $(\bar{1}10)$ surface of a $\text{Al}_x\text{Ga}_{1-x}\text{As}/\text{GaAs}$ heterostructure after 18 h of oxidation, taken at constant force in contact mode. Nine layers of $\text{Al}_x\text{Ga}_{1-x}\text{As}$ with increasing Al mole fraction x and thickness are embedded between GaAs-layers of a nominal thickness of 75 nm.

barrier. It was shown that activated adsorption leads to a formation of a thin oxide film after 10^6 L oxygen; this roughly corresponds to an exposure time of 0.1 ms in air, much shorter than our observation time scale. After this virtually instantaneous formation of an initial oxide layer, the growth of the

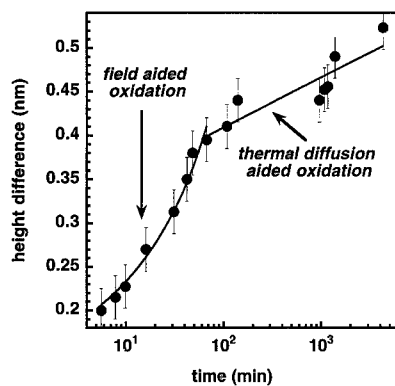


Fig. 3. Mean height difference between oxidized GaAs and $\text{Ga}_{0.5}\text{In}_{0.5}\text{P}$ as a function of exposure time in air.

oxide proceeds in the so-called *field-aided oxidation* mode. A strong electric field induced by adsorbates bonded to surface states is set up across the oxide layer, which pulls substrate or oxygen ions through the non reacting oxide layer. This model, first proposed by Cabrera and Mott for metal oxidation [16], yields an inverse logarithmic growth law for the oxide thickness h as a function of time t which, in our case of high exposures, gives:

$$\frac{1}{h} = a + \frac{1}{h_1} \ln(t). \quad (1)$$

The fitting parameter $h_1 = eV/kT$ is proportional to the *Mott potential* V , set across the oxide film. For long exposure times and sufficiently thick films, the field assisted oxidation is not effective any more and thermal diffusion becomes the dominant mode, leading to a logarithmic growth law. We fitted Eq. (1) to the GaAs height data obtained by the AFM and found a good agreement up to 70 min of exposure. For longer times we observed logarithmic growth behavior of $h(t)$. This agrees well with the model of

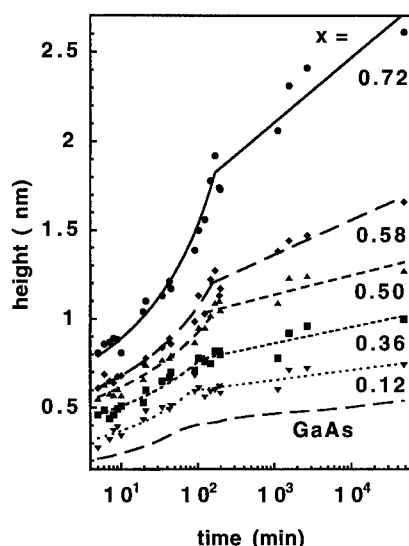


Fig. 4. Mean height of oxidized $\text{Al}_x\text{Ga}_{1-x}\text{As}$ with respect to $\text{Ga}_{0.5}\text{In}_{0.5}\text{P}$ for different Al mole fraction as a function of exposure time in air. The corresponding data for the oxidation of GaAs are given by the dashed line at the bottom.

field aided oxidation followed by diffusion related oxide growth, similar to the behavior in metals [17].

To properly account for the oxidation of GaAs in the $\text{Al}_x\text{Ga}_{1-x}\text{As}/\text{GaAs}$ structure, we added the height of oxidized GaAs from Fig. 3 to the measured mean height difference between oxidized $\text{Al}_x\text{Ga}_{1-x}\text{As}$ and GaAs, taken from the data of Fig. 2. In Fig. 4 we plot this sum as a function of time for different Al-concentrations, together with the corresponding curve for GaAs, shown as a dashed line at the bottom of the figure. The initial $\text{Al}_x\text{Ga}_{1-x}\text{As}$ height increases with increasing Al mole fraction x . For each composition, the time dependence of the height can be modeled in a way similar to that for GaAs. The oxide growth proceeds up to a certain exposure time in the *field-aided oxidation* mode, followed by thermal diffusion induced growth. The time at which a transition between the two modes of growth is observed slightly increases with increasing x , from 70–150 min for $x=0.12$ and $x=0.72$, respectively. The coefficient h_1 , which is assumed to be proportional to the Mott potential V , and the slopes of the fits in the diffusion controlled time range also increase with increasing x . This behavior can be explained either by the higher electrochemical

potential of aluminium compared with gallium or by a higher mobility of the smaller Al-ions, leading in both cases to faster oxide growth. The roughness of the $\text{Al}_x\text{Ga}_{1-x}\text{As}$ -oxide surface is similar to the roughness of the GaAs-oxide surface for mole fraction x up to 0.5 and then slowly increases with increasing x . In the extreme case of an 80 nm thick AlAs-layer embedded in GaAs, we observed very fast oxide formation (30 nm height after 5 min), resulting in a rough, high (200 nm after a day) and broad (150 nm) oxide region, which is presumably the result of three dimensional growth of porous oxide. The dimensions of the original AlAs-layer can only be roughly deduced from the resulting height profile of the AlAs-oxide.

From the discussion above we conclude that the mode of oxide growth on the cleaved surface of $\text{Al}_x\text{Ga}_{1-x}\text{As}$ ($x < 0.7$) proceeds in a way similar to the oxidation of GaAs, differing only quantitatively in the reaction rates. The smooth surface over large areas and the low growth rate of the oxide (< 1 nm/h) indicate quasi-epitaxial formation of these thin films. After 200 min of oxidation a quasi stable height profile is reached, which is only slowly changing with time. The height differences between GaAs and $\text{Al}_x\text{Ga}_{1-x}\text{As}$ as a function of x can be used for inferring the Al-concentration from the height profile of a given sample at a given exposure time.

For Al-concentrations in the range $0 < x < 0.72$, we used the difference in height to identify composition and thickness of layers deposited on NP-substrates. As an example for this application we show cross-sectional AFM images of two samples: one consisting of GaAs-layers, nominally 60 nm thick, separated by 4 nm thick $\text{Al}_{0.5}\text{Ga}_{0.5}\text{As}$ -markers (Fig. 5), the other with $\text{Al}_{0.5}\text{Ga}_{0.5}\text{As}$ -layers (50 nm) and nominally 3 nm thin GaAs-markers (Fig. 6), both grown under similar conditions on NP-substrates as described above. The nominal thickness values are given for growth on a planar (001) surface. The thin marker layers are in both cases easy to distinguish, and we can thus observe the planarization process of the grown layers and the formation of QWRs, and can measure the crystalline directions and growth rates of the observed facets. The oxide height difference between the $\text{Al}_{0.5}\text{Ga}_{0.5}\text{As}$ -layer and the GaAs-substrate is in both cases around 0.5 nm, comparable

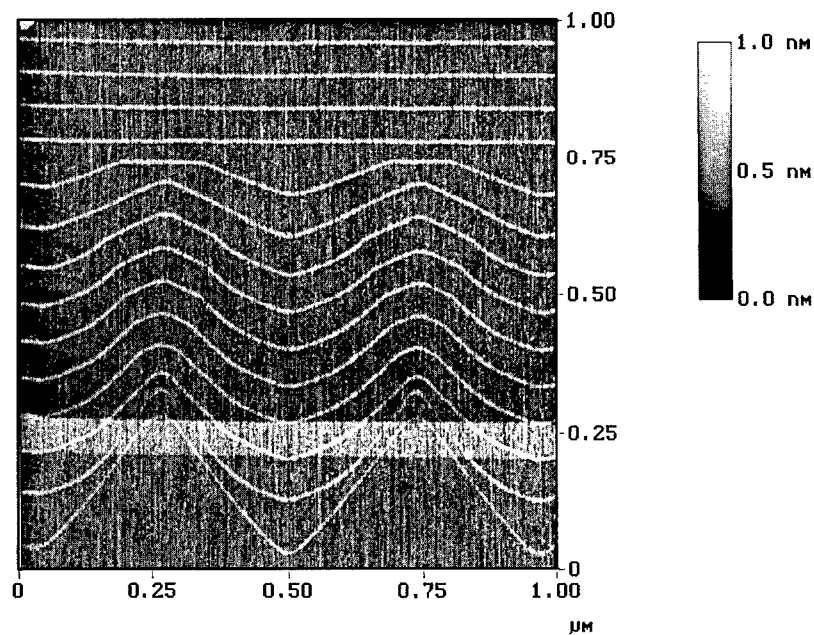


Fig. 5. AFM height image of the cleaved $\bar{1}10$ surface of a nonplanar GaAs/ $\text{Al}_{0.5}\text{Ga}_{0.5}\text{As}$ heterostructure after 3 h of exposure to air. Several $\text{Al}_{0.5}\text{Ga}_{0.5}\text{As}$ -layers of a nominal thickness of 4 nm were grown at a temperature of 750°C, sandwiched between nominally 62 nm thick GaAs-layers on a nonplanar GaAs substrate, consisting of V-shaped grooves (0.5 μm wide, 0.25 μm deep, 0.5 μm pitch). The light stripe running horizontally through the structure is due to imperfect cleave.

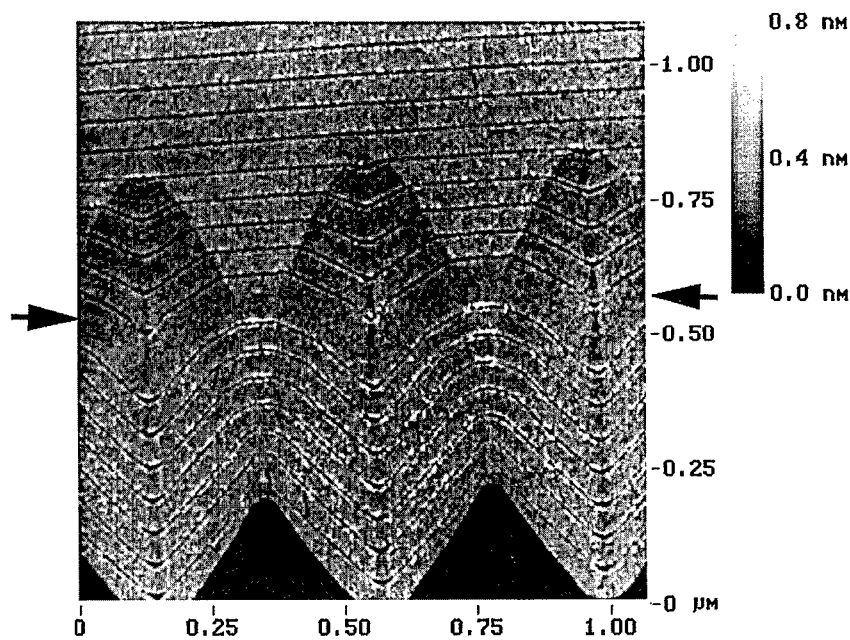


Fig. 6. AFM height image of the cleaved $\bar{1}10$ surface of a nonplanar $\text{Al}_{0.5}\text{Ga}_{0.5}\text{As}/\text{GaAs}$ heterostructure after 3 h of exposure to air. Several GaAs layers of a nominal thickness of 2.5 nm were grown sandwiched between 50 nm thick $\text{Al}_{0.5}\text{Ga}_{0.5}\text{As}$ on a nonplanar GaAs substrate, consisting of V-shaped grooves (0.5 μm wide, 0.25 μm deep, 0.5 μm pitch). The growth temperature for the first seven layers was 750°C and then decreased to 650°C during growth of the 100 nm thick $\text{Al}_{0.5}\text{Ga}_{0.5}\text{As}$ layer, indicated by the arrow.

to the height difference obtained after three hours of oxidation of the $\text{Al}_{0.5}\text{Ga}_{0.5}\text{As}/\text{GaAs}$ calibration heterostructure. The relatively large diameter of the AFM tip (about 30 nm) hinders a penetration of the groove, resulting in a reduced height difference ($h \sim 0.12$ nm instead of 0.5 nm) in the case of the thin GaAs-layer and in a larger measured width (15 nm instead of 4 nm) of the thin $\text{Al}_{0.5}\text{Ga}_{0.5}\text{As}$ ridge (Fig. 6). A simple model, describing the imaging of a structure (groove or ridge) which is smaller than the diameter of the tip [18], shows that the measured height of a thin ridge should be correct, whereas its width should appear larger, as found in the experiments. In the case of a groove, the depth appears reduced, but the imaged width corresponds to the real value. We compared cross sectional TEM images of the sample shown in Fig. 6 with the AFM picture and obtained a good agreement for the dimension of the GaAs-layer, with an uncertainty of 0.5 nm in the lateral dimension of the layer, probably determined by lateral oxide growth.

In Fig. 6, the region where the AlGaAs-growth proceeded on the (001) surface appears lighter

(higher) than the region, corresponding to the growth inside the grooves. This behavior, observed consistently in cross-sectional AFM or TEM-images of such structures, is due to a different incorporation rate of Al or Ga-atoms on different crystal facets. The Al mole fraction difference between both regions is 0.07, found by translating the height difference to x -values. We can also distinguish a dark band in the center of the V-groove, formed along the [001]-direction, which is the result of Ga-accumulation in this region during growth [14].

3.2. AFM of the (001) surface

Two dimensional growth is assumed to be the major process in OMCVD on (001) surfaces. Adsorption of atoms or molecules on the surface, followed by two-dimensional diffusion and preferential attachment to steps or kinks, leads to the formation of growth islands or large terraces, separated by steps of one or a few monolayer height. The migration of these steps over the growing surface can be determined by in situ spectroscopy during OMCVD

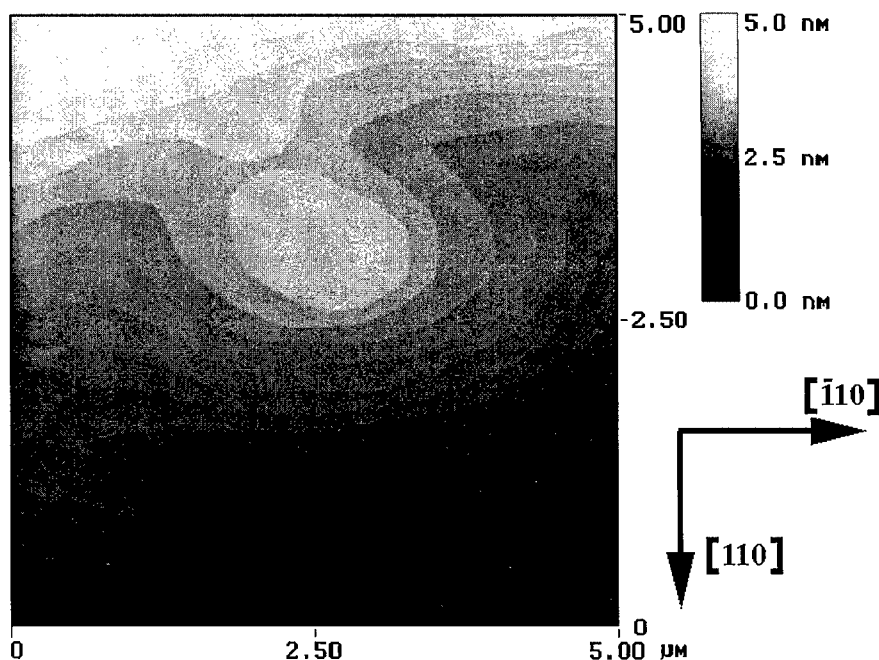


Fig. 7. AFM height image of the (001) surface ($\pm 0.1^\circ$ oriented) of GaAs, grown at 750°C on an n-type substrate, exposed for more than 40 h to air.

[19–23]. Several features of surface morphology, such as step density and height, island size or terrace width, are characteristic of a given set of growth parameters, including temperature, partial pressures of organometallics and hydrides, or the initial orientation of the substrate. Ex situ AFM-imaging in air, after the growth process is completed, can be applied to visualize surface morphology if the modification of the morphology due to oxidation and contamination is small enough. As we showed above the oxide growth on the (110) surface nearly saturates at a thickness of ~ 0.6 nm for GaAs and < 2 nm for $\text{Al}_{0.58}\text{Ga}_{0.42}\text{As}$ after several days of exposure. We also saw that the surface of this oxide stays atomically smooth (RMS of 0.05 nm) up to Al-concentration of $x = 0.5$. Since the oxide growth rate on the (001) surface was found to be lower than on the (110) surface in the case of high temperatures [24], it can be assumed that the oxidation rate at room temperature is as well lower. In addition, the surface is covered after growth during the sample cooling under AsH_3 -overpressure with at least two layers of

arsenic, forming a $c(4 \times 4)$ reconstruction [20,22,25,26], which probably delays oxidation process.

The (001)-GaAs and (001)-InP surfaces we studied ex situ with AFM were grown at 750°C and 695°C , cooled down under AsH_3 - or PH_3 -overpressure and, after unloading from the reactor, exposed to air for at least 40 h. On a large number of samples, which appeared flat under optical and scanning electron microscopes, we observed large terraces separated by more or less parallel monolayer steps (Fig. 7 and Fig. 8). We measured the rms-roughness of the terraces surface by calculating variance of height values over an area defined on a single terrace. The roughness is lower for tapping mode (rms = 0.04 nm) than for contact mode (rms = 0.1 nm), probably due to lower noise of the AFM-apparatus in this mode. Similar values of roughness were found for (001)-InP, (001)-GaAs and graphite surfaces. We therefore conclude that the surfaces are at least as smooth as the measured rms-value, and thus used tapping mode for obtaining images of

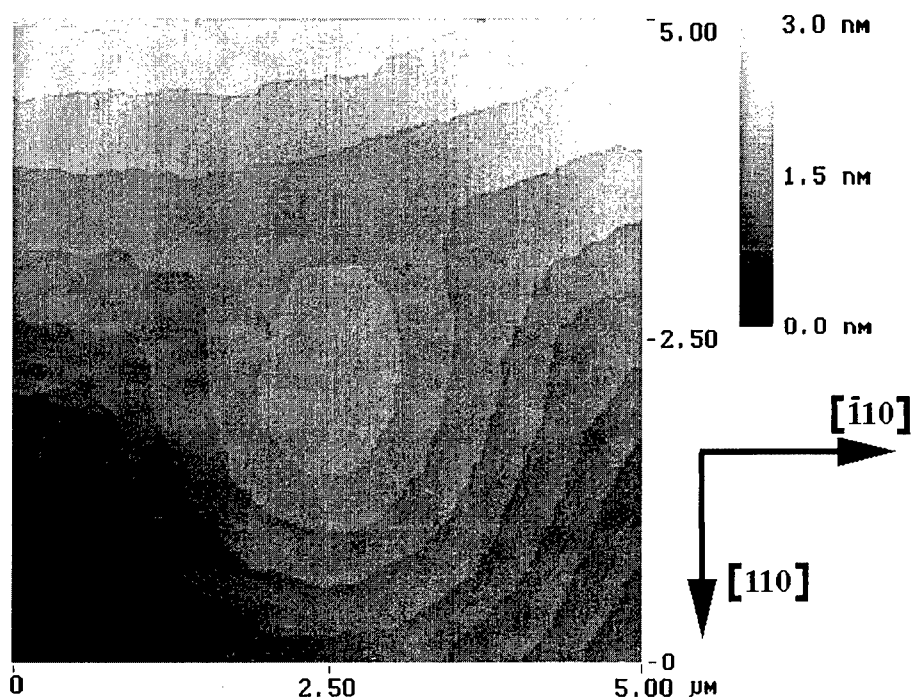


Fig. 8. AFM height image of the (001) surface ($\pm 0.03^\circ$ oriented) of InP, grown at 695°C on a semi-insulating substrates (Fe-doped), exposed for more than 40 h to air.

higher quality, including the images shown in Fig. 7 and Fig. 8. We carefully analyzed the step height and found a mean value of 0.275 ± 0.02 nm for GaAs and 0.295 ± 0.02 nm for InP. These values correspond to the height of a monolayer ($a/2$) of GaAs and InP, and show that the corresponding oxides, probably grown pseudomorphically, depict well the underlying structure and step height of the original surface. Since the lateral extent of the oxide growth can be assumed to be smaller than 0.6 nm, as found in the cross-sectional studies of the $(\bar{1}10)$ surface, we can conclude that the AFM image of the sample after oxidation well represents the original surface morphology.

The typical flow direction of the steps was $[120]$ on the (001) GaAs- and $[110]$ on the (001) InP-surface, and is probably determined by the initial substrate miscut. The average spacing between the terraces was found to be 140 nm and 340 nm for semi-insulating and n-doped GaAs-substrates, and 620 nm for Fe-doped InP, corresponding to initial misorientations of $\sim 0.12^\circ$, 0.048° and 0.027° , respectively. The edges of the steps are more rounded in the case of the GaAs-surface. For InP the step edges show kinks, with borders oriented along the $[\bar{1}10]$ - and $[110]$ -direction. In both cases, isolated growth islands appear typically on the terraced surface and can be explained by 2D-island nucleation growth. The mean radius of 670 nm of the GaAs islands gives a lower limit for the adatom diffusion length at these conditions, in agreement with the findings (~ 800 nm) of Kisker et al. [19], based on grazing incidence X-ray scattering (GIXS) data, obtained in situ during GaAs-growth using tertiary butyl arsine. We performed additional investigations of surfaces of (Al, Ga, In) (As, P) grown at different growth conditions and observed a similar behavior.

4. Conclusions

We have demonstrated a simple and efficient method for imaging III–V-heterostructures by top and cross-sectional AFM. In the cross sectional studies, we have used the composition dependence of the thin native oxide growth on the cleaved surface to image the layer composition. The oxidation proper-

ties of $\text{Al}_x\text{Ga}_{1-x}\text{As}$ in air were also investigated with this technique. While the AFM image does not have the resolution of TEM or STM (we estimate the resolution to be ~ 1 nm), it is far superior to cross-sectional SEM and can be obtained without complicated sample preparation. Our studies demonstrate that AFM imaging of heterostructures in air is capable of detecting GaAs-layers, embedded between AlGaAs, with a thickness as small as 1 nm, with an accuracy of ± 0.5 nm. The Al mole fraction can be determined with an accuracy of 0.1 using a calibration curve measured at a specific time after cleaving. The application to other heterostructures (i.e. $\text{Ga}_{0.5}\text{In}_{0.5}\text{P}/\text{GaAs}$), where oxidation differences are not as pronounced as for $\text{Al}_x\text{Ga}_{0.5}\text{As}/\text{GaAs}$, is possible, but demands an AFM with lower noise and higher z -resolution. AFM images of the oxidized (001) surface of GaAs and InP, after several days of exposure to air, provide structural information about the surface morphology after OMCVD growth. Such images can be used to investigate the growth mechanisms with monolayer resolution as a function of growth parameters.

Acknowledgements

This work was supported by Fonds National Suisse de la Recherche Scientifique. We wish to thank R. Bauknecht (ETHZ-IQE) and E. Gini (ETHZ-IQE) for their help in OMCVD growth, A. Rudra (EPFL-IMO) for supply of the CBE-grown sample, P. Ils (EPFL-IMO) and U. Marti (EPFL-IMO) for preparation of nonplanar substrates and A. Gustafsson (EPFL-IMO) for TEM investigations.

References

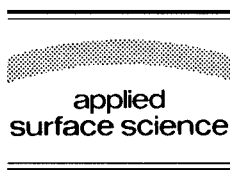
- [1] G. Binnig, C.F. Quate and C. Gerber, *Phys. Rev. Lett.* 72 (1986) 930.
- [2] M.B. Johnson, U. Maier, H.P. Meier and H.W.M. Salemink, *Appl. Phys. Lett.* 63 (1993) 1273.
- [3] S. Gwo, K.J. Chao, A.R. Smith, C.K. Shih, K. Sadra and B.G. Streetman, *J. Vac. Sci. Technol. B* 11 (1993) 1509.
- [4] K. Pond, R. Maboudian, V. Bressler-Hill, D. Leonard, X.-S. Wang, K. Self, W.H. Weinberg and P.M. Petroff, *J. Vac. Sci. Technol. B* 11 (1993) 1374.
- [5] J.A. Stroscio, R.M. Feenstra and A.P. Fein, *Phys. Rev. Lett.* 58 (1987) 1668.

- [6] R.M. Silver, J.A. Dagata and W. Tseng, *J. Appl. Phys.* 76 (1994) 5122.
- [7] W. Mönch, *Surf. Sci.* 168 (1986) 577.
- [8] W. Mönch, *Springer Series in Surface Science*, Vol. 26, ISBN 3-540-54423-2, p. 288.
- [9] K.A. Bertness, J.-J. Yeh, D.J. Friedman, P.H. Mahowald, A.K. Wahi, T. Kendelewicz and W.E. Spicer, *Phys. Rev. B* 38 (1988) 5406.
- [10] C.C. Hsu, T.K.S. Wong and I.H. Wilson, *Appl. Phys. Lett.* 63 (1993) 1839.
- [11] C.C. Hsu, J.B. Xu and I.H. Wilson, *Appl. Phys. Lett.* 65 (1994) 1394.
- [12] T. Fukui, J. Ishizaki, S. Hara, J. Motohisa and H. Hasegawa, *J. Cryst. Growth* 146 (1995) 183.
- [13] E. Kapon, D.M. Hwang and R. Bhat, *Phys. Rev. Lett.* 63 (1989) 430.
- [14] E. Kapon, M. Walther, M. Grundmann, J. Christen, C. Caneau, D.M. Hwang, E. Colas, R. Bhat, G.H. Song and D. Bimberg, *Superlatt. Microstruct.* 12 (1992) 491.
- [15] C.D. Thurmond, G.P. Schwartz, G.W. Kammlott and B. Schwartz, *J. Electrochem. Soc.* 127 (1980) 1366.
- [16] F. Cabrera and N.F. Mott, *Rep. Progr. Phys.* 12 (1948) 163.
- [17] A.T. Fromhold, *Theory of Metal Oxidation* (North-Holland, Amsterdam, 1976).
- [18] B. Dwir, F. Reinhardt, G. Biasiol and E. Kapon, *J. Mater. Sci. B*, to be published.
- [19] D.W. Kisker, G.B. Stephenson, P.H. Fuoss, F.J. Lamelas, S. Brennan and P. Imperatori, *J. Cryst. Growth* 124 (1992) 1.
- [20] F. Reinhardt, W. Richter, A.B. Müller, D. Gutsche, P. Kurpas, K. Ploska, K. Rose and M. Zorn, *J. Vac. Sci. Technol. B* 11 (1993) 1427.
- [21] M. Zorn, J. Jönsson, A. Krost, W. Richter, J. Zettler, K. Ploska and F. Reinhardt, *J. Cryst. Growth* 145 (1994) 53.
- [22] F. Reinhardt, *Dissertation Technical University of Berlin*, ISBN 3-928943-11-1.
- [23] J.E. Epler and H.P. Schweizer, *Appl. Phys. Lett.* 65 (1993) 1839.
- [24] D.N. Butcher and B.J. Sealy, *J. Phys. D: Appl. Phys.* 11 (1978) 1451.
- [25] M. Kasu, N. Kobayashi and H. Yamaguchi, *Appl. Phys. Lett.* 63 (1993) 678.
- [26] I. Kamiya, D.E. Aspnes, H. Tanaka, L.T. Florez, E. Colas, J.P. Harbison and R. Bhat, *Appl. Surf. Sci.* 60/61 (1992) 534.



ELSEVIER

Applied Surface Science 104/105 (1996) 539–545



Site occupation of Si atoms deposited on vicinal GaAs(001)-(2 × 4) surfaces

A.R. Avery^a, J.L. Sudijono^b, T.S. Jones^{a,*}, B.A. Joyce^b

^a Department of Chemistry and Interdisciplinary Research Centre for Semiconductor Materials, Imperial College, London SW7 2AY, UK

^b Interdisciplinary Research Centre for Semiconductor Materials, Imperial College, London SW7 2AB, UK

Received 28 June 1995; accepted 25 October 1995

Abstract

Scanning tunnelling microscopy (STM) and reflection high energy electron diffraction (RHEED) have been used to study the deposition of Si in the presence of an arsenic flux at 560°C on vicinal GaAs(001)-(2 × 4) surfaces grown in situ by molecular beam epitaxy (MBE). RHEED studies showed that the surface structure changed from (2 × 4) to asymmetric (3 × 1) at a Si coverage of ~0.1 ML, before a symmetric (3 × 1) structure was formed at a coverage of ~0.4 ML. Deposition of low coverages of Si (<0.1 ML) resulted in a disordered surface with STM images showing a high degree of kinking of the (2 × 4) surface. The disorder is caused by Si atoms occupying the vacant Ga sites in the missing dimer trenches of the clean (2 × 4) surface. With increasing Si coverage, neighbouring Si atoms in the trenches are eventually covered with As, bridging the missing dimer trenches and forming elongated rectangular units. The number of these units becomes greater as the coverage of Si is increased and there is a change in periodicity from 8 to 12 Å along $\bar{1}10$ consistent with the appearance of the symmetric (3 × 1) RHEED pattern. Detailed studies carried out on vicinal surfaces, offcut by 1° towards both (111)A and (111)B planes, showed that for coverages up to 0.5 ML of Si, the distribution of the Si is uniform across the surface and there is no preferential interaction with the step edges.

1. Introduction

The interaction of Si with GaAs(001) surfaces has been the focus of a number of studies in the last few years primarily because of the interest in applications such as Si δ -doping [1] and the passivation of GaAs surfaces by Si for improved ohmic contacts [2]. Reflection high energy electron diffraction (RHEED) studies of Si deposition on GaAs(001) have revealed a number of different structural changes depending

on the initial surface reconstruction, the substrate temperature and the presence or absence of As during the deposition process [3–14]. In general, the presence of a three-fold periodicity in the RHEED pattern only occurs when Si is deposited in the presence of an As flux [11–14].

For the formation of Si δ -doped structures on GaAs(001) surfaces, it is necessary to carry out the deposition at low substrate temperatures (400°C) in order to minimise the spreading of the Si atoms away from the δ -plane [15,16]. Under these conditions, deposition takes place on the As-rich c(4 × 4) reconstruction [17]. RHEED studies have shown that

* Corresponding author. Tel.: +44-171-5945794; fax: +44-171-5945801; e-mail: t.jones@ic.ac.uk.

the structure changes to an asymmetric (3×1) and then a symmetric (3×1) after the deposition of 0.5 ML of Si [11,12]. Recent STM measurements suggest that the additional As layer of the $c(4 \times 4)$ reconstruction acts as a surfactant, leading to a dimer exchange mechanism at the surface and the formation of a series of ordered 'needle-like' islands [12,14,18].

RHEED studies at higher substrate temperatures on the GaAs(001)-(2×4) surface also show the transition from an asymmetric to symmetric (3×1) structure with increasing Si coverage [4]. Detailed STM studies have shown that the Si preferentially occupies vacant Ga sites in the missing dimer trenches of the (2×4) reconstruction [13]. The resulting three-fold periodicity in the diffraction pattern is a consequence of the Si being covered with As and the surface is characterised by a series of rectangular blocks of As dimers.

It has recently been suggested that Si doping wires may be formed on vicinal GaAs(001)-(2×4) surfaces due to the preferential attachment of Si atoms at step edges [19–21]. In order to investigate further any possible influence of steps in the adsorption of Si at the GaAs(001) surface, we have carried out an STM and RHEED study for deposition on vicinal surfaces at 560°C in the presence of an As flux. For these deposition conditions, we find that the adsorption behaviour is not influenced by the step edges; the Si preferentially occupies vacant Ga sites in the missing dimer trenches of the (2×4) reconstruction and there is no evidence for the formation of Si wires.

2. Experimental

The experiments were performed in a combined ultra high vacuum STM (Omicron) and molecular beam epitaxy (MBE) growth chamber (DCA Instruments, Finland) linked via a gate valve. The n^+ Si-doped GaAs(001) substrates were mounted with indium onto molybdenum plates and transferred to UHV without any ex situ preparation. After initial outgassing at 300°C and removal of the native oxide at 600°C, buffer layers of 500 nm thickness were grown at 0.5 ML s^{-1} , at a substrate temperature of 560°C and an As_4 pressure of 2.4×10^{-6} mbar. A

silicon dopant concentration of 5.8×10^{17} atoms cm^{-3} , calibrated by secondary ion mass spectrometry (SIMS) depth profiling of a staircase structure with up to 5×10^{18} atoms cm^{-3} of Si, was used throughout growth except for the last 100 ML. The grown samples were then annealed for approximately 10 min at 560°C under an As_4 flux. The (2×4) surface reconstruction was monitored by RHEED throughout the growth and annealing process. The samples were then cooled to 400°C over a period of about 2 min and transferred quickly to the STM chamber for imaging.

Si deposition onto the (2×4) surface was achieved by exposure to a Si flux of about 5×10^{10} atoms $cm^{-2} s^{-1}$ at 560°C in the presence of an As_4 flux. The RHEED patterns were monitored throughout the deposition. After annealing for a further 5 to 10 min in the presence of the same As_4 flux, the samples were again cooled to 400°C and transferred quickly to the STM chamber for imaging. Surfaces prepared in this way were found to be stable and to remain uncontaminated for several days. Filled states STM images were taken at room temperature in a constant current mode, with negative sample biases of 2 to 3 V, tunnelling currents of 0.2 to 0.5 nA, with a typical vertical resolution of better than 1 Å.

3. Results

The RHEED pattern for the clean GaAs(001)-(2×4) surface had sharp $2/4$ streaks and equal intensity $1/4$ order features in the $[\bar{1}10]$ direction [17]. A relatively wide area STM image ($800 \text{ Å} \times 800 \text{ Å}$) of the clean surface, offset by 1° towards (111)A, is shown in Fig. 1a. The image shows the well-known dimer row structure with the surface grown under these conditions characterised by relatively large domains of ordered dimer rows [17,22,28]. Higher resolution images show that the bright rows are due to pairs of arsenic dimers and the dark rows are caused by the absence of two dimers per unit cell [17,22,28]. A 1° offset produces a nominal terrace width of 150 Å. The 2.8 Å steps visible in Fig. 1a clearly show signs of bunching, although the mean terrace width is still consistent with a 1° offset. These A-type step edges, aligned along $[\bar{1}10]$, are Ga-terminated and are relatively straight when compared to the As-terminated B-type steps [24].

After deposition of 0.05 ML of Si, the $2/4$ rod of the four-fold RHEED pattern for the $[\bar{1}10]$ azimuth became faint, consistent with an increase in the amount of disorder on the surface. This was accompanied by a broadening of the half order rods of the two-fold pattern in the $[110]$ direction. The corresponding STM image ($750 \text{ \AA} \times 750 \text{ \AA}$), after deposition onto the vicinal (2×4) surface offcut by 1° towards (111)A, shows that the As dimer rows are disrupted with the disorder manifesting itself uniformly across the surface (Fig. 1b). Importantly, there appears to be *no* preferential interaction of Si with the A-type step edges at this coverage under these conditions. Similar images were obtained for

deposition under the same conditions on both the singular (2×4) surface and the vicinal surface offcut by 1° towards (111)B [13].

Further exposure to Si (> 0.1 ML) resulted in a splitting of the half order rods in the $[110]$ azimuth. At this coverage, all the fractional order rods of the four-fold pattern disappeared and a so-called asymmetric (3×1) RHEED pattern was observed [4]. The STM image ($500 \text{ \AA} \times 500 \text{ \AA}$) shown in Fig. 1c corresponds to the deposition of 0.15 ML of Si on the vicinal (001) surface offcut by 1° towards (111)A. The surface is still relatively disordered and is characterised by a series of rectangles whose long direction is perpendicular to the step edges, i.e. along

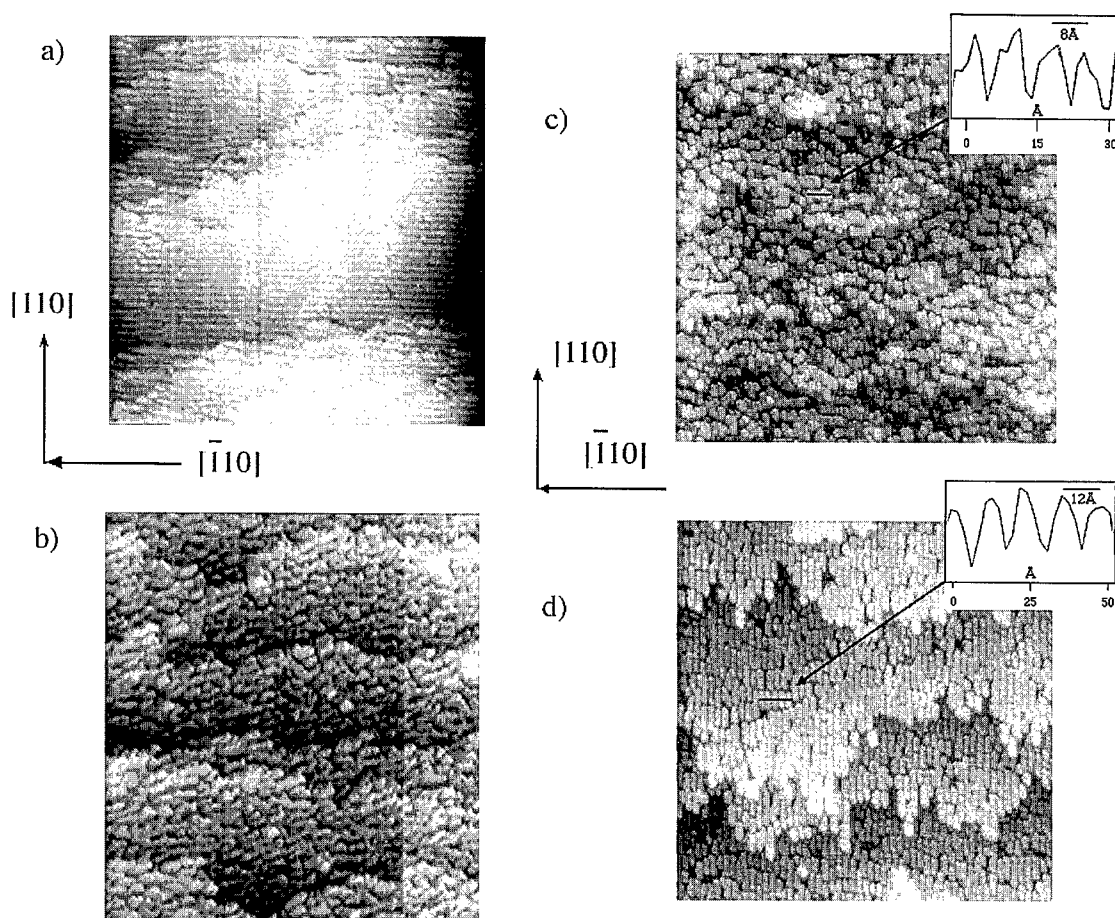


Fig. 1. Filled states STM images of (a) the clean GaAs(001)-(2×4) surface offcut by 1° towards (111)A and the same surface after the deposition of (b) 0.05 ML, (c) 0.15 ML, and (d) 0.5 ML of Si at 560°C in the presence of an As_4 flux. Image dimensions are (a) $800 \text{ \AA} \times 800 \text{ \AA}$, (b) $750 \text{ \AA} \times 750 \text{ \AA}$, (c) $500 \text{ \AA} \times 500 \text{ \AA}$, and (d) $500 \text{ \AA} \times 500 \text{ \AA}$.

[110]. These rectangles consist of As dimers and occupy the same, outermost atomic layer as the As dimers of the clean surface. Cross-sectional measurements indicate that the periodicity along $\bar{1}10$ is 8 Å and is the same as that for the As dimers on the clean (2×4) surface.

Further increases in Si coverage (typically between 0.4 and 0.5 ML) result in the formation of a symmetric (3×1) RHEED pattern. An example of an STM image ($500 \text{ Å} \times 500 \text{ Å}$) for 0.5 ML of Si is shown in Fig. 1d. There is an increase in both the density and mean length of the rectangular units and also a higher degree of ordering. The periodicity along $\bar{1}10$ is now 12 Å and close inspection of the image reveals a wider, more pronounced gap between the rectangular units. The change in periodic-

ity from 8 Å to 12 Å as the Si coverage is increased correlates with the RHEED observations which show a gradual transition from the asymmetric (3×1) to symmetric (3×1) structure. STM images for Si coverages in between those shown in Fig. 1c and d are characterised by a mixture of 8 Å and 12 Å periodicities. When the symmetric (3×1) structure is formed at 0.5 ML the periodicity is always 12 Å.

The formation of the rectangular units and the change in periodicity from 8 to 12 Å at the higher Si coverages is also seen on the singular GaAs(001) surface and on vicinal surfaces with different offcuts [13]. Fig. 2 compares STM images ($500 \text{ Å} \times 500 \text{ Å}$) taken after the deposition of 0.5 ML of Si under identical conditions on vicinal surfaces offcut by 1° towards (a) (111)A and (b) (111)B. Both STM images show a high degree of ordering and the characteristic rectangular blocks with a periodicity along $\bar{1}10$ of 12 Å. The images also clearly illustrate that the adsorption behaviour of Si is not influenced by the step edges for deposition under these conditions.

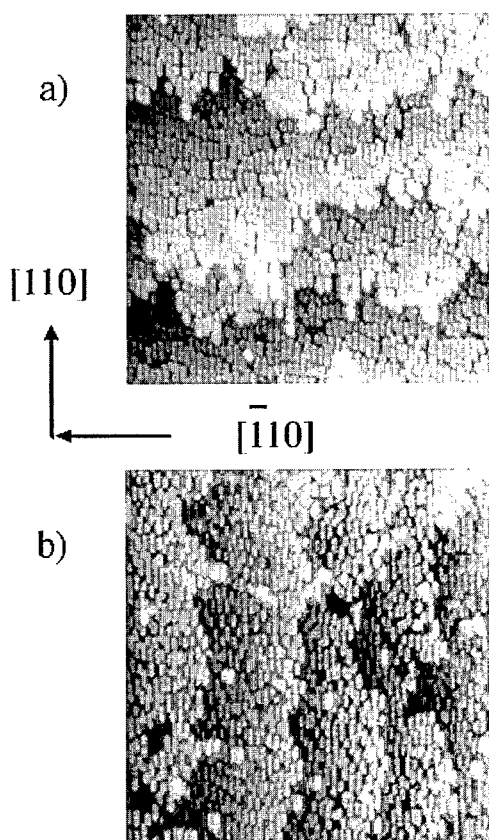


Fig. 2. Filled states STM images after the deposition of 0.5 ML of Si in the presence of an As_4 flux at 560°C onto a vicinal GaAs(001)- (2×4) surface offcut by 1° towards (a) (111)A and (b) (111)B. Image dimensions are $500 \text{ Å} \times 500 \text{ Å}$.

4. Discussion

It is clear from the STM images shown that the step edges have no influence on the adsorption behaviour of Si on vicinal GaAs(001)- (2×4) surfaces for deposition at high substrate temperatures in the presence of an arsenic flux. Since the same adsorption behaviour is seen on both singular and vicinal surfaces, it is essential to be clear about the structure of the clean surface in order to understand the site occupancy of Si in this coverage regime. Several models have been proposed for the (2×4) reconstructed GaAs (001) surface based on the idea of missing dimers. The main difficulty has been to establish the number of dimers per unit cell, as structures containing either two or three dimers per cell are both consistent with a four-fold periodicity. It has recently been established from combined STM and RHEED studies, that the two dimer model is the only structure that exists, even though different RHEED patterns can be obtained which exhibit a (2×4) symmetry [17,22,28]. The STM images clearly show that the variation in the RHEED patterns can be explained simply on the basis of different degrees of ordering, with the most ordered struc-

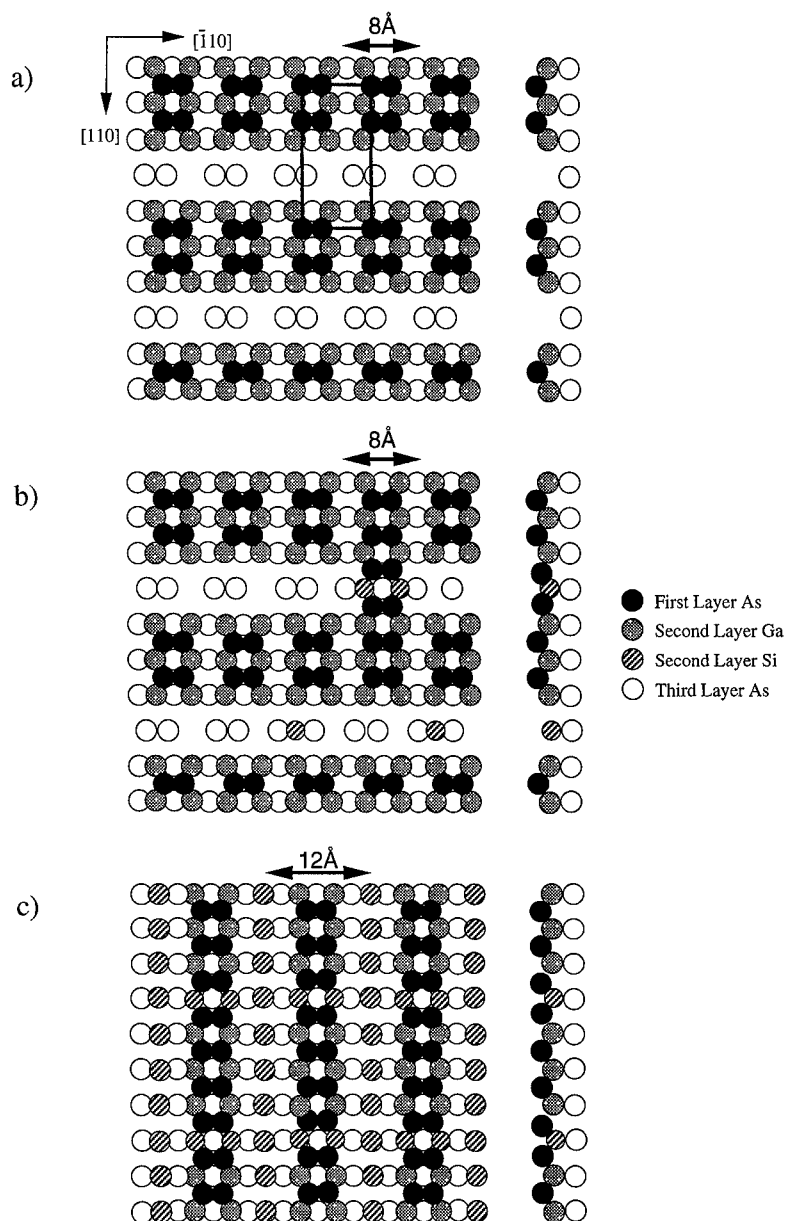


Fig. 3. (a) A structural model for the clean GaAs(001)-(2x4) surface showing two As dimers and two missing dimers per unit cell. The As dimer bond in the top layer is aligned along $\bar{1}10$ and there are Ga atoms absent from the missing dimer trenches. The exposed third layer As atoms also form dimers. (b) A schematic diagram showing the filling of the trenches by Si atoms which occupy the vacant Ga sites in the original (2x4) structure. At a sufficiently high coverage, the Si atoms occupy adjacent sites along $\bar{1}10$ and are covered by As atoms which form dimers. This leads to the appearance of rectangular units in the STM images with the long direction of the rectangle along 110 and a periodicity of 8 Å along $\bar{1}10$. The kinks which are caused by the presence of small amounts of Si have been omitted for clarity. (c) A schematic diagram showing how at coverages > 0.25 ML, Si displaces second layer Ga atoms and results in a row-like structure of Si atoms in Ga sites along 110 . The As dimers in the top layer are spaced further apart and the periodicity is increased along $\bar{1}10$ to 12 Å, consistent with the introduction of a three-fold periodicity in the RHEED pattern.

ture having a RHEED pattern with equal intensity in the fractional order streaks [17,28]. The corresponding STM image (Fig. 1a) is characterised by large domains of straight dimer rows, with the two dimer structure having no second layer Ga atoms in the missing dimer trench and with the exposed third layer As atoms also forming dimers (Fig. 3a) [17,22,23,25,26,28]. Acceptance of this structure, specifically the absence of the Ga atoms in the missing dimer trenches, is crucial to an understanding of the behaviour of Si on GaAs(001) in this low coverage regime.

For low coverages of Si, the atoms occupy the empty Ga sites in the missing dimer trenches of the clean (2×4) surface (Fig. 3b). The arrival of the first Si atoms on these empty sites induces disorder which manifests itself in the form of kinks in the STM image (Fig. 1b). Kinking of the (2×4) surface has also been observed for GaAs(001) samples with a high level of Si (n-type) bulk doping [27]. This has been shown to arise from the autocompensation of Si donors by the surface, which creates acceptor states in the form of kinks in order to keep the Fermi level mid-gap. Recently, we have shown that the highly ordered (2×4) surface of the type shown in Fig. 1a, rearranges with kink formation when cooled to about 520°C in an arsenic flux [17,28]. This suggests that kinks can *also* be caused by the addition of either As or Si to the (2×4) surface and that they arise from the large number of vacancies in the Ga layer and at a temperature which is high enough (in this case 560°C) for the Ga atoms and vacancies to be mobile [28].

As the Si coverage is increased, the Si atoms are forced to occupy trench sites which are adjacent to sites which have already been occupied by Si atoms. Under our experimental conditions, the Si is deposited in the presence of an arsenic flux. Consequently, adjacent Si atoms are covered by As atoms which can then dimerise in a similar fashion to the growth of clean GaAs (Fig. 3b). The STM does not, therefore, image Si atoms as these occupy the second layer. It is the As atoms in the top layer which appear in the images shown in Fig. 1c and d. This in-filling of the missing dimer trench bridges the gap between the original As dimers of the clean surface and is responsible for the presence of the elongated rectangular units having 8 Å periodicity along $[110]$

(Fig. 3b). The periodicity is the same as for this direction on the clean (2×4) reconstructed surface. The frequency with which adjacent trenches along $[110]$ are filled in this manner determines the length of a specific rectangular unit. In the case of very low coverages of silicon, the Si atoms are present in low enough concentration that pairs of adjacent Si atoms do not occur and there are no rectangular blocks seen in the STM images. The only effects at these very low coverages (0.05 ML) is kinking of the dimer rows and a disordered surface (Fig. 1b).

The number of empty Ga sites in the missing dimer trenches of the original (2×4) surface which can subsequently be occupied by Si atoms is 0.25 ML. However, the STM images, which are characterised by the rectangular blocks of As dimers, correspond to the deposition of 0.5 ML of Si (Fig. 2). It is therefore necessary to account for the additional 0.25 ML which must occupy alternative sites. Since the Si–As bond is stronger than the Ga–As bond [6], a Si–Ga exchange process can occur with the deposited Si replacing second layer Ga atoms. A possible structural model based on such an exchange is shown in Fig. 3c and is consistent with the formation of the rectangular units of arsenic having a greater periodicity (12 Å) along $[110]$ at the higher Si coverages.

This structural model also explains the change in RHEED pattern from asymmetric (3×1) to symmetric (3×1) as the Si coverage is increased. The asymmetric pattern, which occurs at lower Si coverages, arises as a result of the introduction of three-fold periodic units into an otherwise two-fold periodic surface. As the population of units with 12 Å periodicity increases with Si coverage, the half order rods of the original two-fold pattern split further until, when the surface consists entirely of 12 Å periodic units, it exhibits the symmetric three-fold pattern.

5. Conclusions

The real space imaging capability of STM has been used to study directly the effects of the deposition of Si at 560°C on vicinal GaAs(001)- (2×4) surfaces grown by MBE. The offcut direction has little effect upon the incorporation of silicon for coverages up to 0.5 ML of Si. Low Si coverages

cause extensive disruption in the form of kinking across the surface. This effect is uniform and there is no preference for incorporation of Si at step edges. The Si atoms preferentially occupy Ga sites which are vacant in the missing dimer trenches of the original (2×4) reconstructed surface. With increasing coverage, the Si atoms are covered by As and result in rectangular units whose long direction is along $[110]$, i.e. perpendicular to the original As dimer rows. These have a periodicity of 8 Å in the $[\bar{1}10]$ direction. As the coverage increases to 0.5 ML the arrangement of these units becomes more ordered and there is a gradual change in periodicity from 8 Å to 12 Å. The change in the RHEED pattern from (2×4) to asymmetric (3×1) and symmetric (3×1) can be explained simply by the loss of four-fold order due to kinks and the subsequent arrangement of the rectangular units, and an increase in the population of the 12 Å periodic units on the surface at the expense of those with an 8 Å spacing. When the entire surface displays this new periodicity, the RHEED pattern is symmetric (3×1) .

Recent RHEED studies on vicinal GaAs(001) surfaces reported a (3×2) structure at low Si coverages and was interpreted as being due to the preferential attachment of Si atoms at step edges [19–21]. Under our deposition conditions, a (3×2) structure is only observed at much higher Si coverages (> 0.65 ML). Subsequent STM images suggest that there is no influence of the substrate misorientation and that Si doping wires are not formed under these particular deposition conditions.

Acknowledgements

This work was supported by the Engineering and Physical Sciences Research Council (EPSRC) UK under grant number GRJ97540.

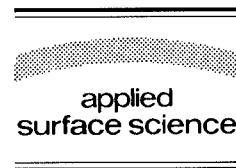
References

- [1] J.J. Harris, *J. Mater. Sci.: Mater. Electron.* 4 (1993) 93.
- [2] G.G. Fountain, S.V. Hattangady, D.J. Vitkavage, R.A. Rudner and R.J. Markunas, *Electron. Lett.* 24 (1988) 1135.
- [3] M. Akazawa, H. Ishii and H. Hasegawa, *Jpn. J. Appl. Phys.* 30 (1991) 3744.
- [4] M.R. Fahy, M.J. Ashwin, J.J. Harris, R.C. Newman and B.A. Joyce, *Appl. Phys. Lett.* 61 (1992) 1805.
- [5] H.J. Gillespie, G.E. Crook and R.J. Matyi, *Appl. Phys. Lett.* 60 (1992) 721.
- [6] R.Z. Bachrach, R.D. Bringans, M.A. Olmstead and R.I.G. Uhrberg, *J. Vac. Sci. Technol. B* 5 (1987) 1135.
- [7] P.C. Zalm, P.M.J. Marée and R.I.J. Olthof, *Appl. Phys. Lett.* 46 (1985) 597.
- [8] L. Sorba, G. Bratina, G. Ceccone, A. Antonini, J.F. Walker, M. Micovoc and A. Franciosi, *Phys. Rev. B* 43 (1991) 2450.
- [9] K. Adomi, S. Strite, H. Morkoç, Y. Nakamura and N. Otsuka, *J. Appl. Phys.* 69 (1991) 220.
- [10] H. Tanino, S. Amano, H. Kawanami and H. Matsuhata, *J. Appl. Phys.* 70 (1991) 7068.
- [11] D.A. Woolf, K.C. Rose, J. Rumberg, D.I. Westwood, F. Reinhardt, S.J. Morris, W. Richter and R.H. Williams, *Phys. Rev. B* 51 (1995) 4691.
- [12] A.R. Avery, D.M. Holmes, J.L. Sudijono, T.S. Jones, M.R. Fahy and B.A. Joyce, *J. Cryst. Growth* 150 (1995) 202.
- [13] A.R. Avery, J.L. Sudijono, T.S. Jones and B.A. Joyce, *Surf. Sci.* 340 (1995) 57.
- [14] J.L. Sudijono, A.R. Avery, B.A. Joyce and T.S. Jones, *J. Mater. Sci.*, in press.
- [15] M.J. Ashwin, M. Fahy, J.J. Harris, R.C. Newman, D.A. Sansom, R. Addinall, D.S. McPhail and V.K.M. Sharma, *J. Appl. Phys.* 73 (1993) 633.
- [16] L. Hart, M.R. Fahy, R.C. Newman and P.F. Fewster, *Appl. Phys. Lett.* 62 (1993) 2218.
- [17] A.R. Avery, D.M. Holmes, J.L. Sudijono, T.S. Jones and B.A. Joyce, *Surf. Sci.* 323 (1995) 91.
- [18] A.R. Avery, J.L. Sudijono, D.M. Holmes, T.S. Jones and B.A. Joyce, *Appl. Phys. Lett.* 66 (1995) 3200.
- [19] C.E.C. Wood, *J. Appl. Phys.* 71 (1992) 1760.
- [20] L. Daweritz, K. Hagenstein and P. Schutzendube, *J. Cryst. Growth* 127 (1993) 1051.
- [21] L. Daweritz and H. Kostial, *Appl. Phys. A* 58 (1994) 81.
- [22] T. Hashizume, Q.K. Xue, J. Zhou, A. Ichimiya and T. Sakurai, *Phys. Rev. Lett.* 73 (1994) 583.
- [23] M. Wassermeier, V. Bressler-Hill, A. Maboudian, K. Pond, X.S. Wang, W.H. Weinberg and P.M. Petroff, *Surf. Sci.* 278 (1992) L147.
- [24] M.D. Pashley, K.W. Haberern and J.M. Gaines, *Appl. Phys. Lett.* 58 (1991) 406.
- [25] D.J. Chadi, *J. Vac. Sci. Technol. A* 5 (1987) 834.
- [26] J.E. Northrup and S. Froyen, *Phys. Rev. B* 50 (1994) 2015.
- [27] M.D. Pashley and K.W. Haberern, *Phys. Rev. Lett.* 67 (1991) 2697.
- [28] A.R. Avery, C.N. Goringe, D.M. Holmes, J.L. Sudijono and T.S. Jones, *Phys. Rev. Lett.* 76 (1996) 3344.



ELSEVIER

Applied Surface Science 104/105 (1996) 546–551



Characterization of nanostructures by virtue of the phenomena due to the electron–phonon interaction

E.P. Pokatilov, V.M. Fomin^{*}, S.N. Klimin, S.N. Balaban

Department of Theoretical Physics, State University of Moldova, str. Mateevici 60, 277009 Kishinev, Moldova

Received 28 June 1995; accepted 4 December 1995

Abstract

Investigations of polarons in a polar cylindrical quantum wire are carried out for various barrier potentials at the interface. It is shown that dependencies of the ground-state energy and the effective mass on the radius of the wire may be used in order to determine the mechanical boundary conditions in a heterostructure under consideration. In the presence of a magnetic field directed along the wire axis, the Schrödinger equation with a centred parabolic potential within the wire is solved exactly and the energy spectrum depending on the magnetic field is obtained. As far as a splitting and a pinning of the energy levels of magnetopolarons are revealed to depend on the electron–phonon interaction, they can be used for an effective characterization of the state of interfaces in nanostructures. A relative intensity of absorption for the different polarizations of light determines the degree of non-perfectness of the interfaces. The geometrical features of interface can be characterized by means of the cyclotron and the cyclotron-phonon resonances.

The electron–phonon interaction in polar semiconductor low-dimensional systems such as quasi-planar multiheterostructures and superlattices (2D), wire-like (quasi-1D) and dot-like (quasi-0D) structures have recently attracted great interest [1–3], due to the more complex phonon spectra than those in a three-dimensional (3D) system. As it was shown in first theoretical works in this field [4–6], the polar optical vibration spectra in low-dimensional structures include bulk-like confined (slab) and interface phonon modes. In [4] the polar optical vibrational modes of an ionic slab in vacuum were obtained in the dispersionless approximation within the frame-

work of the dielectric continuum model (DCM). The equations of motion of the vibrational excitations in the heterostructure, considered within the framework of a continuum approximation, must be supplemented by both electrostatic and mechanical boundary conditions (BCs). The electrostatic BCs have the universal form for all types of heterojunctions. The mechanical BCs may also assume a general form proceeding from the requirement of continuity of stresses and displacements [2]. However, the mechanical BCs are chosen usually in one of the following forms: (1) $P(n) = 0$ [1,2]; (2) $P^\perp(n) = 0$, $P^\parallel(n) \neq 0$ [4]; (3) $P^\perp(n) \neq 0$, $P^\parallel(n) = 0$ [7], where $P^\perp(n)$ and $P^\parallel(n)$ are the components of the polarization vector in the n -th layer directed along the interface and along the growth axis, respectively. In the first case of ‘squeezed’ interface ions, the vibrations occurring in the neighboring media are inde-

^{*} Corresponding author. Present address: Departement Natuurkunde, Universitaire Instelling Antwerpen (UIA), Universiteitsplein 1, B-2610 Wilrijk, Belgium.

pendent. In other cases, the interface modes appear which allow penetration of both vibrations and corresponding electrostatic potentials from one medium into another one.

For an adequate theoretical description of the vibrational excitations and the electron–phonon interaction in mesoscopic heterostructures, it is crucial, to identify the mechanical BCs which are characteristic of a given heterojunction. This can be performed by comparison of theoretically deduced features of the electron–phonon phenomena in the structures with various types of the mechanical BCs.

In order to reveal these peculiarities, we have considered the polaron problem for a cylindrical quantum wire with finite potential barrier V_0 at the interface [8]. The electron–phonon Hamiltonian was obtained within a continuum model with the mechanical BCs of the type 3. The internal (1) and surrounding (2) media were considered to be polar. In order to achieve higher accuracy, the virtual transitions through all quantum states were taken into account within the second-order perturbation theory, including those belonging to the continuum part of spectrum. In a simple cylindrical quantum-well structure four types of active phonon modes exist [7]: (1) cylindrical bulk-in (confined in the well) LO-phonon modes with the frequency ω_{1L} ; (2) cylindrical bulk-out (belonging to the barrier) LO-phonon modes with the frequency ω_{2L} ; (3) cylindrical interface-optical phonon modes with a relatively high frequency Ω_1 (which is close to ω_{2L}); (4) analogous phonon modes with a lower frequency Ω_2 which is close to ω_{1L} . Existence of the vibrations with the frequencies $\Omega_1 \approx \omega_{2L}$ in the first medium and $\Omega_2 \approx \omega_{1L}$ in the second is indicative of a penetration of the vibrations through the interface. The kinetic energy of the longitudinal motion of a polaron is

$$E_{\parallel}(k) = \frac{\hbar^2 k^2}{2m_{\parallel}^*},$$

$$m_{\parallel}^* = m_{\parallel} \left(1 + s_p \frac{\alpha_{F1}}{6} \right) = m_{\parallel} + \Delta m_p^*, \quad (1)$$

where α_{F1} is the Pekar–Fröhlich coupling constant in the central layer, γ_p describes a polaron effective mass correction due to all phonon modes.

We have studied in detail all contributions to the ground-state energy and the effective mass Δm_p^* for

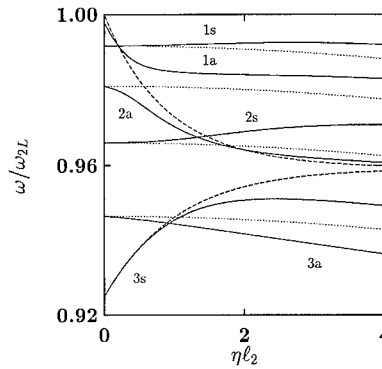


Fig. 1. Vibrational eigenfrequencies for the quantum well AlAs/GaAs/AlAs of thickness $l_2 = 34 \text{ \AA}$ as a function of the module of the in-plane wave vector η . Dotted lines: bulk modes $\omega_{2L}(Q_2)$ with $Q_2 = (\eta, q_2)$, q_2 being a transverse component of the phonon wave vector; dashed lines: interface DCM-modes; heavy lines: hybridized modes; s and a denote symmetrical and antisymmetrical modes, respectively.

a typical cylindrical structure. The results of calculations are presented in Fig. 1. It is easy to see the maxima of both the polaron ground-state energy and the effective mass plotted as a function of the radius R of the cylinder, due to the interaction between an electron and the interface vibrations. Moreover, the interface mode with the frequency Ω_1 plays a leading role in this interaction. In both limiting cases of large and small radii, an electron is placed sufficiently far away from the interface. This circumstance explains why the interface contributions to the polaron parameters depend on the radius R non-monotonously. The total polaron energy ΔE_p reaches the bulk value in $\text{Al}_{0.3}\text{Ga}_{0.7}\text{As}$ at small $R/R_p \rightarrow 0$, R_p being the polaron radius, and reaches the bulk value in GaAs in the limiting case $R/R_p \rightarrow \infty$. These limits are provided by the interaction with cylindrical bulk-in and bulk-out phonon modes, respectively. In spite of essential distinction between electron and polaron states in a slab and in cylinder, qualitatively the results of our work are similar to those of Ref. [9]. Indeed, in both cases for a cylindrical barrier, on the one hand, and for the planar barrier, on the other hand, there are the minima and maxima of the both functions ΔE_p and $\Delta m_p^*/\Delta m_{\text{GaAs}}$ for small radii. For a cylindrical well, these extrema exist at a larger size of the quantum well. For example, in the GaAs/ $\text{Al}_{0.3}\text{Ga}_{0.7}\text{As}$ -structures the mentioned extrema appear for a slab of thickness 20 \AA , but for a

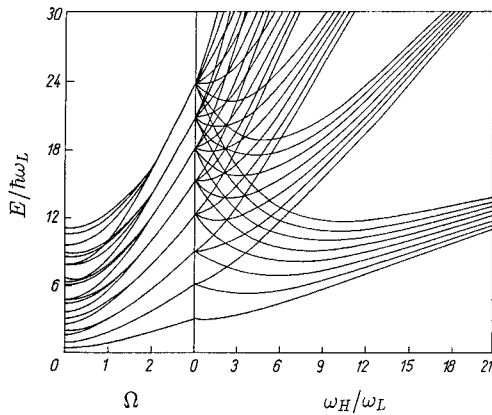


Fig. 2. Left-hand panel: the electron energy spectrum as a function of the confinement parameter Ω for $R/R_p = 4$, where R_p is a polaron radius in the absence of magnetic field. Right-hand panel: the size-quantization-oscillator energy levels as a function of the electron cyclotron frequency ω_H at a fixed value of Ω .

cylinder of diameter 60 Å. The maximum value of $\Delta m_p^* / \Delta m_{\text{GaAs}}$ for a cylindrical quantum well is larger than that for a slab and reaches about 2.5% of the electron mass m_{\parallel} . Note that in the example of the heterostructure GaAs/Al_{0.3}Ga_{0.7}As considered above, the electron–phonon coupling constants α_{F1} and α_{F2} are small. In heterostructures with the larger values of α_{F2} , the above-stated non-monotonous behaviour is expressed considerably stronger. The experimental observation would be indicative of the mechanical BCs which allow a penetration of the vibrations from one medium into another.

We have investigated *magnetopolaron* states in a cylindrical quantum wire with two-dimensional parabolic potential inside the cylinder and the barrier potential at its interface [10]. Fig. 2 (left-hand panel) represents the electron energy spectrum as a function of the confinement parameter Ω for a typical radius $R/R_p = 4$, where R_p is a polaron radius in the absence of magnetic field. It provides a clear view of the splitting of higher levels by the barrier field and of the generation of lower levels. In a weak magnetic field, the splitting of levels takes place, and degeneracy is absent. In this limiting case the value of splitting is determined by the term $\hbar\omega_H m/2$, where ω_H is the electron cyclotron frequency. In the opposite limiting case of a strong magnetic field, $\omega_H \gg \Omega$

and the magnetic radius $a_H \ll a_0$ (where a_0 is the Bohr radius), the energy levels are given as

$$E = \hbar\omega_H \left(n + \frac{1}{2}\right), \quad (2)$$

where $n \equiv r - 1 + (m + |m|)/2$ is a Landau quantum number. The right-hand panel of Fig. 2 shows the conversion of size-quantization-oscillator energy levels into Landau ones with increasing ω_H at a fixed value of Ω . Further, it is important to note mutual crossing and inversion of levels with positive m with respect to levels with negative m .

In the approximation of Wigner–Brillouin perturbation theory (see [11]) we have the following equation for a polaron energy:

$$E = E_{\gamma_0, n_\chi}^0 - \sum_{\gamma, n_\chi} \frac{|\langle \Psi_{\gamma, n_\chi} | \hat{H}_{e-ph} | \Psi_{\gamma_0, n_\chi}^0 \rangle|^2}{E_{\gamma, n_\chi}^0 - E}, \quad (3)$$

where $|\Psi_{\gamma_0, n_\chi}^0\rangle = \Psi(\rho; \gamma)|n_\chi\rangle$ is an eigenfunction of the unperturbed Hamiltonian \hat{H}^0 composed of an electron at the level $\gamma(\nu, m, k)$ with a set of electron quantum numbers ν and of n_χ phonons with a set of phonon quantum numbers χ , which belongs to the eigenvalue E_{γ, n_χ}^0 , the electron–phonon interaction \hat{H}_{e-ph} being considered as a perturbation. Fig. 3a and b represent the resulting polaron energy $E = E_{\gamma_0, 0_\chi}^0 + \Delta E_p(\gamma)$, where $E_{\gamma_0, 0_\chi}^0$ is the unperturbed energy and $\Delta E_p(\gamma)$ is the polaron correction, as a function of the electron cyclotron frequency. For the case when a simple resonance takes place, the electron level $(-1, 1)$ crosses the virtual level $(0, 1)$, but if there are two resonances, the level $(1, 1)$ crosses virtual levels $(0, 1)$ and $(-1, 1)$. Note that a cyclotron transition $(-1, 1) \rightarrow (1, 1)$ with $\Delta m = 2$ is forbidden.

It is noteworthy that in planar structures states with a certain value of the angular momentum are possible only when the magnetic field is perpendicular to the interface, but in this case the frequency of a cyclotron transition does not depend on the size of a layer. The resonance condition reads

$$E_{\gamma_0}(R, \mathcal{H}) = E_\gamma(R, \mathcal{H}) + \hbar\omega, \quad (4)$$

whence it follows that the resonant value of the magnetic field depends on the phonon energy $\hbar\omega$. Because of the inequality $\Omega_1 > \omega_{1L}$, the cyclotron–phonon resonance at the transition $(0, 1) \rightarrow (-1, 1)$ assisted by an interface phonon with the frequency

Ω_1 , takes place at lower values of the magnetic field than the respective resonance assisted by a bulk-in phonon. On the contrary, the cyclotron-phonon resonance at the transition $(0, 1) \rightarrow (1, 1)$ assisted by an interface phonon Ω_1 , takes place at higher values of the magnetic field than that assisted by a bulk-in phonon. This distinct qualitative difference between the resonances for two polarizations of light allows to identify their relation to definite phonon branches. The dependence of a cyclotron-phonon resonant frequency ω_H^0 on R is presented in Fig. 4 for three selected values of the confinement parameter Ω . From the curve 1, which corresponds to a transition $(0, 1) \rightarrow (-1, 1)$ at $\Omega/\omega_L = 1.5$, it follows that $\omega_H^0/\omega_L > 1$ for all values of the radius. At small $\Omega/\omega_L = 0.5; 0.1$, two types of resonance are possi-

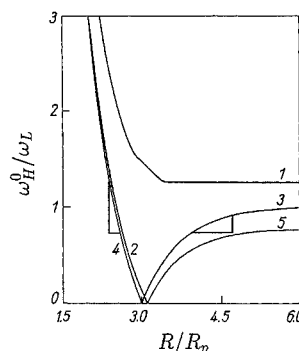


Fig. 4. The dependence of a cyclotron frequency ω_H^0 on the radius for three values of the confinement parameter $\Omega/\omega_L = 0.1, 0.5$ and 1.5 for various transitions: transition $(0, 1) \rightarrow (-1, 1)$ at $\Omega/\omega_L = 1.5$ (1); $(0, 1) \rightarrow (-1, 1)$ at $\Omega/\omega_L = 0.5$ (2); $(0, 1) \rightarrow (1, 1)$ at $\Omega/\omega_L = 0.1$ (3); $(0, 1) \rightarrow (-1, 1)$ at $\Omega/\omega_L = 0.1$ (4); $(0, 1) \rightarrow (1, 1)$ at $\Omega/\omega_L = 0.5$ (5).

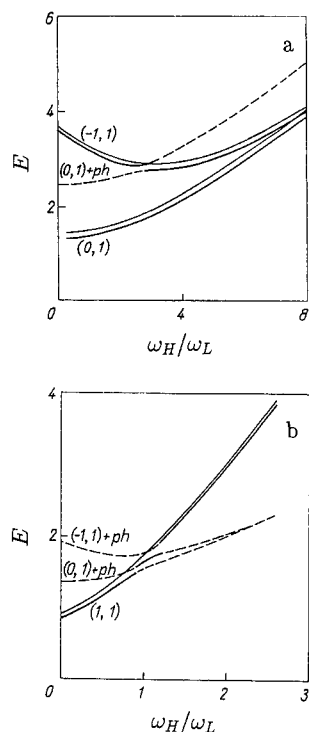


Fig. 3. Numerical plot of the polaron energy $E = E_{\gamma_0,0}^0 + \Delta E_p(\gamma)$, where $E_{\gamma_0,0}^0$ is the unperturbed energy and $\Delta E_p(\gamma)$ is the polaron correction, versus ω_H/ω_L , for parameters of GaAs. Thin curves: the electron level $E_{\gamma}^0/\hbar\omega_L$; dashed curves: virtual levels $(E_{\gamma}^0 + \hbar\omega_L)/\hbar\omega_L$; heavy curves: polaron levels $(E_{\gamma}^0 + \Delta E_p(\gamma))/\hbar\omega_L$ at $R/R_p = 2$ (a) and 4 (b). The lines are labelled by (m, r) , where m is the quantum number of angular momentum and r is a number of a solution.

ble, namely, $(0, 1) \rightarrow (-1, 1)$ (the curve 2 for $\Omega/\omega_L = 0.5$ and the curve 4 for $\Omega/\omega_L = 0.1$), and $(0, 1) \rightarrow (1, 1)$ (the curve 3 for $\Omega/\omega_L = 0.1$, and the curve 5 for $\Omega/\omega_L = 0.5$). From Fig. 4 it is evident, that there exists such a value of a radius R_0 at which a cyclotron transition occurs in a vanishing magnetic field. This value found from Eq. (4) at $\mathcal{H} = 0$ is determined by the parameters of the structure: a charge carrier effective mass and frequencies of optical vibrations. At $R = R_0$ a difference between size-quantized levels becomes equal to the optical phonon energy, and a magneto-size resonance turns into a purely size resonance. The absorption rate is determined by a number of cylinders of the radius $R = R_0$ in a statistical ensemble. At large $R/R_p \gg 1$ we find that $\omega_H^0 = |\omega_L^2 - \Omega^2|/\omega_L$ does not depend on the radius and has the limit $\omega_H^0 = \omega_H$ at $\Omega = 0$. It is interesting to note the existence of the interval of R values where $0 \leq \omega_H^0 < \omega_L$, at $\Omega/\omega_L \leq \sqrt{2}$. This dependence of the cyclotron frequency on the radius implies that for an ensemble of ideal cylinders the *cyclotron-phonon absorption* of the clockwise and counter clockwise polarized light has sharply different features. Namely, at $\omega_H^0 < \omega_L$, the frequency ω_H^0 decreases (increases) for a clockwise (counter clockwise) polarized light. Thus, a critical radius R_0 separates two regions: at $R < R_0$ a transition for a clockwise polarization of light takes place, while at $R > R_0$ that for a counter polarization. For an ensemble of cylinders with various radii far away from the

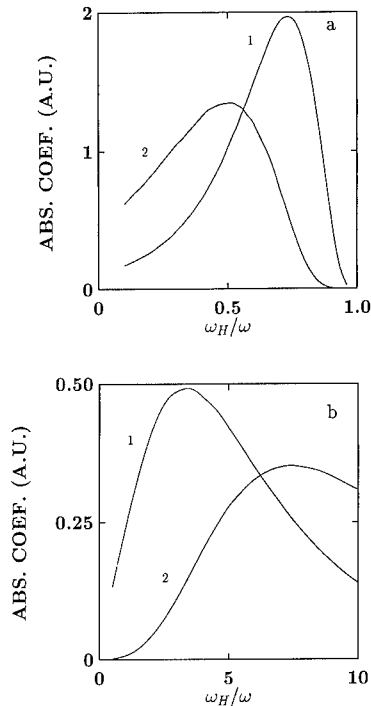


Fig. 5. The light absorption coefficient due to direct transitions $(0, 1) \rightarrow (1, 1)$ (a) and $(0, 1) \rightarrow (-1, 1)$ (b) versus the cyclotron frequency measured in units of the light frequency ω for a Gaussian statistical ensemble of quantum wires with the standard deviation of the radius $\Delta R/\bar{R} = 0.25$ and various mean radii: $\bar{R}_1/R_p = 2$ (1a); $\bar{R}_2/R_p = 1.67$ (2a); $\bar{R}_1/R_p = 1$ (1b); $\bar{R}_2/R_p = 0.9$ (2b).

point R_0 , there will occur a diffused absorption at a given polarization of light in dependence on a magnetic field. For a non-perfect cylindrical interface the electron states have no definite angular momentum, therefore absorption of light of both polarizations will be at one and the same frequency. Thus, a relative intensity of absorption for the two polarizations of light can be used for characterization of interfaces, as far as it determines the degree of their non-perfectness.

In Fig. 5a and b the light absorption coefficient due to direct transitions, $(0, 1) \rightarrow (1, 1)$ and $(0, 1) \rightarrow (-1, 1)$, respectively, is plotted versus the cyclotron frequency for a Gaussian statistical ensemble of quantum wires. It is instructive to mention that for a transition $(0, 1) \rightarrow (1, 1)$ the resonance curves are narrower than for another transition considered, and have opposite dependence on the average radius.

As it follows from the Fig. 5a for a transition $(0, 1) \rightarrow (1, 1)$, when decreasing the mean radius \bar{R} , a cyclotron-phonon resonance peak shifts to the smaller values of the magnetic field, while the absorption coefficient quickly rises with the field at the right from the peak and relatively slowly at the left from it. At the same time, it is evident from the Fig. 5b for a transition $(0, 1) \rightarrow (-1, 1)$, that when increasing \bar{R} , an absorption resonance peak shifts to the smaller values of the field, while the behavior of the absorption coefficient is opposite to that for the former transition. The sharpness and asymmetry of the resonance peaks at a symmetrical distribution of the radii in the statistical ensemble, is explained by the dependence of the resonance frequency ω_H^0 on the radius R . The width of a cyclotron-phonon resonance peak due to the inhomogeneous absorption, may be estimated by the formula:

$$\Delta\omega_H^0(\bar{R}, \Delta R) = |\omega_H^0(\bar{R} + \Delta R) - \omega_H^0(\bar{R} - \Delta R)|, \quad (5)$$

where $\Delta R = (\overline{\Delta R^2})^{1/2}$ is the mean squared deviation of the radius from its average value \bar{R} in the considered statistical ensemble of wires. In two triangles drawn in Fig. 4, vertical and horizontal sides determine $\Delta\omega_H^0$ and $2\Delta R$, respectively, and the points $\omega_H^0(\bar{R})$ for the corresponding values of \bar{R} are marked. It is seen from the dependencies $\Delta\omega_H^0(\bar{R})$ at fixed ΔR , that at \bar{R} increasing, $\Delta\omega_H^0(\bar{R})$ decreases for both types of transitions, in accordance with the results of calculation of the absorption coefficient $\Gamma(\omega_H)$.

For the explanation of asymmetry of the two types of absorption, it is necessary to note that the resonant frequencies ω_H^0 ($(0, 1) \rightarrow (1, 1)$) form a band of a finite width: $0 - (\omega_H^0)_{\max}$, where $(\omega_H^0)_{\max} = \lim_{R \rightarrow \infty} \omega_H^0(R)$, whereas resonant frequencies ω_H^0 ($(0, 1) \rightarrow (-1, 1)$) form an infinitely wide band. Therefore the absorption coefficient $\Gamma(\omega_H)$ for a transition $(0, 1) \rightarrow (1, 1)$ sharply vanishes at large values of ω_H , namely, when they occur to be outside the band of the resonant frequencies. At small ω_H , the absorption coefficient $\Gamma(\omega_H)$ can have a finite value which is determined by a number of wires of the radius R_0 in the considered statistical ensemble. The profile of the decrease of the absorption coefficient $\Gamma(\omega_H)$ for a transition $(0, 1) \rightarrow (-1, 1)$ at the

absorption band edges is determined by the distribution of cylinders, therefore the absorption bands are substantially wider than in the preceding case.

Summarizing the results, we note that:

(i) the absence of the resonant absorption for a counter clockwise polarized light at $\bar{R} > R_0$ in the magnetic field region $0 < \omega_H < \omega_{ph}$ (where ω_{ph} is a frequency of either bulk-like or interface phonons) may witness the strong quantization of the electron spectrum, $E(1, 1) - E(0, 1) > \hbar \omega_{ph}$ due to a potential inside the cylinder (for example, a parabolic potential);

(ii) the resonant absorption of circularly polarized light allows to determine R via a point of maximum of the absorption band. The parameters of the Gaussian distribution can be determined through the spectral distribution of the absorption rate;

(iii) the absorption of light for both polarizations at the same values of the magnetic field is indicative of fluctuations of the cross-section of a quantum wire.

It is noteworthy that if in Eq. (4) ω means the frequency of the electromagnetic field absorbed in the conditions of the cyclotron resonance, we arrive at the same dependencies of the cyclotron frequency on the cylinder radius, as those presented in Fig. 4 for the cyclotron-phonon resonance. As a consequence, all above-mentioned conclusions can be extended to the case of the cyclotron resonance.

Thus, the results obtained afford a new possibility

of characterization of the geometrical features of interface by means of the cyclotron and cyclotron-phonon resonances.

Acknowledgements

This work has been supported by the International Science Foundation (grant No. RZD000).

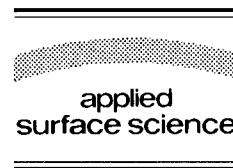
References

- [1] M. Cardona, *Superlatt. Microstruct.* 5 (1989) 27.
- [2] M.P. Chamberlain, M. Cardona and B.K. Ridley, *Phys. Rev. B* 48 (1993) 14356.
- [3] E.P. Pokatilov, V.M. Fomin and S.I. Beril, *Kolebatelnye Vozbuzhdeniya, Polyarony i Eksitony v Mnogosloynnykh Sistemakh i Sverkhreshetkakh* (Shtiintsa, Kishinev, 1990).
- [4] R. Fuchs and K. Kliewer, *Phys. Rev.* 140 (1965) A2076.
- [5] R. Ruppin and R. Engleman, *Rep. Progr. Phys.* 33 (1970) 149.
- [6] V.V. Bryksin and Y.A. Firsov, *Fiz. Tverd. Tela* 13 (1971) 496.
- [7] S.N. Klimin, E.P. Pokatilov and V.M. Fomin, *Phys. Status Solidi (b)* 184 (1994) 373.
- [8] S.N. Klimin, E.P. Pokatilov and V.M. Fomin, *Phys. Status Solidi (b)* 190 (1995) 441.
- [9] G.Q. Hai, F.M. Peeters and J.T. Devreese, *Phys. Rev. B* 48 (1993) 4666.
- [10] E.P. Pokatilov, S.N. Klimin, S.N. Balaban and V.M. Fomin, *Phys. Status Solidi (b)* 189 (1995) 433.
- [11] G. Lindemann, R. Lassnig, W. Seidenbuch and E. Gornik, *Phys. Rev. B* 28 (1983) 4693.



ELSEVIER

Applied Surface Science 104/105 (1996) 552–556



Porous silicon layers as a model system for nanostructures

U. Rossow^{a,*}, U. Frotscher^b, C. Pietryga^b, D.E. Aspnes^a, W. Richter^b

^a *Physics Department, North Carolina State University, Raleigh, NC 27695-8202, USA*

^b *Institut für Festkörperphysik, TU Berlin, PN6-1, D-10623 Berlin, Germany*

Received 28 June 1995; accepted 28 August 1995

Abstract

In this paper we show that the lineshapes of the dielectric functions of porous p-doped silicon layers are strongly correlated to their original bulk doping concentrations. Features in the dielectric functions of layers formed from heavily doped bulk material correspond to bulk critical points, with an additional feature in the visible that results from the electronic structure of silicon that has been changed by the presence of inner surfaces. These results suggest that the layers remain highly connected. For lightly doped starting material the bulk-related features are much broader, with some samples exhibiting only an E_2 interband critical point feature that is shifted to higher energies. This shift, which can be understood in terms of strong confinement of the carriers, suggests reduced connectivity in these layers.

1. Introduction

The nanostructure of porous silicon layers has a high inner surface area and the carriers are confined to small regions. Such layers can easily be prepared by a HF-based electrochemical process, so these layers are attractive for studies of the optical and electronic properties of nanocrystalline material. The nanostructure is considered to consist of weakly linked nanocrystallites. This is an idealization of the real picture, and it has been suggested that these layers have a fractal structure [1].

Here, we show that the lineshapes of the dielectric functions of porous silicon layers formed from p-type silicon are strongly correlated with the doping concentration of the starting material, and therefore the

nanostructures of the layers. Our conclusions are based on dependences observed with variations of starting material (doping concentration), preparation conditions (current densities, electrolyte composition, illumination) and post-preparation treatments.

2. Experimental

Data were obtained from 1.8 to 5.5 eV with a spectroscopic ellipsometer of the rotating analyzer type [2]. The information depth varies strongly with photon energy, here ranging from 5 nm to a few 100 nm and being shallowest near 4.2 eV. The data were converted into so-called effective or pseudodielectric functions $\langle \epsilon \rangle$ [2,3], which describe the effective response of the layer and substrate to the incident light. For most samples investigated here the absorption in the layer is strong enough to suppress bulk contributions.

* Corresponding author. Fax: +1-919-5151333; e-mail: rossow@unity.ncsu.edu.

The porous layers were prepared on p-type doped on-axis silicon wafers with resistivities from 0.01 to 10 Ω cm. The wafers were etched in the dark in an electrolytic solution consisting of 50% HF diluted 1:1 by high purity ethanol. For some experiments the electrolyte was modified by adding NH_4F or H_2O_2 or by dilution with water. Typical current densities and etching times were 20 to 40 mA cm^{-2} and 210 s, respectively. For lightly doped wafers this yields layers with porosities of about 65% and thicknesses of approximately 5 μm . The samples were investigated either directly after preparation or after storage in dry nitrogen. Some of the layers were further oxidized in air or by ozone or H_2O_2 .

3. Results and discussion

Fig. 1 shows the porosity dependence of the imaginary parts of the dielectric functions $\text{Im}\langle\epsilon\rangle$ of layers formed on highly doped silicon substrates. The porosity is determined by the current density during etching, with higher current densities yielding higher porosities. As the porosity increases the volume fraction of the remaining Si skeleton decreases, leading to the reduction of the magnitude of $\text{Im}\langle\epsilon\rangle$ with increasing porosity as can be seen in Fig. 1. Note that all spectra have similar lineshapes above 3.5 eV.

For low porosities, two features labeled A and B appear around 3 eV along with a shoulder near 4.2 eV. The shoulder is related to the E_2 interband critical point of bulk silicon [3]. The spectral position of feature B is about 3.3 eV for the sample with 30%

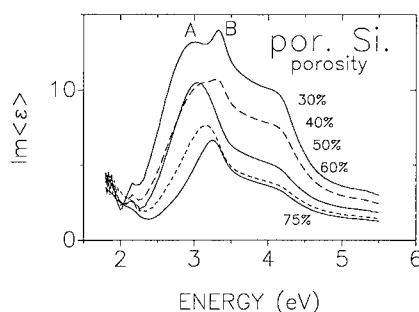


Fig. 1. Porosity dependence of $\text{Im}\langle\epsilon\rangle$ of layers formed on highly doped silicon wafers. The porosity is determined by the current density during etching.

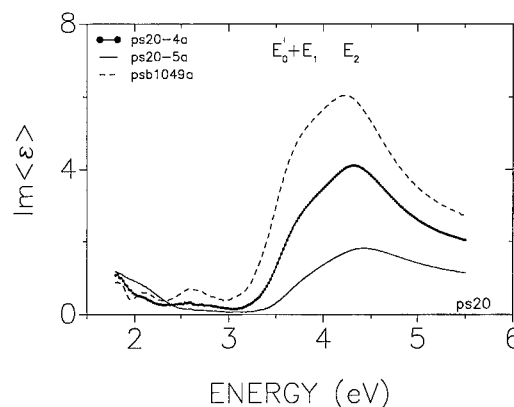


Fig. 2. $\text{Im}\langle\epsilon\rangle$ for three different porous silicon layers formed on lightly doped Si wafers. Layer parameters as follows: psb1049a: 7 μm , 70% porosity; ps20-4a: 5 μm , 65%; ps20-5a: as ps20-4a but oxidized for 1 min in H_2O_2 /ethanol. The 3.7 eV shoulder has nearly vanished for the oxidized sample ps20-5a.

porosity. This is approximately the energy of the interband critical points E'_0 and E_1 . As discussed in [4,5] only a mixture of E'_0 and E_1 is expected for nanocrystalline material due to the broadening of the interband critical points in nanostructures. Therefore, feature B can be assigned to $E'_0 + E_1$. The origin of the feature A, which was reported earlier in [4,6], is unclear. We believe that this feature is due to a modification of the electronic structure of the silicon in the skeleton by the presence of the inner surfaces, and will discuss this more fully elsewhere [7].

Fig. 2 shows $\text{Im}\langle\epsilon\rangle$ for three different porous layers formed on lightly doped starting material. These lineshapes are qualitatively different from those of highly doped silicon. The $E'_0 + E_1$ feature is recognizable only as shoulder on a broad peak E_2 near 4.3 eV. Aside from some variations in absolute values and low-energy lineshapes these spectra are typical for lightly doped samples.

As shown in [8,9] lineshape analysis reveals that the $E'_0 + E_1$ and E_2 spectral positions vary from 3.4 to 3.8 eV and 4.2 to 4.5 eV depending on porosity and post-preparation treatment. Comparing the values of the threshold energies E_g and broadening parameters Γ of the interband critical points obtained by lineshape analysis with the dependencies of E_g and Γ on crystallite diameter as given in [5] reveals a discrepancy between values obtained for $E'_0 + E_1$ and E_2 . For sample psb1049a shown in Fig. 2 the former yields extrapolated values of 2 to 4 nm

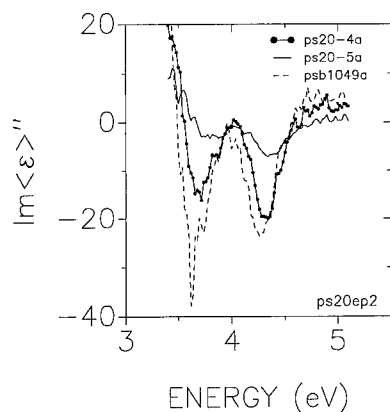


Fig. 3. $d^2\text{Im}\langle\epsilon\rangle/dE^2$ for the spectra of Fig. 2.

while the latter indicate nanocrystallite diameters of about 18 to 20 nm. The E_2 spectral positions for typical layers formed on lightly p-doped material are above 4.3 eV and therefore out of the range studied in [5].

To explain this behavior we first note that the amplitudes and energies of the $E'_0 + E_1$ shoulders in $\text{Im}\langle\epsilon\rangle$ shown in Fig. 2 depend rather strongly on the individual sample and preparation conditions. For ps20-5a the shoulder is hardly visible, whereas in ps20-4a it is clearly seen. To examine the threshold energy we calculated the second energy derivative of $\text{Im}\langle\epsilon\rangle$ for these samples. The results are shown in Fig. 3. The $E'_0 + E_1$ minimum near 3.7 eV is strongest for psb1049a and nearly vanishes for ps20-5a. As the amplitude decreases the feature moves to higher energies. The same is true for the E_2 feature near 4.4 eV. These trends can be understood as a result of percolation. In microcrystalline silicon the crystallites are strongly connected and the $E'_0 + E_1$ feature is clearly visible. We can assume that a relaxation of the momentum conservation due to the presence of interfaces will have its strongest effect on the electronic states. Momentum relaxation reaches its limit in amorphous material, which exhibits total relaxation of momentum conservation and a single broad peak in $\text{Im}\langle\epsilon\rangle$ at 3.8 eV. If momentum relaxation were dominant we could therefore expect the E_2 peak to shift to lower energies in agreement with [5]. However, for isolated nanocrystallites carrier confinement comes into play which is expected to shift all energies to higher values. The latter situation

clearly applies to the samples shown in Fig. 2. We can therefore conclude that with increasing confinement (separation of the nanocrystallites) the E_2 gap will shift to higher energies and the $E'_0 + E_1$ structure will vanish. This also explains the difference between the spectra for lightly and highly doped starting material. For heavily doped starting material $E'_0 + E_1$ is much more pronounced than for lightly doped starting material. Consequently, the nanostructure of layers on heavily doped wafers must be strongly interconnected, in agreement with the fact that the feature sizes are larger in heavily doped silicon [10].

We must still decide whether the main (average) crystallite diameter is 2–4 nm as inferred from $E'_0 + E_1$, or 18–20 nm as inferred from E_2 . We can make this decision with an oxidation experiment. We suppose that we have an ordered array of cylinders of radius r along the [001] direction. We now oxidize the cylinders, which reduces their radius by Δr . For this microstructure the original volume fraction f_{Si} of silicon is given by

$$f_{\text{Si}} = \frac{V_{\text{Si}}}{V} = n\pi r^2, \quad (1)$$

where V is the total volume of the layer, V_{Si} is the volume of silicon before oxidation, and n is the area density of the cylinders.

Oxidation changes the volume fraction of silicon to f'_{Si} . For small Δr we have

$$f'_{\text{Si}} = f_{\text{Si}} \left(1 - 2 \frac{\Delta r}{r} \right). \quad (2)$$

To determine f'_{Si} we measure $\langle\epsilon\rangle$ of a freshly prepared sample, repeat the measurement after the sample has oxidized, then use the Bruggeman effective medium approximation to find out how much SiO_2 must be added to convert $\langle\epsilon\rangle$ to $\langle\epsilon'\rangle$, where $\langle\epsilon'\rangle$ is the measured dielectric function of the oxidized layer. The result of the calculation is shown in Fig. 4. To obtain this result we supposed that $\langle\epsilon\rangle$ is the host dielectric function and neglected contributions from surface states, deviations of the dielectric function of oxide layer from that of SiO_2 (suboxides), and changes in the microstructure. Considering these approximations the fit is excellent. The resulting value of f_{ox} is 0.22.

To relate this result to f'_{Si} we need to relate f'_{Si} to

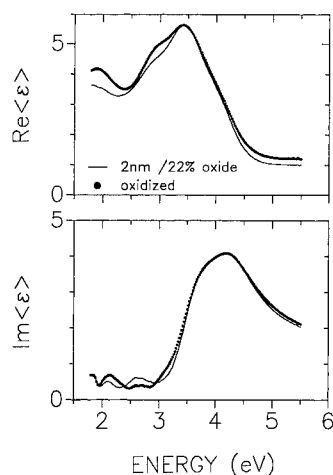


Fig. 4. Points: spectrum of psb1049a that was obtained after the sample was heated in UHV to desorb the hydrogen and stored in air. Line: result of the Bruggeman effective medium calculation described in the text. A 2 nm thick oxide layer on the porous layer was taken into account in the procedure.

f_{ox} . We assume that the ratio of volume fraction of silicon to void remains constant, corresponding to the procedure given above. Thus in consuming skeletal silicon the void fraction also becomes smaller. A decrease in the void fraction is reasonable because oxidized silicon needs more space. We suppose also, that a completely oxidized porous layer will be dense, which is an approximation. It therefore follows that

$$f_{\text{Si}} = \frac{V'_{\text{Si}}}{V - V_{\text{ox}}}, \quad (3)$$

where $V'_{\text{Si}} = f'_{\text{Si}}V$. Substituting this expression into Eq. (3) yields

$$\frac{f'_{\text{Si}}}{f_{\text{Si}}} = \frac{V - V_{\text{ox}}}{V} = 1 - f_{\text{ox}}. \quad (4)$$

Combining Eqs. (2) and (4) yields

$$\frac{\Delta r}{r} = \frac{1}{2}f_{\text{ox}}. \quad (5)$$

The prefactor 1/2 of f_{ox} is only valid for cylinders and would be 1/3 for spheres. Since we are only interested in an estimate we neglect this difference.

We obtain finally

$$r = \frac{2\Delta r}{f_{\text{ox}}}. \quad (6)$$

The value of Δr will range from 0.3 to 1.5 nm for normal oxidation. The latter value is expected to be realized after 1 week of oxidation, which is the case here. With $f_{\text{ox}} = 0.22$ from Fig. 4 we obtain a value of 17 nm, which is in reasonable agreement with 18 to 20 nm range derived from the lineshape analysis of E_2 . Therefore, if the nanocrystallites are interconnected the carriers are confined to regions that are large compared to those that are considered to be necessary to create a pseudo direct gap in silicon.

4. Summary and conclusion

We have shown that the dielectric functions of porous silicon layers formed on p-doped silicon substrates are different for lightly and heavily doped starting material. For heavily doped material the dielectric function resembles that of bulk silicon with some broadening of the interband critical points. An additional feature is observed in the visible range. The origin of this feature is still being clarified, but clearly originates from a change of the electronic structure of the silicon in the skeleton caused by the presence of the inner surfaces.

In lightly doped material the lineshape is dominated by a broad feature at energies near, but above, that of the E_2 interband critical point of bulk silicon. This blue shift together with the vanishing of the additional shoulder of the combined $E'_0 + E_1$ interband critical point feature indicates a loss of interconnectivity of the nanocrystallites. For material that is still interconnected we estimated the main feature size to be of the order of 20 nm. The size range giving the highest PL efficiency is not yet clear.

Acknowledgements

It is a pleasure to acknowledge M.G. Berger (KFA Jülich, Germany) for heavily doped material, and financial support from the German Ministry of Research and Technology (BMBF) under contract No. 01BA401/3, the CEC Esprit Basic Research under action No. 6878 'EASI', the Alexander von Humboldt Foundation, and the U.S. Office of Naval Research (ONR) under contract N-00014-93-1-0255.

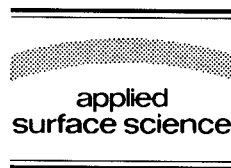
References

- [1] C.C. Matthai, J.L. Gavartin and A.A. Cafolla, *Thin Solid Films* 255 (1995) 174.
- [2] D.E. Aspnes and A.A. Studna, *Appl. Opt.* 14 (1975) 220.
- [3] D.E. Aspnes and A.A. Studna, *Phys. Rev. B* 27 (1983) 983.
- [4] U. Rossow, H. Münden, M. Thönissen and W. Theiß, *J. Lumin.* 57 (1993) 205.
- [5] S. Logothetidis, H.M. Polatoglou and S. Ves, *Solid State Commun.* 68 (1988) 1075.
- [6] F. Ferrieu, A. Halimaoui and D. Bensahel, *Solid State Commun.* 84 (1992) 293.
- [7] U. Rossow, D.E. Aspnes, U. Frotscher and W. Richter, to be published.
- [8] U. Rossow, U. Frotscher, W. Richter, H. Münden, M. Thönissen and M.G. Berger, *Mater. Res. Soc. Symp. Proc.* 358 (1995) 429; in: *Microcrystalline and Nanocrystalline Semiconductors*, Eds. L. Brus, M. Hirose, R.W. Collins, F. Koch and C.C. Tsai.
- [9] U. Rossow, U. Frotscher, C. Pietryga, W. Richter and D.E. Aspnes, *Appl. Surf. Sci.* 102 (1996) 413.
- [10] V. Lehmann, *Thin Solid Films* 255 (1995) 1.



ELSEVIER

Applied Surface Science 104/105 (1996) 557–562



Influence of surface reconstruction on MBE growth of layered GaSe on Si(111) substrates

H. Reqqass^a, J.-P. Lacharme^a, M. Eddrief^a, C.A. Sébenne^{a,*}, V. Le Thanh^a,
Y.L. Zheng^b, J.-F. Pétroff^b

^a Laboratoire de Physique des Solides, ERS 113, CNRS, Université Pierre et Marie Curie, 75252 Paris Cédex 05, France

^b Laboratoire de Minéralogie Cristallographie, URA 9, CNRS, Université Pierre et Marie Curie, 75252 Paris Cédex 05, France

Received 28 June 1995; accepted 25 October 1995

Abstract

Very thin GaSe films, about 100 Å thick, have been epitaxially grown by molecular beam epitaxy on differently ordered Si(111) substrates, namely: the clean 7×7 reconstructed surface with its dangling bonds, the H-passivated 1×1 surface and the Ga-passivated $\sqrt{3} \times \sqrt{3}$ R30° reconstructed one. For each substrate, the GaSe layer and its interface with Si have been studied by low energy electron diffraction, Auger electron spectroscopy and photoemission yield spectroscopy. Upon sequential removal of the GaSe film by Joule heating in ultrahigh vacuum, it is shown that, (i) the band offsets are not sensitive to the initial surface structure of the substrate, (ii) the uniformity of the GaSe layer and of the Fermi level position is questionable on Si(111) $\sqrt{3}$ -Ga, (iii) the density of gap states in the GaSe layer increases upon ageing in air.

1. Introduction

It has been shown that high quality semiconducting layered GaSe films can be grown by molecular beam epitaxy (MBE) on Si(111) 7×7 surfaces from oxidized wafers [1]. Crystalline GaSe films with large single domains have been obtained in which the epitaxy occurs with the hexagonal edges of GaSe aligned with those of Si(111). Other perfectly smooth Si(111) substrates, well-ordered at the atomic scale, can be used such as the H-passivated 1×1 surface [2] or the Ga-passivated $\sqrt{3} \times \sqrt{3}$ R30° reconstructed

surface [3] as well as the clean 7×7 reconstructed one as obtained at low temperature [4]. These substrate structures will be noted in short Si 7×7 , Si-H and Si $\sqrt{3}$ -Ga. Good van der Waals epitaxy of GaSe on Si-H has been already demonstrated [5].

It appears essential to investigate the structural and electronic properties at the interfaces between the 'three dimensional' silicon crystal and the anisotropic, 'two dimensional' GaSe crystalline film. This would help understand better this successful van der Waals epitaxy and check what is the influence of the initial surface structure. The structural properties of the GaSe layer and of the interfaces have been investigated by transmission electron microscopy (TEM) [6] for which a cut through the interface region was prepared by a thinning proce-

* Corresponding author.

ture. To study both electronic and structural properties by surface characterization techniques, we have followed another procedure by which the GaSe/Si(111) heterostructures are progressively annealed under ultra-high vacuum (UHV) until the Si(111) surface is clean.

In a previous paper [7] we reported on such an approach in which the systems GaSe/Si 7×7 and GaSe/Si-H have been sequentially studied by Auger electron spectroscopy (AES), and low energy electron diffraction (LEED). Photoemission yield spectroscopy (PYS) measurements, from which Fermi level position and band offsets can be estimated, had also been performed. They have been reported for the former heterostructure [8].

For the present paper, the same experimental procedure and the same measurements (AES, LEED, PYS) have been performed on GaSe/Si-H and GaSe/Si $\sqrt{3}$ -Ga. The interface properties of the various heterostructures will be compared to each other, knowing of course that the procedure may have some influence on the interface morphology and therefore on the electronic properties. The low photon energy used in PYS (4 to 7 eV) favors a relatively large electron escape depth, over 10 Å. In case of uniform layers, it enables to get straightforward information on band discontinuities and gap states.

2. Experiment

The MBE grown GaSe/Si(111) heterostructures were prepared in a Riber system as described elsewhere [1]. The Si substrates were low doped n-type wafers about 500 μm thick from Siltronics. First, all substrates were H-passivated using a buffered solution of HF according to the method proposed in [2], then they were introduced into the MBE vacuum system taking special care for the loading and pumping procedure. They could be used as such for the GaSe film growth on the Si-H substrate. In order to prepare a clean and smooth 7×7 reconstructed Si(111) surface, the H-passivated wafer was heated to 600°C in ultra-high vacuum (UHV) [3]. The Si-Ga $\sqrt{3}$ substrate was prepared by deposition of a few monolayers of Ga on the cleaned Si 7×7 followed by annealing in the 650°C range to remove the excess of Ga and reach the $\sqrt{3}$ reconstruction as

observed by reflection high energy electron diffraction (RHEED).

The Si(111) substrate, once heated to 450°C, was covered by a crystalline film of GaSe by setting the Se to Ga flux ratio between 8.5 and 11.5. The thickness of the film was about 100 Å for the new samples while it had been about 300 Å in the previous heterostructures [7,8].

After GaSe deposition, the wafers were exposed to air and cut into samples for different characterizations. Before the transfer to the UHV system for surface measurements, the new samples were kept at most one month under primary vacuum. They will be referred to as 'freshly prepared' samples. Whereas the previous heterostructures had been stored at least three months in air in a dust free container.

For surface studies, the samples were $20 \times 5 \times 0.5$ mm³ GaSe/Si(111) parallelepipeds. They were mounted on a sample holder in a ultra-high vacuum chamber which has been described earlier [9]. The sample bridged two refractory metal electrodes through which it could be Joule-heated at any temperature up to 1200°C under the control of optical pyrometers (either standard or IR). The base pressure in the system was below 2×10^{-10} Torr and did not change upon sample heating below 500°C. Upon heating at higher temperatures, the pressure raised at most into the high 10^{-10} Torr range. A heating cycle lasted 5 min by rapidly fixing a constant current through the sample and turning it off suddenly at the end. The highest temperature reached during a heating cycle will be called the annealing temperature T_A . After each heating cycle, once the sample was back to room temperature, the photoemission yield spectrum was measured, then, the Auger electron spectra were recorded, using a normally incident primary beam of 10 μA at 2 keV and a cylindrical mirror analyzer, and the LEED diagram was observed.

3. Results and discussion

The RHEED diagrams observed during the growth process showed that whatever the initial surface structure of the substrate, the GaSe film was singly oriented, with the *c*-axis normal to the layer and to the (111) plane of Si, and with its [10.0] direction

parallel to the $[1\bar{1}0]$ direction of the substrate. This is confirmed by TEM studies [6] which, in all cases, reveal sharp interfaces where the distortion-free regions are of the order of several hundred Å along the surface.

The LEED and Auger results of the freshly prepared systems are given in Fig. 1 as a function of annealing temperature with T_A around and above the growth temperature. The peak to peak intensities of the low energy Auger structures of Se, Ga and Si are reported, as well as the oxygen signal.

Let us consider the GaSe/Si-H heterostructure first (Fig. 1a). Both Se and Ga show roughly constant Auger signals below 600°C when the surface exhibits the 1×1 GaSe(00.1) LEED diagram. In the same T_A range, there is no detectable low energy Auger signal from Si, whereas a faint and constant high energy signal is observed. These results are consistent with the presence of a uniform, non oxi-

dized GaSe film. After annealing at 600°C, the LEED diagram becomes that of Si(111) 1×1 ; both Se and Ga Auger signals suffer an important decrease while the Si signal at 91 eV remains barely detectable. The GaSe is fully removed by annealing slightly beyond 600°C as inferred from the very small value and disappearance of the Se signal, and the sharp increase of the Si (91 eV) structure. There remains a fraction of a monolayer of Ga which induces a $\sqrt{3} \times \sqrt{3}$ R30° reconstruction of Si(111), and some oxygen appears at the silicon surface. It is then necessary to anneal the sample at 680°C to get rid of the gallium and observe a 1×1 diagram of the substrate.

These results are in many ways similar to those reported previously on GaSe/Si 7×7 and GaSe/Si-H [7], in particular the sudden disappearance of the GaSe layers beyond 600°C in spite of the different film thickness. Also, the sequence of LEED

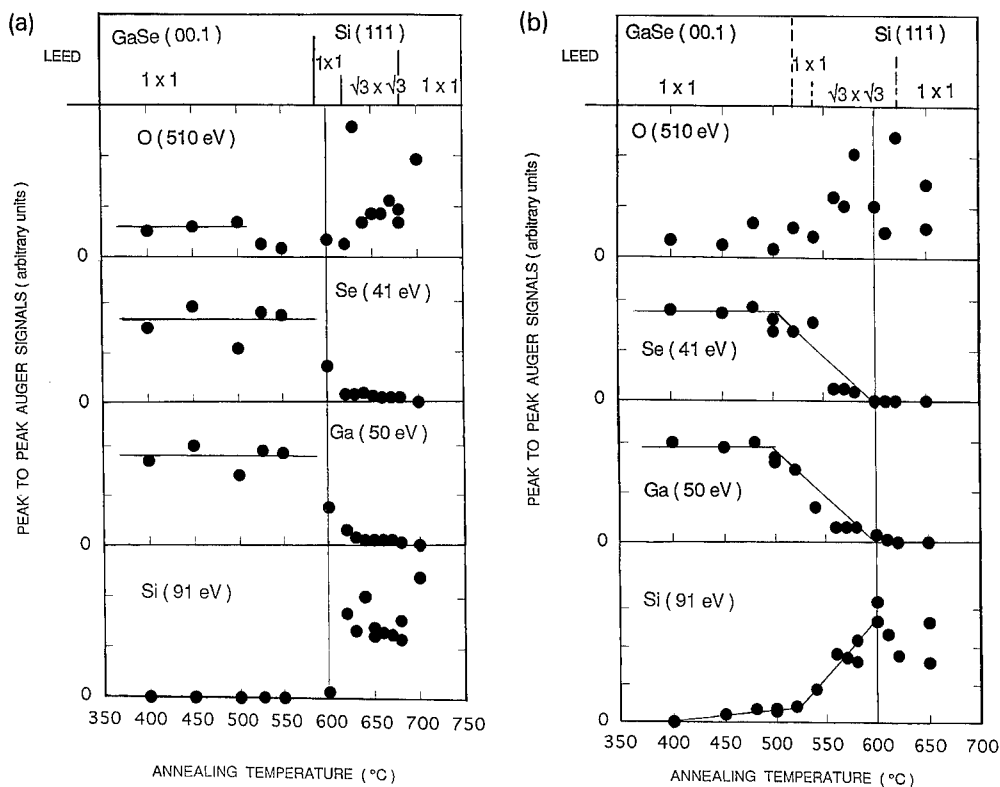


Fig. 1. Evolution with annealing temperature of the peak to peak Auger signal intensities of oxygen, selenium, gallium and silicon measured at room temperature, together with the surface unit mesh as deduced from LEED, after UHV annealing of freshly prepared GaSe/Si(111) heterostructures where a 100 Å thick layer of GaSe had been grown on (a) Si(111) 1×1 -H and (b) Si(111) $\sqrt{3} \times \sqrt{3}$ R30°-Ga substrates.

diagrams and the T_A values at which changes occur are the same as with GaSe/Si 7×7 . The main differences arise from the initial oxygen content of the films: it is very small in the freshly prepared samples whereas it is important in the two heterostructures which have been stored in air. The initial presence of oxidized Ga modified the evolution of both Se and Ga signals at T_A below 600°C [7]. One should notice also that in spite of the large initial oxygen content, the GaSe/Si 7×7 system is the only one which, after annealing at 570°C, gives an oxygen free surface that remains clean upon further annealings [7]. The other heterostructures appear to have some oxygen at the interface.

A much different behaviour is observed for GaSe grown on Si(111) $\sqrt{3}$ -Ga (Fig. 1b). Besides an overall increasing oxygen content, a silicon Auger signal has already appeared after 450°C annealing. This Si signal increases slowly up to about 500°C annealing while both Se and Ga Auger signals remain roughly constant. Then, after annealings at increasing temperatures from 500 to 600°C, the Si signal increases regularly while both the Se and Ga signals decrease in parallel. In LEED, as in the other cases, the GaSe 1×1 diagram gives place to Si 1×1 , then to Si $\sqrt{3}$ -Ga, but the changes occur at lower temperatures. It appears also that the Ga signal and the corresponding $\sqrt{3}$ -Ga reconstruction disappear after annealing at temperatures lower than for the other cases. This may be related to the relatively high oxygen content at the interface which may partly combine with Ga enabling the latter to thermally desorb as an oxide.

The morphological behaviour of our systems can be qualitatively understood in a simple manner. Except in the case of Si $\sqrt{3}$ -Ga substrate, the thermal erosion of GaSe occurs layer by layer. The layer edges are expected to be much less stable than the layer Se plane, so when a hole appears by thermal bond breaking in the top layer, its size increases very fast and the top layer is removed while the layer beneath is still intact. In the case of GaSe grown on Si $\sqrt{3}$ -Ga, the evolution of the Si (91 eV) Auger signal (Fig. 1b) suggests that the GaSe film is no longer continuous after annealing in the 450–500°C temperature range. Some holes have appeared in the film which make the Si substrate visible and expose free layer edges over possibly several layers. Beyond 500°C, thermal erosion would start from the hole

edges. The origin of the holes is not known. We tentatively propose they may be related to the presence of Ga nanoclusters as a result of the Si $\sqrt{3}$ -Ga substrate preparation.

Let us consider now the electronic properties of the GaSe/Si(111) systems, as deduced from photoemission yield measurements. In PYS, the number of photoemitted electrons per incident photons, whatever their kinetic energy, is measured as a function of photon energy $h\nu$. This technique is sensitive to filled electronic states, and, since $h\nu$ ranges from 4.2 to 6.7 eV, it probes the possible presence of gap states and the top of the valence band. At the low photon energy end of the spectra, an integrated Fermi distribution function is used to fit the threshold and obtain the work function of the system. The ionization energy at the onset of the valence band contribution can be determined from the high photon energy part of the spectra as long as the surface is homogeneous. Upon successive annealings at increased temperatures, one expects to switch from GaSe to Si valence band contribution. We shall focus our attention on two points. First, the electronic properties of the GaSe films grown on the various substrates will be compared not only between themselves but also to those of a clean cleaved GaSe bulk crystal. Then, the electronic properties of the heterojunctions will be considered.

In Fig. 2 various photoemission yield spectra are displayed, corresponding to the various substrates under study. They have been selected as having undergone UHV annealing at the highest temperature compatible with a negligible contribution from the Si substrates. They are thus characteristic of the GaSe films. Curves 1 and 2 correspond to the samples which had been stored in air, GaSe/Si 7×7 annealed at 570°C, and GaSe/Si-H annealed at 580°C, respectively. Curves 3 and 4 are from the freshly prepared samples, GaSe/Si-H annealed at 550°C, and GaSe/Si $\sqrt{3}$ -Ga annealed at 520°C, respectively. Also given in Fig. 2 is (R) the measured yield curve for a cleaved bulk GaSe crystal and its best fit with a power law $(h\nu - E_i)^\alpha$ which gives an ionization energy $E_i = 5.90 \pm 0.05$ eV and a purely phenomenological exponent $\alpha = 3.5$ (R has been divided by 10 to have a better view of the results). This reference curve has been used to estimate the ionization energy corresponding to each spectrum

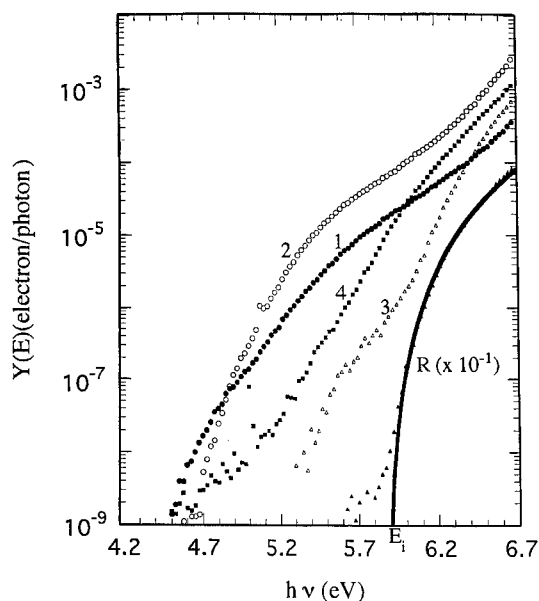


Fig. 2. Photoemission yield spectra, in semilogarithmic coordinates, of a clean cleaved GaSe bulk crystal (R) fitted with a power law $(h\nu - 5.9)^{3.5}$, and of various GaSe/Si(111) heterostructures after UHV annealing at T_A : (1) 300 Å GaSe on Si(111) 7×7 , stored in air, $T_A = 570^\circ\text{C}$; (2) 300 Å GaSe on Si(111) 1×1 -H, stored in air, $T_A = 580^\circ\text{C}$; (3) 100 Å GaSe on Si(111) 1×1 -H, freshly prepared, $T_A = 550^\circ\text{C}$; (4) 100 Å GaSe on Si(111) $\sqrt{3} \times \sqrt{3}$ R30°-Ga, freshly prepared, $T_A = 520^\circ\text{C}$. For clarity of the figure, the reference curve R has been attenuated 10 times, i.e. shifted by one decade along the ordinate axis.

from the best fit at high photon energy where the GaSe valence band states dominate. In most cases, the ionization energy of the GaSe film is found very close to that of the reference.

Obviously, the reference curve does not display any gap states. It is not the case for curves 1 and 2 which show a large contribution of filled gap states between Fermi level E_F and valence band edge E_v , E_F being at least 1.2 eV above E_v in both cases. This corresponds to the two heterostructures which had been stored in air for several months, at an annealing stage where gallium oxide has been removed. In the case of freshly prepared samples, the gap state densities are much smaller. These most likely arise from structural defects of the GaSe films and from impurities such as oxygen inserted in the layered material. The smallest density of gap states is observed with GaSe grown on Si-H (Fig. 2 – curve 3). This is consistent with a uniform film in that case

as compared to a disrupted one on $\text{Si}\sqrt{3}$ -Ga (Fig. 2 – curve 4). It is also consistent with the TEM results [6] according to which the Si-H substrate provides films with the best crystalline perfection.

With the presently investigated heterostructures, like with GaSe/Si 7×7 [8], as the annealing temperatures are raised beyond those of Fig. 2, a growing contribution of the substrate valence band states is observed. It leads to a photoemission yield spectrum characteristic of the $\text{Si}\sqrt{3}$ -Ga surface. This evolution is seen in Fig. 3 where the ionization energies and work functions deduced from photoemission yield spectra are shown against annealing temperature for both freshly prepared samples as well as for GaSe/Si 7×7 . The switch from GaSe ionization energy to $\text{Si}\sqrt{3}$ -Ga ionization energy, which coincides here with direct determinations [10], is always clear. The work function was not always easy to determine. In particular with the Si-H substrate, it is probably overestimated in the 540°C range because the density of gap states is too small; in that case, only an upper limit can be evaluated.

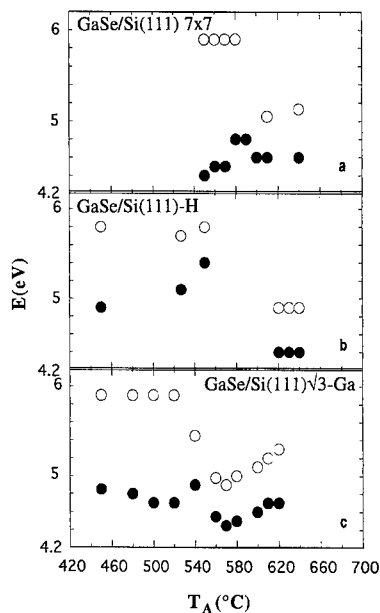


Fig. 3. Evolution of ionization energy (○) and work function (●) deduced from photoemission yield spectra upon UHV annealing at T_A of GaSe/Si(111) heterostructures: (a) 300 Å GaSe on Si(111) 7×7 , stored in air; (b) 100 Å GaSe on Si(111) 1×1 -H, freshly prepared; (c) 100 Å GaSe on Si(111) $\sqrt{3} \times \sqrt{3}$ R30°-Ga, freshly prepared.

Because the escape depth of photoemitted electrons is relatively large (above 10 Å) in the photon energy range investigated, silicon valence band contribution can already be detected while Si is still fully covered by GaSe. This signal comes from the interface before it is destroyed by thermal erosion. It has been observed with the present GaSe/Si–H heterostructure as well as with GaSe/Si 7×7 [8]. In both cases, the photoemission yield curve looks like an attenuated spectrum from a Si $\sqrt{3}$ –Ga surface. It suggests that there might exist a Si $\sqrt{3}$ –Ga structure at the interface whatever the initial substrate structure.

From the ionization energies of GaSe (5.9 eV) and Si $\sqrt{3}$ –Ga (4.9 eV), and taking the Fermi level as energy reference, band offsets at the heterojunction can be evaluated. This approach is only valid if the system remains uniform upon GaSe erosion, which is not the case of GaSe/Si $\sqrt{3}$ –Ga. The following values are obtained for the band offsets: $\Delta E_v = 0.9 \pm 0.1$ eV and $\Delta E_c = 0.0 \pm 0.1$ eV for both GaSe/Si(111) 7×7 and GaSe/Si(111) 1×1 -H. In the former case, E_F is 0.45 eV above the Si valence band edge at the interface and maybe slightly higher at 0.50 eV in the latter case, for Si-n substrates. Slightly different values of the band offsets have been given in [7] for GaSe/Si 7×7 because a value of 5.8 eV had been assumed for the ionization energy of the clean GaSe (00.1) face by comparison with other selenides.

In summary the main conclusions of the present work are the following:

- The photoemission yield spectrum of crystalline GaSe valence states is well represented by a power law $(h\nu - E_i)^\alpha$ where the ionization energy E_i is 5.90 ± 0.05 eV and $\alpha = 3.5$.

- The band scheme (band offsets, Fermi level position) of the GaSe/Si(111) heterostructures is found almost insensitive to the substrate surface as soon as it is smooth and well ordered: the conduction bands are essentially aligned.

- Oxygen contamination at the interface has been avoided only upon GaSe growth on clean Si(111) 7×7 substrates.

- High densities of gap states in the GaSe epitaxial layer seem related to impurity insertion upon storage in air.

- The thermal erosion of GaSe is strongly anisotropic and nanoinhomogeneities, for example induced by some Ga excess, decrease by about 200° the stability in UHV.

Acknowledgements

The authors are grateful to Dr. A. Chevy of Laboratoire de Physique des Milieux Très Condensés at Université Pierre et Marie Curie for providing us with the GaSe bulk crystal, and to Dr. F. Proix for many fruitful discussions and critical reading of the manuscript.

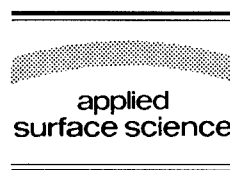
References

- [1] V. Le Thanh, M. Eddrief, C.A. Sébenne, A. Sacuto and M. Balkanski, *J. Cryst. Growth* 135 (1994) 1.
- [2] G.S. Higashi, Y.J. Chabal, G.W. Trucks and K. Raghovachari, *Appl. Phys. Lett.* 56 (1990) 656.
- [3] C.A. Sébenne, in: *Properties of Silicon*, EMIS Datareviews Ser. No. 4, INSPEC 19(10) (1988) 754, and references therein.
- [4] V. Le Thanh, M. Eddrief, C.A. Sébenne, P. Dumas, A. Taleb-Ibrahimi, R. Günther, Y.J. Chabal and J. Derrien, *Appl. Phys. Lett.* 64 (1994) 3308.
- [5] K.-Y. Liu, K. Ueno, Y. Fujitawa, K. Saiki and A. Koma, *Jpn. J. Appl. Phys.* 32 (1993) L434.
- [6] A. Koëbel, Y. Zheng, J.-F. Pétroff, M. Eddrief and C.A. Sébenne, *J. Cryst. Growth* 154 (1995) 269.
- [7] H. Reqqass, J.-P. Lacharme, C.A. Sébenne, M. Eddrief and V. Le Thanh, *Surf. Sci.* 331–333 (1995) 464.
- [8] H. Reqqass, J.-P. Lacharme, C.A. Sébenne, M. Eddrief and V. Le Thanh, *Appl. Surf. Sci.* 92 (1996) 357.
- [9] D. Bolmont, P. Chen, C.A. Sébenne and F. Proix, *Phys. Rev. B* 24 (1981) 4552.
- [10] N. Safta, J.-P. Lacharme, C.A. Sébenne and A. Akremi, *J. Phys.: Condens. Matter* 5 (1993) 6623.



ELSEVIER

Applied Surface Science 104/105 (1996) 563–569



Heteroepitaxial growth of InSb on Si(001) surface via Ge buffer layers

M. Mori, D.M. Li, M. Yamazaki, T. Tambo, H. Ueba, C. Tatsuyama *

Department of Electronics and Information Engineering, Faculty of Engineering, Toyama University, 3190 Gofuku, Toyama 930, Japan

Received 28 June 1995; accepted 5 September 1995

Abstract

InSb was grown on the Si(001), Ge(001) and Ge/Si(001) substrates by the coevaporation of elemental In and Sb sources. The grown films were characterized by AES (Auger electron spectroscopy), optical microscope, XRD (X-ray diffraction), SEM (scanning electron microscope) and ECP (electron channeling pattern), as a function of growth conditions, such as growth temperature and flux ratio of Sb/In. The thickness of grown InSb films was about 0.8–1.2 μm . In contrast with the direct growth on Si(001) surface, InSb easily grows heteroepitaxially on Ge(001) and Ge/Si(001) substrates, for wide growth conditions. The surface morphology and the crystal quality of the grown films strongly depend on the flux and/or composition ratio of Sb/In. It is found that the optimized flux ratio is about 4.5 to obtain the stoichiometric InSb films with smooth surface at growth temperature of 300°C. However, the XRD spectrum and ECP pattern reveal that better crystal quality is obtained for the In-rich films rather than the stoichiometric films.

1. Introduction

InSb is an interesting III–V semiconductor, since it has the highest electron mobility of all semiconductors, and has a narrow band gap. These properties make it attractive material for a magnetic sensor and a long wave length infrared detector. The heteroepitaxial growth of InSb on GaAs substrate has been reported by several groups using different deposition techniques such as molecular beam epitaxy (MBE) [1–4], metalorganic chemical vapor deposition (MOCVD) [5–8], and metalorganic magnetron sput-

tering [9–11]. A thin buffer layer of InSb grown by atomic layer epitaxy has also been used for the growth of InSb on GaAs [12]. Another materials such as sapphire [13,14] and InP [15] have also been used for the substrate. The heteroepitaxial growth of InSb on Si(001) surface has attracted much interest from a view point of the integration of such InSb devices and Si-LSI (large scale integrated circuits) on Si(001) substrate. However, it is very difficult to grow heteroepitaxial InSb on Si(001) substrate, since the large lattice mismatch of about 19% between InSb and Si. Rao et al. [16] have grown InSb epilayer on Si(001) substrate with a 2 μm thick MBE-grown GaAs buffer layer by metalorganic magnetron sputtering. Chyi et al. [17] have also used GaAs as a buffer layer for the MBE growth of InSb on Si(001)

* Corresponding author. Tel.: +81-764-411271; fax: +81-764-418432; e-mail: tatsuyam@jpnt.yam.

substrate. The lattice mismatch between InSb and substrate decreases down to about 15%. By using GaAs buffer layer, they got the improved electron mobility in InSb films on Si(001) compared to that without buffer layer. AlAs has also been used as a buffer layer for the growth of InSb on GaAs and Si substrates [18].

Here, we propose for the first time to use Ge buffer layer for the heteroepitaxial growth of InSb on Si(001) substrate. The heteroepitaxial growth and the structural characterization of Ge on Si(001)- 2×1 surface have already been reported [19,20]. The lattice mismatch between Ge and InSb is down to about 15%, as well as the GaAs buffer layer. In the present work, the comparative study on the growth of InSb on Si(001), Ge(001) and Ge/Si(001) substrates will be reported. The grown films will be characterized by in situ AES (Auger electron spectroscopy), optical microscope, XRD (X-ray diffraction), SEM (scanning electron microscope) and ECP (electron channeling pattern).

2. Experimental

InSb was grown on Si(001), Ge(001) and Ge/Si(001) substrates by the evaporation of separated In and Sb sources in a high vacuum chamber equipped with AES and LEED systems (base pressure 5×10^{-9} Torr). A clean 2×1 surface of p-type Si(001) with resistivity about $20 \Omega \text{ cm}$ was prepared by annealing at 950°C for 20 min. The Ge(001) substrate with resistivity of $60 \Omega \text{ cm}$ was cleaned by heating at 800°C for 20 min. In the case of Ge/Si(001) substrate, the Ge film with thickness of about $4,000 \text{ \AA}$ was grown at 400°C on Si(001) surface as a buffer layer in MBE (molecular beam epitaxy) chamber. After introducing the Ge/Si(001) substrate into the high vacuum growth chamber, it was annealed at 800°C for 10 min. The heating of these substrates was performed by direct current. The substrate dimension was about $8 \times 10 \times 0.5 \text{ mm}^3$. These cleaning procedures yielded the clear 2×1 LEED (low-energy electron diffraction) pattern of individual surface. InSb was grown on these substrates by the coevaporation of 6-nine pure In and Sb from separated sources. The fluxes of In and Sb were monitored separately by quartz oscillators. The flux

ratio of Sb/In was changed by adjusting Sb flux under a constant In flux. The substrate temperature was measured by an alumel–chromel thermocouple attached to the substrate holder and also by a pyrometer. The composition of grown films was estimated by measuring peak-to-peak intensity in the first

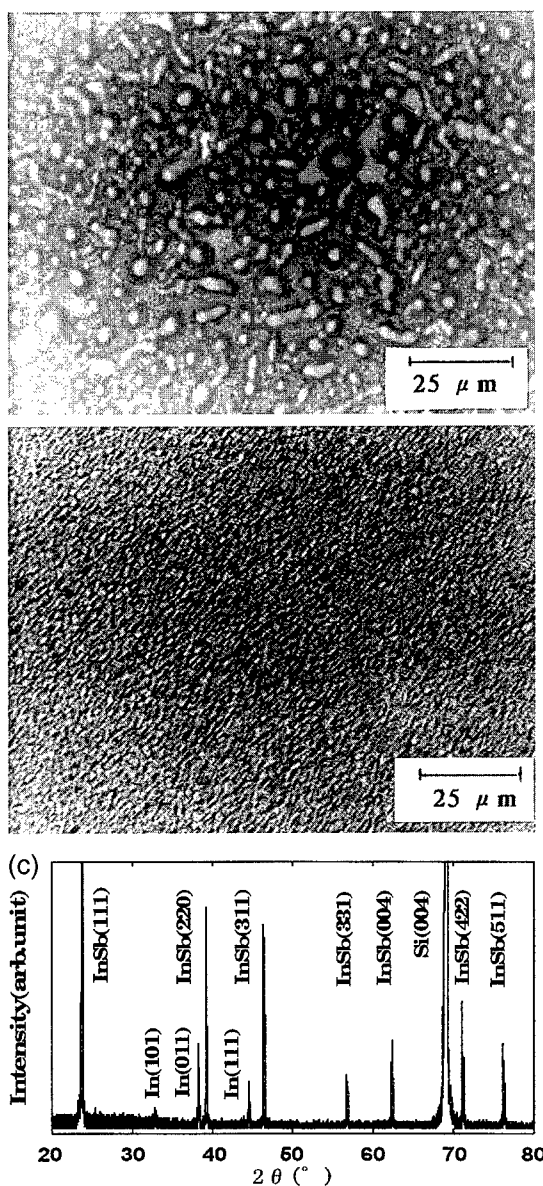


Fig. 1. Growth of InSb on Si(001) substrate with flux ratio of 4.0. (a) Optical microscope photograph of the sample grown at 300°C , (b) optical microscope photograph of the sample grown at 370°C on the 230°C -grown layer, (c) XRD spectrum of the sample (b).

derivative mode of In-Mnn and Sb-MNN AES signals at 404 and 454 eV, respectively. XRD using Cu-K α X-rays, SEM and ECP operating at 15 or 30 kV and optical microscope were used for the characterization of the grown films as a function of growth conditions, such as growth temperature between 100 and 400°C, and flux ratio of Sb/In from 1 to 6. ECP pattern was taken in the beam locking mode with scanning angle of 5.2–6.5°. The growth rate was about 3 Å/s, and the thickness of grown InSb films was about 0.8–1.2 μm .

3. Results and discussion

3.1. Direct growth of InSb on Si(001) substrate

Fig. 1 shows some results on the direct growth of InSb on Si(001) substrate, where (a) depicts an optical microscope photograph of InSb surface grown

on Si(001) substrate at 300°C by using flux ratio of 4.0. The composition ratio of the film estimated by AES is 0.76. As seen in the figure, the surface consists of many agglomerated islands. Although the detail of the surface morphology depended on the flux/and/or composition ratio of Sb/In, it was needed to grow at lower temperature than 250°C for the growth of InSb films with smooth surface. The two-step temperature growth was effective. And, as shown in Fig. 1(b), the growth at higher temperature such as 370°C on the 230°C pre-grown layer results in the growth of InSb with smooth surface. However, XRD spectrum reveals that the InSb film is polycrystalline, irrespective of the growth conditions, as shown in Fig. 1(c). The strongest peak related to InSb is the (111) line, while the (004) peak is very weak, thereby suggesting no epitaxial relation between grown film and substrate. In-related peaks are also seen in the XRD spectrum. Chyi et al. [17] have reported the direct heteroepitaxial growth of InSb on

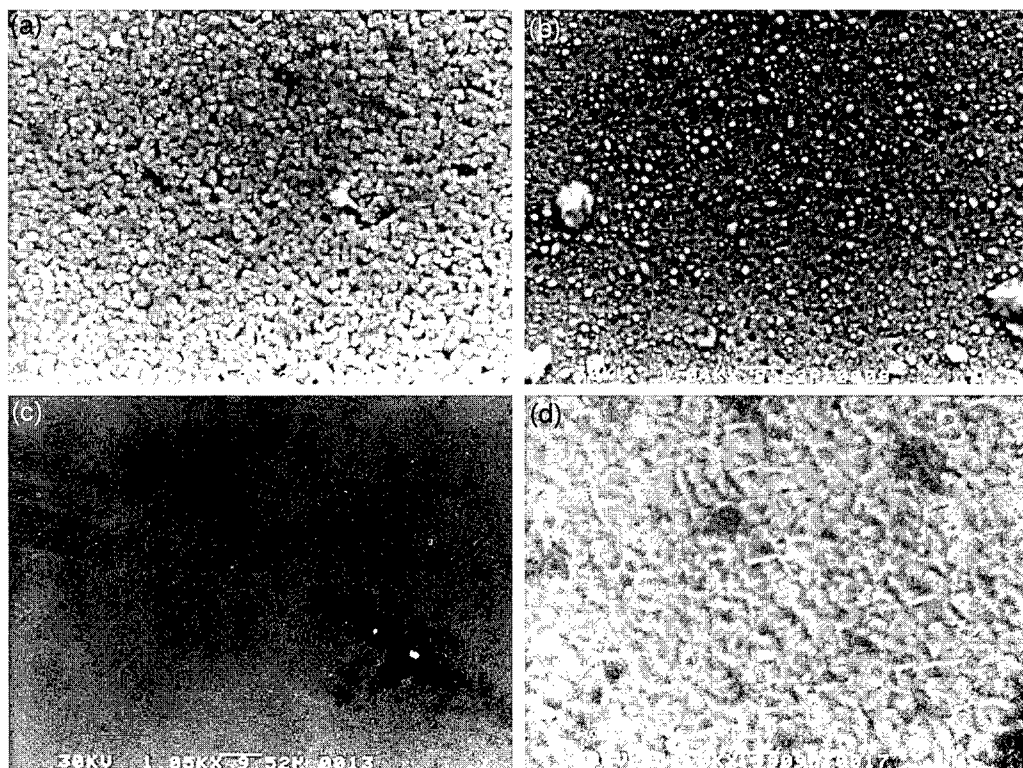


Fig. 2. SEM images of InSb grown on Ge(001) substrate at 300°C under the flux ratio of (a) 3.0, (b) 4.0 and (c) 5.0. The corresponding composition ratio of Sb/In are 0.72, 0.82 and 1.29, respectively.

Si(001) substrate without buffer layer by using molecular beam epitaxy. However, there seems to be a very narrow channel in the growth conditions for the direct heteroepitaxy of InSb on Si(001) substrate [21].

3.2. Growth on Ge(001) substrate

Fig. 2(a, b, c and d) show SEM images of InSb surfaces grown on Ge(001) substrate at 300°C, where

the samples (a), (b) and (c) were grown at flux ratio of 3.0, 4.0 and 5.0, respectively. Sample (d) is the magnification of (c). The corresponding composition ratio estimated by AES is 0.72, 0.82 and 1.29, respectively. The grown films with flux ratio 3.0 and 4.0 are In-rich, while the film grown at flux ratio 5.0 is Sb-rich. As seen in the figures, it is found that the flux ratio and/or composition ratio of Sb/In plays a crucial role in determining the surface morphology of the grown films. The surface of the sample (a)

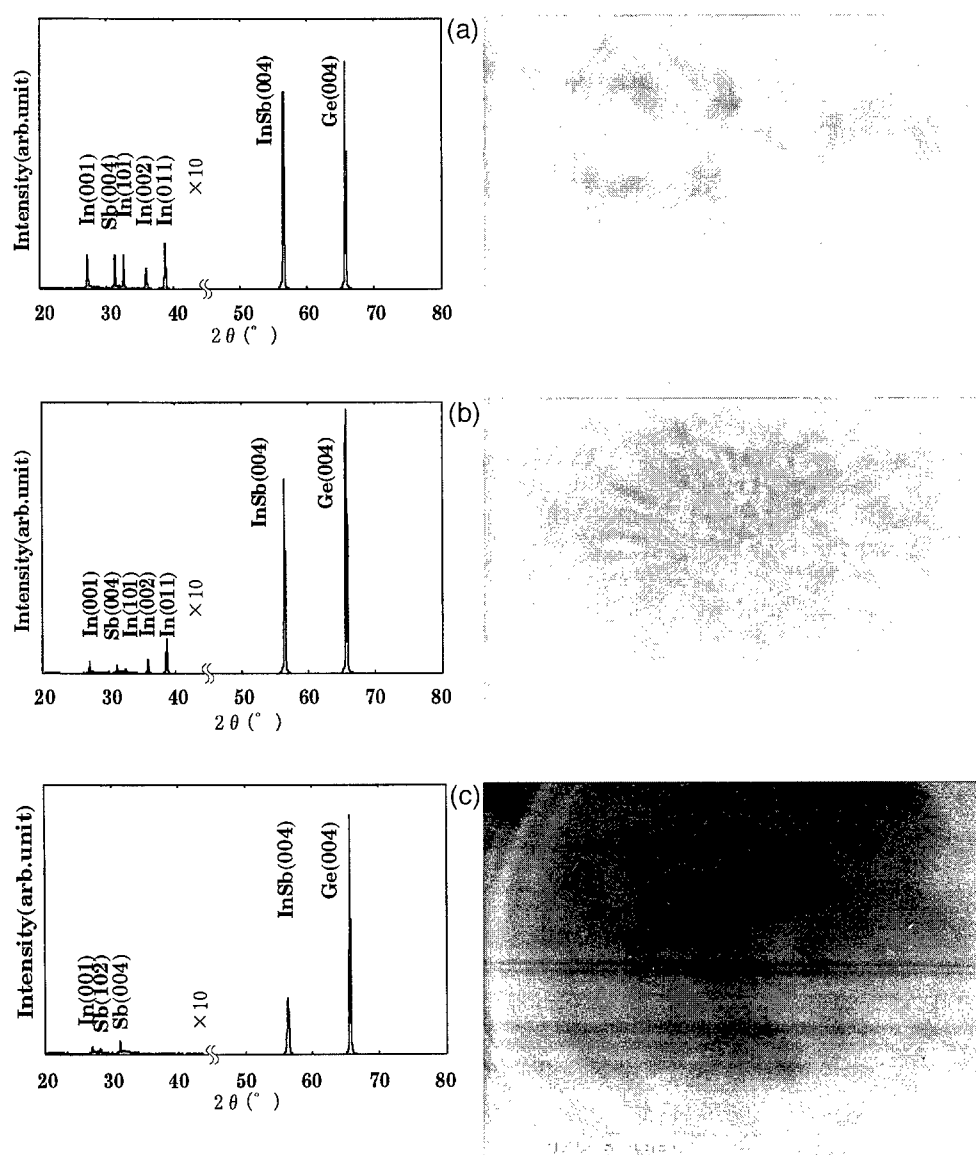


Fig. 3. XRD spectra (left) and ECP patterns (right). The samples are the same as Fig. 2.

grown at flux ratio of 3.0 shows many grains. On the surface of sample (b), there exist many small precipitates, may be In-droplets. The surface becomes smoother and smoother with increase in the flux ratio and/or composition ratio, and the surface of the film grown at flux ratio 5.0 was mirror-like in eye observation, and no structures are seen in Fig. 2(c). However, the magnified SEM image of the sample (c) shows the mosaic structure as shown in Fig. 2(d). The similar behavior of the surface morphology depending on the flux ratio has also been observed for the growth of InSb on GaAs [2]. Fig. 3 shows XRD spectra (left) and ECP patterns (right) of the same samples as shown in Fig. 2. As shown in XRD spectra, all of these InSb films are (001) orientated, in strong contrast to the growth on Si(001). However, the relative intensity of the InSb(004) peak to that of the Ge(004) peak is the largest in (a), and it is very small in (c), thereby suggesting the crystal quality of (a) is the best of all three samples. Similar tendency between crystal quality and composition ratio of the films is also seen in ECP patterns shown on the right of Fig. 3, where sample (a) displays cross pattern, suggesting the film is single crystalline, although the crystal quality is not so good. The ring patterns appearing in ECP of (a) demonstrate that the orientation of the grains in the film plane is limited to small region less than 20 μm . On the other hand, the sample (c) shows only weak ring patterns, indicating the film is amorphous-like even if it includes only very small parts of InSb crystal as observed by XRD. Thus, the mosaic structures observed in the magnified SEM image shown in Fig. 2(d) may be grains including much Sb. Therefore, the smoothness of the surface morphology observed by optical microscopy and/or SEM does not necessarily correspond to the crystal quality of the films.

XRD spectra of the samples also include some additional weak peaks in the low diffraction angle region corresponding to In and Sb crystals. The intensity of these peaks seems to be related to that of InSb(004) peak, that is, the intensity of In- and Sb-related peaks of the sample (a) is strongest of all three samples.

The relationship between the flux ratio and the composition ratio of Sb/In mentioned above, suggests that the films with stoichiometric composition

will be obtained for the growth at the flux ratio of about 4.5.

3.3. Growth on Ge/Si(001) substrate

In the previous section, it has been demonstrated that InSb easily grows heteroepitaxially on Ge(001) surface. Based on the results, InSb was grown on Si(001) substrate with a 4,000 Å thick MBE-grown

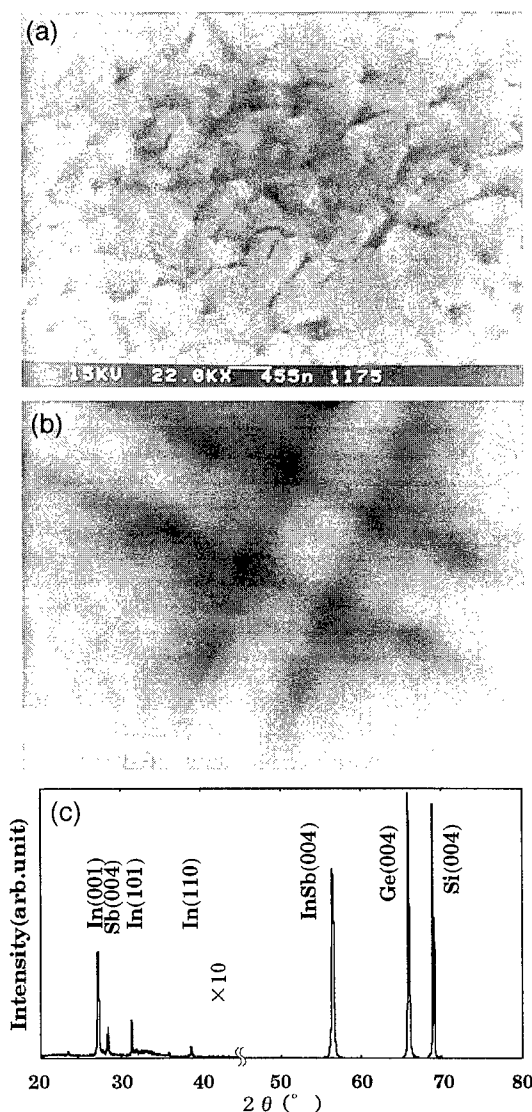


Fig. 4. InSb film with composition of 1.03 on Ge/Si(001) substrate grown at 300°C with flux ratio of 4.5, (a) SEM image, (b) ECP pattern and (c) XRD spectrum.

Ge buffer layer. Fig. 4(a–c) show SEM photograph, ECP pattern and XRD spectrum, respectively, of the InSb film grown at 300°C with flux ratio of 4.5. The composition ratio determined by AES is 1.03, being closely to stoichiometry. The surface appeared smooth and mirror-like. In the SEM image, the surface consists of plate-like grains with grain size of

about 0.5–2.0 μm , which is much different from the surface morphology of Sb-rich films shown in Fig. 2(c) and (d). XRD spectrum exhibits only (004) peak with respect to InSb as shown in Fig. 4(c). ECP shows cross patterns corresponding to (022) and (004) planes as seen in Fig. 4(b), although (004) pattern is very weak. It is noted that the ring pattern which was observed for InSb surface on Ge(001) does not appear in the present case, suggesting the film is monocrystalline in the wide region at least over 20 μm .

Fig. 5(a) and (b) show the SEM image and ECP pattern, respectively, of the In-rich film with composition ratio of 0.7 grown at 300°C. Fig. 5(c) depicts the ECP pattern of the surface of Ge/Si(001) substrate for the comparison. As seen in Fig. 5(a), the surface of this sample is covered by many clear shaped InSb islands, which is very different from the images shown in Fig. 2 and Fig. 4. ECP displays clearer cross patterns corresponding to both (022) and (004) planes than that of Fig. 4(b). These results indicate that the film with In-rich composition results in the better crystal quality rather than that with stoichiometric composition, even if the surface morphology degrade in the In-rich films. However, the broadness of the pattern and the lack of the detail in the ECP pattern of Fig. 5(b), relative to that of the Ge/Si(001) shown in Fig. 5(c), indicate that the InSb film still has a higher density of defects than Ge layer.

It should be important to improve the crystal quality of the InSb films with stoichiometric composition. It may be effective in the improvement of the crystal quality to grow at higher temperature. However, the growth at 400°C resulted in the agglomeration of the films. The two-step temperature growth is believed to be useful, as well as the growth on Si(001) substrate, for the growth of the InSb films with smooth surface at higher temperature. Such works are now in progress.

4. Conclusion

In conclusion, it has been shown that InSb films easily grow heteroepitaxially on Ge(001) and Ge/Si(001) substrates for wide deposition conditions. Ge was used for the first time as a buffer layer

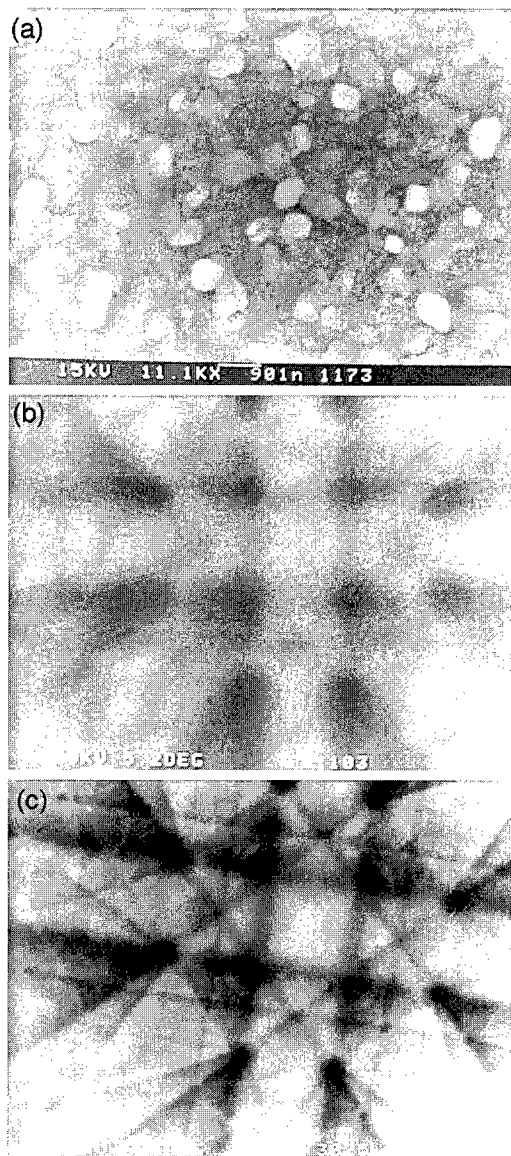


Fig. 5. (a) SEM image, and (b) ECP pattern of InSb with composition ratio of 0.7 on the Ge/Si(001) substrate grown at 300°C; (c) ECP pattern of the Ge/Si(001) substrate.

for the heteroepitaxial growth of InSb on Si(001) substrate. For the growth at 300°C, the flux ratio of 4.5 resulted in the growth of InSb with a nearly stoichiometric composition, and with a smooth surface. However, the better crystal quality was obtained in the In-rich films rather than in the stoichiometric films for the growth temperature of 300°C.

Acknowledgements

The authors would like to express their thanks to Mr. K. Matsuda at Department of Materials, Science and Technology of Toyama University for his cooperation in the SEM and ECP observations. A part of this work was financially supported by Cosel Foundation.

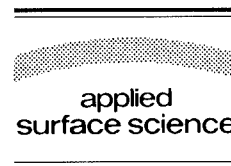
References

- [1] A.J. Noreika, M.H. Francombe and C.E.C. Wood, *J. Vac. Sci. Technol. A* 1 (1983) 558.
- [2] J.-I. Chyi, S. Kalen, N.S. Kumar, C.W. Litton and H. Morkoc, *Appl. Phys. Lett.* 53 (1988) 1092.
- [3] G.M. Williams, C.R. Whitehouse, C.F. McConville, A.G. Cullis, T. Ashley, S.J. Courtney and C.T. Elliott, *Appl. Phys. Lett.* 53 (1988) 1189.
- [4] J.L. Davis and P.E. Thompson, *Appl. Phys. Lett.* 54 (1989) 2235.
- [5] P.K. Chiang and S.M. Bedair, *Appl. Phys. Lett.* 46 (1985) 383.
- [6] B.M. Biefield and G.A. Hebner, *Appl. Phys. Lett.* 57 (1990) 1563.
- [7] D.K. Gaskill, G.T. Stauff and N. Bottka, *Appl. Phys. Lett.* 58 (1991) 1905.
- [8] Y. Yamamura and N. Watanabe, *Jpn. J. Appl. Phys.* 31 (1992) L68.
- [9] J.B. Webb, C. Halpin and J.P. Noad, *J. Appl. Phys.* 60 (1986) 2949.
- [10] T. Ohshima, S. Yamauchi and T. Hariu, *Jpn. J. Appl. Phys.* 28 (1989) L13.
- [11] Z.C. Feng, S. Perkowitz, T.S. Rao and J.B. Webb, *J. Appl. Phys.* 68 (1990) 5363.
- [12] P.E. Thompson, J.L. Davis, I. Waterman, R.J. Wagner, D. Gammon, D.K. Gaskill and R. Stahlbush, *J. Appl. Phys.* 69 (1991) 7166.
- [13] K.D. Jamison, A. Bensaula, A. Ignatiev, C.F. Huang and W.S. Chan, *Appl. Phys. Lett.* 54 (1989) 1916.
- [14] T. Miyazaki, M. Mori and S. Adachi, *Appl. Phys. Lett.* 58 (1991) 116.
- [15] J.E. Oh, P.K. Bhattacharya, Y.C. Chen and S. Tsukamoto, *J. Appl. Phys.* 66 (1989) 3616.
- [16] T.S. Rao, J.B. Webb, D.C. Houghton, J.M. Baribeau, T. Moore and J.P. Noad, *Appl. Phys. Lett.* 53 (1988) 51.
- [17] J.-I. Chyi, D. Biswas, S.V. Iyer, N.S. Kumar, H. Morkoc, R. Bean, K. Zanio, H.-Y. Lee and H. Chen, *Appl. Phys. Lett.* 54 (1989) 1989.
- [18] L.K. Li, Y. Hsu and W.I. Wang, *J. Vac. Sci. Technol. B* 1 (1993) 872.
- [19] M. Asai, H. Ueba and C. Tatsuyama, *J. Appl. Phys.* 58 (1985) 2577.
- [20] Y. Hida, T. Tamagawa, H. Ueba and C. Tatsuyama, *J. Appl. Phys.* 67 (1990) 7274.
- [21] G.E. Franklin, D.H. Rich, H. Hong, T. Miller and T.-C. Chiang, *Phys. Rev. B* 45 (1992) 3426.



ELSEVIER

Applied Surface Science 104/105 (1996) 570–574



Ga–Se films grown on a GaAs(001) surface at high temperature using a thermal evaporation of GaSe

T. Izumi, H. Nishiwaki, T. Tambo^{*}, C. Tatsuyama

Department of Electronics & Information Engineering, Faculty of Engineering, Toyama University, 3190 Gofuku, Toyama 930, Japan

Received 28 June 1995; accepted 28 September 1995

Abstract

The initial stage of heteroepitaxial growth of Ga–Se films on GaAs(001) surface using a single evaporation source of GaSe has been studied as a function of growth temperature by means of in-situ LEELS (low-energy electron-loss spectroscopy), XPS (X-ray photoemission spectroscopy) and AES (Auger electron spectroscopy). The thick films were studied ex-situ by XRD (X-ray diffraction). In the LEELS spectra, the film grown at 450°C had a different structure from the film grown at 400°C. In the XRD pattern, weak but clear signals of Ga₂Se₃ were observed. The AES intensity ratio of Ga and Se also showed that the films were composed of Ga-rich Ga₂Se₃. The film grown at 430°C evolved the structure from high temperature phase (mainly Ga-rich Ga₂Se₃) to low temperature phase (GaSe) with increase in thickness. At 450°C, not the Ga₂Se₃ but the crystalline GaSe film grew on a GaAs(111)A surface.

1. Introduction

The GaSe is a typical III–VI layered compound. The surface of crystalline GaSe is very stable because there are no dangling bonds. The band gap of GaSe is 2.0 eV, and the GaSe thin film is a good window and protection material for a GaAs device with the band gap of 1.43 eV. There is another stoichiometric compound, Ga₂Se₃. The Ga₂Se₃ is a three-dimensional crystal different from GaSe. The band gap is still under discussion and likely to be larger than 2.0 eV. The phase diagram of the Ga–Se system has been studied by the differential thermal analysis [1]. And there, the phases of GaSe and

Ga₂Se₃ were found, but the phases of Ga₂Se [2] and Ga₃Se₂ [3] were not found. It has been known that the compound of Ga₂Se is unstable and can only be obtained by sublimation method [2].

We have studied the growth condition and the structure of Ga–Se film on a GaAs(001) surface by using a thermal evaporation of GaSe [4], where the substrate temperature largely influenced the film structure. The films grown at temperatures lower than 250°C were amorphous, even though they were evolved to crystalline GaSe by the post annealing at 400°C for 30 min. The LEELS spectra of films with only about 30 Å grown at temperatures between 250 and 400°C were essentially the same as that of cleaved GaSe surface. The LEELS spectra of the film with thickness of 30 Å grown at 400°C had not a peak with loss energy of 16 eV which appears in a spectrum of cleaved GaSe. The spectrum was named

^{*} Corresponding author.

as “high temperature phase” which will be identified to be Ga_2Se_3 in the present paper. In the case of the thickness of about 30 Å, the 400°C may be a critical temperature whether the crystalline GaSe phase grows or the high temperature phase grows.

Using the similar thermal evaporation method of layered compound, GaSe and Ga_2Se_3 film have been fabricated on glass or mica substrate under a pressure of 10^{-5} Torr by Yudasaka and Nakanishi [5]. Their evaporation source was a GaSe bulk in a molybdenum boat. GaSe epitaxial films could not be formed, although epitaxial films of InSe which is the same III–VI layered compound could be formed.

It has been known that a heterovalent exchange reaction between Se and GaAs surface which results in the formation of Ga_2Se_3 takes place for both Se-passivation [6] and molecular beam epitaxy (MBE) [7]. In the case of Se-passivation such as annealing of GaAs substrates in a H_2Se atmosphere, $\beta\text{-Ga}_2\text{Se}_3$ has been formed at higher temperature than 780 K (507°C) [6]. In order to prepare the Ga_2Se_3 film by MBE, a substrate temperature of 500°C and a VI/III ratio as large as 150 to 180 were required [7]. Compared with these, the present experiments are characterized in using the thermal evaporation of GaSe single crystal as a source. In this case, very high Se/Ga ratios required in MBE could not be obtained, and the molecules evaporated by the thermally decomposition of the GaSe source have been reported to be Ga_2Se and Se [5].

In the present paper, we study the Ga–Se films grown on a GaAs(001) surface at temperatures between 400 and 450°C. They are characterized by using LEELS, AES, XPS and XRD. The results will demonstrate that GaSe films or Ga_2Se_3 films easily grow on GaAs substrates without the use of H_2Se gas or metal sources, and the control of VI/III ratio. The difference in the growth of GaSe and Ga_2Se_3 on GaAs(001) depending on the growth temperature and film thickness will be discussed. The Ga–Se film grown on GaAs(111)A surface at the high temperature will also be characterized.

2. Experimental

GaSe films were grown in an ultra-high vacuum chamber with a base pressure of 2×10^{-9} Torr. The

substrates were non-doped n-type GaAs(001) and GaAs(111)A wafer with resistivity of 5 Ω cm and carrier density of $4 \times 10^{14} \text{ cm}^{-3}$. The substrate surface was cleaned by Ar^+ ion sputtering with an accelerated voltage of 1 kV, and subsequent annealing at 450°C for 30 min.

The ingot of GaSe single crystals grown by the Bridgman method was used as the source for the thermal evaporation. They were heated in a coiled tungsten wire which was wrapped in a shroud of liquid nitrogen. The evaporation rate was held to 0.1 Å/s at all growth temperatures using a quartz thickness monitor cooled by water. The substrate temperature was varied between 400 and 450°C with resistive heating by a tungsten filament. The thickness of the Ga–Se films grown at different temperatures were a few to 1000 Å on a display of the thickness monitor.

The electronic structure, the chemical state and the chemical composition were observed by LEELS, XPS and AES at some thicknesses during the growth. A double-pass cylindrical mirror analyzer (PHI 15-255G) including a co-axial electron gun accepted electrons with an incident angle of 42.3°. The center axis was inclined by 30° from the sample surface normal. In this geometry the probe depth of an electron with a primary energy of 100 eV is less than 2.5 Å. Ga(LMM) and Se(LMM) AES lines with kinetic energies of 1070 eV and 1315 eV were used to estimate the chemical composition ratio of Se/Ga. The crystal structure of films with nominal thickness of 1000 Å was determined by XRD.

3. Results and discussion

We have studied the initial stage of heteroepitaxial Ga–Se films on a GaAs(001) surface using surface analyses mentioned above. LEELS analysis has a specially high sensitivity to a surface. The crystalline GaSe film as reported in Ref. [4] grew on a GaAs(001) surface at 400°C. Typical LEELS spectra of Ga–Se films grown at 450 and 430°C on GaAs(001) surfaces are shown in Fig. 1 and Fig. 2, respectively. The film thickness in figures represents the value obtained by a quartz thickness monitor.

In Fig. 1 (450°C), a small amount of difference at the peak position and the missing of a peak at energy

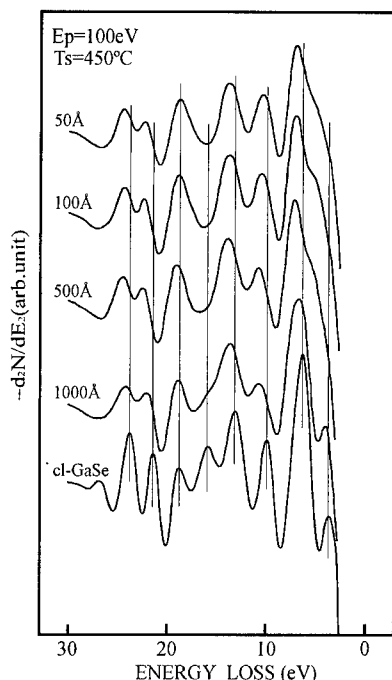


Fig. 1. LEELS spectra of Ga–Se film grown at 450°C on a GaAs(001) surface. The observed spectra are so-called high temperature phase different from that of cleaved GaSe as shown at the bottom.

of 16 eV are observed in the spectra of films from 50 to 500 Å compared with the spectrum of cleaved GaSe drawn at the bottom, while the peak at energy of 16 eV is obscurely observed at 1000 Å. The high temperature phase is characterized by missing of a peak with loss energy of 16 eV in the LEELS spectrum and the small energy shift of several other peaks to higher energy side. The appearance of the high temperature phase means a creation of a new derivative different from stoichiometric GaSe. At 450°C, the deposition growth rate is thought to be very low and the re-evaporation rate on the surface is thought to be very high. Really, the very thick film could not grow on a GaAs(001) surface at 450°C.

The Ga–Se film grown at temperatures between 400 and 450°C becomes a matter of concern. The LEELS spectra at 430°C are shown in Fig. 2. Although the spectrum of the film with thickness of 50 Å shows the growth of high temperature phase, the spectrum evolves from the high temperature phase to the crystalline GaSe phase with increasing thickness of film. The spectra of films with thickness of over

250 Å perfectly reveals the same spectrum as that of cleaved GaSe single crystal.

In order to make clear what is the derivative, the chemical states, the chemical composition and the crystal structure of the film were measured using XPS, AES and XRD methods. The XRD patterns of the films grown at 400, 430 and 450°C are shown in Fig. 3. The thickness of the films is 1000 Å displayed on the quartz thickness monitor. The XRD pattern of the film grown at 400°C shows (001)-orientated GaSe signals with intensities of a few thousand counts per second. This confirms that the crystalline GaSe grows along the *c*-axis on a GaAs(001) surface at 400°C. On the other hand, the XRD pattern of the film grown at 450°C shows small peaks related to Ga_2Se_3 . The weak intensity of the peaks is due to very thin film thickness rather than 1000 Å. Although the intensity is weak, it is found that only (001)-orientated Ga_2Se_3 grows. The XRD pattern of film grown at 430°C only showed a weak diffraction peak of GaSe(004).

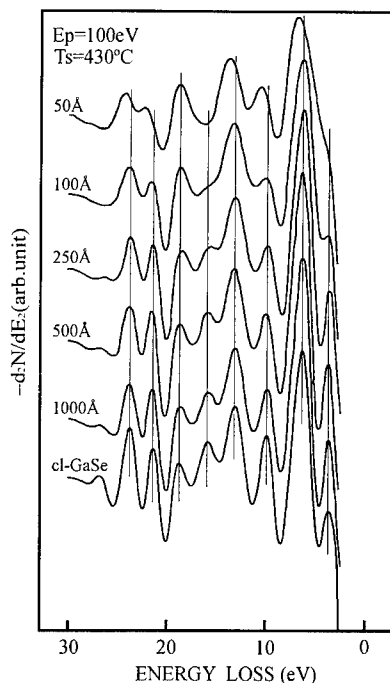


Fig. 2. LEELS spectra of Ga–Se film grown at 430°C on a GaAs(001) surface. The spectrum shows the high temperature phase Ga–Se at the initial deposition, and then it evolves to the spectrum of crystalline GaSe.

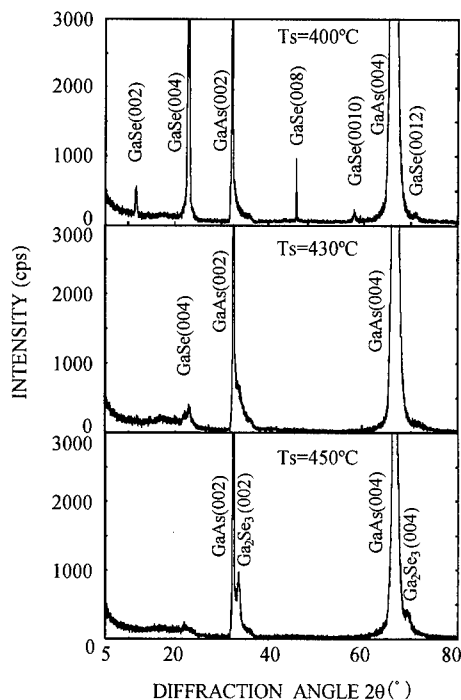


Fig. 3. XRD patterns of the films grown at different growth temperatures. They are all 1000 Å thick obtained from a quartz thickness monitor.

Fig. 4 shows the ratio of chemical composition of Ga and Se estimated by AES as a function of growth temperature. The sensitivity is normalized to the peak-to-peak intensity of the stoichiometric GaSe crystal. Although the composition ratio between 350 and 400°C is constant at 0.97, it increases to 1.36 with raising the growth temperature. It is noted that the films are Ga-rich not only in the crystalline GaSe

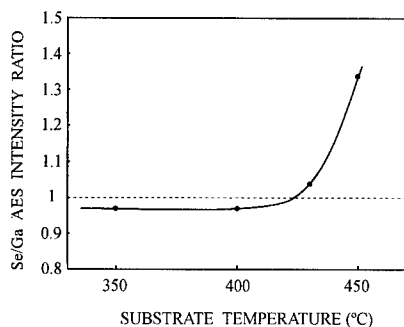


Fig. 4. Composition ratio of Se to Ga obtained from their AES peak-to-peak intensities as a function of growth temperature.

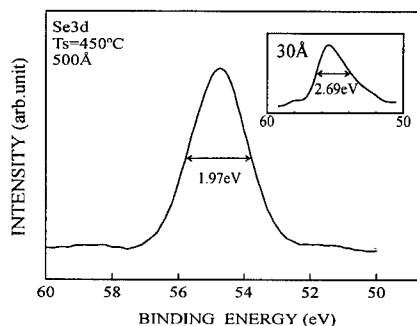


Fig. 5. Se 3d X-ray photoemission spectrum of film grown at 450°C with thickness of 500 Å. The inset represents Se 3d spectrum of film with thickness of 30 Å [4].

phase but also in the high temperature phase, Ga_2Se_3 . Li et al. [9] have reported that a highly developed reconstruction structure has been observed at the interface between vacancy-ordered Ga_2Se_3 and $\text{GaAs}(001)$ by the analysis of electron diffraction pattern and high resolution transmission electron microscope images. The Ga–Se film was prepared by molecular beam epitaxy method. In the reconstruction structure, each Se atom had three nearest neighbor Ga atoms [9]. The reconstruction structure is Ga-rich for defect zincblende Ga_2Se_3 . The Ga-rich Ga_2Se_3 film grown at 450°C in the present work would have the same structure as the reconstruction one in Ref. [9].

The XPS spectrum of Se 3d was selected to observe the chemical bonding of the high temperature phase, since the Ga element is common for the Ga–Se film and the GaAs substrate. Fig. 5 shows the Se 3d X-ray photoemission spectrum of the film grown at 450°C with thickness of 500 Å. The FWHM of this spectrum is wider than that of GaSe by about 0.2 eV. According to the result of XRD, the spectrum originates from Ga_2Se_3 . Recently, high resolution photoemission spectra of Ga_2Se_3 film formed on $\text{GaAs}(001)$ were measured and deconvoluted into two components of Se in Ga_2Se_3 by Markl et al. [8]. A binding energy of the spectrum in Fig. 5 is in agreement with their data. Inset in the figure shows a Se 3d spectrum of the film with thickness of 30 Å from Ref. [4]. The full width at half maximum (FWHM) of this spectrum is clearly wider than the spectrum of Ga_2Se_3 . The differential part between the two spectra is lower binding energy side in the

inset. It corresponds to $\text{Ga}_y\text{-Se}$ ($y > 1$) [4]. Thus, the component of $\text{Ga}_y\text{-Se}$ disappears with increase in thickness and only the Ga_2Se_3 component remains.

Some interpretations are considered for the disappearing of a bonding of $\text{Ga}_y\text{-Se}$ ($y > 1$) with increase in thickness. The first interpretation is that the $\text{Ga}_y\text{-Se}$ ($y > 1$) is a Ga_2Se molecule evaporated from the GaSe source [5], and in the initial deposition some of Ga_2Se molecules transform to the Ga_2Se_3 [5], while others remain on the GaAs substrate. With increasing deposition, it is thought that the rate of transformation becomes large since the Ga_2Se is deposited on the Ga_2Se_3 layer [5]. Therefore, the Ga_2Se will be introduced at the interface of the Ga_2Se_3 film and GaAs substrate. The second interpretation is that both $\text{Ga}_y\text{-Se}$ ($y > 1$) and Ga_2Se_3 are formed on the GaAs surface by Se molecules included in the evaporated species, because Se molecules evaporated from the source GaSe first react with the surface atoms of the substrate at the initial step. In the case of S-passivation of GaAs(001), the S 2p spectrum with two components has also been observed at a S/GaAs(001) surface prepared by $(\text{NH}_4)_2\text{S}_x$ -treated GaAs [10]. The third interpretation is that the signal of $\text{Ga}_y\text{-Se}$ ($y > 1$) is originated from the Se atoms which occupied the As sites below the surface. The phenomenon has been shown at the 3d spectrum of the (2×1) Se-stabilized GaAs(001) surface [11], where there are also two chemically shifted components, which are tentatively attributed to the Se atoms terminating the surface (adsorption) and those occupying the As sites below the surface (heterovalent exchange reaction). According to these interpretations, it is reasonable that the signal intensity of $\text{Ga}_y\text{-Se}$ ($y > 1$) decreases with increasing of film thickness.

We have tried to grow a Ga–Se film on a GaAs(111)A surface at 450°C. The cleaning method of the GaAs surface was the same as the GaAs(001). The deposition condition was also the same. The LEELS spectrum shows the same loss structure as crystalline GaSe even for the thickness of 50 Å, thereby suggesting the growth of GaSe different from on $\text{Ga}_2\text{Se}_3/\text{GaAs}(001)$. Considering the atom alignment, a six-fold symmetry for GaSe(001) surface coincides with that for GaAs(111). In order to make the growth mechanism clear, we are planning to observe the atomic structures at the initial stage of

the growth using RHEED (reflection high energy electron diffraction) and STM (scanning tunneling microscopy).

4. Conclusion

We have studied the initial stage of the heteroepitaxial growth of Ga–Se films on GaAs(001) and GaAs(111)A surface using a single evaporation source of GaSe. The (001)-oriented GaSe and the (001)-oriented Ga_2Se_3 grew on a GaAs(001) surface at 400 and 450°C, respectively. At growth temperature of 430°C, the crystal structure evolved from Ga_2Se_3 to the (001)-oriented GaSe with increase in the thickness. The $\text{Ga}_y\text{-Se}$ ($y > 1$) is thought to be formed near the interface between the GaAs substrate and the Ga_2Se_3 film grown at 450°C. The films grown at 450°C on GaAs(111)A has the (001)-oriented GaSe structure, which is different from the structure for films grown at 450°C on GaAs(001).

Acknowledgements

We greatly thank Dr. Ueba for his useful discussion.

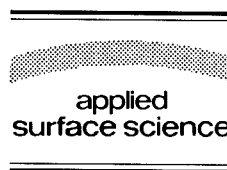
References

- [1] H. Suzuki and R. Mori, *Jpn. J. Appl. Phys.* 13 (1974) 417.
- [2] W. Kelmm and H.U. von Vogel, *Z. Anorg. Allgem. Chem.* 219 (1934) 45.
- [3] J.C.J.M. Terhell and R.M. Lieth, *Phys. Status Solidi* 10 (1972) 529.
- [4] K. Fujita, T. Izumi, K. Ohsaki, T. Tambo, H. Ueba and C. Tatsuyama, *Thin Solid Films* 247 (1994) 134.
- [5] M. Yudasaka and K. Nakanishi, *Thin Solid Films* 156 (1988) 145.
- [6] D.R. Zhan, A. Krost, M. Kolodziejczyk and W. Richer, *J. Vac. Sci. Technol. B* 10 (1992) 2077.
- [7] T. Okamoto, A. Yamada, M. Konagai and K. Takahashi, *J. Cryst. Growth* 138 (1994) 204.
- [8] A. Markl, M. von der Emde, C. Nowak, W. Richter and D.R.T. Zahn, *Surf. Sci.* 331–333 (1995) 631.
- [9] D. Li, Y. Nakamura, N. Otsuka, J. Qiu, M. Kobayashi and R.L. Gunshor, *J. Cryst. Growth* 111 (1991) 1038.
- [10] H. Sugahara, M. Oshima, H. Oigawa and Y. Nannichi, *J. Vac. Sci. Technol. A* 11 (1993) 52.
- [11] S. Takatani, T. Kikawa and M. Nakazawa, *Phys. Rev. B* 45 (1992) 8498.



ELSEVIER

Applied Surface Science 104/105 (1996) 575–579



MOCVD growth of Ga_2Se_3 on GaAs(100) and GaP(100): a Raman study

M. von der Emde^a, D.R.T. Zahn^{a,*}, T. Ng, N. Maung^b, G.H. Fan^b, I.B. Poole^b,
J.O. Williams^b, A.C. Wright^b

^a Professur für Halbleiterphysik der TU Chemnitz–Zwickau, D-09107 Chemnitz, Germany

^b North East Wales Institute, Plas Coch, Wrexham, Clwyd LL11 2AW, Wales, UK

Received 28 June 1995; accepted 26 September 1995

Abstract

Due to its luminescence in the blue–green spectral range, Ga_2Se_3 has become a subject of extensive research. Thin epitaxial Ga_2Se_3 layers were grown on GaAs(100) and GaP(100) for the first time by metalorganic chemical vapour deposition (MOCVD). The structural and optical properties were investigated by transmission electron microscopy, Raman spectroscopy and photoluminescence (PL). Raman spectra were taken in a temperature range from 100 K to 600 K using excitation energies of Ar^+ and Kr^+ ion lasers. Additionally the photoluminescence of the layers was measured using ultraviolet (UV) excitation. The results of this study are compared and discussed with those of other growth techniques.

1. Introduction

In the last years epitaxial Ga_2Se_3 layers have been grown successfully on III–V semiconductors using molecular beam epitaxy (MBE) [1–3], metalorganic MBE (MOMBE) [4] and the heterovalent exchange reaction (HER) [5]. This defect zincblende semiconductor [6] is discussed as a potential material for optoelectronic applications due to the interesting optical properties, e.g. light emission in the visible spectral range. While the results of several transmission electron microscopy (TEM) and X-ray diffraction studies show the same structural properties of

the Ga_2Se_3 layers for all growth methods [3,5,7–9], studies of the optical properties, e.g. photoluminescence, lead to different results [2,10–12]. In this work the MOCVD growth of Ga_2Se_3 layers and the resulting structural and optical properties were investigated.

2. Experimental

Epitaxial Ga_2Se_3 films of several hundred nanometer thickness were grown on GaAs(100) and GaP(100) in a conventional MOCVD reactor using trimethylgallium (TMG) and H_2Se as precursors. The GaAs crystals were prepared by degreasing and etching in $\text{H}_2\text{SO}_4:\text{H}_2\text{O}_2:\text{H}_2\text{O}$, and the GaP(100) substrates (10° off), were etched in $\text{HNO}_3:\text{HCl}:\text{H}_2\text{O}$

* Corresponding author. Tel.: +49-371-5313036; fax: +49-371-5313060; e-mail: zahn@physik.tu-chemnitz.de.

and the surfaces were reduced using $(\text{NH}_4)_2\text{S}_x$ as described by Wang [13]. In order to improve the crystal quality of the Ga_2Se_3 layers, the growth temperature (T_s) and the $\text{H}_2\text{Se}/\text{TMG}$ flux ratio were varied in the range from 630 K to 830 K and up to 20, respectively. The structural properties of these layers were investigated by transmission electron microscopy (TEM).

The samples were studied by Raman spectroscopy under various conditions using the microscope stage of a Dilor XY triple monochromator equipped with a CCD camera for multichannel detection. All measurements were performed with a magnification of 50–80, resulting in a focus diameter of $< 5 \mu\text{m}$ and backscattering geometry with both the incident and scattered light polarised parallel to the [011] direction of the substrate. Typically a spectral resolution of 2.3 cm^{-1} was achieved (100 μm slit width and 2.41 eV excitation energy). To investigate the temperature dependence between 100 K and 600 K, the samples were placed in an optical cryostat under the microscope. A broad range of excitation energies (1.83 eV to 2.71 eV) provided by Ar^+ and Kr^+ lasers was applied for the resonance measurements.

Additional photoluminescence measurements were performed at 300 K using the 3.81 eV line of a HeCd laser.

3. Results and discussion

The results of the TEM investigations of the parameter variation reveal optimized Ga_2Se_3 growth for $T_s = 725 \text{ K}$ and a Se:Ga ratio of 4:1 on both substrates. Epitaxial layers of the Ga_2Se_3 in the ordered cubic defect zincblende structure [6] with domain sizes of 10 nm were obtained. The crystal quality of Ga_2Se_3 layers on GaP is superior to GaAs as expected from the smaller lattice mismatch (0.3% for GaP, 4% for GaAs). For higher growth temperatures as well as Se:Ga ratios only growth of polycrystalline material was observed. A more detailed description of the MOCVD growth and the TEM study can be found in Ref. [14].

The variation of the growth parameters was then investigated by Raman spectroscopy. As an example typical spectra of samples grown on GaAs at 625 K using two different Se:Ga ratios are shown in Fig. 1.

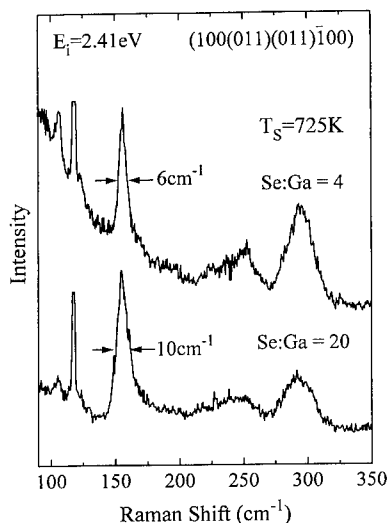


Fig. 1. Raman spectra of Ga_2Se_3 on GaAs(100) taken at 300 K: Comparison of two different Se:Ga flux ratios for a constant substrate temperature of 725 K.

For both ratios the complex phonon structure of Ga_2Se_3 [15] can be observed. The analysis of these spectra using a curve fitting procedure reveals a higher crystal quality of the sample grown with a Se:Ga ratio of 4:1. For example the full width at half maximum (FWHM) of the 155 cm^{-1} peak is 6 cm^{-1} at the lower ratio compared to 10 cm^{-1} at the higher value. For the variation of T_s and the Se:Ga flux ratios the results of the Raman spectroscopy are in agreement with the TEM investigations and confirm the optimized growth parameters of $T_s = 725 \text{ K}$ and Se:Ga of 4:1 for both substrates. In comparison to the results of recent Ga_2Se_3 growth experiments using MBE, MOMBE and HER the substrate temperature is 50–130 K lower. This behaviour is somewhat surprising since it is known that in III–V and II–VI semiconductor growth the substrate temperatures are usually higher for MOCVD. On the other hand, the precursors used and flux ratios are very different and do not allow an exact comparison. However, the structural ordering and the homogeneity of the layers grown by MOCVD is of comparable quality to samples grown by the other techniques. High quality samples grown at the optimized parameters are the subject of the following investigations.

The temperature dependence of the Raman spectra was investigated in the range from 100 K to 600

K. In Fig. 2 the spectra of Ga_2Se_3 on GaP at various temperatures are shown. For increasing temperatures a broadening from 5 cm^{-1} (100 K) up to 10 cm^{-1} (600 K) of the 155 cm^{-1} peak and a decreasing intensity of the Ga_2Se_3 related features can be observed. At low temperatures the structures at 250 cm^{-1} to 300 cm^{-1} increase with respect to the 155 cm^{-1} peak. The curve fitting analysis of these spectra reveal linear frequency shifts to lower energies with increasing temperature as expected from the thermal expansion of the samples. The slopes of the corresponding shifts are listed together with the results of a similar study of Ga_2Se_3 layers grown by HER [17] in Table 1. For the HER-grown material the peaks at 250 cm^{-1} and 290 cm^{-1} show a temperature dependence, which is comparable to the frequency shifts for the phonons in GaAs (TO: $2.0\text{ cm}^{-1}/100\text{ K}$; LO: $1.8\text{ cm}^{-1}/100\text{ K}$) and ZnSe (LO: $2.4\text{ cm}^{-1}/100\text{ K}$). In comparison the low frequency peaks reveal much weaker slopes. This behaviour is related to the origin of the phonon structures. As mentioned in Ref. [15] the peaks at 250 cm^{-1} and 290 cm^{-1} are due the short range interaction in the defect-zincblende unit cell, while the low frequency peaks are related to the long range ordering of the monoclinic superstructure of the $\beta\text{-Ga}_2\text{Se}_3$ [6]. The

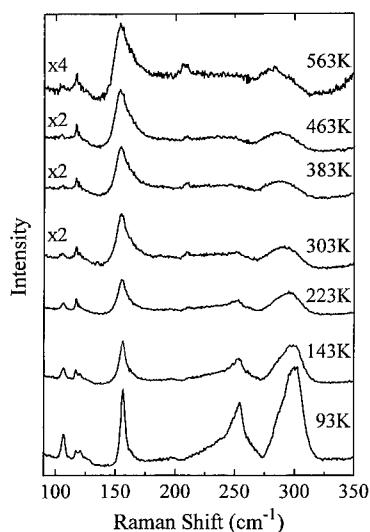


Fig. 2. Temperature dependence of Raman spectra of $\text{Ga}_2\text{Se}_3/\text{GaP}(100)$, recorded in $(100(011)(011)\bar{1}00)$ geometry with 2.41 eV excitation energy. The spectra for higher temperatures were multiplied by the labeled factors.

Table 1

Comparison of the temperature induced shifts of the strongest Ga_2Se_3 peaks between this study and Ref. [17]

$\nu_{300\text{ K}}$ (cm^{-1})	$d\nu/dT$ ($\text{cm}^{-1}/100\text{ K}$) [17]	$d\nu/dT$ ($\text{cm}^{-1}/100\text{ K}$)
105	−0.1	−0.45
118	−0.1	−0.3
155	−0.5	−0.77
250	−1.3	−0.4
290	−2.1	−2.3

slopes obtained from the MOCVD samples show a similar behaviour with slightly higher values, except the slope of the 250 cm^{-1} peak. While the higher slopes are likely to be explained by the disordered nature of the bottom layer in HER growth [8], which may cause a change in the thermal expansion of this material, the reason for the anomalous weak temperature dependence of the 250 cm^{-1} peak is still unresolved.

Also the enhancement of the high energy features at low temperatures is in agreement with the previous study and is explained due to resonance enhancement of the Raman cross section [17].

While epitaxial Ga_2Se_3 layers show very similar behaviour of the phonon modes for all growth techniques, there are still large differences in the reported value for the fundamental band gap and the photoluminescence data of this material. A PL peak was observed using 2.41 eV excitation at 2.1 eV (50 K) for MBE growth [2] and a band gap in this spectral region was supported by transmission spectra [10]. For HER growth PL spectra using blue and green laser excitation show photoluminescence at 2.5 eV (50 K). This agrees well with features observed by reflection measurements and resonant Raman scattering [12]. These samples show another PL feature at approximately 3.1 eV (2 K) when UV excitation is used, this result was also confirmed by low temperature reflection measurements [11].

The excitation energy dependence of the Raman spectra was measured at room temperature in the range from 1.83 eV to 2.71 eV . For Ga_2Se_3 on GaP these spectra are shown in Fig. 3. A dramatic change of the spectra take place at approximately 2.3 eV , where the substrate related signals (GaP multiphonon

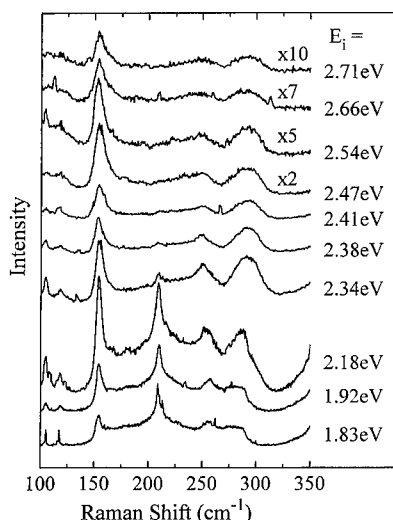


Fig. 3. Evolution of Raman spectra of $\text{Ga}_2\text{Se}_3/\text{GaP}(100)$ with various excitation energies, measured at 300 K in $(100)(011)(011)\bar{1}00$ geometry. Note the GaP multiphonon scattering around 200 cm^{-1} for excitation energies $< 2.4\text{ eV}$.

processes [16]), which dominate the spectra for low energy excitation, disappear and the Ga_2Se_3 features become dominant over the whole spectral range. This behaviour is obviously due to a strong increase of the absorption constant of the Ga_2Se_3 layer in this energy range. The intensity of the 155 cm^{-1} peak of

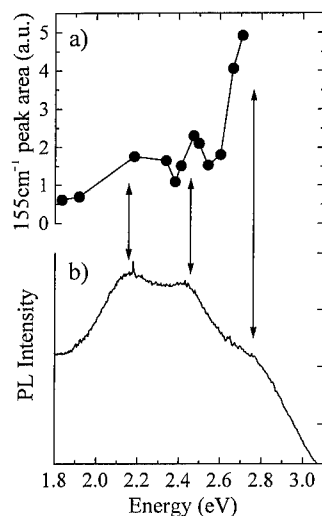


Fig. 4. Results of resonance experiment (a) and PL (b) of $\text{Ga}_2\text{Se}_3/\text{GaP}$ at 300 K. Resonance enhancements and structures in the PL spectra can be observed at 2.1 eV, 2.5 eV and $> 2.7\text{ eV}$.

these spectra, taking into account the correction of the spectrometer sensitivity is plotted in Fig. 4a. Resonance enhancement can be observed near 2.5 eV and 2.7 eV, which is an indication for electronic transition energies in Ga_2Se_3 . This resonance behaviour is found to be almost independent of the substrate material. In order to substantiate these results photoluminescence spectra were taken at room temperature using UV excitation. A typical spectrum is shown in Fig. 4b which reveals broad light emitting PL bands centered at 2.1 eV, 2.5 eV and 2.7 eV.

These values are consistent with previous results of HER grown material [11]. All these results strongly suggest the existence of a Ga_2Se_3 band gap near 3 eV at 300 K and various donor or acceptor related transitions depending on the growth method.

4. Conclusions

MOCVD was successfully applied for the first time to epitaxial growth of Ga_2Se_3 on $\text{GaAs}(100)$ and $\text{GaP}(100)$. The optimized growth parameters were determined by a variation of T_s and the Se:Ga flux ratio and a structural analysis of the samples using TEM and Raman spectroscopy. The temperature and excitation energy dependence of the Raman spectra are consistent with the results of Ga_2Se_3 layers grown by other techniques. Light emitting transitions in the blue–green spectral range were obtained from the PL measurements and were confirmed by resonant Raman scattering. This result is a further indication for the potential of this material for optoelectronic applications.

Acknowledgements

The authors acknowledge the financial support by the Deutsche Forschungsgemeinschaft (Za146/4-2), the SERC, and the DAAD/British Council ARC programme.

References

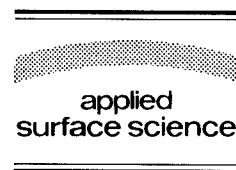
- [1] N. Teraguchi, M. Konagai, F. Kato and K. Takahashi, J. Cryst. Growth 115 (1991) 798.

- [2] T. Okamoto, A. Yamada, M. Konagai and K. Takahashi, *J. Cryst. Growth* 138 (1994) 204.
- [3] D. Li, Y. Nakamura, N. Otsuka, J. Qui, M. Kobayashi and R.L. Gunshor, *Surf. Sci.* 267 (1992) 181.
- [4] N. Teraguchi, F. Kato, M. Konagai and K. Takahashi, *Jpn. J. Appl. Phys.* 28 (1989) L2134.
- [5] D.R.T. Zahn, A. Krost, M. Kolodziejczyk and W. Richter, *J. Vac. Sci. Technol. B* 10 (1992) 2077.
- [6] D. Lübbbers and V. Leute, *J. Solid State Chem.* 43 (1982) 339.
- [7] A.C. Wright, J.O. Williams, A. Krost, W. Richter and D.R.T. Zahn, *J. Cryst. Growth* 121 (1992) 111.
- [8] A.C. Wright, J.O. Williams, M. von der Emde, D.R.T. Zahn, A. Krost and W. Richter, *Inst. Phys. Conf. Ser.* 143 (1993) 433.
- [9] T. Okamoto, A. Yamada, M. Konagai, K. Takahashi and N. Suyama, in: *Proc. Control of Semiconductor Interfaces*, 2.–12.11.1993, Karuizawa, Japan, Eds. I. Ohdomari, M. Oshima and A. Hiraki.
- [10] T. Okamoto, N. Kojima, A. Yamada, M. Konagai, K. Takahashi, Y. Nakamura and O. Nittono, *Jpn. J. Appl. Phys.* 31 (1992) L143.
- [11] M. von der Emde, U. Rossow, G. Kudlek, A. Hoffmann, A. Krost, W. Richter, S. Morley, A.C. Wright, J.O. Williams and D.R.T. Zahn, in: *Proc. ICFSI-4*, 14.–18.6.93, Jülich, Germany, Eds. B. Lengeler, H. Lüth, W. Mönch and J. Pollmann.
- [12] M. von der Emde, A. Märkl, A. Krost, W. Richter, Y.S. Raptis, J. Cai, E. Anastassakis and D.R.T. Zahn, in: *Proc. 4th German–Greek Workshop*, 23.–24.9.93, Berlin, Germany, Eds. G. Kaiser and N. Constantopoulos.
- [13] A.C. Wright, private communication.
- [14] A.C. Wright, T.L. Ng, N. Maung, G.H. Fan, I.B. Poole and J.O. Williams, *ICMOVPE*, accepted.
- [15] E. Finkmann, A. Tauc, R. Kershaw and A. Wold, *Phys. Rev. B* 11 (1975) 3785.
- [16] M. Cardona, *Light Scattering in Solids*, Topics in Applied Physics (Springer, Berlin, 1983).
- [17] M. von der Emde, A. Märkl, W. Richter, Y.S. Raptis, J. Cai, E. Anastassakis and D.R.T. Zahn, in: *Proc. ICORS-14*, 22.–26.8.94, Hong Kong, Eds. N.T. Yu and X.Y. Li.



ELSEVIER

Applied Surface Science 104/105 (1996) 580–585



Temperature dependence of interdiffusion-induced III–V compound formation at the interface between Al, Ga, In layers and Sb substrates

V. Wagner^{a,*}, W. Richter^a, J. Geurts^b

^a *Institut für Festkörperphysik, Berlin University of Technology, Hardenbergstr. 36 Sekr. PN6-1, D-10623 Berlin, Germany*

^b *I. Physikalisches Institut, RWTH Aachen, P.O. Box, D-52056 Aachen, Germany*

Received 28 June 1995; accepted 4 December 1995

Abstract

The reactivity and diffusion of atoms at III–V interfaces is studied from group-III overlayers on group-V substrates. The interfaces are formed by an MBE-like deposition of Al, Ga, and In on UHV-cleaved Sb(111) substrates at temperatures sufficiently low to suppress the III–V formation, followed by a continuous temperature ramp. A systematic investigation of the temperature dependence of the formation of III–V compounds during the temperature ramp is presented. It allows insight into the diffusion barriers involved. The process is monitored by Raman spectroscopy as the main tool. Besides, the initial and final state is characterized by AES and LEED. The threshold temperature observed increases with the group-III species from InSb (–15°C) over GaSb (40°C) to AlSb (165°C). A layer-like reactive growth is found for InSb, while AlSb and GaSb tend to island formation.

1. Introduction

Due to the reduced size of modern semiconductor devices the diffusion and reactivity of atoms at interfaces attract increasing attention. This paper concerns the investigation of the diffusion barriers at reactive metal–semiconductor interfaces. For this purpose a group-III layer is deposited in UHV on UHV-cleaved antimony (111) surfaces. From the initial reactive metal-III metal-V interface the heterostructure III/III–V/V evolves containing the

well-known III–V zincblende semiconductor. The reaction leads to an epitaxial (111) oriented semiconductor layer on the (111) antimony substrate [1,6–10]. After the formation of the first closed monolayer the growth is strongly affected by the diffusion behaviour of the group-III and group-V atoms in the newly formed semiconductor layer [10]. Therefore the possibility of studying the diffusion properties at ultra-thin III–V layers is achieved.

An experimental technique which is very well suited for monitoring this intermixing diffusion process is Raman spectroscopy. By this method the III–V compounds which are possibly formed are directly identified by means of their characteristic lattice vibration frequencies. Thus, it allows a contin-

* Corresponding author. Fax: +49-32-81724595; e-mail: vwagner@fundp.ac.be.

uous monitoring of the process. For the *in situ* Raman monitoring two different strategies may be followed. The first one is the continuous spectral observation during the group-III deposition at a fixed substrate temperature [1–3]. Alternatively, the group-III element is deposited first at a sufficiently low Sb substrate temperature to prevent a III–Sb compound formation. Subsequently the temperature is increased gradually, while simultaneously monitoring the Raman spectrum in order to catch the dynamics of the compound formation.

In this paper the latter approach is followed. While increasing slowly the temperature the amount of the reacted phase at the buried interface is detected through the measured Raman intensity at the compound phonon frequency. This allows the deduction of the compound layer thickness and thus of the diffusion rate in the semiconductor layer.

In addition, the growth mode of the initial group-III layer and the completeness of the reaction at the end of the temperature ramp is checked by Auger electron spectroscopy (AES).

2. Experimental

The initial clean antimony (111) surfaces were obtained by cleavage in UHV environment. Afterwards a group-III layer — indium, gallium or aluminium — was evaporated from a Knudsen cell. Sufficiently low substrate temperatures were chosen to suppress a compound formation in this early stage of the experiment (In: -110°C , Ga: -100°C , Al: $+23^{\circ}\text{C}$). Already this deposition process was monitored by Raman spectroscopy revealing the attenuation of the Sb-A_{1g} and Sb-E_g substrate modes at 153 cm^{-1} and 114 cm^{-1} , respectively. During the deposition process no Raman signals at the vibrational frequencies of the compounds are detected. The evaluation of the pure group-III phases is not possible by this technique, since these phases have no optical phonon modes. The deposition was stopped when the intensity of the Sb-A_{1g} and Sb-E_g phonons had dropped to approximately half of its initial value. In this way information from the topmost substrate layers is still obtainable. This criterion led to film thicknesses of 40 Å indium, 70 Å gallium and 40 Å aluminium. After finishing the deposition an analysis

by Auger electron spectroscopy was performed to check for remaining substrate features.

As the next step the sample temperature was slowly increased while continuously Raman spectra were taken with a rate of one spectrum per minute. The speed of the temperature ramp was set to 1°C per minute ($1.4^{\circ}\text{C}/\text{min}$ for aluminium), controlled by thermocouples. The temperature difference between the sample surface and the thermocouple data is estimated to be $\pm 20^{\circ}\text{C}$. Nevertheless the ramp speed of $1^{\circ}\text{C}/\text{min}$ is expected to be valid also for the sample surface. The temperature ramp was continued until structures in the compound frequency range appeared in the Raman spectra. The maximum temperatures were In: 25°C , Ga: 160°C , Al: 290°C .

Finally, the temperature was decreased below the observed onset temperature of the compound formation while Raman monitoring was continued. This procedure was performed in order to distinguish between the influence of the irreversible diffusion process and a possible reversible temperature influence on the Raman spectrum.

The Raman spectra were recorded using a Dilor XY triple monochromator equipped with a multi-channel detector. This spectrometer is coupled to the UHV chamber, such that Raman spectra can be recorded while the deposition or heating process is in progress [2]. The Raman spectra were excited with an Ar^{+} -laser using the 514.5 nm line for indium, the 496.5 nm line for gallium, and the 457.9 nm line in the case of aluminum deposition. Thus resonance enhancement was achieved for detection of the expected III–V compounds [4]. The laser power used was equal or less than 50 mW and diagonal polarisation configuration was used.

3. Results and discussion

The decrease of the substrate phonon intensity in the Raman spectra during the first stage of the experiment — the deposition of the ad-layer — is shown in Fig. 1. Obviously, for In and Al deposition the decay is more pronounced than for Ga. For all deposited materials we performed simulations of the expected substrate intensity attenuation assuming a two-dimensional growth, based on the optical constants of the overlayers at the applied laser wave-

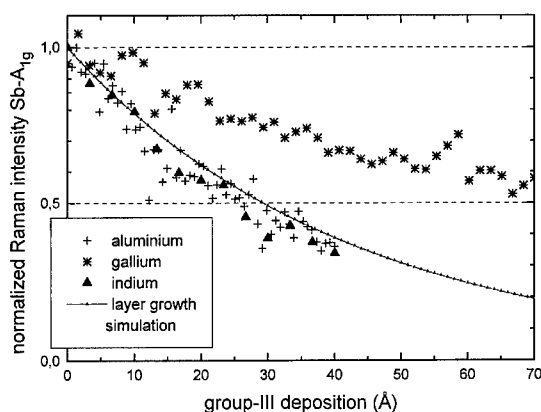


Fig. 1. Attenuation of the Sb-A_{1g} Raman line during the group-III deposition process. The model calculation for a planar overlayer growth fits well for the indium and aluminum case.

length [5]. The calculated result for In is also shown in Fig. 1. Those for Al and Ga (not shown here) would nearly coincide with the curve for In. The experimentally detected antimony Raman intensities follow the exponential-like decrease consistent with a flat and closed metallic top layer for the case of In and Al deposition. For Ga deposition the decay is much weaker than predicted by the model for two-dimensional growth.

These data are explained consistently by two-dimensional growth for In and Al, but island growth for Ga. This interpretation is further confirmed by AES spectra, which reveal only for the 70 Å gallium-covered sample still features of the antimony substrate.

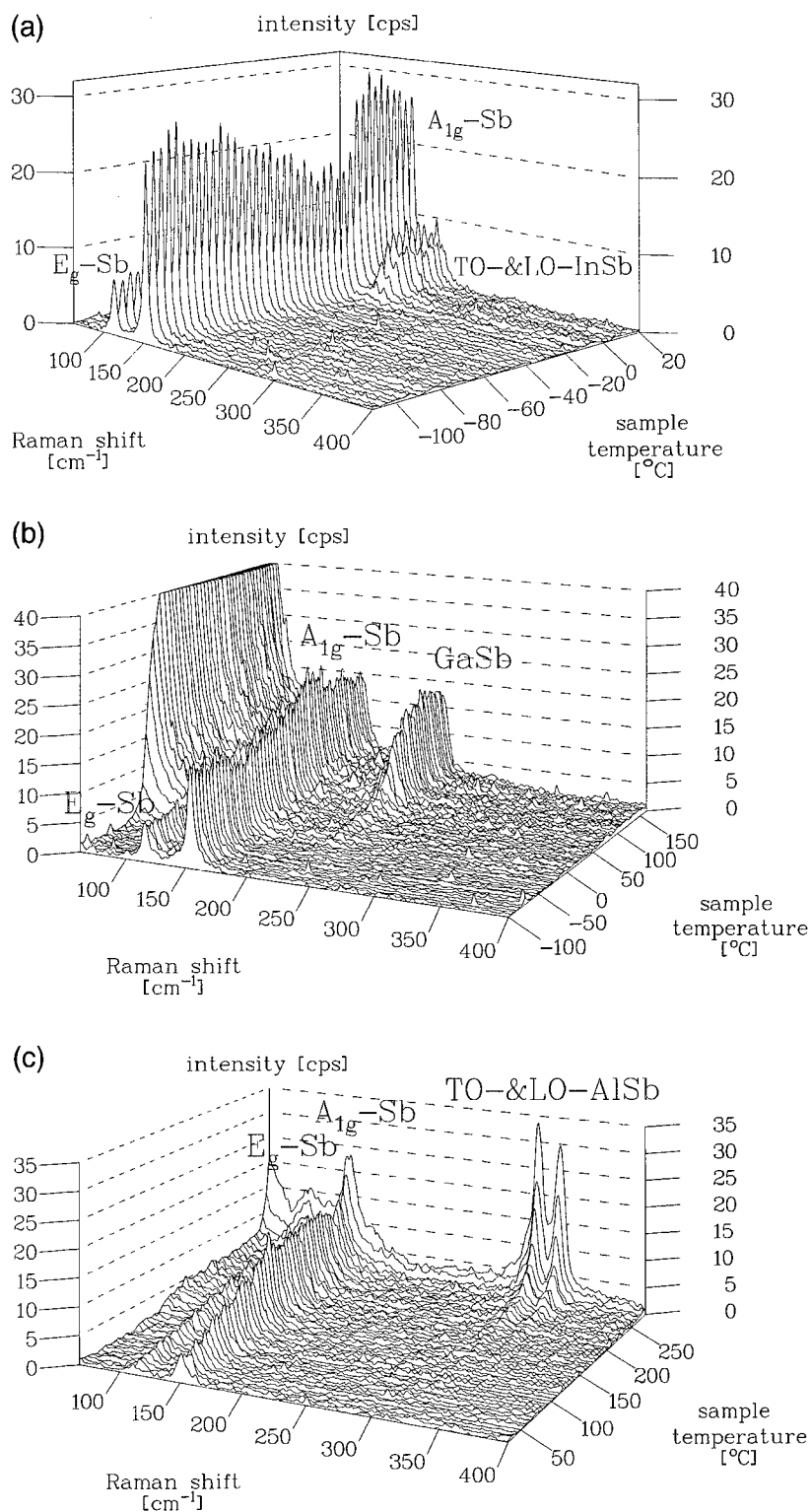
Results of the subsequent stage of the experiment, the temperature ramp, are presented in Fig. 2. Three-dimensional plots show the evolution of the Raman spectra with increasing sample temperature. In all cases temperatures high enough for compound formation can be reached in the experiment.

Three main features can be observed in the three diagrams of Fig. 2: the appearance of the compound-related phonon modes, the intensity change of the substrate modes, and the increase of elastically scattered light in the low frequency region of the spectra.

During the temperature ramp of the indium covered sample the peak heights of the substrate phonons are continuously decreasing (Fig. 2a), most probably due to a temperature induced broadening and/or change of resonance. This behaviour continues until new features are clearly observable at about -10°C in the spectral range of 190 cm^{-1} . The new features are two peaks at 181 cm^{-1} and 191 cm^{-1} revealing the formation of InSb by the appearance of TO- and LO-phonon lines at the expected frequencies. The evaluation of their temperature-dependent intensity shows that the compound formation starts at -15°C (see Fig. 3). In parallel, the intensity of the Sb increases, which is explained by the reduced light absorption in the InSb compound layer compared to the absorption in metallic indium. This argument holds even in spite of the 2.6 times increased InSb film thickness compared to the thickness of the initial metallic indium layer. In contrast to the aluminium and gallium case no increase of the elastically scattered light due to an increasing surface roughness is observed. This proves the flatness of the obtained compound surface. The evaluation of the InSb layer thickness over the sample temperature is plotted in Fig. 3. For this plot the Raman intensities of the InSb modes were transformed to a reacted layer thickness assuming a stacked layer model In/InSb/Sb during the reaction. Beside attenuation also interference effects in the layer were taken into account. An exponential increase of the layer thickness with increasing temperature is obtained. With the aid of a simple diffusion model an activation energy of $3.3\text{ eV} \pm 25\%$ can be attributed to the diffusion process.

After finishing the temperature ramp the LEED pattern of the compound surface exhibits a 2×2 superstructure, as it was reported for an indium-rich InSb(111) surface [11]. Both the lattice constant from the LEED pattern and the InSb phonon positions in the Raman spectra state a relaxation of the 100 Å ad-layer, as expected from the large lattice mismatch of 6% with respect to the antimony substrate. During the subsequent reversed temperature ramp the observed scattered intensity of the InSb stays nearly

Fig. 2. Online Raman spectra taken during a temperature ramp for (a) In, (b) Ga, and (c) Al layer on antimony substrates. The compound formation is manifested by the appearance of the compound related phonon lines.



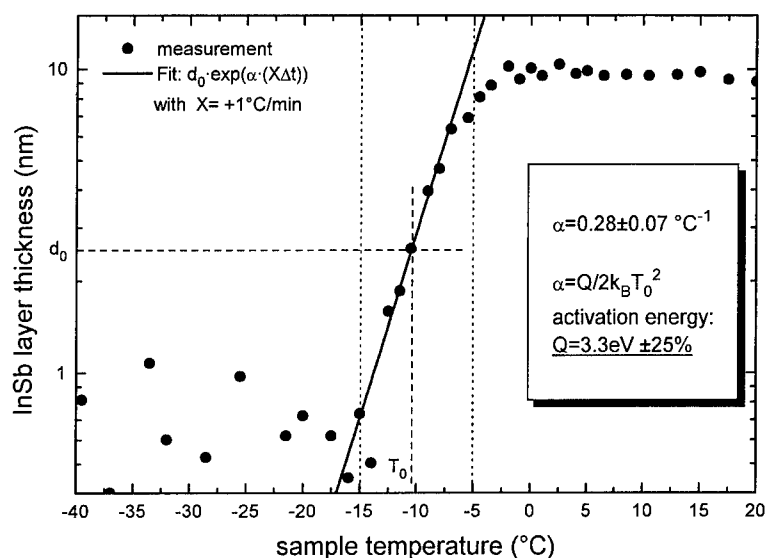


Fig. 3. Thickness of the reacted layer, deduced from the intensity of the InSb Raman lines, vs. sample temperature. The observed exponential increase corresponds to an activation energy of $3.3 \text{ eV} \pm 25\%$.

unaltered. This proves that the observed dynamics during the increasing temperature ramp indeed have to be attributed to the diffusion and a thermal modification of the light scattering efficiency is negligible. Besides, also Auger spectroscopy shows persistent indium and antimony features.

The data presented in this paper are consistent with a similar heating experiment for a 100 nm thick In layer on Sb(111) using perturbed gamma-gamma angular correlation (PAC) analysis, which was performed by Wesche et al. They found InSb formation over the range from -50°C to $+50^\circ\text{C}$ [12].

For gallium (Fig. 2b) the T-ramp leads to a two step behaviour. A first step at about -15°C reveals a strong increase of the diffusely reflected light and at the same time the onset of a small structure at the GaSb phonon frequency (230 cm^{-1}). In a second step from $40 \dots 70^\circ\text{C}$ the intensity of the GaSb mode increases by a factor of three. This increase is accompanied by a further roughening of the surface as indicated by a further step in the elastical straylight intensity, which is beyond the vertical scale of the picture. During the GaSb formation the Sb signal does by no means vanish. This proves that the GaSb is present in the form of islands. The small decrease of the antimony substrate modes during the major part of GaSb formation from the Ga islands is at-

tributed to an enhancement of the lateral coverage of the surface due to the island volume gain by a factor of 2.9 because of the increase of the volume related to each gallium atom by this factor during GaSb formation. Only very weak LEED features are observed from the compound surface.

Aluminium (Fig. 2c) shows a similar two step compound formation procedure. During the temperature ramp the straylight intensity increases for temperatures up to 160°C , subsequently it stays constant until a temperature of 260°C is reached, and increases again until the temperature ramp is stopped. The substrate modes follow this intensity behaviour. The first unambiguous observation of AlSb modes requires a temperature as high as about 170°C . The increase of the AlSb signal follows an exponential law ($10^{\alpha \Delta T}$) over one and a half decade in the temperature interval $170 \dots 265^\circ\text{C}$ with the pre-factor $\alpha = 0.016/^\circ\text{C}$. For the last range $265 \dots 280^\circ\text{C}$ the pre-factor increases to ca. $\alpha = 0.04/^\circ\text{C}$. The roughening of the surface up to 160°C can be explained by a continuous enhancement of the mobility of the aluminium atoms at the surface, leading to a partial rearrangement until at ca. 165°C the first formation of the AlSb compound occurs, as deduced from the evaluation of the temperature-dependent intensity of the AlSb modes.

The stronger increase of the AlSb phonon intensities beyond about 265°C indicates the evolution of a new process, perhaps a strain relaxation of the film, resulting in an increased growth by diffusion along grain boundaries. This is underscored by the behaviour of the AlSb mode frequencies. Together with the changed growth mode at 265°C the frequencies of both, the TO- and LO-AlSb phonon, exhibit a stronger down shift with increasing temperature. This is interpreted as a relaxation-induced shift in addition to the temperature-induced one.

Also for the cases of AlSb and GaSb the reverse temperature ramp confirms the irreversible diffusion process and the negligible temperature effect on the light scattering efficiency.

Due to the more complicated temperature dependence of the GaSb and AlSb formation and, moreover, the non-planar growth of the III–Sb compound for these materials the activation energy cannot be determined quantitatively with the model applied for InSb. However, we may state that the observed trend of a retarded diffusion of GaSb and especially AlSb with respect to InSb fully agrees with our earlier results for deposition at 300 K. Here InSb layers of good quality were formed, while the GaSb was inferior and AlSb did not appear at all [3]. The easy diffusion of InSb may seem surprising since this compound has a considerably lower formation enthalpy than GaSb and AlSb. We attribute the strong diffusion to an enhancement, caused by the formation of cracks in the InSb due to the high lattice mismatch of 6% to the Sb substrate.

4. Conclusions

In this paper a systematic investigation of the formation temperatures of antimony based III–V compounds was presented. In this context Raman monitoring with multichannel detection has turned out to be very suitable for the detection of the onset and observation of the development of the interface

reaction. The threshold temperature observed was found to increase with the group-III species from InSb (–15°C) over GaSb (40°C) to AlSb (165°C). A layer-like formation was found for InSb, while AlSb and GaSb tend to island formation.

Acknowledgements

This project was supported by the Ministerium für Wissenschaft und Forschung des Landes Nordrhein-Westfalen (FRG) within the Bennigsen-Foerder program. We thank Professor P. Grosse (RWTH-Aachen) for providing the antimony substrates.

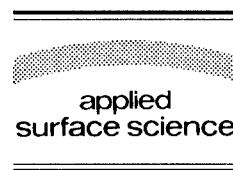
References

- [1] V. Wagner, D. Drews, D.R.T. Zahn, J. Geurts and W. Richter, *Europhys. Conf. Abstr.* 13th General Conf. of the Condensed Matter Div. European Physical Society (EPS), 17A (1993) p. 1532.
- [2] V. Wagner, D. Drews, N. Esser, D.R.T. Zahn, J. Geurts and W. Richter, *J. Appl. Phys.* 75 (1994) 7330.
- [3] V. Wagner, D. Drews, N. Esser, W. Richter, D.R.T. Zahn and J. Geurts, in: *Proc. 4th Int. Conf. on the Formation of Semiconductor Interfaces ICSFI-4*, 14–18 June 1993, ISBN 981-02-1559-2 (1994) p. 546.
- [4] W. Richter, *Springer Tracts in Modern Physics*, Vol. 78, Ed. G. Hoehler (Springer, Berlin, 1976).
- [5] M. Ramsteiner, C. Wild and J. Wagner, *Appl. Opt.* 28 (1989) 4017.
- [6] J.-L. Guyaux, R. Sporken, R. Caudano, V. Wagner, J. Geurts, N. Esser and W. Richter, *Surf. Sci.* 338 (1995) 204.
- [7] R. Sporken, P. Louette, R. Caudano, J. Barth, J. Ghijsen, R.L. Johnson and H.W. Richter, *J. Vac. Sci. Technol. B* 5 (1987) 1057.
- [8] R. Sporken, P. Louette, J. Gerard, R. Caudano and J.P. Delrue, *Fresenius Z. Anal. Chem.* 329 (1987) 370.
- [9] R. Sporken, P. Xhonneux, R. Caudano and J.P. Delrue, *J. Vac. Sci. Technol. A* (1988) 1565.
- [10] R. Sporken, P.A. Thiry, E. Petit, J.J. Pireaux, R. Caudano, J. Ghijsen, R.L. Johnson and L. Ley, *Phys. Rev. B* 35 (1987) 7927.
- [11] G.J. Russell, *Surf. Sci.* 55 (1976) 380.
- [12] R. Wesche, W. Keppner, T. Klas, R. Platzer, J. Voigt and G. Schatz, *Hyperfine Interactions* 34 (1987) 573.



ELSEVIER

Applied Surface Science 104/105 (1996) 586–594



STM study of the organic semiconductor PTCDA on highly-oriented pyrolytic graphite

C. Kendrick, A. Kahn^{*}, S.R. Forrest

Department of Electrical Engineering and Advanced Technology Center for Photonics and Optoelectronic Materials, Princeton University, Princeton, NJ 0854, USA

Received 1 July 1995; accepted 26 September 1995

Abstract

Monolayer and multilayer films of the archetype organic semiconductor 3,4,9,10-perylenetetracarboxylic dianhydride are deposited at room temperature in ultrahigh vacuum on freshly cleaved highly-oriented pyrolytic graphite (HOPG) and analyzed by scanning tunneling microscopy (STM). STM images of monolayer films show a 'herringbone' structure with two molecules per unit cell and dimensions which are in good agreement with prior studies. High-resolution STM images acquired under a variety of bias voltages indicate an electronic inequivalence of the two molecules within the unit cell. Although the image of the most prominent of these molecules resembles a figure eight over a wide range of sample biases, a difference in shape between filled and empty states appears at the smallest bias voltages. These differences are compared to molecular orbital calculations for the highest occupied and lowest unoccupied molecular orbitals of an isolated molecule and found to correlate rather well. Moiré fringes are observed with much larger periodicity than those previously reported by Ludwig et al., and can be explained by the incommensurate nature of the overlayer, which grows quasi-epitaxially, constrained mostly by the symmetry of the substrate. The first reported results of STM on multilayer films is presented showing crystalline domains in multiples of 60°, the rotational symmetry of the HOPG (0001) surface. In most cases, edges of these domains are observed to preferentially align along the *a*-axis of the unit cell. Finally, given this evidence of stable tunneling with molecular resolution on monolayer and multilayer films, mechanisms for STM image contrast on PTCDA films are discussed.

1. Introduction

Organic thin films have received an increasing amount of attention for their application to electrical and optoelectronic devices [1–6]. Specifically, these films possess the attractive properties of photosensitivity, birefringence, and optical non-linearity. Re-

cently, the demonstration of the growth of highly ordered films using Langmuir–Blodgett (LB) and high vacuum organic molecular beam deposition (OMBD) processes [7] has further made organic thin films research a promising area of investigation. Organic molecular crystals made from commercially available dye pigments, such as phthalocyanine- and perylene-based compounds, have several practical advantages in addition to interesting optical and electrical properties. They have inherent thermodynamic

^{*} Corresponding author.

stability and are compatible with ultrahigh vacuum (UHV) deposition and processing, though, perhaps their greatest advantage is the relaxed constraint of lattice matching of the film to the substrate lattice due to the flexible nature of van der Waals bonding, characteristic of these crystalline molecular solids.

In this paper we focus on studying the interface between the archetype crystalline molecular semiconductor PTCDA (3,4,9,10-perylenetetracarboxylic dianhydride) and highly-oriented pyrolytic graphite (HOPG) as observed by scanning tunneling microscopy (STM). This materials system has several advantages for study as a prototypical organic thin film interface. First, because the layering direction in bulk PTCDA is close to the growth direction, the first few monolayers relax into a flat lying configuration [8] which facilitates observation of the molecules by STM. Second, the HOPG substrate is flat and chemically inert, allowing a preferential alignment of the interface molecules over large areas. This general phenomenon of orientation to the substrate even in the absence of lattice matching is termed 'quasi-epitaxy' (QE) and has been described elsewhere [9]. The interface of PTCDA with HOPG has been previously studied with STM, LEED, and X-ray diffraction [8,10] and separately by RHEED and STM [11]. However, there remains some controversy over the exact orientation and epitaxial (or quasi-epitaxial) nature of the thin film with respect to the substrate lattice, as well as the contrast mechanism in STM images. In this contribution, we present data supporting the assumptions of QE (over conventional epitaxial) growth and address issues of STM image contrast.

2. Experiment

Experiments were conducted in an ultrahigh vacuum system consisting of an STM chamber connected to a surface analysis chamber. The STM and surface analysis chambers have base pressures of $\sim 1 \times 10^{-10}$ Torr. A load lock attached to the analysis chamber facilitated fast sample transfer as well as preparation of the STM tips. Both electrochemically etched tungsten tips and mechanically sheared Pt–Ir tips [12] were used in these experiments, however, the Pt–Ir tips were typically more stable over long

periods of time. Thin films of PTCDA were characterized using a home-built UHV-STM based on the design of Demuth et al. [13] with the added capability of stable operation at small tunneling currents (15–30 pA). This STM is well suited to the study of organic thin films due to their relatively low conductivity. All images shown in this paper were taken in constant-current mode (using tip currents of 100 to 300 pA and voltages from -800 to $+750$ mV) with a scan rate of approximately 2–3 min/frame.

The surface analysis chamber is equipped with low energy electron diffraction (LEED), Auger electron spectroscopy (AES), and argon ion sputtering. The PTCDA source material was purified by gradient sublimation as described previously [11,14] and loaded into an effusion cell within the surface analysis chamber. The HOPG substrate was cleaved and immediately transferred into vacuum via the load lock. PTCDA was deposited onto the room temperature substrate at a rate of 3–4 Å/min, as measured by a quartz-crystal thickness monitor. The film thicknesses studied in these experiments ranged from sub-monolayer coverage up to 2–3 monolayers (ML).

3. Results and discussion

3.1. Monolayer films

3.1.1. Unit cell characterization

In Fig. 1a is shown a high-resolution image of a 1 ML thick film of PTCDA. Notice the shape of the two molecules within the unit cell: one characteristically appears as a figure-eight while the other less well resolved molecule appears as two parallel lines. We first characterize the surface unit cell and its orientation to the substrate, and will later return to the origin of these features.

Correct calibration of distances measured by STM was verified by the close agreement between past observation of Si(111)- 7×7 surfaces and observation of the HOPG substrate adjacent to a PTCDA monolayer during the present experiment. The dimensions of the PTCDA rectangular unit cell, which is outlined in Fig. 1a, were averaged over several different images and samples to minimize errors due to thermal drift. The unit cell parameters were found to be: $a = 13.2 \pm 0.45$ Å and $b = 19.5 \pm 0.6$ Å.

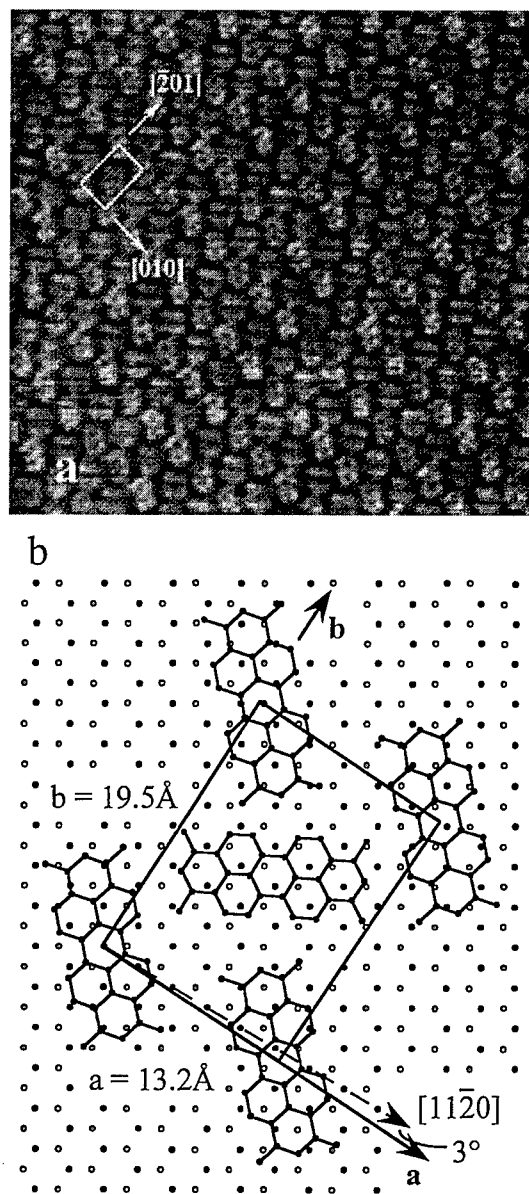


Fig. 1. Characterization of a monolayer of PTCDA on HOPG. (a) $200 \text{ \AA} \times 200 \text{ \AA}$ constant-current STM image showing a unit cell containing two molecules and crystallographic directions ($I_{\text{tip}} = 0.2 \text{ nA}$, $V_s = -800 \text{ mV}$). (b) Schematic representation of a monolayer showing unit cell dimensions and orientation to the substrate.

These measurements agree well with those reported previously [8,11] and are consistent with a possible enlargement of the bulk 2D unit cell in the (102) plane ($a = 11.96 \text{ \AA}$, $b = 19.91 \text{ \AA}$) on which growth

begins. Similar behavior for the growth of the first few monolayers has been observed for PTCDA on Au(111) [15] and for PTCDA on alkali halide substrates [16,17]. The orientation of the PTCDA with respect to the HOPG was obtained by maneuvering the tip into a small hole in the overlayer. This measurement assures that, in spite of the presence of randomly oriented domains in HOPG, the correct angular relationship between the substrate and the overlayer was observed. A small angle of $3^\circ \pm 3^\circ$ was observed between the a -axis ($[010]$ direction) of the PTCDA and the $[11\bar{2}0]$ direction of graphite, in agreement with the result of previous studies in which small misalignments of the PTCDA film to the graphite were measured [8,11]. Although our angular measurement is only accurate within a few degrees because of thermal drifts during imaging, we expect the angle to be non-zero based on the observation of moiré fringe patterns explained below. These results for the dimensions and orientation of the monolayer unit cell are compiled in the schematic representation of Fig. 1(b).

3.1.2. Moiré pattern in STM images

As mentioned above, moiré patterns were observed under certain tunneling conditions. An example of this is shown in Fig. 2. Here we clearly see a

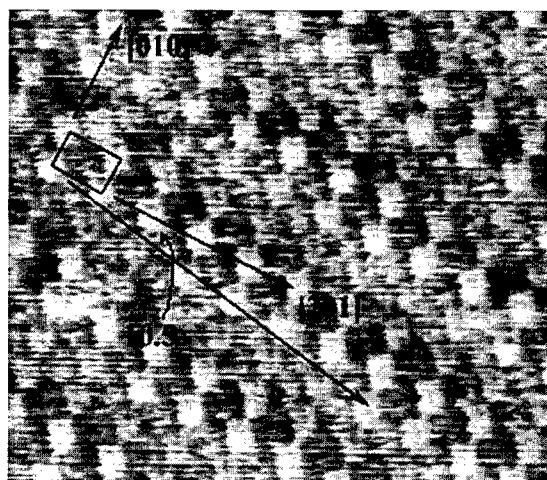


Fig. 2. $200 \text{ \AA} \times 200 \text{ \AA}$ image of a monolayer of PTCDA showing moiré fringes (parallel to the long arrow) which make an angle of 10.5° with the b -axis of the unit cell (shorter arrow; $I_{\text{tip}} = 0.1 \text{ nA}$, $V_s = -500 \text{ mV}$).

striated superstructure at an angle of 10.5° with respect to the b -axis ($[\bar{2}01]$ direction) of the PTCDA unit cell. This result differs from a previous study [8] in which moiré fringes were observed *parallel* to the b -axis, and where a *commensurate* 1×3 reconstruction was proposed as a possible explanation. That there is such close agreement in measurements of lattice misalignment angle and yet significantly different values for measurements of moiré fringe angle does not necessarily pose an inconsistency. First, we note that the moiré fringes parallel to the b -axis were observed [8] on films deposited at slightly elevated temperatures ($\sim 100^\circ\text{C}$), whereas all our films were grown on room temperature HOPG. A small difference in the alignment of the film with respect to the substrate could result from different growth conditions. Second, because of the large lattice mismatch

between the PTCDA and substrate, it is possible to adjust the surface unit cell dimensions and/or orientation by an amount less than the spatial resolution of the STM to obtain a precise reconstruction. However, due to the weak nature of the van der Waals bond, we believe it is unreasonable to assume that the molecules form a rigid reconstruction on such a scale equivalent to the repeat distance in the moiré pattern ($\sim 119 \text{ \AA}$ along the $[010]$ direction and $\sim 215 \text{ \AA}$ along the $[\bar{2}01]$ direction). Instead, our results imply that the overlayer is *incommensurate* with the substrate beneath, consistent with previous quantitative analyses of QE growth of such lattice mismatched overlayers [9].

Such moiré fringe patterns can be explained by several hypotheses. McTague and Novaco have predicted mass-density waves (MDWs) [18,19] to exist

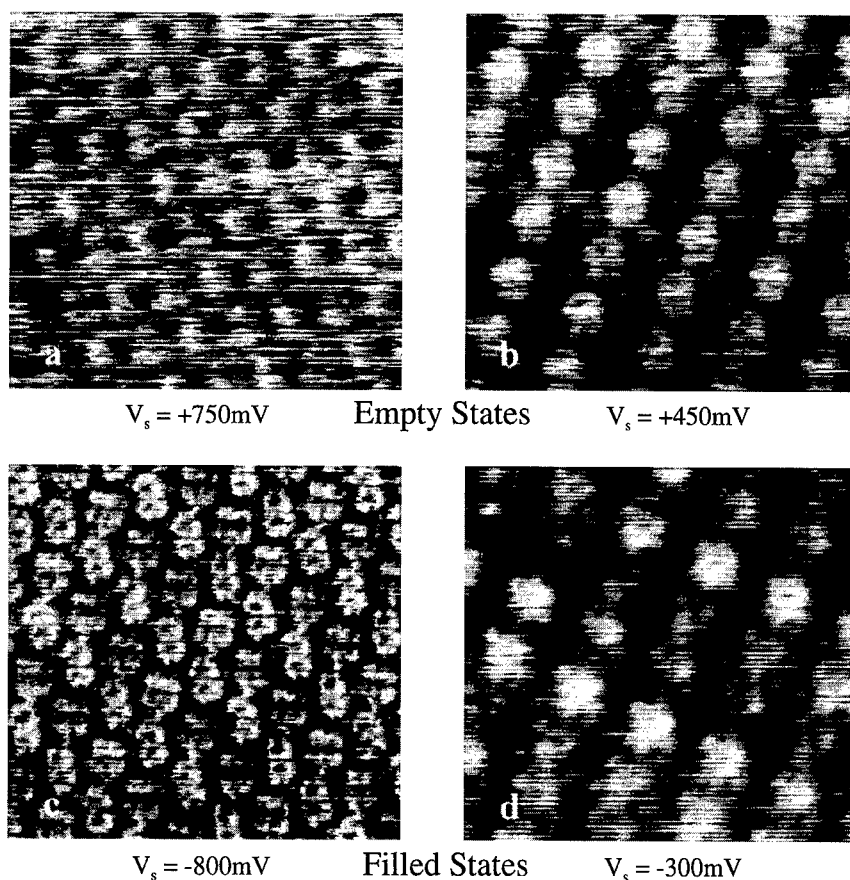


Fig. 3. $100 \text{ \AA} \times 100 \text{ \AA}$ STM images showing equal intensity of molecules for $|V_s| > 650 \text{ mV}$ and heightened intensity of one molecule for $|V_s| < 650 \text{ mV}$ ((a, b, d) $I = 0.1 \text{ nA}$, (c) $I = 0.2 \text{ nA}$).

as a strain-relief mechanism for monolayer films where adsorbate–substrate interactions are weak. Due to the relatively large unit cell size of the PTCDA overlayer and the limited spatial resolution of the STM, however, it is not possible to verify the existence of such a MDW from our data. An alternative and simpler explanation for such a moiré pattern is an electronic interaction between the symmetry of the film and that of the substrate which would create an interference pattern. Similar patterns have been observed by STM for van der Waals epitaxy of transition metal dichalcogenides [20] such as MoSe_2 on MoS_2 . In this situation, a small angular misalignment of the film produces a large change in the angle of the moiré pattern. Ref. [20] shows that it is possible to construct a diagrammatic interference pattern analogous to that observed by STM. This was done for the case of PTCDA on HOPG, however, due to the very large lattice mismatch, the interference effect can be easily seen with the naked eye only when the lattices are moved in relation to one another, hence we cannot show such a representation here. To summarize, both of these explanations are consistent with an incommensurate overlayer having a structure which, to first order, does not depend on the lattice constant of the substrate, but which tends to slightly misalign from a symmetry axis in order to reduce strain [9].

3.1.3. Voltage dependent imaging

In an effort to better understand the contrast mechanism in STM images of PTCDA, monolayers of the organic molecules were studied over a wide range of sample biases ($-1.0 \text{ V} < V_s < +1.0 \text{ V}$). This voltage dependency is shown in the four images of Fig. 3(a–d). In Fig. 3(a) and (c) both molecules in the unit cell are imaged with equal intensity, although Fig. 3(a) does not show the best resolution due to a poor tip. In general we find that, for biases $|V_s| > 650 \text{ mV}$, the two molecules appear with about equal contrast. Upon decreasing the bias voltage to $|V_s| < 650 \text{ mV}$, we find that the row containing the figure-eight molecule always appears with higher relative intensity than the alternating rows. This is apparent in Fig. 3(b) and (d).

At present it is not known whether this voltage dependent contrast of the PTCDA layer is an electronic or a topographic effect. Note, however, that the two molecules in the bulk (102) plane are not exactly coplanar, but instead are slightly offset in the direction perpendicular to the plane [7], a situation which might also hold for monolayer films on HOPG. If so, one would expect the slight difference in height between the two molecules to be most observable when the tip is closest to the film (i.e. low bias voltages). Assuming a roughly constant density of states over the voltage range studied, reducing the

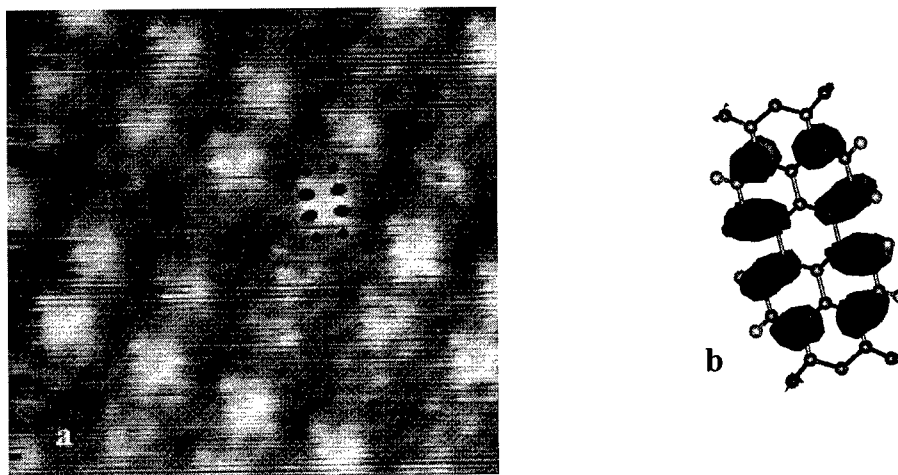


Fig. 4. (a) Low bias filled state STM image ($I_{\text{tip}} = 0.1 \text{ nA}$, $V_s = -250 \text{ mV}$, $100 \text{ \AA} \times 100 \text{ \AA}$). (b) Molecular orbital calculation for the HOMO of an isolated molecule.

tip-sample separation would produce a greater corrugation simply due to the exponential relationship between tunneling current and gap distance. Thus, the contrast dependency could be explained from a purely topographic point of view.

As has already been mentioned, however, the surface unit cell is found to be expanded from that of the bulk, pointing to a configuration in which both molecules could lie flat in the substrate plane. An alternative explanation of the contrast, therefore, is that the molecules within the rows of lower contrast have their long molecular axis aligned closely with a symmetry axis of the substrate. The interaction of these molecules with the substrate would then be greater, causing a symmetric energy shift of the highest occupied and lowest unoccupied molecular orbitals to lower and higher potential energies respectively. In this case, the molecules imaged with higher intensity at low biases would actually be less strongly bound, their associated molecular orbitals having greater overlap with tip wave-functions than their more tightly bound neighbors. In contrast, the overlap of each orbital at higher biases would be approximately the same, giving rise to an equal intensity for both molecules in the STM images as observed. It is also possible that a combination of these two mechanisms, topographic and electronic, contribute in some degree to the observed voltage dependent contrast.

Fig. 4(a) and Fig. 5(a) are STM images of filled and empty states, respectively. The images are taken at the lowest bias voltages below which the contrast of the PTCDA monolayer becomes unobservable. Under these conditions, we are able to image the PTCDA molecules with submolecular resolution and find a difference in the local electronic density of states. To interpret these images, Fig. 4(b) and Fig. 5(b) show the results of molecular orbital calculations [21] for the isolated PTCDA molecule based on the semi-empirical Zerner's intermediate neglect of differential overlap (ZINDO) method. These plots reflect the electronic probability density contour of the HOMO and LUMO states of PTCDA. When compared to the STM images, the spatial correlation of the calculated HOMO and LUMO to the filled and empty state images is quite good. The HOMO contour plot (Fig. 4(b)) shows where the highest energy electrons are located. According to the calculation, the highly electronegative oxygen atoms in the carbonyl groups at either end of the molecule capture an excess charge of approximately $0.4e^-$ from their carbon nearest neighbors. Nevertheless, the energy of these states lie lower than the HOMO, and there appears to be no significant contribution of the end groups to the STM images. Instead, it is the carbon-carbon π -bonds in the perylene core which contribute most significantly to determining the HOMO energy. It appears that in both filled and

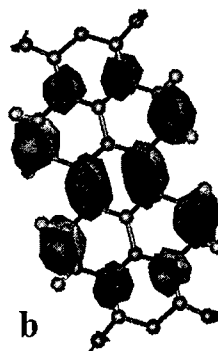
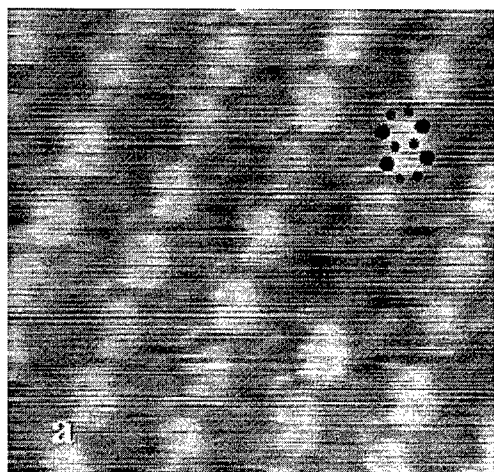


Fig. 5. (a) Low bias empty state STM image ($I_{\text{tip}} = 0.1$ nA, $V_s = +250$ mV, $100 \text{ \AA} \times 100 \text{ \AA}$). Note the missing molecule in the middle-right of the picture. (b) Molecular orbital calculation for the LUMO of an isolated molecule.

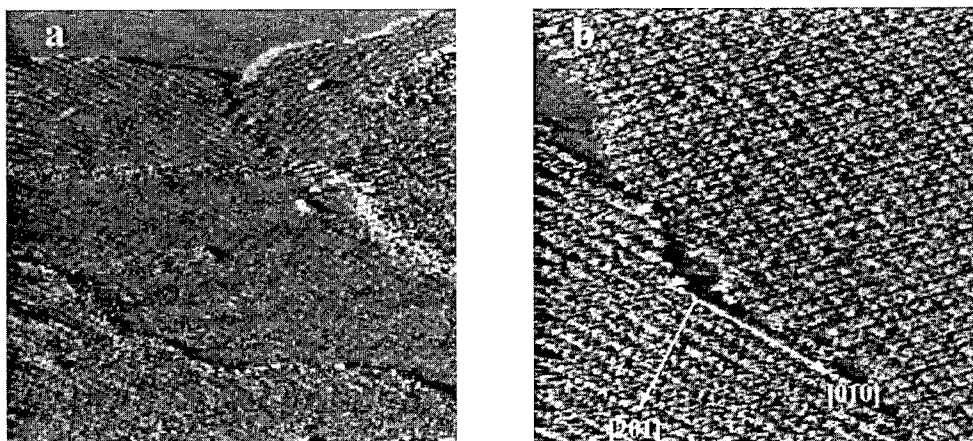


Fig. 6. (a) $750 \text{ \AA} \times 750 \text{ \AA}$ differentially filtered STM image ($I_{\text{tip}} = 0.1 \text{ nA}$, $V_s = +700 \text{ mV}$) showing several PTCDA steps of monolayer height in addition to clean graphite at the top of the image. (b) A close-up scan ($375 \text{ \AA} \times 375 \text{ \AA}$, $I_{\text{tip}} = 0.1 \text{ nA}$, $V_s = +700 \text{ mV}$) of the domain boundary near the top of (a) showing a domain orientation of approximately 120° as well as preferential edge alignment along the $[010]$ direction.

empty state images, the features which dominate the tunneling process are the π -bonds directed perpendicular to the surface. It is also interesting that these molecules can be imaged at biases much lower than the energy separation between the HOMO and the LUMO (estimated to be 2.2 eV from the lowest exciton energy [8], and 2.8 eV from the ZINDO calculation [21]). This may be due to broad band-tails [22], polarization effects, and/or substrate–overlayer interactions which could introduce allowed states

between the HOMO and the LUMO, effectively reducing the energy gap for the tunneling process.

Finally, for $|V_s| < 200 \text{ mV}$, the contrast of the PTCDA monolayer rapidly decreases and is replaced by the smoother corrugation of the graphite surface. When the sample bias is well below 200 mV, we find that it is possible to sweep the monolayer away and expose the HOPG substrate, as has been observed by others [8,11]. However, we also find that imaging of HOPG at a bias just below 200 mV does

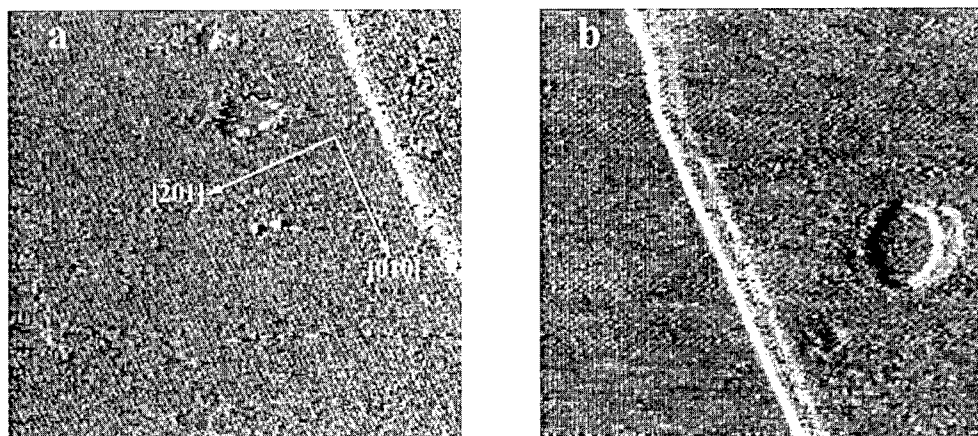


Fig. 7. (a) STM image of a step-up from monolayer to second layer coverage determined by observation of the graphite substrate in a small hole near the top of the image. The fine striations in the vertical direction are heightened contrast parallel to the a -axis of the unit cell to which the step-edge is also aligned. (b) Detailed image of the step where the 1st monolayer is clearly visible through a hole in the second layer. Note: ghost shadowing is due to a transient double-tip effect ($1500 \text{ \AA} \times 1500 \text{ \AA}$, $I_{\text{tip}} = 0.1 \text{ nA}$, $V_s = +900 \text{ mV}$).

not disturb the PTCDA monolayer. This result suggests that the total tunneling current probably consists of contributions from both the HOPG and PTCDA.

3.2. Multilayer films

In this section we report the first studies performed on multilayer films of PTCDA having typical coverages of from 1–3 ML. STM images of multilayer films were differentially filtered in order to increase the contrast. Therefore, regions of the surface at which the tip height changes rapidly appear in these images either as very light or very dark, depending on the sign of the slope at that point.

Fig. 6 and Fig. 7 show multilayer films from two different samples, each elucidating a specific property of the films. In Fig. 6(a) there are several layers visible. The smooth texture at the very top of the image indicates the surface of clean graphite which has a smaller corrugation than that of PTCDA. The middle of the image contains a trough which is bordered on top and bottom by a multilayer film in which molecular ordering appears. Fig. 6(b) shows a close-up of this area in which domains of PTCDA are found oriented at approximately 120° to each other. Domains oriented in multiples of 60° have also been observed by STM [11]. Although bulk HOPG possesses only a 3-fold rotational symmetry (space group $P6_3/mmc$), one would expect to see domains oriented in multiples of 60° if the PTCDA monolayer interacts significantly with only the surface of HOPG. In this case, domains of PTCDA would align to the 6-fold rotationally symmetric plane group ($p6mm$) of the HOPG (0001) surface.

Fig. 7 shows images giving detail on two sides of a PTCDA step from 1 ML up to 2 ML coverage. The film thickness determination follows from the observation of a small hole in Fig. 7(a) which shows the characteristic smooth texture of the graphite surface and another hole, observed in Fig. 7(b), which clearly shows the corrugation of a PTCDA layer. Furthermore, it can be seen in Fig. 7(a) that the orientation of the domains is the same in each of the two layers, and that the step-edge is aligned precisely along the a -axis. To our knowledge, this image constitutes the first evidence obtained via STM of highly oriented QE in multilayer organic films. Fig. 6(b) also shows

a preferential alignment (indicated by arrow) of the step-edge along the same side of the unit cell. The observation of preferential alignment of step-edges along the a -axis in both Fig. 6(b) and Fig. 7(a) could imply an anisotropy of the *intra*-layer binding forces which are greater perpendicular to the b -axis than they are perpendicular to the a -axis leading to low-energy steps along the [010] direction. In addition, we observe no isolated molecules on areas of clean HOPG. This is consistent with the fact that PTCDA grows quasi-epitaxially on HOPG at room temperature (and below [11]), and implies that there is high surface molecular mobility at room temperature and that molecules have a lower energy when attached to an island.

Finally, these first reported STM images of multilayer PTCDA films provide strong evidence that the molecules participate directly in the tunneling process and do not simply modify the local barrier height of the substrate, as has been previously suggested [8]. Furthermore, the growth characteristics of the films are consistent with those expected from the assumptions of QE. Specifically, growth begins as an ordered overlayer which is not lattice matched to the substrate and continues in a *quasi-epitaxial*, slightly strained, layer-by-layer manner [9,11,15]. We note, in addition that the small angle observed between the PTCDA and the $[11\bar{2}0]$ HOPG axis is consistent with energy minimization calculations [9] which suggest that the overlayer orientation is determined by energy minimization with respect to the substrate. Due to the low energy of the vdW bond, however, the strain induced by the lattice mismatch is not sufficient to strongly distort the overlayer, consistent with our observations.

4. Summary

We have used STM to characterize the initial stages of growth for the molecular semiconductor PTCDA on HOPG starting from the sub-monolayer regime and continuing through the first few monolayers. We have found that growth starts on the (102) plane of PTCDA, with the molecules lying flat on the HOPG substrate in a rectangular cell slightly distorted with respect to the 2D unit cell in the bulk (102) plane. A small angular misalignment of the

film with respect to the substrate was found by directly imaging both the film and the substrate. This misalignment was further supported by the significant angle which moiré fringes were found to make with the *b*-axis of the unit cell. By studying the monolayer films over a wide range of sample biases a difference in contrast was observed between the two molecules comprising the PTCDA unit cell. Possible explanations of this contrast were presented based on both topographic and electronic arguments. At the lowest biases, we observed a difference between the shape of the individual molecules for filled and empty state images. These shapes were found to correlate well with molecular orbital calculations for the isolated molecule. However, the details of STM contrast for these organic films is not yet well understood. Finally, in the first reported STM study of multilayer films, we found that domains of PTCDA tend to orient in multiples of 60° with respect to each other, most probably due to a significant interaction of PTCDA monolayers with only the surface of HOPG. Lastly, evidence of preferential step-edge alignment along the *a*-axis of the unit cell was observed, which may indicate an anisotropy of the intra-layer forces within the (102) plane of PTCDA during the initial stages of growth.

Acknowledgements

The authors wish to thank the AFOSR (G. Pomrenke and C. Lee) and the NSF MRSEC program for their support of this work. We also thank Professor M.E. Thompson for generously providing molecular orbital calculations of PTCDA, and for informative discussions.

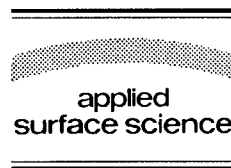
References

- [1] G. Horowitz, *Adv. Mater.* 2 (1990) 287.
- [2] C.W. Tang and S.A. Van Slyke, *Appl. Phys. Lett.* 51 (1987) 913.
- [3] S.R. Forrest, M.L. Kaplan and P.H. Schmidt, *J. Appl. Phys.* 55 (1984) 1492.
- [4] F.F. So and S.R. Forrest, *IEEE Trans. Electron Devices* ED-36 (1989) 66.
- [5] V. Prabhakar, S.R. Forrest, J.P. Lorenzo and K. Vaccaro, *IEEE Photonics Tech. Lett.* 2 (1990) 724.
- [6] C. Rompf, B. Hilmer and W. Kowalsky, *Jpn. J. Appl. Phys.* 33 (1994) 832.
- [7] A.J. Lovinger, S.R. Forrest, M.L. Kaplan, P.H. Schmidt and T. Venkatesan, *J. Appl. Phys.* 55 (1984) 476.
- [8] C. Ludwig, J. Gompf, W. Glatz, J. Petersen, W. Eisenmenger, M. Möbus and N. Karl, *Z. Phys. B* 86 (1992) 397.
- [9] S.R. Forrest and Y. Zhang, *Phys. Rev. B* 49 (1994) 11297.
- [10] C. Ludwig, J. Gompf, J. Petersen, R. Strohmaier and W. Eisenmenger, *Z. Phys. B* 93 (1994) 365.
- [11] S.R. Forrest, P.E. Burrows, E.I. Haskal and F.F. So, *Phys. Rev. B* 49 (1994) 11309.
- [12] Nanotips, Digital Instruments, Inc., Santa Barbara, CA 93103.
- [13] J.E. Demuth, R.J. Hamers, R.M. Tromp and M.E. Welland, *J. Vac. Sci. Technol. A* 4 (1986) 1320.
- [14] S.R. Forrest, M.L. Kaplan and P.M. Schmidt, *Annu. Rev. Mater. Sci.* 17 (1987) 189.
- [15] P. Fenter, P.E. Burrows, P. Eisenberger and S.R. Forrest, *J. Cryst. Growth* 152 (1995) 65.
- [16] M. Möbus, M. Schreck and N. Karl, *Thin Solid Films* 175 (1989) 89.
- [17] M. Möbus, N. Karl and T. Kobayashi, *J. Cryst. Growth* 116 (1992) 495.
- [18] J.P. McTague and A.D. Novaco, *Phys. Rev. B* 19 (1979) 5299.
- [19] A.D. Novaco and J.P. McTague, *Phys. Rev. Lett.* 38 (1977) 1286.
- [20] A. Koma, *Surf. Sci.* 267 (1992) 29.
- [21] J. Cronin and M.E. Thompson, private communication (1995).
- [22] Y. Hirose, PhD Thesis, Princeton University (1995).



ELSEVIER

Applied Surface Science 104/105 (1996) 595–600



Low-energy yield spectroscopy determination of band offsets: application to the epitaxial Ge/Si(100) heterostructure

L. Di Gaspare^{*}, G. Capellini, C. Chudoba, M. Sebastiani, F. Evangelisti

Dipartimento di Fisica "E. Amaldi", III Università di Roma, and INFM, Unità di Roma III, v. Vasca Navale 84, 00146 Rome, Italy

Received 28 June 1995; accepted 28 September 1995

Abstract

We apply a new experimental method for determining band lineups at the Ge/Si(100) heterostructure. This method uses a modern version of an old spectroscopy: the photoelectric yield spectroscopy excited with photons in the near UV range. It is shown that both substrate and overlayer valence-band tops can be identified in the yield spectrum, thus allowing a direct and precise determination of the band lineup. We find an offset of 0.36 ± 0.02 eV for heterojunctions whose overlayers were grown according to the Stranski–Krastanov mechanism.

1. Introduction

Due to its basic as well as technological interest, the band lineup at the Si/Ge interface was investigated extensively both theoretically [1–4] and experimentally, by applying a variety of techniques [5–10]. Among such techniques, photoemission spectroscopy is one of the most used and powerful. The main advantage of the photoemission technique, beside its surface sensitivity, is that it provides a signal which is directly proportional to the density of states and, therefore, the sought information is obtained with a small amount of assumptions. However, it has also several shortcomings, which limit its accuracy (see Ref. [11] for a discussion).

We have shown in a previous paper [12] on the characterization of crystalline/amorphous silicon heterojunctions that high accuracy and reliability can be obtained by applying a 'modern' version of an 'old' technique [13–15], i.e. photoelectric yield spectroscopy excited with low energy photons (visible and near-UV range) and operated in the constant final state mode (see below). This technique provides both a high resolution and a high dynamical range. Moreover, since the escape depth of electrons increases at low kinetic energies, a thicker near-surface region can be sampled (typically 40–50 Å), allowing a wider thickness range for the heterojunctions that can be analyzed. Both substrate and overlayer valence band edges can be identified on the same spectrum, thus providing a direct measure of the valence band discontinuity. In the photoemission measurements this kind of analysis, referred to as 'direct technique' in Ref. [11], is only feasible when the band offset is very large. In the present paper we

^{*} Corresponding author.

present data obtained on the Ge/Si(100) heterojunctions.

2. Experimental

The heterojunctions were grown in situ by low pressure chemical vapour deposition in a preparation chamber whose basic pressure was $\sim 8 \times 10^{-11}$ Torr. P-type ($\rho = 5 \Omega \text{ cm}$) mirror polished Si(100) wafers were used as substrates. The cleaning procedure consisted in: ex situ chemical wet etching; hydrogen plasma for removing surface carbon contamination; heating up to 1000°C in H_2 atmosphere for the removal of the SiO_2 layer. The cleanness of the resulting surfaces was monitored by XPS and the surface quality by RHEED. The contamination was beyond the detection limit and the surfaces showed 2×1 reconstruction. Ge overlayers were grown from high purity germane without carrier gas at low pressure. Two deposition temperatures were used for the Ge overlayer, namely 350°C and 470°C . The Ge surface was then passivated by exposure to activated hydrogen. Epitaxial quality, strain and surface morphology were characterized in situ by RHEED and ex situ by TEM, SEM, AFM and RHEED. Details will be published elsewhere [16].

As for the yield spectroscopy (YS), the light of a Xe source was monochromatized by a double grating monochromator in order to reduce the stray-light. The exciting photons were in the 3.5–6.5 eV energy range. The photon flux for the normalization of the electron count rate was measured before the experiments by positioning a photomultiplier in front of the entrance window of the analysis chamber. The photoemitted electrons were analyzed by a double-pass cylindrical mirror analyzer. The YS was operated in the constant final state mode (CFS), i.e. the photoemitted electrons of a chosen kinetic energy were collected as a function of photon energy. The samples were negatively biased in order to reduce the background. In these experimental conditions up to seven order of magnitude of signal intensity change as a function of energy could be followed. The system resolution in normal working conditions was 80 meV. The CFS operating mode is at variance with the previous use [13–15] of the YS technique, where

the total yield mode was employed¹. The CFS mode is frequently used with high energy photons in the synchrotron radiation spectroscopy, but was only recently employed by our group with low energy photons [17–19].

Typical electron kinetic energies chosen for the CFS-YS were 0.1–0.2 eV above the vacuum level. For such a low kinetic energy the conservation at the free surface of k parallel implies that the electrons which can escape into the vacuum are distributed in a narrow cone around the direction perpendicular to the surface. Hence, the final state for the transitions involved in the CFS-YS is fixed both in energy and in k direction. The interpretation of the signal becomes straightforward, contrary to the total yield case where a variety of functional dependencies were found [20], related to the electronic structure in a very indirect way. In the case of emission from localized states and surface states, it is expected that the transitions are *non-direct*. With the usual assumption that matrix elements are slowly varying functions of the energy, the CFS-YS spectrum is directly proportional to the density of initial states. In the case of transitions from extended states, we must distinguish between two possibilities. If the transitions are *direct* and k is conserved in the optical transition, a narrow peak in the CFS spectrum is expected when the photon energy is such that the final state is in the chosen escape cone. The CFS-YS becomes, substantially, an angle-resolved photoemission spectroscopy. Quite to the contrary, if the transitions are *indirect* and the missing k is provided by, e.g. the phonons, the CFS-YS intensity is again proportional to the density of initial states. More details on the comparison between CFS-YS and total yield spectroscopy can be found in Ref. [17].

The Fermi level energy position E_F on the CFS-YS spectra was determined in two ways. In the first procedure, the cutoff at the lowest binding energy due to the occupation probability was fitted with the Fermi function. Since the density of gap states which pin the Fermi level is high enough also on hydrogenated surfaces (see below) this procedure is usu-

¹ In the total yield mode all photoemitted electrons are collected, regardless their kinetic energy, and the current intensity is analyzed as a function of photon energy.

ally a reliable one. In the second procedure, the Fermi level was first located on the UPS spectra excited with $h\nu = 6.02$ eV photons by measuring a freshly evaporated gold layer. Then E_F was positioned on the corresponding yield spectra by bringing to coincidence the signals from the valence band edge in the two spectroscopies.

3. Results and discussion

We present preliminarily the CFS-YS data of the clean Si(100) and Ge(100) surfaces. The spectra are reported in Fig. 1 and Fig. 2, where the intensity is displayed on a linear as well as on a logarithmic scale. In order to remove the 'intrinsic' surface-state band and 'expose' the bulk valence band edge, both surfaces were hydrogenated. It is worth noticing, however, that the yield spectra are only slightly changed by the hydrogenation process, since the escape depth is rather large and the relative intensity of the surface states is already low. A study of the CFS-YS spectra as a function of hydrogenation and their comparison with the UPS spectra are reported elsewhere [21]. From the spectrum of Fig. 1 on the linear scale we see that in silicon there is a very sharp rise of emission at ~ 5.3 eV, resulting in a 'quasi' linear edge followed by a second structure at ~ 6.0 eV. Based on the evolution as a function of the final state energy and on the analysis of the energy band structure, we attribute the onset at ~ 5.3 eV to indirect transitions from the top of the valence

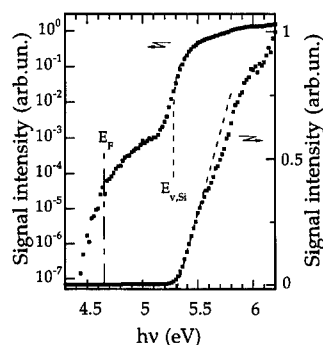


Fig. 1. CFS-YS spectrum of a Si(100) sample. The signal intensity is displayed on a linear scale on the right and on a logarithmic scale on the left. The dashed line represents the $E - E_{v,Si}$ dependence. The energy position E_F of the Fermi level is also shown.

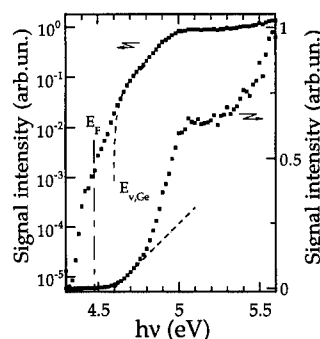


Fig. 2. CFS-YS spectrum of a Ge(100) sample. The signal intensity is displayed on a linear scale on the right and on a logarithmic scale on the left. The dashed line represents the $E - E_{v,Ge}$ dependence. The energy position E_F of the Fermi level is also shown.

band. The higher energy structure could be due either to direct transitions setting in or to indirect transitions from the L_3' critical point in the valence-band density of states.

The same spectrum reported on a logarithmic scale allows us to follow the evolution of the states inside the gap, thanks to the high dynamical range of the CFS-YS. For $h\nu < 5.3$ eV there is a steep decrease of emission as expected for transitions originating at the valence-band top. The exponential behaviour which extends to ~ 5.15 eV results from the broadening due to the experimental resolution. At still lower energies a broad band of deep defects is present, spanning the energy gap with decreasing intensity down to the Fermi level E_F . Based on the close similarity with the yield spectra of a-Si:H, we attribute [12] these states to isolated dangling bonds and/or small cluster of dangling bonds due to surface defects, which do not 'participate' to the surface reconstruction. These dangling bonds are reduced in number but not completely eliminated by the hydrogen passivation.

The edge at ~ 5.3 eV is used for defining the top $E_{v,Si}$ of the valence band. According to the usual procedure followed in the determination of band discontinuities by photoemission spectroscopies, we define $E_{v,Si}$ from the linear extrapolation to zero as shown schematically in Fig. 1. It should be kept in mind, however, that this definition is somewhat arbitrary and, as such, can entail a systematic error in the determination of the valence-band discontinuity at the interface.

Although at first glance the Ge(100) CFS-YS spectrum (Fig. 2) appears rather different from that of the silicon, a closer scrutiny reveals that the essential features are very similar. From the spectrum displayed on the linear scale it is apparent that there is a rise of emission at ~ 4.6 eV followed by a prominent structure at ~ 5.0 eV. On the logarithmic plot we see that the intensity is falling off very fast around 4.6 eV. Contrary to the Si case, in Ge the Fermi level is very close to the fast falling off. However, a shoulder due to the deep states is still visible at ~ 4.5 eV, despite the Fermi function cutoff. We attribute the onset at ~ 4.6 eV to indirect transitions from the top of the valence band and, similarly to the Si case, use it to define the top $E_{v,Ge}$ of the valence band. The resulting energy separation ($E_F - E_{v,Ge}$) between the Fermi level and the valence-band top is 0.10 ± 0.02 eV, in good agreement with previous reports [22,23] that in germanium E_F is pinned very close to the valence-band top.

The CFS-YS spectrum of a Ge/Si(100) heterojunction is shown in Fig. 3 for a 7 Å thick overlayer. Structural characterizations show that the Ge overlayer is epitaxial but partially relaxed and covers uniformly the Si substrate. With reference to the figure we see that there is a perfect agreement with the spectrum of the pure Ge down to ~ 0.3 eV below the Ge valence band top, while the emission from the heterojunction is larger at higher binding energies. A straightforward interpretation of this behavior is that the parting of the two spectra at high binding energy signals the beginning of the emission from the Si valence band and that the Si emission is negligibly small at lower binding energies. The agreement shown in Fig. 3c between the difference spectrum and that of the Si edge confirms this interpretation. Hence, the two band tops $E_{v,Si}$ and $E_{v,Ge}$ are clearly identified on the same spectrum and, consequently, the band offset ΔE between substrate and overlayer can be measured directly with high precision. The values of ΔE measured on the heterojunctions investigated in the present work are reported in the third column of Table 1.

As a test of the CFS-YS method, the heterojunctions were also characterized by XPS. As a first consistency check, we have estimated the band offset by using the Si core level according to the following procedure. First of all, a common binding energy

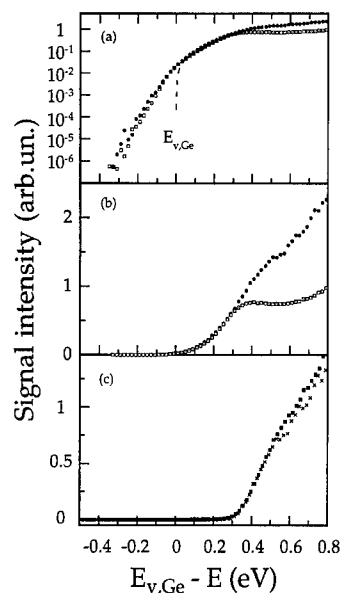


Fig. 3. (a) CFS-YS spectrum (dots) of a Ge/Si(100) heterojunction compared to that (open squares) of a Ge sample. The spectra are aligned to the Ge valence band top, determined as described in the text. (b) Same as (a) but with the intensity displayed on a linear scale. (c) Difference between the two spectra (crosses) of panel (b) (i.e. the Ge/Si heterojunction spectrum minus the Ge spectrum) compared to the spectrum (full squares) of a Si sample.

scale was obtained for the CFS-YS and XPS data by determining the Fermi level energy position for both kinds of spectra. Then, the energy separation $\Delta E_{val,core}$ between the valence band top and the $2p_{3/2}$ core level in bulk Si was determined by measuring a pure Si(100) sample. Finally, the energy

Table 1

Deposition temperature T_D , valence band offsets ΔE and ΔE^* , as measured by two different procedures (see text), and overlayer thickness for the heterojunctions investigated in the present work. The thickness was estimated by using core level intensities

Sample	T_D (°C)	ΔE (eV)	ΔE^* (eV)	Ge thickness (Å)
1	350	0.34	0.46	7
2	350	0.49	0.53	15
3	350	0.51	0.68	30
4	470	0.37	0.41	<11>
5	470	0.35	0.38	<11>
6	470	0.37	0.36	<11>
7	470	0.34	0.34	<11>

position of the Si valence-band top in the heterojunction spectra was obtained by adding $\Delta E_{\text{val,core}}$ to the value of the Si $2p_{3/2}$ core level as measured on the heterojunctions. The found value for $\Delta E_{\text{val,core}}$ is 98.66 eV. The values of the band offset ΔE^* , obtained with this procedure, are reported in the fourth column of Table 1. We see that on the average the agreement is good, confirming the soundness of the CFS-YS method.

Let us comment briefly on the values we have obtained for the valence-band offset. AFM and TEM analysis showed that the deposition at 350°C was of the layer-by-layer type, resulting in very flat overlayers. The 470°C deposition was of the Stranski–Krastanov type. These last four samples were practically identical and consisted of approximately four monolayers of Ge covering uniformly the Si substrate followed by large islands. The Ge overlayer was relaxed. The offset values measured on these samples are very close each other and their spread probably represents the uncertainty of the experimental method. Therefore, we can quote $\Delta E = 0.36 \pm 0.02$ eV for the offset in this kind of heterojunctions.

The measurements on the three 350°C samples were the first of a systematic investigation we have undertaken as a function of thickness and strain on layer-by-layer grown heterostructures. Unfortunately, RHEED analysis showed a partial relaxation of the overlayer and, therefore, the value of the strain could not be quantified. We believe that the spread of offset values is a consequence of real differences in the heterojunctions themselves. Beside the level of relaxation that could vary from sample to sample, we point out two more possible effects that can influence the offset, i.e. the presence of residual strain at the Si/Ge interface and the effect of quantum confinement in the Ge overlayer. Concerning the former effect, it was pointed out by Peressi and Baroni [24] that also in fully relaxed heterostructures a transition region two or three monolayers thick of residual strain and/or overstrain at the interface should be present. Its influence can not be neglected in heterojunctions with very thin and uniform overlayers like our sample 1. As for the latter effect, we note that the Ge electronic states close to the valence band top should feel quantum confinement if the Ge thickness is very small and that also should affect the measured offset.

Finally, we would like to compare our results with previous determinations. Our value for the offset in the Stranski–Krastanov heterostructures agrees with the determination of Kuech et al. [5], who found $\Delta E = 0.39 \pm 0.04$ by reverse bias capacitance measurements on p-Ge/n-Si(100) heterojunctions grown by CVD. It is also in good agreement with the finding ($\Delta E = 0.4 \pm 0.1$ eV) by Mahowald et al. [7] on Si/Ge(111) heterojunctions. Measurements on strained heterojunctions give higher values for the offset, as theoretically expected, due to the variation in the valence band structure brought about by the strain. Yu et al. [9] find $\Delta E = 0.83$ eV for a strained overlayer and $\Delta E = 0.49$ eV when the average Ge valence band top is considered, Schwartz et al. [8] find $\Delta E = 0.74$ eV for a strained overlayer. Preliminary measurements performed by us with the CFS-YS technique on strained junctions show a similar increase in the offset.

4. Conclusions

We have applied low-energy yield spectroscopy to the study of the heterojunctions, in the effort of finding a technique which could determine band offsets directly and avoid some of the shortcomings of the photoemission methods. CFS-YS excited with photons in the near UV range exhibits two interesting features, a larger sampling depth of the near surface region and a much higher dynamical range. We have shown that, by taking advantage of these features, it is possible to locate both substrate and overlayer valence-band tops on the same spectrum and obtain a direct determination of the band offset.

Acknowledgements

We are grateful to L. Ranieri for his valuable help during the experiment and to A. Miriametro and R. Moretto for their skilful technical assistance. This work was partially supported by the Consiglio Nazionale delle Ricerche under the contract No. 93.01269.CT02. L.D.G. is a recipient of a post-doctoral fellowship from the III University of Rome.

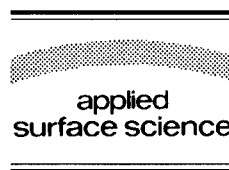
References

- [1] W.A. Harrison, *Electronic Structure and the Properties of Solids* (Freeman, San Francisco, 1980) p. 253; W.A. Harrison and J. Tersoff, *J. Vac. Sci. Technol. B* 4 (1986) 1068.
- [2] J. Tersoff, *Phys. Rev. B* 30 (1984) 4874.
- [3] C.G. Van de Walle and R.M. Martin, *Phys. Rev. B* 34 (1986) 5621.
- [4] L. Colombo, R. Resta and S. Baroni, *Phys. Rev. B* 44 (1991) 5572.
- [5] T.F. Kuech, M. Maenpaa and S.S. Lau, *Appl. Phys. Lett.* 39 (1981) 245.
- [6] G. Margaritondo, N.G. Stoffel, A.D. Katnani and F. Patella, *Solid State Commun.* 36 (1980) 215; G. Margaritondo, A.D. Katnani, N.G. Stoffel, R.R. Daniels and T.-X. Zhao, *Solid State Commun.* 43 (1982) 163.
- [7] P.H. Mahowald, R.S. List, W.E. Spicer, J. Woicik and P. Pianetta, *J. Vac. Sci. Technol. B* 3 (1985) 1252.
- [8] G.P. Schwartz, M.S. Hybertsen, J. Bevk, R.G. Nuzzo, J.P. Mannaerts and G.J. Gualtieri, *Phys. Rev. B* 39 (1989) 1235.
- [9] E.T. Yu, E.T. Croke, D.H. Chow, D.A. Collins, M.C. Phillips, T.C. McGill, J.O. McCaldin and R.H. Miles, *J. Vac. Sci. Technol. B* 8 (1990) 908.
- [10] J.F. Morar, P.E. Batson and J. Tersoff, *Phys. Rev. B* 47 (1993) 4107.
- [11] R.S. List and W.E. Spicer, *J. Vac. Sci. Technol. B* 6 (1988) 1228.
- [12] M. Sebastiani, L. Di Gaspare, G. Capellini, C. Bittencourt and F. Evangelisti, *Phys. Rev. Lett.* 75 (1995) 3352.
- [13] G.W. Gobeli and F.G. Allen, *Phys. Rev.* 127 (1962) 141.
- [14] C.A. Sebenne, *Nuovo Cimento* 39 B (1977) 768; P. Chen, D. Bolmont and C.A. Sebenne, *J. Phys. C: Solid State Phys.* 15 (1982) 6101; P. Chen, D. Bolmont and C.A. Sebenne, *Solid State Commun.* 46 (1983) 689.
- [15] S. Griep and L. Ley, *J. Non-Cryst. Solids* 59/60 (1983) 253; K. Winer and L. Ley, *Phys. Rev. B* 36 (1987) 6072.
- [16] L. Di Gaspare, G. Capellini, F. Evangelisti, M. Rossi and G. Vitali, to be published.
- [17] S.L. Wang, F. Patriarca and F. Evangelisti, in: *Amorphous Silicon Technology 1992*, Eds. M.J. Thompson, Y. Hamakawa, P.G. Le Comber, A. Madan and E.A. Schiff, *MRS Symp. Proc. No. 258* (Materials Research Society, Pittsburgh, PA, 1992) p. 241.
- [18] M. De Seta and F. Evangelisti, *Phys. Rev. Lett.* 71 (1993) 2477.
- [19] F. Patriarca, M. Sebastiani, S.L. Wang, I. Chambouleyron and F. Evangelisti, *J. Non-Cryst. Solids* 164–166 (1993) 833.
- [20] E.O. Kane, *Phys. Rev.* 127 (1962) 131; J.M. Ballantyne, *Phys. Rev. B* 6 (1972) 1436.
- [21] L. Di Gaspare, M. Sebastiani, G. Capellini and F. Evangelisti, to be published.
- [22] E. Landemark, C.J. Karlsson, L.S.O. Johansson and R.I.G. Uhrberg, *Phys. Rev. B* 49 (1994) 16523.
- [23] T. Miller, E. Rosenwinkel and T.C. Chiang, *Phys. Rev. B* 30 (1984) 570.
- [24] M. Peressi and S. Baroni, *Phys. Rev. B* 49 (1994) 7490.



ELSEVIER

Applied Surface Science 104/105 (1996) 601–607



Ultra-thin AlAs films on GaAs (001) investigated by high-resolution electron-energy-loss spectroscopy

J.-L. Guyaux^{a,*}, Ph. Lambin^b, M.D. Lange^{a,1}, R. Sporken^a, P.A. Thiry^a,
R. Caudano^a

^a *Laboratoire Interdisciplinaire de Spectroscopie Electronique, Facultés Universitaires Notre-Dame de la Paix, Rue de Bruxelles 61, B-5000 Namur, Belgium*

^b *Laboratoire de Physique du Solide, Facultés Universitaires Notre-Dame de la Paix, Rue de Bruxelles 61, B-5000 Namur, Belgium*

Received 28 June 1995; accepted 30 August 1995

Abstract

High-resolution electron-energy-loss spectroscopy has been applied to AlAs ultra-thin films grown by molecular beam epitaxy on GaAs (001). Below 12 AlAs monolayers, the loss intensities deviate from the prediction of the long-wavelength dielectric properties of AlAs and GaAs. Microscopic lattice-dynamics calculations of the surface dielectric response of AlAs/GaAs slabs have been performed. A better qualitative agreement with the experimental results is obtained when some cation intermixing is assumed to take place at the interface between the two media.

1. Introduction

The most frequent application of molecular beam epitaxy (MBE) growth is heteroepitaxy, namely, the epitaxial growth of a layer with chemical composition and sometimes structural parameters different from those of the substrate. Since the properties of the heterointerface play a major role in optoelectronic devices such as laser heterojunctions or 2 DEG FET transistors, many efforts have been devoted to improve and characterize these interfaces.

Interface roughness in quantum well structures is frequently studied by photoluminescence (PL) measurements. In a GaAs quantum well, the energy of the excitonic recombination line is a direct measure of the local width of the well, over the spatial extension of the exciton, through the quantization of the electronic energy-level in the square potential [1]. These studies have shown that the AlGaAs/GaAs interface is formed by large islands (larger than the exciton diameter) of half a lattice parameter height, and the lateral size of the islands is increased by interrupting the growth at the interface. On the other hand, the inverse interface (GaAs on AlGaAs) is pseudo-smooth, meaning that the lateral roughness is much lower than the exciton radius.

Optical phonons in AlAs/GaAs multilayers are strongly influenced by the interfaces and have been

* Corresponding author. Fax: +32-81-724595; e-mail: jean-loup.guyaux@fundp.ac.be.

¹ Presently at Physics Branch, Research and Technology division, Naval Air Warfare Centre Weapons Division, China Lake, CA 93555-6001, USA.

studied extensively by Raman spectroscopy [2]. In a superlattice, the superperiodicity along the growth direction induces a folding of the first Brillouin zone which produces additional modes at the zone center. These modes are affected to some extent by interface roughness [3]. From both PL and Raman experiments, it became clear that atomic roughness takes place at the interfaces and both techniques agree to claim that it occurs largely at the inverse interface (GaAs on AlGaAs).

The actual details of the interface roughness are rather complicated, as indeed recent transmission electron microscopy analyses revealed that even the AlGaAs/GaAs interface contains substantial atomic roughness [4]. More recently, cross-sectional scanning tunneling microscopy images recorded on short period AlAs/GaAs superlattices also showed a certain degree of interfacial roughness at the atomic scale at both interfaces [5]. A possible interpretation is that the interface presents in-plane terrace as large as 100 nm alongside with 'atomic scale roughness' meaning that Ga and Al are somewhat intermixed. In relationship with this interpretation, we have investigated the macroscopic optical phonons of MBE grown AlAs_n/GaAs epitaxial layers by high-resolution electron-energy-loss spectroscopy (HREELS), which is a useful tool for this kind of study [6]. The combined HREELS-MBE technique allowed us to investigate the AlAs/GaAs single interface instead of the usual multi-interface heterostructures such as quantum wells or superlattices. The data are first analyzed based on the well-known dielectric theory [7]. Test calculations based on lattice dynamics were then performed, to emphasize the effect of the interfacial 'atomic scale roughness' on the HREELS spectrum.

2. Experimental

The experiments were carried out in an ultra-high vacuum system combining HREELS and a MBE reactor. The samples can thus be transferred from the growth chamber into the spectrometer without being exposed to air. For the MBE growth, the substrate temperature was measured with an optical pyrometer, calibrated by observing the desorption of the gallium oxide by reflection high-energy electron diffraction (RHEED).

The (001)-oriented GaAs substrates (1 cm × 1 cm, semi-insulating, $> 10^{-7} \Omega \text{ cm}$) were prepared by a standard etching procedure ($\text{H}_2\text{SO}_4 : \text{H}_2\text{O}_2 : \text{H}_2\text{O} = 5 : 1 : 1$ at room temperature) before being loaded into the ultra-high vacuum chamber. They are mounted with indium on molybdenum sample holders. A thick buffer of GaAs was then grown on a (2 × 4)-As stabilized surface at a substrate temperature of 580°C. Prior to the growth of the AlAs film at the same temperature, the GaAs buffer was kept under As flux during 120 s, so as to improve the surface smoothness. The AlAs thickness was measured by the direct counting of the RHEED oscillations [8] of the (00) diffraction spot in the [110] direction, except for the thicker layers (above about 15 ML), whose thickness was extrapolated from the growth rate of the thin layers. Up to 50 monolayers of AlAs, the same (2 × 4) reconstruction as for GaAs was observed. For thicker layers, the AlAs surface exhibits a (2 × 2) reconstruction. A new sample was grown for each thickness of the AlAs overlayer.

The HREELS spectrometer uses two hemispherical capacitors as electron monochromator and analyzer. With the pass energies used in this experiment, the nominal energy resolution (full width at half maximum, FWHM) is 48 cm^{-1} . Experimentally, we obtain a FWHM of the quasi-elastic peak around 45 cm^{-1} . This indicates that our spectral resolution is not limited by the quality of the samples but by the spectrometer itself. We have not attempted to increase the resolution (by changing the pass energies) in order to keep a reasonable signal/noise ratio.

3. Results and discussion

The HREELS spectra were measured in the dipole scattering geometry (specular reflection). Fig. 1 shows a series of such spectra, recorded on AlAs_n/GaAs (001) heterostructures where n denotes the number of AlAs monolayers. These spectra were recorded with 10 eV electrons at an incidence angle of 45° with respect to surface normal. Besides a strong quasi-elastic peak, we observe characteristic energy loss peaks, as well as their corresponding energy gains. These features will first be discussed in

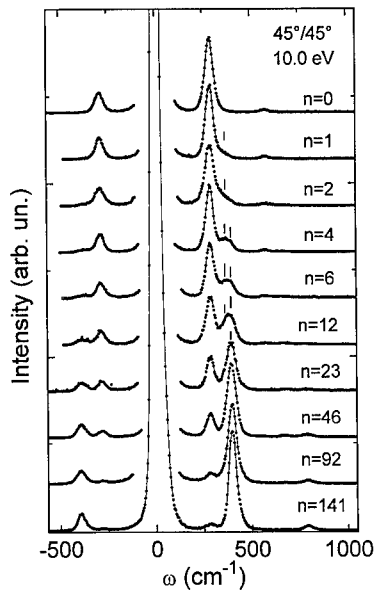


Fig. 1. HREELS spectra recorded with 10 eV electrons in specular reflection at an incidence of 45° versus the normal to the surface for AlAs_n/GaAs (001) for $n = 1 \dots 141$.

the framework of the dielectric theory; a more subtle analysis based on lattice dynamics will then be presented briefly.

Under specular reflection, the long-range of the coulomb field accompanying the moving electron implies that the probing electron interacts mainly with the macroscopic excitations ($Q \cong 0.1$ nm). In the first Born approximation, the HREELS spectrum is described by

$$P(h\omega) = \int_D d^2Q A(Q, \omega) \text{Im}[g(Q, \omega)], \quad (1)$$

where A is a kinematic cross section depending on the geometry of the scattering, and $g(Q, \omega)$ is the response of the target to an external field having the form of a plane wave with frequency ω and wave vector Q parallel to the surface. $\text{Im}[g(Q, \omega)]$ is the surface loss function of the target and presents sharp absorption peaks located at frequencies corresponding to the poles of $g(Q, \omega)$. $P(h\omega)$ gives the frequency resolved energy-loss spectrum at $T = 0$ K. A theoretical simulation of the entire spectrum is obtained by constructing the quantum mechanical loss distribution at a temperature T , which accounts for multiple excitation processes [7]. After convolu-

tion of the spectrum with the experimental response function of the spectrometer, the theoretical spectrum can be compared with the experimental one.

Due to the long-wavelength nature of the modes excited in HREELS, the response function can be deduced from electrostatics and is given by

$$g(Q, \omega) = \frac{\xi(Q, \omega) - 1}{\xi(Q, \omega) + 1}, \quad (2)$$

where $\xi(Q, \omega)$ is the effective dielectric function of the target.

The theoretical formulation of the dielectric model for a two-layer system has been established a long time ago [9]; an AlAs layer of thickness d on a semi-infinite GaAs substrate is described by:

$$\xi(Q, \omega) = \varepsilon_{\text{AlAs}} \frac{\varepsilon_{\text{AlAs}} \tanh(Qd) + \varepsilon_{\text{GaAs}}}{\varepsilon_{\text{GaAs}} \tanh(Qd) + \varepsilon_{\text{AlAs}}}, \quad (3)$$

where $\varepsilon_{\text{AlAs}}(\omega)$ and $\varepsilon_{\text{GaAs}}(\omega)$ are the long-wavelength bulk dielectric functions of AlAs and GaAs, and are expressed as $\varepsilon(\omega) = \varepsilon_\infty + \rho\omega_{\text{TO}}^2/(\omega_{\text{TO}}^2 - \omega^2)$ where ε_∞ is the electronic dielectric constant, ρ the oscillator strength and ω_{TO} the bulk transverse optical frequency (TO).

In the case of a GaAs (AlAs) semi-infinite sample, the pole of the surface loss function reduces to the well known condition for surface vibration, $\xi = -1$ where ξ is the bulk dielectric function of GaAs (AlAs). The optical dielectric parameters of GaAs or AlAs found in the literature [10] were slightly adjusted to best reproduce the HREELS spectrum recorded on semi-infinite GaAs and, in the case of AlAs, on a thick AlAs film grown on GaAs. The fitted optical parameters used for AlAs and GaAs are given in Table 1.

The analysis of the poles of $g(Q, \omega)$ shows that an AlAs film of thickness d deposited on a semi-in-

Table 1

Infrared optical constants of AlAs and GaAs: the optical parameters were obtained from fits of the dielectric theory to the experimental HREELS spectra recorded on thick AlAs and GaAs samples grown by MBE

	ε_∞	ρ	ω_{TO} (cm ⁻¹)
AlAs	8.16	1.88	360
GaAs	10.9	2.01	267

finite GaAs substrate has three branches of optical phonons, called the Fuchs–Kliwer modes (FK). The two lowest frequency branches come from the assumed sharp transition between AIAs and GaAs. They are called interface modes according to the localization at the interface of the electric field they generate. According to their frequencies, they can be labeled as GaAs and AIAs-like interface modes. The third mode, highest in frequency, generates an evanescent electric field centered at the termination of the overlayer at the free surface, and is called an AIAs-like surface mode.

From the HREELS spectrum of Fig. 1 we can state the following.

(i) The spectrum recorded on the GaAs surface ($n = 0$) shows only one main peak located around 288 cm^{-1} in the loss part of the spectrum. This is the fingerprint of the surface FK mode of GaAs.

(ii) From the very beginning of AIAs coverage (1 ML), a weak shoulder appears to the right of the GaAs main peak at a frequency around 365 cm^{-1} . This is the AIAs-like interface mode. The peak near 288 cm^{-1} is now called an interface GaAs mode.

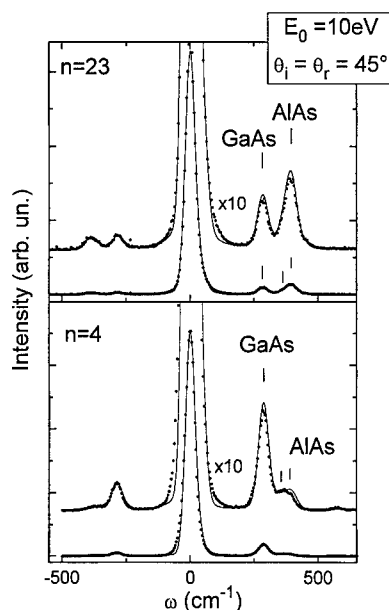


Fig. 2. HREELS spectra of two AlAs/GaAs (001) heterostructures obtained with 10 eV electrons in specular reflection. The dots represent the experimental data; the solid curves are the results of the dielectric theory.

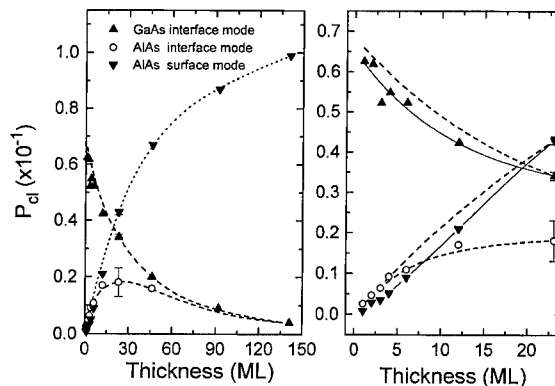


Fig. 3. Intensity of the two AlAs-like surface and interface modes as well as the interface GaAs modes versus overlayer thickness as predicted by the dielectric theory. The symbols are the experimental data following the procedure described in the text.

(iii) The new feature increases in intensity when the number of AIAs monolayers increases while the GaAs interface mode decreases to almost zero at high AIAs coverage. From the spectrum recorded on AlAs₄/GaAs, we can state that the AIAs related feature is composed of two peaks which merge into a single sharp one when the thickness of the AIAs overlayer increases. Within the electrostatic approximation, these two peaks are attributed to the interface and surface AIAs-like modes. At high coverage, the loss region is dominated by the strong AIAs surface peak near 395 cm^{-1} .

Fig. 2 shows the comparison between measured HREELS spectra of 4 and 23 monolayers of AIAs on GaAs (001). The continuous line is the result of the dielectric theory. While the agreement is excellent for the thicker layer, some discrepancies are observed for the case of 4 monolayers. Indeed, the macroscopic approach predicts too high an intensity for both the GaAs interface mode and the AIAs surface mode. This has led us to compare the experimental intensities of the loss peaks with the calculated ones as a function of thickness.

The intensities of each of the modes can be extracted from $\text{Im}[g(Q, \omega)]$ because the long-wavelength bulk dielectric function of GaAs and AIAs are described by one single Lorentzian oscillator. In the case of small oscillator damping, $\text{Im}(g)$ can be written, as a sum of three δ functions. The oscillator

strength of these modes depends on the target parameters and on the thickness of the AlAs overlayer. Using the optical parameters for AlAs and GaAs from Table 1, the loss probability corresponding to each of the modes is calculated as a function of the AlAs thickness. The result is shown by the dashed curves in Fig. 3.

The experimental loss intensities were obtained by adjusting the weight of the delta functions without changing their frequency, until the experimental spectrum is well fitted after accounting for multiple scattering and instrumental broadening. The result is superimposed on the calculated curves in Fig. 3. The larger error bar for the AlAs interface mode is due to the fact that this mode is weak and located close to the stronger AlAs surface mode. On the left panel of Fig. 2, we observe a good overall agreement between the dielectric theory and the experimental intensities. However, for small overlayer thicknesses (< 10 ML; right panel of Fig. 3), some discrepancies appear. In particular, the dielectric theory overestimates both the GaAs interface mode and the AlAs surface mode.

This deviation of the dielectric theory from the experimental results for thin AlAs films led us to perform lattice-dynamics calculations in order to test the validity of the dielectric approximation for ultra-thin films of AlAs on GaAs. These calculations will be summarized below and the main conclusions will be discussed. A more detailed description will be the subject of a separate publication [11].

Dynamical calculations were performed with a recent valence overlap shell model of GaAs (model OSM 5, see Ref. [12]). In the present calculations, AlAs was described with the same set of parameters except for the cation mass. The surface dielectric response function is easily obtained from lattice dynamics for the case of an isolated slab [13]. For that reason, shell-model calculations were performed for various (001) slabs composed of n monolayers of AlAs on top of $30 - n$ monolayers of GaAs which simulate the substrate. One monolayer is defined as one cation plane plus one anion plane. The number of monolayers in the slab (30) was taken as large as possible within reasonable limits imposed by the computing load [13].

The lattice-dynamics response function is not directly comparable to the experimental spectrum for the two following reasons:

(i) As the phonons of relevance here generate a macroscopic polarization field, the surfaces at both ends of the slab interact with each other;

(ii) the shell model was not optimized to provide realistic dielectric constants and we did not attempt to improve it.

For these reasons, a comparison between the lattice-dynamics response function and the experimental data is only possible via additional 'test' spectra obtained by the dielectric theory which can be made consistent on the one hand with the experimental data, when using the parameters of Table 1 in the semi infinite geometry, and on the other hand with the lattice dynamics, by using the slab geometry and the set of dielectric parameters deduced from the shell model at the Γ point.

The lattice-dynamics surface loss functions of $\text{AlAs}_n/(\text{GaAs})_{30-n}$ (001) slabs were compared with the corresponding dielectric spectra. When $n > 5$, the lattice-dynamics response function is very close to the electrostatic predictions. For $n < 5$, lattice dynamics yields more than two distinct peaks in the surface response function of the AlAs layer. The multiple-peak structure is a consequence of the confinement of the optical phonons in the AlAs overlayer [14]. However, such multi peak phonon spectra give approximately the same weight as that calculated by the dielectric theory.

The small deviation of the electrostatic approach from the lattice dynamics one does not truly explain the discrepancy between the experimental data and the dielectric theory. In particular, the AlAs-like surface mode and the GaAs-like interface mode have too high an intensity as compared to the experimental data. On the other hand, it has been mentioned above that the weight of the loss peaks is not significantly different when calculated by the dielectric theory or by lattice dynamics.

We now show that a reduction of the intensities of the AlAs-like surface and the GaAs-like interface modes can be caused by interfacial alloying. A theoretical argument in favor of this interpretation is that interfacial disorder has already been recognized to have a significant effect on the vibrational properties of ultra-thin AlAs/GaAs superlattices [15]. As mentioned in the introduction, there are in addition several experimental indications for atomic disorder exists at the AlGaAs/GaAs interfaces [4,5].

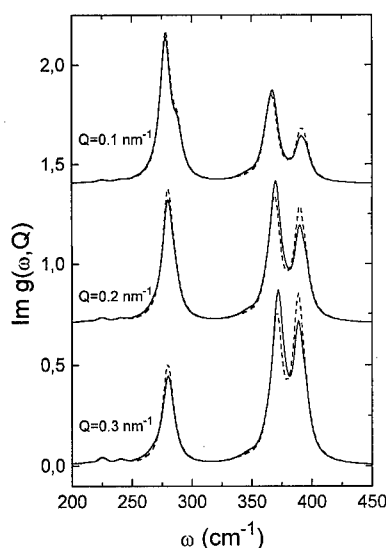


Fig. 4. The lattice-dynamics surface dielectric response of $\text{AlAs}_6/\text{GaAs}_{24}$ (001) slab for selected surface wavevectors. The dashed curves were obtained by assuming an abrupt change of composition at the interface whereas the solid curves were computed for a slab where the Al atoms at the interface are randomly mixed (50%) with the Ga atoms.

In order to investigate the effects of interfacial broadening on the HREELS spectrum of AlAs/GaAs heterostructures, the composition of the Al and Ga planes around the interface has been mixed at random with equal probabilities. The corresponding surface response function of the $\text{AlAs}_6/\text{GaAs}_{24}$ system is shown in Fig. 4 for selected wavevector values. The dashed curves represent the perfectly abrupt interface and the solid curves correspond to the mixed interface. The effect of interfacial mixing is consistent with the behavior of our HREELS data in Fig. 2. The interfacial intermixing creates a slight decrease of the GaAs loss structure intensity at 280 cm^{-1} and a significant decrease of the AlAs surface mode located at 390 cm^{-1} . There is also an enhancement of the AlAs-like interface mode around 370 cm^{-1} . When the wavevector Q of the external electric field is increased, the response of the bottom interface of the slab is lowered, since the spatial extension of the potential along the normal to the surface decreases like $\exp(-QD)$ where D is the overall slab thickness. As a consequence, the shoulder seen on the right hand side of the GaAs FK mode at 285 cm^{-1} vanishes when the value of Q is

increased above 0.2 nm^{-1} , and the effect of disorder at the interface is enhanced since the external field is more and more localized in the top part of the film. The effects of interfacial mixing should then approach those encountered in the case of a semi-infinite GaAs substrate which could not be dealt with in our theoretical calculations.

In order to better understand the effect of interface disorder on the long-wavelength FK modes, we have analyzed the eigenvectors of the modes contributing to the surface response of the $\text{AlAs}_6/\text{GaAs}_{24}$ system.

A first trend is that the AlAs-like modes are confined in the AlAs overlayer. The same is true for the GaAs vibrations which stay localized in the GaAs substrate. Due to the large separation between the GaAs and AlAs optical phonons, a vibration involving Al–As motion (Ga–As) cannot propagate through the neighboring GaAs (AlAs) layer since its frequency falls in a forbidden region. GaAs (AlAs) acts as an infinite barrier to the propagation of AlAs (GaAs) vibrations [16].

The broadening of the interface enhances the confinement of the AlAs surface as well as the GaAs mode. This can be understood because the mixture of the Al and Ga cations in the planes around the interface produces an alloy-like medium with composition $\text{Al}_{0.5}\text{Ga}_{0.5}\text{As}$. This alloy develops both AlAs- and GaAs-like vibrations (two mode behavior) [17] whose frequencies are well below those of pure AlAs or GaAs. It follows that the GaAs or AlAs bulk vibrations can not propagate through the $\text{Al}_{0.5}\text{Ga}_{0.5}\text{As}$ intermediate layer. The broadened interface therefore acts as a barrier (see Ref. [16] in the case when $x > 0.25$) which pushes the AlAs or the GaAs vibrations out. These modes, being confined within a smaller number of atomic planes, have their surface response lowered because the oscillator strength is proportional to the number of oscillating dipoles.

On the contrary, the interfacial alloying reduces the confinement of the phonons responsible for the AlAs interface modes simply because the AlAs-like mode of the intermediate material $\text{Al}_{0.5}\text{Ga}_{0.5}\text{As}$ has a frequency close to the interfacial FK phonon [18]. As a consequence, these vibrations can propagate somewhat in the interfacial region and their dielectric response is increased (Fig. 4).

4. Conclusion

We have grown AlAs/GaAs (001) heterostructures by MBE and analyzed the corresponding surface and interface phonon spectra by HREELS in the specular geometry. The spectra were first analyzed by the dielectric theory, which is in excellent agreement with the experiment if the thickness of the AlAs layer exceeds about 4 nm. For thinner layers, the dielectric theory overestimates the GaAs-like interface phonon and the AlAs surface phonon intensities. To check the validity of the macroscopic dielectric theory, lattice-dynamics calculations of the surface response function were performed. These calculations show that the discrepancies between experiment and dielectric theory cannot be explained by the failure of the dielectric theory for small thickness alone. By including some interface roughness in the lattice-dynamics calculations, it is shown that the surface response function is rather sensitive to the details of the interface atomic structure. Microscopic lattice-dynamics calculations are in much better agreement with the experimental results when some cation intermixing is introduced at the interface.

Acknowledgements

This work is supported by the Belgian Fund for Joint Basic Research, and by the Interuniversity Research Projects (PAI/UIA) on “Materials characterization” and “Sciences of interfacial and mesoscopic structures” sponsored by the Belgian Prime Minister’s office (Federal Services for Scientific, Technical and Cultural affairs). R.S. and Ph.L. are supported by the Belgian Fund for Scientific Research (FNRS).

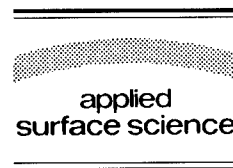
References

- [1] D. Bimberg, D. Mars, J.N. Niller, R. Bauer and D. Oerel, *J. Vac. Sci. Technol. B* 4 (1986) 1014.
- [2] B. Jusserand and M. Cardona, *Light Scattering in Solids V*, Eds. Cardona and G. Güntherodt (Springer, Heidelberg, 1989).
- [3] G. Fasol, M. Tanaka, H. Sakaki and Y. Horokoshi, *Phys. Rev. B* 38 (1988) 6056.
- [4] A. Ourmazd, D.W. Taylor, Cunningham and C.W. Tu, *Phys. Rev. Lett.* 62 (1989) 933.
- [5] A.R. Smith, K.-J. Chao, C.K. Shih, Y.C. Shih and B.G. Streetman, *Appl. Phys. Lett.* 66 (1995) 478, and to be published.
- [6] Ph. Lambin, J.-P. Vigneron, A.A. Lucas, P.A. Thiry, M. Liehr, J.-P. Pireaux, R. Caudano and T.J. Kuech, *Phys. Rev. Lett.* 56 (1986) 1842.
- [7] A.A. Lucas, J.P. Vigneron, Ph. Lambin, P.A. Thiry, M. Liehr, J.J. Pireaux and R. Caudano, *Int. J. Quantum Chem.* 19 (1986) 687.
- [8] J.H. Neave, B.A. Joyce, P.J. Dobson and N. Norton, *Appl. Phys. A* 31 (1983) 1.
- [9] H. Ibach and D.L. Mills, in: *Electron Energy Loss Spectroscopy and Surface Vibrations* (Academic Press, New York, 1982).
- [10] S. Adachi, *J. Appl. Phys.* 58 (1985) S1.
- [11] J.L. Guyaux, Ph. Lambin, M.-D. Lange, R. Sporken, P.A. Thiry and R. Caudano, *Phys. Rev. B*, to be submitted.
- [12] D. Strauch and B. Dorner, *J. Phys.: Condens. Matter* 2 (1990) 1457.
- [13] P. Senet, Ph. Lambin, J.-P. Vigneron, I. Derycke and A.A. Lucas, *Surf. Sci.* 226 (1990) 307; Ph. Lambin, P. Senet and A.A. Lucas, *Phys. Rev. B* 12 (1991) 6416.
- [14] P. Senet, Ph. Lambin and A.A. Lucas, *Phys. Rev. Lett.* 74 (1995).
- [15] S. Baroni, P. Giannozzi and E. Molinari, *Phys. Rev. B* 41 (1990) 3870; B. Jusserand, *Phys. Rev. B* 42 (1990) 7256.
- [16] C. Molteni, L. Colombo, L. Miglio and G. Benedek, *Phys. Rev. B* 50 (1994) 11684.
- [17] B. Jusserand and J. Sapriel, *Phys. Rev. B* 24 (1981) 7194.
- [18] J.-L. Guyaux, P.A. Thiry, Ph. Lambin, R. Sporken and R. Caudano, *Phys. Rev. B* 18 (1993) 4380.



ELSEVIER

Applied Surface Science 104/105 (1996) 608–614



Band structure evolution in InAs overlayers on GaAs(110)

Z.Q. He ^{a,*}, L. Ilver ^a, J. Kanski ^a, P.O. Nilsson ^a, P. Songsiriritthigul ^a, G. Holmén ^a,
U.O. Karlsson ^b

^a Department of Physics, Chalmers University of Technology, S-41296 Göteborg, Sweden

^b Department of Physics, Materials Physics, Royal Institute of Technology, S-10044 Stockholm, Sweden

Received 28 June 1995; accepted 30 August 1995

Abstract

An angle-resolved photoemission study of MBE grown InAs/GaAs(110) hetero-structures was carried out to investigate the establishment of valence bands as a function of overlayer thickness. The valence band spectra were found to change gradually up to thicknesses well above 10 nm. The data are interpreted in terms of excitations within the overlayer from a combination of substrate and overlayer initial states, the former tailing into the overlayer.

1. Introduction

Much effort is focused to the search for semiconductor systems with properties superior to those of presently available materials for particular applications [1]. New and unique properties can be obtained by combining different materials in nanometer scale structures. The key components in such systems are heterointerfaces. Within limits dictated by lattice mismatch and interface chemistry, the structures can be tailored to the designer's particular needs. Progress in this area is closely linked to improvements of growth techniques such as molecular beam epitaxy (MBE). The present state of art allows building of multilayer stacks or microstructures with high purity and ordered structure, controlled on an atomic scale [2].

Superlattices and quantum wells have been utilised for decades. Since the periodicity is usually in the order of tens or hundreds of nanometers, which is essentially longer than the coherence length of the valence electrons, it is not surprising that great success has been achieved without detailed knowledge of the interface electronic states. Structures with shorter range periodicity open the possibility to use materials with relatively large lattice mismatch. InAs/GaAs, with a lattice misfit of 7.16%, is a good example of such a hetero-system [3,4]. This particular combination has attracted increasing attention for its promising prospects in optoelectronic device applications [5–7]. The periodicity is here restricted to at most a few monolayers, which imposes limitations in device construction. For future use of ultra-thin layers, including interfaces with large lattice misfit, extensive investigations of such systems are necessary. So far several studies have been concerned with structural properties, while less attention has been paid to heterointerfacial electronic properties [7].

* Corresponding author. Tel.: +46-31-7723330; fax: +46-31-165176; e-mail: flxhe@fy.chalmers.se.

We present here a valence band and core level photoemission study of InAs/GaAs(110) heterojunction formation. While our main interest is focused on the electronic properties, a necessary point of concern is structural characterisation. This work is also motivated by a fundamental question concerning energy band structure in nanometer scale systems. An obvious consequence of constrained dimensions is energy quantisation, as observed e.g. via optical properties of quantum well structures. Another, less trivial effect relates to the electronic interaction between the different materials in a layered structure. One example of this is the observation of a thickness dependent band gap in α -Sn layers on CdTe(110) [8].

2. Experimental

The experiments were carried out at the Swedish national synchrotron radiation laboratory MAX-lab. At one of the photoelectron beamlines a dedicated molecular beam epitaxy (MBE) system has been attached, allowing in situ growth and analysis. GaAs(110) substrates ($n = 10^{17} \text{ cm}^{-3}$) were obtained by cleaving $0.8 \times 0.8 \text{ cm}^2$ bars in air, cutting them into slices and cleaning with organic solvents. The substrates were In-mounted onto transferable Mo sample holders.

The layers were grown in the MBE chamber, containing six conventional effusion cells, equipment for RHEED and an IR pyrometer. Prior to growth every sample was heated to a temperature of 590°C in a protective As_4 beam to remove the residual oxide on the surface. As a clear 3-D RHEED pattern appeared, the temperature was lowered to 570°C . To obtain an abrupt interface with InAs, an atomic scale flat surface is needed. It was achieved by careful buffer-layer preparation. GaAs homoepitaxy was performed with a As_4 :Ga flux ratio of about 6:1. A few hundred nanometers were grown until good quality 2-D RHEED patterns were observed. As expected, the (110) surface was nonreconstructed, just as a surface prepared by cleaving.

The growth on the GaAs(110) surface was followed by InAs deposition at 400°C . As the optimum growth condition is not available from the literature, the surface phase diagram on (100) surface by New-

stead et al. [9] was used as a reference, and a V/III flux ratio of 4:1 was used for every InAs overlayer growth. The growth front was monitored by RHEED observation and the in-plane lattice parameter was checked by measuring the separation of the integral order streaks of the RHEED patterns. For the first few monolayers, the lattice parameter was kept to the same value as that of the substrate i.e. the epilayers were fully strained. Above this thickness relaxation occurs. Contrary to the behaviour on (100) surface, however, the relaxation is not accompanied by 3D nucleation and surface roughening. For all coverages the surfaces showed good 2D RHEED patterns with streaks in both azimuths, which is a strong evidence for a layer-by-layer growth of the epilayers. This growth has been studied in detail by other groups using transmission electron microscopy and X-ray diffraction [10]. It was concluded that due to the surface geometry asymmetric strain relief is preferred on (110) surface. This is realised via the nucleation of a regular array of Lomer-type dislocations in the $[1\bar{1}0]$ direction and the generation of 60° dislocations in the $[001]$ direction.

As mentioned in the introduction, a well ordered and layered epilayer is desired for this study as disorder or inhomogeneity would be expected to reduce all effects of long range electronic interaction across the interface. InAs/GaAs interfaces are generally believed to be abrupt on an atomic scale [11] and good surface morphology is naturally obtained as a result of the layer by layer growth.

All photoemission measurements were performed in the p-polarisation geometry, at 45° incidence angle. The photoelectron spectra were recorded using an angle resolving, goniometer mounted, hemispherical electrostatic energy analyser with an angle of acceptance of $\pm 2^\circ$, movable in the horizontal and vertical planes. The overall energy resolution was approximately 0.1 eV for core level data and 0.2 eV for valence band data. All spectra presented in this paper were collected in the plane of light incidence. The surface Fermi level position was determined by the photoemission from a clean molybdenum foil in contact with the sample.

The In deposition rate was estimated from measurements of RHEED oscillations. This was realised by subtracting the growth rate of GaInAs (i.e. with both Ga and In sources open) from that of GaAs.

After the spectroscopic analysis all samples were investigated with Rutherford back scattering (RBS) to verify the overlayer thicknesses. Since the RHEED-derived growth rate was obtained from a difference between two nearly equal oscillation frequencies, the RBS values were considered as more reliable ($\sim 5\%$ accuracy). These are the values quoted in the following.

3. Results and discussion

The InAs overlayer formation was studied via core level and valence band spectra, with the goal to investigate at which thickness the overlayer starts to develop bulklike properties. The surface sensitivity of photoemission makes the method well suitable for this purpose. Since the electronic interaction between overlayer and substrate materials is strongest at the very interface, the intrinsic properties of the overlayer material should first show up at the surface.

Fig. 1a shows the In 3d and Ga 3d core levels in a sequence of epilayer thicknesses. The spectra were decomposed by a computer routine assuming equally shaped peaks with fixed spin-orbit splittings. Peak widths (combined Gaussian/Lorentzian shapes), branching ratios and peak positions were treated as fitting parameters. Examples of such fittings are shown in Fig. 1b. For brevity only normal emission spectra are displayed. A Ga surface component is found at $+0.29$ eV relative to the bulk binding energy, and a surface component of In 4d is located at $+0.27$ eV. These values are the same as previously published core level shifts at the (110) surfaces of GaAs [12] and InAs [13]. After the first exposure, we can already observe a bulk In 4d component. According to RBS measurements on this sample the epilayer is about 5 ML thick. We would therefore in principle expect to see three different In components, corresponding to the first (surface), second (sandwiched) and third (interface) atomic layers. The fact that only two components are clearly resolved shows that the local environments at the interface and sand-

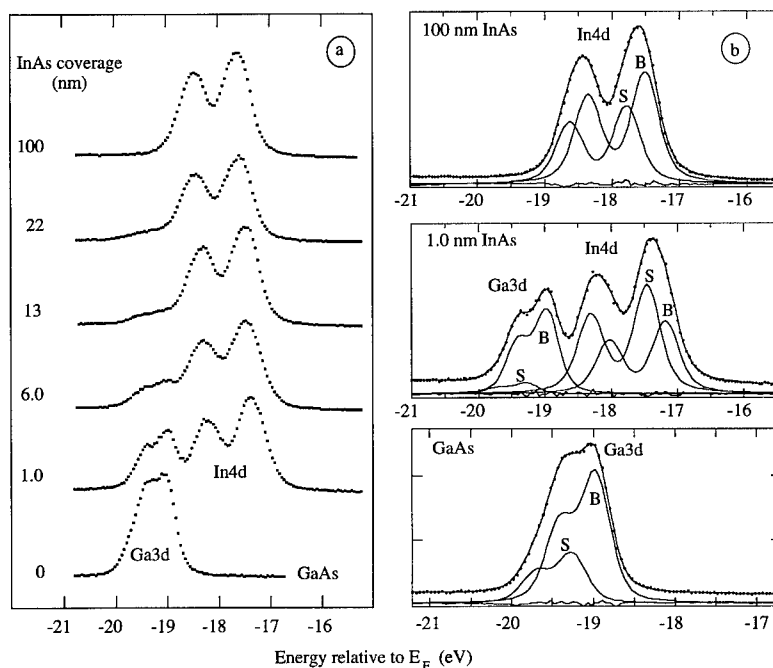


Fig. 1. (a) Ga 3d and In 4d core level spectra from GaAs(110) with InAs epilayers of different thicknesses. (b) Spectral decomposition of the Ga 3d and In 4d emission. The fittings were made with the following parameters: $\Delta E_{\text{Gauss}} = 0.33$ eV, $\Delta E_{\text{Lor}} = 0.15$ eV and $\Delta E_{\text{s-o}} = 0.43$ eV for Ga 3d and $\Delta E_{\text{Gauss}} = 0.33$ eV, $\Delta E_{\text{Lor}} = 0.22$ eV and $\Delta E_{\text{s-o}} = 0.84$ eV for In 4d. The residues presented at the bottom of each panel are drawn on the same scale as the spectra.

wich sites are similar, both being close to bulk InAs. The 'bulk' component increases at further growth until saturated at a thickness of ~ 3 nm where the photoelectron probing depth is reached. Concerning the Ga 3d level we see that after the first exposure a strong peak is still present. From the spectral decomposition shown in Fig. 1b we see that at this stage the Ga 3d emission is bulk related, i.e. mainly due to excitations in the substrate. The surface component is clearly more reduced than the bulk one. Due to the low amplitude its position is difficult to determine with high precision, but according to the fit shown in this figure it appears somewhat closer to the bulk component. The relative size of this new surface component was found to depend on the substrate temperature during the initial growth, and was practically quenched for growth temperatures below 200°C . It is interesting to note that a small Ga signal also exists further up to thick epilayers, well exceeding the photoelectron probing depth. This indicates a slightly more complicated structure than a plain two dimensional InAs overlayer. Since the structural information from RHEED unambiguously shows that the epilayer is two-dimensional, we can rule out that the persistent Ga 3d emission is an effect of overlayer perforation. It is therefore concluded that this surface component must come from Ga atoms within or on top of the epitaxial InAs layer. From available

information about InAs growth on GaAs we know that the interface is abrupt [11], and consequently no interdiffusion of elements takes place across the interface. Therefore, the observed Ga must originate from an exchange process during formation of the first atomic overlayer. By this mechanism there can be at most one monolayer Ga present in the overlayer. Since the Ga signal falls off very slowly with increasing overlayer thickness, we believe that the Ga atoms are mainly located at the surface and are only slowly incorporated in the overlayer (although ternary GaInAs compounds are stable over the whole composition range). From the relative intensities of the core level signals we conclude that the amount Ga is $\sim 10\%$ of a monolayer. This small quantity of 'floating' material is assumed not to have any significant influence on the bulk electronic properties of the heterostructure, and is in any case not influencing the final conclusions of this work. Actually this kind of species-floating phenomenon is rather common in heterostructure growth [14]. Information about the spatial distribution of a particular element is in principle also contained in the core level data via their angular dependence and presence of (surface) shifted components. In our case, the evaluation of the Ga spectral shape is rather difficult as it appears as a small shoulder on the nearby strong In 4d peak. It is clear, however, that the intensity of the Ga signal

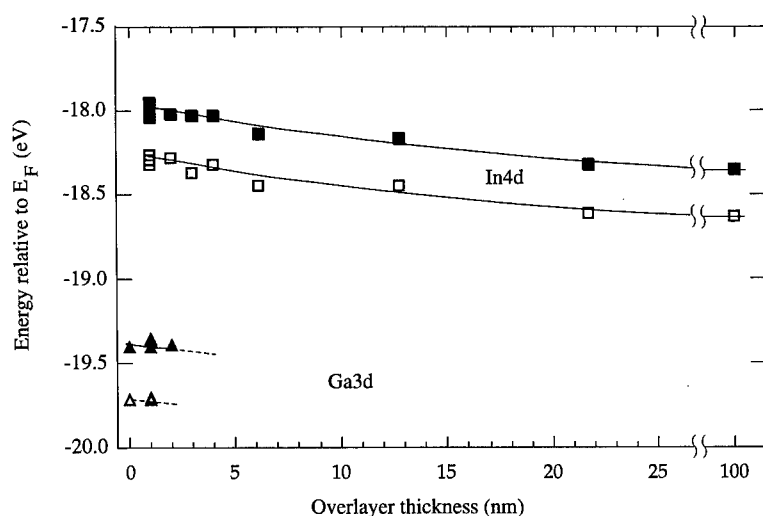


Fig. 2. Ga $3d_{5/2}$ and In $4d_{5/2}$ positions as function of overlayer thickness. The open symbols represent the positions of surface shifted components.

does not change very much over a thickness range of nanometers. Another factor which complicates quantitative analysis of these core level intensities is strong photoelectron diffraction reported in several studies of InAs [13]. In Fig. 1 this effect is manifested by a lower intensity of the surface In 4d component in the spectrum recorded at 60° emission angle than at normal emission. This observation by itself shows that the pseudomorphic overlayer is highly ordered.

Changes in the surface Fermi level pinning were determined precisely using the strong In 4d emission. In Fig. 2 the In 4d and Ga 3d peak positions relative to the surface Fermi level are plotted as a function of epilayer thickness. The In 4d peak starts at 18.0 eV below E_F and falls gradually with increased epilayer thickness. The total observed shift is 0.35 eV and at high coverages the pinning is in fact above the conduction band minimum. This was directly observed as a small photoemission peak above the valence band maximum (not shown here). Such emission has been previously reported from various InAs surfaces [15], and is considered to reflect the presence of a quasi-two-dimensional electron gas, which extends ~ 15 nm into the crystal. It is significant to note that the electron gas found in the present experiment is only developed in epilayers thicker than ~ 10 nm. Factors which determine the bulk core level position in the surface region are band bending and interface dipole. The interface dipole is usually considered to be established during the initial stage of interface formation. Assuming that the surface conditions are equivalent throughout the series, i.e. that the above discussed Ga has no effect on the surface Fermi level pinning, our observations would suggest that the bulk properties are not fully developed until a thickness of ~ 20 nm.

A more direct test of these overlayer properties is obtained from the valence band data. Fig. 3 shows normal emission valence band spectra for the same series of InAs epilayers as in Fig. 1. Due to the delocalised nature of the electronic states involved, interpretation of this type of data is more complicated than for core level spectra. It is thus not possible here to define the spatial location of the excitation sites. For thick heterojunctions one could divide the space into four regions, namely the two bulk regions and the two interface regions at each

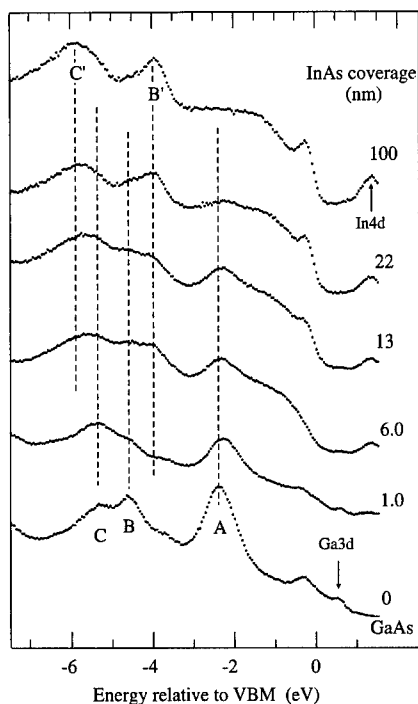


Fig. 3. Normal emission valence band spectra from clean GaAs(110) and after growth of InAs epilayers of varying thickness. The spectra were excited with 19 eV photons. The labelled peaks are interpreted as excitations involving bulk states of GaAs and InAs.

side of the interface. From the electronic point of view each of these regions extends over a range defined by the electron coherence length. What makes the present situation particularly complicated is the fact that the overlayer dimensions are of the same size as the coherence length.

The structures labelled A, B and C in the spectrum of clean GaAs in Fig. 3 are interpreted as bulk interband excitations. Just above the valence band maximum a shoulder-like structure can be observed, originating from the Ga 3d level which is excited in second order. The photon energy chosen in this case allows thus simultaneous registration of the intensity of a state localised in the substrate and states which are delocalised. Furthermore, at this photon energy the bulk states that are probed in normal emission are located near the K-point of the bulk Brillouin zone. This is the reason for the relatively high intensity of peak A in the spectrum of clean GaAs. Another reason for concentrating on data recorded at

this photon energy and normal emission is that under these conditions the spectrum from clean GaAs is distinctly different from that of InAs.

After growth of 1.0 nm InAs, which corresponds to ~ 5 ML the RHEED pattern shows that the overlayer is almost fully relaxed. In the valence band spectrum (Fig. 3) we note that all features are attenuated. This is a rather expected result considering that the thickness at this point is about the same as the mean free path. The presence of the Ga 3d structure shows that the overlayer is transparent for electrons excited on the substrate side of the interface. No obvious overlayer related structures are seen in this spectrum. Spectra recorded at other photon energies show more pronounced overlayer induced spectral changes at this coverage. The effects that we are interested in here are, however, most readily observed in spectra excited with 19 eV photons.

Turning to thicker epilayers, we observe that the Ga 3d emission is gradually reduced and is hardly detectable in the 6 nm spectrum. The residual Ga signal discussed in connection with Fig. 1 is not seen here, due to a relatively smaller Ga 3d/In 4d excitation cross section at 19 eV photon energy [16]. More significant for the present discussion is the attenuation of Ga 3d intensity from its initial value for the clean GaAs surface. In relation to this we can consider the Ga 3d emission as completely quenched in spectra with epilayers exceeding 10 nm thickness. In the valence band we can follow one clear development, namely the appearance and growth of a structure labelled B'. Glancing at the spectrum from the 100 nm epilayer it is clear that this structure is related to bulk electronic states in InAs. More specifically, it reflects an interband excitation of the third valence band. Looking back at spectra from thinner layers we note that this feature is practically absent in the 1 nm epilayer spectrum and that even at ~ 10 nm thickness it is not fully developed. The last observation gives further support for a two-dimensional growth mode, as already concluded from RHEED observations, since any tendency to island formation should at this stage result in three-dimensional particles.

Parallel with this development we see that the GaAs-specific interband excitations are attenuated. Despite this, they can still be observed at large InAs coverages. The attenuation of the GaAs-specific ex-

citations occurs over a similar thickness range as the development of InAs structures. The interband excitation A is discernible even in the 22 nm spectrum. As already pointed out, emission from the localised Ga 3d state is completely quenched at this stage. We can thus rule out the possibility that these interband excitations occur within the GaAs substrate. It must then be concluded that the GaAs bulk states which are observed in our spectra are present within the InAs epilayer. In other words, the corresponding GaAs wave functions must tail into the overlayer material over distances as large as 10–20 nm. It should be stressed that this conclusion is only based on the presence of a continuous two-dimensional overlayer, and does not depend on overlayer properties like strain or surface structure.

At this point it deserves repeating that each of the spectra presented here was obtained from a new epilayer grown under the same conditions on a new substrate. With modified growth parameters, e.g. a less well-ordered initial surface or reduced growth temperature, the substrate related valence band structures were reduced faster. The corresponding LEED and RHEED patterns were significantly broadened, although clear 1×1 surface periodicity could still be observed. These observations suggest that the long-range tailing proposed here depends critically on the interface quality.

Investigations of photon energy and angular dependence of these substrate related structures show clearly that they represent direct (momentum conserving) excitations. This can only be explained if both initial and final states probed in this case are of similar nature in the substrate and overlayer. In other words the data suggest that the wave vectors of the decaying states are preserved. A detailed interpretation of the present data must, however, be based on a thorough analysis of the electronic structure in a composite system like InAs/GaAs.

4. Conclusion

The photoemission results discussed here show that valence states at the InAs/GaAs(110) interface may tail across the interface over distances of ~ 10 nm. The extent of this tailing appears to depend on the interface quality. With a well ordered structure it

seems that true bulk properties in the overlayers develop only at thicknesses exceeding this distance. This result has significant implications for the understanding of electronic properties of heterojunctions, e.g. band offsets.

Acknowledgements

We wish to thank the MAX-lab staff for all technical support. Grants from the Swedish Natural Science Research Council are gratefully acknowledged. One of the authors (Z.Q.H.) is indebted to the Swedish Institute for financial supports and would also like to thank S.M. Wang for valuable discussions.

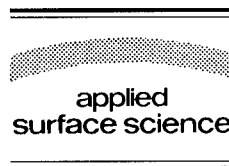
References

- [1] K. Adomi, J.I. Chyi, S.F. Fang, T.C. Shen, S. Strite and H. Morkoc, *Thin Solid Films* 205 (1991) 182.
- [2] K. Ploog, *Angew. Chem. Int. Ed. Engl.* 27 (1988) 593.
- [3] O. Brandt, K. Ploog, L. Tapfer, M. Hohenstein, R. Bierwolf and F. Phillipp, *Phys. Rev. B* 45 (1992) 8443.
- [4] M. Ilg, M.I. Alonso, A. Lehmann, K.H. Ploog and M. Hohenstein, *J. Appl. Phys.* 74 (1993) 7188.
- [5] S.D. Benjamin, T. Zhang, Y.L. Hwang, M.S. Mytych and R.M. Kolbas, *Appl. Phys. Lett.* 60 (1992) 1800.
- [6] M.L. Dotor, P. Huertas, J. Melendez, A. Mazuelas, M. Garriga, D. Golmayo and F. Briones, *Electron. Lett.* 28 (1992) 997.
- [7] H. Toyoshima, K. Onda, E. Mizuki, N. Samoto, M. Kuzuhara, T. Itoh, T. Anan and T. Ichibashi, *J. Appl. Phys.* 69 (1991) 3941.
- [8] L.-W. Tu, G.K. Wong and J.B. Ketterson, *Appl. Phys. Lett.* 55 (1989) 1327.
- [9] S.M. Newstead, R.A.A. Kubiak and E.H.C. Parker, *J. Cryst. Growth* 81 (1987) 49.
- [10] X. Zhang, D.W. Pashley, J.H. Neave, P.N. Fawcett, J. Zhang and B.A. Joyce, *J. Cryst. Growth* 132 (1993) 331.
- [11] J.M. Moison, C. Guille, F. Houzay, F. Barthe and M. Van Rompay, *Phys. Rev. B* 40 (1989) 6149.
- [12] W. Ranke, J. Finster and H.J. Kuhr, *Surf. Sci.* 187 (1987) 112.
- [13] J.N. Andersen and U.O. Karlsson, *Phys. Rev. B* 41 (1990) 3844.
- [14] K. Horn, *Appl. Phys. A* 51 (1990) 289.
- [15] C.B.M. Andersson, U.O. Karlsson, L. Ilver, J. Kanski, P.O. Nilsson, L.Ö. Olsson and M.C. Håkansson, in: *Proc. 22nd Int. Conf. on the Physics of Semiconductors, Vancouver, 1994*, Ed. D.J. Lockwood (World Scientific, Singapore, 1995) p. 489.
- [16] J.J. Yeh and I. Lindau, *At. Data Nucl. Data Tables* 32 (1985) 1.



ELSEVIER

Applied Surface Science 104/105 (1996) 615–620



Measurements of the energy band offsets of $\text{Si}_{1-x}\text{Ge}_x/\text{Si}$ and $\text{Ge}_{1-y}\text{C}_y/\text{Ge}$ heterojunctions

F. Chen^{a,*}, M.M. Waite^b, S. Ismat. Shah^c, B.A. Orner^a, S.S. Iyer^d, J. Kolodzey^a

^a Electrical Engineering Department, 140 Evans Hall, University of Delaware, Newark, DE 19716, USA

^b Physics Department, University of Delaware, Newark, DE 19716, USA

^c E.I. Du Pont De Nemours & Company Inc., Wilmington, DE 19880, USA

^d Sibond LLC Inc., Hopewell Junction, NY 12533, USA

Received 28 June 1995; accepted 6 October 1995

Abstract

Discontinuities in the energies of the conduction and valence bands at semiconductor heterojunctions are important parameters for device design. We describe experiments using X-ray photoelectron spectroscopy with measurements of valence-band energies with respect to core-levels of metastable, coherently strained $\text{Si}_{1-x}\text{Ge}_x$ alloy layers and of thick $\text{Ge}_{1-y}\text{C}_y$ alloy layers. For strained $\text{Si}_{1-x}\text{Ge}_x$ alloys on Si, we have found that the valence band offset increased with the Ge fraction x with most of the offset in the valence band. We obtained a valence band offset of 0.22 eV for $x = 0.23$, in good agreement with theoretical calculations. For $\text{Ge}_{1-y}\text{C}_y$ alloys, we found very little shift in the valence band energies with the C fraction y . Since the optical bandgap of GeC increased with the C fraction y , most of the offset for $\text{Ge}_{1-y}\text{C}_y/\text{Ge}$ heterojunction was in the conduction band. Based on the measurements of the energy band offsets of $\text{Si}_{1-x}\text{Ge}_x/\text{Si}$, we infer that the major portion of bandgap discontinuity of $\text{Ge}_{1-y}\text{C}_y$ on Si is in the valence band. $\text{Ge}_{1-y}\text{C}_y$ alloys are new metastable materials that open up a new region for group IV heterostructures.

Knowledge of the band offsets at heterointerfaces is important for assessing the degree of carrier confinement, and therefore is important for high-speed optoelectronic device operation. Many theories have reported calculations of valence-band offsets at heterojunctions. For examples, Tersoff [1] and Cardona and Christensen [2] calculated semiconductor band offsets using interface dipole theory and dielectric midgap energy theory, respectively. Frensley and

Kroemer [3] proposed a pseudopotential model to predict the semiconductor band offsets. For certain heterojunction systems, the above theories yield fairly different results.

Several experimental techniques have been studied during the last few years for the quantitative determination of semiconductor band offsets at heterojunctions [4–6]. Among them, X-ray photoelectron spectroscopy (XPS) of the atomic core-levels represents the most reliable method for obtaining valence-band offsets (ΔE_v) [7]. The valence band energies can be measured with respect to deep atomic core levels which are relatively unaffected by the heterointerface. If the bandgap E_g is known, the

* Corresponding author. Tel.: +1-302-8318959; fax: +1-302-8314316; e-mail: fchen@ee.udel.edu.

conduction band offsets can also be determined, and thus whole band structure will be clear.

In this paper, we present and discuss the results of an XPS investigation of $\text{Si}_{1-x}\text{Ge}_x/\text{Si}$ and $\text{Ge}_{1-y}\text{C}_y/\text{Ge}$ heterojunction valence-band offsets (VBO) by using metastable, coherently strained $\text{Si}_{1-x}\text{Ge}_x$ alloys on Si and thick $\text{Ge}_{1-y}\text{C}_y$ alloys on Si. The $\text{Si}_{1-x}\text{Ge}_x/\text{Si}$ system is well-known and there are many theoretical and experimental results regarding to its valence-band offsets. We compared our measurements of $\text{Si}_{1-x}\text{Ge}_x/\text{Si}$ to published data to check our XPS data analysis method which was proposed by Shih and Spicer [8]. Our interest was to find the band energies at the heterointerface of $\text{Ge}_{1-y}\text{C}_y$ and Ge with respect to Si by measuring the band energy position using thick $\text{Ge}_{1-y}\text{C}_y$ and Ge layers. $\text{Ge}_{1-y}\text{C}_y$ alloys are a novel material system for the physics and device of group IV semiconductors [9]. In principle, it can be lattice matched to Si substrates by adjusting the composition. Its optical bandgap (E_g) depends on the C fraction y [10].

In order to avoid the demands posed by XPS core-level spectroscopy such as preparing good interface quality samples and ensuring negligible band bending over the portion of the sample probed, we followed the potentially simplified method proposed by Shih and Spicer [8]. They postulated that the core-level positions were approximately independent of alloy composition, thus they substituted bulk samples for the actual interface to study valence-band offsets. They tested their method by deducing the VBO in the $\text{HgTe}-\text{CdTe}$ system and obtained an accurate lineup. This approach was also studied in a theoretical analysis by Wei and Zunger [11] with good results. By using this technique, we can easily determine the band offsets without performing a measurement located precisely at the heterointerface.

In our study, we used the Si_{2p} core-level as a reference level for the $\text{Si}_{1-x}\text{Ge}_x/\text{Si}$ system, and the Ge_{3d} core-level for the $\text{Ge}_{1-y}\text{C}_y/\text{Ge}$ system. Before any heterostructure data analysis, we first estimated the core-level shifts due to the alloy composition, and justified the approximation of core-level constancy.

Strict and consistent calculation of core-level shifts due to the alloy composition requires using a Born-Haber cycle calculation which is used to relate binding-energy shifts to changes of bond energies due to

the excitation of core electrons [12]. However, Morar et al. used a model based on linear-response theory [13] to estimate the shift of the Si_{2p} core-level energy in $\text{Si}_{1-x}\text{Ge}_x$ alloys due to different Ge composition. They found that for strain-free $\text{Si}_{1-x}\text{Ge}_x$ alloys with $x \leq 0.3$, the maximum Si_{2p} core-level shift was ~ 15 meV. We used the same approach to estimate the Ge_{3d} core-level shift of $\text{Ge}_{1-y}\text{C}_y$ alloys due to adding small amount of carbon. Energetic shifts in the core levels are interpreted in terms of changes in the total valence charge surrounding each atom. They can be directly associated with the electronegativity and ionicity. The hydrostatic component of strain can also cause core-level shifts. Because the strain configuration depends on details of the growth conditions for the different samples, we can determine the band offsets without these strain effects first, and then add the tetragonal distortion caused by strain for the particular sample later if strain is present. Thus the total core-level shift ΔE_{core} can be written as:

$$\Delta E_{\text{core}} = n_C \Delta,$$

$$\Delta = \Delta_d + (r_{\text{GeC}} - r_{\text{Ge bulk}}) \frac{dE_{\text{CL}}}{dr} = \Delta_r + \Delta_d,$$

and where n_C is the number of C neighbors of each Ge atom, Δ_d is the electronic shift of the core-level corresponding to the dielectric response to a first-order local perturbation, r_{GeC} is the bond length for $\text{Ge}_{1-y}\text{C}_y$ alloys, and $r_{\text{Ge bulk}}$ is the bulk Ge covalent bond length. Δ_r is the core-level shift associated with the atomic displacement. With consisting of a superposition of spherical atomic density [14], we obtained $\Delta_d \sim -83.45$ meV and $dE_{\text{CL}}/dr \sim 630$ meV/Å, giving $\Delta \sim 225$ meV. The total core-level shift for $\text{Ge}_{1-y}\text{C}_y$ is $4y\Delta$. For a small amount of C (1–3% for our SGC samples), the maximum shift is ~ 27 meV. Therefore we conclude that the core-level is approximately constant for our GeC alloys to within ± 27 meV.

Two groups of molecular beam epitaxy grown samples were used for this study. The first was metastable strained $\text{Si}_{1-x}\text{Ge}_x$ alloys on Si substrates, and the second was thick $\text{Ge}_{1-y}\text{C}_y$ alloys on Si substrates. The $\text{Si}_{1-x}\text{Ge}_x$ samples were grown in a VG-80 solid source MBE system using e-beam evaporation for Si and a thermal effusion cell for Ge. The

$\text{Ge}_{1-y}\text{C}_y$ alloys were grown by solid source in an EPI 620 MBE system. The base pressure of the GeC growth chamber was below 5×10^{-11} Torr, and growth pressures were typically near 5×10^{-9} Torr [10]. The Ge beam was produced by thermal evaporation from a solid polycrystalline Ge source in a pyrolytic boron nitride crucible, and the C beam was produced by sublimation from a pyrolytic graphite filament carbon source. The substrates used in the $\text{Ge}_{1-y}\text{C}_y$ experiments were p-type (100) Si wafers ($\rho = 13\text{--}17 \Omega \text{ cm}$) that had been chemically cleaned before being inserted into the vacuum chamber. Details of growth conditions are given in [10]. The substrate temperature during the film growth was 570°C .

XPS measurements were performed using an SSX-100 spectrometer with a monochromatic Al K α X-ray source ($h\nu = 1487 \text{ eV}$). The background base pressure for the analysis chamber was $T = 10^{-9}$ Torr. Because of exposure to air, samples were sputtered with Ar^+ ions of energy 2 keV for 30 min to remove surface oxidation.

We determined the absolute valence band maximum (VBM) position by finding the relative difference between the VBM and the core-level in each material. We decided not to fit theoretically calcu-

lated density of valence-band energy distribution states to the complete XPS spectrum since the calculated theoretical critical points of the density of states of GeC are not yet well known. Near the valence-band maximum, the density of states varies as the square root of energy. Assuming that Vegard's law is valid for the interpolation of alloy hole effective masses of the endpoint compositions near the VBM, we can compare the VBM of these alloys accurately after dividing out the characteristic hole effective mass. The inset in Fig. 1 and Fig. 2 shows the measured alignment of the VBM for $\text{Si}_{1-x}\text{Ge}_x$ and $\text{Ge}_{1-y}\text{C}_y$ samples respectively. For $\text{Si}_{1-x}\text{Ge}_x$ alloys, we compare the VBM of metastable, coherently strained $\text{Si}_{0.92}\text{Ge}_{0.08}$ and $\text{Si}_{0.77}\text{Ge}_{0.23}$ alloy layers with the VBM of bulk Si substrate. For $\text{Ge}_{1-y}\text{C}_y$ alloys, we compare the VBM of thick $\text{Ge}_{0.984}\text{C}_{0.016}$ and $\text{Ge}_{0.968}\text{C}_{0.032}$ alloy layers with the VBM of a thick pure Ge layer. The core-level energy positions were defined as the center of the peak width at half of the peak maximum height. After alignment of the adjusted valence band edges of these materials, the relative positions of the core-level binding energies referred to the VBM can be determined very precisely to within 30 meV (systematic errors can be canceled) [8]. This change reflects the movement of

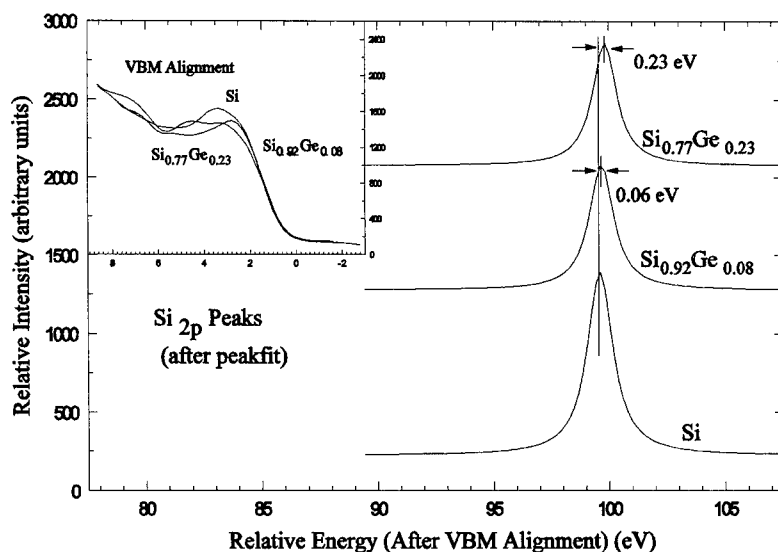


Fig. 1. The Si_{2p} core-level of Si, $\text{Si}_{0.92}\text{Ge}_{0.08}$, and $\text{Si}_{0.77}\text{Ge}_{0.23}$ with the valence band maximum (VBM) taken as zero binding energy. Inset: Alignment of the VBMs by shifting energy scales after counting the effects of characteristic hole effective mass for each material. Energy shifts near peaks are the VBO with respect to Si.

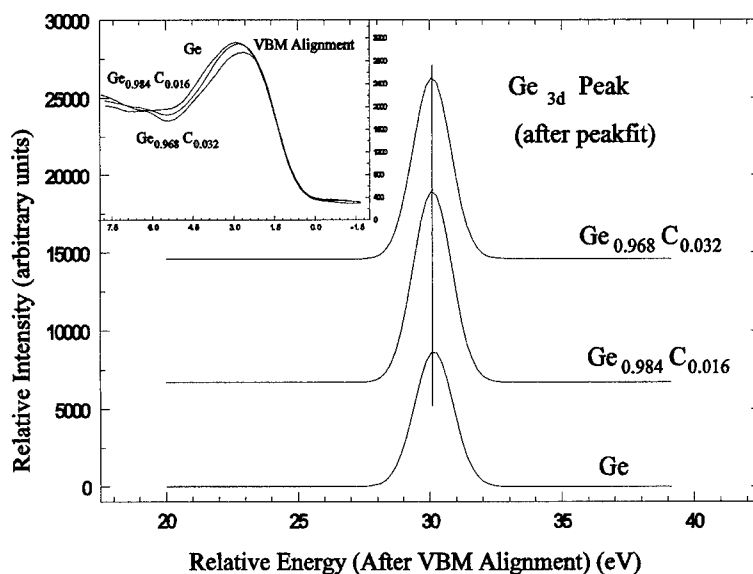


Fig. 2. The Ge_{3d} core-level of Ge, Ge_{0.984}C_{0.016}, and Ge_{0.968}C_{0.032} with the valence-band maximum (VBM) taken as zero binding energy. Inset: Alignment of the VBMs by shifting energy scales after counting the effects of characteristic hole effective mass for each material. No VBO was found for Ge_{1-y}C_y on Ge.

the VBM with alloy composition if we neglect the contribution from core-level shift, thus the VBO can be deduced. Results for VBO of SiGe/Si and GeC/Ge system of different alloy composition can be read directly from Fig. 1 and Fig. 2. Fig. 3 shows our VB offset results for Si_{1-x}Ge_x/Si system compared with the theoretical prediction of $\Delta E_v = 740x$ meV where x is the Ge fraction [15] and with

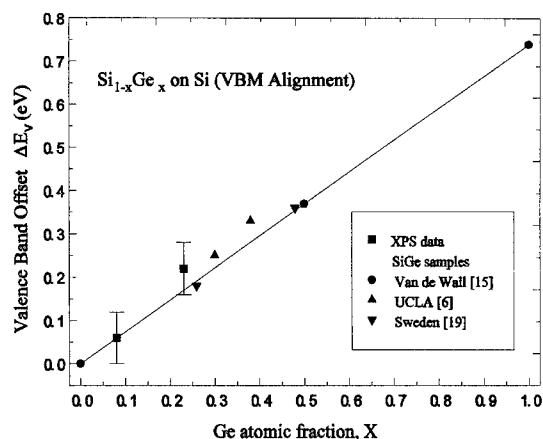


Fig. 3. Valence band offsets in strained Si_{1-x}Ge_x on Si substrate heterostructures: the solid line indicates theoretical prediction of $0.74x$ eV.

experimental data done by different research groups using various techniques. On the other hand, our results of VB offsets for Ge_{1-y}C_y/Ge indicated that there was almost no valence band discontinuity between Ge_{1-y}C_y as the C fraction varied from 0.01 to 0.03. This was surprising at first, but, using the diamond bandgap of 5.45 eV [16,17], and by applying the electron-affinity Anderson–Shockley model to Ge/C, we note that Ge and C indeed lineup across the heterointerface theoretically. This prediction was consistent with our XPS results and with measurements by other groups [18]. Fourier transform infrared spectroscopy (FTIR) optical absorption data showed that the optical bandgap of the Ge_{1-y}C_y alloys varied linearly with composition throughout the composition range investigated [10]. For $y = 0.032$ (SGC32), the bandgap E_g increased by 250 meV with respect to the bulk Ge bandgap. Combining the results from XPS and FTIR, the conduction band alignment of unstrained Ge_{1-y}C_y and Ge heterojunction was determined. Fig. 4 shows the whole band structure of GeC/Ge heterojunction system. As previously, the core-level shifting was assumed to be zero in this picture. Combining the results of band alignment for Ge/Si and Ge_{1-y}C_y/Ge gives the alignment of Ge_{1-y}C_y on Si which is also shown in

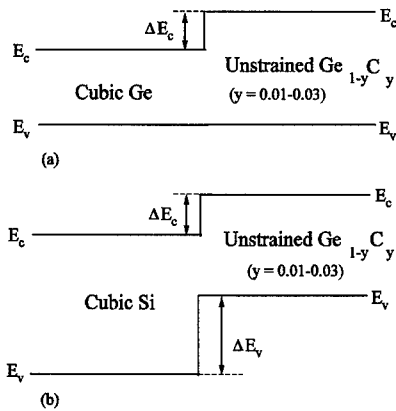


Fig. 4. Flat-band diagram showing the bandgap alignment for (a) thick $\text{Ge}_{1-y}\text{C}_y$ on Ge, and (b) thick $\text{Ge}_{1-y}\text{C}_y$ on Si. The major portion of bandgap discontinuity of $\text{Ge}_{1-y}\text{C}_y/\text{Ge}$ system is in the conduction band, whereas the major discontinuity of $\text{Ge}_{1-y}\text{C}_y/\text{Si}$ is in the valence band. Numerical values of the offsets for our samples are given in Table 1 and Table 2.

Fig. 4. If we count the core-level shifting calculated previously, the precision of the results of this study is ± 60 meV.

In conclusion, we used the XPS method and a data analysis approach proposed by Shih and Spicer to deduce energy band lineups in $\text{Si}_{1-x}\text{Ge}_x/\text{Si}$ and $\text{Ge}_{1-y}\text{C}_y/\text{Ge}$ systems. Convenient core levels (Si_{2p} and Ge_{3d}) serve as reference levels. The results obtained for $\text{Si}_{1-x}\text{Ge}_x/\text{Si}$ are in good agreement with pseudopotential calculations [3], and experimental data. The $\text{Ge}_{1-y}\text{C}_y/\text{Ge}$ VB offsets are approximately constant for C fractions y between 0.01 and 0.03. The optical bandgap increases with C fraction y , implying that the major portion of bandgap discontinuity of $\text{Ge}_{1-y}\text{C}_y/\text{Ge}$ system is in the conduction band. So it has type III (one band continuous) band-edge lineups. Combining the results of band alignment for $\text{Si}_{1-x}\text{Ge}_x/\text{Si}$ and $\text{Ge}_{1-y}\text{C}_y/\text{Ge}$, we infer that the major portion of bandgap discontinuity

Table 2

Sample properties and valence-band offsets for $\text{Ge}_{1-y}\text{C}_y$

Sample i.d.	C atomic fraction	Thickness (Å)	Measured ΔE_v (meV)
SGC10	0	6240	—
SGC30	0.016	4300	10 ± 60
SGC32	0.032	3500	20 ± 60

of $\text{Ge}_{1-y}\text{C}_y/\text{Si}$ is in the valence band and it has type II (staggered) band-edge lineups. Our measurements are the first experimental determination of VB offsets for $\text{Ge}_{1-y}\text{C}_y/\text{Ge}$ systems. The $\text{Ge}_{1-y}\text{C}_y/\text{Ge}$ and $\text{Ge}_{1-y}\text{C}_y/\text{Si}$ heterostructures have high potential for carriers confinement on band-engineered devices.

Acknowledgements

This work was supported by grants from the AFOSR (AFOSR-91-0370), AASERT (AASERT-F49620-92-J-0340), the ONR (N00014-93-1-0393), and from W.L. Gore & Associates.

References

- [1] J. Tersoff, Phys. Rev. B 30 (1984) 4874.
- [2] M. Cardona and N.E. Christensen, J. Vac. Sci. Technol. B 5 (1987) 1285.
- [3] W.R. Frensley and H. Kroemer, Phys. Rev. B 16 (1977) 2642.
- [4] R.W. Grant, J.R. Woldrop and E.A. Kraut, Phys. Rev. Lett. 40 (1978) 656.
- [5] G. Margaritondo, N.G. Stoffel, A.D. Katnani and F. Patella, Solid State Commun. 36 (1980) 215.
- [6] S. Khorram, C.H. Chern and K.L. Wang, Mater. Res. Soc. Symp. 220 (1991).
- [7] H. Kroemer, Surf. Sci. 132 (1983) 543.
- [8] C.K. Shih and W.E. Spicer, Phys. Rev. Lett. 58 (1987) 2594.
- [9] J. Kolodzey, S. Zhang, P. O'Neil, E. Hall, R. McAnnally and C.P. Swann, in: Proc. Int. Conf. on Silicon Carbide and Related Materials, Washington, DC, 1993, Inst. Phys. Conf. Ser., No. 137 (1993) ch. 3, p. 357.
- [10] J. Kolodzey, P.A. O'Neil, S. Zhang, B. Orner, K. Roe, C.P. Swann, K.M. Unruh, M.M. Waite and S. Ismat Shah, Appl. Phys. Lett. 67 (1995) 1865.
- [11] S. Wei and A. Zunger, Phys. Rev. Lett. 59 (1987) 144.

Table 1

Sample properties and valence-band offsets for $\text{Si}_{1-x}\text{Ge}_x$

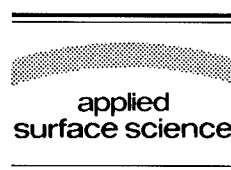
Sample i.d.	Ge atomic fraction	Thickness (Å)	Measured ΔE_v (meV)	Theoretical calculation (meV)
IBM27	0.08	2075	60 ± 60	59
IBM28	0.23	915	220 ± 60	170

- [12] R. Enderlein and W.A. Harrison, *Phys. Rev. B* 30 (1984) 1867.
- [13] J.F. Morar, P.E. Batson and J. Tersoff, *Phys. Rev. B* 47 (1993) 4107.
- [14] C.G. Van de Walle and R.M. Martin, *Phys. Rev. B* 34 (1986) 8.
- [15] C.G. Van de Walle and R.M. Martin, *Phys. Rev. B* 34 (1986) 5621.
- [16] F.J. Himpsel, J.A. Knapp, J.A. Van Vechten and D.E. Eastman, *Phys. Rev. B* 20 (1979) 624.
- [17] B.B. Pate, *Surf. Sci.* 165 (1986) 83.
- [18] K. Rim, S. Takagi, J.J. Welser, J.L. Hoyt and J.F. Gibbons, *Mater. Res. Soc. Symp. Proc.*, Spring Meeting, 1995.
- [19] W.X. Ni, J. Knall and G.V. Hansson, *Phys. Rev. B* 36 (1987) 7744.



ELSEVIER

Applied Surface Science 104/105 (1996) 621–625



The conduction barrier at the interface between low temperature grown GaAs and undoped GaAs

K.D. Maranowski^{a,*}, J.P. Ibbetson^b, K.L. Campman^a, A.C. Gossard^{a,b}

^a Department of Electrical and Computer Engineering, University of California at Santa Barbara, Santa Barbara, CA 93106, USA

^b Materials Department, University of California at Santa Barbara, Santa Barbara, CA 93106, USA

Received 28 June 1995; accepted 4 December 1995

Abstract

We have examined current transport across the interface between low temperature grown (LTG) GaAs and GaAs grown at normal temperatures, both n^+ -doped and undoped. The two types of interface, LTG GaAs/ n^+ GaAs and LTG GaAs/undoped GaAs, exhibit ohmic and rectifying behavior, respectively. In the ohmic case, electrons can easily tunnel from the defect hopping band of the LTG GaAs, in which the Fermi level is pinned, into the conduction band of the n^+ GaAs-layer. In the second case, the interface acts like a Schottky barrier since electrons must be thermally emitted from the defect hopping band of the LTG GaAs up into the conduction band of the undoped GaAs. By fitting the temperature dependence of the current–voltage relationship using thermionic emission theory, we obtain a simple, direct measure of the Fermi level depth in the LTG GaAs.

1. Introduction

As studies of low temperature grown GaAs (LTG GaAs) move toward device applications, it becomes necessary to understand the electronic properties of the interface between LTG GaAs and normal temperature grown GaAs. In this paper, we use current–voltage measurements at varying temperatures to investigate transport across the interface between LTG GaAs and both undoped GaAs and n^+ GaAs grown at normal ($\sim 600^\circ\text{C}$) growth temperatures.

The growth of GaAs at low temperature ($\sim 200^\circ\text{C}$) leads to the incorporation of ~ 1 –2% excess As [1].

This non-stoichiometry is manifested as high concentrations of defects, specifically As anti-sites (As_{Ga}), Ga vacancies (V_{Ga}), and As interstitials (As_i). The high concentration ($\sim 3 \times 10^{19} \text{ cm}^{-3}$) of As_{Ga} anti-sites gives rise to a dense deep donor band [2]. Look et al. [3] have shown that, for anneal temperatures up to 600°C , hopping conduction through this deep donor band is the dominant conduction process through the LTG GaAs. The Fermi level in the LTG GaAs is pinned in the donor band as the donor levels are partially compensated by $\sim 10^{19} \text{ cm}^{-3}$ deep acceptors (believed to be V_{Ga}) [1]. For higher annealing temperatures ($> 600^\circ\text{C}$), hopping conductivity is reduced by several orders of magnitude and the LTG GaAs becomes highly resistive [3].

The potential for high resistivity in annealed LTG GaAs has led to its application as an insulating layer in metal–insulator–semiconductor field effect tran-

* Corresponding author. Tel.: +1-805-8938154; fax: +1-805-8933262; e-mail: 6500kdm@ucsbuxa.ucsb.edu.

sistors (MISFETs) [4–6] as well as a barrier layer between a back gate and two-dimensional electron gas (2DEG) [7]. In the second case, it was found that the leakage current between the back gate and the 2DEG was limited by the *interface* between LTG GaAs and undoped GaAs rather than the LTG GaAs itself. Here, we have studied the transport across the interface in order to measure directly the Fermi level pinning depth in the LTG GaAs.

2. Experimental

All samples were grown by molecular beam epitaxy in a Varian modular Gen II system. In all cases, the low temperature growth was performed under an As_2 over pressure at 225°C as measured by the substrate thermocouple (since pyrometry is not possible at such a low temperature). Also, all samples were grown on semi-insulating GaAs substrates. The first sample, sample A, contained a 5000 Å heavily Si-doped ($\sim 5 \times 10^{18} \text{ cm}^{-3}$) n^+ back contact. (The Si shutter was closed for the final 20 Å of this layer in order to incorporate any Si diffusing to the surface before the low temperature growth.) Then the substrate temperature was ramped down to 225°C and a 1000 Å LTG GaAs-layer was grown. The second sample, sample B, was identical to sample A except that the n^+ -layer was separated from the LTG GaAs-layer by a 1500 Å undoped GaAs-layer. The growth structures and temperatures are shown in Fig. 1.

To investigate the LTG/normal interface for LTG $\text{Al}_x\text{Ga}_{1-x}\text{As}$, we grew two more samples, C and D. The structure for these samples is as follows: 5000 Å heavily Si-doped ($\sim 5 \times 10^{18} \text{ cm}^{-3}$) n^+ back contact, a 1500 Å linearly graded layer (using the digital alloy technique [8] with a period of 20 Å) from $x = 0$ (GaAs) to $\text{Al}_x\text{Ga}_{1-x}\text{As}$, a 1000 Å LTG $\text{Al}_x\text{Ga}_{1-x}\text{As}$ -layer, and a 100 Å LTG GaAs cap. For sample C, $x = 0.15$ and for sample D, $x = 0.3$.

After the samples were removed, anneals were done on separate pieces of each wafer. The two annealing conditions were 400°C for 30 s and 500°C for 30 s, both performed with a rapid thermal annealer. Under these annealing conditions, hopping will be the dominant conduction mechanism, as explained above. Samples were then processed with

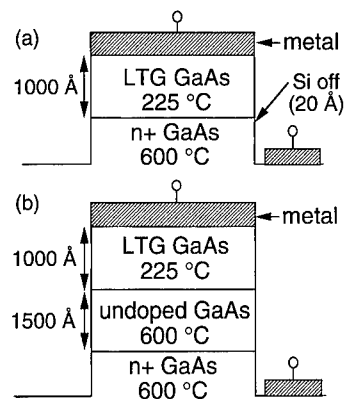


Fig. 1. Growth structure and temperatures for sample A (a) and sample B (b). The two samples are identical except that sample B has a 1500 Å undoped GaAs-layer inserted between the n^+ back contact and the LTG GaAs-layer.

conventional wet etching of a mesa to form vertical diode structures. Standard AuGe metallization (Ni/AuGe/Ni/Au) was used for contacts. All of the top contacts (on the LTG GaAs) were non-alloyed. Broad-area back contacts to the n^+ GaAs-layer were also non-alloyed except for the pieces of sample A and B which had already undergone the 400°C/30 s and 500°C/30 s anneals. For these pieces of samples A and B, the back contacts were annealed at 380°C for 15 s. In all cases, ohmic contacts to the n^+ -layer were obtained.

3. Results and discussion

Fig. 2(a, b) illustrates the fundamental difference in the current versus voltage relationships for samples A and B. Sample A is clearly ohmic, while sample B exhibits rectifying behavior. The reason for this difference lies solely with the nature of the current transport across the interface between the LTG GaAs and the normal temperature grown GaAs. For both samples, the surface metal will make an ohmic tunneling contact to the defect hopping band of the LTG GaAs since the surface pinning depth of GaAs is close ($< 0.2 \text{ eV}$) to the Fermi level pinning in the LTG GaAs. In addition, the surface depletion depth will be very small for the LTG GaAs due to the high trap density, and so electrons can easily tunnel into the LTG GaAs hopping band. Yamamoto

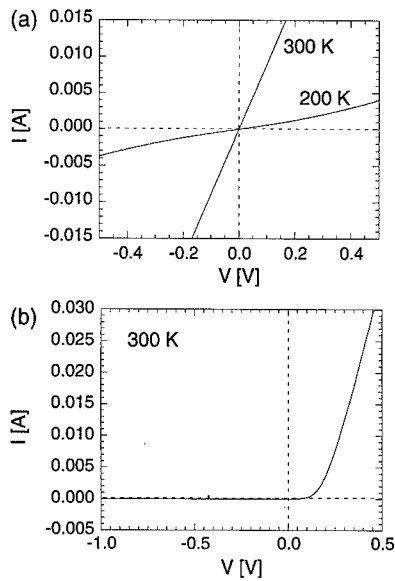


Fig. 2. Current versus voltage curves showing the difference between the ohmic behavior of sample A (a) and the rectifying behavior of sample B (b).

et al. [2] have demonstrated this type of non-alloyed contact to LTG GaAs having a small specific contact resistance (mid $10^{-3} \Omega \text{ cm}^2$).

Now, in order to explain the different I versus V behavior, we must examine the band diagram at the LTG GaAs/normal GaAs interface. Looking at the band diagram of sample A (Fig. 3(a)), we see that electrons are able to tunnel from the defect hopping band of the LTG GaAs into the conduction band of the n^+ GaAs as long as the n^+ -doping is sufficiently high, thus yielding the ohmic behavior. (Similar ohmic behavior [9] has been seen previously for the case of LTG GaAs on n -type ($1.6 \times 10^{17} \text{ cm}^{-3}$) GaAs.) In the case of sample B (Fig. 3(b)), when electrons reach the end of the defect hopping band of the LTG GaAs, tunneling is insignificant because of the 1500 Å spacer layer. Instead, electrons must be thermally emitted into the conduction band of the undoped GaAs at the interface. (This is equivalent to saying that the transport across the interface is limited to the small number of electrons in the conduction band due to the Boltzmann tail at finite temperature.) Therefore, the LTG GaAs/undoped GaAs interface acts like a Schottky barrier with a barrier height Φ_B which is equal to the Fermi level depth in

the LTG GaAs referenced to the conduction band (i.e. $\Phi_B = E_C - E_F$ in the LTG GaAs). For transport in the other direction (to the left in Fig. 3(b)), injected electrons that cross the interface will rapidly recombine and fall down into the empty donors. Electrons will then be swept out by hopping conduction through the LTG GaAs to the metal contact. The LTG GaAs-layer therefore acts as a series resistance, which, although fairly large, will not limit the current flow until the diode is turned on (i.e. until the barrier is reduced to several times kT).

Since the LTG GaAs/undoped GaAs interface acts like a Schottky barrier, the Fermi level pinning depth in the LTG GaAs can be directly obtained from the temperature dependence of the reverse bias saturation current using standard thermionic emission theory of Schottky barriers. Thermionic emission theory gives:

$$I = I_s \left[\exp \left(\frac{qV - IR_s}{nkT} \right) - 1 \right], \quad (1)$$

where I is the current, I_s is the reverse bias saturation current, q is the electronic charge, V is the applied voltage, R_s is the series resistance, n is the

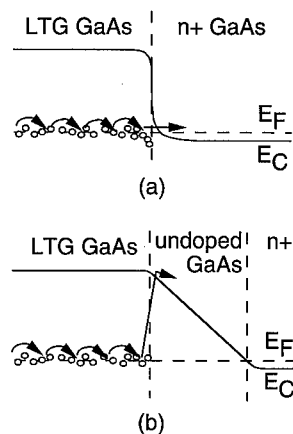


Fig. 3. Schematic band diagrams for the LTG GaAs/ n^+ GaAs interface of sample A (a) and the LTG GaAs/undoped GaAs interface of sample B (b). The small circles represent the defect states that make up the hopping band. In (a), electrons can readily tunnel across the interface, giving the ohmic behavior of sample A. In contrast, the LTG GaAs/undoped GaAs interface in (b) acts like a Schottky barrier since electrons must be thermally emitted from the defect hopping band of the LTG GaAs into the conduction band of the undoped GaAs.

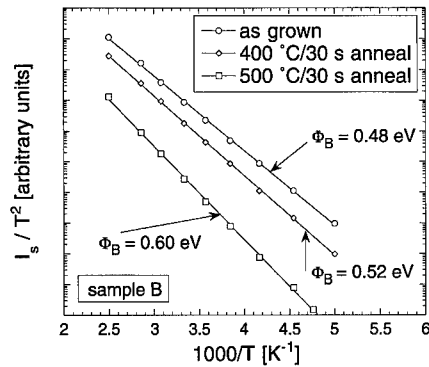


Fig. 4. Plot of I_s/T^2 versus $1000/T$ for sample B. The slope of each linear fit gives the barrier height Φ_B of the Schottky-like barrier in accordance with Eq. (2).

ideality factor, k is Boltzmann's constant, and T is temperature. The saturation current I_s is obtained by fitting the forward bias characteristic to Eq. (1). The saturation current has the following temperature dependence:

$$I_s \propto T^2 \exp\left(\frac{-q\Phi_B}{kT}\right), \quad (2)$$

where Φ_B is the barrier height. A plot of I_s/T^2 versus $1/T$ on a semi-log plot will give a straight line with a slope equal to $-q\Phi_B/k$. Thus the barrier height can be obtained by fitting to a straight line as shown in Fig. 4 for sample B.

The barrier heights obtained from the above fitting procedure are given in Table 1 for sample B (LTG GaAs), sample C (LTG $\text{Al}_{0.15}\text{Ga}_{0.85}\text{As}$) and sample D (LTG $\text{Al}_{0.3}\text{Ga}_{0.7}\text{As}$). Recalling that the barrier height is simply the Fermi level depth in the LTG GaAs, our value for the Fermi level pinning in the unannealed LTG GaAs, 0.48 eV, is in good agreement with the 0.47 eV value obtained by Shen

et al. [10] by photoreflectance. Additionally, our results for the movement of the Fermi level with anneal temperature seem to confirm the two-donor-level model proposed by Look et al. [3], in which the first donor is about 0.5 eV below the conduction band and the second deeper donor is 0.65 eV below the conduction band. In this model, when the acceptor density increases and the shallower donor density decreases at the 500°C anneal, the remaining shallow donors are emptied, and thus the Fermi level drops into the second deeper donor band.

Results for sample C (LTG $\text{Al}_{0.15}\text{Ga}_{0.85}\text{As}$) and sample D (LTG $\text{Al}_{0.3}\text{Ga}_{0.7}\text{As}$) are also given in Table 1. The deeper Fermi level pinning for the LTG AlGaAs explains the higher resistivity of AlGaAs annealed at $> 600^\circ\text{C}$ relative to LTG GaAs. It is also interesting to note that the Fermi level pinning depth in the AlGaAs samples seems to track the conduction band offset relative to GaAs.

4. Conclusions

We have examined the current transport across the interface between LTG GaAs and normal temperature grown GaAs. For an LTG GaAs/ n^+ GaAs interface, ohmic behavior is observed due to tunneling from the defect hopping band of the LTG GaAs into the conduction band of the n^+ GaAs. The LTG GaAs/undoped GaAs interface, on the other hand, acts like a Schottky barrier with a barrier height equal to the Fermi level pinning depth in the LTG GaAs. Therefore, we have determined the Fermi level depth in the LTG GaAs by fitting the temperature dependence of the current–voltage curves using thermionic emission theory, and these results agree with the proposed two-donor-level model.

Table 1
Barrier heights Φ_B for samples B, C, and D (all numbers are in eV)

	Sample B (LTG GaAs)	Sample C (LTG AlGaAs $x = 0.15$)	Sample D (LTG AlGaAs $x = 0.3$)
As grown	0.48	0.59	0.67
400°C/30 s anneal	0.52	0.58	0.69
500°C/30 s anneal	0.60	0.71	0.77

Acknowledgements

We gratefully acknowledge the technical support of John English. This work was supported by the Air Force Office of Scientific Research under Grant No. AFOSR-F49620-94-1-0158 and Grant No. AFOSR-F49620-94-1-0040 and by the NSF Science and Technology Center for Quantized Electronic Structures (QUEST). One of the authors (K.M.) acknowledges support from AFOSR AASERT Grant No. F49620-94-1-0377.

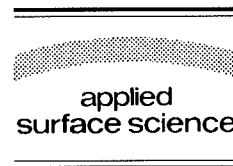
References

- [1] D.C. Look, *Thin Solid Films* 231 (1993) 61.
- [2] H. Yamamoto, Z.-Q. Fang and D.C. Look, *Appl. Phys. Lett.* 57 (1990) 1537.
- [3] D.C. Look, D.C. Walters, G.D. Robinson, J.R. Sizelove, M.G. Mier and C.E. Stutz, *J. Appl. Phys.* 73 (1993) 306.
- [4] L.-W. Yin, Y. Hwang, J.H. Lee, R.M. Kolbas, R.J. Trew and U.K. Mishra, *IEEE Electron Device Lett.* EDL-11 (1990) 561.
- [5] C.L. Chen, L.J. Mahoney, K.B. Nichols, M.J. Manfra, B.F. Gramstorff, K.M. Molvar, R.A. Murphy and E.R. Brown, *IEEE Electron Device Lett.* EDL-16 (1995) 199.
- [6] C.L. Chen, F.W. Smith, B.J. Clifton, L.J. Mahoney, M.J. Manfra and A.R. Calawa, *IEEE Electron Device Lett.* EDL-12 (1991) 306.
- [7] K.D. Maranowski, J.P. Ibbetson, K.L. Campman and A.C. Gossard, *Appl. Phys. Lett.* 66 (1995) 3459.
- [8] A.C. Gossard, M. Sundaram and P.F. Hopkins, in: *Epitaxial Microstructures*, Ed. A.C. Gossard (Academic Press, Boston, MA, 1994) p. 153.
- [9] D.C. Look, C.E. Stutz and K.R. Evans, *Appl. Phys. Lett.* 57 (1990) 2570.
- [10] H. Shen, F.C. Rong, R. Lux, J. Pamulapati, M. Taysing-Lara, M. Dutta, E.H. Poindexter, L. Calderon and Y. Lu, *Appl. Phys. Lett.* 61 (1992) 1585.



ELSEVIER

Applied Surface Science 104/105 (1996) 626–630



$(\text{II-VI})_m/(\text{IV}_2)_n$ (110) superlattice: interfacial chemistry, electronic structure, and optical property

E.G. Wang^{a,b,*}^a Texas Center for Superconductivity and Space Vacuum Epitaxy Center, University of Houston, Houston, TX 7720, USA^b Institute of Physics, Chinese Academy of Sciences, P.O. Box 603, Beijing 100080, China

Received 28 June 1995; accepted 9 December 1995

Abstract

The detail calculations of the electronic and optical properties of the $(\text{ZnS})_n/(\text{Si}_2)_m$ and $(\text{ZnSe})_n/(\text{Ge}_2)_m$ (110) superlattices are performed by a semiempirical tight-binding method with a wide range of $n, m \leq 20$. Interfacial band structures and planar average of charge densities of states are presented for the ZnS–Si and ZnSe–Ge (110) boundaries. An empty interface band is identified in the upper region of the gap of the ZnS/Si superlattice, which extends over an extended region of k space. No interface state, however, is found in the thermal gap of the ZnSe/Ge system. Furthermore, some widely used pseudobinary semiconductor alloys in the interface region are studied to show the important role of interfacial chemistry in II–VI compound growth on silicon. Finally, the calculated absorption spectra of the superlattice are found to be quite different from those of the corresponding bulks, but fairly close to their average.

1. Introduction

There is great interest in the multilayer growth of II–VI compounds for optoelectronic device applications in the visible-to-ultraviolet range. Recent progress in high-vacuum deposition technology has allowed the heteroepitaxial growth to integrate the superior properties of II–VI wide band-gap compounds with the mature technology of IV semiconductors [1,2]. Early theoretical considerations of electronic structure at an interface were confined to ZnSe–Ge heterojunctions [3], or only to a five–five layer superlattice [4]. Until recently there has been a

theoretical attempt to understand the electronic structure of ZnS/Si superlattice [5]. Although less studied in the past than III–V compound superlattice, multilayers formed from II–VI and IV semiconductors now belong to a rapidly growing field of solid-state research. Therefore, it is of crucial importance to fully explore the knowledge of the interfacial chemistry, electronic structure, and optical property of II–VI/IV superlattices.

In this paper, a detailed tight-binding study of the $(\text{ZnS})_n/(\text{Si}_2)_m$ and $(\text{ZnSe})_n/(\text{Ge}_2)_m$ ($n, m \leq 20$) superlattices is reported. The lattice mismatch in these systems is less than 0.4%. Therefore, the ZnS–Si and ZnSe–Ge interface is nonpolar when the superlattices are grown along (110) direction. A zero-field model [5–8] is well established for the lattice-matched II–VI/IV (110) superlattices.

* E-mail: ewang@uh.edu.

2. Tight-binding technique

The tight-binding eigenstates of a superlattice can be expanded as a linear combination of atomic orbitals:

$$\begin{aligned} |k, \lambda\rangle &= \sum_{\xi, \alpha} \langle \xi, r_\alpha, k | k, \lambda \rangle | \xi, r_\alpha, k \rangle \\ &= \sum_{\xi, \alpha} C_{\xi\alpha}(k, \lambda) | \xi, r_\alpha, k \rangle \end{aligned} \quad (2.1)$$

where λ denotes the band index, ξ is a quantum number that runs over the basis orbitals, s, s^*, p_x, p_y , and p_z on the different types of sites α in a unit cell. The N wavevectors k lie in the first Brillouin zone with the origin of the l th unit cell at R_l , and r_α represents the positions of the atoms in this unit cell. The eigenwave function can be obtained by solving the Schrödinger equation.

The absorption coefficient of a superlattice is given by [5,9] (apart from a constant factor)

$$\begin{aligned} \alpha(\hbar\omega) &= \frac{1}{\omega} \sum_k \sum_{\lambda, \lambda'} |\epsilon \cdot P_{\lambda, \lambda'}(k, k)|^2 \delta(E_{\lambda'}(k) \\ &\quad - E_\lambda(k) - \hbar\omega) \end{aligned} \quad (2.2)$$

With the eigenstates given in (2.1), one can obtain the momentum matrix element as

$$\begin{aligned} P_{\lambda, \lambda'}(k, k') &= \langle k, \lambda | p | k', \lambda' \rangle \\ &= \frac{1}{N} \sum_{\xi, \xi', \alpha, \alpha'} C_{\xi\alpha}^*(k, \lambda) C_{\xi'\alpha'}(k', \lambda') \\ &\quad \times \sum_{l, l'} \exp\{i[k' \cdot (R_{l'} + r_{\alpha'}) - k \cdot (R_l + r_\alpha)]\} \\ &\quad \times \langle \xi, r_\alpha, R_l | p | \xi', r_{\alpha'}, R_{l'} \rangle \end{aligned} \quad (2.3)$$

where $\langle \xi, r_\alpha, R_l | p | \xi', r_{\alpha'} + \tau_\alpha, R_{l'} \rangle$ are determined by comparing the theoretical computed values of bulks with their experimental results. Considering the strongly localized atomic orbitals in the tight-binding model, the momentum matrix elements between atoms beyond the nearest neighbors are neglected [9].

The intramaterial elements in the tight-binding Hamiltonian can be uniquely formed by using the corresponding bulk parameters. While for the inter-material elements at ideal interface, a simple average of the bulk parameters have been used. These bulk

parameters are determined by fitting the first-principles calculations and experimental results. Yamaguchi's formulae [7] has been adopted to yield a self-consistent result at X-point energies. These parameters are tested against some well established bulk results [5].

3. Results and discussion

3.1. Localized state at ideal interface

The planar average of the charge densities of the X and Γ band-edge states are shown in Fig. 1 and Fig. 2 for $(\text{ZnS})_{16}/(\text{Si}_2)_{16}$ and $(\text{ZnSe})_{16}/(\text{Ge}_2)_{16}$ (110) superlattices with ideal interface, respectively. At first we assume their valence-band offset ΔE_v to be 1.90 eV (ZnS/Si) and 1.46 eV (ZnSe/Ge) given by Harrison theory [10]. A clearly localized state is found at the interface of the ZnS/Si system, where the Zn–Si and S–Si bonds are equally appeared. The interface state extends over an extended region of k space. Its relative position is changed by varying ΔE_v , but it does not disappear from the gap for all possible valence-band offsets.

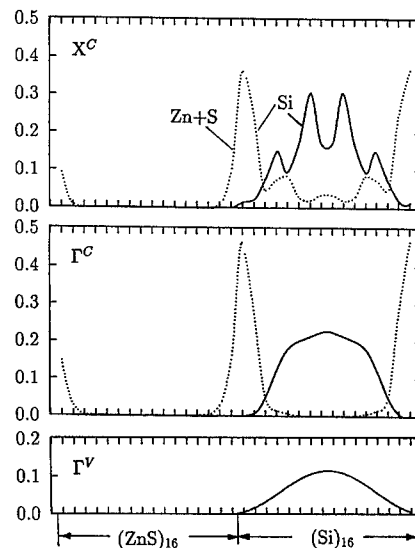


Fig. 1. Calculated planar average of the charge densities of the interface (dashed lines) and the confined band-edge (solid lines) states at Γ and X points for $(\text{ZnS})_{16}/(\text{Si}_2)_{16}$ (110) superlattice with ideal interface.

For ZnSe/Ge superlattice, however, we do not find any interface state in the thermal gap (Fig. 2). The Zn–Ge interface state is pushed into the valence-band region, in agreement with the experimental consensus [11] and the self-consistent pseudopotential results [4].

In addition, from Fig. 1 and Fig. 2, one can see that all the band-edge states are confined in the two dimensional silicon and germanium ‘wells’, respectively. Therefore, it is reasonable to believe that these states originate from those of IV semiconductors by the zone folding effects.

3.2. Interfacial chemical interaction

In order to check the influence of interfacial chemistry, two pseudobinary semiconductor alloy [12] $\text{ZnSi}_x\text{S}_{1-x}/\text{Si}_{1-x}\text{S}_x$ (A) and $\text{Zn}_{1-y}\text{Si}_y\text{S}/\text{Zn}_y\text{Si}_{1-y}$ (B) are used in the interface region to allow a continuous range of materials parameters, tunable by changing the composition x and y . The difference between the two distinct interfaces is: the A form in which the S–Si atoms are mixed within bilayers perpendicular to the growth

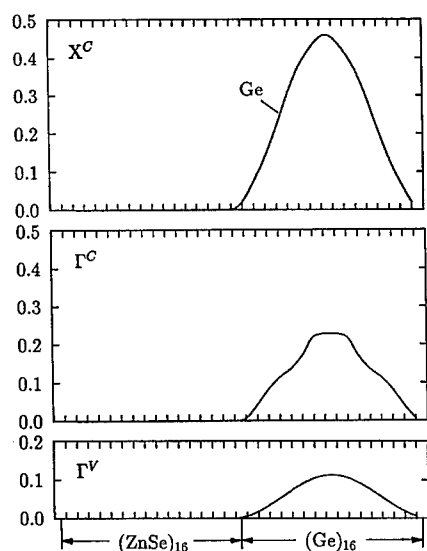


Fig. 2. Calculated planar average of the charge densities of the confined band-edge states at Γ and X points for $(\text{ZnSe})_{16}/(\text{Ge}_2)_{16}$ (110) superlattice with ideal interface. No interface states are found in the thermal gap of this system.

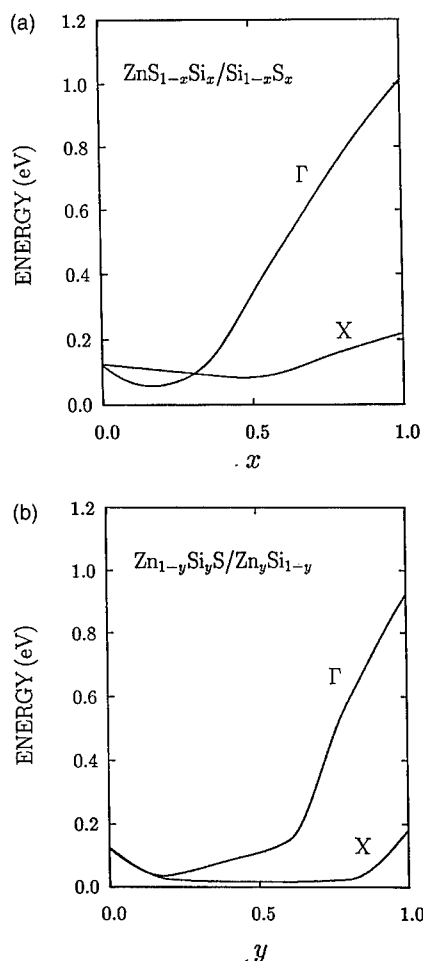


Fig. 3. Difference of the interface states and the confined conduction band-edge states versus the composition x and y of the pseudobinary semiconductor alloy $\text{ZnSi}_x\text{S}_{1-x}/\text{Si}_{1-x}\text{S}_x$ (a) and $\text{Zn}_{1-y}\text{Si}_y\text{S}/\text{Zn}_y\text{Si}_{1-y}$ (b) at some high symmetry points, where $\Gamma = \Gamma^C - \Gamma^I$ and $X = X^C - X^I$.

direction, and the B form in which the Zn–Si atoms are mixed within bilayers. A series of tight-binding parameters in the interface region can be written as

$$E(\text{AC}_x\text{B}_{1-x}) = (1-x)E(\text{AB}) + xE(\text{C}), \quad (3.1)$$

$$E(\text{C}_{1-x}\text{B}_x) = xE(\text{AB}) + (1-x)E(\text{C}), \quad (3.2)$$

$$E(\text{A}_{1-y}\text{C}_y\text{B}) = (1-y)E(\text{AB}) + yE(\text{C}), \quad (3.3)$$

and

$$E(\text{A}_y\text{C}_{1-y}) = yE(\text{AB}) + (1-y)E(\text{C}). \quad (3.4)$$

Fig. 3(a) and (b) show the difference between the interface state and the confined conduction band-edge state at some high symmetry points by continuously changing the composition x and y , where $\Gamma = \Gamma^C - \Gamma^I$ and $X = X^C - X^I$. For the limiting cases of $x = y = 1$, the interface states at Γ move away from the conduction band-edge and become occupy-like. It is found that the interface states are mainly localized at Γ point when y is in the range of 0.4–0.7 for $\text{Zn}_{1-y}\text{Si}_y\text{S}/\text{Zn}_y\text{Si}_{1-y}$ alloy. While the behavior of the interface states in the above alloys with x and $y > 0.7$ appear to have no major difference.

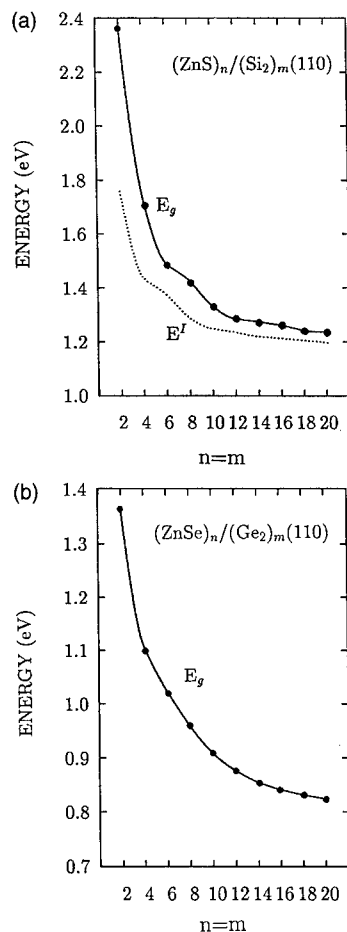


Fig. 4. Band gap E_g of $(\text{ZnS})_n/(\text{Si}_2)_m$ (a) and $(\text{ZnSe})_n/(\text{Ge}_2)_m$ (b) (110) superlattices as a function of the number of layers $n = m$. The relative positions of the interface band E^I and X point are also drawn in (a). The zero of energy is the valence band maximum of the superlattices.

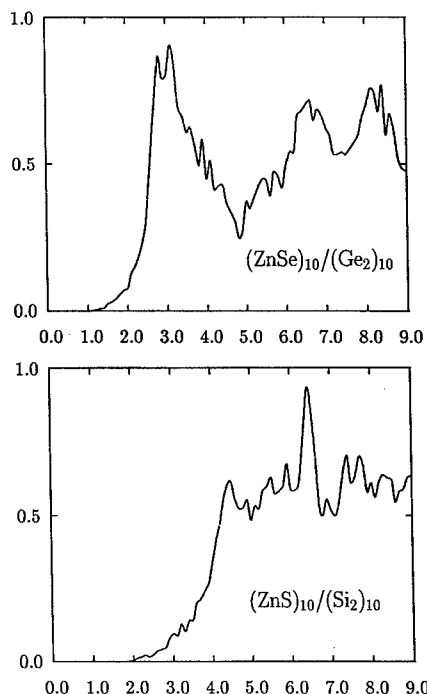


Fig. 5. Total joint densities of states (JDOS) corresponding to the overall optical transitions in II–VI/IV (110) superlattices.

3.3. Band structure

The fundamental band gaps of the $(\text{ZnS})_n/(\text{Si}_2)_m$ and $(\text{ZnSe})_n/(\text{Ge}_2)_m$ (110) superlattices with ideal interface are given as a function of $n = m$ in Fig. 4(a) and (b), respectively. We also plot the interface band E^I , dashed line in Fig. 4(a), for ZnS/Si system. Our calculation shows that the lowest transition is the indirect Γ -to- X' for ZnS/Si superlattices, where X' is near to X point. For ZnSe/Ge system, it is the Γ -to-M ($n = m \leq 8$) and Γ -to- X' ($n = m > 8$). The quantum confinement is most dramatic, as the gap rises sharply by decreasing superlattice period.

3.4. Optical absorption

In the present calculations, 28 special points in the $1/8$ irreducible two-dimensional Brillouin zone (k_x, k_y) and two special points in the $1/2$ one-dimensional Brillouin zone (k_z) are accepted. The calculated joint densities of states (JDOS) corresponding to the optical transitions [13,14] are given

in Fig. 5 for II–VI/IV (110) superlattices with $n = m = 10$.

Three main peaks are identified for these structures. The one located at lower energy range originates from the IV-group semiconductor and the others from II–VI compound by comparison with the absorption spectra of bulks. For example of the ZnSe/Ge superlattice, these peaks are around 3.2 eV, 6.5 eV, and 8.4 eV, respectively. It is noted that the first originates from Ge (3.9 eV [15]), the second from ZnSe (6.6 eV [16]), and the third from ZnSe (8.3 eV [16]). In addition, we find that these peak positions in the superlattice are modified more from their bulks with the change of Ge than with that of ZnSe.

4. Conclusion

A detailed investigation of the interfacial chemistry, electronic structure, and optical transition in $(\text{II-VI})_n/(\text{IV})_m$ (110) superlattices has been performed for a wide range of $n, m \leq 20$ by using a semiempirical tight-binding method. An empty interface band is identified in the upper region of the gap in ZnS/Si system, which extends over a quite different region of k space. For the ZnSe/Ge system, no interface band is found in the thermal gap, while the Zn–Ge localized state is pushed into the valence-band region. The influence of interfacial chemical interaction on the localized state has been studied for pseudobinary semiconductor alloys in the boundary region. It is found that the interfacial chemistry has a dominant role in II–VI compound growth on Si substrate. Three main peaks are identified in the absorption spectra of these superlattices. The one located at lower energy range originates from the IV-group semiconductor, and the others from II–VI compounds. These results presented in this work

should establish the understanding of the fundamental electronic and optical properties of the superlattices fabricated from II–VI and IV semiconductor.

Acknowledgements

The author wishes to thank Dr. C.S. Ting at the Texas Center for Superconductivity, University of Houston, and Dr. C.F. Chen at University of Nevada for their interest. The work was supported in part by the ARO Grant DAAH04-94-G-0075 and the NSF under Cooperative Agreement OSR-9353227. The author also wishes to acknowledge a summer visiting appointment at Princeton University and an Outstanding Young Award by CAS.

References

- [1] L.T. Romano, R.D. Bringans, J. Knall, D.K. Biegelsen, A. Garcia and J.E. Northrup, *Phys. Rev. B* 50 (1994) 4416.
- [2] X.-C. Zhou and W.P. Kirk, *Mater. Res. Soc. Symp. Proc.* 318 (1994) 207.
- [3] J. Pollmann and S.T. Pantelides, *Phys. Rev. B* 21 (1980) 709.
- [4] W.E. Pickett and M.L. Choen, *Phys. Rev. B* 18 (1978) 939.
- [5] E.G. Wang and C.S. Ting, *Phys. Rev. B* 51 (1995) 9791.
- [6] T. Saito and T. Ikoma, *Phys. Rev. B* 45 (1992) 1762.
- [7] E. Yamaguchi, *J. Phys. Soc. Jpn.* 57 (1988) 2461.
- [8] J. Shen, J.D. Dow and S.Y. Ren, *J. Appl. Phys.* 67 (1990) 376.
- [9] Y.C. Chang and J.N. Schulman, *Phys. Rev. B* 31 (1985) 2069.
- [10] W.A. Harrison, *Electronic Structure and the Properties of Solids* (Freeman, San Francisco, CA, 1980).
- [11] A.G. Milnes and D.L. Feucht, *Heterojunctions and Metal–Semiconductor Junctions* (Academic Press, New York, 1972).
- [12] S.M. Sze, *Physics of Semiconductor Devices* (Wiley, New York, 1981); M. Jaros, *Rep. Prog. Phys.* 48 (1985) 1091.
- [13] Z. Xu, *Solid State Commun.* 76 (1990) 1143.
- [14] D.E. Aspnes and A.A. Studna, *Phys. Rev. B* 27 (1983) 985.
- [15] C.S. Wang and B.M. Klein, *Phys. Rev. B* 24 (1981) 3393.
- [16] J.L. Freeouf, *Phys. Rev. B* 7 (1973) 3810.

Charge transfer and electronic activation at an Sb δ -layer in Si(001)

J.M.C. Thornton ^{a,*}, R.J. Cole ^a, D.J. Gravesteijn ^b, P. Weightman ^a

^a IRC in Surface Science, University of Liverpool, Liverpool L69 3BX, UK

^b Philips Research Laboratories, 5600 JA Eindhoven, The Netherlands

Received 28 June 1995; accepted 30 August 1995

Abstract

Thin sheets of dopant atoms (δ -layers) have been shown to give unprecedented microscopic control over interfaces between semiconductors, though there exists very little understanding of the fundamental changes in the electronic structure in the vicinity of the δ -doped layer. Recent work in electron spectroscopy has shown that the combination of environmentally determined photoelectron and Auger electron shifts within the Auger parameter can provide insight into the differences in local electron screening and charge transfer. In this work, we apply the technique to the study of Sb δ -layers in epitaxially grown Si(001) and have been able to determine for the first time using spectroscopic techniques the existence of two different environments for Sb in Si, and that only 17% of the donor atoms are electrically active.

1. Introduction

One of the current major themes of semiconductor research is the creation of high doping levels with sharp spatial profiles for use in high-speed devices such as heterojunction bipolar transistors (HBTs). The problems in fabrication are particularly hard to overcome for n-type dopants in silicon, where strong surface segregation and a low incorporation probability [1] during growth severely limits the doping profile attainable. Antimony is one of the n-type dopants which has been widely used in high concentration and δ -doping studies [2–5], which although it segregates strongly and is therefore hard to control, does have the practical advantage of being easy to evaporate from a Knudsen cell.

A number of different approaches have been made to the problem of creating highly concentrated δ -layers of Sb in Si with perhaps the best understood so far being that of solid phase epitaxy (SPE) [4,6]. In this technique, a near to complete monolayer of Sb is deposited onto an epitaxially prepared Si substrate surface followed by a layer of Si at low temperature. The Si is amorphous at the temperatures used, though the overlayer can be recrystallized by annealing, with only very limited diffusion of the Sb away from the original position of the layer. The main advantage this particular preparation method offers is that it yields complete incorporation of the Sb in the Si, though this does not extend to the electrical activity of the dopant atoms. In order to be electrically active, the Sb dopant atoms require either a pre- or post-growth annealing stage [7,8]. Complete incorporation is an important factor in our experiments which are surface sensitive, and so might be

* Corresponding author.

confused by the existence of both surface and buried environments of Sb. For this reason we have concentrated our studies on SPE grown samples, and have investigated the local chemical and electronic environment of the Sb dopant atoms.

The analysis of Auger parameter shifts has been used with considerable success to describe ground state charge transfer and core-hole screening effects in both bulk and surface environments of semiconductors [9–11]. In particular, the As/Si(001) and As/Si(111) systems have been studied in detail, with clear differences apparent in the measured Auger parameter between the two interface environments [11]. We now extend and apply these techniques to the study of Sb δ -layers in Si(001) with a view to understanding dopant ionization and local dielectric properties.

2. Experimental

Sb-doped δ -layers were grown on (001) oriented 4-in. diameter Si substrates of p-type 1000 Ω cm float-zone material. Following the thermal desorption of the native oxide, a buffer layer of Si was grown epitaxially at a temperature of 685°C to a thickness of 1500 Å. Details of the molecular beam epitaxy (MBE) apparatus and technique have been published elsewhere [12]. A layer of Sb was then deposited from a Knudsen cell onto this prepared surface to a concentration of 3.5×10^{14} cm⁻² as measured subsequently using Rutherford backscattering spectrometry (RBS). After cooling to room temperature, amorphous Si layers of 25 Å and 45 Å thickness were deposited over the Sb. The top layers were then recrystallized by ramping the temperature up to 560°C and cooling back to room temperature. No extra annealing time was needed due to the very small thickness of the Si overlayer, which were chosen to permit electron spectroscopic techniques to be used to detect the Sb δ -layer.

The samples were transferred to an electron spectrometer [13], where the spectra from core-electron features (Sb 3d, 4d) were measured. These could be excited by Al K α radiation, which was monochromated to give a total instrumental resolution of 0.4 eV. Spectra were obtained at both normal emission, and at an angle of 50° between the sample normal

and the electron emission in order to investigate the surface species and depth distribution of the Sb.

The samples were also investigated using higher energy synchrotron radiation ($h\nu = 4500$ eV) to excite the Sb L_{2,3}M_{4,5}M_{4,5} transitions. This was performed on beamline IRC-4.2 at Daresbury laboratory, UK. The photoelectrons were collected with a similar hemispherical analyser to the 'in-house' spectrometer, though in this case the sensitivity was enhanced by operating at a reduced resolution, corresponding to a Gaussian broadening of 0.6 eV.

3. Results

The Sb 3d_{3/2} and 4d core-levels obtained from the sample grown with a 25 Å Si top-layer are shown by the dots in Fig. 1 and Fig. 2 are representative of both of the specimens, though as expected the Sb features showed a reduction in absolute intensity when measured for the specimen with the 45 Å top-layer. The spectra shown in Fig. 1 and Fig. 2 were collected at normal emission, and are shown together with 'best fits' to the data obtained using a curve-fitting analysis program. The parameters used to fit the data are shown in Table 1.

The Sb 3d_{3/2} peak is shown here rather the more intense 3d_{5/2} due to the proximity of the latter to the O 1s core-level photoemission line, which occurs in the spectral region between the two Sb spin-orbit split components. Fortunately, the Sb 3d spin-orbit

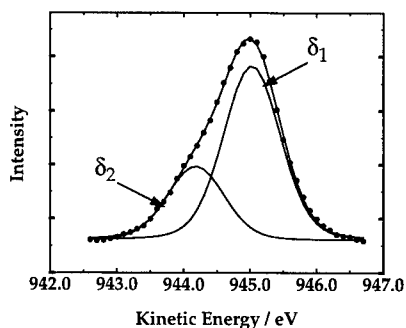


Fig. 1. A normal emission XPS spectrum of the Sb 3d_{3/2} core-level from a δ -layer, buried by 25 Å in Si(001). The spectrum is shown fitted with two components separated by 0.85 eV in energy (δ_1 and δ_2) which are believed to be substitutional and precipitate respectively.

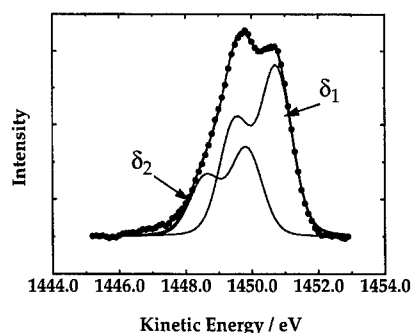


Fig. 2. An XPS spectrum of the Sb 4d core-level under the same conditions as in Fig. 1.

split components are separated in energy by approximately 9 eV, so the $3d_{3/2}$ is not affected significantly by the O 1s emission. The fact that the Sb 4d spectrum does not have the form of a single spin-orbit doublet makes it immediately clear that Sb is present in more than one environment. An analysis of the peak shapes using a curve-fitting routine established that both 3d and 4d core-levels consist of two components; one large peak (labelled δ_1), and a smaller one (δ_2) 0.85 eV to higher binding energy. The spectral profiles of both Sb core-levels can be attributed to an envelope of two identically shaped contributions, 0.85 eV apart and with a relative intensity ratio of 1.9:1 ($\delta_1 : \delta_2$). We can eliminate the possibility that one of the Sb components arises from surface oxidized Sb since the angle-dependent studies showed no change in the relative intensity of the two components with take-off angle.

The results showed that the specimens had a thin silicon dioxide layer at the surface and no surface Sb as confirmed by the lack of change in the core-level line-shape and no increase relative to the bulk Si signal with electron take-off angle. It was found that the Sb core-levels did not alter in lineshape with emission angle, and did not increase in intensity relative to the bulk Si 2p emission at grazing emission angles as found for the O 1s and the Si 2p associated with SiO_2 . This confirms the view that all the Sb remains buried in the Si top-layer, and did not diffuse to the surface during growth, where it would have oxidized on removal of the specimen from the UHV growth apparatus. Furthermore, the absence of any dependence of both the Sb 4d and $3d_{3/2}$ core-level lineshapes on emission angle indicates that the

environments giving rise to the δ_1 and δ_2 components have the same depth distribution.

In seeking an explanation for the presence of two Sb sites we note that the extremely high concentration of Sb at the δ -layer is well above the maximum doping level achieved in this material system [4], and that precipitation of Sb might be expected [6]. We therefore attribute the two environments that we observe to arise from substitutional Sb in the host lattice and from small Sb clusters, with in each case a contribution to the lineshape from inhomogeneous broadening arising from a statistical spread of sites. It is difficult to associate the δ_1 and δ_2 features with each form of Sb since a comparison with the absolute binding energies of the bulk material are not necessarily valid in an electronic structure distorted by very localized and high doping levels. The results of RBS measurements on these and similar samples show that between 50% and 80% of the Sb can be expected to be on substitutional sites, and on this basis we attribute the most intense component in the photoemission data (δ_1) to be due to substitutionally located Sb. It then follows that the smaller component (δ_2) is due to 'bulk-like' Sb clusters. This is of course a simplified view of the real Sb environments which may exist under these conditions as may be seen from the width of the Gaussian broadening contribution needed to fit the Sb core-levels (Table 1). This was between 0.9 and 1.0 eV for each site, and since the resolution of the spectrometer used to collect these data was measured using a clean Ag Fermi-edge to be 0.40 eV it is clear that there is a substantial inhomogeneous broadening contribution to the measured peak widths. We attribute this additional broadening to a spread of environments associated with the main 'substitutional' and 'precipitate' sites.

Table 1
Curve fitting parameters

	Sb 3d	Sb 4d
Lorentzian width	0.16 eV	0.18 eV
Gaussian width	0.90 eV	0.99 eV
Spin-orbit splitting	9 eV	1.25 eV
Relative intensity of spin-orbit components	0.66	0.66
Binding energy difference ($\delta_2 - \delta_1$)	0.85 eV	0.87 eV
Intensity ratio (δ_1 / δ_2)	1.9	1.9

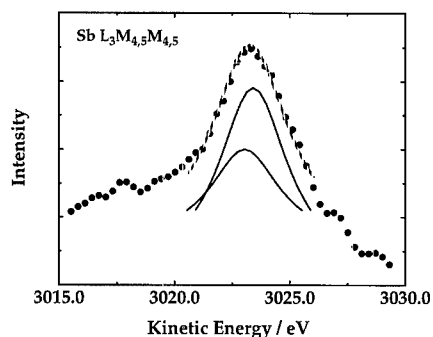


Fig. 3. The Sb $L_3M_{4.5}M_{4.5}$ Auger transition obtained using synchrotron radiation with an energy 4500 eV from the same buried δ -layer of Sb as in Fig. 1 and Fig. 2. A fit to the $L_3M_{4.5}M_{4.5}^1G_{22}34$ showing the maximum acceptable shift between two components consisting of Lorentzian peaks (FWHM = 2.8 eV) broadened with a 0.6 eV Gaussian instrumental contribution is also shown overlayed. The components are offset for clarity.

The Sb LMM (~ 3000 eV) group of Auger features were measured making use of synchrotron radiation, though the MNN is the preferred group due to its intrinsically narrower width, and greater sensitivity of the electron analyser used at these energies. From these samples, however, it proved to be difficult to measure the MNN group due to the close proximity in energy of the oxygen KLL Auger emission.

The higher energy Sb $L_3M_{4.5}M_{4.5}$ Auger transition at approximately 3023 eV is shown in Fig. 3. This feature is naturally rather broad (~ 3 eV) though has the advantage of not being complicated by any nearby peaks in emission from Si or its oxide. The full width half maximum (FWHM) of this peak is 2.8 eV, which is very close to that predicted, though less than previously measured for the bulk material [14]. Considering our use of a higher resolution setting for the electron analyser (~ 0.6 eV compared with ~ 1.5 eV [14]) this is not too surprising. The natural linewidth is the dominant factor in the measurement here, though from the narrowness of the peak it is clear that no large energy shift occurs between the components of the two known environments. The result of only a small shift between environments being possible is of great significance since one would expect ionized Sb and bulk elemental Sb to exhibit a large difference in the initial state Auger parameter, yet these data show otherwise.

This may be demonstrated by fitting the Auger peak-shape with two Lorentzian peaks of 2.8 eV FWHM and with a 2:1 intensity ratio, which are broadened with a Gaussian of 0.6 eV to account for the resolution of the electron analyser. The data is easily fitted with a kinetic energy shift of zero, and regardless of relative energy, a shift greater than 0.4 eV gives an unacceptable representation of the data. A fit in the extreme case of a 0.4 eV energy difference is shown in Fig. 3 as a dashed line, together with the two components.

Significant advances have been made recently in the analysis of local electronic structure by combining environmentally determined XPS and Auger shifts in terms of Auger parameters [9–11,15]. This progress has been dependent on the development of a model relating the potential in an atomic core to the valence charge. Early versions of the potential model adopted a linear relationship between the core potential V and the valence charge q ,

$$V = V_{\text{core}} + kq + U,$$

where V_{core} is the contribution from the core electrons and the nucleus, U represents the contribution from the polarization of the extra-atomic environment and k is the linear parameter. This model, however, is unable to account for differences in the Auger parameter of a number of free atoms and elemental metals, and it is necessary to allow for two higher order terms in k which is written

$$k(N_{\text{nl}}, q) = a + bN_{\text{nl}} + dq,$$

where b represents the contraction of the valence charge when a core electron is removed ($N = 1$) and d represents the expansion (contraction) of the valence charge as valence electrons are added (subtracted) from the atom. It is found that when a , b and d are evaluated from the results of atomic structure calculations, it is possible to account for the Auger parameter differences between free atoms and elemental metals and the results are consistent with the expected valence charges in the elemental metals. The potential parameters a , b and d were evaluated using the Dirac–Fock atomic structure code of Desclaux [16] and were found to have values of 15.20, 1.75 and 1.55 respectively for Sb which therefore gives a value of $k(N_{\text{nl}}, q)$ for Sb in the ground state of 7.45.

With an effective model for the core-potential in the atom, it is now possible to relate changes in that potential ΔV to the ground state charge transfer Δq . It is important to realise, however, that any changes in the measured kinetic or binding energies of Auger and core-level features (ΔE_k and ΔE_b) are determined by both ΔV and the relaxation energy ΔR . We must therefore consider both the initial-state and final-state Auger parameters $\Delta\beta$ and $\Delta\alpha$ which are defined by

$$\Delta\beta = 3\Delta E_b + \Delta E_k \sim 2\Delta V$$

and

$$\Delta\alpha = \Delta E_b + \Delta E_k \sim 2\Delta R.$$

As indicated in the above expressions, the differences in the initial and final state Auger parameters approximate to the differences in the initial state potential and final screening between the two environments. The initial state Auger parameter $\Delta\beta$ is the measure of changes in the charge within the valence shell and by using the potential model, it is given approximately by [17]

$$\Delta\beta \approx 2\Delta qk.$$

This is possible because both sites are in the same specimen, so there is no difference in the surface dipole and workfunction which would affect the environmental contribution to the core potential. The local site neutrality in the precipitate means that the environmental contribution can be set to zero for this site. For the substitutional Sb, a Madelung-like contribution arising from charge transfer between the Sb and Si neighbours might be expected, though this will depend largely on the difference in the electronegativities of Si and Sb. These are very close, however, and no significant ionicity is known to occur in an Sb–Si bond. The measurement of core-level and Auger transition electron spectra can therefore give us directly the change in the valence charge on an atom.

In the core-level data discussed earlier, the difference in binding energy between precipitated Sb (Sb^0) and substitutional Sb (Sb^+) was seen to be 0.85 eV. The corresponding maximum kinetic energy difference between Auger features was estimated at 0.4 eV. It is not possible to distinguish the two compo-

Table 2
Cases A, B and C

	$\Delta\alpha(\delta_1\delta_2)$	$\Delta\beta(\delta_1\delta_2)$	Δq
Case A	1.65	3.35	0.18
Case B	0.05	1.75	0.14
Case C	0.85	2.55	0.17

nents in the Auger spectra, and so it is not possible to unequivocally determine the appropriate Auger parameters. We have therefore considered both alternatives by using the largest possible difference in Auger features in order to place maximum limits on our estimations. These are shown as case A and case B in Table 2.

Using these Auger parameters to calculate the initial state charge transfer Δq we find it to be between 0.14 and 0.18 electrons per substitutional Sb atom. The extremes of this range are worst cases, with the zero shift possibility (the middle of the acceptable fit range) considered as case C in Table 2, which leads to the estimate of Δq as 0.17 i.e. 17% of the substitutional Sb donors are donating an electron to a delocalized state. This is very close to the estimates of $\sim 20\%$ made following electrical measurements on similar structures [4].

4. Conclusions

The initial and final state Auger parameters have been measured for Sb in Si(001), where the Sb is in a highly concentrated δ -layer close to the sample surface. These have been used to estimate the charge transfer from the Sb dopant atoms into the Si conduction band and therefore the dopant activation level. We have found that approximately 1/3 of the Sb present is in the form of precipitates, in close agreement with RBS measurements from the same structures. The remaining 2/3 of the Sb is located on substitutional sites in the Si host lattice, and we estimate that between 14 and 18% of the Sb is electrically active. This is in excellent agreement with electrical measurements from similar Sb δ -layer structures in Si. We believe these to be the first direct spectroscopic measurements of dopant concentration and activation level in a semiconductor.

Acknowledgements

The authors would like to acknowledge the help from A.W. Robinson and V.R. Dhanak in performing these measurements, T.P. Morrison and A.A. Cafolla in developing analysis software, and support from the Basic Research Action of ESPRIT (EASI; 6878) funded by the European Commission.

References

- [1] H. Jorke, *Surf. Sci.* 193 (1989) 569.
- [2] K.D. Hobart, D.J. Godbey and P.E. Thompson, *Appl. Phys. Lett.* 61 (1992) 76.
- [3] E.V. Thomsen, O. Hansen, K. Harrekilde-Petersen, J.L. Hansen, S.Y. Shiryayev and A. Nylandsted Larsen, *J. Vac. Sci. Technol. B* 12 (1994) 3016.
- [4] A.A. van Gorkum, K. Nakagawa and Y. Shiraki, *Jpn. J. Appl. Phys.* 26 (1987) L1933.
- [5] H.-J. Gossmann, E.F. Schubert, D.J. Eaglesham and M. Cerullo, *Appl. Phys. Lett.* 57 (1990) 2440.
- [6] C. van Opdorp, L.J. van IJzendoorn, C.W. Fredriksz and D.J. Gravesteijn, *J. Appl. Phys.* 72 (1992) 4047.
- [7] A. Casel, H. Kibbel and F. Schäffler, *Thin Solid Films* 183 (1989) 351.
- [8] A.A. van Gorkum, K. Nakagawa and Y. Shiraki, *J. Appl. Phys.* 65 (1989) 2485.
- [9] S.D. Waddington, P. Weightman, J.A.D. Matthew and A.D.C. Grassie, *Phys. Rev. B* 39 (1989) 10239.
- [10] J.A. Evans, A.D. Laine, P. Weightman, J.A.D. Matthew, D.A. Woolf, D.I. Westwood and R.H. Williams, *Phys. Rev. B* 46 (1992) 1513.
- [11] R.J. Cole, J.A. Evans, P. Weightman, J.A.D. Matthew, D.A. Woolf and D.I. Westwood, *Phys. Rev. B* 49 (1994) 7528.
- [12] A.A. van Gorkum, G.F.A. van de Walle, R.A. van de Heuvel, D.J. Gravesteijn and C.W. Fredriksz, *Thin Solid Films* 184 (1990) 207.
- [13] P. Weightman, *Phys. Scr. T* 41 (1992) 277.
- [14] G.G. Kleiman, R. Landers, P.A.P. Nascente and S.G.C. de Castro, *Phys. Rev. B* 46 (1992) 1970.
- [15] R.J. Cole, D.A.C. Gregory and P. Weightman, *Phys. Rev. B* 49 (1994) 5657.
- [16] J.P. Desclaux, *Comput. Phys. Commun.* 9 (1975) 31.
- [17] T.D. Thomas and P. Weightman, *Phys. Rev. B* 33 (1986) 5406.



ELSEVIER

Applied Surface Science 104/105 (1996) 637–645

applied
surface science

A scanning tunnelling microscopy study of local surface modifications induced by misfit dislocation formation in strained-layer heteroepitaxy

G. Springholz ^{*}, G. Bauer

Institut für Halbleiterphysik, Johannes Kepler Universität Linz, Altenbergerstraße 69, 4040 Linz, Austria

Received 28 June 1995; accepted 30 August 1995

Abstract

The surface modifications caused by misfit dislocation formation in strained-layer heteroepitaxy of 2.1% lattice-mismatched EuTe on PbTe (111) are studied using ultra-high vacuum scanning tunnelling microscopy (STM). It is shown that at the critical layer thickness straight monolayer step lines appear on the surface due to the glide of threading dislocations grown-in from the PbTe buffer layer, in agreement with the classical Matthews–Blakeslee mechanism for strain relaxation. Due to the local lattice distortions around the misfit dislocation segments at the layer/substrate interface, local wave-like deformations with an amplitude equal to the normal component of the Burgers vector are induced on the surface above the misfit dislocations. However, the exact form of the surface deformation depends on the orientation of the Burgers vector. Since the local surface deformations are a direct signature of the dislocations at the interface, the formation of a network of misfit dislocation becomes directly visible even by STM.

1. Introduction

Progress in strained-layer heteroepitaxial growth techniques has opened many possibilities for the fabrication of novel modulated semiconductor heterostructures (see e.g. Ref. [1]). Because of the large number of possible combinations of different materials in strained-layer heteroepitaxy, device characteristics unattainable with lattice-matched systems can be achieved. However, the actual performance of a strained-layer heterostructure device is not only affected by misfit dislocations formed during the strain relaxation process, but also by the roughness of the

heterointerfaces. In heteroepitaxy, the latter strongly depends on the evolution of the surface morphology during growth, which itself is strongly influenced by the strains in the layers. For perfect 2D layer-by-layer growth, usually, the coherency strain due to the layer/substrate lattice-mismatch is fully accommodated by a biaxial elastic lattice deformation until a critical layer thickness is reached beyond which a network of misfit dislocations is formed in order to reduce the strain energy in the layer. However, for a lattice-mismatched wetting overlayer, the form of a completely uniform overlayer is often not the lowest free energy configuration in thermodynamic equilibrium [2–5], since the formation of a pronounced surface corrugation (strain induced coherent islanding) offers an additional very effective channel for

^{*} Corresponding author. Tel.: +43-732-2468 9602; fax: +43-732-2468650; e-mail: g.springholz.@hlphys.uni-linz.ac.at.

strain relaxation based on purely elastic effects, and a growth mode transition from 2D to 3D growth occurs (Stranski–Krastanov growth mode).

In this paper, the surface modifications caused by the formation of misfit dislocation are studied by UHV scanning tunnelling microscopy (STM) for molecular beam epitaxy of EuTe on PbTe (111). Both materials crystallize in the rock salt structure and their lattice-mismatch is 2.1%. Besides the large difference in the energy band gaps of PbTe and EuTe, resulting in a tunability of the band gap from 190 meV to 2 eV, the combination of the antiferromagnet EuTe with the non-magnetic PbTe is interesting for the study of magnetic interactions and inter-layer-coupling in low dimensional short period (EuTe)_n/(PbTe)_m superlattices [6]. Due to the 2.1% lattice-mismatch, EuTe usually grows in a Stranski–Krastanov growth mode, with a transition from 2D layer-by-layer growth to 3D island growth after the first 2–4 monolayers (ML) [7]. When the substrate temperature is reduced, however, this strain-induced coherent islanding can be kinetically suppressed and strain relaxation occurs only via misfit dislocation formation. We find that the formation of misfit dislocation segments by the usual Matthews–Blakeslee mechanism [8] produces glide line steps on the epitaxial surface which are easily detected by STM. In addition, the local lattice distortions around the misfit dislocations induce a pronounced local surface deformation. The shape of the resulting surface profile depends mainly on the orientation of the Burgers vector and the layer thickness. The local changes in the surface profile can be utilized to enhance the contrast between dislocated and dislocation free surface areas and thus, the formed complicated dislocation networks can be made directly visible by STM, similar as in a bright field electron microscopy imaging.

2. Experimental

The growth experiments were carried out in a Riber MBE system with separate effusion cells for

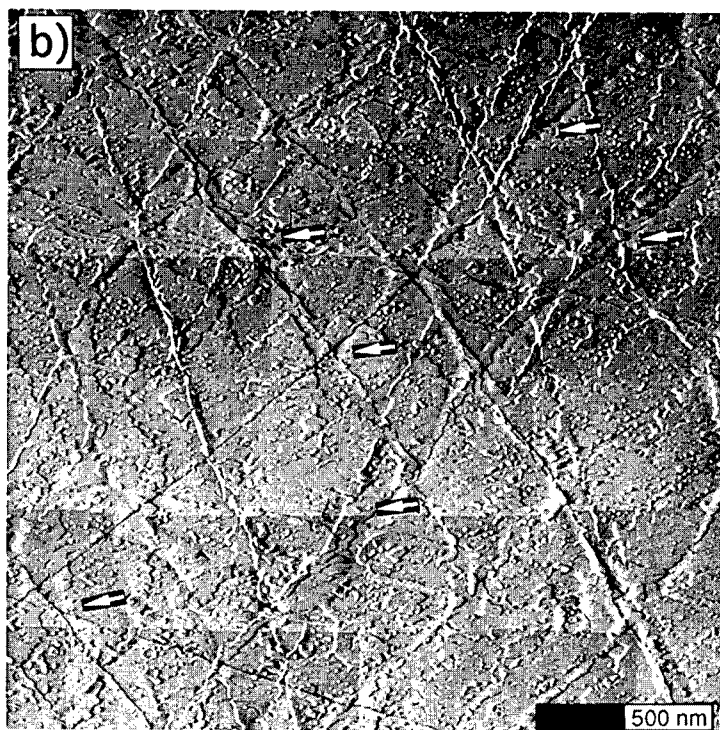
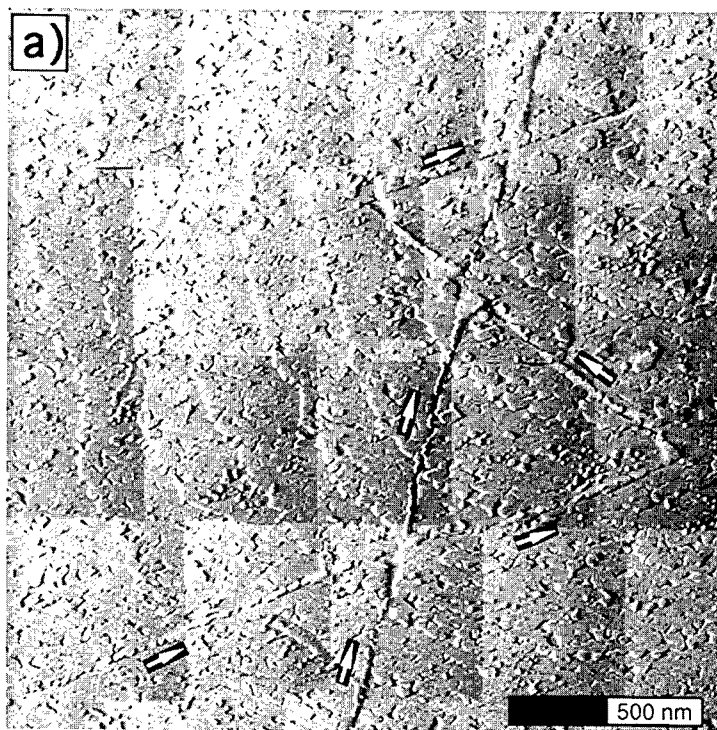
PbTe, Eu and Te, as described in detail in Ref. [7]. First, several μm thick PbTe buffer layers were deposited on freshly cleaved BaF₂ (111) substrates (lattice-mismatch of 4.2%). Because of the complete strain relaxation and their high structural perfection [9], these buffer layers serve as ‘virtual’ substrates for the subsequent overlayer deposition. EuTe growth is controlled by the Eu flux impinging on the surface and excess Te₂ flux is supplied due to its high re-evaporation rate. For the study of the surface structure, EuTe growth was stopped after well defined growth sequences, and after rapid cooling to room temperature, the samples were transferred to an attached UHV-chamber equipped with a BEETLE STM. Large-scale STM images were mounted together from several $0.5 \times 0.5 \mu\text{m}^2$ STM images recorded in a reproducible step and scan mode.

3. The surface evolution of EuTe on PbTe (111)

In the following the surface evolution of EuTe on PbTe (111) is studied for 2D layer-by-layer growth conditions [7], i.e., for a substrate temperature of 270°C and Eu and Te₂ fluxes of 0.4 and 1.2 ML/s, respectively. For the EuTe (111) surface, one ML corresponds to a layer thickness of 3.8 Å or to a flux of 5.54×10^{14} atoms/cm². For the given growth conditions, up to a layer thickness of 42 ML pronounced RHEED intensity oscillations are observed after which an abrupt damping of the RHEED oscillations sets in, indicating an abrupt surface roughening transition [10]. In order to clarify the origin of this roughening transition, the growth was interrupted at various EuTe coverages up to 70 ML, and after rapid cooling, the samples were transferred to the STM chamber for imaging of the surface structure.

As described in Ref. [10], the surfaces of the initial PbTe buffer layers are extremely smooth. The main surface features are large growth spirals formed around the core of threading dislocations that originate from the growth of PbTe on the 4.2% lattice-mismatched BaF₂ substrates. The density of the ob-

Fig. 1. STM surface images EuTe epitaxial layers grown on PbTe (111) with layer thicknesses of (a) 25 and (b) 30 ML. As indicated by the arrows, additional step lines appear on the surface due to glide of grown-in threading dislocations. The grey scale in the images corresponds to the local derivative of the height in the horizontal direction.



served threading dislocations is of the order of 10^7 cm^{-2} , in good agreement with transmission electron microscopy studies [11]. The smooth spiral step edges are exactly one monolayer in height (3.73 Å) and the totally flat terraces between the steps have widths of the order of 1000–2000 Å. Since no 2D islands are nucleated on top of the flat terraces PbTe growth mainly proceeds in a step flow growth mode.

Representative STM images of EuTe layers grown on these PbTe buffer surfaces are shown in Fig. 1. Due to the layer-by-layer growth mode, initially, the basic spiralled surface structure of the PbTe buffer layer is replicated on the EuTe surface (Fig. 1a). However, due to the much shorter adatom surface diffusion lengths in EuTe MBE growth on a local length scale, the surface is much more corrugated, i.e., small monolayer islands are nucleated on the terraces of the growth spirals and the spiral step edges become extremely ragged. Starting at a EuTe layer thickness of about 17 ML, however, completely new surface features are observed on the epitaxial surface. As indicated by arrows in Fig. 1a, these surface features are totally straight monolayer step lines of tens of μm in length, which are oriented parallel to certain crystallographical directions. These monolayer surface step lines cut right through all other surface features such as 2D islands and spiral step edges, and are formed very rapidly compared to the usual step propagation rate due to adatom incorporation from the incoming flux. As growth is continued, at first the number of surface step lines increases only very gradually with EuTe coverage, but beyond 40 ML increases very rapidly by one order of magnitude [12].

In large scale STM images, the end points of the newly formed surface step lines can be identified as the penetration points of the threading dislocations which apparently have moved by several micrometers parallel to the surface. Such a dislocation glide process is exactly what is expected for the classical Matthews–Blakeslee mechanism for strain relaxation [8]. In this model, the coherency stress results in a force acting on the threading dislocations grown-in from the substrate. This force increases linearly with layer thickness and it is opposed by the dislocation line tension. At the critical layer thickness, the coherency force exceeds the dislocation line tension, and thus, the threading dislocations start to move

parallel to the surface and bend over to form strain-relaxing misfit dislocation segments at the layer/substrate interface. However, due to the normal component of the Burgers vector, not only a misfit dislocation segment is produced, but also a monolayer surface step line at the point where the glide plane intersects with the epitaxial surface. This is exactly what is observed by STM.

Initially, the observed surface step lines only include angles of 60° with respect to each other (see Fig. 1a). This is consistent with the primary (100)[011] glide system typical for the lead salt compounds, where misfit dislocation segments parallel to the sixfold $\langle\bar{1}10\rangle$ directions are formed upon lateral movement of threading dislocations. Since for this dislocation configuration the $1/2[011]$ type Burgers vectors \mathbf{b} are normal to the dislocation line direction, these misfit dislocation segments are of pure edge character and thus effectively relieve in-plane strain. However, as the layer thickness increases dislocations also along other crystallographical directions are observed, resulting in angles of 30° , 90° , and of 20° , 40° and 80° between surface step lines (see arrows in Fig. 1b)). Thus, at larger layer thicknesses secondary glide systems are activated in the strain relaxation process. From the observed additional $\langle\bar{2}11\rangle$ and $\langle\bar{3}21\rangle$ misfit dislocation line directions, dislocation glide must also take place in the $(\bar{2}11)[011]$ and $(\bar{3}11)[011]$ glide systems. For these glide systems, the dislocation self energy is almost the same as for the (100)[011] glide system, but the relieved strain per misfit dislocation is somewhat smaller due to the partial screw character of the dislocations. Therefore, the corresponding Matthews–Blakeslee critical layer thickness is somewhat larger, i.e., is 14.1, 17.0 and 20.3 ML for the for the (100)[011], $(\bar{3}11)[011]$ and the $(\bar{2}11)[011]$ glide systems, respectively.

The appearance of these secondary glide systems is based on the fact that up to EuTe layer thicknesses of about 40 ML, the epitaxial layers are found to be highly metastable since only a very small fraction of the total misfit strain is relieved [12]. E.g., the misfit dislocation line density observed at 25 ML EuTe (Fig. 1a) corresponds to a relaxed strain of only 1.5×10^{-4} . Since this is less than 1% of the total of the misfit strain of 2.1%, up to a thickness of 35 ML, the EuTe layers can still be considered as being

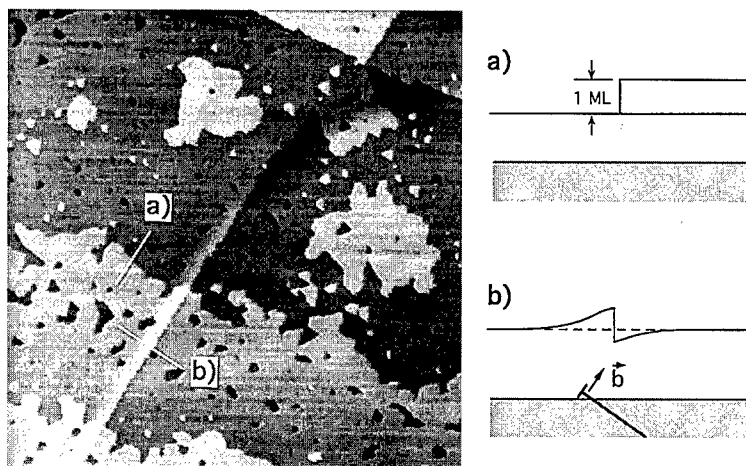


Fig. 2. STM height image ($0.5 \times 0.5 \mu\text{m}^2$) of a 25 ML EuTe layer on PbTe (111) including a single dislocation glide step. The surface profiles along the lines marked (a) and (b) are shown schematically on the right hand side of the figure.

essentially fully strained with respect to the PbTe buffer. Thus, when the critical layer thickness for a secondary glide system is exceeded, dislocation glide in this system becomes possible.

4. Local surface distortions induced by misfit dislocations

Up to now, we have only treated the glide steps created by the misfit dislocation formation process. However, the local lattice distortions around the misfit dislocations at the interface also cause a significant local deformation of the epitaxial surface [13,14]. This is shown in the STM surface image of a 25 ML EuTe layer in the vicinity of a single misfit

dislocation (Fig. 2). As indicated on the right hand side of Fig. 2, each step observed on the surface corresponds to a height change of exactly one monolayer (profile along line a), which is reflected by an abrupt change of the grey level in the STM image. In contrast, across a dislocation glide step (profile along b), there is an additional wave-like surface distortion which compensates the glide step of the dislocation, i.e., at distances more than 200 \AA away from the glide step, the surface height is the same on both sides of the dislocation in spite of the monolayer glide step in between.

As is illustrated in Fig. 3, the type of surface distortion strongly depends on the orientation of the Burgers vector. For an arbitrary dislocation lying at a fixed distance below the surface, the Burgers vector

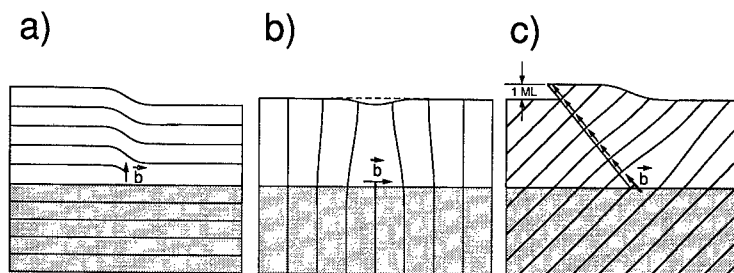


Fig. 3. Schematic illustration of the surface distortions induced by misfit dislocations at the layer/substrate interface for different orientations of the Burgers vector \vec{b} : (a) \vec{b} normal to the interface, which causes a wave-like surface deformation, (b) \vec{b} parallel to the interface, resulting in a Lorentzian shape surface deformation, (c) usual misfit dislocation with \vec{b} inclined to the interface. The corresponding asymmetric surface deformation is a result of the superposition of surface deformations of type (a) and (b).

\mathbf{b} can be split into three parts: (1) a component b_{\perp} normal to the interface, (2) an edge component $b_{\parallel, \text{edge}}$ parallel to the interface, and (3) a screw component $b_{\parallel, \text{screw}}$, also parallel to the interface plane. As shown in Fig. 3a, the b_{\perp} component corresponds to an additional lattice plane removed or inserted parallel to the surface. Therefore, a symmetric wave-like surface deformation is induced for which the total deformation amplitude is equal to b_{\perp} . In contrast, the $b_{\parallel, \text{edge}}$ component corresponds to an additional lattice plane inserted or removed in the direction normal to the surface (Fig. 3b), which results in a Lorentzian shaped depression or elevation of the surface above the misfit dislocation [14]. Since for the screw component $b_{\parallel, \text{screw}}$, the lattice displacements are all parallel to the surface, no surface normal displacements are induced by this component. For an arbitrary misfit dislocation whose Burgers vector is inclined to the interface, the resulting surface distortion is given by the superposition of the deformations of the corresponding b_{\perp} and $b_{\parallel, \text{edge}}$ components, and thus an asymmetric wave-like surface distortion is induced. In Fig. 3c, also the monolayer surface step caused by the glide of the lattice planes in the direction \mathbf{b} is included, showing

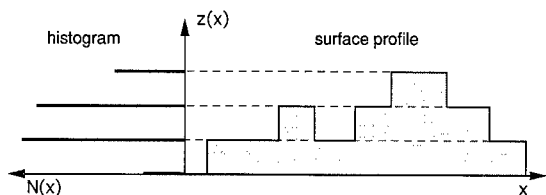
that the surface glide step is displaced from the position of the misfit dislocation in the horizontal direction. It should be noted, that as growth is continued, this surface glide step moves away from its original position due to adatom incorporation at the step edge, whereas the local surface deformation is spatially fixed above the misfit dislocation. Thus, from the distance between the glide step and the local surface distortion information on the time scale of the dislocation formation can be obtained.

It is clear that the local surface deformations are a direct fingerprint of the misfit dislocations lying at the interface and in the STM height images the misfit dislocations show up as lines at which a gradual contrast change takes place in absence of a surface step. This is shown in the STM height image of a 30 ML EuTe layer on PbTe (111) depicted in Fig. 4. At this stage a complicated network of misfit dislocations has formed and at the intersections between dislocations a number of dislocation reactions are observed. In particular, two misfit dislocations with $1/2[011]$ type Burgers vector can react to form a single misfit dislocation with a Burgers vector of $1/2[110]$ type. This new dislocation has a Burgers vector parallel to the interface and thus produces a



Fig. 4. STM height image of a 30 ML EuTe layer on PbTe (111) showing the formation of a complicated network of misfit dislocations.

a) coherent stepped surface



b) incoherent stepped surface

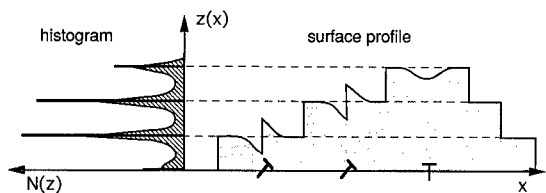


Fig. 5. Schematic illustration of the surface profile and histogram, (a) for an ideal stepped surface, and (b) for a stepped surface of an incoherent epitaxial layer with misfit dislocations at the interface. In case (a), only surface heights z equal to an integer number times the monolayer thickness d_{ML} are present, whereas in case (b) due to the local surface deformations induced by misfit dislocations a continuous distribution of z -values exists.

groove-like surface depression as shown in Fig. 3b. Such a misfit dislocation cannot be formed by the usual Matthews–Blakeslee mechanism.

Based on the existence of local surface deformations due to interfacial misfit dislocations, the contrast in the STM images can be adjusted such that these deformed surface regions appear as black areas in the STM images, just like in a bright field transmission electron microscopy image. As is illustrated in Fig. 5a, the surface of a stepped but fully coherent epitaxial layer consists only of surface areas with surface heights z equal to a multiple of $n \times d_{ML}$, where n is an integer number and d_{ML} is the height of one monolayer. Thus, the surface histogram $N(z)$ consist only of delta functions at $z = n \times d_{ML}$, i.e., $N(z)$ is zero for $z \neq n \times d_{ML}$. In contrast, for a dislocated incoherent epitaxial layer, the local surface deformations result in the presence of surface areas with $z \neq n \times d_{ML}$ (see Fig. 5b). If these surface areas are now assigned to grey level 0, they appear as black areas in the STM image, signifying a local deviation from the surface of a perfect crystal.

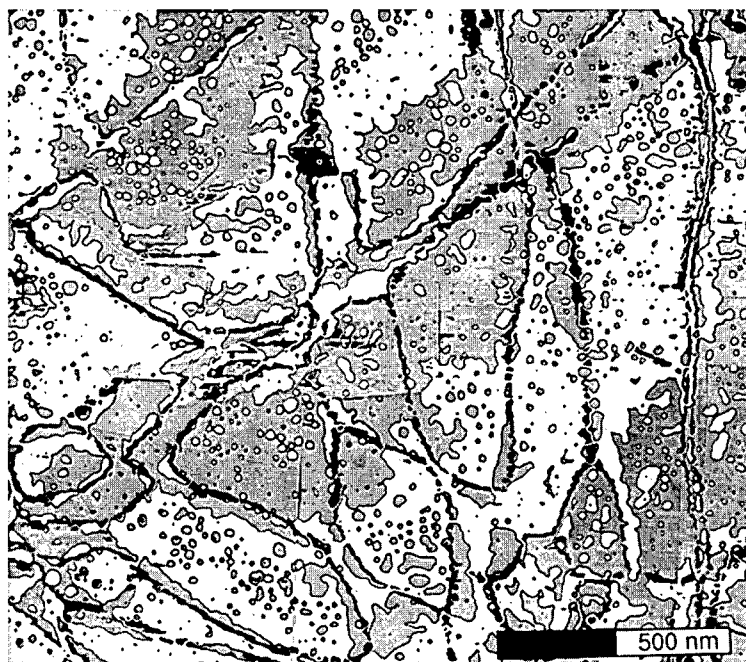


Fig. 6. Modified representation of the STM image shown in Fig. 4 with enhanced contrast between regular surface areas (alternating white/grey), and surface areas displaced by the strain fields of misfit dislocations (black). The grey scale in the image is adjusted such that surface areas with a height within intervals of $(n \times d_{ML}) \pm \Delta$ appear alternating white/grey (n : integer number and $\Delta = d_{ML}/10$), whereas surface areas with other z -values appear black.



Fig. 7. STM height image of a 65 ML EuTe layer on PbTe (111) showing the formation of multiple step surface elevations due to pile-up of misfit dislocations.

In other words, the misfit dislocations responsible for the local surface displacements will show up as black lines in the STM image.

The contrast between the dislocated and the dislocation free surface areas is further enhanced if a constant white or grey intensity level is assigned to the surface areas in registry with the surface of a perfect crystal, i.e., for $z = n \times d_{\text{ML}}$. For a real STM surface image, this condition has to be somewhat relaxed in order to take into account the background noise level, i.e., a surface area is assumed to be in registry with a perfect crystal if z lies within an interval of $n \times d_{\text{ML}} \pm \Delta$, where Δ is $1/10$ of d_{ML} in our case. Fig. 6 shows the such modified STM image of the 30 ML EuTe layer of Fig. 4. In order to retain the information on the overall surface structure, the perfect surface areas appear alternating with n as white or grey surface areas. Now surface features such as 2D islands and spiral step edges growth and the surface deformations due to misfit dislocations can be easily distinguished, and the thus formed misfit dislocation network becomes directly visible.

When epitaxial growth is continued beyond 40 ML, the number of misfit dislocations drastically increases forming a dense network of misfit dislocations [10,12]. At this stage, the original spiral structure on the surface vanishes since the surface structure is now totally dominated by the high density of surface step lines generated by the dislocation glide processes. Since the freshly created surface step lines are continuously overgrown by the subsequently deposited material, the individual 'older' step lines

eventually become very ragged and are no longer clearly visible. At places where several dislocations intersect multiple-step triangular-shaped islands are formed. As is shown in Fig. 7 for 65 ML EuTe coverage, this type of surface feature is progressively enhanced when growth is continued, leading to a significant roughening of the epitaxial surface, which is also reflected by the increase of the RMS roughness of the EuTe surface by a factor of 4 [10]. As long as the average spacing of the formed glide steps on the surface is much larger than the EuTe adatom surface diffusion length of about 200 Å the 2D layer-by-layer growth mode is essentially unperturbed. However, at about 40 ML the average spacing between these newly formed step lines becomes comparable to the adatom surface diffusion length and thus more and more impinging adatoms are incorporated at these surface step edges instead of nucleating 2D islands. As a result, the growth mode changes from the initial layer-by-layer growth to a step flow growth mode, which explains the rapid damping of the RHEED intensity oscillations at a EuTe layer thickness of about 42 ML.

5. Conclusions

Misfit dislocation formation in strained-layer heteroepitaxy of 2.1% lattice-mismatched EuTe on PbTe (111) was studied using scanning tunnelling microscopy. It was found that the formation of misfit dislocation segments by the glide of grown-in thread-

ing dislocations produces a monolayer surface step line along the glide line directions. When the layer thickness significantly exceeds the critical layer thickness, the formation of misfit dislocations not only along the $\langle 110 \rangle$ direction, but also along the $\langle \bar{2}11 \rangle$ and $\langle \bar{3}21 \rangle$ directions is observed, which indicates the activation of secondary glide systems, although the Matthews–Blakeslee critical layer thickness calculated for the primary glide system agrees quite well with the EuTe layer thickness of 17 ML at which the first monolayer step lines appear on the epitaxial surface. In addition to the glide steps, the lattice-distortions around the misfit dislocation segments induce significant local distortions of the surface above the dislocation, which can be detected by STM as wave-like surface displacements. The exact form of this local surface distortion depends on the orientation of the Burgers vector and its width is proportional to the layer thickness. Therefore, the local surface deformations are a clear fingerprint of the misfit dislocation at the interface and by a modification of the contrast in the STM images, the formed dislocation network can be directly observed and reactions between misfit dislocations can be observed.

Acknowledgements

This work was supported by the Deutsche Forschungsgemeinschaft (No. SP 466/1-1) and by

the Gesellschaft für Mikroelektronik, Vienna, Austria.

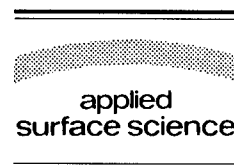
References

- [1] See e.g. *Semiconductors and Semimetals*, Vols. 32 and 33, Ed. T.P. Pearsall (Academic Press, Boston, MA, 1991).
- [2] D.J. Eaglesham and M. Cerullo, *Phys. Rev. Lett.* 64 (1990) 1943.
- [3] C.W. Snyder, B.G. Orr, D. Kessler and L.M. Sander, *Phys. Rev. Lett.* 66 (1991) 3032.
- [4] D.J. Srolovitz, *Acta Met.* 37 (1989) 621.
- [5] C. Ratsch and A. Zangwill, *Surf. Sci.* 293 (1993) 123.
- [6] J.J. Chen, Z.H. Wang, M.S. Dresselhaus, G. Dresselhaus, G. Springholz and G. Bauer, *Solid State Electron.* 373 (1994) 107.
- [7] G. Springholz and G. Bauer, *Phys. Rev. B* 48 (1993) 10998.
- [8] J.W. Matthews and A.E. Blakeslee, *J. Cryst. Growth* 27 (1974) 118.
- [9] E. Koppensteiner, G. Springholz, P. Hamberger and G. Bauer, *J. Appl. Phys.* 74 (1993) 6062.
- [10] G. Springholz, N. Frank and G. Bauer, *Appl. Phys. Lett.* 64 (1994) 2970; *Thin Solid Films* 267 (1995) 15.
- [11] P. Pongratz, H. Clemens, E.J. Fantner and G. Bauer, *Inst. Phys. Conf. Ser.* 76 (1985) 331.
- [12] N. Frank, G. Springholz and G. Bauer, *Phys. Rev. Lett.* 73 (1994) 2236.
- [13] M.A. Lutz, R.M. Feenstra, F.K. LeGoues, P.M. Mooney and J.O. Chu, *Appl. Phys. Lett.* 66 (1995) 724.
- [14] R. Stalder, H. Sirringhaus, N. Onda and H. von Känel, *Appl. Phys. Lett.* 59 (1991) 1960.



ELSEVIER

Applied Surface Science 104/105 (1996) 646–651



Reconstruction and chemical ordering at the surface of strained (In, Ga) As epilayers

M. Sauvage-Simkin^{a,b,*}, Y. Garreau^b, R. Pinchaux^{b,c}, A. Cavanna^{b,1}, M.B. Véron^b,
N. Jedrecy^a, J.P. Landesman^d, J. Nagle^d

^a Laboratoire de Minéralogie-Cristallographie, CNRS, Universités P. et M. Curie et D. Diderot, 4 Place Jussieu, F-75252 Paris-Cedex 05, France

^b Laboratoire pour l'Utilisation du Rayonnement Electromagnétique (LURE), Batiment 209D, Université Paris-Sud, F-91405 Orsay, France

^c Université P. et M. Curie, 4 Place Jussieu, F-75252 Paris-Cedex 05, France

^d Laboratoire Central de Recherches, Thomson-CSF, F-91404 Orsay, France

Received 28 June 1995; accepted 10 October 1995

Abstract

An evidence for a cation chemical ordering in 2×3 reconstructed surfaces of strained $\text{In}_x\text{Ga}_{1-x}\text{As}$ layers, locking the composition at the value $\text{In}_{0.67}\text{Ga}_{0.33}\text{As}$, has been obtained by grazing incidence X-ray diffraction. For lower surface concentrations, the reconstruction becomes incommensurate $2 \times n$ and is described by introducing a random distribution of indium-free faults in the commensurate 2×3 phase. A quantitative account of the intensity distribution is obtained.

1. Introduction

Indium surface segregation in a gallium arsenide matrix is a major problem for device elaboration since it generates composition gradients at interfaces in $\text{In}_x\text{Ga}_{1-x}\text{As}/\text{GaAs}$ heterostructures and at the surface of ternary alloys. If a good modelisation of the indium in-depth distribution, measured in photoluminescence [1] or photoelectron spectroscopy [2] experiments, has been obtained by the introduction of a surface segregation energy, no interpretation is

available yet in terms of atomic structure for the specific reconstructions observed in these systems and never present at the surface of strain free III–V binary compounds, namely a commensurate 2×3 [3] and an incommensurate $2 \times n$ [4].

Being sensitive to long and short range order in the surface and near surface region, grazing incidence X-ray diffraction (GIXD) is an optimal tool to address this question. An unambiguous assignment of the atoms involved in the surface structure is possible as far as their atomic numbers are sufficiently different, which is obviously the case for indium and gallium.

In the present work, it will be demonstrated that the 2×3 reconstruction observed in arsenic rich experimental conditions corresponds to a unique structure with a chemical ordering between indium and gallium leading to an indium surface concentra-

* Corresponding author. Fax: +33-1-64464148; e-mail: sauvage@lure.u-psud.fr.

¹ Present address: Laboratoire de Microstructures et de Micro-electronique, CNRS–CNET, BP 107, 196 Av. H. Ravera, F-92225, Bagneux (France).

tion of 0.67. The transition towards an incommensurate structure, as the indium surface concentration decreases, is readily explained by the multiplication of faulted sequences with indium free structural blocks forming local patches with the clean GaAs $c(4 \times 4)$ configuration.

2. Experimental

A series of samples has been prepared in the molecular beam epitaxy (MBE) growth chamber attached to the ultra-high vacuum (UHV) surface diffractometer (LURE, synchrotron radiation facility, Orsay, France, bending magnet beam line D25a and wiggler beam line DW12). Thick GaAs substrates, $18 \times 13 \times 2 \text{ mm}^3$, cut within 0.1 deg. of the nominal (001) orientation and mechanochemically polished were deoxidized in a solution ethanol–10% HCl and further annealed in the vacuum chamber at 600°C under an As flux until a sharp 2×4 RHEED pattern was observed. A 5000 Å thick GaAs buffer layer was grown in standard conditions and from then on, two different procedures were adopted. In a first approach, fully strained, ternary alloys with nominal compositions $\text{In}_{0.20}\text{Ga}_{0.80}\text{As}$ and $\text{In}_{0.28}\text{Ga}_{0.72}\text{As}$ calibrated by use of the RHEED oscillations frequency were grown at 520°C and a rate of about 0.5 ML/s. After cooling under the arsenic flux, the RHEED pattern turned from a diffused 1×1 at the growth temperature into a $2 \times n$ (with n close to 3). For the nominal concentration $x = 0.2$ two samples were prepared with thicknesses 3 ML (9 Å) and 6 ML, whereas only one sample with thickness 3 ML was prepared with $x = 0.28$. In the following these three samples will be referred to as T_1 , T_2 and T_3 . In the second approach, a single InAs layer was deposited at 450°C and further covered by a GaAs cap of respectively 0, 1, 5 and 10 ML, the four samples of this second series will be referred to as G_0 , G_1 , G_5 and G_{10} . The first two samples showed a clear $x3$ reconstruction on cooling whereas sample G_5 showed a slightly more diffused incommensurate xn RHEED pattern (with $n < 3$) and sample G_{10} presented very diffused streaks mostly centred on half-order positions.

The two growth procedures are expected to deliver samples with variable indium surface concen-

trations which can be roughly evaluated from the data published in the literature [1,2].

After completion of the growth process, each sample has been transferred, under vacuum, on the diffractometer stage and surface diffraction data were collected under grazing incidence at the critical angle for total reflection: 0.28° for samples T_1 , T_2 and T_3 studied at a wavelength of 1.488 Å and 0.2° for the others studied at $\lambda = 1$ Å. Since the geometry of the diffractometer did not allow for a perpendicular momentum transfer, only hkl reflections with $l \neq 0$ have been measured carrying the information on the surface structure projected on the surface plane.

3. Results and discussion

3.1. The commensurate 2×3 surface

Although their preparation conditions were quite different, the four samples T_2 , T_3 (ternary alloys at 20% and 28% In), G_0 and G_1 (uncapped and 1 ML GaAs capped InAs strained monolayer) showed a commensurate 2×3 reconstruction. Moreover, the measured fractional peak intensities were found identical within the 10% experimental accuracy in samples G_0 and G_1 , whereas those measured in the two ternary samples were linearly related to the other two through a mere scaling factor (Fig. 1). Prior to any further analysis it can thus be anticipated that the surface structure is the same in the four cases which

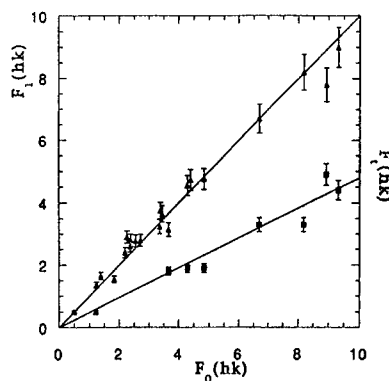


Fig. 1. Structure factors of sample G_1 (triangles) and T_3 (squares) as a function of the corresponding structure factors in sample G_0 the linear correlation demonstrates the identity of the surface structure in the three samples.

means either that the reconstruction is due to a similar arsenic distribution on an undisplaced chemically disordered cation layer or, in contrast, that indium exodiffusion ensures an identical cation last layer in the three samples.

The analysis was first performed on sample G_0 data. The surface unit cell is referred to the face centred cubic basis vectors as follows:

$$a_s = [\bar{1}\bar{1}0], \quad b_s = \frac{3}{2}[110], \quad c_s = [001].$$

Reflections are indexed in the corresponding reciprocal basis and although all indices are integer in such a basis, superstructure reflections will be referred to as fractional peaks whereas those common with the 1×1 bulk derived reciprocal lattice are called integer orders to match the usual vocabulary. 27 independent fractional orders and seven integer orders have been measured and used for the refinement procedure. The trial model was inspired from the structural elements identified in arsenic rich surfaces namely chemisorbed As dimers on an As terminal plane along $[110]$ and As dimers bonded to cations along $[\bar{1}\bar{1}0]$ combined to produce the required 2×3 symmetry, a schematic of the model is presented in Fig. 2. According to Pashley [5], it is known that the surface neutrality condition cannot be fulfilled with

such a dimer concentration and this question will be addressed later on.

The origin for the surface and bulk coordinates is taken on the Ga atom in the second cation layer below the surface. The free parameters for the fit were an overall scale factor, the y coordinates of As(1) and As(3), the x coordinate of As(2), the x and y coordinates of In(1), In(2) being kept fixed and finally two Debye–Waller coefficients for surface and bulk atoms, respectively. Assuming first that the last cation layer was a complete indium layer, lead to a χ^2 residue of 6.7 with the overall dynamics of the data sufficiently well reproduced to ensure that the model carried part of the real structure. In a second step, a partial occupancy of the indium layer by gallium atom was allowed and a reduction to 2.6 of the residue was obtained for a full indium occupancy of the In(1) site and an almost complete substitution by gallium of the In(2) site: the minimum value was obtained for 0.82 Ga and 0.18 In but this minimum is rather flat between 0.7 and 1 Ga atom on the site whereas the residue raises rapidly below 0.7 Ga.

The comparison between observed and calculated structure factors is displayed in Fig. 3. The reliability factor R defined as:

$$R = \frac{\sum |F_{hkl}^{obs} - F_{hkl}^{calc}|}{\sum F_{hkl}^{obs}}$$

is equal to 16% for this structure proposition.

The atomic positions at the surface are listed in Table 1, together with the As dimer length, directly derived from the data since the dimers are assumed parallel to the surface plane. The pattern for the z coordinates is only tentative and selected to ensure interatomic bond lengths close to the strain free values in binary materials (Ga–As = 2.45 Å and In–As = 2.61 Å), out-of-plane data, to be collected in a future experiment will enable to finalize the 3D description of the atomic arrangement. However, a total energy minimization performed with the density functional theory [6] on a model 2×2 unit cell having the same local configuration as As(2), In(1) and As(3) gave x , y , z coordinates for the three atoms very similar to the ones quoted in Table 1. The analysis of sample G_1 data with the same model gave a χ^2 value of 2.4 with atomic parameters

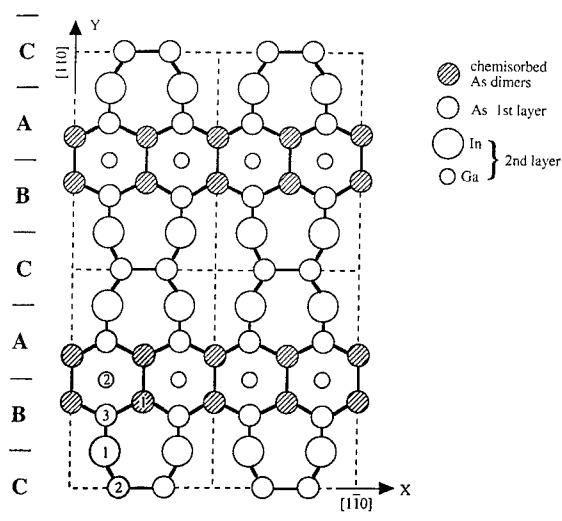


Fig. 2. Projected model of the atomic arrangement in the surface 2×3 unit cell. Labels refer to the atoms whose coordinates are listed in Table 1.

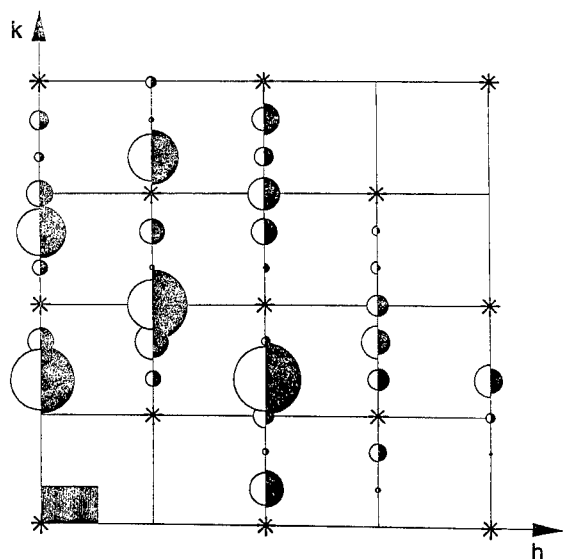


Fig. 3. Comparison between observed (black semicircles) and calculated (white semicircles) structure factors for the best fit in sample I. A square grid outline the 1×1 bulk derived reciprocal lattice where stars mark the location of bulk allowed nodes. The shaded rectangle indicate the 2×3 reciprocal unit cell used for the hk indexation.

within the accuracy of the present determination and the more limited data sets collected with samples T_2 and T_3 were equally compatible with the model.

The main conclusion of this analysis is that a chemical order in the cation top layer locks the surface composition at $\text{In}_{0.67}\text{Ga}_{0.33}\text{As}$ and stabilizes the 2×3 reconstruction both in ternary alloys and in monolayer thick heterostructures where an almost complete exchange between In and Ga takes place in the last two surface layers. Since the intensity of integer orders is not so well reproduced, it was attempted to model the cation distribution in the deeper layers: for sample G_0 and G_1 , it was not

possible to make a definite assignment since in both cases, the data are compatible with an amount of 0–0.2 In in the second cation layer. For the ternary T_3 , the best agreement is obtained with 0.4 In in the second layer over a nominal bulk at 0.25.

As mentioned before, such a model does not fulfil the surface neutrality condition. There is an excess positive charge located on the As(3) site which can be balanced by non-dimerized arsenic along $[1\bar{1}0]$. Indeed, the distribution of As(2) dimers is highly disordered and the expected half-order lines for the $2 \times$ reconstruction are too diffuse to be measured.

4. The incommensurate $2 \times n$ phases

As outlined above, sample G_5 and the ternary alloy T_1 showed an incommensurate $2 \times n$ reconstruction with n slightly smaller than 3. Since in both cases, the In surface concentration was expected to be smaller than for the preceding samples, the structure was assumed to be a faulted 2×3 where the In rich element would be randomly removed. When one considers the model in Fig. 2 it can be decomposed into three blocks A, B and C, A and B being Ga rich and C containing the In atoms. Describing the system as a one dimensional stacking along $[1\ 1\ 0]$, the sequence in the ideal 2×3 structure is ABCABCABC, however, if one introduces a probability $p \neq 1$ of finding C after the AB pair, the surface is no longer perfectly periodic and faulted sequences of the type ABABCABCABABABC are found. At the other end, the periodic case ABABABAB, obtained for $p = 0$, corresponds to the arrangement of the GaAs(001) surface, reconstructed $c(4 \times 4)$, provided an ordered distribution of missing chemisorbed As dimers is allowed. The expected diffraction pattern

Table 1
Atomic coordinates in unit $a_0/\sqrt{2}$ along x , $3a_0/\sqrt{2}$ along y and a_0 along z with $a_0 = 5.6532 \text{ \AA}$

Atom	In(1)	Ga, In(2)	As(1)	As(2)	As(3)
x	0.25	0.25	0.5	0.345 ± 0.015	0.25
y	0.150 ± 0.003	0.50	0.400 ± 0.004	0	0.350 ± 0.004
z	$-0.42 (-0.50)$	-0.50	$0.045 (0.0)$	$-0.10 (-0.25)$	$-0.21 (-0.25)$

The z coordinates are tentatively chosen to keep Ga–As and In–As distances close to their strainfree values 2.45 and 2.63 \AA , respectively, and are only given to show the displacement trends from GaAs bulk derived positions marked between brackets.

Dimer bondlength: As(1)–As(1) = $2.40 \pm 0.03 \text{ \AA}$ As(2)–As(2) = $2.48 \pm 0.03 \text{ \AA}$.

of such a surface can be calculated by use of the diffuse scattering formalism: in the Born approximation the diffracted amplitude for a momentum transfer Q is given by

$$A(Q) = \sum_{\text{all sites } n} F_n e^{-iQr_n}$$

where F_n stands for the scattering factor of the block with position vector r_n (F_A , F_B or F_C). The diffracted intensity

$$I(Q) = A(Q) \times A(Q)^*$$

is then given by

$$\begin{aligned} I(Q) &= \sum_{n'} \sum_n F_n F_{n'}^* e^{-iQ(r_n - r_{n'})} \\ &= \sum_m \langle F_n F_{m+n}^* \rangle e^{iQr_m} \end{aligned}$$

where $\langle F_n F_{m+n}^* \rangle$ is the average structure factor product for two blocks separated by the vector r_m and can be expressed in terms of the probability $P_{XY}(m)$ for an X block in concentration c_X to have a Y block as an m th neighbour, with X (resp. Y) = A, B or C:

$$\langle F_n F_{m+n}^* \rangle = \sum_X c_X \sum_Y P_{XY}(n) F_X F_Y^*$$

With the specific constraints of the model: AB undissociable and probability p to find a C element after an AB pair, the literal expressions of the P_{XY} can be derived by a recurrent matrix algebra procedure as a function of p and m and the intensity distribution can be calculated [7]. The major consequence for $p \neq 1$ is the occurrence of maxima shifted from commensurate positions and weighted by a generalized structure factor. In sample G_5 the observed shift lead to a value of 0.6 for p from which the expected intensity has been simulated. Fig. 4 shows the comparison between the calculated distribution along the reciprocal row $[2, k]$ and the measured values at the local maxima, the only free parameters being a scale factor and the probability p since the atomic positions were those derived from the commensurate structure. The agreement assesses that the model gives an accurate interpretation for the origin of the incommensurate phase. The surface composition, derived from the p value according to $[\text{In}]_s = p(1+p)/2 + p$ is found equal to 0.37, close to the value 0.3 estimated from the literature [1].

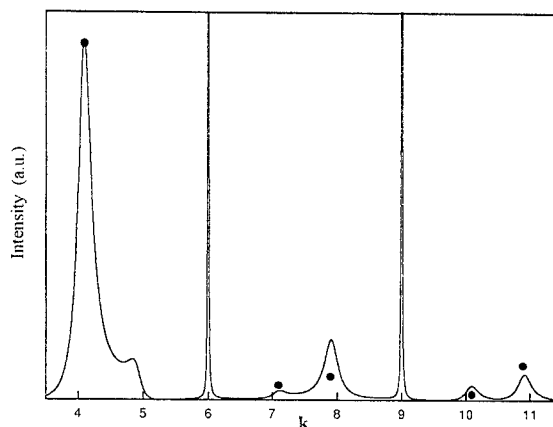


Fig. 4. Calculated intensity distribution along the reciprocal row $h=4$ as a function of k in the incommensurate phase. Measured satellites integrated intensities are marked by bold dots.

The peak shift in the ternary alloy T_1 was slightly smaller than in sample G_5 and the corresponding p value was 0.65 leading to a surface indium concentration of 0.4. This amount, significantly smaller than the equilibrium value at the surface of a nominal alloy with 20% of indium is explained by the 3 ML thickness of the deposit which did not allowed the steady state to be reached contrary to the 6 ML sample with the same nominal composition (sample T_2).

Finally the X-ray diffraction pattern collected with sample G_{10} showed a superposition of broad maxima at half-order positions along the k -axis which correspond to a dilute surface alloy together with sharper half and quarter-order peaks characteristic of the $c(4 \times 4)$ GaAs (001) surface.

The present study has thus given a clue for the occurrence of a common 2×3 reconstruction at the surface of strained ultrathin heterostructures in the InAs/GaAs system, stabilizing the surface indium concentration at 0.67 with a chemical ordering between In and Ga. The transition towards an incommensurate phase as the indium surface concentration decreases is clearly interpreted and leads naturally to the configuration of the clean GaAs(001) arsenic saturated $c(4 \times 4)$ surface. The unique ability of X-ray diffraction to probe the atomic ordering not only in the top layer but in the whole near surface region has enabled to reach the essential features of these complex systems.

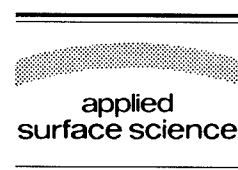
References

- [1] J.M. Gérard and J.Y. Marzin, *Phys. Rev. B* 45 (1992) 6313.
- [2] J. Nagle, J.P. Landesman, M. Larive, C. Mottet and P. Bois, *J. Cryst. Growth* 127 (1993) 550.
- [3] J.M. Moison, C. Guille, F. Houizay, F. Barthe and M. Van Rompay, *Phys. Rev. B* 40 (1989) 6149.
- [4] J.M. Moison, C. Guille and M. Bensoussan, *Phys. Rev. Lett.* 58 (1987) 2555.
- [5] M.D. Pashley, *Phys. Rev. B* 40 (1989) 10481.
- [6] L. Bellaïche, K. Kune, M. Sauvage-Simkin and Y. Garreau, in preparation.
- [7] T.R. Welberry, *Rep. Prog. Phys.* 48 (1985) 1543.



ELSEVIER

Applied Surface Science 104/105 (1996) 652–655



Interface abruptness in strained III–V heterostructures

M.R. Bruni, S. Kačiulis^{*,1}, G. Mattogno, G. Righini

Istituto di Chimica dei Materiali, CNR, P.O. Box 10, I-00016 Monterotondo Scalo, Italy

Received 28 June 1995; accepted 13 December 1995

Abstract

Highly strained $\text{In}_{0.53}\text{Ga}_{0.47}\text{As}/\text{InAs}/\text{In}_{0.53}\text{Ga}_{0.47}\text{As}$ heterostructures and InAs layers were grown on InP (100) substrates by using molecular beam epitaxy (MBE). The samples have been investigated by means of selected-area X-ray spectroscopy (SAXPS) combined with low energy ion sputtering. The heterointerface widths in the $\text{In}_{0.53}\text{Ga}_{0.47}\text{As}/\text{InAs}/\text{In}_{0.53}\text{Ga}_{0.47}\text{As}$ samples grown under diverse MBE conditions (standard and virtual surfactant) have been analysed. The thickness of the ternary sublayer formed between the InAs and InP substrate has been studied in the samples deoxidized under the flux of arsenic (AsH_3) or phosphorus (PH_3). The suitability of SAXPS depth profiling technique for the qualitative characterization of ultra-thin heterostructures is discussed considering the limitations of experimental depth resolution.

1. Introduction

The growth and characterization of strained $\text{InAs}/\text{In}_x\text{Ga}_{1-x}\text{As}$ and InAs/InP heterostructures is a very important topic of research in semiconductor materials. The studies of strained InAs epilayers permit an understanding both of the fundamentals of the epitaxy process and of novel physical properties of strained III–V materials, which have a promising future in modern semiconductor optoelectronics [1,2]. The major part of numerous experimental works has been always dedicated to the molecular beam epitaxy (MBE) growth and material characterization by reflected high-energy electron diffraction (RHEED), high-resolution X-ray diffraction (HRXRD) and photoluminescence (PL) techniques. Nevertheless, many

important problems of MBE growth (e.g., the determination of optimal growth temperatures for different III–V sublayers, the control of the surface and heterointerface quality, etc.) remain unresolved until now. An ideal heterostructure must contain atomically flat and abrupt interfaces, but even the use of modern MBE technique does not guarantee such a high quality of the material. The real heterointerface abruptness is limited by initial surface roughness and unwanted atomic displacements during growth process. The most pronounced phenomena reported in the case of In-containing compounds are the surface segregation and interface diffusion of indium [3–7] and the substitution of P atoms by As [7–12].

It was recently demonstrated that the MBE growth under virtual surfactant conditions [13] can minimize the effect of indium interdiffusion at the heterointerfaces. One of the purposes of the current work was to grow highly strained heterostructures (InAs quantum wells embedded into $\text{In}_{0.53}\text{Ga}_{0.47}\text{As}$ matrix) and

^{*} Corresponding author.

¹ On leave from Semiconductor Physics Institute, Goštauto 11, LT-2600 Vilnius, Lithuania.

to compare the quality of the samples produced at different growth conditions: standard (As-stable surface) and virtual surfactant (In-stable surface). Selected area X-ray photoelectron spectroscopy (SAXPS) combined with low energy ion sputtering has been used for the sample characterization. The same depth profiling technique has been employed for the investigation of InAs/InP heterointerfaces grown after different cleaning procedures of InP substrate: deoxidation under the flux of arsenic or phosphorus.

2. Experimental

The $\text{In}_{0.53}\text{Ga}_{0.47}\text{As}/\text{InAs}/\text{In}_{0.53}\text{Ga}_{0.47}\text{As}$ samples were produced following a virtual surfactant model of the MBE growth. It means, the In-stable conditions were maintained during the growth of InAs sublayer by closing the As shutter. As it was reported in Ref. [13], these growth conditions are expected to produce a sharper InAs/ $\text{In}_x\text{Ga}_{1-x}\text{As}$ interface. The growth was carried out by solid source MBE technique using a Varian GEN II modular system. The (100) oriented epi-ready InP:Fe substrates were utilized. Prior to the growth, the substrates were deoxidized under arsenic flux. Then heterostructures of various thicknesses of InAs quantum well were grown using the procedure described elsewhere [7,14,15]. For comparison, another series of samples were grown under standard MBE conditions, i.e. with the As shutter opened (As-stable surface).

Strained InAs/InP heterostructures were fabricated by growing InAs epilayers directly on InP substrates. In this case, a gaseous source of arsenic (AsH_3) was employed. Before the growth, surface oxides were removed by heating under the flux of AsH_3 or PH_3 for 10 min at $T = 520\text{--}530^\circ\text{C}$, i.e. maintaining the same conditions as in our previous studies of InP deoxidation under the flux of arsenic from the solid source [7,12,15].

The SAXPS depth profiling was performed in a VG Scientific Escalab MkII spectrometer. Photoelectrons (excited by an Al $K\alpha$ X-ray source) were collected from a sample area of about 3 mm in diameter. The low energy ($E_i = 1.0$ keV) Ar^+ ion beam was rastered over the window in the gold

mask, producing a sample current density $j \approx 3 \mu\text{A cm}^{-2}$. Elemental depth profiles were derived from the areas of the In $3d_{5/2}$, Ga $2p_{3/2}$, As $2p_{3/2}$ and P $2p$ photoelectron peaks. More experimental details on the SAXPS depth profiling have been reported elsewhere [6,16].

3. Results and discussion

The main restriction in the application of any depth profiling technique (AES, XPS or SIMS) is a limit of experimental depth resolution [17,18]. This question is particularly important in the case of strained III–V semiconductor heterostructures, where the maximum thickness of strained sublayers cannot exceed the critical value ($d = 10\text{--}12$ ML, i.e. $d = 3\text{--}4$ nm for the samples containing InAs). Previous studies of III–V semiconductor quantum wells and superlattices by SAXPS depth profiling [6,7,16,19] manifested that the main factor determining the depth resolution Δz is photoelectron information depth Δz_A .

In this work, with the aim to exclude any doubts about the possible influence of the ion sputtering [16–19], the depth profiles of the same $\text{In}_{0.53}\text{Ga}_{0.47}\text{As}/\text{InAs}/\text{In}_{0.53}\text{Ga}_{0.47}\text{As}$ sample with $d = 10$ ML were obtained at Ar^+ ion energy $E_i = 1.0$ and 1.5 keV (Fig. 1). The depth profiles were normalised to the corresponding peak area S_0 in the

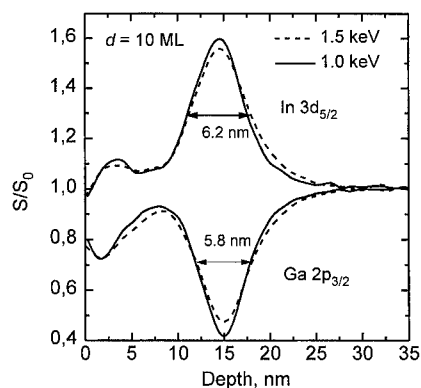


Fig. 1. Depth profiles ($E_i = 1.0$ and 1.5 keV, respectively) of the $\text{In}_{0.53}\text{Ga}_{0.47}\text{As}/\text{InAs}/\text{In}_{0.53}\text{Ga}_{0.47}\text{As}$ sample with $d = 10$ ML. The peak areas S are normalized to the corresponding peak area S_0 in the $\text{In}_{0.53}\text{Ga}_{0.47}\text{As}$ layer. The experimental values of FWHM are indicated by arrows.

'bulk' $\text{In}_{0.53}\text{Ga}_{0.47}\text{As}$ buffer layer. The results obtained at the different energies are almost identical, i.e. the SAXPS depth resolution Δz at low E_i values is really determined by photoelectron information depth which is $\Delta z_\lambda = 4.5$ and 2.1 nm for the In 3d and Ga 2p peaks, respectively [16]. The experimental values of FWHM (full width half maximum or minimum for In or Ga, respectively) ca. 6 nm are caused by the convolution of the instrumental response function (which must be Gaussian in the case of photoelectron escape depth) and the elemental concentration distribution function, i.e. the real profile. For the same reason, both the indium and gallium profiles have the shape of a rounded top with a maximum (for In) or minimum (for Ga) value very different from the real ones (1/0.53 and 0, respectively). However, the low values of FWHM indicate that the real heterointerfaces must be described by the step-function in respect to the scale of photoelectron information depth, i.e. they are really steep.

The comparison of the results for the samples containing two InAs sublayers ($d = 12$ and 6 ML) grown by standard MBE process (As-stable surface) and under virtual surfactant conditions (In-stable surface) is given in the Fig. 2. These depth profiles clearly exhibit that the InAs sublayers grown under virtual surfactant conditions are more confined. In fact, only diverse abruptness of the real elemental profiles convoluted with the same instrumental re-

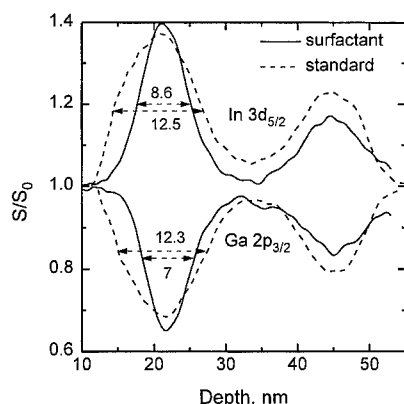


Fig. 2. Depth profiles ($E_i = 1.0$ keV) of the $\text{In}_{0.53}\text{Ga}_{0.47}\text{As}/\text{InAs}/\text{In}_{0.53}\text{Ga}_{0.47}\text{As}$ double quantum wells ($d = 12$ and 6 ML, respectively) grown at different MBE conditions: standard and virtual surfactant. The experimental values of FWHM are indicated by arrows.

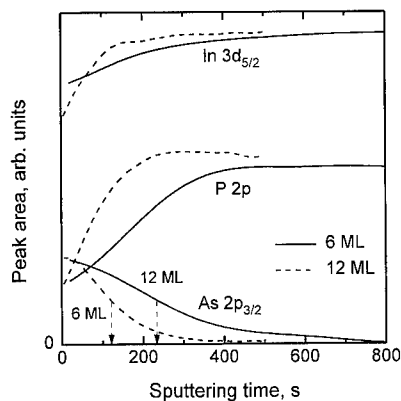


Fig. 3. Depth profiles ($E_i = 1.0$ keV) of the InAs layers ($d = 6$ and 12 ML) grown on InP substrates deoxidized under AsH_3 flux.

sponse function can yield such a noticeable difference in the shape of experimental profiles. Since the growth times of both samples were exactly identical, only one explanation of this result is that the heterointerfaces grown under virtual surfactant conditions are steeper and the effective thickness of the InAs layer is slightly reduced. Of course, for the reconstruction of real profiles, it would be possible to apply a simple deconvolution procedure [19], although, this procedure is not justified in our case, where $d/\Delta z_\lambda < 1$.

The depth profiles of the InAs/InP samples with $d = 12$ and 6 ML (InP substrate deoxidized under AsH_3 flux) are presented in Fig. 3. If we determine the thickness of InAs layer as $d = z$ at a 50% change in the $\text{As } 2p_{3/2}$ peak, which has the smallest value of the Δz_λ [7,12], then the remaining tail of the arsenic signal is related to the interfacial sublayer of $\text{InAs}_x\text{P}_{1-x}$. The existence of thick $\text{InAs}_x\text{P}_{1-x}$ sublayer has been observed previously by using SAXPS, SIMS and Raman spectroscopy in the samples deoxidized under As flux from the solid source [7,12,15]. It should be noted that, in the samples deoxidized under AsH_3 flux, the thickness ratio $d_{\text{InAsP}}/d_{\text{InAs}}$ is higher, i.e. the $\text{InAs}_x\text{P}_{1-x}$ sublayer is thicker than in the samples deoxidized under molecular arsenic flux. A logical experiment for the understanding of the mechanism of ternary sublayer's formation would be to clean the substrate without the arsenic, i.e. under phosphorus flux, and to grow InAs layer on it. However, the depth profiles of the samples deoxidized under PH_3 flux were identical to the ones

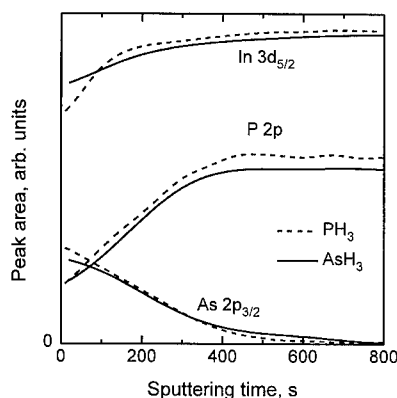


Fig. 4. Depth profiles ($E_i = 1.0$ keV) of the InAs layers ($d = 12$ ML) grown on InP substrates deoxidized under the flux of AsH_3 or PH_3 .

cleaned in AsH_3 , as can be seen from Fig. 4. Therefore, only a topmost part of the interfacial sublayer (1–2 ML thick, accordingly to Refs. [9,10]) is formed by direct $\text{As} \rightarrow \text{P}$ substitution during the deoxidation under arsenic flux or during the initial stage of InAs growth (samples deoxidized in PH_3). The major part of ternary compound is formed due to the subsequent diffusion of As atoms into the deeper sub-surface region of hot InP substrate.

4. Conclusions

The $\text{In}_{0.53}\text{Ga}_{0.47}\text{As}/\text{InAs}/\text{In}_{0.53}\text{Ga}_{0.47}\text{As}$ heterostructures with steep interfaces were successfully grown by using both sets of MBE conditions investigated. However, the abruptness of the heterointerfaces produced under virtual surfactant (In-stable) conditions was improved in respect to the ones grown at standard (As-stable) conditions. This fact testified that, in the virtual surfactant growth, the effect of segregation and interdiffusion of indium is reduced significantly.

The main reason of the formation of thick interfacial $\text{InAs}_x\text{P}_{1-x}$ sublayer at InP substrate is the diffusion of As atoms into substrate during deoxidation under arsenic and InAs growth.

The SAXPS depth profiling technique can be used for comparative characterization of ultra-thin III–V heterostructures quantum wells, taking into account the limitations of depth resolution, which is determined mainly by photoelectron information depth.

Acknowledgements

This work was supported by the National Research Council (CNR) of Italy under the auspices of the 'Progetto Finalizzato Materiali Speciali per Tecnologie Avanzate'. We thank Dr. M.G. Simeone for the helpful discussions. One of us (S.K.) is grateful for a research fellowship provided by CNR of Italy.

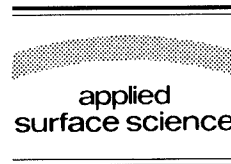
References

- [1] Ed. T.P. Pearsall, *Semicond. Semimet.* 32/33 (1990).
- [2] E. Tournié, H.-P. Schoenherr, K. Ploog, C. Giannini and L. Tapfer, *Appl. Phys. Lett.* 61 (1992) 846.
- [3] K. Muraki, S. Fukatsu, Y. Shiraki and R. Ito, *Appl. Phys. Lett.* 61 (1992) 557.
- [4] J.M. Moison, C. Guille, F. Houzay, F. Barthe and M. Van Rompay, *Phys. Rev. B* 40 (1989) 6149.
- [5] J.M. Moison, F. Houzay, F. Barthe, J.M. Gérard, B. Jusserand, J. Massies and F.S. Turco-Sandroff, *J. Cryst. Growth* 111 (1991) 141.
- [6] M.R. Bruni, S. Kačiulis, G. Mattogno, M.G. Simeone, S. Viticoli and F. Martelli, in: *Formation of Semiconductor Interfaces*, Eds. B. Lengeler, H. Lüth, W. Mönch and J. Pollmann (World Scientific, Singapore, 1994) p. 672.
- [7] M.R. Bruni, N. Gambacorti, S. Kačiulis, G. Mattogno, M.G. Simeone and S. Viticoli, *Mater. Sci. Eng. B* 28 (1994) 228.
- [8] J.M. Moison, M. Bensoussan and F. Houzay, *Phys. Rev. B* 34 (1986) 2018.
- [9] G. Hollinger, D. Gallet, M. Gendry, C. Santinelli and P. Viktorovitch, *J. Vac. Sci. Technol. B* 8 (1990) 832.
- [10] D.E. Aspnes, M.C. Tamargo, M.J.S. Brasil, R.E. Nahory and S.A. Schwarz, *Appl. Phys. Lett.* 64 (1994) 3279.
- [11] M.R. Bruni, S. Kačiulis, G. Mattogno and M.G. Simeone, *Vuoto Sci. Tecnol.* 23/1 (1994) 89.
- [12] M.R. Bruni, N. Gambacorti, S. Kačiulis, G. Mattogno, M.G. Simeone, L. Quagliano, N. Tomassini and B. Jusserand, *J. Cryst. Growth* 150 (1995) 123.
- [13] E. Tournié and K. Ploog, *J. Cryst. Growth* 135 (1994) 97.
- [14] M.R. Bruni, N. Gambacorti, S. Kačiulis, G. Mattogno, M.G. Simeone and S. Viticoli, *Mater. Sci. Forum* 203 (1996) 231.
- [15] M.R. Bruni, N. Gambacorti, S. Kačiulis, G. Mattogno and M.G. Simeone, *Vuoto Sci. Tecnol.* 25 (1996), in press.
- [16] M.R. Bruni, S. Kačiulis, G. Mattogno, M.G. Simeone, S. Viticoli and F. Martelli, *Appl. Surf. Sci.* 72 (1993) 89.
- [17] S. Hofmann, *Appl. Surf. Sci.* 70/71 (1993) 9.
- [18] K. Witmaack, *Surf. Interf. Anal.* 21 (1994) 323.
- [19] S. Kačiulis, G. Mattogno, G. Treideris and S. Viticoli, *J. Electron Spectrosc. Rel. Phen.* 70 (1994) 145.



ELSEVIER

Applied Surface Science 104/105 (1996) 656–660



Ab-initio electronic structure calculation of the InAs multiple quantum wells in bulk GaAs

Nacir Tit ^{a,*}, Maria Peressi ^b

^a International Centre for Theoretical Physics, P.O. Box 586, 34100 Trieste, Italy

^b Dipartimento di Fisica Teorica dell'Università di Trieste, Strada Costiera 11, 34014 Trieste, Italy

Received 28 June 1995; accepted 26 September 1995

Abstract

We present a theoretical investigation of the electronic structure of an InAs monomolecular plane inserted in bulk GaAs. Our calculations are based on the ab-initio self-consistent pseudopotential method. Both electrons and holes are found to be strongly localized in the vicinity of the inserted InAs monolayer, which therefore acts as a quantum well for all charge carriers. Moreover, using a finite-square-well model, we show that the energy gap increases with the increasing GaAs barrier thickness and also show the formation of a localized electron/hole state in the gap in the limit of a single InAs quantum well. This latter result successfully explains the intense and narrow low temperature photoluminescence spectra, experimentally observed in the InAs/GaAs single-monolayer quantum well systems.

1. Introduction

Lattice-mismatched heterojunctions have recently attracted a great interest for the possibility to tune band offsets and, therefore, to control the transport and optical properties of microelectronic devices. In this respect, the strain effect plays a predominant role and has been traditionally manipulated using various substrate compositions. This latter method, however, has suffered from misfit dislocations during the growth. On the other hand, this problem can be avoided in the case of dopant-monolayer/host crystal system. Namely, it is due to the recent advances in growth technology that one-monolayer

thick of InAs has been synthesized in GaAs using the flow-rate-modulation epitaxy (FME) [1]. The recent photoluminescence experiments [1–3], done on this latter heterostructure at very low temperatures (2 K), have shown very intense and narrow spectra and demonstrated that the inserted InAs monolayer is playing the role of a quantum well for both electrons and holes. In addition to this, Sato and Horikoshi [2,3] have studied superlattices, consisting of two InAs monolayers separated by few monolayers of GaAs, and reported an increasing bandgap, E_g , with the distance between the two InAs monolayers. Hence, such monolayer-plane-host-crystal system offers an additional flexibility to the bandgap engineering and the artificial control of charge carrier distribution and, as a consequence, is expected to yield new interesting optoelectronic devices. Indeed, the electronic and optical properties of this latter het-

* Corresponding author. Present address: Physics Department, United Arab Emirates University, P.O. Box 17551, Al-Ain, United Arab Emirates.

erostructure has been the subject of several recent experimental and theoretical works [1–5].

The scope of this paper is to calculate and analyse the electronic structure of the InAs/GaAs(001) strained-layer superlattices (SSL) using the ab-initio self-consistent pseudopotential method. We also use a finite-square-well model to estimate the carrier confinement energies and to study the variation of the bandgap versus the barrier thickness. Our results show that, in the limit of a single quantum well, the interband electron-heavy-hole transition is about 0.04 eV smaller than the bandgap of the host GaAs crystal. This is consistent with the predictions of the photoluminescence experiment. In the next section, we describe our computational method, then in Section 3 we give and discuss our results. The last section summarizes our conclusions.

2. Computational details

Our numerical calculations are based on the state-of-the-art density functional theory (DFT) [6], within the local density approximation, applied in the momentum space formalism [7]. We use a plane wave basis set up to a kinetic energy cutoff E_{cut} ($= 20$ Ry), the norm-conserving pseudopotentials [8]¹, and the special-point technique (the (333) Monkhorst–Pack cubic mesh appropriately folded for various supercell shapes and sizes [9]) to perform the k -space integration. In our present work, we use supercells containing five GaAs monolayers and one InAs plane (total of 12 atoms) to simulate the InAs/GaAs (001) monomolecular-plane-host-crystal systems.

In Ref. [10], we reported the valence band offset (VBO) at the GaAs/InAs interface, where the GaAs was the substrate and the InAs was the overlayer. We found that the VBO = 0.28 eV, where the spin-orbit effects were included in the calculations and the InAs valence band edge is higher in energy. In our present work, we use this result, together with the calculated bandgaps of the two constituents under their strained (or cubic) configurations. In addi-

tion to this, we use a finite-square-well model to estimate the charge carrier confinement energies as well as to study the variation of the superlattice bandgap E_g versus the GaAs barrier thickness. Our results compare favourably with the photoluminescence experimental data.

3. Results and discussion

We first give a brief description of our supercell atomic structure. Our calculated equilibrium bulk lattice parameters for the two constituents are: $a_{\text{GaAs}} = 10.65$ au and $a_{\text{InAs}} = 11.25$ au. These values give a lattice mismatch of 5.5%, slightly below the experimental value. It has been, recently, experimentally observed [5] that for InAs inserted in GaAs the macroscopic theory of elasticity (MTE) breaks down in the monolayer (ML) limit. In particular, the measured strain is much higher than expected according to the MTE and it rather corresponds to bulk bond length conservation (BLC). This observation is supported by the theoretical calculations of Ref. [4], whereas different findings are conversely reported in Ref. [11]. We found that — with respect to our numerical accuracy — the supercells describing the inserted InAs monolayer in the two different strain states (MTE and BLC) are very similar in total energy, also after additional internal relaxations which make the atomic forces vanish. In the final optimized structures, the interplanar In–As distance is intermediate between the MTE and BLC predictions, and a small compressive strain affects the GaAs plane adjacent to the inserted InAs, as similarly found in other superlattices [12,13] in the region close to the interface. More accurate calculations (e.g. improving cell size, kinetic energy cutoff, number of special points) would be required to definitely establish the true equilibrium structure. Since this is not the main purpose of the present work, in the following we consider the strain state of the InAs ML as predicted by BLC, according to the experimental observations [5].

The calculated energy gaps of bulk GaAs, bulk and strained InAs are 1.07 eV (the experimental value is 1.52 eV [14]), 0.58 eV (experimental 0.42 eV [14]) and 0.19 eV, respectively, taking properly into account strain splitting effects for InAs. We

¹ The pseudopotentials used here have been generated by Giannozzi (unpublished) using a scheme originally proposed by Car and Von Barth (unpublished).

have previously found [10] that the non-relativistic valence band offsets (VBO) at GaAs/InAs interface amounts to 0.26 eV, almost independent of the local strain in the interface region, with GaAs valence band edge lower in energy. The corresponding conduction band offset (CBO) is $\text{CBO} = \Delta E_g - \text{VBO} = 0.62$ eV, where the GaAs conduction band edge is higher in energy and $\Delta E_g = 0.88$ eV is the band gap difference between bulk GaAs and strained InAs. Hence, the inserted InAs layer acts as a quantum well (QW) for electrons and holes, giving the so-called type-I heterostructure. Spin-orbit (SO) effects can be taken into account and added a posteriori to our calculations (see Ref. [13]) using the experimental SO parameters [14], $\Delta_0 = 0.34$ eV for GaAs and 0.38 eV for InAs. The corrected band gaps of bulk GaAs and strained InAs are 0.96 and 0.06 eV, respectively. The VBO and the bandgap difference ΔE_g increase by about 0.02, whereas the CBO remain unchanged.

In Fig. 1a, we display the band structure of a hypothetical supercell containing pure GaAs in the cubic configuration, namely $(\text{GaAs})_6$. We have chosen the top of valence band as our reference (zero) of energy. In Fig. 1b, we show the bands of a supercell

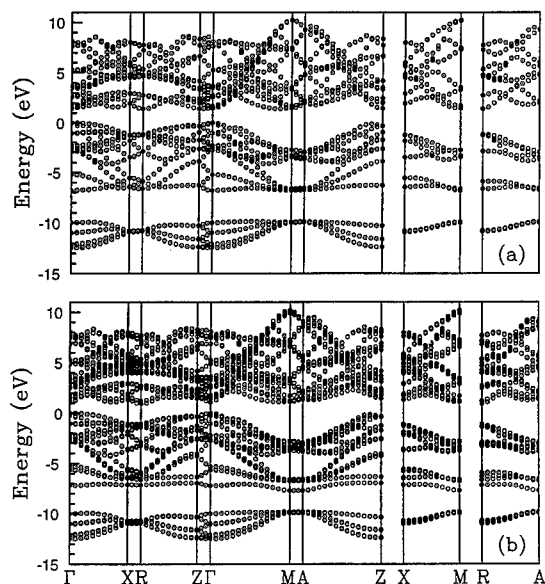


Fig. 1. Band structures calculated at $E_{\text{cut}} = 14$ Ry for the following supercells: (a) $(\text{GaAs})_6$, which is in the cubic structure; (b) $\text{InAs}/(\text{GaAs})_5$, where the In–As bond length is conserved as in its bulk equilibrium configuration.

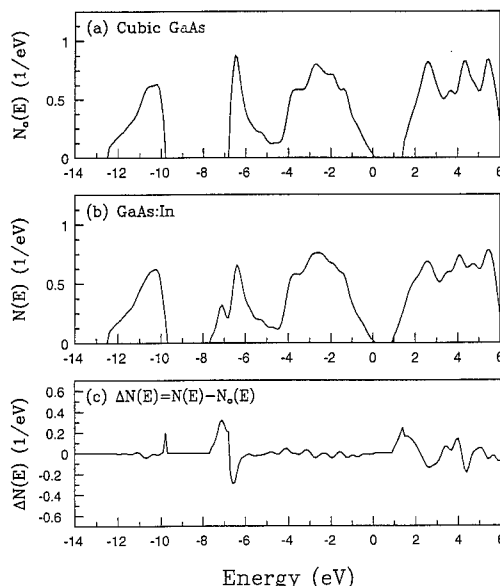


Fig. 2. Density of states calculated at $E_{\text{cut}} = 14$ Ry for: (a) $(\text{GaAs})_6$ which is in the cubic structure similar to the one of Fig. 1a; (b) $\text{InAs}/(\text{GaAs})_5$ where the In–As bond length is conserved as in its bulk configuration. The difference of density of states between (b) and (a), $N(E) - N_0(E)$, is displayed in (c) to illustrate the effects of the inserted InAs monolayer.

containing one InAs monomolecular plane inserted in GaAs bulk (namely corresponding to $\text{InAs}/(\text{GaAs})_5$ structure), where the In–As bond length is as in the bulk. It is clearly seen that the degeneracies of several bands are lifted under the reduced symmetry of this new structure. The lowest group consisting of 6 bands, located below the valence band, seems to be not much affected by the substitution of In-atom because it is composed of the As s-states. The bandgap is diminished to $E_g = 0.76$ (0.87) eV including (neglecting) the SO effects. This value is a little smaller than the GaAs bandgap (see below for further details).

In Fig. 2a, we show the calculated density of states, $N_0(E)$, for the same supercell used in Fig. 1a. Similarly, in Fig. 2b we show the DOS, $N(E)$, corresponding to the same supercell used in Fig. 1b. This latter DOS, in turn, reflects the splits of the manifold states that occurred in all the bands, as well as the reduction of the energy gap. In Fig. 2c, we display the difference $\Delta N(E) = N(E) - N_0(E)$ to stress the new features caused by the insertion of the InAs monolayer.

Since the electron density $n(\mathbf{r})$ and the electrostatic potential $V(\mathbf{r})$ are periodic in the planes nominal to the growth direction (z -axis) and since we are interested only in the z -dependence, we show in Fig. 3 (solid curve with left scale) the (xy) planar average of the electronic charge density $\bar{n}(z)$ for: (a) a hypothetical InAs/(GaAs)₅ supercell where one Ga atom (layer) is substituted by In atom (layer) but all bond lengths are kept fixed as in the original GaAs structure; (b) a realistic supercell of InAs/(GaAs)₅, where the In–As bond length is conserved as in its bulk-like structure. The electronic charge density is normalized to eight electrons per cell. Moreover, in order to get rid of the microscopic bulk oscillations and blow up the interface features, we apply the macroscopic average as described in Refs. [10] and [15] to get $\bar{\bar{n}}(z)$, shown by the dotted curves with the scale on the right. Fig. 3a shows that even for the ‘hypothetical’ InAs/(GaAs)₅ structure, there is already a depletion of electronic valence charge in the InAs region. This depletion increases with the increasing In–As bond length as shown by the dotted curve of Fig. 3b. This observation is consistent, as will be described below, with the creation of hole states in the vicinity of the inserted InAs layer.

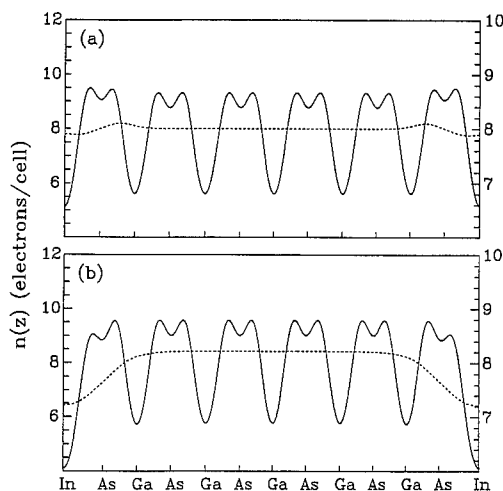


Fig. 3. Planar, $\bar{n}(z)$, and double macroscopic, $\bar{\bar{n}}(z)$, averaged electronic charge densities are shown in solid curve (with left scale) and dotted curve (with right scale) respectively. The shown results correspond to the following: (a) Hypothetical InAs/(GaAs)₅ supercell where all bond lengths are the same as that of GaAs; (b) Realistic InAs/(GaAs)₅ supercell where the In–As bond length is taken to be the same as in its bulk equilibrium configuration.

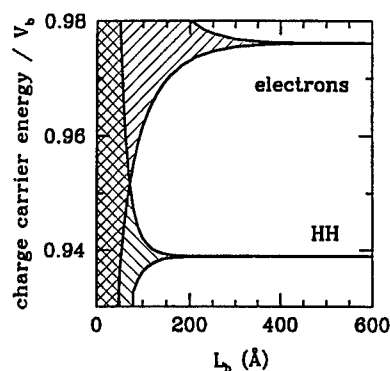


Fig. 4. The evolution of the lowest (highest) allowed band for electrons (heavy holes) in InAs/GaAs(001) strained supercell when the barrier thickness L_b is increased. The figure reports the ratio between the charge carrier energy (calculated from the bottom of the well) and the barrier height V_b versus L_b (which is given in Å units).

To study the decrease of the strained superlattice bandgap, one may use a much simpler one-dimensional finite square well model [16]. The VBO and CBO described above (with the inclusion of spin-orbit effects) represent the barrier height V_b for holes and electrons, respectively. For both charge carriers, the respective well and barrier thicknesses are taken to be: $L_w = 0.5a_{\perp}(\text{InAs}) = 3.27$ Å and $L_b = 2.5a_{\perp}(\text{GaAs}) = 14.10$ Å, where $a_{\perp}(\text{XAs})$ is the lattice parameter of the material XAs along the growth direction of the superlattice. The other parameters used in the finite-square-well model are the effective masses of the heavy holes (HH) and electrons in the well and in the barrier: $m_w^{\text{HH}} = 0.41$, $m_b^{\text{HH}} = 0.45$, $m_w^{\text{el}} = 0.023$ and $m_b^{\text{el}} = 0.0665$ in units of free electron mass [16].

In Fig. 4, we show the results of the square well model for our system. We display the variation of the confinement charge carrier energy E_{conf} (measured from the bottom of the well) versus the barrier thickness L_b . We have plotted the ratio E_{conf}/V_b , so that the plot is general, independent on the barrier height. In the case of our supercell geometry ($L_b = 14.1$ Å), it is evident that: (i) the very small well thickness makes the confinement energies very high, and this explains why the supercell energy gap is closer to the one of bulk GaAs rather than to the one of strained InAs; (ii) the confinement energies for the electrons and HH are 0.50 and 0.22 eV, respectively, so that the superlattice energy gap derived

from this model is, $E_g(\text{SSL}) = E_g(\text{InAs}) + E_{\text{conf}}^{\text{HH}} + E_{\text{conf}}^{\text{el}} = 0.78$ eV, in good agreement with the value 0.76 eV obtained from our ab-initio supercell calculations (with the inclusion of spin–orbit effects).

Fig. 4 also shows that by increasing the barrier thickness (L_b), the confinement energies for electrons and HH increase and the bandwidth reduces down to reach the limit of isolated energy levels (single quantum well, SQW, regime) rather than broadened bands. In this latter regime, reached for $L_b \geq 400$ Å, the interband e–HH transition energy is reduced by 0.04 eV from the calculated bandgap of the host GaAs crystal. This result is consistent with the recent photoluminescence experiments [1–3] which reported a transition energy about 0.04–0.07 eV smaller than the experimental GaAs energy gap. We stress that the inaccuracies of our calculations for the band gaps (due to the underestimation of the DFT to band gaps) tend to cancel out when comparing similar quantities; it is therefore more reasonable to compare with the experiments the differential quantity $\Delta E = E_g(\text{GaAs}) - E(\text{e–HH})$ rather than the absolute value $E(\text{e–HH})$.

4. Conclusions

We presented our ab-initio self-consistent pseudopotential calculations of the electronic structure of an InAs monomolecular plane inserted in bulk GaAs. Moreover, we have used a finite-square-well model to estimate the charge carrier confinement energies and to study the variation of the superlattice bandgap E_g versus the barrier thickness.

Our results show that the InAs/GaAs strained dopant-monolayer/host-crystal system forms a type-I heterostructure, where the InAs slab acts as a quantum well localizing both electrons and holes. The multiple quantum well regime is predicted to be for a barrier thicknesses $L_b > 400$ Å. Whereas superlattice-like structure is expected for smaller barrier thicknesses.

Finally, in the case of a single quantum well ($L_b \rightarrow \infty$), one obtains an interband e–HH transition

of 0.04 eV smaller than the bandgap of the host GaAs crystal. This result is consistent with the photoluminescence experiments. Hence, such heterostructure could find fascinating applications for the bandgap engineering and the control of the spatial charge carrier distribution.

Acknowledgements

We are indebted to thank Prof. Stefano Baroni for stimulating discussions and Dr. Mohamed El-Hadi Lazzouni for some computational help. One of us (N.T.) would also like to thank Prof. Yu Lu for the invitation to visit the International Center for Theoretical Physics in Trieste, where this work has been accomplished.

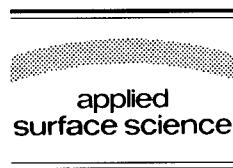
References

- [1] M. Sato and Y. Horikoshi, *J. Appl. Phys.* 66 (1989) 851.
- [2] M. Sato and Y. Horikoshi, *J. Appl. Phys.* 69 (1991) 7697.
- [3] M. Sato and Y. Horikoshi, *Surf. Sci.* 267 (1992) 195.
- [4] K. Shiraishi and E. Yamaguchi, *Phys. Rev. B* 42 (1990) 3064.
- [5] O. Brandt and K. Ploog, *Phys. Rev. Lett.* 68 (1992) 1339.
- [6] P. Hohenberg and W. Kohn, *Phys. Rev. B* 136 (1965) B864; W. Kohn and L.J. Sham, *Phys. Rev. B* 140 (1965) A1133.
- [7] J. Ihm, A. Zunger and M.L. Cohen, *J. Phys. C* 12 (1979) 4409.
- [8] D.R. Hamann, M. Schlüter and C. Chiang, *Phys. Rev. Lett.* 43 (1979) 1494.
- [9] H.J. Monkhorst and J.P. Pack, *Phys. Rev. B* 13 (1976) 5188.
- [10] N. Tit, M. Peressi and S. Baroni, *Phys. Rev. B* 48 (1993) 17607.
- [11] J.E. Bernard and A. Zunger, *Appl. Phys. Lett.* 65 (1994) 165.
- [12] M. Peressi and S. Baroni, *Phys. Rev. B* 49 (1994) 7490.
- [13] M. Peressi, L. Colombo, A. Baldereschi, R. Resta and S. Baroni, *Phys. Rev. B* 48 (1993) 12047.
- [14] Landolt–Börnstein, Eds., *Numerical Data and Functional Relationships in Science and Technology*, Vol. 17a (Springer, New York, 1982).
- [15] L. Colombo, R. Resta and S. Baroni, *Phys. Rev. B* 44 (1991) 5572.
- [16] G. Basard, *Wave Mechanics Applied to Semiconductors Heterojunctions* (Les Editions de Physique, Paris, 1988).



ELSEVIER

Applied Surface Science 104/105 (1996) 661–668



Medium energy ion scattering (MEIS) studies on Si/GaSb/Si- and Si/CaF₂/Si(111) layer systems

T. Tappe, A. Chatziparaskewas, J. Schäffer, J. Schlosser, J. Schmalhorst,
B. Schmiedeskamp *

Fakultät für Physik, Universität Bielefeld, D-33615 Bielefeld, Germany

Received 28 June 1995; accepted 11 September 1995

Abstract

The layer systems Si/GaSb/Si and Si/CaF₂/Si(111) are fabricated by MBE. The thickness of the interlayers are about 1 monolayer and a few nm. The composition and geometric structure of the layer systems is studied with MEIS. The systems are well suited for MEIS-studies because both the GaSb and CaF₂-signals in the MEIS spectra can be separated from the silicon background. CaF₂ has almost the same lattice constant as silicon. It turns out that Si/CaF₂/Si(111) can be grown epitaxially for an interlayer thickness of about 5 nm. This has been earlier found by other groups for layer systems with larger thicknesses. An attempt to produce corresponding systems with a CaF₂ thickness of only 1 monolayer resulted in diffusion of CaF₂ from the interface. The lattice constant of GaSb is about 12% larger than that of silicon making epitaxial growth by far more difficult. Partly epitaxial GaSb-islands are observed for deposition at about 200°C. In this case, the attempt to produce a system with GaSb thickness of only 1 monolayer by overgrowth of GaSb with silicon at 200°C and heating the system to 600°C yields an epitaxial silicon cap layer. GaSb remains at the interface. For the quantitative analysis of the MEIS data Monte Carlo calculations of the ion trajectories are performed for comparison with the experimental spectra. The simulations take into account all shadowing and blocking effects in the layer systems. The simulations show that MEIS is an excellent method to determine the orientation of GaSb-dipoles quantitatively.

1. Introduction

Heterostructure systems with thin interlayers in the monolayer range might be favourite systems for new applications in semiconductor engineering. Especially systems with thin dipolelayers are of interest due to the probability of manipulating the bandoffset [1–3]. Most studies in this area have been made on III–V heterostructures with thin group IV materials (Si,Ge) as interlayers [3–7]. Some work has also

been reported on III–V interlayers in group IV semiconductors [8]. Theory suggests that the size of the bandoffset is strongly related to the geometric structure of the interface and especially to the orientation of the interface dipole [9]. Experimental studies of the geometrical structure at the interface have, however, not been performed up to now. Earlier MEIS studies [10] on GaAs/Si/AlAs with silicon interlayers in the monolayer range have contributed to an understanding of the variation of the bandoffset with silicon interlayer thickness but a detailed characterization of the interface structure was not possible due to the fact that the MEIS signal from the silicon

* Corresponding author.

interlayer is too weak and hidden by the AlAs background.

This work describes first results of a project, in which ultrathin interlayers (thickness \approx monolayer) of heavier materials are incorporated between a silicon substrate and an epitaxial silicon caplayer. The composition and geometric structure of the systems is studied with MEIS. As first candidates for the interlayer material, GaSb and CaF_2 were chosen, because their signals in the MEIS spectra can be separated from the silicon background. Before systems with thicknesses in the monolayer range are produced the deposition conditions for CaF_2 and GaSb are optimized by deposition and characterization of thick films (several nm).

2. Experimental

The layer systems are grown by molecular beam epitaxy (MBE) on well oriented (miscut $< 0.5^\circ$) Si(100) and Si(111) substrates. The substrates are loaded into the MBE system by means of a vacuum transfer system and mounted on a heatable manipulator. The substrate temperature is measured by means of a thermocouple which is fixed at the heater and close to the substrate. The temperature measurement is calibrated by means of a thermocouple at the sample surface (only possible if samples are loaded by hand at atmospheric pressure) and at temperatures above 800°C with a pyrometer. To remove the oxide from the substrate surface, the sample is annealed at 500°C for five min and then heated to 850°C for two min.

CaF_2 , Ga and Sb are evaporated from effusion cells with boron nitride crucibles. The deposition rates are 0.3 nm per min in the case of CaF_2 and 1 nm per min for GaSb at a substrate temperature of 200°C . Evaporation of CaF_2 from a Ta crucible, which was made first, results in an incorporation of small amounts of Ta ($< 0.2\%$) into the systems. Silicon is evaporated by electron beam evaporation. After deposition the samples are transferred to the MEIS system.

For the MEIS studies we use a 300 keV He^+ ion beam. The beam spot on the sample is rectangular with 1.8 mm horizontal size and 0.9 mm vertical size. The samples are mounted on a high precision

manipulator, which allows three rotations and two translations lateral to the beam. The energy of the backscattered ions is determined by use of a toroidal electrostatic analyser (TEA). The energy resolution $\Delta E/E$ of the whole system (energy width of ion beam and TEA resolution) is 5×10^{-3} . The TEA accepts an angular distribution of 20° in the scattering plane simultaneously. The angular resolution is better than $\pm 0.15^\circ$. A typical ion dose during a measurement with TEA is $100 \mu\text{C}$. Measurements can also be performed with a surface barrier detector. In this case the energy resolution is only 9 keV FWHM but the required ion dose for an energy distribution of backscattered particles is reduced to about $1 \mu\text{C}$. The yields measured with the surface barrier detector were converted into number of monolayers by the method given in [11]. For the TEA measurements the energy dependence of the analyser transmission and of the He-charge state were in addition taken into consideration. They have been determined in detail elsewhere [12].

3. Results and discussion

3.1. $\text{CaF}_2/\text{Si}(111)$ and $\text{Si}/\text{CaF}_2/\text{Si}(111)$

CaF_2 is a good candidate for an epitaxial interlayer in silicon, because the lattice mismatch is only 0.6% at room temperature. A dipole can occur if the bonds of CaF_2 with the silicon substrate and the silicon cap layer are different, e.g. Si–F bonds at the top interface and Si–Ca bonds at the substrate interface. There have been a couple of earlier studies on the system Si/ CaF_2 /Si [13] which show an epitaxial growth of CaF_2 on Si(111) and Si(100) with thicknesses in the range between 50 and 100 nm. To our knowledge studies on CaF_2 interlayer systems with smaller thickness (< 5 nm), and especially of 1 ML CaF_2 , have up to now not been reported. Systems with 1 ML CaF_2 on Si(111) have been investigated very intensively [14–16]. For this case one observes formation of a monolayer CaF, i.e. one F atom desorbs into the vacuum.

Fig. 1a shows the MEIS spectra for a system with 15 nm CaF_2 on Si(111). The CaF_2 is deposited at a substrate temperature of 700°C . The spectra show the results for ion incidence along a random direction

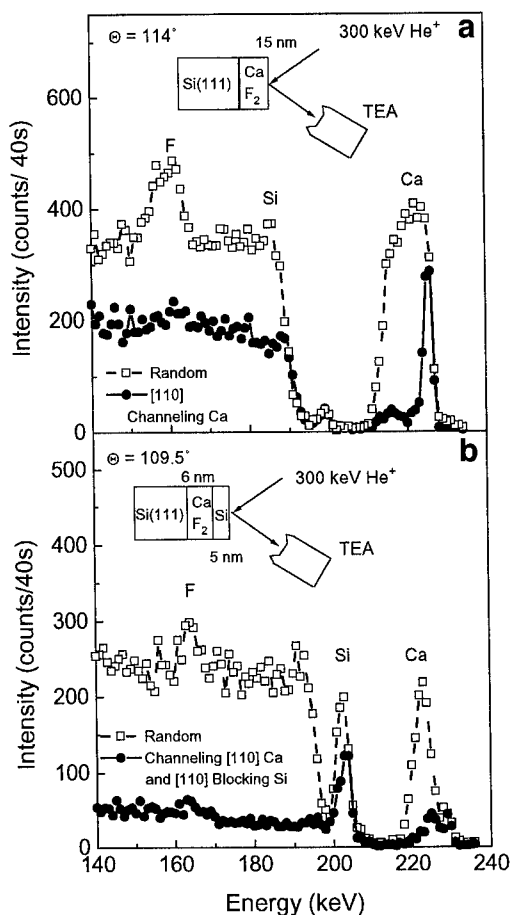


Fig. 1. (a) Top: MEIS spectra for 15 nm CaF₂/Si(111). (b) Bottom: MEIS spectra for 5 nm Si/CaF₂/Si(111).

(□) and for ion incidence along the [110] axis in CaF₂ (●). In the random spectrum (□) the backscattering signal due to Ca is found between 210 and 230 keV, the signal due to backscattering from F is obtained between 150 and 170 keV. All other contributions belong to backscattering from silicon. The ratio of the integrated peak intensities of Ca and F is 2.5. This value is expected for CaF₂, because the scattering cross section is proportional to the square of the atomic number. The Ca and F yield is drastically reduced for channelling along the [110] axis (●), while the silicon yield is only reduced to about 50% of the random yield. In a corresponding measurement for the same ion incidence direction but with $\theta = 109.5^\circ$ we observe, however, also a drastic reduction of the silicon yield due to [110] blocking in

the silicon substrate. This is due to the fact that — as reported in earlier work [17,18] — the CaF₂ layer is rotated by 180° with respect to Si(111).

Fig. 1b shows the MEIS spectra for a system of 5 nm Si on 6 nm CaF₂ on Si(111). The CaF₂ layer was deposited at 700°C. The silicon layer was grown at a substrate temperature (T_{Sub}) of 200°C and annealed to 600°C immediately after deposition. We obtain a peak at 225 keV due to backscattering from Ca, at 205 keV due to backscattering from the silicon toplayer and at 165 keV due to F. All other contributions belong to backscattering from the substrate. Again a spectrum for ion incidence along random directions (□) and parallel to the [110] channelling direction in CaF₂ (●) is displayed. In this case the spectrum for $\theta = 109.5^\circ$ is shown resulting in a reduction of the silicon substrate yield due to [110] blocking. Comparing the different intensities of the Ca random and channelling yields we find a good epitaxial growth for CaF₂ (also the F signal vanishes in the channelling spectra) while the silicon toplayer is not perfectly epitaxial: the blocking yield is only 40% of the random yield. We obtain a double peak for the Ca signal with single peaks at 229 and 224 keV. This indicates that 10% of the CaF₂ is at the surface which is probably due to the fact that only 90% of the CaF₂ is covered with Si-islands. Some groups have reported that for thicknesses < 10 nm silicon island growth for silicon on CaF₂ occurs [17].

Results for 1 ML CaF₂ in silicon are given in Fig. 2. CaF₂ was deposited at $T_{\text{Sub}} = 700^\circ\text{C}$. To get a smooth silicon overlayer we deposited silicon at a temperature of about 150°C [19]. The yield between 200 and 205 keV is due to backscattering from the silicon toplayer and the yield below 200 keV due to backscattering from the silicon substrate. There is no difference in the channelling and random yield between 200 and 205 keV. The silicon toplayer is thus not epitaxial. The peak at 226 keV is due to backscattering from Ca at the interface. (A signal from Ca at the surface would occur at 230 keV.) If the sample is stepwise annealed to 550, 700 and 850°C each step for 5 min, the Ca signal moves to higher energy and becomes broader (see Fig. 2b). The peak vanishes at 850°C. On the other hand, we find a very good crystallization of the silicon toplayer while the temperature is too low for a desorption of silicon from the sample. It is also compatible

with the MEIS data, that the heating results in the growth of epitaxial Si-islands and Ca occurs then at the surface. An F signal was not visible for any measurement. This suggests either that F is not built in under our preparation conditions or ion damage and a displacement of F occurs during the ion bombardment. One should also note, however, that for this system and experimental geometry we work at the detection limit for F. This will be studied in more detail in the near future using a scattering geometry (smaller θ) which is more sensitive to F detection and minimizes the ion damage on the sample.

3.2. Si / GaSb / Si

GaSb has a lattice constant that is about 12% larger than that of silicon. This will make an epitaxial growth of smooth GaSb layers on silicon by far more difficult. We hope, however, that, nevertheless, for thin interlayers in the monolayer range an epitaxial growth is possible. The system Si/GaSb/Si is well suited for MEIS studies, because both the Ga- and Sb signal can be separated from the silicon background. For thin layers (1–10 ML), the Ga- and Sb signal will also be separated, this makes studies of the geometric structure easier. In addition the cross section for ion backscattering is considerably larger for Ga and Sb than for silicon. Deposition of Ga and Sb at $T_{\text{Sub}} = 450^\circ\text{C}$ results in Ga islands and a monolayer Sb layer on silicon (see Fig. 3a). Stoichiometric GaSb has been found by a deposition below $T_{\text{Sub}} = 400^\circ\text{C}$ while the Sb supply is considerably larger than that of Ga. 200°C is the temperature for GaSb homoepitaxy. It turned out that deposition of Ga and Sb on Si(111) at 200°C results in flat partially epitaxial GaSb islands. Fig. 3b shows results obtained for these deposition conditions. 12 nm GaSb islands on Si(111) are overgrown by 14 nm Si at 200°C . The ratio of Ga- and Sb peak intensities is roughly 2.7 as expected for GaSb. There is no difference visible between the Ga- and Sb yield for channelling and random ion incidence. A corresponding experiment with surface barrier detector shows, however, that such a difference exists indeed (inset Fig. 3b), if the ion dose is kept below ca. $10 \mu\text{C}$. GaSb turns out to be extremely sensitive to radiation damage by the ion beam. Similar radiation damage sensitivities have been earlier reported by

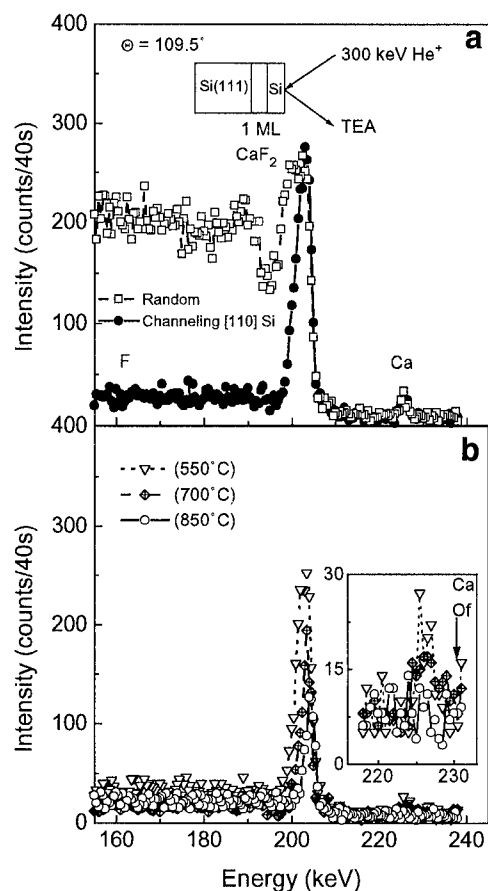


Fig. 2. MEIS spectra for 7.5 nm Si/1 ML CaF_2 /Si(111). (a) Top: spectra for ion incidence along [110] and a random direction. (b) Bottom: spectra for ion incidence along [110] after deposition and after annealing at 3 different temperatures.

Smit and van der Veen for GaSb(110) [20]. Despite this fact they were able to perform an excellent characterisation of the surface geometric structure. They used backscattering geometries with $\theta = 45$ and 60 degrees (the backscattering cross section is then by a factor of ca. 20 larger than in the present case) and used about 20 different spots on the sample for one structure analysis. By this procedure they kept the ion dose on the sample below 6×10^{14} ions/ cm^2 corresponding to $2 \mu\text{C}$ in our case. For our case of buried III–V layers this technique was also applied, but it resulted in an overlap of the Ga and Sb signal either due to GaSb island formation or/and thickness variation of the silicon cap layer.

In Fig. 4, we present our results for 1 ML GaSb

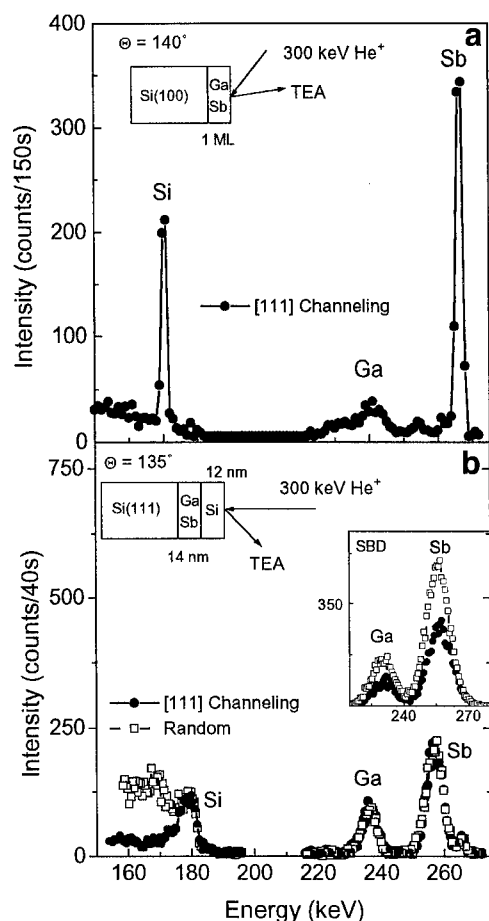


Fig. 3. (a) Top: MEIS spectra for Ga and Sb on Si(100). The total Ga and Sb amount corresponds to 1 ML GaSb. Deposition occurred at 450°C. The broad distribution of Ga is probably due to Ga islands. (b) Bottom: MEIS spectra for 14 nm Si/12 nm GaSb/Si(111), deposition at 200°C; inset: measurement with surface barrier detector, $\theta = 170^\circ$.

on Si(100). The GaSb layer is covered by a 12 nm silicon layer in order to obtain a crystalline silicon cap layer. Silicon is in this case deposited at $T_{\text{Sub}} = 200^\circ\text{C}$ and annealed at 600°C after deposition. Again the results for random ion incidence (\square) and for ion channelling along the [100] axis are given. Comparing the random- and channelling yield intensities of silicon we find a sharp surface peak, a strongly reduced yield behind it and an interface edge between 170 and 180 keV. This is the backscattering contribution of the toplayer which turns, thus, out to be of high epitaxial quality. Two antimony peaks,

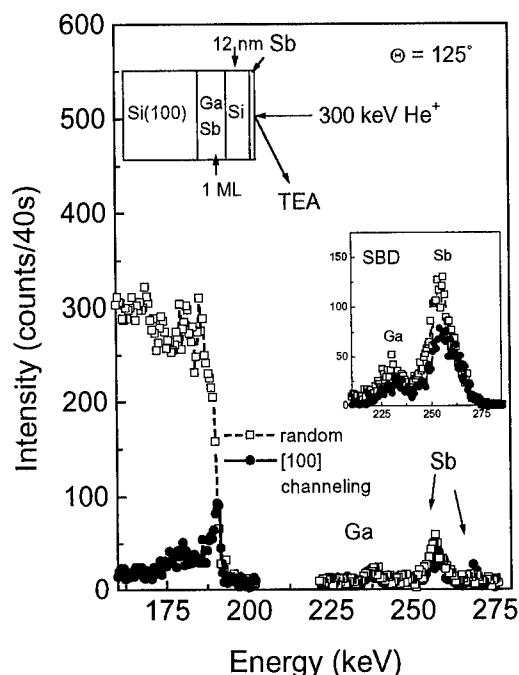


Fig. 4. MEIS spectra for 12 nm Si/1 ML GaSb/Si(100); inset: measurement with surface barrier detector, $\theta = 170^\circ$.

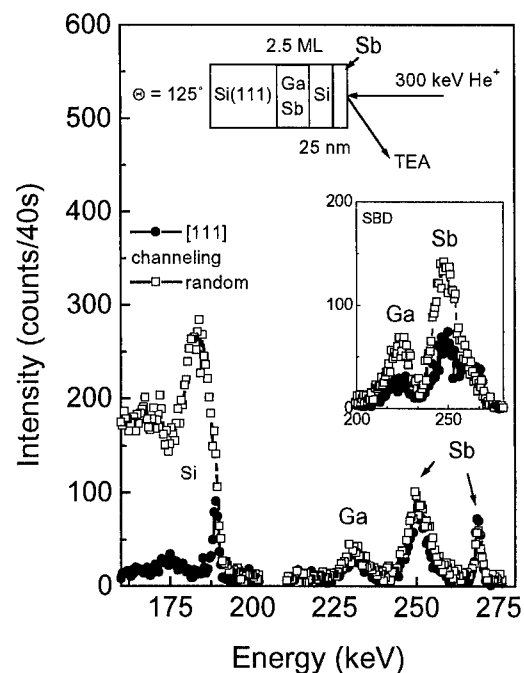


Fig. 5. MEIS spectra for 25 nm Si/2.5 ML GaSb/Si(111); inset: measurement with surface barrier detector, $\theta = 170^\circ$.

one due to backscattering from the surface and one from the interface are found at 270 and at 258 keV. A Ga peak due to backscattering from the interface is found at 238 keV. There is, however, no Ga signal due to backscattering from the surface. This result means that a small amount of antimony diffuses to the surface during the silicon deposition or annealing the sample at 600°C but in contrast to the CaF_2 interlayer GaSb remains at the interface and an excellent cap layer is obtained already at annealing temperatures of 600°C which is possibly due to an influence of Sb. A significant difference for the random and channelling yield in both, gallium and antimony is again not obtained in the spectra. In order to find out whether GaSb is deposited without epitaxial order or whether this order is destroyed by the ion beam, an additional experiment is made with the surface barrier detector. The inset in Fig. 4 shows the results for a random (\square) and [100] channelling (\bullet) ion incidence and for an ion dose of $1 \mu\text{C}/\text{mm}^{-2}$. A significant reduction (30%) in the

channelling yield is found. The peak width in the TEA spectra of the Sb and Ga interface peak in Fig. 4 is broader than that one would expect for one monolayer. Two explanation can be given. Firstly, it is possible that the GaSb has been grown in partially epitaxial islands with an average thickness of 3 nm, so that only 10% of the silicon surface is covered by the GaSb. This would also explain the good epitaxial growth of the silicon toplayer. Secondly, it is possible that we have a smooth and abrupt GaSb layer which is partially epitaxial and that the silicon toplayer has a surface roughness of about 3 nm, which results in the same MEIS spectra. To distinguish between both cases, TEM investigations will be made. MEIS results on Si/GaSb/Si(111) which was deposited at the same conditions as the sample of Fig. 4 are presented in Fig. 5. We find an even better epitaxial silicon toplayer and a GaSb layer which remains located at the interface after annealing at 600°C. The intensities of the GaSb peak from the interface are compatible with 2.5 ML GaSb.

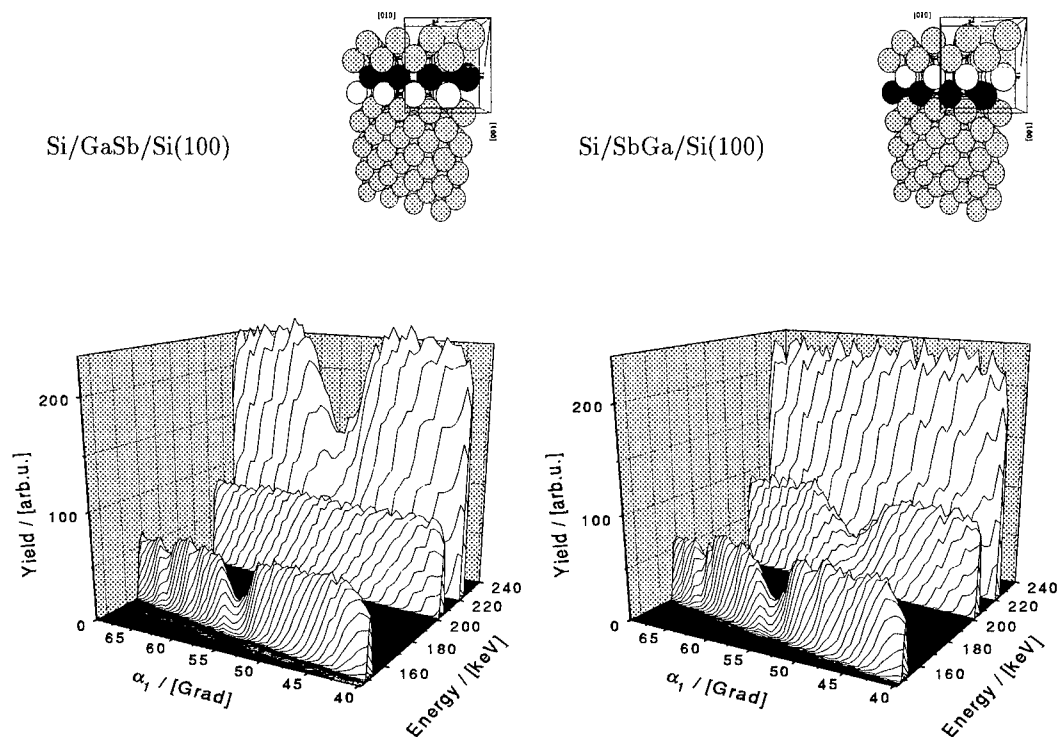


Fig. 6. Computersimulation of MEIS spectra. Top: models of the layer system with GaSb in two opposite dipole orientations. Bottom: calculated MEIS spectra for normal incidence of 250 keV He^+ along the systems in the upper part of this figure. The backscattered ions are collected in the (110) plane close to the [111] blocking direction.

4. Monte Carlo simulations of MEIS spectra

A Monte Carlo program has been written [21,22] which allows to perform calculations of MEIS spectra for arbitrary directions of ion incidence, arbitrary detection directions of the analyzer and several different types of epitaxial layer systems. The basic principles are identical with those in Refs. [23] and [24]. In contrast to those works which were optimized for surface structure analysis and calculated the outgoing trajectories as an inverse channelling process, we calculate the trajectories of outgoing particles from different depths of the layer system in the direction of the TEA. Energy losses can then be incorporated in the calculations in a more natural way also for systems with large number (e.g. 200) of monolayers. The upper part of Fig. 6 shows the model of a layer system with GaSb dipoles. In the lower part, the calculated spectra for the two different dipole orientations are given. Ion incidence occurs normal to the surface. In the one case the Ga yield is reduced at detection angles near 54.7° which corresponds to a [111] blocking direction, in the other case it is the Sb yield which is reduced. This simple example shows that the orientation of dipoles can quantitatively be determined by MEIS, if experiments are successful enough in the preparation of such samples.

5. Conclusion

We have presented first results of a project in which ultrathin (thickness \approx monolayer) interlayers are incorporated between a silicon substrate and a silicon cap layer. The geometric structure of these systems is studied by MEIS. A 15 nm CaF_2 film grown at 700°C turns out to be epitaxial, smooth and rotated by 180° with respect to the Si(111) substrate. Deposition of 5 nm silicon on such CaF_2 films at $T_{\text{Sub}} = 200^\circ\text{C}$ and heating to 600°C after deposition, results in a sample with about 10% CaF_2 at the surface, probably due to island growth of silicon. The silicon layer is only partially epitaxial. Deposition of a monolayer CaF_2 at 700°C and subsequent silicon deposition at 200°C results in a system with Ca at the interface and no detectable amount of CaF_2 at the surface. The 7.5 nm silicon cap layer is amorphous. Heating the sample to 700°C results in a

silicon epitaxy of about 4 nm of the silicon cap layer but after this procedure Ca is again detectable at the surface either due to Ca diffusion to the surface or due to creation of silicon islands. After heating to 850°C the MEIS spectrum is identical with that of a Si(111) crystal. Si epitaxy has therefore occurred up to the surface of the cap layer but CaF_2 is then neither found at the interface nor at the surface of the sample.

The lattice constant of GaSb is about 12% larger than that of silicon making epitaxial growth by far more difficult. Partially epitaxial GaSb islands are observed for deposition at $T_{\text{Sub}} = 200^\circ\text{C}$. These layers are extremely sensitive to radiation damage by the incident ion beam. In a system with one monolayer GaSb on Si(100) with a 12 nm caplayer of silicon which is deposited at $T_{\text{Sub}} = 200^\circ\text{C}$ GaSb remains at the interface when the sample is annealed at 600°C . The cap layer is then almost completely epitaxial and for GaSb some epitaxy is also detected.

In order to get even more quantitative information from the MEIS spectra a computer program has been developed, which allows to calculate MEIS spectra and which takes into consideration all shadowing, channelling and blocking effects. An example calculation for GaSb dipole layers in silicon shows that MEIS is well suited to determine dipole orientations at such interfaces.

Acknowledgements

We would like to thank Prof. H.O. Lutz for the possibility to make use of the ion accelerator and corresponding equipment. Collaboration and technical assistance by his group is gratefully acknowledged. This work was financially supported by the Deutsche Forschungsgemeinschaft (Grant No. Schm-1034/1-1) and by the Ministerium für Wissenschaft und Forschung des Landes NRW.

References

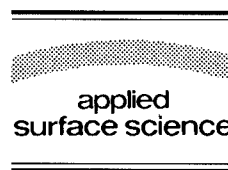
- [1] F. Capasso, *Science* 235 (1987) 172; *Appl. Surf. Sci.* 56–58 (1992) 723.
- [2] G. Margaritondo, *Surf. Sci.* 168 (1986) 439.
- [3] G. Margaritondo, J.T. McKinley, D. Rioux and D.W. Niles, *Appl. Surf. Sci.* 56–58 (1992) 713.

- [4] L. Sorba, G. Bratina, G. Ceccone, A. Antonini, J.F. Walker, M. Micovic and A. Franciosi, *Phys. Rev. B* 43 (1991) 2450.
- [5] T. dell'Orto, J. Almeida, C. Coluzza, A. Baldereschi, G. Margaritondo, M. Cantile, S. Yildirim, L. Sorba and A. Franciosi, *Appl. Phys. Lett.* 64 (1994) 2111.
- [6] G. Biasiol, L. Sorba, G. Bratina, R. Nicolini, A. Franciosi, M. Peressi, S. Baroni, R. Resta and A. Baldereschi, *Phys. Rev. Lett.* 69 (1992) 1283.
- [7] M. Cantile, L. Sorba, S. Yildirim, P. Faraci, G. Biasiol, A. Franciosi, T.J. Miller and M.I. Nathan, *Appl. Phys. Lett.* 64 (1994) 988.
- [8] J.T. McKinley, Y. Hwu, B.E.C. Koltenbah, G. Margaritondo, S. Baroni and R. Resta, *Appl. Surf. Sci.* 56–58 (1992) 762.
- [9] A. Muñoz, N. Chetty and R.M. Martin, *Phys. Rev. B* 41 (1990) 2976.
- [10] B. Schmiedeskamp, T. Tappe, B. Heidemann, J. Schlosser, G. Haindl, U. Kleineberg, T. Albers and M. Neumann, in: *Formation of Semiconductor Interfaces*, Eds. B. Lengeler, H. Lüth, W. Mönch and J. Pollmann (World Scientific, Singapore, 1994) S. 637–640.
- [11] W.K. Chu, J.W. Mayer and M.A. Nicolet, *Backscattering spectrometry* (Academic Press, New York, 1978) ch. 5.
- [12] B. Heidemann, Thesis, Universität Bielefeld (1994).
- [13] E. Kasper and J.C. Bean, Eds., *Silicon–Molecular Beam Epitaxy* (CRC Press, Boca Raton, FL, 1988).
- [14] F.J. Himpsel, U.O. Karlsson, J.F. Morar, D. Rieger and J.A. Yarmoff, *Phys. Rev. Lett.* 56 (1986) 1497.
- [15] M.A. Olmstead, R.I.G. Uhrberg, R.D. Bringans and R.Z. Bachrach, *Phys. Rev. B* 35 (1987) 7526.
- [16] R.M. Tromp and M.C. Reuter, *Phys. Rev. Lett.* 61 (1988) 1756.
- [17] H. Ishiwara, Ref. [13], ch. 5.
- [18] H. Ishiwara and T. Asano, *Appl. Phys. Lett.* 40 (1982) 66.
- [19] B. Schmiedeskamp, A. Kloidt, H.J. Stock, U. Kleineberg, T. Döhring, M. Pröpper, S. Rahn, K. Hilgers, B. Heidemann, T. Tappe, U. Heinzmann, M. Krumrey, P. Müller, F. Scholze and K.F. Heidemann, *Optical Eng.* 33 (1994) 1314.
- [20] L. Smit and J.F. van der Veen, *Surf. Sci.* 166 (1986) 183.
- [21] J. Schlosser, Diplomarbeit, University of Bielefeld (1994).
- [22] J. Schlosser et. al., in preparation.
- [23] J.W.M. Frenken, R.M. Tromp and J.F. van der Veen, *Nucl. Instr. Meth. B* 17 (1986) 334.
- [24] P.F.A. Alkemade, W.C. Turkenburg and J. Vrijmoeth, *Nucl. Instr. Meth. B* 64 (1992) 716.



ELSEVIER

Applied Surface Science 104/105 (1996) 669–678



Clustering on surfaces at finite areal coverages

R. Barel, Y. Mai, G.R. Carlow, M. Zinke-Allmang *

Department of Physics, University of Western Ontario, London, Ontario, Canada N6A 3K7

Received 28 June 1995; accepted 11 September 1995

Abstract

Clustering is a phase separation process often observed in growth on surfaces and of technological relevance in heteroepitaxy. Cluster size distributions for three-dimensional cluster ripening on surfaces has been studied to test predictions for the dependence of ripening on finite areal cluster fractions. We show that the distribution broaden relative to the mean field model and also exceed the increase in width predicted in simulations for three-dimensional systems caused by the interaction between neighboring clusters. The observed data are in significant disagreement with the model and the simulations in respect of the skewness of the cluster size distributions which can be associated with unexpectedly intensive coalescence effects even at areal coverages as low as 10%.

1. Introduction

Phase separation phenomena on surfaces are an active field of fundamental research in non-equilibrium thermodynamics. Many theoretical and simulation studies offer increasing insight into phenomena such as the self-similar evolution of the surface morphology. A growing number of experimental studies try to test the complex and divers predictions [1–3].

Epitaxial growth of thin semiconductor films is an interesting case to apply these concepts and to try to benefit from the results. This ranges from just identifying growth parameters to suppress adverse effects of phase separation to intentionally employing these phenomena to improve structural film features or to achieve otherwise unaccessible patterns. Examples include the growth of tilted superlattices, the use of surfactants to improve the quality of metastable heteroepitaxial films and ‘low temperature epitaxy’ where epitaxial growth involves nucleation and island growth to complete a new layer.

A detailed understanding of the phase separation processes is required to systematic apply these concepts in epitaxial growth. This level has not been reached. In particular, transitions between different cluster growth processes are not well characterized [4] and even the description of well defined processes, such as ripening, is still over-simplified for typical film growth conditions.

* Corresponding author.

A problem of this type is studied in this paper: deviations of the cluster size distribution from theoretical predictions for late stage ripening, i.e., the growth of larger clusters at the expense of smaller clusters due to the capillarity effect. The dependence of the cluster size distribution on the areal fraction of clusters on the surface will be quantified, indicating that an increasing areal cluster coverage (a) leads to increasing interaction between neighboring clusters which results in a broadening of the distributions and (b) increases significantly the probability of coalescence events, i.e., the merging of clusters upon contact, which can be linked to a skewness of the distribution with a tail toward larger cluster sizes.

2. Theoretical concepts

During deposition of a molecular beam on a substrate, the increasing saturation of adatoms shifts the system often into a regime of the surface phase diagram where the single phase is not stable any more. As a result, the system shows a propensity toward surface phase separation processes through clustering [5]. The clustering process best understood theoretically is Ostwald ripening. A description of ripening on surfaces has to be based on the Gibbs–Thomson effect, mass conservation, the mass transport mechanism of monomers and any applicable cluster–cluster interaction effect. To obtain an analytical solution, the cluster–cluster interactions have to be neglected, leading to a mean-field description applicable at zero volume fraction of the dense cluster phase. This description has first been given by Lifshitz and Slyozov (LSW-theory [6]). A necessary condition for the late stage is that the free adatom diffusion fields of all individual clusters overlap. As a consequence clusters larger than the average size will have an equilibrium concentration which is smaller than the actual free adatom concentration and grow, clusters smaller than the average size dissolve at the same time with a net transport of material from smaller to larger clusters. The quantitative predictions of the LSW theory include:

(i) A power law for the growth of the average sized cluster with time. Limiting the discussion to cases where the mass transport is limited by surface diffusion, we get

$$r_c(t) = r_0(1 + t/\tau_n)^{1/n} \quad (1)$$

where $r_c(t)$ is the critical cluster radius, i.e., the radius of those clusters which are in equilibrium at time t with the free adatom concentration, τ is a temperature dependent time constant and $n = 3$ for three-dimensional clusters in solution or two-dimensional islands on a surface and $n = 4$ for three-dimensional clusters on a surface.

(ii) A cluster size distribution $f(r, t)$ which becomes time independent if rescaled using the critical cluster size at time t ('statistical self-similarity'). Two distributions will be considered in this paper, the distribution for three-dimensional clusters in a solution [5,6]:

$$f(\rho, t) = \frac{\nu_{33} \rho^2}{(1 + t/\tau)^{4/3}} \left(\frac{3}{3 + \rho} \right)^{7/3} \left(\frac{-3/2}{\rho - 3/2} \right)^{11/3} \exp \left[\frac{\rho}{\rho - 3/2} \right] \quad (2a)$$

with $\rho = r/r_c(t) < 3/2$ (dashed curve in Fig. 1) and the distribution for three-dimensional clusters on a surface [5,6]:

$$f(\rho, t) = \frac{\nu_{32} \rho^3}{(1 + t/\tau)} \frac{\exp \left[\frac{2/3}{\rho - 4/3} \right] \exp \left[-\frac{1}{6\sqrt{2}} \tan^{-1} \left(\frac{\rho + 4/3}{4\sqrt{2/3}} \right) \right]}{(4/3 - \rho)^{19/6} (\rho^2 + 8\rho/3 + 16/3)^{23/12}} \quad (2b)$$

with $\rho < 4/3$ (solid curve in Fig. 1). ν_{33} and ν_{32} are numerical constants.

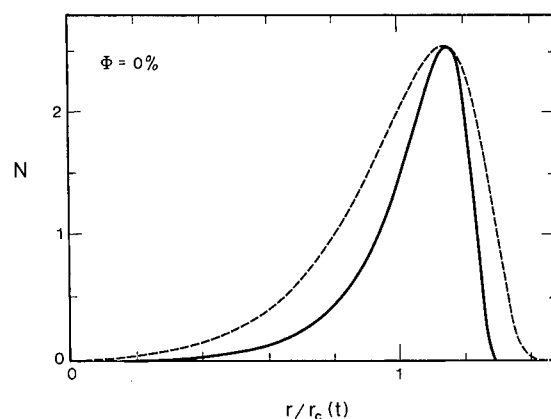


Fig. 1. Cluster size distributions for Ostwald ripening dominated cluster growth (LSW model). The dashed line represents three-dimensional clustering in solution (Eq. (2a)) and the solid line represents three-dimensional clustering on a surface (Eq. (2b)).

The power law has been confirmed experimentally for several systems on surfaces [7]. Less successful were attempts to match experimental cluster size distributions with the model predictions in Eqs. (2a) and (2b) and this issue is the topic of the current study.

The starting point are several recent simulation studies which predict a connection between the deviations from the ideal cluster size distribution and the areal fraction of clusters which is associated with local interactions of neighboring clusters. Grant et al. [8] recently published a theoretical study on this effect which critically discusses the underlying physical concepts of these simulations. If this connection can be demonstrated experimentally, we would not only obtain better predictions for cluster size distributions, but also gain insight in the interaction of clusters on surfaces.

The simulations include the cooperative effects of the droplets which give rise to the dependence on the droplet volume fraction beyond the LSW mean field theory [8–14]. Statistical mechanics methods are used to incorporate effects due to interactions between immobile, spatially correlated droplets. The correlations are generated by a cumulative effect of droplet interactions with time through the diffusion field, analogous to the well-known correlations between particles generated by intermolecular forces in gas dynamics. In some studies, particular focus was given to the effect of diffusive correlations between nearest neighboring clusters, showing their particular relevance in the development of the distribution. The growth of clusters in that study was specifically limited to the diffusive influence in the immediate vicinity of a cluster.

Since the simulations are usually done for either two-dimensional islanding on a surface or three-dimensional clustering in solution, however, we have to keep in mind that they do not strictly apply to clustering in thin film growth, which is the experimental case discussed in this paper¹. In particular the surface coverage fraction itself becomes a decreasing function of time, increasing the likelihood of coalescence processes which occur at very high areal cluster coverages.

3. Results and sample analysis

Results are reported in this section for four different systems, (i) Ga on Si(111), (ii) Ge on Si(100), (iii) Sn on Si(111) and (iv) In on Si(111); the Ga, Sn and In samples were prepared in the same ultra-high vacuum

¹ Note that a recent simulation of the geometry present in thin film growth has been done by Atwater and Yang [15] but cannot be used for comparison due to the use of an alternative mass transport mechanism which results in another power law than underlying our experimental data.

deposition system with a base pressure of 1×10^{-10} mbar (University of Western Ontario), the Ge data are based on previously published measurements done at Bell Laboratories [4]. Si substrates were prepared by the Shiraki method [16]. Metal deposition was obtained from Knudsen cells with the sample held at room temperature. Annealing was done as a post-deposition process to ensure mass conservation conditions during cluster growth. Material loss due to desorption can be ruled out based on independent measurements of desorption rates (see e.g. [17]). The amount of deposited material was measured after completion of the experiment using ex-situ ion scattering techniques [18].

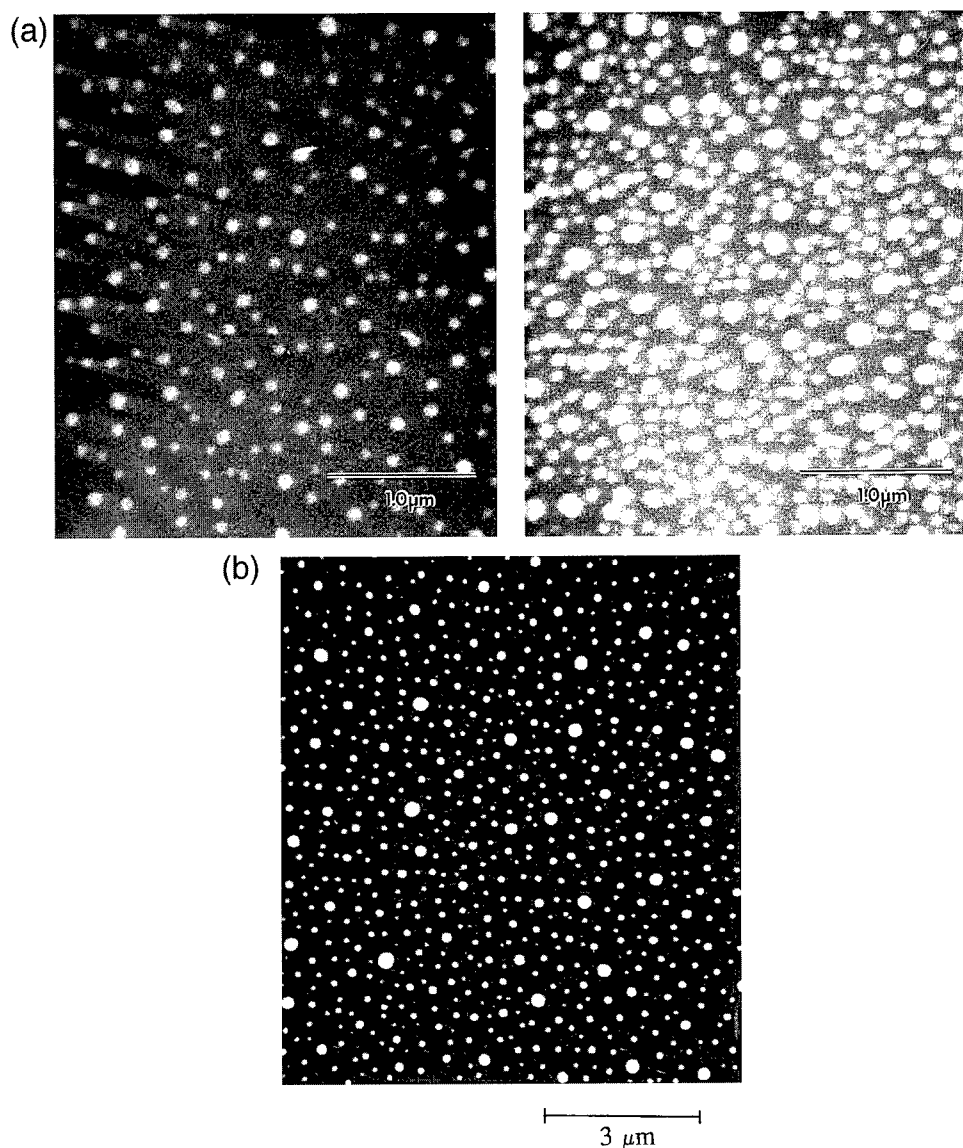


Fig. 2. (a) Two SEM micrographs for Ga/Si(111) at 7.2 ML equivalent coverage corresponding to an areal coverage of 8.3% (left) and 48 ML equivalent coverage corresponding to an areal coverage of 24.6% (right). (b) SEM micrograph for In/Si(111) at 21.8 ML equivalent coverage corresponding to an areal coverage of 11.3%.

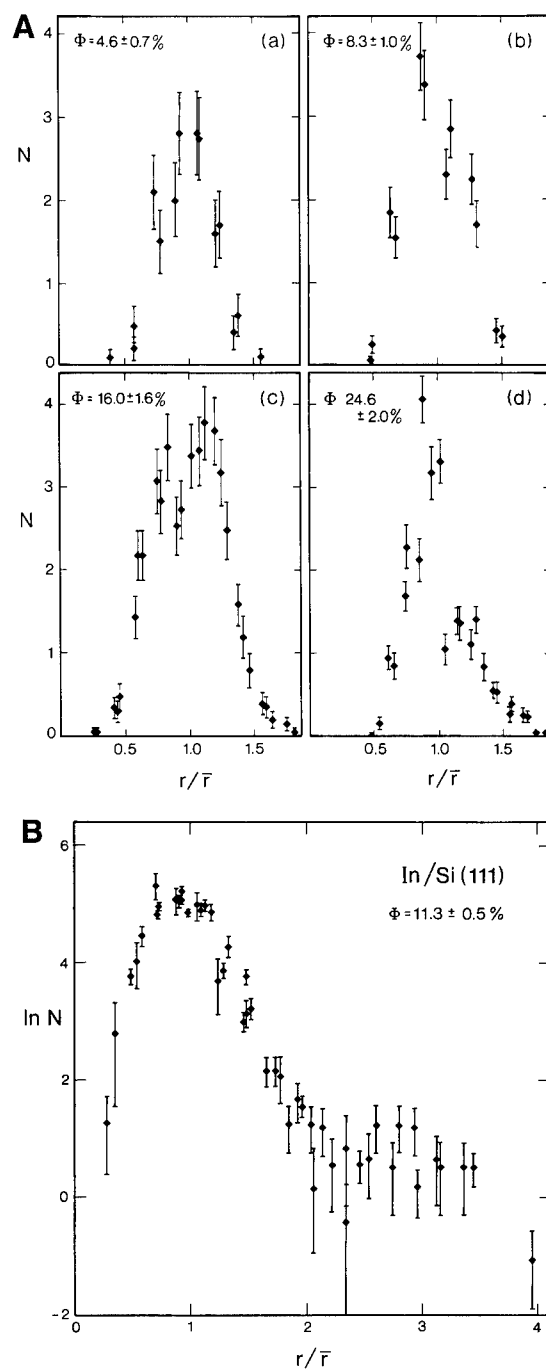


Fig. 3. (A) Cluster size distributions for Ga/Si(111), (a) 3.4 ML, (b) 7.2 ML, (c) 17.5 ML and (d) 49 ML equivalent coverage. N is number of clusters per unit area and per bin width, \bar{r} the mean radius as defined in Eq. (3). (B) Cluster size distribution for In/Si(111) with equivalent 21.8 ML coverage after annealing at 375°C for 35 min. Shown is $\ln(N)$ versus r/\bar{r} to emphasize smaller cluster numbers in the tails of the distribution.

The specific preparation conditions were (a) for Ga/Si: coverages ranging from 2.5×10^{15} atoms/cm² (3.3 monolayer (ML)) to 4×10^{16} at/cm² (48 ML), each identically annealed at 535°C for 30 min, resulting in average cluster radii of 500 Å; (b) for In/Si: samples with 6.4 and 21.8 ML, post-deposit annealed at 375°C for 35 min, resulting in typical cluster radii of 500–1000 Å; and (c) for Sn/Si: coverages of 5 and 50 ML, post-deposit annealed at 400°C for 20 to 240 min, resulting in average cluster sizes in the range of 1–2 μm [19]. (d) The Ge/Si data are based on 9 ML deposition with 10 min annealing at 650°C, resulting in average cluster radii of 3000 Å [4].

Cluster size distributions were studied in all cases with ex-situ electron microscopic techniques. Fig. 2a shows two micrographs for Ga/Si(111) at 7.2 ML equivalent coverage (left) and 48 ML equivalent coverage (right); Fig. 2b shows a micrograph of In/Si(111) at 21.8 ML equivalent coverage. Note the qualitative tendency toward a bimodal size distribution for the In and the higher coverage Ga samples.

From the micrographs cluster size distributions were obtained. To limit the influence of lateral thermal gradients across the surface, clusters in a smaller area (within 1×1 mm²) near the center of the sample were analyzed. Cluster size distributions for four Ga coverages, (a) 3.4, (b) 7.2, (c) 17.5 and (d) 49 ML on Si(111) are shown in Fig. 3a. Normalized numbers of clusters (per unit area and per bin width) are plotted versus r/\bar{r} , with \bar{r} the mean radius as defined in Eq. (3).

$$\bar{r}(t_0) = \int_0^\infty r f(r, t_0) dr \text{ with } \int_0^\infty f(r, t_0) dr = 1 \quad (3)$$

Each plot represents typically 1000 clusters analyzed on three to five micrographs taken at the same magnification. The distribution for the sample with the lowest coverage represents only about 500 clusters due to the low cluster density on the surface. As a result data at low coverages carry a larger statistical error.

Cluster size distributions in the cases of In and Sn on Si(111) were obtained with a computer based image analysis program typically based on 2000 clusters from five to ten micrographs at magnifications ranging from 10k to 50k. Fig. 3b shows the In cluster size distribution obtained for a sample with equivalent 21.8 ML coverage after annealing at 375°C for 35 min. Note that in this plot the logarithmic normalized number of clusters is shown versus r/\bar{r} . This representation is more sensitive to lower numbers of clusters as required for the discussion of coalescence effects.

In many theoretical studies, changes of the cluster size distribution with volume fraction are quantified by calculating the first moments of the cluster size distributions. We will consider the standard deviation (σ) and the skewness (K_s), with

$$\sigma^2 = \int_0^\infty \left(\frac{r}{\bar{r}(t_0)} - 1 \right)^2 f(r, t_0) dr$$

$$K_s = \frac{1}{\sigma^3} \int_0^\infty \left(\frac{r}{\bar{r}(t_0)} - 1 \right)^3 f(r, t_0) dr \quad (4)$$

The standard deviation is a measure of the width of the distribution and the skewness is a measure of the asymmetry of the distribution.

4. Discussion

Fig. 4a and 4b show plots of $\Delta\sigma/\sigma(\Phi=0)$ with $\Delta\sigma = \sigma(\Phi) - \sigma(\Phi=0)$, i.e., the relative change in the standard deviation (in percent) with areal coverage, Φ . Both figures show the same data, with Fig. 4a using a linear Φ -axis and Fig. 4b using a logarithmic Φ -axis to highlight the dependence on smaller coverages. This representation was chosen instead of a plot of σ vs. Φ for the following reason: the standard deviation and

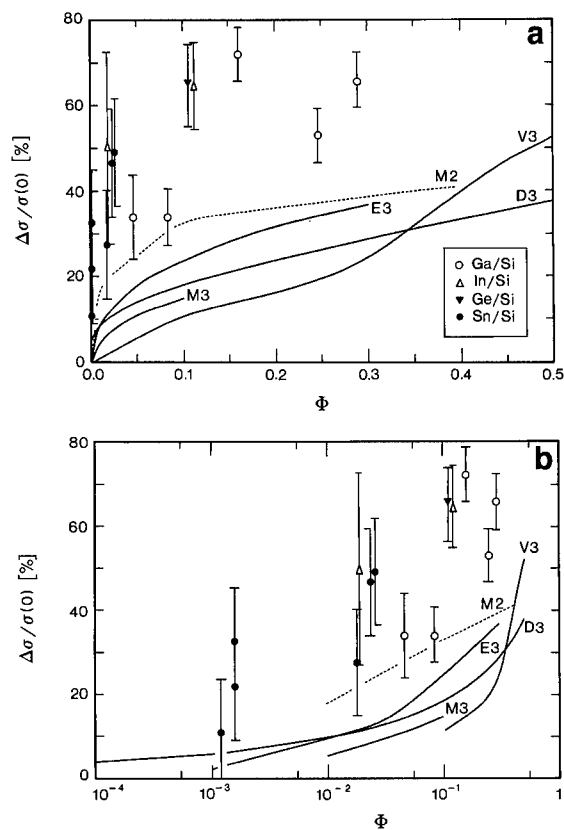


Fig. 4. Plots of the relative increase of the standard deviation width of the cluster size distributions (in %) versus areal coverage fraction Φ . (a) linear Φ axis, (b) logarithmic Φ axis to highlight smaller coverages. Solid lines represent simulations for three-dimensional systems by Marqusee et al. (M3 [9]), Enomoto et al. (E3 [10]), Voorhees et al. (V3 [11]) and Davies et al. (D3 [12]). The dashed line is a simulation for a two-dimensional system by Marqusee (M2 [13]). The symbols for the experimental data are indicated in the inset.

skewness values vary for the two distributions in Eqs. (2a) and (2b) with $\sigma = 0.21$ and $K_s = -0.9$ for Eq. (2a) and $\sigma = 0.16$ and $K_s = -1.3$ for Eq. (2b). This can be seen in Fig. 1 where the solid curve has a narrower peak and the peak is skewed stronger to higher $r/r_c(t)$ -values. Thus, absolute values of σ can only be compared if the same underlying geometry is given; in the current case, where simulations are only available for entirely three- or two-dimensional systems, a comparison with the relative change is more appropriate.

The solid lines represent simulations for three-dimensional systems; the label M3 identifies work by Marqusee et al. [9], E3 work by Enomoto et al. [10], V3 work by Voorhees et al. [11] and D3 work by Davies et al. [12]. For volume fractions $\leq 6\%$, Grant et al. [8] confirmed in a theoretical study the predictions by Marqusee and Enomoto using a mean field model. The dashed line is a simulation for a two-dimensional system by Marqusee [13]. For areal fractions up to 8.5% Grant et al. [8] again found agreement between the simulation and a mean field model approach. The variable symbols represent experimental data for different systems as indicated in the inset.

The experimental cluster size distributions show clear deviations from both, the basic LSW theory ($\Delta\sigma/\sigma(0) = 0$) and the simulation predictions. Standard deviations of experimental distributions exceed the LSW value by 40% and more. This trend continues to cluster densities as small as 0.1% (see Fig. 4b). The experimental data exceed also the simulation values for finite volume fractions, typically by a factor of two. The

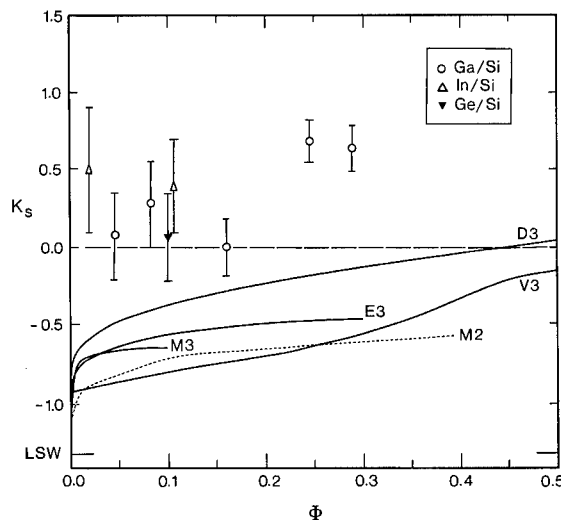


Fig. 5. Skewness of cluster size distributions versus the areal coverage Φ . Notations are the same as for Fig. 4.

qualitative features of the simulations, i.e., that broadening increases with volume fraction with a steeper increase below 10%, are also present in the experimental data.

Fig. 5 shows a plot of the skewness of the distributions, K_s , as defined in Eq. (4), versus the areal coverage, Φ . Although, $K_s(\Phi=0)$ also depends on the dimensionality of the system, the absolute value is shown to emphasize the variation in sign. Notations of solid, dashed lines and symbols are the same as in Fig. 4. Note that the statistical error on K_s increases significantly for smaller areal coverages, and therefore no values are shown for the Sn/Si system.

Again, the experimental cluster size distributions show clear deviations from both, the basic LSW theory (labelled LSW on the axis of the plot) and the simulation predictions for three- or two-dimensional systems. The data disagree in this case also qualitatively. While the simulations predict distributions with negative skewness which become more symmetric with increasing volume fraction, the experimental data show consistently positive skewness values with the tail toward larger cluster sizes increasingly distinguishable for larger areal coverages.

Thus, Fig. 4 and Fig. 5 show that the experimental data follow a similar trend toward broader distributions as seen in simulations, with a stronger absolute effect, but that the origin of a tail toward larger cluster sizes in the distributions is not predicted in simulations. Two physical concepts explain these findings, (i) the degree of cluster–cluster interactions of three dimensional clusters on a surface (a case not directly studied in simulations) and (ii) concurrent coalescence during the evolution of the morphology.

4.1. Cluster–cluster interactions

As shown in a large number of simulations, cluster–cluster interactions tend to widen the cluster size distribution and increase the value of the skewness of the distribution toward zero (i.e., symmetric distribution curves). This effect also applies in the current system, since the presence of diffusive fields around clusters underlies the cluster growth process in the same fashion as assumed in the simulations.

Further support of the concept comes from a second prediction of the simulations which has been confirmed for the experimental data: using the model with neighboring cluster interactions through diffusive fields (a) the volume fraction dependence does not change the time dependence of the cluster radius growth (power law) but (b) has a minor effect on the absolute growth rate. This variation in growth rate as a function of areal coverage

has been studied experimentally for Sn/Si [19] and a rate increase of the same order of magnitude as in the simulations was observed.

The larger broadening of the experimental distributions is due to the difference in dimensionality to the simulations since we study three-dimensional clusters on surfaces. This implies that the areal coverage for the present data is a decreasing function of time, $d\Phi(t)/dt < 0$, and the analyzed distribution will carry information of previously higher areal fractions. This contrasts the current study with all available simulations for diffusion limited growth of three- or two-dimensional systems, where the volume fraction or areal fraction will practically be conserved during late stage cluster growth.

4.2. Concurrent coalescence

The qualitative disagreement in skewness data is caused by significant coalescence rates, an effect not considered in the simulations. The higher areal coverage sample in Fig. 2a and the sample in Fig. 2b show a qualitative tendency toward bi-modal distributions. As Fig. 3A and 3B show, a genuine bi-modal character has not been developed, however, particularly the logarithmic representation of the In/Si distribution shows clearly a range of few, but large clusters extending significantly beyond the extrapolated slope of the peak of the distribution. For Ga/Si this feature is less distinct and contributes more directly to the steepness of the peak at larger cluster sizes. A tendency toward bi-modality of a distribution is closely linked to coalescence growth [2,20]. Even in a non-mass conserved system, where coalescence growth may dominate the evolution of the cluster size distribution, the actual formation of a distinctive minimum in the distribution will take rather long [20]. For immobile clusters, von Smoluchowski showed already that rate of growth will be inversely proportional to the volume fraction for coalescence [21], but if coalescence occurs in a system, the growth rate will be higher than for ripening growth as shown in an experimental study for Ga/GaAs(001) [2]. Thus the result of coalescence events will always be visible at the upper end of a cluster size distribution which is dominated by ripening growth.

5. Conclusion and outlook

We have shown that the width of the cluster size distributions for three-dimensional cluster ripening on surfaces broadens relative to the mean field model (LSW theory) and also exceeds the increase in width predicted in simulations of three-dimensional clustering in solution or two-dimensional islanding on surfaces. The physical origin of this effect is the interaction between neighboring clusters through the diffusive field. The excess broadening in the experiments is caused by the decreasing areal fraction in the case of three-dimensional clustering on a surface.

The observed data are in significant disagreement with the mean field model and the simulation results in respect of the skewness of the cluster size distributions. This can be linked to coalescence events which can be shown to play an important role even at areal coverage fractions of only 10%. Again, the decreasing areal coverage fraction during the evolution of the morphology in the present experimental study allows an enhancement of this effect.

Of fundamental interest are the implications on the concept of self-similarity which is analytically predicted for the mean field model [6]. In the case of three-dimensional clusters in solution or two-dimensional islanding on surfaces, the simulations suggest that self-similarity holds at any (time independent) volume fraction, but that the cluster size distributions are different from the LSW model. In our case, the areal coverage will asymptotically reach zero and we conclude therefore that all observed cluster size distributions in this geometry are transient to the LSW prediction. Particularly the relevance of the areal coverage on the likelihood of coalescence events in the observed distributions suggests that a system of higher areal coverage resembles the morphology of the system at an earlier time during the evolution toward the self-similar state.

Acknowledgements

We thank Y. Chen for technical assistance and J. Gill for the computer-based sample analysis program. Financial support for this work was received from the Natural Sciences and Engineering Research Council of Canada and the Ontario Center for Materials Research (OCMR). RJB acknowledges also a scholarship of the OCMR.

References

- [1] T.D. Lowes and M. Zinke-Allmang, *Phys. Rev. B* 49 (1994) 16678.
- [2] M. Zinke-Allmang, L.C. Feldman and W. van Saarloos, *Phys. Rev. Lett.* 68 (1992) 2358.
- [3] M.G. Lagally, R. Kariotis, B.S. Swartzentruber and Y.-W. Mo, *Ultramicroscopy* 31 (1989) 87.
- [4] M. Zinke-Allmang, *J. Vac. Sci. Technol. B* 10 (1992) 1984.
- [5] M. Zinke-Allmang, L.C. Feldman and M.H. Grabow, *Surf. Sci. Rep.* 16 (1992) 377.
- [6] I.M. Lifshitz and V.V. Slyozov, *J. Phys. Chem. Solids* 19 (1961) 35; *Sov. Phys. JETP* 35 (1959) 331; C. Wagner, *Z. Elektrochem.* 65 (1961) 581; B.K. Chakraverty, *J. Phys. Chem. Solids* 28 (1967) 2401.
- [7] M. Zinke-Allmang and L.C. Feldman, *Appl. Surf. Sci.* 52 (1991) 357.
- [8] J.H. Yao, K.R. Elder, H. Guo and M. Grant, *Phys. Rev. B* 47 (1993) 14110.
- [9] J.A. Marqusee and J. Ross, *J. Chem. Phys.* 80 (1984) 536.
- [10] Y. Enomoto, M. Tokuyama and K. Kawasaki, *Acta Met.* 34 (1986) 2119.
- [11] P.W. Voorhees and M.E. Glicksman, *Acta Met.* 32 (1984) 2001, 2013.
- [12] C.K.L. Davies, P. Nash and R.N. Stevens, *Acta Met.* 28 (1980) 179.
- [13] J.A. Marqusee, *J. Chem. Phys.* 81 (1984) 976.
- [14] P.W. Voorhees, *J. Statist. Phys.* 38 (1985) 231; C.S. Jayanth and P. Nash, *J. Mater. Sci.* 24 (1989) 3041; M. Tokuyama, Y. Enomoto and K. Kawasaki, *Physica A* 143 (1987) 183; *A* 123 (1984) 386; *A* 134 (1986) 323; A.J. Ardell, *Phys. Rev. B* 41 (1990) 2554.
- [15] H.A. Atwater and C.M. Yang, *J. Appl. Phys.* 67 (1990) 6202.
- [16] A. Ishizaka and Y. Shiraki, *J. Electrochem. Soc.* 133 (1986) 666.
- [17] M. Zinke-Allmang and L.C. Feldman, *Surf. Sci.* 191 (1987) L749.
- [18] L.C. Feldman and J.W. Mayer, in: *Fundamentals of Surface and Thin Film Analysis* (Prentice-Hall, Englewood Cliffs, NJ, 1986).
- [19] G.R. Carlow and M. Zinke-Allmang, *Can. J. Phys.* 72 (1994) 812; *Surf. Sci.* 328 (1995) 311.
- [20] F. Family and P. Meakin, *Phys. Rev. A* 40 (1989) 3836.
- [21] M. von Smoluchowski, *Z. Phys. Chem. (Leipzig)* 92 (1917) 129; *Phys. Z.* 17 (1916) 585.



ELSEVIER

Applied Surface Science 104/105 (1996) 679–684

applied
surface science

Preparation and properties of thin polycrystalline $\text{MnSi}_{1.73}$ films

St. Teichert^{a,*}, R. Kilper^a, J. Erben^a, D. Franke^a,
B. Gebhard^a, Th. Franke^a, P. Häussler^a, W. Henrion^b, H. Lange^b

^a Institute of Physics, Technical University Chemnitz-Zwickau, D-09107 Chemnitz, Germany

^b Department Photovoltaics, Hahn-Meitner-Institute, Rudower Chaussee 5, D-12489 Berlin, Germany

Received 28 June 1995; accepted 14 September 1995

Abstract

Thin $\text{MnSi}_{1.73}$ films were prepared by a DC sputter method in a high vacuum deposition chamber. As target material a MnSi_2 silicide target was used. Films were deposited onto quartz substrates at different temperatures (330–875 K) without any annealing steps after the sputter process. The composition of the samples was determined by Rutherford backscattering spectroscopy. Within the detection limit of this method no contamination in the films was found. The crystalline structure of the films was analyzed by transmission electron microscopy. At substrate temperatures of 530 K always a tetragonal crystalline phase of $\text{MnSi}_{1.73}$ was observed. The specific resistivity and the Hall mobility of the samples were determined in the temperature range from 300 to 25 K. The results of the electrical measurements verify the low crystallization temperature of the films. The character of the electrical transport in the crystalline films is strongly influenced by the preparation temperature. With rising substrate temperature the sign of the temperature coefficient of resistivity at room temperature changes from negative to positive values. At room temperature Hall mobilities in the region of $1.4 \text{ cm}^2 \text{ V}^{-1} \text{ s}^{-1}$ were obtained. The temperature dependence of the electrical transport properties can be interpreted in the picture of a degenerated semiconductor. With optical measurements at room temperature an indirect gap of 0.46 eV was determined. The structure of the transmission spectra was influenced by the different heat treatments in the sample preparation.

1. Introduction

Semiconducting transition metal silicides could play an important role in the advanced silicon technology for new optoelectronic devices as well as in the development of thermoelectric applications. In higher manganese silicides (HMS) with a composition near $\text{MnSi}_{1.73}$ the existence of a direct gap between 0.68 and 0.83 eV [1,2] has been reported from measurements of the optical absorption coefficient.

The analysis of electrical resistivity and the Hall coefficient in the intrinsic conduction region yields gap values between 0.4 and 0.7 eV [1,3–6]. Generally, the electrical properties of bulk [4], single crystalline [3,5] and polycrystalline thin films [4,6] of HMS can be described in the picture of a highly degenerated p-type semiconductor. Typical values for the hole concentration are 7×10^{20} up to $3 \times 10^{21} \text{ cm}^{-3}$, which are independent of the temperature in the extrinsic conduction region, the Hall mobility at room temperature is about $1 \text{ cm}^2 \text{ V}^{-1} \text{ s}^{-1}$.

Usually, the thin film preparation of HMS is performed by a solid phase reaction of a Mn film

* Corresponding author. Tel.: +49-371-5313114; fax: +49-371-5313077; e-mail: teichert@physik.tu-chemnitz.de.

deposited onto a Si substrate with a one [2,7] or a two [6,8,9] step annealing process. The lowest temperatures reported for observing the HMS with one annealing step are about 760 to 775 K.

This paper reports about structural, electrical and optical properties on HMS thin films, prepared by a one step process onto insulating substrates (quartz, SiO_2) held at different temperatures during the deposition.

2. Experimental

For the preparation of the HMS films a DC triode sputtering process of a silicide target with a nominal composition MnSi_2 has been used. The layers were deposited onto heated substrates without subsequent annealing steps, typical sputter parameters are described elsewhere [10]. The electrical and optical transmission measurements were performed on films deposited onto quartz substrates with a thickness of about 50 nm. For the determination of the optical absorption edge the layer thickness used was 400 nm. The composition of the samples was determined by Rutherford backscattering spectroscopy (RBS). To analyse the crystal structure and the grain size with transmission electron microscopy (TEM) some samples were prepared onto oxidised silicon substrates. The determination of the Hall coefficient and the resistivity were carried out with a standard DC van der Pauw technique [11] in the temperature range from 300 to 25 K with maximal available fields up to 1 T. For all samples a linear dependence of the Hall voltage on the applied electric current or

on the magnetic field was observed. The thermopower of the films was measured with a method using the change of the thermoelectric voltage while varying the temperatures T_1 and T_2 at two corners of the sample in the temperature range from 300 to 20 K. The optical measurements were performed in the transmission and reflection mode with a UV–VIS–NIR Lambda 19 (Perkin–Elmer) spectrometer in the spectral range from 0.3 to 6.2 eV. To exclude effects of light scattering in the polycrystalline samples an integrating sphere was used.

3. Results and discussion

The RBS analysis of the films shows a composition of $\text{MnSi}_{1.78}$, indicating a small excess of silicon with respect to the HMS. The contamination level of other elements was below the detection limit of about 1 at%. The crystallite size determined by Brightfield TEM for a sample with $T_{\text{sub}} = 530$ K is below 20 nm, at substrate temperatures > 640 K crystallite sizes between 40 and 70 nm were found. The diffraction pattern of films prepared at temperatures ≥ 530 K could be attributed to the tetragonal $\text{Mn}_{15}\text{Si}_{26}$ phase [12]. It must be noted, that many other tetragonal phases in the vicinity of the composition $\text{MnSi}_{1.73}$ have been reported, for example $\text{Mn}_{11}\text{Si}_{19}$ [13], $\text{Mn}_{26}\text{Si}_{45}$ [14] or $\text{Mn}_{27}\text{Si}_{47}$ [15]. The unit cell of these structures consists of a Mn and a Si sublattice, the c -axis is the result of the approximate smallest common multiple of these two sublattices [2]. De Ridder et al. [16] have shown, that the c -axis of the Si subcell changes continuously and that the

Table 1
Room temperature values of electrical transport coefficients

T_{sub} (K)	ρ ($10^{-3} \Omega \text{ cm}$)	R_{H} ($\text{cm}^3 \text{ A}^{-1} \text{ s}^{-1}$)	μ_{H} ($\text{cm}^2 \text{ V}^{-1} \text{ s}^{-1}$)	S ($\mu\text{V K}^{-1}$)
330	1.1	6.6×10^{-5}	0.06	25
485	47.6	0.03	0.63	141
530	31.2	0.0284	0.91	204
590	18.9	0.0193	1.02	175
640	17.4	0.0197	1.13	190
710	12.6	0.0183	1.45	188
755	10.4	0.0151	1.45	168
785	9.58	0.0137	1.43	165
840	8.01	0.0113	1.41	164
875	7.72	0.0095	1.23	143

description of the HMS as a superstructure of two tetragonal subcells is the result of an average over large areas. However, with the common TEM used here, it is not possible to distinguish between the different tetragonal superstructures, therefore the observed tetragonal structure from the diffraction pattern will be referred here as HMS. The occurrence of the crystalline HMS at substrate temperatures as low as 530 K could be confirmed by the comparison of the electrical properties at room temperature (Table 1). The change of the Hall mobility by one order of magnitude between samples prepared at 330 and 485 K, respectively, and the strong rise of the thermopower shows the starting of crystallization in the films. With further increasing of the substrate temperature and an improvement of the crystalline quality of the films the following results could be observed: The room temperature resistivity decreases to $7.7 \times 10^{-3} \Omega \text{ cm}$, which is about two times higher than those reported for bulk material [4] or for thin films [1,7]. The sign of the Hall coefficient R_H as well as of the thermopower S is positive for all samples, indicating, that predominantly hole conduction occurs. By using the equation $p = (eR_H)^{-1}$ for determination of the hole concentration may be found values between 2×10^{20} and $6.6 \times 10^{20} \text{ cm}^{-3}$. These carrier concentrations are lower than previously re-

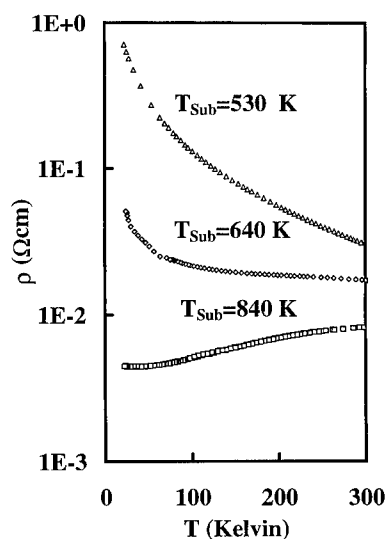


Fig. 1. Specific resistivity versus temperature for different preparation temperatures.

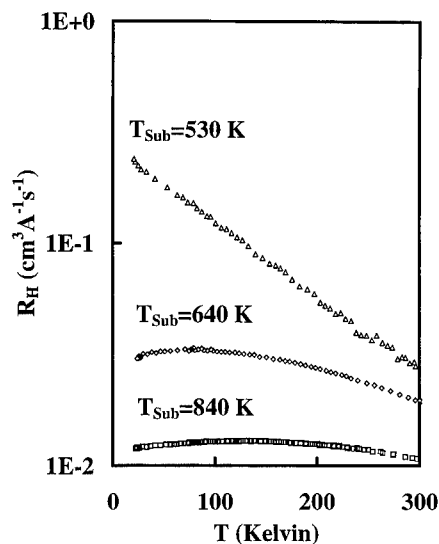


Fig. 2. Hall coefficient as a function of the temperature.

ported values. It may be suggested, that the higher resistivity is a result of the lower carrier concentration. This assumption is supported by the results for the Hall mobility of samples prepared between 710 and 840 K. The change of the resistivity from 17×10^{-3} to $8 \times 10^{-3} \Omega \text{ cm}$ is accompanied by an increasing of the carrier concentration, which leads to a constant Hall mobility at room temperature.

The transport coefficients in the temperature region for 25 to 300 K are plotted for representative samples in Figs. 1–4. The temperature coefficient of the resistivity at higher temperatures changes with increasing substrate temperature from negative to positive. The curve, observed at $T_{\text{sub}} = 840 \text{ K}$, is comparable with the results found in other experiments on HMS [4,7]. At low temperatures a minimum in the resistivity occurs. One origin for the increase of the resistivity of the sample prepared at 530 K is the decrease of the carrier concentration as indicated by the increasing of the Hall coefficient. On the other hand, the Hall mobility is lower than for the other samples. Possible sources for this behaviour are stronger scattering due to grain size effects or grain boundaries with respect to the higher quality samples. For these scattering mechanisms, an activated character of the conductivity as well as for the Hall mobility would be expected. From the Arrhenius plot, not shown here, it could be seen, that

there are no linear regions, a determination of a typical activation energy is not possible. With improving crystalline quality the degenerate character of the Hall coefficient rises. The hole density is only weakly temperature dependent for the highest substrate temperatures. The highest mobility values at low temperatures could be observed in this case. Usually, the mobility of semiconductors decreases with increase of the degenerate character, the opposite result here allows the conclusion, that the reason for the degeneracy is an intrinsic property of the HMS, occurring in films of improved quality. The shape of the Hall mobility curve shows a maximum, shifting to lower energies with increasing absolute value in the mobility. As the main scattering mechanism at higher temperatures acoustic phonon scattering can be assumed, whereas at lower temperatures impurity scattering is preferred. The mobility due to phonon scattering in the degenerate case [18] is proportional to $T^{-1/2}$, for ionized impurities it is expected to be proportional to $T^{3/2}$. However, it must be kept in mind, that these dependencies occur by including the assumption of a parabolic density of states at the valence band edge. In the case of HMS with the strong degeneracy of the carriers, the forming of band tail states should be taken into account by interpreting the data. A more detailed analysis of the data will be given elsewhere.

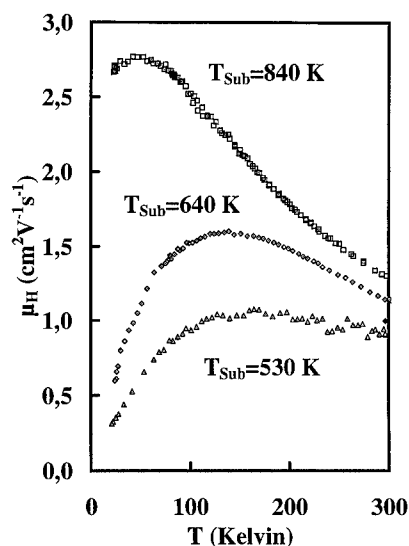


Fig. 3. Hall mobility plotted versus temperature.

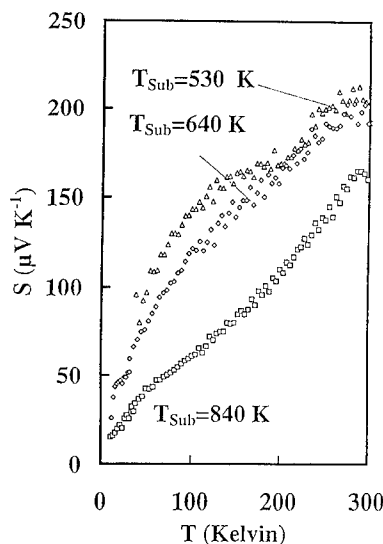


Fig. 4. Thermopower plotted versus temperature.

The determination of the transmission was performed in the energy range from 0.5 to 6.2 eV on samples with a thickness of about 50 nm (Fig. 5). The remarkable change of the transmission on the long wavelength side with increasing substrate temperature shows the transition from a metallic like free electron absorption to a semiconductor like behaviour. It must be noted, that the most drastic rise of transmission occurs between samples prepared at 330 and 530 K, a further enlargement of the substrate temperature changes the transmission properties only weakly. This is in addition to the electrical and structural properties a clear evidence for the formation of crystalline HMS at temperatures as low as 530 K and for the improving of the film quality with rising substrate temperature. A second feature of the transmission spectra, occurring at elevated substrate temperatures, is a transmission window at a photon energy of about 1.95 eV. This enhanced transmission in the region of interband transitions must be attributed to a strong minimum in the combined density of states. To our knowledge, there has been no such behaviour of the density of states in other semiconducting silicides. This transmission window seems to be a typical property of the band-structure of the HMS, because an improved crystalline quality gives a further decrease of the absorption in this spectral region. It can be expected, that in

single crystalline films of HMS this effect becomes more pronounced.

For the measurement of the absorption edge a sample with 400 nm thickness prepared at 530 K was used. For illustration of the fundamental transition the square and the square root of the absorption coefficient versus the photon energy are plotted in Fig. 6. In the case of a direct transition a proportionality between α^2 and the incident photon energy could be expected [17]. The intercept of the linear region with the energy axis gives the minimum direct energy required for the optical transition. The result of a least square fit is here 0.78 eV for the direct gap. However, the scatter of the data allows not a high accuracy in the determination of the gap energy, good fits will be observed with energies between 0.75 and 0.8 eV. This result is in good agreement with previously reported results [1,2]. The direct gap is preceded by an indirect one, as evidenced by the proportionality between $\alpha^{1/2}$ and the photon energy. In this case the square root of the absorption coefficient should exhibit two linear branches, corresponding to transitions including the absorption or emission of a phonon. The intercept with the energy axis at the low energy side is the gap energy minus the phonon energy, on the higher energy side the intercept gives the energy gap plus

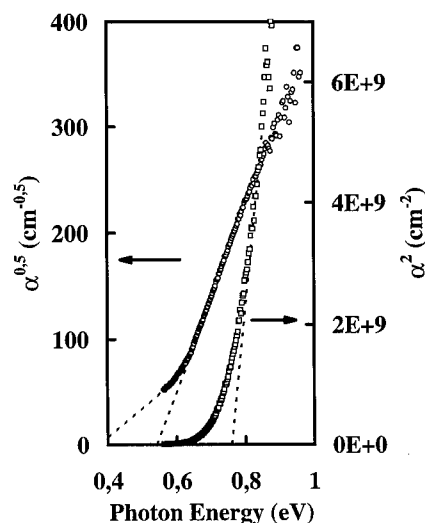


Fig. 6. Absorption edge for direct and indirect transition.

the phonon energy, respectively. The analysis of the data yields a gap energy of 0.46 eV with an accompanied phonon of 60 to 70 meV. It must be mentioned that the two linear regions are well pronounced. A necessary condition for the observation of a clear indirect gap is the existence of larger ordered areas in the sample. Bost and Mahan [1] found with their analysis for indirect transitions a gap of about 0.54 eV, whereas the result of the resistivity measurements in the intrinsic conduction regime leads to a minimum gap energy of 0.68 eV. However, taking into account the complicated crystal structure of the HMS a variation of the gap energy with the continuous change of the lattice properties could be expected.

4. Summarizing remarks

The influence of the preparation temperature on the structural, electrical and optical properties was studied on thin films of HMS. The main results of the experiments are the following:

(1) By preparing HMS thin films onto heated substrates the occurrence of the tetragonal structure is observed at $T_{\text{sub}} = 530$ K. Further increasing of the substrate temperature leads to an increase of the crystallite size.

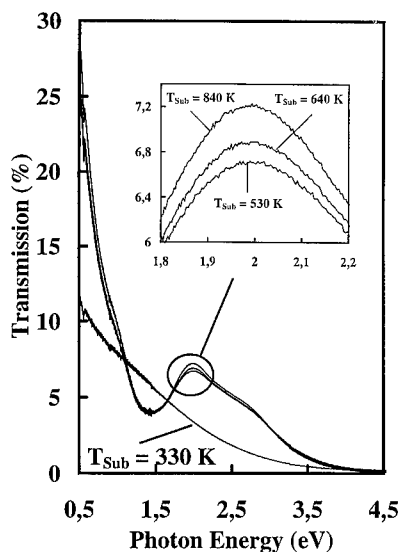


Fig. 5. Transmission spectra for samples with a thickness of about 50 nm.

(2) The hole concentration and the degenerate character of the charge carriers, respectively, increases with improving of the crystalline quality. Room temperature values of the Hall mobility and the thermopower are in the same order as in single crystalline material.

(3) The HMS exhibits an indirect gap of 0.46 eV assisted by phonons with an energy of about 65 meV, a direct transition is observed at about 0.78 eV. In the transmission spectra a window exists corresponding to a minimum of the combined density of states at about 2 eV.

Acknowledgements

This work was supported by the project FKZ 251/531 of BMFT Germany.

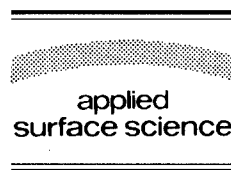
References

- [1] M.C. Bost and J.E. Mahan, *J. Electron. Mater.* 16 (1987) 389.
- [2] L. Zhang and D.G. Ivey, *J. Mater. Sci.* 2 (1991) 116.
- [3] E.N. Nikitin, W.J. Tarasov, A.A. Andreev and L.N. Schumilowa, *Fiz. Tw. Tela* 11 (1969) 3389.
- [4] I. Nishida, *J. Mater. Sci.* 7 (1972) 435.
- [5] I. Kawasumi, M. Sakata, I. Nishida and K. Masumoto, *J. Mater. Sci.* 16 (1981) 355.
- [6] C. Krontiras, K. Pomoni and M. Roilos, *J. Phys. D: Appl. Phys.* 21 (1988) 509.
- [7] M. Eizenberg and K.N. Tu, *J. Appl. Phys.* 53 (1982) 6885.
- [8] K. Sundström, S. Petersson and P. Tove, *Phys. Status Solidi (a)* 20 (1973) 653.
- [9] Y.C. Lian and L.J. Chen, *Appl. Phys. Lett.* 48 (1986) 359.
- [10] S. Teichert, R. Kilper, T. Franke, J. Erben, P. Häussler, W. Henrion, H. Lange and D. Panknin, *Appl. Surf. Sci.* 91 (1995) 56.
- [11] L.J. van der Pauw, *Philips Res. Rep.* 13 (1958) 1.
- [12] H.W. Knott, M.H. Mueller and L. Heaton, *Acta Cryst.* 23 (1967) 549.
- [13] O. Schwomma, A. Preisinger, H. Nowotny and A. Wittman, *Monatsh. Chem.* 95 (1964) 1527.
- [14] H. Fliecher, H. Völlenkle and H. Nowotny, *Monatsh. Chem.* 98 (1967) 2173.
- [15] G. Zwilling and H. Nowotny, *Monatsh. Chem.* 102 (1971) 672.
- [16] R. de Ridder, G. van Tandeloo and S. Amelinckx, *Phys. Status Solidi (a)* 33 (1976) 383.
- [17] P.S. Kirejev, *Physik der Halbleiter* (Akademie Verlag, Berlin, 1974) p. 490.
- [18] V.L. Bonc-Bruevic and S.G. Kalasnikov, *Halbleiterphysik* (VEB Deutscher Verlag der Wissenschaften, Berlin, 1982) p. 451.



ELSEVIER

Applied Surface Science 104/105 (1996) 685–689



A summary and perspective on the Fifth International Conference on the Formation of Semiconductor Interfaces, Princeton, NJ

Hans Lüth

Institut für Schicht- und Ionentechnik, Forschungszentrum Jülich GmbH, D-52425 Jülich, Germany

Received 1 September 1995; accepted 5 September 1995

It has become a tradition of this conference to have a summary talk at its end, in which concluding remarks highlight the program and put it into perspective relative to the general development in the research field of 'Semiconductor Interfaces'. I have accepted the honour to give this final concluding talk, even though I feel the burden to report about work of which I often have but circumstantial knowledge. I want to emphasize in this context that the following judgements are based on a personal view that is biased by my own research experience in subsets of this field.

In order to judge the quality level of the contributions and, particularly, their relevance in addressing up-to-date issues, one might ask oneself, does the program reflect recent developments and meet the needs of other research branches that rely on results from our own work?, and, who are our clients? Such questions are easily answered for the field of basic research on semiconductor interfaces. By tradition and by taking into account common historical roots the major impact of semiconductor interface science is on

1. Microelectronics
2. Optoelectronics
3. Sensor and actuator technology

Particularly in times of shrinking research budgets, it behooves us to understand the problems in these more applied fields of industrial research. Interface physics and chemistry can certainly benefit by help-

ing to clarify important technological questions and by developing new ideas and directions of addressing interface related problems in these fields.

What are some of the important near-term challenges in the above listed areas that might also entice and redirect the work of interface scientists? Some aspects will be mentioned. In microelectronics the development of basic CMOS technology to higher integration levels reaches a serious development barrier in the first decade of the next century, when feature sizes in the 50 nm range with gate oxide thicknesses below 5 nm become necessary in DRAMs for information capacities beyond 1 Gbit (Fig. 1). Research on extremely thin SiO₂ layers and its interfaces to Si is therefore necessary to shift the limits of CMOS technology as far as possible. Even with modified CMOS device concepts as e.g. vertical MOSFETs etc., severe physical limitations such as leakage due to tunnelling through the ultrathin oxide layers, electromigration in vias and interconnects, etc. hinder further miniaturisation. On the other hand, quantum effects, e.g. tunnelling, might be used in new device concepts that would allow more complex functions on the chip with relaxed feature size constraints and, consequently, more relaxed lithographic requirements. Quantum devices of novel functionality and/or increased compactness that show promise for commercialization would immediately enhance the importance of work on semiconductor heterointerfaces, modification of surfaces on a nanometre

scale and the formation of nanostructures. Taking into account the success of III–V heterostructures with reasonably high band offsets in the design of novel heterostructure devices, there is strong interest in new types of Si based heterostructures with higher band discontinuities than for the SiGe/Si system. This would open new possibilities for Si-based quantum electronics that might be compatible with advanced CMOS technology. Similarly important is further research on III–V semiconductor heterostructures and interfaces for the improvement of optoelectronic and photonic devices, such as lasers, light emitting diodes (LED's), detectors and optoelectronic and photonic switches. A new impact in this field is expected from the development of large band gap materials, in particular SiC, GaN, GaAlN and ZnSe-related materials, which would open the visible and near UV spectral range to semiconductor optoelectronics.

Large band gap materials also play an important role in power electronics and sensor technology at elevated temperatures: in general, sensor and actuator technology benefits appreciably from interface studies, as well as from the development of surface modification and patterning techniques. In particular with respect to biosensors, the interaction of organic molecules with semiconductor surfaces is of central interest.

From these general considerations, one might define the following topics of central interest for semiconductor interface research in the present situation.

1. Si/insulator interface
2. Si-heterostructures
3. Interface structure, layer growth and surface passivation
4. Fabrication of nanometre structures
5. Analytical tools on nanometre scale
6. Organic molecules on semiconductors
7. Wide band gap heterostructures

The ICFSI-5 in Princeton was an excellent conference as its program covered more or less these important topics of semiconductor interface research. In all these fields a number of interesting contributions were presented. In the following some highlights — of course biased by personal view and understanding — are briefly discussed.

1. Si/insulator interface

The Si/SiO₂ interface, because of its importance for MOSFET performance, particularly attracts attention in areas of ultrathin SiO₂ films and degradation effects due to hot electrons in short channel devices. Cartier gave an interesting contribution about the passivation and generation of defects in which he

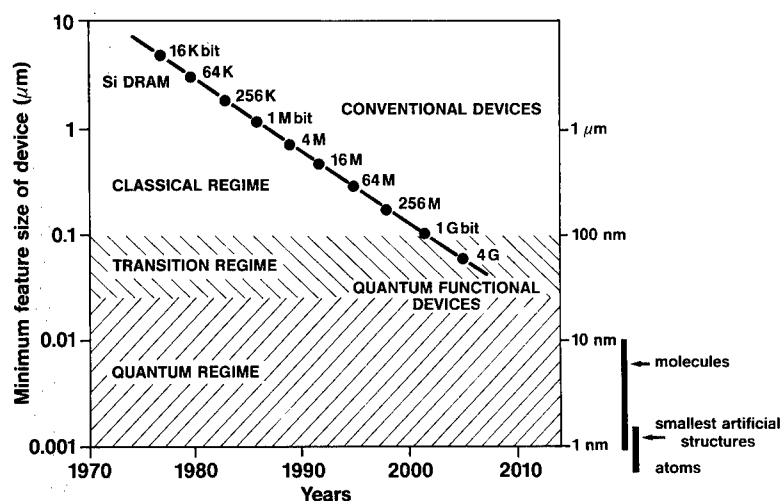


Fig. 1. Plot of the minimum feature size of Si DRAM chips versus time (Moore plot). Beyond the 1 Gigabit information capacity physical limits start to complicate the conventional 'main stream' CMOS technology. Below feature sizes of 50 nm quantum electronics might yield new perspectives for further developments.

discussed the importance of embedded hydrogen versus the well established hole model. The latter defect model seems to be valid preferentially for thicker SiO_2 layers. Lucovsky et al. reported about nitrated Si/SiO_2 interfaces produced by low temperature plasma processing and rapid thermal annealing. Their conclusions concerning defect formation, e.g. as over-coordinated O (oxonium) or N (ammonium) and their removal, fit well into the picture of hydrogen defects as presented by Cartier. Peng et al. determined the density of microvoids (ca. $10^9/\text{cm}^2$) and vacancies (ca. $10^{10}/\text{cm}^2$) from positron annihilation studies of SiO_2/Si interfaces. Another interesting contribution about the electronic structure of SiO_2/Si interfaces was presented by Pasquarello et al. From first principles calculations of Si 2p core level shifts they could explain the reported experimental data solely on covalent band structure models, without taking into account effects due to dangling bonds.

Lu et al. used very high-resolution medium energy ion scattering (MEIS) in combination with X-ray photoelectron spectroscopy to study the initial stages of Si oxidation. The unexpected fast thermal oxidation at very low SiO_2 film thickness (< 10 nm) is ascribed to a combination of interfacial, near interfacial and surface reactions.

2. Si-heterostructures

Advanced Si technology beyond CMOS suffers from the fact that no perfect Si-based heterostructures exist with large band gap and correspondingly large band offsets to Si. SiGe/Si is certainly the best developed material system in this respect, and has already been used in devices such as HEMT's and HBT's. However, even for thicker pseudomorphic and highly stressed SiGe layers valence band offsets of only 0.3 eV can be reached. In contrast to Si, not much is known so far about reactions of technological relevance on the surface of the Ge–Si alloy system. In this context the paper by Tettelin et al. on plasma assisted oxidation of LPVPE grown SiGe layers presented interesting new results about the presence of a Ge-rich interlayer at the SiGe/Oxide interface.

Of related interest are epitaxial, wide band gap

materials and dielectrics on Si. For the latter, CaF_2 layers are interesting candidates, even though the crystallographic quality of the layers reached so far is not sufficient for the manufacture of tunnel devices. Much more work is needed, which was reflected at this conference by two contributions: Sokolov et al. studied structural transformations, i.e. phase transitions, at $\text{CaF}_2/\text{Si}(111)$ interfaces, whereas Wollschläger and Meier performed a LEED investigation and observed multilayer growth before the completion of the first monolayer. These results helped shed some light on the problems that arise in attempts to improve the CaF_2 epitaxy on Si.

3. Surfactants, passivation and layer growth

For all kind of semiconductor devices the interface quality is of the utmost importance and can be affected by the geometrical structure and roughness at the interface and by the ensuing role of electronic structure related to interface states. Surface and interface scattering, as well as gate control in field effect structures are strongly affected. Besides growth studies of layers in general (including surface and interface roughness), the effect of surfactants during the growth and the techniques of passivating a surface with a low density of interface states continue to be major research fields.

Ploog et al. gave an interesting overview with a number of recent experimental results about the role of surfactants in III–V MBE. The distinction between reactive and non-reactive surfactants helps to identify the right surfactant material for a specific epitaxial process. In particular, the improvement of strained InAs and InGaAs layer growth with In as a 'virtual' surfactant gave novel insights into the interplay between 2D and 3D layer growth modes.

Some interesting papers that emphasized structural characterisation techniques (STM, UHV–TEM) were given by Williams, LeGoues and Voigtländer. The STM allows a detailed characterization of growth on an atomic scale. Examples included a dynamic mode for taking movies during the growth of Si and Ge, and the investigation and explanation of step bunching on Si surfaces. UHV–TEM studies by LeGoues presented new insights into the nucleation process and the effect of glide dislocations on relief-

ing stress in highly strained SiGe layers on Si. Theoretical contributions are essential for a deeper understanding. In this context Tersoff considered stress induced roughening during epitaxial growth and pointed out that in contrast to relaxation there is no critical thickness for stress induced roughening. Kaminski and Suris described simulations of the smoothing of a crystal surface during growth interruption by surface migration of 2D holes and 2D nuclei.

In the field of surface passivation, contributions by Sundararaman et al. and by Mitchell et al. treated the sulfur passivation of InP, whereas Xu et al. gave some interesting results about the chemical bonds on nitrated GaAs surfaces.

4. Growth and characterization of nanostructures

With respect to future quantum electronics, the growth and characterization of nanostructures based on semiconductor heterostructures is a growing and very important research field, where many of the surface and interface techniques are used with great success. The growth of quantum wires attracts a lot of interest. Sakaki discussed in his contribution the effects of interface quality on the characteristics of nanostructures and pointed out that, due to the inverse L^3 dependence of the quantization energies on feature size, the properties of quantum wires depend sensitively on potential fluctuations at the interfaces. Since lithographic techniques are difficult to apply in the 10 nm size range, self assembled nanostructures during epitaxial growth play an increasing role. Priester and Lannoo explained in their theoretical paper the transformation of 2D platelets into 3D islands (for the case of InAs on GaAs shown in the contribution of Moisson) by a repulsive interaction.

Hartmann et al. demonstrated the growth of SiGe quantum wires in lithographically structured V-groves on Si and reported about the electron-microscopic determination of inhomogeneous concentration profiles of Ge across the wire. An interesting contribution was given by Hess on the application of a near-field optical probe to study the local variations of photons emitted from nanostructures. The application of STM cross sectional techniques for the

characterization of nanostructures was presented in several papers, in particular by Pfister et al., Lew et al. and Avery et al.

5. Wide band gap material

Future developments of optoelectronics in the visible and near UV spectral range, as well as in high power electronics and sensor technology for elevated temperature applications are intimately related to a better understanding and implementation of epitaxial processes of wide band gap materials such as the group III nitrides, diamond (C) and SiC. Also in this research field ICFSI-5 included a good overview and some late exciting results. Dupuis reviewed in his talk the work on MOCVD of high quality III–V nitrides. Several exciting theoretical papers contributed to a better understanding of the difficult growth processes of wide band gap materials: De Vita et al. reported about first-principle-calculations of phase transitions from diamond to graphite. His beautiful molecular pictures of different stages of the phase transition gave the impression that it may be very useful for researchers in the epitaxial growth field to first let the computer do the physics of a difficult technological process. Pollmann et al. and Käckell et al. presented interesting new results about structure and electronic properties of IV, III–V, II–VI surfaces. In particular the comparison of the SiC surfaces with those of GaAs(110) is instructive. For the experimentally difficult field of GaN growth and doping, the theoretical results presented by van der Walle about the formation energies of several defects in that material are of major importance.

6. Organic molecules on semiconductors

The interface between organic materials and semiconductors is another novel field where the ICFSI has entered. Koma extensively discussed the effect of various surface preparation techniques on the adsorption behaviour of organic molecules. Hirose et al. reported about more complex systems consisting of metal contacts on organic material deposited on a semiconductor. For these systems, the chemical

properties derived from synchrotron photoemission studies could be related to the electrical behaviour of the contact.

7. Continuing issues

A number of papers at this conference treated long standing problems such as space charge layers, Fermi level pinning, metal/semiconductor contacts etc. Out of the large number of very nice results which were presented, I will only mention three: Aristov and Le Lay reported on photoemission from a two-dimensional electron gas at the InAs(110) surface. They could clearly resolve two occupied sub-bands within the quantized accumulation layer. Qi et al. used the extremely interface sensitive second-order non-linear optical spectroscopy to study the distribution of metal induced gap states (MIGS) at metal/GaAs(001) interfaces. Studies of this type are at their beginning and promise a great deal of interesting spectral information about interfaces.

Hashizume et al. presented a novel in-situ electrochemical process for the preparation of metal/GaAs and metal/InP junctions. This process leads to high quality, defect free Schottky interfaces and unpinned Fermi levels on InP. The authors used this process with success for the fabrication of an InP-MESFET.

8. Concluding remarks

In my opinion ICFSI-5 in Princeton was again a great success in this conference series, which started in Europe in 1985 (Marseille, France). The measure of success is based on the number of papers, on the high calibre of relevant contributions and especially on the high level and extent of the discussions, which is largely a consequence of its format.

The conference series started as a European–Japanese alternative to the USA-based conference on Physics and Chemistry of Semiconductor Interfaces (PCSI). ICFSI-5 in Princeton was the first one to be organized in the USA. In my judgement this internationalization is a very good development that broadens the basis of ICFSI, which has now become a ‘world conference’, with added participation from East Asian and from Eastern European countries.

Our special thanks are due to the organizers of the conference for the opportunity to attend such an interesting and exciting meeting. Not only the scientific quality and diversity of the contributions are acknowledged, but also the delightful site of Princeton University and the distracting social events contributed much to the success of ICFSI-5.



ELSEVIER

Applied Surface Science 104/105 (1996) 690–698

applied
surface science

Author index

- Aiba, T., see Hattori, T. 104/105 (1996) 323
Akita, Y., see Koyama, M. 104/105 (1996) 253
Allinger, Th., see Stietz, F. 104/105 (1996) 169
Almeida, J., see Coluzza, C. 104/105 (1996) 196
Alperovich, V.L., A.G. Paulish, H.E. Scheibler, V.I. Tynnyi and A.S. Terekhov, Unpinned behavior of the Fermi level and photovoltage on p-(100)GaAs surface facilitated by deposition of cesium 104/105 (1996) 228
Alvarado, S.F., see Pfister, M. 104/105 (1996) 516
Alvarez, J.C., see Sokolov, N.S. 104/105 (1996) 402
Andersson, M.O., see Farmer, K.R. 104/105 (1996) 369
Angerer, W., see Qi, J. 104/105 (1996) 188
Angermann, H., K. Kliefoth and H. Flietner, Preparation of H-terminated Si surfaces and their characterisation by measuring the surface state density 104/105 (1996) 107
Angermann, H., see Flietner, H. 104/105 (1996) 342
Anyele, H.T., see Levermann, A.H. 104/105 (1996) 124
Aquino, A.A. and T.S. Jones, A comparative study of the adsorption and thermal decomposition of triethylgallium and trimethylgallium at GaAs(100) surfaces studied by electron energy loss spectroscopy 104/105 (1996) 304
Aristov, V.Yu., M. Grehk, V.M. Zhilin, A. Taleb-Ibrahimi, G. Indlekofer, Z. Hurych, G. Le Lay and P. Soukiassian, Sb or Cs covered InAs(110) surfaces: moving E_F into conduction band and quantized 2D electron channel 104/105 (1996) 73
Aspnes, D.E., see Rossow, U. 104/105 (1996) 137
Aspnes, D.E., see Rossow, U. 104/105 (1996) 552
Astaldi, C., see De Padova, P. 104/105 (1996) 349
Avery, A.R., J.L. Sudijono, T.S. Jones and B.A. Joyce, Site occupation of Si atoms deposited on vicinal GaAs(001)-(2 × 4) surfaces 104/105 (1996) 539
Bailey, P., see Thornton, J.M.C. 104/105 (1996) 234
Balaban, S.N., see Pokatilov, E.P. 104/105 (1996) 546
Bangert, U., see Hartmann, A. 104/105 (1996) 502
Barbo, F., see Coluzza, C. 104/105 (1996) 196
Barel, R., Y. Mai, G.R. Carlow and M. Zinke-Allmang, Clustering on surfaces at finite areal coverages 104/105 (1996) 669
Barrett, N., see Orlowski, B.A. 104/105 (1996) 282
Bauer, G., see Springholz, G. 104/105 (1996) 637
Baumann, P.K. and R.J. Nemanich, Characterization of cobalt–diamond (100) interfaces: electron affinity and Schottky barrier 104/105 (1996) 267
Bechstedt, F., see Käckell, P. 104/105 (1996) 45
Bechstedt, F., see Käckell, P. 104/105 (1996) 141
Bechstedt, F., see Käckell, P. 104/105 (1996) 490
Behringer, R.E., V. Natarajan and G. Timp, Surface diffusion limitation in laser focused atomic deposition 104/105 (1996) 291
Beitia, C., see Roy, M. 104/105 (1996) 158
Bell, G.R., C.F. McConville and T.S. Jones, Plasmon excitations and the effects of surface preparation in n-type InAs(001) studied by electron energy loss spectroscopy 104/105 (1996) 17
Benjamin, M.C., M.D. Bremser, T.W. Weeks, Jr., S.W. King, R.F. Davis and R.J. Nemanich, UV photoemission study of heteroepitaxial AlGaN films grown on 6H-SiC 104/105 (1996) 455
Bergossi, O., see Coluzza, C. 104/105 (1996) 196
Bertolo, M., see Coluzza, C. 104/105 (1996) 196
Bianco, A., see Coluzza, C. 104/105 (1996) 196
Biasiol, G., see Reinhardt, F. 104/105 (1996) 529
Björkqvist, M., see Göthelid, M. 104/105 (1996) 113
Bolotin, I.L., see Grazhulis, V.A. 104/105 (1996) 68
Borensztein, Y., see Roy, M. 104/105 (1996) 147
Borensztein, Y., see Roy, M. 104/105 (1996) 158
Borsella, E., see De Padova, P. 104/105 (1996) 349
Bozhko, S.I., see Grazhulis, V.A. 104/105 (1996) 68
Brandt, O., see Braun, W. 104/105 (1996) 35
Brandt, O., see Yang, H. 104/105 (1996) 461
Braun, W., O. Brandt, M. Wassermeier, L. Däweritz and K. Ploog, Kinematical RHEED simulation of different structure models for the GaAs (311)A surface 104/105 (1996) 35
Bremser, M.D., see Benjamin, M.C. 104/105 (1996) 455
Bruni, M.R., S. Kačulis, G. Mattogno and G. Righini, Interface abruptness in strained III–V heterostructures 104/105 (1996) 652

- Buchanan, D.A., see Farmer, K.R. 104/105 (1996) 369
- Bulanov, O.R., see Grazhulis, V.A. 104/105 (1996) 68
- Bullock, E.L., see Johansson, L.S.O. 104/105 (1996) 88
- Burgess, S.R., B.C.C. Cowie, S.P. Wilks, P.R. Dunstan, C.J. Dunscombe and R.H. Williams, A surface extended X-ray absorption fine structure study of tellurium adsorbed onto Si(100) 104/105 (1996) 152
- Burstein, E., see Talaat, H. 104/105 (1996) 479
- Cairns, J., see Evans, D.A. 104/105 (1996) 240
- Campman, K.L., see Maranowski, K.D. 104/105 (1996) 621
- Canning, A., see De Vita, A. 104/105 (1996) 297
- Capellini, G., see Di Gaspare, L. 104/105 (1996) 595
- Car, R., see De Vita, A. 104/105 (1996) 297
- Car, R., see Pasquarello, A. 104/105 (1996) 317
- Carlow, G.R., see Barel, R. 104/105 (1996) 669
- Caudano, R., see Guyaux, J.-L. 104/105 (1996) 601
- Cavanna, A., see Sauvage-Simkin, M. 104/105 (1996) 646
- Cerasari, S., see Coluzza, C. 104/105 (1996) 196
- Chang, Y.-L., S.I. Yi, S. Shi, E. Hu, W.H. Weinberg and J. Merz, Hydrogen ion treatments of oxidized GaAs(100) and AlGaAs(100) surfaces: surface stoichiometry and electronic properties 104/105 (1996) 422
- Chatziparaskewas, A., see Tappe, T. 104/105 (1996) 661
- Chen, F., M.M. Waite, S. Ismat Shah, B.A. Orner, S.S. Iyer and J. Kolodzey, Measurements of the energy band offsets of $\text{Si}_{1-x}\text{Ge}_x/\text{Si}$ and $\text{Ge}_{1-y}\text{C}_y/\text{Ge}$ heterojunctions 104/105 (1996) 615
- Cheong, C., see Koyama, M. 104/105 (1996) 253
- Chizhov, I., see Lin, X.F. 104/105 (1996) 223
- Cho, K. and J.D. Joannopoulos, Intrinsic surface atom manipulations in STM and AFM 104/105 (1996) 286
- Chudoba, C., see Di Gaspare, L. 104/105 (1996) 595
- Cole, R.J., see Thornton, J.M.C. 104/105 (1996) 631
- Coluzza, C., J. Almeida, T. dell'Orto, F. Barbo, M. Bertolo, A. Bianco, S. Cerasari, S. Fontana, O. Bergossi, M. Spajer and D. Courjon, Spatially resolved internal and external photoemission of Pt/n-GaP Schottky barrier 104/105 (1996) 196
- Comicioli, C., see De Padova, P. 104/105 (1996) 349
- Courjon, D., see Coluzza, C. 104/105 (1996) 196
- Cowie, B.C.C., see Burgess, S.R. 104/105 (1996) 152
- Cricenti, A., P. Perfetti, B. Nesterenko, G. LeLay and C. Sebenne, Si(110)16 \times 2 and Si(110)2 \times 3-Sb surfaces studied by photoemission and optical spectroscopy 104/105 (1996) 118
- Crotti, C., see De Padova, P. 104/105 (1996) 349
- Dai, H.L., see Li, C.M. 104/105 (1996) 57
- Davis, R.F., see Benjamin, M.C. 104/105 (1996) 455
- Däweritz, L., see Braun, W. 104/105 (1996) 35
- De Andrés, P.L., see Saiz-Pardo, R. 104/105 (1996) 183
- De Padova, P., R. Larciprete, C. Ottaviani, C. Quaresima, P. Perfetti, E. Borsella, C. Astaldi, C. Comicioli, C. Crotti, M. Matteucci, M. Zacchigna and K. Prince, Synchrotron radiation photoelectron spectroscopy of the O(2s) core level as a tool for monitoring the reducing effects of ion bombardment on SnO_2 thin films 104/105 (1996) 349
- De Vita, A., G. Galli, A. Canning and R. Car, Graphitization of diamond (111) studied by first principles molecular dynamics 104/105 (1996) 297
- Debauche, C.P., see Farmer, K.R. 104/105 (1996) 369
- Deelman, P.W., T. Thundat and L.J. Schowalter, AFM and RHEED study of Ge islanding on Si(111) and Si(100) 104/105 (1996) 510
- Dell'Orto, T., see Coluzza, C. 104/105 (1996) 196
- Del Sole, R., see Roy, M. 104/105 (1996) 158
- Del Sole, R., see Shkrebtii, A.I. 104/105 (1996) 176
- Dhanak, V.R., see Johal, T.K. 104/105 (1996) 257
- Di Cioccio, L., see Semond, F. 104/105 (1996) 79
- Di Gaspare, L., G. Capellini, C. Chudoba, M. Sebastiani and F. Evangelisti, Low-energy yield spectroscopy determination of band offsets: application to the epitaxial Ge/Si(100) heterostructure 104/105 (1996) 595
- Dieker, C., see Hartmann, A. 104/105 (1996) 502
- Ding, X.M., see Xu, Q.J. 104/105 (1996) 468
- Dorsey, D.L., see Venkatasubramanian, R. 104/105 (1996) 448
- Dougherty, D.J., see House, J.L. 104/105 (1996) 472
- Drews, D., A. Schneider, D.R.T. Zahn, D. Wolframm and D.A. Evans, Raman monitoring of selenium decapping and subsequent antimony deposition on MBE-grown ZnSe(100) 104/105 (1996) 485
- Dudzik, E., A. Leslie, E. O'Toole, I.T. McGovern, A. Patchett and D.R.T. Zahn, An ARUPS/NEXAFS study of the $\text{H}_2\text{S}/\text{InP}(110)$ adsorbate system 104/105 (1996) 101
- Dunscombe, C.J., see Burgess, S.R. 104/105 (1996) 152
- Dunstan, P.R., see Burgess, S.R. 104/105 (1996) 152
- Dwir, B., see Reinhardt, F. 104/105 (1996) 529
- Eddrief, M., see Reqqass, H. 104/105 (1996) 557
- Edwards, K.A., see Levermann, A.H. 104/105 (1996) 124
- Elbe, A., see Polyakov, V.M. 104/105 (1996) 24
- Elissa, L., see Talaat, H. 104/105 (1996) 479
- Erben, J., see Teichert, St. 104/105 (1996) 679
- Erfurth, W., see Stietz, F. 104/105 (1996) 169
- Esser, N., see Shkrebtii, A.I. 104/105 (1996) 176
- Evangelisti, F., see Di Gaspare, L. 104/105 (1996) 595
- Evans, D.A., see Thornton, J.M.C. 104/105 (1996) 234
- Evans, D.A., D. Wolframm, D. Gnoth, J. Cairns, A.C. Wright, M. Evans, J. Riley, D. Westwood and D.A. Woolf, Metal overlayers on the MBE-grown ZnSe-(001) surface 104/105 (1996) 240
- Evans, D.A., see Drews, D. 104/105 (1996) 485
- Evans, M., see Evans, D.A. 104/105 (1996) 240

- Falkenberg, G., see Levermann, A.H. 104/105 (1996) 124
- Fan, G.H., see von der Emde, M. 104/105 (1996) 575
- Farmer, K.R., C.P. Debauche, A.R. Giordano, P. Lundgren, M.O. Andersson and D.A. Buchanan, Weak fluence dependence of charge generation in ultra-thin oxides on silicon 104/105 (1996) 369
- Fefer, E., L. Kronik, M. Leibovitch, Y. Shapira and W. Riedl, In-situ monitoring of surface chemistry and charge transfer at semiconductor surfaces 104/105 (1996) 61
- Feidenhans'l, R., see Levermann, A.H. 104/105 (1996) 124
- Fenske, F., A. Schöpke, S. Schulze and B. Selle, Analytical studies of nickel silicide formation through a thin Ti layer 104/105 (1996) 218
- Finetti, P., see Johal, T.K. 104/105 (1996) 257
- Flietner, H., see Angermann, H. 104/105 (1996) 107
- Flietner, H., W. Füssel, N.D. Sinh and H. Angermann, Density of states and relaxation spectra of etched, H-terminated and naturally oxidized Si-surfaces and the accompanied defects 104/105 (1996) 342
- Flores, F., see Saiz-Pardo, R. 104/105 (1996) 183
- Flores, F., see Levy Yeyati, A. 104/105 (1996) 248
- Fomin, V.M., see Pokatilov, E.P. 104/105 (1996) 546
- Fontana, S., see Coluzza, C. 104/105 (1996) 196
- Forrest, S.R., see Kendrick, C. 104/105 (1996) 586
- Franke, D., see Teichert, St. 104/105 (1996) 679
- Franke, Th., see Teichert, St. 104/105 (1996) 679
- Frost, M.R. and C.W. Magee, Characterization of nitrided SiO₂ thin films using secondary ion mass spectrometry 104/105 (1996) 379
- Frotscher, U., see Rossow, U. 104/105 (1996) 552
- Furthmüller, J., see Käckell, P. 104/105 (1996) 45
- Furuta, S., see Ikeda, H. 104/105 (1996) 354
- Füssel, W., see Flietner, H. 104/105 (1996) 342
- Galli, G., see De Vita, A. 104/105 (1996) 297
- Gandhi, S., see Lucovsky, G. 104/105 (1996) 335
- Garfunkel, E., see Gusev, E.P. 104/105 (1996) 329
- Garreau, Y., see Sauvage-Simkin, M. 104/105 (1996) 646
- Gebhard, B., see Teichert, St. 104/105 (1996) 679
- Geurts, J., see Wagner, V. 104/105 (1996) 580
- Giordano, A.R., see Farmer, K.R. 104/105 (1996) 369
- Gnoth, D., see Evans, D.A. 104/105 (1996) 240
- Goldmann, A., see Stietz, F. 104/105 (1996) 169
- Goncalves-Conto, S., see von Känel, H. 104/105 (1996) 204
- Gossard, A.C., see Maranowski, K.D. 104/105 (1996) 621
- Göthelid, M., S. Odasso, G. LeLay, M. Björkqvist, E. Janin, U.O. Karlsson and T.M. Grehk, Ge(111)3 × 1:K/Sn; on the influence of tin substitution in a metal induced 3 × 1 reconstruction 104/105 (1996) 113
- Gravesteijn, D.J., see Thornton, J.M.C. 104/105 (1996) 631
- Grazhulis, V.A., S.I. Bozhko, I.L. Bolotin, O.R. Bulanov and A.M. Ionov, Electronic structure of the valence band of GdS_x and Gd₃S₄ 104/105 (1996) 68
- Grehk, M., see Aristov, V.Yu. 104/105 (1996) 73
- Grehk, T.M., see Göthelid, M. 104/105 (1996) 113
- Guillot, C., see Orlowski, B.A. 104/105 (1996) 282
- Gunnella, R., see Johansson, L.S.O. 104/105 (1996) 88
- Gusev, E.P., H.C. Lu, T. Gustafsson and E. Garfunkel, The initial oxidation of silicon: new ion scattering results in the ultra-thin regime 104/105 (1996) 329
- Gustafsson, T., see Gusev, E.P. 104/105 (1996) 329
- Guyaux, J.-L., Ph. Lambin, M.D. Lange, R. Sporken, P.A. Thiry and R. Caudano, Ultra-thin AlAs films on GaAs (001) investigated by high-resolution electron-energy-loss spectroscopy 104/105 (1996) 601
- Haier, P., see Shkrebtii, A.I. 104/105 (1996) 176
- Harada, J., see Sokolov, N.S. 104/105 (1996) 402
- Hartmann, A., C. Dieker, U. Bangert, R. Loo, L. Vescan and H. Lüth, Photoluminescence and transmission electron microscopy investigation of SiGe quantum wires grown on patterned Si substrates 104/105 (1996) 502
- Hattangady, S.V., see Lucovsky, G. 104/105 (1996) 335
- Hattori, T., T. Aiba, E. Iijima, Y. Okube, H. Nohira, N. Tate and M. Katayama, Initial stage of oxidation of hydrogen-terminated silicon surfaces 104/105 (1996) 323
- Hattori, T., see Nohira, H. 104/105 (1996) 359
- Hauser, J.R., see Lucovsky, G. 104/105 (1996) 335
- Häussler, P., see Teichert, St. 104/105 (1996) 679
- He, Z.Q., L. Ilver, J. Kanski, P.O. Nilsson, P. Songsiririthigul, G. Holmén and U.O. Karlsson, Band structure evolution in InAs overlayers on GaAs(110) 104/105 (1996) 608
- Henrion, W., see Teichert, St. 104/105 (1996) 679
- Hill, I.G., see Mitchell, C.E.J. 104/105 (1996) 434
- Holmén, G., see He, Z.Q. 104/105 (1996) 608
- Hong, M., see Passlack, M. 104/105 (1996) 441
- Horita, K., see Koyama, M. 104/105 (1996) 253
- Horita, K., see Koh, M. 104/105 (1996) 364
- Hotta, K., see Ikeda, H. 104/105 (1996) 354
- Hou, X.Y., see Xu, Q.J. 104/105 (1996) 468
- House, J.L., D.J. Dougherty, G.S. Petrich, L.A. Kolodziejki, E.P. Ippen and G.-C. Hua, Growth and characterization of ZnSe/GaAs single quantum well structures 104/105 (1996) 472
- Howes, P.B., see Levermann, A.H. 104/105 (1996) 124
- Hu, E., see Chang, Y.-L. 104/105 (1996) 422
- Hua, G.-C., see House, J.L. 104/105 (1996) 472
- Hurych, Z., see Aristov, V.Yu. 104/105 (1996) 73
- Hurych, Z., see Semond, F. 104/105 (1996) 79
- Hwang, H.L., see Wang, K.C. 104/105 (1996) 373
- Hybertsen, M.S., see Pasquarello, A. 104/105 (1996) 317
- Ibbetson, J.P., see Maranowski, K.D. 104/105 (1996) 621
- Iijima, E., see Hattori, T. 104/105 (1996) 323

- Ikeda, H., K. Hotta, S. Furuta, S. Zaima and Y. Yasuda, Influences of hydrogen on initial oxidation processes of H-terminated Si(100) surfaces 104/105 (1996) 354
- Ilver, L., see He, Z.Q. 104/105 (1996) 608
- Indlekofer, G., see Aristov, V.Yu. 104/105 (1996) 73
- Ionov, A.M., see Grazhulis, V.A. 104/105 (1996) 68
- Ippen, E.P., see House, J.L. 104/105 (1996) 472
- Ishigami, R., see Yuhara, J. 104/105 (1996) 163
- Ishikawa, D., see Yuhara, J. 104/105 (1996) 163
- Ismat Shah, S., see Chen, F. 104/105 (1996) 615
- Itoh, Y., see Sokolov, N.S. 104/105 (1996) 402
- Iyer, S.S., see Chen, F. 104/105 (1996) 615
- Izumi, A., K. Kawabata, K. Tsutsui, N.S. Sokolov, S.V. Novikov and A.Yu. Khilko, Growth of $\text{CdF}_2/\text{CaF}_2/\text{Si}(111)$ heterostructure with abrupt interfaces by using thin CaF_2 buffer layer 104/105 (1996) 417
- Izumi, T., H. Nishiwaki, T. Tambo and C. Tatsuyama, Ga- Se films grown on a $\text{GaAs}(001)$ surface at high temperature using a thermal evaporation of GaSe 104/105 (1996) 570
- Janin, E., see Göthelid, M. 104/105 (1996) 113
- Jaussaud, C., see Semond, F. 104/105 (1996) 79
- Jedrecy, N., see Sauvage-Simkin, M. 104/105 (1996) 646
- Jing, Z., see Lucovsky, G. 104/105 (1996) 335
- Joannopoulos, J.D., see Cho, K. 104/105 (1996) 286
- Johal, T.K., P. Finetti, V.R. Dhanak, A.W. Robinson, A. Patchett, D.R.T. Zahn and R. McGrath, A normal incidence X-ray standing wave study of sulphur adsorption on $\text{InP}(110)$ 104/105 (1996) 257
- Johansson, L.S.O., R. Gunnella, E.L. Bullock, C.R. Natoli and R.I.G. Uhrberg, Surface core-level shift photoelectron diffraction from $\text{As}/\text{Si}(111)$ 104/105 (1996) 88
- Johnson, M.B., see Pfister, M. 104/105 (1996) 516
- Johnson, R.L., see Levermann, A.H. 104/105 (1996) 124
- Jones, T.S., see Bell, G.R. 104/105 (1996) 17
- Jones, T.S., see Aquino, A.A. 104/105 (1996) 304
- Jones, T.S., see Avery, A.R. 104/105 (1996) 539
- Joyce, B.A., see Avery, A.R. 104/105 (1996) 539
- Kačiulis, S., see Bruni, M.R. 104/105 (1996) 652
- Käckell, P., J. Furthmüller and F. Bechstedt, Ab initio calculations of the reconstructed (100) surfaces of cubic silicon carbide 104/105 (1996) 45
- Käckell, P., W.G. Schmidt and F. Bechstedt, Se-induced 3d core-level shifts of $\text{GaAs}(110)$ 104/105 (1996) 141
- Käckell, P. and F. Bechstedt, Heterocrystalline SiC : ab initio calculations for the interface structure of combinations of cubic and hexagonal SiC 104/105 (1996) 490
- Kahn, A., see Kendrick, C. 104/105 (1996) 586
- Kaminski, A.Yu. and R.A. Suris, Smoothing of crystal surfaces during growth interruption 104/105 (1996) 312
- Kanski, J., see He, Z.Q. 104/105 (1996) 608
- Kapon, E., see Reinhardt, F. 104/105 (1996) 529
- Karlsson, U.O., see Göthelid, M. 104/105 (1996) 113
- Karlsson, U.O., see He, Z.Q. 104/105 (1996) 608
- Katayama, M., see Hattori, T. 104/105 (1996) 323
- Kawabata, K., see Izumi, A. 104/105 (1996) 417
- Kendrick, C., A. Kahn and S.R. Forrest, STM study of the organic semiconductor PTCDA on highly-oriented pyrolytic graphite 104/105 (1996) 586
- Khilko, A.Yu., see Izumi, A. 104/105 (1996) 417
- Kilper, R., see Teichert, St. 104/105 (1996) 679
- Kim, B.M., C.A. Ventrice, Jr., T. Mercer, R. Overney and L.J. Schowalter, Molecular beam epitaxial growth of thin CaF_2 films on vicinal $\text{Si}(111)$ surfaces 104/105 (1996) 409
- King, S.W., see Benjamin, M.C. 104/105 (1996) 455
- Kishida, A., see Koh, M. 104/105 (1996) 364
- Kliefoth, K., see Angermann, H. 104/105 (1996) 107
- Klimin, S.N., see Pokatilov, E.P. 104/105 (1996) 546
- Koh, M., see Koyama, M. 104/105 (1996) 253
- Koh, M., K. Horita, B. Shigeta, T. Matsukawa, A. Kishida, T. Tani, S. Mori and I. Ohdomari, Radiation immunity of pMOSFETs and nMOSFETs examined by means of MeV He single ion microprobe 104/105 (1996) 364
- Kolodzey, J., see Chen, F. 104/105 (1996) 615
- Kolodziejewski, L.A., see House, J.L. 104/105 (1996) 472
- Köpp, M., see Shkrebtii, A.I. 104/105 (1996) 176
- Kowalski, B.J., see Orłowski, B.A. 104/105 (1996) 282
- Koyama, M., Y. Akita, C. Cheong, M. Koh, T. Matsukawa, K. Horita, B. Shigeta and I. Ohdomari, Quantitative analysis of degradation in Schottky diode characteristics induced by single ion implantation 104/105 (1996) 253
- Kronik, L., see Fefer, E. 104/105 (1996) 61
- Krüger, P., see Pollmann, J. 104/105 (1996) 1
- Ku, J.-H. and R.J. Nemanich, The Schottky barrier of Co on strained and unstrained $\text{Si}_x\text{Ge}_{1-x}$ alloys 104/105 (1996) 262
- Kwo, J.R., see Passlack, M. 104/105 (1996) 441
- LaBella, V.P., see Ventrice Jr., C.A. 104/105 (1996) 274
- Lacharme, J.-P., see Orłowski, B.A. 104/105 (1996) 282
- Lacharme, J.-P., see Reqqass, H. 104/105 (1996) 557
- Laine, A.D., see Thornton, J.M.C. 104/105 (1996) 234
- Lambin, Ph., see Guyaux, J.-L. 104/105 (1996) 601
- Landesman, J.P., see Sauvage-Simkin, M. 104/105 (1996) 646
- Lange, H., see Teichert, St. 104/105 (1996) 679
- Lange, M.D., see Guyaux, J.-L. 104/105 (1996) 601
- Lannoo, M., see Priester, C. 104/105 (1996) 495
- Lapeyre, G.J., see Polyakov, V.M. 104/105 (1996) 24
- Lapeyre, G.J., see Stietz, F. 104/105 (1996) 169

- Larciprete, R., see De Padova, P. 104/105 (1996) 349
- Lee, D.R., see Lucovsky, G. 104/105 (1996) 335
- Leibovitch, M., see Fefer, E. 104/105 (1996) 61
- Le Thanh, V., see Reqqass, H. 104/105 (1996) 557
- LeLay, G., see Aristov, V.Yu. 104/105 (1996) 73
- LeLay, G., see Göthelid, M. 104/105 (1996) 113
- LeLay, G., see Cricenti, A. 104/105 (1996) 118
- Leslie, A., see Dudzik, E. 104/105 (1996) 101
- Levermann, A.H., P.B. Howes, K.A. Edwards, H.T. Anyele, C.C. Matthai, J.E. Macdonald, R. Feidenhans'l, L. Lottermoser, L. Seehofer, G. Falkenberg and R.L. Johnson, The atomic structure of the Si(111) ($2\sqrt{3} \times 2\sqrt{3}$)R30°-Sn reconstruction 104/105 (1996) 124
- Levy, M., see Luo, Y. 104/105 (1996) 49
- Levy Yeyati, A., A. Martín-Rodero, F. Flores, J. Ortega and R. Rincón, Metal-insulator transition for K on GaAs(100)-As rich surfaces 104/105 (1996) 248
- Lew, A.Y., C.H. Yan, C.W. Tu and E.T. Yu, Characterization of arsenide/phosphide heterostructure interfaces by scanning tunneling microscopy 104/105 (1996) 522
- Li, C.M., T. Sjödin, Z.C. Ying and H.L. Dai, Photoexcited carrier diffusion near a Si(111) surface and in the Si bulk 104/105 (1996) 57
- Li, D.M., see Mori, M. 104/105 (1996) 563
- Lin, X.F., I. Chizhov, H.A. Mai and R.F. Willis, Scanning tunneling spectroscopy examination of surface electronic structures of Si(111)($2\sqrt{3} \times 2\sqrt{3}$)30°-Sn surface 104/105 (1996) 223
- Loferski, J.J., see Wang, K.C. 104/105 (1996) 373
- Loo, R., see Hartmann, A. 104/105 (1996) 502
- Lottermoser, L., see Levermann, A.H. 104/105 (1996) 124
- Lu, H.C., see Gusev, E.P. 104/105 (1996) 329
- Lu, Z.H., see Mitchell, C.E.J. 104/105 (1996) 434
- Lucovsky, G., D.R. Lee, S.V. Hattangady, H. Niimi, S. Gandhi, C. Parker, Z. Jing, J.L. Whitten and J.R. Hauser, Local atomic structure and electrical properties of nitrated Si-SiO₂ interfaces produced by low-temperature plasma processing and rapid thermal annealing, and explained by ab-initio quantum chemistry calculations 104/105 (1996) 335
- Lundgren, P., see Farmer, K.R. 104/105 (1996) 369
- Luo, Y., D.A. Slater, M. Levy and R.M. Osgood Jr., Chemical preparation of CdTe(100) and (110) surfaces using atomic hydrogen 104/105 (1996) 49
- Lüth, H., see Hartmann, A. 104/105 (1996) 502
- Lüth, H., A summary and perspective on the Fifth International Conference on the Formation of Semiconductor Interfaces, Princeton, NJ 104/105 (1996) 685
- Macdonald, J.E., see Levermann, A.H. 104/105 (1996) 124
- Magee, C.W., see Frost, M.R. 104/105 (1996) 379
- Mai, H.A., see Lin, X.F. 104/105 (1996) 223
- Mai, Y., see Barel, R. 104/105 (1996) 669
- Mangat, P.S., see Semond, F. 104/105 (1996) 79
- Mannaerts, J.P., see Passlack, M. 104/105 (1996) 441
- Mantese, L., see Rossow, U. 104/105 (1996) 137
- Maranowski, K.D., J.P. Ibbetson, K.L. Campman and A.C. Gossard, The conduction barrier at the interface between low temperature grown GaAs and undoped GaAs 104/105 (1996) 621
- Marti, U., see Pfister, M. 104/105 (1996) 516
- Martin, D., see Pfister, M. 104/105 (1996) 516
- Martín-Rodero, A., see Levy Yeyati, A. 104/105 (1996) 248
- Martinotti, D., see Orlowski, B.A. 104/105 (1996) 282
- Matsuda, M., see Nohira, H. 104/105 (1996) 359
- Matsukawa, T., see Koyama, M. 104/105 (1996) 253
- Matsukawa, T., see Koh, M. 104/105 (1996) 364
- Matteucci, M., see De Padova, P. 104/105 (1996) 349
- Matthai, C.C., see Levermann, A.H. 104/105 (1996) 124
- Mattogno, G., see Bruni, M.R. 104/105 (1996) 652
- Maung, N., see von der Emde, M. 104/105 (1996) 575
- McConville, C.F., see Bell, G.R. 104/105 (1996) 17
- McGovern, I.T., see Dudzik, E. 104/105 (1996) 101
- McGrath, R., see Johal, T.K. 104/105 (1996) 257
- McLean, A.B., see Mitchell, C.E.J. 104/105 (1996) 434
- Meier, A., see Wollschläger, J. 104/105 (1996) 392
- Mercer, T., see Kim, B.M. 104/105 (1996) 409
- Merz, J., see Chang, Y.-L. 104/105 (1996) 422
- Mitchell, C.E.J., I.G. Hill, A.B. McLean and Z.H. Lu, Sulfur passivated InP(100): surface gaps and electron counting 104/105 (1996) 434
- Miyazaki, T., see Sugino, T. 104/105 (1996) 428
- Mönch, W., see Nienhaus, H. 104/105 (1996) 95
- Mori, M., D.M. Li, M. Yamazaki, T. Tambo, H. Ueba and C. Tatsuyama, Heteroepitaxial growth of InSb on Si(001) surface via Ge buffer layers 104/105 (1996) 563
- Mori, S., see Koh, M. 104/105 (1996) 364
- Morier-Genoud, F., see Pfister, M. 104/105 (1996) 516
- Morita, K., see Yuhara, J. 104/105 (1996) 163
- Müller, E., see von Känel, H. 104/105 (1996) 204
- Nagle, J., see Sauvage-Simkin, M. 104/105 (1996) 646
- Natarajan, V., see Behringer, R.E. 104/105 (1996) 291
- Natoli, C.R., see Johansson, L.S.O. 104/105 (1996) 88
- Negm, S., see Talaat, H. 104/105 (1996) 479
- Nemanich, R.J., see Ku, J.-H. 104/105 (1996) 262
- Nemanich, R.J., see Baumann, P.K. 104/105 (1996) 267
- Nemanich, R.J., see Benjamin, M.C. 104/105 (1996) 455
- Nesterenko, B., see Cricenti, A. 104/105 (1996) 118
- Ng, T., see von der Emde, M. 104/105 (1996) 575
- Nienhaus, H. and W. Mönch, Fluorine adsorption on GaAs(110) surfaces and the onset of etching after XeF₂ exposures 104/105 (1996) 95
- Niimi, H., see Lucovsky, G. 104/105 (1996) 335

- Nilsson, P.O., see He, Z.Q. 104/105 (1996) 608
- Nishiwaki, H., see Izumi, T. 104/105 (1996) 570
- Noguez, C., see Roy, M. 104/105 (1996) 158
- Nohira, H., see Hattori, T. 104/105 (1996) 323
- Nohira, H., H. Sekikawa, M. Matsuda and T. Hattori, Effect of chemical preoxidation treatment on the structure of SiO₂/Si interfaces 104/105 (1996) 359
- Novikov, S.V., see Izumi, A. 104/105 (1996) 417
- Nys, J.P., see Tételin, C. 104/105 (1996) 385
- Odasso, S., see Göthelid, M. 104/105 (1996) 113
- Ohdomari, I., see Koyama, M. 104/105 (1996) 253
- Ohdomari, I., see Koh, M. 104/105 (1996) 364
- Okube, Y., see Hattori, T. 104/105 (1996) 323
- Olshanetsky, B.Z., Atomic phenomena on Si surfaces at adsorption of transition metals 104/105 (1996) 130
- Onda, N., see von Känel, H. 104/105 (1996) 204
- Opila, R.L., see Passlack, M. 104/105 (1996) 441
- Orlowski, B.A., B.J. Kowalski, N. Barrett, D. Martinotti, C. Guillot, J.-P. Lacharme and C.A. Sébenne, Valence band of Cd_{1-x}Fe_xSe/Fe in resonant photoemission spectra 104/105 (1996) 282
- Orner, B.A., see Chen, F. 104/105 (1996) 615
- Ortega, J., see Levy Yeyati, A. 104/105 (1996) 248
- Osgood Jr., R.M., see Luo, Y. 104/105 (1996) 49
- O'Toole, E., see Dudzik, E. 104/105 (1996) 101
- Ottaviani, C., see De Padova, P. 104/105 (1996) 349
- Overney, R., see Kim, B.M. 104/105 (1996) 409
- Overney, R.M., see Sokolov, N.S. 104/105 (1996) 402
- Pamula, V.K., see Venkatasubramanian, R. 104/105 (1996) 448
- Parker, C., see Lucovsky, G. 104/105 (1996) 335
- Pasquarello, A., M.S. Hybertsen and R. Car, Comparison of structurally relaxed models of the Si(001)-SiO₂ interface based on different crystalline oxide forms 104/105 (1996) 317
- Passlack, M., M. Hong, R.L. Opila, J.P. Mannaerts and J.R. Kwo, GaAs surface passivation using in-situ oxide deposition 104/105 (1996) 441
- Patchett, A., see Dudzik, E. 104/105 (1996) 101
- Patchett, A., see Johal, T.K. 104/105 (1996) 257
- Paulish, A.G., see Alperovich, V.L. 104/105 (1996) 228
- Peressi, M., see Tit, N. 104/105 (1996) 656
- Perfetti, P., see Cricenti, A. 104/105 (1996) 118
- Perfetti, P., see De Padova, P. 104/105 (1996) 349
- Petrich, G.S., see House, J.L. 104/105 (1996) 472
- Pétroff, J.-F., see Reqqass, H. 104/105 (1996) 557
- Pfister, M., M.B. Johnson, S.F. Alvarado, H.W.M. Salemink, U. Marti, D. Martin, F. Morier-Genoud and F.K. Reinhardt, Surface and subsurface imaging of indium in InGaAs by scanning tunneling microscopy 104/105 (1996) 516
- Pietryga, C., see Rossow, U. 104/105 (1996) 552
- Pinchaux, R., see Sauvage-Simkin, M. 104/105 (1996) 646
- Ploog, K., see Braun, W. 104/105 (1996) 35
- Ploog, K.H., see Yang, H. 104/105 (1996) 461
- Pokatilov, E.P., V.M. Fomin, S.N. Klimin and S.N. Balaban, Characterization of nanostructures by virtue of the phenomena due to the electron-phonon interaction 104/105 (1996) 546
- Pollmann, J., P. Krüger, M. Rohlfing, M. Sabisch and D. Vogel, Ab initio calculations of structural and electronic properties of prototype surfaces of group IV, III-V and II-VI semiconductors 104/105 (1996) 1
- Polyakov, V., see Stietz, F. 104/105 (1996) 169
- Polyakov, V.M., A. Eibe, J. Wu, G.J. Lapeyre and J.A. Schaefer, Investigation of the space charge regime of epitaxially grown GaAs (100) by high-resolution electron energy-loss spectroscopy 104/105 (1996) 24
- Poole, I.B., see von der Emde, M. 104/105 (1996) 575
- Priester, C. and M. Lannoo, Highly mismatched heteroepitaxy: 2D platelets assisted nucleation of self-assembled 3D quantum dots 104/105 (1996) 495
- Prince, K., see De Padova, P. 104/105 (1996) 349
- Qi, J., W. Angerer, M.S. Yeganeh, A.G. Yodh and W.M. Theis, Midgap states observed by nonlinear optical spectroscopy of metal:GaAs junctions 104/105 (1996) 188
- Quaresima, C., see De Padova, P. 104/105 (1996) 349
- Ramaswamy, G., see Ventrice Jr., C.A. 104/105 (1996) 274
- Reinhardt, F., B. Dwir, G. Biasiol and E. Kapon, Atomic force microscopy of III-V nanostructures in air 104/105 (1996) 529
- Reinhart, F.K., see Pfister, M. 104/105 (1996) 516
- Reqqass, H., J.-P. Lacharme, M. Eddrief, C.A. Sébenne, V. Le Thanh, Y.L. Zheng and J.-F. Pétroff, Influence of surface reconstruction on MBE growth of layered GaSe on Si(111) substrates 104/105 (1996) 557
- Richter, W., see Shkrebtii, A.I. 104/105 (1996) 176
- Richter, W., see Rossow, U. 104/105 (1996) 552
- Richter, W., see Wagner, V. 104/105 (1996) 580
- Riedl, W., see Fefer, E. 104/105 (1996) 61
- Righini, G., see Bruni, M.R. 104/105 (1996) 652
- Riley, J., see Evans, D.A. 104/105 (1996) 240
- Rincón, R., see Saiz-Pardo, R. 104/105 (1996) 183
- Rincón, R., see Levy Yeyati, A. 104/105 (1996) 248
- Robinson, A.W., see Johal, T.K. 104/105 (1996) 257
- Rohlfing, M., see Pollmann, J. 104/105 (1996) 1
- Rossow, U., L. Mantese, T. Yasuda and D.E. Aspnes, Hydrogenated and oxidized vicinal Si(001) surfaces investigated by reflectance-difference spectroscopy 104/105 (1996) 137

- Rossow, U., U. Frotscher, C. Pietryga, D.E. Aspnes and W. Richter, Porous silicon layers as a model system for nanostructures 104/105 (1996) 552
- Roy, M. and Y. Borenstein, Optical study of potassium growth on the Si(100) surface 104/105 (1996) 147
- Roy, M., C. Beitia, Y. Borenstein, A. Shkrebtii, C. Noguez and R. Del Sole, Optical spectroscopy study of hydrogenation of the Si(111)-7 × 7 surface 104/105 (1996) 158
- Sabisch, M., see Pollmann, J. 104/105 (1996) 1
- Saiz-Pardo, R., R. Rincón, P.L. de Andrés and F. Flores, Schottky-barrier formation at passivated surfaces: covalent and ionic semiconductors 104/105 (1996) 183
- Sakamoto, Y., see Sugino, T. 104/105 (1996) 428
- Salemink, H.W.M., see Pfister, M. 104/105 (1996) 516
- Sauvage-Simkin, M., Y. Garreau, R. Pinchaux, A. Cavanna, M.B. Véron, N. Jedrecy, J.P. Landesman and J. Nagle, Reconstruction and chemical ordering at the surface of strained (In, Ga)As epilayers 104/105 (1996) 646
- Schaefer, J.A., see Polyakov, V.M. 104/105 (1996) 24
- Schaefer, J.A., see Stietz, F. 104/105 (1996) 169
- Schäffer, J., see Tappe, T. 104/105 (1996) 661
- Scheibler, H.E., see Alperovich, V.L. 104/105 (1996) 228
- Schlosser, J., see Tappe, T. 104/105 (1996) 661
- Schmalhorst, J., see Tappe, T. 104/105 (1996) 661
- Schmidt, W.G., see Käckell, P. 104/105 (1996) 141
- Schmiedeskamp, B., see Tappe, T. 104/105 (1996) 661
- Schneider, A., see Drews, D. 104/105 (1996) 485
- Schöpke, A., see Fenske, F. 104/105 (1996) 218
- Schowalter, L.J., see Ventrice Jr., C.A. 104/105 (1996) 274
- Schowalter, L.J., see Kim, B.M. 104/105 (1996) 409
- Schowalter, L.J., see Deelman, P.W. 104/105 (1996) 510
- Schulze, S., see Fenske, F. 104/105 (1996) 218
- Schwarz, C., see von Känel, H. 104/105 (1996) 204
- Sebastiani, M., see Di Gaspare, L. 104/105 (1996) 595
- Sébenne, C., see Cricenti, A. 104/105 (1996) 118
- Sébenne, C.A., see Orłowski, B.A. 104/105 (1996) 282
- Sébenne, C.A., see Reqqass, H. 104/105 (1996) 557
- Seehofer, L., see Levermann, A.H. 104/105 (1996) 124
- Sekikawa, H., see Nohira, H. 104/105 (1996) 359
- Selle, B., see Fenske, F. 104/105 (1996) 218
- Semond, F., P. Soukiasian, P.S. Mangat, Z. Hurych, L. di Cioccio and C. Jaussaud, Synchrotron radiation study of Cs/carbon-rich β -SiC(100) and Cs/silicon-rich β -SiC(100) surfaces: metallization and interface formation 104/105 (1996) 79
- Shapira, Y., see Fefer, E. 104/105 (1996) 61
- Shi, S., see Chang, Y.-L. 104/105 (1996) 422
- Shigeta, B., see Koyama, M. 104/105 (1996) 253
- Shigeta, B., see Koh, M. 104/105 (1996) 364
- Shinabe, S., see Yao, T. 104/105 (1996) 213
- Shirafuji, J., see Sugino, T. 104/105 (1996) 428
- Shkrebtii, A., see Roy, M. 104/105 (1996) 158
- Shkrebtii, A.I., N. Esser, M. Köpp, P. Haier, W. Richter and R. Del Sole, Electronic properties of antimony monolayers on III-V (110) surfaces: a comparative study by reflectance anisotropy spectroscopy and microscopic tight-binding calculations 104/105 (1996) 176
- Shusterman, Yu.V., see Sokolov, N.S. 104/105 (1996) 402
- Sinh, N.D., see Flietner, H. 104/105 (1996) 342
- Sjodin, T., see Li, C.M. 104/105 (1996) 57
- Slater, D.A., see Luo, Y. 104/105 (1996) 49
- Sokolov, N.S., J.C. Alvarez, Yu.V. Shusterman, N.L. Yakovlev, R.M. Overney, Y. Itoh, I. Takahashi and J. Harada, Structural transformations at $\text{CaF}_2/\text{Si}(111)$ interfaces 104/105 (1996) 402
- Sokolov, N.S., see Izumi, A. 104/105 (1996) 417
- Songsiririthigul, P., see He, Z.Q. 104/105 (1996) 608
- Soukiasian, P., see Aristov, V.Yu. 104/105 (1996) 73
- Soukiasian, P., see Semond, F. 104/105 (1996) 79
- Spajer, M., see Coluzza, C. 104/105 (1996) 196
- Sporken, R., see Guyaux, J.-L. 104/105 (1996) 601
- Springholz, G. and G. Bauer, A scanning tunnelling microscopy study of local surface modifications induced by misfit dislocation formation in strained-layer heteroepitaxy 104/105 (1996) 637
- Stietz, F., Th. Allinger, V. Polyakov, J. Woll, A. Goldmann, W. Erfurth, G.J. Lapeyre and J.A. Schaefer, Segregation of In atoms at clean and hydrogen passivated InP(100) surfaces 104/105 (1996) 169
- Sudijono, J.L., see Avery, A.R. 104/105 (1996) 539
- Sugino, T., Y. Sakamoto, T. Miyazaki and J. Shirafuji, Interface properties of PN_x/InP structures by in-situ remote plasma processes 104/105 (1996) 428
- Suris, R.A., see Kaminski, A.Yu. 104/105 (1996) 312
- Takahashi, I., see Sokolov, N.S. 104/105 (1996) 402
- Talaat, H., L. Elissa, S. Negm and E. Burstein, Photomodulation Raman scattering spectroscopy of ZnSe/GaAs heterostructure interface 104/105 (1996) 479
- Taleb-Ibrahimi, A., see Aristov, V.Yu. 104/105 (1996) 73
- Tambo, T., see Mori, M. 104/105 (1996) 563
- Tambo, T., see Izumi, T. 104/105 (1996) 570
- Tanii, T., see Koh, M. 104/105 (1996) 364
- Tappe, T., A. Chatziparaskewas, J. Schäffer, J. Schlosser, J. Schmalhorst and B. Schmiedeskamp, Medium energy ion scattering (MEIS) studies on Si/GaSb/Si- and Si/ $\text{CaF}_2/\text{Si}(111)$ layer systems 104/105 (1996) 661
- Tate, N., see Hattori, T. 104/105 (1996) 323
- Tatsuyama, C., see Mori, M. 104/105 (1996) 563
- Tatsuyama, C., see Izumi, T. 104/105 (1996) 570

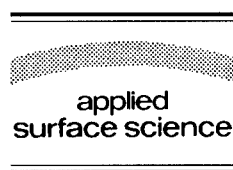
- Teichert, St., R. Kilper, J. Erben, D. Franke, B. Gebhard, Th. Franke, P. Häussler, W. Henrion and H. Lange, Preparation and properties of thin polycrystalline Mn-Si_{1.73} films 104/105 (1996) 679
- Terekhov, A.S., see Alperovich, V.L. 104/105 (1996) 228
- Tételin, C., X. Wallart, L. Vescan and J.P. Nys, Plasma assisted oxidation of SiGe layers at 500°C: interface characterization 104/105 (1996) 385
- Theis, W.M., see Qi, J. 104/105 (1996) 188
- Thiry, P.A., see Guyaux, J.-L. 104/105 (1996) 601
- Thornton, J.M.C., P. Weightman, P. Bailey, D.A. Woolf, A.D. Laine and D.A. Evans, Development of the Na/GaAs(111)A-(2 × 2) interface at room and low temperature 104/105 (1996) 234
- Thornton, J.M.C., R.J. Cole, D.J. Gravesteijn and P. Weightman, Charge transfer and electronic activation at an Sb δ-layer in Si(001) 104/105 (1996) 631
- Thundat, T., see Deelman, P.W. 104/105 (1996) 510
- Timp, G., see Behringer, R.E. 104/105 (1996) 291
- Tit, N. and M. Peressi, Ab-initio electronic structure calculation of the InAs multiple quantum wells in bulk GaAs 104/105 (1996) 656
- Trampert, A., see Yang, H. 104/105 (1996) 461
- Tsutsui, K., see Izumi, A. 104/105 (1996) 417
- Tu, C.W., see Lew, A.Y. 104/105 (1996) 522
- Tynni, V.I., see Alperovich, V.L. 104/105 (1996) 228
- Ueba, H., see Mori, M. 104/105 (1996) 563
- Uhrberg, R.I.G., see Johansson, L.S.O. 104/105 (1996) 88
- Venkatasubramanian, R., V.K. Pamula and D.L. Dorsey, Influence of physisorbed arsenic on RHEED intensity oscillations during low-temperature GaAs molecular beam epitaxy 104/105 (1996) 448
- Ventrice Jr., C.A., V.P. LaBella, G. Ramaswamy, H.-P. Yu and L.J. Schowalter, Hot-electron scattering at Au/Si-(100) Schottky interfaces measured by temperature dependent ballistic electron emission microscopy 104/105 (1996) 274
- Ventrice, Jr., C.A., see Kim, B.M. 104/105 (1996) 409
- Véron, M.B., see Sauvage-Simkin, M. 104/105 (1996) 646
- Vescan, L., see Tételin, C. 104/105 (1996) 385
- Vescan, L., see Hartmann, A. 104/105 (1996) 502
- Vogel, D., see Pollmann, J. 104/105 (1996) 1
- Von der Emde, M., D.R.T. Zahn, T. Ng, N. Maung, G.H. Fan, I.B. Poole, J.O. Williams and A.C. Wright, MOCVD growth of Ga₂Se₃ on GaAs(100) and GaP(100): a Raman study 104/105 (1996) 575
- Von Känel, H., E. Müller, S. Goncalves-Conto, C. Schwarz and N. Onda, Structural properties of epitaxial silicide layers on Si 104/105 (1996) 204
- Wagner, V., W. Richter and J. Geurts, Temperature dependence of interdiffusion-induced III-V compound formation at the interface between Al, Ga, In layers and Sb substrates 104/105 (1996) 580
- Waite, M.M., see Chen, F. 104/105 (1996) 615
- Wallart, X., see Tételin, C. 104/105 (1996) 385
- Wang, E.G., (II-VI)_m/(IV₂)_n (110) superlattice: interfacial chemistry, electronic structure, and optical property 104/105 (1996) 626
- Wang, K.C., H.L. Hwang, J.J. Loferski and T.R. Yew, Studies on low temperature silicon grain growth on SiO₂ by electron cyclotron resonance chemical vapor deposition 104/105 (1996) 373
- Wang, X., see Xu, Q.J. 104/105 (1996) 468
- Wassermeier, M., see Braun, W. 104/105 (1996) 35
- Weeks, Jr., T.W., see Benjamin, M.C. 104/105 (1996) 455
- Weightman, P., see Thornton, J.M.C. 104/105 (1996) 234
- Weightman, P., see Thornton, J.M.C. 104/105 (1996) 631
- Weinberg, W.H., see Chang, Y.-L. 104/105 (1996) 422
- Westwood, D., see Evans, D.A. 104/105 (1996) 240
- Whitten, J.L., see Lucovsky, G. 104/105 (1996) 335
- Wilks, S.P., see Burgess, S.R. 104/105 (1996) 152
- Williams, J.O., see von der Emde, M. 104/105 (1996) 575
- Williams, R.H., see Burgess, S.R. 104/105 (1996) 152
- Willis, R.F., see Lin, X.F. 104/105 (1996) 223
- Wolfframm, D., see Evans, D.A. 104/105 (1996) 240
- Wolfframm, D., see Drews, D. 104/105 (1996) 485
- Woll, J., see Stietz, F. 104/105 (1996) 169
- Wollschläger, J. and A. Meier, Diffraction spot profile analysis for heteroepitaxial surfaces applied to the initial growth stages of CaF₂ adlayers on Si(111) 104/105 (1996) 392
- Woolf, D.A., see Thornton, J.M.C. 104/105 (1996) 234
- Woolf, D.A., see Evans, D.A. 104/105 (1996) 240
- Wright, A.C., see Evans, D.A. 104/105 (1996) 240
- Wright, A.C., see von der Emde, M. 104/105 (1996) 575
- Wu, J., see Polyakov, V.M. 104/105 (1996) 24
- Xu, Q.J., X.M. Ding, X.Y. Hou and X. Wang, Nitridation of GaAs surfaces stimulated by nitrogen glow discharge 104/105 (1996) 468
- Yakovlev, N.L., see Sokolov, N.S. 104/105 (1996) 402
- Yamazaki, M., see Mori, M. 104/105 (1996) 563
- Yan, C.H., see Lew, A.Y. 104/105 (1996) 522
- Yang, H., O. Brandt, A. Trampert and K.H. Ploog, Initial stage of growth of GaN/GaAs(001) in plasma-assisted molecular beam epitaxy 104/105 (1996) 461
- Yao, T., S. Shinabe and M. Yoshimura, Atomistic study of the formation process of Ni silicide on the Si(111)-7 × 7 surface with scanning tunneling microscopy 104/105 (1996) 213
- Yasuda, T., see Rossow, U. 104/105 (1996) 137
- Yasuda, Y., see Ikeda, H. 104/105 (1996) 354

- Yeganeh, M.S., see Qi, J. 104/105 (1996) 188
Yew, T.R., see Wang, K.C. 104/105 (1996) 373
Yi, S.I., see Chang, Y.-L. 104/105 (1996) 422
Ying, Z.C., see Li, C.M. 104/105 (1996) 57
Yodh, A.G., see Qi, J. 104/105 (1996) 188
Yoshimura, M., see Yao, T. 104/105 (1996) 213
Yu, E.T., see Lew, A.Y. 104/105 (1996) 522
Yu, H.-P., see Ventrice Jr., C.A. 104/105 (1996) 274
Yuhara, J., R. Ishigami, D. Ishikawa and K. Morita, Dissolution and segregation of monolayer Cu, Ni and Co atoms on the Si(111)- $\sqrt{3} \times \sqrt{3}$ -Ag surface induced by thermal annealing 104/105 (1996) 163
Zacchigna, M., see De Padova, P. 104/105 (1996) 349
Zahn, D.R.T., see Dudzik, E. 104/105 (1996) 101
Zahn, D.R.T., see Johal, T.K. 104/105 (1996) 257
Zahn, D.R.T., see Drews, D. 104/105 (1996) 485
Zahn, D.R.T., see von der Emde, M. 104/105 (1996) 575
Zaima, S., see Ikeda, H. 104/105 (1996) 354
Zheng, Y.L., see Reqqass, H. 104/105 (1996) 557
Zhilin, V.M., see Aristov, V.Yu. 104/105 (1996) 73
Zinke-Allmang, M., see Barel, R. 104/105 (1996) 669



ELSEVIER

Applied Surface Science 104/105 (1996) 699–719



Subject index

Alkali metals

- Sb or Cs covered InAs(110) surfaces: moving E_F into conduction band and quantized 2D electron channel, V.Yu. Aris-tov, M. Grehk, V.M. Zhilin, A. Taleb-Ibrahimi, G. Indlekofer, Z. Hurych, G. Le Lay and P. Soukiassian 104/105 (1996) 73
- Synchrotron radiation study of Cs/carbon-rich β -SiC(100) and Cs/silicon-rich β -SiC(100) surfaces: metallization and interface formation, F. Semond, P. Soukiassian, P.S. Mangat, Z. Hurych, L. di Cioccio and C. Jaussaud 104/105 (1996) 79
- Ge(111)3 \times 1:K/Sn; on the influence of tin substitution in a metal induced 3 \times 1 reconstruction, M. Göthelid, S. Odasso, G. LeLay, M. Björkqvist, E. Janin, U.O. Karlsson and T.M. Grehk 104/105 (1996) 113
- Optical study of potassium growth on the Si(100) surface, M. Roy and Y. Boren-sztejn 104/105 (1996) 147
- Development of the Na/GaAs(111)A-(2 \times 2) interface at room and low tempera-ture, J.M.C. Thornton, P. Weightman, P. Bailey, D.A. Woolf, A.D. Laine and D.A. Evans 104/105 (1996) 234
- Metal-insulator transition for K on GaAs-(100)-As rich surfaces, A. Levy Yeyati, A. Martín-Rodero, F. Flores, J. Ortega and R. Rincón 104/105 (1996) 248

Alloys

- The Schottky barrier of Co on strained and unstrained $\text{Si}_x\text{Ge}_{1-x}$ alloys, J.-H. Ku and R.J. Nemanich 104/105 (1996) 262

Aluminium

- Hydrogen ion treatments of oxidized GaAs(100) and AlGaAs(100) surfaces: surface stoichiometry and electronic properties, Y.-L. Chang, S.I. Yi, S. Shi, E. Hu, W.H. Weinberg and J. Merz 104/105 (1996) 422

- UV photoemission study of heteroepitaxial AlGaIn films grown on 6H-SiC, M.C. Benjamin, M.D. Bremser, T.W. Weeks, Jr., S.W. King, R.F. Davis and R.J. Nemanich 104/105 (1996) 455
- Temperature dependence of interdiffusion-induced III-V compound formation at the interface between Al, Ga, In layers and Sb substrates, V. Wagner, W. Richter and J. Geurts 104/105 (1996) 580
- Ultra-thin AlAs films on GaAs (001) inves-tigated by high-resolution electron-en-ergy-loss spectroscopy, J.-L. Guyaux, Ph. Lambin, M.D. Lange, R. Sporken, P.A. Thiry and R. Caudano 104/105 (1996) 601

Annealing

- Dissolution and segregation of monolayer Cu, Ni and Co atoms on the Si(111)- $\sqrt{3} \times \sqrt{3}$ -Ag surface induced by thermal annealing, J. Yuhara, R. Ishigami, D. Ishikawa and K. Morita 104/105 (1996) 163
- Local atomic structure and electrical proper-ties of nitrided Si-SiO₂ interfaces pro-duced by low-temperature plasma pro-cessing and rapid thermal annealing, and explained by ab-initio quantum chem-istry calculations, G. Lucovsky, D.R. Lee, S.V. Hattangady, H. Niimi, S. Gandhi, C. Parker, Z. Jing, J.L. Whitten and J.R. Hauser 104/105 (1996) 335

Antimony

- Sb or Cs covered InAs(110) surfaces: mov-ing E_F into conduction band and quan-tized 2D electron channel, V.Yu. Aris-tov, M. Grehk, V.M. Zhilin, A. Taleb-Ibrahimi, G. Indlekofer, Z. Hurych, G. Le Lay and P. Soukiassian 104/105 (1996) 73
- Raman monitoring of selenium decapping and subsequent antimony deposition on MBE-grown ZnSe(100), D. Drews, A. Schneider, D.R.T. Zahn, D. Wolfframm and D.A. Evans 104/105 (1996) 485

- Temperature dependence of interdiffusion-induced III-V compound formation at the interface between Al, Ga, In layers and Sb substrates, V. Wagner, W. Richter and J. Geurts 104/105 (1996) 580
- Charge transfer and electronic activation at an Sb δ -layer in Si(001), J.M.C. Thornton, R.J. Cole, D.J. Gravesteijn and P. Weightman 104/105 (1996) 631

Arsenic

- Surface core-level shift photoelectron diffraction from As/Si(111), L.S.O. Johansson, R. Gunnella, E.L. Bullock, C.R. Natoli and R.I.G. Uhrberg 104/105 (1996) 88
- Influence of physisorbed arsenic on RHEED intensity oscillations during low-temperature GaAs molecular beam epitaxy, R. Venkatasubramanian, V.K. Pamula and D.L. Dorsey 104/105 (1996) 448
- Characterization of arsenide/phosphide heterostructure interfaces by scanning tunneling microscopy, A.Y. Lew, C.H. Yan, C.W. Tu and E.T. Yu 104/105 (1996) 522
- Interface abruptness in strained III-V heterostructures, M.R. Bruni, S. Kačiulis, G. Mattogno and G. Righini 104/105 (1996) 652

Atomic force microscopy

- Intrinsic surface atom manipulations in STM and AFM, K. Cho and J.D. Joannopoulos 104/105 (1996) 286
- Studies on low temperature silicon grain growth on SiO₂ by electron cyclotron resonance chemical vapor deposition, K.C. Wang, H.L. Hwang, J.J. Loferski and T.R. Yew 104/105 (1996) 373
- Structural transformations at CaF₂/Si(111) interfaces, N.S. Sokolov, J.C. Alvarez, Yu.V. Shusterman, N.L. Yakovlev, R.M. Overney, Y. Itoh, I. Takahashi and J. Harada 104/105 (1996) 402
- Molecular beam epitaxial growth of thin CaF₂ films on vicinal Si(111) surfaces, B.M. Kim, C.A. Ventrice, Jr., T. Mercer, R. Overney and L.J. Schowalter 104/105 (1996) 409
- AFM and RHEED study of Ge islanding on Si(111) and Si(100), P.W. Deelman, T. Thundat and L.J. Schowalter 104/105 (1996) 510
- Atomic force microscopy of III-V nanostructures in air, F. Reinhardt, B. Dwir, G. Biasiol and E. Kapon 104/105 (1996) 529

Auger electron spectroscopy

- Chemical preparation of CdTe(100) and (110) surfaces using atomic hydrogen, Y. Luo, D.A. Slater, M. Levy and R.M. Osgood Jr. 104/105 (1996) 49
- Fluorine adsorption on GaAs(110) surfaces and the onset of etching after XeF₂ exposures, H. Nienhaus and W. Mönch 104/105 (1996) 95
- Atomic phenomena on Si surfaces at adsorption of transition metals, B.Z. Olshansky 104/105 (1996) 130
- Optical study of potassium growth on the Si(100) surface, M. Roy and Y. Borenstein 104/105 (1996) 147
- A surface extended X-ray absorption fine structure study of tellurium adsorbed onto Si(100), S.R. Burgess, B.C.C. Cowie, S.P. Wilks, P.R. Dunstan, C.J. Dunscombe and R.H. Williams 104/105 (1996) 152
- Dissolution and segregation of monolayer Cu, Ni and Co atoms on the Si(111)- $\sqrt{3} \times \sqrt{3}$ -Ag surface induced by thermal annealing, J. Yuhara, R. Ishigami, D. Ishikawa and K. Morita 104/105 (1996) 163
- Analytical studies of nickel silicide formation through a thin Ti layer, F. Fenske, A. Schöpke, S. Schulze and B. Selle 104/105 (1996) 218
- Local atomic structure and electrical properties of nitrided Si-SiO₂ interfaces produced by low-temperature plasma processing and rapid thermal annealing, and explained by ab-initio quantum chemistry calculations, G. Lucovsky, D.R. Lee, S.V. Hattangady, H. Niimi, S. Gandhi, C. Parker, Z. Jing, J.L. Whitten and J.R. Hauser 104/105 (1996) 335
- Plasma assisted oxidation of SiGe layers at 500°C: interface characterization, C. Tételin, X. Wallart, L. Vescan and J.P. Nys 104/105 (1996) 385
- Hydrogen ion treatments of oxidized GaAs(100) and AlGaAs(100) surfaces: surface stoichiometry and electronic properties, Y.-L. Chang, S.I. Yi, S. Shi, E. Hu, W.H. Weinberg and J. Merz 104/105 (1996) 422
- UV photoemission study of heteroepitaxial AlGaN films grown on 6H-SiC, M.C. Benjamin, M.D. Bremser, T.W. Weeks, Jr., S.W. King, R.F. Davis and R.J. Nemanich 104/105 (1996) 455
- Influence of surface reconstruction on MBE growth of layered GaSe on Si(111) substrates, H. Reqqass, J.-P. Lacharme, M. Eddrief, C.A. Sébenne, V. Le Thanh, Y.L. Zheng and J.-F. Pétroff 104/105 (1996) 557

- Heteroepitaxial growth of InSb on Si(001) surface via Ge buffer layers, M. Mori, D.M. Li, M. Yamazaki, T. Tambo, H. Ueba and C. Tatsuyama 104/105 (1996) 563
- Ga-Se films grown on a GaAs(001) surface at high temperature using a thermal evaporation of GaSe, T. Izumi, H. Nishiwaki, T. Tambo and C. Tatsuyama 104/105 (1996) 570

Cadmium

- Valence band of $\text{Cd}_{1-x}\text{Fe}_x\text{Se}/\text{Fe}$ in resonant photoemission spectra, B.A. Orłowski, B.J. Kowalski, N. Barrett, D. Martinotti, C. Guillot, J.-P. Lacharme and C.A. Sébenne 104/105 (1996) 282
- Growth of $\text{CdF}_2/\text{CaF}_2\text{Si}(111)$ heterostructure with abrupt interfaces by using thin CaF_2 buffer layer, A. Izumi, K. Kawabata, K. Tsutsui, N.S. Sokolov, S.V. Novikov and A.Yu. Khilko 104/105 (1996) 417

Cadmium telluride

- Chemical preparation of $\text{CdTe}(100)$ and (110) surfaces using atomic hydrogen, Y. Luo, D.A. Slater, M. Levy and R.M. Osgood Jr. 104/105 (1996) 49

Calcium fluoride

- Diffraction spot profile analysis for heteroepitaxial surfaces applied to the initial growth stages of CaF_2 adlayers on $\text{Si}(111)$, J. Wollschläger and A. Meier 104/105 (1996) 392
- Structural transformations at $\text{CaF}_2/\text{Si}(111)$ interfaces, N.S. Sokolov, J.C. Alvarez, Yu.V. Shusterman, N.L. Yakovlev, R.M. Overney, Y. Itoh, I. Takahashi and J. Harada 104/105 (1996) 402
- Molecular beam epitaxial growth of thin CaF_2 films on vicinal $\text{Si}(111)$ surfaces, B.M. Kim, C.A. Ventrice, Jr., T. Mercer, R. Overney and L.J. Schowalter 104/105 (1996) 409
- Growth of $\text{CdF}_2/\text{CaF}_2\text{Si}(111)$ heterostructure with abrupt interfaces by using thin CaF_2 buffer layer, A. Izumi, K. Kawabata, K. Tsutsui, N.S. Sokolov, S.V. Novikov and A.Yu. Khilko 104/105 (1996) 417
- Medium energy ion scattering (MEIS) studies on $\text{Si}/\text{GaSb}/\text{Si}$ - and $\text{Si}/\text{CaF}_2/\text{Si}(111)$ layer systems, T. Tappe, A. Chatziparaskewas, J. Schäffer, J. Schlosser, J. Schmalhorst and B. Schmiedeskamp 104/105 (1996) 661

Carbides

- UV photoemission study of heteroepitaxial AlGaN films grown on 6H-SiC, M.C. Benjamin, M.D. Bremser, T.W. Weeks, Jr., S.W. King, R.F. Davis and R.J. Nemanich 104/105 (1996) 455

Chemical vapour deposition

- Studies on low temperature silicon grain growth on SiO_2 by electron cyclotron resonance chemical vapor deposition, K.C. Wang, H.L. Hwang, J.J. Loferski and T.R. Yew 104/105 (1996) 373
- UV photoemission study of heteroepitaxial AlGaN films grown on 6H-SiC, M.C. Benjamin, M.D. Bremser, T.W. Weeks, Jr., S.W. King, R.F. Davis and R.J. Nemanich 104/105 (1996) 455
- Photoluminescence and transmission electron microscopy investigation of SiGe quantum wires grown on patterned Si substrates, A. Hartmann, C. Dieker, U. Bangert, R. Loo, L. Vescan and H. Lüth 104/105 (1996) 502
- MOCVD growth of Ga_2Se_3 on $\text{GaAs}(100)$ and $\text{GaP}(100)$: a Raman study, M. von der Emde, D.R.T. Zahn, T. Ng, N. Maung, G.H. Fan, I.B. Poole, J.O. Williams and A.C. Wright 104/105 (1996) 575

Cobalt

- Atomic phenomena on Si surfaces at adsorption of transition metals, B.Z. Olshanetsky 104/105 (1996) 130
- Dissolution and segregation of monolayer Cu, Ni and Co atoms on the $\text{Si}(111)-\sqrt{3} \times \sqrt{3}$ -Ag surface induced by thermal annealing, J. Yuhara, R. Ishigami, D. Ishikawa and K. Morita 104/105 (1996) 163
- Structural properties of epitaxial silicide layers on Si, H. von Känel, E. Müller, S. Goncalves-Conto, C. Schwarz and N. Onda 104/105 (1996) 204
- The Schottky barrier of Co on strained and unstrained $\text{Si}_x\text{Ge}_{1-x}$ alloys, J.-H. Ku and R.J. Nemanich 104/105 (1996) 262
- Characterization of cobalt-diamond (100) interfaces: electron affinity and Schottky barrier, P.K. Baumann and R.J. Nemanich 104/105 (1996) 267

Copper

- In-situ monitoring of surface chemistry and charge transfer at semiconductor surfaces, E. Fefer, L. Kronik, M. Leibovitch, Y. Shapira and W. Riedl 104/105 (1996) 61
- Dissolution and segregation of monolayer Cu, Ni and Co atoms on the Si(111)- $\sqrt{3} \times \sqrt{3}$ -Ag surface induced by thermal annealing, J. Yuhara, R. Ishigami, D. Ishikawa and K. Morita 104/105 (1996) 163

Depth profiling

- Analytical studies of nickel silicide formation through a thin Ti layer, F. Fenske, A. Schöpke, S. Schulze and B. Selle 104/105 (1996) 218
- Characterization of nitrided SiO₂ thin films using secondary ion mass spectrometry, M.R. Frost and C.W. Magee 104/105 (1996) 379
- Plasma assisted oxidation of SiGe layers at 500°C: interface characterization, C. Tételin, X. Wallart, L. Vescan and J.P. Nys 104/105 (1996) 385
- GaAs surface passivation using in-situ oxide deposition, M. Passlack, M. Hong, R.L. Opila, J.P. Mannaerts and J.R. Kwo 104/105 (1996) 441
- Interface abruptness in strained III-V heterostructures, M.R. Bruni, S. Kačulis, G. Mattogno and G. Righini 104/105 (1996) 652

Diamond

- Characterization of cobalt-diamond (100) interfaces: electron affinity and Schottky barrier, P.K. Baumann and R.J. Neumanich 104/105 (1996) 267
- Graphitization of diamond (111) studied by first principles molecular dynamics, A. De Vita, G. Galli, A. Canning and R. Car 104/105 (1996) 297

Doping effects

- Charge transfer and electronic activation at an Sb δ -layer in Si(001), J.M.C. Thornton, R.J. Cole, D.J. Gravesteijn and P. Weightman 104/105 (1996) 631

Electrical properties

- Quantitative analysis of degradation in Schottky diode characteristics induced by single ion implantation, M. Koyama, Y. Akita, C. Cheong, M. Koh, T. Mat-

- sukawa, K. Horita, B. Shigeta and I. Ohdomari 104/105 (1996) 253
- Density of states and relaxation spectra of etched, H-terminated and naturally oxidized Si-surfaces and the accompanied defects, H. Flietner, W. Füssel, N.D. Sinh and H. Angermann 104/105 (1996) 342
- The conduction barrier at the interface between low temperature grown GaAs and undoped GaAs, K.D. Maranowski, J.P. Ibbetson, K.L. Campman and A.C. Gos-sard 104/105 (1996) 621

Electron diffraction

- Kinematical RHEED simulation of different structure models for the GaAs (311)A surface, W. Braun, O. Brandt, M. Wassermeyer, L. Däweritz and K. Ploog 104/105 (1996) 35
- Surface core-level shift photoelectron diffraction from As/Si(111), L.S.O. Johansson, R. Gunnella, E.L. Bullock, C.R. Natoli and R.I.G. Uhrberg 104/105 (1996) 88
- Smoothing of crystal surfaces during growth interruption, A.Yu. Kaminski and R.A. Suris 104/105 (1996) 312
- Structural transformations at CaF₂/Si(111) interfaces, N.S. Sokolov, J.C. Alvarez, Yu.V. Shusterman, N.L. Yakovlev, R.M. Overney, Y. Itoh, I. Takahashi and J. Harada 104/105 (1996) 402
- Molecular beam epitaxial growth of thin CaF₂ films on vicinal Si(111) surfaces, B.M. Kim, C.A. Ventrice, Jr., T. Mercer, R. Overney and L.J. Schowalter 104/105 (1996) 409
- Sulfur passivated InP(100): surface gaps and electron counting, C.E.J. Mitchell, I.G. Hill, A.B. McLean and Z.H. Lu 104/105 (1996) 434
- Influence of physisorbed arsenic on RHEED intensity oscillations during low-temperature GaAs molecular beam epitaxy, R. Venkatasubramanian, V.K. Pamula and D.L. Dorsey 104/105 (1996) 448
- Initial stage of growth of GaN/GaAs(001) in plasma-assisted molecular beam epitaxy, H. Yang, O. Brandt, A. Trampert and K.H. Ploog 104/105 (1996) 461
- Growth and characterization of ZnSe/GaAs single quantum well structures, J.L. House, D.J. Dougherty, G.S. Petrich, L.A. Kolodziejski, E.P. Ippen and G.-C. Hua 104/105 (1996) 472
- AFM and RHEED study of Ge islanding on Si(111) and Si(100), P.W. Deelman, T. Thundat and L.J. Schowalter 104/105 (1996) 510
- Characterization of arsenide/phosphide heterostructure interfaces by scanning tun-

- neling microscopy, A.Y. Lew, C.H. Yan, C.W. Tu and E.T. Yu 104/105 (1996) 522
- Site occupation of Si atoms deposited on vicinal GaAs(001)-(2 × 4) surfaces, A.R. Avery, J.L. Sudijono, T.S. Jones and B.A. Joyce 104/105 (1996) 539

Electron energy loss spectroscopy

- Plasmon excitations and the effects of surface preparation in n-type InAs(001) studied by electron energy loss spectroscopy, G.R. Bell, C.F. McConville and T.S. Jones 104/105 (1996) 17
- Investigation of the space charge regime of epitaxially grown GaAs (100) by high-resolution electron energy-loss spectroscopy, V.M. Polyakov, A. Elbe, J. Wu, G.J. Lapeyre and J.A. Schaefer 104/105 (1996) 24
- Electronic structure of the valence band of GdS_x and Gd₃S₄, V.A. Grazhulis, S.I. Bozhko, I.L. Bolotin, O.R. Bulanov and A.M. Ionov 104/105 (1996) 68
- Fluorine adsorption on GaAs(110) surfaces and the onset of etching after XeF₂ exposures, H. Nienhaus and W. Mönch 104/105 (1996) 95
- Segregation of In atoms at clean and hydrogen passivated InP(100) surfaces, F. Stietz, Th. Allinger, V. Polyakov, J. Woll, A. Goldmann, W. Erfurth, G.J. Lapeyre and J.A. Schaefer 104/105 (1996) 169
- A comparative study of the adsorption and thermal decomposition of triethylgallium and trimethylgallium at GaAs(100) surfaces studied by electron energy loss spectroscopy, A.A. Aquino and T.S. Jones 104/105 (1996) 304
- Influences of hydrogen on initial oxidation processes of H-terminated Si(100) surfaces, H. Ikeda, K. Hotta, S. Furuta, S. Zaima and Y. Yasuda 104/105 (1996) 354
- Ga-Se films grown on a GaAs(001) surface at high temperature using a thermal evaporation of GaSe, T. Izumi, H. Nishiwaki, T. Tambo and C. Tatsuyama 104/105 (1996) 570
- Ultra-thin AlAs films on GaAs (001) investigated by high-resolution electron-energy-loss spectroscopy, J.-L. Guyaux, Ph. Lambin, M.D. Lange, R. Sporken, P.A. Thiry and R. Caudano 104/105 (1996) 601

Electron microscopy

- Segregation of In atoms at clean and hydrogen passivated InP(100) surfaces, F.

- Stietz, Th. Allinger, V. Polyakov, J. Woll, A. Goldmann, W. Erfurth, G.J. Lapeyre and J.A. Schaefer 104/105 (1996) 169
- Spatially resolved internal and external photoemission of Pt/n-GaP Schottky barrier, C. Coluzza, J. Almeida, T. dell'Orto, F. Barbo, M. Bertolo, A. Bianco, S. Cerasari, S. Fontana, O. Bergossi, M. Spajer and D. Courjon 104/105 (1996) 196
- Structural properties of epitaxial silicide layers on Si, H. von Känel, E. Müller, S. Goncalves-Conto, C. Schwarz and N. Onda 104/105 (1996) 204
- Analytical studies of nickel silicide formation through a thin Ti layer, F. Fenske, A. Schöpke, S. Schulze and B. Selle 104/105 (1996) 218
- Metal overlayers on the MBE-grown ZnSe(001) surface, D.A. Evans, D. Wolframm, D. Gnoth, J. Cairns, A.C. Wright, M. Evans, J. Riley, D. Westwood and D.A. Woolf 104/105 (1996) 240
- Hot-electron scattering at Au/Si(100) Schottky interfaces measured by temperature dependent ballistic electron emission microscopy, C.A. Ventrice Jr., V.P. LaBella, G. Ramaswamy, H.-P. Yu and L.J. Schowalter 104/105 (1996) 274
- Studies on low temperature silicon grain growth on SiO₂ by electron cyclotron resonance chemical vapor deposition, K.C. Wang, H.L. Hwang, J.J. Loferski and T.R. Yew 104/105 (1996) 373
- Molecular beam epitaxial growth of thin CaF₂ films on vicinal Si(111) surfaces, B.M. Kim, C.A. Ventrice, Jr., T. Mercer, R. Overney and L.J. Schowalter 104/105 (1996) 409
- Interface properties of PN_x/InP structures by in-situ remote plasma processes, T. Sugino, Y. Sakamoto, T. Miyazaki and J. Shirafuji 104/105 (1996) 428
- Initial stage of growth of GaN/GaAs(001) in plasma-assisted molecular beam epitaxy, H. Yang, O. Brandt, A. Trampert and K.H. Ploog 104/105 (1996) 461
- Photoluminescence and transmission electron microscopy investigation of SiGe quantum wires grown on patterned Si substrates, A. Hartmann, C. Dieker, U. Bangert, R. Loo, L. Vescan and H. Lüth 104/105 (1996) 502
- Heteroepitaxial growth of InSb on Si(001) surface via Ge buffer layers, M. Mori, D.M. Li, M. Yamazaki, T. Tambo, H. Ueba and C. Tatsuyama 104/105 (1996) 563
- Clustering on surfaces at finite areal coverages, R. Barel, Y. Mai, G.R. Carlow and M. Zinke-Allmang 104/105 (1996) 669

Epitaxy

- Investigation of the space charge regime of epitaxially grown GaAs (100) by high-resolution electron energy-loss spectroscopy, V.M. Polyakov, A. Elbe, J. Wu, G.J. Lapeyre and J.A. Schaefer 104/105 (1996) 24
- Structural properties of epitaxial silicide layers on Si. H. von Känel, E. Müller, S. Goncalves-Conto, C. Schwarz and N. Onda 104/105 (1996) 204
- Unpinned behavior of the Fermi level and photovoltage on p-(100)GaAs surface facilitated by deposition of cesium, V.L. Alperovich, A.G. Paulish, H.E. Scheibler, V.I. Tynnyi and A.S. Terekhov 104/105 (1996) 228
- Surface diffusion limitation in laser focused atomic deposition, R.E. Behringer, V. Natarajan and G. Timp 104/105 (1996) 291
- Smoothing of crystal surfaces during growth interruption, A.Yu. Kaminski and R.A. Suris 104/105 (1996) 312
- Diffraction spot profile analysis for heteroepitaxial surfaces applied to the initial growth stages of CaF_2 adlayers on Si(111), J. Wollschläger and A. Meier 104/105 (1996) 392
- Growth of $\text{CdF}_2/\text{CaF}_2\text{Si}(111)$ heterostructure with abrupt interfaces by using thin CaF_2 buffer layer, A. Izumi, K. Kawabata, K. Tsutsui, N.S. Sokolov, S.V. Novikov and A.Yu. Khilko 104/105 (1996) 417
- Influence of physisorbed arsenic on RHEED intensity oscillations during low-temperature GaAs molecular beam epitaxy, R. Venkatasubramanian, V.K. Pamula and D.L. Dorsey 104/105 (1996) 448
- UV photoemission study of heteroepitaxial AlGaIn films grown on 6H-SiC, M.C. Benjamin, M.D. Bremser, T.W. Weeks, Jr., S.W. King, R.F. Davis and R.J. Nemanich 104/105 (1996) 455
- Growth and characterization of ZnSe/GaAs single quantum well structures, J.L. House, D.J. Dougherty, G.S. Petrich, L.A. Kolodziejwski, E.P. Ippen and G.-C. Hua 104/105 (1996) 472
- Raman monitoring of selenium decapping and subsequent antimony deposition on MBE-grown ZnSe(100), D. Drews, A. Schneider, D.R.T. Zahn, D. Wolframm and D.A. Evans 104/105 (1996) 485
- Highly mismatched heteroepitaxy: 2D platelets assisted nucleation of self-assembled 3D quantum dots, C. Priester and M. Lannoo 104/105 (1996) 495
- Influence of surface reconstruction on MBE growth of layered GaSe on Si(111) substrates, H. Reqqass, J.-P. Lacharme, M. Eddrief, C.A. Sébenne, V. Le Thanh, Y.L. Zheng and J.-F. Pétroff 104/105 (1996) 557
- Heteroepitaxial growth of InSb on Si(001) surface via Ge buffer layers, M. Mori, D.M. Li, M. Yamazaki, T. Tambo, H. Ueba and C. Tatsuyama 104/105 (1996) 563
- Ga-Se films grown on a GaAs(001) surface at high temperature using a thermal evaporation of GaSe, T. Izumi, H. Nishiwaki, T. Tambo and C. Tatsuyama 104/105 (1996) 570
- MOCVD growth of Ga_2Se_3 on GaAs(100) and GaP(100): a Raman study, M. von der Emde, D.R.T. Zahn, T. Ng, N. Maung, G.H. Fan, I.B. Poole, J.O. Williams and A.C. Wright 104/105 (1996) 575
- Low-energy yield spectroscopy determination of band offsets: application to the epitaxial Ge/Si(100) heterostructure, L. Di Gaspare, G. Capellini, C. Chudoba, M. Sebastiani and F. Evangelisti 104/105 (1996) 595
- Band structure evolution in InAs overlayers on GaAs(110), Z.Q. He, L. Ilver, J. Kanski, P.O. Nilsson, P. Songsiriritthigul, G. Holmén and U.O. Karlsson 104/105 (1996) 608
- A scanning tunnelling microscopy study of local surface modifications induced by misfit dislocation formation in strained-layer heteroepitaxy, G. Springholz and G. Bauer 104/105 (1996) 637
- Reconstruction and chemical ordering at the surface of strained (In, Ga)As epilayers, M. Sauvage-Simkin, Y. Garreau, R. Pinchaux, A. Cavanna, M.B. Véron, N. Jedrecy, J.P. Landesman and J. Nagle 104/105 (1996) 646
- Clustering on surfaces at finite areal coverages, R. Barel, Y. Mai, G.R. Carlow and M. Zinke-Allmang 104/105 (1996) 669

Etching

- Fluorine adsorption on GaAs(110) surfaces and the onset of etching after XeF_2 exposures, H. Nienhaus and W. Mönch 104/105 (1996) 95

Europium

- A scanning tunnelling microscopy study of local surface modifications induced by misfit dislocation formation in strained-layer heteroepitaxy, G. Springholz and G. Bauer 104/105 (1996) 637

Evaporation

- The Schottky barrier of Co on strained and unstrained $\text{Si}_x\text{Ge}_{1-x}$ alloys, J.-H. Ku and R.J. Nemanich 104/105 (1996) 262
- Ga- Se films grown on a GaAs(001) surface at high temperature using a thermal evaporation of GaSe, T. Izumi, H. Nishiwaki, T. Tambo and C. Tatsuyama 104/105 (1996) 570

Gadolinium

- Electronic structure of the valence band of GdS_x and Gd_3S_4 , V.A. Grazhulis, S.I. Bozhko, I.L. Bolotin, O.R. Bulanov and A.M. Ionov 104/105 (1996) 68

Gallium

- In-situ monitoring of surface chemistry and charge transfer at semiconductor surfaces, E. Fefer, L. Kronik, M. Leibovitch, Y. Shapira and W. Riedl 104/105 (1996) 61
- UV photoemission study of heteroepitaxial AlGa N films grown on 6H-SiC, M.C. Benjamin, M.D. Bremser, T.W. Weeks, Jr., S.W. King, R.F. Davis and R.J. Nemanich 104/105 (1996) 455
- Initial stage of growth of GaN/GaAs(001) in plasma-assisted molecular beam epitaxy, H. Yang, O. Brandt, A. Trampert and K.H. Ploog 104/105 (1996) 461
- Influence of surface reconstruction on MBE growth of layered GaSe on Si(111) substrates, H. Reqqass, J.-P. Lacharme, M. Eddrief, C.A. Sébenne, V. Le Thanh, Y.L. Zheng and J.-F. Pétroff 104/105 (1996) 557
- Temperature dependence of interdiffusion-induced III-V compound formation at the interface between Al, Ga, In layers and Sb substrates, V. Wagner, W. Richter and J. Geurts 104/105 (1996) 580
- Interface abruptness in strained III-V heterostructures, M.R. Bruni, S. Kačiulis, G. Mattogno and G. Righini 104/105 (1996) 652

Gallium antimonide

- Medium energy ion scattering (MEIS) studies on Si/GaSb/Si- and Si/ CaF_2 /Si-(111) layer systems, T. Tappe, A. Chatziparaskewas, J. Schäffer, J. Schlosser, J. Schmalhorst and B. Schmiedeskamp 104/105 (1996) 661

Gallium arsenide

- Investigation of the space charge regime of epitaxially grown GaAs (100) by high-resolution electron energy-loss spectroscopy, V.M. Polyakov, A. Elbe, J. Wu, G.J. Lapeyre and J.A. Schaefer 104/105 (1996) 24
- Kinematical RHEED simulation of different structure models for the GaAs (311)A surface, W. Braun, O. Brandt, M. Wassermeier, L. Däweritz and K. Ploog 104/105 (1996) 35
- Fluorine adsorption on GaAs(110) surfaces and the onset of etching after XeF_2 exposures, H. Nienhaus and W. Mönch 104/105 (1996) 95
- Se-induced 3d core-level shifts of GaAs(110), P. Käckell, W.G. Schmidt and F. Bechstedt 104/105 (1996) 141
- Schottky-barrier formation at passivated surfaces: covalent and ionic semiconductors, R. Saiz-Pardo, R. Rincón, P.L. de Andrés and F. Flores 104/105 (1996) 183
- Midgap states observed by nonlinear optical spectroscopy of metal:GaAs junctions, J. Qi, W. Angerer, M.S. Yeganeh, A.G. Yodh and W.M. Theis 104/105 (1996) 188
- Unpinned behavior of the Fermi level and photovoltage on p-(100)GaAs surface facilitated by deposition of cesium, V.L. Alperovich, A.G. Paulish, H.E. Scheibler, V.I. Tynnyi and A.S. Terekhov 104/105 (1996) 228
- Development of the Na/GaAs(111)A-(2×2) interface at room and low temperature, J.M.C. Thornton, P. Weightman, P. Bailey, D.A. Woolf, A.D. Laine and D.A. Evans 104/105 (1996) 234
- Metal-insulator transition for K on GaAs-(100)-As rich surfaces, A. Levy Yeyati, A. Martín-Rodero, F. Flores, J. Ortega and R. Rincón 104/105 (1996) 248
- A comparative study of the adsorption and thermal decomposition of triethylgallium and trimethylgallium at GaAs(100) surfaces studied by electron energy loss spectroscopy, A.A. Aquino and T.S. Jones 104/105 (1996) 304
- Hydrogen ion treatments of oxidized GaAs(100) and AlGaAs(100) surfaces: surface stoichiometry and electronic properties, Y.-L. Chang, S.I. Yi, S. Shi, E. Hu, W.H. Weinberg and J. Merz 104/105 (1996) 422
- GaAs surface passivation using in-situ oxide deposition, M. Passlack, M. Hong, R.L. Opila, J.P. Mannaerts and J.R. Kwo 104/105 (1996) 441
- Influence of physisorbed arsenic on RHEED intensity oscillations during low-temperature GaAs molecular beam epitaxy, R.

- Venkatasubramanian, V.K. Pamula and D.L. Dorsey 104/105 (1996) 448
- Initial stage of growth of GaN/GaAs(001) in plasma-assisted molecular beam epitaxy, H. Yang, O. Brandt, A. Trampert and K.H. Ploog 104/105 (1996) 461
- Nitridation of GaAs surfaces stimulated by nitrogen glow discharge, Q.J. Xu, X.M. Ding, X.Y. Hou and X. Wang 104/105 (1996) 468
- Growth and characterization of ZnSe/GaAs single quantum well structures, J.L. House, D.J. Dougherty, G.S. Petrich, L.A. Kolodziejski, E.P. Ippen and G.-C. Hua 104/105 (1996) 472
- Photomodulation Raman scattering spectroscopy of ZnSe/GaAs heterostructure interface, H. Talaat, L. Elissa, S. Negm and E. Burstein 104/105 (1996) 479
- Raman monitoring of selenium decapping and subsequent antimony deposition on MBE-grown ZnSe(100), D. Drews, A. Schneider, D.R.T. Zahn, D. Wolfframm and D.A. Evans 104/105 (1996) 485
- Surface and subsurface imaging of indium in InGaAs by scanning tunneling microscopy, M. Pfister, M.B. Johnson, S.F. Alvarado, H.W.M. Salemin, U. Marti, D. Martin, F. Morier-Genoud and F.K. Reinhart 104/105 (1996) 516
- Site occupation of Si atoms deposited on vicinal GaAs(001)-(2 × 4) surfaces, A.R. Avery, J.L. Sudijono, T.S. Jones and B.A. Joyce 104/105 (1996) 539
- Ga-Se films grown on a GaAs(001) surface at high temperature using a thermal evaporation of GaSe, T. Izumi, H. Nishiwaki, T. Tambo and C. Tatsuyama 104/105 (1996) 570
- MOCVD growth of Ga₂Se₃ on GaAs(100) and GaP(100): a Raman study, M. von der Emde, D.R.T. Zahn, T. Ng, N. Maung, G.H. Fan, I.B. Poole, J.O. Williams and A.C. Wright 104/105 (1996) 575
- Ultra-thin AlAs films on GaAs (001) investigated by high-resolution electron-energy-loss spectroscopy, J.-L. Guyaux, Ph. Lambin, M.D. Lange, R. Sporken, P.A. Thiry and R. Caudano 104/105 (1996) 601
- Band structure evolution in InAs overlayers on GaAs(110), Z.Q. He, L. Ilver, J. Kanski, P.O. Nilsson, P. Songsiriritthigul, G. Holmén and U.O. Karlsson 104/105 (1996) 608
- The conduction barrier at the interface between low temperature grown GaAs and undoped GaAs, K.D. Maranowski, J.P. Ibbetson, K.L. Campman and A.C. Gosard 104/105 (1996) 621
- Reconstruction and chemical ordering at the surface of strained (In, Ga)As epilayers, M. Sauvage-Simkin, Y. Garreau, R. Pinchaux, A. Cavanna, M.B. Véron, N. Jedrecy, J.P. Landesman and J. Nagle 104/105 (1996) 646
- Ab-initio electronic structure calculation of the InAs multiple quantum wells in bulk GaAs, N. Tit and M. Peressi 104/105 (1996) 656

Gallium phosphide

- Electronic properties of antimony monolayers on III-V (110) surfaces: a comparative study by reflectance anisotropy spectroscopy and microscopic tight-binding calculations, A.I. Shkrebtii, N. Esser, M. Köpp, P. Haier, W. Richter and R. Del Sole 104/105 (1996) 176
- Electronic properties of antimony monolayers on III-V (110) surfaces: a comparative study by reflectance anisotropy spectroscopy and microscopic tight-binding calculations, A.I. Shkrebtii, N. Esser, M. Köpp, P. Haier, W. Richter and R. Del Sole 104/105 (1996) 176
- Spatially resolved internal and external photoemission of Pt/n-GaP Schottky barrier, C. Coluzza, J. Almeida, T. dell'Orto, F. Barbo, M. Bertolo, A. Bianco, S. Cerasari, S. Fontana, O. Bergossi, M. Spajer and D. Courjon 104/105 (1996) 196
- MOCVD growth of Ga₂Se₃ on GaAs(100) and GaP(100): a Raman study, M. von der Emde, D.R.T. Zahn, T. Ng, N. Maung, G.H. Fan, I.B. Poole, J.O. Williams and A.C. Wright 104/105 (1996) 575

Gallium selenide

- MOCVD growth of Ga₂Se₃ on GaAs(100) and GaP(100): a Raman study, M. von der Emde, D.R.T. Zahn, T. Ng, N. Maung, G.H. Fan, I.B. Poole, J.O. Williams and A.C. Wright 104/105 (1996) 575

Germanium

- Ge(111)3 × 1:K/Sn; on the influence of tin substitution in a metal induced 3 × 1 reconstruction, M. Göthelid, S. Odasso, G. LeLay, M. Björkqvist, E. Janin, U.O. Karlsson and T.M. Grehk 104/105 (1996) 113
- The Schottky barrier of Co on strained and unstrained Si_xGe_{1-x} alloys, J.-H. Ku and R.J. Nemanich 104/105 (1996) 262
- Plasma assisted oxidation of SiGe layers at 500°C: interface characterization, C. Tételin, X. Wallart, L. Vescan and J.P. Nys 104/105 (1996) 385

- Photoluminescence and transmission electron microscopy investigation of SiGe quantum wires grown on patterned Si substrates, A. Hartmann, C. Dieker, U. Bangert, R. Loo, L. Vescan and H. Lüth 104/105 (1996) 502
- AFM and RHEED study of Ge islanding on Si(111) and Si(100), P.W. Deelman, T. Thundat and L.J. Schowalter 104/105 (1996) 510
- Heteroepitaxial growth of InSb on Si(001) surface via Ge buffer layers, M. Mori, D.M. Li, M. Yamazaki, T. Tambo, H. Ueba and C. Tatsuyama 104/105 (1996) 563
- Low-energy yield spectroscopy determination of band offsets: application to the epitaxial Ge/Si(100) heterostructure, L. Di Gaspare, G. Capellini, C. Chudoba, M. Sebastiani and F. Evangelisti 104/105 (1996) 595
- Measurements of the energy band offsets of $\text{Si}_{1-x}\text{Ge}_x/\text{Si}$ and $\text{Ge}_{1-y}\text{C}_y/\text{Ge}$ heterojunctions, F. Chen, M.M. Waite, S. Ismat Shah, B.A. Orner, S.S. Iyer and J. Kolodzey 104/105 (1996) 615

Gold

- Metal overlayers on the MBE-grown ZnSe(001) surface, D.A. Evans, D. Wolfframm, D. Gnoth, J. Cairns, A.C. Wright, M. Evans, J. Riley, D. Westwood and D.A. Woolf 104/105 (1996) 240
- Hot-electron scattering at Au/Si(100) Schottky interfaces measured by temperature dependent ballistic electron emission microscopy, C.A. Ventrice Jr., V.P. LaBella, G. Ramaswamy, H.-P. Yu and L.J. Schowalter 104/105 (1996) 274

Graphite

- Graphitization of diamond (111) studied by first principles molecular dynamics, A. De Vita, G. Galli, A. Canning and R. Car 104/105 (1996) 297
- STM study of the organic semiconductor PTCDA on highly-oriented pyrolytic graphite, C. Kendrick, A. Kahn and S.R. Forrest 104/105 (1996) 586

Hall effect

- Preparation and properties of thin polycrystalline $\text{MnSi}_{1.73}$ films, St. Teichert, R. Kilper, J. Erben, D. Franke, B. Gebhard, Th. Franke, P. Häussler, W. Henrion and H. Lange 104/105 (1996) 679

Halogens

- Fluorine adsorption on GaAs(110) surfaces and the onset of etching after XeF_2 exposures, H. Nienhaus and W. Mönch 104/105 (1996) 95

Heterostructures

- Photomodulation Raman scattering spectroscopy of ZnSe/GaAs heterostructure interface, H. Talaat, L. Elissa, S. Negm and E. Burstein 104/105 (1996) 479
- Characterization of arsenide/phosphide heterostructure interfaces by scanning tunneling microscopy, A.Y. Lew, C.H. Yan, C.W. Tu and E.T. Yu 104/105 (1996) 522
- Interface abruptness in strained III-V heterostructures, M.R. Bruni, S. Kačiulis, G. Mattogno and G. Righini 104/105 (1996) 652

Hydrogen

- Chemical preparation of CdTe(100) and (110) surfaces using atomic hydrogen, Y. Luo, D.A. Slater, M. Levy and R.M. Osgood Jr. 104/105 (1996) 49
- Preparation of H-terminated Si surfaces and their characterisation by measuring the surface state density, H. Angermann, K. Kliefloth and H. Flietner 104/105 (1996) 107
- Hydrogenated and oxidized vicinal Si(001) surfaces investigated by reflectance-difference spectroscopy, U. Rossow, L. Mantese, T. Yasuda and D.E. Aspnes 104/105 (1996) 137
- Optical spectroscopy study of hydrogenation of the Si(111)- 7×7 surface, M. Roy, C. Beitia, Y. Borensztein, A. Shkrebtii, C. Noguez and R. Del Sole 104/105 (1996) 158
- Segregation of In atoms at clean and hydrogen passivated InP(100) surfaces, F. Stietz, Th. Allinger, V. Polyakov, J. Woll, A. Goldmann, W. Erfurth, G.J. Lapeyre and J.A. Schaefer 104/105 (1996) 169
- Initial stage of oxidation of hydrogen-terminated silicon surfaces, T. Hattori, T. Aiba, E. Iijima, Y. Okube, H. Nohira, N. Tate and M. Katayama 104/105 (1996) 323
- Density of states and relaxation spectra of etched, H-terminated and naturally oxidized Si-surfaces and the accompanied defects, H. Flietner, W. Füssel, N.D. Sinh and H. Angermann 104/105 (1996) 342
- Influences of hydrogen on initial oxidation processes of H-terminated Si(100) surfaces, H. Ikeda, K. Hotta, S. Furuta, S. Zaima and Y. Yasuda 104/105 (1996) 354

- Hydrogen ion treatments of oxidized GaAs(100) and AlGaAs(100) surfaces: surface stoichiometry and electronic properties, Y.-L. Chang, S.I. Yi, S. Shi, E. Hu, W.H. Weinberg and J. Merz 104/105 (1996) 422

Indium

- In-situ monitoring of surface chemistry and charge transfer at semiconductor surfaces, E. Fefer, L. Kronik, M. Leibovitch, Y. Shapira and W. Riedl 104/105 (1996) 61
- Segregation of In atoms at clean and hydrogen passivated InP(100) surfaces, F. Stietz, Th. Allinger, V. Polyakov, J. Woll, A. Goldmann, W. Erfurth, G.J. Lapeyre and J.A. Schaefer 104/105 (1996) 169
- Surface and subsurface imaging of indium in InGaAs by scanning tunneling microscopy, M. Pfister, M.B. Johnson, S.F. Alvarado, H.W.M. Salemink, U. Marti, D. Martin, F. Morier-Genoud and F.K. Reinhart 104/105 (1996) 516
- Temperature dependence of interdiffusion-induced III-V compound formation at the interface between Al, Ga, In layers and Sb substrates, V. Wagner, W. Richter and J. Geurts 104/105 (1996) 580
- Interface abruptness in strained III-V heterostructures, M.R. Bruni, S. Kačialis, G. Mattogno and G. Righini 104/105 (1996) 652

Indium antimonide

- Heteroepitaxial growth of InSb on Si(001) surface via Ge buffer layers, M. Mori, D.M. Li, M. Yamazaki, T. Tambo, H. Ueba and C. Tatsuyama 104/105 (1996) 563

Indium arsenide

- Plasmon excitations and the effects of surface preparation in n-type InAs(001) studied by electron energy loss spectroscopy, G.R. Bell, C.F. McConville and T.S. Jones 104/105 (1996) 17
- Sb or Cs covered InAs(110) surfaces: moving E_F into conduction band and quantized 2D electron channel, V.Yu. Aris-tov, M. Grehk, V.M. Zhilin, A. Taleb-Ibrahimi, G. Indlekofer, Z. Hurych, G. Le Lay and P. Soukiassian 104/105 (1996) 73
- Electronic properties of antimony monolayers on III-V (110) surfaces: a comparative study by reflectance anisotropy spectroscopy and microscopic tight-binding calculations, A.I. Shkrebtii, N.

- Esser, M. Köpp, P. Haier, W. Richter and R. Del Sole 104/105 (1996) 176
- Reconstruction and chemical ordering at the surface of strained (In, Ga)As epilayers, M. Sauvage-Simkin, Y. Garreau, R. Pinchaux, A. Cavanna, M.B. Véron, N. Jedrecy, J.P. Landesman and J. Nagle 104/105 (1996) 646
- Ab-initio electronic structure calculation of the InAs multiple quantum wells in bulk GaAs, N. Tit and M. Peressi 104/105 (1996) 656

Indium phosphide

- In-situ monitoring of surface chemistry and charge transfer at semiconductor surfaces, E. Fefer, L. Kronik, M. Leibovitch, Y. Shapira and W. Riedl 104/105 (1996) 61
- Segregation of In atoms at clean and hydrogen passivated InP(100) surfaces, F. Stietz, Th. Allinger, V. Polyakov, J. Woll, A. Goldmann, W. Erfurth, G.J. Lapeyre and J.A. Schaefer 104/105 (1996) 169
- Electronic properties of antimony monolayers on III-V (110) surfaces: a comparative study by reflectance anisotropy spectroscopy and microscopic tight-binding calculations, A.I. Shkrebtii, N. Esser, M. Köpp, P. Haier, W. Richter and R. Del Sole 104/105 (1996) 176
- A normal incidence X-ray standing wave study of sulphur adsorption on InP(110), T.K. Johal, P. Finetti, V.R. Dhanak, A.W. Robinson, A. Patchett, D.R.T. Zahn and R. McGrath 104/105 (1996) 257
- Interface properties of PN_x /InP structures by in-situ remote plasma processes, T. Sugino, Y. Sakamoto, T. Miyazaki and J. Shirafuji 104/105 (1996) 428
- Sulfur passivated InP(100): surface gaps and electron counting, C.E.J. Mitchell, I.G. Hill, A.B. McLean and Z.H. Lu 104/105 (1996) 434
- Band structure evolution in InAs overlayers on GaAs(110), Z.Q. He, L. Ilver, J. Kanski, P.O. Nilsson, P. Songsiririt-thigul, G. Holmén and U.O. Karlsson 104/105 (1996) 608

Infrared spectroscopy

- Initial stage of oxidation of hydrogen-terminated silicon surfaces, T. Hattori, T. Aiba, E. Iijima, Y. Okube, H. Nohira, N. Tate and M. Katayama 104/105 (1996) 323

Interfaces

- Sb or Cs covered InAs(110) surfaces: moving E_F into conduction band and quantized 2D electron channel, V.Yu. Aris-

- tov, M. Grehk, V.M. Zhilin, A. Taleb-Ibrahimi, G. Indlekofer, Z. Hurych, G. Le Lay and P. Soukiassian 104/105 (1996) 73
- Synchrotron radiation study of Cs/carbon-rich β -SiC(100) and Cs/silicon-rich β -SiC(100) surfaces: metallization and interface formation, F. Semond, P. Soukiassian, P.S. Mangat, Z. Hurych, L. di Cioccio and C. Jaussaud 104/105 (1996) 79
- Development of the Na/GaAs(111)A-(2 \times 2) interface at room and low temperature, J.M.C. Thornton, P. Weightman, P. Bailey, D.A. Woolf, A.D. Laine and D.A. Evans 104/105 (1996) 234
- Hot-electron scattering at Au/Si(100) Schottky interfaces measured by temperature dependent ballistic electron emission microscopy, C.A. Ventrice Jr., V.P. LaBella, G. Ramaswamy, H.-P. Yu and L.J. Schowalter 104/105 (1996) 274
- Comparison of structurally relaxed models of the Si(001)-SiO₂ interface based on different crystalline oxide forms, A. Pasquarello, M.S. Hybertsen and R. Car 104/105 (1996) 317
- Effect of chemical preoxidation treatment on the structure of SiO₂/Si interfaces, H. Nohira, H. Sekikawa, M. Matsuda and T. Hattori 104/105 (1996) 359
- Plasma assisted oxidation of SiGe layers at 500°C: interface characterization, C. Tételin, X. Wallart, L. Vescan and J.P. Nys 104/105 (1996) 385
- Growth of CdF₂/CaF₂/Si(111) heterostructure with abrupt interfaces by using thin CaF₂ buffer layer, A. Izumi, K. Kawabata, K. Tsutsui, N.S. Sokolov, S.V. Novikov and A.Yu. Khilko 104/105 (1996) 417
- Interface properties of PN_x/InP structures by in-situ remote plasma processes, T. Sugino, Y. Sakamoto, T. Miyazaki and J. Shirafuji 104/105 (1996) 428

Ion bombardment

- Synchrotron radiation photoelectron spectroscopy of the O(2s) core level as a tool for monitoring the reducing effects of ion bombardment on SnO₂ thin films, P. De Padova, R. Larciprete, C. Ottaviani, C. Quaresima, P. Perfetti, E. Borsella, C. Astaldi, C. Comicioli, C. Crotti, M. Matteucci, M. Zacchigna and K. Prince 104/105 (1996) 349
- Radiation immunity of pMOSFETs and nMOSFETs examined by means of MeV He single ion microprobe, M. Koh, K. Horita, B. Shigeta, T. Matsukawa, A.

- Kishida, T. Tanii, S. Mori and I. Ohdomari 104/105 (1996) 364

Ion implantation

- Quantitative analysis of degradation in Schottky diode characteristics induced by single ion implantation, M. Koyama, Y. Akita, C. Cheong, M. Koh, T. Matsukawa, K. Horita, B. Shigeta and I. Ohdomari 104/105 (1996) 253

Ion scattering

- Dissolution and segregation of monolayer Cu, Ni and Co atoms on the Si(111)- $\sqrt{3} \times \sqrt{3}$ -Ag surface induced by thermal annealing, J. Yuhara, R. Ishigami, D. Ishikawa and K. Morita 104/105 (1996) 163
- Analytical studies of nickel silicide formation through a thin Ti layer, F. Fenske, A. Schöpke, S. Schulze and B. Selle 104/105 (1996) 218
- The initial oxidation of silicon: new ion scattering results in the ultra-thin regime, E.P. Gusev, H.C. Lu, T. Gustafsson and E. Garfunkel 104/105 (1996) 329
- Medium energy ion scattering (MEIS) studies on Si/GaSb/Si- and Si/CaF₂/Si-(111) layer systems, T. Tappe, A. Chatziparaskewas, J. Schäffer, J. Schlosser, J. Schmalhorst and B. Schmiedeskamp 104/105 (1996) 661
- Preparation and properties of thin polycrystalline MnSi_{1.73} films, St. Teichert, R. Kilper, J. Erben, D. Franke, B. Gebhard, Th. Franke, P. Häussler, W. Henrion and H. Lange 104/105 (1996) 679

Iron

- Structural properties of epitaxial silicide layers on Si, H. von Känel, E. Müller, S. Goncalves-Conto, C. Schwarz and N. Onda 104/105 (1996) 204
- Valence band of Cd_{1-x}Fe_xSe/Fe in resonant photoemission spectra, B.A. Orłowski, B.J. Kowalski, N. Barrett, D. Martinotti, C. Guillot, J.-P. Lacharme and C.A. Sébenne 104/105 (1996) 282

Lead

- Metal overlayers on the MBE-grown ZnSe(001) surface, D.A. Evans, D. Wolframm, D. Gnoth, J. Cairns, A.C.

- Wright, M. Evans, J. Riley, D. Westwood and D.A. Woolf 104/105 (1996) 240

Lead telluride

- A scanning tunnelling microscopy study of local surface modifications induced by misfit dislocation formation in strained-layer heteroepitaxy, G. Springholz and G. Bauer 104/105 (1996) 637

Low energy electron diffraction

- Chemical preparation of CdTe(100) and (110) surfaces using atomic hydrogen, Y. Luo, D.A. Slater, M. Levy and R.M. Osgood Jr. 104/105 (1996) 49
- Atomic phenomena on Si surfaces at adsorption of transition metals, B.Z. Olshanetsky 104/105 (1996) 130
- Optical study of potassium growth on the Si(100) surface, M. Roy and Y. Borenstein 104/105 (1996) 147
- A surface extended X-ray absorption fine structure study of tellurium adsorbed onto Si(100), S.R. Burgess, B.C.C. Cowie, S.P. Wilks, P.R. Dunstan, C.J. Dunscombe and R.H. Williams 104/105 (1996) 152
- Dissolution and segregation of monolayer Cu, Ni and Co atoms on the Si(111)- $\sqrt{3} \times \sqrt{3}$ -Ag surface induced by thermal annealing, J. Yuhara, R. Ishigami, D. Ishikawa and K. Morita 104/105 (1996) 163
- Segregation of In atoms at clean and hydrogen passivated InP(100) surfaces, F. Stietz, Th. Allinger, V. Polyakov, J. Woll, A. Goldmann, W. Erfurth, G.J. Lapeyre and J.A. Schaefer 104/105 (1996) 169
- Diffraction spot profile analysis for heteroepitaxial surfaces applied to the initial growth stages of CaF₂ adlayers on Si(111), J. Wollschläger and A. Meier 104/105 (1996) 392
- Sulfur passivated InP(100): surface gaps and electron counting, C.E.J. Mitchell, I.G. Hill, A.B. McLean and Z.H. Lu 104/105 (1996) 434
- UV photoemission study of heteroepitaxial AlGaIn films grown on 6H-SiC, M.C. Benjamin, M.D. Bremser, T.W. Weeks, Jr., S.W. King, R.F. Davis and R.J. Nemanich 104/105 (1996) 455
- Influence of surface reconstruction on MBE growth of layered GaSe on Si(111) substrates, H. Reqqass, J.-P. Lacharme, M. Eddrief, C.A. Sébenne, V. Le Thanh, Y.L. Zheng and J.-F. Pétroff 104/105 (1996) 557

Luminescence

- Photoluminescence and transmission electron microscopy investigation of SiGe quantum wires grown on patterned Si substrates, A. Hartmann, C. Dieker, U. Bangert, R. Loo, L. Vescan and H. Lüth 104/105 (1996) 502

Manganese

- Preparation and properties of thin polycrystalline MnSi_{1.73} films, St. Teichert, R. Kilper, J. Erben, D. Franke, B. Gebhard, Th. Franke, P. Häussler, W. Henrion and H. Lange 104/105 (1996) 679

Metal-oxide-semiconductor structure (MOS)

- Radiation immunity of pMOSFETs and nMOSFETs examined by means of MeV He single ion microprobe, M. Koh, K. Horita, B. Shigeta, T. Matsukawa, A. Kishida, T. Tanii, S. Mori and I. Ohdomari 104/105 (1996) 364

Molecular beam epitaxy

- Metal overlayers on the MBE-grown ZnSe(001) surface, D.A. Evans, D. Wolfframm, D. Gnoth, J. Cairns, A.C. Wright, M. Evans, J. Riley, D. Westwood and D.A. Woolf 104/105 (1996) 240
- Molecular beam epitaxial growth of thin CaF₂ films on vicinal Si(111) surfaces, B.M. Kim, C.A. Ventrice, Jr., T. Mercer, R. Overney and L.J. Schowalter 104/105 (1996) 409
- Initial stage of growth of GaN/GaAs(001) in plasma-assisted molecular beam epitaxy, H. Yang, O. Brandt, A. Trampert and K.H. Ploog 104/105 (1996) 461
- Photomodulation Raman scattering spectroscopy of ZnSe/GaAs heterostructure interface, H. Talaat, L. Elissa, S. Negm and E. Burstein 104/105 (1996) 479
- Interface abruptness in strained III-V heterostructures, M.R. Bruni, S. Kačuliš, G. Mattogno and G. Righini 104/105 (1996) 652
- Medium energy ion scattering (MEIS) studies on Si/GaSb/Si- and Si/CaF₂/Si(111) layer systems, T. Tappe, A. Chatziparaskewas, J. Schäffer, J. Schlosser, J. Schmalhorst and B. Schmiedeskamp 104/105 (1996) 661

Molecular dynamics

- Graphitization of diamond (111) studied by first principles molecular dynamics, A. De Vita, G. Galli, A. Canning and R. Car 104/105 (1996) 297

Nickel

- Atomic phenomena on Si surfaces at adsorption of transition metals, B.Z. Olshanetsky 104/105 (1996) 130
- Dissolution and segregation of monolayer Cu, Ni and Co atoms on the Si(111)- $\sqrt{3} \times \sqrt{3}$ -Ag surface induced by thermal annealing, J. Yuhara, R. Ishigami, D. Ishikawa and K. Morita 104/105 (1996) 163
- Atomistic study of the formation process of Ni silicide on the Si(111)- 7×7 surface with scanning tunneling microscopy, T. Yao, S. Shinabe and M. Yoshimura 104/105 (1996) 213
- Analytical studies of nickel silicide formation through a thin Ti layer, F. Fenske, A. Schöpke, S. Schulze and B. Selle 104/105 (1996) 218

Nitrides

- Characterization of nitrided SiO₂ thin films using secondary ion mass spectrometry, M.R. Frost and C.W. Magee 104/105 (1996) 379
- Interface properties of PN_x/InP structures by in-situ remote plasma processes, T. Sugino, Y. Sakamoto, T. Miyazaki and J. Shirafuji 104/105 (1996) 428
- UV photoemission study of heteroepitaxial AlGaN films grown on 6H-SiC, M.C. Benjamin, M.D. Bremser, T.W. Weeks, Jr., S.W. King, R.F. Davis and R.J. Nemanich 104/105 (1996) 455
- Initial stage of growth of GaN/GaAs(001) in plasma-assisted molecular beam epitaxy, H. Yang, O. Brandt, A. Trampert and K.H. Ploog 104/105 (1996) 461

Nitrogen

- Local atomic structure and electrical properties of nitrided Si-SiO₂ interfaces produced by low-temperature plasma processing and rapid thermal annealing, and explained by ab-initio quantum chemistry calculations, G. Lucovsky, D.R. Lee, S.V. Hattangady, H. Niimi, S. Gandhi, C. Parker, Z. Jing, J.L. Whitten and J.R. Hauser 104/105 (1996) 335

- Nitridation of GaAs surfaces stimulated by nitrogen glow discharge, Q.J. Xu, X.M. Ding, X.Y. Hou and X. Wang 104/105 (1996) 468

Optical properties

- Optical study of potassium growth on the Si(100) surface, M. Roy and Y. Borenstein 104/105 (1996) 147
- Optical spectroscopy study of hydrogenation of the Si(111)- 7×7 surface, M. Roy, C. Beitia, Y. Borensztein, A. Shkrebtii, C. Noguez and R. Del Sole 104/105 (1996) 158
- Electronic properties of antimony monolayers on III-V (110) surfaces: a comparative study by reflectance anisotropy spectroscopy and microscopic tight-binding calculations, A.I. Shkrebtii, N. Esser, M. Köpp, P. Haier, W. Richter and R. Del Sole 104/105 (1996) 176
- Midgap states observed by nonlinear optical spectroscopy of metal:GaAs junctions, J. Qi, W. Angerer, M.S. Yeganeh, A.G. Yodh and W.M. Theis 104/105 (1996) 188

Oxidation

- Hydrogenated and oxidized vicinal Si(001) surfaces investigated by reflectance-difference spectroscopy, U. Rossow, L. Mantese, T. Yasuda and D.E. Aspnes 104/105 (1996) 137
- Initial stage of oxidation of hydrogen-terminated silicon surfaces, T. Hattori, T. Aiba, E. Iijima, Y. Okube, H. Nohira, N. Tate and M. Katayama 104/105 (1996) 323
- The initial oxidation of silicon: new ion scattering results in the ultra-thin regime, E.P. Gusev, H.C. Lu, T. Gustafsson and E. Garfunkel 104/105 (1996) 329
- Density of states and relaxation spectra of etched, H-terminated and naturally oxidized Si-surfaces and the accompanied defects, H. Flietner, W. Füssel, N.D. Sinh and H. Angermann 104/105 (1996) 342
- Influences of hydrogen on initial oxidation processes of H-terminated Si(100) surfaces, H. Ikeda, K. Hotta, S. Furuta, S. Zaima and Y. Yasuda 104/105 (1996) 354
- Plasma assisted oxidation of SiGe layers at 500°C: interface characterization, C. Tételin, X. Wallart, L. Vescan and J.P. Nys 104/105 (1996) 385
- GaAs surface passivation using in-situ oxide deposition, M. Passlack, M. Hong, R.L. Opila, J.P. Mannaerts and J.R. Kwo 104/105 (1996) 441

Oxides

- Weak fluence dependence of charge generation in ultra-thin oxides on silicon, K.R. Farmer, C.P. Debauche, A.R. Giordano, P. Lundgren, M.O. Andersson and D.A. Buchanan 104/105 (1996) 369

Phosphorus

- Interface properties of PN_x/InP structures by in-situ remote plasma processes, T. Sugino, Y. Sakamoto, T. Miyazaki and J. Shirafuji 104/105 (1996) 428
- Characterization of arsenide/phosphide heterostructure interfaces by scanning tunneling microscopy, A.Y. Lew, C.H. Yan, C.W. Tu and E.T. Yu 104/105 (1996) 522

Photochemistry

- Photoexcited carrier diffusion near a Si(111) surface and in the Si bulk, C.M. Li, T. Sjodin, Z.C. Ying and H.L. Dai 104/105 (1996) 57

Photoelectron spectroscopy

- Chemical preparation of CdTe(100) and (110) surfaces using atomic hydrogen, Y. Luo, D.A. Slater, M. Levy and R.M. Osgood Jr. 104/105 (1996) 49
- Electronic structure of the valence band of GdS_x and Gd_3S_4 , V.A. Grazhulis, S.I. Bozhko, I.L. Bolotin, O.R. Bulanov and A.M. Ionov 104/105 (1996) 68
- Sb or Cs covered InAs(110) surfaces: moving E_F into conduction band and quantized 2D electron channel, V.Yu. Aris-tov, M. Grehk, V.M. Zhilin, A. Taleb-Ibrahimi, G. Indlekofer, Z. Hurych, G. Le Lay and P. Soukiasian 104/105 (1996) 73
- Synchrotron radiation study of Cs/carbon-rich $\beta\text{-SiC}(100)$ and Cs/silicon-rich $\beta\text{-SiC}(100)$ surfaces: metallization and interface formation, F. Semon, P. Soukiasian, P.S. Mangat, Z. Hurych, L. di Cioccio and C. Jaussaud 104/105 (1996) 79
- Surface core-level shift photoelectron diffraction from As/Si(111), L.S.O. Johansson, R. Gunnella, E.L. Bullock, C.R. Natoli and R.I.G. Uhrberg 104/105 (1996) 88
- An ARUPS/NEXAFS study of the $\text{H}_2\text{S}/\text{InP}(110)$ adsorbate system, E. Dudzik, A. Leslie, E. O'Toole, I.T. McGovern, A. Patchett and D.R.T. Zahn 104/105 (1996) 101

- Ge(111) 3×1 :K/Sn; on the influence of tin substitution in a metal induced 3×1 reconstruction, M. Göthelid, S. Odasso, G. LeLay, M. Björkqvist, E. Janin, U.O. Karlsson and T.M. Grehk 104/105 (1996) 113
- Si(110) 16×2 and Si(110) 2×3 -Sb surfaces studied by photoemission and optical spectroscopy, A. Cricenti, P. Perfetti, B. Nesterenko, G. LeLay and C. Sebenne 104/105 (1996) 118
- Segregation of In atoms at clean and hydrogen passivated InP(100) surfaces, F. Stietz, Th. Allinger, V. Polyakov, J. Woll, A. Goldmann, W. Erfurth, G.J. Lapeyre and J.A. Schaefer 104/105 (1996) 169
- Spatially resolved internal and external photoemission of Pt/n-GaP Schottky barrier, C. Coluzza, J. Almeida, T. dell'Orto, F. Barbo, M. Bertolo, A. Bianco, S. Cerasari, S. Fontana, O. Bergossi, M. Spajer and D. Courjon 104/105 (1996) 196
- Development of the Na/GaAs(111)A-(2×2) interface at room and low temperature, J.M.C. Thornton, P. Weightman, P. Bailey, D.A. Woolf, A.D. Laine and D.A. Evans 104/105 (1996) 234
- Metal overlayers on the MBE-grown ZnSe(001) surface, D.A. Evans, D. Wolfram, D. Gnoth, J. Cairns, A.C. Wright, M. Evans, J. Riley, D. Westwood and D.A. Woolf 104/105 (1996) 240
- The Schottky barrier of Co on strained and unstrained $\text{Si}_x\text{Ge}_{1-x}$ alloys, J.-H. Ku and R.J. Nemanich 104/105 (1996) 262
- Characterization of cobalt-diamond (100) interfaces: electron affinity and Schottky barrier, P.K. Baumann and R.J. Nemanich 104/105 (1996) 267
- Valence band of $\text{Cd}_{1-x}\text{Fe}_x\text{Se}/\text{Fe}$ in resonant photoemission spectra, B.A. Or-lowski, B.J. Kowalski, N. Barrett, D. Martinotti, C. Guillot, J.-P. Lacharme and C.A. Sébenne 104/105 (1996) 282
- Initial stage of oxidation of hydrogen-terminated silicon surfaces, T. Hattori, T. Aiba, E. Iijima, Y. Okube, H. Nohira, N. Tate and M. Katayama 104/105 (1996) 323
- Synchrotron radiation photoelectron spectroscopy of the O(2s) core level as a tool for monitoring the reducing effects of ion bombardment on SnO_2 thin films, P. De Padova, R. Larci-prete, C. Ottaviani, C. Quaresima, P. Perfetti, E. Borsella, C. Astaldi, C. Comicioli, C. Crotti, M. Matteucci, M. Zacchigna and K. Prince 104/105 (1996) 349
- Effect of chemical preoxidation treatment on the structure of SiO_2/Si interfaces, H. Nohira, H. Sekikawa, M. Matsuda and T. Hattori 104/105 (1996) 359

- Growth of $\text{CdF}_2/\text{CaF}_2\text{Si}(111)$ heterostructure with abrupt interfaces by using thin CaF_2 buffer layer, A. Izumi, K. Kawabata, K. Tsutsui, N.S. Sokolov, S.V. Novikov and A.Yu. Khilko 104/105 (1996) 417
- Interface properties of PN_x/InP structures by in-situ remote plasma processes, T. Sugino, Y. Sakamoto, T. Miyazaki and J. Shirafuji 104/105 (1996) 428
- Sulfur passivated $\text{InP}(100)$: surface gaps and electron counting, C.E.J. Mitchell, I.G. Hill, A.B. McLean and Z.H. Lu 104/105 (1996) 434
- GaAs surface passivation using in-situ oxide deposition, M. Passlack, M. Hong, R.L. Opila, J.P. Mannaerts and J.R. Kwo 104/105 (1996) 441
- UV photoemission study of heteroepitaxial AlGaIn films grown on 6H-SiC , M.C. Benjamin, M.D. Bremser, T.W. Weeks, Jr., S.W. King, R.F. Davis and R.J. Nemanich 104/105 (1996) 455
- Nitridation of GaAs surfaces stimulated by nitrogen glow discharge, Q.J. Xu, X.M. Ding, X.Y. Hou and X. Wang 104/105 (1996) 468
- Ga-Se films grown on a GaAs(001) surface at high temperature using a thermal evaporation of GaSe, T. Izumi, H. Nishiwaki, T. Tambo and C. Tatsuyama 104/105 (1996) 570
- Band structure evolution in InAs overlayers on GaAs(110), Z.Q. He, L. Ilver, J. Kanski, P.O. Nilsson, P. Songsiriritthigul, G. Holmén and U.O. Karlsson 104/105 (1996) 608
- Measurements of the energy band offsets of $\text{Si}_{1-x}\text{Ge}_x/\text{Si}$ and $\text{Ge}_{1-y}\text{C}_y/\text{Ge}$ heterojunctions, F. Chen, M.M. Waite, S. Ismat Shah, B.A. Orner, S.S. Iyer and J. Kolodzey 104/105 (1996) 615
- Charge transfer and electronic activation at an Sb δ -layer in $\text{Si}(001)$, J.M.C. Thornton, R.J. Cole, D.J. Gravesteijn and P. Weightman 104/105 (1996) 631
- Interface abruptness in strained III-V heterostructures, M.R. Bruni, S. Kačičius, G. Mattogno and G. Righini 104/105 (1996) 652

Photoemission

- Low-energy yield spectroscopy determination of band offsets: application to the epitaxial $\text{Ge}/\text{Si}(100)$ heterostructure, L. Di Gaspare, G. Capellini, C. Chudoba, M. Sebastiani and F. Evangelisti 104/105 (1996) 595

Plasma processing

- Local atomic structure and electrical properties of nitrided Si-SiO_2 interfaces pro-

- duced by low-temperature plasma processing and rapid thermal annealing, and explained by ab-initio quantum chemistry calculations, G. Lucovsky, D.R. Lee, S.V. Hattangady, H. Niimi, S. Gandhi, C. Parker, Z. Jing, J.L. Whitten and J.R. Hauser 104/105 (1996) 335
- Plasma assisted oxidation of SiGe layers at 500°C : interface characterization, C. Tételin, X. Wallart, L. Vescan and J.P. Nys 104/105 (1996) 385
- Interface properties of PN_x/InP structures by in-situ remote plasma processes, T. Sugino, Y. Sakamoto, T. Miyazaki and J. Shirafuji 104/105 (1996) 428
- Initial stage of growth of GaN/GaAs(001) in plasma-assisted molecular beam epitaxy, H. Yang, O. Brandt, A. Trampert and K.H. Ploog 104/105 (1996) 461

Platinum

- Spatially resolved internal and external photoemission of Pt/n-GaP Schottky barrier, C. Coluzza, J. Almeida, T. dell'Orto, F. Barbo, M. Bertolo, A. Bianco, S. Cerasari, S. Fontana, O. Bergossi, M. Spajer and D. Courjon 104/105 (1996) 196

Quantum effects

- Hydrogen ion treatments of oxidized GaAs(100) and AlGaAs(100) surfaces: surface stoichiometry and electronic properties, Y.-L. Chang, S.I. Yi, S. Shi, E. Hu, W.H. Weinberg and J. Merz 104/105 (1996) 422
- Growth and characterization of ZnSe/GaAs single quantum well structures, J.L. House, D.J. Dougherty, G.S. Petrich, L.A. Kolodziejski, E.P. Ippen and G.-C. Hua 104/105 (1996) 472
- Highly mismatched heteroepitaxy: 2D platelets assisted nucleation of self-assembled 3D quantum dots, C. Priester and M. Lannoo 104/105 (1996) 495
- Photoluminescence and transmission electron microscopy investigation of SiGe quantum wires grown on patterned Si substrates, A. Hartmann, C. Dieker, U. Bangert, R. Loo, L. Vescan and H. Lüth 104/105 (1996) 502
- Characterization of nanostructures by virtue of the phenomena due to the electron-phonon interaction, E.P. Pokatilov, V.M. Fomin, S.N. Klimin and S.N. Balaban 104/105 (1996) 546
- Ab-initio electronic structure calculation of the InAs multiple quantum wells in bulk GaAs, N. Tit and M. Peressi 104/105 (1996) 656

Raman scattering

- Electronic properties of antimony monolayers on III-V (110) surfaces: a comparative study by reflectance anisotropy spectroscopy and microscopic tight-binding calculations, A.I. Shkrebtii, N. Esser, M. Köpp, P. Haier, W. Richter and R. Del Sole 104/105 (1996) 176
- Photomodulation Raman scattering spectroscopy of ZnSe/GaAs heterostructure interface, H. Talaat, L. Elissa, S. Negm and E. Burstein 104/105 (1996) 479
- Raman monitoring of selenium decapping and subsequent antimony deposition on MBE-grown ZnSe(100), D. Drews, A. Schneider, D.R.T. Zahn, D. Wolfframm and D.A. Evans 104/105 (1996) 485
- MOCVD growth of Ga₂Se₃ on GaAs(100) and GaP(100): a Raman study, M. von der Emde, D.R.T. Zahn, T. Ng, N. Maung, G.H. Fan, I.B. Poole, J.O. Williams and A.C. Wright 104/105 (1996) 575
- Temperature dependence of interdiffusion-induced III-V compound formation at the interface between Al, Ga, In layers and Sb substrates, V. Wagner, W. Richter and J. Geurts 104/105 (1996) 580

Scanning tunneling microscopy

- The atomic structure of the Si(111) ($2\sqrt{3} \times 2\sqrt{3}$)R30°-Sn reconstruction, A.H. Levermann, P.B. Howes, K.A. Edwards, H.T. Anyele, C.C. Matthai, J.E. Macdonald, R. Feidenhans'l, L. Lottermoser, L. Seehofer, G. Falkenberg and R.L. Johnson 104/105 (1996) 124
- Atomistic study of the formation process of Ni silicide on the Si(111)- 7×7 surface with scanning tunneling microscopy, T. Yao, S. Shinabe and M. Yoshimura 104/105 (1996) 213
- Hot-electron scattering at Au/Si(100) Schottky interfaces measured by temperature dependent ballistic electron emission microscopy, C.A. Ventrice Jr., V.P. LaBella, G. Ramaswamy, H.-P. Yu and L.J. Schowalter 104/105 (1996) 274
- Intrinsic surface atom manipulations in STM and AFM, K. Cho and J.D. Joannopoulos 104/105 (1996) 286
- Surface diffusion limitation in laser focused atomic deposition, R.E. Behringer, V. Natarajan and G. Timp 104/105 (1996) 291
- Surface and subsurface imaging of indium in InGaAs by scanning tunneling mi-

- croscopy, M. Pfister, M.B. Johnson, S.F. Alvarado, H.W.M. Salemink, U. Marti, D. Martin, F. Morier-Genoud and F.K. Reinhart 104/105 (1996) 516
- Characterization of arsenide/phosphide heterostructure interfaces by scanning tunneling microscopy, A.Y. Lew, C.H. Yan, C.W. Tu and E.T. Yu 104/105 (1996) 522
- Site occupation of Si atoms deposited on vicinal GaAs(001)-(2 × 4) surfaces, A.R. Avery, J.L. Sudijono, T.S. Jones and B.A. Joyce 104/105 (1996) 539
- STM study of the organic semiconductor PTCDA on highly-oriented pyrolytic graphite, C. Kendrick, A. Kahn and S.R. Forrest 104/105 (1996) 586
- A scanning tunnelling microscopy study of local surface modifications induced by misfit dislocation formation in strained-layer heteroepitaxy, G. Springholz and G. Bauer 104/105 (1996) 637

Schottky barrier

- Schottky-barrier formation at passivated surfaces: covalent and ionic semiconductors, R. Saiz-Pardo, R. Rincón, P.L. de Andrés and F. Flores 104/105 (1996) 183
- Spatially resolved internal and external photoemission of Pt/n-GaP Schottky barrier, C. Coluzza, J. Almeida, T. dell'Orto, F. Barbo, M. Bertolo, A. Bianco, S. Cerasari, S. Fontana, O. Bergossi, M. Spajer and D. Courjon 104/105 (1996) 196
- Development of the Na/GaAs(111)A-(2 × 2) interface at room and low temperature, J.M.C. Thornton, P. Weightman, P. Bailey, D.A. Woolf, A.D. Laine and D.A. Evans 104/105 (1996) 234
- Metal overlayers on the MBE-grown ZnSe(001) surface, D.A. Evans, D. Wolfframm, D. Gnoth, J. Cairns, A.C. Wright, M. Evans, J. Riley, D. Westwood and D.A. Woolf 104/105 (1996) 240
- Quantitative analysis of degradation in Schottky diode characteristics induced by single ion implantation, M. Koyama, Y. Akita, C. Cheong, M. Koh, T. Matsukawa, K. Horita, B. Shigeta and I. Ohdomari 104/105 (1996) 253
- The Schottky barrier of Co on strained and unstrained Si_xGe_{1-x} alloys, J.-H. Ku and R.J. Nemanich 104/105 (1996) 262
- Characterization of cobalt-diamond (100) interfaces: electron affinity and Schottky barrier, P.K. Baumann and R.J. Nemanich 104/105 (1996) 267

Hot-electron scattering at Au/Si(100)
Schottky interfaces measured by temperature dependent ballistic electron emission microscopy, C.A. Ventrice Jr., V.P. LaBella, G. Ramaswamy, H.-P. Yu and L.J. Schowalter 104/105 (1996) 274

The conduction barrier at the interface between low temperature grown GaAs and undoped GaAs, K.D. Maranowski, J.P. Ibbetson, K.L. Campman and A.C. Gosard 104/105 (1996) 621

Secondary ion mass spectrometry

Local atomic structure and electrical properties of nitrided Si-SiO₂ interfaces produced by low-temperature plasma processing and rapid thermal annealing, and explained by ab-initio quantum chemistry calculations, G. Lucovsky, D.R. Lee, S.V. Hattangady, H. Niimi, S. Gandhi, C. Parker, Z. Jing, J.L. Whitten and J.R. Hauser 104/105 (1996) 335

Characterization of nitrided SiO₂ thin films using secondary ion mass spectrometry, M.R. Frost and C.W. Magee 104/105 (1996) 379

Selenium

In-situ monitoring of surface chemistry and charge transfer at semiconductor surfaces, E. Fefer, L. Kronik, M. Leibovitch, Y. Shapira and W. Riedl 104/105 (1996) 61

Se-induced 3d core-level shifts of GaAs(110), P. Käckell, W.G. Schmidt and F. Bechstedt 104/105 (1996) 141

Valence band of Cd_{1-x}Fe_xSe/Fe in resonant photoemission spectra, B.A. Orlovski, B.J. Kowalski, N. Barrett, D. Martinotti, C. Guillot, J.-P. Lacharme and C.A. Sébenne 104/105 (1996) 282

Growth and characterization of ZnSe/GaAs single quantum well structures, J.L. House, D.J. Dougherty, G.S. Petrich, L.A. Kolodziejski, E.P. Ippen and G.-C. Hua 104/105 (1996) 472

Raman monitoring of selenium decapping and subsequent antimony deposition on MBE-grown ZnSe(100), D. Drews, A. Schneider, D.R.T. Zahn, D. Wolfram and D.A. Evans 104/105 (1996) 485

Influence of surface reconstruction on MBE growth of layered GaSe on Si(111) substrates, H. Reqqass, J.-P. Lacharme, M. Eddrief, C.A. Sébenne, V. Le Thanh, Y.L. Zheng and J.-F. Pétroff 104/105 (1996) 557

Ga-Se films grown on a GaAs(001) surface at high temperature using a thermal evaporation of GaSe, T. Izumi, H. Nishiwaki, T. Tambo and C. Tatsuyama 104/105 (1996) 570

Semiconductors

Ab initio calculations of structural and electronic properties of prototype surfaces of group IV, III-V and II-VI semiconductors, J. Pollmann, P. Krüger, M. Rohlfing, M. Sabisch and D. Vogel 104/105 (1996) 1

Weak fluence dependence of charge generation in ultra-thin oxides on silicon, K.R. Farmer, C.P. Debauche, A.R. Giordano, P. Lundgren, M.O. Andersson and D.A. Buchanan 104/105 (1996) 369

STM study of the organic semiconductor PTCDA on highly-oriented pyrolytic graphite, C. Kendrick, A. Kahn and S.R. Forrest 104/105 (1996) 586

A summary and perspective on the Fifth International Conference on the Formation of Semiconductor Interfaces, Princeton, NJ, H. Lüth 104/105 (1996) 685

Silicides

Structural properties of epitaxial silicide layers on Si, H. von Känel, E. Müller, S. Goncalves-Conto, C. Schwarz and N. Onda 104/105 (1996) 204

Atomistic study of the formation process of Ni silicide on the Si(111)-7×7 surface with scanning tunneling microscopy, T. Yao, S. Shinabe and M. Yoshimura 104/105 (1996) 213

Analytical studies of nickel silicide formation through a thin Ti layer, F. Fenske, A. Schöpke, S. Schulze and B. Selle 104/105 (1996) 218

Preparation and properties of thin polycrystalline MnSi_{1.73} films, St. Teichert, R. Kilper, J. Erben, D. Franke, B. Gebhard, Th. Franke, P. Häussler, W. Henrion and H. Lange 104/105 (1996) 679

Silicon

Photoexcited carrier diffusion near a Si(111) surface and in the Si bulk, C.M. Li, T. Sjödin, Z.C. Ying and H.L. Dai 104/105 (1996) 57

Surface core-level shift photoelectron diffraction from As/Si(111), L.S.O. Johansson, R. Gunnella, E.L. Bullock, C.R. Natoli and R.I.G. Uhrberg 104/105 (1996) 88

- Preparation of H-terminated Si surfaces and their characterisation by measuring the surface state density, H. Angermann, K. Kliefoth and H. Flietner 104/105 (1996) 107
- Si(110) 16×2 and Si(110) 2×3 -Sb surfaces studied by photoemission and optical spectroscopy, A. Cricenti, P. Perfetti, B. Nesterenko, G. LeLay and C. Sebenne 104/105 (1996) 118
- The atomic structure of the Si(111) ($2\sqrt{3} \times 2\sqrt{3}$)R30°-Sn reconstruction, A.H. Lev-ermann, P.B. Howes, K.A. Edwards, H.T. Anyele, C.C. Matthai, J.E. Mac-donald, R. Feidenhans'l, L. Lottermoser, L. Seehofer, G. Falkenberg and R.L. Johnson 104/105 (1996) 124
- Atomic phenomena on Si surfaces at ad-sorption of transition metals, B.Z. Ol-shanetsky 104/105 (1996) 130
- Hydrogenated and oxidized vicinal Si(001) surfaces investigated by reflectance-dif-ference spectroscopy, U. Rossow, L. Mantese, T. Yasuda and D.E. Aspnes 104/105 (1996) 137
- Optical study of potassium growth on the Si(100) surface, M. Roy and Y. Boren-sztein 104/105 (1996) 147
- A surface extended X-ray absorption fine structure study of tellurium adsorbed onto Si(100), S.R. Burgess, B.C.C. Cowie, S.P. Wilks, P.R. Dunstan, C.J. Dunscombe and R.H. Williams 104/105 (1996) 152
- Optical spectroscopy study of hydrogena-tion of the Si(111)- 7×7 surface, M. Roy, C. Beitia, Y. Borensztein, A. Shkrebtii, C. Noguez and R. Del Sole 104/105 (1996) 158
- Dissolution and segregation of monolayer Cu, Ni and Co atoms on the Si(111)- $\sqrt{3} \times \sqrt{3}$ -Ag surface induced by thermal annealing, J. Yuhara, R. Ishigami, D. Ishikawa and K. Morita 104/105 (1996) 163
- Schottky-barrier formation at passivated surfaces: covalent and ionic semicon-ductors, R. Saiz-Pardo, R. Rincón, P.L. de Andrés and F. Flores 104/105 (1996) 183
- Quantitative analysis of degradation in Schottky diode characteristics induced by single ion implantation, M. Koyama, Y. Akita, C. Cheong, M. Koh, T. Mat-sukawa, K. Horita, B. Shigeta and I. Ohdomari 104/105 (1996) 253
- The Schottky barrier of Co on strained and unstrained Si_xGe_{1-x} alloys, J.-H. Ku and R.J. Nemanich 104/105 (1996) 262
- Hot-electron scattering at Au/Si(100) Schottky interfaces measured by temper-ature dependent ballistic electron emis-sion microscopy, C.A. Ventrice Jr., V.P. LaBella, G. Ramaswamy, H.-P. Yu and L.J. Schowalter 104/105 (1996) 274
- Comparison of structurally relaxed models of the Si(001)-SiO₂ interface based on different crystalline oxide forms, A. Pasquarello, M.S. Hybertsen and R. Car 104/105 (1996) 317
- Initial stage of oxidation of hydrogen-terminated silicon surfaces, T. Hattori, T. Aiba, E. Iijima, Y. Okube, H. Nohira, N. Tate and M. Katayama 104/105 (1996) 323
- The initial oxidation of silicon: new ion scattering results in the ultra-thin regime, E.P. Gusev, H.C. Lu, T. Gustafsson and E. Garfunkel 104/105 (1996) 329
- Local atomic structure and electrical proper-ties of nitrided Si-SiO₂ interfaces pro-duced by low-temperature plasma pro-cessing and rapid thermal annealing, and explained by ab-initio quantum chem-istry calculations, G. Lucovsky, D.R. Lee, S.V. Hattangady, H. Niimi, S. Gandhi, C. Parker, Z. Jing, J.L. Whitten and J.R. Hauser 104/105 (1996) 335
- Density of states and relaxation spectra of etched, H-terminated and naturally oxi-dized Si-surfaces and the accompanied defects, H. Flietner, W. Füssel, N.D. Sinh and H. Angermann 104/105 (1996) 342
- Influences of hydrogen on initial oxidation processes of H-terminated Si(100) sur-faces, H. Ikeda, K. Hotta, S. Furuta, S. Zaima and Y. Yasuda 104/105 (1996) 354
- Effect of chemical preoxidation treatment on the structure of SiO₂/Si interfaces, H. Nohira, H. Sekikawa, M. Matsuda and T. Hattori 104/105 (1996) 359
- Weak fluence dependence of charge genera-tion in ultra-thin oxides on silicon, K.R. Farmer, C.P. Debauche, A.R. Giordano, P. Lundgren, M.O. Andersson and D.A. Buchanan 104/105 (1996) 369
- Studies on low temperature silicon grain growth on SiO₂ by electron cyclotron resonance chemical vapor deposition, K.C. Wang, H.L. Hwang, J.J. Loferski and T.R. Yew 104/105 (1996) 373
- Plasma assisted oxidation of SiGe layers at 500°C: interface characterization, C. Tételin, X. Wallart, L. Vescan and J.P. Nys 104/105 (1996) 385
- Diffraction spot profile analysis for het-eroepitaxial surfaces applied to the ini-tial growth stages of CaF₂ adlayers on Si(111), J. Wollschläger and A. Meier 104/105 (1996) 392
- Structural transformations at CaF₂/Si(111) interfaces, N.S. Sokolov, J.C. Alvarez, Yu.V. Shusterman, N.L. Yakovlev, R.M. Overney, Y. Itoh, I. Takahashi and J. Harada 104/105 (1996) 402

- Molecular beam epitaxial growth of thin CaF_2 films on vicinal $\text{Si}(111)$ surfaces, B.M. Kim, C.A. Ventrice, Jr., T. Mercer, R. Overney and L.J. Schowalter 104/105 (1996) 409
- Growth of $\text{CdF}_2/\text{CaF}_2\text{Si}(111)$ heterostructure with abrupt interfaces by using thin CaF_2 buffer layer, A. Izumi, K. Kawabata, K. Tsutsui, N.S. Sokolov, S.V. Novikov and A.Yu. Khilko 104/105 (1996) 417
- UV photoemission study of heteroepitaxial AlGaIn films grown on 6H-SiC , M.C. Benjamin, M.D. Bremser, T.W. Weeks, Jr., S.W. King, R.F. Davis and R.J. Nemanich 104/105 (1996) 455
- Photoluminescence and transmission electron microscopy investigation of SiGe quantum wires grown on patterned Si substrates, A. Hartmann, C. Dieker, U. Bangert, R. Loo, L. Vescan and H. Lüth 104/105 (1996) 502
- AFM and RHEED study of Ge islanding on $\text{Si}(111)$ and $\text{Si}(100)$, P.W. Deelman, T. Thundat and L.J. Schowalter 104/105 (1996) 510
- Site occupation of Si atoms deposited on vicinal $\text{GaAs}(001)-(2 \times 4)$ surfaces, A.R. Avery, J.L. Sudijono, T.S. Jones and B.A. Joyce 104/105 (1996) 539
- Porous silicon layers as a model system for nanostructures, U. Rossow, U. Frotscher, C. Pietryga, D.E. Aspnes and W. Richter 104/105 (1996) 552
- Influence of surface reconstruction on MBE growth of layered GaSe on $\text{Si}(111)$ substrates, H. Reqqass, J.-P. Lacharme, M. Eddrief, C.A. Sébenne, V. Le Thanh, Y.L. Zheng and J.-F. Pétroff 104/105 (1996) 557
- Heteroepitaxial growth of InSb on $\text{Si}(001)$ surface via Ge buffer layers, M. Mori, D.M. Li, M. Yamazaki, T. Tambo, H. Ueba and C. Tatsuyama 104/105 (1996) 563
- Low-energy yield spectroscopy determination of band offsets: application to the epitaxial $\text{Ge}/\text{Si}(100)$ heterostructure, L. Di Gaspare, G. Capellini, C. Chudoba, M. Sebastiani and F. Evangelisti 104/105 (1996) 595
- Measurements of the energy band offsets of $\text{Si}_{1-x}\text{Ge}_x/\text{Si}$ and $\text{Ge}_{1-y}\text{C}_y/\text{Ge}$ heterojunctions, F. Chen, M.M. Waite, S. Ismat Shah, B.A. Orner, S.S. Iyer and J. Kolodzey 104/105 (1996) 615
- Charge transfer and electronic activation at an Sb δ -layer in $\text{Si}(001)$, J.M.C. Thornton, R.J. Cole, D.J. Gravesteijn and P. Weightman 104/105 (1996) 631
- Medium energy ion scattering (MEIS) studies on $\text{Si}/\text{GaSb}/\text{Si}$ - and $\text{Si}/\text{CaF}_2/\text{Si}(111)$ layer systems, T. Tappe, A. Chatziparaskewas, J. Schäffer, J. Schlosser, J. Schmalhorst and B. Schmiedeskamp 104/105 (1996) 661

Silicon carbide

- Ab initio calculations of the reconstructed (100) surfaces of cubic silicon carbide, P. Käckell, J. Furthmüller and F. Bechstedt 104/105 (1996) 45
- Synchrotron radiation study of $\text{Cs}/\text{carbon-rich } \beta\text{-SiC}(100)$ and $\text{Cs}/\text{silicon-rich } \beta\text{-SiC}(100)$ surfaces: metallization and interface formation, F. Semond, P. Soukiassian, P.S. Mangat, Z. Hurych, L. di Cioccio and C. Jaussaud 104/105 (1996) 79
- Heterocrystalline SiC : ab initio calculations for the interface structure of combinations of cubic and hexagonal SiC , P. Käckell and F. Bechstedt 104/105 (1996) 490

Silicon oxide

- Comparison of structurally relaxed models of the $\text{Si}(001)\text{-SiO}_2$ interface based on different crystalline oxide forms, A. Pasquarello, M.S. Hybertsen and R. Car 104/105 (1996) 317
- The initial oxidation of silicon: new ion scattering results in the ultra-thin regime, E.P. Gusev, H.C. Lu, T. Gustafsson and E. Garfunkel 104/105 (1996) 329
- Local atomic structure and electrical properties of nitrided Si-SiO_2 interfaces produced by low-temperature plasma processing and rapid thermal annealing, and explained by ab-initio quantum chemistry calculations, G. Lucovsky, D.R. Lee, S.V. Hattangady, H. Niimi, S. Gandhi, C. Parker, Z. Jing, J.L. Whitten and J.R. Hauser 104/105 (1996) 335
- Effect of chemical preoxidation treatment on the structure of SiO_2/Si interfaces, H. Nohira, H. Sekikawa, M. Matsuda and T. Hattori 104/105 (1996) 359
- Studies on low temperature silicon grain growth on SiO_2 by electron cyclotron resonance chemical vapor deposition, K.C. Wang, H.L. Hwang, J.J. Loferski and T.R. Yew 104/105 (1996) 373
- Characterization of nitrided SiO_2 thin films using secondary ion mass spectrometry, M.R. Frost and C.W. Magee 104/105 (1996) 379

Silver

- Dissolution and segregation of monolayer Cu , Ni and Co atoms on the $\text{Si}(111)-\sqrt{3} \times \sqrt{3}$ - Ag surface induced by thermal annealing, J. Yuhara, R. Ishigami, D. Ishikawa and K. Morita 104/105 (1996) 163

- Metal overlayers on the MBE-grown ZnSe(001) surface, D.A. Evans, D. Wolfram, D. Gnoth, J. Cairns, A.C. Wright, M. Evans, J. Riley, D. Westwood and D.A. Woolf 104/105 (1996) 240
- Sputter deposition*
- Preparation and properties of thin polycrystalline $\text{MnSi}_{1.73}$ films, St. Teichert, R. Kilper, J. Erben, D. Franke, B. Gebhard, Th. Franke, P. Häussler, W. Henrion and H. Lange 104/105 (1996) 679
- Sulphides*
- Electronic structure of the valence band of GdS_x and Gd_3S_4 , V.A. Grazhulis, S.I. Bozhko, I.L. Bolotin, O.R. Bulanov and A.M. Ionov 104/105 (1996) 68
- Sulphur*
- A normal incidence X-ray standing wave study of sulphur adsorption on $\text{InP}(110)$, T.K. Johal, P. Finetti, V.R. Dhanak, A.W. Robinson, A. Patchett, D.R.T. Zahn and R. McGrath 104/105 (1996) 257
- Sulfur passivated $\text{InP}(100)$: surface gaps and electron counting, C.E.J. Mitchell, I.G. Hill, A.B. McLean and Z.H. Lu 104/105 (1996) 434
- Superlattices*
- $(\text{II-VI})_m/(\text{IV}_2)_n$ (110) superlattice: interfacial chemistry, electronic structure, and optical property, E.G. Wang 104/105 (1996) 626
- Tellurium*
- A surface extended X-ray absorption fine structure study of tellurium adsorbed onto $\text{Si}(100)$, S.R. Burgess, B.C.C. Cowie, S.P. Wilks, P.R. Dunstan, C.J. Dunscombe and R.H. Williams 104/105 (1996) 152
- Thin films*
- The Schottky barrier of Co on strained and unstrained $\text{Si}_x\text{Ge}_{1-x}$ alloys, J.-H. Ku and R.J. Nemanich 104/105 (1996) 262
- UV photoemission study of heteroepitaxial AlGaIn films grown on 6H-SiC , M.C. Benjamin, M.D. Bremser, T.W. Weeks, Jr., S.W. King, R.F. Davis and R.J. Nemanich 104/105 (1996) 455
- Initial stage of growth of $\text{GaN}/\text{GaAs}(001)$ in plasma-assisted molecular beam epitaxy, H. Yang, O. Brandt, A. Trampert and K.H. Ploog 104/105 (1996) 461
- Growth and characterization of ZnSe/GaAs single quantum well structures, J.L. House, D.J. Dougherty, G.S. Petrich, L.A. Kolodziejski, E.P. Ippen and G.-C. Hua 104/105 (1996) 472
- Ga-Se films grown on a $\text{GaAs}(001)$ surface at high temperature using a thermal evaporation of GaSe, T. Izumi, H. Nishiwaki, T. Tambo and C. Tatsuyama 104/105 (1996) 570
- MOCVD growth of Ga_2Se_3 on $\text{GaAs}(100)$ and $\text{GaP}(100)$: a Raman study, M. von der Emde, D.R.T. Zahn, T. Ng, N. Maung, G.H. Fan, I.B. Poole, J.O. Williams and A.C. Wright 104/105 (1996) 575
- Preparation and properties of thin polycrystalline $\text{MnSi}_{1.73}$ films, St. Teichert, R. Kilper, J. Erben, D. Franke, B. Gebhard, Th. Franke, P. Häussler, W. Henrion and H. Lange 104/105 (1996) 679
- Tin*
- $\text{Ge}(111)3 \times 1:\text{K}/\text{Sn}$; on the influence of tin substitution in a metal induced 3×1 reconstruction, M. Göthelid, S. Odasso, G. LeLay, M. Björkqvist, E. Janin, U.O. Karlsson and T.M. Grehk 104/105 (1996) 113
- The atomic structure of the $\text{Si}(111)(2\sqrt{3} \times 2\sqrt{3})\text{R}30^\circ\text{-Sn}$ reconstruction, A.H. Levermann, P.B. Howes, K.A. Edwards, H.T. Anyele, C.C. Matthai, J.E. Macdonald, R. Feidenhans'l, L. Lottermoser, L. Seehofer, G. Falkenberg and R.L. Johnson 104/105 (1996) 124
- Schottky-barrier formation at passivated surfaces: covalent and ionic semiconductors, R. Saiz-Pardo, R. Rincón, P.L. de Andrés and F. Flores 104/105 (1996) 183
- Tin oxide*
- Synchrotron radiation photoelectron spectroscopy of the $\text{O}(2s)$ core level as a tool for monitoring the reducing effects of ion bombardment on SnO_2 thin films, P. De Padova, R. Larciprete, C. Ottaviani, C. Quaresima, P. Perfetti, E. Borsella, C. Astaldi, C. Comicioli, C. Crotti, M. Matteucci, M. Zacchigna and K. Prince 104/105 (1996) 349

Titanium

- Analytical studies of nickel silicide formation through a thin Ti layer, F. Fenske, A. Schöpke, S. Schulze and B. Selle 104/105 (1996) 218

Tunneling

- Scanning tunneling spectroscopy examination of surface electronic structures of Si(111)($2\sqrt{3} \times 2\sqrt{3}$)30°-Sn surface, X.F. Lin, I. Chizhov, H.A. Mai and R.F. Willis 104/105 (1996) 223

X-ray absorption

- An ARUPS/NEXAFS study of the H₂S/InP(110) adsorbate system, E. Dudzik, A. Leslie, E. O'Toole, I.T. McGovern, A. Patchett and D.R.T. Zahn 104/105 (1996) 101
- A surface extended X-ray absorption fine structure study of tellurium adsorbed onto Si(100), S.R. Burgess, B.C.C. Cowie, S.P. Wilks, P.R. Dunstan, C.J. Dunscombe and R.H. Williams 104/105 (1996) 152

X-ray diffraction

- The atomic structure of the Si(111) ($2\sqrt{3} \times 2\sqrt{3}$)R30°-Sn reconstruction, A.H. Levermann, P.B. Howes, K.A. Edwards, H.T. Anyele, C.C. Matthai, J.E. Macdonald, R. Feidenhans'l, L. Lottermoser, L. Seehofer, G. Falkenberg and R.L. Johnson 104/105 (1996) 124
- Growth of CdF₂/CaF₂Si(111) heterostructure with abrupt interfaces by using thin CaF₂ buffer layer, A. Izumi, K. Kawabata, K. Tsutsui, N.S. Sokolov, S.V. Novikov and A.Yu. Khilko 104/105 (1996) 417
- Initial stage of growth of GaN/GaAs(001) in plasma-assisted molecular beam epitaxy, H. Yang, O. Brandt, A. Trampert and K.H. Ploog 104/105 (1996) 461
- Characterization of arsenide/phosphide heterostructure interfaces by scanning tunneling microscopy, A.Y. Lew, C.H. Yan, C.W. Tu and E.T. Yu 104/105 (1996) 522
- Heteroepitaxial growth of InSb on Si(001) surface via Ge buffer layers, M. Mori, D.M. Li, M. Yamazaki, T. Tambo, H. Ueba and C. Tatsuyama 104/105 (1996) 563
- Ga-Se films grown on a GaAs(001) surface at high temperature using a thermal evaporation of GaSe, T. Izumi, H. Nishiwaki, T. Tambo and C. Tatsuyama 104/105 (1996) 570

- Reconstruction and chemical ordering at the surface of strained (In, Ga)As epilayers, M. Sauvage-Simkin, Y. Garreau, R. Pinchaux, A. Cavanna, M.B. Véron, N. Jedrecy, J.P. Landesman and J. Nagle 104/105 (1996) 646

X-ray scattering

- Structural transformations at CaF₂/Si(111) interfaces, N.S. Sokolov, J.C. Alvarez, Yu.V. Shusterman, N.L. Yakovlev, R.M. Overney, Y. Itoh, I. Takahashi and J. Harada 104/105 (1996) 402

X-ray spectroscopy

- Segregation of In atoms at clean and hydrogen passivated InP(100) surfaces, F. Stietz, Th. Allinger, V. Polyakov, J. Woll, A. Goldmann, W. Erfurth, G.J. Lapeyre and J.A. Schaefer 104/105 (1996) 169

X-ray standing wave

- A normal incidence X-ray standing wave study of sulphur adsorption on InP(110), T.K. Johal, P. Finetti, V.R. Dhanak, A.W. Robinson, A. Patchett, D.R.T. Zahn and R. McGrath 104/105 (1996) 257

Zinc

- Growth and characterization of ZnSe/GaAs single quantum well structures, J.L. House, D.J. Dougherty, G.S. Petrich, L.A. Kolodziejski, E.P. Ippen and G.-C. Hua 104/105 (1996) 472
- Raman monitoring of selenium decapping and subsequent antimony deposition on MBE-grown ZnSe(100), D. Drews, A. Schneider, D.R.T. Zahn, D. Wolframm and D.A. Evans 104/105 (1996) 485

Zinc selenide

- Metal overlayers on the MBE-grown ZnSe(001) surface, D.A. Evans, D. Wolframm, D. Gnoth, J. Cairns, A.C. Wright, M. Evans, J. Riley, D. Westwood and D.A. Woolf 104/105 (1996) 240
- Photomodulation Raman scattering spectroscopy of ZnSe/GaAs heterostructure interface, H. Talaat, L. Elissa, S. Negm and E. Burstein 104/105 (1996) 479